

Mariyamni Awang · Berihun Mamo Negash  
Nur Asyraf Md Akhir · Luluan Almanna Lubis  
Abdul Ghani Md. Rafek *Editors*

# ICIPEG 2016

Proceedings of the International  
Conference on Integrated Petroleum  
Engineering and Geosciences

ICIPEG 2016



Mariyamni Awang · Berihun Mamo Negash  
Nur Asyraf Md Akhir · Luluan Almana Lubis  
Abdul Ghani Md. Rafek  
Editors

# ICIPEG 2016

Proceedings of the International Conference  
on Integrated Petroleum Engineering  
and Geosciences

*Editors*

Mariyamni Awang  
Faculty of Geosciences and Petroleum  
Engineering  
Universiti Teknologi PETRONAS  
Seri Iskandar, Perak  
Malaysia

Luluan Almanna Lubis  
Faculty of Geosciences and Petroleum  
Engineering  
Universiti Teknologi PETRONAS  
Seri Iskandar, Perak  
Malaysia

Berihun Mamo Negash  
Faculty of Geosciences and Petroleum  
Engineering  
Universiti Teknologi PETRONAS  
Seri Iskandar, Perak  
Malaysia

Abdul Ghani Md. Rafek  
Faculty of Geosciences and Petroleum  
Engineering  
Universiti Teknologi PETRONAS  
Seri Iskandar, Perak  
Malaysia

Nur Asyraf Md Akhir  
Faculty of Geosciences and Petroleum  
Engineering  
Universiti Teknologi PETRONAS  
Seri Iskandar, Perak  
Malaysia

ISBN 978-981-10-3649-1

ISBN 978-981-10-3650-7 (eBook)

DOI 10.1007/978-981-10-3650-7

Library of Congress Control Number: 2016963307

© Springer Nature Singapore Pte Ltd. 2017

This work is subject to copyright. All rights are reserved by the Publisher, whether the whole or part of the material is concerned, specifically the rights of translation, reprinting, reuse of illustrations, recitation, broadcasting, reproduction on microfilms or in any other physical way, and transmission or information storage and retrieval, electronic adaptation, computer software, or by similar or dissimilar methodology now known or hereafter developed.

The use of general descriptive names, registered names, trademarks, service marks, etc. in this publication does not imply, even in the absence of a specific statement, that such names are exempt from the relevant protective laws and regulations and therefore free for general use.

The publisher, the authors and the editors are safe to assume that the advice and information in this book are believed to be true and accurate at the date of publication. Neither the publisher nor the authors or the editors give a warranty, express or implied, with respect to the material contained herein or for any errors or omissions that may have been made. The publisher remains neutral with regard to jurisdictional claims in published maps and institutional affiliations.

Printed on acid-free paper

This Springer imprint is published by Springer Nature

The registered company is Springer Nature Singapore Pte Ltd.

The registered company address is: 152 Beach Road, #22-06/08 Gateway East, Singapore 189721, Singapore

*The original version of this chapter was revised: For detailed information please see Erratum. The erratum to this chapter is available at [10.1007/978-981-10-3650-7\\_71](https://doi.org/10.1007/978-981-10-3650-7_71)*

# Preface

We return with the proceedings of the 4th International Conference on Integrated Petroleum Engineering and Geosciences (ICIPEG 2016) which was one of the conferences in the World Engineering, Science and Technology Congress (ESTCON 2016). The chapters in this proceeding are double-blind peer-reviewed. The theme “Blue Ocean Strategies in E&P to Meet Global Energy Challenges” was aimed to attract papers on research that address the oil and gas industry with out-of-the-box approaches and pushing the boundaries of conventional applications. The theme also implies the need to consider current and future challenges such as low oil prices and increasingly stringent environmental limits. The subjects range from exploration, reservoir, field development, and production operation to health, safety and environment. We hope that our readers will find these proceedings beneficial, and perhaps we will meet at ICIPEG 2018. The program schedule and all information regarding the conference may be accessed from the home page <http://usite.utp.edu.my/icipeg2016/>.

Seri Iskandar, Malaysia

Mariyamni Awang  
Berihun Mamo Negash  
Nur Asyraf Md Akhir  
Luluan Almanna Lubis  
Abdul Ghani Md. Rafek

# Plenary Speakers and Reviewers

## Plenary Speakers

Prof. Roland N. Horne, School of Earth, Energy & Environmental Sciences,  
Stanford University

Prof. Joseph J. Lambiase, Chulalongkorn University, Bangkok, Thailand

Dr. Ahmad Bazlee Matzain, Amaray Pty Ltd., Australia

## Reviewers

Abdul Rafek

Ahmad Majdi Abdul-Rani

Ahmad Zuhairi Abdullah

Ahmed Mohamed Ahmed Salim

Awalludin Harun

Badrul Mohamed Jan

Christopher Lenn

Hassan Baioumy

Khaled Elraies

Lo Shyh Zung

Mariyamni Bt. Awang

M. Suhaili Ismail

Martin Brewer

Mohamad Nasir Mohamad Ibrahim

Raj Tewari

Sonny Irawan

Wan Ismail Wan Yusoff

Weng Sum Chow

Alpheus Igbokoyi

Manuel Pubellier

Septoratto Siregar

# Conference Organizing Committee

## **Chairman**

AP. Dr. Ismail B.M. Saaid

## **Co-Chairman**

AP. Dr. Abdul Hadi Abd Rahman

## **Secretary**

Muhammad Noor Amin B. Zakariah

Azeb D. Habte

Dinesh A/L Kanesan

Salina Bt Mat Nawi

Siti Nur Fatimah Bt Manap

## **Treasurer**

AP. Dr. Chow Weng Sum

Mohamad Shaufi Bin Sokiman

## **Publication**

Prof. Dr. Mariyamni Bt Awang

Berihun Mamo Negash

Nur Asyraf Bt Md Akhir

Prof. Dr. Abdul Ghani Md Rafek

Luluan Almanna Lubis

## **Technical**

AP. Dr. Eswaran Padmanabhan

AP. Dr. Syed Mohammad Mahmood

Dr. Chew Kew Hong

Dr. Muhammad Ayoub

## **Sponsorship**

Jasmi Ab Talib

Khairul Arifin Mohd Noh

Awalludin B. Harun

**IT/Multimedia**

Khairul B. Azhar  
Munirah Bt Musa

**Webmaster**

Khor Wei Chung  
Muhammad Luqman B. Hasan

**Logistic**

Dr. Mysara Eissa Mohyaldinn Elhaj  
M. Azfar Mohamed  
Amirul Qhalis B. Abu Rashid  
Jukhairi B. Selamat  
Khairunnizam B.A. Wahid  
Saiful Nizam B. Ismail  
Zuraini B. Ismail  
Shahrul Rizzal B.M. Yusof

**Food and Beverage**

Mazlin Idress  
Yasmin Bt Rosli  
Farah Bt Abdul Latif  
Nabilla Afzan Hj Abdul Aziz

**Event Management**

M. Ayyub B.M. Syayuti  
Siti Nur Fathiyah Bt Jamaludin  
M. Aslam B. Md Yusof  
Muhammad Aqram B. Shahidan  
Dr. Mohd Azuwan Maoinser  
Juhairi Aris B. Mohd Shuhli

**Promotion**

AP. Askury B. Abd Kadir  
AP. Dr. Lo, Shyh-Zung  
AProf. Wan Ismail B. Wan Yusoff  
Dr. Ahmed Mohamed Ahmed Salim  
Choong Chee Meng  
Nor Syazwani Bt Zainal Abidin  
AP. Dr. Xianhua Liu  
Dr. Abdul Haque Tunio  
Dr. Maqsood Ahmad  
Dr. Mohammed Idrees Ali  
Azif Zamir

**Public Relation**

A. Halim B. Abdul Latiff  
Dr. Sia Chee Wee

Dr. Amin Shoushtari  
Dr. Syahrir Ridha  
Dr. Shiferaw Regassa  
Dr. Mohamed Abdalla Ayoub  
Titus N. Ofei  
Nur Huda Bt Mohd Jamin

**Secretariat/Registration**

Noor Ilyana Bt Ismail  
Nur Hidayah Bt Abdul Karim  
Che Rafidah Bt Abd Aziz  
Nor Baizura Bt Mokhtar  
Shahrul Iqbal B. Shahrul Adzahar  
Noor Ashyima Bt Mohd Zainal Abidin



## Acknowledgements

We would like to express our gratitude to all who have submitted and presented their research work at ICIPEG 2016 which took place at the Kuala Lumpur Convention Centre, from 15 August 2016 to 17 August 2016. We would also like to appreciate external and internal reviewers for the tremendous efforts and dedication of their valuable resource and time while reviewing over 200 papers submitted. Moreover, we would like to extend our utmost appreciation to the three esteemed plenary speakers for delivering their respective fascinating talks in line with the theme of the conference “Blue Ocean Strategies in E&P to Meet Global Energy Challenges.” Professor Roland N. Horne from School of Earth, Energy & Environmental Sciences, Stanford University, has spoken about the application of machine learning under the title “Big Data and Machine Learning in Reservoir Analysis.” Professor Joseph J. Lambiasi from Chulalongkorn University, Thailand, has spoken on “Comprehensive Depositional and Stratigraphic Models as an Exploration Tool.” Last but not least, Dr. Ahmad Bazlee Matzain from Amaray Pty Ltd., Australia, has highlighted cutting edge flow assurance technologies under the title “Flow Assurance Technologies—Where Do They Stand?”.

# Contents

## Part I Reservoir Numerical Simulation and Characterization

<b>History Matching Using Proxy Modeling and Multiobjective Optimizations</b> . . . . .	3
B.M. Negash, Mohammed A. Ayoub, Shiferaw Regassa Jufar and Aban John Robert	
<b>New Insight in Sand and Petrophysical Properties Prediction Using Attenuation Attributes</b> . . . . .	17
M. Hermana, S.Z. Shamsuddin, C.W. Sum and D.P. Ghosh	
<b>Optimizing Injection-Perforated Layers of Lateral Continuous Shale During Secondary Recovery—A Simulation Approach</b> . . . . .	27
M.A. Ayoub, H.S. Baladram and Berihun M. Negash	
<b>Sensitivity Analysis of Sandstone Rock Elastic Properties to Effective Pressure Using a New Rock Physics Workflow and Its Application for Time-Lapse Seismic Data Analysis</b> . . . . .	45
Shahram Danaei and Deva Ghosh	
<b>Comparison of Liquid CO<sub>2</sub> Injection with a Common Tertiary Recovery Method Using Non-Isothermal Simulations</b> . . . . .	61
Zakaria Hamdi and Mariyamni Awang	
<b>A Simulation Study of Foam Generation Across Vertical Heterogeneity</b> . . . . .	71
U. Djuraev, S.R. Jufar, P. Vasant and H. Hematpour	
<b>Part II Enhanced Oil Recovery</b>	
<b>Pressure-Transient Behavior of Injection/Falloff Tests</b> . . . . .	83
A.D. Habte, M. Onur, I.B.M. Saaid and T.N. Ofei	

<b>Evaluation of Bentonite Colloids for Potential Use as an In-Depth Fluid Diversion Agent</b> . . . . .	97
Abdelazim Abbas Ahmed, Ismail Mohd Saaid and Nur Asyraf Md Akhir	
<b>Investigating Effect of Chemical Composition on Emulsion Stability and Rag Layer Growth During Separation</b> . . . . .	107
Ahmed Basyouni, Khaled A. Elraies and Hussain H. Al-Kaieym	
<b>Field-Scale Investigation of Miscible CO<sub>2</sub> Injection in a Heterogeneous Shaly Sand Reservoir</b> . . . . .	115
Ahmed Khalil Jaber, Mariyamni B. Awang and Christopher P. Lenn	
<b>A Review on the Application of Ionic Liquids for Enhanced Oil Recovery</b> . . . . .	133
Alvinda Sri Hanamertani, Rashidah M. Pilus and Sonny Irawan	
<b>Comparison Study on Anionic Surfactants and Mixed Surfactant Behavior in SAG Foam Process</b> . . . . .	149
Hamed Hematpur, Syed Mohammad Mahmood, Saeed Akbari and Negar Hadian Nasr	
<b>Potential of Fly Ash as a Foam Stabilizing Additive</b> . . . . .	157
Ishaq Ahamad, Mariyamni Awang and Mudasser Mumtaz	
<b>Optimization of Water Recycle at Steam Flood EOR Using Genetic Algorithm</b> . . . . .	167
Karina Aryanti Permatasari, Totok R. Biyanto, Sony Andriyanto, Sonny Irawan and Ridho Bayuaji	
<b>Seismic Stimulation and Induced Seismicity in Oil Reservoirs: A Review of Applications to Enhanced Oil Recovery (EOR)</b> . . . . .	183
Md. Irfan, Christopher Peter Lenn and Deva Ghosh	
<b>Controlling Gas Mobility in Water-Alternating Gas Injection by Surfactant Blend Formulations</b> . . . . .	195
Muhammad Khan Memon, Khaled Abdalla Elraies and Mohammed Idrees Al-Mossawy	
<b>A Review on CO<sub>2</sub> Foam for Mobility Control: Enhanced Oil Recovery</b> . . . . .	205
Shehzad Ahmed, Khaled Abdalla Elraies, Isa M. Tan and Mudassar Mumtaz	
<b>Palm Fatty Acid Methyl Ester in Reducing Interfacial Tension in CO<sub>2</sub>-Crude Oil Systems</b> . . . . .	217
Aminah Qayyimah Mohd Aji and Mariyamni Awang	

**Part III Unconventional Resources**

**Effect of Porosity to Methane Hydrate Formation in Quartz Sand . . . .** 231  
 Mazlin Idress, Mazuin Jasamai, Ismail M. Saaid, Bhajan Lal,  
 Behzad Partoon and Khalik M. Sabil

**Permeability Evaluation in Hydrate-Bearing Sand  
 Using Tubular Cell Setup . . . . .** 241  
 Mazuin Jasamai, Ismail M. Saaid, Mazlin Idress, Bhajan Lal,  
 Behzad Partoon and Khalik M. Sabil

**Mineralogical and Petrographic Characterization: An Indication  
 of Fractability of Shale Gas Reservoir  
 in the Blue Nile Basin, Sudan . . . . .** 251  
 Monera A. Shoieb, Nor Syazwani Zainal Abidin, Chow Weng Sum  
 and Yassir Ibrahim

**Effect of Surfactant on Wettability Change and Enhanced  
 Shale Gas Recovery . . . . .** 259  
 Muhammad Ayoub, Syed M. Mahmood, Mysara E. Mohyaldinn,  
 Shiferaw Regassa Jufar and Mudassar Mumtaz

**Part IV Advances in Geophysics and Reservoir Geoscience**

**A Diagenetic Facies Model for Characterizing Yanan Formation,  
 Ordos Basin, North Central China . . . . .** 271  
 Ahmed Mohamed Ahmed Salim, Berihun Mamo Negash  
 and Abubaker Mohamed Ahmed Alansari

**Core Lithofacies Analysis of Reservoir Interval (Albian—  
 Cenomanian) Bentiu Formation of SE Muglad Basin, Sudan . . . . .** 279  
 Ahmed Ali Hassan Taha, Abdel Hadi Abd Rahman, Wan Yusoff Wan  
 Ismail, Ahmed Mohamed Ahmed Salim and Jamal Rajab

**Geology of the Bertam Valley to Pos Betau—Focusing on  
 Geomechanical Properties of Andesite . . . . .** 295  
 Pua Ming Jia and Askury Abd Kadir

**Fractures of Gunung Ledang Granite: Insight to Post-Cretaceous  
 Structural Event . . . . .** 305  
 Choong Chee Meng, Askury Abdul Kadir,  
 Muhammad Noor Amin Zakariah, Abdul Ghani Rafek,  
 Chow Weng Sum and Nurul Syafiqah Harun

**Sedimentology of Potential Tertiary Fluvial Deposits in Kluang,  
 Johor, Malaysia . . . . .** 313  
 Choong Chee Meng, Nur Huda M. Jamin,  
 Muhammad Azfar Mohamed and Chin Soon Mun

<b>3D Reservoir Characterization of Field Deta, Termit Basin, Niger . . . .</b>	323
Eevon Chang and Lo Shyh Zung	
<b>Reservoir Characterization of Lacustrine Environment, Doba Basin, Southern Chad: Radioactive Sand Delineation . . . . .</b>	337
M.S. Nur Fathiha, S.Z. Lo and A.S. Ahmed Mohamed	
<b>Application of Seismic Imaging for Shallow Crustal Structure Delineation . . . . .</b>	351
H. Haiqal Hazreeq and M.N. Khairul Ariffin	
<b>Hydrocarbon Bond Variation in Some Shales from Batu Gajah, Malaysia . . . . .</b>	363
Syed Muhammad Ibad Mahmoodi and Eswaran Padmanabhan	
<b>Heterogeneity in Hydrocarbon and Organic Mater Distribution Patterns in the Offshore West Baram Delta, Sarawak Basin . . . . .</b>	373
J. Ben-Awuah and E. Padmanabhan	
<b>Characteristics of Pore Pressure and Effective Stress Changes in Sandstone Reservoir Through Velocity Analysis Approach Due to Hydrocarbon Production . . . . .</b>	385
Adha Kurniawan, Wan Yusoff Wan Ismail, Lubis Luluan Almanna and Mhd Hanapiah Nurhajeerah	
<b>Taking Seismic Acquisition Artifacts Beyond Mitigation. . . . .</b>	403
Mohamed Mahgoub, Deva Ghosh, Abdul Halim Abdullatif and Fernando Neves	
<b>An Innovative Low-Cost Approach for Discontinuity Roughness Quantification of Sandstone at Bukit Merah, Perak, Malaysia . . . . .</b>	413
Salimun Norsyafiqah and Abdul Rafek Ghani	
<b>Bilinear Extrapolation for Geocellular Reservoir Connectivity and Flow Simulation . . . . .</b>	421
Numair Ahmed Siddiqui, Abdul Hadi A. Rahman and Chow Weng Sum	
<b>Triaxial Compression Test Characteristics of Limestone from Gunung Lang, Malaysia . . . . .</b>	431
T.L. Goh, A.S. Serasa, A.G. Rafek, A. Abd Kadir, N. Simon, N. Surip, A. Hussin and K.E. Lee	
<b>Analysis on the Trend of Pore Pressure in Miri Area, Baram Delta . . . . .</b>	441
M.H. Nurhajeerah, W.Y. Wan Ismail, A.Z. Muhammad Noor and A. Kurniawan	

**Fracture Network Analysis of Metasedimentary Rock in East Coast Terengganu—An Analogue to Fractured Basement in Malay Basin** . . . . . 453  
 P.C. Ooi, S.N.F. Jamaludin and A.H.A. Latif

**Full Waveform Inversion: A Multiscale Approach to Tackle Gas Cloud Problem** . . . . . 469  
 Srichand Prajapati

**Feasibility Study of Various Litho-Fluid Indicators for Better Hydrocarbon Prediction in Malay and Adjacent Basin** . . . . . 481  
 Syaza Zuhaira Shamsuddin, Maman Hermana, D.P. Ghosh and Ahmed Mohamed Ahmed Salim

**Growth Timing of Southern Field High Carbonates, Central Luconia Province** . . . . . 491  
 W.K. Chung and D. Ghosh

**Seismic Wave Simulation Using a TTI Pseudo-acoustic Wave Equation** . . . . . 499  
 S.Y. Moussavi Alashloo, D. Ghosh and W.I. Wan Yusoff

**Separation of Seismic Diffraction and Reflection Using Dip Frequency Filtering** . . . . . 509  
 Yasir Bashir, Deva P. Ghosh and Chow Weng Sum

**Locating Optimum Receiver Position in Seismic Acquisition: Example from Carbonate Region** . . . . . 517  
 Abdul Halim Abdul Latiff, Zulfadhli Mohd Zaki, Siti Nur Fathiyah Jamaludin and Nurul Mu'azzah Abdul Latiff

**Seismic Waveform Classification of Reservoir Properties Using Geological Facies Through Neural Network** . . . . . 525  
 Afiqah Zahraa and Deva Ghosh

**Part V Advanced Geological Concepts in Carbonates and Sedimentary Basins**

**The Isoelectric Points of Some Selected Black Shales from the Setap Formation—Sarawak Basin** . . . . . 539  
 E.L. Fosu-Duah, E. Padmanabhan and J.A. Gámez Vintaned

**Diagenetic Process and Their Effect on Reservoir Quality in Miocene Carbonate Reservoir, Offshore, Sarawak, Malaysia** . . . . . 545  
 Hammad Tariq Janjuhah, Ahmed Mohammad Ahmed Salim, Deva Parsed Ghosh and Ali Wahid

<b>Lithostratigraphy of Paleozoic Carbonates in the Kinta Valley, Peninsular Malaysia: Analogue for Paleozoic Successions.</b> . . . . .	559
Haylay Tsegab, Chow Weng Sum and Jasmi Ab Talib	
<b>Sedimentology of the Lambir Formation (Late Miocene), Northern Sarawak, Malaysia.</b> . . . . .	569
A.R. Abdul Hadi, K. Zainey, M.S. Ismail and N. Mazshurraiezal	
<b>Sandstone Facies Reservoir Properties and 2D-Connectivity of Siliciclastic Miri Formation, Borneo.</b> . . . . .	581
Numair Ahmed Siddiqui, Abdul Hadi A. Rahman, Chow Weng Sum and Muhammad Murtaza	
<b>Review of Tectonic Evolution of Sabah, Malaysia.</b> . . . . .	597
Samira Ghaheri and Mohd Suhaili Bin Ismail	
<b>Stratigraphy and Palaeoichnology of “Black Shale” Facies: Chert Unit of the Semanggol Formation, Perak.</b> . . . . .	605
Farahana Azwa Drahman and José Antonio Gámez Vintaned	
<b>Part VI Drilling, Well Completion, Production and Operation</b>	
<b>Advanced Porosity Modeling and Lithology Analysis Based on Sonic Log and Core Data for Arkose Sandstone Reservoir: Habban Field</b> . . . . .	617
A. Al-Hasani, I.M. Saaed, A.M. Salim and H.T. Janjuhah	
<b>The Roles of Polar Compounds in the Stability and Flow Behavior of Water-in-Oil Emulsions.</b> . . . . .	643
A.A. Umar, I.M. Saaed and A.A. Sulaimon	
<b>Geomorphology and Hydrology of 2014 Kelantan Flood</b> . . . . .	655
A.R. Abdul Hadi, M.R.A. Ghani, Jasmi Talib and I. Nur Afiqah	
<b>Nano Additives in Water Based Drilling Fluid for Enhanced-Performance Fluid-Loss-Control</b> . . . . .	669
Ali Samer Muhsan, Norani M. Mohamed, Usman Siddiqui and Muhammad U. Shahid	
<b>Effect of Different Injection Rates of Biopolymer Drag-Reducing Agent (DRA) on Formation Permeability.</b> . . . . .	677
Muhammad Luqman Bin Hasan, Jagathesh Jantararas and Juhairi Aris B. Mohd Shuhli	
<b>Examination and Improvement of Salama Model for Calculation of Sand Erosion in Elbows</b> . . . . .	687
Mysara Eissa Mohyaldinn, Mokhtar Che Ismail, Muhammad Ayoub and Syed Mohammad Mahmood	

**Total Acid Number Reduction in Naphthenic Acids Using Ionic Liquid-Assisted Hot Water** ..... 697  
 P.C. Mandal, N.F.B. Salleh and D. Ruen-ngam

**Pressure Transient Behaviour of Horizontal Wells in a Bounded Reservoir with Gas Cap and Aquifer** ..... 709  
 Tsani Sabila and Azeb Habte

**Effect of Synthesized Biopolymer from Coconut Residue as Drag Reducing Agent in Water Injection Well** ..... 721  
 T.M. Alghuribi, M.S. Liew and N.A. Zawawi

**Rheological Performance of Potassium Formate Water-Based Muds for High-Temperature Wells** ..... 733  
 T.N. Ofei, R.M. Al Bendary and A.D. Habte

**A Pre-drill Computer Model for Predicting Post-drill Well Gradients** ..... 741  
 T.N. Ofei and D.J. Jorge

**A Comparison of Drilling Fluid Power for Coiled Tubing Drilling of Microholes in Hard Rock: Water Versus Supercritical CO<sub>2</sub>** ..... 755  
 Xianhua Liu, Brian Evans and Ahmed Barifcani

**Drilling Hydraulic Power Optimization in Coiled Tubing Drilling of Hard Rock** ..... 773  
 Xianhua Liu

**Optimizing Well Structures and Trajectories for Maximizing Oil Recovery** ..... 783  
 Noorfadzreena Mahmud and Xianhua Liu

**Anionic Surfactant for Enhancing the Performance of Water-Based Mud** ..... 795  
 Putri Yunita, Sonny Irawan, Dina Kania and Deni Subara

**Hydrocarbon Fire and Explosion’s Safety Aspects to Avoid Accident Escalation for Offshore Platform** ..... 801  
 Muhammad Imran, M.S. Liew, Mohammad Shakir Nasif, Usama Muhammad Niazi and Airil Yasreen

**Developing Optimum Production Strategy of Kailashtilla Gas Field and Economic Analysis** ..... 809  
 H. Mahmud, M.M. Huque and P.C. Mandal

**Erratum to: Pressure-Transient Behavior of Injection/Falloff Tests** ..... E1  
 A.D. Habte, M. Onur, I.B.M. Saaid and T.N. Ofei



**Part I**  
**Reservoir Numerical Simulation**  
**and Characterization**

# History Matching Using Proxy Modeling and Multiobjective Optimizations

**B.M. Negash, Mohammed A. Ayoub, Shiferaw Regassa Jufar and Aban John Robert**

**Abstract** Various studies have witnessed the wide application of assisted history matching for the calibration of dynamic reservoir models. Although the proposed algorithms have the potential to improve the history matching process in some synthetic cases, most of them have failed or have partially succeeded when applied to real, complex reservoirs. Thus far, identifying the most efficient optimization strategy for history matching has remained a challenging topic for research. In this paper, a sequential approach is adopted whereby a reservoir model is replaced by a proxy model, and multiobjective optimization algorithms are applied on misfit functions that were defined by the combination of the proxy models and historical data. The proposed approach was tested on a case study involving a benchmark synthetic reservoir model with 14 years of production data. The data were freely provided by Imperial College London. The effectiveness of using individual optimization algorithms was quantified by using normalized root-mean-square error. The proposed approach is found to be efficient, robust, and flexible.

**Keywords** History matching · Response surface · Design of experiment · Proxy modeling · Multiobjective optimization

## 1 Introduction

Most often, initial simulation models do not reproduce the exact behavior of reservoirs. This has a detrimental effect on prediction results and hence on reservoir management. Uncertainty in measured or inferred subsurface parameters that are utilized while building reservoir simulation models contributes to the effect. Conventionally, this problem is solved by tuning selected uncertain reservoir

---

B.M. Negash (✉) · M.A. Ayoub · S.R. Jufar · A.J. Robert  
Universiti Teknologi PETRONAS, 32610 Bandar Seri Iskandar,  
Perak Darul Ridzuan, Malaysia  
e-mail: bmamo.negash@utp.edu.my

parameters one at a time (OAT), a process referred to as manual history matching. The process is iteratively performed until an acceptable match between simulation and observation data is reached. Consequently, this trial-and-error approach is computationally expensive and highly dependent on the knowledge of the engineer involved. It is only favored for calibrating simple reservoir models but fall short in complex multidimensional reservoir problems. This study seeks to overcome this difficulty through the application of proxy modeling and multiobjective optimization algorithms for computer-assisted history matching.

This paper proposes and validates the use of response surface method (RSM), design of experiment (DOE), proxy modeling, and application of suitable optimization algorithms. A medium-sized benchmark synthetic reservoir model referred to as PUNQ-S3 reservoir model has been used to evaluate the performance of the proposed methodology. The model and its historical production data have been set as a benchmark case study and are freely provided by Imperial College London (UCL). It can be accessed in [1].

## 2 Literature Review

Reservoir engineers and research scientists have for long worked to develop viable options to calibrate complex reservoir models. Thus far, most researchers have taken advantage of recent advances in computer technology to speed up the history matching process [2]. This innovative technique has given rise to a new research area within reservoir engineering called computer-assisted history matching (AHM). There is a growing interest on the niche area of AHM, and a number of methods and results are being reported [3, 4]. Moreover, strengths and limitations are presented in a number of literatures for instance in [5]. The techniques approached history matching as an optimization problem which requires minimization of an objective function. The benefit is that multivariable sensitivity analysis and multiobjective optimization can be carried out simultaneously [6]. This eliminates one at-a-time parameter variation, thus saving time.

Assisted history matching can be approached as a direct or indirect optimization problem. Direct method is where the entire history matching job is solved by using a simulator. This involves optimizing set of uncertain parameters following subsequent simulation runs. This study investigates an indirect approach to assisted history matching. In this approach, the role of reservoir simulators is replaced by a proxy model, such as linear, nonlinear, or kriging polynomial, relating input parameters and reservoir responses. Proxy model eliminates the burden of waiting for long simulation runs and therefore permits rapid convergence of objective function [7]. Figure 1 shows the sequence of indirectly assisted history matching.

*Gu, Y. and D.S. Oliver, 2005* [8], employed the ensemble Kalman filter (EnKF) for the purpose of history matching and demonstrated its efficacy on PUNQ-S3 reservoir model. The authors approached the problem of history matching as a

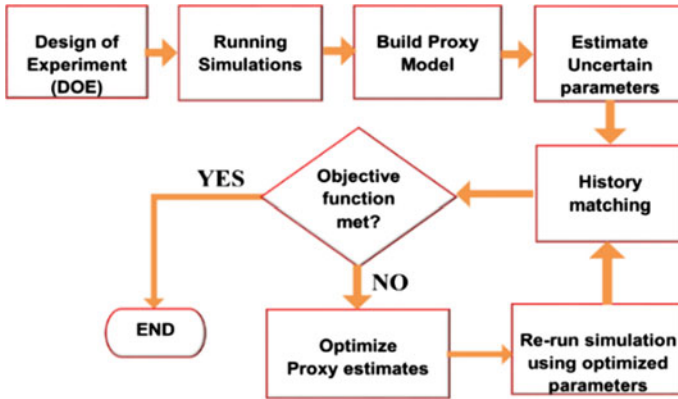


Fig. 1 Indirect assisted history matching

nonlinear state estimation problem and utilized Monte Carlo method on the ensemble of reservoir models. Currently, EnKF has a lot of publicity in the research community [4]. However, one of the key issues for EnKF is how to prevent the ensemble from collapsing and producing too narrow a probabilistic forecast. This phenomenon and some attempts to remedy it are well explained in [9]. A related issue is that each updated realization (i.e., ensemble member) is a linear combination of the initial realizations; thus, the ability of the EnKF to obtain a good estimate of the true solution is highly dependent on the quality of the initial ensemble, which needs to accurately reflect the uncertainty in the ensemble estimate, often a major challenge in real-field applications. Moreover, EnKF is a Bayesian approach. However, [5] pointed out that Bayesian approaches to history matching problem simply assume the existence of only a single minimum, which is not always the case.

Zubarev [10] have concluded that the use of proxy model as a substitute for mechanistic reservoir models is not justified and hence not recommended. However, recently, an extensive article on the application of proxy models as the next generation of uncertainty tools to history matching problem is presented by [11]. This paper strongly argues that a major pitfall of proxy modeling is that it is a “black box” model, and therefore, measuring quality is difficult. This has resulted in less popularity of the technique by practitioners. In this study, the application of proxy model together with an optimization algorithm is demonstrated using the PUNQ-S3 benchmark synthetic reservoir model.

### 3 Methodology

The methodology consists of replacing the reservoir model, which was built using physical laws, by polynomial proxy models which are functions of sensitive reservoir parameters. This is achieved through the use of DOE and RSM. A number of objective functions are then defined by combining the proxy models and historical production and pressure data. Finally, minimum objective functions were obtained using optimization algorithms. Thus, the parameter values obtained are plugged into the original reservoir model to update. The procedure can be repeated to improve the history matching process. The detail steps are as outlined in Fig. 1.

#### 3.1 Case Study

PUNQ-S3 is a synthetic reservoir model owned by Elf Exploration and Production Company. The reservoir model was constructed by a group of European Research Universities/Centers and Companies under the courtesy of the European Union [12]. It was developed purposely for Production Forecasting with Uncertainty Quantification (named, PUNQ) and has become a benchmark for researchers to test new methods for history matching. The model consists of 5 layers at a top depth of 2430 m dipping at  $1.5^\circ$  and consists of  $19 \times 28 \times 5$  grid blocks. A total of 1761 blocks are active and covers a uniform area of  $180 \times 180 \text{ m}^2$ . The top structure on the model is shown in Fig. 2. A fault strikes through the east and south of the model, while the north and west are strongly connected to a large (Carter Tracy) aquifer and bounded by a gas cap. Due to the presence of an aquifer and a gas cap

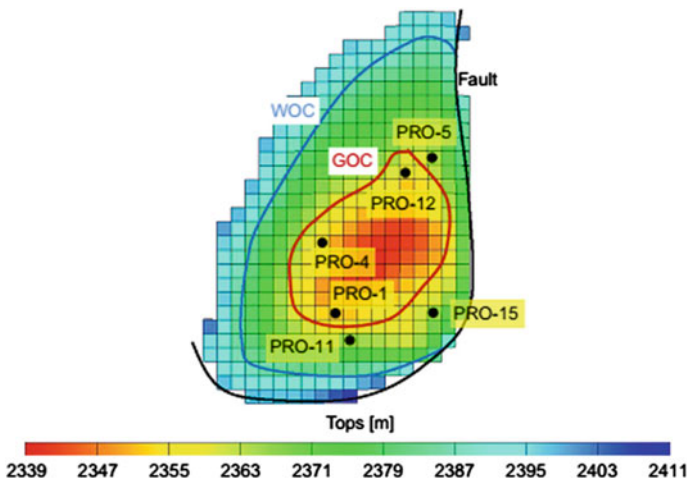


Fig. 2 Top structure of the PUNQ-S3 reservoir model

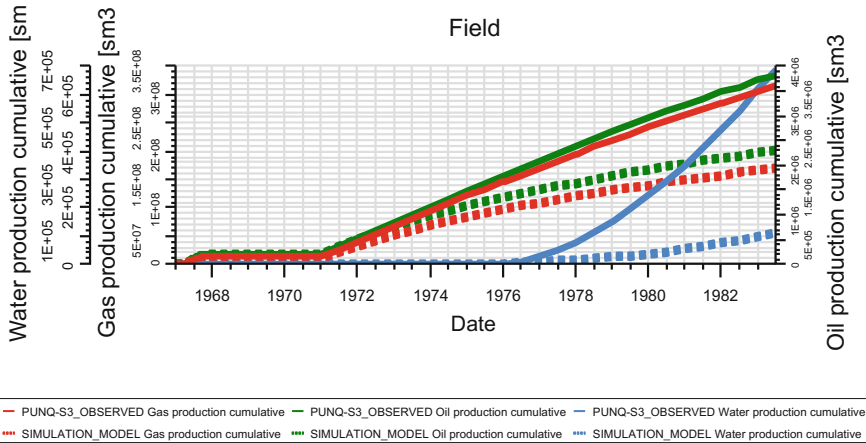


Fig. 3 Observed versus simulation model FOPT

in Layer 1, no injection wells were considered. There are six production wells in this reservoir (PRO-1, PRO-4, PRO-5, PRO-11, PRO-12, and PRO-15), and production schedule was put under well-flow constraints and constant monitoring. Wells are scheduled to flow for the first year to allow for well testing followed by build-up test for three years prior to resuming production.

When production commenced, a period of 2 weeks was needed to shut-in the well for every year of production to enable pressure data gathering for surface analysis. The uncertain parameters in this model are the porosity, permeability, and transmissibility which must be adjusted. The available historical production data include WBHP, WGOR, WWCT, FOPT, FGPT, and FWPT. These data are compared against simulation data as shown in Fig. 3 for field cumulative productions. The interest of this study is to minimize the mismatch between the observed and simulated production rates.

The proposed workflow used to evaluate history matching of the synthetic PUNQ-S3 case study is shown in Fig. 1. The flowchart shows a generalized procedure for assisted history matching in eight (8) subsequent steps.

### 3.2 Design of Experiment (DOE) and Reservoir Simulation

DOE involves generating random values of factors (input variables) by using their initial minimum and maximum ranges. The uncertain parameters in this study are the multipliers for porosity, permeability, and transmissibility as shown in Table 1. For 7 parameters, 84 experimental values were randomly generated from DOE as inputs for reservoir simulation.

**Table 1** Uncertain reservoir input variables

Factors	Low	High
A: PORO	0.68	1.0
B: MULTPERMX	0.7	1.0
C: MULTPERMY	0.7	1.0
D: MULTPERMZ	0.35	1.0
E: MULTX	0.15	1.0
F: MULTY	0.15	1.0
G: MULTZ	0.05	1.0

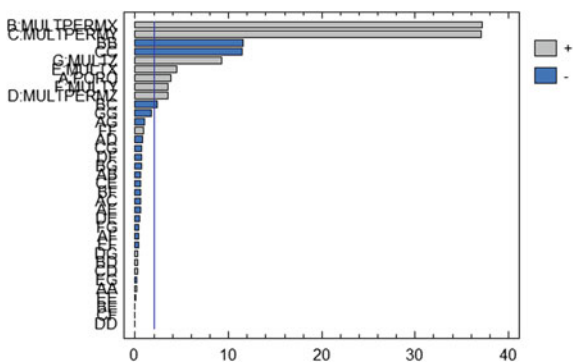
The experiments were run at different time steps for each of the six (6) wells. The 15 responses for WBHP, 15 responses for WWCT, and 15 responses for WGOR in each of the six wells were selected at specified time steps of the simulation. The simulation result was used to complete the DOE in order to fit a response surface (proxy model). In total, each well produced  $84 \times 15 \times 3 = 3780$  responses and  $3780 \times 6$  responses for all the six wells.

### 3.3 Building and Validation of Proxy Model

A multidimensional nonlinear regression proxy model that represents feasible regions of the search space was built through RSM and DOE. During DOE, the 7 input parameters interacted to produce 37 combinations of uncertain parameters over the feasible region.

Figure 4 shows an estimated effect of these parameters on well bottom-hole pressure at time step one (WBHP\_1). As observed, there is a unique influence of each parameter on WBHP\_1. Parameters in blue have a negative impact on the model as compared to those in gray. Parameters which pose less influence on the model were removed from the analysis while retaining most of the influential parameters as illustrated in Fig. 5. The proxy was validated with the retained parameters in order to improve its accuracy for further analysis.

**Fig. 4** Standardized Pareto chart for WBHP\_1 (before screening)



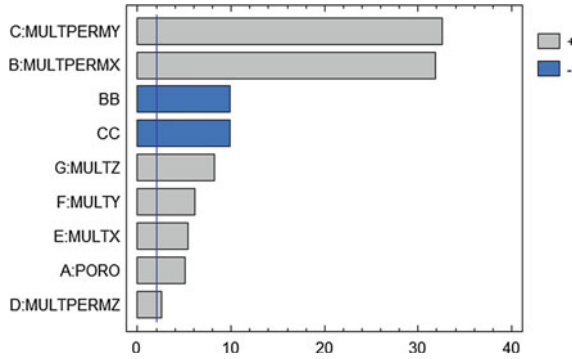


Fig. 5 Standardized Pareto chart for WBHP\_1 (after parameter screening)

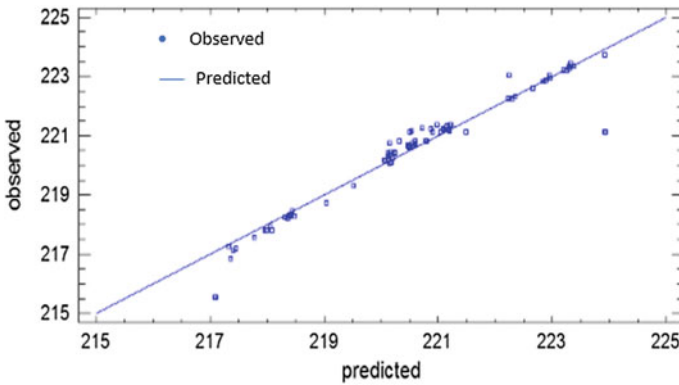


Fig. 6 Curve fitting of observed versus proxy predicted WBHP\_1

The proxy model is said to be accurate if it reproduces the same behavior trend as the simulation model. This is judged by quantifying its R-squared ( $R^2$ ) error which should be close to unity (1) as revealed by Fig. 6. Equation 1 is used to quantify this error.

$$R^2 = 1 - \frac{\sum_i (Y_{obs,i} - Y_{sim,i})^2}{\sum_i (Y_{obs,i} - Y_{obs,i})^2} \tag{1}$$



### 3.4 Objective Function

The objective function is an expression that is used to minimize the mismatch between predicted and observed responses. Different types of regression equations are used to quantify objective function and including linear least square, generalized least square, and weighted least square [13]. In this study, linear least square, shown in Eq. (2), is used to define the misfit between the proxy model and the historical production data:

$$\sum_{i=1}^N (Y_{\text{obs}} - Y_{\text{sim}})^2 \quad (2)$$

Moreover, normalized root-mean-square error (NRMSE) approach, presented in Eq. 3, has been used to validate the efficacy of the proposed approach:

$$NRMSE = \sqrt{\frac{\sum_{i=1}^N (Y_{\text{obs}} - Y_{\text{sim}})^2}{\sum_{i=1}^N (\bar{Y}_{\text{obs}} - Y_{\text{sim}})^2}} \quad (3)$$

where N is the number of experiments,  $Y_{\text{obs}}$  is the observed response,  $Y_{\text{sim}}$  is the simulation response, and  $\bar{Y}_{\text{obs}}$  is the average observed data.

With the help of the constructed proxy model, the objective function is defined prior to performing the optimization process. This enables calculation of the misfit between observed and simulated data. History matching is successful when the difference between the predicted and the observed responses has been reduced to a specified selection criterion. NRMSE (Eq. 3) as described previously is used to quantify this difference.

### 3.5 Optimization Process

The ultimate goal of optimization is determining the values of uncertain reservoir parameters that minimize the objective function to an acceptable tolerance. In this workflow, multiobjective global optimization algorithms have been applied. The idea was to compare the effectiveness of MOGA and MOGAA as tools to find the best uncertain parameters for history matching. The best algorithm is selected based on its convergence rate and minimal objective function.

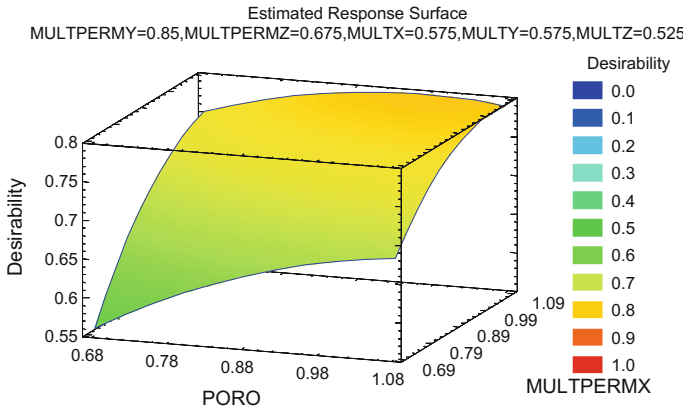


Fig. 7 Estimated response surface for multiple responses

## 4 Results and Discussion

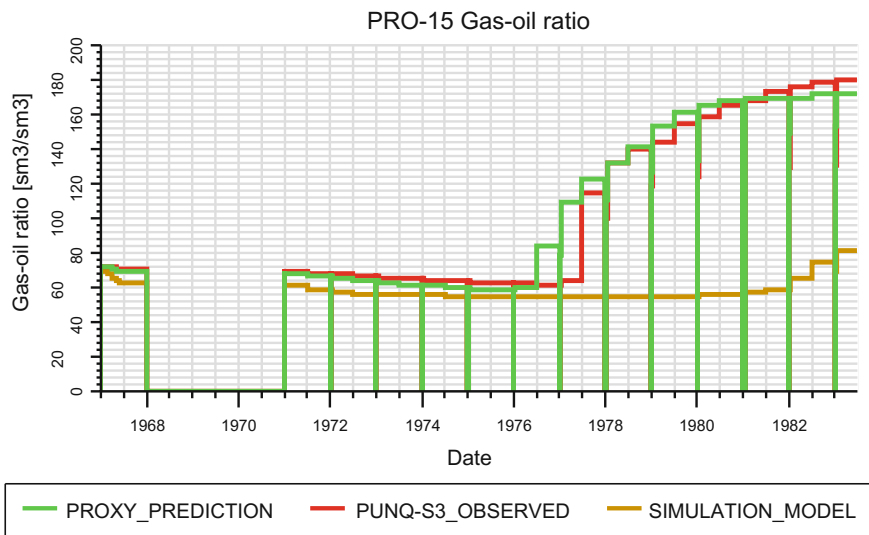
The proposed workflow for assisted history matching has been successfully applied with appreciable outcome. Response surface and design of experiment are the most critical attributes in the success of this work. As observed in Fig. 4, the influence of the 7 input parameters and their interactions on well responses was scrutinized. Through a stepwise validation process, the accuracy of the proxy model was improved to fit the simulation model. This makes it a potential driver replacing the use of reservoir simulator for global optimization of the uncertain reservoir parameters. The established proxy is cost-effective and fast, and can handle large number of uncertain parameters simultaneously. It was used to estimate the 7 uncertain reservoir parameters over a feasible region (response surface).

### 4.1 Proxy Predicted Results

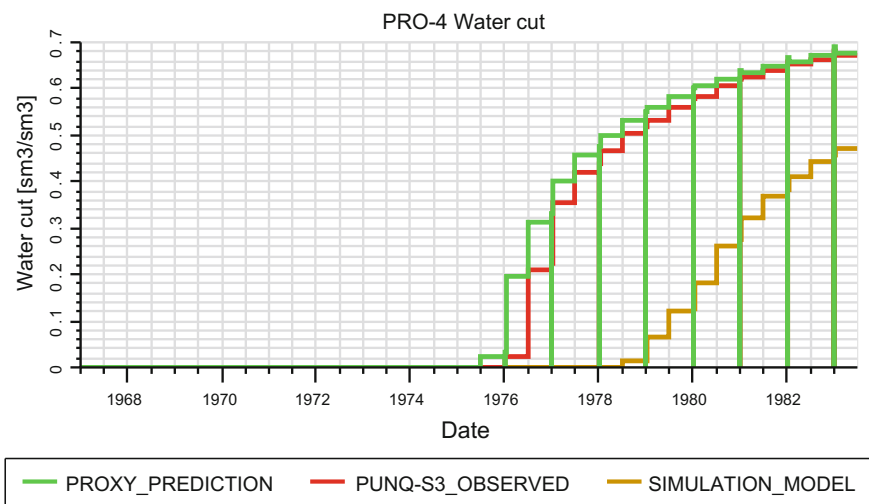
Figure 7 shows a 3D desirability plot of the overall desirability function for porosity and horizontal permeability plane where a value of 1 indicates the perfect response and 0 indicates a completely undesired value. Several values of porosity,

Table 2 optimized parameters for history matching

Factor	Simulation	Proxy model	MOGA	MOGAA
PORO	0.68	0.84	0.89	0.916
MULTPERMX	0.70	0.85	0.86	1.107
MULTPERMY	0.70	0.85	0.91	0.953
MULTPERMZ	0.35	0.675	0.72	0.890
MULTX	0.15	0.575	0.56	0.750
MULTY	0.15	0.575	0.56	1.005
MULTZ	0.05	0.525	0.92	0.774



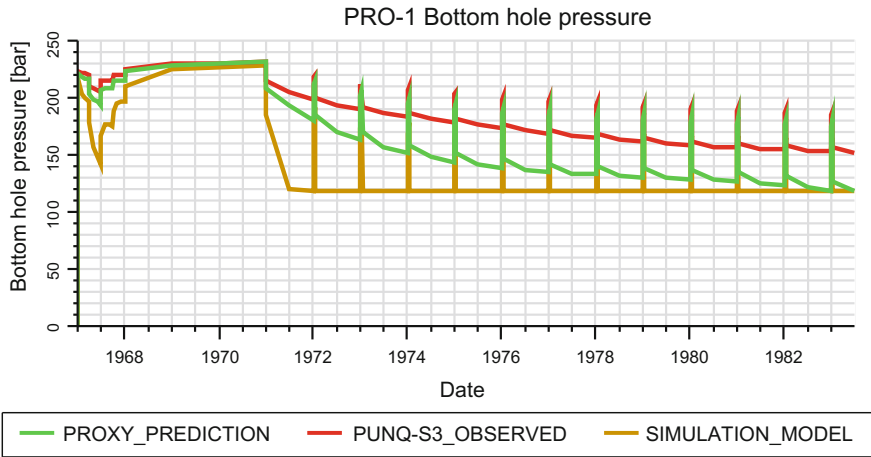
**Fig. 8** PRO-15 gas–oil ratio profile (without optimization)



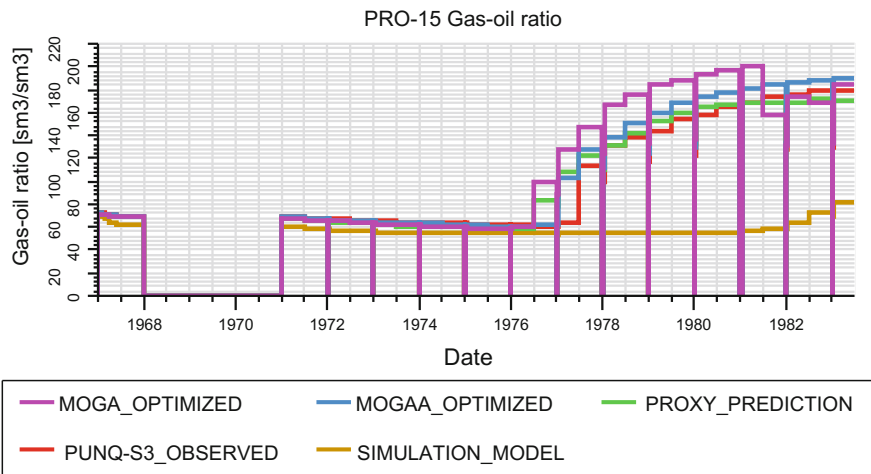
**Fig. 9** PRO-4 water-cut production profiles (without optimization)

permeability, and transmissibility multipliers were tested each time during the simulation to identify the best matching combinations.

An improved match was realized following the successive simulation runs by employing the estimated proxy parameters (Table 2) as illustrated in Figs. 8 and 9.



**Fig. 10** PRO-1 bottom-hole pressure profile (without optimization)



**Fig. 11** Optimized PRO-15 gas–oil ratio profile

However, NRMSE % calculation revealed a significant mismatch in WBHP (Fig. 10). A different approach was used to minimize this error by using reliable optimization strategies as discussed in case 2.

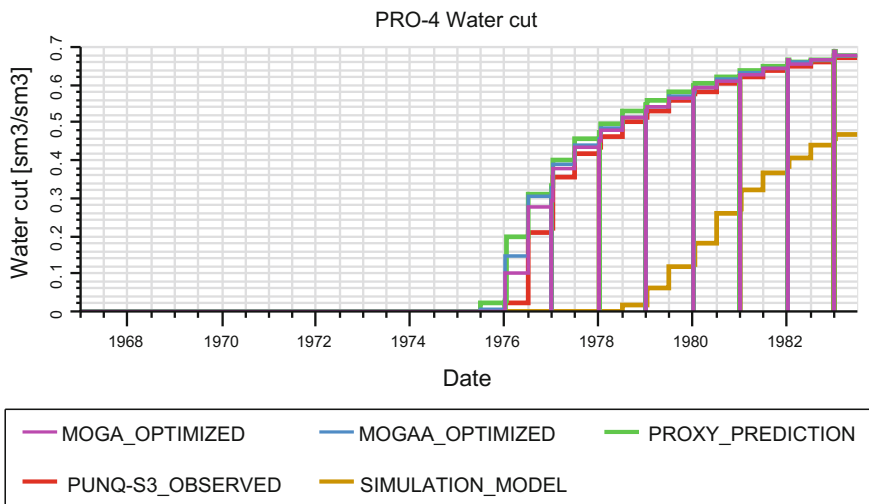


Fig. 12 Optimized PRO-4 water-cut profile

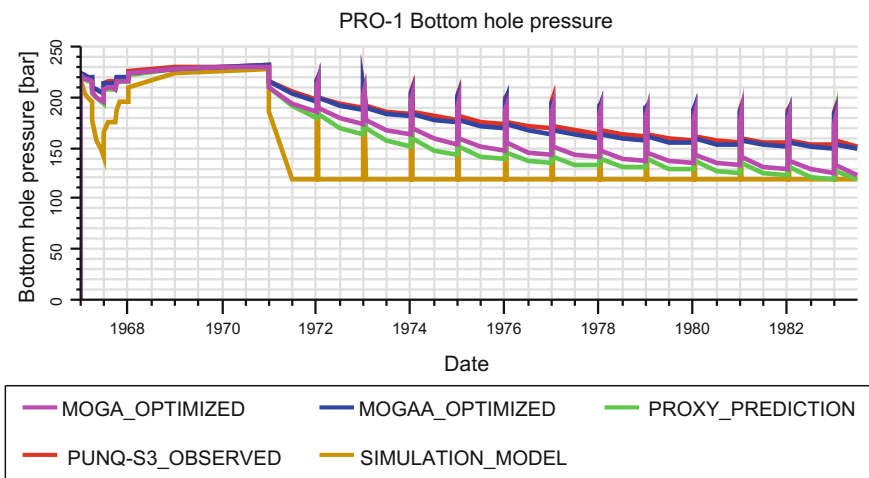


Fig. 13 Optimized PRO-1 bottom-hole pressure profiles

Table 3 Error quantification for FOPT

Period	Response type	Before history matching	Proxy prediction	MOGA prediction	MOGAA prediction
History	FOPT	54.83	0.06	0.017	0.00019
	FGPT	35.48	3.40	2.45	1.45
	FWPT	156.28	5.63	4.67	4.40
Forecast	FOPT	336.29	61.87	51.91	11.19
	FGPT	367.80	60.60	23.89	16.22
	FWPT	196.87	43.86	36.68	23.37

## 4.2 Optimization of the Proxy Models Using Goal Attainment and Genetic Multiobjective Algorithms

In the second case, the estimated proxy parameters in case 1 were optimized using multiobjective genetic algorithm (MOGA) and multiobjective genetic goal attainment algorithm (MOGAA). Interestingly, application of the two algorithms provided a satisfactory history matching for all the well responses (WBHP, WWCT, and WGOR) as shown in Figs. 11, 12, and 13. Specifically, MOGAA resulted in a 0.0019% NRMSE which is much better when compared with MOGAA which is resulted in a NRMSE of 0.016%. Errors resulting from the application of either proxy model, MOGA, or MOGAA were quantified using the defined NRMSE and compared to the error before history matching as shown in Table 3. It is observed that the error diminishes drastically with the introduction of optimization algorithms.

## 5 Conclusion

An integrated workflow for history matching using computer-aided techniques has been demonstrated. The importance of proxy modeling for sensitivity analysis and its potential to improve history matching has been illustrated. It is proven that the use of proxy model for predicting uncertain reservoir parameters is faster and more convenient than the traditional one that varies one at-a-time approach. The introduction of MOGA and MOGAA in the workflow provides a significant improvement in the history matching results. It is hoped that the developed approach can be applicable for real-field case studies and related optimization problems.

**Acknowledgements** The authors would like to thank Elf Exploration Company and Imperial College of Earth Sciences and Engineering for making PUNQ-S3 model dataset available online. The authors also thank Universiti Teknologi PETRONAS for providing access to the commercial software required to complete the work.

## References

1. Imperial college London, D.o.E.S. <https://www.imperial.ac.uk/engineering/departments/earth-science/research/research-groups/perm/standard-models/eclipse-dataset/>. 2015/09/10].
2. Wu, X.-H., L. Bi, and S. Kalla, Effective parametrization for reliable reservoir performance predictions. *International Journal for Uncertainty Quantification*, 2012. **2**(3).
3. Oliver, D.S. and Y. Chen, Recent progress on reservoir history matching: a review. *Computational Geosciences*, 2011. **15**(1): p. 185–221.
4. Rwechungura, R.W., M. Dadashpour, and J. Kleppe. Advanced History Matching Techniques Reviewed. in *SPE Middle East Oil and Gas Show and Conference*. 2011: Society of Petroleum Engineers.
5. Tavassoli, Z., J.N. Carter, and P.R. King, Errors in History Matching.

6. Verga, F., M. Cancelliere, and D. Viberti, Improved application of assisted history matching techniques. *Journal of Petroleum Science and Engineering*, 2013. **109**: p. 327–347.
7. Arief, I.H., Computer assisted history matching: A comprehensive study of methodology. 2013.
8. Gu, Y. and D.S. Oliver, History matching of the PUNQ-S3 reservoir model using the ensemble Kalman filter. *SPE journal*, 2005. **10**(02): p. 217–224.
9. Yang, X. and T. DelSole, The diffuse ensemble filter. *Nonlinear Processes in Geophysics*, 2009. **16**(4): p. 475–486.
10. Zubarev, D.I. Pros and cons of applying proxy-models as a substitute for full reservoir simulations. in *SPE Annual Technical Conference and Exhibition*. 2009: Society of Petroleum Engineers.
11. Goodwin, N., Bridging the Gap Between Deterministic and Probabilistic Uncertainty Quantification Using Advanced Proxy Based Methods, Society of Petroleum Engineers.
12. Dehghan Monfared, A., et al., A Global Optimization Technique Using Gradient Information for History Matching. *Energy Sources, Part A: Recovery, Utilization, and Environmental Effects*, 2014. **36**(13): p. 1414–1428.
13. Sisman, Y. and S. Bektas, Linear regression methods according to objective functions. *ACTA MONTANISTICA SLOVACA*, 2012. **17**(3): p. 209–217.

# New Insight in Sand and Petrophysical Properties Prediction Using Attenuation Attributes

M. Hermana, S.Z. Shamsuddin, C.W. Sum and D.P. Ghosh

**Abstract** Sand body and its petrophysical properties prediction such as porosity, net-to-gross, and water saturation are essential task in reservoir characterization. In common technology, those properties are estimated based on elastic inversion result. However, because of non-unique problem in the lithology and fluid, the prediction of sand body and other petrophysical properties are still not optimized. This paper discusses a new approach in sand and petrophysical properties prediction based on “scaled quality factor” of  $SQ_p$  and  $SQ_s$  attributes which is derived from attenuation attribute through rock physics approximation. The discussion included the testing of  $SQ_p$  and  $SQ_s$  attributes on model and well log data and application of these attributes for petrophysical properties prediction by using probabilistic neural network technology. The results show that  $SQ_p$  and  $SQ_s$  attributes work properly on unconsolidated rock and the Marmousi model; the lithological effect can be distinguished effectively. All hydrocarbon sands in the Marmousi model are able to be captured by  $SQ_s$  attribute and were distinguished from wet sand. By testing on well logs, the response of  $SQ_p$  is similar with gamma ray logs which indicate the lithology. Meanwhile,  $SQ_s$  attribute is similar with resistivity log which indicates fluid. Combination of those two attributes as input for probability neural network engine is able to improve petrophysical properties prediction such as volume of shale, porosity, and water saturation. Application of this approach on Malaysian offshore data showed that sand reservoir is identified accurately as low volume of shale, good porosity, and water saturation and it was confirmed with well data on the area.

**Keywords** Attenuation · Elastic properties · Rock physics · Petrophysical

---

M. Hermana (✉) · S.Z. Shamsuddin · C.W. Sum · D.P. Ghosh  
Department of Geosciences, Universiti Teknologi PETRONAS,  
32610 Seriiskandar, Perak Darul Ridzuan, Malaysia  
e-mail: mherjody@yahoo.com

© Springer Nature Singapore Pte Ltd. 2017  
M. Awang et al. (eds.), *ICIPEG 2016*,  
DOI 10.1007/978-981-10-3650-7\_2



## 1 Introduction

Seismic method has been applied widely in the oil and gas industry for lithology and pore fluid and also petrophysical properties prediction. However, the current technology is still based on the interpretation of seismic amplitude such as direct hydrocarbon indicator (DHI) as bright spots and elastic properties derived from compressibility and density of the rock matrix and pore fluid. Other techniques include the use of elastic parameters which are extracted from amplitude versus offset (AVO) attribute [1], elastic impedance (EI) as a result of AVO rotation technique [2], acoustic impedance (AI) or  $P$ -impedance, shear impedance ( $S$ -impedance), the ratio of  $P$ -velocity and  $S$ -velocity ( $V_p/V_s$ ), and density as a result of simultaneous inversion. The successful implementations of these methods for reservoir characterization have been reported. Nevertheless, the ambiguity in lithology and pore fluid determination also contributed to the limitation of this method. Hence, the prediction of sand body and characterization of the reservoir including petrophysical properties prediction based on seismic amplitude are still not optimized.

The main objective of this work is to solve the problem mentioned above and to improve the petrophysical properties prediction based on new approach by using neural network technique. In order to improve the prediction results, we have developed new attributes which are called as  $SQ_p$  and  $SQ_s$  attributes, and then, those attributes are used as input for neural network engine. As example of this approach, a data set from Malaysian offshore has been used with success.

## 2 Attenuation Attribute

During the propagation, the seismic wave cannot be isolated from attenuation. The attenuation mechanism will suffer from the amplitude, frequency, and phase of seismic data. The degree of attenuation depends on many factors; however, the intrinsic attenuation of the medium is a main contributor.

In rock physics view, the incoming seismic wave in a medium encourages the unbounded fluid in the pore to vibrate around the equilibrium position. This vibration produces a new wave field that opposes the incoming wave. As consequences, some energy of incoming wave will be transformed into heat due to the effect of damping. The initial energy of incoming wave will be attenuated. The degree of vibration is depending on the frame of rock, pore, and number and type of fluid inside pore. Therefore, the attenuation can be correlated with the rock physics and petrophysical properties of the medium.

Mavko [3] related the attenuation in term of quality factor ( $Q$ ) with the basic elastic properties: bulk modulus ( $M$ ) and shear modulus ( $G$ ). The maximum quality factor of  $P$  ( $Q^p$ ) or  $S$ -wave ( $Q_s$ ) can be estimated by using Kramers–Kronig relation:

$$\begin{aligned} 2Q_p^{-1} &= \frac{M_\infty - M_0}{\sqrt{M_0 M_\infty}} \\ 2Q_s^{-1} &= \frac{G_\infty - G_0}{\sqrt{G_0 G_\infty}} \end{aligned} \quad (1)$$

By assuming the  $M = \sqrt{M_0 M_\infty}$  and  $G = \sqrt{G_0 G_\infty}$  as average of properties at low- and high-frequency condition, and adopting the Hudson crack theory, Mavko formulated the  $Q_p$  and  $Q_s$  for a weak anisotropy as [3]:

$$\begin{aligned} Q_p^{-1} &= \frac{2}{3} \varepsilon \frac{(M/G - 2)^2}{(M/G - 1)} \\ Q_s^{-1} &= \frac{8}{3} \varepsilon \frac{(M/G)}{(3M/G - 2)} \end{aligned} \quad (2)$$

where  $\varepsilon$  is a crack density that can be correlated with aspect ratio and secondary porosity. These parameters are still difficult to be extracted directly from seismic. For this reason, we used the aspect ratio for sand is 0.1 [4] as reference and we do an approximation on secondary porosity from density. The Eq. (2) now becomes:

$$\begin{aligned} SQ_p &\equiv \frac{5}{6} \frac{1}{\rho} \frac{(M/G - 2)^2}{(M/G - 1)} \\ SQ_s &\equiv \frac{10}{3} \frac{1}{\rho} \frac{(M/G)}{(3M/G - 2)} \end{aligned} \quad (3)$$

where  $SQ_p$  and  $SQ_s$  are defined as scaled quality factor of  $P$  and  $S$ -wave, respectively;  $\rho$  is density; and  $M/G$  is approximated with  $(V_p/V_s)$ . With this formulation, now all the parameters can be calculated from basic elastic properties.

### 3 Methodology

To test the effectiveness of  $SQ_p$  and  $SQ_s$  attributes, a series of tests has been done. The first test was performed on rock physics model, the soft sediment model which consists of shale and sand with various porosity and water saturation. The effectiveness of these attributes is indicated by the optimum separation between shale background with gas saturated sand. The crossplot between conventional method and new attribute are provided to show the performance of those attributes in discriminating effect of lithology and fluid. The next test is by applying  $SQ_s$  attribute on the Marmousi model which has complexity in structure and geology. This model consists of sand shale lamination with different fluid types (water, oil, and gas). The final test is the implementation of  $SQ_p$  and  $SQ_s$  attributes on well log

data. A well log data from Malaysian offshore was utilized. The effectiveness of these attributes is compared with gamma ray as lithology indicator and resistivity log as fluid indicator.

In the next stage, the  $SQp$  and  $SQs$  attributes are applied for petrophysical properties prediction by using probabilistic neural network (PNN). The  $SQp$ ,  $SQs$ , and its ratio were used as input for this engine in porosity, volume of shale, and water saturation prediction. Two wells are used in the training stage, and another well is used for justification and crossvalidation. Multi-attribute analysis was performed to have the best prediction results. After the training stage is validated, the training data sets are used to predict the 3D cubic of water saturation, volume of shale, and porosity from 3D cube of  $SQp$ ,  $SQs$ , and its ratio. Those attributes are derived from elastic inversion result of Malaysian offshore. The inversion was performed by using a set of partial-stack seismic data with constrained sparse spike inversion method to produce P-velocity, S-wave, and density where the attributes are calculated from.

## 4 Results and Discussion

### 4.1 Attributes Test on Model

There are two models used in the testing of  $SQp$  and  $SQs$  attributes: rock physics model with unconsolidated rock model which is used to observe more details on how new attributes are able to separate the lithology and pore fluid and 2D Marmousi model which consists of different lithology and fluid.

The unconsolidated rock/soft sediment model consists of shale with various porosity ranging from 1 to 40% and sand with various porosity and water saturation (porosity ranges from 10 to 40%, while the water saturation ranges from 0 to 100% of gas). The responses of  $SQp$  and  $SQs$  are described in the crossplot and compared with industry method,  $Vp/Vs$ -AI. The results showed that shale can be distinguished from sand with various porosity and water saturation. Shale is distributed in vertical axis, while sand with various water saturations is distributed along horizontal axis. The separations among them are almost orthogonal (Fig. 1b).

For the comparison, Fig. 1a showed a crossplot in the  $Vp/Vs$ -AI domain, where the gas sand is figured out far away from shale back ground line. In this case, both conventional method and new attribute still can easily identify the lithology and pore fill. Fortunately, the  $SQp$ - $SQs$  crossplot gives us more orthogonal separation which is telling us that the lithology can be distinguished optimally from fluid effect.

In geological model of 2D Marmousi model, the  $SQs$  attribute gives a significant improvement on hydrocarbon sand delineation. Figure 2 shows the  $SQs$  section

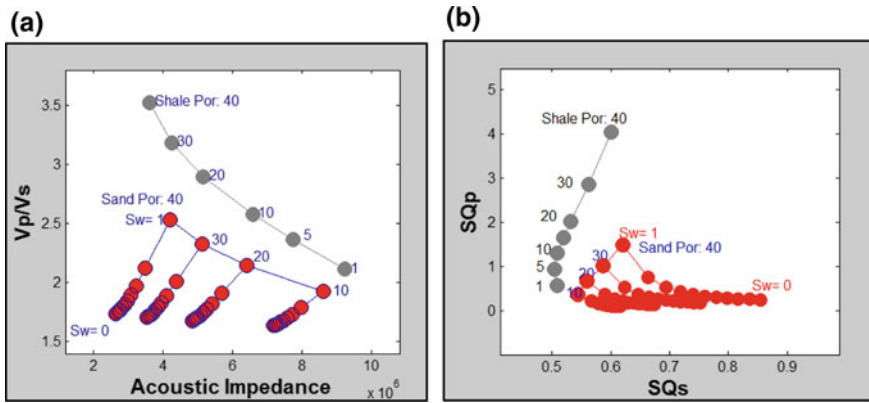


Fig. 1 a Shale–sand model in VpVs—AI crossplot, and b the  $SQp$ – $SQs$  crossplot

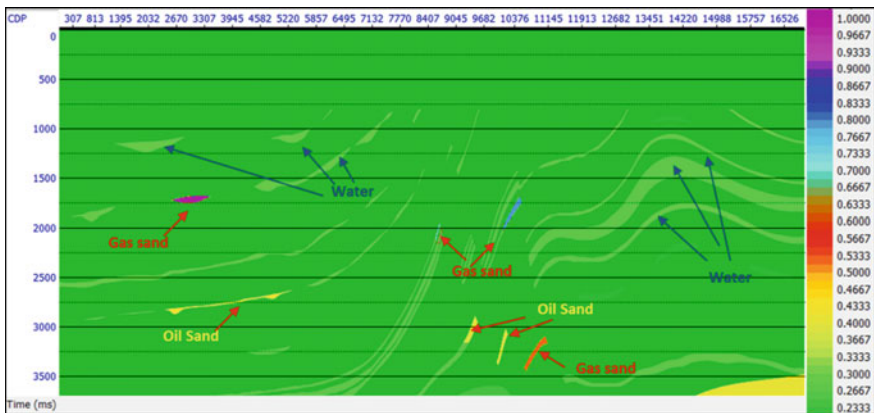


Fig. 2  $SQs$  attribute responses on Marmousi model

derived from Marmousi model. In these results, all hydrocarbon sand is highlighted and it was distinguished from wet sand and shale background. This results show that the  $SQs$  attribute can effectively be used for hydrocarbon sand body prediction.

### 4.2 Well Log Responses

The tests of  $SQp$ – $SQs$  attribute on well logs are performed on Malaysian offshore data. The results showed that the response of  $SQp$  attribute is similar with gamma

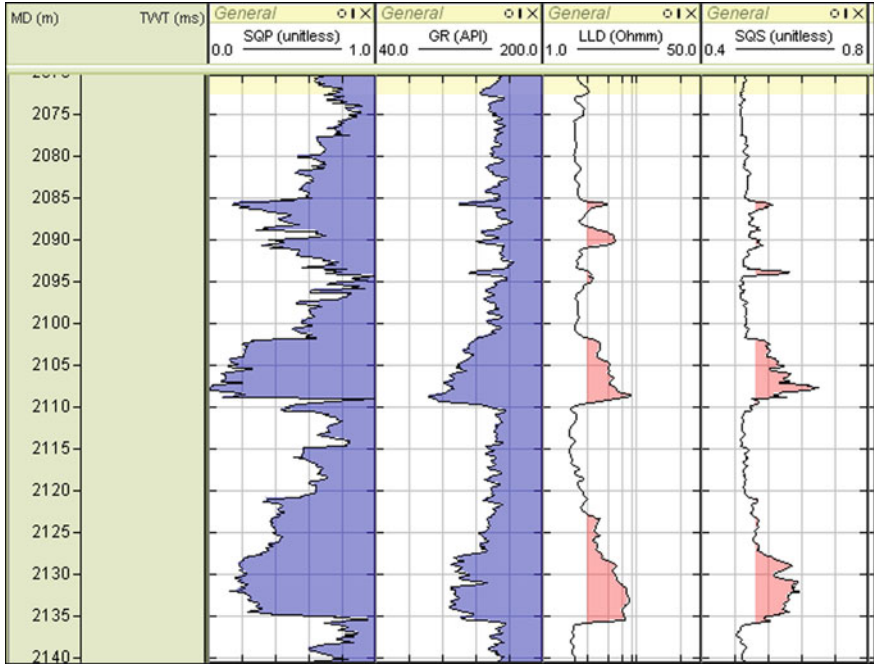


Fig. 3 *SQp* and *SQs* attribute responses compared with gamma ray and resistivity logs

ray logs, while the *SQs* attributes are similar with resistivity log (Fig. 3). All sand formations are shown as low gamma ray is figured also as low *SQp*. Shale with high gamma ray also is shown as high *SQp*. The coefficient correlation between gamma ray and *SQp* logs is more than 0.8 which shows that the *SQp* attribute also can be used as lithology indicator. In *SQs* log, all hydrocarbon sand formation that showed high resistivity also showed high *SQs*. Not only hydrocarbon, but coal also appears similarly. Coal has very high *SQs*, and it appears as a spike in resistivity log. This results show that the *SQs* attribute also can be used as an affective fluid indicator like resistivity. The coefficient correlation between *SQs* and resistivity logs is more than 0.85.

In another example, we applied this attribute on fractured basement reservoir. The *SQp* attribute was compared with the fracture density/porosity log. The results showed that the *SQp* log has similar response as fracture density logs and brittleness log (E). High fracture density region was associated with high *SQp*, and this result showed that this attribute is sensitive with the lithology and petrophysical properties. The *SQs* attribute response showed that high *SQs* is also associated with the “butterfly” pattern of neutron and density plot (Fig. 4).

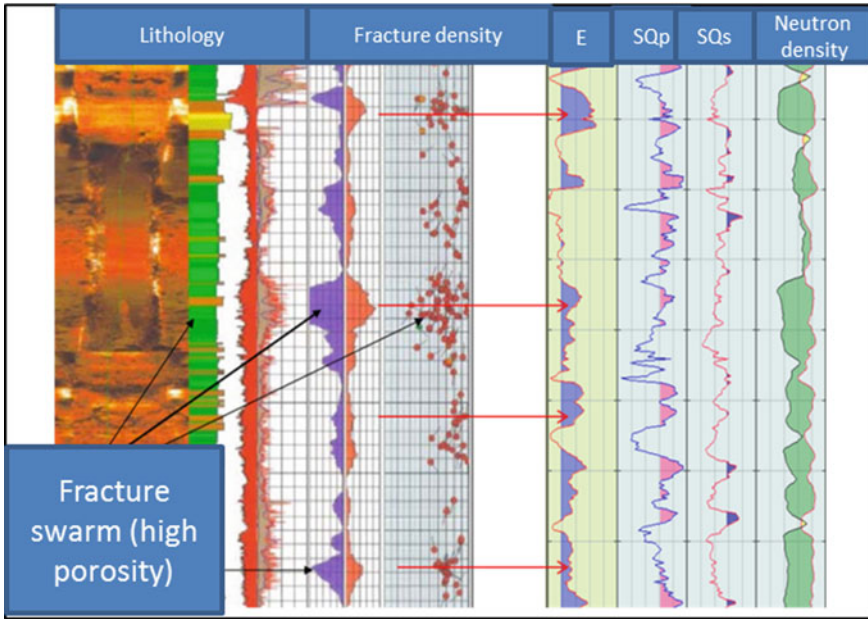
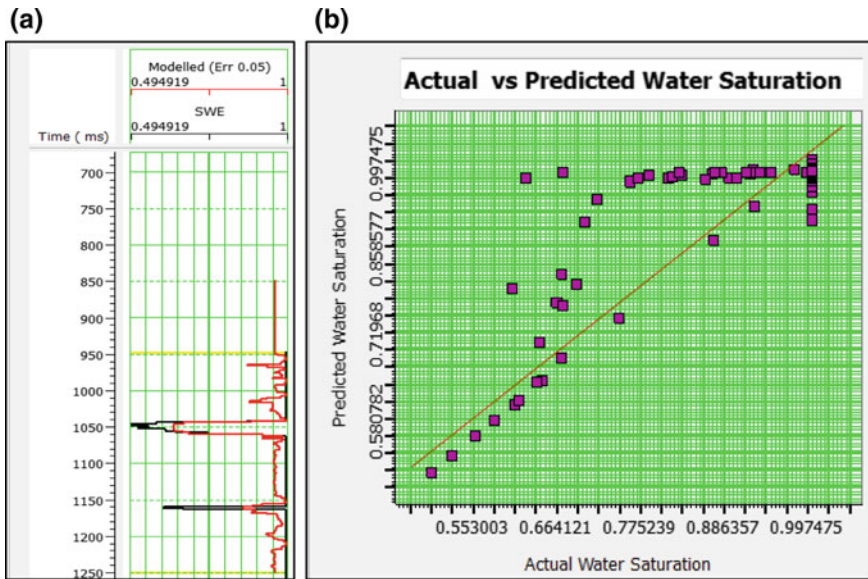


Fig. 4  $SQp$  and  $SQs$  attribute on fractured basement reservoir

### 4.3 Application of $SQp$ and $SQs$ Attributes for Petrophysical Properties Prediction

Workflow for  $SQp$  and  $SQs$  attribute derivation has been applied on a real data set from Malaysian offshore. The 3D data available for analysis are near-angle stack approximately  $5-15^\circ$ , mid-angle stack approximately from  $15$  to  $25^\circ$ , and far-angle stack approximately  $25-40^\circ$  with the time sampling  $4$  ms. In general, the quality of these 3D seismic data is good. The lateral continuity and fault discontinuity are clear. The dominant frequency is around  $35-40$  Hz at major reservoir zones. Hydrocarbon sand was discovered in the A and B reservoir formations; at this horizon, the interval velocity is about  $3400$  m/s; hence, the tuning thickness around this formation is about  $12$  m. From well data, the net thickness of hydrocarbon sand was identified at  $18-28$  m. As a consequence, the top and bottom of the reservoir can be tracked clearly. The main reservoir (reservoir A) is identified as strong amplitude (bright spot) in the seismic data.

The main target of this analysis is to estimate the petrophysical properties, i.e., porosity, volume of shale, and water saturation, in 3D from attenuation attribute:  $SQp$  and  $SQs$ . The  $SQp$  attribute,  $SQs$  attribute, and its ratio derived from well log data are used as an input for the training probabilistic neural network (PNN) engine.



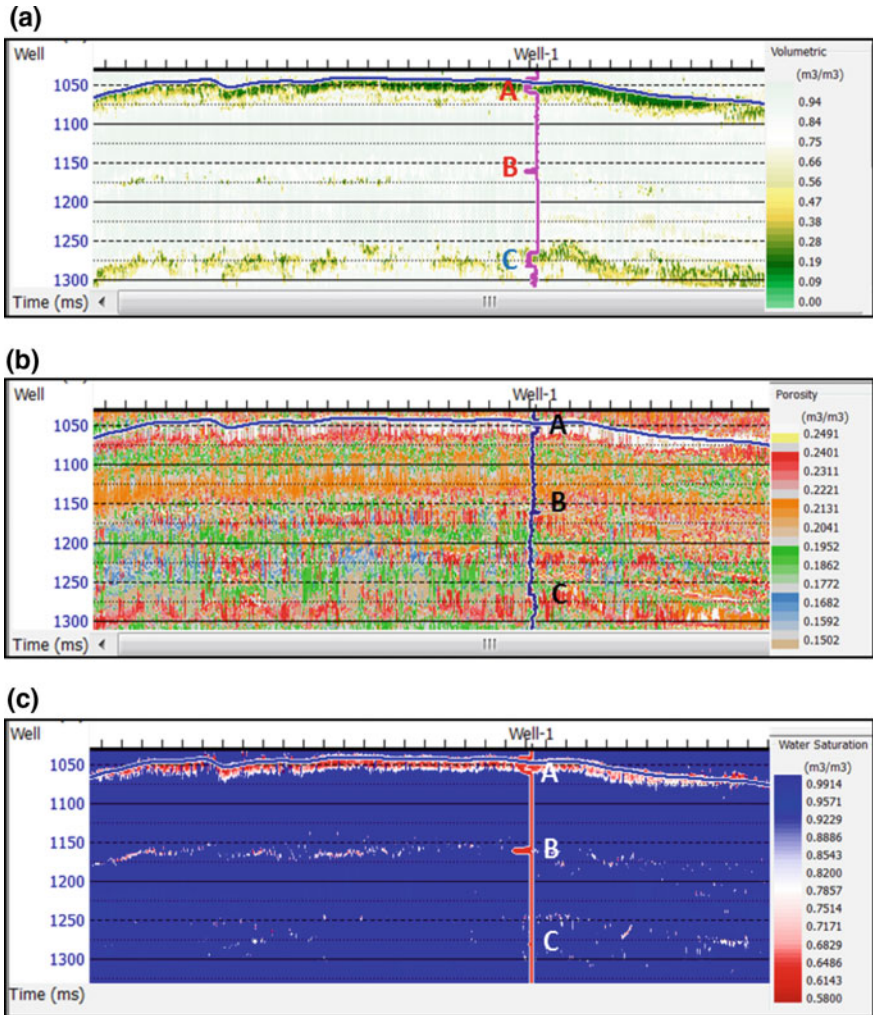
**Fig. 5** **a** Predicted and actual water saturation logs and **b** crossplot between predicted and actual water saturation

The number of internal attributes that effects on the prediction is determined during multi-attribute analysis. The results are shown in Fig. 5. Figure 5a shows the estimated and predicted water saturation in the training well. The actual data are represented with back color, while predicted is red color coded. After validation step, the correlation between actual and predicted volume of shale is shown in Fig. 5b. The coefficient correlation is more than 0.95.

After validation and the results are satisfied, the training data sets are used to estimate 3D petrophysical properties. The inputs are 3D cubes of  $SQp$ ,  $SQs$ , and its ratio. The predicted petrophysical properties, volume of shale, porosity, and water saturation section, are demonstrated in Fig. 6.

Figure 6 shows a cross section of petrophysical properties: water saturation, volume of shale, and porosity with respected inserted curve. The sand formations which consist of A (gas sand), B (gas sand), and C (wet sand) formations are recognized as low area in the estimated volume of shale section. These formations have been confirmed with well logs (Fig. 6a). The main gas sand reservoir which is represented by A and B formations has estimated water saturation about 60% and porosity about 20–30%. All those properties matched with log of the blind well.





**Fig. 6** Predicted petrophysical properties: **a** volume of shale section with  $V_{shale}$  log inserted, **b** porosity section with porosity log inserted, and **c** water saturation section with water saturation log inserted

## 5 Conclusion

The  $SQ_p$  and  $SQ_s$  attributes derived from attenuation–rock physics approximation are potential to be used for sand and fluid indicator, respectively. The tests that have been conducted showed that the  $SQ_p$  has similar response with gamma ray and it is sensitive with lithology changes, while  $SQ_s$  attribute has similar response as resistivity which is sensitive with fluid content.



Application of new approach for petrophysical properties prediction on Malaysian offshore showed that these attributes can be used as an effective input for probabilistic neural network engine which is able to improve the accuracy on prediction.

## References

1. P. M. Gidlow, G. C. Smith, and P. Vail, "Hydrocarbon Detection Using Fluid Factor Traces: A Case Study," *Geophys. Prospect.*, vol. 35, pp. 993–1014, 1987.
2. D. N. Whitcombe, "Short Note Elastic impedance normalization," vol. 67, no. 1, pp. 60–62, 2002.
3. G. Mavko, T. Mukerji, and J. P. Dvorkin, *The Rock Physics Handbook*. 2009.
4. L. Zhao, D. Han, Q. Yao, F. Yan, U. Houston, M. Nasser, and M. Oil, "Modeling the effect of pore and crack interactions on the effective elastic properties of fractured porous rocks," *SEG Houst. 2013 Annu. Meet.*, pp. 2900–2904, 2013.

# Optimizing Injection-Perforated Layers of Lateral Continuous Shale During Secondary Recovery—A Simulation Approach

M.A. Ayoub, H.S. Baladram and Berihun M. Negash

**Abstract** Shale studies are essential for the optimization of the reservoir performance as its presence can significantly reduce the oil reserves. Contingent on the degree of communication, reservoir dynamics can vary considerably, leading to several key issues including well completion and perforation strategy and enhanced recovery program. The principal aim of this study is to investigate the optimum location to inject water in waterflooding scheme or gas for an immiscible water-alternating gas (WAG) scheme in the presence of lateral extension of continuous shale in the reservoir. A sensitivity analysis of the optimum injection place is conducted with respect to various locations of the shale orientation. The objectives of this project include studying the trend of the vertical distribution of lateral shale and its effect on the recovery factor, conducting a comparative study between the performance of two flooding techniques; waterflooding and immiscible water-alternating gas (WAG) injection and to further optimize the resulting best cases of injection-perforated intervals. The simulation work of this project was carried out using Schlumberger Eclipse 100 simulator.

**Keywords** Lateral shale · Waterflooding · Water-alternating gas

---

M.A. Ayoub (✉) · H.S. Baladram · B.M. Negash  
Petroleum Engineering Department, Universiti Teknologi PETRONAS,  
Perak 32610, Malaysia  
e-mail: Abdalla.ayoub@petronas.com.my

H.S. Baladram  
e-mail: haifa.b.ily@gmail.com

B.M. Negash  
e-mail: Abdalla.ayoub@petronas.com.my

## 1 Introduction

The majority of heterogeneous reservoirs usually contain shaly segments. Shale is considered to be one of the most abundant sedimentary rocks found on the earth's crust. It is known that shale has a low matrix permeability. In petroleum geology, organic shale are source rocks and seal rocks that trap oil and gas. In reservoir engineering, shale segments are considered as flow barriers.

During the field development plan, shale volume must be considered when calculating stock tank initially in-place (STOIIP) as shale reduces the oil pay zone/net-to-gross (NTG). The higher the shale thickness, the lower the NTG ratio and thus the lower the STOIIP. Therefore, it is important to study the effects of shale orientation at various locations in the reservoir in order to optimize the reservoir management and reservoir production performance.

WAG injection is normally applied as an enhanced oil recovery method, meaning that the oil field has been in production for some time and has experienced both primary depletion and waterflooding as well.

The main target is to achieve an additional recovery compared to other possible injection operations. WAG process has been applied to rocks from very low-permeability chalk up to high-permeability sandstone [1]. WAG is classified into many types including miscible WAG, immiscible WAG, hybrid WAG, and others. However, the most commonly used process for heterogeneous reservoirs is the immiscible WAG process. It is usually applied with the aim of improving the frontal stability or contacting the unswept zones. Application has been in reservoirs where gravity stable gas injection cannot be applied, because of limited gas resources or the reservoir properties like low dip of strong heterogeneities. In addition to sweep, the microscopic displacement efficiency may be improved as well [1].

This simulation study aims (1) to investigate the trend of varying continuous shale orientation and its effect on the recovery factor, (2) identify the optimum place to inject waterflooding and immiscible WAG in the presence of lateral continuous shale, with respect to various locations of the shale orientation and (3) perform a comparative study and optimize the performance of both waterflooding and immiscible WAG injection for heterogeneous reservoirs having lateral shale.

## 2 State of the Art

### 2.1 *Waterflooding Performance in Stratified Reservoirs*

Timing of waterflooding has a crucial impact on the success rate, especially in stratified reservoirs [2]. Significant oil is recovered when waterflooding is conducted at or above the bubble point. Satter et al. [2] recommended that performing waterflooding at early phases of reservoir development leads to “a quicker payout period”.

In a stratified reservoir with the presence of shale, the authors have pointed out that the most effective waterflooding recovery is when the layer permeability increases from top to bottom. Greater vertical-to-horizontal permeability ratios will result in higher primary and waterflooding recoveries due to more efficient vertical sweep within the layer.

### 2.2 *Immiscible WAG—Effects of Permeability Ordering of Layers and Interlayer Communication in Stratified Reservoirs with the Presence of Shale*

As stated previously, WAG performs 25–50% more efficiently in a stratified reservoir with upward fining sequence, hence permeabilities increasing from top to bottom [3]. Several factors greatly affect WAG injection. Heterogeneity strongly affects WAG performance significantly especially with regard to anisotropy and stratification, ratio of viscous to gravity forces, and communication between different zones in the reservoir. They all have strong influence on the vertical conformance of the water–gas displacement process [4].

Moreover, Surguchev et al. [4] observed that if gas and water were traveling in the reservoir at equivalent speed, oil displacement by WAG would be achieved at optimum conditions. Influence of WAG injection parameters such as water–gas ratio, injection rates, and number of cycles would affect in different ways the recovery efficiency from the high- to low-permeability layers. Depending on the oil reserves in the layers, optimum conditions of WAG injection should be investigated.

Al-Mamari et al. [5] performed a comparative study on the effect of miscible water-alternating gas within shaly porous media when using numerical simulation versus experimental studies of oil recovery. Their paper included intensive studies on sweep efficiency and shale as barrier to flow. However, their study had no base case, i.e., 100% of oil initially in-place was recovered at the end of both the experiment and the simulation study [5]. In addition, Mohammadi et al. [6] carried out an intensive pore-level screening study on effect of the miscible/immiscible floods of water, polymer, surfactant, and hydrocarbon solvent injection with the

presence of shale. However, their study did not investigate the effects of WAG, rather only the effects of miscible/immiscible floods of water [6].

### 2.3 Proposed Approach

The simulation work of this project has been carried out by using Schlumberger Eclipse 100 simulator. Figure 1 explains the steps to be followed to design a model for optimizing the WAG injection process in a heterogeneous reservoir by using the Eclipse 100 software.

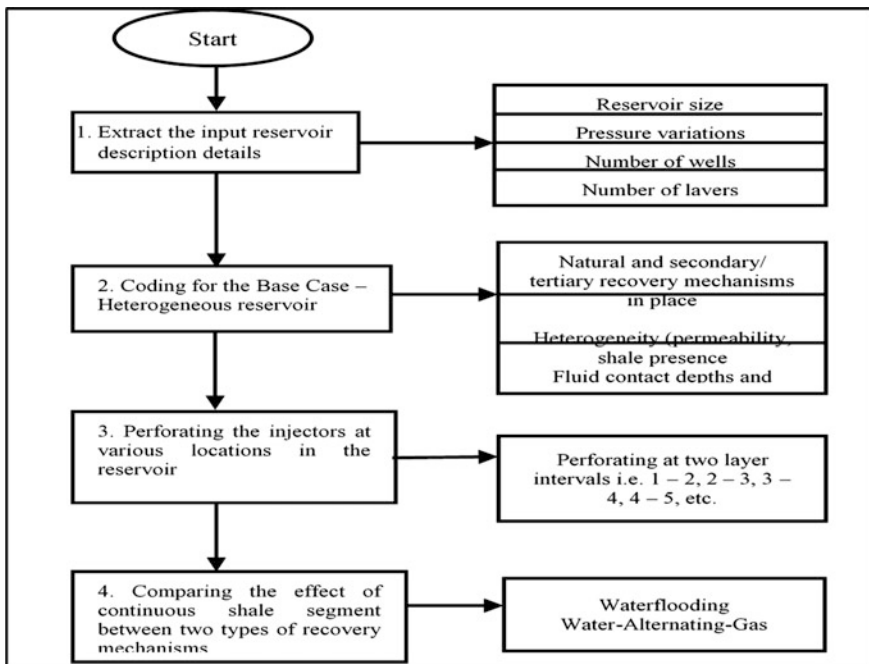


Fig. 1 Research methodology

**Table 1** Initial reservoir properties

Reservoir parameters	Value
Formation	Shaly sand
Grid cell dimensions	88.8934
Length (DX) (ft)	373.3524
Width (DY) (ft)	4.53125
Height (DZ) (ft)	
Volume of grid cells ( $X \times Y \times Z$ ) (ft <sup>3</sup> )	150385.6817
Average porosity <sup>a</sup>	0.20
Average net-to-gross NTG	1
Reservoir permeability (mD) <sup>a</sup>	50–480
Initial water saturation	0.27
Initial reservoir pressure $P_{\text{initial}}$ (psi)	4500
Oil density (lb/ft <sup>3</sup> )	49.1
Oil viscosity (cP)	0.628–0.665
Reservoir depth (ft)	72.5
Water–oil contact (ft)	4300

<sup>a</sup>Heterogeneous and anisotropic**Table 2** Well locations in the model

Well name	Well location ( $I, J, K$ )
PROD1	1, 1, 17
PROD2	1, 5, 17
PROD3	21, 1, 17
PROD4	21, 5, 17
INJ1	11, 3, 17

### 2.3.1 Reservoir Data

The reservoir properties have mainly been extracted from Genrich's [7] SPE paper titled "A Simplified Model to Predict Heterogeneity Effects on WAG Flooding Performance" [7]. Some of these properties are highlighted in Table 1.

### 2.3.2 Description of the Base Case Model

The base case model refers to the field at initial conditions, before the addition of any shale segments. The model has dimensions of 21, 5, and 17 in  $I$ ,  $J$ , and  $K$  directions, respectively. Five wells, four producers, and a single injector were placed in the grid locations as shown in Table 2. The five-spot pattern for well placement was used for this study. Table 3 summarizes the main input data for this study's base case model. There are a total of 17 layers in the reservoir with variation

**Table 3** Input data for base case model

Input	Base case model
Number of wells	5
Types of wells	Vertical well
Depletion method	Natural depletion method
Production control mode	Well control by oil rate
Oil rate	1000 bbl/day

**Table 4** Input data for permeability variation

Layers	Horizontal permeability (md)	Vertical permeability (md)
1–7	200	50
8–12	180	45
13–17	480	192

in permeability of each layer listed in Table 4. The same model was also used to compare between the waterflooding and WAG flooding performance, i.e., which of the two scenarios managed to efficiently recover more oil. Minimal changes were made to the model run by WAG, such as making the injector well inject both water and gas, and other input parameters remained intact.

### 2.3.3 Simulation Cases

The following cases were simulated:

1. Base case with waterflooding.
2. Base case with WAG.
3. Using waterflooding technique—effects of adding and changing the position of the lateral shale segment in the reservoir, i.e., varying the shale location distribution to top, middle, and bottom layers.
4. Using immiscible WAG technique—effects of adding and changing the position of the lateral shale segment in the reservoir, i.e., varying the shale location distribution to top, middle, and bottom layers.

## 3 Results and Discussion

Figure 2 shows that there is a recovery factor of 10.79% after 2 years of production life. Since the reservoir does not have an aquifer or gas cap, we can conclude that the solution gas drive is the natural drive of the reservoir. Table 5 summarizes the results of the natural drive of the reservoir.

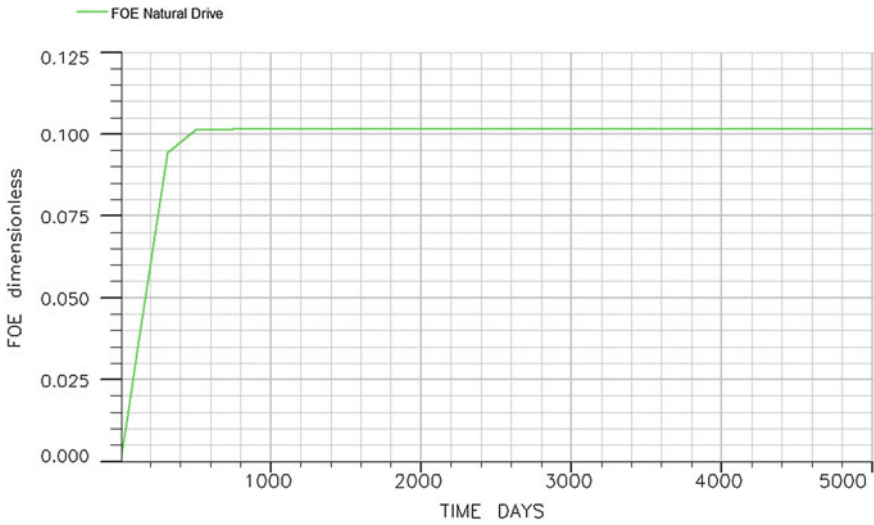


Fig. 2 The natural drive field recovery of oil

Table 5 Base case simulation results

Natural drive	FOPT (MSTB)	FWPT (MSTB)	FOE (%)	FWCT (%)
	603.062	64.326	10.15	2.61

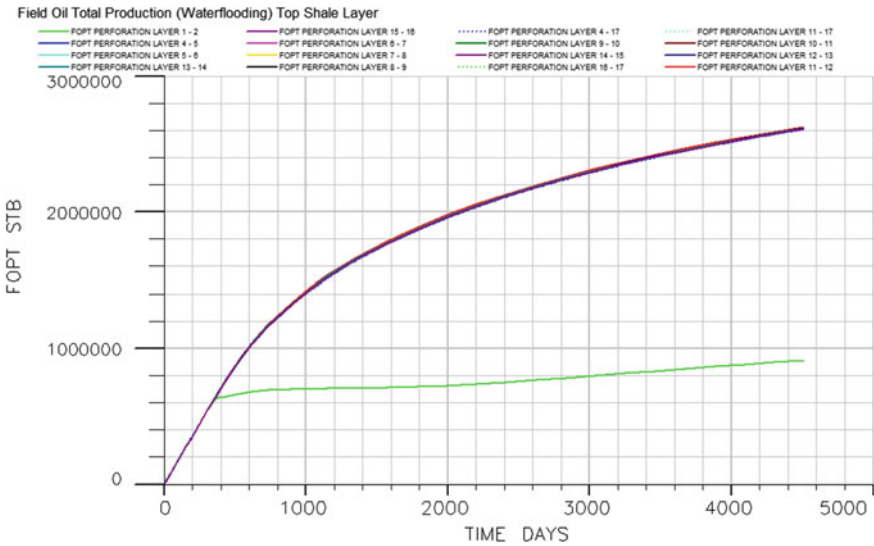


Fig. 3 Field oil production total for shale layer located at the top of the reservoir



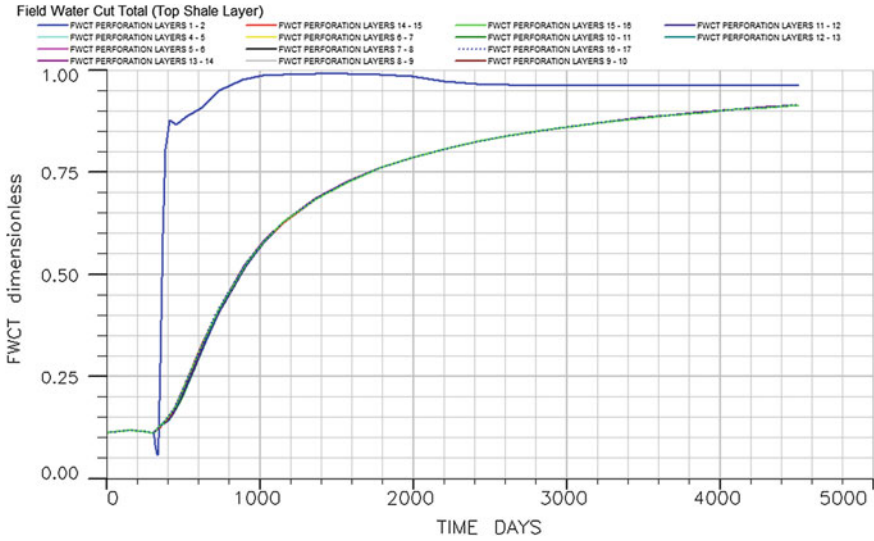


Fig. 4 Field water cut total for shale layer located at the top of the reservoir

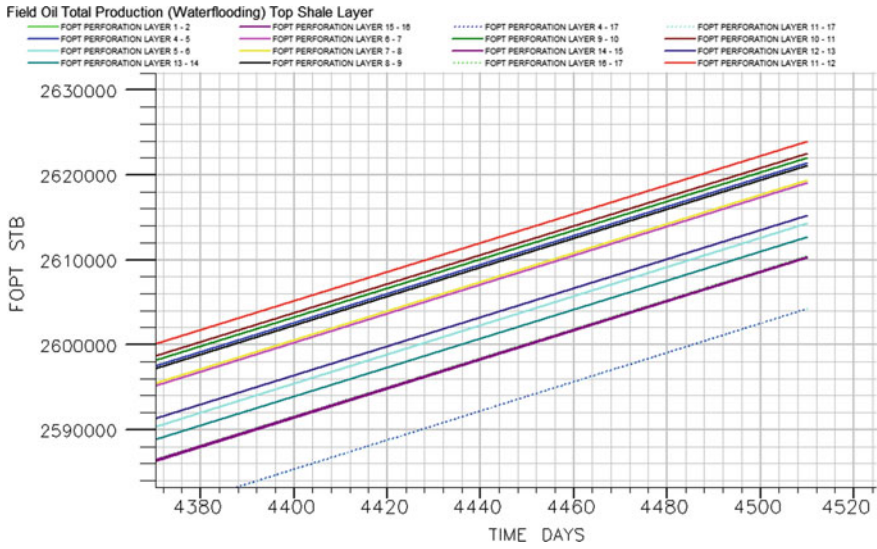
### 3.1 Recovery Method 1—Waterflooding

- Case A: Shale layer is located at the top

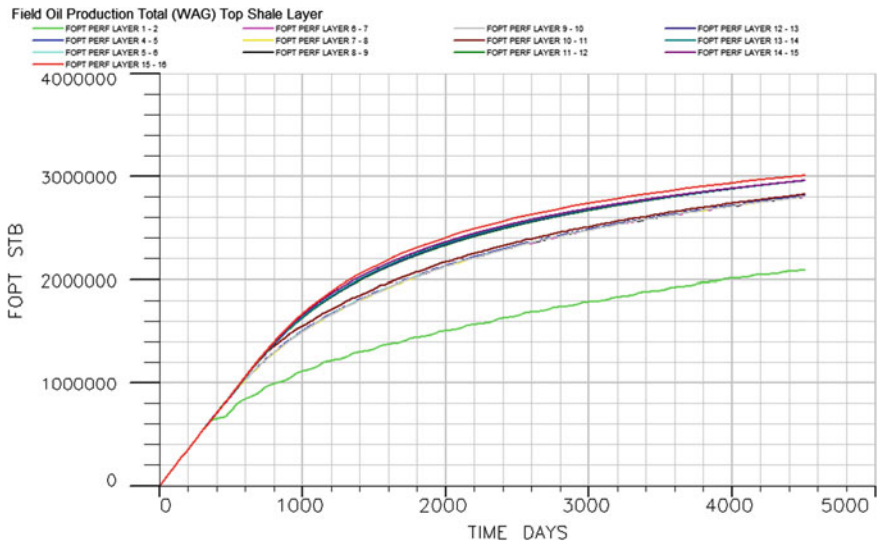
For case A, the shale layer is located at layer 3. A total of 14 cases have been run, and the cases include water injected above and below the shale layer. This is illustrated in Fig. 3. Perforating above the shale layer (represented by the lime green line) leads to much lower recovery than perforating below the shale layer, when shale is present at the top side of the reservoir.

The field water production total (FWPT) graph shows that perforation in layer 1–2 led to early water breakthrough, and this is illustrated in Fig. 4. The most likely explanation for this is because layers 1–2 are swept by the water, but at the same time, the shale layer acts as a barrier to flow, thus preventing the injected water from sweeping the bottom layers. The shale layer pushed the water injected toward the producers leading to early water breakthrough. Figure 5 shows the most optimum injection perforation interval at layers 11–12. It performs slightly better than the perforation interval of 10–11. The reason behind 11–12 performing better than the others is the reservoir vertical permeability. Therefore, perforating at layers 11–12 showed the highest field oil recovery and highest cumulative oil production, which is shown clearly in Fig. 5.

- Case B: Shale layer is located at the middle



**Fig. 5** Zoomed section to emphasize the difference between the FOPT for the different cases of perforation intervals above the shale layer in Fig. 4



**Fig. 6** Field oil production total for shale layer located at the top of the reservoir using immiscible WAG

**Table 6** Summary of middle shale layer simulation results at 4510 days ( $\sim 12.3$  years)

Recovery method	Waterflooding	FOPT (MMSTB) Field oil production total	Reduction in total oil production ( $\times 10^3$ bbl)	FWPT (MMSTB) Field water production total	FOE (%) Field oil efficiency	FWCT (%) Field water cut total
	Shale layer location: layer 9					
Perforated layers	Location from shale layer					
1–2	Above	1.646677	–	7.37332	27.72	96.05
10–11	Below	1.583789	62.888	7.43621	26.66	95.63
11–12	Below	1.57873	67.947	7.44127	26.58	95.63
12–13	Below	1.569374	77.303	7.45063	26.42	95.63
2–3	Above	1.569111	77.566	7.45089	26.42	96.03
16–17	Below	1.566301	80.376	7.4537	26.37	95.59
13–14	Below	1.566268	80.409	7.45373	26.37	95.62
15–16	Below	1.566169	80.5081	7.45383	26.37	95.59
14–15	Below	1.566059	80.618	7.45394	26.36	95.60
7–8	Above	1.551072	95.605	7.46893	26.11	96.01
6–7	Above	1.548915	97.762	7.47109	26.08	96.01
5–6	Above	1.548546	98.131	7.47146	26.07	96.02
4–5	Above	1.548024	98.653	7.471977	26.06	96.02
3–4	Above	1.547637	99.04	7.47236	26.05	96.02

In case B, the shale layer is located at layer 9. Figure 6 shows a comparison between all the different injection perforation cases. Perforating in layers 1–2 (i.e., the lime green line) performed slightly better than the other cases. A summary of all the layer perforation results is listed in Table 6.

We can see from Table 6 that layers 1–2 and 10–11 performed better than the other perforation layers. This can be attributed to injector perforated at 1–2 being located at the topmost of the reservoir, above the shale layer, whereas injector perforated at 10–11 is located right below the shale layer. This arrangement led to the highest oil recoveries due to the impact of gravity segregation. As water is denser than oil, it will sink down, thus sweeping the oil in the reservoir and pushing it toward the producers.

- Case C: Shale layer is located at the bottom

For case C, the shale layer is located at layer 15. Unlike when shale layer was located at the top, perforating below the shale layer leads to a much lower recovery than perforating above the shale layer. This is illustrated in Table 7. Similar explanation applies whereby the perforation in layers 16–17 led to early water breakthrough. The most likely explanation for this behavior is because layers 16–17 are swept by the water, but at the same time, the shale layer acts as a barrier to flow, thus preventing the injected water from sweeping the bottom layers.

**Table 7** Summary of bottom shale layer simulation results at 4510 days (~12.3 years)

Recovery method	Waterflooding	FOPT (MMSTB) Field oil production total	Reduction in total oil production (bbl)	FWPT (MMSTB) Field water production total	FOE (%) Field oil efficiency	FWCT (%) Field water cut total	
	Shale layer location: layer 15						
Perforated layers	Location from shale layer						
1–2	Above	2.568913	–	6.451087	43.25	93.74	
2–3		2.532493	36.42	6.487508	42.63	93.70	
11–12		2.53211	36.803	6.48789	42.63	93.71	
10–11		2.530968	37.945	6.489032	42.61	93.70	
9–10		2.529788	39.125	6.490212	42.59	93.70	
8–9		2.528993	39.92	6.491007	42.58	93.70	
7–8		2.527445	41.468	6.492555	42.55	93.70	
6–7		2.52558	43.333	6.494415	42.52	93.69	
5–6		2.52428	44.633	6.495718	42.50	93.69	
12–13		2.524166	44.747	6.495834	42.49	93.70	
4–5		2.523307	45.606	6.496693	42.48	93.69	
3–4		2.522502	46.411	6.497498	42.47	93.68	
13–14		2.520311	48.602	6.49969	42.43	93.68	
16–17		Below	0.910311	1658.602	8.10969	15.32	96.84

### 3.2 Recovery Method 2—Immiscible Water-Alternating Gas

Different scenarios have been run to investigate the immiscible water-alternating gas (top, bottom, and middle) as has been done for the previous cases, and the results have been compared as well.

- Case A: Shale layer is located at the top

The least cumulative oil production was produced when the injection perforation is above the shale layer (layers 1–2). This is shown as the lime green line in Fig. 6. Table 8 shows that layers 1–2 have the lowest FOPT. A possible explanation for that is because the shale block acts as a barrier to flow. When it is located at the top of the reservoir, it prevents the injected water perforating at layers 1–2 from sweeping through and sweeping the oil from the bottom of the reservoir and drives it toward the producers. At the same time, the block of shale causes the gas to quickly breakthrough and moves out the producers. This effect is brought about due to gravity segregation, where water tends to sink to the bottom of the reservoir and gas moving up and sweeping the top of the reservoir.

This is in line with Genrich’s [7] observation in which he highlighted that the streaks with low vertical permeability distributed close to the center of the reservoir yield the most noticeable enlargement of the segregated zone and hence the best recovery.

**Table 8** Summary of top shale layer simulation results at 4510 days (~ 12.3 years)

Recovery method	Immiscible water-alternating gas	FOPT (MMSTB) Field oil production total	Reduction in total oil production (bbl)	FWPT (MMSTB) Field water production total	FOE (%) Field oil efficiency	FWCT (%) Field water cut total	
	Shale layer location: layer 3						
Perforated layers	Location from shale layer						
15–16	Below	3.007454	–	6.01255	50.63	93.90	
11–12		2.958931	48.523	6.06107	49.81	92.11	
14–15		2.958723	48.731	6.06128	49.81	93.14	
12–13		2.957423	50.031	6.06258	49.79	92.35	
13–14		2.957163	50.291	6.06284	49.78	92.75	
10–11		2.827804	179.65	6.1922	47.61	90.70	
4–5		2.809792	197.662	6.21021	47.30	90.23	
9–10		2.805784	201.67	6.21422	47.23	90.18	
8–9		2.805006	202.448	6.21499	47.22	90.18	
7–8		2.804582	202.872	6.21542	47.21	90.20	
5–6		2.803999	203.455	6.216	47.20	90.21	
6–7		2.802899	204.555	6.2171	47.19	90.19	
1–2		Above	2.091078	916.376	6.9127	35.20	88.47

For the case of WAG, there is a competition between injecting at the lower most layers of the reservoir and perforating before the start of high-permeability zone. Both are performing well, with a slight favorable reservoir performance when the injection is selected at the lower most layers of the reservoir.

The most likely explanation for this is when you place the injection perforation right before the start of the high-permeability zone (i.e., layers 13–17, with a permeability of 480 md), the injected water can easily sweep the oil from the high-permeability zone leading to high recovery factor (i.e., when perforation layer is 11–12, the recovery factor is 49.81%).

However, from the results in Table 8, we can conclude that for WAG, it is better to perforate the lower most layers of the reservoir. The reason behind this is gas being less dense than water and oil, when injected at the bottom layers, travels upwards and sweeps majority of the oil from the higher permeability zones. Therefore, when the perforation layer is 15–16, the recovery factor (RF) is 50.63%.

- Case B: Shale layer is located at the middle

Figure 7 shows the cumulative oil production for shale layer located in the middle of the reservoir. The dark blue and purple lines represent perforation at layers 14–15 and 16–17, respectively. It can be seen that perforating layers 16 and 17 until 3650 days has resulted in higher total oil production. Meanwhile, after 3650 days of production, perforation at layers 14 and 15 has given a higher cumulative oil.

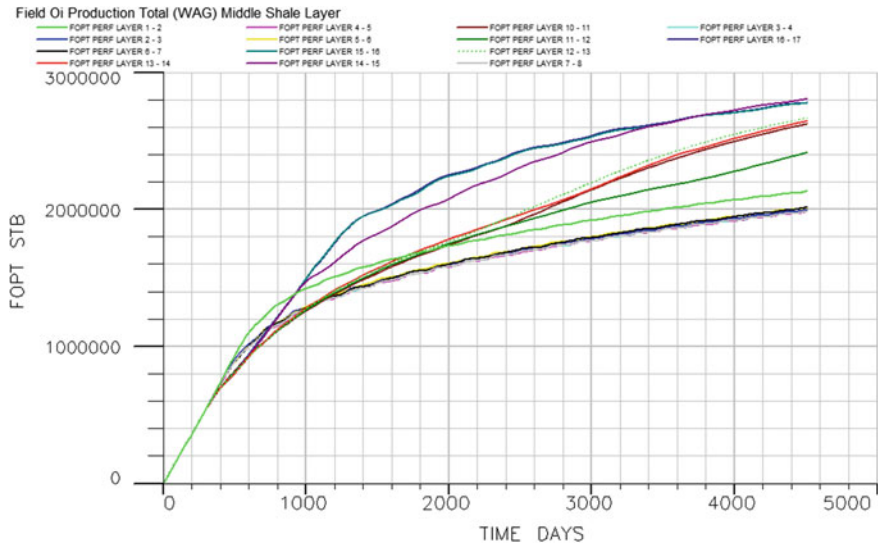


Fig. 7 Field oil production total for shale layer located in the middle of the reservoir

Table 9 Summary of bottom shale layer simulation results at 4510 days (~12.3 years)

Recovery method	Immiscible water-alternating gas	FOPT (MMSTB) Field oil production total	Reduction in total oil production (bbl)	FWPT (MMSTB) Field water production total	FOE (%) Field oil efficiency	FWCT (%) Field water cut total
	Shale layer location: layer 15					
Perforated layers	Location from shale layer					
13-14	Above	2.904948	–	6.115053	48.90	91.54
11-12		2.899786	5162	6.120214	48.82	93.85
1-2		2.890782	14166	6.129218	48.67	92.40
12-13		2.890485	14463	6.129515	48.66	92.81
10-11		2.881821	23127	6.138179	48.51	93.68
9-10		2.791788	113160	6.228212	47.00	91.27
2-3		2.783122	121826	6.236879	46.85	91.11
8-9		2.774179	130769	6.245821	46.70	91.03
7-8		2.772145	132803	6.247855	46.67	91.04
6-7		2.770275	134673	6.249725	46.64	91.04
5-6		2.76983	135118	6.250171	46.63	91.05
4-5		2.769117	135831	6.250884	46.62	91.06
3-4		2.768509	136439	6.251491	46.61	91.06
16-17	Below	2.12737	777578	6.89263	35.81	96.53

From Table 9, injection perforation located below the shale layer performs better than perforations done above the shale layer. It can be seen from the results listed that layers 14–15 performed the best, followed by perforation layers 16–17 and 15–16. Unlike the previous case of WAG, when the shale is located at the top, where layers 11–12 produced the highest recovery factor; here, when the shale is located at the middle, layers 11–12 produce a lower recovery factor. This result shows that when the shale block is located in the middle of the reservoir, the most optimum location to inject WAG is in the middle of the high-permeability layers (i.e., in this example, it is between layers 13–17) rather than injecting right above the permeable layers. This effect is mainly caused by gravity segregation.

- Case C: Shale layer is located at the bottom

The injection of WAG above the shale layer is better than injecting it below, when the shale layer is at the bottom as can be illustrated by Fig. 8. The blue line represents injection perforation below the shale layer, at layers 16–17, and it can clearly be seen that it is much lower than injecting above the shale layer.

From Table 9, layers 13–14 performed the best, followed by layers 11–12 and 1–2. The results indicate that for immiscible WAG, it is better to place the injectors at the top of the reservoir, or at the very bottom of the reservoir before the shale layer, rather than perforating above the shale layer, but in the middle of the reservoir. This is again due to gravity segregation. Placing the injectors at the very top or very bottom of the reservoir gives maximum benefits for injected fluid to travel either downward or upward, hence sweeping a larger area of the original oil in-place.

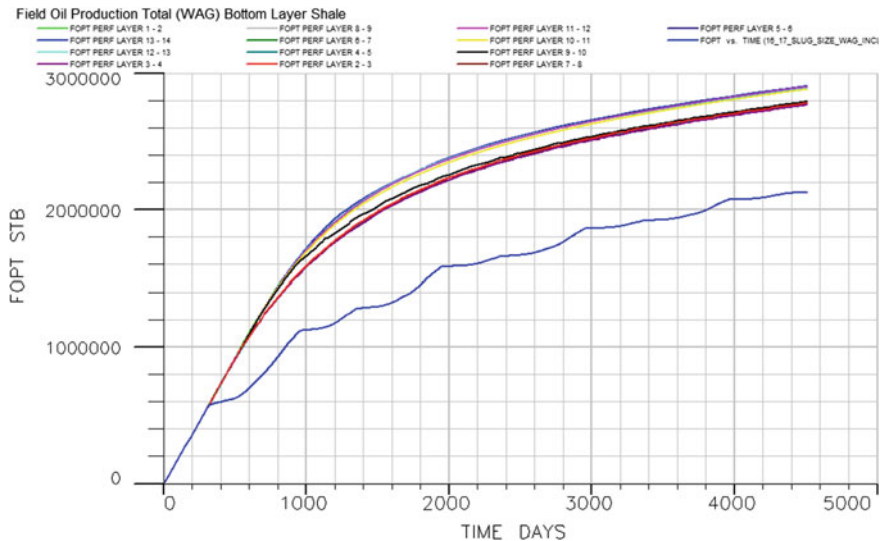
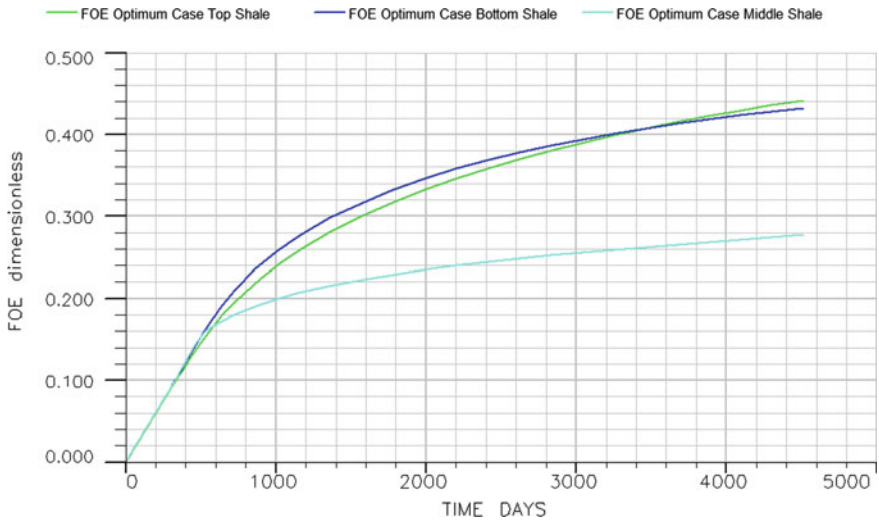
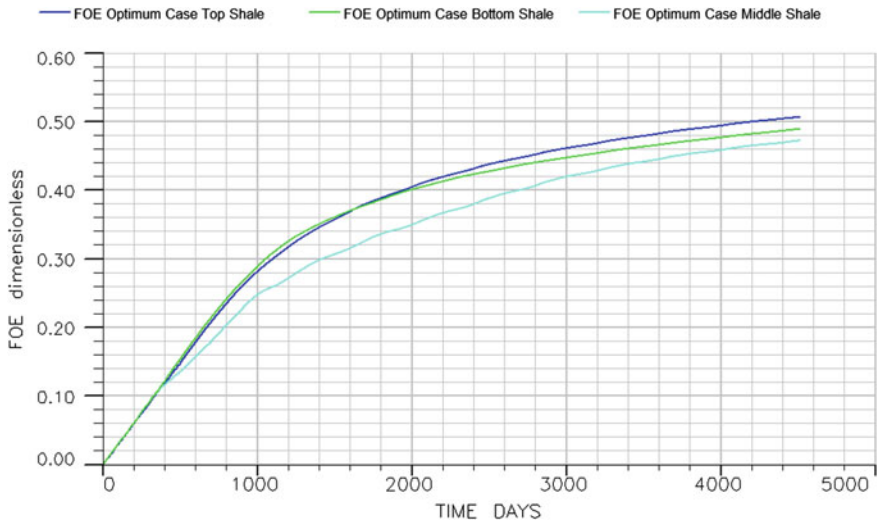


Fig. 8 Field oil production total for shale layer located in the *bottom* of the reservoir



**Fig. 9** Comparison of *top*, *middle*, and *bottom* optimum injection perforation intervals for waterflooding



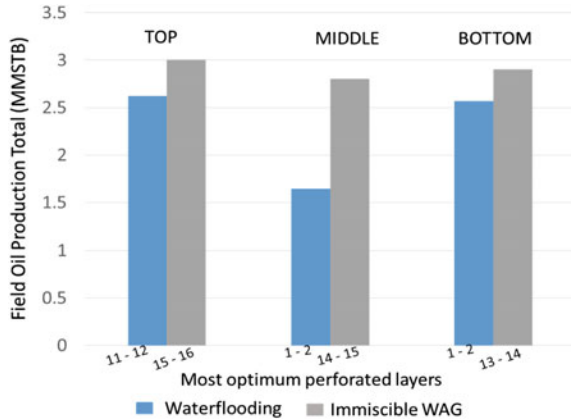
**Fig. 10** Comparison of *top*, *middle*, and *bottom* optimum injection perforation intervals for WAG

### 3.2.1 Comparison Study

As shown in Figs. 9 and 10, the highest field oil recovery is obtained when the shale layer is present at the top of the reservoir for both waterflooding and WAG injection. Similar trend was observed for both recovery methods. Initially, the bottom shale



**Fig. 11** Comparison between waterflooding and WAG for the most optimum case when shale is present at the *top* layer



layer indicates that the recovery factor is higher when shale layer is present at the bottom section of the reservoir. However, after 3670 days of production under waterflooding and 2000 days of production under WAG, the performance of the reservoir when shale is located at the top shows higher field oil recovery. These findings coincide with the previous work reported in the literature [7].

Furthermore, Figs. 9 and 10 show that both waterflooding and WAG have the same trend, whereby shale at the top layer produced the highest oil recovery, followed by shale present at the bottom, and lastly the shale present at the middle of the reservoir.

In addition, Fig. 11 shows the comparison between waterflooding and immiscible WAG for the most optimum cases when shale is present at the top, middle, and bottom layers.

All graphs show that WAG consistently performs better than waterflooding. That is mainly because in the case of immiscible WAG, the additional injection of gas helped to sweep the oil that was unswept by the water. These findings coincide with the previous work reported in the literature. In addition, for both recovery methods, waterflooding, and immiscible WAG, shale at the top layer produced the highest oil recovery, followed by shale present at the bottom, and lastly shale present at the middle of the reservoir.

## 4 Conclusion and Future Work

1. For the studied reservoir, the optimum perforation layers for the injectors when shale is located at the top were found to be layers 11–12 for waterflooding and 15–16 for WAG. The optimum perforation interval when shale is at the middle

of the reservoir was found to be injecting at layers 1–2 for waterflooding and 14–15 for WAG. The optimum perforation interval when shale is at the bottom of the reservoir was found to be injecting at layers 1–2 for waterflooding and 13–14 for WAG.

2. For waterflooding, the best perforation intervals were compared to investigate the best case of shale location. It was found that reservoir performance was most efficient when the lateral shale layer is present at the top of the reservoir. Similar findings were obtained for WAG, with the same trend, which coincides with the reports from the literature.
3. Optimizing the injection perforation location reduced the gas coning effect that occurs with WAG. In addition, WAG yielded higher reservoir performance compared to waterflooding, for the heterogeneous reservoir studied.

**Acknowledgements** The authors would like to express their deepest gratitude to Universiti Teknologi PETRONAS for providing all necessary assistance to accomplish this research. Special thanks go to Mr. Abdul Azim Abbas for his invaluable support during the early stages of model generation.

## References

1. Christensen, J. R., et al. (2001). "Review of WAG field experience." *SPE Reservoir Evaluation & Engineering* 4(02): 97–106.
2. Satter, A., Iqbal, G. M. & Buchwalter, J. (2008). *Practical Enhanced Reservoir Engineering: Assisted with Simulation Software*.
3. Sorbel, J. (2015). *Water Alternating Gas in Stratified Reservoirs. A Sensitivity Study of WAG Parameters*.
4. Surguchev et al. (1992). *Screening of WAG Injection Strategies for Heterogeneous Reservoirs*.
5. Al-Mamari, F., et al. (2007). *Numerical Simulation and Experimental Studies of Oil Recovery via First-Contact Miscible Water Alternating Gas Injection within Shaly Porous Media*. SPE/EAGE Reservoir Characterization and Simulation Conference, Society of Petroleum Engineers.
6. Mohammadi S, Ghazanfari MH, Masihi M, Kharrat R. *Experimental Study of Miscible Displacement with Hydrocarbon Solvent in Shaly Heavy Oil Reservoirs using Five-Spot Micromodels: The Role of Shale Geometrical Characteristics*. *Journal of Porous Media*. 2012; 15(5).
7. Genrich, J. F. (1986, January). *A Simplified Model to Predict Heterogeneity Effects on WAG Flooding Performance*. In *SPE Annual Technical Conference and Exhibition*. Society of Petroleum Engineers.

# Sensitivity Analysis of Sandstone Rock Elastic Properties to Effective Pressure Using a New Rock Physics Workflow and Its Application for Time-Lapse Seismic Data Analysis

Shahram Danaei and Deva Ghosh

**Abstract** Sensitivity analysis of sandstone rock frame to pressure has been an appealing area of research in upstream oil and gas industry. Knowledge of the effects of various pressures on sandstone elastic properties has been used to interpret 3D seismic data and also to use time-lapse seismic data sets to monitor the dynamic changes in an oil and gas reservoir. Rock physics models build a relation between rock elastic properties and reservoir pressure; therefore, two rock physics approaches are used commonly to illustrate the dependency of rock elastic parameters to pressure. The first approach is empirical equations, and the second is to use contact theory models. Laboratory-derived empirical equations are used to relate rock elastic properties to pressure variations. Besides these equations, contact theory models also are used to investigate the sandstone rock elastic properties to pressure changes. The aim of this research is to present a new rock physics workflow to predict the effect of different pressures on dry sandstone rock elastic properties. Hertz–Mindlin contact theory in conjunction with the pore space stiffness theory is cooperated to model the pressure effects on dry rock seismic properties. This new rock physics workflow is calibrated with laboratory measurements on core samples. The results of the developed rock physics workflow show a perfect fit with the pressure laboratory measurements on core samples. Unlike other contact theory rock physics models, our workflow requires less time with a straightforward approach. An application of this rock physics workflow for time-lapse seismic feasibility modeling is also included in this research.

**Keywords** 4D seismic data · Rock physics model · Pressure sensitivity analysis

---

S. Danaei (✉) · D. Ghosh

Department of Geosciences, Faculty of Geosciences and Petroleum Engineering,  
Universiti Teknologi PETRONAS, 31750 Tronoh, Perak, Malaysia  
e-mail: shahram\_g03167@utp.edu.my

## 1 Introduction

Seismic wave propagation into oil and gas reservoir rock depends on various factors, namely lithology, porosity, temperature, and reservoir pore fluid. These factors control the elastic properties of the reservoir rock and therefore alter the seismic responses significantly. Any changes in reservoir pore fluid saturation and pressure induced by production and/or injection will affect seismic velocity. Fluid saturation and pressure changes are among the most important changes observed at the location of oil and gas reservoirs. These changes need to be analyzed, and the effects should be modeled in great details. The effect of fluid saturation changes on seismic velocity is investigated comprehensively by different researchers. The most commonly used theoretical approach for fluid saturation changes employs the low-frequency Gassmann fluid substitution theory [1]. On the other hand, the effect of pore pressure changes is less understood. Reservoir pressure changes result in three potential seismic effects [2]:

1. A change in fluid modulus  $K_f$  and in density  $\rho$ .
2. An increase in gas saturation if pressure declines below the bubble point
3. Changes in the porosity of the reservoir–rock frame and in the bulk and shear moduli ( $K_{dry}$  and  $\mu_{dry}$ ).

Pore pressure changes during the productive life of a reservoir can result in significant changes in pore fluid properties [3]. Fluid density, compressibility, and also viscosity are the main properties that affect the seismic wave propagation; therefore, any changes in these properties will be demonstrated in the seismic responses. Pore pressure change can similarly affect the stiffness of rock and directly influence the dry rock elastic properties. The main focus of this research is to examine the effect of different pressure on rock frame elastic moduli ( $K_{dry}$  and  $\mu_{dry}$ ). For this purpose, core measurement is one technique that shows the effect of different pore pressures on seismic velocities at laboratory scale, but this technique has its own shortcomings [4]. Core measurements are subject to sampling biases, to damage, and most core measurements are obtained at ultrasonic frequencies [2]. Another alternative approach is to model the effect of different pressures on seismic responses using theoretical or empirical rock physics modeling.

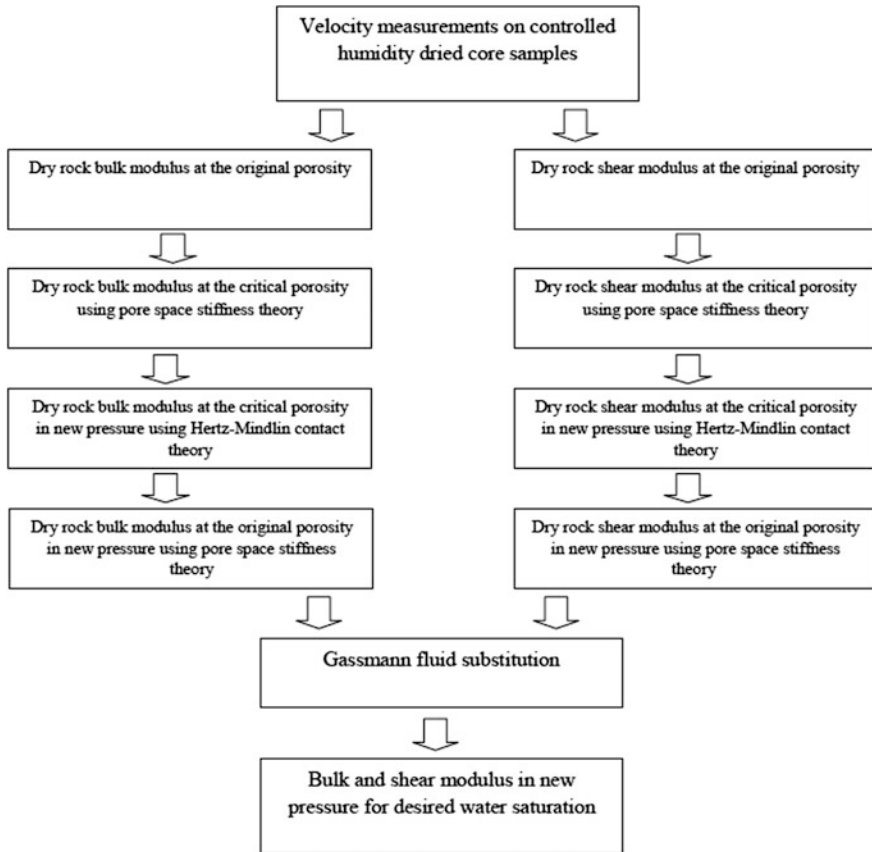
Rock physics modeling provides a link between reservoir dynamic properties and seismic responses. The modeling investigates the effects of different water saturations and pressures on elastic properties of reservoir rock. Rock physics models use either theoretical physics-based or empirical measurement-based models [2]. In this research, a new semi-theoretical physics-based model has been presented and calibrated with the core measurements from the Deep Basin in Alberta Canada. The simplest theoretical model to predict rock elastic properties changes as a function of pressure is the Hertz–Mindlin geo-mechanical modeling [5]. Hertz–Mindlin contact theory is the only theoretical model relates effective pressure to rock elastic moduli. Using Hertz–Mindlin contact theory needs a

description of grain packing or pore geometry and some simplifying assumptions [2]. In this research, a new rock physics workflow has been presented to estimate the effects of different pressures on sandstone dry rock seismic properties. Hertz–Mindlin contact theory has been used in conjunction with the pore space stiffness theory to build a framework to model the impacts of various pressures on dry rock elastic moduli. Using Hertz–Mindlin contact theory requires an estimation of rock elastic properties at the critical porosity [6]. Pore space stiffness theory is used to extrapolate the dry rock elastic properties to the critical porosity. This extrapolation to the critical porosity avoids parameterizing the model in terms of grain and contact properties that may have a lot of uncertainties related to them [6]. After extrapolation of elastic moduli to the critical porosity, Hertz–Mindlin contact theory will be used indirectly to investigate the effects of various pressures on rock elastic properties.

Our new rock physics model has been validated using core measurement on dry rock samples. Two sandstone core samples from the Cadotte member (West central Alberta) have been provided to examine and calibrate our rock physics model and implement any possible amendment to increase the accuracy of rock physics model. The results prove the capability of our rock physics workflow to predict the changes in the rock frame elastic properties resulted from pressure changes. At the end, an application of this rock physics workflow for 4D seismic feasibility study is discussed and shown on a field in Malaysian basins.

## 2 Methodology

Knowledge of the pressure dependence of elastic rock properties is useful for the analysis of rocks in sedimentary basins, including for the prediction of pore pressure and geo-mechanical effects, and also for the time-lapse seismic monitoring of subsurface fluid flow as occurs in hydrocarbon, groundwater, and CO<sub>2</sub> sequestration reservoirs. Laboratory measurements on core samples are one technique to gain valuable understanding of pressure effects on rock elastic properties. Another technique is to develop rock physics models to demonstrate the responses of rock elastic properties to various pressures. These models estimate the effective elastic moduli of rocks in terms of various pressures. There exist two approaches to model the effect of pressure on seismic velocities. Firstly, empirical models based on mathematical dependence of rock elastic properties to pressure. These mathematical relations employ different parameters with some assumptions. Eberhart-Phillips et al. [17], Avseth et al. [18], and Macbeth [19] equations are the examples of empirical modeling. Secondly, theoretical models which are based on contact medium theory. These rock physics models describe the relation between rock properties and its correspondence seismic properties. Using contact models and volume average of the elastic properties of the minerals for sandstone rock, the effects of various pressures on rock elastic properties can be estimated.



**Fig. 1** Rock physics workflow to model the effect of different pressures on dry rock frame

In this research, a rock physics workflow based on contact theory has been presented to investigate the effect of pressure on seismic velocity. This rock physics workflow is validated on two sandstone core samples. This research has been followed by an elaboration for the use of this rock physics workflow for time-lapse seismic data analysis. Our rock physics model consists of Hertz–Mindlin contact theory, Pore space stiffness theory, and also Gassmann fluid substitution. Figure 1 shows the steps involved in this rock physics workflow.

The first step in this rock physics workflow is to calculate the rock frame elastic moduli at the original porosity; therefore, there are three approaches for this calculation: (1) velocity measurements on controlled humidity-dried core, (2) application of empirical relationship or effective medium theory, or (3) direct calculation from well-log observation [1]. In this research, the first approach has been taken and the elastic moduli of dry sandstone frame are calculated using laboratory measurements on two core samples. Both bulk and shear moduli in this research have

been calculated for two dry sandstone core samples at the original porosity and in a given pressure. The second step is to calculate pressure-dependent seismic velocity of dry rock frame. Hertz–Mindlin contact model is the sole theoretical model which relates pressure to elastic moduli of rock frame at the critical porosity. Using Hertz–Mindlin contact theory requires an estimation of rock elastic properties at the critical porosity and also to parameterize the model in terms of grain and contact properties [6]. Instead of calculating these values from Hertz–Mindlin theory directly, the moduli are extrapolated to the critical porosity from the original porosity using pore space stiffness theory. This extrapolation of elastic moduli to the critical porosity avoids the uncertainties related to the use of Hertz–Mindlin contact theory.

Using Hertz–Mindlin contact theory indirectly, the effect of different pressures is modeled at the critical porosity, and finally to close the loop the pressure-changed values of elastic moduli are back-extrapolated to the original porosity using pore space stiffness theory. Finally, Gassmann fluid substitution theory could be used to deliver the pressure-changed elastic moduli to the desired water saturation.

## 2.1 Hertz–Mindlin Contact Theory

Hertz–Mindlin model is a theoretical model based on Hertz contact law which relates the elastic moduli of dry rock to the applied effective pressure [7]. Hertz contact law provides that two elastic bodies pressed together with a force will form a contact surface elliptic in shape, and Hertz–Mindlin theory considers the addition of a monotonically increasing tangential force across the contact surface [8]. This model assumes unconsolidated sand as a random pack of identical spheres and relates effective elastic properties of the medium to the effective pressure [7]. Two equations to estimate shear and bulk moduli are as follows:

$$K_{\text{eff}} = \sqrt[3]{\frac{C^2(1-\varphi)\mu^2}{18\pi^2(1-\vartheta)^2}P} \quad (1)$$

$$\mu_{\text{eff}} = \frac{5-4\vartheta}{5(2-\vartheta)} \sqrt[3]{\frac{3C^2(1-\varphi)\mu^2}{2\pi^2(1-\vartheta)^2}P} \quad (2)$$

where  $\varphi$  is the critical porosity,  $\vartheta$  and  $\mu$  are the Poisson's ratio and shear modulus of the solid grains,  $C$  is the average number of contacts per grain, and  $P$  is the effective pressure. This model suggests a power law relation between the effective bulk and shear moduli and the net confining pressure  $P$ , and proposes a power dependence of effective module as  $P^{\frac{1}{3}}$  [7]. For rock physics modeling, this model calculates the elastic moduli at the critical porosity and Hashin–Shtrikman upper or lower bounds are used to estimate the values of bulk and shear moduli at the different porosities.

By knowing the values of elastic moduli at the critical porosity (calculated by Hertz–Mindlin contact equation) as one end member and another elastic moduli at the zero porosity (Mineral elastic moduli) as another end member, Hashin–Shtrikman upper or lower bounds are used to estimate the values of bulk and shear moduli at the different porosities. Hashin–Shtrikman lower and upper bounds are used for soft and hard sandstones, respectively. One can use the Hertz–Mindlin contact theory and also Hashin–Shtrikman lower bound (HMHS) to observe the effect of different pressures on dry rock elastic moduli, but there are some issues related to using the Hertz–Mindlin contact theory and also Hashin–Shtrikman lower bound (HMHS) at the same time.

1. There are various parameters in Hertz–Mindlin equations related to grain size and its contacts which make the calculation complicated and time-consuming.
2. Dry rock bulk-to-shear ratio calculated using Hertz–Mindlin contact theory is far from the constant ratio approach presented by Murphy et al. [20].
3. All the calculations for bulk and shear moduli are conducted at the critical porosity and should be related to other porosities using different bounds.
4. The mathematical calculation is complicated and time-consuming when using Hashin–Shtrikman lower bound to relate the dry rock elastic moduli to different porosities.

To avoid running the calculation for different parameters and simplify the mathematical calculations, bulk and shear moduli are extrapolated to the critical porosity using pore space stiffness theory. This extrapolation procedure provides the elastic moduli values at the critical porosity where Hertz–Mindlin contact theory is used indirectly to estimate the elastic moduli in different pressures [9]. The changed elastic moduli due to the pressure change can be calculated using the ratio of the initial and final pressures according to the following equations [9]:

$$\frac{K_{\text{new}}}{K_{\text{old}}} = \left( \frac{P_{\text{new}}}{P_{\text{old}}} \right)^{\infty} \quad (3)$$

$$\frac{\mu_{\text{new}}}{\mu_{\text{old}}} = \left( \frac{P_{\text{new}}}{P_{\text{old}}} \right)^{\infty} \quad (4)$$

$K_{\text{new}}$  and  $\mu_{\text{new}}$  are the bulk and shear moduli of the dry rock at the critical porosity with effective pressure  $P_{\text{new}}$ , and  $K_{\text{old}}$  and  $\mu_{\text{old}}$  are the bulk and shear moduli of the dry rock at the critical porosity with effective pressure  $P_{\text{old}}$ . In these two equations, the coefficient ( $\infty$ ) is driven from laboratory core measurements.

As stated before, to investigate the effect of different pressures on elastic moduli using Eqs. (3) and (4), the elastic moduli have to be extrapolated to the critical porosity. Pore space stiffness theory is used for extrapolation purposes, and after the implementation of Eqs. (3) and (4), the new values of elastic moduli at the critical porosity are back-extrapolated to the original porosity using pore space stiffness theory.



## 2.2 Pore Space Stiffness Theory

In our rock physics workflow, the elastic moduli of dry rock in the original porosity are extrapolated to the critical porosity using pore space stiffness theory. To model dry rock elastic moduli of rock frame at different porosities, one approach is to use pore space stiffness, which is the inverse of the dry rock space compressibility at a constant pore pressure [10]. Using the Betti–Rayleigh reciprocity theorem [11], it can be seen that the pore space stiffness in a constant pressure,  $K_\phi$ , is related to the dry rock bulk modulus, the mineral bulk modulus and porosity using the following relationship [12]:

$$\frac{1}{K_{\text{dry}}} = \frac{1}{K_m} + \frac{\phi}{K_\phi} \quad \text{or} \quad \frac{K_{\text{dry}}}{K_m} = \frac{1}{1 + \frac{\phi}{K}} \quad K = \frac{K_\phi}{K_m} \quad (5)$$

In this equation,  $K_{\text{dry}}$  is the rock frame bulk modulus,  $K_m$  is the mineral bulk modulus,  $\phi$  is the porosity, and  $K_\phi$  is the pore space stiffness. Equation (5) is one of the equations which relate the dry rock bulk modulus to the porosity of frame rock; therefore, this equation is used to extrapolate the rock frame bulk modulus from original porosity to the critical porosity, and also after pressure changed using Eqs. (3) and (4), pore space stiffness will be used to back-extrapolate the elastic moduli to the original porosity. At the critical porosity, the pore space stiffness will decrease and the equation can be written as [4]:

$$\frac{K_{\text{dry at critical porosity}}}{K_m} = \frac{1}{1 + \frac{\phi_{\text{critical porosity}}}{K}} \quad K = \frac{K_\phi}{K_m} \quad (6)$$

where  $K_\phi$  can be estimated from the in situ case. The procedure used to extrapolate the dry bulk modulus to the critical porosity and also after pressure changed to back extrapolate from the critical porosity to the original porosity is depicted in Fig. 2.

In Fig. 2, the green dots represent the values of dry bulk modulus in the old pressure. The direction of arrow shows the extrapolation from the original porosity to the critical porosity. The red dots in the Fig. 2 illustrate the new values of dry bulk modulus after pressure changed using Eqs. (3) and (4). The direction of arrow shows the direction of the back extrapolation from critical porosity to the original porosity in new pressure.

Using Hertz–Mindlin contact theory in conjunction with pore space stiffness theory, dry frame bulk modulus is investigated with different pressures. It is worth saying that the procedure to model the effect of various pressures on shear modulus is similar to the aforementioned steps for dry rock bulk modulus. After modeling the elastic moduli changes due to pressure alterations, Gassmann fluid substitution can be used to simulate the effect of different water saturations.

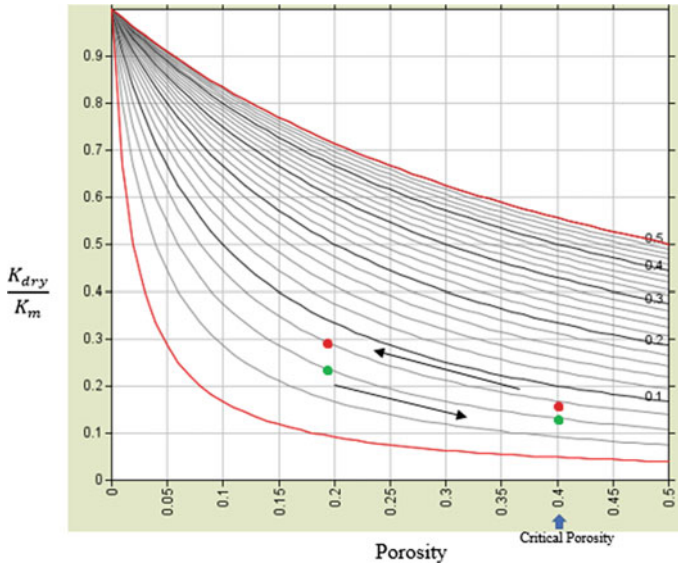


Fig. 2 Pore space stiffness theory to extrapolate elastic moduli from original to critical porosity

### 3 Results

An appropriate rock physics model should be consistent with the available well and core data, surface and borehole seismic as well as production and reservoir engineering data sets [13]. To examine the accuracy and its elastic properties' prediction capability, every rock physics model has to be calibrated with laboratory measurement on core samples or well-log observations. Our rock physics workflow also is calibrated with experimental data sets. This calibration means that the model-based pressure dependence of rock elastic properties are displayed against the actual laboratory measurement on core samples and updates will be implemented on rock physics model.

This rock physics workflow has been calibrated and tested on two core samples. The first core sample (core sample number 1) had been taken from the Cadotte member of the Peace River Formation located in Deep Basin Alberta [14]. These two sandstone core samples are mainly composed of quartz and chert, which have been subjected to intense silica cementation (quartz overgrowth development) because of pressure solution along grain contacts [14]. Pressure solution is driven by stress differences and involves dissolution at grain contacts during high stress and precipitation at grain contact on pore spaces under low pressure [14].

Laboratory measurements had been conducted to record the responses of dry core sample to different pressures. The confining pressure had been altered from 15 to 55 MPa, and the corresponding dry rock sample elastic properties are calculated.

**Table 1** Values of dry core elastic moduli in various pressure both modeled and measured

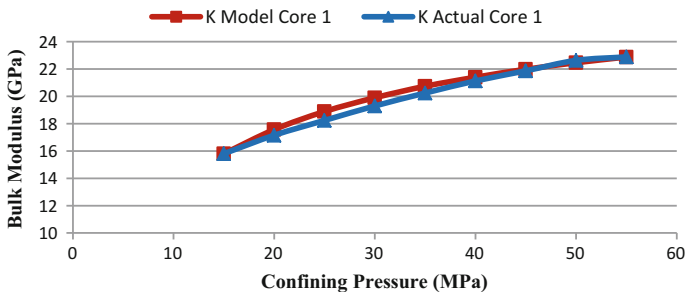
Confining pressure	Measured bulk modulus	Modeled bulk modulus	Measured shear modulus	Modeled shear modulus
15	15.807	15.807	14.340	14.340
20	17.155	17.57	16.142	16.70
25	18.24	18.89	17.621	18.49
30	19.5	19.90	19.031	19.84
35	20.243	20.74	20.25	20.90
40	21.130	21.40	21.343	21.761
45	21.87	21.983	22.313	22.46
50	22.635	22.466	23.27	23.041
55	22.89	22.88	23.98	23.53

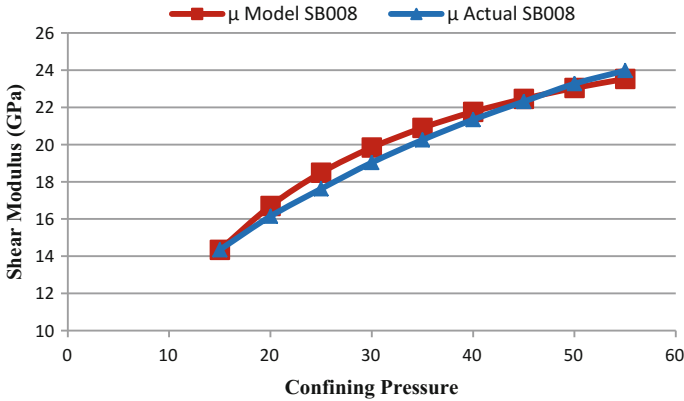
The bulk and shear moduli had been calculated in different pressures as shown in Table 1.

Our new rock physics model has been tested on the first sandstone core sample with the average porosity of 0.055. The mineral bulk and shear moduli are 25.2 and 24.8 GPa, respectively. The dry frame elastic moduli of the sample are calculated at the 15 MPa confining pressure using the velocity measurement on controlled humidity dried core sample. For dry rock bulk modulus, the value is 15.807 GPa, and for shear modulus this value is 14.340 GPa. These values of dry frame elastic moduli are considered as the old pressure values, and our rock physics model has calculated the dry frame elastic moduli in different confining pressure ranging from 15 to 55 MPa. The values of  $\alpha$  in our rock physics workflow are 1.16 to predict the dry rock bulk modulus and 0.86 to model the dry frame shear modulus.

Figure 3 shows the comparison between the measured bulk modulus and the modeled one using our rock physics workflow. In Fig. 4, a comparison between the measured and the modeled shear modulus is shown.

Our rock physics model also has been tested on the second core sample. The second core sample (core sample number 2) had been taken from the same well and

**Fig. 3** Comparison between the measured and the modeled values of bulk modulus in various pressures



**Fig. 4** Comparison between the dry rock shear modulus for laboratory measurements in *blue* and modeled one in *red*

**Table 2** Values of dry core elastic moduli in various pressure both modeled and measured

Confining pressure	Measured bulk modulus	Modeled bulk modulus	Measured shear modulus	Modeled shear modulus
20	19.162	19.162	16.557	16.557
25	20.3	20.73	17.97	18.33
30	21.657	21.98	19.42	19.77
35	22.84	23.01	20.77	20.98
40	24	23.881	21.94	21.98
45	24.95	24.62	22.99	22.84
50	25.87	25.26	23.96	23.59

formation unit as the first core sample. The average porosity of this core sample is less than the first core sample and is 0.044. The mineral bulk and shear moduli are 32 and 31 GPa, respectively. The dry rock elastic moduli also are calculated at the 20 MPa confining pressure. For that porosity and in that specific confining pressure, the dry rock bulk modulus is 19.162 GPa, and for shear modulus the value is 16.557 GPa. The laboratory measurement had been conducted on dry rock core sample and the elastic moduli were observed in different confining pressures ranging from 20 to 55 MPa. Our rock physics model has been tested for this core sample in different confining pressure ranging from 20 to 55 MPa. It is worth mentioning that the coefficient  $\alpha$  for our rock physics model is different for this core sample. For bulk modulus modeling, this coefficient is 1.26, and for the shear modulus modeling the value is 1.09. The value of elastic moduli in various pressures is calculated using our rock physics workflow. Table 2 shows the modeling of the value of elastic moduli in the range of confining pressure from 20 to 55 MPa.

Figure 5 shows the comparison between the modeled and measured dry rock bulk modulus for the core sample number 2. Figure 6 also depicts the same comparison for the dry rock shear modulus.

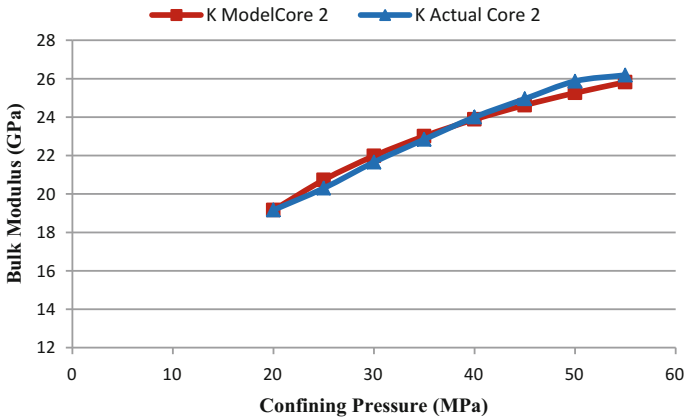


Fig. 5 Comparison between the dry rock bulk modulus for measured and modeled values

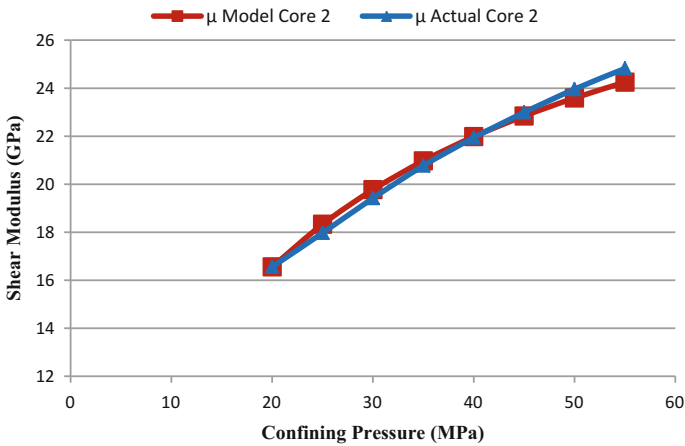
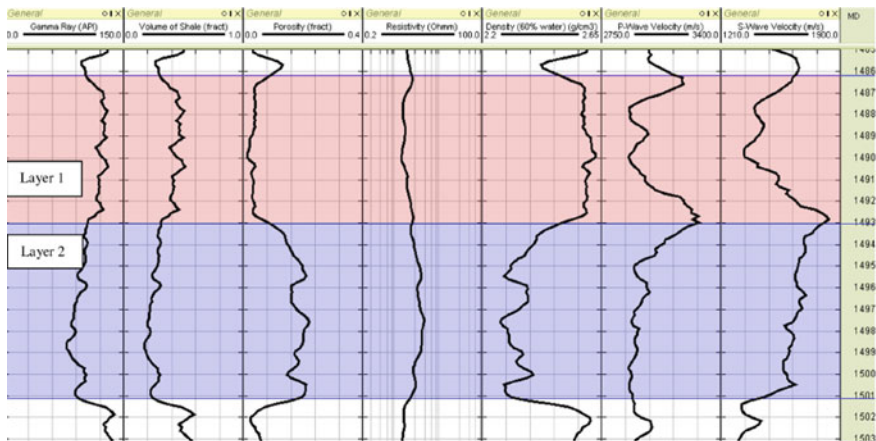


Fig. 6 Measured values of dry rock shear modulus versus the modeled ones using our rock physics model

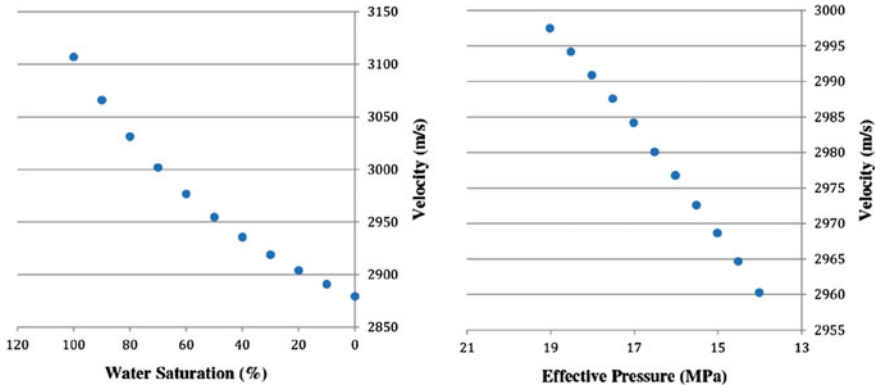
## 4 Application for 4D Seismic Data Analysis

The production and/or injection from/into a hydrocarbon reservoir results in dynamic changes in reservoir pore pressure and saturation. The rock physics modeling relates reservoir dynamic changes to the seismic responses; therefore, it can be used for time-lapse seismic data analysis. Variation in rock frame properties with applied effective pressure is a critical ingredient in assessing the feasibility of time-lapse seismic monitoring and in inversion for dynamic reservoir properties from seismic data [15]. Four-dimensional feasibility modeling, or feasibility study, is the name given to modeling the seismic changes that are expected to result from predicted production or injection scenarios and determining whether and how they can be observed [16]. Our rock physics workflow can be used in time-lapse seismic feasibility modeling to investigate the effect of different pressures and saturations on seismic responses. Building a reliable rock physics model is an essential step in 4D feasibility modeling to find out the best possible time to repeat 3D seismic survey. The application of this rock physics workflow is presented here through the feasibility modeling of a field in Malaysian basins. Our feasibility modeling is conducted in one dimension using well-log observations. Figure 7 shows the well-log observations using our 4D seismic feasibility modeling.

Different production and/or injection scenarios have been considered for layer 2 of this field, and consequently different seismic velocities are modeled using our rock physics workflow and Gassmann fluid substitution to investigate the effect of various saturations and pressures on seismic responses. The ultimate goal of 4D seismic feasibility modeling is to understand the effect of reservoir dynamic



**Fig. 7** Well-log observations for a field located in Malaysian basins using for 4D seismic feasibility modeling



**Fig. 8** Responses of seismic velocity to various water saturations and pressures based on our rock physics model

changes on seismic velocities and to find out the best possible time to repeat 3D seismic survey over the same area. Figure 8 shows the responses of seismic velocity to different pressures and also saturation changes.

## 5 Conclusion and Discussion

The effect of pressure variations on sandstone rock samples has gained an undeniable paramount importance in oil and gas industry, especially for the time-lapse seismic data analysis. To link reservoir dynamic parameters to rock elastic properties, rock physics modeling is used commonly. Fluid saturation and pressure in the reservoir change continuously in accordance to the production and/or injection activities; therefore, one attempt is to model seismic velocity changes due to these dynamic changes in the reservoir.

Hertz–Mindlin geo-mechanical modeling has been used in this research to investigate the alteration of dry rock elastic moduli to the various pressures. Hertz–Mindlin contact theory in conjunction with pore space stiffness theory is cooperated to model the dry rock elastic properties due to pressure changes. In oil and gas industry, Hertz–Mindlin contact theory commonly is used with Hashin–Shtrikman lower or upper bounds to model elastic moduli of dry rock samples, but using Hertz–Mindlin contact theory and Hashin–Shtrikman lower bound requires a time-consuming and complicated mathematical calculation. In contrast, our rock physics workflow needs less time with a straightforward mathematical calculation.

This rock physics workflow has an advantage of calculation dry elastic moduli with an acceptable industrial accuracy. One main problem in rock physics modeling (both theoretical and empirical) is that the modeled shear modulus is far from the actual shear modulus but using pore space stiffness theory in our rock physics

workflow, the modeled shear modulus has a better agreement with the actual measured shear modulus.

Our new rock physics workflow models the effect of various pressures on dry sandstone elastic properties. This rock physics workflow has to be calibrated with laboratory measurements on core samples; therefore, it is a semi-theoretical approach compared to the empirical or theoretical methods. One major shortcoming of core measurements is to use an ultrasonic frequency which is not compatible with seismic frequency. To use our rock physics workflow with Gassmann fluid substitution equation avoids frequency-dispersion effects by using dry core samples.

**Acknowledgements** The authors of this research papers want to express their deepest gratitude and thanks to PETRONAS for providing data and funding for this research. We are also so thankful of Universiti Teknologi PETRONAS and University of Alberta, especially Tiewei He and Dr. Schmitt letting us to use the data and providing support for this research.

## References

1. T. M. Smith, C. H. Sondergeld, and C. S. Rai, "Gassmann fluid substitutions: A tutorial," *GEOPHYSICS*, vol. 68, pp. 430–440, 2003.
2. D. H. Johnston, *Practical applications of time-lapse seismic data*. U.S.A.: Society of Exploration Geophysicists, 2013.
3. J. L. Packwood, *Rock Physics for Hydrocarbon Recovery Monitoring*: Stanford University, 1997.
4. S. Danaei, M. Hermana, A. G. Rafek, and D. Ghosh, "Time-lapse seismic feasibility modelling and AVO sensitivity analysis for quantification of pressure-saturation effects in fields located in Malaysian basins," presented at the Offshore Technology Conference, Kuala Lumpur, Malaysia, 2016.
5. M. Landro and K. Duffaut, "Vp-Vs Ratio Versus Effective Pressure And Rock Consolidation - a Comparison Between Rock Models And Time-lapse AVO Studies," presented at the SEG Annual Meeting, Denver, Colorado, 2004.
6. A. Das, B. Roy, P. G. Folstad, B. Lyngnes, B. Smith, and A. Grandi, "A rock physics modelling workflow for compacting chalk reservoirs: Ekofisk Case study," presented at the Second International Workshop on Rock Physics, Southampton, 2013.
7. N. Islam, "Time-lapse seismic observations and effects of reservoir compressibility at Teal South oil field," Doctor of Philosophy in Geological Engineering, Department of Geological and Mining Engineering and Science, Michigan Technological University, 2014.
8. D. A. Terry, C. C. Knapp, and J. H. Knapp, "Effective medium models and rock physics analysis for marine gas hydrates in Northern Gulf of Mexico," in *International Conference on Gas Hydrates*, Edinburgh, Scotland, United Kingdom, 2011.
9. B. A. Smith, F. D. Lane, and S. Danudjaja, "Interpreting 4D seismic response to change in effective pressure with rock physics modeling," presented at the Offshore Technology Conference, Houston, Texas, U.S.A., 2004.
10. B. H. Russell and T. Smith, "The relationship between dry rock bulk modulus and porosity-An empirical study," Consortium for Research in Elastic Wave Exploration Seismology, CREWES research report2007.
11. G. Mavko and T. Mukerji, "Seismic pore space compressibility and Gassmann's relation," *GEOPHYSICS*, vol. 60, pp. 1743–1749, 1995.



12. B. Russell, "A Gassmann-consistent rock physics template," *Canadian Society of Exploration Geophysicists*, vol. 38, 2013.
13. M. R. Saberi, "Rock physics integration: from petrophysics to simulation," presented at the 10th Biennial International Conference and Exposition Society of Petroleum Geophysicists, India, Kochi, India, 2013.
14. T. He, "P- and S-wave velocity measurement and pressure sensitivity analysis of AVA response," Master of science, Department of Physics, University of Alberta, Alberta, Canada, 2006.
15. C. MacBeth, "A classification for the pressure-sensitivity properties of a sandstone rock frame," *GEOPHYSICS*, vol. 69, pp. 497–510, 2004.
16. R. Calvert, *Insights and methods for 4D reservoir monitoring and characterization*. Tulsa, U.S.A.: SEG, EAGE, 2005.
17. D. Eberhart-Phillips, D. H. Han, and M. D. Zoback, "Empirical relationships among seismic velocity, effective pressure, porosity, and clay content in sandstone", *Geophysics*, vol. 54, no. 1, pp. 82–89, 1989.
18. P. Avseth, and T. Mukerji, "Seismic lithofacies classification from well logs using statistical rock physics", *Petrophysics*, vol. 43, no. 2, 2002.
19. C. MacBeth, J. Soldo, and M. Floricich, "Going Quantitative with 4D Seismic Analysis", *74th Ann. Internat. Mtg, Society of Exploration Geophysicist* P2283–2286, 2004.
20. W. Murphy, A. Reischer, and K. Hsu. "Modulus decomposition of compressional and shear velocities in sand bodies", *Geophysics*, vol. 58, no. 2, pp. 227–239, 1993.

# Comparison of Liquid CO<sub>2</sub> Injection with a Common Tertiary Recovery Method Using Non-Isothermal Simulations

Zakaria Hamdi and Mariyamni Awang

**Abstract** For the past decades, carbon dioxide injection has been used as a successful tertiary recovery method. The main advantage of CO<sub>2</sub> can be referred as its miscibility with the crude oil which can lead to higher recovery. Generally, a large quantity of CO<sub>2</sub> exploration can often be explored as gas or supercritical phase, but low-temperature CO<sub>2</sub> is produced in some downstream facilities such as cryogenic separation units. This low-temperature CO<sub>2</sub> opened a novel opportunity to evaluate the potential of low-temperature CO<sub>2</sub> injection for enhanced oil recovery methods. Recent studies showed that usage of liquid CO<sub>2</sub> instead of its supercritical form can increase the efficiency significantly. But its effectiveness in comparison with other tertiary methods is not investigated yet. In this paper, first, a non-isothermal compositional simulation is conducted by using a commercial simulator and by injecting low-temperature CO<sub>2</sub>. Then, the results are compared with an equivalent solvent injection scenario. The results show that, after 2 pore volumes of liquid CO<sub>2</sub> injection, a total recovery of 75.79% is obtained, which shows 17.43% increase in comparison with solvent injection. The results of this study proved a significant advantage for low-temperature CO<sub>2</sub> injection in comparison with common tertiary methods to improve oil recovery that can be implemented in the field.

**Keywords** Enhanced oil recovery · Reservoir simulation · CO<sub>2</sub> injection · Tertiary recovery

## List of symbols

$C_1$  Methane  
 $C_2$  Ethane  
 $C_3$  Propane

---

Z. Hamdi (✉) · M. Awang  
Department of Petroleum Engineering, Universiti Teknologi PETRONAS,  
Seri Iskandar, Malaysia  
e-mail: Zakaria\_g01743@utp.edu.my

M. Awang  
e-mail: Mariyamni\_Awang@petronas.com.my

$C_{4+}$	Lumped component including $C_4$ – $C_6$
$C_{7+}$	Lumped component including $C_7$ – $C_9$
$C_{10+}$	Lumped component including $C_{10}$ – $C_{19}$
$C_{20+}$	Lumped component including $C_{20}$ – $C_{29}$
$C_{30+}$	Lumped component including $C_{30}$ – $C_{68}$
$CO_2$	Carbon dioxide
$K_r$	Phase relative permeability, mD
$MW$	Molecular weight, gr
$P$	Pressure, psi
$P_c$	Critical pressure, psi
$S_{oi}$	Initial oil saturation, %
$S_{wi}$	Initial water saturation, %
$T$	Temperature, °F
$T_c$	Critical temperature, °F
$\mu$	Viscosity, cP
$\phi$	Porosity, %

## 1 Introduction and Literature Review

For the past a few decades,  $CO_2$  flooding has proven to be an acceptable tertiary recovery in enhanced oil recovery (EOR) [1–3].  $CO_2$  causes a massive viscosity reduction due to component exchange between oil and  $CO_2$  [4–10]; it is reported that the addition of  $CO_2$  in the crude oil may reduce the crude oil viscosity by a factor of 10 even for heavy crude oils [11, 12]. Besides that, dissolution of  $CO_2$  in the oil results in oil swelling, solution gas drive, and oil extraction in which those mechanisms can help to increase oil recovery [7–10, 13]. But the major benefit of  $CO_2$  flooding is its miscibility with the oil. The minimum miscibility pressure (MMP) of  $CO_2$  and crude oil is lower than other gases such as methane and nitrogen. But low viscosity and low density of  $CO_2$  may lead to gravity override [14, 15].

While increasing oil production, EOR by  $CO_2$  can also facilitate the storage of  $CO_2$  in the oil reservoir [16–20]. As a result, it may provide some economic benefits [21].

Carbon dioxide is known as a greenhouse gas that contributes to global warming [20, 22–24].  $CO_2$  emitted into the atmosphere is the main reason for global warming [25]. Injection of  $CO_2$  into the oil reservoir is one of the possible solutions in the reduction of  $CO_2$  in the atmosphere [16–19].

$CO_2$  is a colorless, odorless gas in standard condition but its phase is highly dependent on the temperature and pressure as shown in Fig. 1.

Generally, miscible  $CO_2$  drive is the preferred displacement mechanism than immiscible  $CO_2$  drive, because oil recovery in the miscible case is much more than

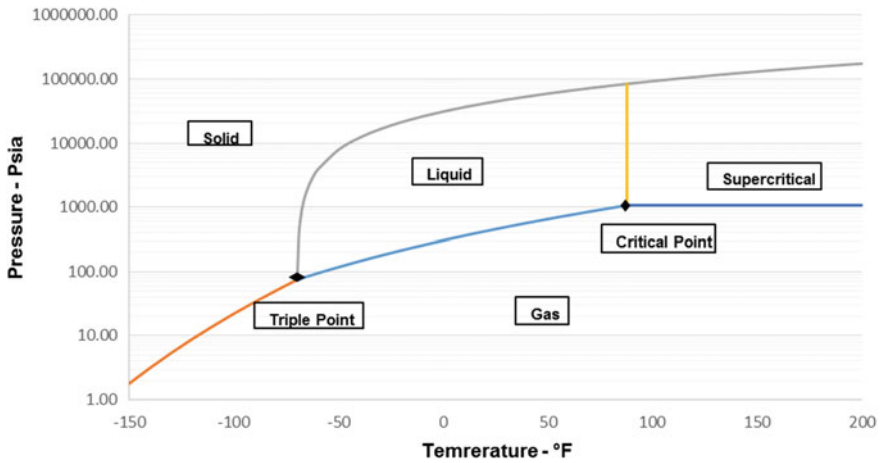


Fig. 1 CO<sub>2</sub> phase diagram

an immiscible case; recovery by miscible CO<sub>2</sub> drive typically exceeds 80% oil in place [26, 27]. The MMP indicates the miscibility or immiscibility of carbon dioxide in oil during carbon dioxide flooding. The carbon dioxide MMP is a direct function of temperature and it increases linearly corresponding to temperature [26]. The MMP is high at high temperatures. That is why most of the time achieving miscible flooding is impossible for at high-temperature reservoirs. There are situations where CO<sub>2</sub> cannot be injected at minimum miscibility pressure. For example, when the fracture pressure of the formation is lower than MMP, injection at MMP causes the formation to fracture and leads to CO<sub>2</sub> loss, and consequently the failure of the displacement.

But Yellig et al. (1980) reported, with every 50 °F drop in temperature, the CO<sub>2</sub> MMP decreases by about 600–700 psi (Fig. 2). So decreasing of reservoir temperature can be a suitable option for aiming to miscible displacement and improving oil recovery in high-temperature reservoirs. Also, it is expected that gravity override is eliminated by temperature reduction due to increase in the density of CO<sub>2</sub>. Therefore, low-temperature injection (temperatures lower than the critical temperature of CO<sub>2</sub>, i.e., 87 °F) may lead to a successful miscible flooding method.

Several Malaysian gas fields have high CO<sub>2</sub> content, up to 70% of the reservoir. One of the available ways of CO<sub>2</sub> removal is cryogenic separation. Disposal of—60 °C CO<sub>2</sub> is a potential problem. As a result, CO<sub>2</sub> from cryogenic separation has the potential of being used for EOR purposes by decreasing the reservoir temperature near the wellbore and decreasing MMP.

At cryogenic temperatures, fracturing of the formation will occur and this concept has been applied commercially to fracture wells. However, for large volumes of cryogenic CO<sub>2</sub> liquid, the use of the liquid for EOR and for sequestration requires much more investigation.

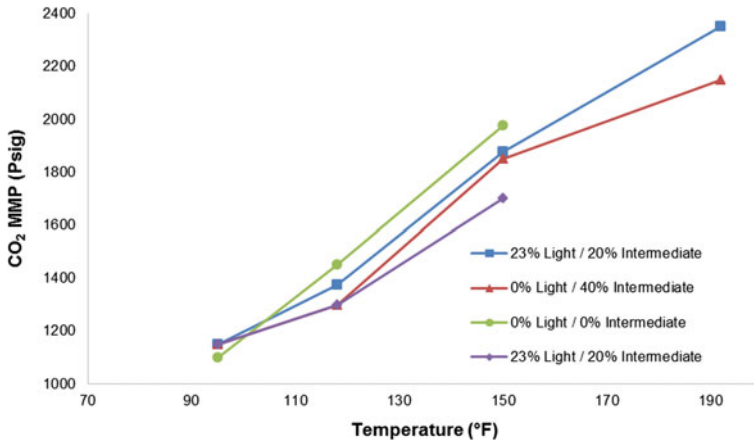


Fig. 2 Experimental data showing CO<sub>2</sub> MMP reduction by decrease in temperature [28]

The majority of the hydrocarbon reservoirs have temperature and pressure above the critical point of CO<sub>2</sub> [29–31]. So the CO<sub>2</sub> in normal condition will be in supercritical phase. A recent study has shown that when CO<sub>2</sub> is injected in low temperature, the reservoir temperature may change locally based on the pressure and volume of the injected CO<sub>2</sub> and recovery factor may increase [32]. Also, liquid CO<sub>2</sub> is more viscous and will cause better mobility of the oil, and furthermore, the stored CO<sub>2</sub> would be more than high-temperature CO<sub>2</sub> storage.

The latest study showed that low-temperature injection is always a profitable method, but it is limited due to the difficulty of decreasing the injection temperature lower than the critical temperature of CO<sub>2</sub> [33]. Therefore, the objective of this study is to compare the low-temperature CO<sub>2</sub> injection (liquid) in a high-temperature reservoir with an equivalent common tertiary method that is a common solvent flooding.

## 2 Methodology

The non-isothermal CO<sub>2</sub> flooding in the reservoir is conducted by Eclipse 300. The model has 6400 grids (40 × 40 × 10) in the form of a box with homogeneous properties for all grids so only the direct effect of temperature will have the impact on the recovery factor. The size of the first few grids was small near the injection well (as small as 2 ft in the horizontal plane) so the effect of temperature can be calculated with better precision. Initial grid properties of the reservoir are shown in Table 1. The size of the reservoirs is taken as 1000 ft × 1000 ft × 80 ft. Since the aim is to focus on CO<sub>2</sub> flooding, a natural depletion of 6 years is first applied to the simulation. Early simulations showed that after 6 years no more production is

**Table 1** Initial properties of the reservoir

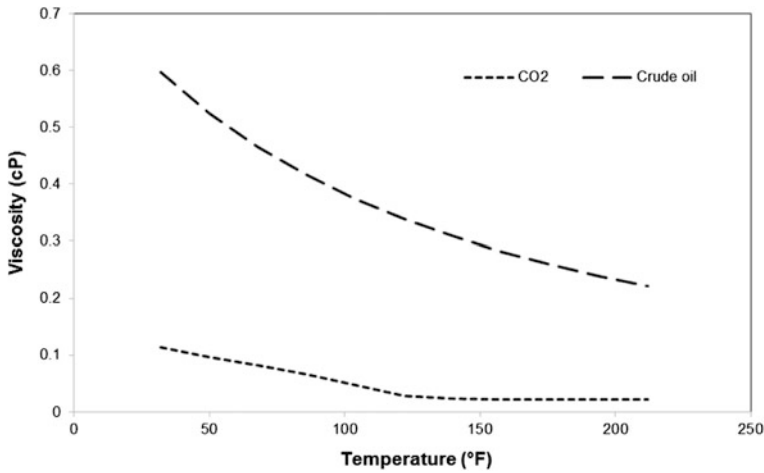
Parameter	Amount
Porosity ( $\Phi$ )	25%
Depth	8400 ft
$S_{oi}$	72.9%
$S_{wi}$	27.1%
Initial temperature of the reservoir	200 °F
Initial pressure of the reservoir	4000 Psi
Permeability in X-direction	400 mD
Permeability in Y-direction	400 mD
Permeability in Z-direction	40 mD

recorded. The reservoir temperature is taken as 200 °F, which is high enough to make it possible for us to study a wide range of injection temperatures less than this amount. No gas cap is available in this model. Also, water zone is far below so it is not affecting our simulations. The location of the wells is in the form of a quarter of 5-spot pattern, taking one injection well and one production well at the beginning and the end of the box. The injection pressure is 2000 psi while the minimum bottom hole pressure of the production well is set to 1000 psi. Both wells are having a diameter of 0.6 ft, and the top layer depth is taken 8400 ft.

The crude oil properties used in these simulations are derived from Tapis crude. The pressure–volume–temperature (PVT) calculations (using modified Peng–Robinson equation of state [34]) are done by PVTi, a software package. Thermal compositional runs require the lowest components possible for higher precision and accuracy. Therefore, lumping of the crude oil is done in such a way that the phase envelope of the crude remains constant. The original crude oil gas chromatography test that has been done earlier shows hydrocarbons up to C<sub>68</sub>. The lumping work reduced the number of components to 10, keeping the properties close enough to the original phase envelope. This is important and yet vital step as detailed debugging showed many oscillations in temperature and pressure changes from Newton iteration. Similar problems were reported and found in the literature previously [35, 36].The properties of the fluid are shown in Table 2.

**Table 2** Basic fluid properties of crude oil

Component	Mole (%)	MW (gr)	$P_c$ (psia)	$T_c$ (°R)
CO <sub>2</sub>	1.22	44.01	1071.33	548.46
N <sub>2</sub>	0.10	28.01	492.31	227.16
C <sub>1</sub>	37.67	16.04	667.78	343.08
C <sub>2</sub>	6.35	30.07	708.34	549.77
C <sub>3</sub>	3.37	44.10	615.76	665.64
C <sub>4+</sub>	9.98	74.66	511.18	854.08
C <sub>7+</sub>	7.49	119.12	402.09	1063.19
C <sub>10+</sub>	10.49	197.64	264.59	1282.51
C <sub>20+</sub>	14.92	363.86	132.15	1574.12
C <sub>30+</sub>	8.41	461.75	93.16	1700.70



**Fig. 3** Viscosities of CO<sub>2</sub> and C4 + calculated in different temperatures

The viscosity of the crude oil is calculated using Lohrenz–Bray–Clark model [37]. But viscosity of CO<sub>2</sub> is derived from previous experimental results as Lohrenz–Bray–Clark model is not giving reliable results for CO<sub>2</sub> viscosity. The obtained viscosities are shown in Fig. 3. These viscosity values are to be entered into the simulator as one of the requirements of non-isothermal injection of CO<sub>2</sub>.

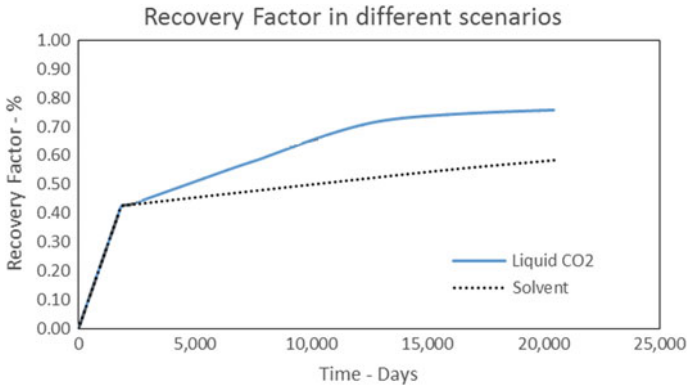
In the first step, primary depletion is considered for 6 years. The water flooding is neglected as previous studies showed the effectiveness of tertiary method vs. water flooding [29]. Then, the two scenarios are simulated. First, 40 °F CO<sub>2</sub> injection at 100 Mscf/day is done for an extended period of time. The second scenario is to use a common solvent as the tertiary flooding agent with the same injection condition. The solvent composition taken from the literature is 80% C<sub>1</sub> and 20% C<sub>3</sub> [38]. The results are then compared especially in terms of oil recovery and compositional recovery.

### 3 Results and Discussion

As described earlier, the simulations are run in each case, while they are closely monitored in case of inability of the simulator to converge. If that was the case, the PVT data is checked and modified with respect to operating temperature and pressure.

For both scenarios, 2 pore volumes of the fluids is injected. The duration of primary depletion is taken the same, 6 years. As shown in Fig. 4, the recovery factor for primary recovery for both cases is recorded to be 43%.

The results show that ultimate recovery for liquid CO<sub>2</sub> injection is 75.79%. For solvent injection case, much lower crude oil is recovered, that is, 58.36%, which is



**Fig. 4** Recovery factor versus. time in different scenarios

17.43% lower than the liquid CO<sub>2</sub> injection. According to the obtained results, solvent injection is not profitable method especially while considering the economic point of view of the methane and propane usage.

The main reason behind the high recovery of CO<sub>2</sub> in comparison with other case is its miscibility with the crude oil. The low-temperature of CO<sub>2</sub> can decrease the miscibility pressure significantly. While at the same condition, the solvent cannot lower the minimum miscibility pressure much.

Analyzing the compositional recovery of liquid CO<sub>2</sub>, one can find that CO<sub>2</sub> has much higher impact on the extraction of heavier components. This is important as currently lighter crudes are being produced at the early life of the reservoir, leaving heavier crudes in place. Furthermore, due to the low viscosity of CO<sub>2</sub>, miscible flooding will cause lower viscosity and better mobility of the mixture. So, liquid CO<sub>2</sub> can be performed in three main ways, namely extraction of the heavier components, viscosity reduction, and lowering minimum miscibility pressure.

One of the significances of the liquid CO<sub>2</sub> is in injection rate. As mentioned before, the simulator injection rate was set to 100 MScf/day. This number is obviously different in terms of cubic feet for different fluids. Considering the density of the two fluids at given pressure and temperature, the surface injection rate will be 200 and 1362 ft<sup>3</sup>/day for liquid CO<sub>2</sub> and solvent, respectively. This shows the significant benefit of the drastically low amount of liquid CO<sub>2</sub> in comparison with solvent. Obviously, if the surface injection was considered, the difference between recovery of liquid CO<sub>2</sub> and the other fluids was much more.

## 4 Conclusion

The liquid CO<sub>2</sub> injection simulation is made based on the injection temperature to compare the before mentioned recovery method and solvent injection scenario in a high-temperature reservoir.



The results suggest that by using low injection temperature of CO<sub>2</sub>, it is expected that higher recovery than solvent injection is achieved. In the studied case, the difference in recovery is recorded to be up to 17.43% higher than in solvent case, respectively. The main advantage of liquid CO<sub>2</sub> can be expressed as the ability to recover heavier components as well as performing miscible displacement at lower pressure.

As a result, considering the two cases studied, low-temperature injection seems to be always a profitable method, but again, it is limited due to the difficulty of decreasing the injection temperature lower than the critical temperature of CO<sub>2</sub> and it is only applicable where large quantities of low-temperature CO<sub>2</sub> are available. Meanwhile, it is proven to be a promising method even while considering heavy crudes and it can be handled with a much lower injection rate of liquid CO<sub>2</sub> in comparison with other methods.

## 5 Future Work

The model can be used to verify future displacement experiments. Also, a more accurate PVT data is needed, preferably with more experimental data to fit. Other parameters such as relative permeability, surface tension, injectivity, and composition-based recovery are obtained but not presented in this study due to the limitations of the conference. Also, the effect of reducing the temperature on the parameters can be analyzed and traced along the reservoir.

**Acknowledgements** The authors would like to thank Universiti Teknologi PETRONAS for assistantship support and software licensing of Eclipse by Schlumberger.

## References

1. Lake, L.W., *Enhanced oil recovery*. 1989, Englewood Cliffs, N.J: Prentice Hall.
2. Green, D.W., G.P. Willhite, and S.o.P.E. (U.S.), *Enhanced oil recovery/ Don W. Green, G. Paul Willhite*. 1998.
3. Moritis, G., *EOR Continues to Unlock the Oil Resources*. Oil and Gas Journal, 2004: pp. 45–52.
4. Latil, M., *Enhanced Oil Recovery*. 1980, Paris, France: Éditions Technip.
5. Lake, L.W., *Enhanced Oil Recovery*. 1989, New Jersey: Prentice Hall Incorporated. 550.
6. Green, D.W. and G.P. Willhite, *Enhanced Oil Recovery*. Vol. 6 of of SPE textbook series. 1998, New York: Henry L. Doherty Memorial Fund of AIME, Society of Petroleum Engineers.
7. Holm, L.W., *CO<sub>2</sub> Flooding: Its Time Has Come*. J. Pet. Technol., 1982. **34**(12): pp. 2739–2745.
8. Holm, L.W. and V.A. Josendal, *Effect of Oil Composition on Miscible-Type Displacement by Carbon Dioxide*. Soc. Pet. Eng. J., 1982. **22**(1): pp. 87–98.
9. Orr, F. and J. Taber, *Use of carbon dioxide in enhanced oil recovery*. Science, 1984. **224** (4649): pp. 563–569.

10. Blunt, M., F.J. Fayers, and F.M. Orr, *Carbon Dioxide in Enhanced Oil Recovery*. Energy Convers. Manage., 1993. **34**(9): pp. 1197–1204.
11. Rojas, G.A., et al., *Scaled Model Studies of CO<sub>2</sub> Floods*. SPE Reservoir Eng., 1991. **6**(2): pp. 169–178.
12. Quraini, A.A., M. Sohrabi, and M. Jamiolahmady, *Heavy Oil Recovery by Liquid CO<sub>2</sub>/Water Injection*, in *EUROPEC/EAGE Conference and Exhibition*. 2007, Society of Petroleum Engineers: London, U.K.
13. Bondor, P., *Applications of Carbon Dioxide in Enhanced Oil Recovery*. Energy Convers. Manage., 1992. **33**(5): pp. 579–586.
14. Stalkup, F.I., *Miscible Displacement*. 1983: Henry L. Doherty Memorial Fund of AIME, Society of Petroleum Engineers of AIME.
15. Orr, F.M. and J.J. Taber, *Displacement of Oil by Carbon Dioxide: Final Report*. 1981: U.S. Department of Energy.
16. Kovscek, A. and M. Cakici, *Geologic Storage of Carbon Dioxide and Enhanced Oil Recovery. II. Cooptimization of Storage and Recovery*. Energy conversion and Management, 2005. **46**(11): pp. 1941–1956.
17. Ren, S., et al., *Monitoring on CO<sub>2</sub> EOR and Storage in a CCS Demonstration Project of Jilin Oilfield China*, in *SPE Annual Technical Conference and Exhibition*. 2011, Society of Petroleum Engineers: Denver, Colorado, USA.
18. Gozalspour, F., S. Ren, R., and B. Tohid, *CO<sub>2</sub>EOR and Storage in Oil Reservoir*. Oil Gas Sci. Technol., 2005. **60**(3): pp. 537–546.
19. Kovscek, A.R., *Screening Criteria for CO<sub>2</sub> Storage In Oil Reservoirs*. Pet. Sci. Technol., 2002. **20**(7–8): pp. 841–866.
20. Rackley, S., *Carbon Capture and Storage*. 2009, Burlington, Massachusetts: Butterworth-Heinemann.
21. Espie, T., *A New Dawn for CO<sub>2</sub> EOR*, in *International Petroleum Technology Conference*. 2005, International Petroleum Technology Conference: Doha, Qatar.
22. Hepple, R.P. and S.M. Benson, *Geologic Storage of Carbon Dioxide as a Climate Change Mitigation Strategy: Performance Requirements and the Implications of Surface Seepage*. Environ. Geol., 2005. **47**(4): pp. 576–585.
23. Kongsjorden, H., O. Kårstad, and T.A. Torp, *Saline Aquifer Storage of Carbon Dioxide in the Sleipner Project*. Waste Management, 1998. **17**(5): pp. 303–308.
24. Schrag, D.P., *Storage of Carbon Dioxide in Offshore Sediments*. Science, 2009. **325**(5948): pp. 1658–1659.
25. Jeong, S.-m., T. Sato, and B. Chen, *Diffusion Simulation of CO<sub>2</sub> Discharged in Mesoscale Deep Ocean by Using Moving-Nesting Grid Technique*. Int. J. Offshore Polar Eng., 2010. **20**(1): pp. 48–53.
26. Jarrell, P.M., et al., *Practical Aspects of CO<sub>2</sub> Flooding*. Vol. 22. 2002, Texas: SPE Monograph.
27. Stalkup, F.I., *Carbon Dioxide Miscible Flooding: Past, Present, And Outlook for the Future*. SPE Journal of Petroleum Technology, 1978. **30**(8).
28. Yellig, W.F. and R.S. Metcalfe, *Determination and Prediction of CO<sub>2</sub> Minimum Miscibility Pressures (includes associated paper 8876)*. SPE Journal of Petroleum Technology, 1980. **32**(1): pp. 160–168.
29. Ireland, S., et al., *Experimental Investigation of Liquid-CO<sub>2</sub> and CO<sub>2</sub>-Emulsion Application for Enhanced Heavy Oil Recovery*, in *75th EAGE Conference & Exhibition incorporating SPE EUROPEC*. 2013, Society of Petroleum Engineers: London, United Kingdom.
30. Frailey, S.M., et al., *Investigation of Liquid CO<sub>2</sub> Sequestration and EOR in Low Temperature Oil Reservoirs in the Illinois Basin*, in *SPE/DOE Symposium on Improved Oil Recovery*. 2004, Society of Petroleum Engineers: Tulsa, Oklahoma.
31. Sohrabi, M., M. Jamiolahmady, and A.A. Quraini, *Heavy Oil Recovery by Liquid CO<sub>2</sub>/Water Injection*, in *EUROPEC/EAGE Conference and Exhibition*. 2007, Society of Petroleum Engineers: London, U.K.

32. Hamdi, Z. and M. Awang, *Improving Oil Recovery by Cold CO<sub>2</sub> Injection: A Simulation Study*. International Journal of Petroleum and Geoscience Engineering (IJPGE), 2013. **1**(3): pp. 167–177.
33. Hamdi, Z., M. Bt. Awang, and B. Moradi, *Low Temperature Carbon Dioxide Injection in High Temperature Oil Reservoirs*, in *International Petroleum Technology Conference*. 2014, International Petroleum Technology Conference.
34. Robinson, D.B. and D.Y. Peng, *The Characterization of the Heptanes and Heavier Fractions for the GPA Peng-Robinson Programs*. 1978: Gas Processors Association.
35. Khan, S.A., G.A. Pope, and K. Sepehrnoori, *Fluid Characterization of Three-Phase CO<sub>2</sub>/Oil Mixtures*, in *SPE/DOE Enhanced Oil Recovery Symposium*. 1992, 1992 Copyright 1992, Society of Petroleum Engineers, Inc.: Tulsa, Oklahoma.
36. Jr, A.G.L., L.X. Nghiem, and T.G. Harding, *Three-Phase Hydrocarbon Thermodynamic Liquid-Liquid-Vapour Equilibrium in CO<sub>2</sub> Process*, in *SPE Reservoir Characterisation and Simulation Conference and Exhibition*. 2011, Society of Petroleum Engineers: Abu Dhabi, UAE.
37. Lohrenz, J., B.G. Bray, and C.R. Clark, *Calculating Viscosities of Reservoir Fluids From Their Compositions*. 1964.
38. Killough, J.E. and C.A. Kossack, *Fifth Comparative Solution Project: Evaluation of Miscible Flood Simulators*. Society of Petroleum Engineers.

# A Simulation Study of Foam Generation Across Vertical Heterogeneity

U. Djuraev, S.R. Jufar, P. Vasant and H. Hematpour

**Abstract** Many studies have been performed, and valuable conclusions have been drawn to augment understanding about foam generation process and its impact on ultimate oil recovery. However, the behavior of foam in vertically heterogeneous reservoir remains unresolved. Hence, this challenge creates a need to investigate the matter comprehensively, which essentially is the goal of this study. In this work, the simulation runs were conducted for two configurations of vertical heterogeneity: First, the low-permeable layer is on top of the high-permeable layer. Second, the simulation runs are conducted for “vice versa” configuration. In each configuration, five scenarios were defined to investigate the effect of permeability contrast ratio. Furthermore, for all cases, the comparison was made with the case of gas injection in the absence of foam. The results suggest that foam generation was not beneficial when it was applied in the reservoir with low-permeable layer on top of the high-permeable one. It failed to challenge the conventional gas injection process with respect to case studies developed in the project, as very little, or no strong foam was generated. By contrast, as the foam was generated in the reservoir with high permeability on top with low-permeable layer in the bottom, it succeeded to control the gas–oil ratio and mobility of injected gases quite effectively.

**Keywords** Foam flooding · Reservoir simulation · Vertical heterogeneity · Mobility reduction

---

U. Djuraev (✉) · S.R. Jufar  
Department of Petroleum Engineering, Universiti Teknologi Petronas,  
Seri Iskandar 32610, Perak, Malaysia  
e-mail: ulugbek.dj@gmail.com

P. Vasant  
Department of Fundamental & Applied Sciences, Universiti Teknologi Petronas,  
Seri Iskandar 32610, Perak, Malaysia

H. Hematpour  
Petroleum Engineering Department, Research Institute of Petroleum Industry,  
Tehran, Iran

## 1 Introduction

In a porous medium, the foam is defined as a gas dispersed in a liquid where the liquid is in continuous phase, whereas the gas is at least partly discontinuous by lamellae [1]. Basically, this definition includes both bulk foams, where one's bubble size is much smaller than the size of the pores and the other one, whose average bubble size is greater than the pore dimensions. Foam is called "unstable" when the lamellae are short lived, and longer-lived foams or "stable" foams travel from pore to pore. This phenomenon lowers the mobility of the gas phase and consequently increases the sweep efficiency of the gas injection process. This reduction of mobility is illustrated by a parameter called mobility reduction factor (MRF). MRF is used in local steady-state modeling to describe foam rheology.

There are three essential foam generation mechanisms: leave-behind, snap-off, and lamella division. In general, the generation of "strong" foam greatly depends upon the snap-off mechanism [2]. As it was mentioned earlier, the desired form of foam is a discontinuous-gas foam generation, which entails a snap-off occurrence and/or lamella division. In case of the snap-off, the non-wetting phase (invading gas) crosses the threshold of a pore restriction initially filled with wetting liquid (surfactant solution) and creates foam bubbles. Moreover, the lamella division mechanism also contributes to the formation of a strong foam. However, lamella division and leave-behind mechanisms lay beyond the scope of this paper and thus will not be discussed in details.

The snap-off mechanisms are pivotal process when it is desired to generate a "strong" foam. This was tested experimentally and observed by many eminent researchers [3]. Furthermore, it was pointed out that the pore radius must be at least twice greater than the radius of the pore throat, as it would essentially deliver the needed reduction in capillary pressure to yield "strong" foam [4]. The determination of required permeability contrast is crucial in this paper. Despite having an increase in permeability between layers, a certain critical value should exist in order to be able to simulate real applications of foam generation more accurately. Tanzil et al. [4] illustrated a mathematical expression that quantified the desired critical number. As such, according to the authors, the snap-off foam bubbles form at an abrupt increase in permeability between layers, whereby the permeability contrast must equal at least four.

There are many factors that affect the foam generation in porous media. However, in this study, we narrowed them down to certain factors, which, in turn, depend on heterogeneity of reservoirs—permeability contrast ratio in vertical direction.

In petroleum industry, there are four different foam flooding methods: (1) surface pregenerated foam is injected into the reservoir formation, (2) surfactant-alternating-gas (SAG) foam, where surfactant and gas slugs are injected in alternating the order for a specific period of time [5], (3) based on previous studies

[6, 7], surfactant solutions in supercritical CO<sub>2</sub> are too used to create foam once the solution encounters the existing water in the reservoir, and (4) a simultaneous coinjection of both gas and surfactant solution into the same reservoir, albeit into different sections of well [8, 9]. In this study, all simulation studies were performed under the surfactant-alternating-gas method.

In this study, the influence of a layer’s vertical permeability on the behavior of SAG foam process was examined via mobility reduction factor, gas–oil ratio, and oil recovery.

## 2 Methodology

### 2.1 Reservoir Model and Model’s Parameters

In order to simulate a SAG foam process, following assumptions were considered: The reservoir has no-flow boundaries, and there are one injection well and one production well placed diagonally in a quarter portion of an inverted 5-spot injection pattern. The reservoir heterogeneity is represented by various vertical permeability values. As such, there are five high-permeable layers and five low-permeable layers. Each layer has identical thickness and is a homogeneous porous medium with identical properties in all Cartesian directions. In this study, firstly, the simulations are run with the high-permeable layer placed on top of the low-permeable layer. Secondly, the simulation studies are conducted with the low-permeable layer which is on top of the high-permeable layer. The table below shows the model’s properties (Table 1).

**Table 1** Reservoir properties

Properties\Cases	Case 1	Case 2	Case 3	Case 4	Case 5
Reservoir dimensions	50 × 50 × 10				
Grid size (ft.)	100				
Porosity	0.3				
High-permeable layer thickness	20				
Low-permeable layer thickness	30				
Permeability ratio	2:1 1:2	3:1 1:3	4:1 1:4	5:1 1:5	10:1 1:10
$k_x = k_y = k_z$ (high-permeable layer) (mD)	100	150	200	250	500
$k_x = k_y = k_z$ (low-permeable layer) (mD)	50				
Surfactant solution (3% wt.) injection rate (stb/day)	100,000				
Gas flooding, surface injection rate (mscf/day)	100,000				

## 2.2 *Simulation Procedure*

As mentioned before, the main aim of this study is to investigate the foam behavior in heterogeneous reservoir. In order to achieve this objective, all simulations were run in Eclipse E100, developed by Schlumberger. In this work, 10 different runs were performed, where the half of these runs were performed with the high-permeable layer placed on the top, and the rest was conducted with the high-permeable layer placed in the bottom. All configurations were examined by different permeability ratios. The SAG foam process was applied in such a way, where one slug of surfactant solution (91 days) is followed by gas slug for 7020 days. This scenario represents one cycle of SAG foam process. The results of simulations are illustrated in Fig. 1.

## 3 Results and Discussion

### 3.1 *Gas Mobility Reduction Factor*

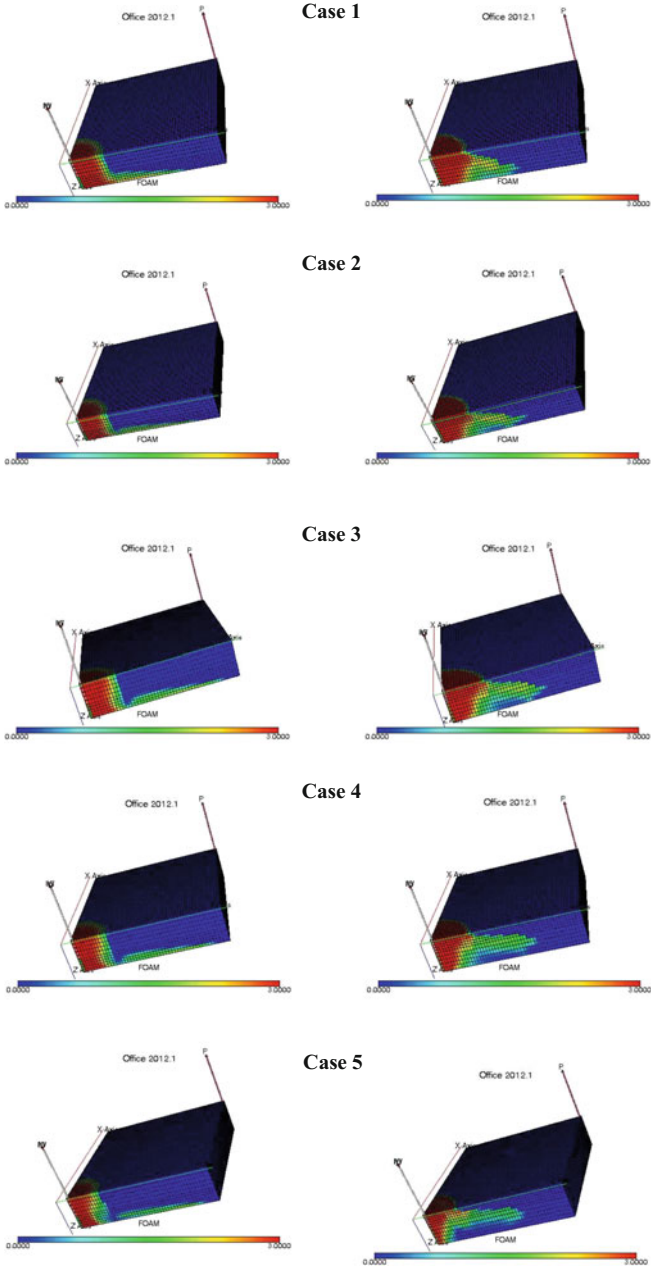
As mentioned before, the gas mobility reduction factor can adequately represent the strength of the foam. Therefore, MRF was examined to investigate the effect of permeability ratio on the generation of the foam. Fig. 2 shows the behavior of foam when high-permeable layer was located in the bottom. The results reveal that in Case 3, the required condition was met for snap-off mechanism and thus produced relatively “strong” foam. However, the succeeding cases had no significant impact on the mobility of the gas.

Figure 3 depicts how drastically the gas mobility reduced due to foam being generated when the high permeability was located on top. Same as in Fig. 2, Case 3 met the required condition for the snap-off. This implies that “strong” foam was predominantly generated by the snap-off mechanism, and thus, more bubbles were transported into the high-permeable formation. However, in case of very abrupt permeability contrast (Case 5), the gas mobility factor yielded nearly the same result as in Case 3, although it is obvious that “strong foam” did prevail nonetheless. The reason why such an abrupt permeability ratio did not have a high impact on the gas mobility is, probably, because of the high permeability value itself. That being said, the foam bubbles were transported at much faster rates deep into the reservoir, with little time to alter the gas mobility.

The difference between the values of Figs. 2 and 3 can be delineated by the phase segregation phenomena. Since the gas phase tends to go upward due to density differences between reservoir fluids, this phenomenon would play a supportive role to increase the gas dominance in the top layers, which in turn leads to foam destruction.

**Low permeability on the top**

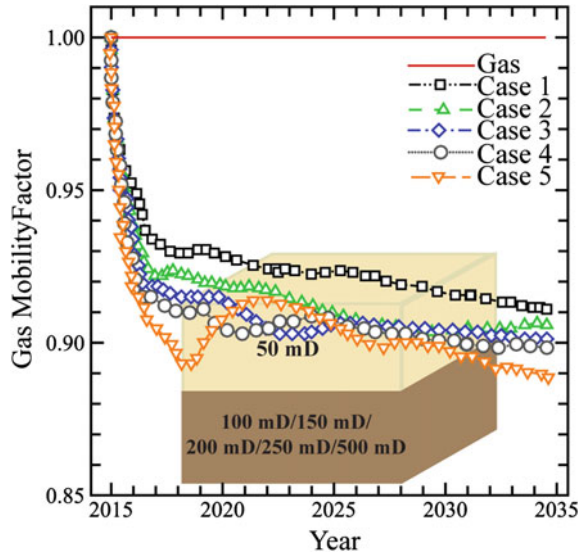
**High permeability on the top**



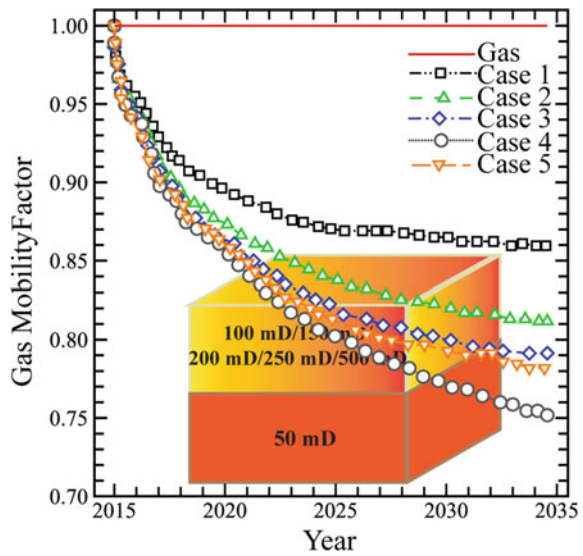
**Fig. 1** 3D simulation results for all scenarios



**Fig. 2** Gas mobility reduction factor (high permeability at bottom)



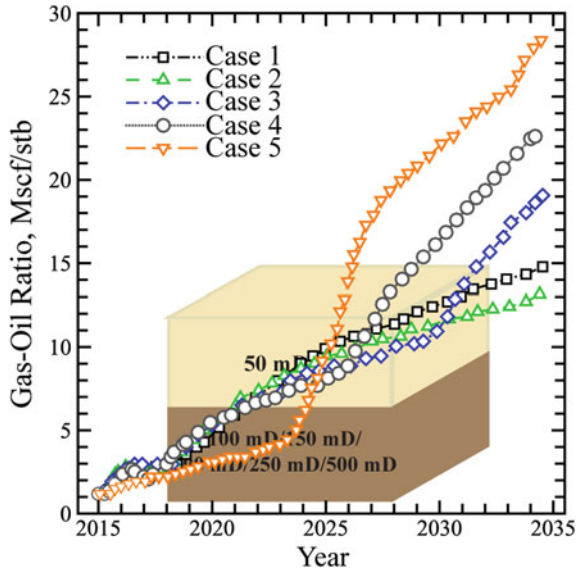
**Fig. 3** Gas mobility reduction factor (high permeability at top)



### 3.2 Gas–Oil Ratio

This section examines the effect of foam generation on gas–oil ratio, where Fig. 4 depicts the when the high permeability was located in the bottom. This figure indicates that the trend of gas–oil ratio is quite different from others factors. Moreover, from the figure, we can clearly see the breakthrough time. In fact, the

**Fig. 4** Gas–oil ratio (high permeability at bottom)



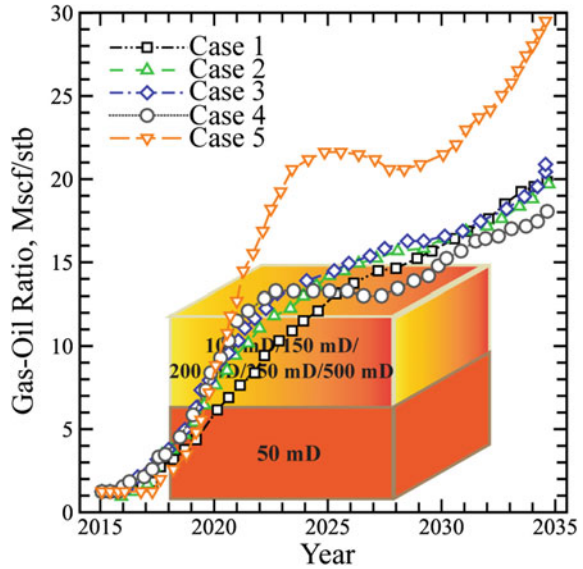
breakthrough time was not considerably delayed by increasing the permeability of the bottom layer. The main changes in breakthrough time occurred between Cases 3–4.

As discussed in previous section, the foam generation can reduce the gas mobility, and therefore, it can also delay the breakthrough time. However, in the scenario below, the increasing permeability ratio did not reduce the breakthrough time significantly. Hence, these results are very contradictory. Fig. 5 shows the gas–oil ratio behavior for all foam cases when the high-permeable layer was located on the top. These results show that the foam generation had a negligible effect on the ratio, because due to the high permeability factor, the gas mobility reduction overcomes effect of foam. The behavior of gas–oil ratio in Case 5 is quite consistent with this statement.

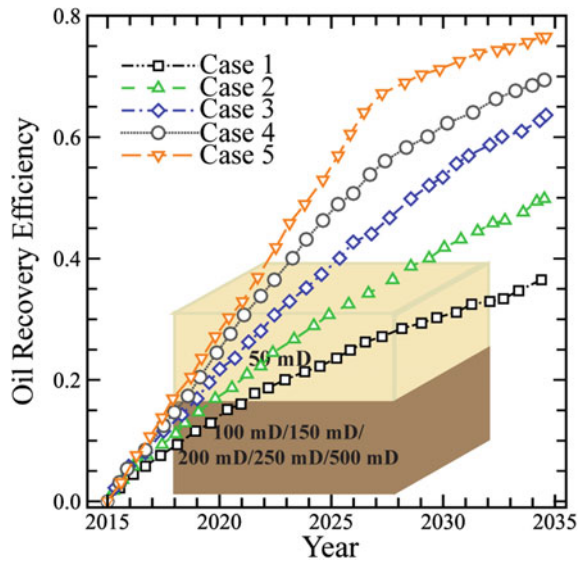
### 3.3 Recovery Ratio

The “strong” foam leads to a significant gas mobility reduction, and therefore, it increases the sweep efficiency and recovery factor [10]. The oil recovery efficiency with the high-permeable layer located in the bottom is illustrated in Fig. 6. This figure shows that the recovery factor increased significantly when the permeability ratio was modified from Case 2 to Case 3. This behavior implies that in the third case, the condition for “strong” foam generation was satisfied. In fact, the recovery was dramatically improved in the last two cases, as we can see from the figure below. Such remarkable results suggest that with increase in the permeability layer

**Fig. 5** Gas–oil ratio (high permeability at top)



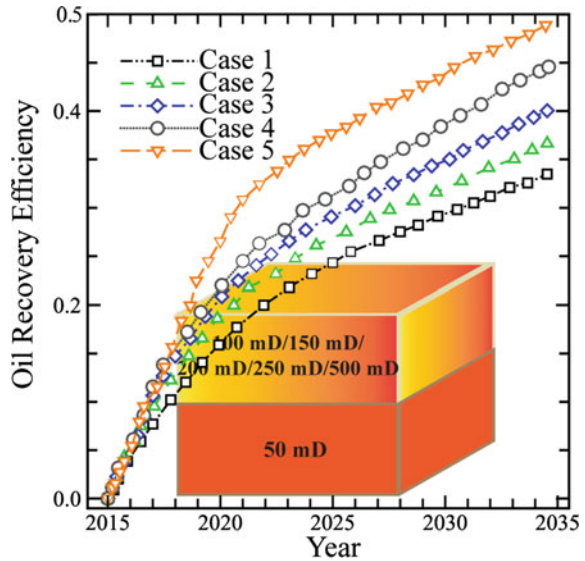
**Fig. 6** Oil recovery (high permeability at bottom)



in the bottom of the reservoir, and having foam prevailing on top, we significantly delay the gas breakthrough. This, in turn, results in high oil recovery.

As shown in Fig. 7, the oil recovery did not benefit from the configuration, where the high-permeable layer was located on top. As a matter of fact, the figure shows that there were no significant changes when permeability ratio shifted from

**Fig. 7** Oil recovery (high permeability at top)



Case 2 to Case 3 and so forth. The comparison between the two different reservoir configurations suggests that foam had a detrimental effect on the recovery due to overriding phenomenon of the gas phase.

## 4 Conclusion

This study illustrates a number of cases, where the impact of foam generation processes has been examined and compared to their gas injection counterparts. The results obtained were discussed for a scenario where the low-permeable layer is on top of the formation, and the results obtained were discussed for a scenario where the high-permeable layer was on top of the low-permeable one. The following conclusion was drawn from this study:

- The foam that was generated in the high-permeable zone being located in the top layer was weaker than in the “vice versa” case. The gas mobility reduction factor behavior was an appropriate proof for this, because the gas override phenomena occurred and gas tended to go upward in the reservoir.
- The strength of foam was enhanced with increasing the permeability ratio between two layers (heterogeneity). However, there was a threshold ratio value, above which the mobility reduction factor did not change significantly. As such, the results of gas mobility reduction factor and oil recovery testify this conclusion.

- The foam generation has a great effect on breakthrough time and gas–oil ratio, especially when the strong foam was generated in case of low-to-high permeability scenario.
- The oil recovery was maximized by increasing the permeability ratios in reservoirs with low-to-high permeability configuration. However, in case of high-to-low permeability configuration, the oil recovery was not affected significantly.

**Acknowledgements** The authors are grateful to Dr. Masoud Rashidi and Department of Petroleum Engineering at Universiti Teknologi PETRONAS for graduate assistantship support.

## References

1. G. J. Hirasaki, “The Steam-Foam Process—Review of Steam-Foam Process Mechanisms,” *Soc. Pet. Eng.*, p. SPE-19518-MS, 1989.
2. W. R. Rossen, “Foam Generation at Layer Boundaries in Porous Media,” *SPE J.*, vol. 4, no. 4, pp. 409–412, 1999.
3. A. H. Falls, G. J. Hirasaki, T. W. Patzek, D. A. Gauglitz, D. D. Miller, and T. Ratulowski, “development of a mechanistic foam simulator.pdf,” *Soc. Pet. Eng.*, 1988.
4. T. Dickson, G. Hirasaki, and C. Miller, “Mobility of Foam in Heterogeneous Media: Flow Parallel and Perpendicular to Stratification,” *SPE J.*, vol. 7, no. January, pp. 1–4, 2002.
5. A. Afsharpoor, G. S. Lee, and S. I. Kam, “Mechanistic simulation of continuous gas injection period during surfactant-alternating-gas (SAG) processes using foam catastrophe theory,” *Chem. Eng. Sci.*, vol. 65, no. 11, pp. 3615–3631, 2010.
6. E. Ashoori, T. van der Heijden, and W. Rossen, “Fractional-Flow Theory of Foam Displacements With Oil,” *SPE J.*, vol. 15, no. April, pp. 20–22, 2010.
7. V. Q. Le, Q. P. Nguyen, A. W. Sanders, and T. Dow, “A Novel Foam Concept with CO<sub>2</sub> Dissolved Surfactants,” in *The SPE/DOE Improved Oil Recovery Symposium held in Tulsa, Oklahoma, 19–23 April, 2008*, pp. 1–15.
8. H. L. Stone, “A Simultaneous Water and Gas Flood Design with Extraordinary Vertical Gas Sweep,” in *Proceedings of SPE International Petroleum Conference in Mexico, 2004*.
9. W. Rossen, C. van Duijn, Q. Nguyen, C. Shen, and A. Vikingstad, “Injection Strategies To Overcome Gravity Segregation in Simultaneous Gas and Water Injection Into Homogeneous Reservoirs,” *SPE J.*, vol. 15, no. March, 2010.
10. H. Hematpur, M. Karimi, and M. Rashidi, “A brief review on foam flow modeling through porous media,” *Int. J. Pet. Geosci. Eng.*, pp. 104–119, 2014.

**Part II**  
**Enhanced Oil Recovery**

# Pressure-Transient Behavior of Injection/Falloff Tests

A.D. Habte, M. Onur, I.B.M. Saaid and T.N. Ofei

**Abstract** Pressure-transient tests can provide useful information for characterization and evaluation of reservoirs under secondary and tertiary processes if they are properly designed and analyzed. In this work, we present the dimensionless pressure and pressure-derivative behavior of gas injection and falloff periods following water injection with skin and outer-boundary effects. To generate the bottom-hole flowing pressure, Laplace transform finite difference (LTFD) method with quasi-stationary assumption is used. The solution method decouples the saturation and pressure equations that describe slightly compressible three-phase flow. The pressure equation is solved using LTFD method, whereas the saturation equation is solved separately using the upwind scheme finite volume method, which is Riemann solver-free. As expected, skin effect is significant in the early times for gas injection period following water–oil displacement, but it becomes insignificant as time increases. For gas injection period following both favorable and unfavorable water–oil mobility ratio displacement with positive skin, the pressure drop starts decreasing after sometime as the front approaches the skin zone boundary, which results in negative derivative values. The effect of outer-boundary condition is also significant for gas injection period following unfavorable water–oil displacement. The pressure drop starts decreasing as the constant-pressure outer-boundary starts being felt. This leads to an increase in injectivity. However, the no-flow boundary condition exhibits a resistance in flow that leads to a reduction in injectivity.

---

The original version of this chapter was revised: For detailed information please see Erratum. The erratum to this chapter is available at [10.1007/978-981-10-3650-7\\_7](https://doi.org/10.1007/978-981-10-3650-7_7)

---

A.D. Habte (✉) · I.B.M. Saaid · T.N. Ofei  
Department of Petroleum Engineering, Universiti Teknologi PETRONAS,  
Bandar Seri Iskandar, Perak 32610, Malaysia  
e-mail: azeb.habte@utp.edu.my

M. Onur  
Department of Petroleum Engineering, University of Tulsa, Tulsa, Oklahoma, USA

### List of symbols

B	Formation volume factor, v/v
c	Isothermal fluid compressibility, $\text{psi}^{-1}$
h	Thickness, ft
k	Absolute permeability, md
p	Pressure, psi
r	Radial distance, ft
S	Saturation, fraction
t	Time, h
$\mu$	Viscosity, cp
$\rho$	Density, lbm/ft
$\phi$	Porosity, fraction
$\Delta$	Difference operator

### Subscript

f	Formation
g	Gas
i	Initial
o	Oil
r	Relative
w	Water

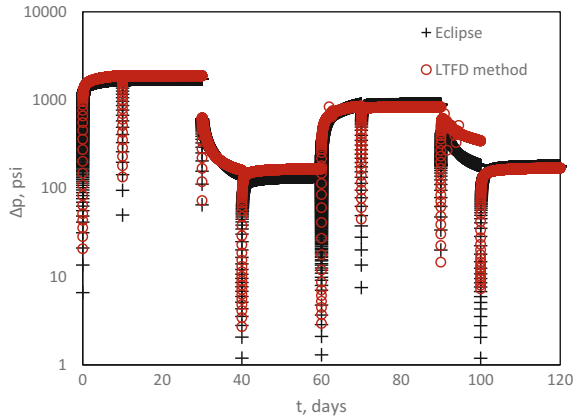
## 1 Introduction

In our previous work [1], a mathematical model for water injection problem was formulated by decoupling the saturation and pressure equations. To determine the saturation profile at any time, the well-known Buckley–Leverett [2] frontal advance formula for two-phase flow is used, whereas the pressure equation is solved using Laplace transform finite difference method with a quasi-stationary assumption. The solution allows one to perform calculation at times of interest, and no iteration is needed as that of the standard numerical methods. The model simulates pressure-transient tests with multiple-rate injection and falloff periods accurately and efficiently.

Because the solution gives accurate results for variable-rate tests, it was successfully extended to immiscible water alternating gas (IWAG) injection problem to predict the bottom-hole flowing pressure during injection and falloff tests. To approximate the saturation profile for the case of three-phase flow, a finite volume method with upwind scheme for hyperbolic conservation laws is used [3, 4]. The method is accurate and simple, in that it is free from Riemann solver. For an accurate simulation of bottom-hole flowing pressure at early times, logarithmic



**Fig. 1** Comparison of pressure drop from the LTFD method and numerical (Eclipse) method for IWAG injection



gridding in solving both saturation and pressure equations is used. In the solution, the results obtained at the end of a flow period are used as the initial condition for the successive flow period and the saturation profile is considered stationary during falloff period. It was shown that despite the assumption of incompressible fluid for gas phase in the calculation of saturation and quasi-stationary, the comparison of the pressure and pressure-derivative curves from our model (LTFD) and Eclipse 100 shows a good match. Figure 1 shows the pressure drop comparison of our model (LTFD) and Eclipse 100 for two (2) WAG cycles with test schedule presented in Table 1 [5]. As is shown in the figure, the two graphs match well.

In this report, the pressure-transient behavior of water injection/falloff periods and gas injection/falloff periods following water in the presence of skin and constant-pressure outer-boundary condition in terms of dimensionless variables is studied. Stenger et al. [6] presented interpretation of pressure falloff test acquired from two vertical IWAG injection wells in a carbonate reservoir using the concept of radial composite model with two zones. They showed that at early times, the falloff pressure-derivative curve of water injection following gas shows a hump, and a straight line with slope of positive quarter (+1/4 slope line) is observed instead of a zero slope on the falloff-derivative curve following water injection

**Table 1** Flow period

Time period, days	Test
0–10	1st water injection
10–30	1st water falloff
30–40	1st gas injection
40–60	1st gas falloff
60–70	2nd water injection
70–90	2nd water falloff
90–100	2nd gas injection
100–120	2nd gas falloff

period which is an indication of a progressive mixing of injected water with gas (high mobility). However, their study does not include effects of skin and outer-boundary condition, which are inevitable in real well test data.

Water and gas are injected alternately into an oil reservoir with 4500 STB/D injection rate and 1:1 WAG ratio for 10 days, and each flow period is followed by falloff period for 20 days. Favorable ( $M = 0.07$ ) and unfavorable ( $M = 2.045$ ) water–oil mobility ratios are considered. Skin factor values of 3 and  $-1$  are investigated to understand the dimensionless pressure and pressure-derivative signature of injection wells in the presence of skin.

## 2 Mathematical Model

### 2.1 Saturation Equation

For a nonlinear problem with discontinuity, the solution to the quasi-linear problem might converge to a function that is not a weak solution of the problem (i.e., it does not satisfy the entropy condition). Leveque (1992) [7] suggested the use of the conservative method starting from the conservation equation.

The saturation equation for two conservation laws can be written as follows:

$$\frac{\partial}{\partial T}u + \frac{\partial}{\partial R}f(u) = 0 \quad (1)$$

where

$$u = \begin{bmatrix} S_w \\ S_g \end{bmatrix} \quad (2)$$

$$f = \begin{bmatrix} f_w \\ f_g \end{bmatrix} \quad (3)$$

$$T = \frac{q_t t}{\pi h \phi r_e^2} \quad (4)$$

$$r_D = \frac{r}{r_e} \quad (5)$$

$$R = r_D^2 \quad (6)$$

and

- $S_m$  = saturation of m-phase
- $f_m$  = fractional flow of m-phase
- $\phi$  = porosity
- $q_t$  = total flow rate

Equation 1 is a nonlinear equation of systems (not scalar) where the fractional flow  $f$  is a function of saturation  $u$ . The standard first-order upwind scheme solution for a hyperbolic conservation laws (Eq. 1) has the form:

$$u_i^{n+1} = u_i^n - \frac{\Delta T}{\Delta R_i} (f(u_i^n) - f(u_{i-1}^n)) \tag{7}$$

where

$$u_i^n = \frac{1}{\Delta R_i} \int_{R_i - (1/2)\Delta R_i}^{R_i + (1/2)\Delta R_i} u(R, T^n) dR \tag{8}$$

$i$  and  $n$  are grid and time step indices, respectively.

The stability and convergence of the method are guaranteed by CFL (Courant) number defined as follows:

$$v = \frac{\Delta T}{\Delta R} \max_i |\eta^i| \tag{9}$$

where  $\eta$  is the wave speed [4].

### 2.2 Pressure Equation

As mentioned before, the diffusivity equation for a radial system is solved using LTFD method, and the saturation-dependent coefficients calculated from Eq. (7) are introduced at each grid block and time. The pressure solution is presented below:

At  $t = 0$ , i.e.,  $r = r_w$  (see Fig. 2), the pressure solution in Laplace space is given as follows [1]:

$$\left( 1 + \frac{k C_D}{k_s \hat{M}} \Delta Z_1 s \right) \bar{p}_{wD} - \bar{p}_{D1} = \frac{k}{k_s} \left( \frac{\Delta Z_1}{s} + \frac{C_D \Delta Z_1}{\hat{M}} p_{wD}(t_D = 0) \right) \tag{10}$$

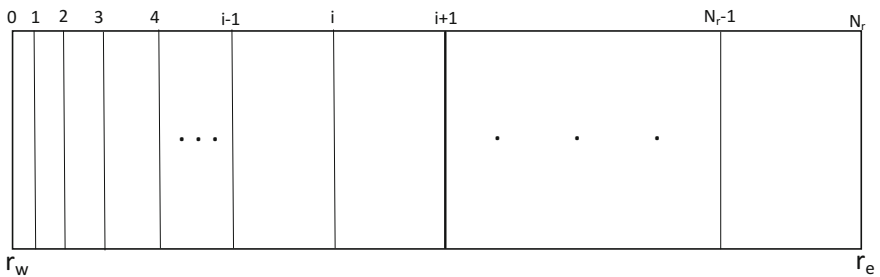


Fig. 2 Point-centered logarithmic gridding

For the interior grid points, the difference equation becomes

$$-T_{i-1}\bar{p}_{D_{i-1}} + (T_i + T_{i-1} + \tilde{V}_i s)\bar{p}_{D_i} - T_i\bar{p}_{D_{i+1}} = \tilde{V}_i p_{D_i}(t_D=0) \quad (11)$$

where we have defined

$$T_i = \frac{\hat{\lambda}_i D_i}{\Delta Z_{i+1}} \quad (12)$$

$$T_{i-1} = \frac{\hat{\lambda}_i D_{i-1}}{\Delta Z_i} \quad (13)$$

$$\Delta Z_{i+1} = Z_{i+1} - Z_i \quad (14)$$

$$\Delta Z_i = Z_i - Z_{i-1} \quad (15)$$

$$\tilde{V}_i = e^{2Z_i} \Delta Z_i c_{iD_i} \quad (16)$$

For no-flow outer-boundary condition ( $i = N_r$ ) by setting  $T_{N_r} = 0$ , Eq. 11 becomes

$$-T_{N_r-1}\bar{p}_{D_{N_r-1}} + (T_{N_r-1} + \tilde{V}_{N_r} s)\bar{p}_{D_{N_r}} = \tilde{V}_{N_r} p_{D_{N_r}}(t_D = 0) \quad (17)$$

For constant-pressure outer-boundary condition, the pressure at grid point  $i = N_r$  is known from the boundary; therefore, the pressure difference equation needs to be modified for the grid point  $i = N_r - 1$ . Thus, the resulting difference equation at grid point  $i = N_r - 1$  becomes

$$-T_{N_r-2}\bar{p}_{D_{N_r-2}} + (T_{N_r-1} + T_{N_r-2} + \tilde{V}_{N_r-1} s)\bar{p}_{D_{N_r-1}} = \tilde{V}_{N_r-1} p_{D_{N_r-1}}(t_D = 0) \quad (18)$$

where the dimensionless terms are defined by:

$$p_D = \frac{\hat{\lambda}_i h}{141.2 q_w B_w} \Delta p \quad (19)$$

where  $\Delta p$  is the pressure change defined as  $\Delta p = p_{wf} - p_i$  for injection period and  $\Delta p = p_{ws} - p_i$  for falloff period, and

$$t_D = \frac{0.0002637 \hat{\lambda}_o}{\phi \hat{c}_{1o} r_w^2} t \quad (20)$$

$$r_D = \frac{r}{r_w} \quad (21)$$

$$\lambda_{tD} = \frac{\lambda_t(r, t)}{\hat{\lambda}_o} \quad (22)$$

$$\lambda_t(r, t) = k(r) \left( \frac{k_{rw}(r, t)}{\mu_w} + \frac{k_{ro}(r, t)}{\mu_o} + \frac{k_{rg}(r, t)}{\mu_g} \right), \quad r_w \leq r \leq r_f \quad (23)$$

$$\lambda_t(r, t) = \hat{\lambda}_o = \frac{k(r)k_{ro}(S_{wi})}{\mu_o}, \quad r_f \leq r \leq r_e \quad (24)$$

$$\hat{\lambda}_t = k \left( \frac{k_{rw}(S_w)}{\mu_w} + \frac{k_{rg}(S_g)}{\mu_g} + \frac{k_{ro}(1 - S_w - S_g)}{\mu_o} \right) \quad (25)$$

For water injection periods,

$$\hat{\lambda}_t = k \left( \frac{k_{rw}(S_{wi})}{\mu_w} + \frac{k_{rg}(S_g)}{\mu_g} + \frac{k_{ro}(1 - S_g - S_{wi})}{\mu_o} \right) \quad (26)$$

for gas injection periods.

$$c_{tD} = \frac{c_t(r, t)}{\hat{c}_{to}} \quad (27)$$

$$c_t(r, t) = S_w(r, t)c_w + (1 - S_w(r, t) - S_g(r, t))c_o + S_g(r, t)c_g + c_f \quad (28)$$

$$\hat{c}_{to} = S_{wi}c_w + (1 - S_{wi})c_o + c_f \quad (29)$$

### 3 Results and Discussion

In this section, the dimensionless pressure and pressure-derivative behavior of gas injection following water is presented. The radial direction is discretized into 300 grid blocks logarithmically to ensure that the grid points near the wellbore are refined enough to yield accurate flowing bottom-hole pressures and the Laplace space is inverted to real time numerically using Stehfest algorithm. Other fluid and rock properties are given in Table 2.

#### 3.1 Water Injection and Falloff Periods

A detailed study of the LTFD method for the water injection into an oil reservoir problem and dimensionless pressure and pressure-derivative behavior of water

**Table 2** Fluid and rock properties at average reservoir conditions

Average reservoir conditions	
$p$ , psi 3200	
$T$ , ° F 250	
Fluid and rock properties	
$B_o$ , rb/stb 1.53	$\rho_g$ , lbm/ft <sup>3</sup> 8.01
$B_w$ , rb/stb 1.02	$S_{wi}$ , fraction 0.31
$B_g$ , rb/Mscf 1.035	$S_{gc}$ , fraction 0.06
$\mu_g$ , cp 0.02	$S_{orw}$ , fraction 0.373
$c_o$ , psi <sup>-1</sup> $1.5 \times 10^{-5}$	$S_{org}$ , fraction 0.125
$c_w$ , psi <sup>-1</sup> $2.3 \times 10^{-6}$	$k_{rw}(@S_{or})$ 0.09
$c_f$ , psi <sup>-1</sup> $3 \times 10^{-6}$	$k_{rg}(@S_{or})$ 0.45
$\rho_o$ , lbm/ft <sup>3</sup> 36.7	$k_{ro}(@S_{wi})$ 0.88
$\rho_w$ , lbm/ft <sup>3</sup> 70	$k_{ro}(@S_{gi})$ 0.88
$h$ , ft 56	$k$ , md 200
<b>Favorable mobility ratio</b>	$k_s$ , md 56.46 (for $S = 3$ )
$\mu_o$ , cp 2.0	$k_s$ , md 1311 (for $S = -1$ )
$\mu_w$ , cp 0.48	$\phi$ , fraction 0.2
<b>Unfavorable mobility ratio</b>	<b>Infinite acting reservoir</b>
$\mu_o$ , cp 3.0	$r_e$ , ft 10,000
$\mu_w$ , cp 0.15	<b>Constant-pressure outer-boundary condition</b>
	$r_e$ , ft 700

injection and falloff periods with skin and outer-boundary effects is presented in [1]. At very early time, if wellbore storage has no effect, the pressure-derivative curve will have a horizontal line with a value inversely proportional to the endpoint mobility of oil [8, 9]. The value of the derivative can be mathematically expressed as follows [10]:

$$\Delta p' = \frac{70.6q\mu_o B}{kk_{ro}(S_{wi})h} \quad (30)$$

Hence, the dimensionless pressure-derivative value based on the definition in Eq. 19 becomes

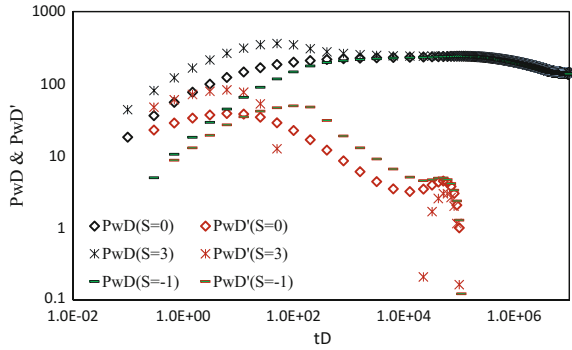
$$p'_{wD} = 0.5\hat{M} \quad (31)$$

However, if the skin effect is present near the wellbore, the dimensionless pressure derivative has a value that can be estimated from [1]:

$$p'_{wD} = 0.5\hat{M} \frac{k}{k_s} \quad (32)$$

As time becomes sufficiently large and the area completely flooded by water is significant, there will be a second horizontal line on the derivative curve following a transition period that reflects the endpoint mobility of water. The pressure-derivative value on the line can be determined as follows:

**Fig. 3** Dimensionless pressure and pressure-derivative behavior of gas injection period with and without skin factor ( $\widehat{M} = 0.43$ )



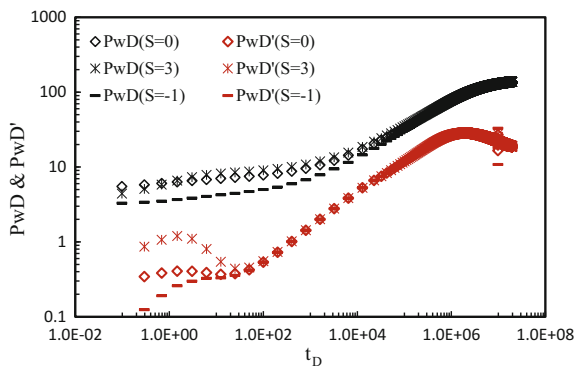
$$\Delta p' = \frac{70.6q\mu_w B}{kk_{rw}(1 - S_{or})h} \tag{33}$$

Applying the dimensionless pressure-derivative definition to Eq. 19 gives

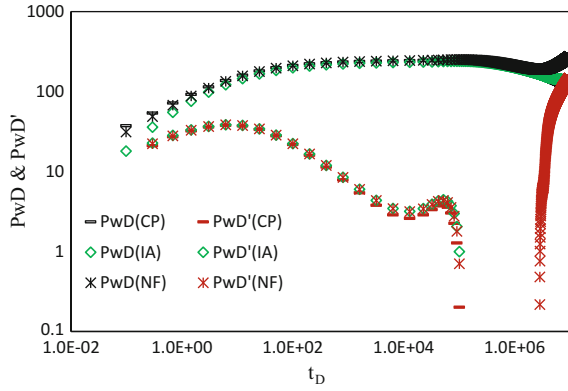
$$p'_{wD} = 0.5 \tag{34}$$

During falloff, assuming that the previous injection period is long enough to establish a completely flooded zone around the wellbore, the first radial flow on the derivative curve reflects the endpoint mobility of water and the dimensionless pressure derivative has a value of 0.5 as the infinite acting period (Eq. 8). As time increases, for a reservoir that is large enough so that the outer-boundary effect will not be felt early, the well starts detecting the oil zone and the dimensionless pressure derivative can be expressed by Eq. 6 (Figs 3 and 4). This behavior is shown in Figs. 5 and 6. Skin factor has insignificant effect during falloff period, except at very early time. The very early time dimensionless pressure derivative can be approximated using

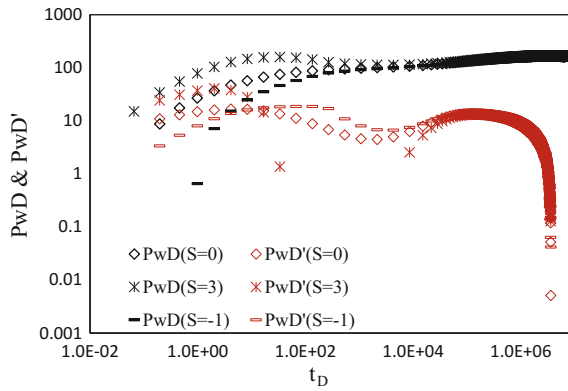
**Fig. 4** Dimensionless pressure and pressure-derivative behavior of gas injection falloff period with and without skin factor ( $\widehat{M} = 0.43$ )



**Fig. 5** Dimensionless pressure and pressure-derivative behavior of gas injection period with constant-pressure outer-boundary condition ( $\hat{M} = 0.43$ )



**Fig. 6** Dimensionless pressure and pressure-derivative behavior of gas injection period with and without skin factor ( $\hat{M} = 2.05$ )



$$P'_{wD} = 0.5 \frac{k}{k_s} \tag{35}$$

For constant-pressure outer-boundary case, the pressure at late times starts decreasing which results in negative dimensionless pressure-derivative value expressed in Eq. 13, whereas for the favorable mobility ratio case, the pressure increases with a constant positive slope which can also be determined from Eq. 13 [9].

$$P'_{wD} = \frac{1}{2} (1 - \hat{M}) \tag{36}$$



### 3.2 Gas Injection and Falloff Periods

For the gas injection, the pressure and saturation distribution at the end of the water injection falloff period is used as the initial conditions in Eqs. 10, 11, 17, and Eq. 7, respectively. Figure 3 presents the dimensionless pressure and pressure derivative of the gas injection period with and without skin factor for favorable endpoint mobility ratio. At early times, the pressure and pressure-derivative curves of the positive skin are higher than the curves of the zero skin curves and the negative skin curves have lower values, which are expected because skin causes an additional pressure drop. In all cases, the pressure change starts to decrease after sometimes and the derivative curves exhibit negative values as time increases [5]. This is due to the high mobility and compressibility of gas, which makes it easier to be injected with less pressure drop.

Due to the high mobility contrast between gas and the reservoir fluids, the well starts detecting the injected fluid at early times and the pressure derivative exhibits a value inversely proportional to the harmonic average of the total mobility in the area where mobility changes rapidly with time [5]. Therefore, the early time dimensionless pressure-derivative values can be estimated from Eq. 31, where the mobility ratio is defined as follows:

$$\widehat{M} = \frac{\widehat{\lambda}_g}{\bar{\lambda}_t} \quad (37)$$

where

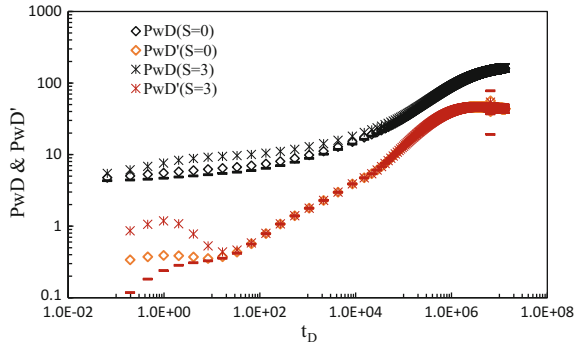
$$\widehat{\lambda}_g = \frac{k_{rg}(S_{g,max})}{\mu_g} \quad (38)$$

and

$\bar{\lambda}_t$  is the harmonic average of the total mobility in the area flooded by gas. However, this period is short and can be dominated by effect of wellbore storage. When skin factor is incorporated, the value can be approximated by Eq. 32, where the mobility ratio is defined in Eq. 37.

Similar to the water injection falloff period, the saturation distribution during the gas injection falloff period is obtained from the end of the injection period and it is considered to be stationary. The dimensionless pressure and pressure-derivative curves for the falloff period with and without skin are presented in Fig. 4. Figure 4 shows that the early time data reflect the information in the completely flooded zone. For the case without skin ( $S = 0$ ), the dimensionless pressure derivative converges to a value expressed in Eq. 34, and for the cases with skin factor, the value can be approximated by Eq. 35. However, the period occurs very early and the duration is short, thus difficult to see a stabilized horizontal line. Following the early time period, there is a long transition period, which is caused by the high

**Fig. 7** Dimensionless pressure and pressure-derivative behavior of gas injection falloff period with and without skin factor ( $\widehat{M} = 2.05$ )



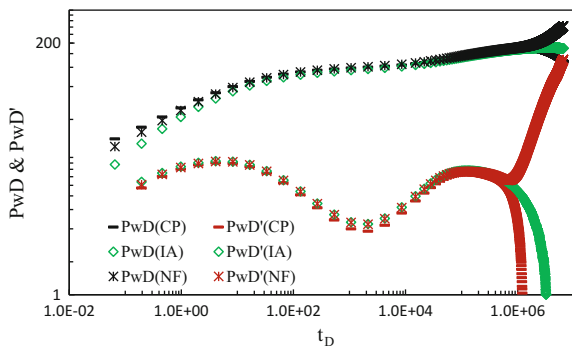
mobility of gas, which results in highly unfavorable mobility ratio. As time increases, the pressure derivative exhibits a value which is inversely proportional to the oil zone and the dimensionless pressure derivative can be estimated from Eq. 31.

Figure 5 shows the dimensionless pressure and pressure-derivative behavior for different outer-boundary conditions. The curves do not show significant difference in the transient behavior of the injection period from the one presented for infinite acting reservoir in Fig. 3 for  $S = 0$ .

For the unfavorable water–oil mobility ratio case, the pressure drop increases for longer period and then starts to decrease, which causes negative pressure-derivative values. However, the positive skin factor curve exhibits two negative derivative zones (in the middle and late times). Similar to the water injection case, when the front approaches the radius of skin, it feels the sudden change of mobility from low to high, which causes the decrease in the pressure drop and negative derivative values (Fig. 6). After sometime, the pressure adjusts to the undamaged zone permeability and the pressure drop starts to increase. As time increases, it becomes easier for the gas to flow with lower pressure drop, thus the negative values in the derivative curve at late times.

Figure 7 shows the falloff period pressure and pressure-derivative signature. As is shown in the figure, skin has insignificant effect, except at early times.

**Fig. 8** Dimensionless pressure and pressure-derivative behavior of gas injection period with constant-pressure outer-boundary condition ( $\widehat{M} = 2.05$ )



Outer-boundary effect is significant on the pressure and pressure-derivative curves of a gas injection period following unfavorable mobility water injection at late times (Fig. 8). At late times, the pressure curve shows a significant reduction in the pressure drop compared to the infinite acting reservoir case in Fig. 6. This is because the water that is injected before gas moves faster than oil, which reduces the resistance for gas to flow, thus a reduction in the pressure drop.

## 4 Conclusions

The dimensionless pressure and pressure-derivative behavior of gas injection following water with and without skin and with outer-boundary effect is studied. The effect of skin and outer-boundary condition on the transient behavior depends on whether the previous water–oil displacement is favorable or unfavorable. For the favorable mobility case, the skin effect is significant in middle times, whereas the effect of constant-pressure outer-boundary condition is insignificant. For the unfavorable mobility case, as that of the water injection period, positive skin factor causes the pressure drop to decrease in the middle time, which results in negative pressure-derivative values. When the wellbore starts feeling the constant-pressure outer boundary, the pressure drop decreases significantly, which indicates high gas injectivity. However, for the case of no-flow outer-boundary condition, the pressure drop starts increasing in both favorable and unfavorable mobility ratio injections, which leads to a reduction in injectivity.

**Acknowledgements** The authors would like to thank the Universiti Teknologi PETRONAS (UTP) for providing the necessary financial support and research facility to conduct this study.

## References

1. A. D. Habte, and M. Onur, “Laplace-Transform Finite-Difference and Quasistationary Solution Method for Water-Injection/Falloff Tests,” Society of Petroleum Engineers. doi:[10.2118/168221-PA](https://doi.org/10.2118/168221-PA).
2. S. E. Buckley, and M. C. Leverett, “Mechanism of Fluid Displacement in Sands,” *Trans., AIME* 146, 107, 1942. doi:[10.2118/942107-G](https://doi.org/10.2118/942107-G).
3. R. J. LeVeque, “Finite-Volume methods for hyperbolic problems,” University of Cambridge, 2004.
4. K. A. Lie, and R. Juanes, “A front-tracking method for the simulation of three-phase flow in porous media,” *Computational Geosciences* 9: 29–59, 2005.
5. A. D. Habte, M. Onur, and I. M. B. Saaid, “Pressure Transient Behavior of Immiscible Water Alternating Gas (IWAG) Injection with and without Relative Permeability Hysteresis Effects,” *Proceedings of the 3rd International Conference on Integrated Petroleum Engineering and Geoscience (ICIPEG)*, Malaysia, Springer, Singapore, 3–5 June, 2014.
6. A. B. Stenger, S. A. Al-Kendi, A. F. Al-Ameri, and A. B. Al-Katheeri, “Interpretation of immiscible WAG Pressure–Falloff Tests,” presented at the Abu Dhabi International Petroleum Exhibition and conference, Abu Dhabi, UAE, 1–4 November 2010, paper SPE 137062.

7. R. J. LeVeque, "Numerical Methods for Conservation Laws," 2nd edn, Birkh user Verlag, Berlin, 1992.
8. M. Abbaszadeh and M. Kamal, "Pressure transient testing of water-injection wells," *SPEE*, vol 4, no. 1, pp. 115–124, 1989, paper SPE 16744-PA.
9. R. B. Bratvold and R. N. Horne, "Analysis of Pressure-Falloff Tests Following Cold-Water Injection," *SPEE* 5 (3): 293–302, 1990, paper SPE-18111-PA.
10. A. M. M. Peres and A. C. Reynolds, "Theory and analysis of injectivity tests on horizontal wells," *SPEJ* 8 (2): 147–159, 2003, paper SPE 84957-PA.

# Evaluation of Bentonite Colloids for Potential Use as an In-Depth Fluid Diversion Agent

Abdelazim Abbas Ahmed, Ismail Mohd Saaid  
and Nur Asyraf Md Akhir

**Abstract** In this study, API-grade bentonite sample was characterized using XRD and FTIR techniques. The effect of gravity and centrifugal sedimentation on bentonite colloid size and size distribution was examined. Also, rheological properties of 1000-, 2000-, and 3000-ppm dispersions were measured using Anton Paar rheometer. Finally, stability and critical salt concentration (CSC) were determined by using Turbiscan Classic. The objective is to evaluate the potential application of these dispersed particles as an in-depth fluid diversion. XRD data indicate the presence of a smectite with minor amounts of impurities such as quartz and dolomite. Sedimentation was found effective for preparing a controlled size dispersion which can be adjusted to target high water production zones. Different colloidal dispersions of different mean hydrodynamic sizes are obtained ranging from 340 nm down to 260 nm in average with less than 8  $\mu\text{m}$  as the maximum diameter. These sizes fall in the range of existing IFD that often used for improving sweep efficiency in heterogeneous rock matrix. Bentonite dispersions exhibited a water-like viscosity at low concentrations studied, which is in favor of IFD. However, increasing salt concentration and temperature sharply increased viscosity. The stability of bentonite colloids is reduced with increasing solution salinity above CSC. In addition, the CSC was found dependent on the colloidal concentrations. At 3000 ppm, bentonite dispersion showed a higher critical salt concentration. For low salinity formation water and low salinity dispersion make-up water, controlled bentonite colloids could be effectively stabilized and transported in porous media and serve as IFD for improving sweep efficiency. However, at higher salinity conditions, bentonite aggregation and stability will become an issue.

---

A.A. Ahmed (✉) · I.M. Saaid · N.A. Md Akhir  
Department of Petroleum Engineering, University Technology Petronas,  
Tronoh, Perak, Malaysia  
e-mail: abdulazim\_abass@yahoo.com

## 1 Introduction

A major issue for the oil and gas industries is the high water production from many fields. Reducing high water production while improving oil recovery from these fields is a key challenge. In-depth fluid diversions (IFDs) have recently emerged and posed a frequent business need for operating companies and research groups [1]. Rather than close wellbore conformance treatment, polymer gels are applied in injector wells for in-depth fluid diversion [2]. Several gel systems have been used, including weak gels, sequential in situ gels, colloidal dispersion gels (CDGs), preformed particle gels (PPGs), and microgels. These gels are mainly different in their size and plugging mechanism [3]. The main objective of IFDs is to preferentially block the high permeable layer (thief zone) and divert the following injected water or chemicals to low permeable unswept zones [4–7]. There are four ideal properties required for IFD: Firstly, the IFD dispersion should have a water-like viscosity to achieve selective injection in high permeable layer; secondly, particle size must be small enough to propagate into formation without sand face plugging; thirdly, particle dispersion stability; and finally, dispersed particles should have capability to plug the thief zones by either swelling, adsorption or log jamming effect. Although IFD has been proved for improving sweep efficiency in heterogeneous reservoirs, application at high temperature is limited, because most of the recently developed IFDs are formulated using polymers with an organic/inorganic cross-linker, which are risky to be applied at very high reservoir temperature (e.g.,  $>100$  °C). In addition, some IFDs are required to cool down the area in the vicinity of the wellbore to create a thermal front that can delay early particle swelling in case of high-temperature conditions [8]. Consequently, there is a need to develop a thermally stable particle for high-temperature applications.

Although bentonite particles are most abundant, naturally occurring, low-cost resource with high thermal stability (up to 200 °C), its application as IFD in rock matrix treatment has not been reported. This paper reports on experiments carried out to characterize and investigate the API-grade bentonite properties for possible use as a novel IFD.

The objective of the present study was to explore the feasibility of using bentonite colloid dispersion, as an in-depth fluid diversion (IFD) for improving oil recovery of heterogeneous oil reservoir. The effect of operating parameters such as initial concentration, salinity, and temperature on the rheological behavior was examined. Different gravity separation methods were conducted to separate dispersed bentonite colloids into defined size fractions.

## 2 Experimental

### 2.1 Materials

A commercial API-grade bentonite samples were used for this study. The samples were obtained from the Australia Bentonite Company and used without any further treatment. Sodium chloride was used in preparation for solution salinity, and ammonium acetate, potassium chloride, and isopropyl were used for determining cation exchange capacity (CEC), which were purchased from Sigma-Aldrich.

### 2.2 Methods

#### 2.2.1 Sample Characterization

##### (a) FTIR Spectra Analysis

The FTIR spectra were gathered with a Thermo Nicolet FTIR spectrometer. The transmittance bands somewhere around 400 and 4000  $\text{cm}^{-1}$  were performed and broke down as shown in Fig. 1. The wide adsorption groups at 3620  $\text{cm}^{-1}$  and 3404 are credited to extending vibrations of structural OH groups of bentonite structure and bounded water, respectively. The groups at 2883  $\text{cm}^{-1}$ , 2159  $\text{cm}^{-1}$ , and 2030  $\text{cm}^{-1}$  are due to organic impurities in the bentonite. The band at 1632  $\text{cm}^{-1}$  is in charge of bending H–O–H vibration in water. The adsorption band at 1031  $\text{cm}^{-1}$  is because of Si–O-twisting vibration. The band relating to Al–Al–OH is seen at 910  $\text{cm}^{-1}$ . A sharp band at 794  $\text{cm}^{-1}$  shows quartz admixture in the

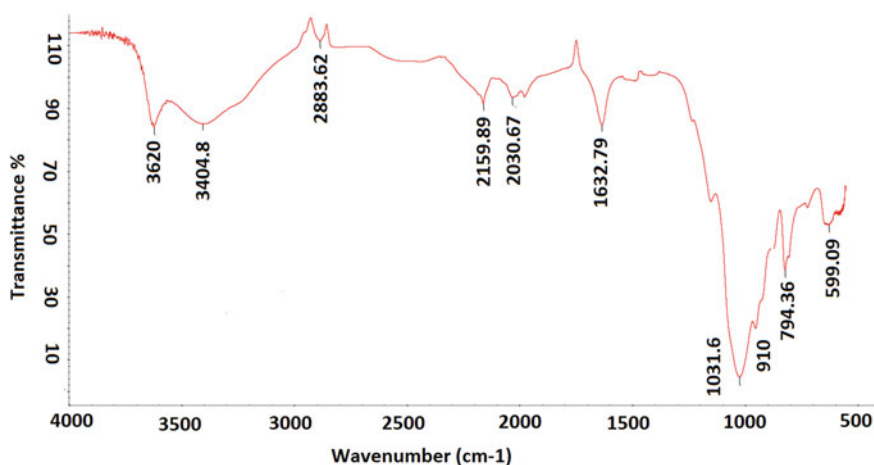


Fig. 1 FTIR spectra for bentonite sample

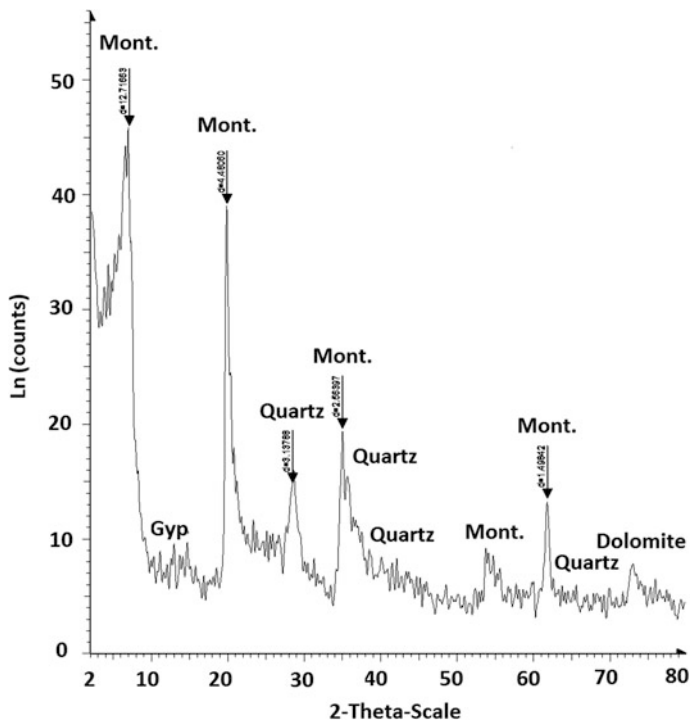


Fig. 2 XRD for bentonite sample

specimen, which has been affirmed likewise by X-ray diffraction. The groups at 599 are because of Al–O–Si-bending vibrations.

(b) X-ray diffraction analysis

The bentonite mineralogy is identified by utilizing XRD investigation (Fig. 2). XRD information demonstrates the vicinity of a smectite (most likely montmorillonite) with minor measures of impurities, for example, quartz, gypsum, and dolomite.

(c) Cation Exchange Capacity (CEC)

The CEC of bentonite sample was determined using the standard method according to ASTM 7503. The ASTM 7503 method involves the displacement of the inter-layer cations with the index cation (Ammonium  $\text{NH}_4$ ). The CEC was 118 meq/100 g.



## 2.2.2 Bentonite Colloid Fractionation

The bentonite sample was separated by gravity using sedimentation and centrifugal techniques. The separation methodology was adopted from Reference [9]. 10 g of bentonite was dispersed in deionized water and stirred for 24 h for hydration. Then, particles were separated by two gravity methods and centrifuged at 1000 and 2000 rpm, and static sedimentation was carried out for 3–7 days. The colloid size distributions of bentonite in all dispersions are determined by dynamic light scattering (DLS).

## 2.2.3 Rheological Properties

Dispersion viscosity measurements were performed using MCR Anton Paar rheometer with a double cap. The viscosity was determined for 1000-, 2000-, and 3000-ppm dispersions at a consistent shear rate  $30 \text{ s}^{-1}$  and at various temperatures extending from 25 to 90 °C.

## 2.2.4 Critical Salt Concentration (CSC)

A Turbiscan Classic was used to determine the CSC of the studied concentrations by the variation in measuring mean value of transmitting light across the sample for different NaCl concentrations. A salt concentration where the mean value of transmitting light started sharply expanding was assumed as CSC.

# 3 Results and Discussions

## 3.1 Bentonite Colloid Fractionation

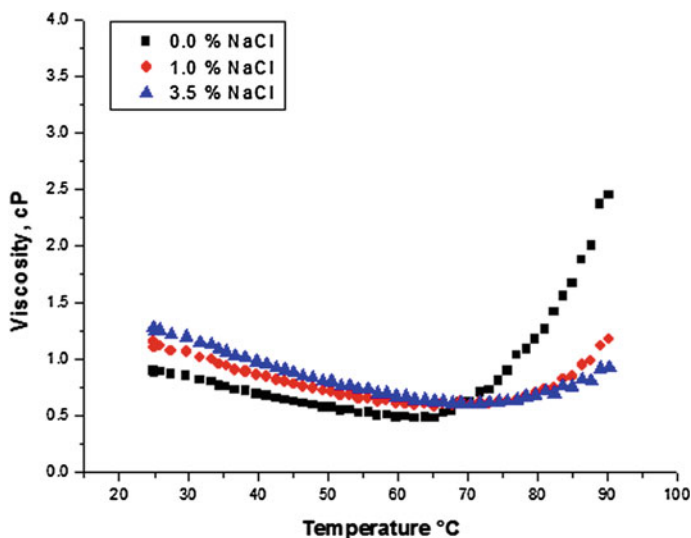
As described in the Methods section, the size of the particles was obtained through DLS at 25 °C. It is obvious that colloid particle size can be reduced by sedimentation or centrifuge methods. Bentonite colloids showed polydisperse and wide particle size distribution curve as shown in Table 1. These results are consistent with the findings in the literature [10, 11]. The results indicate that a narrow distribution curve can be obtained by centrifuge in comparison with sedimentation.

**Table 1** Condition and mean size obtained

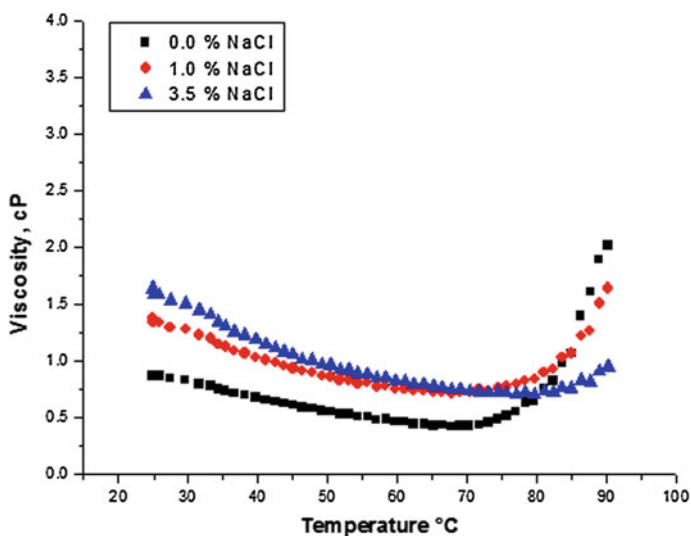
Separation process	Average particle size, nm	Max particle size, nm
Bentonite_1000 RPM_0.5 h	260	≤ 2000
Bentonite_2000 RPM_1 h	295	≤ 1000
Bentonite_3 days sedimentation	340	≤ 8000
Bentonite_7 days sedimentation	260	≤ 7000

### 3.2 Dispersion System Viscosity

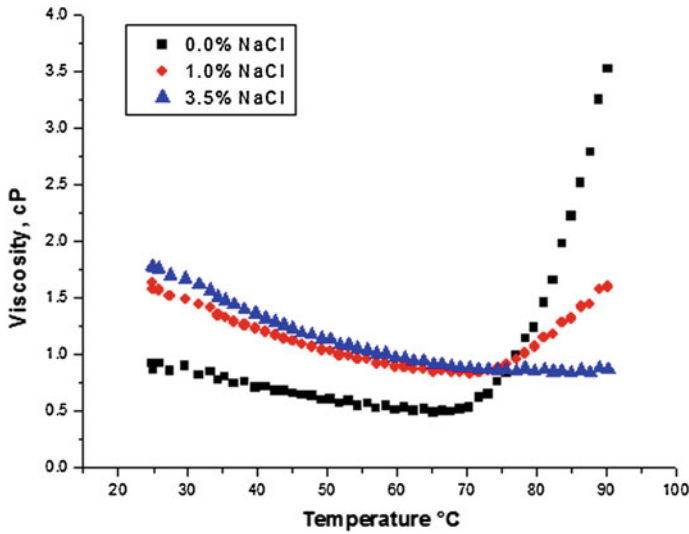
Bentonite colloid dispersion viscosity is dependent on the colloidal concentrations, salinity of the solvent, and temperature. The results shown in Figs. 3, 4, and 5 indicate that increase in concentration and salinity increases apparent viscosity. It is



**Fig. 3** Effect of temperature on 1000 ppm bentonite dispersion at NaCl concentrations 0–3.5% (w/w)



**Fig. 4** Effect of temperature on 2000 ppm bentonite dispersion at NaCl concentrations 0–3.5% (w/w)



**Fig. 5** Effect of temperature on 3000 ppm bentonite dispersion at NaCl concentrations 0–3.5% (w/w)

also found from results that increase in temperature results in a decrease in viscosity of the dispersions. However, at a transition temperature ( $\sim 70$  °C), dispersion viscosity started to increase sharply. The reason is that bentonite particles' interaction and face-to-edge association are much more and the resultant combination causes aggregation of particles, so the viscosity is increased [12, 13]. As the result of face-to-edge association collapsed and face-to-face association enhanced, the viscosity after transition temperature with higher salt concentration showed a lesser value.

### 3.3 Critical Salt Concentration

The particles in a colloidal suspension might be dispersed or might form 3D network structures having basic units that are in the range of colloidal dimensions. A sol is a liquid or semi-liquid colloidal system [14]. A gel is a colloidal system having a continuous network structure and a finite yield stress. A surely understood idea in the hypothesis of colloids that is utilized to assess the ionic quality impact of a specific electrolyte on the stability of a colloid is the critical salt concentration (CSC) [15]. As indicated by DLVO hypothesis, the CSC quality is characterized as the electrolyte concentration at which the repulsion forces is less than or equal to the total attractive energy [16]. These aggregations could be distinguished by measuring various mean values of transmitting light over time for the middle sample portion. Table 2 shows the measured CSC for 1000, 2000, and 3000 ppm

**Table 2** CSC from variation of mean value of transmission

Concentrations	CSC, wt% NaCl
1000 ppm	0.01
2000 ppm	0.025
3000 ppm	0.05

bentonite dispersions after 1 h. It can be seen that particles coagulate for NaCl concentration higher than 0.01, 0.035, and 0.05% (w/w) for 1000, 2000, and 3000 respectively.

## 4 Conclusions

Bentonite colloid dispersions in a different size portion were prepared in this study. The average particle size and size distribution depend on a sedimentation period and centrifugation. Bentonite particle could be separated into a desired particle of IDF (>10  $\mu\text{m}$ ). The rheological behavior of bentonite dispersion systems as a function of concentration and salinity is investigated at various temperatures of 25–90 °C. The results reveal that the viscosity of systems increases obviously with the addition of NaCl and decrease in temperature. In contrast, above a transition temperature, viscosity decreases with the addition of NaCl. Aggregation kinetics was used to estimate the effect of salinity on the colloidal stability of bentonite dispersion. The critical salt concentration (CSC) was also determined for various concentrations. It was found that the CSC increases with increasing bentonite concentrations. In terms of particle size, bentonite colloid could be controlled within the IFD size range. However, for temperature higher than transition temperature and salinity higher than CSC, bentonite colloids could not be used before treatment, because dispersion system stability is important for transporting the particles deep into the formation.

## References

1. Ahmed, A. A, Saaid, I. M., (2015), In-depth Permeability Modifier for Improvement of Sweep Efficiency in a Heterogeneous Oil Reservoir: A Review, *RJASET*, 9(1): pp. 18–28.
2. Han, M., Alshehri, A., Krinis, D. and Lyngra, S., 2014, State-of-the-art of in-depth fluid diversion technology: enhancing reservoir oil recovery by gel treatments, SPE 172186, presented at SPE Saudi Arabia section annual technical symposium and exhibition, Alkhobar, Saudi Arabia.
3. Delshad, M., Sepehrnoori, K., Bai, B. and Hu, Y., 2013, Water Management in Mature Oil Fields using Preformed Particle Gels, SPE 165356-MS, presented at SPE Western Regional & AAPG Pacific Section Meeting 2013 Joint Technical Conference, pp. 19–25 April, Monterey, California, USA.

4. Mack, J. and J. Smith, 1994. In-depth colloidal dispersion gels improve oil recovery efficiency. Proceeding of the SPE/DOE Improved Oil Recovery Symposium. Tulsa, Oklahoma, USA, April pp. 17–20.
5. Bai, B., 2007. Conformance control by preformed particle gel: Factors affecting its properties and applications. Paper SPE 89468, Aug 2007, pp: 415–421.
6. Robert, D.S. and R.Z. Laua, 2011. Reservoir conformance improvement. Society of Petroleum Engineers, Richardson, TX.
7. Spildo, K., Skauge, A., and Aarra, M., 2009, A new polymer application for north sea reservoirs, SPE 113460, presented at the SPE/DOE Symposium on improving oil recovery, Tulsa, USA.
8. Seright, R., Zhang, G., Akanni, O., Wang, D., 2012, A comparison of polymer flooding with in-depth profile modification, SPE, Presented at Canadian unconventional resources conference, Calgary, Canada.
9. Norrfors, k., Bouby, M., Heck, S., Finck, N., Marsac, R., Schäfer, T., Geckeis, H. and Woldb, S., 2015, Montmorillonite colloids: I. Characterization and stability of dispersions with different size fractions, applied clay science, pp. 179–189.
10. Neretnieks, I., Liu, L. and Moreno, L., 2009, Mechanisms and models for bentonite erosion, Technical Report, Royal Institute of Technology, KTH.
11. Frimmel, F., Kammer, F. and Flemming, H., 2007, Colloidal Transport in Porous Media, Springer Science & Business Media, pp 39.
12. Annis, R. 1997. Retention of synthetic-based drilling material on cuttings discharged to the Gulf of Mexico. Technical Report (API), Washington, DC.
13. Alderman, N., Gavignet, D. and Maitland, G., High Temperature, High Pressure Rheology of Water-Based Muds, SPE18035, presented at the SPE 63rd Annual Technical Conference and Exhibition, Houston, Texas, USA.
14. Arthur, R., 2011, Handling of Hydrogeochemical Relations in Erosion and Swelling Pressure Models for the Buffer and Backfill., Part I. A Review of Surface-Chemical Concepts Used in Models of Buffer Erosion. Report No., STUK-TR 10. Helsinki, Finland.
15. Hiemenz, P., 1986. Principles of Colloid and Surface Chemistry, second ed., Marcel Dekker, New York.
16. García-García, S., Wold, S. and Jonsson, M., 2007, Kinetic determination of critical coagulation concentrations for sodium- and calcium-montmorillonite colloids in NaCl and CaCl<sub>2</sub> aqueous solutions, JCIS, pp. 512–519.

# Investigating Effect of Chemical Composition on Emulsion Stability and Rag Layer Growth During Separation

Ahmed Basyouni, Khaled A. Elraies and Hussain H. Al-Kaieym

**Abstract** Alkaline–surfactant–polymer (ASP) flooding is a promising chemical enhanced oil recovery (EOR) method, currently applied in many oilfields in China, USA, India, and Malaysia. ASP has been the worldwide focus of research and field trials for the last decade. In a Malaysian EOR oilfield, a range of ASP concentrations were reported to breakthrough into the separator feed which results in forming stable/tight crude oil emulsions. Stable emulsion makes oil/water separation costly, time-consuming, and contributes to several operational problems in the surface facilities. The contribution of ASP components to the stability of produced emulsions has not been fully investigated. This paper discusses the design of experiments used to investigate the effect of water cut, alkaline concentration, surfactant concentration, polymer concentration, and temperature effect on stabilization of ASP-produced emulsion. A series of batch and continuous experiments are utilized to investigate the effect of various ASP compositions on the coalescence rate, rag layer growth, rheological properties, and droplet size of the generated emulsion after ASP flooding.

**Keywords** Enhanced oil recovery • Emulsion stability • Rag layer • Alkaline • Surfactant • Polymer

---

A. Basyouni (✉) · K.A. Elraies  
Department of Petroleum Engineering, Universiti Teknologi PETRONAS,  
Tronoh, Perak 32610, Malaysia  
e-mail: a.basyouni91@gmail.com

K.A. Elraies  
e-mail: khaled.elraies@petronas.com.my

H.H. Al-Kaieym  
Department of Mechanical Engineering, Universiti Teknologi PETRONAS,  
Tronoh, Perak 32610, Malaysia  
e-mail: hussain\_kayiem@utp.edu.my

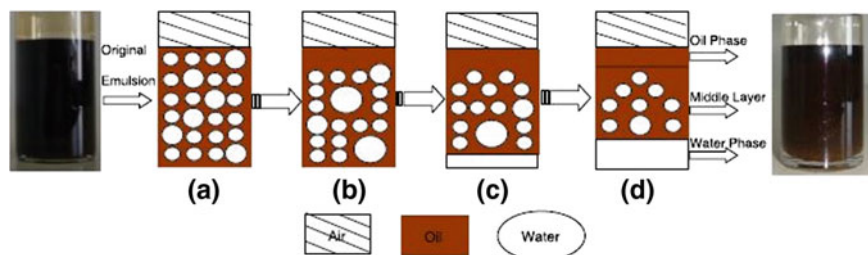
## 1 Introduction and Literature Review

Crude oil is usually produced associated with mixtures of water, gas, chemicals, and solids [1, 2]. Throughout the production system, the mixture suffers excessive turbulence that causes one phase of droplets to disperse into the other phase creating an emulsion [1]. Generally, emulsion is thermodynamically unstable and high turbulence such as shaking, stirring, or homogenizing is needed to form an emulsion [3, 4]. However, over time an emulsion tends to return to the stable state of original phases comprising it as shown in Fig. 1. The stability of an emulsion is increased when an emulsifier (emulsifying agent) present in the emulsion system [3, 6]. Emulsifiers have the tendency to adsorb at the oil/water interface creating interfacial film around the dispersed-phase droplets. The interfacial film hinders droplet coalescence making oil/water phase separation challenging [2, 4]. Formation of stable emulsion is one of the associated problems with crude oil produced by ASP flooding. That is mainly caused due to the presence of chemical components produced with the crude oil at the separator [2, 3, 7, 8].

### 1.1 Emulsification by Alkaline, Surfactant, and Polymer

Crude oil contains natural emulsifiers such as asphaltenes and resins. In addition, surfactant reduces the interfacial tension between the oil and water surfaces, thus forming stable emulsion. Alkali also contributes to the formation of stable emulsions as alkali generates in situ surfactant as a result of a chemical reaction between the alkali used and the crude oil and/or rock acids [7]. Polymer with high concentrations was also found to increase emulsification tendency and stability [6].

In alkaline–surfactant–polymer (ASP) flooding, oil recovery can increase up to 20% of the original oil in place [9, 10]. The incremental recovery factor from flooding individual chemical of alkaline, surfactant, or polymer was found in the range of 10 to 15% whereas the oil recovery factor from the three chemicals combined (i.e., ASP) was found to be 45.3% in a laboratory investigation [10]. On the one hand, emulsification is one of the main contributing factors to the significant



**Fig. 1** Emulsion tendency to separate over time into the original phases of oil and water [5]

upsurge in oil recovery and reduction in water cut. On the other hand, emulsification is a disadvantage at the transportation and separation stages as the combination of alkaline, surfactant, and polymer causes produced emulsion to be more stable [11]. The associated problems with ASP-produced stable emulsions can be summarized as follows: 1. difficulty to separate water from oil, 2. difficulty to treat produced water, and 3. Operational problems at surface facilities [3, 6, 12].

Some studies [3, 6, 13–15] explained the main reasons behind the stable emulsion formation associated with ASP-produced liquid as follows: (1) reduced interfacial tension (IFT) by alkaline and surfactant which makes it difficult for oil droplets to approach and coalesce, (2) increased viscosity of displacing fluid by polymers which reduces oil rising velocity, and (3) the shear and excessive turbulence experienced by produced liquid during the production process.

## 1.2 Rag Layer

Rag layer (also referred to as emulsion layer) is a thick viscous layer that forms at the interface between oil and water in almost all separation vessels. Rag layers reduce the efficiency of phase separation process which makes it undesirable [2, 7]. The main controllers of rag layer growth are the settling/creaming and coalescence rates of the dispersed-phase droplets. The rag layer grows faster when settling/creaming and coalescence rates are low [2]. Settling/creaming rate is influenced by the continuous-phase viscosity, phase densities, and the size of droplets whereas coalescence rate depends on the size of droplets and interfacial properties [8, 16, 17]. Coalescence rate is also affected by the materials adsorbed at the oil/water interface such as emulsifying agents, clays, and solids [18–20]. The coalescence rate reduces drastically when such materials present at the oil/water interfacial region. They act as a barrier that hinders droplets coalescence [21].

The strength and viscoelasticity of a rag layer are influenced by how the adsorbed materials (i.e., emulsifiers, chemicals, clays, solids) in it are packed. The closer the adsorbed materials are packed, the stronger and more viscoelastic is the rag layer. Therefore, it is difficult for the dispersed droplets to break the layer and coalesce. Then, the emulsion is stable [3]. In addition, the rag layer strength is increased when different materials are adsorbed and mixed emulsifiers are present [15]. When the layer is damaged, its viscoelastic properties can heal the layer and therefore returns to hinder droplet coalescence [3]. Hence, the strength of rag layer and its viscoelastic behavior plays an important role in stabilizing emulsions and reducing separation efficiency.

Khatri et al. [2] stated that the factors contributing to the growth of rag layer in oil–water separation are not yet noticeably identified. The author stated that one of the main controllers of rag layer growth is the emulsion droplets' coalescence rate. Thus, the effect of asphaltene, solids, and surfactant on coalescence rate of oil/water emulsion was investigated. The results indicated that coalescence rate of droplets depends on the type of emulsifiers used and their concentrations [2].



However, there is not yet a study that established a clear understanding about the effect of alkaline, surfactant, and polymer on coalescence rate and rag layer growth of ASP-produced emulsion.

## **2 Methodology**

### **2.1 Material**

Typically, the materials required to prepare crude oil/water emulsion stabilized by alkaline–surfactant–polymer (ASP) are crude oil samples, water, and ASP components. For this study, crude oil sample and reservoir brine are obtained from an identified field in Malaysia. The crude oil sample has high wax content of 18.8 wt% and high API gravity of 42° API. The chemicals used are anionic AOS surfactant, Na<sub>2</sub>CO<sub>3</sub> alkaline, and GLP 100 polymer supplied by PETRONAS Company.

### **2.2 Crude Oil Characterization**

To investigate the emulsion behavior of a given crude oil, the amount of natural emulsifiers such as wax, resins, asphaltene, and solids should be identified. On the other hand, alkaline is strongly influenced by the organic acids of crude oil, and thus, Total Acid Number (TAN) should be measured. In addition, measurements of crude oil density and viscosity are obtained.

For density measurement, DM40 density meter provided by Mettler Toledo is utilized using DIN 51757 (German Institute for Standardization) standards. Specific gravity was measured using the same equipment following ISO 12185 (International Organization for Standardization). Then, API gravity was calculated using ASTM D1250 (American Society for Testing and Materials) standards. For measuring TAN, Titrator T70 provided by Mettler Toledo is utilized. Wax content was obtained using MQC-23-32 NMR analyzer provided by Oxford Instruments in accordance with ASTM D7171-05 standard.

### **2.3 Preparation of Emulsion**

Emulsion samples will be prepared in the laboratory by mixing the crude oil and brine/ASP solutions. The solutions can be prepared by adding the ASP components with the respective concentrations to the brine. ASP compositions will vary the concentrations of alkaline, surfactant, and polymer between 500–1000 ppm,

200–600 ppm, and 400–800 ppm, respectively. Magnetic stirrer is used for 5 min to ensure that the solution is well mixed.

Both of the crude oil sample and brine/ASP solution are preheated at the oven for a minimum of 30 min at 60 °C. The crude oil sample and the brine/ASP solution is then mixed at 12,000 RPM for 2 min using an IKA T25 digital variable speed disperser.

## 2.4 Emulsion Separation Tests

Three types of tests will be conducted: batch test, continuous test, and decay test. The methodology and experimental procedures are obtained from Khatri et al. [2]. Each separation test will be carried out to provide the change in the height of oil, water, and emulsion layer over time.

### 1. Batch test

After preparing the emulsion sample, the emulsion is poured into a graduated test tube and allowed to coalesce while placed at the oven. The heights of the three layers (i.e., oil, water, and emulsion) will be measured over time. The layer heights are recorded until steady-state condition, i.e., no more changes in the emulsion layer height, which indicates that droplet coalescence process has been aborted.

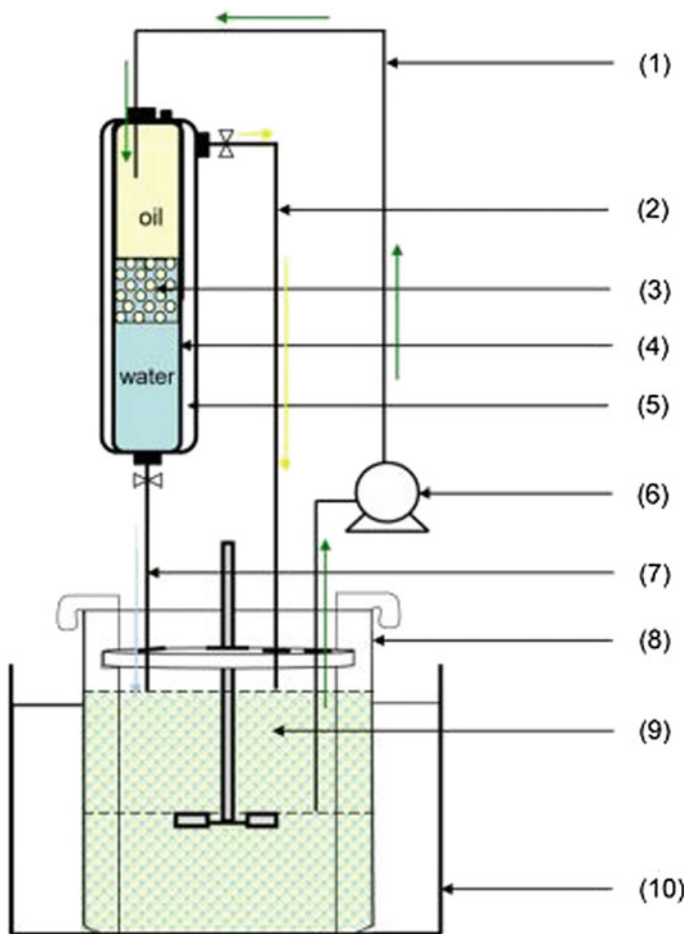
### 2. Continuous test

Continuous separation is carried out using continuous separator apparatus. Schematic diagram of the continuous separator apparatus is shown in Fig. 2. The apparatus uses a graduated glass separator with a volume of 1 L and a cross-sectional area of 14.4 cm<sup>2</sup>. To prepare the emulsion, an IKA T25 digital variable speed disperser is utilized. To inject the emulsion into the separator, 5-m feed tubing is used with TACMINA pump with capability of flow rate between 5 and 300 ml/min.

In the continuous test, equal volumes of preheated water and crude oil will be filled in the separator. The emulsion sample will be prepared the same way it was prepared for the batch test. After the emulsion is prepared, the disperser will be stopped and the pump will be used to inject the emulsion into the separator at different flow rates. As a result, the emulsion will accumulate in the separator at the water/oil interface. The emulsion layer height will be measured over time throughout the test.

### 3. Decay test

When the continuous test is completed, the pump will be turned off and water and oil valves will be closed. The aim of this step is to allow undisturbed coalescence to occur. The height of emulsion layer, free oil, and free water will be measured over time the same way to the batch experiment until the emulsion layer reaches constant height indicating no more coalescence.



**Fig. 2** Schematic diagram of the continuous separator: 1 Feeding tube; 2 oil outlet tubing; 3 emulsion layer; 4 glass separator; 5 water jacket; 6 pump; 7 water outlet tubing; 8 beaker; 9 oil–water emulsion; 10 water bath [2]

### 2.5 Emulsion Characterization

Further experimental investigations are conducted to characterize the effect of chemicals on rheological properties of emulsion layer, droplet size and their distribution, and zeta potential of droplets. Turbiscan is also utilized in order to measure the precise amount of water separated from the emulsion over time, which indicates the level of tightness of emulsion.

### 3 Conclusion

The stability of chemical EOR-produced emulsion is subject to the types of chemicals, their concentrations, and the properties of oil and water. Crude oil characterization is essential to identify the natural emulsifiers and the potential influencing factors to the emulsion stability of ASP-produced liquid. Proper emulsion sample preparation is required to ensure that the prepared emulsion simulates the produced emulsion at the separator. In addition, characterizing ASP-produced emulsion is important to define the main factors contributing to its tightness. Measuring droplet coalescence rate, rheological properties, interfacial properties, and droplet size and their distributions are important tools to develop clear understanding about the mechanism of which the emulsion is stabilized. Most of the studies conducted to investigate emulsion stability utilized mainly in batch experiments which is also known as static bottle test. Utilizing continuous separation experiments (dynamic test) obtains reliable results since it resembles the actual separation process at the field separator.

### References

1. Kokal, S. L. (2005). Crude oil emulsions: A state-of-the-art review. *SPE Production & facilities*, 20(01), pp. 5–13.
2. Khatri N. L., Andrade, J., Baydak, E. N., & Yarranton, H. W. (2011). Emulsion layer growth in continuous oil–water separation. *Colloids and Surfaces A: Physicochemical and Engineering Aspects*, 384(1), pp. 630–642.
3. Sheng J. (2010). *Modern chemical enhanced oil recovery: theory and practice*. Gulf Professional Publishing.
4. McLean, J. D., Spiecker, P. M., Sullivan, A. P., & Kilpatrick, P. K. (1998). The role of petroleum asphaltene in the stabilization of water-in-oil emulsions. In *Structures and Dynamics of Asphaltenes* (pp. 377–422). Springer US.
5. Kang, W., Guo, L., Fan, H., Meng, L., & Li, Y. (2012). Flocculation, coalescence and migration of dispersed phase droplets and oil–water separation in heavy oil emulsion. *Journal of Petroleum Science and Engineering*, 81, pp. 177–181.
6. Di, W., Meng, X., Zhao, F., Zhang, R., Yan, C., Wang, Q., & Liang, H. (2001, January). Emulsification and stabilization of ASP flooding produced liquid. In *SPE International Symposium on Oilfield Chemistry*. Society of Petroleum Engineers.
7. Czarnecki, J., Moran, K., & Yang, X. (2007). On the “rag layer” and diluted bitumen froth dewatering. *The Canadian Journal of Chemical Engineering*, 85(5), pp. 748–755.
8. Hartland S., & Vohra, D. K. (1980). Effect of interdrop forces on the coalescence of drops in close-packed dispersions. *Journal of Colloid and Interface Science*, 77(2), pp. 295–316.
9. Kang, W., & Wang, D. (2001, January). Emulsification characteristic and de-emulsifiers action for alkaline/surfactant/polymer flooding. In *SPE Asia Pacific Improved Oil Recovery Conference*. Society of Petroleum Engineers.
10. Olsen, D. K., Hicks, M. D., Hurd, B. G., Sinnokrot, A. A., & Sweigart, C. N. (1990, January). Design of a novel flooding system for an oil-wet Central Texas carbonate reservoir. In *SPE/DOE Enhanced Oil Recovery Symposium*. Society of Petroleum Engineers.

11. Chang, H. L., Hou, H., Wu, F., & Gao, Y. (2013, July). Chemical EOR Injection Facilities-From Pilot Test to Field-Wide Expansion. In SPE Enhanced Oil Recovery Conference. Society of Petroleum Engineers.
12. Sheng, J. J. (2014). A comprehensive review of alkaline-surfactant-polymer (ASP) flooding. *Asia-Pacific Journal of Chemical Engineering*, 9(4), pp. 471-489.
13. Deng, S., Bai, R., Chen, J. P., Yu, G., Jiang, Z., & Zhou, F. (2002). Effects of alkaline/surfactant/polymer on stability of oil droplets in produced water from ASP flooding. *Colloids and Surfaces A: Physicochemical and Engineering Aspects*, 211(2), pp. 275-284.
14. Nguyen, D. T., Sadeghi, N., & Houston, C. W. (2011, January). Emulsion Characteristics and Novel Demulsifiers for Treating Chemical EOR Induced Emulsions. In SPE Enhanced Oil Recovery Conference. Society of Petroleum Engineers.
15. Kang, W. L. (2001). Study of chemical interactions and drive mechanisms in Daqing ASP flooding.
16. Hartland S., & Jeelani, S. A. K. (1988). Prediction of sedimentation and coalescence profiles in a decaying batch dispersion. *Chemical engineering science*, 43(9), pp. 2421-2429.
17. Dickinson E., Murray, B. S., & Stainsby, G. (1988). Coalescence stability of emulsion-sized droplets at a planar oil-water interface and the relationship to protein film surface rheology. *Journal of the Chemical Society, Faraday Transactions 1: Physical Chemistry in Condensed Phases*, 84(3), pp. 871-883.
18. Chen F., Finch, J. A., Xu, Z., & Czarnecki, J. (1999). Wettability of fine solids extracted from bitumen froth. *Journal of adhesion science and technology*, 13(10), pp. 1209-1224.
19. Sztukowski D. M., & Yarranton, H. W. (2005). Oilfield solids and water-in-oil emulsion stability. *Journal of colloid and interface science*, 285(2), pp. 821-833.
20. Jiang T., Hirasaki, G. J., Miller, C. A., & Moran, K. (2008). Using silicate and pH control for removal of the rag layer containing clay solids formed during demulsification. *Energy & Fuels*, 22(6), pp. 4158-4164.
21. Saadatmand, M., Yarranton, H. W., & Moran, K. (2008). Rag layers in oil sand froths. *Industrial & Engineering Chemistry Research*, 47(22), pp. 8828-8839.

# Field-Scale Investigation of Miscible CO<sub>2</sub> Injection in a Heterogeneous Shaly Sand Reservoir

Ahmed Khalil Jaber, Mariyamni B. Awang and Christopher P. Lenn

**Abstract** Carbon dioxide flooding is considered one of the most commonly used miscible gas injection to improve oil recovery, and its applicability has grown significantly due to its availability, greenhouse effect, and easy achievement of miscibility relative to other gasses. Therefore, miscible CO<sub>2</sub> injection is considered one of the most feasible methods worldwide. For long-term strategies in Iraq and the Middle East, most oil fields will need to improve oil recovery as oil reserves are falling. This paper presents a study of the effect of various miscible CO<sub>2</sub> injection scenarios on the performance of the highly heterogeneous clastic reservoir in Iraq. An integrated field-scale reservoir simulation model of miscible CO<sub>2</sub> flooding is accomplished. The compositional simulator, Eclipse-300, has been used to investigate the feasibility of miscible CO<sub>2</sub> injection process. The process of the continuous CO<sub>2</sub> injection was optimized to start in January 2056 as an improved oil recovery method after natural depletion and waterflooding processes have been performed, and it will continue until January 2063. The minimum miscibility pressure (MMP) for CO<sub>2</sub> was determined using empirical correlation as a function of crude oil composition and its properties. Ten miscible CO<sub>2</sub> injection options were undertaken to investigate the reservoir performance. These options included applying a wide range of the CO<sub>2</sub> injection rates ranged between 1.25 and 50 MMScf/day. All development options were analyzed with respect to net present value (NPV) calculations to confirm the more feasible CO<sub>2</sub> development strategy.

---

A.K. Jaber (✉)

Iraqi Ministry of Oil & Universiti Teknologi PETRONAS,  
Perak Sari-Iskandar, Malaysia  
e-mail: ahmedkhalil1974@yahoo.com

M.B. Awang

Petroleum Engineering Department, Universiti Teknologi PETRONAS,  
Perak Sari-Iskandar, Malaysia  
e-mail: mariyamni\_awang@utp.edu.my

C.P. Lenn

Head of Center COREOR, Universiti Teknologi PETRONAS,  
Perak Sari-Iskandar, Malaysia  
e-mail: christopher.lenn@utp.edu.my

The results showed that the application of CO<sub>2</sub> injection option of a 20 MScf/day attained the highest recovery of 28% by January 2063 among the others. The recovery growth was so minor by increasing the CO<sub>2</sub> injection rate above this level. Based on economic findings, the option of 20 MScf/day also attained the highest net present value. The results showed that after January 2063, the oil recovery attained by the different CO<sub>2</sub> injection options are less than the one attained by the waterflooding process. Therefore, the miscible CO<sub>2</sub> injection became unviable economically after January 2063.

**Keywords** Field scale · Miscible CO<sub>2</sub> injection · Shaley sand reservoir · Heterogeneous reservoir

### List of symbols

NPV	Net present value, US\$
FOE	Field recovery factor, fraction
FOPT	Field oil production total, STB
FOPR	Field oil production rate, STB/day
FWCT	Field water cut total, fraction
FPR	Field pressure, psia
CAPEX	Capital expenditure, US\$
OPEX	Operational expenditure, US\$
NCF	Net cash flow, US\$
T	Future time, year
T	Cumulative investment (or production) period
I	Interest rate, fraction

### Abbreviations

M Mobility ratio

### Greek

$v$	Velocity of the displacing phase
$\mu$	Viscosity of the displacing phase
$\sigma$	Interfacial tension between oil and water
$\theta$	Contact angle between oil–water interface and the rock surface

## 1 Introduction

Carbon dioxide flooding appeared in the 1930s and had a great development in the 1970s [1, 2]. Over forty years of production practice, CO<sub>2</sub> flooding has become a leading EOR technique for light and medium oils [2, 3]. CO<sub>2</sub> flooding is beneficial

for both the environment and the petroleum industry by injecting the harmful CO<sub>2</sub> to increase oil recovery. This reduces greenhouse gasses (GHG) emissions by sequestration CO<sub>2</sub> in the reservoir, thus reducing heat trap in the atmosphere. CO<sub>2</sub> injection has been proven as a successful technology worldwide, with less minimum miscibility pressure than nitrogen and hydrocarbon gasses. The studied reservoir is the Nahr Umr reservoirs which considered one of the most important producing reservoirs in the south of Iraq. This reservoir in many southern Iraqi fields needs to apply improved oil recovery methods (IOR) shortly to extract more oil and increase oil recovery. It is very necessary to screen, investigate, and optimize the proper IOR method. CO<sub>2</sub> injection has a great potential enhancing and increasing oil recovery. However, it does not recover all the oil, regardless of whether the reservoir has been previously flooded with water. Typically, recovery addition with miscible CO<sub>2</sub> displacement is around 10–20%, by injecting an equivalent of 80% HCPV with CO<sub>2</sub> [2, 4].

The reservoir under study is the Nahr Umr reservoir in the Subba oil field that is described as a heterogeneous clastic reservoir. The heterogeneity index was determined based on Lohrenz coefficient calculations [5]; this is based on the flow capacity distribution to measure the contrast in permeability relative to the homogeneous case. The average Lohrenz coefficient value of different core samples of the Nahr Umr reservoir was found equal to 0.814, indicating that the Nahr Umr reservoir is a highly heterogeneous reservoir. The Subba oil field has a short production history, for 6 months only as an experimental period during the 1990s. The production of the field was not last due to some technical issues at that time.

Due to the reservoir heterogeneity, the optimum infill placement wells were optimized based on sweet spots determined by the dynamic opportunity index analyses [2, 6]. There were 50 infill wells, and accordingly, 21 injectors were decided to be involved in development scenarios. The waterflooding process was optimized to start up in January 2028 and continued until January 2056 with 3000 bbl/day, water injection rate. The CO<sub>2</sub> injection proposed to commence in January 2056 as an IOR method after waterflooding process and tested until January 2076. The compositional flow simulation model, Eclipse-300, was used to construct the flow simulations runs. Eclipse-300 allows to model multicomponent hydrocarbon flow to get a detailed description of phase behavior and compositional changes, and it uses a cubic equation of state. The obtained results are analyzed depending on the NPV analysis and present value of producing oil that conducted in each case.

## 2 Background

CO<sub>2</sub> flooding process can be classified as miscible and immiscible. In the immiscible flooding process, the relatively high reservoir pressure results in CO<sub>2</sub> dissolution, oil viscosity reduction, lowering interfacial tension, oil swelling, and dissolved-gas drive [2]. In the miscible flooding mechanism, the process involves the generation of the miscibility at minimum miscible pressure between the CO<sub>2</sub>



and reservoir oil, lowering the interfacial tension between oil and CO<sub>2</sub> and swelling of the oil due to the transferring of CO<sub>2</sub> into the oil and then lowering the oil viscosity and density and finally the increasing oil recovery factor. The miscibility between the CO<sub>2</sub> and crude oil was achieved through multiple contact miscibility process. CO<sub>2</sub> was, first, condensed into the crude oil (transferring of CO<sub>2</sub> to the oil), making oil lighter. The lighter components of the oil vaporized or were extracted by the remainder of the CO<sub>2</sub>, making CO<sub>2</sub> denser with a higher viscosity. The formed CO<sub>2</sub> is called the richest phase, as mass transfer continued between CO<sub>2</sub> and oil, the formed CO<sub>2</sub> become more like oil regarding fluid properties. The relative permeability of the gas (displacing phase) will reduce, and the mobility ratio was reduced. The capillary number and microscopic displacement efficiency were increased, and then, the recovery factor was increased. The capillary number was defined by the following equation [2].

$$N_{ca} = \frac{\text{Viscouse Forces}}{\text{Capillary Forces}} = \frac{v\mu}{\sigma \cos \theta} \quad (1)$$

where  $v$  and  $\mu$  are the velocity and the viscosity of the displacing phase, respectively,  $\sigma$  is the interfacial tension between oil and water, and  $\theta$  is the contact angle between oil–water interface and the rock surface measured between the rock surface and the denser phase. This takes place because the purposes of any EOR method are to increase the capillary number that leads to a favorable mobility ratio ( $M < 1.0$ ).

### 3 Problem Statement

Many clastic reservoirs in the south of Iraq need to apply the IOR methods in the near futures, as many reservoirs go to maturity [2]. The miscible CO<sub>2</sub> flooding process considers one of the best candidate methods to be applied to these reservoirs [2]. This study addresses the NPV criterion to investigate the most viable miscible CO<sub>2</sub> flooding option.

### 4 Objectives of Study

The objective of the current study is to investigate the feasibility of miscible CO<sub>2</sub> flooding performance in a highly heterogeneous reservoir through the analysis of the full-field-scale flow simulation model. Six options of miscible CO<sub>2</sub> flooding were examined for future reservoir performance prediction.

## 5 Reservoir Characterization

The Subba oil field is located in southeast of Iraq, some of 110 km to the northwest of Basra and 12 km northwest of the Luhais oil field [2]. This oil field is described as a giant field with bottom and edge aquifer support. There were 14 wells drilled in this field that penetrated the Nahr Umr formation, but only six of them were completed in the Nahr Umr reservoir [2]. The dimensions of the Subba oil field are about 30 km long and 7 km wide. The Nahr Umr reservoir is considered one of the most important productive reservoirs in southern Iraqi oil fields, which comprises an important place in the stratigraphic column of the Lower Cretaceous Albian Nahr Umr [2]. It has a double dome separated by a shallow saddle. The largest one is located in the south of the field and the smallest one in the north of the field [2]. This field has not been developed for over the last forty years; since it was produced in 1990 for a short experimental period from the Nahr Umr reservoir. The reservoir holds medium gravity oil with  $<30^\circ$  API,  $<3$  c.p viscosity, and  $>55\%$  molar composition of C<sub>5</sub>–C<sub>20</sub> components. The reservoir temperature equals to 178° F. The crest of the reservoir occurs at a depth of (–2400) m SSTVD [2, 6]. According to this screening, the CO<sub>2</sub> flooding considers the most proper method to improve oil recovery from this reservoir after primary and secondary depletion strategies.

## 6 Static Model

The static model was constructed based on the petrophysical interpretation results [2, 7], structural contour maps of the Nahr Umr geological layers, and the data from 14 wells penetrated the reservoir. These data comprised well coordinates, formation tops, core data, log interpretation results, facies, and permeability curves [2, 6–8]. The log interpretation results include shale volume, porosity, and water saturation. The petrophysical property distribution, such as permeability, porosity, and saturation was constructed based on the facies model. The resultant 3-dimensional cellular model formed the basis for the reservoir simulation model that was used to optimize the reservoir development scenarios. The facies consists mainly of four rock types include fluvial sandstone, tidal sandstone for the reservoir, siltstone, and shale for non-reservoir. The Nahr Umr reservoir has a heterogeneous permeability profile, including very high permeability for sandstone and very low permeability for shale.

## 7 Structural Modeling

The model cells were defined as 200 m × 200 m in the X- and Y-directions with 36 cell layers deep [2]. This size of cells was efficient to capture the reservoir characteristic and the reservoir petrophysical property changes as well as to ensure that

the derived geological grids could be exported into the simulation model directly; hence, avoiding grid upscaling. The number of layers in the geological model was adjusted to ensure the match between the upscaled and wells' facies. Then, a better definition was set for discrete flow units and the boundaries that separated the flow units in the reservoir. The total numbers of cells considered in the geological model set 101 and 196 in X-direction and Y-direction, respectively, and considering 36 cells in Z-direction. The total number of cells in the geological model became 712656 cells.

## 8 Boundary Conditions

In this study, flow boundaries from the surrounding aquifer, bottom, and edge have been considered as they have proven from well logs, well tests, and log production test [2]. The Carter–Tracy analytical aquifer model [10] was adopted in the reservoir simulation flow model to represent the water influx drive mechanism.

## 9 Fluid Properties

Fluid properties of the reservoir are shown in Table 1 [2]. The Peng–Robinson cubic equation of state was employed in the compositional simulation model. One-stage separation at standard conditions was utilized.

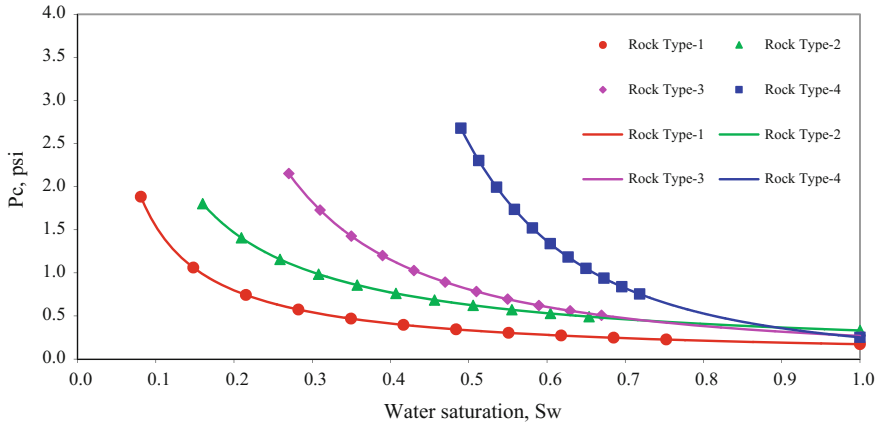
## 10 Capillary Pressure and Relative Permeability

The Nahr Umr reservoir in the Subba oil field consists of four rock types, as was proved from core analysis, mud logs, well logs, flow zone indicator analysis, and capillary pressure analysis [2]. These rock types included fluvial sandstone, tidal

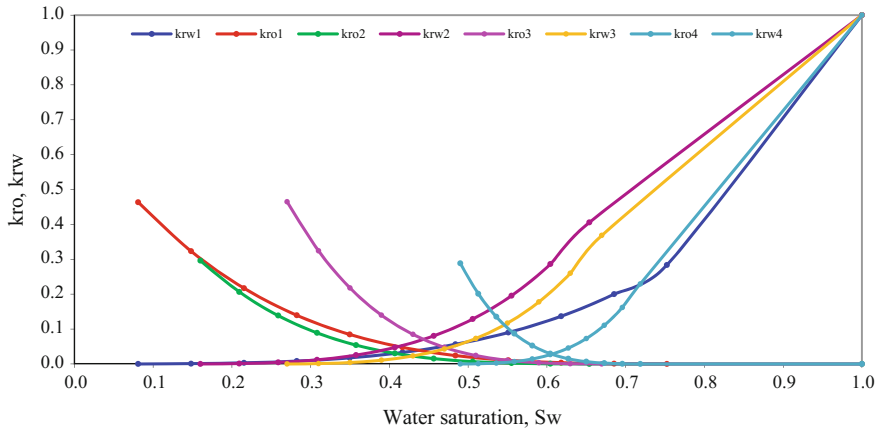
**Table 1** Reservoir fluid properties [6, 9]

Property	Value
T, °F	178
Pb, psia	1103
$\rho_o$ , °API	28.7
$\mu_o$ @ Pb, cp	1.6183
$\beta_o$ @ Pb, rbb/STB	1.2283
$\gamma_w$	1.1678
$\mu_{o^*}$ @ Pinit, cp	0.7000
$\gamma_g$	0.6534
$\beta_w$ @ Pinitial, rbb/STB	1.0160

sandstone for the reservoir, siltstone, and shale for non-reservoir. Figures 1 and 2 show the oil–water system capillary pressure and relative permeability curves for the four rock types. Figure 3 shows oil–gas relative permeability curves for the two active rock types in the simulation model. In this study, gas and oil are considered as miscible components, what means that there is no capillary pressure between oil and gas.



**Fig. 1** Capillary pressure curves for Nahr Umr reservoir [6]



**Fig. 2** Water–oil relative permeability curves for Nahr Umr reservoir [6]

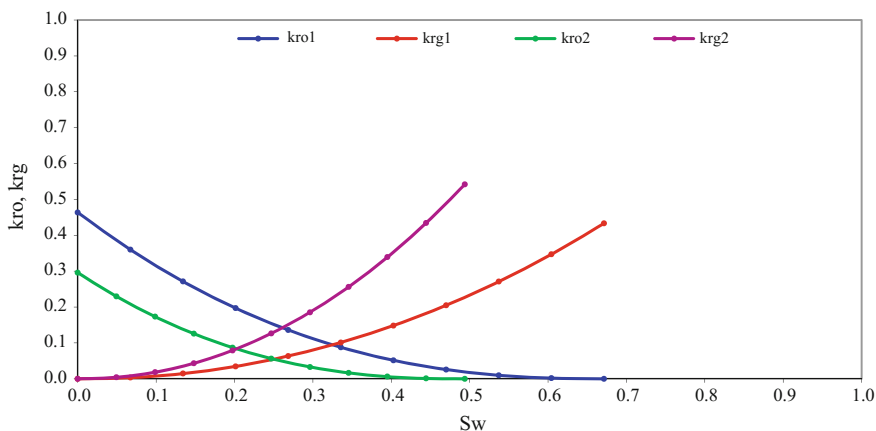


Fig. 3 Gas-oil relative permeability curves for NahrUmr reservoir [21]

## 11 PVT Model

The PVT model was accomplished by employing IPM-PVTP fluid thermodynamic software from Petroleum Experts Ltd. The Podbielniak compositional analysis is conducted for a bottom-hole fluid sample of the reservoir. Fluid properties are calibrated with the EOS compositional model to match the measured laboratory data [2]. 10 components of reservoir fluid sample until C6+ are used to generate the cubic Peng–Robinson EOS [2]. The model adjusts the component's properties to match the observed fluid properties. In this study, the single-stream mode is utilized to match the laboratory data, which includes only adjusting properties, i.e., the component properties of one stream are changed to match its laboratory data. The component composition is kept with no change, while the critical temperature ( $T_c$ ) and critical pressure ( $P_c$ ) of the fluid components are selected as regression parameters to be tuned in order to obtain the laboratory data matched to the all fluid properties except the fluid viscosity, which is predicted separately by using Lohrenz, Bray and Clark model [2, 5]. This correlation used the composition, specific gravity and, more importantly, critical volume ( $V_c$ ) which was the dominated parameter, and it was the most significant input parameter for this model.

It is very unlikely that a satisfactory match for the observe properties would be obtained before applying a multivariable nonlinear regression process. Therefore, a nonlinear regression analysis is carried out to get the match between the experimental and the modeled fluid properties. The following experimental results are used as match parameters [2]:

1. Bubble-point pressure from the differential liberation dataset.
2. Fluid density at the bubble-point pressure from the differential liberation dataset.

3. Oil formation volume factor ( $\beta_o$ ) versus pressure from the differential liberation dataset.
4. Oil density versus pressure from the differential liberation dataset.
5. Solution GOR ( $R_s$ ) versus pressure from the differential liberation dataset.
6. Stock tank oil density for the differential liberation dataset.

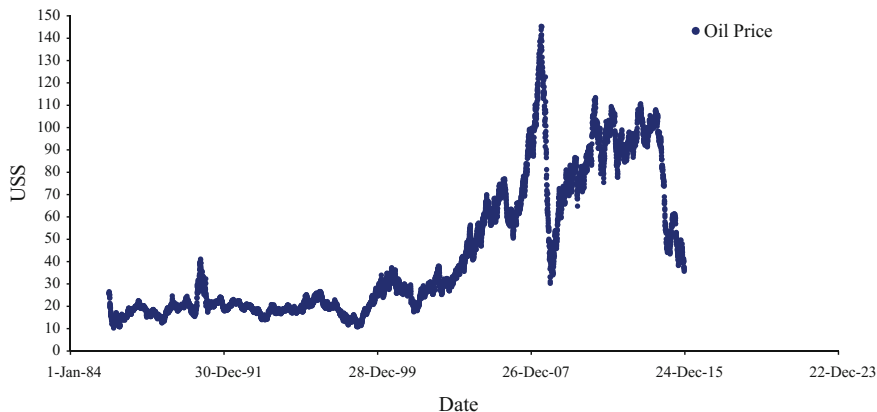
## 12 Minimum Miscibility Pressure (MMP)

The minimum miscibility pressure is the minimum pressure for a specific temperature at which miscibility can occur independently of the overall composition [11]. For the miscible CO<sub>2</sub> injection project, the reservoir pressure must be maintained at the minimum miscibility pressure or higher. The MMP is reported to be a function of temperature and fluid compositions. Several methods for determination of the MMP have been proposed: slim tube experiments, calculations with EOS, and correlations. There was no availability of slim tube experiments' results or the experiments required to conduct the EOS analysis for the reservoir. Therefore, it depended on the available correlations to determine the minimum miscibility pressure. Several empirical correlations were tested, including Glass [12]; Yellig and Metcalfe [13]; Yuan, et al. [14]; Cronquist [15]; and Alston, et al. [16]. The MMP calculated by Glass [12] method was found equal to 2421 psia. This was considered in the current work, because the average molecular weights of fluid samples used in the Glass correlation, almost near the molecular weight of the Nahr Umr reservoir fluid [2]. Moreover, it gave an average value among other correlations.

## 13 Economic Evaluation

To prove the success of any project, economic calculations have to perform to examine the project profitability. The technical success of the project alone sometimes is not enough to give the final decision on project success. As many projects have proven to be technical successes but not economical ones [2].

To build a sound business decision, it requires economic criteria for measuring the value of the proposed investments and financial opportunities [2, 17]. The objectives of carrying out an economic analysis were to select the best development strategy for the field based on minimizing costs and high profit. The net present value is considered as one of the most economical criteria that are widely used to include the time value of money and is considered as a measure of profit. It is defined as the aggregate of all project cash flows for a specified period, discounted back to a common point in time. In this study, a fixed discount rate of 10% per annum was considered. NPV was determined by calculating the present worth of all



**Fig. 4** Statistic history of oil prices [22]

the future net cash flows and summing them up. The future cash flow includes all sales revenue of producing oil and gas minus the costs of water handling, water reinjection, capital expenditure (CAPEX), operational expenditures (OPEX), and transportation cost of oil discounted at a 10% annual rate. The operation cost escalation was considered to be 1.5% [2, 18]. This includes lifting costs, water handling, reinjection, and recycles costs. The inflation rate in oil prices was considered in this study as it causes prices to rise over time. Oil prices had a big fall at mid-2014 to US\$ 44 and had stopped falling at the end of the same year and then fell again to US\$ 36 at the end of 2015 as shown in Fig. 4. The variability of oil prices makes it difficult to expect the exact trend of the inflation rate. As oil prices move up or down, inflation follows in the same direction. The reason why this happens is that oil is a major input in the economy, and it is used in critical activities such as fueling transportation and heating homes. If the input costs rise, so should the cost of the end products. In this study, a ratio of 5% inflation rate per annum was assumed to be more reasonable to keep pace with the oil market. Gas prices were assumed to be constant over the project life.

The cost of existing producing wells was considered already incurred during the natural depletion phase of the field. The royalty and taxes were neglected in this analysis as the oil fields are owned and developed by the Iraqi government. The NPV was computed using the following formula [217, 19]:

$$NPV = \sum_{t=1}^T \frac{NCF_t}{(1+i)^t} \tag{2}$$

$$NCF(t) = Revenue - CAPEX - OPEX - Water\ handling\ and\ reinjection - Transportation\ cost - CO_2\ price - CO_2\ Recycle\ cost \tag{3}$$

**Table 2** Economic parameters for Nahr Umr reservoir [2]

Parameter	Value
Interest rate (%)	10
Oil price (\$/STB)	50
Net gas price (\$/MSCF)	3.5
Water handling (\$/STB)	0.373
Water reinjection (\$/STB)	0.559
OPEX (\$/STB)	1.5
Well CAPEX (MM\$)	5
Average crude oil transportation cost (\$/STB)	2.7
Water injection facilities (MM\$)	17
Production facilities (MM\$)	100
CO <sub>2</sub> capturing and compression (\$/MSCF)	0.85
CO <sub>2</sub> transportation (\$/MSCf)	0.25
CO <sub>2</sub> recycle (\$/MSCf)	0.35
CAPEX of CO <sub>2</sub> separation, treatment, and reinjection (MM\$)	22

where

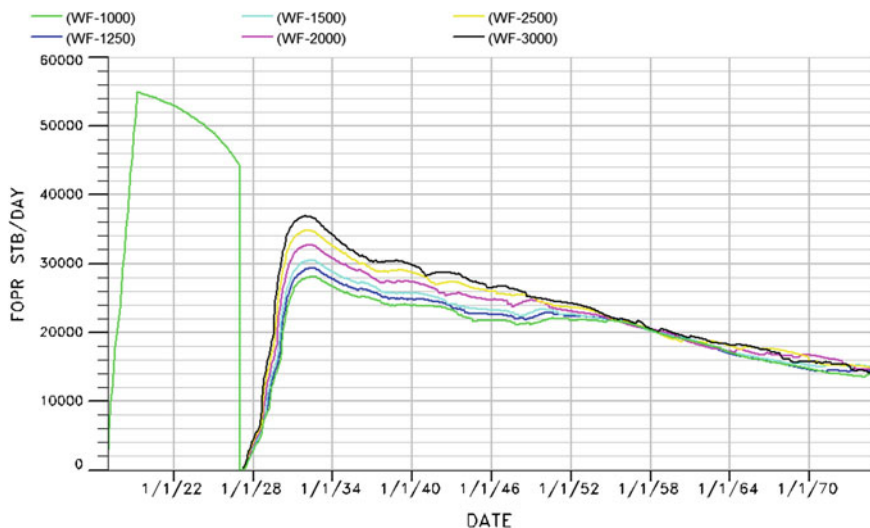
NPV	net present value, US\$
NCF	net cash flow, US\$
CAPE	Capital expenditures, US\$
OPEX	Operational expenditures, US\$
CO <sub>2</sub> price	Carbon dioxide, US\$
t	Future time, year
T	Cumulative investment (or production) period, year
i	Interest rate, dimensionless

To perform the NPV calculations, the economic parameter shown in Table 2 was used in this study [1, 2, 17, 20]. The capital expenditures include the cost of production facilities, water injection facilities, injection well drilling, completion, cementing, perforation, and acidizing services. The water handling and reinjection processes included the following: pumping, electricity, treatment equipment, storage equipment, piping, and maintenance.

## 14 Waterflooding Simulation

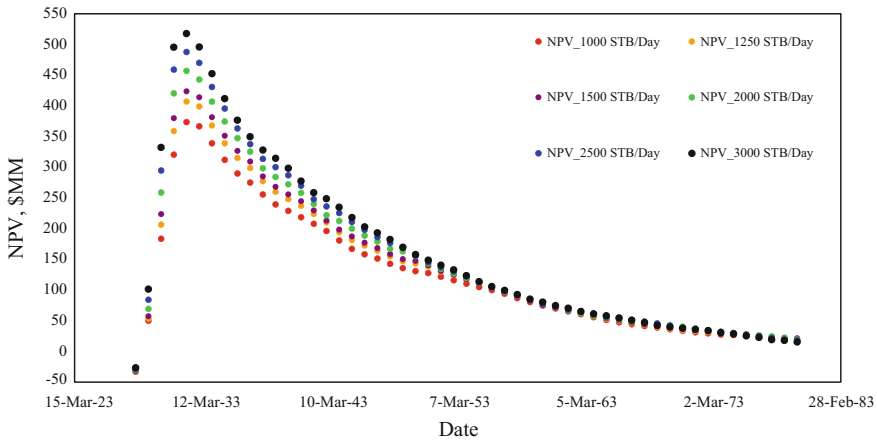
The waterflooding technique has proved to be the most popular and successful secondary oil recovery mechanism. This recovery method has been used on numerous oil fields worldwide [2]. However, after the secondary recovery process, there is still a significant amount of oil trapped in the reservoir. In this study, the waterflooding process was tried after the natural depletion of the reservoir. There





**Fig. 5** Reservoir performance under different waterflood scenarios [2]

have been six producers already drilled; these producers were located almost in the middle of the formation. There were 50 infill drillings suggested as the optimum well locations [26]. The waterflooding process was achieved through 21 injectors [2]. These injectors were located depending on the reservoir heterogeneity and in a way that would provide enough support to the producers. The waterflooding process has been optimized to start in January 2027 as a secondary recovery method after depletion of the reservoir, naturally, for 10 years. Several waterflooding options were tried with different injection rates at each injector as follows: 1000, 1250, 1500, 2000, 2500, and 3000 STB/day. The waterflooding process has been optimized to halt in January 2056 and start the miscible  $\text{CO}_2$  flooding process. The simulator runs were conducted using the compositional simulator E300 for the compatibility purpose to import the restart file data of the waterflooding case into the  $\text{CO}_2$  compositional simulator runs. The setup for the simulation model was the following: all producer wells were set on the constant production rate of 3000 STB/day, with a bottom-hole pressure limit of MMP for the  $\text{CO}_2$  injection. The production at the well stopped as the water cut level of 80% was reached. The injection rates were adjusted to avoid the pressure increase over the formation fracture pressure. The results are presented in Fig. 5. As it can be seen, the injection rate option of 3000 STB/day has reflected the higher reservoir production rate. The results were analyzed economically depending on the NPV calculations; these results are presented in Fig. 6. The higher NPV was also realized at the injection rate option of 3000 STB/day. This case was considered as the base of which the  $\text{CO}_2$  miscible injection process was continued.



**Fig. 6** NPV for different waterflood scenarios [2]

## 15 CO<sub>2</sub> Injection Simulation

This technique involves injecting a certain amount of CO<sub>2</sub> continuously until the required slug size is reached. Usually, continuous miscible CO<sub>2</sub> injections have excellent microscopic displacement efficiency [2]. However, they often suffer from poor macroscopic sweep efficiency due to the formation of viscous fingers that propagate through the CO<sub>2</sub> passing much of the hydrocarbon that has not been contacted. This happens because of the low viscosity of the CO<sub>2</sub> compared to the oil and it results in an adverse mobility ratio. In this study, the miscible CO<sub>2</sub> injection was started up after the waterflooding process had been completed. The optimum waterflooding strategy was chosen as the base to continue the CO<sub>2</sub> injection process. In this issue, several compositional simulation runs were conducted to optimize to the optimum CO<sub>2</sub> injection rate that reflected the highest net present value. A wide range of injection rates was trying to examine the reservoir performance under the miscible CO<sub>2</sub> injection. These rates included 1.25, 2.5, 5, 10, 15, 20, 25, 30, 35, 40, 45, and 50 MM Scf/day. The setup for the simulations was the following: all producers were set at the constant production rate of 3000 STB/day, with the bottom-hole pressure limit of MMP. The CO<sub>2</sub> was injected at a constant rate for each development strategy, with the maximum bottom-hole injection pressure limit of the formation fracture pressure. The production wells were closed when the water cut reached the limit of 95%, and the injection rates were adjusted to avoid a pressure increase over the fracture pressure. All the results were analyzed relative to the net present value calculations as the economic criterion. The results showed that the injection rate option of 50 MScf/day has reflected the higher oil recovery for the first 6 years of the reservoir production as shown in Fig. 7.

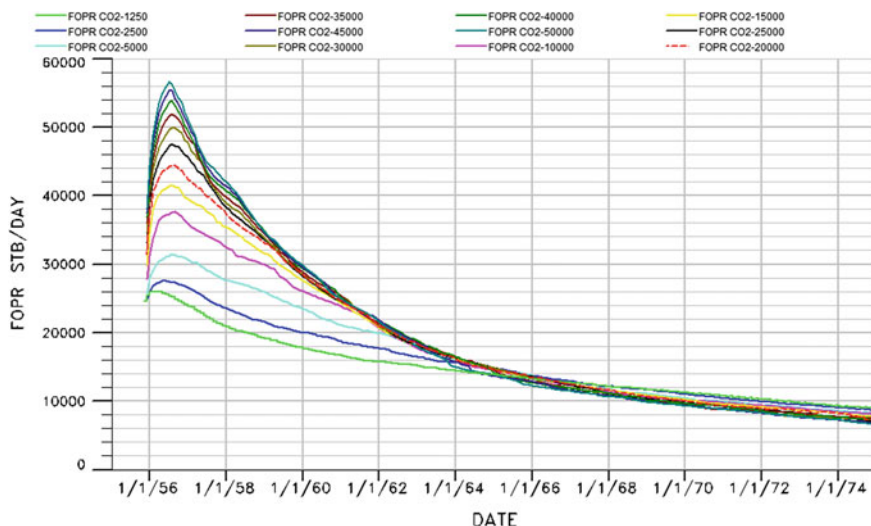
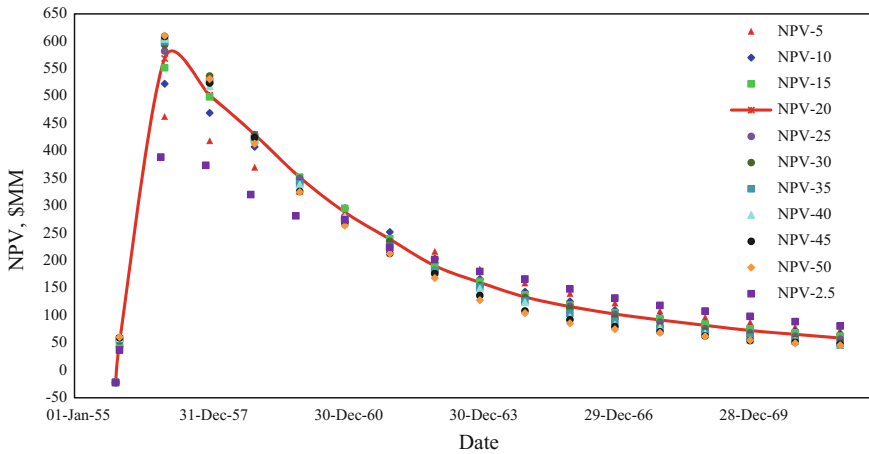


Fig. 7 Reservoir flow rate under different CO<sub>2</sub> flooding scenarios

However, the injection rate option of 20 MScf/day has reflected the higher NPV as shown in Fig. 8. This injection rate was considered as an optimal CO<sub>2</sub> injection rate for the all CO<sub>2</sub> flooding modes.

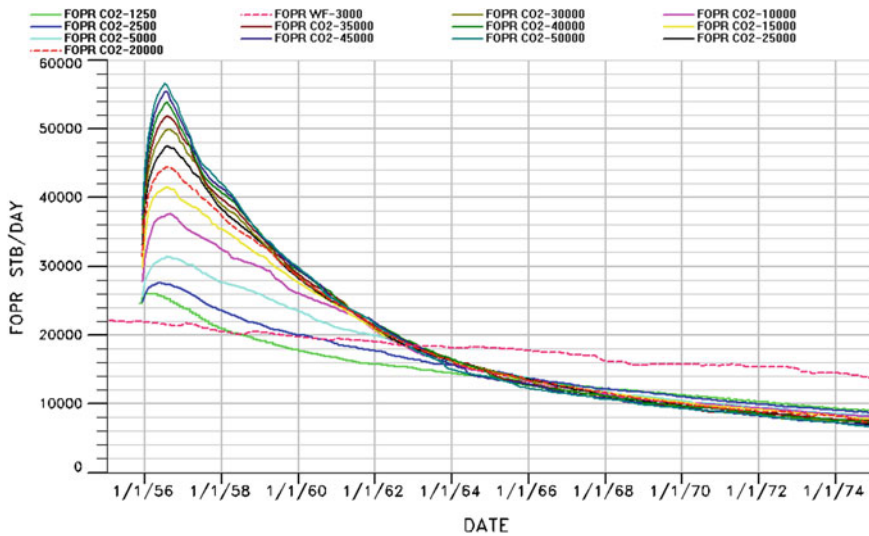
## 16 Results and Discussion

There have been 12 cases constructed in this work to examine the continuous CO<sub>2</sub> flooding process to improve the oil recovery in the highly heterogeneous clastic reservoir. The same waterflooding injection scheme was converted later to CO<sub>2</sub> flooding. The field development plan is proposed to start up in January 2017 through the naturally depleted reservoir with 56 wells. The waterflooding process has been optimized to commence in January 2027 with 21 injectors because the reservoir pressure became close to the saturation pressure. These injectors are located according to reservoir heterogeneity, and in that way, they can provide enough support to the producers. Six waterflood scenarios were tried with different injection rates ranging between 1000 and 3000 STB/day. The CO<sub>2</sub> flood was started up when the reservoir pressure reached close to the MMP to improve the volumetric efficiency of the CO<sub>2</sub>. Because, the oil viscosity reached a lower value at this pressure, an increase in the mobility of the oil occurred in turn, improving the stability of the displacement front that controls the sweeping efficiency.



**Fig. 8** NPV for different CO<sub>2</sub> scenarios

The results of the waterflooding process showed that the waterflood scenario with the 3000 STB/day injection rate was the best option because it attained the highest oil recovery and the NPV as shown in Figs. 5 and 6. It has been mentioned that all the waterflooding scenarios were intersected at the same point in January 2056; because there was an almost incomparable oil recovery obtained for the different injection rates after this date. On this date, the miscible CO<sub>2</sub> flooding was suggested to proceed as the reservoir pressure reached 2875 psia. This pressure was adequate to start the miscible CO<sub>2</sub> process in respect to the MMP value. Several miscible CO<sub>2</sub> flooding scenarios were examined at different injection rates ranging between the low injection rate of 1.25 MScf/day and the high injection rate of a 50 MScf/day. All results of the flooding options were analyzed with respect to the NPV calculations. It was found that the miscible CO<sub>2</sub> flooding scenario with 20 MMScf/day reflected the highest oil recovery as shown in Fig. 7. The recovery growth was insignificant by increasing the CO<sub>2</sub> injection rate above this level. In terms of the economic profitability, the scenario of the 20 MMScf/day also reflected the highest NPV as shown in the Fig. 8. This flow rate was considered the optimum CO<sub>2</sub> injection rate. As shown in Fig. 9, the reservoir flow rates for different CO<sub>2</sub> injection options were met at the same point in January 2063. After this date, the oil recovery attained by the different CO<sub>2</sub> injection options fell below the one attained by the waterflooding process. Thus, the CO<sub>2</sub> injection process became unviable, economically, after January 2063.



**Fig. 9** Reservoir performance comparisons under different CO<sub>2</sub> flooding scenarios and waterflooding scenario

## 17 Conclusion

The observations and conclusions drawn from this study are summed up below:

1. This study is enough to give an answer to what will be the performance of a clastic reservoir in southern Iraq during the miscible CO<sub>2</sub> flooding process.
2. The Glass [12] method was found to be more suitable to calculate the MMP for the Nahr Umr reservoir.
3. To some extent, the miscible CO<sub>2</sub> flooding has been proven successful to increase the sweep efficiency and then the oil recovery in the studied reservoir. However, particular attention should be paid to the application of this process due to the mobility contrast of the CO<sub>2</sub>, which leads to the instability of the displacement front and gas channeling.
4. The ultimate recovery reached the highest value of 28% by January 2063 at the option of a 20 MScf/day. Based on the economic findings, this option has also reflected the highest NPV.
5. There is no economic profitability from the continuation of the CO<sub>2</sub> flooding after January 2063 for all the scenarios. Because the oil recovery attained by the waterflooding process was higher after this date compared to the one achieved by the different CO<sub>2</sub> injection options, the produced gas was escalated and most probable, CO<sub>2</sub> channeling happened due to the high heterogeneity of the reservoir and mobility contrast.

6. The compositional simulator model-E300 was used to model the waterflood process for the purpose of compatibility. This was performed to import the restart data files generated by the waterflooding case into the CO<sub>2</sub> injection compositional simulator model.

**Acknowledgements** The authors would like to thank the Iraqi Ministry of Oil for permission to publish this paper and to PETRONAS Oil Company that support this work.

## References

1. W. J. Al-Mudhafer, "A Practical Economic Optimization Approach with Reservoir Flow Simulation for Infill Drilling in A Mature Oil Field," in North Africa Technical Conference and Exhibition, 2013.
2. A. K. Jaber and M. B. Awang, "Field-scale investigation of different miscible CO<sub>2</sub>," Journal of Petroleum Exploration and Production Technology, pp. 1–22.
3. R. B. Grigg and D. S. Schechter, "State of the Industry in CO<sub>2</sub> Floods," in SPE annual technical conference and exhibition, 1997.
4. M. Garcia Quijada, "Optimization of a CO<sub>2</sub> flood design Wesson Field-west Texas," Texas A&M University, 2006.
5. J. Lohrenz, B. G. Bray, and C. R. Clark, "Calculating viscosities of reservoir fluids from their compositions," Journal of Petroleum Technology, vol. 16, pp. 1,171–1,176, 1964.
6. A. K. Al-Khazraji and M. T. Shuker, "Development of Heterogeneous Immature Brownfield with Waterdrive Using Dynamic Opportunity Index: A Case Study from Iraqi Oil fields," in SPE North Africa Technical Conference and Exhibition, 2015.
7. A. K. Jaber and M. T. Shuker, "Integrated Petrophysical Evaluation of a Heterogeneous Shaly-Sand Reservoir: A Case Study in Nahr Umr Formation-Subba Giant Oil Field, Iraq," Research Journal of Applied Sciences, Engineering and Technology, vol. 8, pp. 2388–2402, 2014.
8. A. K. Jaber and M. T. Shuker, "Multiple Linear Regression Approach for the Permeability Calculation from Well Logs: A Case Study in Nahr Umr Formation-Subba Oil Field, Iraq," International Journal of Science and Research (IJSR) vol. 3, 2014.
9. A. K. Al-Khazraji and M. T. Shuker, "Optimal Field Development of Immature Clastic Heterogeneous Brownfield with Waterdrive: Subba Field, South Iraq Case Study," in SPE North Africa Technical Conference and Exhibition, 2015.
10. Schlumberger Corporation, "ECLIPSE Reservoir Simulation Software Manual," 2013.
11. R. Shpak, "Modeling of Miscible WAG Injection Using Real Geological Field Data," 2013.
12. O. Glass, "Generalized minimum miscibility pressure correlation (includes associated papers 15845 and 16287)," Society of Petroleum Engineers Journal, vol. 25, pp. 927–934, 1985.
13. W. Yellig and R. Metcalfe, "Determination and Prediction of CO<sub>2</sub> Minimum Miscibility Pressures (includes associated paper 8876)," Journal of Petroleum Technology, vol. 32, pp. 160–168, 1980.
14. H. Yuan, R. T. Johns, A. M. Egwuenu, and B. Dindoruk, "Improved MMP correlation for CO<sub>2</sub> floods using analytical theory," SPE Reservoir Evaluation & Engineering, vol. 8, pp. 418–425, 2005.
15. C. Cronquist, "Carbon dioxide dynamic miscibility with light reservoir oils," in Proc. Fourth Annual US DOE Symposium, Tulsa, 1978, pp. 28–30.
16. R. Alston, G. Kokolis, and C. James, "CO<sub>2</sub> minimum miscibility pressure: a correlation for impure CO<sub>2</sub> streams and live oil systems," Society of Petroleum Engineers Journal, vol. 25, pp. 268–274, 1985.

17. A. Satter and G. C. Thakur, *Integrated petroleum reservoir management: a team approach*: PennWell Books, 1994.
18. Y. Ghomian, "Reservoir simulation studies for coupled CO<sub>2</sub> sequestration and enhanced oil recovery," PhD Dissertation, Texas at Austin University, Texas., 2008.
19. J. Nwaozo, "Dynamic optimization of a water flood reservoir," UNIVERSITY OF OKLAHOMA, 2006.
20. L. J. AL-Khatteeb, "The Geopolitics of Natural Gas, Natural Gas in the Republic of Iraq," ed: Center for Energy Studies, Rice University's Baker Institute and Harvard Kennedy School, 2013.
21. A. K. Al-Khazraji and M. B. Awang, "Evaluation of Miscible CO<sub>2</sub>-Flooding to Improve Oil Recovery in a Clastic Heterogeneous Reservoir," in IADC/SPE Asia Pacific Drilling Technology Conference, 2016.
22. "MacroTrends Historical Data."

# A Review on the Application of Ionic Liquids for Enhanced Oil Recovery

Alvinda Sri Hanamertani, Rashidah M. Pilus and Sonny Irawan

**Abstract** Research is extensively ongoing on the application of ionic liquids (ILs) in technological application, particularly its application in the enhanced oil recovery (EOR). Research in this field, however, is often limited to researchers determining ionic liquids' specific behavior in the aqueous solutions. A comprehensive study is necessary to provide a complete possible understanding of the ionic liquids' surface interaction as the self-organization and micelle formation ability of ionic liquids in aqueous solution have significant effect on their applications and the environment. ILs that have surface activity are able to exhibit the critical micelle concentration (CMC) and reduce the interfacial tension (IFT) to the noticeable value even at high salinity and temperature conditions. The application of ILs as cosurfactant is also favorable to support the surfactant performance in minimizing the IFT values. This review indicates that further investigation is required to study the interphase behavior of ionic liquids in a more complex system where hydrocarbons, salts, surfactants, and other chemical additives are present. The alteration in behavior and system properties due to the interaction of ionic liquid with surfactant may determine its effectiveness in emulsion and foaming studies. These two studies are essential in the application of ionic liquids in oil and gas reservoirs, particularly water and chemical flooding to increase the recovery of oil.

**Keywords** Ionic liquid • EOR • Surfactant • Surface activity • Critical micelle concentration • Interfacial tension

---

A.S. Hanamertani (✉) · R.M. Pilus (✉) · S. Irawan  
Department of Petroleum Engineering, University Teknologi PETRONAS,  
32610 Seri Iskandar, Perak Darul Ridzuan, Malaysia  
e-mail: alvindamertani12@gmail.com

R.M. Pilus  
e-mail: rashidah\_mp@utp.edu.my



## 1 Introduction

The application of new technologies in petroleum industry has been continuously investigated in order to conquer many challenges that occurred throughout the crude oil displacement from reservoir to production facilities and further into the refinery process [1]. For example, the exploitation of heavy and extra heavy crude oils encounters problems in several areas such as production, transportation, refining, up to their conversion to usable oil and petrochemicals with higher commercial value. Within the last few years, ionic liquids (ILs) have attracted researchers' attention because of their remarkable properties and potential capabilities to be applied in petroleum industries. The term ionic liquid has been used to describe the salts that melt below 100 °C, whereas room temperature ionic liquids (RTILs) specifically refer to those salts that are electrolytes forming liquid at room temperature range or even below. Their low melting point, nonvolatile, highly polar, and chemically inert nature make them a much investigated reagent or solvent for separation and extraction process [2]. The effectiveness of some ionic liquids to alter heavy crude oil properties, such as viscosity and API gravity, was reported by Nares et al. [3]. ILs have also shown the ability in preventing the precipitation of asphaltene during enhanced oil recovery (EOR) process where CO<sub>2</sub> injection technique was applied. It was observed to effectively break the asphaltene association in which the difference in charge densities between opposite ions in ILs acts to inhibit the precipitation of asphaltene [4]. Additionally, the surface-active ILs can also be used as demulsification agents to break water/oil emulsion which is a necessary process before oil refining [5]. These findings have sparked further investigations on ILs' potential in EOR process.

Previous works highlighted the high interfacial tension (IFT) between oil and the displacing fluid as one of the fundamental reasons for the difficulty in mobilizing residual oil. As such, surfactant flooding has become one of the most promising methods among chemical EOR processes as this technique focuses on IFT reduction and wettability alteration in order to increase the capillary number, hence oil production. Surfactant molecules are able to adsorb at the interface of oil and water due to their amphiphilic structures, thereby reducing the amount of work required to increase the interface area which is favorable for oil mobilization. Thus, surfactant application in EOR was observed to enhance the displacement of oil and sweep efficiency [6]. However, the tendency of surfactant to be adsorbed on the reservoir rock surface has been regarded as the limitation of surfactant flooding. Some studies have also ascertained that most surfactants are not able to tolerate harsh reservoir conditions. The reduced performance of surfactant at high temperatures and salinity has led to new technologies, chemicals, and formulations being explored [7–10]. The addition of chemicals that support surfactant performance in chemical process has been considered to bring about an ultralow IFT required for an efficient oil displacement process.

Based on the continuous studies, ILs, which are known as “green chemicals,” have been regarded as potential alternates to surfactant since some of them exhibit

the surface activity and noticeable effect on micelle formation [11]. Some researchers have tried to investigate the capability of ILs as supporting or alternative chemicals in order to improve the techniques applied in EOR. This review will provide the information on ILs' interfacial behavior gathered from recent studies to gain in-depth understanding of its application in EOR scenario and pave the way for the production of better ILs that may fulfill the requirement of specific EOR and/or reservoirs.

## 2 Interfacial Phenomena

Petroleum reservoirs typically contain multiple fluid phases, either two (gas/water or oil/water) or three fluid phases (gas/oil/water). The forces at the interface of these immiscible phases are known as the interfacial tension. The main attempt of EOR technique is to minimize the interfacial tension between oil and formation brine, thus improving the displacement efficiency. The variation in oil/water interfacial tension highly influences fluid displacement in a reservoir, and therefore, an important property has to be studied before the EOR process. Based on the previous studies, IFT values are highly dependent on temperature and pressure [12]. However, the plots may give inconsistent trends of IFT values due to its dependency on some other equally important parameters, such as salinity, type of oil, liquid composition, or concentration of additives. Therefore, the whole fluid system and experimental conditions need to be considered in order to evaluate the interfacial behavior.

The presence of suitable chemical which has surface activity, like surfactant, is required to modify the interfacial properties, particularly surface tension or IFT reduction. The surface activity of surfactant is due to its ability to be adsorbed at the interface and form aggregates which are called micelles. At the interface, surfactant molecules will direct the hydrophobic tail to be apart from the water system. Once the surfactant molecules have completely saturated the surface, micelle formation or "micellization" occurs. Micellization is a phenomenon when self-organization of surfactant molecules occurs by the hydrophilic head groups rearranging themselves to be in contact with the water system and simultaneously adjusting to the repulsion forces between themselves, thus forming the outer part of a micelle. The surfactant concentration at which the micelles begin to form at large amount after the interface region has been saturated by surfactant molecules is called critical micelle concentration (CMC). The accumulation of surfactant molecules at the interface results in IFT reduction. A drastic decline in IFT value indicates the significant formation of micelles. Surfactant molecule distribution from the bulk phase to the interface is influenced by the diffusion and adsorption process. The diffusion process is responsible for molecule distribution from the bulk phase to the subsurface region before reaching the interface area, while the adsorption process controls molecule movement from subsurface to the interface. The adsorption of surfactant molecules at the interface is dependent on the nature of the amphiphilic structure possessed by

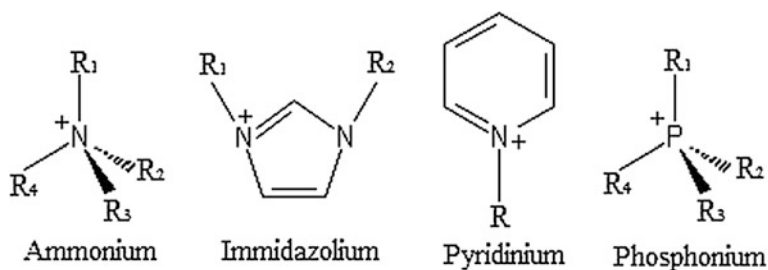
surfactant, the vacant space available to be adsorbed, and the possible interaction occurring at the interface, such as electrical repulsion or attraction [13, 14].

Surfactant solution used for EOR flooding is normally at the concentration above CMC in order to form micelle solution. The formation of micelles is effective in carrying oil molecules which will be attached with surfactant hydrophobic tails. For ionic surfactant, the concentration above the CMC is required to conduct the efficient process, while for nonionic surfactants, it is sufficient to apply the concentration around CMC value [9]. CMC has to be determined before surfactant application to know the economical concentration needed to form significant amount of micelles, which is important in determining the molecule adsorption at the interface. Currently, many studies have reported the ability of ILs to form micelle, hence reducing IFT of oil–water systems even at harsh conditions of salinity and temperature.

### 3 Ionic Liquids

Ionic liquids (ILs) are ionic compounds and typically composed of both cationic and anionic species which have melting point less than 100 °C. The cation can be obtained from organic source, while the anion can be from organic or inorganic source. ILs are usually classified based on their cationic part, such as (1) ammonium, (2) imidazolium, (3) pyridinium, and (4) phosphonium (Fig. 1) [15]. The physical and chemical properties of ILs can be modified by changing the cation and anion in their molecule structure [16]. The anions commonly used for IL preparation include chloride [Cl]<sup>−</sup>, bromide [Br]<sup>−</sup>, iodide [I]<sup>−</sup>, hexafluorophosphate [PF<sub>6</sub>]<sup>−</sup>, tetrafluoroborate [BF<sub>4</sub>]<sup>−</sup>, methane sulfonate (mesylate) [CH<sub>3</sub>SO<sub>3</sub>]<sup>−</sup>, bis (trifluoromethanesulfonyl) imide [(CF<sub>3</sub>SO<sub>2</sub>)<sub>2</sub>N]<sup>−</sup>, and nitrate [NO<sub>3</sub>]<sup>−</sup> [15, 17].

Besides melting at low temperatures, ILs have beneficial properties such as wide liquid range and high thermal stability and hence suitable for high-temperature applications such as the reservoirs [18, 19]. Certain ILs containing the imidazolium ring exhibit very high thermal stability and tend to be more stable than ammonium ILs [20]. The interaction of ILs with other compounds is dependent on the nature of



**Fig. 1** The common cationic structures of ILs

their cation and anion. Certain types of ILs have amphiphilic structure, containing both hydrophobic tail groups and hydrophilic head groups with surface activity, for example, imidazolium-based ionic liquids containing hydrophobic chain longer than four carbon atoms [21]. In general, the properties of ILs highly depend on the structures, the combination of anions and cations, and the ionic interaction. These factors can also affect the ability of ILs to alter the interfacial behavior of EOR processes. A screening of several ILs before investigating their capability in improving oil recovery is important to be carried out. Some screening parameters might be carried out according to the property of ILs such as their solubility in water and brine, surface activity, and stability at high temperature.

## 4 Surface Activity of Ionic Liquids

ILs, which have surface activity, similar to surfactant, are able to be adsorbed at water/oil interface with particular arrangement. The amphiphilic structures possessed by some ILs are able to influence the distribution of IL molecules at the surface and the repulsion between the ionic heads. Owing to these characteristics, similar to surfactant behavior, ILs are able to form micelles or aggregates in aqueous solution at certain concentration. The aggregation of ILs in aqueous system is affected by the attractive interaction between hydrophobic chains, the hydrogen bond, and Coulombic interaction. It was also reported that the CMC of ILs is influenced by the length of hydrophobic chain, counter ion bonding, number of aggregations, and temperature [22–24].

In enhancing oil recovery, like surfactants, it is necessary for ILs to reduce the interfacial tension between water and oil. Studies have confirmed that some ILs exhibit the critical micelle concentration (CMC) and lower the IFT to the noticeable value, given in Table 1. The major observations are IFT between oil and water decreases as IL concentration increases and the ability of ILs in reducing IFT increases when it is prepared in formation brine. The presence of salt has successfully affected the surface activity of ILs by forming electrical attraction between opposite charges. The closed arrangement of IL molecules at the surface due to their interaction with salt ions leads to significant IFT reduction. At CMC, an imidazolium-based IL is even able to drastically reduce the IFT, from 38.02 mN/m to the lowest value of 0.81 mN/m [11]. According to these studies, the reduction of IFT occurred when IL molecules accumulate at the interface; thus, the neutralization of the positive charges from the cationic part of ILs by negative charges from salt ions expands the oil and brine contact area.

The surface activity of ILs of different alkyl chain length or different cation moiety gives rise to different IFT reduction ability. Investigations on imidazolium-based IL and pyridinium-based IL with eight and twelve carbon chains, namely 1-octyl-3-methylimidazolium chloride ( $[\text{C}_8\text{mim}][\text{Cl}]$ ), 1-dodecyl-3-methylimidazolium chloride ( $[\text{C}_{12}\text{mim}][\text{Cl}]$ ), 1-dodecyl pyridinium chloride ( $[\text{C}_8\text{Py}][\text{Cl}]$ ), and 1-dodecyl pyridinium chloride ( $[\text{C}_{12}\text{Py}][\text{Cl}]$ ), showed

**Table 1** CMC of several types of ILs and the IFT obtained at CMC

Ionic liquid	CMC (ppm)	Brine system	IFT at CMC (mN/m)	Reference
[C <sub>12</sub> mim][Cl]	2000	–	7.23	[11]
	100	Formation brine	0.81	[11, 14]
	250	Formation brine	0.83	[25]
[C <sub>8</sub> mim][Cl]	1000	–	16.77	[14]
	500	Formation brine	11.12	[14]
[C <sub>12</sub> Py][Cl]	500	–	8.72	[14]
	250	Formation brine	7.10	[14]
[C <sub>8</sub> Py][Cl]	nd <sup>a</sup>	–	> 21.89	[14]
	750	Formation brine	18.24	[14]
Tetra-alkyl ammonium sulfate (Ammoeng 102)	250	20% wt. NaCl and CaCl <sub>2</sub>	1.65	[26, 27]

<sup>a</sup>Not detected

that the pyridium-based and imidazolium-based ILs with long hydrocarbon chain (C<sub>12</sub>) have the tendency to be more effective in reducing IFT than the ILs with shorter hydrocarbon chain (C<sub>8</sub>). This result agrees with the study conducted by Javadian et al. [21] which confirms that ILs with longer alkyl chain will have higher surface activity due to higher tendency to have intermolecular interaction with the hydrocarbon chain. Thus, ILs with longer hydrophobic chain will reach CMC at low concentration compared to the ILs with shorter hydrophobic chain [21].

## 5 The Reduction of Ionic Liquids/Crude Oil IFT in the Presence of Salt

ILs prepared in formation brine tend to have lower IFT value compared to ILs prepared in distilled water, especially for imidazolium-based ILs. In general, all types of ILs are able to reduce IFT in the absence or presence of salt ions. The presence of opposite ions in salt leads to the counterion attraction. Ions with negative charges can attract the positive charges attached to the cationic part of ILs, thus reducing the electrical repulsion between cationic charges of IL head groups. This interaction, producing electrostatic stabilization, improves the IL molecule adsorption at the interface. Therefore, IL molecules will compactly occupy the brine/oil interface which leads to the higher IFT reduction. The extent of IFT reduction takes into account the capability of ionic liquid in optimizing their adsorption at hydrophilic and hydrophobic interface and in tolerating the high salinity condition, especially in the presence of divalent ions. Adequately compact IL molecule arrangement at the interface can facilitate the formation of micelles at low concentration of ILs.

In distilled water however, in the absence of salt ions, the IL molecules tend to repel each other until certain arrangement with lower number of IL molecules (due to high surface charge density) is reached. The same salinity condition can reduce the CMC of imidazolium-based IL ( $[C_{12}mim][Cl]$ ) to very low concentration more significantly compared to that of pyridinium-based IL with the same length of alkyl chain. This is due to the lower hydrophobicity of the imidazolium ion as compared to the pyridinium ion [14]. The presence of negative ions in salts can reduce the repulsion between imidazolium ions more effectively since they have higher affinity to water compared to pyridinium ions. The tendency of cationic group in ILs to attract water can support its interaction with salt anion.

Some studies on the effect of salt concentration on IFT between crude oil and IL solution revealed that some ILs have high salinity tolerance at which ILs still have good performance in reducing IFT. In contrast, the salinity tolerance of some conventional surfactants is not very high since they showed the trend that IFT is not persistently decreasing with increasing salt concentrations. It is dependent on factors such as the charge type and concentration of surfactant used [28]. In EOR process, the salinity of formation water should meet the salinity tolerance range of the particular surfactant or IL used in order for the water/oil IFT to decrease. Table 2 shows the result from previous studies on declining IFT trend with rising salt concentration using ILs.

$[C_{12}mim][Cl]$  was reported to persistently reduce the IFT at salinity condition ranging from 10,000 up to 100,000 ppm of NaCl, and the significant IFT reduction at 100,000 ppm of salt showed the stability of IL at high saline solutions compared to the conventional surfactants. The IFT values achieved were also constant over time. The pyridinium-based ILs with longer hydrophobic tail chain length reduced

**Table 2** Interfacial tension between crude oil and different IL solutions with increasing salt concentration

Salt concentration (ppm)	IFT (mN/m)						
	$[C_{12}mim][Cl]$	$[C_8mim][Cl]$	$[C_6mim][HSO_4]$	$[C_4mim][Cl]$	$[C_{12}Py][Cl]$	$[C_8Py][Cl]$	Ammoeng 102
10,000	6.2 [11] <sup>c</sup>	14.57 [31] <sup>b</sup>	16.36 [31] <sup>b</sup>	15.24 [31] <sup>b</sup>			
25,000	3.9 [11] <sup>c</sup>						
50,000	2.4 [11] <sup>c</sup>	12.33 [31] <sup>b</sup>	14.85 [31] <sup>b</sup>	13.75 [31] <sup>b</sup>			
100,000	0.56 [11] <sup>c</sup>	10.48 [31] <sup>b</sup>	13.85 [31] <sup>b</sup>	12.64 [31] <sup>b</sup>			4.8c at 25 °C [9] <sup>d</sup> 3.36 at 60 °C [26] <sup>a</sup>
150,000		1.78 [14] <sup>b</sup>			2.57 [14] <sup>b</sup>	11.23 [14] <sup>b</sup>	
200,000		1.43 [14] <sup>b</sup>	11.37 [31] <sup>b</sup>	9.86 [31] <sup>b</sup>	1.00 [14] <sup>b</sup>	11.86 [14] <sup>b</sup>	1.65 at 60 °C [26] <sup>a</sup>
250,000		1.37 [14] <sup>b</sup>			1.47 [14] <sup>b</sup>	11.98 [14] <sup>b</sup>	
300,000		1.29 [14] <sup>b</sup>			0.91 [14] <sup>b</sup>	12.01 [14] <sup>b</sup>	

IL concentration: <sup>a</sup>250 ppm; <sup>b</sup>1000 ppm; <sup>c</sup>1250 ppm; <sup>d</sup>2000 ppm

IFT better up to 300,000 ppm salt concentration. A study on different type of ILs showed that a low concentration of tetra-alkyl ammonium sulfate IL (Ammoeng 102) could reduce IFT in an increasing salinity from 100,000 to 200,000 ppm of brine containing NaCl and CaCl<sub>2</sub>. Moreover, the imidazolium-based ILs of different alkyl chain length and anion types ([C<sub>n</sub>mim][X], *n* = 12 and 16, X = Cl<sup>-</sup>, Br<sup>-</sup>) also showed a declining IFT trend with the increase of salinity in the presence of different salts (NaCl, KCl) [29].

The salt ions in aqueous system may present a competition with cations and anions of ILs in attracting water molecules. For instance, [C<sub>12</sub>mim]<sup>+</sup> and Na<sup>+</sup> from NaCl attract water molecules for undergoing hydration. However, the strong hydration is obtained by Na<sup>+</sup> ions due to the smaller size and high surface charge density, inducing the [C<sub>12</sub>mim]<sup>+</sup> ions to be adsorbed at the interface. It leads to a decrease in IFT, and the same trend is also observed for [C<sub>16</sub>mim][Cl] and [C<sub>16</sub>mim][Br]. The investigation reveals that the system containing IL with longer alkyl chain length and bigger size of anion exhibits higher reduction of IFT that in order for the short-alkyl-chain ILs to produce equal IFT value, it is necessary for its concentration to be higher than the long-chain ILs [29, 30].

## 6 Effect of Temperature on Ionic Liquids/Crude Oil IFT

In addition to salinity, the temperature effect should be investigated to assess the capability of IL to persistently reduce the IFT through the rising temperature in the reservoir. Table 3 reports the change of IFT value of oil and some ionic liquid solutions as temperature increases. The trend of increasing IFT with temperature was observed in [C<sub>12</sub>mim][Cl], [C<sub>8</sub>mim][Cl], [C<sub>8</sub>Py][Cl], and [C<sub>12</sub>Py][Cl] ILs for the temperature range of 20–60 °C. However, the ammonium-based IL (Ammoeng 102) showed a decreasing trend on IFT with increasing temperature from 20 °C to 90 °C and better when compared to commercial surfactant (Triton X-100) at the same set conditions. Their results showed that the IFT values vary with the type of ILs used and depended on the total concentration, the surfactant-to-IL-mass ratio, and the temperature. Additionally, based on the initial findings, the capability of ammonium-based ILs is better than that of phosphonium-based ILs in reducing IFT value at different temperature up to 90 °C. In terms of pressure, Bin-Dahbag and coworkers reported that IFT between oil and Ammoeng 102 solution slightly increases with pressure up to 4000 psig at different temperatures [26, 27].

The increasing IFT values due to rising temperature can be affected by the IL molecule distribution change at the interface. There are two factors that can influence the interfacial behavior, particularly when temperature changes: the limitation of molecule movement at the interface and dehydration of hydrophilic head and/or hydrophobic tail groups [32]. At high temperature, dehydration of molecules either at the interface or in the bulk phase will occur due to thermal motion which leads to higher entropy of the system. Furthermore, the change of IFT by temperature might be affected by emulsion alteration from oil-in-water at low

**Table 3** Interfacial tension between crude oil and different IL solutions with increasing temperature

Temperature (°C)	IFT (mN/m)					
	[C <sub>12</sub> mim][Cl] <sup>a</sup>	[C <sub>8</sub> mim][Cl] <sup>c</sup>	[C <sub>4</sub> mim][Cl] <sup>b</sup>	[C <sub>12</sub> Py][Cl] <sup>c</sup>	[C <sub>8</sub> Py][Cl] <sup>c</sup>	Ammoeng 102 <sup>a</sup>
15			22.57 [31]			
20	0.5 [11]	1.29 [14]		0.91 [14]	12.1 [14]	4.8 [9]
25			19.03 [31]			
30	0.9 [11]	1.74 [14]		1.47 [14]	13.12 [14]	
35			18.56 [31]			
40	1.35 [11]	2.11 [14]		2.09 [14]	15.6 [14]	4.2 [9]
45			17.96 [31]			
50	2.1 [11]	2.42 [14]		2.54 [14]	16.01 [14]	
60	2.7 [11]	2.91 [14]		2.76 [14]	16.45 [14]	3.5 [9]
80						2.9 [9]
90						2.3 [9]

<sup>a</sup>2000 ppm IL in brine<sup>b</sup>5000 ppm IL in brine<sup>c</sup>10,000 ppm IL, 300,000 ppm of NaCl concentration

temperature to water-in-oil as temperature increases. The emulsion inversion occurs after reaching phase inversion temperature (PIT). At the temperature below PIT, the IFT value might decrease with rising temperature due to the conformation of molecule arrangement at the interface. The oil/water interface will be saturated when the PIT is reached causing the maximum reduction of IFT. Then, at the temperature higher than PIT, the IL molecules tend to be distributed on to oil phase, causing the emulsion inversion, similar to surfactant behavior [25, 33].

## 7 Effect of Ionic Liquids on the Performance of Surfactant

In chemical EOR processes, the performance of surfactant under reservoir conditions can be optimized by the presence of cosurfactant, such as alcohol or synthetic surfactant [34, 35]. Cosurfactant that can enhance surfactant properties, such as thermal stability and salinity tolerance, may improve the effectiveness of surfactant in reducing oil/water IFT at harsh condition of reservoirs. Studies have shown that surfactant/IL mixture of ammonium-based IL and a commercial surfactant (Triton X-100) with the mass ratio of 1:1 at total concentration 200 and 2000 ppm in 10% wt. brine is able to reduce IFT value at and above temperature 40 °C, compared to other mass ratios containing higher amount of surfactant [9]. This means the



presence of IL at specific ratio and temperature, is possible to change IFT trend of a surfactant in saline condition.

The presence of ILs in surfactant solution has also been reported to modify the critical micelle concentration (CMC) and micellization behavior of surfactant as observed in the varying surface activities of cetyl trimethylammonium bromide (CTAB) as a function of structural properties of imidazolium-based ILs [21]. Apart from decreasing the CMC of a surfactant, ILs influence the micellization of surfactant based on their concentration and molecular structure (type of anion and hydrocarbon chain length). ILs with long hydrophobic chain (more than four carbon atoms) are able to produce the hydrophobic effect, while the ILs with the short chain mainly act as electrolytes. The IL molecules may interact with surfactant to form mixed micelles through hydrogen bonding formation, hydrophobic interactions, and electrical repulsion stabilization between ionic heads of surfactant. These three interactions lead to further alteration of CMC. In addition, an increase in the size of the hydrophilic anions could reduce the CMC. The hydration of the bigger anions is more difficult; thus, they tend to be attached on the micelle surface which is favorable for micellization.

Some ILs, such as  $[C_6mim][Cl]$ ,  $[C_6mim][Br]$ ,  $[C_4mim][Cl]$ , and  $[C_4mim][Br]$ , can reduce electrostatic repulsion between anionic groups of SDS (sodium dodecyl sulfate) even at low concentration, indicated by a decrease of surface tension and CMC. The factors identified to be responsible for this phenomenon are electrostatic and hydrophobic interaction, hydrogen bonding, and electrolyte effect. It was observed that the higher reduction of CMC was reached by the mixture solutions containing IL with longer alkyl chain due to the stronger hydrophobic effect it produced. Beyaz et al. [36] who worked on SDS and several types of imidazolium-based ILs (e.g. 1,3-dimethylimidazolium iodide ( $[Me_2Im][I]$ ), 1-butyl-3-methylimidazolium chloride ( $[C_4mim][Cl]$ ), 1-hexyl-3-methylimidazolium chloride ( $[C_6mim][Cl]$ ), 1-methyl-3-octylimidazolium chloride ( $[C_1OIm][Cl]$ ), and 1-methyl-3-octylimidazolium tetrafluoroborate ( $[C_1OIm][BF_4]$ )) as additives, also reported that an increase in the length of hydrocarbon chain leads to the decrease of CMC of SDS which is favorable for micellization. The presence of  $[C_6mim][Cl]$ ,  $[C_1OIm][Cl]$ , and  $[C_1OIm][BF_4]$  IL consistently reduces CMC compared to  $[Me_2Im][I]$  and  $[C_4mim][Cl]$ . Since the anionic head groups of SDS and cationic head groups of IL undergo electrical attraction accompanied by the electrolyte effect and hydrophobic interaction between their alkyl chains, the ILs here can be considered as a cosurfactant. It indicates the synergetic effect toward interfacial behavior that can be produced when using a mixture of IL and surfactant [36, 37].

Additionally, the interaction between surfactant and IL can affect the properties of micelles, such as micelle size and morphology. Previous study reported the growing size of surfactant micelles from 5 nm to approximately 20–30 nm due to the interaction between IL  $[C_6mim][Br]$  and cationic surfactant. The interactions at the outer and inner parts of micelles induce the micelle morphology transition from spherical to cylindrical. Further micellar growth can be influenced by a higher IL concentration due to better electrostatic stabilization of micelles at the surface. The addition of ILs into surfactant solution could also increase the aggregation number

and size due to the reduction of electrical repulsion between anionic head groups of surfactant. The micellar transition from spherical micelles to vesicle or wormlike micelles can be achieved by the addition of ILs with long alkyl chain (longer than  $C_6$ ) since the interaction between hydrophobic parts is considered as a key role in the formation of large mixed micelles. The morphology modification has a great importance for some applications; for example, the formation of cylindrical micelles is preferable in foam application because it has higher viscosity than spherical micelles, which is generally formed in the single surfactant system [38]. Consequently, the formation of long cylindrical micelles is considered to improve foam stability by reducing the liquid drainage through the thin liquid film, the so-called lamellae [39].

## 8 Ionic Liquids for EOR Flooding

Studies discussed earlier had supported the possible utilization of ILs for flooding process to enhance oil recovery. The ability of  $[C_{12}mim][Cl]$  ionic liquid to increase the oil recovery efficiency has been investigated at certain condition [11]. Based on the study, an increase in IL concentration has led to an increment of oil recovery efficiency. The IL solutions prepared in brine have resulted in the reduction of oil/water IFT indicating feasibility in saline environment of the reservoir, and the presence of salt induces the complete adsorption of IL molecules at the interface providing a large area for water/oil contact, hence ultimately improving oil displacement. The presence of some ILs is also capable of altering the wettability from slightly oil wet to medium water wet condition as IL concentration increases. In the application of ammonium-based IL in flooding process, it is preferred to initially carry out the secondary flooding with low-salinity brine prior to IL flooding. The tertiary flooding of IL with high salinity condition is favorable to get the optimum recovery than that of IL prepared with low salinity condition [26]. 1-ethyl-3-methylimidazolium tosylate,  $[C_2mim][OTs]$ , has shown its ability to enhance oil recovery, especially the aromatic hydrocarbon [40]. The oil recovery using this IL solution with volume 4 times greater than the pore volume is almost two times more than that using brine solution or surfactant solution. The high electrostatic interaction and aromatic character are the essential factors affecting the oil recovery. The electrostatic interaction refers to the interaction between the ionic groups of IL and the counterion from sand surface which allows the wettability alteration and consequently improves oil displacement. Meanwhile, the ability of IL to interact with the aromatic content in oil is affected by the aromaticity of IL through  $\pi$ - $\pi$  interactions. These studies have confirmed that the application of ILs can be considered as an alternative or additional stage to the conventional EOR flooding processes.

## 9 Conclusion

This review highlights the application of ILs for EOR purpose, especially its surface activity as determined by several studies. ILs have the ability to effectively reduce interfacial tension at high salinity and temperature conditions and increase the oil recovery efficiency on the laboratory scale. These results indicate the possibility of using ILs in harsh condition of reservoir. The application of ILs as cosurfactant is also favorable to support the surfactant performance in minimizing the IFT values. However, the IFT values acquired from a mixture system are dependent on the type of ILs applied, mass ratio, total concentration, and temperature. As studies also showed that in oil recovery process, some interactions may occur between ILs and other components such as oil, brine, surfactant, and reservoir rock surface; hence, several fields do require further investigation. A study on the interfacial behavior of a more complex system in the presence of ILs at various conditions can be conducted to strengthen the understanding of system dependence toward particular conditions, such as salinity, temperature, and pressure. Therefore, it is important to design and conduct basic experiments on reservoir conditions for the utilization of ILs to be feasible for EOR purposes.

The capability of ILs to modulate micellar transition which ultimately results in higher viscosity due to the large number of aggregates will be very useful for foam studies whereby the ILs can be expected to support the surfactant performance in generating stable foam. The results derived from some studies that investigate the ability of ILs to alter many aspects, such as surface activity, interfacial behavior, surfactant properties, micellar size, and morphology formed in the system, become very important to be explored for further application in emulsion or foaming studies. On the other hand, since the ILs have the tendency to be adsorbed on the reservoir rock by the strong electrostatic interaction between the negative charge at the rock surfaces and the cationic charge of IL cations, the study on the IL adsorption on the reservoir rock surface must be carried out in depth to avoid chemical loss during flooding. However, if the adsorption of ILs is favorable for maintaining the function of surfactant in alternating oil–water emulsion, a deeper study on IL interaction and distribution on the reservoir rock along with the environmental impact should also be considered.

**Acknowledgements** The authors gratefully acknowledge Universiti Teknologi PETRONAS (UTP) for providing financial support through the Graduate Research Assistant (GRA) Scheme.

## References

1. M.-H. José-Alberto and A. Jorge, "Current knowledge and potential applications of ionic liquids in the petroleum industry," in *Ionic liquids: Applications and Perspectives*, A. Kokorin, Ed., ed Rijeka, Croatia: InTech, pp. 439–456, 2011.
2. J. D. Holbrey and K. R. Seddon, "Ionic Liquids," *Clean Products and Processes*, vol. 1, p. 223, 1999.
3. R. Nares, P. Schacht-Hernandez, M. A. Ramirez-Garnica, and M. d. C. Cabrera-Reyes, "Upgrading Heavy and Extra Heavy Crude Oil with Ionic Liquid," presented at the International Oil Conference and Exhibition, Veracruz, Mexico, 2007.
4. Y. F. Hu and T. M. Guo, "Effect of the structures of ionic liquids and alkylbenzene-derived amphiphiles on the inhibition of asphaltene precipitation from CO<sub>2</sub>-injected reservoir oils," *Langmuir*, vol. 21, pp. 8168–8174, 2005.
5. D. Guzmán-Lucero, P. Flores, T. Rojo, and R. Martínez-Palou, "Ionic liquids as demulsifiers of water-in-crude oil emulsions: study of the microwave effect," *Energy & Fuels*, vol. 24, pp. 3610–3615, 2010.
6. D. W. Green and G. P. Willhite, *Enhanced Oil Recovery*. Richardson, TX: Henry L. Doherty Memorial Fund of AIME, Society of Petroleum Engineers, 1998.
7. M. R. Azam, I. M. Tan, L. Ismail, M. Mushtaq, M. Nadeem, and M. Sagir, "Static adsorption of anionic surfactant onto crushed Berea sandstone," *Journal of Petroleum Exploration and Production Technology*, vol. 3, pp. 195–201, 2013.
8. J. J. Sheng, "Status of surfactant EOR technology," *Petroleum*, vol. 1, pp. 97–105, 2015.
9. M. S. Benzagouta, I. M. AlNashef, W. Karnanda, and K. Al-Khidir, "Ionic liquids as novel surfactants for potential use in enhanced oil recovery," *Korean Journal of Chemical Engineering*, vol. 30, pp. 2108–2117, 2013.
10. W. Karnanda, M. S. Benzagouta, A. AlQuraishi, and M. M. Amro, "Effect of temperature, pressure, salinity, and surfactant concentration on IFT for surfactant flooding optimization," *Arabian Journal of Geosciences*, vol. 6, pp. 3535–3544, 2012.
11. A. Z. Hezave, S. Dorostkar, S. Ayatollahi, M. Nabipour, and B. Hemmateenejad, "Investigating the effect of ionic liquid (1-dodecyl-3-methylimidazolium chloride ([C<sub>12</sub>mim][Cl])) on the water/oil interfacial tension as a novel surfactant," *Colloids and Surfaces A: Physicochemical and Engineering Aspects*, vol. 421, pp. 63–71, 2013.
12. W. Wang and A. Gupta, "Investigation of the Effect of Temperature and Pressure on Wettability Using Modified Pendant Drop Method," presented at the SPE Annual Technical Conference and Exhibition, Dallas, Texas, 1995.
13. S. Fu, W. Zhou, Z. Wang, B. Yin, J. Liu, D. Sun, et al., "Study on dynamic interfacial tension of 3-dodecyloxy-2-hydroxypropyl trimethyl ammonium bromide at liquid/liquid interface," *Fluid Phase Equilibria*, vol. 269, pp. 93–97, 2008.
14. A. Z. Hezave, S. Dorostkar, S. Ayatollahi, M. Nabipour, and B. Hemmateenejad, "Effect of different families (imidazolium and pyridinium) of ionic liquids-based surfactants on interfacial tension of water/crude oil system," *Fluid Phase Equilibria*, vol. 360, pp. 139–145, 2013.
15. J. Wang and H. Wang, "Aggregation in Systems of Ionic Liquids," in *Structures and Interactions of Ionic Liquids*. vol. 151, S. Zhang, J. Wang, X. Lu, and Q. Zhou, Eds., ed Heidelberg: Springer-Verlag Berlin Heidelberg, 2014.
16. S. Zhang, N. Sun, X. He, X. Lu, and X. Zhang, "Physical Properties of Ionic Liquids: Database and Evaluation," *Journal of Physical and Chemical Reference Data*, vol. 35, pp. 1475–1517, 2006.
17. K. Dong, Q. Wang, X. Lu, Q. Zhou, and S. Zhang, "Structure, Interaction and Hydrogen Bond," in *Structures and Interactions of Ionic Liquids*, S. Zhang, J. Wang, X. Lu, and Q. Zhou, Eds., ed Berlin, Heidelberg: Springer Berlin Heidelberg, 2014, pp. 1–38.
18. A. Kokorin, *IONIC LIQUIDS: APPLICATIONS AND PERSPECTIVES*. Rijeka, Croatia: InTech, 2011.

19. S. Zhang, J. Wang, X. Lu, and Q. Zhou, *Structures and interactions of ionic liquids*. Heidelberg: Springer-Verlag, 2014.
20. H. Tokuda, K. Hayamizu, K. Ishii, M. A. B. H. Susan, and M. Watanabe, "Physicochemical Properties and Structures of Room Temperature Ionic Liquids. 2. Variation of Alkyl Chain Length in Imidazolium Cation," *The Journal of Physical Chemistry B*, vol. 109, pp. 6103–6110, 2005.
21. S. Javadian, V. Ruhi, A. A. Shahir, A. Heydari, and J. Akbari, "Imidazolium-Based Ionic Liquids as Modulators of Physicochemical Properties and Nanostructures of CTAB in Aqueous Solution: The Effect of Alkyl Chain Length, Hydrogen Bonding Capacity, and Anion Type," *Industrial & Engineering Chemistry Research*, vol. 52, pp. 15838–15846, 2013.
22. H. Zhang, K. Li, H. Liang, and J. Wang, "Spectroscopic studies of the aggregation of imidazolium-based ionic liquids," *Colloids and Surfaces A: Physicochemical and Engineering Aspects*, vol. 329, pp. 75–81, 2008.
23. J. Luczak, J. Hupka, J. Thöming, and C. Jungnickel, "Self-organization of imidazolium ionic liquids in aqueous solution," *Colloids and Surfaces A: Physicochemical and Engineering Aspects*, vol. 329, pp. 125–133, 2008.
24. C. Jungnickel, J. Luczak, J. Ranke, J. F. Fernández, A. Müller, and J. Thöming, "Micelle formation of imidazolium ionic liquids in aqueous solution," *Colloids and Surfaces A: Physicochemical and Engineering Aspects*, vol. 316, pp. 278–284, 2008.
25. A. Z. Hezave, S. Dorostkar, S. Ayatollahi, M. Nabipour, and B. Hemmateenejad, "Dynamic interfacial tension behavior between heavy crude oil and ionic liquid solution (1-dodecyl-3-methylimidazolium chloride ([C<sub>12</sub>mim][Cl])<sup>+</sup> distilled or saline water/heavy crude oil) as a new surfactant," *Journal of Molecular Liquids*, vol. 187, pp. 83–89, 2013.
26. M. Bin-Dahbag, A. AlQuraishi, and M. Benzagouta, "Efficiency of ionic liquids for chemical enhanced oil recovery," *Journal of Petroleum Exploration and Production Technology*, vol. 5, pp. 353–361, 2014.
27. M. S. Bin-Dahbag, A. A. Al Quraishi, M. S. Benzagouta, M. M. Kinawy, I. M. Al Nashef, and E. Al Mushaegeh, "Experimental study of use of ionic liquids in enhanced oil recovery," *Journal of Petroleum & Environmental Biotechnology*, vol. 4, 2014.
28. B. Kumar, "Effect of Salinity on the Interfacial Tension of Model and Crude Oil Systems," Master Thesis, Department of Chemical and Petroleum Engineering, University of Calgary, Calgary, Alberta, 2012.
29. S. Asadabadi and J. Saien, "Effects of pH and salinity on adsorption of different imidazolium ionic liquids at the interface of oil–water," *Colloids and Surfaces A: Physicochemical and Engineering Aspects*, vol. 489, pp. 36–45, 2016.
30. J. Saien and S. Asadabadi, "Salting out effects on adsorption and micellization of three imidazolium-based ionic liquids at liquid–liquid interface," *Colloids and Surfaces A: Physicochemical and Engineering Aspects*, vol. 444, pp. 138–143, 2014.
31. S. Sakthivel, S. Velusamy, R. L. Gardas, and J. S. Sangwai, "Use of Aromatic Ionic Liquids in the Reduction of Surface Phenomena of Crude Oil–Water System and their Synergism with Brine," *Industrial & Engineering Chemistry Research*, vol. 54, pp. 968–978, 2015.
32. H. Matsubara, A. Onohara, Y. Imai, K. Shimamoto, T. Takiue, and M. Aratono, "Effect of temperature and counterion on adsorption of imidazolium ionic liquids at air–water interface," *Colloids and Surfaces A: Physicochemical and Engineering Aspects*, vol. 370, pp. 113–119, 2010.
33. Z. Ye, F. Zhang, L. Han, P. Luo, J. Yang, and H. Chen, "The effect of temperature on the interfacial tension between crude oil and gemini surfactant solution," *Colloids and Surfaces A: Physicochemical and Engineering Aspects*, vol. 322, pp. 138–141, 2008.
34. S. B. Sandersen, "Enhanced Oil Recovery with Surfactant Flooding," PhD Dissertation, Department of Chemical and Biochemical Engineering, Technical University of Denmark, Kongens Lyngby, Denmark, 2012.
35. J. J. Sheng, "Surfactant Flooding," in *Modern Chemical Enhanced Oil Recovery*, ed Boston: Gulf Professional Publishing, 2011, pp. 239–335.

36. A. Beyaz, W. S. Oh, and V. P. Reddy, "Ionic liquids as modulators of the critical micelle concentration of sodium dodecyl sulfate," *Colloids and Surfaces B: Biointerfaces*, vol. 35, pp. 119–124, 2004.
37. F. Comelles, I. Ribosa, J. J. Gonzalez, and M. T. Garcia, "Catanionic surfactant formation from the interaction of the cationic surfactant hexadecyltrimethylammonium bromide (CTAB) and the ionic liquid 1-butyl-3-methylimidazolium octyl sulfate (bmim-octyl SO<sub>4</sub>) in aqueous solution," *Colloids and Surfaces A: Physicochemical and Engineering Aspects*, vol. 484, pp. 136–143, 2015.
38. M. J. Rosen and J. T. Kunjappu, "Micelle Formation by Surfactants," in *Surfactants and Interfacial Phenomena*, M. J. Rosen and J. T. Kunjappu, Eds., 4 ed Hoboken, NJ, USA: John Wiley & Sons, Inc., 2012, pp. 123–201.
39. S. C. Sharma, L. K. Shrestha, and K. Aramaki, "Foam Stability Study of Dilute Aqueous Nonionic Fluorinated Surfactant Systems," *Journal of Nepal Chemical Society*, vol. 22, p. 8, 2007.
40. J. F. B. Pereira, R. Costa, N. Foios, and J. A. P. Coutinho, "Ionic liquid enhanced oil recovery in sand-pack columns," *Fuel*, vol. 134, pp. 196–200, 2014.

# Comparison Study on Anionic Surfactants and Mixed Surfactant Behavior in SAG Foam Process

Hamed Hematpur, Syed Mohammad Mahmood, Saeed Akbari and Negar Hadian Nasr

**Abstract** In order to increase the gas injection's sweep efficiency, the assisted foam process has been introduced. The foam can be created when the gas phase moves through surfactant solution under certain conditions. Although several surfactant types are able to generate foam through porous media, finding the appropriate surfactant to achieve the best performance is the goal of foam-assisted process. In this study, the behavior of two different types of surfactant was investigated. However, there are various surfactant types; the objective of this study was to elaborate the performance of mixed surfactant and an anionic surfactant in porous media. To achieve this target, the static tests, as well as dynamic tests, were conducted in the oil-free medium. For dynamic test, core flooding was conducted which included core sample, core flooding apparatus, two surfactant types, and nitrogen as injected gas. The static tests were interpreted in terms of foam height, while the dynamic experiments were analyzed in terms of liquid recovery and pressure drop. The results show that the mixed surfactant has better efficiency compared to anionic surfactant. Furthermore, the behavior of foam reveals the consistency of the dynamic experiments with static experiments.

**Keywords** Foam flooding · Anionic surfactant · Mixed surfactant · Mobility reduction

---

H. Hematpur · S.M. Mahmood (✉) · S. Akbari · N.H. Nasr  
Petroleum Engineering Department, Universiti Teknologi Petronas,  
Tronoh, Malaysia  
e-mail: mohammad.mahmood@petronas.com.my

H. Hematpur  
Petroleum Engineering Department, Research Institute of Petroleum Industry,  
Tehran, Iran

## 1 Introduction

The foam-assisted process has been introduced to tackle the drawbacks of gas injection [1]. This revealed that foam process can significantly increase the sweep efficiency [2]. The foam can be created by adding a surfactant to the liquid phase in the gas injection process. The increase in the front stability, due to the decrease in interfacial tension, results in raising the sweep efficiency of foam compared to gas injection. Therefore, the foam is utilized to prevent channeling and fingering phenomenon of gas, consequently amounting the sweep efficiency of flooding process.

Foam in porous media is a scattering of gas in liquid such that the liquid phase is continuous and some parts of the gas phase are discontinuous [3]. Considering the number of lamellae in foam texture, the foam might be categorized into two categories: weak foam with coarse texture (large bubble size) and strong foam with fine texture (small bubble size). The strong foam reduces the gas mobility and increases the sweep efficiency, compared to weak foam.

There are four different methods to perform the foam flooding in industry: First, the foam is generated on the surface and then injected into the reservoir. Second, the surfactant and gas are injected one after another periodically, in a process referred to as surfactant-alternating-gas (SAG). In this method, whenever the gas encounters the existing surfactant solution the foam can be generated [4]. Third, as stated by previous studies [5, 6] some surfactants are able to dissolve into supercritical CO<sub>2</sub>; accordingly, the foam can be created once this solution faces the existing water in the reservoir. Fourth, both gas and surfactant solution are simultaneously injected into the reservoir but in different sections of well [7, 8]. In this study, all core flooding was performed under the surfactant-alternating gas method.

It is realized that the lamellae of foam are generated due to three different mechanisms: Firstly, during the invasion of gas into liquid saturated area, the lenses can be deserted behind, and this mechanism is called “leave-behind.” Secondly, another mechanism is called “snapped-off” in which gas bubbles are created due to the driving force of gas applied on the gas–liquid interface, and this interface is pushed toward the pore throat. Also, the fluctuation in capillary pressure leads to the snapped-off mechanism. Thirdly, the pressure gradient affects pre-existing lamellae and forces it to move; consequently, it divides into many at the pore junction. This mechanism is called “lamellae division” [9].

As mentioned before, to create the foam the surfactant solution is required. The surfactant is a substance that is energetically favorable to adsorb onto the surfaces or interfaces between phases [10]. Surfactants can reduce interfacial tension between two phases and also allow easier spreading of the wetting phase on solid [11].

Considering the hydrophilic moiety of the molecule, surfactants are categorized into one of the four groups: anionic, cationic, nonionic, and zwitterionic (amphoteric). An anionic surfactant carries a net negative charge on its head group, while a cationic surfactant carries a positive charge. If a surfactant contains a head group with both positive and negative charged groups, it is termed zwitterionic. The



nonionic surfactant does not have charged group in its hydrophilic moiety. These surfactants are different in their applications because they have the different characteristics in applications. For instance, some of these surfactants show the appropriate performance to generate the foam. Three primary factors to select appropriate surfactant for enhanced oil recovery are the stability of the foam, foam adsorption, and recovery factor of the foam injection. The majority of minerals in most of the reservoirs are quartz, kaolinite, etc., which normally have a net negative charge. In order to lower the adsorption, negatively charged surfactants are usually considered [12]. However, sometimes to increase the foam stability or to lower the cost, it has to mix with another surfactant, usually amphoteric surfactant.

In this study, the performance of SAG foam process for two different surfactant types was examined: anionic and mixed surfactant.

## **2 Methodology**

The comparison between the performance of the anionic surfactant (IOS 1518 from Shell Company) and mixed surfactant (PRSB from Petronas Company) is the main aim of this study. To achieve this, two different experiments were conducted: static and dynamic experiments.

### ***2.1 Static Experiment***

In order to conduct the static tests, the surfactant solutions were prepared, 1 wt% of surfactant in 35000 ppm brine. The brine solution is a representative of seawater which is normally used for water injection in a real reservoir. About 100 ml of each sample was added to the measured column. Then, nitrogen was injected, by same flow rate, into surfactant solution to generate the foam to the level of 900 ml. After that, the height of the foam was measured, each 10 min, to investigate the foam stability for each sample. This procedure is also called column test. Figure 1 shows the column test procedure after 1 h.

### ***2.2 Dynamic Experiment***

The dynamic experiment involves the core flooding procedure. The experimental setup used is shown in Fig. 2. This system utilized a vertical core holder to avoid the gas segregation phenomena, a hand pump to supply the confining pressure up to 1000 psi. This set of experiments was performed under the ambient conditions (ambient pressure for the outlet and ambient temperature) and 1000 psi as confining pressure.

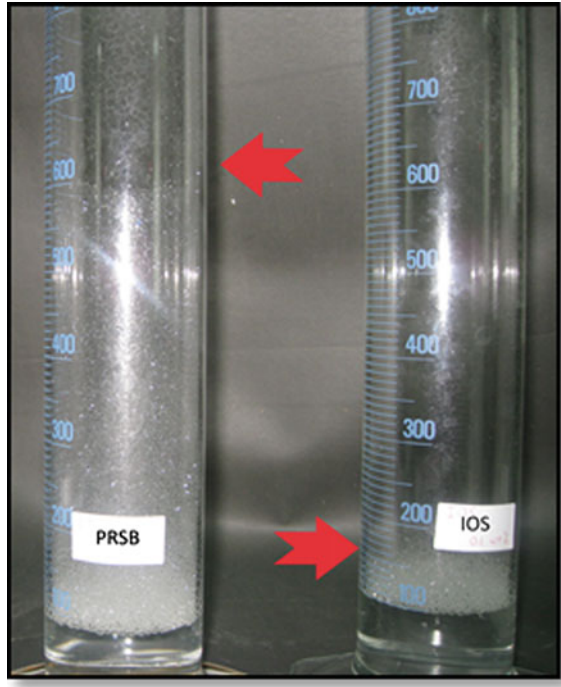


Fig. 1 Column test for two surfactants

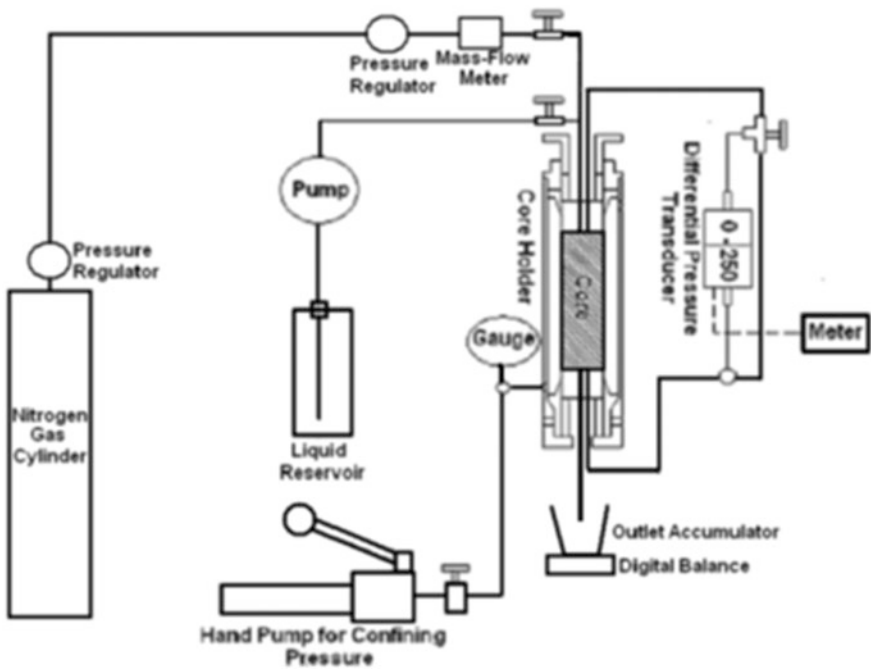


Fig. 2 Core flooding setup

**Table 1** Core properties

Length (cm)	Diameter (cm)	Vp (cc)	$\phi$ (%)	K[air] (mD)
7.157	3.736	23.29631	29.69289	15028.56

The Idaho gray sandstone core was selected to perform experiments due to its high permeability. The core properties were illustrated in Table 1.

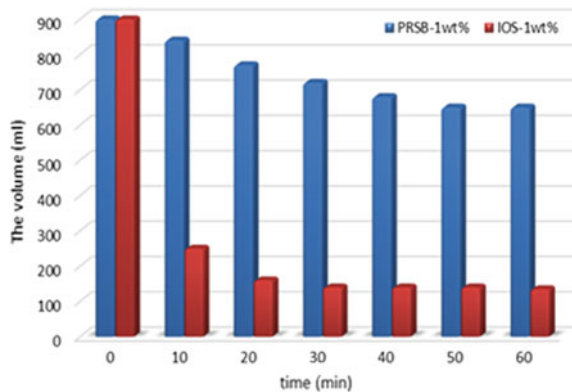
The flow rate of 2 cc/min was adjusted for gas injection rate during core flooding experiments because it is around 8 ft/day which is consistent with real cases. The core flooding procedure is as follows: Firstly, the core sample was saturated by synthetic brine (sea water) via vacuum saturator, and then laid it in the core holder. Secondly, the 5-pore volume of surfactant solution was injected into the core at the rate of 0.5 cc/min to saturate the core by 100% as well as to reach the equilibrium for surfactant adsorption to the rock surface. Finally, the gas was injected into the saturated core to generate the foam. Meanwhile, the pressure drop and liquid recovery were monitored by time.

### 3 Results and Discussion

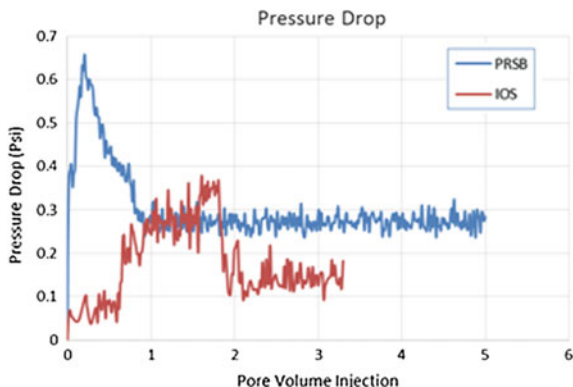
#### 3.1 Static Experiment Results

The results of column tests are depicted in Fig. 3. The significant difference between two surfactant types is obvious in this figure. It shows that the height of IOS foam after 10 min dramatically decreases and reaches to minimum level after 20 min. Despite IOS, PRSB surfactant which is a mixed surfactant leads to more

**Fig. 3** Column test results



**Fig. 4** Pressure drop comparison



stable and stronger foam. The results confirm this improvement in stability by adding amphoteric surfactant to anionic surfactant.

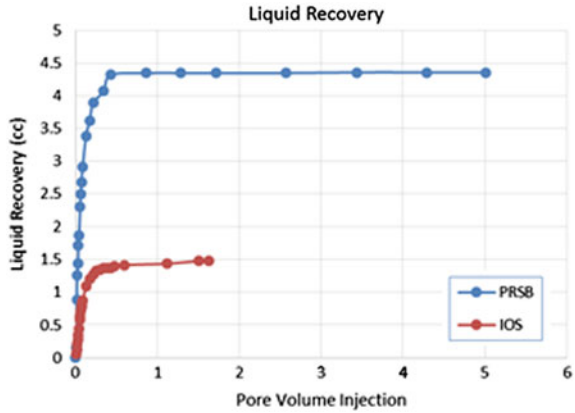
### 3.2 Core Flooding Results

As mentioned before, during the core flooding both liquid recovery and pressure were monitored. The results of pressure drop were illustrated in Fig. 4. This figure shows the foam generation period as well as the strength of the foam. As mentioned before, the foam generation leads to increasing the pressure drop. For strong foam, this increment will be more remarkable. Figure 4 depicts that at the first stage the foam was generated and the pressure drop reached to its maximum value, which can be the representative of critical capillary pressure. However, the pressure drop suddenly decreases to steady state after increasing. This phenomenon has occurred due to the foam destruction at certain pressure drop.

The comparison between two different surfactant types shows that the PRSB surfactant can generate stronger foam compared to the IOS surfactant at the same conditions and using nitrogen as injected gas because it increased the pressure drop more. Furthermore, the fast foam generation of PRSB can be delineated by this figure due to pressure drop's increasing time. It can be concluded that the foaming agent in PRSB surfactant performed better than the IOS surfactant. This result is consistent with the static test which was discussed in the corresponding section.

The liquid recovery can be compared to find out whether the foam performs well or not. The outcome of liquid recovery was shown in Fig. 5. This figure shows that the PRSB foam can produce more liquid than the IOS foam. This result can be explained by the following reason: The foam strength can be shown by gas mobility reduction factor; thus, strong foam has the high reduction in gas mobility [9] and

**Fig. 5** Liquid recovery comparison



consequently has greater sweep efficiency. Moreover, the greater sweep efficiency leads to greater recovery. Hence, PRSB surfactant is more effective to generate the strong foam due to its higher liquid recovery.

## 4 Conclusion

In this study, two different types of surfactants (anionic and mixed surfactant) were investigated through the SAG foam process to find out the effect of using mixed surfactant instead of pure anionic surfactant, moreover to compare the static test results with dynamic results. The following conclusions were drawn from this study:

- PRSB surfactant, which is mixed surfactant, showed better performance to foam generation compared to IOS during the static test. It means that the amphoteric surfactant improves the foam stability.
- The core flooding results also were in line with static test results and show that PRSB surfactant is able to generate the stronger foam. This can be delineated by the pressure drop results.
- The rate of foam generation for PRSB surfactant was higher than IOS when they face nitrogen gas under the same conditions.
- The recovery outcome from core flooding illustrated that PRSB surfactant can increase the sweep efficiency during the flooding procedure. The higher value of gas mobility reduction factor leads to the sweep efficiency amounting.

**Acknowledgements** The authors are grateful to EOR center and Petroleum department of Universiti Teknologi PETRONAS for graduate assistantship support.

## References

1. L. L. Schramm, "Foams: Fundamentals and Applications in the Petroleum Industry," ACS Adv. Chem. Ser. No. 242, 1994.
2. D. C. Bond and C. C. Holbrook, "Gas Drive Oil Recovery Process, Patent Number: 2,866,507," 1958.
3. G. J. Hirasaki, "The Steam-Foam Process—Review of Steam-Foam Process Mechanisms," Soc. Pet. Eng., p. SPE-19518-MS, 1989.
4. A. Afsharpoor, G. S. Lee, and S. I. Kam, "Mechanistic simulation of continuous gas injection period during surfactant-alternating-gas (SAG) processes using foam catastrophe theory," Chem. Eng. Sci., vol. 65, no. 11, pp. 3615–3631, 2010.
5. E. Ashoori, T. van der Heijden, and W. Rossen, "Fractional-Flow Theory of Foam Displacements With Oil," SPE J., vol. 15, no. April, pp. 20–22, 2010.
6. V. Q. Le, Q. P. Nguyen, A. W. Sanders, and T. Dow, "A Novel Foam Concept with CO<sub>2</sub> Dissolved Surfactants," in The SPE/DOE Improved Oil Recovery Symposium held in Tulsa, Oklahoma, 19–23 April, 2008, pp. 1–15.
7. H. L. Stone, "A Simultaneous Water and Gas Flood Design with Extraordinary Vertical Gas Sweep," in Proceedings of SPE International Petroleum Conference in Mexico, 2004.
8. W. Rossen, C. van Duijn, Q. Nguyen, C. Shen, and A. Vikingstad, "Injection Strategies To Overcome Gravity Segregation in Simultaneous Gas and Water Injection Into Homogeneous Reservoirs," SPE J., vol. 15, no. March, 2010.
9. H. Hematpur, M. Karimi, and M. Rashidi, "A brief review on foam flow modeling through porous media," Int. J. Pet. Geosci. Eng., pp. 104–119, 2014.
10. C. A. Miller and P. Neogi, *Interfacial Phenomena: Equilibrium and Dynamic Effects*, Second Edition, Second Edi. Taylor & Francis.
11. H. Hematpour, R. Arabjamloei, M. Nematzadeh, H. Esmaili, and M. Mardi, "An Experimental Investigation of Surfactant Flooding Efficiency in Low Viscosity Oil Using a Glass Micromodel," Energy Sources, Part A Recover. Util. Environ. Eff., vol. 34, no. 19, pp. 1745–1758, Jul. 2012.
12. J. Scamehorn, R. Schechter, and W. Wade, "Adsorption of surfactants on mineral oxide surfaces from aqueous solutions," J. Colloid Interface Sci., vol. 85, no. 2, pp. 463–478, 1982.

# Potential of Fly Ash as a Foam Stabilizing Additive

Ishaq Ahamad, Mariyamni Awang and Mudasser Mumtaz

**Abstract** In chemical EOR (enhanced oil recovery), nanoparticles have gained the potential to improve foam stability, and therefore, a low concentration of surfactant is needed to control gas mobility in the reservoir. The aim is to improve the foam-forming ability and foam stability both in the absence and in the presence of oil. In this paper, the potential of fly ash to produce stable foam was studied. Foam is produced by the sparging of air through a syringe pump. The hydrophilicity of fly ash was also investigated by monitoring the sedimentation time. The fly ash at various concentrations (ppm) was mixed with the best performing anionic foaming surfactant. The anionic surfactants used were AOS14–16 (industrial benchmark). Static foam tests were performed at ambient temperature by the sparging of air through the solution. It was analyzed that fly ash has more potential to stabilize the lamella of the foam. Therefore, the developed alkali-treated nanofly ash results were used in a considerably nanoparticle-assisted EOR.

**Keywords** Fly ash · Nanoparticles · Surfactant · Stabilizing additive

## 1 Introduction

Foams have been considered for capacity to move around control in the arrangement, gas infusion-enhanced oil recuperation (IOR) processes, for blocking and occupying utilizing either predictable or gelled foams, and for gas/oil proportion control at generation wells. In a (various sorts of individuals or things) scope of utilizations, a foam gathers a scope of oil immersions, which requires planning a foam with the essential strength to oil. Center surge tests by various agents propose that oil gets to be destructive to foam at oil immersions above 5–20% [1]. The foam then again is an accumulation of proximately pressed air pockets evaded by meager

---

I. Ahamad (✉) · M. Awang · M. Mumtaz  
Department of Petroleum Engineering, Universiy Teknoloj PETRONAS,  
Seri Iskandar, Malaysia  
e-mail: ishaq281@yahoo.com

movies of oil that buoy on the surface of the oil. It is for the most part corrective, yet it must be dealt with on the off chance that it makes oil-level control infeasible. In thorough cases, the foam can spill out of the machine through breathers, visual observation glasses, and dipsticks. Foam is a proficient warm encasing, so the temperature of the oil can get to be willful.

The usage of nanoparticles for cutting edge CO<sub>2</sub>-EOR foam can possibly prompt incidental early era EOR foams in light of the fact that the nanoparticles can convey supplemental functionalities, for example, para attraction, catalysis, or response control abilities. Silica-predicated nanoparticles have been utilized to create CO<sub>2</sub> foams that have apparent viscosities helpful for EOR. Foam era by coinfusion of CO<sub>2</sub> and polyethylene glycol (PEG)-treated business silica nanoparticles was seen in dot packs. Standardized apparent viscosities up to 16 cP were watched for low fixation (3.00 wt%) nanomolecule scatterings and were at a most extreme when CO<sub>2</sub> thickness was most elevated. Petroleum Recovery Research Center at New Mexico Tech examined foam era at element conditions, and nanosilica molecule balanced out CO<sub>2</sub> foam transference crosswise over permeable media. In the first place, research demonstrated that steady CO<sub>2</sub> foam could be incited when the nanoparticle consideration was in the scope of 4,000–6,000 ppm, using business silica nanoparticles [2].

A “stage molecule” combination system was produced to streamline the testing of nanoparticle viability for foam adjustment. The combinatorial materials science approach (stage particles), in which polymers are adsorbed on “standard” nanoparticle centers to control their surface properties, empowers concurrent testing of various polymers on the same nanoparticles of ideal size. This high-throughput methodology is connected to discover molecule coatings with ideal action at the CO<sub>2</sub>–water interface. Financially delivered Wicker smoldered silica particles with half dichloride dimethylsiloxane surface adjustment were intended to balance out CO<sub>2</sub> foams and demonstrated high security, with under 10% foam determination (by stature) in 24 h. The foams were made out of air pockets littler than 100 μm as a consequence of high adsorption vitality, which added to the high soundness [3,4].

To generate the nanoparticle foam, the temperature was up to 95 °C. The researchers notice the creation of foam with in fractures, which is even more beneficial in carbonate [5]. At the current time, a large amount of coal fly ash is utilized universally as a preservative to concrete. At the present time, a lot of coal fly cinder is used widespread as an additive to concrete. Not just does this utilization take care of a fiery remains transfer issue, yet it likewise brings about an improvement in solid item belonging (added substances that fill this need are termed pozzolans). It is the carbon’s retentive surface territory that is critical in deciding the limit of the carbon to adsorb air-entraining admixtures (AEAs) [6–8]. Nanoparticles are used as a form of EOR which alters the possessions of oil in order to assist in freeing the stuck oil. This is done by injecting particles of 1–100 nm of specific chemical mixes into the reservoir to decrease in oil viscosity, agreeing for an easier mobility of the fluids [9]. CO<sub>2</sub> foams are accumulations of gas bubbles separated from each other by liquid films with 60–97% gas content. Up to 100 times, gas mobility decrease can be attained using CO<sub>2</sub> foam via permeability



decrease and viscosity enhancement. Moreover, CO<sub>2</sub> foams are shear-thinning fluids and are considered an environmentally friendly material [10].

It has affirmed as of late that in part, hydrophobic silica nanoparticles give stable air rises in a fluid stage. The particles were essential size of particles of nm. Conversely, rise of same introductory size balanced out by bits shrank quickly. On the off chance that the particles were excessively hydrophobic, no steady air pockets could be framed by any means. It was watched that no hydrophobic particles tried gave high foam capacity [11–15].

It creates the impression that idle, surface dynamic nanoparticles can give complete foam steadiness. In the meantime, it is perceived that both proteins and particles might be available together in numerous frameworks and, moreover, that proteins might frequently be considered as surface dynamic nanoparticles inside such frameworks [16].

Fly ash kenned by pipe fiery debris is one of the deposits induced and incorporates the fine particles that hoist with the pipe gasses. Fiery debris that can not hoist is termed base cinder. Contingent on the substratum and cosmetics of the coal being blazed, the parts of fly fiery debris fluctuate essentially; however, all fly slag incorporates significant measures of silicon dioxide (SiO<sub>2</sub>) (both formless and crystalline) and calcium oxide (CaO), both being endemic components in numerous coal-bearing rock strata. Lethal constituents rely on the solid coal bed cosmetics, however might incorporate one or a greater amount of the accompanying components or substances found in follow amounts (up to hundreds ppm): arsenic, beryllium, boron, cadmium, chromium, hexavalent chromium, cobalt, lead, manganese, mercury, molybdenum, selenium, strontium, thallium, and vanadium, along with dioxins and PAH compounds [17, 18].

The harsh conditions of reservoir such as high temperature, pressure, and salinity tend to destabilize the foam leading to lower down the sweep efficiency. The main objective of this study is foam performance at reservoir conditions mainly temperature, pressure, and salinity. Applications of nanofly ash are to analyze their potential for the EOR applications.

## 2 Proposed Methodology

The fly ash was collected from a coal power plant inside Malaysia. Anionic foaming surfactants, alpha olefin sulfonate (AOS14–16), were used in this research. AOS14–16 (Bio-Terge AS-40) was obtained from the Stepan Company, USA. Sodium hydroxide (NaOH) was purchased from J. T. Baker, Sweden. The oil used was Tapis crude oil. The API gravity of the Tapis crude was 43.

## 2.1 Fly Ash Test to Determine the Hydrophilic Nanoparticles

Fly ash was treated using sodium hydroxide for adjustment of its pH. For pH-treated fly ash measured with different weight percentage, the weight percentages are 0.1, 0.5, and 0.7 wt% in grams. Before measurement of the pH value, the fly ash first was put into the 20-mL cylindrical sample glass with the weight value stated. Then, 20 mL distil water mixes together with the fly ash inside the cylindrical sample glass until the fly ash mixes up properly, and then, the pH values were noted.

After the fly ash solution was prepared, its stability was measured by using turbidity test. Turbidity reading was taken every 30 min. The reading of turbidity takes after the first shake, and then, for every 30 min, the reading was taken. It shows the particles settle at the bottom of the cylindrical sample glass after every 30 min turbidity was taken.

## 2.2 Static Foam Tests

The static foam ability and foam stability tests were performed based on the foam height and foam drainage in a 1000 ml measuring cylinder. The air was sparged in the solution for the foam generation at a constant flow rate of 2 ml/sec for 30 s. The total volume of each solution used for the foam generation was 150 ml. The percent composition of the surfactants (AOS) with the nanofly ash is shown in Table 1.

The stability of the foam was analyzed by noting the drainage time of the foam generated in the cylinder. The foaming was observed in both the presence and absence of crude oil. For the foam oil study, 10 wt% of the oil was added in the mixture of 150 ml of 1 wt% of the surfactant and fly ash solution. The major variables for the foam height and drainage tests were the type of surfactant and fly ash used.

## 3 Results and Discussions

Figure 1 shows the FESEM analysis of original fly ash. It is evident from the figure that fly ash is having different sizes in the different ranges. Different morphologies were observed in the FESEM analysis of the FA. The majority of the fly ash consisted of spherical particles. The size of the particles was varied in the range of 10–18  $\mu\text{m}$ .

**Table 1** Percentage compositions of the surfactant and nano FA solution

S. ID	AOS (0.1 wt%)	FA = 1000 ppm	Alkali FA = 1000 ppm
A	100	–	–
B	70	30	–
C	70	–	30

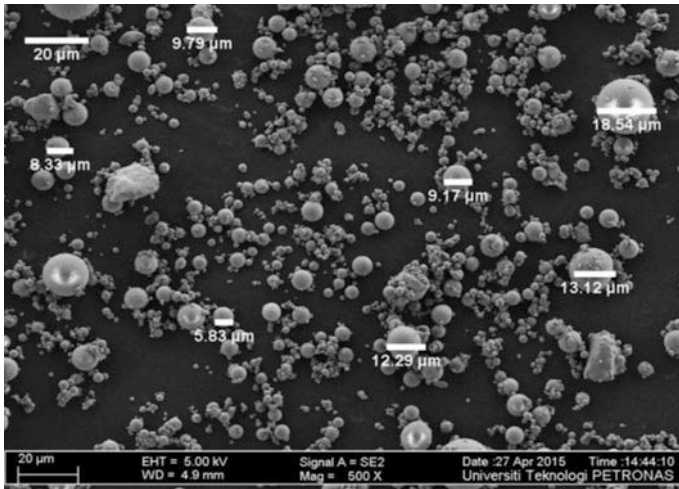


Fig. 1 Particle size of fly ash

### 3.1 Fly Ash pH Value Test to Determine the Hydrophilic Nanoparticles

The pH value was obtained as in Table 2. For every weight percentage, the value of pH was controlled at a closet value with the percentage difference of 11.7%. From the table, we can conclude that the pH value is at the pH condition needed.

### 3.2 Turbidity Test of the Fly Ash for Hydrophilic Nanoparticles

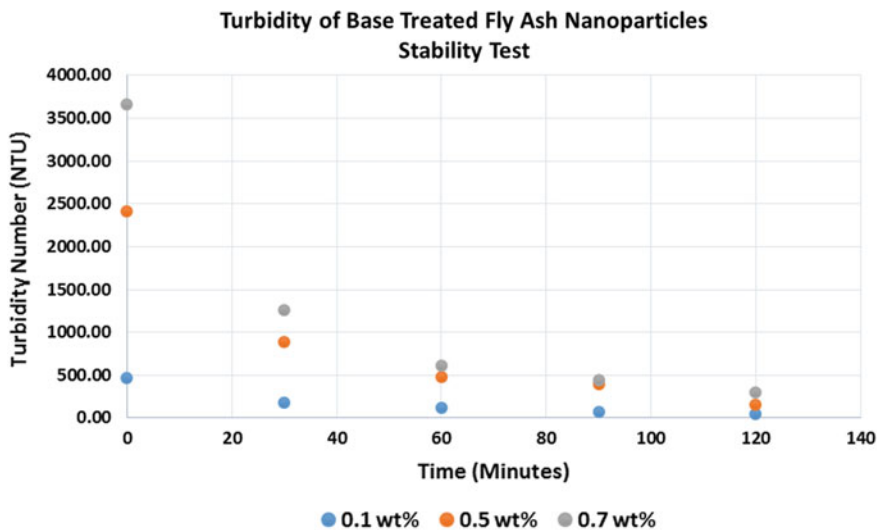
To know the stability of alkali-treated fly ash suspension inside the water, the turbidity test was performed. The sedimentation time of the alkali FA suspension at various concentrations is shown in Table 3 which illustrates the stability of fly ash particle suspension inside the water. Figure 2 shows the graphical plot of the sedimentation time values of alkali FA at various concentrations (0.1, 0.5, and 0.7 wt%). It shows that the alkali-treated fly ash suspended longer. Looking at the time taken from 30 to 90 min, the values 0.5 and 0.7 wt% for both treated fly ashes

Table 2 pH value at a given fly ash composition

No	Weight percentage, wt%	pH
1	0.1	9.60
2	0.5	9.71
3	0.7	9.57

**Table 3** Base-treated fly ash

Time (Min)	Turbidity value of difference weight percentage		
	0.1 wt%	0.5 wt%	0.7 wt%
0	468.50	2415.00	3660.00
30	173.50	885.00	1260.00
60	120.00	483.50	615.00
90	66.00	395.00	439.50
120	51.00	155.00	300.00

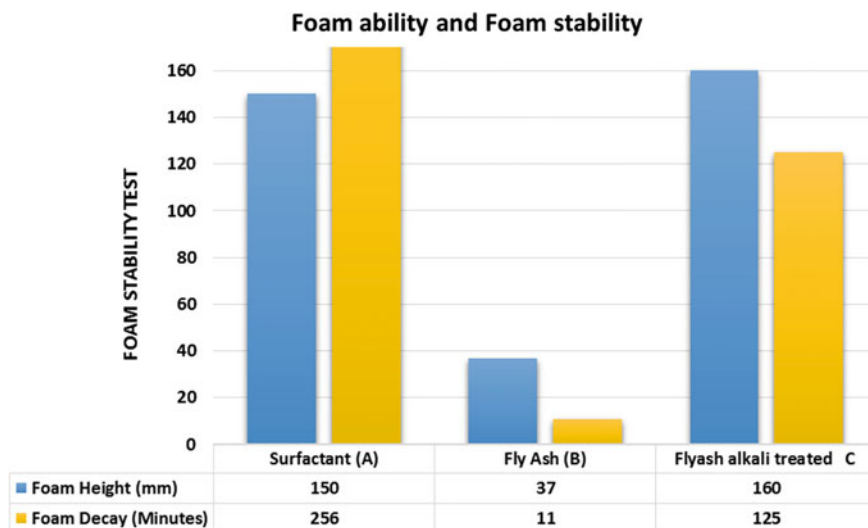


**Fig. 2** The graph of turbidity test for base-treated nanoparticles stability test

showed difference in decreasing turbidity value, but value 0.1 wt% showed difference in reading. The value for the turbidity of alkali-treated fly ash is higher than the base value for every reading taken.

### 3.3 Nano Fly Ash on Foaming

In Fig. 3, the foam ability for samples A and C were almost the same. However, the foam ability of the surfactant mixed with pure fly ash was very low. The formulations were presented in Table 2. The surfactants themselves, AOS (sample A), were found more stable as compared with the combinations of the surfactant with FA particles as shown in Fig. 3. In the mixture of the surfactants with pure fly ash, sample B seems unstable and the foam drainage was comparatively fast. The maximum foam stability was observed for the combinations of AOS mixed with the



**Fig. 3** Foam ability and foam stability

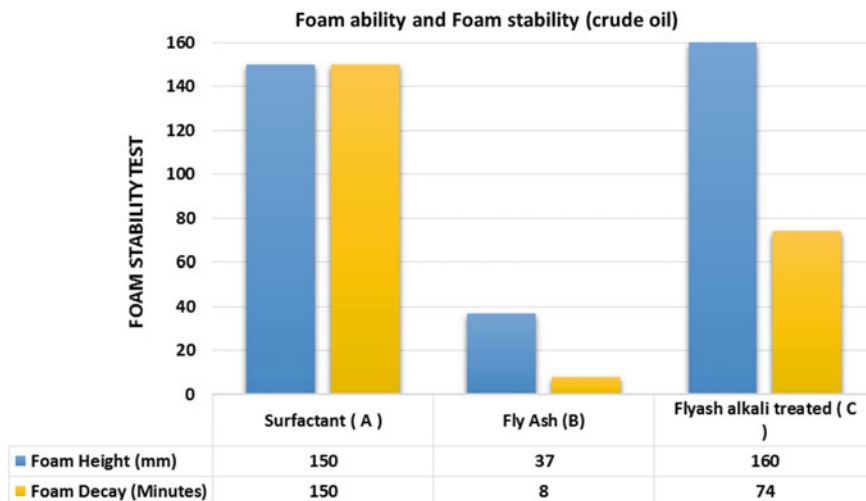
alkali-treated fly ash particles. The foam stability was found to be 180 min for sample C, AOS with AFA (125 of AOS: AFA) for 75% drainage. The performance of AOS to generate the stable foam was found good as compared to fly ash nanoparticles.

### 3.4 Effect of Crude Oil on Foaming

The effect of Tapis crude oil on foaming was studied to identify the tolerance for oil. The foaming of formulated samples with the Tapis crude is shown in Fig. 4.

The foam stability was decreased when the foaming was performed in the presence of oil. The addition of the oil in the solution led to the increase in the foam drainage rate. The formulations presented in Table 2 were each mixed with 10 wt% of the Tapis crude oil. The foam ability and foam stability in terms of height and drainage have been shown in Fig. 4. The foam height and foaming ability of sample A is almost the same with oil but samples B and C showed less foam stability with pure fly ash and alkali-treated fly ash.

The stability of each mixture was examined by noting the drainage time. In the case of surfactants, samples A performed better in the presence of crude oil. But the performance of samples B and C, the AOS mixtures with pure fly ash, was found to be less. However, the performance of sample C, AOS with alkali-treated fly ash AFA (74 of AOS: AFA) for 75% drainage, was superior both in the presence and in the absence of oil. From the static foam test, it was found that the performance of AOS was better in contact with oil.



**Fig. 4** Foam ability and foam stability with crude oil

## 4 Conclusion

The mixture of the surfactant and alkali-treated nanofly ash produced a stronger foam as compared with the fly ash alone. However, fly ash alone had the worst foam drainage resistance. The sample 'C' of the AOS and fly ash gave the best stable foam both in the absence and in the presence of oil. The reduction of the surfactant injection volume tended to lower the cost of the surfactant EOR process. As discussed in this paper, the surfactants performance for the foam generation can be tuned in order to produce the formulation with the nanofly ash essential for a successful EOR.

**Acknowledgements** Special thanks to the chemical engineering Dept., UTP for providing beneficial insights regarding the fly ash behavior analysis. The authors acknowledge the financial support of the UTP-TU-DELFT-SHELL project and University Technology PETRONAS (UTP), Malaysia, and the usage of the EOR center facilities.

## References

- Schramm, L.L.: "Foam Sensitivity to Crude Oil in Porous Media," in *Foams, Fundamentals and Applications in the Petroleum Industry*, L.L. Schramm ~ ed.!, *Advances in Chemistry Series 242*, American Chemical Society, Washington, DC ~ 1994! pp. 165–197.
- Espinosa, et al. 2010, Nanoparticle-Stabilized Supercritical CO<sub>2</sub>, *Foams for Potential Mobility Control Applications*. Paper SPE 129925, presented at SPE Improved Recovery Symposium, Tulsa, 24–28 April. <http://dx.doi.org/10.2118/129925-MS>.

3. NETL. 2011. Nanoparticle-Stabilized CO<sub>2</sub> Foam for CO<sub>2</sub> EOR Application. <http://www.netl.doe.gov/technologies/oilgas/Petroleum/projects/EP/ImprovedRec/FE0005979-NMIMT.html>.
4. Yu, J, ET all R. 2012. Study of Adsorption and Transportation Behavior of Nanoparticles in Three Different Porous Media. Paper SPE 153337, presented at the SPE Improved Oil Recovery Symposium, Tulsa, 16–18 April,
5. Sinisha ET al. national energy technology laboratory, US department of Energy JPT. July 2012.
6. Y.-M. Gao, H.-S. Shim, R.H. Hurt, E.M. Suuberg, N.Y.C. Yang, Effects of carbon on air entrainment in fly ash concrete: the role of soot and carbon black, *Energy Fuels* 11 (1997) 457–462.
7. E. Freeman, Y.-M. Gao, R.H. Hurt, E.M. Suuberg, Interactions of carbon-containing fly ash with commercial air-entraining admixtures for concrete, *Fuel* 76 (1997) 761–765.
8. Kūlaots, Y.M. Gao, R.H. Hurt, E.M. Suuberg, The role of polar surface and mesoporosity in adsorption of organics by fly ash carbon, *ACS Div. Fuel Chem. Prepr.* 43 (1998) 980–984.
9. Ayatollahi, S. and zeraft M.M., 2012. Nanotechnology-Assisted EOR techniques: New solutions to old challenges. SPE 157094 presented at the SPE international oilfield nanotechnology conference, noordwijk, netederlands, 12–14th June.
10. R. SYDANSK AND R. ZERON, 2011, Reservoir Conformance Improvement, SPE publications.
11. Z. Du, M.P. Bilbao-Montoya, B.P. Binks, E. Dickinson, R. Ettelaie, B.S. Murray, Outstanding stability of particle-stabilized bubbles, *Langmuir* 19 (2003) 3106–3108.
12. E. Dickinson, R. Ettelaie, T. Kostakis, B.S. Murray, Factors controlling the formation and stability of air bubbles stabilized by partially hydrophobic silica nano particles. *Langmuir*, 20 (2004) 8517–8525.
13. Manlowe, D.J. and Radke, C.J.: “A Pore-Level Investigation of Foam/Oil Interactions in Porous Media,” *SPERE* ~ November 1990! 495.
14. Lobo, L. and Wasan, D.T.: “Mechanisms of Aqueous Foam Stability In the Presence of Emulsified Non-Aqueous-Phase Liquids: Structure and Stability of the Pseudoemulsion Film,” *Langmuir* ~ 1993! 9, No. 7, 1668.
15. Nikolov, A.D. et al.: “The Effect of Oil on Foam Stability: Mechanisms And Implications for Oil Displacement by Foam in Porous Media,” Paper SPE 15443 presented at the 1986 SPE Annual Technical Conference and Exhibition, New Orleans, 5–8 October.
16. Murray, Brent S., and Rammile Ettelaie. “Foam stability: proteins and nanoparticles.” *Current opinion in colloid & interface science* 9.5 (2004): 314–320.
17. Managing Coal Combustion Residues in Mines, Committee on Mine Placement of Coal Combustion Wastes, National Research Council of the National Academies, 2006.
18. Jump up^ Human and Ecological Risk Assessment of Coal Combustion Wastes, RTI, Research Triangle Park, August 6, 2007, prepared for the U.S. Environmental Protection Agency.

# Optimization of Water Recycle at Steam Flood EOR Using Genetic Algorithm

Karina Aryanti Permatasari, Totok R. Biyanto, Sony Andriyanto,  
Sonny Irawan and Ridho Bayuaji

**Abstract** Steam flood is one of the thermal enhanced oil recovery methods widely used to increase production rate. This method injects steam into reservoir formation that will reduce crude oil viscosity. The steam condensate gives additional pressure to push crude oil toward production well. This method is known to be able to increase recovery factor significantly, but there are several things we need to note. The total cumulative water injected per day could reach 200 MT. This number is equivalent to total energy needed for steam generation, and wastewater (water-cut) on production well. Wastewater typically has complex chemistries, including total dissolved solids (TDS), organic carbon content, and concentration of scale-forming minerals (e.g., carbonates and sulfates). High-cost treatment is needed before wastewater can be re-injected. The optimization steam flood operation is required to maximize crude oil production, minimize energy at steam generation, and minimize wastewater (water-cut) on production well. Model of steam flood operation could be derived from Beggs–Brill method and Darcy equation. Mean error from Beggs–Brill method to PIPESIM software is 4.48% for pressure and 0.98% for temperature. Mean error from Darcy equation to COMSOL simulation is 0.39% for pressure and 0.97% for temperature. Before optimization, steam flood runs in 2.2 kg/s of mass steam injection rate, 600 psia of injection pressure, and 80% of steam quality. The profit of those configurations is 7645.37 USD/day. After optimization using genetic algorithm, steam flood operation could reach global optimum at 6.460 kg/s, 1408.53 psia injection pressure, and 87.86% steam quality. The profit of those optimized parameters is 17618.75 USD/day.

---

K.A. Permatasari (✉) · S. Irawan  
Departement of Petroleum Engineering, Universiti Teknologi PETRONAS,  
Seri Iskandar, Perak, Malaysia

T.R. Biyanto (✉) · S. Andriyanto  
Departement of Physics Engineering, Institut Teknologi Sepuluh Nopember,  
Surabaya, Indonesia  
e-mail: trbiyanto@gmail.com

R. Bayuaji  
Departement of Civil Engineering, Institut Teknologi Sepuluh Nopember,  
Surabaya, Indonesia



**Keywords** Genetic algorithm • Optimization • Steam flood • Water recycle

**List of symbols**

$\lambda$	Input liquid content $q_L/(q_L + q_g)$
A	Area passed by fluid ( $m^2$ )
BOPD	Barrel oil per day (barrel)
$d$	Tube diameter (m)
DWW	Daily wastewater ( $m^3$ )
ES	Energy for steam generation (kJ)
$f_{tp}$	Two-phase friction factor (dimensionless)
$f_{ns}$	Normalized friction factor (dimensionless)
$G_m$	Mixture mass flux rate ( $kg/m^2s$ )
$g_c$	Gravity factor (m/s)
$g$	Gravity acceleration ( $m/s^2$ )
HHV	High heating value of natural gas (kJ/kg)
$H_L$	Liquid holdup fraction (dimensionless)
$H_L(\theta)$	Angle $\theta$ holdup fraction
$H_L(0)$	Horizontal holdup fraction
$h_f$	Enthalpy of saturated liquid in certain injection pressure (kJ/kg)
$h_{fg}$	Enthalpy of saturated liquid to saturated vapor in certain injection pressure (kJ/kg)
$h_{f,25C}$	Enthalpy of saturated liquid in 1 atm, 25 °C (kJ/kg)
k	Permeability of medium ( $cm^2$ )
L	Length of medium (m)
$L_{inj,Prod}$	Distance between well injection and well production (m)
NGC	Natural gas cost (USD/kg)
$\dot{m}$	Steam injection rate (kg/s)
$N_{Re}$	Reynolds number
$\eta$	Displacement efficiency (%)
$\eta_{boiler}$	Boiler efficiency (%)
OP	Oil price (USD/barrel)
PR	Steam flooding profit (USD)
$\rho_L$	Liquid density ( $kg/m^3$ )
$\rho_g$	Gas density ( $kg/m^3$ )
$\Delta P$	Differential pressure from initial to finish (psi)
$\Phi$	Porosity (dimensionless)
q	Volumetric flow rate ( $m^3/s$ )
$q_L$	Liquid volumetric rate ( $m^3/s$ )
$q_g$	Gas volumetric rate ( $m^3/s$ )
$r_{to}$	Tubing outside diameter (cm)
$S_{oi}$	Initial oil saturation
$S_{or}$	Residual oil saturation
$\theta$	Elevation angle from horizontal (°)
$t_f$	Formation temperature (C)

$\mu$	Dynamic viscosity (Pa.s)
$U_{to}$	Heat transfer coefficient ( $w/m^2.K$ )
$v_m$	Mixture rate (m/s)
WTC	Water treatment cost (USD/m <sup>3</sup> )
$x$	Steam quality (fraction or %)
$\Psi$	Inclination correction factor
$z$	Depth (m)
$z_{res}$	Reservoir thickness (m)

## 1 Introduction

Heavy oil is important fossil energy resources to sustain future energy demand. Total accumulation of heavy oil is about 3.396 billion barrel in original oil in place (OOIP). This number spread around the world, and most of them located in Middle East, North America, and South America [1].

Heavy oil has a high viscosity, and it is difficult to exploit heavy crude oil economically and efficiently. Special method needs to be performed in order to boost oil production in heavy oil reservoir, and this method is known as enhanced oil recovery (EOR) [2]. Steam flood is widely used in heavy oil enhanced oil recovery. There are two kinds of well in steam flood operation such as injection well and production well. In steam flood EOR, the steam is injected to reservoir through injection well, and heat from steam will be distributed to reservoir formation. This heat will reduce heavy oil viscosity. The steam condensate gives additional pressure to push crude oil toward production well [3].

The injected steam is generated in steam production facility. The amount of water used in steam flood is about 1600 barrel per day or about 200 MT per day. Boiler needs more than eight tons of natural gas, or more than 7662.09 \$ per day to generate steam. The main waste in steam flood operation is water (in liquid or gas phase) that is lifted to oil production line. The ratio of wastewater to crude oil (water-cut) in production well is equal to volume of injected steam. Wastewater typically has complex chemistries, including total dissolved solids (TDS), organic carbon content, and concentration of scale-forming minerals (e.g., carbonates and sulfates). This water at times may also contain naturally occurring radioactive material (Ra-226 and Ra-228) [4]. High-cost water treatment is needed before wastewater can be re-injected.

More volume of steam injected per day will not only increase the amount of oil in production well, but also increase the amount of wastewater [5]. The increasing steam injection rate will consume more energy in steam production facility.

Then, this process (steam flood operation) is modeled for optimization. Due to the complexity of steam flood operation model, optimization steam flood operation

using genetic algorithm is required to optimize the profit of steam flood operation, by minimizing wastewater (water-cut) on production well, maximizing crude oil production, and minimizing energy at steam generation.

## 2 Methods

Steam flood operation model is divided into 3 models: pressure mathematical model from injection well head to reservoir; pressure gradient and sweep efficiency model in reservoir formation; and pressure mathematical model from reservoir to production well head. First and third models are derived from Beggs and Brill equation. Second model is derived from Darcy equation. Illustration for these models in steam flood operation is shown in Fig. 1.

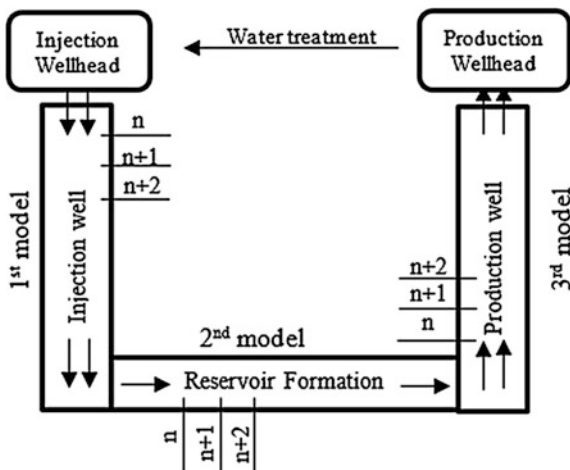
Beggs–Brill method is used in first and third models. In segment  $n$ , pressure gradient is calculated. The output calculation of segment  $n$  then becomes input for segment  $n + 1$ . This chain calculation is needed, because the fluid properties in segment  $n$  and  $n + 1$  are different (viscosity, density, steam fraction, pressure, etc.). Length or depth of every segment is 50 m.

Pressure gradient in second model is derived from Darcy equation. Segmentation is also needed because the fluid properties in segment  $n$  and  $n + 1$  are different. The output calculation of segment  $n$  then becomes input for segment  $n + 1$ . Length of every segment in second model is 10 m.

- Beggs and Brill equation

Beggs and Brill derive pressure gradient equation in multiphase flow by analyzing energy balance and by assuming there are no external forces to fluid flow [6].

Fig. 1 Steam flood scheme and model dividing



The pressure gradient consists of two-phase friction, flow in elevation angle, and change gravitation acceleration. Beggs and Brill equation is given by Eq. (1).

$$\frac{\partial p}{\partial z} = \left(\frac{\partial p}{\partial z}\right)_{\text{friction}} + \left(\frac{\partial p}{\partial z}\right)_{\text{elevation}} + \left(\frac{\partial p}{\partial z}\right)_{\text{acceleration}} \quad (1)$$

Pressure drop in multiphase flow through pipeline is caused by friction between two phases and friction between fluid and pipe wall. Significant pressure drop may occur in bigger mass flow injection rate and rough inner tubing. Pressure drop from friction is defined by the following:

$$\left(\frac{\partial p}{\partial z}\right)_{\text{friction}} = \frac{f_{\text{tp}} \cdot G_m \cdot V_m}{2 \cdot g_c \cdot d} \quad (2)$$

Two-phase friction factor ( $f_{\text{tp}}$ ) from Beggs–Brill is derived from normalized friction factor ( $f_{\text{ns}}$ ) and correlating factor ( $S$ ). Relation between  $f_{\text{tp}}$  and  $f_{\text{ns}}$  is shown in Eq. (3). Normalized friction factor could be calculated using Reynolds number as shown in Eq. 4. Correlating factor ( $S$ ) for Eq. (3) could be calculated using Eqs. (5) and (6).

$$\frac{f_{\text{tp}}}{f_{\text{ns}}} = e^s \quad (3)$$

$$f_{\text{ns}} = \left[ 2 \log \left( \frac{N_{\text{Re}}}{4.5223 \log(N_{\text{Re}} - 3.8215)} \right) \right]^{-2} \quad (4)$$

$$s = \frac{\ln y}{-0.0523 + 3.182 \ln y - 0.8725(\ln y)^2 + 0.01853(\ln y)^4} \quad (5)$$

$$y = \frac{\lambda}{[H_L(\theta)]^2} \quad (6)$$

Elevation loss is caused by hydrostatic pressure loss. This loss occurs in two-phase flow in deviation angle ( $\theta$ ) from horizontal ( $0^\circ$ ). Elevation loss could be predicted by calculating holdup fraction. Holdup fraction is a fraction of liquid volume in fluid flow with total volume in flow. Elevation loss is defined by Eq. (7):

$$\left(\frac{\partial p}{\partial z}\right)_{\text{elevation}} = \frac{g}{g_c} [\rho_L H_L + \rho_g (1 - H_L)] \times \sin \theta \quad (7)$$

In order to calculate holdup fraction in certain deviation angle, holdup fraction in  $0^\circ$  and inclination correction factor ( $\Psi$ ) need to be calculated. Relation between holdup fraction in angle  $\theta$  and inclination correction factor is shown in Eq. (8).

$$\frac{H_L(\theta)}{H_L(0)} = \psi \tag{8}$$

Inclination correction factor ( $\Psi$ ) could be predicted for all phase flow patterns by Eq. (9).

$$\psi = 1 + C(\sin \phi - 1/3(\sin \phi)^3) \tag{9}$$

With  $\phi = 1, 8\theta$ , in downward vertical flow, the value of angle  $\theta$  is  $-90^\circ$ . Then, the value of  $C$  and  $H_L(0)$  depend on flow pattern of fluid in pipelines (Table 1).

Flow pattern could be known by observing Froude number and its relation between  $L_1$  and  $L_2$ . The criteria of flow pattern are as follows:

- If  $N_{FR} < L_1$ , segregated flow pattern
- If  $N_{FR} > L_1$  and  $N_{FR} > L_2$ , distributed flow pattern
- If  $L_1 < N_{FR} < L_2$ , intermittent flow pattern
- $L_1$  and  $L_2$  calculated from Eqs. (10), (11), and (12) are as follows:

$$L_1 = \exp(-4.62 - 3.757X - 0.481X^2 - 0.0207X^3) \tag{10}$$

$$L_2 = \exp(-4.62 - 4.602X - 1.602X^2 - 0.179X^3 + 0.635 \times 10^{-3}X^5) \tag{11}$$

$$X = \ln(\lambda) \tag{12}$$

Acceleration loss is caused by external force in fluid flow, and in this case, it means gravitation force. Gravitation force will change in distance between a point to center of earth. The common depth of oil well is 2 km. The change of gravitation force is relatively small. In this research, change of gravitation force is neglected. So, pressure gradient by Beggs and Brill is as follows:

$$\left(\frac{\partial p}{\partial z}\right) = \frac{f_{tp} \cdot G_m \cdot V_m}{2 \cdot g_c \cdot d} + \frac{g}{g_c} [\rho_L H_L + \rho_g (1 - H_L)] \tag{13}$$

**Table 1** Holdup equation and coefficient  $C$  calculation based on different flow patterns

Flow pattern	$H_L(0)$	$C$
Segregated	$H_L(0) = \frac{0.98 \lambda^{0.4846}}{N_{FR}^{0.0868}}$	$C = (1 - \lambda) \ln \left[ \frac{4.7 N_{LV}^{0.0868}}{\lambda^{0.3692} N_{FR}^{0.5056}} \right]$
Intermittent	$H_L(0) = \frac{0.84 \lambda^{0.5351}}{N_{FR}^{0.0173}}$	$C = (1 - \lambda) \ln \left[ \frac{4.7 N_{LV}^{0.1244}}{\lambda^{0.3692} N_{FR}^{0.5056}} \right]$
Distributed	$H_L(0) = \frac{1.06 \lambda^{0.5824}}{N_{FR}^{0.0609}}$	$C = (1 - \lambda) \ln \left[ \frac{4.7 N_{LV}^{0.1244}}{\lambda^{0.3692} N_{FR}^{0.5056}} \right]$

- Darcy equation and sweep efficiency

Permeability is the ability of porous medium to deliver fluid flow. Based on Henry Darcy’s experiment, volumetric flow rate through porous medium is equal to pressure gradient, area passed by fluid, and 1/length. Darcy equation is written as below:

$$q = k \frac{A\Delta P}{\mu L} \tag{14}$$

Variable that needs to be calculated is  $\Delta P$ . Volumetric flow rate is assumed to be equal to injection volumetric flow rate. In this research, permeability ( $k$ ) is assumed as constant/isotropic. Area ( $A$ ) is an area of fluid flow. Length ( $L$ ) is length of a segment (10 m). Dynamic viscosity ( $\mu$ ) could be changed in different pressures and temperatures. Pressure and temperature from segment  $n$  will influence the value of dynamic viscosity in segment  $n + 1$ .

Reservoir is assumed as cylinder with 100 m in length (distance between injection well and production well) and 30.48 in diameter (reservoir thickness). Permeability of reservoir formation is 1200 mD. Input pressure of the second model is calculated from injection well last segment outputs. The output calculation of the last segment in reservoir then becomes input for  $n$  segment in production well (third model).

After reservoir segmentation and calculation, pressure gradient ( $\Delta P$ ) is used to calculate sweep efficiency. Sweep efficiency is a ratio between change in oil saturation to initial oil saturation. In previous study, sweep efficiency or displacement efficiency is the function of pressure gradient [7]. Displacement efficiency’s empirical equation from pressure gradient is written below as in Eq. (15):

$$\eta = 0.0739 \times \ln\left(\frac{\Delta P}{L}\right) + 0.7111 \tag{15}$$

$$\eta = \frac{S_{or} - S_{oi}}{S_{oi}} \tag{16}$$

$$PV = \phi \times V_{\text{reservoir}} \tag{17}$$

Cumulative oil production of steam flood operation is the change of oil saturation multiplied by pore volume ( $PV$ ). Therefore, production rate ( $BOPD$ ) could be known by dividing cumulative oil production and time during production.

- Optimization

The objective function is to maximize the profit from steam flood operation. Profit is energy cost for steam generation, water treatment cost for wastewater treatment, and crude oil production. The optimized variables are mass flow rate of

steam flood, pressure in well head injection well, and steam quality in injection well. Objective function is written below as in Eq. (18):

$$PR = (OP - BOPD) - \left( \frac{ES}{HHV \times \eta_{\text{boiler}}} \times NGC \right) - (WTC) \quad (18)$$

Oil price is assumed as 45.037 USD/barrel (average oil price from April 1, 2015 to April 1, 2016). The energy needs for steam generation ( $ES$ ) is calculated by Eq. (19). Boiler runs with 88% efficiency [8], and using natural gas ( $HHV = 54$  MJ/kg, and 0.8552 USD/kg) [9].

$$ES = \dot{m} \times [(h_f + (h_{fg} \times x)) - h_{f25c}] \quad (19)$$

Water treatment cost is the function of daily wastewater volume rate [10]. The equation of wastewater treatment cost is shown below as follows:

$$WTC = 0.7952 \times DWW - 93.571 \quad (20)$$

### 3 Result and Discussion

In this research, the input parameters consist of injection/production well characteristic and reservoir characteristic. Parameter inputs are from Hamaca field, Venezuela [3]. Both of these inputs are shown as in Table 2.

First and third models are validated using PIPESIM software. Second model is validated using COMSOL Multiphysics. Normal operating conditions in Hamaca

**Table 2** Well parameter and operating condition

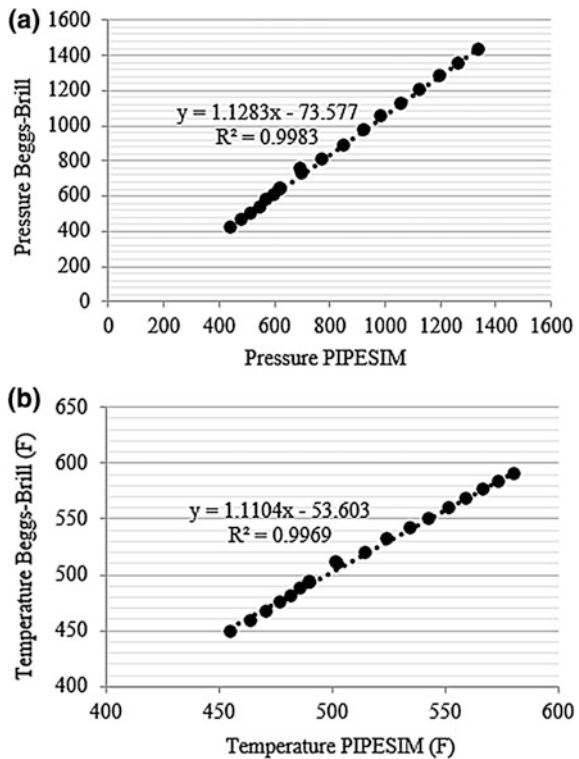
Parameter	Value	Unit
$g_c$	9.80665	$\text{m}^3/\text{kg}\cdot\text{s}^2$
$d$	0.089	m
$z$	1200	m
$r_{to}$	3.648	cm
$U_{to}$	11.356	$\text{W}/\text{m}^2\cdot\text{K}$
$z_{res}$	30.48	m
$L_{inj,prod}$	100	m
$\Phi$	0.3	–
$g$	9.8	$\text{m}/\text{s}^2$
$k$	1200	md
$t_f$	38	C
$\dot{m}$	2.2	kg/s
Injection pressure	600	psia
$x$	0.8	–

field are 2.2 kg/s of mass steam injection rate, 600 psia of injection pressure, and 80% of steam quality [3]. Model validation is performed by modifying mass flow rate of steam injection, injection pressure, and steam quality from normal operating condition. The output of this research model is then compared to the output of PIPESIM and COMSOL.

Mean error from Beggs–Brill method (first and third models) to PIPESIM software is 4.48% for pressure and 0.98% for temperature. Mean error from Darcy equation (second model) to COMSOL simulation is 0.39% for pressure and 0.97% for temperature. The validation result of first, second, and third model is shown in Figs. 2, 3, and 4.

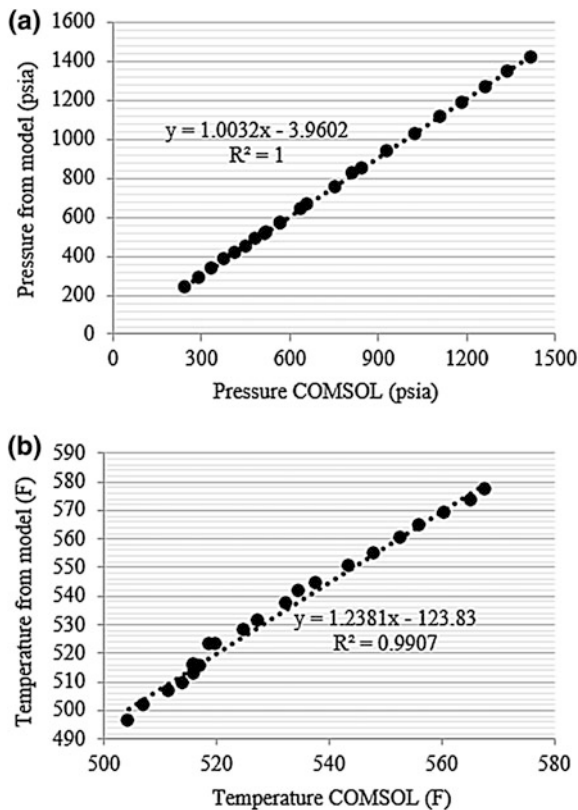
Before optimization, it runs in 2.208 kg/s, 600 psia injection pressure, and 80% steam quality. Energy needs for steam generation could be calculated by Eq. (19) using input  $m_i = 2.208$  kg/s;  $h_{f(600\text{psia})} = 2800.19$  kJ/kg;  $h_{fg(600\text{ psia})} = 1703.00$  kJ/kg;  $x = 0.8$ ; and  $h_{(f\ 25\ C)} = 417.43$  kJ/kg. Daily oil production could be calculated by knowing pressure gradient in reservoir using Darcy Eq. (14). The result of Darcy equation is  $\Delta P = 0.008200772$  Mpa/L, and the result calculation of sweep efficiency using Eq. (15) is  $\eta = 0.356$ . Oil volume and water volume in production

Fig. 2 First model pressure validation (a) and temperature validation (b)





**Fig. 3** Second model pressure validation (a) and temperature validation (b)



well will be 355.54 barrel/day and 134.25 m<sup>3</sup>/day. The plot result of above calculation is shown in Figs. 5, 6, and 7.

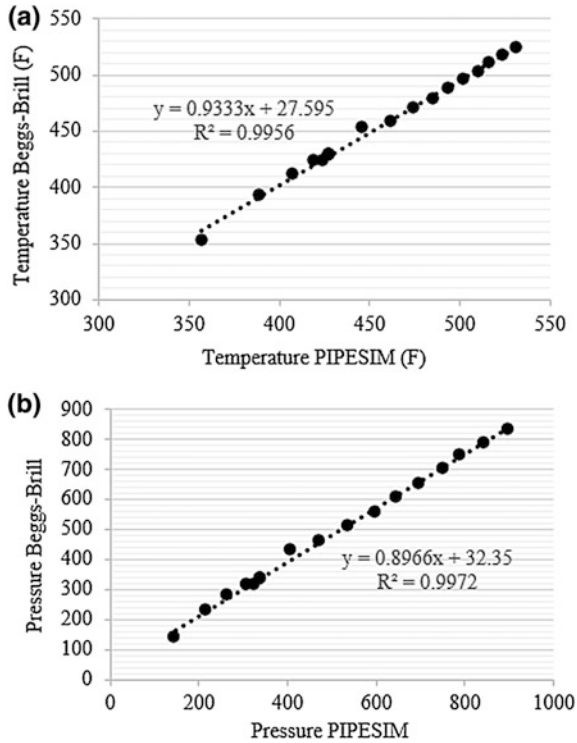
From model and calculation that have been mentioned above, the value of objective function (*PR*) is shown in Table 3.

- Genetic Algorithm

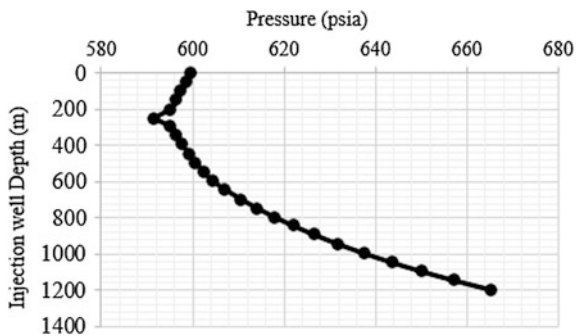
Genetic algorithm is an optimization algorithm adopted from the evolution of natural living such as human. Genetic algorithm maximizes/minimizes an objective function by encoding the solution parameter value to binary. Then, the solution value is evaluated by its fitness. Individual with the best fitness value will be reproduced in order to increase the next-generation quality [9]. Mechanism in genetic algorithm is shown in Fig. 8.

In this research, genetic algorithm (GA) is written in Visual Basic for Applications. Optimization parameters that are used in this GA are 100 population size, 100 maximum number of generation, 20-digit binary encoding, 0.1 mutation probability, and 0.7 crossover mutation probability. The used constraints are as follows:  $0 \text{ kg/s} < \mu < 20 \text{ kg/s}$ , injection pressure less than 3190 psia,  $0 < x < 100$ ,

**Fig. 4** Third model pressure validation (a) and temperature validation (b)



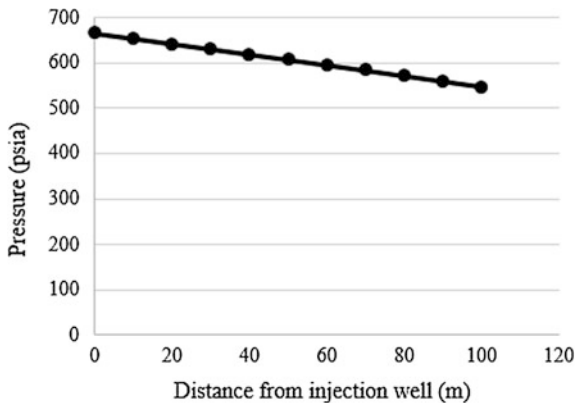
**Fig. 5** Steam pressure plot in injection well (normal operating condition)



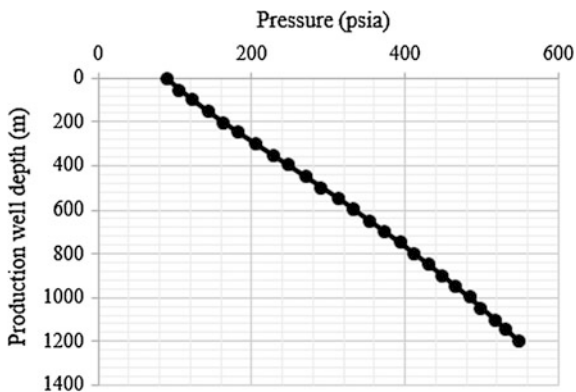
and steam pressure in production well head more than 100 psia. Best fitness plot of each generation is shown in Fig. 9.

After optimization using GA, in order to reach global optimum of objective function ( $PR$ ), steam flood operation is recommended to run in 6.460 kg/s, 1408.53 psia injection pressure, and 87.86% steam quality. From model and calculation using these optimized parameters, the value of objective function ( $PR$ ) is shown in Table 4.

**Fig. 6** Steam pressure plot in reservoir formation (normal operating condition)



**Fig. 7** Steam pressure plot in production well (normal operating condition)



**Table 3** Revenue calculation before optimization

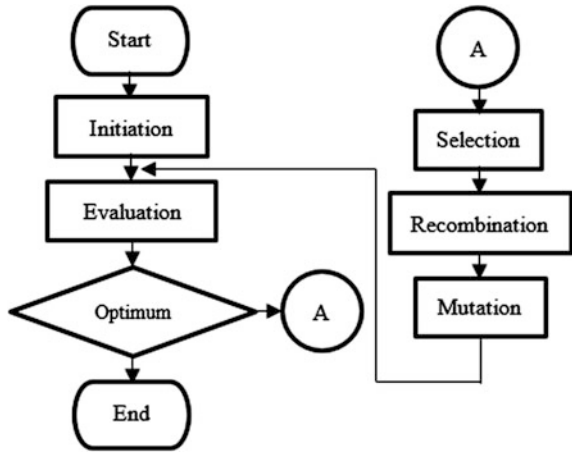
Parameter	Quantity	Subtotal
Daily energy needs	469251913.6 kJ/day	-7011.69 USD/day
Oil volume produced per day	355.54 barrel/day	16012.82 USD/day
Wastewater volume produced per day	134.25 m <sup>3</sup> /day	-1355.75 USD/day
<i>PR</i>		7645.37 USD/day

\*Minus (-) in subtotal column mean as a cost

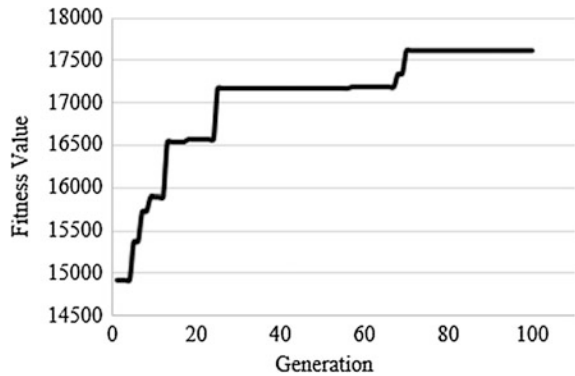
• Discussion

Pressure and temperature mathematical models of steam flood operation using Beggs–Brill method show a good approach about pressure gradient in two-phase flow. As shown in Figs. 2 and 4, the error of these models is relatively small (4.48% for pressure and 0.98% for temperature). This error is because of different methods between PIPESIM and manual calculation. In PIPESIM software, calculation performs until the smallest segment/part (using numeric method). While we are using

**Fig. 8** Mechanism in genetic algorithm



**Fig. 9** Best fitness plot of each generation in genetic algorithm optimization of steam flood operation



**Table 4** Revenue calculation after optimization

Parameter	Quantity	Subtotal
Daily energy needs	1433,768,852 kJ/day	-21609.55 USD/day
Oil volume produced per day	965.93 barrel/day	43502.79 USD/day
Wastewater volume produced per day	404.62 m <sup>3</sup> /day	-4274.47 USD/day
<i>PR</i>		17618.75 USD/day

manual method, segmentation ability of our calculation is limited (in this research, segmentation in first and third models is 50 m). Therefore, manual calculation is like lumped calculation. As mentioned above, the fluid properties in every segment are different.

Darcy equation in second model shows excellent result when validated using COMSOL. Mean error from Darcy equation (second model) to COMSOL

simulation is 0.39% for pressure and 0.97% for temperature. The output of second model, pressure gradient in reservoir formation, is used for change in oil saturation.

Both of these models are valid enough for further calculation. The next calculation is steam flood operation profit. In normal operating condition, steam flood runs in 2 kg/s of mass steam injection rate, 600 psia of injection pressure, and 80% of steam quality. Table 3 shows us that the value of water recycle in normal operating condition is not optimum yet. Although the number of wastewater is relatively small, profit (*PR*) is not at global optimum value. The value of *PR* is 7645.37 USD/day.

The result of genetic algorithm optimization could reach global optimum at 17618.75 USD/day. The optimum operation could be reached when steam flood runs in 6.460 kg/s mass injection rate, 1408.53 psia injection pressure, and 87.86% steam quality. The process GA optimizes this model which is shown in Fig. 8. In Fig. 9, we can see the value of best fitness from each generation is increasing.

## 4 Conclusions

Model of steam flood operation can be derived using Beggs and Brill equation at injection well head to reservoir formation and reservoir formation to production well head, and using Darcy equation to obtain pressure gradient at reservoir formation. Mean error from Beggs–Brill method (first and third models) to PIPESIM software is 4.48% for pressure and 0.98% for temperature. Mean error from Darcy equation (second model) to COMSOL simulation is 0.39% for pressure and 0.97% for temperature. Pressure gradient value can be used to calculate sweep efficiency and wastewater at production well.

Using genetic algorithm, models can be optimized to global optimum. Based on the case in Hamaca field, global optimum of steam operation can be achieved at 6.460 kg/s mass injection rate, 1408.53 psia injection pressure, and 87.86% steam quality. Then, the profit of steam flood operation will be 17,618.75 USD/day.

**Acknowledgements** The authors would like to thank the Department of Petroleum Engineering, Universiti Teknologi PETRONAS, and the Department of Engineering Physics—Institut Teknologi Sepuluh Nopember (ITS) Surabaya, Indonesia, for assistance given to us in this study.

## References

1. A. Bera, “Status of electromagnetic heating for enhanced heavy oil/bitumen recovery and future prospects: A review,” *Applied Energy*, no. 151, pp. 206–226, 2015.
2. H. Gu, “Steam injection for heavy oil recovery: Modelling of wellbore heat efficiency and analysis of steam injection performance,” *Energy Conversion and Management*, vol. 97, pp. 166–177, 2015.

3. A. Dutt, "Modified analytical model for prediction of steam flood performance," *PRODUCTION ENGINEERING*, vol. 2, pp. 117–123, 2012.
4. A. e. a. Fakhru'l-Razi, "Review of technologies for oil and gas produced," *Hazard. Mater*, pp. 170 (2–3), 530–551, 2009.
5. M. A. Allawzi, "Study of the Effect of Steam Injection on Crude Oil Displacement Yield from an Oil Contaminated Soil Bed," *Jordan Journal of Civil Engineering*, vol. 2, pp. 208–217, 2008.
6. H. D. a. B. Beggs, "A Study of Two-Phase Flow in Inclined Pipes," *SPE-AIME*, pp. 616–617, 1973.
7. J. Xu, "Study on relative permeability characteristics affected by displacement pressure gradient: Experimental study and numerical simulation," *Fuel*, pp. 314–323, 2015.
8. A. J. Son, "Energy efficiency measures and conversion of fossil fuel," *Energy Efficiency*, vol. 3, p. 223–236, 2010.
9. C. G. Gutie'rrez-Arriaga, "Multi-objective optimization of steam power plants for sustainable," *Clean Techn Environ Policy*, vol. 15, p. 551–566, 2013.
10. E. J. S. Graham, "Probabilistic cost estimation methods for treatment of water," *International Journal of Greenhouse Gas Control*, vol. 41, p. 316–327, 2015.

# Seismic Stimulation and Induced Seismicity in Oil Reservoirs: A Review of Applications to Enhanced Oil Recovery (EOR)

Md. Irfan, Christopher Peter Lenn and Deva Ghosh

**Abstract** The objective of this paper is to review the literature on seismic stimulation methods for improving efficiency of oil production in mature reservoirs. Seismic stimulation has been reported via anecdotal field experience, analytical studies, numerical simulations, laboratory experiments and oilfield investigations over a 60-year period. New ideas include the mobilization of oil in porous media by capillarity-induced resonance at the dominant frequency. On the basis of critical interpretation of reported work, seismic stimulation appears capable of increasing efficiency of oil production in depleted reservoirs without damaging seismicity effects such as micro-earthquakes. Early pioneers of seismic stimulation techniques were from Russia, and they have promoted it as an alternative technique to conventional enhanced oil recovery (EOR) methods. This stimulation technique can alter the production of oil in low-recovery mature reservoirs at the macroscopic level.

**Keywords** Seismic stimulation · Enhanced oil recovery (EOR) · Mature reservoirs · Earth seismicity

## List of symbols

$\theta$	Contact angle
$R_{pore}$	Pore meniscus radius
$\eta_{oil}, \eta_{water}$	Viscosity of oil and water, respectively
$F_a, F_o$	Seismic force perturbation, background pressure gradient

---

Md.Irfan (✉) · C.P. Lenn  
Department of Petroleum Engineering, Universiti Teknologi PETRONAS,  
Bandar Seri Iskandar, 32610 Tronoh, Perak, Malaysia  
e-mail: md.irfan@zhcet.ac.in

C.P. Lenn  
e-mail: christopher.lenn@petronas.com.my

D. Ghosh  
Department of Petroleum Geosciences, Universiti Teknologi PETRONAS,  
Bandar Seri Iskandar, 32610 Tronoh, Perak, Malaysia  
e-mail: drdeva@petronas.com.my

$\phi$	Porosity
$\rho_f$	Mass density of fluid
$C_a$	Capillary number
$\sigma$	Surface tension
$h, l$	Downstream length of a stuck oil bubble, hydraulic throat radius
$S$	Stimulation number
$T$	Dimensionless frequency number
$k$	Permeability
$R$	Reynolds number
$\eta_f$	Shear viscosity of fluid

## 1 Introduction

The United States Department of Energy (DOE) Office of Basic Energy Science notes that the average primary recovery factor in world reservoirs is approximately 5–10% of the Original oil in place (OOIP) and overall recovery is about 35–45% of the OOIP including primary and secondary recovery methods [1]. Using EOR methods including thermal, gas and chemical techniques, the oil extraction can be ultimately increased 30–60% of OOIP in favourable conditions [2]. In a number of Russian reservoirs, it is reported that the proportion of residual hard-to-recover oil constitutes over 60% of OOIP due to geological and physical factors [3]. The principal causes of hard-to-recover oil are the presence of the higher interfacial tension, low mobility ratios, low permeability, immobile patches of oil (ganglia) in low permeability zones, complicated reservoir heterogeneity, higher capillary pressure and low driving force (viscous force) in the pore constriction (throat) [3].

In order to fulfil growth in energy consumption, big oil companies are in need of new technologies for oil production from low-recovery reservoirs [4]. The Interstate Oil & Gas Compact Commission (1995) reported that 238 Billion Barrels immobile oil from reservoirs in the USA could be recovered by a wave stimulation technique [5]. The capillary saturation curve; the relative permeability curve; and apparent thickening of polymer, CO<sub>2</sub>, or water flooding can be shifted favourably like increased 0.2 MBPD oil in Daqing Oil Field by HPAM [6, 7].

### 1.1 Seismic Stimulation Historical Background

Seismic stimulation technology has played role in residual oil recovery from marginal reservoirs since 1950. The researchers of USA (peaked in the 1970s) and USSR (peaked in the 1970–1980s) have been working on seismic stimulation technology for EOR [8]. During 1950–1987, the Russian workers observed that



vibration generated by natural seismic events, such as earthquake, volcano eruption and tectonic events, has transformed the extraction behaviour of oil wells even at distances of about 200 km from the epicentre [9]. Artificial explosions such as chemical, nuclear and continuously generating seismic vibrations such as railways and highways have also played a role in oil production [10]. Important studies have been done at notable Soviet institutes such as the Institute of Nuclear Geophysics & Geochemistry (VNIIYaGG), the Krylov Institute of Oil & Gas (VNII) and the Institute of Physics of the Earth of the USSR Academy of Sciences [11].

Over the past few years, seismic stimulation technology has been under scrutiny by research laboratories in the USA, Europe, South Korea, China, Russia, Canada and Norway [12, 13]. The laboratories have focused on elastic-wave vibration, acoustic, ultrasound waves, pressure pulsing and vibro-seismic stimulation technology methods. A joint project on ‘Seismic Stimulation for Enhanced Production of Oil Reservoirs’ was initiated by M. Robert at Los Alamos National Laboratory (LANL) with University of California at Berkeley (UCB) and Lawrence Berkeley National Laboratory (LBNL) researchers in 1995 [5]. The major oil companies such as Philips Petroleum Co., Oil and Gas Consultants International and Occidental Petroleum Corporation, in collaboration with the geophysical and service companies such as Halliburton and Seismic Recovery LLC have joined the consortium under DOE [5, 14]. The United States Department of Energy (DOE) project is directed towards innovative seismic stimulation technology for the recovery of the approximate 890 Million barrels of oil and natural gas liquids on Native American & Alaskan Native Corporation lands [5].

## **2 Significance of Studying Seismic Stimulation for Enhanced Oil Recovery**

Demand of energy for transportation and power consumption has increased significantly throughout the world. However, there has been growing concern about additional oil recovery from depleted mature reservoirs, noted in 2002 [15]. In 1986–87, the Russian oil company Nizhnevartovskneftegaz unprecedentedly obtained an extra 300,000 tons of crude oil, attributed to the use of seismic wave vibration. Yevgeny Kozlovsky, Vice-President, Russian Academy of Natural Sciences, estimated that Russia is now losing about 150 million tons of oil production per year due to difficulties in extracting oil from low-recovery reservoirs. [3]. Various Russian oil companies have initiated steps to increase production using ‘wave oscillations’. Well flow rates are stated to have increased by at least 5–10%. Moreover, it has additionally water cut by 5–10% [3]. In seismic wave stimulation, the propagation of the waves depends on elasticity, compressibility factor, grain size, viscosity and density of the rock [16]. The propagation of elastic waves is said to create gravitational separation of gas, oil and water and reduce capillarity forces in mature reservoirs.

## ***2.1 Anecdotal Evidences of Improved Oil Recovery by Seismic Stimulation (Seismicity)***

It has been noted through numerous anecdotal evidences that the generated seismic waves from earthquakes, railway and highways may alter oil production [17]. The result of generated seismic waves on permeability and mobility of saturated rocks has been long-established in laboratory experiments [18]. The electrohydraulic, electromagnetic, vibro-seismic and acoustic methods are very common for getting wave oscillation effects on reservoirs [4]. The Soviet scientist S.M. Gadiyev invented vibrowave method and the devices for its realization. The vibroseis-type sources are used for producing seismic frequency waves at the earth's surface [19]. It has been compared to the effects of teleseismic earthquakes to the effects of vibroseis-type sources on aquifers [20]. The seismic effects of earthquakes on oil extraction have been studied in great details with reference to extensive oilfield case studies. It has been shown that earth seismicity can alter oil extraction [11].

## ***2.2 Oil and Gas Extraction Has Triggered Earthquakes of Damaging Magnitudes***

On the basis of Stanford doctoral student's reported work, the Oklahoma Geological Survey (OGS) issued a statement that the injection of produced water into disposal wells from nearby oil and gas operations is the prime cause of the most of the state's recent (low magnitude) earthquakes [21]. It has been revealed that earth seismicity has increased dramatically over a 6-year period from 2009 to 2014. He states that it has increased from an average of 24 Mag. 3 earthquakes per year in the years 1973–2008 to an average of 193 Mag. 3 earthquakes in 2009–2014, with 688 occurring in 2014 alone [22].

## ***2.3 Mechanism of Induced Seismicity (Earthquakes)***

The human activities such as mining, fluid injection, reservoir impoundment and fluid extraction can induce earthquakes. Many other factors that lead to apropos cause include fluid injection parameters such as injection rate, injection depth, injection pressure, fluid temperature and cumulative injected volume. The reservoir conditions such as rock strength, pore pressure, pore temperature, the existence of pre-existing faults and their positioning related to the local stress field and reservoir permeability are also important for induced earthquakes [23]. Fluid injection can induce earthquakes in four ways: (1) the injection of fluid that is colder than the rock into which it is being injected: it causes thermoelastic deformation; (2) the injection of fluids fills and compressed fluids within pore spaces: it causes

**Table 1** The primary causes of earth seismicity in oil and gas extraction from oilfields

Reference	Earthquake site	Year	Magnitude of seismicity	Primary cause of earthquakes
Zoback M & Walsh R (2015), Rubinstein (2014)	Prague, Oklahoma	2011	5.6	Wastewater disposal
Justin L. & Alireza M (2015)	Trinidad, Colorado	2011	5.3	Wastewater disposal
Horton (2012), Kim (2013), Justin L. & Alireza M (2015)	Guy-Greenbrier, Arkansas	2011	4.7	Waste water disposal
Gail Atkinson (2015), H. Kao (2015)	Central west Alberta (Canada)	2014	4.4	Hydraulic fracturing
Gail Atkinson (2015) H. Kao (2015)	Northeast British Columbia (Canada)	2014	4.4	Hydraulic fracturing
Gan (2013) Frohlich (2013)	Cogdell field Near Snyder, Texas	2006–2011	4.6	Enhanced oil recovery

defonnation (poro-elastic effects); (3) the injection of fluids: it raises pore-fluid pressure within a fault; and (4) fluid stresses holding the fault closed (the normal stress). This results in a lower effective stress [22]. The following three primary types of fluid injection used by the oil industry can induce earthquakes as given in Table 1.

### 2.3.1 Hydraulic Fracturing (Fracking)

Hydraulic fracturing is the prime cause of a small percentage of the earth seismicity (having low magnitudes) observed in the USA. The largest hydraulic fracturing prompted earthquakes up to these dates are two M 4.4 earthquakes in central west Alberta and northeast British Columbia in Canada (British Columbia Oil and Gas Commission, 2014). Despite being invented in 1947, the first report of a felt hydraulic fracturing induced earthquake was in 1991 [24]. Around one million wells were hydraulically fractured in the USA between 1947 and 2010 [25]. Since 2011, several small earthquakes linked to hydraulic fracturing have been reported. The horizontal drilling technology invented in the 1990s combined with hydraulic fracturing, is the key driver for the recent increase in gas and oil extraction in the USA. Hydraulic fracturing has triggered earthquakes, albeit very small often termed as micro-seismic events and they can be used to monitor the fracturing process [26]. These earthquakes are typically on the order of  $-3.0 \leq M \leq 0$  [27].

### 2.3.2 Wastewater Disposal

Most induced seismic activities in the USA are linked to the deep underground disposal of fluids such as wastewater. The disposal of fluid underground is

considered an economic and safe option [28]. These formation brines (also termed produced water or wastewater) are often laden with dissolved salts, minerals and occasionally other materials that make it unsuitable for other uses. The Denver earthquakes of the 1960s were initiated by injection of chemical waste in deep injection wells (Evans et al., 1966; Healy et al., 1968). Several injection-induced earthquakes have been identified since these events. The largest ones are the Trinidad, Colorado and Oklahoma earthquakes [29].

### 2.3.3 Enhanced Oil Recovery

The largest earthquake (2006–2011) known to be induced by enhanced oil recovery (injection) processes was a 4.6 M earthquake in the Cogdell field near Snyder, Texas [30].

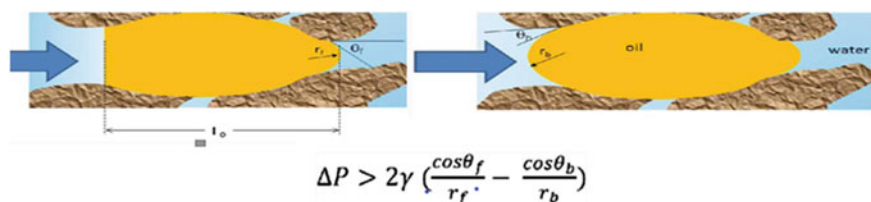
## 3 Analytical Studies for Shaking the Struck Patches of Oil (Ganglia/Blobs) in Pore Space

It has been stated that more than 30% by volume of the pore space might considerably be occupied by the oil (ganglia/blobs) in mature reservoirs [31]. The oil often gets trapped in a pore constriction (throat) by capillary pressure imbalance as shown in Fig. 1 [32, 33].

$$R_{Upstream} \cos\theta < R_{pore} \tag{1}$$

$$R_{Downstream} \cos\theta < R_{pore} \tag{2}$$

The lattice Boltzmann (LB) model (2 Dimensional) is applied for pore-scale numerical simulation. The two-phase flow can be simulated using easy form of the LB model presented by Gunstensen et al. (1991, 1993). It has been simplified by changing the multiple relaxation times in the lattice Boltzmann operator by only



**Fig. 1** A ganglion of oil is usually get trapped in pore constriction (throat), *Source* SPE179574MS

relaxation time  $1/\lambda$ . That is why, lattice BGK algorithm (Qian et al., 1992) has been used [33, 34].

Numerical analysis has been applied to understand the dynamics of the liquid trapped in porous media. Seismic stimulation is a very interesting engineering concept which offers the potential to improve ganglia mobilization and therefore enhances residual oil extraction [35]. The energy of a seismic wave can be converted into the energy of the dominant resonant frequency in the porous media, which locally generate ultrasound. This dominant frequency depends on the fluid saturation, the compactness and size of porous grains. It is independent of the source of energy and frequency spectrum originating at source [9].

## 4 Methodology

Mature reservoirs often have low volumetric sweep efficiency and displacement efficiency [36]. Lake et al. (1989) formulated recovery factor, i.e.,  $R_e = E_v * E_d$ . The main reasons are immobile ganglia in low permeability zones, capillary physics mechanisms and complexity in reservoir heterogeneity [37]. The seismic (mechanical) force is added through seismic stimulation in order to overcome capillary barriers for enhanced oil production. Numerical simulation schemes that investigate how to shake the stuck (trapped) oil patches (ganglia/blobs) through a pore constriction (throat) in mature reservoirs have been classified by the author and are shown in Fig. 2. They will indicate if it is plausible to cause coalescence of patches of oil ganglia that could be easily mobilized for production, well in late oilfield development stages.

**Selected Fields/Basins:** The United States Department of Energy (DOE) funded three large projects for feasibility studies of seismic stimulation as shown in Table 2. Furthermore, Occidental Petroleum Corp. (Oxy) performed seismic stimulation on Elk Hills field in Kern County of California and South Wasson Clear Fork Unit in Permian Basin of Texas. The Garza field in Permian Basin of Texas was also studied for improving oil cut in depleted reservoirs in the USA [14].

In the public domain of literature from Soviet times, the Russians performed seismic vibration projects on Changirtash field in Kirgizstan, Jirmovsky field in Volgogradskiy region, Pravdinsk field in Siberia and Mortymya Teterevsky field in Russia. All these field tests showed significant increase in oil production [14]. In Indonesia field tests, Caltex Pacific Indonesia (CPI) tested the Russian developed vibro-seismic impact technology (VSIT). This stimulation technique reported that the total cumulative enhanced oil production reached 20.2% above the agreed production baseline [5]. Additionally, the pressure pulsing technology termed cold heavy oil production (CHOP) is being used in heavy oil sands of Alberta and Saskatchewan in Canada. This technology is used for producing cold, heavy, high viscosity oil in poorly consolidated young sandstones [38]. The PE Tech (Canadian Service Company) executed pulse technology on sands of Morgan field in Alberta.

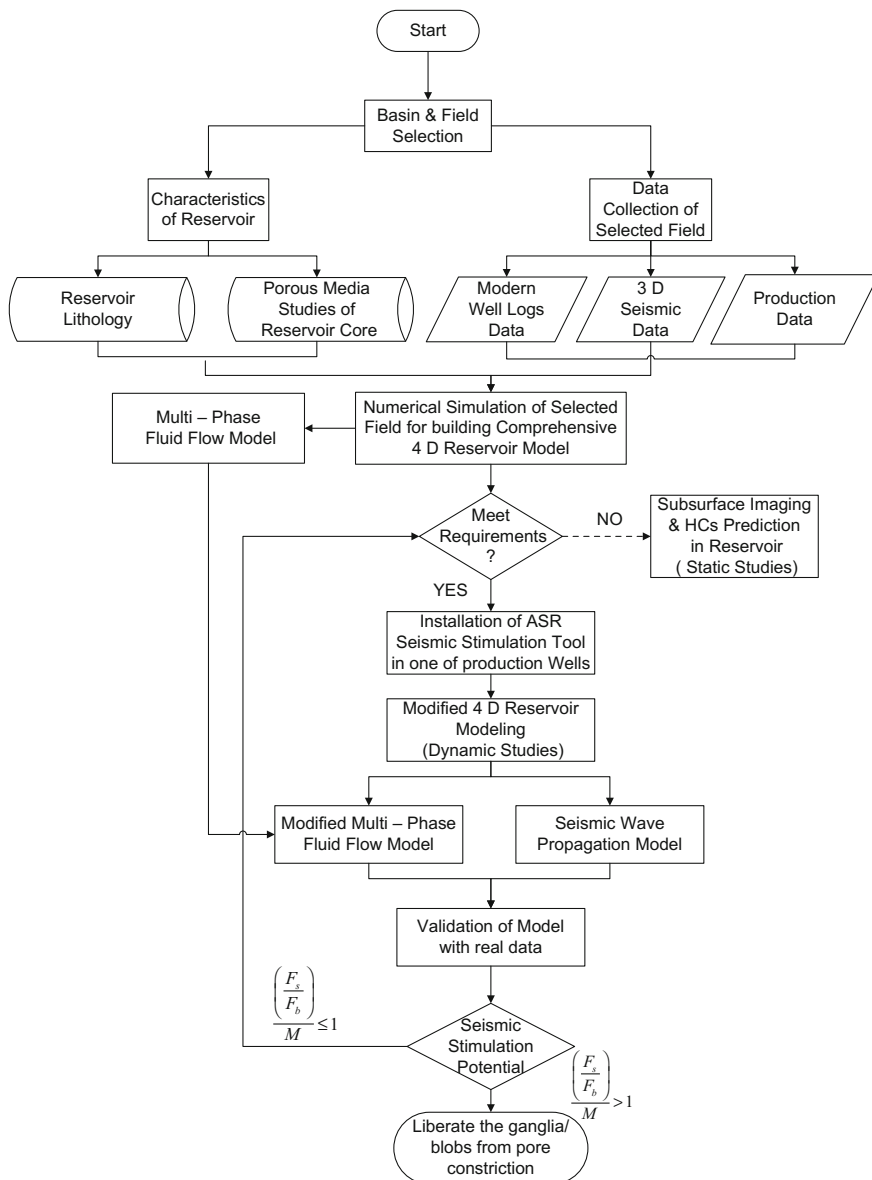


Fig. 2 Flow chart of numerical simulation schemes of seismic stimulation

**Reservoir Characterization:** In the flow chart in Fig. 2, it has been divided into the reservoir lithology and reservoir core formation. The reservoirs can be clastic (or non-clastic) or carbonate (or non-carbonate).

**Table 2** Doe-funded seismic stimulation projects for improving efficiency of oil production

Selected reservoir field	Basin/field location	Performers/consortiums	Principle investigator (P.I)/Co investigator
Lost hills	Kern County near Bakersfield, in California	Joint collaboration of LBNL & LANL	P.I—Steven R. Pride C. I—Peter Robert at LANL & C.I—Ernie Majorat LBNL
Upper Burbank field	Osage County in Oklahoma	Oil and Gas Consultants International	P.I—Robert Westermark
Michigan reservoir	Michigan	Michigan Tech University	P.I—Roger Turbening

For instances, Elk Hills fields, Lost Hills Fields and Permian Basin (Garza Field and South Wasson Clear Fort Unit field) are sandstone, diatomite and dolomite (carbonate) reservoirs, respectively. In reservoir cores, studies are taken for getting data on pore type, pore size distribution, pore throat distribution and formation thickness [39].

**Installation of ASR Seismic Tool in Mature Reservoirs:** Applied Seismic Research (ASR) has manufactured seismic tool for seismic stimulation in reservoirs. The ASR tool comprises three main components [40]. One component consists of the upper plunger (4 feet long having small diameter), 100 feet of sucker rods and a lower plunger (4 feet long having larger diameter). The sucker rods and lower plunger are equipped with travelling valves except upper plunger having no valve. Second component consists of the upper barrel (10 feet long with small diameter), compressional chamber (100 feet long) and lower barrel (10 feet long having large diameter). Third component consists of a cement plug (100 feet long, placed on the top of sand).

**Working principle of ASR Tool:** The seismic tool is installed at the bottom of tubing and rod string in one of production wells in mature reservoir. In down stroke, the travelling valve on the lower plunger is opened. Water is passed into the compression chamber in the down stroke. The travelling valve is enclosed as the both plungers move upward in upstroke. The water gets ‘compressed’ between the plungers. The maximum water pressure of the compression chamber reaches 3–4 K psi. The energy reaches around 100 kJ. The compressed water is released in a time interval of 50 ms. The hydrodynamic shock waves propagate downward into the reservoir in form of seismic wave. It would add a seismic-induced force to background pressure potential so that they would overcome the capillary barrier pressure. It would result in favourable shaking of the stuck oil patches in pores in low permeability reservoir zones. The permeability is effectively increased [41]. A seismic tool measures seismic wave amplitudes received by all wells from the seismic stimulation in the source well.

**Comprehensive 4D Reservoir Model:** With modern well log data, seismic data and production data, a comprehensive 4D reservoir model is numerically generated. It is used for calculations of lithology, net pay, porosity, water saturation and

**Table 3** Conditions for numerical simulation of seismic stimulation

Dimensionless number	Condition
$\frac{\eta_{oil}}{\eta_{water}}$ (Viscosity)	$\frac{\eta_{oil}}{\eta_{water}} \geq 10$
$\frac{F_a}{F_0}$ (Seismic/Pressure)	$\frac{F_a}{F_0} \approx \frac{f}{10^{-4}Hz} \theta > 10$
$R = \left(\frac{\rho_f k^2}{\eta^2 \varphi^2} F_0\right)$	$R \leq 1$
$Ca$ (Capillary number)	$Ca = \frac{2F_0 h l}{\sigma \cos(\varphi)} \left(1 + \frac{F_a}{F_0}\right) > 1$
$S$ (Stimulation number)	$S = \frac{2F_0 h \sqrt{k}}{\sigma \phi \cos(\varphi)} = \frac{2Ca h}{\cos(\varphi) \sqrt{k}} > > Ca$
$T$ (Dynamic criterion)	$T = \frac{l}{\delta_a} = \frac{4f \eta_{oil}}{\sqrt{k} F_a} < 1$
Mobilizing trapped oil	$T < 1 \& \frac{F_a}{F_0} > \frac{1}{S} - 1$

permeability. From static studies of the reservoir, 4D dynamic studies in terms of multiphase fluid flow and wave models are further generated. Numerical simulation is performed prior to, during and after installation of ASR seismic tool [42].

**Dimensionless numbers for seismic stimulation to shake the stuck (trapped) oil patches (ganglia/blobs) in depleted mature reservoir:** In numerical simulations, the dimensionless numbers that characterize seismic stimulation must be identified for actual field experiments [31]. Two flows will be similar if the dimensionless numbers are same irrespective of the fact that some of the material properties or force would be different in two situations as shown in Table 3 [31].

## 5 Conclusions

The implementation of seismic stimulation for EOR is a very interesting reservoir engineering concept. It offers great potential to improve ganglia mobilization from pore constriction in low permeability zone reservoirs. It has also been shown in published work that oil and gas extraction can trigger small-scale earthquakes, further developing the link between seismicity and production. Therefore, extensive studies are warranted for oil extraction through seismic stimulation methods.

**Acknowledgements** MD Irfan is very thankful to Universiti Teknologi PETRONAS, Malaysia, for giving Graduate Assistantship (GA) grant. We are particularly grateful to AMU alumni Dr. Abrar Hakeem for reviewing this manuscript before submission.

## References

1. L. W. Lake, R. Johns, W. Rossen, and G. Pope, *Fundamentals of enhanced oil recovery*: Society of Petroleum Engineers, 2014.
2. E. Tzimas, A. Georgakaki, C. Garcia Cortes, and S. Peteves, "Enhanced oil recovery using CO<sub>2</sub> in the European energy system," *European Commission, JRC*, pp. 26–30, 2005.



3. V. I. e. al, "Wave vibration oil recovery stimulation technology". retrieved from <http://www.oilru.com/or/37/742/>, accessed on March 2016," 2008.
4. S. A. Thomas, W. W. Gilbert, and A. R. Huffman, "Process and apparatus for coupled electromagnetic and acoustic stimulation of crude oil reservoirs using pulsed power electrohydraulic and electromagnetic discharge," ed: Google Patents, 2002.
5. R. Westermark, J. Brett, and D. Maloney, "Enhanced oil recovery with downhole vibration stimulation," in *SPE production and operations symposium*, 2001.
6. T. Hamida and T. Babadagli, "Effect of ultrasonic waves on the capillary imbibition recovery of oil," in *SPE Asia Pacific Oil and Gas Conference and Exhibition*, 2005.
7. A. Clarke, A. M. Howe, J. Mitchell, J. Staniland, and L. A. Hawkes, "How Viscoelastic-Polymer Flooding Enhances Displacement Efficiency," *SPE Journal*, 2015.
8. P. R. Susan Jackson, Ernie Majer, "Advances in Seismic Stimulations Technologies," *National Petroleum Technologies Office at Los Alamos & Lawrence Berkeley National Laboratory, Excerpt in PTTC Network News, 2nd Quarter*, 2011.
9. V. Nikolaevskiy, e. al, "Residual oil reservoir recovery with seismic vibrations," *SPE Production & Facilities*, vol. 11, pp. 89–94, 1996.
10. A. Bolonkin, J. Friedlander, S. Neumann, and S. S. T. Group, "Innovative unconventional oil extraction technologies," *Fuel Processing Technology*, vol. 124, pp. 228–242, 2014.
11. I. A. Beresnev and P. A. Johnson, "Elastic-wave stimulation of oil production: A review of methods and results," *Geophysics*, vol. 59, pp. 1000–1017, 1994.
12. M. Mullakaev, et. al, "Development of ultrasonic equipment and technology for well stimulation and enhanced oil recovery," *Journal of Petroleum Science and Engineering*, vol. 125, pp. 201–208, 2015.
13. V. O. Abramov, M. S. Mullakaev, A. V. Abramova, I. B. Esipov, and T. J. Mason, "Ultrasonic technology for enhanced oil recovery from failing oil wells and the equipment for its implementation," *Ultrasonics sonochemistry*, vol. 20, pp. 1289–1295, 2013.
14. C. Huh, "Improved oil recovery by seismic vibration: a preliminary assessment of possible mechanisms," *Inter national Oil Conference and Exhibition in Mexico*, 2006.
15. M. Höök, R. Hirsch, and K. Aleklett, "Giant oil field decline rates and their influence on world oil production," *Energy Policy*, vol. 37, pp. 2262–2272, 2009.
16. E. Alhomadhi e. al, "Experimental application of ultrasound waves to improved oil recovery during waterflooding," *Journal of King Saud University-Engineering Sciences*, vol. 26, pp. 103–110, 2014.
17. S. Jackson, P. Roberts, and E. Majer, "Advances in seismic stimulation technologies," *PTTC Network News, 2nd Quarter. Available Online at: <http://www.appliedseismicresearch.com/pdf/stateofheart.pdf>*, 2001.
18. L. Han, "Wave Attenuation in Porous Media Under Multiple Energy Excitations and a Statistical Periodicity Ratio Method with its Application in Nonlinear System Behavior Diagnosis," Faculty of Graduate Studies and Research, University of Regina, 2013.
19. O. Ellingsen, "Method to increase the oil production from an oil reservoir," ed: Google Patents, 2002.
20. V. Barabanov, A. Grinevskiy, I. Kissin, and A. Nikolayev, "Some Effects of Imposed Seismic Vibrations on a Water-Saturated Medium. Comparison with Effects of Distant Earthquakes," in *Dokl. USSR Acad. Sci., Earth Sci. Sect.*, 1987, pp. 52–56.
21. F. R. Walsh and M. D. Zoback, "Oklahoma's recent earthquakes and saltwater disposal," *Science advances*, vol. 1, p. e1500195, 2015.
22. J. L. Rubinstein and A. B. Mahani, "Myths and facts on wastewater injection, hydraulic fracturing, enhanced oil recovery, and induced seismicity," *Seismological Research Letters*, vol. 86, pp. 1060–1067, 2015.
23. S. Shapiro and C. Dinske, "Fluid-induced seismicity: Pressure diffusion and hydraulic fracturing," *Geophysical Prospecting*, vol. 57, pp. 301–310, 2009.
24. H. Kanamori and E. Hauksson, "A slow earthquake in the Santa Maria Basin, California," *Bulletin of Seismological Society of America*, vol. 82, pp. 2087–2096, 1992.

25. T. J. Gallegos and B. Varela, "Trends in hydraulic fracturing distributions and treatment fluids, additives, proppants, and water volumes applied to wells drilled in the United States from 1947 through 2010," US Geological Survey 2328–0328, 2015.
26. J. J. Bommer, H. Crowley, and R. Pinho, "A risk-mitigation approach to the management of induced seismicity," *Journal of Seismology*, vol. 19, pp. 623–646, 2015.
27. A. A. Holland, "Earthquakes triggered by hydraulic fracturing in southcentral Oklahoma," *Bulletin of Seismological Society of America*, vol. 103, pp. 1784–1792, 2013.
28. G. Ferguson, "Deep injection of waste water in the western Canada sedimentary basin," *Groundwater*, vol. 53, pp. 187–194, 2015.
29. J. L. Rubinstein, W. L. Ellsworth, A. McGarr, and H. M. Benz, "The 2001–present induced earthquake sequence in the Raton Basin of northern New Mexico and southern Colorado," *Bulletin of the Seismological Society of America*, 2014.
30. W. Gan and C. Frohlich, "Gas injection may have triggered earthquakes in the Cogdell oil field, Texas," *Proceedings of the National Academy of Sciences*, vol. 110, pp. 18786–18791, 2013.
31. S. R. Pride, E. G. Flekkøy, and O. Aursjø, "Seismic stimulation for enhanced oil recovery," *Geophysics*, vol. 73, pp. O23–O35, 2008.
32. I. A. Beresnev, "Theory of vibratory mobilization on nonwetting fluids entrapped in pore constrictions," *Geophysics*, vol. 71, pp. N47–N56, 2006.
33. M. Hilpert, G. H. Jirka, and E. J. Plate, "Capillarity-induced resonance of oil blobs in capillary tubes and porous media," *Geophysics*, vol. 65, pp. 874–883, 2000.
34. M. Hilpert, "Capillarity-induced resonance of blobs in porous media: Analytical solutions, Lattice–Boltzmann modeling, and blob mobilization," *Journal of colloid and interface science*, vol. 309, pp. 493–504, 2007.
35. H. D. Joshi, "A Numerical Approach for Oil Slug Mobilization in a Capillary Tube Under Absence and Presence of External Excitations," Faculty of Graduate Studies and Research, University of Regina, 2013.
36. C. J. Wright and R. A. Gallun, *Fundamentals of oil & gas accounting*: Pennwell Books, 2008.
37. H. Steeb, P. S. Kurzeja, M. Frehner, and S. M. Schmalholz, "Phase velocity dispersion and attenuation of seismic waves due to trapped fluids in residual saturated porous media," *Vadose Zone Journal*, vol. 11, 2012.
38. T. Spanos, B. Davidson, M. Dusseault, D. Shand, and M. Samaroo, "Pressure pulsing at the reservoir scale: a new IOR approach," *Journal of Canadian Petroleum Technology*, vol. 42, 2003.
39. A. Rafiq, D. W. Eaton, A. McDougall, and P. K. Pedersen, "Reservoir characterization using microseismic facies analysis integrated with surface seismic attributes," *Interpretation*, vol. 4, pp. T181–T195, 2016.
40. T. Daley and E. Majer, "Borehole seismic monitoring of seismic stimulation at Occidental Permian Ltd's–South Wason Clear Fork Unit," *Lawrence Berkeley National Laboratory*, 2007.
41. J. E. Elkhoury, E. E. Brodsky, and D. C. Agnew, "Seismic waves increase permeability," *Nature*, vol. 441, pp. 1135–1138, 2006.
42. S. Kostrov and W. Wooden, "In situ seismic stimulation shows promise for revitalizing mature fields," *Oil & gas journal*, vol. 103, pp. 43–49, 2005.

# Controlling Gas Mobility in Water-Alternating Gas Injection by Surfactant Blend Formulations

Muhammad Khan Memon, Khaled Abdalla Elraies  
and Mohammed Idrees Al-Mossawy

**Abstract** Controlling the viscous fingering in water-alternating gas injection, addition of foam with injection water is more favorable. The use of foam surfactant is one of the potential solutions for reducing the gas mobility. The main objective of this study is to generate stable foam for gas mobility control using surfactant blend formulations. Surfactant blend synergistically exhibit better foaming properties than those of individual surfactant. The blend contains anionic as primary surfactant and amphoteric as a foam stabilizer. Surfactant blend improves the foam stability and reduces the destabilizing effect of crude oil. Alpha olefin sulfonate (AOS<sub>C14–16</sub>) is selected as a primary surfactant. Amphoteric surfactant lauryl amido propyl amine oxide (LMDO) is selected as an additive. The foam was generated in the absence of crude oil in porous media by using Berea sandstone core samples at 96 °C and 1400 psi. The increase in differential pressure showed reduction in gas mobility. The average mobility reduction factors of surfactant blend 0.6%AOS and 0.6%AOS + 0.6%LMDO at reservoir conditions were resulted as 2.5 and 4.35, respectively. The experimental results showed that the blend formulations play an imperative role in minimizing gas mobility during water-alternating gas injection.

**Keywords** Foam · Mobility reduction factor · Porous media · Surfactant blend · Surfactant-alternating gas

## 1 Introduction

Foam liquid is generally a surfactant solution with a good ability to sweep oil from reservoirs. Foam surfactant flooding can not only improve macro-sweep volume but also improve micro-displacement efficiency [1, 2]. In general, foam flooding can increase the 10–25% of oil recovery [3]. Foam can improve gas injection conformance

---

M.K. Memon (✉) · K.A. Elraies · M.I. Al-Mossawy  
Petroleum Engineering Department, Universiti Teknologi PETRONAS, Bandar Seri  
Iskandar, 32610 Tronoh, Perak Darul Ridzuan, Malaysia  
e-mail: mkmemon@hotmail.com

and gas mobility control and hence improve sweep efficiency in secondary or tertiary recovery processes.

Mobility is a measure of the ability of a fluid to move through interconnected pore spaces. Mobility reduction factor (MRF) is the ratio of pressure drop caused by the simultaneous flow of gas and liquid through the rock (core sample) in the presence or absence of surfactant [4–7].

Mathematically,

$$MRF = \frac{\Delta p(CO_2 \text{ with foam})}{\Delta p(CO_2 \text{ Without foam})}$$

or

$$MRF = \frac{\Delta p_{\text{Foam}}}{\Delta p_{\text{without foam}}} \quad (1)$$

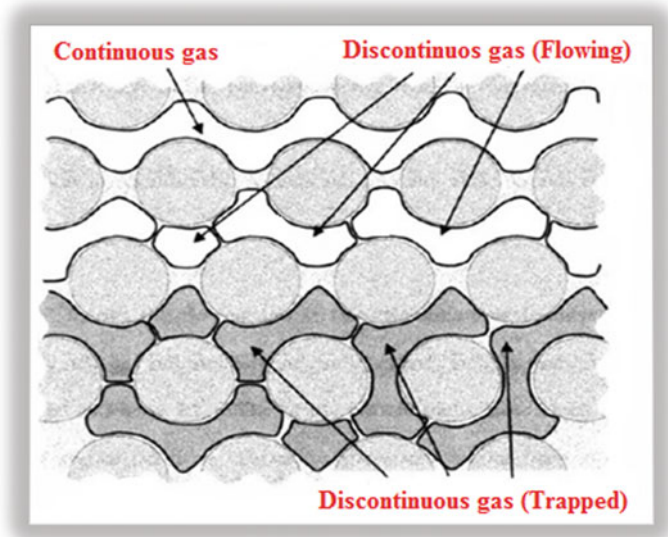
The MRF mechanism was studied by Sanchez and Schechter in 1989. They suggested MRF increase with increasing pressure. A high pressure increases the number of snap-off sites that generate a higher number of lamellae. A lower surfactant concentration is required at high pressure [8]. Strong stable foam should be needed for reducing CO<sub>2</sub> mobility in the porous media. Several published literatures suggested that the strong foam can be generated at relatively high oil saturations [9–11]. This can be measured by MRF. Mobility reduction factor depends on the following main factors:

- The composition of gas and brine,
- Nature of the surfactant and reservoir,
- The foam quality and low texture,
- The foam flow rate,
- The temperature and pressure at reservoir conditions.

The injection of foam surfactant has advantages as compared to other chemicals because it reduces the injected gas mobility more than liquid mobility [12]. Further, the maximum generated foam volume and foam half time are indications of strong stability and better performance of surfactants [13]. In this study, four surfactants were tested and evaluated based on the mobility reduction factor. The experiments were performed by using sandstone core at reservoir conditions.

## 2 Literature Review

Addition of foam surfactant with water-alternating gas (WAG) injection can reduce gas mobility. Mobility control is achieved by WAG and SWAG due to instantaneous flow of two phases (gas and surfactant) [14–16]. In these processes, foam is generated by simultaneous injection of two phases that resulted an increase in the gas apparent viscosity and therefore increases the gas saturation. The increase in gas



**Fig. 1** Gas-flowing and gas-trapped phenomena in porous media [20, 21]

saturation results in the decrease of oil saturation and relative permeability of oil. Thus, the foam generation improves mobility control in the process [17]. Figure 1 presents the concept of reducing gas mobility. Gas bubbles are surrounded by thin films of liquid (lamellae). These lamellae surrounded by foam bubbles may be stationary or in motion. The ability of foam to reduce the gas mobility depends strongly on its texture (bubble size or number of lamellae per unit volume). The gas trapped by stationary lamellae is immobilized and reduces the gas saturation [18]. Stationary lamellae alter gas flow paths and block the movement of gas flow resulting in the reduction of gas relative permeability. Lamellae in motion along the pore walls increase the resistance to flow of the flowing gas. This cannot increase the actual gas viscosity because only moving portion of gas increases resistance to flow. The effect of moving lamellae resulted an increase in apparent gas viscosity. Therefore, foam surfactant reduces the gas mobility by reducing the gas relative permeability and increasing the apparent gas viscosity [19].

In the foam surfactant WAG injection process, the injected foam surfactant controls the gas mobility using the following three techniques:

- a. Minimizing gravity segregation,
- b. Blocking gas flow,
- c. Reducing the early breakthrough time.

### 3 Methodology

#### 3.1 Materials

##### 3.1.1 Foam Surfactants

Alpha olefin sulfonate (AOS<sub>C14-16</sub>) and lauryl amido propyl amine oxide (LMDO) were provided by Stepan Company, USA.

##### 3.1.2 Composition of Injection Water

Sodium chloride (NaCl) was purchased from Fischer Company, UK, and magnesium chloride (MgCl<sub>2</sub>.6H<sub>2</sub>O), potassium chloride (KCL), sodium bicarbonate (NaHCO<sub>3</sub>), sodium sulfate (Na<sub>2</sub>SO<sub>4</sub>), and calcium chloride (CaCl<sub>2</sub>.2H<sub>2</sub>O) were purchased from R & M Chemicals, UK. Table 1 presents the composition of synthetic brine used as injection water.

##### 3.1.3 CO<sub>2</sub> Gas

Pure CO<sub>2</sub> gas was selected. The density of CO<sub>2</sub> at 96 °C and 1400 psia was measured as 0.18 gm/cm<sup>3</sup>. Viscosity at 96 °C was measured as 0.018 cp.

##### 3.1.4 Berea Sandstone

Berea sandstone is considered as excellent sandstone for the laboratory experiments, particularly in enhanced oil recovery (EOR). Table 2 presents the properties of Berea core samples.

**Table 1** Composition of injection water

Salt	mg/L
Sodium	10603
Chloride	18807
Calcium	354
Magnesium	1219
Potassium	325
Bicarbonate	163
Sulfate	2636
Total salinity (ppm)	34107

**Table 2** Berea sandstone properties

Properties	Core A	Core B
Diameter of core sample, cm	3.80	3.81
Length of core sample, cm	7.62	7.62
Area of core sample, cm <sup>2</sup>	11.40	11.40
Pore volume, ml	16.76	17
Porosity, %	19.3	20.3
Brine permeability, md	142	163.6

### 3.2 Mobility Reduction Factor

Mobility reduction factor (MRF) is the ratio of steady pressure drop across a core sample with foam and brine flowing at the same rate. Higher differential pressure indicates greater reduction in gas mobility by using surfactant formulations. MRF measurement was taken by HTHP relative permeability system (RPS 8000–10000, TEMCO, Inc., USA).

Figure 2 presents the equipment of RPS used for the MRF experiments. All MRF measurements were taken at steady state with an injection flow rate of 0.8 cm<sup>3</sup>/min. To generate the foam in the Berea sandstone core samples, experiments were performed at a reservoir temperature 96 °C and pressure 1400 psi.



**Fig. 2** High-temperature high-pressure (HTHP) relative permeability system for the MRF experiments

### 4 Results and Discussions

The purpose of the MRF is to evaluate the blocking effect of selected formulations. Two surfactant formulations were evaluated to determine the foam quality and its flow behavior by using Berea sandstone core samples. Before the start of the MRF experiments, core samples were vacuumed with brine for 48 h. After that, core sample was settled in the core holder. Accumulators A, B, and C were filled with CO<sub>2</sub>, brine, and surfactant solution. These all were settled inside the oven at temperature 96 °C and pressure 1400 psi. Other required data were put in the software. Figure 3 presents the schematic diagram of experiments performed at reservoir conditions. First of all, core sample was saturated with brine. Surfactant solution was injected before and after CO<sub>2</sub> injection with an injection rate of 0.8 cm<sup>3</sup>/min. The fluids (brine, CO<sub>2</sub>, and surfactant solution) were injected from the accumulators A, B, and C to the core by using syringe-type pump. The effluent was collected in the graduated cylinder. Each fluid was injected up to steady-state conditions.

Table 3 presents the MRF of tested foam surfactant formulations. Equation 1 was used for calculating the mobility reduction factor. Constant differential pressure values were used from the foam flooding experiments by using Berea core samples.

Figure 4 presents the differential pressure profile of foam surfactant 0.6%AOS. The average differential pressure ( $\Delta p$ ) of the measured foam surfactant 0.6%AOS

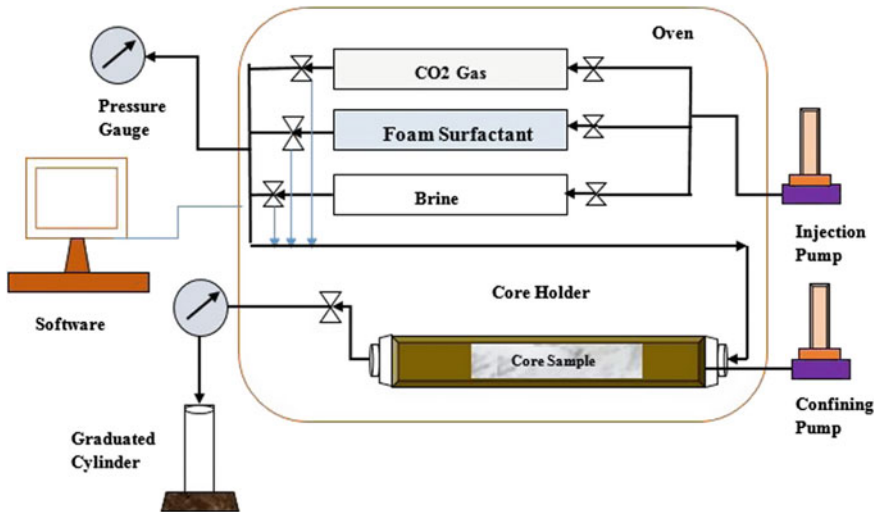


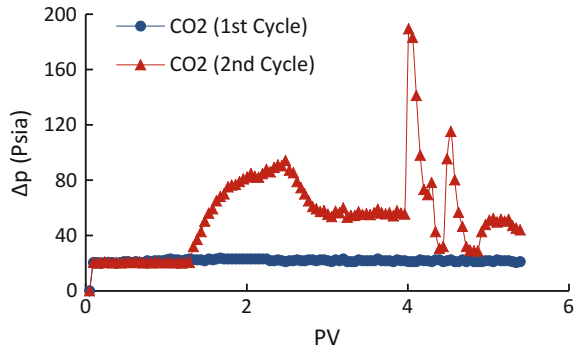
Fig. 3 Schematic diagram of core flooding

Table 3 Mobility reduction factor and foam quality

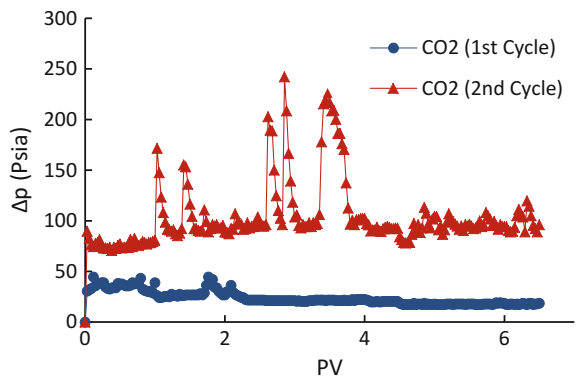
Core ID	Surfactant formulations	$\Delta p$ CO <sub>2</sub> (no foam)	$\Delta p$ CO <sub>2</sub> (with foam)	MRF
1	0.6%AOS	21.8	56.3	2.5
2	0.6%AOS + 0.6%LMDO	23.8	103.4	4.35



**Fig. 4** Pressure differential profile of foam surfactant 0.6%AOS



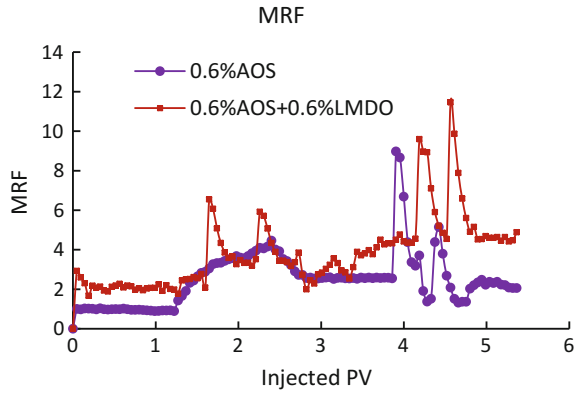
**Fig. 5** Pressure differential profile of foam surfactant blend 0.6%AOS + 0.6% LMDO



was 21.8 psi when CO<sub>2</sub> was dissolved in brine. The value of average Δp was increased as 56.3 psi when the second slug of CO<sub>2</sub> was injected. MRF value was increased due to the discontinuous gas phase created by snap-off inside a core that resulted in the reduction of gas permeability. Figure 5 presents the differential pressure profile of foam surfactant blend 0.6%AOS + 0.6%LMDO. The average Δp was 23.8 psi when CO<sub>2</sub> was dissolved in brine. The value of average Δp was increased as 103.4 psi when the second slug of CO<sub>2</sub> was injected. The increase in Δp is due to the addition of cosurfactant that increases the foam and blocking gas pathways to reduce the gas permeability. Further, high trapped gas saturation due to foam generation inside core usually reduces gas mobility [22]. According to the Sheng (2013), MRF value greater than one shows the presence of foam in the core at reservoir conditions. MRF range is considered as 1–10000. If MRF is less than one (MRF < 1), it means there is no foam generated by surfactant solution inside the core [23].

The MRF value of blended surfactant formulation showed greater than single surfactant tested in the porous media. Figure 6 presents the comparison of MRF values of 0.6%AOS and surfactant blend formulation 0.6%AOS + 0.6%LMDO.

**Fig. 6** MRF of 0.6%AOS and blend of 0.6%AOS + 0.6%LMDO



## 5 Conclusions

- The MRF of foam surfactant formulations is measured at reservoir conditions (96 °C and 1400 psi).
- The MRF of 0.6%AOS + 0.6%LMDO surfactant blend was found higher as compared to 0.6%AOS single surfactant.
- Higher differential pressure ( $\Delta p$ ) values by the MRF experiment indicated greater reduction of gas mobility. Therefore, MRF result showed that the maximum gas mobility was controlled by blend of 0.6%AOS + 0.6%LMDO surfactant formulation.

**Acknowledgements** We would like to acknowledge the Universiti Teknologi PETRONAS, Malaysia, for supporting this research work.

## References

1. E. Ashoori, T. van der Heijden, and W. Rossen, "Fractional-flow theory of foam displacements with oil," *SPE Journal*, vol. 15, pp. 260–273, 2010.
2. R. F. Li, R. B. Le Bleu, S. Liu, G. J. Hirasaki, and C. A. Miller, "Foam mobility control for surfactant EOR," in *SPE Symposium on Improved Oil Recovery*, 2008.
3. R. F. Li, W. Yan, S. Liu, G. Hirasaki, and C. A. Miller, "Foam mobility control for surfactant enhanced oil recovery," *SPE Journal*, vol. 15, pp. 928–942, 2010.
4. L. L. Schramm, "Foam sensitivity to crude oil in porous media," *ACS Advances in Chemistry Series*, vol. 242, pp. 165–200, 1994.
5. G. Hirasaki, C. Miller, R. Szafranski, J. Lawson, and N. Akiya, "Surfactant/foam process for aquifer remediation," in *International Symposium on Oilfield Chemistry*, 1997.
6. K. Mannhardt, J. Novosad, and L. Schramm, "Comparative evaluation of foam stability to oil," *SPE Reservoir Evaluation & Engineering*, vol. 3, pp. 23–34, 2000.
7. R. E. Blauer and C. Kohlhaas, "Formation fracturing with foam," in *Fall Meeting of the Society of Petroleum Engineers of AIME*, 1974.

8. J. M. Sanchez and R. S. Schechter, "Surfactant effects on the two-phase flow of steam-water and nitrogen-water through permeable media," *Journal of Petroleum Science and Engineering*, vol. 3, pp. 185–199, 1989.
9. T. Blaker, M. G. Aarra, A. Skauge, L. Rasmussen, H. K. Celius, H. A. Martinsen, *et al.*, "Foam for gas mobility control in the Snorre field: the FAWAG project," *SPE Reservoir Evaluation & Engineering*, vol. 5, pp. 317–323, 2002.
10. S. Chou, "Conditions for generating foam in porous media," in *SPE Annual Technical Conference and Exhibition*, 1991.
11. V. Chukwueke, M. Bouts, and C. Van Dijkum, "Gas shut-off foam treatments," in *SPE/DOE Improved Oil Recovery Symposium*, 1998.
12. H. Cubillos, J. Montes, C. Prieto, and P. Romero, "Assessment of foam for GOR control to optimize miscible gas injection recovery," in *SPE Improved Oil Recovery Symposium*, 2012.
13. M. K. Memon, M. T. Shuker, and K. A. Elraies, "Study of blended surfactants to generate stable foam in presence of crude oil for gas mobility control," *Journal of Petroleum Exploration and Production Technology*, pp. 1–9, 2016.
14. M. Sohrabi, G. Henderson, D. Tehrani, and A. Danesh, "Visualisation of oil recovery by water alternating gas (WAG) injection using high pressure micromodels-water-wet system," in *SPE Annual Technical Conference and Exhibition*, 2000.
15. D. J. Stephenson, A. G. Graham, and R. W. Luhning, "Mobility control experience in the Joffre Viking miscible CO<sub>2</sub> flood," *SPE Reservoir Engineering*, vol. 8, pp. 183–188, 1993.
16. D. Robie Jr, J. Roedell, and R. Wackowski, "Field Trial of Simultaneous Injection of CO<sub>2</sub> and Water, Rangely Weber Sand Unit, Colorado," in *SPE Production Operations Symposium*, 1995.
17. S. Farnazeh and M. Sohrabi, "A Review of the status of Foam applications in enhanced oil recovery," in *Society of Petroleum Engineers. SPE-164917. Presentation at the EAGE Annual Conference & Exhibition incorporating SPE Europe held in London*, 2013.
18. F. Friedmann, W. Chen, and P. Gauglitz, "Experimental and simulation study of high-temperature foam displacement in porous media," *SPE reservoir engineering*, vol. 6, pp. 37–45, 1991.
19. M. Kloet, W. J. Renkema, and W. R. Rossen, "Optimal Design Criteria for SAG Foam Processes in Heterogeneous Reservoirs," in *EUROPEC/EAGE Conference and Exhibition*, 2009.
20. A. Kovscek and C. Radke, "Fundamentals of Foam Transport in Porous Media. L. Schramm, ed., Foams: Fundamentals and Applications in the Petroleum Industry, 115–163. Washington DC," in *ACS Symposium Series*, 1994.
21. D. Tanzil, G. J. Hirasaki, and C. A. Miller, "Mobility of foam in heterogeneous media: Flow parallel and perpendicular to stratification," in *SPE Annual Technical Conference and Exhibition*, 2000.
22. A. Gandomkar, R. Kharrat, M. Motealleh, H. Khanamiri, M. Nematzadeh, and M. Ghazanfari, "An experimental investigation of foam for gas mobility control in a low-temperature fractured carbonate reservoir," *Petroleum Science and Technology*, vol. 30, pp. 976–985, 2012.
23. J. Sheng, *Enhanced oil recovery field case studies*: Gulf Professional Publishing, 2013.

# A Review on CO<sub>2</sub> Foam for Mobility Control: Enhanced Oil Recovery

Shehzad Ahmed, Khaled Abdalla Elraies, Isa M. Tan  
and Mudassar Mumtaz

**Abstract** Injection of gas is increased nowadays, and among various kinds, the mainly used gas in past 30 years for EOR purpose is CO<sub>2</sub>. The recovery mechanisms associated with CO<sub>2</sub> flooding are oil viscosity reduction, oil swelling, and the phase transition due to miscible displacement. On the other hand, high mobility of CO<sub>2</sub> and reservoir heterogeneities are the two major factors that are responsible for poor sweep efficiency. CO<sub>2</sub> is having low density, and it results in the gravity override and starts moving toward the top of the reservoir causing an unfavorable mobility ratio. The combination of surfactant with CO<sub>2</sub> generates foam which is a promising and cost-effective method in improving the sweep efficiency. The focus of research nowadays is to obtain foam with high stability and low mobility because it is directly related to sweep efficiency. Due to overwhelming interest in foam EOR, some new surfactants have been produced with the objective to meet wide range of reservoir condition and for targeting difficult reservoir design and operating conditions. In this paper, recent experimental research for laboratory screening and evaluation of surfactant is highlighted and the foam mobility in the porous media has been reviewed. The parameters important for the generation of efficient foam for the purpose of EOR have also been reviewed.

**Keywords** Surfactant · CO<sub>2</sub> flooding · CO<sub>2</sub> foam flooding · Foam mobility

## 1 Introduction

In EOR process, the main objective is the economical enhancement of sweep efficiency governed by mobility ratio which is the ratio of effective permeability and viscosity of fluid [1]. The fluid mobility controls the relative ease with which fluid

---

S. Ahmed (✉) · K.A. Elraies  
Department of Petroleum Engineering, University Teknologi PETRONAS,  
32610 Seri Iskandar, Perak, Malaysia  
e-mail: shehzadahmed904@yahoo.com

I.M. Tan · M. Mumtaz  
Department of Fundamental and Applied Sciences, University Teknologi PETRONAS,  
32610 Seri Iskandar, Perak, Malaysia

moves through a reservoir. In a case where the mobility of displacing fluid is more, a stable interface will not be achieved causing the phenomenon of viscous fingering [2, 3]. Such kind of oil displacement mechanism is called unfavorable or non-ideal displacement.

High mobility of CO<sub>2</sub> and reservoir heterogeneities are the two major factors that are responsible for poor sweep efficiency. CO<sub>2</sub> is having low density, and it results in the gravity override [4] and starts moving toward the top of the reservoir resulting in negative effect on sweep efficiency. The use of foam in EOR processes can effectively improve the sweep efficiency [1–3, 5]. This is due to the reason that the resistance to the flow of the individual phase is significantly higher than that of individual phase that is making up foams [1, 6, 7].

Foam is a dispersion of gas in liquid, and it is produced when a liquid containing a small concentration of surfactant solution comes in contact with a gas. Displacement of foams gives relatively high resistance to flow in porous media, and due to this reason, foams are very useful in EOR processes. Foam helps in flow restriction of the injected fluids in fractures or high permeability streaks [1, 4]. It is also helpful in diverting the flow from thicker fractures to thinner [4]. In displacement process, it improves the mobility ratio by reducing injected phase mobility.

In this paper, concept of foam for the purpose of controlling the mobility of injected CO<sub>2</sub> and reducing the layering effect is studied. The proper designing of foam is necessary to obtain the desired properties of foam, i.e., high stability, high viscosity, and low mobility during its transport in porous media. Some commercially used surfactants, their screening, and the evaluations at different scenarios are described in detail, and also, their performance has been reviewed. This paper also includes a brief literature review on foam mobility in porous media. Different parameters controlling mobility of CO<sub>2</sub> foam have been elaborated, and the works of different authors have been summarized.

## 2 Foams and Foaming Agents

Surfactants are required to produce foams and are known as foaming agents. Numerous surfactants are available and suitable for the generation of foam, and the surfactant selection process depends on their specific application on the basis of laboratory test and the empirical relationships. Foam for reservoir application is defined as a gas–liquid mixture such that the liquid phase is continuous, whereas some part of the gas is made discontinuous by a thin film called lamella [8]. There is lack of theoretical quantitative relationship in literature that can help in detailed prediction of properties of the foams [1, 9–11].

Designing a foaming agent is the most critical step of CO<sub>2</sub> foam flooding process. The promising surfactants have good solubility in water, for example, the surfactants such as anionic and nonionic having high ethylene oxide (EO) groups attached [12, 13]. Temperature is another factor that suppresses the solubility of

surfactant in brine, and therefore, it requires special attention to evaluate CO<sub>2</sub> foams as the targeted reservoir conditions using reservoir fluid and its core samples [14].

One of the constraints associated with surfactant-based EOR process is surfactant adsorption on reservoir rock, and it is very important to consider during the design of chemical formulation for a particular reservoir. For sandstone reservoirs, cationic surfactants should be avoided due to high adsorption on the negatively charged surface of sandstone [15]. Due to this reason, the commonly used surfactants in sandstone reservoir are anionic, nonionic, and amphoteric. In case of carbonate reservoirs, due to the positive charge on surface, the adsorption of anionic surfactant is high and the cationic surfactants give good results [15, 16].

Numerous surfactants have been presented up till now for the generation of CO<sub>2</sub> foam in laboratory with each one having unique properties. Based on the past laboratory studies, Chaser CD 1045 and Alipal CD 128 performed excellently in terms of foam generation [15, 17–21] and these surfactants have shown good results in many pilot tests. Chaser CD 1045 is a blend that contains anionic alpha olefin sulfonates, amphoteric, ethoxylates, and nonionic alkyl phenol. Beside this, there are many other famous surfactants for EOR applications that include Chaser CD 1040 [17], Chaser CD 1050 [17], NES-25 [18], Shell Enordet X2001 [17, 18, 22], Shell alpha olefin sulfonates (AOS) 14–16 [23], DOWFAX unethoxylated alkyl biphenyl disulfonates [22], Neodol 25–9 [24], TRS 18 and 40 (a blend of Witco petroleum sulfonates), Witcolate 1247H and 1276, and Witconate AOS12 [25].

Another study concluded that alcohol ethoxy glyceryl sulfonate (AEGS), alcohol ethoxy ethyl sulfonates (AESo) as the promising surfactants. The conclusion was made after studying air-based foams using forty surfactants and testing them using CO<sub>2</sub> foam [26].

The branches of surfactants have prominent effect on the interfacial tension (IFT) at the interface of CO<sub>2</sub>-water, and it has been studied in detail using different surfactants [27]. Some of the new surfactants that are twin-tailed, water soluble, nonionic, and ethoxylated surfactant were used for the stabilization of CO<sub>2</sub> in water emulsion for improving mobility ratio [28]. These surfactants were dioctylglycerine-based consisting 9–12 EO groups and were found more effective at reducing CO<sub>2</sub>-water interfacial tension. Ethomeen C12, a CO<sub>2</sub> soluble ethoxylated amines, was proved to a good CO<sub>2</sub> foamer at high-pressure and high-temperature conditions with low adsorption for carbonates [29].

The design of CO<sub>2</sub> soluble surfactants for different reservoir conditions and their identification is the focus of research nowadays. These could be single-tail or twin-tailed ethoxylates, a hydrocarbon based that are slightly CO<sub>2</sub> soluble (up to 0.5 wt%) and good soluble in aqueous phase. Surfactants with branched carbon chain give better performance, and sometimes, the tails may also contain CO<sub>2</sub>-philic oxygenated functional groups. The solution containing CO<sub>2</sub>-rich surfactant solution has the ability to generate in situ foams upon mixing with the reservoir brine and the different strategies for mobility, and conformance control can be designed by introducing these surfactants to both CO<sub>2</sub> and brine.

### 3 General Foam Properties

#### 3.1 Foam Quality

Frictional flow of gas through porous media is termed as foam quality [30], and mathematically, it is expressed as

$$f = V_g / (V_g + V_l) \quad (1)$$

where  $f$  is the foam quality,  $V_g$  is the gas volume in foam, and  $V_l$  is the liquid volume in foam.

Foam quality affects the behavior of foam flow and is expressed in percentages. Khatib et al. (1988) determined the mobility of the foam at fixed flow rate and observed a slight decrease in foam mobility at increasing foam quality from 50 to 98% [31, 32]. They also noticed an increase in foam mobility at foam quality higher than 98%. De Vries and Wit (1990) reported similar results; i.e., with the increase of foam quality at a fixed flow rate, a decrease in foam mobility was observed until a break point beyond which mobility was found increasing [33]. Patton et al. (1983) [34] and Hirasaki and Lawson (1985) [35] found that mobility decreases as foam quality increases [16, 36]. However, Lee and Heller (1991) [37] reported that foam mobility increases with increasing the foam quality. Yaghoobi and Heller (1994) observed a slight increase in foam mobility till 85% foam quality, and afterward, the mobility of foam was found increasing rapidly [17]. Moradi et al. (1997) found high resistance factor between 50 and 70% foam quality [38].

Foam quality in the sandstone has shown no dependence on shear rate at low value of 60%, but for 60–80%, a slight shear thinning behavior was observed and the distinct shear thinning behavior was noted for driest foam of 90% foam quality [38]. In one study performed using sandstone, it was shown that mobility of foam decreases by a factor of two during the increase of foam quality from 20 to 80% [31].

#### 3.2 Foam Texture

The texture of foam can be defined as the number of lamellae per unit volume. Knowledge of foam texture is significant to study foam rheology, and there are lack of reliable methods to obtain a direct measurements. However, it is common to indirectly deduce the foam texture from apparent gas viscosity and pressure profile. The dynamic mechanism of lamella creation and coalescence is very important mechanism and must be considered to estimate the foam texture in porous media [39].

### 3.3 Foam Stability

Foam stability is the time taken during the collapse of half of the foam. There are three methods to test the stability of the foam [40]. First method is the lifetime of a single bubble, second is the steady-state foam volume under the given gas flow condition and shearing/shaking, whereas the third method is the rate of collapse of static foam. Rothmel et al. (1998) found that the foam stability is not dependent on the inherent properties such as critical micelle concentration and hydrophile to lipophile balance [41]. Mulligan and Eftekhari (2003) used ten commercial surfactants of different types, and stability was checked at different foam qualities [42]. It was found that Triton X-100 and JBR425 surfactant have shown better foam stability [42]. Later, Wang and Mulligan (2004) performed series of experiments with rhamnolipid solution at three different concentrations (i.e., 0.5, 1, and 1.5 wt %) and came to the conclusion that the enough foam stability could be obtained for injection purposes at low concentration of 0.5 wt% [43]. They also noticed that concentration of surfactant and foam quality has a significant effect on foam stability [43]. Normally, the foam stability increases with increasing surfactant concentration, and the region with highest foam stability was found to be within 90–99% foam quality [39].

## 4 CO<sub>2</sub> Foam Behavior

Chang and Grigg (1999) concluded from their experimental study that the increase of flow rate increases the foam mobility [31]. However, the increase of flow rate decreases the foam resistance factor. Foam resistance factor tells about the magnitude of mobility reduction during the foam tests in laboratory [14, 44]. Foam resistance factor is the ratio of CO<sub>2</sub>/brine mobility and foam mobility. If there is no foam generation in porous media, the mobility of CO<sub>2</sub>/surfactant solution is almost the same as CO<sub>2</sub>/brine mobility, and hence, the foam resistance factor will be one [31]. It was concluded that mobility of foam decreases as the foam quality increases. With the increase of foam quality from 33 to 80%, the foam resistance factor was found increasing. However, at foam quality of 20 and 33%, minimum value of foam resistance factor was appeared [31].

## 5 Laboratory Screening and Evaluation of Surfactant Formulations for Foam EOR

There are many studies that have focused on the laboratory screening of surfactant formulation and their evaluation for the foam EOR process [12, 45, 46]. Most studies targeted the foam stability, foam ability, and adsorption, and little literature



is available on systematic procedure for formulation screening and evaluation during foam process. The systematic procedure that includes the solubility, chemical and thermal stability, foam ability, foam stability, and surfactant adsorption at various reservoir conditions was presented recently by Cui (2014) [47]. Furthermore, the surfactant partition coefficients and IFT are also important parameters for foam EOR [48, 49]. During the transport of foam in porous media, surfactant must have good solubility at the reservoir conditions. The harsh reservoir conditions, such as high salinity, high temperature, and high pH, are the major constraints associated with this process, e.g., salting out of sodium dodecylsulfonate surfactant at high salinity brine condition especially in the presence of cations (i.e., Ca ++ and Mg ++ ) [50].

The solubility of switchable cationic surfactants is dependent on the pH, e.g., solubility of surfactants in water is low at neutral and poor at high pH [12]. So it is important to check the solubility of surfactant at the desired reservoir conditions prior to the other evaluations, and for this purpose, a glass pipette method could be utilized [51, 52]. For elevated temperature conditions, sulfonate surfactants are preferred over sulfate surfactant because sulfates degrade at high-temperature condition [53]. Adkins et al. synthesized carboxylate surfactant and was found to be useful for high temperature and salinity conditions [54]. Talley (1988) [53] and Adkins [54] performed phase behavior experiments for the investigation of surfactant stability at high salinity and high-temperature conditions.

Foam stability and foamability are of prime importance during surfactant evaluation for foam EOR. Bulk foam tests and porous media tests are the two main experimental methods that are being used for the screening of surfactant formulations. The bulk foam tests have the half-life of foam and column height as the common parameters [12, 45]. In porous media foam tests, the parameters of interests are pressure gradient, apparent viscosity, and mobility reduction factor (MRF) [35].

## **6 Different Parameters Effecting CO<sub>2</sub> Foam Mobility Reduction**

### ***6.1 Surfactant Concentration***

The concentration of surfactant is of prime importance, and the critical micelle concentration (CMC) of surfactant is the common characteristic associated with surfactant solution. CO<sub>2</sub> foam can be obtained at surfactant concentration below CMC, but the generated foam would be very weak. Adsorption of surfactant is low when a surfactant having high CMC value is utilized at a concentration lower than CMC, and this dilute concentration propagates slowly through the porous media and weak foam for mobility control forms [55]. The maximum mobility reduction is

obtained when the CO<sub>2</sub> foam flooding is performed at a surfactant concentration higher than CMC.

In short, the concentration of surfactant during CO<sub>2</sub> foam ranges from 0.01 to 1 wt% and this is the range over which a significant reduction in the mobility of CO<sub>2</sub> was observed. The concentration of surfactant lower than 0.05 wt% does not form the lamellae, whereas the concentration of surfactant higher than 0.5 wt% may not add a prominent improvement in mobility reduction.

## 6.2 *Permeability*

The major aim of the CO<sub>2</sub> foam flooding process is to divert the flow of CO<sub>2</sub> from high-permeable channel to low-permeable upswept zone that is oil rich. An experimental study showed that the apparent viscosity of CO<sub>2</sub> foam in high-permeable (70–300mD) core is two to three times greater than the low-permeable core with 0.5–6mD [37]. It is proven that the reduction of mobility is large in higher permeability core sample as compared to the low permeability [18]. Not all the surfactants reduce the mobility of the foam to greater extent; therefore, proper assessment of surfactant is required to obtain the desired results. Surfactants such as CD 1045 and CD 1050 were found effective in reducing the mobility of foam in high-permeable cores, whereas CD 1040 and CD 1050 surfactants have generated effective foam in low-permeable cores. The concentration used was 500 ppm, and the injection was performed at 0.4 ft/day Darcy velocity. Enordet X2001 showed the desired results in achieving selective mobility reduction with the increase of permeability. However, for the case of CD 1050 and CD 1045, an increase in mobility with the increase of permeability was noted. Surfactant CD 1040 gave noticeably high mobility reduction in the low-permeable cores. The performance of surfactant is dependent on the concentration and the injection rate [56].

## 6.3 *Temperature*

It is not possible to change the temperature of reservoir during CO<sub>2</sub> foam flood; therefore, the design of process at high temperature higher than 80 °C is a challenging job and it requires careful consideration. The favorable aspect of high-temperature flood is the decrease in surfactant adsorption. In case of high-temperature reservoir, the solubility of surfactant in brine decreases and the degradation of surfactant takes place. The stability of foam decreases with the increase of temperature especially above 60 °C, and the interfacial tension between the brine and the CO<sub>2</sub> decreases [57].

## 6.4 Pressure

Increases of pressure help in increasing the stability of foam [57]. High pressure gives a denser CO<sub>2</sub> which increases the interaction with the carbon chain of surfactant. A micromodel explained that the sweep efficiency at a pressure just below the minimum miscibility (MMP) is as high as it is in high-pressure foam flood above MMP. It was proved that good sweep efficiency can be achieved by using minimum CO<sub>2</sub> if the foam flooding is performed at MMP instead of very high pressure [58].

## 6.5 Brine Composition

Reservoir brine having high salinity and hardness destabilizes foam, and the intensity of destabilization is dependent on the type of surfactant used. There are some surfactants having good properties for the generation of efficient foam, e.g., Chaser CD 1045 that has good tolerance to hard brine [57]. When the surfactant is dissolved in CO<sub>2</sub> instead of brine, then the effect of salinity is more noticeable; such kind of system basically contains low concentration of nonionic surfactants, and dissolved solid in brine suppresses the surfactant solubility in brine and hence drives the surfactant toward the CO<sub>2</sub> phase [59].

## 7 Conclusion

CO<sub>2</sub> flooding is the most widely used economical and effective EOR technique. Combination of foam with CO<sub>2</sub> helps in avoiding early breakthrough and controlling the mobility of CO<sub>2</sub> in reservoir by diverting CO<sub>2</sub> to the less permeable zone, reducing fingering and gravitational override, thus gives a stabilize front. Foam with good stability, viscosity, and mobility in porous media at reservoir conditions is mostly desired, and therefore, proper designing of foam is necessary to obtain the desired foam properties.

There are various commercially available surfactants that act as main player in foam mobility control process. Strength of the foam plays dominant role in controlling the mobility and related directly with the sweep efficiency. Surfactant adsorption and instability are the two major constraints associated with the transport of surfactant in the porous media.

Foam mobility is sensitive to several factors, i.e., surfactant concentration, permeability, foam quality, brine salinity, pressure, and temperature. These parameters have major impact on foam mobility, and there is no substitute in foam design for evaluating the mobility reduction of foam in cores using reservoir fluid under different reservoir conditions and the commercially available surfactants.

## References

1. D. W. Green and G. P. Willhite, *Enhanced Oil Recovery*: Henry L. Doherty Memorial Fund of AIME, Society of Petroleum Engineers, 1998.
2. V. A. Kuuskraa, M. L. Godec, and P. DiPietro, "CO<sub>2</sub> Utilization from "Next Generation" CO<sub>2</sub> Enhanced Oil Recovery Technology," *Energy Procedia*, vol. 37, pp. 6854–6866, 2013.
3. H. O. Lee and J. P. Heller, "Laboratory Measurements of CO<sub>2</sub>-Foam Mobility," *SPE Reservoir Engineering*, pp. 193–197, 1990/5/1/ 1990.
4. W. Yan, C. A. Miller, and G. J. Hirasaki, "Foam sweep in fractures for enhanced oil recovery," *Colloids and Surfaces a-Physicochemical and Engineering Aspects*, vol. 282, pp. 348–359, Jul 20 2006.
5. A. H. Falls, J. J. Musters, and J. Ratulowski, "The Apparent Viscosity of Foams in Homogeneous Bead Packs," *SPE journal*, 1989/5/1/ 1989.
6. D. Liu and W. E. Brigham, "Transient foam flow in porous media with CAT Scanner," DOE/BC/14600–19; Other: ON: DE92001022 United States10.2172/5573805Other: ON: DE92001022Mon Jun 30 08:31:13 EDT 2008OSTI; NTIS; GPO Dep.NETL; EDB-92-055397English, 1992.
7. S. Marsden, "Foams in Porous Media. U.S. Department of Energy" Stanford U. Petroleum Research Inst., Stanford, California., DE-AC03–81SF11564, 1986.
8. S. H. Talebian, R. Masoudi, I. M. Tan, and P. L. Zitha, "Foam assisted CO<sub>2</sub>-EOR; concepts, challenges and applications," in *SPE Enhanced Oil Recovery Conference*, 2013.
9. J. P. Heller, C. L. Lien, and M. S. Kuntamukkula, "Foamlike Dispersions for Mobility Control in CO<sub>2</sub> Floods," 1985/8/1/ 1985s.
10. J. H. Duerksen, "Laboratory Study of Foaming Surfactants as Steam-Diverting Additives," *SPE journal*, 1986/1/1/ 1986.
11. S. E. Dellinger, J. T. Patton, and S. T. Holbrook, "CO<sub>2</sub> Mobility Control," *SPE journal*, 1984/4/1/ 1984.
12. Y. Chen, A. S. Elhag, B. M. Poon, L. Cui, K. Ma, S. Y. Liao, *et al.*, "Switchable Nonionic to Cationic Ethoxylated Amine Surfactants for CO<sub>2</sub> Enhanced Oil Recovery in High-Temperature, High-Salinity Carbonate Reservoirs," *SPE journal*, 2014/4/1/ 2014.
13. R. Gupta, K. Mohan, and K. K. Mohanty, "Surfactant screening for wettability alteration in oil-wet fractured carbonates," in *SPE Annual Technical Conference and Exhibition*, 2009.
14. D. L. Kuehne, R. H. Frazier, J. Cantor, and W. Horn, Jr., "Evaluation of Surfactants for CO<sub>2</sub> Mobility Control in Dolomite Reservoirs," 1992.
15. B. Bai, R. B. Grigg, Y. Svec, and Y. Wu, "Adsorption of a foam agent on porous sandstone and its effect on foam stability," *Colloids and Surfaces A: Physicochemical and Engineering Aspects*, vol. 353, pp. 189–196, 2010.
16. G. Yin, R. B. Grigg, and Y. Svec, "Oil Recovery and Surfactant Adsorption during CO<sub>2</sub>-Foam Flooding," 2009.
17. H. Yaghoobi, "Laboratory Investigation of Parameters Affecting CO<sub>2</sub>-Foam Mobility in Sandstone at Reservoir Conditions," 1994.
18. J.-S. Tsau and J. Heller, "Evaluation of surfactants for CO<sub>2</sub>-foam mobility control," in *Permian Basin Oil and Gas Recovery Conference*, 1992.
19. H. Yaghoobi, J. Tsau, and R. Grigg, "Effect of Foam on CO Breakthrough: Is This Favorable to Oil Recovery?," in *SPE Permian Basin Oil and Gas Recovery Conference*, 1998.
20. F. Khalil and K. Asghari, "Application of CO-Foam as a Means of Reducing Carbon Dioxide Mobility," *Journal of Canadian petroleum technology*, vol. 45, 2006.
21. B. Bai, R. Grigg, Y. Liu, and Z.-W. Zeng, "Adsorption Kinetics of Surfactant Used in CO<sub>2</sub>-Foam Flooding Onto Berea Sandstone," in *SPE Annual Technical Conference and Exhibition*, 2005.
22. M. Kuhlman, H. Lau, and A. Falls, "Surfactant criteria for successful carbon dioxide foam in sandstone reservoirs," *SPE Reservoir Evaluation & Engineering*, vol. 3, pp. 35–41, 2000.

23. Z. Xue, K. Panthi, Y. Fei, K. P. Johnston, and K. K. Mohanty, "CO<sub>2</sub>-Soluble Ionic Surfactants and CO<sub>2</sub> Foams for High-Temperature and High-Salinity Sandstone Reservoirs," *Energy & Fuels*, vol. 29, pp. 5750–5760, 2015.
24. M. I. Kuhlman, "Visualizing the effect of light oil on CO<sub>2</sub> foams," *Journal of Petroleum Technology*, vol. 42, pp. 902–908, 1990.
25. J. Prieditis and G. Paulett, "CO<sub>2</sub>-Foam Mobility Tests at Reservoir Conditions in San Andres Cores," in *SPE/DOE Enhanced Oil Recovery Symposium*, 1992.
26. J. Borchardt, D. Bright, M. Dickson, and S. Wellington, "Surfactants for CO<sub>2</sub> foam flooding," in *SPE Annual Technical Conference and Exhibition*, 1985.
27. S. S. Adkins, X. Chen, Q. P. Nguyen, A. W. Sanders, and K. P. Johnston, "Effect of branching on the interfacial properties of nonionic hydrocarbon surfactants at the air–water and carbon dioxide–water interfaces," *Journal of colloid and interface science*, vol. 346, pp. 455–463, 2010.
28. A. Sanders, Q. P. Nguyen, N. Nguyen, S. Adkins, and K. P. Johnston, "Twin-Tailed Surfactants for Creating CO<sub>2</sub>-in-Water Macroemulsions for Sweep Enhancement in CO<sub>2</sub>-EOR," in *Abu Dhabi International Petroleum Exhibition and Conference*, 2010.
29. L. Cui, K. Ma, M. Puerto, A. A. Abdala, I. Tanakov, L. J. Lu, *et al.*, "Mobility of Ethomeen C<sub>12</sub> and Carbon Dioxide (CO<sub>2</sub>) Foam at High Temperature/High Salinity and in Carbonate Cores," *SPE Journal*, 2016.
30. K. Ma, G. Ren, K. Mateen, D. Morel, and P. Cordelier, "Literature Review of Modeling Techniques for Foam Flow Through Porous Media," presented at the SPE Improved Oil Recovery Symposium, Tulsa, Oklahoma, USA, 2014.
31. S.-H. Chang and R. B. Grigg, "Effects of Foam Quality and Flow Rate on CO<sub>2</sub>-Foam Behavior at Reservoir Temperature and Pressure," 1999/6/1/ 1999.
32. Z. I. Khatib, G. J. Hirasaki, and A. H. Falls, "Effects of Capillary Pressure on Coalescence and Phase Mobilities in Foams Flowing Through Porous Media," 1988/8/1/ 1988.
33. A. S. de Vries and K. Wit, "Rheology of Gas/Water Foam in the Quality Range Relevant to Steam Foam," 1990/5/1/ 1990.
34. J. T. Patton, S. T. Holbrook, and W. Hsu, "Rheology of Mobility-Control Foams," *Society of Petroleum Engineers*, vol. 23, 1983/6/1/ 1983.
35. G. J. Hirasaki and J. B. Lawson, "Mechanisms of Foam Flow in Porous Media: Apparent Viscosity in Smooth Capillaries," *SPE journal*, 1985/4/1/ 1985.
36. S. S. Marsden and S. A. Khan, "The Flow of Foam Through Short Porous Media And Apparent Viscosity Measurements," 1966/3/1/ 1966.
37. H. O. Lee, J. P. Heller, and A. M. W. Hoefer, "Change in Apparent Viscosity of CO<sub>2</sub> Foam With Rock Permeability," *SPE journal*, 1991/11/1/ 1991.
38. A. Moradi-Araghi, E. Johnston, D. Zornes, and K. Harpole, "Laboratory evaluation of surfactants for CO<sub>2</sub>-foam applications at the South Cowden unit," in *International Symposium on Oilfield Chemistry*, 1997.
39. Zhang ZF, V: Freedman, and L. Zhong, "Foam Transport in Porous Media- A Review," Pacific Northwest National:laboratory, Richland, WA2009 2009.
40. L. L. Schramm, *Emulsions, Foams, and Suspensions: Fundamentals and Applications*: Wiley, 2006.
41. R. K. Rothmel, R. W. Peters, E. St. Martin, and M. F. DeFlaun, "Surfactant Foam/Bioaugmentation Technology for In Situ Treatment of TCE-DNAPLs," *Environmental Science & Technology*, vol. 32, pp. 1667–1675, 1998/06/01 1998.
42. C. N. Mulligan and F. Eftekhari, "Remediation with surfactant foam of PCP-contaminated soil," *Engineering Geology*, vol. 70, pp. 269–279, 11// 2003.
43. S. Wang and C. Mulligan, "Rhamnolipid Foam Enhanced Remediation of Cadmium and Nickel Contaminated Soil," *Water, Air, and Soil Pollution*, vol. 157, pp. 315–330, 2004/09/01 2004.
44. S.-H. Chang and R. B. Grigg, "Laboratory Flow Tests Used To Determine Reservoir Simulator Foam Parameters for EVGSAU CO<sub>2</sub> Foam Pilot," 1994.

45. R. F. Li, G. Hirasaki, C. A. Miller, and S. K. Masalmeh, "Wettability Alteration and Foam Mobility Control in a Layered, 2D Heterogeneous Sandpack," *SPE journal*, 2012/12/1/ 2012.
46. K. Ma, L. Cui, Y. Dong, T. Wang, C. Da, G. J. Hirasaki, *et al.*, "Adsorption of cationic and anionic surfactants on natural and synthetic carbonate materials," *Journal of Colloid and Interface Science*, vol. 408, pp. 164–172, 10/15/ 2013.
47. L. Cui, "Application of Foam for Mobility Control in Enhanced Oil Recovery (EOR) Process," Doctor of Philosophy Department of Chemical and Biomolecular Engineering, Rice University, Houston Texas, 2014.
48. D. Wang, J. Cheng, Z. Yang, L. Qun, W. Wu, and H. Yu, "Successful Field Test of the First Ultra-Low Interfacial Tension Foam Flood," 2001.
49. E. Ashoori, T. van der Heijden, and W. Rossen, "Fractional-Flow Theory of Foam Displacements With Oil," *SPE journal*, vol. 15, 2010/6/1/ 2010.
50. P. Somasundaran, K. P. Ananthapadmanabhan, M. S. Celik, and E. D. Manev, "A Thermodynamic Model of Redissolution of Calcium Sulfonate Precipitates in NaCl Solutions," *SPE journal*, vol. 24, 1984/12/1/ 1984.
51. J. R. Barnes, J. Smit, J. Smit, G. Shpakoff, K. H. Raney, and M. Puerto, "Development of Surfactants for Chemical Flooding at Difficult Reservoir Conditions," 2008.
52. M. Puerto, G. J. Hirasaki, C. A. Miller, and J. R. Barnes, "Surfactant Systems for EOR in High-Temperature, High-Salinity Environments," *SPE journal*, vol. 17, 2012/3/1/ 2012.
53. L. D. Talley, "Hydrolytic Stability of Alkylethoxy Sulfates," *SPE journal*, 1988/2/1/ 1988.
54. S. Adkins, G. W. P. Pinnawala Arachchilage, S. Solairaj, J. Lu, U. Weerasooriya, and G. A. Pope, "Development of Thermally and Chemically Stable Large-Hydrophobe Alkoxy Carboxylate Surfactants," 2012.
55. M. Kuhlman, A. Falls, S. Hara, T. Monger-McClure, and J. Borchardt, "CO<sub>2</sub> foam with surfactants used below their critical micelle concentrations," *SPE reservoir engineering*, vol. 7, pp. 445–452, 1992.
56. H. Yaghoobi and J. P. Heller, "Effect of capillary contact on CO<sub>2</sub>-foam mobility in heterogeneous core samples," in *Permian Basin Oil and Gas Recovery Conference*, 1996.
57. Y. Liu, R. B. Grigg, and R. K. Svec, "CO<sub>2</sub> foam behavior: influence of temperature, pressure, and concentration of surfactant," in *SPE Production Operations Symposium*, 2005.
58. S.-H. Chang, F. Martin, and R. Grigg, "Effect of Pressure on CO<sub>2</sub> Foam Displacements: A Micromodel Visualization Study," in *SPE/DOE Improved Oil Recovery Symposium*, 1994.
59. E. Torino, E. Reverchon, and K. P. Johnston, "Carbon dioxide/water, water/carbon dioxide emulsions and double emulsions stabilized with a nonionic biocompatible surfactant," *Journal of colloid and interface science*, vol. 348, pp. 469–478, 2010.

# Palm Fatty Acid Methyl Ester in Reducing Interfacial Tension in CO<sub>2</sub>–Crude Oil Systems

Aminah Qayyimah Mohd Aji and Mariyamni Awang

**Abstract** The interfacial tension (IFT) is one of the most important parameters affecting the ability of CO<sub>2</sub> to become miscible with crude oil. The high IFT difference between CO<sub>2</sub> and crude oil resulted to more problems during the displacement such as fingering and segregation. Extensive research on chemicals to be used as additives in reducing the IFT between CO<sub>2</sub> and crude oil has been done. However, large amounts of chemical are required with field application. This paper presents a preliminary study on the application of fatty acid methyl ester (FAME) from palm to reduce the IFT with crude oil and CO<sub>2</sub>. In this work, FAME is used as an additive in the mixture of CO<sub>2</sub> and crude oil. Vanishing interfacial technique (VIT) was used to determine the effect of the additive on CO<sub>2</sub>–crude oil system. With this finding, an economical approach was obtained which is suitable for mass application in the reservoir.

**Keywords** CO<sub>2</sub> · Crude oil · Interfacial tension (IFT) · Palm fatty acid methyl ester (FAME)

## 1 Introduction

One of the promising techniques widely applied to enhance oil recovery is the CO<sub>2</sub> gas injection [1]. At high pressure and temperature, CO<sub>2</sub> mixes with crude oil, reducing the viscosity and density of the crude oil, improving the crude oil displacement [2]. Higher recovery is achieved with CO<sub>2</sub> miscible displacement than the immiscible flooding [3, 4]. However, miscibility is difficult to attain thus, a reduction in IFT found improving the miscibility. During CO<sub>2</sub> flooding, the interfacial interaction controls the flooding process behavior of crude oil, gas, and brine [5, 6]. The absence of a barrier between CO<sub>2</sub> and crude oil enables fluids to mix and be recovered [7].

---

A.Q.M. Aji (✉) · M. Awang  
Universiti Teknologi PETRONAS, Bandar Seri Iskandar, Perak, Malaysia  
e-mail: aqayyimah@gmail.com

The addition of semi-polar solvent, for example, alcohol, has proven to enhance the miscibility between crude oil and CO<sub>2</sub> [8–10]. Oil, which is nonpolar, will mix with the nonpolar end of alcohol while CO<sub>2</sub>, which possessed a dipole moment, will be mixed at the other end of alcohol, enhancing the solvating power and polarity of CO<sub>2</sub>, thus reducing the IFT between crude oil and CO<sub>2</sub> [11]. Alcohol also has been used as additives together with the surfactant to achieve a lower IFT with crude oil [12].

The economic factor is one of the main important keys to be considered in chemical EOR. Expensive production of chemicals usually hinders the application in the reservoir scales. One way of reducing the chemical production cost is to use less expensive feedstock which contains fatty acids. A fatty acid is a type of a carboxylic acid with a long aliphatic chain, which is either saturated or unsaturated [13].

With long carbon chain and the presence of a carboxyl polar tail, the fatty acid is capable undergone esterification and acid–base reaction. Carboxylic acid had proven to enhance miscibility between CO<sub>2</sub> and crude oil when added to the system [9, 14]. Regardless, the miscibility of supercritical CO<sub>2</sub> with carboxylic acids decreases with carboxylic acids that contain more than 10 carbon atoms [15]. The solubility of CO<sub>2</sub> is decreased with the chain length increment of a crude oil. Esterification usually increases the solubility of carboxylic acids, both aromatic and aliphatic with CO<sub>2</sub> [16, 17].

In this project, the focus is on utilizing FAME from palm biomass as feedstock for chemicals in reducing the IFT between CO<sub>2</sub> and crude oil enhancing the miscibility, thus improving the recovery.

### ***1.1 Fatty Acid Methyl Ester (FAME)***

FAME is a type of fatty acid ester that is produced from transesterification of fatty acids. FAME has chemical characteristics closer to fossil fuels and a mixture of different FAMEs commonly called as biodiesel. FAME also has a higher solubility in CO<sub>2</sub> compared to parent fatty acid [16].

In this paper, FAMEs from different parts of palm tree were used. First is palm crude oil which extracted from the kernel of the palm fruit and palm-pressed fiber (PPF) oil a by-product from oil extraction of oil palm fruits. The PPF oil has unique characteristics resulting from the combination of palm mesocarp fiber, kernel shell, and crushed kernel [18].

### ***1.2 Alkoxy FAME***

Naturally derived alcohols are produced from natural fats and oils by hydrogenation of their fatty acids or FAME [19]. The most common process for manufacturing



natural alcohol is the hydrogenation of FAME in the presence of a catalyst [19, 20]. In this study, the aliphatic FAME underwent alkoxylation with the addition of propanol for branching purposes, to produce alkoxy FAME.

Branched alcohol propoxylated sulfates have emerged to be a good type of surfactant for oil removal creating middle-phase micro-emulsions and presumably achieve low interfacial tension [21]. Another study by Minana-Perez et al. demonstrated that mixtures of ethoxylated and propoxylated formulated to provide optimum performance for various types of oils and with different conditions [22].

Smith et al. have documented optimal condition for epoxidation for the synthesis of saturated fatty acid from the oleic acid of palm oil. Figure 1 below shows an example of alkoxylation of FAME [23].

## 2 Materials and Methods

### 2.1 Material

There are two types of dead crude oil samples used in this study, where both were obtained from Petronas Refinery, Melaka, Malaysia. The properties of crude oil samples were measured at standard 15 °C, the properties of the sample measured listed in Table 2. Industrial-grade CO<sub>2</sub> with 99% purity is used in the experiment to eliminate the impurities that may affect the experimental result.

Two types of FAMEs were used in this study. Palm-pressed fiber and palm crude methyl esters were supplied by Felcra Berhad Nasaruddin Oil Palm Mill, Tronoh, Perak. Palm crude methyl ester is then used to produce the alkoxy FAME.

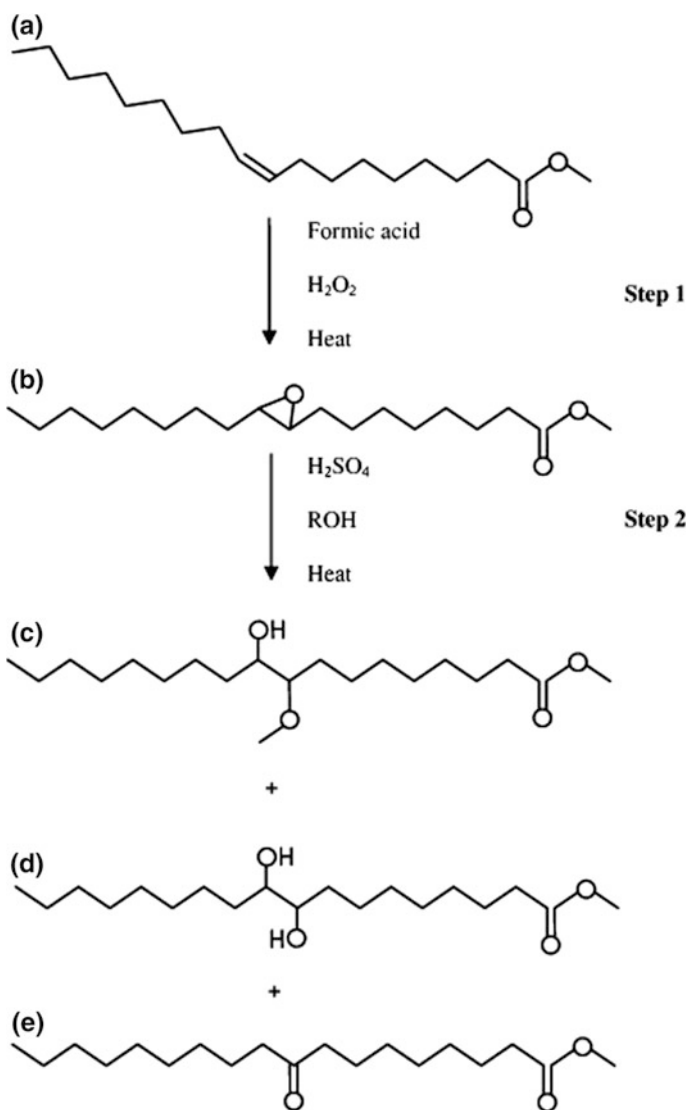
### 2.2 Samples Preparation

The samples were prepared by based on the volumetric ratio [24, 25]. The samples are listed in Table 1. The FAME was added to the crude oil and heated at 60 °C and stirred for 15 min.

### 2.3 Apparatus and Procedure

#### 2.3.1 Fatty Acid Methyl Ester to Alkoxy FAME Conversion

First, the palm crude FAME underwent epoxidation before the alkoxylation process [23, 26]. The process is started with epoxide FAME heated to 60 °C in the reaction glass. A mixture of H<sub>2</sub>SO<sub>4</sub> and 10 mol of 2-propanol is added to the reaction glass



**Fig. 1** Reaction scheme for epoxidation (step 1) and alkoxylation (step 2) of methyl oleate

with the temperature is maintained. The mixture was allowed to react for 2 h before pouring into separation funnel to be settled overnight. Residual catalyst and 2-propanol were removed by repeated water washes and phase separation followed by drying over anhydrous sodium sulfate and filtrated. (Tables 2 and 3)

**Table 1** Samples preparation based on the volumetric ratio concentration

Samples	Crude oil A (% by volume)	Crude oil B (% by volume)	Methyl laurate (% by volume)	Alkoxy FAME (% by volume)
1	100	0	0	0
2	95	0	5	0
3	0	100	0	0
4	0	95	0	5

**Table 2** The properties of crude oil used in the test at 25 °C

Property	Crude oil A	Crude oil B
	Value	Value
Density (g/cm <sup>3</sup> )	0.8114	0.7998
Viscosity (cP)	3.9234	2.434
API gravity	42.9	45.2

**Table 3** FAME's composition analysis

FAME	Palm crude (%)	Palm fiber (%)
Methyl laurate	0.41	66.36
Methyl myristate	1.12	12.89
Methyl palmitate	34.50	19.60
Methyl palmitoleate	0.18	0.25
Methyl stearate	6.30	0.11
Methyl oleate	41.30	0.01
Methyl linoleate	15.36	1.15

### 2.3.2 Compositional Analysis

The gas chromatograph GC-2010 was used to analyze the composition of the FAME and determine the amount of each component present based on AOCS method [27].

### 2.3.3 Density Measurement

Before each experiment, the density of mixtures of crude oil and FAME at desired temperature and pressure were measured by using Anton Paar DMA10 density meter. The density of CO<sub>2</sub> at determined pressure and temperature was calculated by using the table from equations of state and PVT analysis [28]. The density of the mixtures is listed in Table 4.

**Table 4** Density of the mixtures at 90 °C

	Density (g/cm <sup>3</sup> )
Crude oil with methyl laurate	0.7718
Crude oil with alkoxy methyl oleate	0.8346

### **2.3.4 Viscosity Measurement**

Viscosity was measured by using advanced AR-G2 rheometer (TA Instruments, USA) equipped with zero gap geometry and measurement was conducted according to the ASTM D-445 standard at standard 25 °C.

### **2.3.5 IFT Measurement**

All the IFT measurements were done by using Vinci IFT 700 pendant drop measuring equipment. The crude oil was injected into the CO<sub>2</sub> pressure cell at determining pressure and temperature formed pendant drop shape. Once a well-shaped pendant droplet was formed, sequential digital images were recorded and drop analysis software (DAS) was used to measure and calculate the IFT from drop shape produced [29]. The IFT measurement for each temperature and pressure were repeated for pendant oil droplets produced. The IFT measurements were done at constant temperature 90 °C and different pressures ranging from 463 up to 2000 psi.

## **3 Results and Discussions**

### **3.1 *Properties of Crude Oil***

Table 2 shows that both the crude oils are light crude oils, which are suitable for CO<sub>2</sub> miscible flooding.

### **3.2 *Compositional Analysis***

Table 3 shows that the methyl oleate and methyl laurate are the highest composition in both FAMEs tested. FAME is made up of a mixture of various methyl esters, the methyl esters which has the highest percentage affecting the properties of each FAME own.

### **3.3 *Density Measurement***

#### **3.3.1 Effect of FAME Additives on IFT Between Crude Oils And CO<sub>2</sub>**

The measured IFT of the CO<sub>2</sub> and the additives are illustrated in Figs. 2 and 3 for each case, respectively.

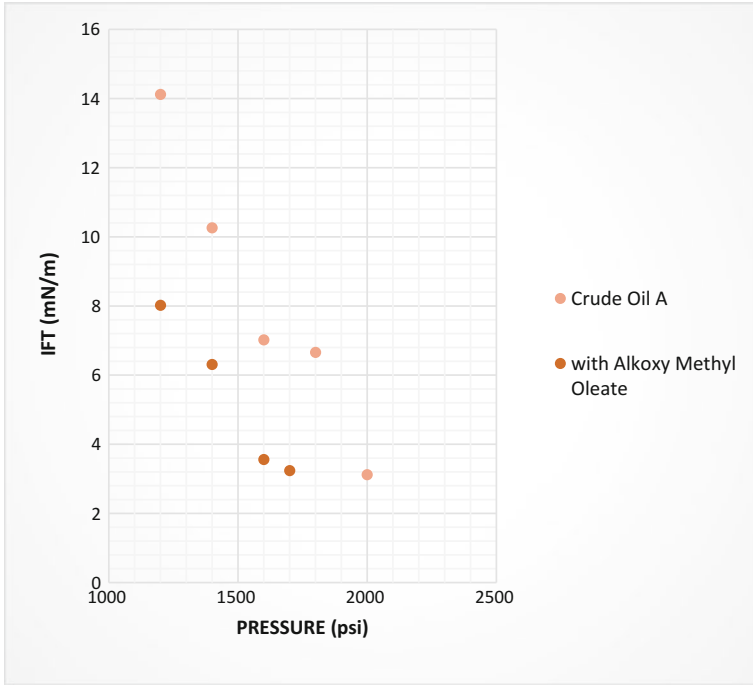


Fig. 2 IFT between CO<sub>2</sub> and crude oil with alkoxy methyl oleate at different pressure

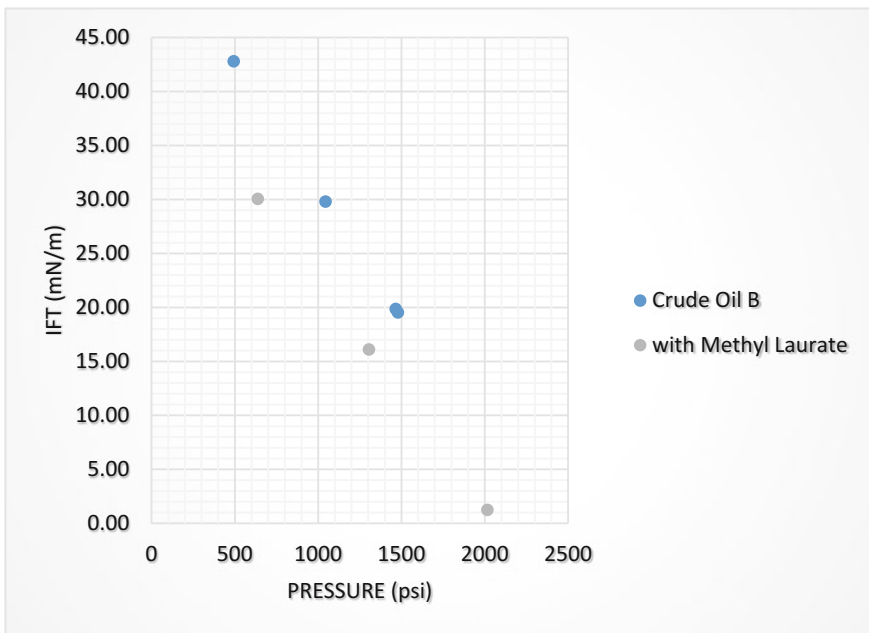


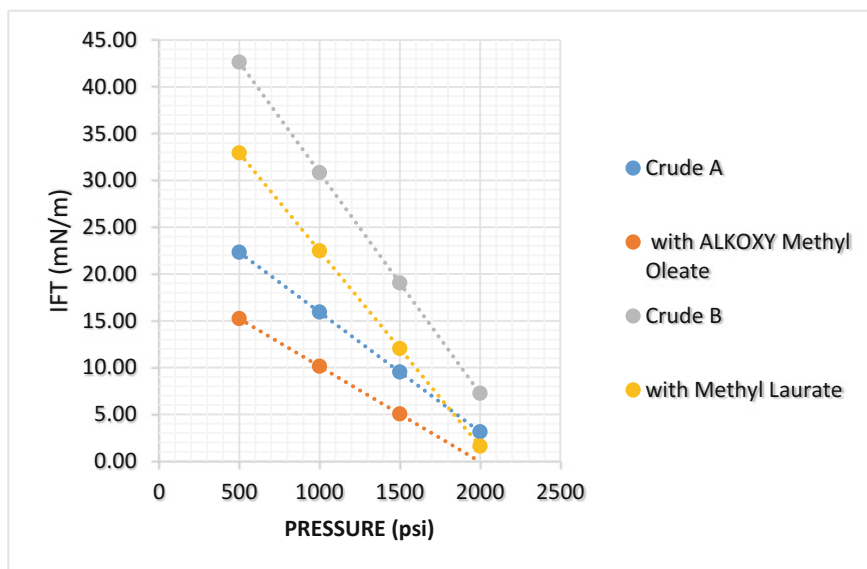
Fig. 3 IFT between CO<sub>2</sub> and crude oil with methyl laurate at different pressure

**Table 5** IFT reduction with pressures

Pressure (psi)	Crude oil A IFT (mN/m)	Error (%)	With alkoxy methyl oleate IFT (mN/m)	Error (%)	IFT difference (%)
500	22.32		15.23		68.25
1000	15.92	5.38	10.13	0.87	63.65
1500	9.52		5.03		52.86
2000	3.12		-0.07		2.25
Pressure (psi)	Crude oil B IFT (mN/m)	Error (%)	With methyl laurate IFT (mN/m)	Error (%)	IFT difference (%)
500	42.63	2.39	32.93		77.24
1000	30.83		22.48		72.90
1500	19.03		12.03		63.20
2000	7.23		1.58	0.50	21.82

For a clear comparison on the effectiveness of both additives with pressure increases, the IFT values were then linearly extrapolated. The pressure taken for the extrapolated IFT was at the pressures 500, 1000, 1500, and 2000 psi. The summary of the IFT values obtained is listed in Table 5 and illustrated in Fig. 4.

Based on the results obtain, it was observed that with the addition of FAME as additives in crude oil shows a great reduction on the IFT. It is also observed that alkoxy methyl oleate reducing the IFT much better compared to methyl laurate.

**Fig. 4** IFT between CO<sub>2</sub> and crude oils with FAME at different pressures

Regardless, the difference in IFT obtained at lower pressure is much more obvious, compared to high pressure where IFT difference becomes less significant. This is directly related to the miscibility of CO<sub>2</sub> at high pressure and temperature with crude oil.

The results support the literature findings that the presence of branching [30] and polar functional groups such as hydroxyl, carboxyl, and carbonyl helps in enhancing the solubility of CO<sub>2</sub> into crude oil [31]. The solubility enhancement with additives causes by the special interactions between the solute and co-solvent molecules [11, 32].

The polar functional group of the co-solvent interacts with CO<sub>2</sub> via dipole-induced dipole interaction while the hydrocarbon chain of the co-solvent interacts with the hydrocarbon via London dispersion force (LDF) [33]. Without the addition of polar chemicals that soluble in crude oil, there would only be LDF among CO<sub>2</sub> and hydrocarbon molecules. With the presence of branches in the outermost layers increased the contact area between CO<sub>2</sub> and crude oil, enhancing the solubility of CO<sub>2</sub> and crude oil that may reduce the IFT [30, 34].

Alkoxy methyl oleate which has both polar functional groups such as hydroxyl and carbonyl shows a great IFT reduction compared to the methyl ester with only carbonyl groups. The presence of branches in the alkoxy methyl oleate enhancing the solubility of CO<sub>2</sub> with crude oil reducing the IFT, which allows the miscibility to occur at lower pressure.

## 4 Conclusions

1. The test shows that addition of FAME to the crude oil enhancing the miscibility by reducing the IFT between CO<sub>2</sub> and crude oil.
2. Alkoxy FAME reducing the IFT much better than the methyl laurate.
3. The difference of IFT become less significant as the pressure increases.

**Acknowledgements** Authors would like to thank Malaysian Ministry of Education for the funding this study via MyRA. Authors would also like to thank Universiti Teknologi PETRONAS for providing all the equipment, enabling the tests to run smoothly. Special thanks to Mr. Emir Rashidi bin Mohd Rashid for his cooperation providing the data that have been used in this work.

## References

1. D. Y. C. Leung, G. Caramanna, and M. M. Maroto-Valer, "An overview of current status of carbon dioxide capture and storage technologies," *Renew. Sustain. Energy Rev.*, vol. 39, pp. 426–443, Nov. 2014.
2. F. M. Orr, J. P. Heller, J. J. Taber, and P. Recovery, "Carbon Dioxide Flooding for Enhanced Oil Recovery," 1982.

3. H. Jiang, L. Nuryaningsih, and H. Adidharma, "SPE 154252 The Influence of O<sub>2</sub> Contamination on MMP and Core Flood Performance in Miscible and Immiscible CO<sub>2</sub> WAG," 2012.
4. B. M. K. Verma, S. Jewell, and U. S. G. Survey, "Fundamentals of Carbon Dioxide-Enhanced Oil Recovery (CO<sub>2</sub> -EOR)—A Supporting Document of the Assessment Methodology for Hydrocarbon Recovery Using CO<sub>2</sub> -EOR Associated with Carbon Sequestration," 2015.
5. D. Yang and Y. Gu, "Interfacial Interactions of Crude Oil-Brine-CO<sub>2</sub> Systems under Reservoir Conditions." Society of Petroleum Engineers, 2004.
6. Z. Yang, M. Li, B. Peng, M. Lin, Z. Dong, and Y. Ling, "Interfacial tension of CO<sub>2</sub> and organic liquid under high pressure and temperature," *Chinese J. Chem. Eng.*, vol. 22, no. 11, pp. 1302–1306, 2014.
7. S. Whittaker and E. Perkins, "Technical aspects of CO<sub>2</sub> EOR and associated carbon storage," no. October, 2013.
8. N. F. Djabbarah, "Miscible oil recovery process using carbon dioxide and alcohol," no. Google Patents, 1990.
9. C. L. Voon and M. Awang, "Practical aspects if CO<sub>2</sub> Flooding," *World Acad. Sci. Eng. Technol. Int. J. Chem. Mol. Nucl. Mater. Metall. Eng.*, vol. 8, no. 4, pp. 2–4, 2014.
10. B. Moradi, M. Awang, A. Bashir, and K. M. Sabil, "Effects of alcohols on interfacial tension between carbon dioxide and crude oil at elevated pressures and temperature," *J. Pet. Sci. Eng.*, vol. 121, pp. 103–109, 2014.
11. Q. Li, C. Zhong, Z. Zhang, and Q. Zhou, "Modeling of the solubility of solid solutes in supercritical CO<sub>2</sub> with and without cosolvent using solution theory," *Korean J. Chem. Eng.*, vol. 21, no. 6, pp. 1173–1177, 2004.
12. M. Awang, I. Dzulkarnain, M. W. Zakaria, and U. T. Petronas, "Enhancement of IFT Reduction in Surfactant Flooding by Branched Alcohols," *Iptc 15140*, no. 1992, p. 15140, 2012.
13. A. K. Chauhan and A. Varma, *A textbook of molecular biotechnology*. New Delhi: I.K. International Pub. House, 2009.
14. Voon Choon Lin, "Reduction of MMP using Oleophilic Chemicals," Universiti Teknologi Petronas, 2015.
15. D. L. Sparks, L. A. Estévez, R. Hernandez, J. McEwen, and T. French, "Solubility of Small-Chain Carboxylic Acids in Supercritical Carbon Dioxide," *J. Chem. Eng. Data*, vol. 55, no. 11, pp. 4922–4927, 2010.
16. M. D. L. de Castro, M. V Cases, and M. T. Tena, *Analytical supercritical fluid extraction*. Springer-Verlag, 1994.
17. W. Brown, C. Foote, B. Iverson, and E. Anslyn, *Organic Chemistry, Enhanced Edition*. Cengage Learning, 2010.
18. B. K. Neoh, Y. M. Thang, M. Z. M. Zain, and A. Junaidi, "Palm pressed fibre oil: A new opportunity for premium hardstock?," *Int. Food Res. J.*, vol. 18, no. 2, pp. 769–773, 2011.
19. S. Van Den Hark, M. Härröd, and P. Møller, "Hydrogenation of fatty acid methyl esters to fatty alcohols at supercritical conditions," *J. Am. Oil Chem. Soc.*, vol. 76, no. 11, pp. 1363–1370, 1999.
20. M. Wilmott, G. E. Harrison, J. Scarlett, M. A. Wood, and D. H. McKinley, "Process for the production of fatty alcohols." Google Patents, 1992.
21. Y. Wu, S. Iglauer, P. Shuler, Y. Tang, and W. A. Goddard, "Branched alkyl alcohol propoxylated sulfate surfactants for improved oil recovery," *Tenside, Surfactants, Deterg.*, vol. 47, no. 3, pp. 152–161, 2010.
22. M. Miñana-Perez, A. Graciaa, J. Lachaise, and J. L. Salager, "Solubilization of polar oils with extended surfactants," *Colloids Surfaces A Physicochem. Eng. Asp.*, vol. 100, no. C, pp. 217–224, 1995.
23. P. C. Smith, Y. Ngothai, Q. D. Nguyen, and B. K. O'Neill, "Alkoxylation of biodiesel and its impact on low-temperature properties," *Fuel*, vol. 88, no. 4, pp. 605–612, Apr. 2009.
24. L. W. Lake, *Enhanced oil recovery*. Prentice Hall, 1989.



25. N. Lindeloff, K. Mogensen, M. Oil, K. S. Pedersen, P. Tybjerg, and R. Noman, "SPE 166270 Investigation of Miscibility Behavior of CO<sub>2</sub> rich Hydrocarbon Systems—With Application for Gas Injection EOR," 2013.
26. S. PC, O. BK, Y. Ngothai, and N. QD, "The addition of alkoxy side-chains to biodiesel and impact on flow properties," *Fuel*, vol. 89, no. 7, pp. 3517–3522, 2010.
27. N. W. Bigelow, W. R. Hardin, J. P. Barker, S. A. Ryken, A. C. MacRae, and R. A. Cattolico, "A Comprehensive GC–MS Sub-Microscale Assay for Fatty Acids and its Applications," *J. Am. Oil Chem. Soc.*, vol. 88, no. 9, pp. 1329–1338, 2011.
28. A. Tarek, *Equations of State and PVT Analysis*. 2007.
29. M. Nobakht, S. Moghadam, and Y. Gu, "Mutual interactions between crude oil and CO<sub>2</sub> under different pressures," *Fluid Phase Equilib.*, vol. 265, no. 1–2, pp. 94–103, 2008.
30. R. Varadaraj, J. Bock, S. Zushma, and N. Brons, "Influence of hydrocarbon chain branching on interfacial properties of sodium dodecyl sulfate," *Langmuir*, vol. 8, no. 1, pp. 14–17, 1992.
31. I. Montes, C. Lai, and D. Sanabria, "Like Dissolves Like: A Classroom Demonstration and a Guided-Inquiry Experiment for Organic Chemistry," *J. Chem. Educ.*, vol. 80, no. 4, pp. 447–449, 2003.
32. Q. Li, Z. Zhang, C. Zhong, Y. Liu, and Q. Zhou, "Solubility of solid solutes in supercritical carbon dioxide with and without cosolvents," *Fluid Phase Equilib.*, vol. 207, no. 1–2, pp. 183–192, May 2003.
33. L. S. Ferreira and J. O. Trierweiler, "Modeling and simulation of the polymeric nanocapsule formation process," *IFAC Proc. Vol.*, vol. 7, no. PART 1, pp. 405–410, 2009.
34. L. Rekvig, M. Kranenburg, B. Hafskjold, and B. Smit, "Effect of surfactant structure on interfacial properties," *Europhys. Lett.*, vol. 63, no. 6, pp. 902–907, 2003.

**Part III**  
**Unconventional Resources**

# Effect of Porosity to Methane Hydrate Formation in Quartz Sand

Mazlin Idress, Mazuin Jasamai, Ismail M. Saaid, Bhajan Lal, Behzad Partoon and Khalik M. Sabil

**Abstract** Natural gas hydrates are recognized as the potential source of methane gas as the current estimates of the global methane hydrates inventory range between 1000 and 10000 Giga Tonnes of carbon. The behavior of methane hydrate formation in porous media is investigated in the Tubular Hydrate Cell at 8 MPa and 276 K. The present work is focused on finding the optimum porosity of the quartz sand with the grain sizes of 600–800  $\mu\text{m}$  that could accelerate the methane hydrate formation. The effect of different porosity ( $\emptyset$  of 0.32, 0.34, 0.37, and 0.4) on the methane hydrate induction time, methane hydrate saturation, and the time taken for methane hydrates to completely form in the unconsolidated sand is investigated. The result shows that the optimum value for porosity is 32% based on the fastest time taken for complete formation and largest value of methane hydrate saturation which is 33.35 h and 6.34%, respectively, at the specified operating conditions.

**Keywords** Induction time · Gas uptakes · Methane hydrate · Formation · Porosity

## 1 Introduction

Natural gas hydrate (NGH) exists in geological formations and constitutes a potentially large natural gas resource for future. The presence of marine gas hydrate throughout the world has been inferred from geophysical, geochemical, and geological evidence mainly by bottom-simulating reflectors (BSRs), chemistry of

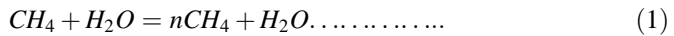
---

M. Idress (✉) · M. Jasamai · I.M. Saaid  
Petroleum Engineering Department, Universiti Teknologi PETRONAS,  
32610 Seri Iskandar, Perak, Malaysia  
e-mail: mazlinidress@petronas.com.my

B. Lal · B. Partoon  
Chemical Engineering Department, Universiti Teknologi PETRONAS,  
Seri Iskandar, Malaysia

K.M. Sabil  
Institute of Petroleum Engineering, Heriot-Watt University Malaysia,  
Putrajaya, Malaysia

sediment pore water, and direct sampling of gas hydrate [1]. Natural gas hydrates are generally defined as inclusion compounds formed from water and light hydrocarbons, mainly methane [2]. The whole structure is stabilized by the interactions between the water molecules forming a lattice and the gas molecules contained within this lattice at high pressure and low temperature. Gas hydrate exists in crystalline, ice-like solid molecule formed when the ‘guest’ molecules such as carbon dioxide (CO<sub>2</sub>), methane (CH<sub>4</sub>), ethane (C<sub>2</sub>H<sub>6</sub>), and nitrogen (N<sub>2</sub>) are altered by the addition or existence of water molecule in the system. Gas hydrates are non-stoichiometric compounds, which denote quantities of reactants which are not in a simple integral ratio or not in the ratio expected from an ideal formula or equation.



Referring to Eq. (1), n is the number of moles of water per mole of gas in hydrate. In natural conditions, when hydrate formed by biogenic methane in bottom sediments, the value of n varies from 5.8 to 6.0. The value of n varies from 7 to 12 during hydrate formation by depth catagenetic gases [3]. The formation of hydrates depends on several parameters such as pressure, temperature, gas composition, salinity, and interfacial surface area which can be affected by the presence of porous media. The different types of porous media will also affect the specific area, pore volume, and pore size distribution of the methane hydrates formed [4]. The methods for recovering natural gas hydrates are still in developing stage. The most practical methods are thermal stimulation, depressurization, and chemical inhibitors [5]. One of the most valuable information needed to reliably predict the production of natural gas from hydrate deposits is the porosity effect on hydrate formation and dissociation within porous medium. Porosity is a measure of how much of a rock has open space. This space can be between grains or within cracks or cavities of the rock. Porosity increased as the particle size increased. It is known that as particle size increases, the surface area decreases [6].

The kinetics of natural gas hydrate formation within geologic materials is limited in current literature with characteristics related to their occurrence in nature. It involves the nucleation mechanism and the induction time, distribution points of these nuclei, and the rate at which hydrates grow within the sediment. This provides a valuable insight into the formation history and mechanisms of natural gas hydrate accumulations [7]. Linga et al. (2012) studied the formation kinetics of various natural gas mixtures in silica sand using stirred vessel and fixed bed reactor and found that the hydrate formation rate in fixed bed reactor is faster than that in the stirred vessel and the percentage of water to hydrate conversion is higher [8]. Sun et al. (2014) studied the phase stability of methane hydrate formation in silica sand particles, and the result shows that phase stability is not affected by the coarse-grained silica sand [9]. From experimental measurement of permeability in partially hydrate-saturated glass beads’ pack which is compared with the measured

value using Masuda model, it is suggested that when the hydrate saturation is less than 35%, the hydrates tend to coat the glass bead, and filling up the pores with minimal interaction with the glass bead when the saturation is more than 35% [10]. From the literature, it is suggested that the hydrate growth dwelled in smaller pore spaces [11]. Clarke et al. (1999) developed a comprehensive predictive thermodynamics model to determine the hydrate formation conditions in the granular porous media. The models required the knowledge of surface energy, mean pore radius, and wetting angle. According to McGrail et al. in 2007, one problem-limiting data collection on gas hydrate properties in porous media is the experimental difficulty associated with the measurement. A pore water freezing model was developed, and it showed good agreement with the experimental measurement. This proves that pore water chemistry is the most important factor that controls the equilibrium of gas hydrate in porous medium [12]. Kleinberg et al. 2003 studied the hydrate growth habit in porous media using nuclear magnetic resonance measurements on hydrate-bearing formation. The samples were artificially formed replicating the water-rich environment. The study discovered that the hydrate is formed in the centers of the pores and suggests that when hydrates are formed from free gas, they occupied the largest pores in consolidated rock due to the availability and low solubility of methane in the water [13]. Other experiments were performed by Garret and Marco to evaluate the methane production from hydrate-bearing quartz sediment. Hydrate formation using a gas invasion technique showed that hydrates tend to form from the top of the reactor and progress downward for prepared sediment samples ranging between 10 and 30% pore space hydrate saturation [14]. Chen et al. reported the synthesis of methane hydrate in porous media and investigated the geochemical characteristics of pore water. The results show that subcooling is one of the most important factors in affecting hydrate formation. Larger subcooling provides more powerful driving force for hydrate formation [15].

The objective of this paper was to investigate the effect of hydrate formation at different porosity settings ranging from 0.32 to 0.40. In this study, sand pack was prepared as a porous medium for hydrate formation and dissociation using quartz sand with the grain sizes of 600–800  $\mu\text{m}$  in Hydrate Tubular Cell. The setting temperature ranges from 20 to 3  $^{\circ}\text{C}$  for hydrate formation at pressure range from 8 MPa to 2 MPa. Methane gas is used as a hydrate former with 100% water saturation in the sand pack. Knowing the physical properties of the rock and existing interactions between the methane hydrate system and the formation is essential for understanding and evaluating the performance of a given reservoir. This study can contribute to increase understanding of gas hydrate formation and dissociation in different sediment settings.

## 2 Experiment

### 2.1 Material

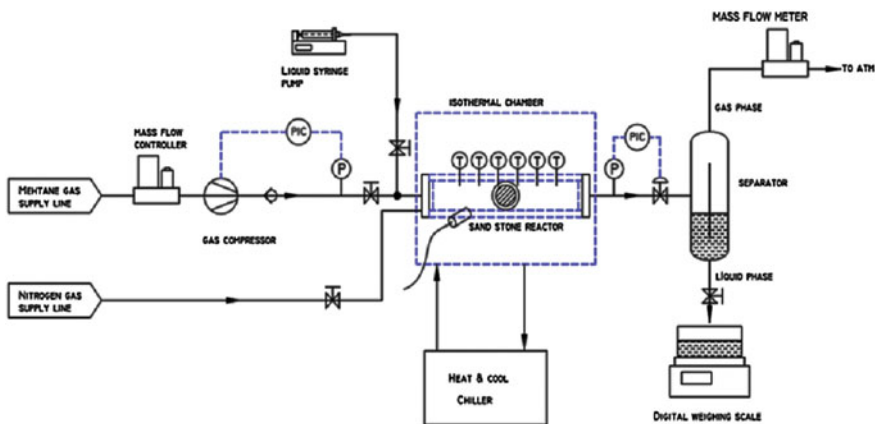
The quartz sand with a 600–800  $\mu\text{m}$  size range is used as porous medium in the experiment. The quartz sand sample was categorized in the range of size using sieve analysis. In the hydrate formation process, deionized water and methane gas with a purity of 0.99 mass fractions were injected into the porous medium. The gas is supplied by Linde Malaysia. Details of the sample are listed in Table 1.

### 2.2 Experimental Apparatus

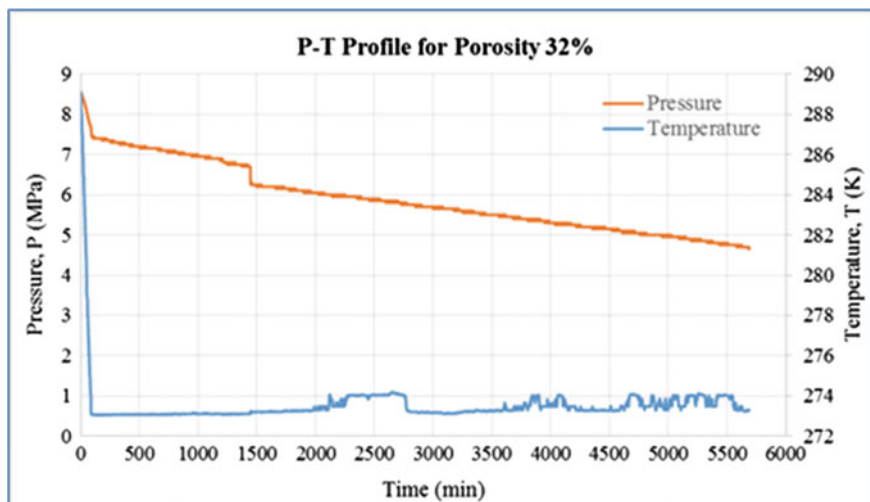
The newly designed Tubular Hydrate Cell is used to simulate gas hydrate formation and dissociation in porous medium via depressurization, thermal stimulation, and inhibitor injection. The experimental apparatus used in this work is shown in Fig. 1. The core component of the apparatus is a high-pressure tubular cell made of SS316

**Table 1** Quartz sand sample

Sample	Porosity (%)	Dry weight (kg)	Water required for 100% saturation (ml)
S100P32	32	3.64	644.65
S100P34	34	3.54	684.91
S100P37	37	3.34	745.35
S100P40	40	3.22	805.78



**Fig. 1** Schematic diagram for experimental apparatus



**Fig. 2** *P-T* profile for porosity of 32%

that can withstand a maximum pressure of 20 MPa with effective volume of 2.01 L. The cell is fixed horizontally in an isothermal chamber with circulating water with the temperature range of 268–323 K. Six thermocouples are inserted along the cell to monitor the temperature changes during the hydrate formation and dissociation as shown in Fig. 2. The system pressure is measured by two pressure transducers located at the inlet and outlet of the tubular hydrate cell. The apparatus is equipped with liquid syringe pump to inject liquid into the porous medium and gas booster to charge in the methane gas to a pre-set pressure. The liquid syringe pump has a range of injection rate up to 100 ml/min and the maximum pressure of up to 15 MPa. The maximum pressure attained by the booster pump is 20 MPa. The two-phase separator with the capacity of 2.01 L is placed at the outlet of the tubular hydrate cell to separate gas and water produced during the dissociation process. A gas flowmeter and a electronic weighing balance are placed at the downstream of the equipment to monitor the fluid flow rates. The experimental data obtained are logged using Indussoftware at prespecified interval.

### 2.3 *Experimental Procedures*

The quartz sand is washed and dried in the oven for 24 h at 373 K to ensure zero moisture inside the quartz sand. The sand was cooled and sieved to obtain the sand with the required range. The sand density is measured to be 2.66 g/mL, and the value is used as a basis to determine the pore volume and porosity of the quartz sand. A total of 3.64 kg dry quartz sand with a size range of 600–800  $\mu\text{m}$  was

tightly compacted in the tubular hydrate cell. Based on the sand density of 2.66 g/mL, and the volume of the cell, the porosity of the sand packed in the cell was determined to be 32%. The cell was placed inside the isothermal chamber with the circulating water at ambient temperature. The cell was vacuumed to remove the air inside the cell. The deionized water was injected into the cell at a constant rate of 10 ml/min using liquid syringe pump until constant differential pressure was observed. At this point, the pores were fully saturated with water. The temperature inside the isothermal chamber was reduced by cooling down the circulating water from the room temperature to the hydrate formation temperature of 276 K. After the system is stabilized at the formation temperature, methane gas is charged from the booster pump into the porous media to increase the system pressure to 8 MPa to prepare for hydrate formation.

Temperature and pressure in the sand bed can be read from the control panel and data acquisition system that are connected to the cell. Temperature and pressure data are recoded at every 10-s interval. Methane hydrate formation was detected by the sharp increase in temperature and a reduction in the cell pressure. As water is denser than methane gas, it tends to accumulate at the bottom part of the sand and gas at the upper part of the cell. This fact may result in more methane hydrates formed at the gas–liquid interface inside the quartz sand. The hydrate formation process lasted for a maximum of six days. The hydrate formation is said to be completed when the system pressure stopped declining and become constant. The experiment is then repeated using freshly packed quartz sand with a porosity of 0.34, 0.37, and 0.40, respectively.

### 3 Results and Discussion

Methane hydrate formation kinetics experiments in porous media are conducted in deionized water using four types of porosity 0.32, 0.34, 0.37, and 0.4 of quartz sand with the grain sizes of 600–800  $\mu\text{m}$  to represent porous media. Tables 2 and 3 provide details of experiments carried out in this study. The effect of porosity of quartz sand on deionized water is studied in detail, and their significance for gas hydrate formation is related. The amount of the gas consumed during the experiment is calculated using Eq. (2):

**Table 2** Methane hydrate induction time for different sand samples

Sample	Porosity (%)	Water saturation (%)	Pressure of hydrate formation (MPa)	Temperature of hydrate formation (K)	Induction time (hour)
S100P32	32	100	6.70	273.20	24.1
S100P34	34	100	5.50	275.75	2.33
S100P37	37	100	7.83	275.72	1.47
S100P40	40	100	7.28	275.70	0.76



**Table 3** Porosity reduction and methane hydrate saturation for different sand samples

Sample	Porosity after hydrate formation (%)	Porosity reduction (%)	Completion of hydrate formation time (h)	Gas uptake (mol/mol)	Hydrate saturation (%)	Hydrate conversion (%)
S100P32	30	6.30	33.35	8.641	6.34	63.75
S100P34	32	5.90	142	4.484	3.27	33.09
S100P37	36	2.70	64.2	3.290	2.48	24.36
S100P40	40	1.00	216	5.361	0.77	39.55

$$(\Delta n_{H,\downarrow})_t = V_C \left[ \left( \frac{P_C}{zRT} \right)_{t=0} - \left( \frac{P_C}{zRT} \right)_t \right] \dots\dots\dots (2)$$

where  $(\Delta n_{H,\downarrow})_t$  denotes the number of moles of gas consumed at time  $t$ . It is the difference in initial number of gas at time  $t = 0$  and number of moles of gas at time  $t$ .  $z$  is the compressibility factor for a given temperature  $T$  and pressure  $P_C$  which is the cell pressure at given time  $t$ .  $z$  is computed by Pitzer’s correlations which is being used widely by many researchers [9].  $V_C$  is the volume of the cell which is 2.01 L.  $R$  is the universal gas constant.

### 3.1 The Effect of Porosity on CH<sub>4</sub> Hydrate Formation

The formation kinetics study was conducted at 276 K at 8 MPa. From Fig. 2, the dissolution phase was started at the beginning of the experiment as methane gas was injected into the cell and diffuses into the liquid phase inside the pores of the sand and becomes saturated. The methane hydrate nucleation starts at the interface of the gas and liquid inside the pores as the gas diffuses into the sand. At this time, there is a sudden increase in temperature due to the exothermic nature of hydrate formation and simultaneous increase in the number of moles of methane gas consumed. The result shows that the larger the porosity, the faster the methane hydrate nucleation will be inside the sand translated by the faster induction time. The induction time occurs as early as 0.76 h for the quartz sand with 40% porosity to 24.1 h for the quartz sand with porosity of 32% as tabulated in Table 2. As the formation progresses, the hydrate crystals continue to grow and the gas uptake also increases accordingly. Since nucleation can take place randomly at any point in the bed, the time at which nucleation occurs can be identified from temperature profiles of the sand bed. As the experiment progresses, there are several temperature spikes observed indicating new nucleation sites within the sand bed.

The number of moles of water consumed at time,  $t$ , is determined from the following equation for various experimental studies:

$$\begin{aligned}
 & \text{water to hydrate conversion (\%)} \\
 & = \frac{\Delta n_{H_2} \times \text{hydration number}}{n_{H_2O}} \times 100 \dots \dots \dots (3)
 \end{aligned}$$

where  $\Delta n_{H_2}$  is the number of moles of gas consumed at the end of the experiment determined using Eq. (2). The hydration number used for the present study is 7.377 [3].  $n_{H_2O}$  is the number of moles of water inside the cell. Table 3 lists the calculated values of water to hydrate conversion at the end of the experimental work. In general, the maximum hydrate conversion of 63.75% is discovered in smallest porosity of 32%. The values decrease from 63.75 to 39.55% as the porosity increased from 32 to 40%.

The observations for hydrate conversion are in agreement with Mekala et al. 2014 that stated as the size of silica sand increased; hydrate conversion decreased. The minimum hydrate conversion is 39.55% using porous media with 40% of porosity. From the literature studies, it is known that smaller particle size provides more surface area for gas hydrate formation compared to larger particle size. Smaller particle sizes lead to lower porosity. Therefore, in porous media with 32% of porosity, it provides larger surface area for gas and liquid contacts to form methane hydrate. This is also proven with the higher gas hydrate saturation value and higher porosity reduction in the quartz sand. The hydrate saturation value decreases as porosity increases, thus leading to higher porosity reduction as porosity of the quartz sand increases. The porosity reduction values also indicated a successful methane hydrate formation inside the pores.

The rate of hydrate formation is determined by the forward differentiation method using Eq. (4). The average gas uptake was computed every minute and reported. The methane gas uptake curves are shown in Fig. 3.

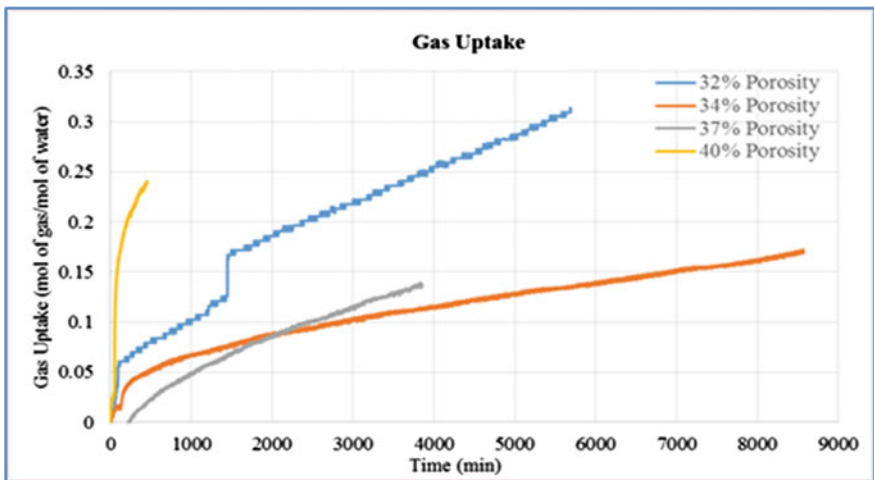


Fig. 3 Gas uptake at different porosity

$$\left(\frac{d\Delta n_{H,\downarrow}}{dt}\right) = \frac{(\Delta n_{H,\downarrow})_{t+\Delta t} - (\Delta n_{H,\downarrow})_t}{\Delta t} \dots\dots\dots (4)$$

Porosity reduction is calculated using Eq. (5):

$$\emptyset_t = \emptyset_i(1 - S_h) \tag{5}$$

where  $\emptyset_t$  is the total porosity of the system in the presence of hydrate,  $\emptyset_i$  is the porosity of the system without hydrate, and  $S_h$  is the hydrate saturation in the system. The hydrate saturation is calculated using Eq. (6):

$$S_h = \frac{nM_h}{V_p\rho_h} \tag{5}$$

where  $S_h$  is the hydrate saturation in the system,  $n$  is the number of gas consumed at the end of the experiment,  $M_h$  is the hydrate molecular weight (g/mol),  $V_p$  is the pore volume of the sample (cm<sup>3</sup>), and  $\rho_h$  is the density of gas hydrate (g/cm<sup>3</sup>).

### 4 Conclusion

The result shows that for quartz sand of 600–800 μm, the smaller the porosity, the faster the methane hydrates formation completion will be and the greater the amount of methane hydrates formed inside the quartz sand. The fastest completion time is 33.34 h for the quartz sand with porosity of 0.32, and the percentage of methane hydrate saturation is 6.34%. This finding is essential to assist in determining the optimum sand properties for different types of sediments.

### References

1. K. A. Kvenvolden, “A review of the geochemistry of methane in natural gas hydrate,” *Org. Geochem*, vol. 23, no. 11/12, pp. 997–1008, 1995.
2. D. Greaves, J. Boxall, J. Mulligan, E. D. Sloan, and C. A. Koh, “Hydrate formation from high water content-crude oil emulsions,” *Chemical Engineering Science*, vol. 63, no. 18, pp. 4570–4579, 2008.
3. Y. F. Makagon, *Hydrates of Hydrocarbon*, p. 382: PennWell Publishing Company, 1997.
4. N.-J. Kim, S.-S. Park, H. T. Kim, and W. Chun, “A comparative study on the enhanced formation of methane hydrate using CM-95 and CM-100 MWCNTs,” *International Communications in Heat and Mass Transfer*, vol. 38, no. 1, pp. 31–36, 2011.
5. X.-S. Li, B. Yang, L.-P. Duan, G. Li, N.-S. Huang, and Y. Zhang, “Experimental study on gas production from methane hydrate in porous media by SAGD method,” *Applied Energy*, vol. 112, pp. 1233–1240, 2013.
6. P. Mekala, M. Busch, D. Mech, R. S. Patel, and J. S. Sangwai, “Effect of silica sand size on the formation kinetics of CO<sub>2</sub> Hydrate in porous media in the presence of pure water and

- seawater relevant for CO<sub>2</sub> sequestration,” *Journal of Petroleum Science and Engineering*, 2014.
7. L. Ruffine, “Exploring methane-hydrate formation and dissociation in geologic materials through laboratory experiments: Kinetic behavior and morphology,” *Fuel*, vol. 141, pp. 173–184, 2015.
  8. P. Babu, S. H. B. Yang, S. Dasgupta, and P. Linga, “Methane Production from Natural Gas Hydrates via Carbon Dioxide Fixation,” *Energy Procedia*, vol. 61, pp. 1776–1779, 2014.
  9. D. Sun, and P. Englezos, “Storage of CO<sub>2</sub> in a partially water saturated porous medium at gas hydrate formation conditions,” *International Journal of Greenhouse Gas Control*, vol. 25, pp. 1–8, 2014.
  10. A. Kumar, B. Maini, P. R. Bishnoi, M. Clarke, O. Zatsepina, and S. Srinivasan, “Experimental determination of permeability in the presence of hydrates and its effect on the dissociation characteristics of gas hydrates in porous media,” *Journal of Petroleum Science and Engineering*, vol. 70, no. 1–2, pp. 114–122, 2010.
  11. M. B. Clennell, M. Hovland, J. S. Booth, P. Henry, and W. J. Winters, “Formation of natural gas hydrates in marine sediments: 1. Conceptual model of gas hydrate growth conditioned by host sediment properties,” *Journal of Geophysical Research*, vol. 104, no. B10, p. 22985, 1999.

# Permeability Evaluation in Hydrate-Bearing Sand Using Tubular Cell Setup

Mazuin Jasamai, Ismail M. Saaid, Mazlin Idress, Bhajan Lal,  
Behzad Partoon and Khalik M. Sabil

**Abstract** Production of natural gas from hydrate-bearing sediments is significantly influenced by permeability variations in the presence of gas hydrate. The quantification on how absolute permeability and relative permeability affect natural gas production from hydrate-bearing sediments is one of the key interests for reservoir engineering studies. This study focuses on the relationship between water saturation, permeability, and porosity in unconsolidated quartz sand. Methane hydrate was formed in quartz sand in high-pressure stainless steel cell using deionized water at 276 K and 8 MPa. The sand pack with porosity of 40% was saturated with 35% water. This study found that porosity of the sample reduced significantly as the sand pack saturated with 35% of water. Porosity reduced from 40 to 37.4% due to the increase of hydrate saturation. Absolute permeability is 108.72 mD, and it was measured before gas hydrate formation. Relative permeability was measured after gas hydrate formation, and results show that relative permeability is 0.49. Formation of hydrate in pores significantly reduces the relative permeability and porosity. Relative permeability from this work is compared with a theoretical model, and the value shows that the relative permeability from this work is close to the value from Masuda model with  $N = 10$ .

**Keywords** Relative permeability · Methane hydrates formation · Kozeny model · Porous media

---

M. Jasamai (✉) · I.M. Saaid · M. Idress  
Petroleum Engineering Department, Universiti Teknologi PETRONAS,  
Bandar Seri Iskandar, Tronoh 32610, Perak, Malaysia  
e-mail: mazuin\_jasamai@utp.edu.my

B. Lal · B. Partoon  
Chemical Engineering Department, Universiti Teknologi PETRONAS,  
Bandar Seri Iskandar, Tronoh 32610, Perak, Malaysia  
e-mail: bhajan.lal@utp.edu.my

K.M. Sabil  
Institute of Petroleum Engineering, Heriot-Watt University Malaysia,  
Precinct 2, Putrajaya 62100, Federal Territory of Putrajaya, Malaysia  
e-mail: k.msabil@hw.ac.uk

## 1 Introduction

Natural gas hydrate (NGH) exists in geological formations and constitutes a potentially large natural gas resource for future. In natural conditions, gas hydrate forms in the presence of water and natural gas, mainly methane at low-temperature and high-pressure environment. Gas hydrate is a solid substance that looks like ice. Naturally occurring methane hydrate is distributed in pore space of sediments. Gas hydrate has the ability to concentrate and store a large volume of natural gas/methane within the water cage cavities where  $1 \text{ m}^3$  of methane hydrate can produce approximately  $164 \text{ m}^3$  of methane gas at standard conditions. Current estimates of the global methane hydrate inventory range more than 445 Gt of carbon [1]. Motivated by these facts, gas hydrate research activities are centered on the exploration of this potentially new energy resource. Research on extraction method is still ongoing to understand the parameters that influence the formation process, directly and indirectly, such as porosity, permeability, water saturation, and lithology of the formation. Yet, many of the aforementioned parameters are not fully investigated in order to show hydrate formation/dissociation mechanisms within the sediments and parameters that influence the process.

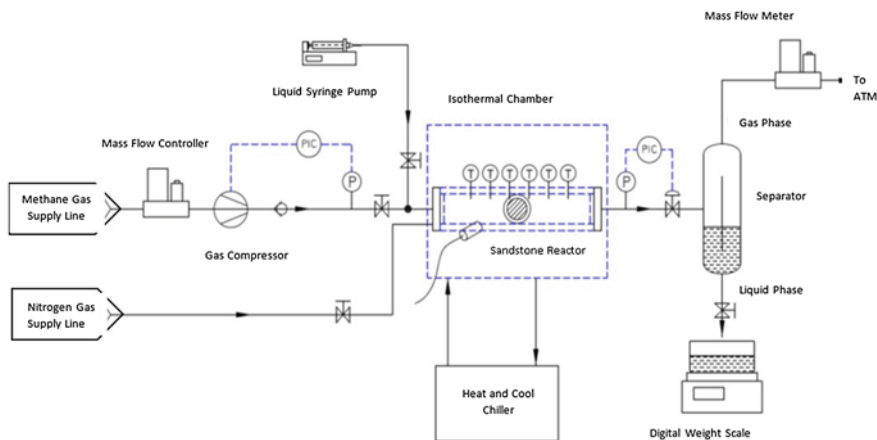
The permeability of a rock is a measure of the ease in which the rock permits the passage of fluids to flow. Therefore, permeability is an important key parameter to determine the fluid flow capacity in order to ensure the successful production of natural gas from natural gas hydrates [2]. The permeability of sediment is determined by measuring gas or liquid flows, and it is affected by the type of fluid flow, porosity, grain size, and packing structure of the sand. Formation of gas hydrate in the pore or at the grain surface will reduce the porosity and indirectly restrict the permeability. After the pores are filled with gas, the flowing path for the fluid to flow will be reduced [3]. The present research on the effect of relative permeability progresses from theoretical and empirical models to the experimental stage. It is an important parameter for predicting natural gas production from gas hydrate reservoir. In 2006, Seol et al. from Lawrence Berkeley National Laboratory, USA, estimate the relative permeability parameters in hydrate-bearing sand using X-ray computed tomography (CT) scanning. The experimental work is to quantify water and hydrate saturations in the sample and estimate parameters related to relative permeability using inversion simulation. Hydrate distribution was reported to be heterogeneous despite relatively uniform initial water saturation and porosity distribution. CT scan results also showed the first visualization of water flow through non-uniformity of hydrate formation in porous media [4]. Sakamoto conducted an experiment at a laboratory scale to analyze the permeability change due to methane hydrate dissociation using hot water injection. His experimental work shows that permeability decreased as methane hydrate saturation increased. Relative permeability curve was shifted to lower water saturation as hydrate saturation increased [5]. It has been observed in nature that hydrate usually exists in unconsolidated sediments. Johnson et al. [6] concluded that measurement of relative permeability in unconsolidated samples would provide meaningful results. Series of experimental results showed that hydrate saturation in the pores could reduce

the permeability of porous media [7]. Kumar et al. performed series of experiments in packed glass beads to test the models developed by Masuda and Kleinberg in measuring gas permeability in the carbon dioxide hydrate sediment and found that experimental results obtained agree with the results from the model. The result shows that for initial water saturation of less than 35%, hydrates tend to form on the grain surfaces, and for water saturation above 35%, the experimental results indicated a hydrate formation in the center of the pore which will reduce permeability more significantly [3]. Sakamoto et al. [5] in his work estimated permeability in methane hydrate reservoir using the model of methane hydrate dissociation. The results showed that methane hydrate derived from both irreducible water saturation and free water will reduce the permeability in reservoirs, thus reducing the porosity as hydrate occupied the pores [5]. It is important to understand the flow properties in hydrate-bearing sediments as hydrate dissociation produces water and gas. The main properties need to understand are relative permeability of aqueous solution,  $K_{ra}$ , relative permeability of the gas,  $K_{rg}$ , and the relationship of capillary pressure,  $P_{cap}$ , to the saturation of fluid phases. Delli and Grozic [8] used a three-dimensional cubic pore network model to study the effect of hydrate particle formation and growth habit on the permeability. A key prediction of the simulation is permeability will reduce exponentially with the increase of hydrate saturation [9]. The prediction is consistent with previously developed permeability models where the degree of permeability reduction depends on the growth habit of hydrates either coating the grains or filling the pore spaces [10]. This study focuses on the relationship between water saturation, permeability, and porosity in unconsolidated quartz sand. In this study, methane and water acted as fluid phase flowing in the porous media. Hydrate formations in the system form from initial water saturation at 276 K at 8 Mpa.

## 2 Experimental

### 2.1 Materials

The quartz sand with particle distribution is between 600 and 800  $\mu\text{m}$  with an average size of 700  $\mu\text{m}$  range used as the porous medium in the experiment. The coefficient of uniformity is 1.44. The sample is characterized as well sorted as the uniformity coefficient is less than 3. The specific gravity is 2.66. Deionized water and methane gas with a purity of 99.95 mol% are used for hydrate formation. The gas is supplied by Linde Malaysia. Deionized water was prepared using TKA-LabTower setup from Thermo Scientific.



**Fig. 1** Schematic diagram for experimental apparatus

## 2.2 Experimental Apparatus

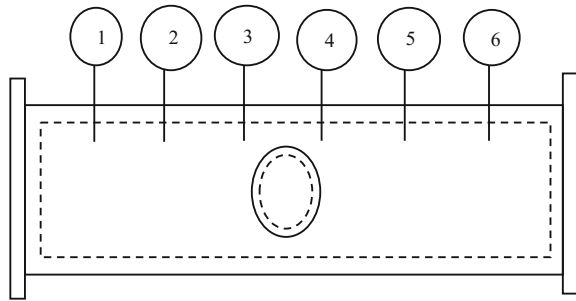
The newly designed high-pressure stainless steel cell was used to simulate the gas hydrate formation and dissociation in the porous medium. The schematic of experimental apparatus is shown in Fig. 1. The core component of the apparatus is a high-pressure cell made of SS316 that can withstand a maximum pressure of 20 MPa with an effective volume of 2.01 L. The cell is fixed horizontally in an isothermal liquid bath chamber. The circulating coolant temperature can be controlled in a range of 268–323 K. Six thermocouples are installed along the cell to monitor the temperature changes during hydrate formation and dissociation. The temperature is measured with  $\pm 0.05$  K. The system pressure is measured by two pressure transducers with an accuracy of  $\pm 0.05$  MPa located at the inlet and outlet of the tubular hydrate cell. The apparatus is equipped with a high-pressure liquid syringe pump to inject liquid into the porous medium and gas booster to charge in the gas into the cell. The liquid syringe pump has a range of injection rate up to 100 ml/min and the maximum pressure of up to 15 MPa. The maximum attainable pressure of the booster pump is 20 MPa. The two-phase separator with the capacity of 2.01 L is placed at the outlet of the tubular hydrate cell to separate gas and water produced during the dissociation process. A gas flowmeter and electronic weighing balance are placed at the downstream of the equipment to monitor the fluid flow rates. The experimental data obtained are logged using data logging system at a 1-s interval.

## 2.3 Experimental Procedure

The quartz sand is washed and dried in the oven for 24 h at 373 K to ensure zero moisture inside the quartz sand. After cooling, the sand was sieved to obtain the



**Fig. 2** Tubular cell and location of thermocouples



sand with the required range. Using ASTM D 6913, particle sand was sieved and into the desired size range and the mass of each range was determined. The density is 2.66 g/cm<sup>3</sup>. The sand mainly composed of silica.

The sand was packed in the tubular cell shown in Fig. 2. The cell was made of 316 stainless steel (SS316) with a maximum pressure of 20 MPa. The internal diameter of the cell and its internal length are 8.5 cm and 35.5 cm that led to the internal volume of 2.01 L. Six resistance temperature detectors (RTDs) are installed at the top surface of the cell as shown in Fig. 2. The sand was filled gradually into the cell with intermittent knocking outside of the cell surface using a rubber hammer to ensure the decent compaction was achieved. Mass of the sand filled in the cell was calculated knowing the volume of grain ( $V_g$ ) and grain density ( $\rho_g$ ). About 3 220 g of sand was packed into the tubular cell to achieve the porosity of 40%. Properties of the sand pack are summarized in Table 1. The average permeability of the sand pack was determined using Darcy’s equation with measured data of pressure drop across the cell when gas was injected at constant pressure.

The cell was placed inside the isothermal chamber and put under vacuum for 1 h to remove all the air trapped inside. The known amount of gas was injected into the cell at a constant pressure of 3 MPa. Differential pressure was observed. The absolute permeability to gas is calculated using modified Darcy’s equation for gas as in Eq. (1).

$$K_a = \frac{Q2\mu LP_2}{A(P_1^2 - P_2^2)} \tag{1}$$

$Q$  is the gas flow rate (m<sup>3</sup>/s),  $L$  is the length of the cell (m),  $\mu$  is the viscosity of gas (Pa·s),  $P_1$  is the inlet pressure, and  $P_2$  is the outlet pressure (Pa).

**Table 1** Properties of sand pack

Properties	Details
Mass of sand (g), $m$	3 220
Bulk volume (cm <sup>3</sup> ), $V_b$	2014.45
Grain volume (cm <sup>3</sup> ), $V_g$	1269.1
Grain density (g/cm <sup>3</sup> ), $\rho_g$	2.66
Pore volume (cm <sup>3</sup> ), $V_p$	805.8
Porosity (fraction), $\emptyset$	0.40
Absolute permeability (mDarcy)	108.7
Grain size (μm)	600–800

After the process of hydrate formation was completed, the pressure will stabilize around 3 MPa. To ensure the complete formation of hydrate, the system pressure slightly increases and the system left overnight to ensure the complete formation of hydrate. For permeability measurement, the pressure drop across the cell was measured after the complete formation of hydrate. Effective permeability to gas is measured. The relative permeability at particular hydrate saturation was calculated using Eq. (2). The relative permeability ( $K_{rg}$ ) is a useful dimensionless parameter measure that quantifies the ability of a fluid to flow relative to another in the porous media. It is the ratio of effective permeability of a fluid at given hydrate saturation to the absolute permeability of the porous media.

$$K_{rg} = \frac{K_r}{K_a} \quad (2)$$

### 3 Results and Discussion

#### 3.1 Methane Hydrate Formation

From Fig. 3, constant pressure and temperature prior to hydrate formation validated that there was no leakage in the system. The dissolution phase starts at the beginning of the experiment as methane gas was injected into the cell and diffuses into the liquid phase inside the pores of the sand and becomes saturated. The methane hydrate nucleation starts at the interface of the gas and liquid inside the pores as the gas diffuses into the sand. The stabilization starts at time  $t = 100$  min. The induction time of the formation process is at time  $t = 216$  min. Taking into account the stabilization time that starts at  $t = 100$  min, the induction time starts 116 min after stabilization or 1.9 h for water saturation of 35%. Induction time includes time taken for the crystal to form which is not visible at macroscopic levels. In practice, induction time is defined as the time elapsed until the appearance

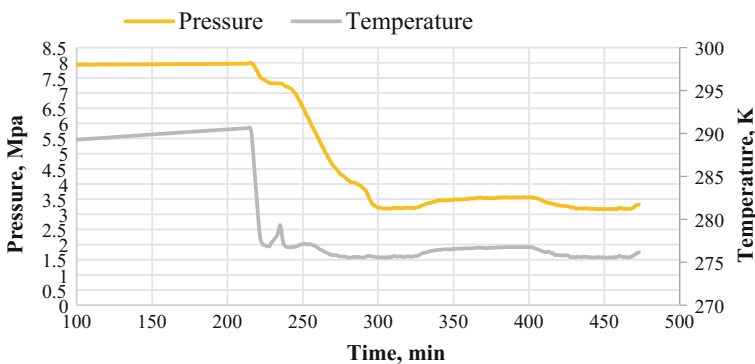
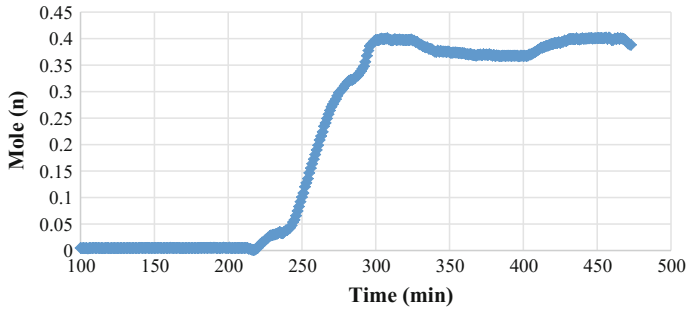


Fig. 3 Pressure and temperature profile during hydrate formation at  $S_w = 35\%$



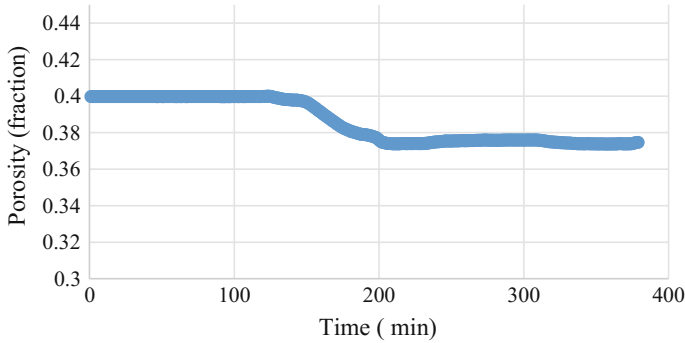
**Fig. 4** Gas consumption profile during hydrate formation at  $S_w = 35\%$

of the detectable volume of the hydrate or can be observed as a detectable number of moles of gas consumed in the system. From Fig. 3, after 1.9 h, a concurrent drop in pressure and rise in temperature were observed, which indicates massive hydrate formation. Sudden pressure drop happens as the gas in the system is being consumed to form methane hydrate. Temperature spike indicates that heat has been released as the formation of hydrate is an exothermic process. Figure 4 shows that the number of moles of gas consumed during the formation process. As shown in this figure at  $t = 216$  min, sudden pressure drop is due to methane gas being consumed. This indicate gas hydrate formation as the gas in the system is being trapped with in the cage of water cavities. This observation is in agreement with a description from Sloan and Koh in 2008, which mentioned earlier gas consumption increases slowly as the formation occurs and reaches its maximum rate over time. The temperature rise resulted from the latent heat produced during hydrate formation as hydrate formation is an exothermic process. Hydrate formation is being observed using the same indication for water saturation of 50 and 100%.

Table 2 shows the summary of the results for gas hydrate formation at 35% water saturation. Hydrate formation pressure is at 7.34 Mpa. Hydrate formation temperature was measured at 276.85 K. The induction time taken is 1.9 h after the stabilization, 5.43 h to completely form gas hydrate inside the sand pack. The porosity reduced due to the accumulation of gas hydrate in pores during gas hydrate formation. This is one of the factors that can confirm the presence of hydrate in the pores. Figure 5 shows results of porosity reduction for unconsolidated sample with

**Table 2** Summary of results after hydrate formation

Water saturation, $S_w$ (%)	0.35
Initial porosity, $\emptyset$ (%)	40
Porosity after hydrate formation	37.4
% of porosity reduction	6.5
Hydrate saturation, $S_h$ (%)	6.35
Pressure of hydrate formation (Mpa)	7.34
Temperature of hydrate formation ( $^{\circ}C$ )	276.85
Induction time (h)	3.6
Completion of hydrate formation time (h)	5.43



**Fig. 5** Porosity reduction profile at  $S_w = 35\%$

35% water saturation. It is observed that porosity reduction is 6.5% during hydrate formation with water saturation of 35%. This is due to the higher hydrate saturation within the pores when unconsolidated sand was saturated with 35% water saturation. Porosity reduction is calculated using Eq. (4)

$$\phi_r = \phi_i(1 - S_h) \quad (4)$$

where  $\phi_r$  is the total porosity of the system in the presence of hydrate and  $\phi_i$  is the porosity of the system without hydrate.  $S_h$  is the hydrate saturation in the system. Hydrate saturation is calculated using Eq. (5).

$$S_h = \frac{nM_h}{V_p\rho_h} \quad (5)$$

where  $S_h$  is the hydrate saturation in the system,  $n$  is the amount of gas consumed at the end of the experiment,  $M_h$  is the hydrate molecular weight (g/mol),  $V_p$  is the pore volume of the sample ( $\text{cm}^3$ ), and  $\rho_h$  is the density of gas hydrate ( $\text{g}/\text{cm}^3$ ). Hydrate saturation is highest with unconsolidated sample that saturated with 35% water which is 6.5%. This result is in agreement with [5] which concluded that methane hydrate derived from both irreducible water saturation and free water will reduce the permeability in reservoirs, thus reducing the porosity as hydrate occupied the pores.

### 3.2 Permeability Evaluation Before and After Hydrate Formation

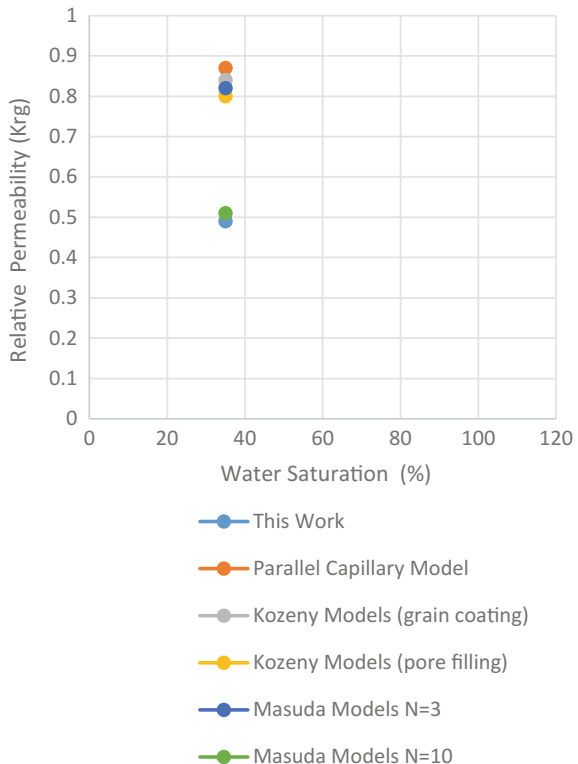
Understanding on how the presence of hydrate in porous media influences water and the gas flow is critical to predict gas recovery from hydrate deposits. Permeability is the main property that needs to be evaluated in the hydrate-bearing sand. Table 3 shows the summary of results calculated from parameters measured during the experiment. Absolute permeability does not show any significant change with variation of water saturation. After hydrate formation, permeability was measured

**Table 3** Summary of permeability before and after hydrate formation

Water saturation, $S_w$ (%)	0.35
Porosity (%), $\emptyset$	40
Permeability (D), $K_0$	108.72
Effective permeability, $K_g$	53.59
Relative permeability, $K_{rg}$	0.49
Parallel capillary model	0.87
Kozeny models (grain coating)	0.84
Kozeny models (pore filling)	0.80
Masuda models $N = 3$	0.82
Masuda models $N = 10$	0.51

again. Effective permeability to gas is calculated using the information from the experiment. From absolute permeability and effective permeability, relative permeability was calculated using Eq. (2). Relative permeability ( $K_{rg}$ ) is a useful measure that quantified the ability of the fluid to flow relative to another in the porous media. Relative permeability measured after gas hydrate formation is 0.49. Relative permeability value from this work is compared with the value from the theoretical model. From Fig. 6, the results from this work show that the value is close to Masuda model with  $N = 10$ .  $N$  is the permeability reduction exponent which depends on the pore structure. The value of  $N$  is taken as 3 and 10 in this work.

**Fig. 6** Comparison of relative permeability from this work with theoretical model



## 4 Conclusion

A newly designed high-pressure cell was found to be capable of forming gas hydrates in the porous medium in this study. From the study, the average absolute permeability calculated for the quartz sand of 600–800  $\mu\text{m}$  particle size and the porosity of 40% without methane hydrate is 108.7 mD. Water saturation at 35% in unconsolidated sample affects hydrate saturation, porosity reduction, and relative permeability. This study found that porosity of the sample reduced significantly as the sand pack saturated with 35% of water. Porosity reduced from 40 to 37.4% due to the increase of hydrate saturation. Relative permeability to gas is calculated from the experimental data, and results show that relative permeability to gas increase is 0.49. This study found that water saturation gives high impact to porosity and relative permeability reduction in porous media. Therefore, further study that varies the water saturation from lower to higher needs to be conducted to investigate the effect of water saturation variation on porosity and permeability reduction.

## References

1. K. Wallmann, E. Pinero, E. Burwicz, M. Haeckel, C. Hensen, A. Dale, and L. Ruepke, "The Global Inventory of Methane Hydrate in Marine Sediments: A Theoretical Approach," *Energies*, vol. 5, no. 12, pp. 2449–2498, 2012.
2. B. Li, X.-S. Li, G. Li, J.-L. Jia, and J.-C. Feng, "Measurements of Water Permeability in Unconsolidated Porous Media with Methane Hydrate Formation," *Energies*, vol. 6, no. 7, pp. 3622–3636, 2013.
3. A. Kumar, B. Maini, P. R. Bishnoi, M. Clarke, O. Zatsepina, and S. Srinivasan, "Experimental determination of permeability in the presence of hydrates and its effect on the dissociation characteristics of gas hydrates in porous media," *Journal of Petroleum Science and Engineering*, vol. 70, no. 1–2, pp. 114–122, 2010.
4. Y. Seol, and T. J. Kneafsey, "Methane hydrate induced permeability modification for multiphase flow in unsaturated porous media," *Journal of Geophysical Research*, vol. 116, no. B8, 2011.
5. Y. Sakamoto, T. Komai, K. Miyazaki, N. Tenma, T. Yamaguchi, and G. Zvoloski, "Laboratory-Scale Experiments of the Methane Hydrate Dissociation Process in a Porous Media and Numerical Study for the Estimation of Permeability in Methane Hydrate Reservoir," *Journal of Thermodynamics*, vol. 2010, pp. 1–13, 2010.
6. A. Johnson, S. Patil, and A. Dandekar, "Experimental investigation of gas-water relative permeability for gas-hydrate-bearing sediments from the Mount Elbert Gas Hydrate Stratigraphic Test Well, Alaska North Slope," *Marine and Petroleum Geology* vol. 28, no. 2, pp. 419–426, 2009.
7. A. Johnson, S. Patil, and A. Dandekar, "Experimental investigation of gas-water relative permeability for gas-hydrate-bearing sediments from the Mount Elbert Gas Hydrate Stratigraphic Test Well, Alaska North Slope," *Marine and Petroleum Geology*, vol. 28, no. 2, pp. 419–426, 2011.
8. M. L. Delli, J. L. H. Grozic, "Experimental determination of permeability of porous media in the presence of gas hydrates," *Journal of Petroleum Science and Engineering*, vol. 120, pp. 1–9, 2014.
9. H. Liang, Y. Song, Y. Liu, M. Yang, and X. Huang, "Study of the permeability characteristics of porous media with methane hydrate by pore network model," *Journal of Natural Gas Chemistry*, vol. 19, no. 3, pp. 255–260, 2010.
10. R. L. Kleinberg, "Deep sea NMR: Methane hydrate growth habit in porous media and its relationship to hydraulic permeability, deposit accumulation, and submarine slope stability," *Journal of Geophysical Research*, vol. 108, no. B10, 2003.

# Mineralogical and Petrographic Characterization: An Indication of Fractability of Shale Gas Reservoir in the Blue Nile Basin, Sudan

Monera A. Shoieb, Nor Syazwani Zainal Abidin, Chow Weng Sum and Yassir Ibrahim

**Abstract** The production of gas and oil that plays an unconventional role in the world has affected the finances and the energy securities. The mineralogical characterization of shale rocks has a significant effect on the efficiency of shale gas, especially for drilling and production operations. This paper aims to study about the qualitative and semiquantitative minerals present in the shale samples of the Blue Nile and Dinder formations by using samples from two drilled wells. Twelve samples were analyzed in detail with the following mineralogical techniques: X-ray diffraction (XRD) and scanning electron microscopy (SEM) with energy dispersive x-ray spectroscopy (EDS). The XRD and SEM results show that the shale samples have clay minerals such as illite, kaolinite, and chlorite, as well as non-clay minerals such as quartz and pyrite. Other minerals compositions are feldspar, dolomite, and calcite. Scanning electron microscope (SEM) provides a high-resolution image of geometry, and EDS confirms the minerals that found in XRD. These types of minerals will be used to aid the exploration and development of shale gas, especially in the fractability.

**Keywords** Shale gas · Blue Nile Basin · Clay mineral · Fractability

---

M.A. Shoieb (✉) · N.S.Z. Abidin · C.W. Sum · Y. Ibrahim  
Geoscience Department, Universiti Teknologi PETRONAS,  
32610 Bandar Seri Iskandar, Perak Darul Ridzuan, Malaysia  
e-mail: Monera1710@gmail.com

N.S.Z. Abidin  
e-mail: NorSyazwani.z@petronas.com.my

C.W. Sum  
e-mail: chow\_wengsum@petronas.com

Y. Ibrahim  
e-mail: yasirovic2009@gmail.com

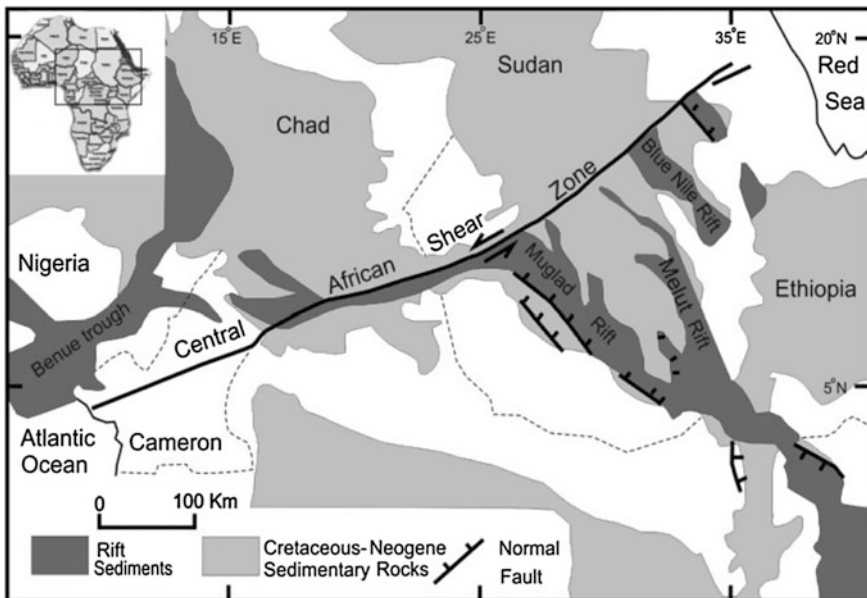
## 1 Introduction

Shale gas is a natural unconventional gas that is produced from low-porosity and low-permeability shale rich in organic matter [1]. Interestingly, the production of shale gas has increased remarkably worldwide due to its potential for an essential natural gas supply source. It is geographically widely distributed with major capacities in the USA [2, 3], UK [4, 5], and other countries.

It is important to know about the mineralogy of a shale formation, especially for drilling and production operations. Mineralogy can provide information about the geological setting [6]. Shale has low matrix porosity and permeability, so in order to take production in commercial quantities from this type of reservoir, we have to do fracturing to increase the permeability, and ministrals give information about the fractability [7]. High-productive shale gas wells in North America generally have clay fractions less than 40% (wt%) and quartz fractions exceeding 40%. Sondhi and Britt et al. [6, 8] concluded that fractures are more prevalent and are created more easily in silica-rich and carbonate-rich shales than in clay-rich shales.

Blue Nile Basin is the area under investigation (Fig. 1), which is located in the eastern part of North Sudan, and it is one of the several Mesozoic basins in Sudan associated with the Central African Rift System (CARS) (Fig. 1).

According to the previous studies reviewed, no systematic mineralogical characterization for fracturing has been carried out in this basin. Therefore, the major



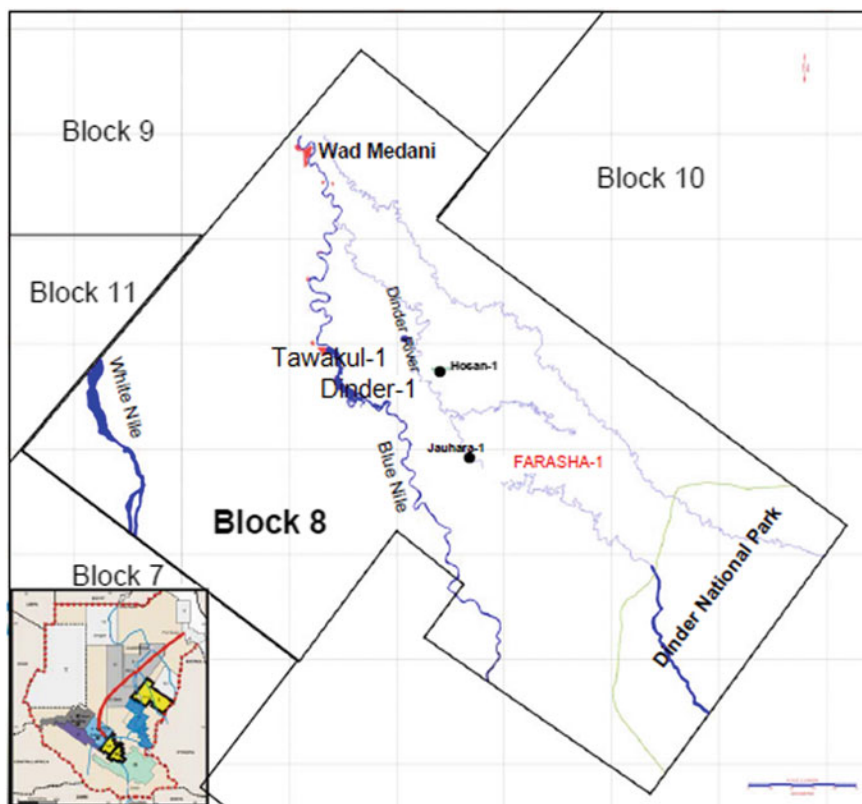
**Fig. 1** Regional tectonic map of central African rifted basins showing the Blue Nile Basin and study area [9]



goals of this work are to visually evaluate the mineralogy of the shale quantitatively and qualitatively; their impact on the fractability; and, hence, the production of shale gas in the Blue Nile Basin by integrating the mineralogical and petrographic techniques such as X-ray diffraction (XRD), energy dispersive x-ray spectroscopy (EDS) and scanning electron microscope (SEM). Knowing the mineral composition of shale samples in the focused basin will provide a reference study for the future unconventional resources.

## 2 Materials and Methods

For this study, a number of twelve shale samples were collected from two drilled wells, namely FARASHA-1 (FR-1) and TAWAKUL-1(TW-1) which are located in the east and west of Dinder-1 well (Fig. 2). Geological researchers show that the Blue Nile Formation is the main source rock for the Blue Nile Basin with the



**Fig. 2** Location map of the study area

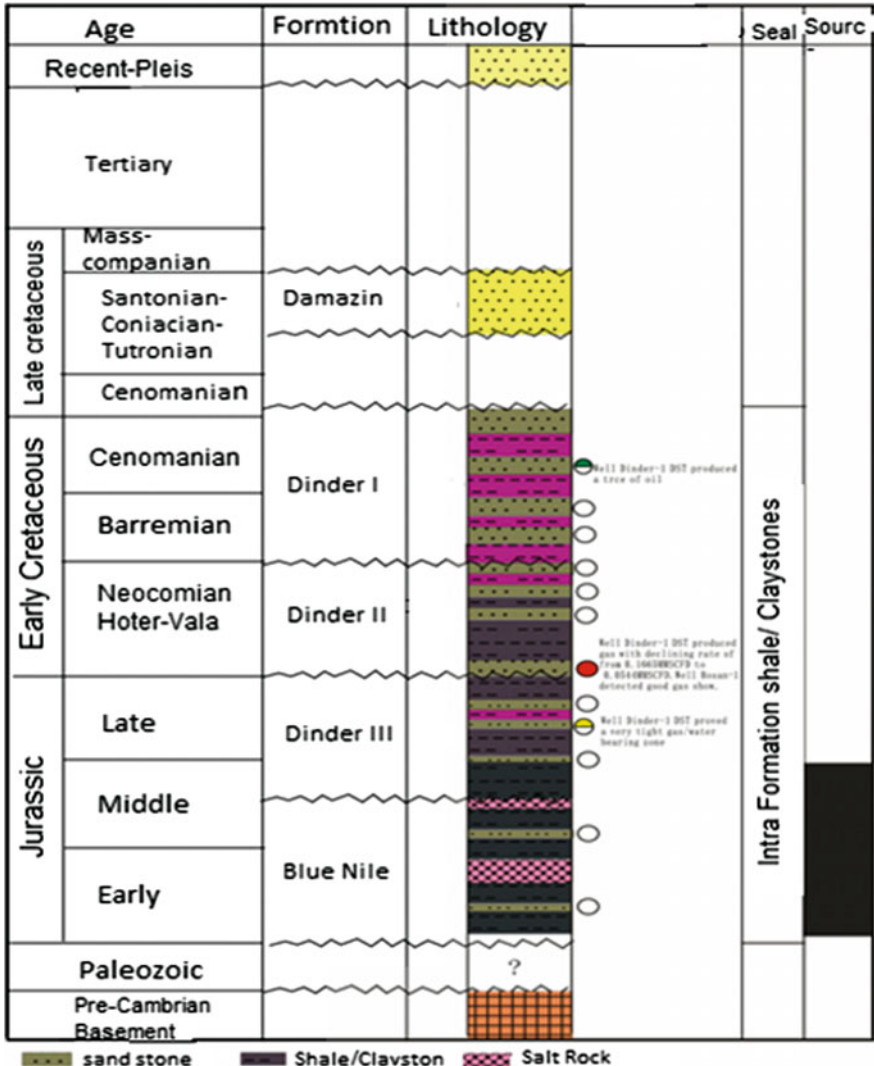


Fig. 3 General stratigraphic column of the Blue Nile Basin, modified after [13]

lacustrine and marginal marine environment. And the stratigraphy of the Blue Nile Formation consists of gray-to-dark-gray claystone and fine sandstone, whereas the Dinder Formation consists of interbedded claystone, siltstone, and sandstone (Fig. 3). All cutting samples were assessed experimentally using X-ray diffraction (XRD) analysis and scanning electron microscope (SEM) with energy dispersive x-ray spectroscopy (EDS). XRD is the most prevalent tool in identifying the unknown crystalline materials [7]. It was performed by grinding the shale sample into powder. SEM is a known tool used for investigating and imaging the

microstructure of rocks, including shale gas [10–12]. This depends on the interaction of the electron as it moves through the material. EDS is a useful method, which gives the estimate of the quantitative crystalline compound that is present in the shale samples.

### 3 Result and Discussion

#### 3.1 X-ray Diffraction (XRD)

The results of all samples show that the Blue Nile and Dinder formations have different mineralogical compositions that consist of quartz, chlorite, calcite, and kaolinite as the main mineral composition. The other constituents are feldspar, dolomite, illite, goethite, and pyrite (Fig. 4). The clay minerals are the most primary mineralogy of the Blue Nile and Dinder shale samples, and non-clay minerals such as quartz and pyrite are the second most abundant phase. The minerals were determined by the combination of d-space and 2 theta data. Clay minerals were also favorable for the development of the shale gas reservoir. In addition, pyrite indicates the existence of organic matter. Illite and chlorite are non-swelling clay

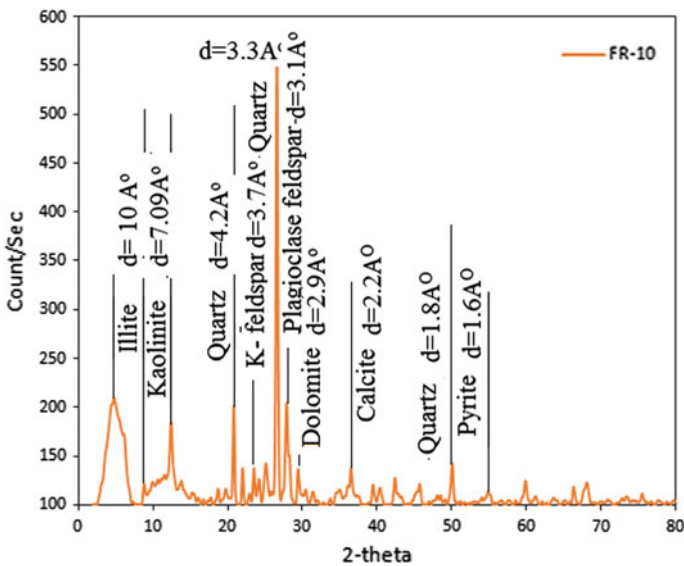


Fig. 4 XRD spectrum of samples from Blue Nile and Dinder formations

minerals, and they improve the brittleness of the shale. However, the presence of brittle minerals such as quartz will be easier in hydraulic fracture.

### 3.2 Scanning Electron Microscope (SEM) and Energy Dispersive X-ray Spectroscopy (EDS)

To image the mineral morphology and determine the chemical composition of the samples, scanning electron microscope (SEM) equipped with energy dispersive x-ray spectroscopy (EDS) analysis was used. Figure 5 shows the SEM images of typical shale sample for TW-1 and FR-1 wells. With increasing magnification, the grain structure can be clearly visualized. Energy dispersive x-ray spectroscopy (EDS) results showed that the elemental composition of shale is dominated by silica,

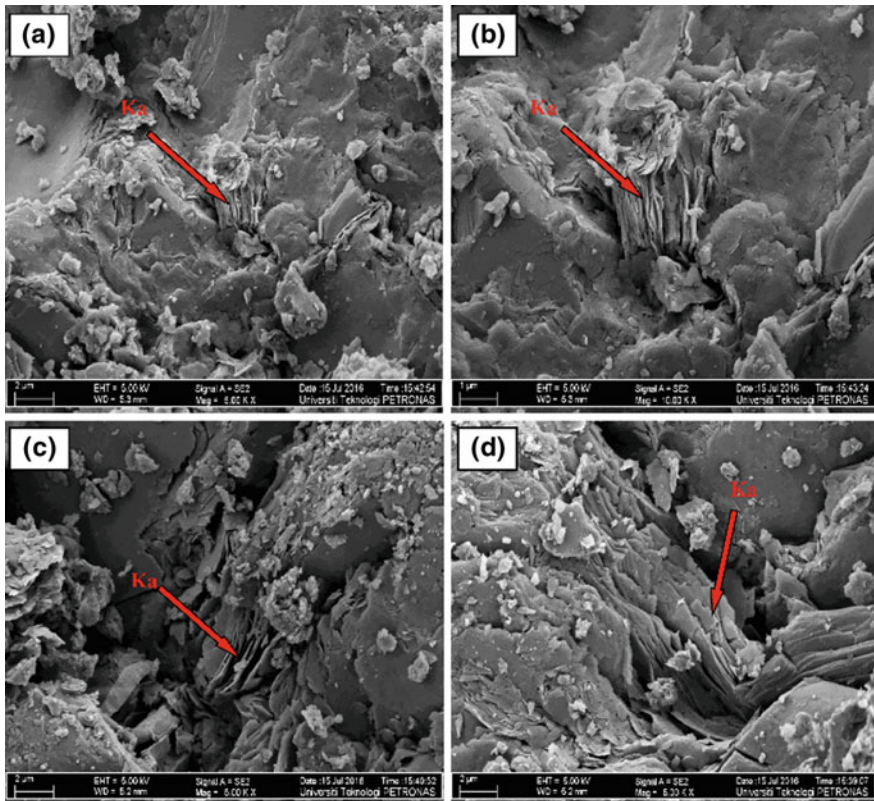


Fig. 5 SEM images of shale specimen in high magnification from FR-1 and TW-1

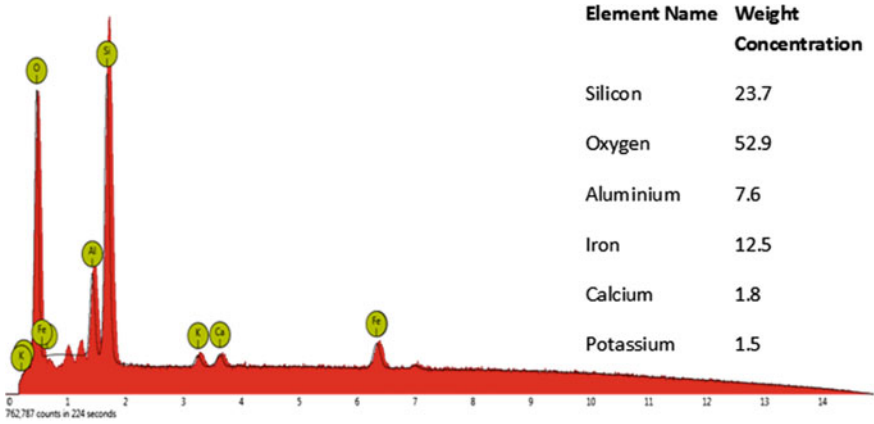


Fig. 6 3 EDS spectrum analyses of shale sample

oxygen, and with similar amounts of ferrous, calcium (ca), and potassium (k). Heavy minerals included strontium (Sr), barium (Ba), and rubidium (Rb). Si and oxygen normally indicate the presence of silica, while Fe, Ca, and potassium indicate the presence of clay minerals as well as mica (Fig. 6).

SEM also could provide information on mineralogy as well as morphology. Mineralogic composition of the shale from SEM is represented by dominant clay mineral (illite) of elongated and crenulated flakes. Potash feldspar is identified by its relatively large irregular shaped grains. Quartz of silt size also present in minor quantity (Fig. 7).

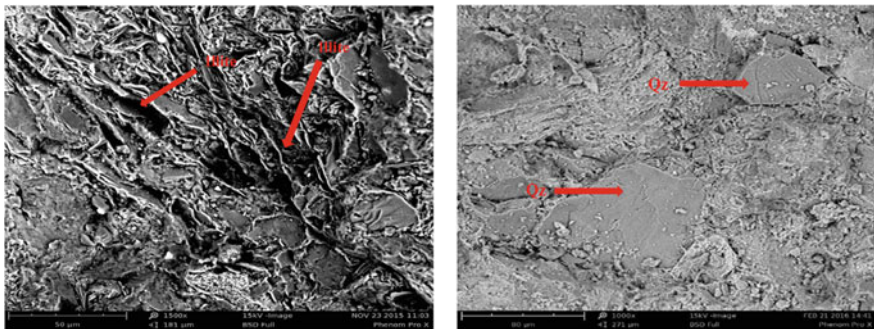


Fig. 7 a illite of elongated and crenulated flakes and b quartz has large irregular shaped grains

## 4 Conclusion

This paper investigated the mineralogical and petrographic characteristics of the shale gas in the Blue Nile and Dinder formations to indicate the fractability of such shale. The shale contained large amounts of different minerals. Clay minerals (illite, kaolinite, and chlorite) and non-clay minerals (quartz and pyrite) were identified in the samples by SEM and EDS, and then confirmed by XRD. From the petrographic characterization, shale was found to compose elongated and crenellated flakes of illite with pores up to 10 microns in size. All results were integrated to provide an indication of shale fractability. Compared to fractability scales in the literature, this shale can be classified as one of the low-to-medium fractal shales. Therefore, to take production in commercial quantities from this type of reservoirs, fracturing is recommended to increase the permeability, because shale has low matrix permeability.

**Acknowledgements** The authors thank Universiti Teknologi PETRONAS for the graduate assistantship of this research project under the “Graduate Assistantship Scheme,” and also thank Ministry of Petroleum in Sudan for providing the samples.

## References

1. K. Perry and J. Lee, “Unconventional gas reservoirs: tight gas, coal seams, and shales,” *Working Document of the NPC Global Oil and Gas Study*, vol. 18, p. 14, 2007.
2. M. W. Peebles, “Evolution of the gas industry,” 1980.
3. D. Donohue, N. Anstey, and N. Morrill, “Shale Gas in the Southern Central Area of New York State, US Dept.,” *Energy, Morgantown*, vol. 4, p. 578, 1981.
4. R. C. Selley, “UK shale gas: the story so far,” *Marine and petroleum geology*, vol. 31, pp. 100–109, 2012.
5. G. Swann and J. Munns, “The hydrocarbon prospectivity of Britain’s onshore basins,” *DTI, London*. p. 17, 2003.
6. N. Sondhi, “Petrophysical characterization of Eagle ford shale,” University of Oklahoma, 2011.
7. A. S. BUTT, “SHALES CHARACTERIZATION USING X-RAY DIFFRACTION,” 2012.
8. L. K. Britt and J. Schoeffler, “The geomechanics of a shale play: what makes a shale prospective,” in *SPE Eastern Regional Meeting*, 2009.
9. J. Fairhead, “Mesozoic plate tectonic reconstructions of the central South Atlantic Ocean: the role of the West and Central African rift system,” *Tectonophysics*, vol. 155, pp. 181–191, 1988.
10. G. Chalmers, R. Bustin, and I. Powers, “A pore by any other name would be as small: the importance of meso- and microporosity in shale gas capacity,” in *AAPG Annual Convention and Exhibition, Denver, Colorado*, 2009, p. 1.
11. F. P. Wang and R. M. Reed, “Pore networks and fluid flow in gas shales,” in *SPE Annual Technical Conference and Exhibition*, 2009.
12. M. E. Curtis, R. J. Ambrose, and C. H. Sondergeld, “Structural characterization of gas shales on the micro- and nano-scales,” in *Canadian Unconventional Resources and International Petroleum Conference*, 2010.
13. G. R. A. o. t. S. R. R. International, “Well evaluation,” *unpublished*, pp. 2–56–2–57, 1991.

# Effect of Surfactant on Wettability Change and Enhanced Shale Gas Recovery

Muhammad Ayoub, Syed M. Mahmood, Mysara E. Mohyaldinn, Shiferaw Regassa Jufar and Mudassar Mumtaz

**Abstract** Shale gas is one of the unconventional gas reservoirs with high potential in the future. One of challenges of shale gas extraction is most of the gas remains adsorbed in the shale reservoirs. Thus, the production of adsorbed gas is very difficult to extract. The purpose of this project is to carry out a comparative analysis on the effect of various surfactants consisting of anionic, cationic, nonionic, and amphoteric surfactants for increasing the productivity of shale gas recovery. This study is based on experimental methodology. Surfactant plays an important role in IFT reduction and changing wettability, thus increasing the gas production. This study has been carried out by using BET machine in order to obtain methane adsorption and desorption isotherm. So, the results of methane adsorption and desorption isotherm without surfactant and with various surfactants were compared. Although the results of adsorption and desorption isotherm after injecting different types of surfactant do not go along with expected trend, adsorption can be decreased since surfactants can encourage methane gas to be desorbed. Anionic, cationic, and amphoteric surfactants can change wettability in shale gas that increases gas adsorption. Amphoteric surfactant can improve the adsorption isotherm of methane gas most effectively; thus, the productivity of shale gas recovery will be maximized.

**Keywords** Adsorption isotherm · BET · Methane · Surfactant · Shale gas

## 1 Introduction

Shale is a fine-grained, rich-clay formation which has been deposited in low-energy environment [13]. In unconventional gas reservoir, shale can entrap the gas in the matrix pore spaces that can carry large amount of gas. Free gas is flowing in the shale

---

M. Ayoub (✉) · S.M. Mahmood · M.E. Mohyaldinn · S.R. Jufar · M. Mumtaz  
WasinWitoontorn, Department of Petroleum Engineering, University Teknologi  
PETRONAS, 32610 Seri Iskandar, Perak, Malaysia  
e-mail: muhammad.ayoub@petronas.com.my

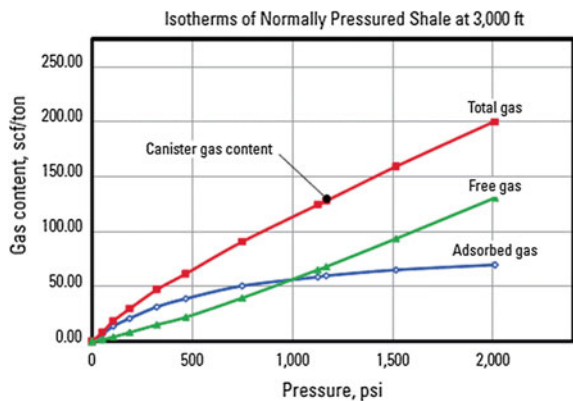


porous media at equilibrium stage. As the free gas passes through the pores or fracture, the gas is absorbed into the pores. The adsorbed gas approaches the organic matter and dissolved gas is generated in kerogen body. Once the drilling operation interferes into the equilibrium stage, gas naturally flows from high pressure to low pressure as free gas, adsorbed gas, and dissolved gas, respectively [9]. In order to introduce the storage mechanism in shale gas, [13] defined the ability of gas to release from or through the surface as desorption. This is the opposite of adsorption which occurs when gas comes in contact with organic matter. Desorption is now noticeable as an important parameter in the natural gas recovery for adsorbed gas in shale [2]. Large amount of shale formation consists of organic matter in the form of kerogen, methane gas to be produced from shale formation (Fig. 1).

Extracting gas from shale formation deals with wettability. Wettability is an important factor controlling the fluid behavior in hydrocarbon recovery process [3]. Wettability is defined as the preferential tendency of one fluid to wet the porous media of the rock in the presence of immiscible fluid. There are four states of wettability such as oil wet, water wet, frictionally wet, and mixed wet. Additionally, [10] defined gas wettability as the displacement capability of gas phase influencing to solid phase under solid–gas–liquid system. This may reduce Gibbs free energy of surface (Fig. 2).

However, to clarify the wettability of shale gas is still under research. [11] stated that one of the methods that can quantify the wettability of shale is to measure spontaneous imbibition of aqueous phase. However, inhibition in shale can cause the connectivity reduction in the fracture after injecting the hydraulic fracturing fluid as the fracturing fluid gets imbibe in the interstitial pores. Industry always uses hydraulic fracturing to increase the production in shale gas process by freshwater. [6] stated that hydraulic fracturing job by injecting water into shale reservoir can cause water to be trapped inside the reservoir. This affects to reduce the relative

**Fig. 1** Isotherm of normally pressured shale at 3,000 ft [12]





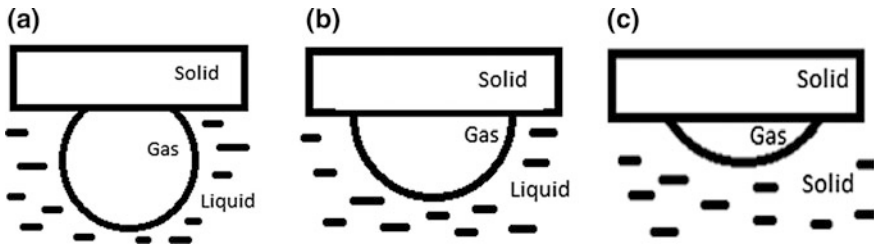


Fig. 2 a Nongas wet. b Intermediately gas wet. c Preferentially gas wet [10]

permeability of gas. By reducing the interfacial tension between water and hydrocarbon, more water can be recovered, thus increasing overall gas production. [6] also supported that surfactants do reduce the IFT between water and hydrocarbon after proving from experiment that surfactants with more than 10 EO groups can reduce interfacial tension between pentane and water from 70 mN/m to approximately 5 mN/m.

Surfactant is an organic compound with chemical structure. It consists of two different components such as hydrophobic group and hydrophilic group. Each group has specific characteristics, for instance, hydrophobic is water-hating or tail and hydrophilic is water-loving or head. Hydrophobic always drives water off and attaches with organic solvent, while hydrophilic likes to attach itself with water molecule. With different interaction, surfactant plays an important role in attacking the interface of two immiscible mediums with decreasing interfacial tension. Anionic surfactant is commonly used in industry and contains approximately half of global production. This surfactant is disassociated in water as affinity of anion and cation forms alkaline metal. Amphoteric surfactant properties are existed when surfactant shows dissociation of both anionic and cationic surfactants. This surfactant is generally expensive. Cationic surfactant is disassociated in water as affinity of anion with cationic polar. Most of cationic surfactants consist of halogen group. Nitrogen compound is very significant part in cationic surfactant. Nonionic surfactant properties are represented obviously by name since the surfactants do not ionize in aqueous solution, because hydrophilic group of nonionic surfactant is dissociable.

Surfactants play an important role to reduce interfacial tension between solid and gas; thus, gas can be released easier. Wettability change by surfactant with increasing in production relates to adsorption and desorption isotherm as the shale gas is generated by adsorption. Therefore, adsorption and desorption of isotherm is possible to evaluate the wettability change in shale gas production.

## 2 Materials and Methods

Sodium dodecyl sulfate-SDS ( $C_{12}H_{24}NaSO_4$ ) is anionic surfactant. Polyethylene glycol tert-octylphenyl ether, Triton X100, is nonionic surfactant. BETAINE ( $C_5H_{11}NO_2$ ) is an amphoteric surfactant. CTAB ( $C_{19}H_{42}BrN$ ) is cationic surfactant. All chemicals were used as received. Surfactant is used to decrease the surface tension and acts as detergents. Their physical and chemical properties make them possible to increase the desorption capacity and decrease the sorption capacity of organic matters, i.e., kerogens has large surface area and more sorption capacity. The properties are summarized in Table 1.

Shale gas sample was collected from local shale formation in Malaysia as the shale gas outcrop. Sample was crushed by hammer and screened through sieve to obtain particles lesser than 63  $\mu$ .

Surfactant solutions were prepared in 1000-mL volumetric flasks. Original surfactants were weighed and mixed with distilled water to get 1 wt% concentration. After preparing each surfactant in 1% wt concentration, crushed shale samples were put in the tube and treated with different categories of surfactants. After 24 h of surfactant treatment, shale samples were centrifuged to separate solution and crushed shale sample. Crushed shale samples were dried in oven for 24 h.

Before proceeding for adsorption and desorption isotherm measurement, the crushed shale samples were dried at 100 °C under vacuum condition for 6 hours. Then, samples were weighed. Adsorption and desorption isotherm was determined by BET Machine (BELSORP MINI-II). Samples after pretreatment were weighed and added in sample cell with one-third of sample cell volume. Sample cells were installed in BET machine. Methane gas was fed into the system under pressure at 101.3 kPa with temperature at 298.2 K (Fig. 3).

## 3 Results and Discussions

This part presents and discusses the experimental results of adsorption and desorption isotherm without surfactant and various surfactants.

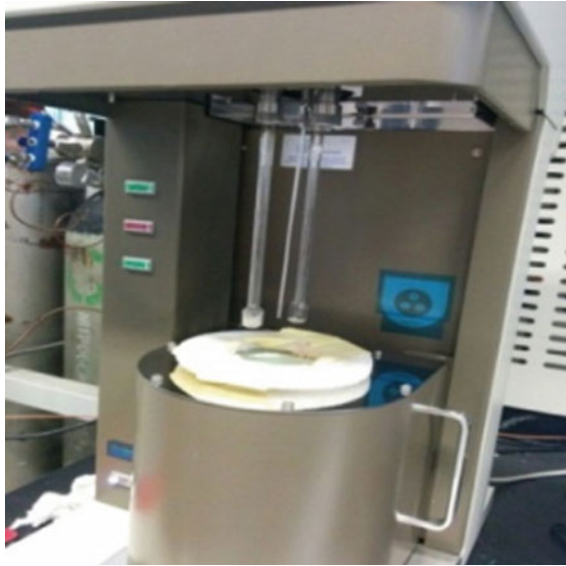
Figure 4 represents the methane adsorption decrease along with the increase in pressure ratio. This isotherm was used as the reference compared with adsorption and desorption isotherm after treating with various surfactants (Figs. 5 and 6).

Surfactants play an important role to reduce the interfacial tension between solid and gas; thus, gas can be released easier. Most of surfactants show the reduction in adsorption and desorption isotherm except anionic surfactant and amphoteric surfactant. Adsorption of gas onto shale gas at particular surfactant concentration can be determined by comparing the performance of methane adsorption and desorption isotherm as illustrated in Figs. 7 and 8.

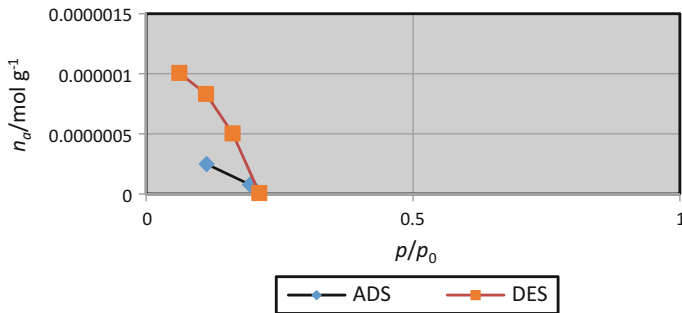
Ionized surfactant can increase the ability of adsorption and desorption compared to nonionic surfactant and without surfactant. From the range of graph in each case, including no surfactant injection and different types of surfactants, amphoteric

**Table 1** Showing properties of four surfactants (1, 4, 5, 7, 8)

Physical/chemical properties	Anionic	Nonionic	Amphoteric	Cationic
Bond	Hydrogen bond	Hydrogen bond	Hydrogen bond	Hydrogen bond
Molecular weight	288.379269 g/mol	<b>80,000</b> mg/L	117.15 g/mol	364.44748 g/mol
Physical description	Dry powder, Liquid and pellets Large crystals	Clear viscous fluid but less viscous than undiluted glycerol	White crystal powder	Dry powder
Water solubility	1,00,000 mg/L	Triton X-100 is soluble at 25 °C in water	In water, 6.11 × 10 + 5 mg/L at 19 °C 160 g/100 mL	1,00,000 mg/L

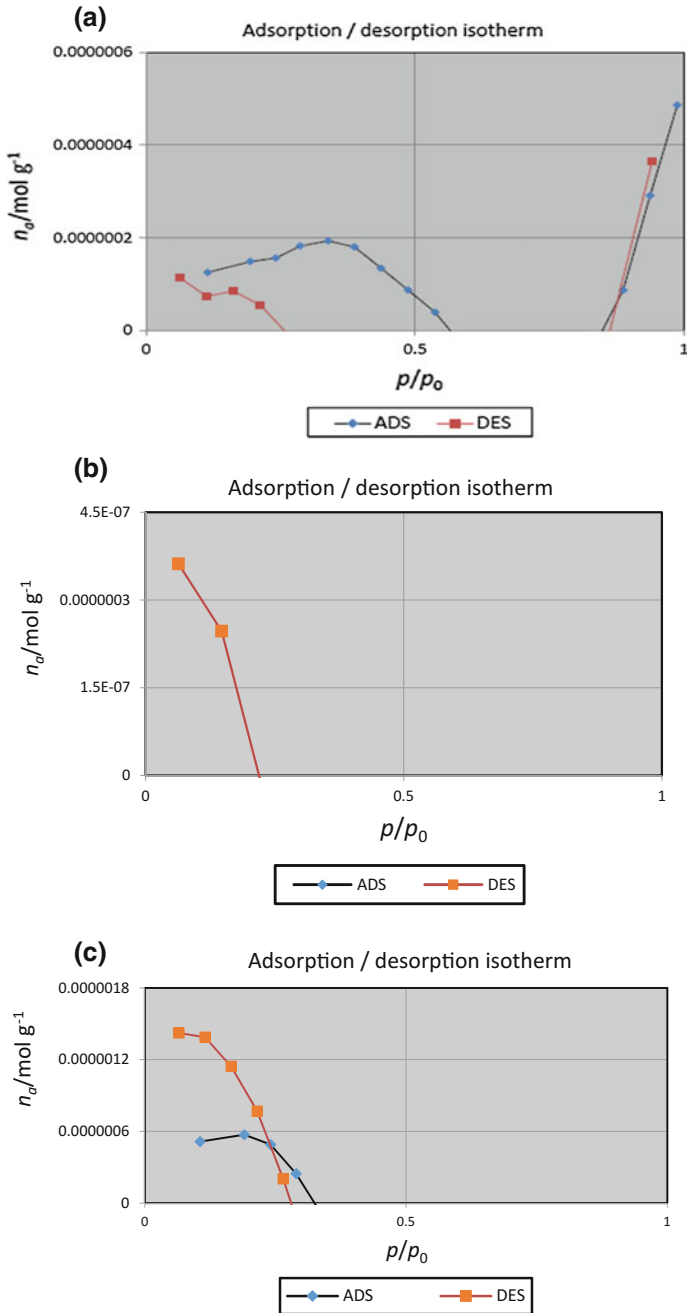


**Fig. 3** Install sample cell in BET machine

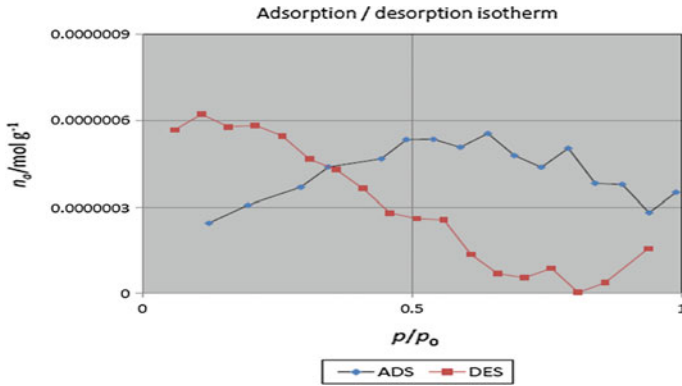


**Fig. 4** CH<sub>4</sub> adsorption and desorption isotherm without surfactant

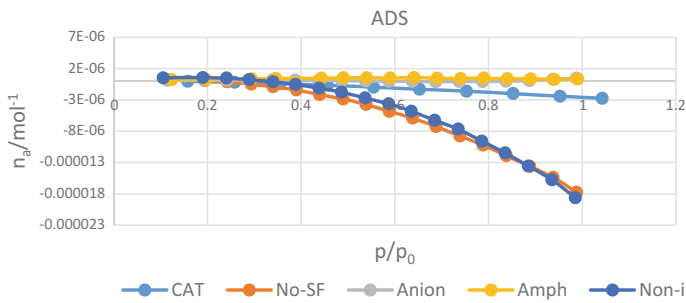
surfactant performs effectively to improve methane adsorption isotherm followed by anionic surfactant and cationic surfactant, respectively. It can be observed that amphoteric surfactant can change the wettability by reducing interfacial tension to produce more gas.



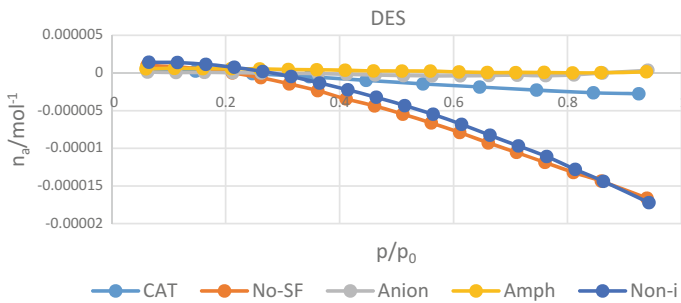
**Fig. 5** **a** represents CH<sub>4</sub> adsorption and desorption isotherm of shale sample after treating with anionic surfactant. **b** represents CH<sub>4</sub> adsorption and desorption isotherm of shale sample after treating with cationic surfactant. **c** represents CH<sub>4</sub> adsorption and desorption isotherm of shale sample after injecting nonionic surfactant



**Fig. 6** CH<sub>4</sub> adsorption and desorption isotherm after injecting **a** anionic **b** cationic **c** nonionic **d** amphoteric surfactant



**Fig. 7** Comparison between each surfactant's performance of methane adsorption isotherm



**Fig. 8** Comparison between each surfactant's performance of methane desorption isotherm

## 4 Conclusion

This project has been conducted to improve the difficulty of adsorbed gas extraction since most of the gas remains adsorbed in the shale reservoirs. Therefore, the experiment has been demonstrated to analyze various surfactants influencing wettability of gas behavior in shale gas and to investigate the potential of injected surfactants to increase the productivity of adsorbed gas recovery in shale gas formation. Adsorption and desorption isotherm without surfactant is tested. Surfactants were used to compare with adsorption and desorption isotherm after treating with different classifications of surfactants. Lastly, the result can be analyzed in accordance with the BET graph in adsorption and desorption isotherm. In conclusion, there is an improvement in methane adsorption isotherm after treating with surfactant. In this experiment, amphoteric surfactant can significantly improve the adsorption isotherm of methane. Wettability can be changed due to the reduction in interfacial tension from surfactant function; thus, shale gas recovery can be increased.

## 5 Recommendation

- This research can be improved by including other classification of surfactants on shale gas formation.
- With the study of wettability, measuring interfacial tension is recommended as the direct method to evaluate wettability change of shale gas.
- This experiment should be extended by using actual shale gas core sample from the field.
- The experiment can be improved by increasing surfactant solution concentration to obtain more visible result.

## References

1. CAMEO Chemicals Dodecyl sulfate, [sodium salt] <http://cameochemicals.noaa.gov/chemical/8602>.
2. Das, J. (2012). Extracting Natural Gas Through Desorption in Shale Reservoirs. *The Way Ahead*, pp. 11–13.
3. Donaldson, E., & Alam, W. (2008). *Wettability*. Houston, Tex: Gulf Publishing Company.
4. DrugBank Cetyl-Trimethyl-Ammonium <http://www.drugbank.ca/drugs/DB01718>.
5. EPA Chemicals under the TSCA1-Hexadecanaminium, N,N,N-trimethyl-, bromide (1:1) <http://www.epa.gov/chemical-data-reporting>.
6. Huynh, U.T. (December, 2013). *Surfactant Characterization to Improve Water Recovery in Shale Gas Reservoirs*.

7. HSDBSODIUM LAURYL SULFATE <http://tonet.nlm.nih.gov/cgi-bin/sis/search/r?dbs+hsdb:@term+@rn+@rel+151-21-3>.
8. ILO-ICSCSODIUMLAURYL Sulfate [http://www.ilo.org/dyn/icsc/showcard.display?p\\_card\\_id=0502](http://www.ilo.org/dyn/icsc/showcard.display?p_card_id=0502).
9. Javadpour, F. (August, 2009). Nanopores and Apparent Permeability of Gas Flow in Mudrocks (Shales and Siltstone). *Journal of Canadian Petroleum Technology*, 48(8), pp. 16–21.
10. Jiang, G., Li, Y. & Zhang, M. (2013). Evaluation of gas wettability and its effects on fluid distribution and fluid flow in porous media. *Petroleum Science*, 10, pp. 515–527.
11. Rezaee, R. (2015). *Fundamental of Gas Shale Reservoirs*. Wiley & Sons, Inc.
12. Schlumberger (2015). Adsorbed gas. *Oilfield Glossary*. Retrieved September 16, 2015 from [http://www.glossary.oilfield.slb.com/en/Terms/a/adsorbed\\_gas.aspx#](http://www.glossary.oilfield.slb.com/en/Terms/a/adsorbed_gas.aspx#).
13. Speight, J. (2013). *Shale gas production processes*. S.I: Gulf Professional.



**Part IV**  
**Advances in Geophysics and Reservoir**  
**Geoscience**

# A Diagenetic Facies Model for Characterizing Yanan Formation, Ordos Basin, North Central China

Ahmed Mohamed Ahmed Salim, Berihun Mamo Negash  
and Abubaker Mohamed Ahmed Alansari

**Abstract** Low-resistivity pay is a popular phenomenon in many sedimentary formations, and is present in clastic reservoirs of Yanan formation, Ordos Basin of North Central China. The reservoir quality of the studied sandstones is affected positively and negatively by several diagenetic processes, our classification is based on precipitation of pyrite and feldspar and clay minerals authigenesis. The main objective of this study is to integrate lithologic and diagenetic information of facies to correctly quantify the reservoir quality. Fifteen sedimentary lithofacies were described based on core description, thin section, and SEM analysis. The quantity and type of clay minerals are examined, using X-ray diffraction technique (XRD) and geochemical analysis using X-ray fluorescence technique (XRF), within the hydrocarbon bearing reservoirs. Facies are lumped together to create a composite database containing eight lithofacies associations. The calibration of log shapes and values by the core is used to establish the suite of logs that would be most suitable for the recognition and discrimination of the various types of facies and facies associations seen in cores before quantitative electro-facies analysis is carried out. Facies association model in the cored intervals is used to predict them in the un-cored intervals. BP-ANN has the most facies prediction power than discriminant function. In particular, with regard to the kaolinite- and pyrite-bearing facies Associations (FA8 and FA6), there is a >90% success rate at predicting the occurrence of them. Facies classification and clustering scheme used in this study are highly successful in prediction of porosity of reservoir rocks. The quality of the reservoirs is generally controlled by the lithologic and diagenetic behavior of rocks forming them.

---

A.M.A. Salim (✉) · B.M. Negash · A.M.A. Alansari  
Faculty of Geoscience & Petroleum Engineering,  
Universiti Teknologi PETRONAS, 32610 Seri Iskandar,  
Perak Darul Ridzuan, Malaysia  
e-mail: mohamed.salim@utp.edu.my

B.M. Negash  
e-mail: bmamo.negash@utp.edu.my

A.M.A. Alansari  
e-mail: Alan.abu@outlook.com

**Keywords** Yanan • Diagenetic facies and porosity

## 1 Introduction

The Ordos basin, with an area of 320,000 km<sup>2</sup>, is situated in the western part of the North China block, within the Yellow River drainage basin. The maximum thickness of the stratigraphic section in the Ordos Basin is in excess of 10 km [1].

The study area is near to the western margin of the fold-thrust belt of Ordos Basin. It covers an area of 848.88 km<sup>2</sup> and tectonically it can be divided into structurally stable eastern part; synclinal form central part and western thrust fault-fold zone. Delta front mouth bar and delta plain distributary channel sandstones in the Yanchang and Yanan Formations, of upper Triassic and Lower Jurassic respectively, are economic oil reservoirs in the area. The risk for successful hydrocarbon exploitation is extremely high because of complex stratigraphic relationships within the formations as well as local variability in reservoir-sandstone thickness, distribution, and quality.

Uplift of the Ordos Basin resulting from an isostatic rebound after the cessation of thrusting and rifting during the last stage of the Late Triassic produced a regional unconformity between Triassic and Jurassic formations. The overlying Lower Jurassic Fuxian Formation was deposited in local depressions developed on the pre-Jurassic erosional surface [2]. Deposition of the Yanan Formation over the western Ordos Basin after a period of uplift during the latest Early Jurassic commenced with the deposition of coarse-grained fluvial sediments at the base of the Yanan Formation. At the upper part of the Yanan Formation, the Ordos Lake of the Yanan period gradually dried and infilled with several parasequences consisting of fluvial and large, gentle-sloped lacustrine deltaic coal-bearing deposits sourced from the uplifted western flanks of the basin.

Yanan formation is well exposed in the central and northern parts of the basin. At the type locality, the formation is composed of two members and ten lithostratigraphic units comprising Yan10 through Yan1 from bottom to top. The lower member consists of fine- to coarse-grained sandstone with a basal conglomerate, and interbedded siltstone and shale in the upper part. The upper member consists of interbedded sandstone, mudstone, shale, and locally, coal and oil shale. In the southernmost part of the basin, Yanan is more complex. The reservoirs have good properties, with an average porosity of 18–20% and an average permeability of 50 md and a maximum permeability of 3000 md [3]. The shallow-lacustrine and swamp mudstones of the upper part of the Yanan Formation serve as a regional seal of the Lower Jurassic oil reservoirs, and the flood-plain mudstones that

superimposed above the sandstones provide direct seals. Stratigraphic traps are the principal trap types of the Jurassic oil accumulations. These traps include the unconformity onlap and pinch-out traps.

Many oil and gas reservoirs are contained in rocks formed by ancient deltas. Deltaic reservoirs often have complex internal architecture and properties [4]. Shales are the fundamental geologic control of the delta reservoir heterogeneity. Shales have variable effects in controlling reservoir behavior [5]. They may affect vertical permeability [6].

The term electrofacies was originally defined as a set of log responses that characterize a bed and permits it to be distinguished from the others [9].

Some efforts have been made to use statistical methods such as discriminant analysis to identify facies from well logs [7]. The past decade has also seen applications of Artificial Neural Network (ANN) [8] and fuzzy logic in facies classification [2]. All methods use a training data set consisting of observed cases with full information about both predictors (in our application, well-log readings) and groups (in our case, facies). Based on the training data set, one creates a rule (called a classifier) by which future observations of predictors can be used to infer probable group memberships.

Chemical processes in shales begin at an intermediate diagenetic level (80–140 °C), including the transformation of smectite to illite and liberation of organic acids from organic matter [9].

## 2 Methodology

The full core was taken from each of four cored wells for sedimentologic and petrophysical analysis. Core plugs (about 10 cm long) were taken at 0.4 + 0.24 m intervals from each cored section for porosity, and permeability measurements.

The detailed petrographical analysis is conducted on 24 thin sections using transmitted light optical microscopy, cathodoluminescence (CL), scanning electron microscopy (SEM) with energy dispersive X-ray spectroscopy (EDS).

Clay mineral analysis using X-ray diffraction technique (XRD) and geochemical analysis using X-ray fluorescence technique (XRF) are also conducted on selected samples from the reservoir intervals.

Well logs used for this study include calipers, induction logs (ILD, ILM) and LL8, dual laterolog (LLD, LLS) and MSFL, Gamma ray (GR), Spontaneous Potential (SP), Acoustic (AC) and borehole-corrected neutron log (CNL), and bulk density (DEN).

The depth shift, standardization, and normalization of logs from different wells is carried out using multi-well histogram and cross-plot displays of various logs as a routine data quality work.

Log readings calibrated by core observations is used for the recognition and discrimination of the various types of facies (F) and facies associations (FA) (training and validation) before quantitative electro-facies analysis is carried out within the whole study area.

Electrofacies analysis in this study is based on the discriminant function analysis and ANN approaches which involve two steps for facies classification and prediction: (1) creation of an electrofacies database with reference to the core-defined facies; and (2) assigning electrofacies to the unknown depth levels with reference to the electrofacies database and a linear discriminant function and pattern-processing of ANN functions.

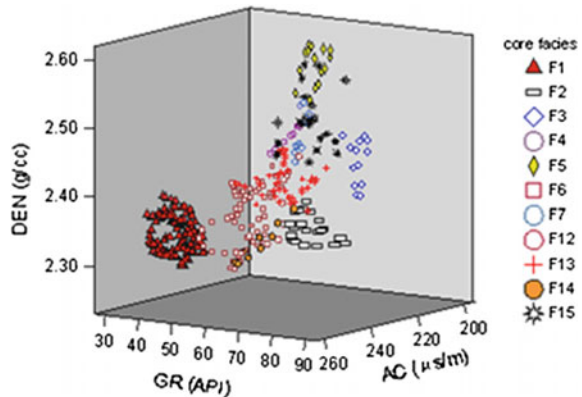
### 3 Results

Fifteen electrofacies (F1, F2, F3, F4, F5, F6, F7, F9, F12, F13, F14, F15, F16, clay and coal) could be created corresponding to fifteen core-defined facies using the same set of cross-plots (Fig. 1).

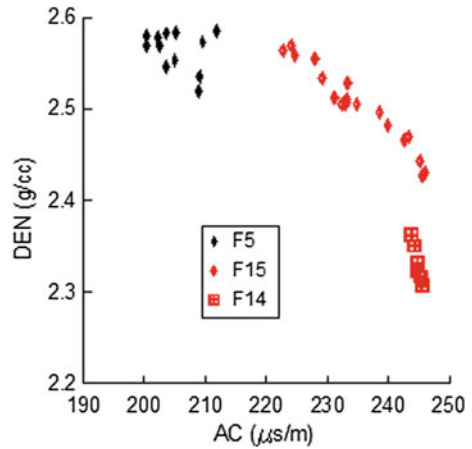
Pyritization is more effective than kaolinitization on DEN and AC (Fig. 2). This made the former affect petrophysical properties more than the latter i.e. kaolinitic sandstone is more porous than pyretic one.

Facies are lumped into facies associations including gravelly sub-litharenite (FA16), medium- to coarse-grained sedimentary sub-litharenite (FA15), fine-grained

**Fig. 1** 3D scatter plot of the study area facies



**Fig. 2** The effect of pyritization and kaolinization on AC-DEN logs

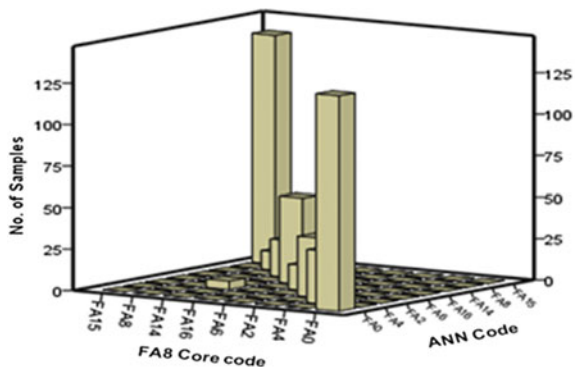


sedimentary sub-litharenite (FA14), arkose sandstone (FA12), kaolinitic sandstone (FA8), pyritic greywacke (FA6), mudstone (FA4) and coal (FA0).

### 3.1 Facies Association Prediction from ANN Approach

All facies associations, except FA14, are classified with 100% accuracy Fig. 3. 18.5% of FA14 is misclassified as FA12 because the igneous fragments can be changed to detritus feldspar of the arkose sandstone. The overall accuracy of this method was 98.9%.

**Fig. 3** 3D barplot of 8 FA using ANN method for training data sets



### 3.2 Discrimination Analysis of the Reservoir Zone Testing Data Set

The best measure of a predictive discrimination power is a classification of observations in the testing dataset. In the discussed example, the result of such a classification is given in Table 1. All facies associations are correctly classified with 100% accuracy percentage.

### 3.3 Porosity Estimation

Estimation of porosity in this work based on facies association (FA) concept. A multiple regression analysis of core porosity with a suit of well logs, GR, DEN, AC, and CNL, was applied based on acceptable correlation coefficient so as to predict porosities in uncored intervals of cored wells and other uncured wells.

Porosity estimation in different depth intervals for different wells, including both training and test data sets, was good (Fig. 4). The accuracy was increasing from fractured lithologies of porous facies, FA15, in A3 and A5 areas, the upper part of the figure, to FA16, FA4, FA8, FA6, and FA14 in A2 and A3 areas lower part of the figure.

**Table 1** Five facies associations’ classification results of the testing dataset

Facies association (FA)		Predicted facies association membership					No. of samples	
		FA15	FA8	FA14	FA16	FA6		
Core facies	Count	FA15	38	0	0	0	0	38
		FA8	0	31	0	0	0	31
		FA14	0	0	21	0	0	21
		FA16	0	0	0	55	0	55
		FA6	0	0	0	0	25	25
	%	FA15	100	0	0	0	0	100
		FA8	0	100	0	0	0	100
		FA14	0	0	100	0	0	100
		A16	0	0	0	100	0	100
		FA6	0	0	0	0	100	100

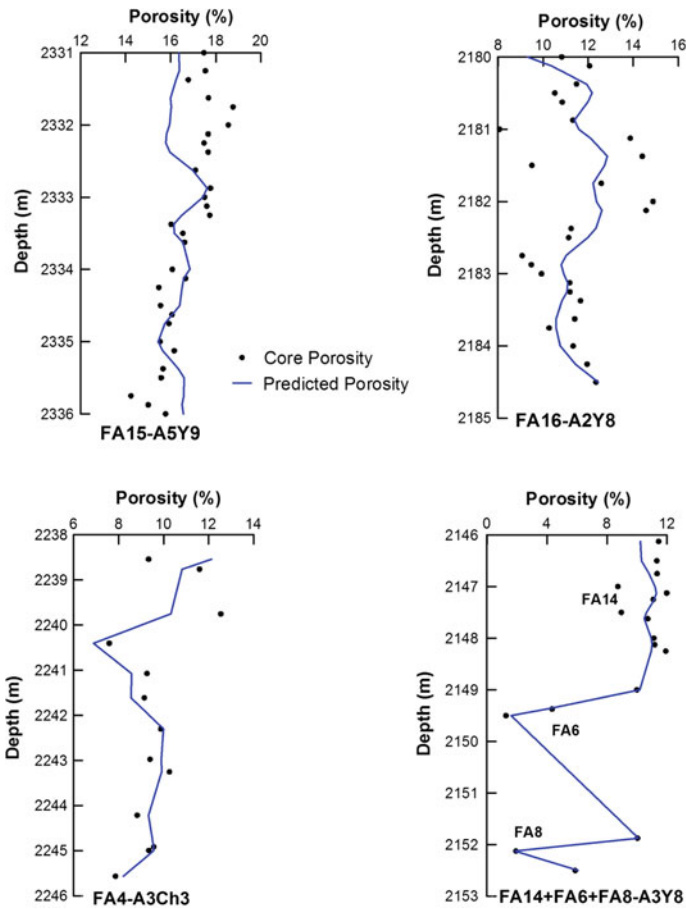


Fig. 4 Core and calculated Porosities for different facies associations

## 4 Conclusion

Well logs and core data; including detailed lithologic and diagenetic information; are integrated to classify facies of reservoir rocks in the study area.

Discrimination of those facies and their associations using back-propagation artificial neural networks (BP-ANN) and discriminant function analysis and a comparison between those techniques has been done.

The prediction accuracy of the eight facies association (FA), for the whole study area, in training dataset by ANN is 98.9%, and the prediction accuracy of the five reservoir sands facies association (FA) by discriminant function analysis using only four well logs, for both training and testing datasets, is 100.0%.



Facies association prediction helped in determining valid porosities for different units of the studied formation.

The above mentioned diagenetic transformations can be considered as some of the causes of low resistivity pays, increasing conductivity by pyrite and forming micro-resistivity by kaolinite.

## References

1. H., Tang, White, C., Zeng, X., Gani, M., Bhattacharya, J., Comparison of multivariate statistical algorithms for wireline log facies classification. AAPG Annual Meeting Abstract, vol. 88, 13, (2004).
2. M., Saggaf, and Nebrija, E., A fuzzy logic approach for the estimation of facies from wire-line logs. AAPG Bull. v.87 (7), 1223–1240(2003).
3. C.D., White, 3D Sedimentologic and geophysical studies of clastic reservoir analogous: facies architecture, reservoir properties and flow behavior within delta front facies elements of the cretaceous Wall Creek member, Frontier formation, Wyoming, DOE Continuation Research Proposal (2001).
4. M. D., Barton, Yeh, J. Angle, E. S. Carrasco, B. N. and Becker, M. R., Architecturally constrained spatial modeling of permeability with a fluvial sandstone body, Cretaceous Acu Formation, Brazil. AAPG Bulletin. 80, 1272–1273 (1996).
5. R. S., Surdam, Dunn, T. L., MacGowan, D. B., and Heasler, H. P., Conceptual models for the prediction of porosity. Evolution with an example from the Frontier Sandstone, Bighorn Basin, Wyoming. In Coalson, E. B., Ed., Petrogenesis and petrophysics of selected sandstone reservoirs of the Rocky Mountain region: Rocky Mt. Assoc. Geol., 7–28, (1989).
6. S. H., Begg, and King, P. R., Modeling the effects of shales on reservoir performance: calculation of effective permeability. 1985 Society of Petroleum Engineers Reservoir Simulation Symposium, Dallas, TX, Feb. 10–13, paper SPE no. 13529 (1985).
7. G., Song, Jurassic channel deposits and the formation of oil pool, southern Ordos basin. In: Sedimentary Facies and Oil, Gas Distribution of Oil-Bearing Basins in China. pp. 217–229. Petroleum Industry Press, Beijing (in Chinese), (1989).
8. A., Bhatt, and Helle, H. B., Determination of facies from well logs using modular neural networks. Pet. Geosci., v.8 (3), 217–228 (2002).
9. O. Serra, and Abbot H., The contribution of logging data to sedimentology and stratigraphy. SPE. 55 the Annual Fall Technical Conference and Exhibition, Dallas, Texas, paper No. 9270 (1980).

# Core Lithofacies Analysis of Reservoir Interval (Albian—Cenomanian) Bentiu Formation of SE Muglad Basin, Sudan

Ahmed Ali Hassan Taha, Abdel Hadi Abd Rahman, Wan Yusoff Wan Ismail, Ahmed Mohamed Ahmed Salim and Jamal Rajab

**Abstract** This study presents the analysis of lithofacies of the subsurface reservoir horizon of Bentiu Formation (Late Albian—Cenomanian) from the SE Muglad basin in Sudan. A detailed core description to analyze and study the different lithofacies, facies association, and architectural elements and to infer the depositional environment is conducted. The study reveals the presence of seven sedimentary lithofacies (massive sandstone, horizontal or parallel-laminated sandstone, planar cross-laminated sandstone, trough cross-laminated sandstone, ripple-laminated sandstone mudstone and sandy mudstone, and conglomerate.) they can be grouped into two major facies as sandstones and conglomerates, and one minor mudstone and sandy mudstone facies. These facies are grouped into five facies associations, which represent the elements of fluvial depositional systems. They can be distinguished from their different stacking patterns. Sandstone which is ranging in grain size from fine to coarse is characterized by massive, cross-laminated, ripple-laminated, parallel-laminated structures, and some bioturbation sedimentary features. These sandstones are also characterized by fining-upward sequence indicating fluvial braided stream depositional environment.

**Keywords** Muglad Basin · Bentiu Formation · Facies analysis · Depositional environment

## 1 Introduction

Muglad Basin is the largest among the Central African Rift System (CARS), and it hosts most of the Sudan and South Sudan proved oil. It extends over a surface area of approximately 120,000 Sq km—trending NW–SE. The northwest end of this basin terminates at the Central African Shear Zone (CASZ), [1]. To the south, the

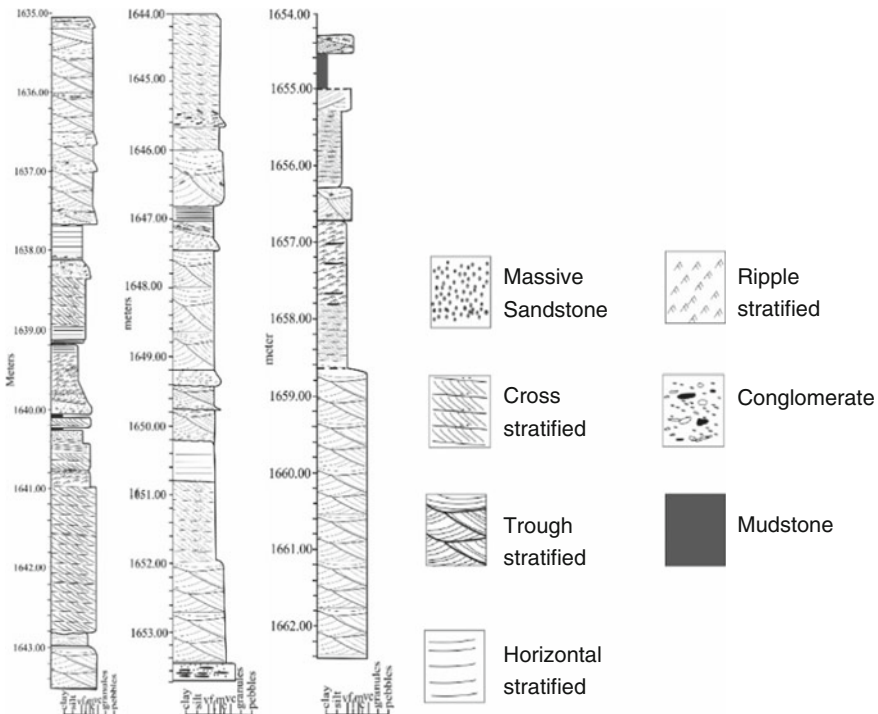
---

A.A. Hassan Taha (✉) · A.H.A. Rahman · W.Y. Wan Ismail · A.M. Ahmed Salim · J. Rajab  
Department of Petroleum Geosciences, Faculty of Geosciences and Petroleum Engineering,  
Universiti Teknologi PETRONAS, Seri Iskandar, Perak, Malaysia  
e-mail: Ahmedtaha75@yahoo.com

Sudanese rift structures tend to funnel together and their extension further is obscured by later Cenozoic volcanic rocks [2]. Volcanic activities in the Muglad Basin are minor compared with a Tertiary rift of East Africa, [3].

The main prolific horizon in this basin is Bentiu Formation followed by Darfur Group Formations. These reservoirs are sourced from Sharaf to Abu Gabra formations. The stratigraphic succession of the Muglad Basin is shown in Fig. 1.

The Bentiu Formation which is the main reservoir interval in the Muglad Basin consists predominantly of thick sandstone sequences interbedded with thin siltstone and claystone facies of continental fluvial environment mainly of braided and meandering streams. This formation which overlies the Abu Gabra Formation terminated at the oldest rifting episode in southwest Sudanese basins. The top of the formation is marked by an unconformity separated by the formation from the overlying Darfur group. On the ground of subsurface lithofacies detailed examination, cores and wire-line logs, [4] subdivided the Bentiu Formation into a lower, middle, and upper part in the Heglig and Unity fields. The lower Bentiu Formation is characterized by interbedded channel/bar sandstone and overbank/floodplain facies, deposited in stacked fining-upward sequences. These sequences seem to have been deposited in moderately deep mixed load high sinuosity streams with limited or no lateral movements. The high sinuosity meandering stream may represent the possible depositional model of this part with the channel, point bar, and



**Fig. 1** Shows detailed core description from the well (A) Heglig oil field SE Muglad Basin SW Sudan

minor channel elements. The middle Bentiu facies indicates deposition in low sinuosity braided stream environment. The fluvial environment represents sand-bed streams, which are intermediate between braided and meandering rivers. This region is characterized by the domination of cylindrical and bell gamma-ray shapes, with the prevalence of the latter. Sandstone facies, especially coarse-grained sandstone, which can be cross-bedded, dominate other facies. The upper Bentiu Formation is characterized by the domination of stacked bell and cylindrical shapes. The bell shapes dominate and are more compact than those found in the middle section. The upper Bentiu was deposited in braided stream environments. This is indicated by the presence of thick stacked sandstone bodies, with interbedded, thin mudstone facies. The most dominant facies consists of coarse-grained sandstone [4]. The Bentiu Sandstone consists of a series of sandstones interbedded with claystone. Sandstones are medium to coarse grained and less consolidated than the overlying formations, generally deposited in a braided stream environment with high  $R_w$  (RRI, 1991).

The reservoir qualities are good according to the petrophysical evaluation and adjacent productive fields both Lower and Upper Cretaceous non-marine sandstones are the principal reservoirs in the Muglad Basin. Channel delta and fan sands of the Abu Gabra Formation and floodplain, braided stream, and alluvial fan sands of the Bentiu formation form a good-quality reservoir. The latter provides the reservoirs in the major Heglig, Unity, and Thar Jath accumulations. Upper Cretaceous non-marine clastic reservoirs are present in the Aradeiba, Zarqa, and Ghazal formations, all of which contribute to fields including Heglig, Unity, Talih West, and Thar Jath. Tertiary non-marine clastic reservoirs are restricted to the Upper Eocene lacustrine–floodplain sediments of the Tendi Formation, which, however, are only of minor importance.

The geological evolution of the basin can be divided into a pre-rift phase, three rift phases, and a sag phase. By the end of the Pan-African Orogeny (550 Ma  $\pm$  100 My), this region had become a consolidated platform. During the rest of the Paleozoic and Early Mesozoic time, this highland platform provided sediments to adjacent subsiding areas. The nearest preserved Paleozoic rocks are continental sediments in northwestern Sudan, near Chad and Libyan borders. The following three rifting phases have occurred in response to crustal extension, which provided the isostatic mechanism for subsidence. Rifting is thought to have started in the Early Cretaceous. Seismic and well data indicate that this initial and strongest rift phase lasted until almost the end of the Albian. The result of the early rift is stratigraphically marked by the basinwide deposition of the thick sandstones of the Bentiu Formation. The second rifting phase occurred during the Turonian–Late Senonian. Stratigraphically, this phase is determined in the widespread deposition of lacustrine and floodplain claystone and siltstones, which abruptly terminated the Bentiu Formation. This phase was characterized by minor volcanism. The end of this phase is marked by the deposition of the thick sandstone of the Paleocene Amal Formation. Final rifting began in the Late Eocene–Oligocene and is reflected in the sediments by a thick sequence of lacustrine and floodplain claystone and siltstones. The only evidence of volcanism in wells is the occurrence of thin Late Eocene

basalt flows in the southern Melut Basin, near Ethiopia. In the Middle Miocene, the basinal areas entered an intracratonic sag phase of very gentle subsidence accompanied by little or no faulting.

## 2 Methodology

The core of about 29.19 ms (~96 ft) from well A on the Heglig oil field was studied at the Data Centre, Ministry of Energy of the Sudan warehouse, and it provides good opportunities for studying the facies of the sedimentary record of the Bentiu Formation. Bentiu Formation is the main reservoir horizon in the SE Muglad Basin.

The main criteria used for defining the facies follow those of [5, 6] which have been adopted by many authors. These criteria mainly look for grain sizes, colors, sedimentary structures, the geometry of sedimentary bodies, and the presence or absence of identifiable plant remains. The codes used for the facies also agree with those used in the study [6]. The core was described carefully in 1:20 scale to insure detail features recognition.

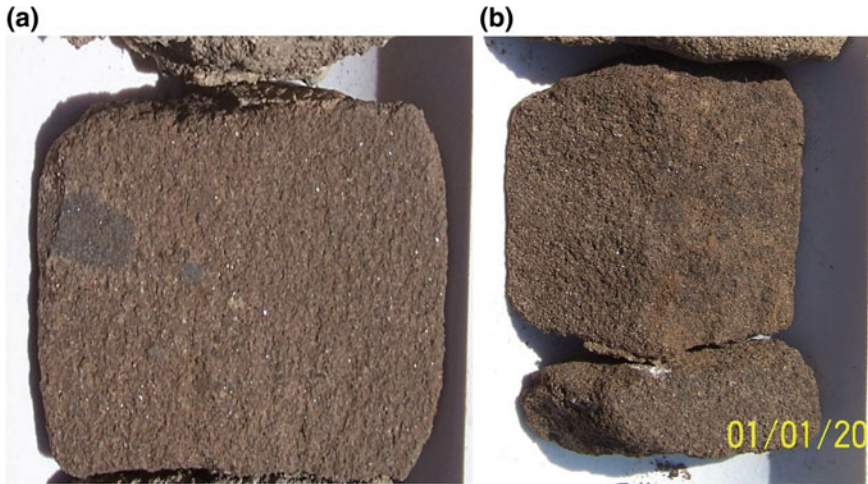
## 3 Result and Discussion

Detailed lithological core logging of about 29.19 m (~96 ft.) coupled with sedimentological studies, the core from selected well from the Heglig oil field in the SE Muglad Basin, Sudan, reveals the presence of seven lithofacies, all are of fluvial environment deposited in braided and meandering stream, and they can be distinguished as shown in Fig. 2:

1. Massive sandstone facies (Sm).
2. Horizontal or parallel-laminated sandstone (Sh).
3. Planar cross-laminated sandstones (Sp).
4. Trough cross-laminated sandstone (St).
5. Ripple-laminated sandstone (Sr).
6. Mudstones and sandy mudstones (Fm).
7. Conglomerate (Gh).

### 3.1 Sedimentary Facies Analysis

Seven facies were recognized in the studied intervals of the Bentiu Formation (Table 1), (core one, core two, and core three of the well A. Most of them are sandstone- to conglomerate-dominated. Mudstone-dominated facies are less.



**Fig. 2** Massive sandstone from core one well HE 28 at depth 1639.32–1639.37 m (a) and 1642.92–1643.12 m (b)

### 3.2 *Massive Sandstone Facies (Sm)*

#### 3.2.1 Description

These facies type was observed in core intervals (1640.25–1640.30) as in Table 2, and the graphic representation is shown in Fig. 1. It ranges in color from brown to dark brown, and light gray to dark gray. Grain size ranges from very coarse to coarse grains, with a gradual fining upward. The grains are sub-rounded to rounded and moderately sorted. Some iron oxides, quartz, and traces of carbonate are occurring as cement as in Fig. 2.

#### 3.2.2 Interpretation

Massive sandstone as shown in Fig. 2 is believed to have been developed in fluvial braided channel bar confirmed the presence of fluvial channel bar and association of trough cross-stratification. Very coarse grained is shown on core one of the wells. These sandstones are cemented with iron oxides and carbonates. This facies shows a cylindrical shape and it can be interpreted as deposited in high energy, low sinuosity braided stream.

**Table 1** Stratigraphic units of the Muglad Basin, SW Sudan, lithology, and deposition environment [8]

Formation		Lithology	Environment	Age	
Kordofan group	Zaraf fm	Predominantly iron-stained sand and silts with minor claystone interbeds	Braided stream/alluvial fans	Recent—Middle Miocene—Oligocene—Late Eocene—Paleocene	Tertiary
	Adoke fm				
	Tendi fm	Predominantly claystone/shale interbedded with sandstones	Fluvial/floodplain and lacustrine		
	Nayil fm				
Amal fm	Predominantly massive medium to coarse sandstone sequences	Braided stream/alluvial fans			
Darfur group	Baraka fm	Predominantly sandstones with minor shale and clay stones interbeds	Fluvial/alluvial fans.	Late Senonian—Turonian	Cretaceous
	Ghazal fm				
	Zarga fm	Predominantly sandstones, shales with interbeds of siltstones and sandstones	Floodplain/lacustrine with fluvial/deltaic channel sands.		
	Arabeiba fm				
Bentiu fm		Predominantly thick sandstone sequences.	Braided/meandering streams.	Cenomanian—Late Albian	
Abugabra fm		Predominantly claystone and shale with fine sandstones and siltstones	Lacustrine/deltaic	Albian—Aptian	
Sharaf fm.		Predominantly claystone and shale with fine sandstones and siltstones	Lacustrine/fluvial floodplain	Barremian—Neocomian	
Basement					

**Table 2** Different facies at different depths in different core intervals

Facies	Core 1 interval	Core 2 interval	Core 3 interval
Massive sandstone facies (Sm)	1640.25–1640.30	–	1656.00–1656.20
Horizontal- or parallel-laminated sandstone (Sh)	1637.60–1638.30 1640.30–1641.10		
Planar cross-laminated sandstones (Sp)		1644.00–1646.00	1654.00–1654.60
Trough cross-laminated sandstone (St)		1646.20–1646.86, 1649.08–1649.30	
Ripple-laminated sandstone (Sr)			1655.00–1655.90, 1656.20–1658.00
Mudstones and sandy mudstones (Fm)	1639.00–1639.24, 1639.80–1639.90		
Conglomerate (Gh)	1639.00	1646.00	

### 3.3 Horizontal- or Parallel-Laminated Sandstone (Sh)

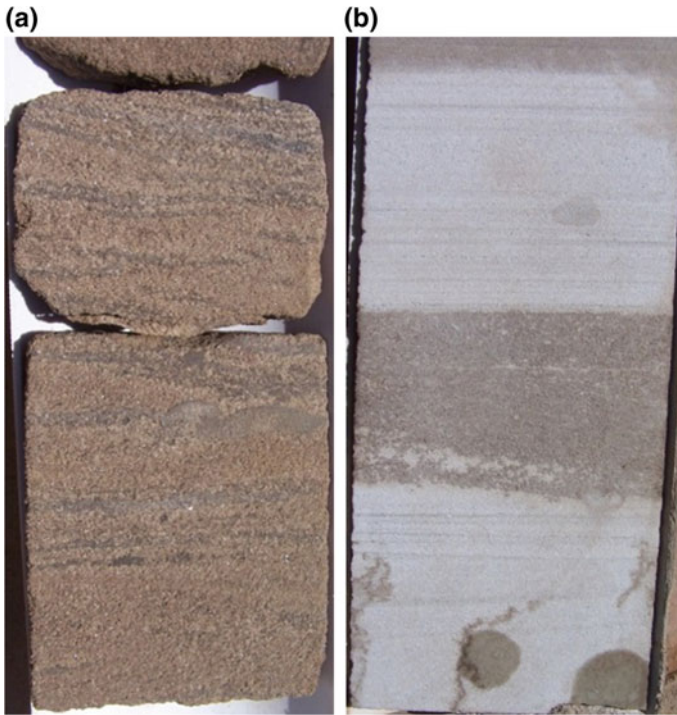
#### 3.3.1 Description

This facies encountered at a depth is shown in Table 1. Figure 3 is the core picture of this facies. It shows grain size range from fine- to very coarse sand size and it shows the ranges in color from gray light brown to creamy brown and red-brown to dark brown. Variably carbonate cemented with scattered small carbonate spherules, contains abundant continuous planar, wavy or convolute argillaceous to silty laminae; phyllosilicates are dominated matrix materials, and mud clasts are also present.

#### 3.3.2 Interpretation

Horizontal- or parallel-laminated sandstone is seen in core one, core two, and core three as shown in Fig. 3. It is very fine to very coarse and it might have deposited in the high energy channel. In core 2, this facies is intercalated with mudstone indicating a change in climate and fluctuation in channel flow. The deposition of this facies with reference to [5] classification may have taken place in the fluvial channel.





**Fig. 3** Parallel- or planar-stratified sandstone, **a** core one well HE 28 at depth 1638.82–1639.22, **b** core two well HE 38 at depth 1641.50–1642.30

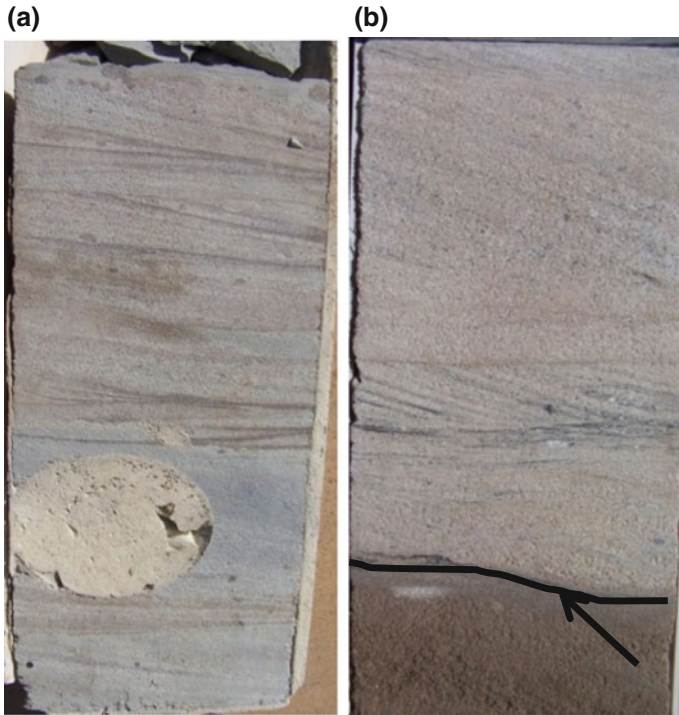
### **3.4 Planar Cross-Laminated Sandstones (*Sc*)**

#### **3.4.1 Description**

This facies observed at depth intervals is shown in Table 1 and Fig. 2. It ranges in color from brownish to gray, and the grain size range is from fine to coarse grained; at the upper interval, it is poorly sorted and well cemented, whereas at the lower interval it is well cemented. Blocky with parallel to sub-horizontal to a tangential low angle to moderate high angle contain scattered coarse quartz grains and mud clasts.

#### **3.4.2 Interpretation**

Planar cross-laminated sandstones (*Sc*) appear in all the three cores of the well A as in Fig. 4, and it ranges in grain size from fine to very coarse. It is probably deposited on a fluvial channel bar or delta distributary channel.



**Fig. 4** Planar cross-stratified sandstone, **a** core one well HE 38 at depth 1633.72– 634.12, **b** core 3 well HE 38 at depth 1658.60–1658.80

### 3.5 *Trough Cross-Laminated Sandstone (St)*

#### 3.5.1 Description

This facies encountered at a depth range as shown in Table 1, it represents fine to medium grain size and it shows gray to brown color. The grains are well rounded to rounded in shape, poorly sorted and well cemented, some mud clasts are present. The matrix is dominant by phyllosilicate minerals.

#### 3.5.2 Interpretation

Trough cross-laminated sandstone (St) is a coarse-grained facies observed in core two of well A as in Fig. 5. As per [5] classification, this facies could be deposited in a migrating 3-D dune in a fluvial channel of a braided stream (Fig. 6).

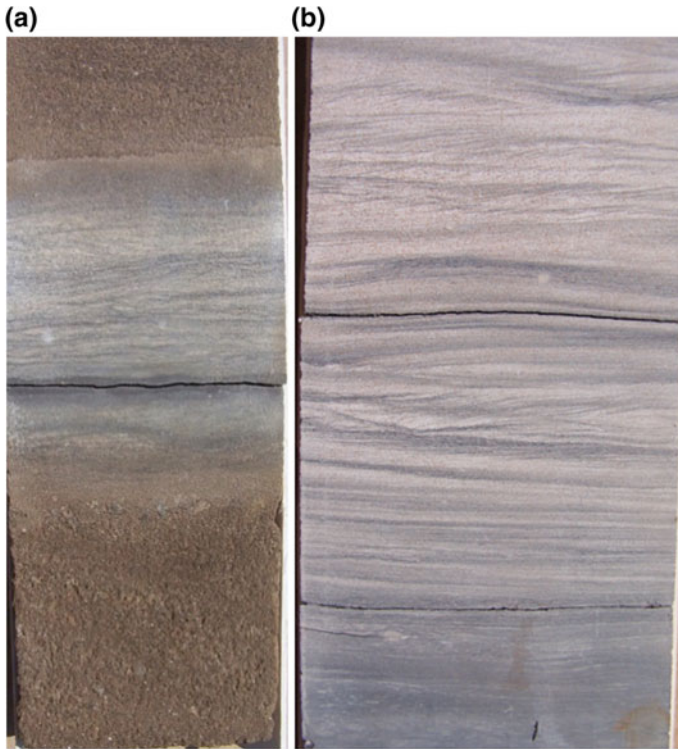


**Fig. 5** Trough cross-stratified sandstone, **a** core three well HE 28 at depth (1660.30–1660.40) **b** core two well HE 38 at depth (1645.20–1645.50)

### 3.6 *Ripple-Laminated Sandstone (Sr)*

#### 3.6.1 Description

This facies found at depth intervals range as shown in the Table 1, light gray to gray in color, very fine to coarse grain sand size, blocky with parallel to sub-parallel to tangential low angle to moderate high angle cross-stratification as in Fig. 6. Partly unevenly carbonate cemented with creamy white laminae. Contain scattered coarse quartz grains and mud clasts.



**Fig. 6** Ripple-laminated sandstone **a** core 1 well HE 28 depth interval 1640.87–1640.97, and **b** core 3 well HE 28 depth interval 1657.70–1657.85

### 3.6.2 Interpretation

Ripple-laminated facies are seen in core three of the well A, as shown in Fig. 1. It ranges in grain size from fine to very coarse indicating bedform channel deposit in a braided river as in Fig. 6.

## 3.7 *Mudstones and Sandy Mudstones (Fm)*

### 3.7.1 Description

This facies found at depth interval shown in the Table 1. Gray in color, blocky massive to locally faintly laminated, sometimes contains white and brown mud clasts and/or fine scattered quartz grains, sometimes bioturbated. Figure 2 resembles FCf facies of [7] classification.



**Fig. 7** Mudstone facies: layered mudstone **a** well HE 28 core 1 depth 1638.25 and massive mudstone **b** well HE core 3 depth 1654.55–1655.00

### 3.7.2 Interpretation

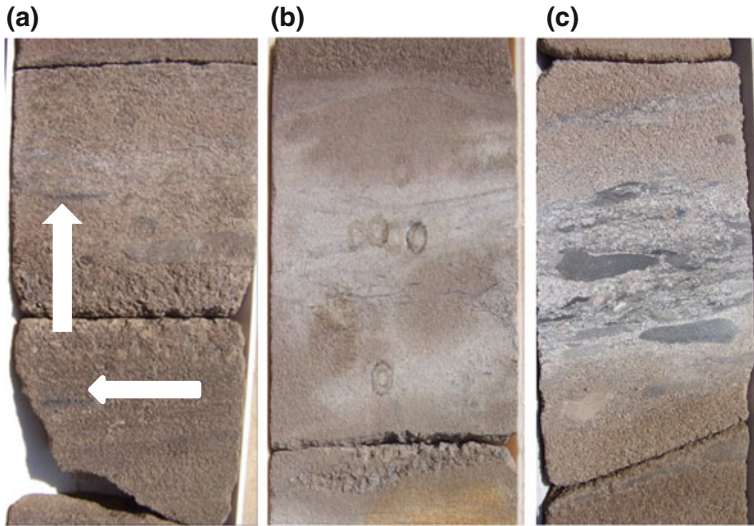
This facies is seen in minor ranges of core one and core two of the well A as shown in Fig. 2. It might deposit in a flood plain in a reduced environment (Fig. 7).

## 3.8 Conglomerate (Gm)

### 3.8.1 Description

Seen at the base of different layers at interval 1639.20 core one and interval 1646.00 core two as shown in Fig. 2 and Table 1 of well A. Characterized with light brown and brown to gray in color, fine to coarse sand size conglomeratic, generally homogeneous and massive. Contains scattered large elongated mud clasts.





**Fig. 8** Conglomerate facies, basal lag conglomerate, well HE 28 core 2 at depth 1647.60 m (a) and 1648.30 m (b) and pebbly shale conglomerate (c) well HE 28 core 1 depth 1636.60 m. white arrows show coal clasts

### 3.8.2 Interpretation

This facies is seen in a small range of interval in core one of the well A as shown in Fig. 2. It might have deposited in alluvial fan environment of as a lag deposit along the fluvial braided stream channel (Fig. 8).

### 3.9 Facies Association

Five facies association were recognized in this study FA1, FA2, FA3, FA4, and FA5. Facies association FA1 is about 2.5 m, grain size range is from coarse to fine, it is brown to light brown sometimes gray, sedimentary structure range from trough cross- to planar cross-stratification at top some pebbly shale conglomerate is also present, and this indicates bank erosion during high flood time gives rise to deposition in channel bar.

Facies association FA2 is about 2 m thick, it represents flood plain association start with conglomerate flowed by ripple lamination and planar tabular cross-stratification and is topped by horizontal stratification, massive mud is seen on top of the ripple stratification. This association indicates that the stream was overflowing; it is bank forming splay giving rise to crevasse splay association.

FA3 facies association about 2 m thick, the cycle started with deposition of planar cross-stratification, ripple cross-stratification, low angle cross-stratification massive sandstone and topped with mudstone. It ranges in grain size from a coarse to very fine and clay, it has a brown color, to gray to light gray. Deposition is thought to take place in channel bar.

FA4 is the fourth facies association range in thickness from less than 1 m to about 5 m average 3 m. It represents the most prominent facies association encountered the study area, it begins with trough cross-stratification followed by planar tabular cross-stratification. In some places, horizontal stratification tops this association, whereas in some other locations this association is topped by mudstone it shows fining-upward trend, the grain size range from very coarse to fine, color ranges from dark brown to brown sometimes gray or black. This association clearly indicates deposition of meander point bar.

FA5 is facies association begins with the deposition of conglomerate followed trough cross-stratification. This represents a repeated cycles of a strong flood.

Based on Miall's classification of architectural element (1987), three main architectural elements were identified:

- Channel deposits.
- Crevasse splay deposits.
- Floodplain deposits.

Based on the core analysis, facies, and facies association interpretation and deposition element, the depositional environment can be braided and meander fluvial system.

## 4 Conclusion

The sedimentological characterization of the core intervals from the Heglig well A, in Muglad Basin, Sudan, has been described at a vertical scale of 1:20 as shown in sedimentological core log as shown in Fig. 2. Seven sedimentary facies are observed and described in detail, consisting of continentally derived clastics dominated by sandy lithofacies with interbedded mudstone and siltstone and minor pebbly to conglomeratic intervals. They can be grouped into four main categories based mainly on their lithology, color, grain sizes, grain sorting, and sedimentary structures. They are sandstone facies, mudstone–siltstone facies, and conglomerate facies. Five facies association were interpreted and three depositional architectural elements were inferred. These elements were considered to be deposited in braided and meandering fluvial stream systems which in part its interval shows intermittent strong flood activity. Core one of well A mainly consists of sandstone with massive, planar-laminated, and cross-laminated structures with conglomeratic units and muddy intervals. Core two of well A is conclusively sandstone shows cross-laminated, trough cross-laminated, planar-laminated structures, with a small

conglomerate interval. Core three of well A shows sandstone which is massive, parallel lamination, cross-ripple laminated structures with silt interval. These facies mostly show fining-upward sequences, and these sequences do not match any of [4] classification for Bentiu Formation. Therefore, we can propose Bentiu Formation as a name for the whole interval from the well A of Heglig oil field.

**Acknowledgements** The author is thankful to Ministry of Petroleum formally Ministry of Energy of the Sudan for supplying data for this study and also thankful to Universiti Teknologi PETRONAS (UTP) for giving the opportunity for this study to be published.

## References

1. S. Browne and J. Fairhead, "Gravity study of the Central African Rift System: A model of continental disruption I. The Ngaoundere and Abu Gabra rifts," *Tectonophysics*, vol. 94, pp. 187–203, 1983.
2. W. Bosworth, "Mesozoic and early Tertiary rift tectonics in East Africa," *Tectonophysics*, vol. 209, pp. 115–137, 1992.
3. J. D. Fairhead, Geophysical controls on sedimentation within the African rift systems. Geological Society, London, Special Publications, 25(1), 19–27, 1986.
4. A. M. Idriss, O. M. Abdullatif, and O. A. Ali, "Depositional Environment and Reservoir Heterogeneity of Bentiu Formation (Albian-Cenomanian), Muglad Rift Basin", 2015.
5. A. Miall, D., "Lithofacies types and vertical profile models in braided river deposits:" a summary. In: *Fluvial sedimentology* (Ed. by Miall, A. D.), vol. Memoir, 5, pp. 597–604, 1978.
6. A. D. Miall, *The geology of fluvial deposits* vol. 575: Springer Berlin, 1996.
7. A. D. Miall, *Recent developments in the study of fluvial facies models*, 1987.
8. T. J. Schull, Rift basins of interior Sudan: petroleum exploration and discovery. *AAPG bulletin*, 72(10), 1128–1142, (1988).



# Geology of the Bertam Valley to Pos Betau—Focusing on Geomechanical Properties of Andesite

Pua Ming Jia and Askury Abd Kadir

**Abstract** This chapter reviews the first geomechanical analysis on exposed andesite along Bertam Valley to Pos Betau, Pahang. This project aims to perform geological analysis by applying geological mapping technique; structural analysis by relating the observed features in the field with the regional tectonic history of Peninsular Malaysia and the formation of Bentong–Raub suture through the construction of rose diagram and stereonet; and finally, the geomechanical analysis to identify the geomechanical properties of andesite. The geological analysis suggested that the study areas are part of an oceanic crust due to the presence of serpentinite and ribbon-bedded chert which are parts of ophiolite. A major compressional force acted along the NNW–SSE direction indicates the major force involved during the tectonic evolution of Peninsular Malaysia. This closely was related to the subduction of Paleo-Tethys Ocean and collision between Sibumasu and Indochina and has resulted in the formation of Bentong–Raub suture zone. In the geomechanical analysis, the unconfined compressive strength (UCS) obtained through the laboratory testing shows similar trends in andesite rock strength which is classified as “high rock strength value.”

**Keywords** Bentong–Raub suture · Andesite · Rock strength

## 1 Introduction

The study area is located near the Pos Betau, Pahang. The road cut is a part of a newly developed road link from Ringlet (Cameron Highlands) to Sg. Koyan (Kuala Lipis) with 20-m wide double-carriage ways. Besides andesite, the study area

---

P.M. Jia (✉) · A.A. Kadir (✉)  
Geoscience Department, Universiti Teknologi PETRONAS,  
32160 Bandar Seri Iskandar, Perak, Malaysia  
e-mail: puamj930901@gmail.com

A.A. Kadir  
e-mail: askury\_akadir@petronas.com.my

consists of granites, phyllite, and serpentinite. The general geology of the area is delineated from geological mapping, petrographic studies, and tectonic history. Meanwhile, the structural analysis is carried out through the construction of rose diagram and stereographic projection. Finally, the geomechanical analysis with an emphasis on the properties of andesite was carried out to review the rock strength and failure envelope of rocks from the Mohr's circle.

During the tectonic evolution, the Bentong–Raub suture zone has been predicted in several publications by describing and illustrating the major tectonic event involved. However, the geomechanical properties of rock, particularly the andesite, have yet to be discussed and studied. Thus, this study is used to discuss the geomechanical properties of andesite with respect to tectonic and structural deformation which is mainly attributed to the Bentong–Raub suture zone.

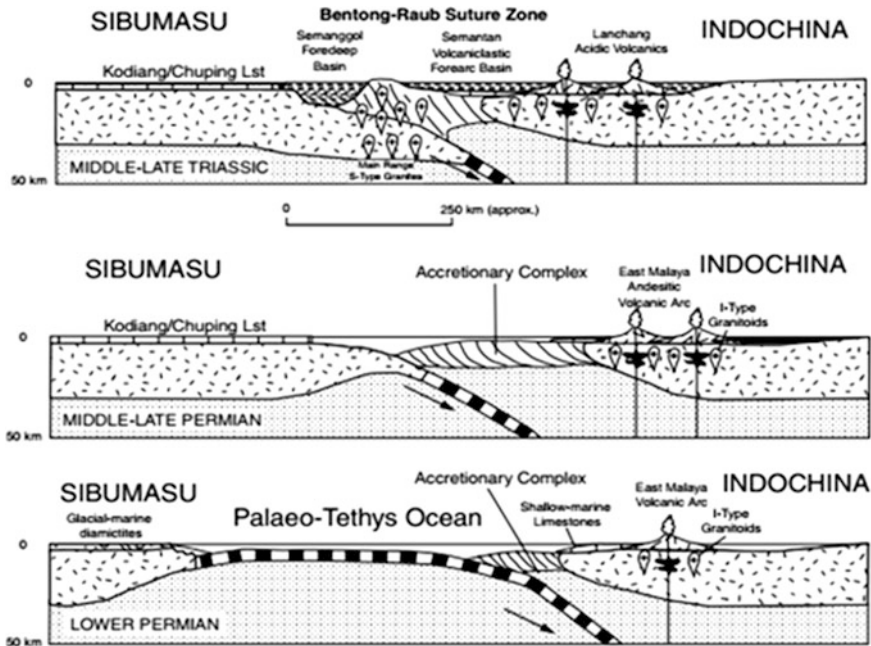
The objective of the study is to prepare a detailed geological map of the transect area. Besides, the structural features of the andesite were discussed and further relating them to the regional tectonic history of the area. The main aim of this project is to identify the geomechanical properties of andesite.

## 2 Bentong–Raub Suture Zone

Bentong–Raub suture is a north–south suture along the eastern foothills of the Main Range that extends from Thailand through Raub and Bentong to the east of Malacca, Peninsular Malaysia. This suture is exposed as an approximately 20-km-wide zone bordering the eastern limit of the Main Range granitoids in Peninsular Malaysia. It comprises *mélange*, oceanic ribbon-bedded cherts, schists, and discontinuous, narrow, and elongated bodies of serpentinitized mafic–ultramafic rock that is interpreted as ophiolite [1]. The Bentong–Raub suture consists of lithologies from both the Indochina and Sibumasu as illustrated in Fig. 1.

The Bentong–Raub suture is significant because it represents the main Paleo-Tethys Ocean which opened in the Devonian when the Indochina, Tarim, South China and North China continental terranes separated from Gondwana. Besides, the Paleo-Tethys Ocean was also destroyed as a result of collision between the Sibumasu and Indochina continental terranes of Southeast Asia. It acts as an important dividing line between the terranes of diversified geology.

Tjia [2] also stated that it is an island arc environment because there are dominant volcanic materials observed. Besides, further observation of crustal–super-crustal rocks and serpentinite lens is observed in the tectonic units of the area, indicating that it is an oceanic environment between the two continental terranes. He also stated that the lithologies that located around the Bentong–Raub suture are well-bedded chert, subparallel-to-parallel olistostrome, weathered massive mudstone, schist and schist-phyllite (Table 1). The olistostrome contains tuffaceous mudstone matrix, tuffaceous phyllite matrix, or phyllite matrix, and they also make up the bedding parallel mylonite zone.



**Fig. 1** Conceptual cross sections illustrating the formation of the Bentong–Raub suture by the subduction of the Paleo-Tethys ocean and collision of the Sibumasu and Indochina terranes [3]

**Table 1** Summary of lithology observed and their respective interpretation

Author	Lithology observed	Interpretation
Hutchison, 1975 [1]	Mélange, oceanic ribbon-bedded cherts, schists, and serpentinized mafic–ultramafic rocks	Ophiolite
Tjia, 1996 [2]	Dominant volcanic material, crustal–supercrustal rocks, serpentinite lens, well-bedded chert, subparallel–parallel olistostrome, schist, and schist-phyllite	Island arc environment
Tjia, 1996 [2]	Eastern: bedded chert with low angle thrust Western: igneous injection complex from eastern Titiwangsa granitoid intruded schist–phyllite sequence	Subduction zone

The primary goal of the structural geology is to use measurements of the present-day rock geometries to uncover information about the history of deformation in the rocks. Depending on the lithospheric condition at the time of deformation, rocks may respond to stress in a brittle or ductile manner. During brittle deformation, rocks fracture with strain localized along a plane, while the rocks to either side remaining unaffected. This can be best shown in faults and joints. This will then ultimately enable us to understand the stress field that resulted in the observed strains and geometries. This understanding of the dynamics of the stress field can be linked to important events in historical geology.

### **3 Methodology**

To identify the lithological features, geological field trip was carried out in the study area. Data and rock specimens are collected with the aid of GPS, compass, hand lens, geological hammer, and measuring tapes. The base map is also one of the most essential information to ensure precise location. The macroscopic and microscopic identifications of rocks are crucial to confirm the lithological types.

#### ***3.1 Discontinuity Data Survey***

A discontinuity survey is done by using scan-line method to collect all the necessary fractured data for rock mass classification. Instead of fractured orientation, the physical properties of fractured plane are noted and described.

#### ***3.2 Petrographic Analysis***

Petrographic study is conducted to identify the texture and mineralogy of rock under the polarized microscope. The rock type is being confirmed with the mineral assemblages, which display their remarkable optical properties under plane and cross-polarized light.

#### ***3.3 Rose Diagram and Stereonet***

Rose diagram and stereonet are very useful tools for structural analysis. Rose diagram is a method of displaying the relative statistical prevalence of various directional trends such as strike direction of fracture and lineaments and illustrates them as a histogram drawn in a circle. We are then able to interpret the maximum and minimum principal compressive stresses. On the other hand, a stereonet is a lower hemisphere plot. A stereographic projection involves plotting 3D data onto a 2D stereonet where it can be manipulated and interpreted. It is then used to represent the orientation of geological planar surfaces.

#### ***3.4 Geomechanical Tests***

Core samples were prepared for geomechanical tests, such as point load, Schmidt Rebound Hammer, uniaxial, and triaxial tests. The strength properties of the andesite can be deduced from the testing, viz. unconfined compressive strength,  $IS_{50}$ , friction angle, and cohesion.

## 4 Results and Discussions

Based on the previous studies, the main lithology observed in this area consists of crustal–supercrustal rocks, subparallel–parallel olistostrome, schist and schist-phyllite, mélange, oceanic ribbon-bedded cherts, and serpentinized mafic-ultramafic rocks which are the rocks generally found at the subduction zone [2]. Structural analysis shows the maximum stresses that are coming from NE–SW direction. The geomechanical properties of andesite which has no published documentation available for reference will be further studied and discussed in the latter part of this paper.

### 4.1 Lithological Map

Based on the geological map that had been constructed (Fig. 2), we are able to match the observed geological feature with several publications [1, 3] and cross-checking them with the findings of this project. The observed granite which is the youngest rock is due to the granite intrusion occurring during the Early Jurassic where the collision between Sibumasu and Indochina ends. The oldest rock such as serpentinite has the most significant features observed in the field. This is because, Hutchison [3] interpreted that Bentong–Raub suture consists of a part of an oceanic crust which had been uplifted due to the collision and overthrusting. Serpentinite is one of the important indicators in identifying package of ophiolites, giving indication of the paleo-ocean. The andesite which is Permian in age undergoes 2 episodic deformations which was firstly caused by the collision and followed by the granite intrusion. This will be further discussed in the structural analysis section.

### 4.2 Structural Analysis

After compiling the  $\sigma_1$  and  $\sigma_3$  values, we are able to observe the major compressional force acting on our area of study that is coming from NNW–SSE direction (Fig. 3). These results are correlatable with the regional tectonic history of Peninsular Malaysia. During the formation of the Bentong–Raub suture, the Paleo-Tethys Ocean undergoes subduction and causing the collision between the Sibumasu and Indochina terranes. This process which takes place throughout the Late Permian to Late Triassic affected all the rocks within the study area. Besides, we are also able to observe second episodic deformation of andesite which are Permian in age, and this deformation could be interpreted relating to the intrusion of younger granite which results in minor compressional force acting on the andesite, causing secondary deformation which has much smaller scale and more minor effect compared to the tectonic forces that acting on them during the subduction period.

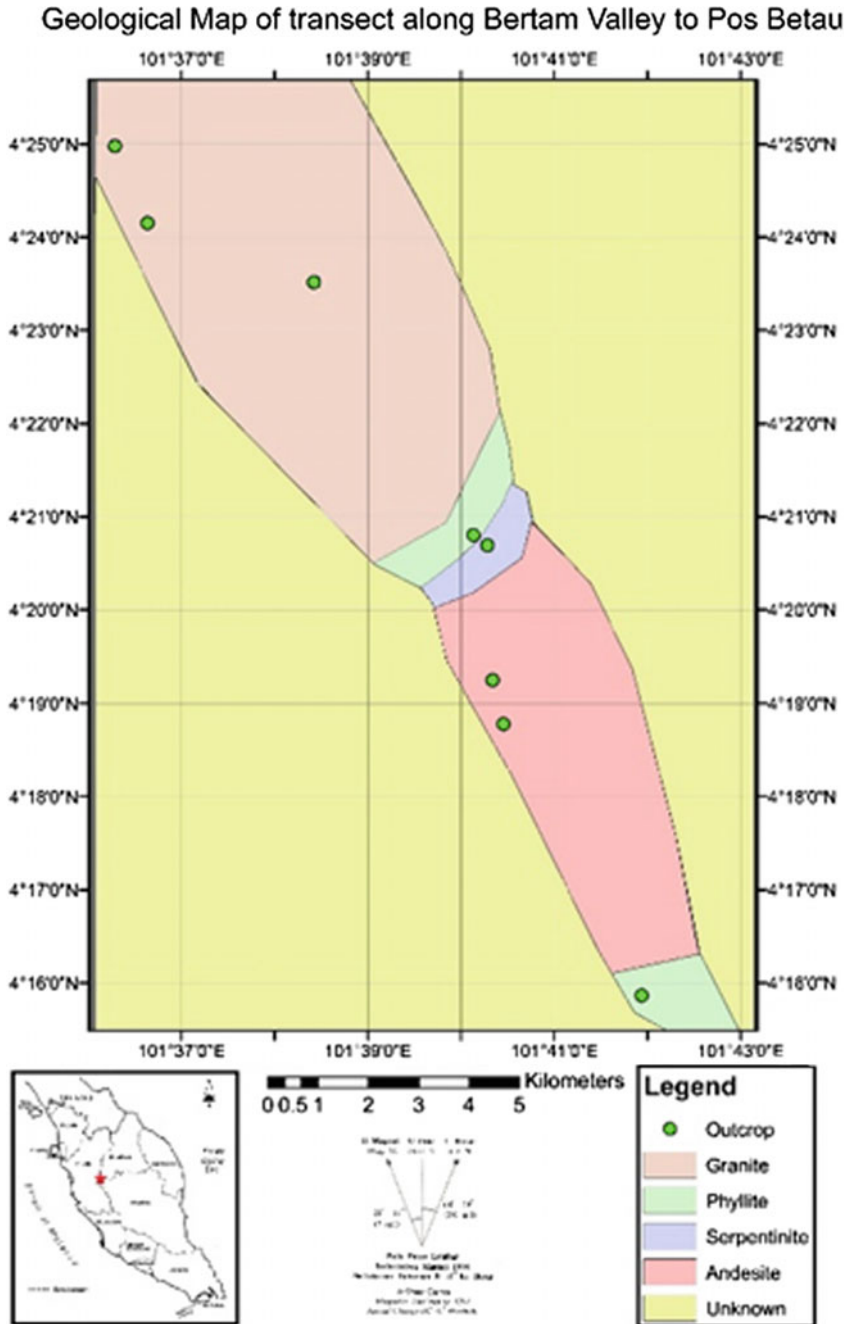


Fig. 2 Geological map of transect along Bertam Valley to Pos Betau

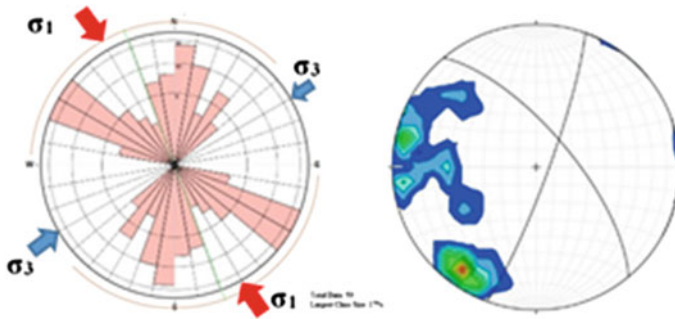


Fig. 3 Rose diagram and stereographic projection for fractures in andesite

### 4.3 Geomechanical Analysis

Based on the correlated UCS value, we are able to observe a similar rock strength value of andesite for all three different rock strength testings. The trends fall in the “very high rock strength” classification [4] as shown in Table 2. This matches with the typical rock strength profile for an igneous rock. Besides, we are able to observe higher UCS value in triaxial compressive strength test. This is due to the confining pressure applied on the rock sample which causes the rock being able to withstand higher axial load. The higher the confining pressure applied on our rock sample, the greater it exhibits ductile behavior which causes the rock being able to withstand greater load before reaching the point of failure.

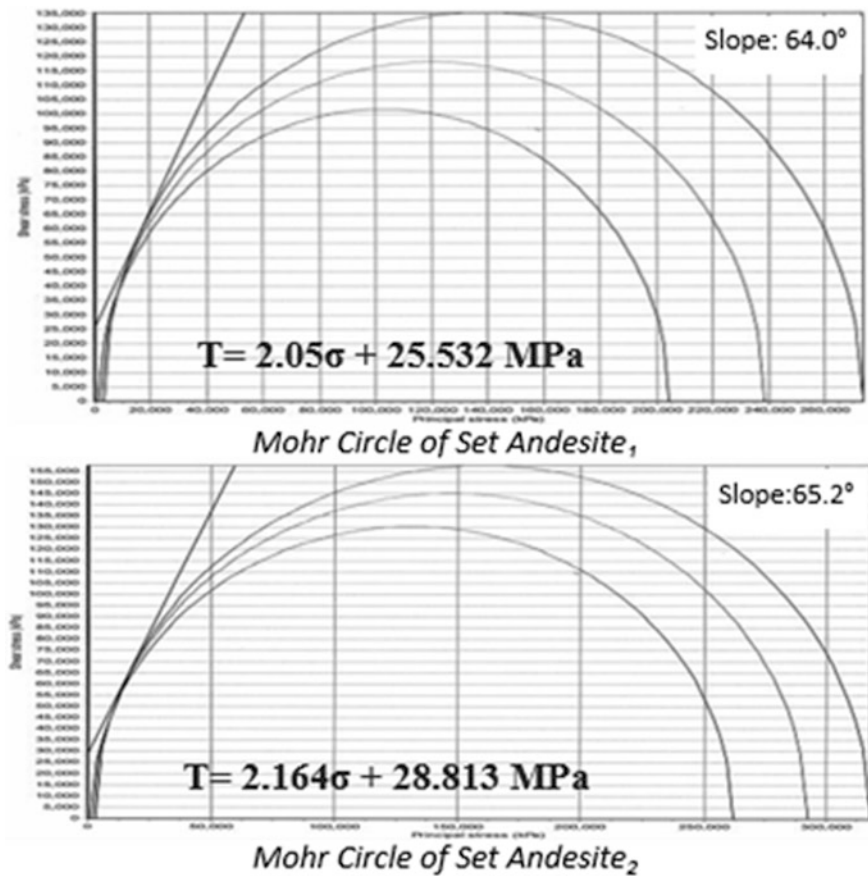
After constructing the Mohr’s circle, we are able to determine the failure envelope for the andesite in our study area (Fig. 4). Therefore, we are able to predict the stress that the andesite can take before its point of failure in different confining pressures. This is particularly important as we are going to relate the properties of the andesite with naturally fractured reservoir that is usually deep within the subsurface with high confining pressure. The andesite is able to withstand a very high friction angle of about  $64.6^\circ$  and has a cohesive strength of 27.17 Mpa.

To delineate the geomechanical properties of andesite and relate them with fractured reservoir, one of the best case studies would be the Anding Field in Malay Basin. According to Mohamad Kadir [5], the rock age and type of Anding Field which located at the southwestern margin of the Malay Basin are suggested to be Permo-Carboniferous metasediments and volcanics, Cretaceous granites, and possible Cretaceous rift fill which match with the age of the andesite in the study area, i.e., Permian in age.

Besides, based on our structural analysis of fractures which trends along the NNW–SSE direction matches with the finding of Mohamad Kadir [5], in which the test results from the wells drilled in the fractured basement within Anding area indicates that most open fracture are trending NNE–SSW and ENE–WSW which same trend with the Principle Stress in Malay Basin while for the closed fractures, they trend along the NW–SE.

**Table 2** UCS comparison between respective geomechanical testings

No.	Sample no.	UCS from point load Test, $\sigma$ (Mpa)	UCS from uniaxial compressive strength test, test, $\sigma$ (Mpa)	UCS from triaxial compressive strength test, test, $\sigma$ (Mpa)
1	Andesite <sub>1</sub>	219.1	205.7	236.9
2	Andesite <sub>2</sub>	213.3	212.3	288.7



**Fig. 4** Mohr's circle for andesite

To further justify our interpretation and correlation with Anding Field, more studies need to be carried out in the eastern part of an onshore Peninsular Malaysia to obtain more data and documentation and to fill up the missing links which exist between this study and the fractured reservoir in Anding area.



## 5 Conclusion

Based on the findings throughout this project, we are able to achieve our objectives through geological analysis, structural analysis, and geomechanical analysis. For geological analysis, the serpentinite and ribbon-bedded chert that we observed in our outcrop further marks the boundary in our geological map, and we are able to confirm that our study area is a part of an oceanic crust which matches with the geological features observed by Hutchison [1], indicating a part of an ophiolite.

The structural analysis shows a major compressional force acting in our area of study which may be related with the subduction on Paleo-Tethys Ocean causing collision of Sibumasu and Indochina terranes, which results in the formation of Bentong–Raub suture zone. This interpretation was further supported by the tectonic evolution model proposed by Metcalfe [3] regarding the formation of Bentong–Raub suture zone and regional tectonic history of Peninsular Malaysia.

Last but not least, the geomechanical properties of andesite enable us to predict the maximum stress of rock able to withstand under different confining pressures. This is important in predicting a naturally fractured reservoir that may have potential to allow accumulation of oil and gas. Although due to lack of documentation, by integrating the findings, we are able to make an initial prediction to relate the geomechanical properties of andesite with the offshore-fractured reservoir in Anding area.

## 6 Recommendation

Further study needs to be performed for andesite samples obtained from Anding Field to compare their geomechanical properties. It will reveal any uncertainties and better understanding on fractured reservoir in the future.

**Acknowledgements** The author would like to thank Universiti Teknologi PETRONAS (UTP) for funding the project.

## References

1. Hutchison, C. S. (1975). Ophiolite in Southeast Asia. *Geological Society of America Bulletin*, 86(6), 797–806.
2. Tjia, H., D., & Almashoor, S. S. (1996). The Bentong Suture in Southwest Kelantan, Peninsular Malaysia. *Geological Society of Malaysia Bulletin*, 39, 195–211.
3. Metcalfe, I. (2000). The Bentong–Raub Suture Zone. *Journal of Asian earth Sciences*, 18, 691–712.

4. Hoek, E., & Brown, E. T. (1997). Practical estimates of rock mass strength. *International Journal of Rock Mechanics and Mining Science & Geomechanics Abstract*, 34(8), 1165–1186.
5. Kadir, M. B. (2010, March). Fractured Basement Exploration Case Study in Malay Basin. In PGCE 2010.

# Fractures of Gunung Ledang Granite: Insight to Post-Cretaceous Structural Event

Choong Chee Meng, Askury Abdul Kadir,  
Muhammad Noor Amin Zakariah, Abdul Ghani Rafek,  
Chow Weng Sum and Nurul Syafiqah Harun

**Abstract** Based on the deformations in the Cretaceous rocks and also the results of the radiometric dating of the fault zones [Zaiton Harun, Late Mesozoic—Early Tertiary faults of Peninsular Malaysia, 9], it is proven that tectonics of onshore Peninsular Malaysia was still active during post-Cretaceous. These deformations may contribute to the basin formation/inversion during Tertiary period in Sundaland. The study area is Cretaceous granite, Gunung Ledang, which is situated in North Johor. The objective of this study is to determine the major fracture sets at regional scales and outcrop scales and reconstruct the structural events. In this study, the focus is on the negative lineaments of Gunung Ledang at a regional scale and the fractures of the Puteri Waterfall at outcrop scale. During site visit, the details of the fracture, e.g., infilling and sense of motions, are recorded. From the observations and analysis, there are 3 negative lineament sets at regional scale: N-S, NE-SW, and ESE-WNW; four fractures sets found at the outcrop scale: N-S, NE-SW, E-W, and NW-SE. The outcrop-scale fractures are all steeply dipping to almost vertically dipping. The crosscutting relationships show that the chronology of the fractures is N-S, NE-SW/E-W, and NW-SE, from oldest to youngest. NE-SW fracture displaces a N-S mega-crystal quartz dyke in left-lateral motion, which deduces a ~ N-S compression. Another possible Riedel system (right-lateral strike-slip) formed on the same NE-SW fractures, which deduce a ~ E-W compression. The chronology of these two events is hard to define because of lack of clear field evidences.

**Keywords** Fractures · Post-Cretaceous · Granite · Gunung Ledang · Puteri Waterfall

---

C.C. Meng (✉) · A.A. Kadir · M.N.A. Zakariah · A.G. Rafek · C.W. Sum · N.S. Harun  
Universiti Teknologi PETRONAS, Bandar Seri Iskandar 32610, Perak, Malaysia  
e-mail: choong.meng@petronas.com.my

© Springer Nature Singapore Pte Ltd. 2017  
M. Awang et al. (eds.), *ICIPEG 2016*,  
DOI 10.1007/978-981-10-3650-7\_26

305

## 1 Introduction

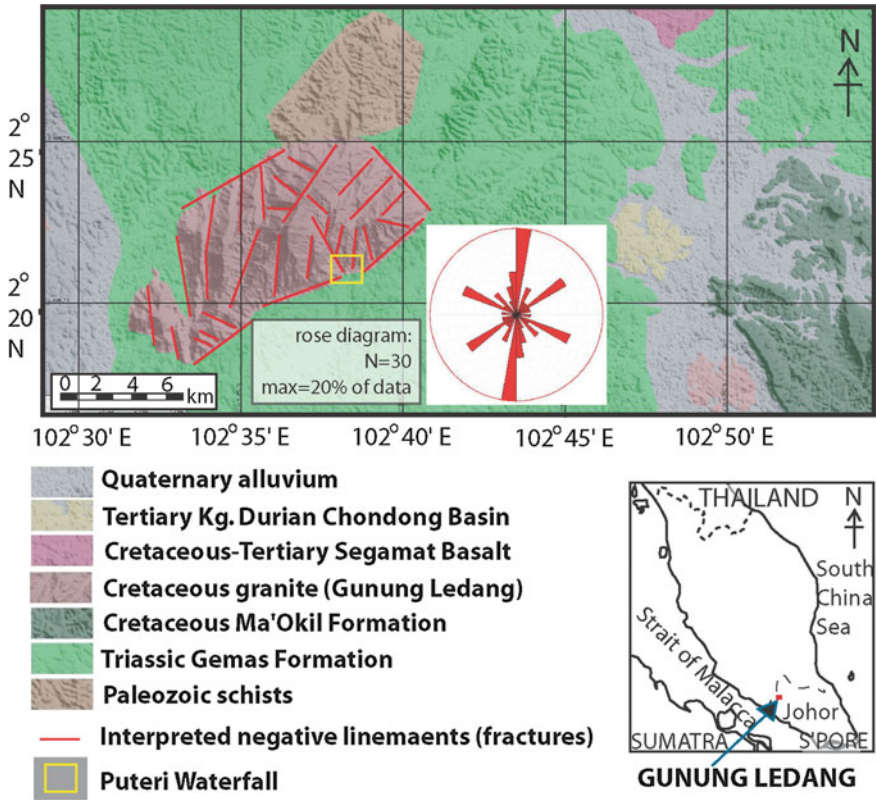
The radiometric dating on the three faults (1. Bukit Berapit area, north Perak; 2. Bukit Tinggi area, Pahang; and 3. Kuala Kelawang area, Negeri Sembilan) in different parts of the Peninsular Malaysia by [9] has given a Late Cretaceous–Tertiary age and it indicated that tectonics was still active in the region during this period. Gunung Ledang or Mount Ophir is one of the granitic intrusions in Peninsular Malaysia which has a relatively younger geological age, i.e., Late Cretaceous. Due to the younger age (Late Cretaceous) of this granite, the structural events and their induced fractures can only be post-Cretaceous. No detail structural analysis has been conducted in this area so far, and thus, the Tertiary structural history remains unclear.

Tertiary geological event is crucial to oil and gas industry because of the hydrocarbon basins of this region mainly developed in this period. Onshore Tertiary (post-Cretaceous) basins of Peninsular Malaysia have been summarized and reviewed by Raj et al. [5] in terms of their tectonic evolution. Among the reviewed Tertiary basins, three of them are located in Johor, i.e., Layang-Layang Basin, Kluang-Niyor Basin, and Kg. Durian Chondong Basin. The formation of these basins is known to be structurally controlled, and it has been verified in Layang-Layang Basin by gravity study [7]. Kg. Durian Chondong Basin is located 10 km to the east of Gunung Ledang. It is postulated that the fractures and fault systems of the Gunung Ledang area are likely to continue into the Kg. Durian Chondong Basin due to the short distance, which could lead to a structurally controlled basin formation.

## 2 Geological Setting of Gunung Ledang Area

The lithological distribution of the Gunung Ledang area is presented in Fig. 1. Gunung Ledang area is composed of rocks from Paleozoic to Quaternary age. Schist is located at the northeastern part of the Gunung Ledang which is believed to be of Paleozoic age. Gemas Formation is widespread in this area. This formation is Triassic in age and composed of interbedded tuffaceous sandstone and shale. Ma'Okil Formation overlies unconformably on the top of Gemas Formation. The dominant facies of Ma'Okil Formation are interbedded argillite and arenite units, rudite and volcanic rocks. Abundant plant and pollen have been encountered in this formation and suggest a Cretaceous age. Segamat Basalt is believed to be formed due to shallow intrusion of dykes and flows [3] during Early Tertiary. Kg. Durian Chondong Basin is of Tertiary age and composed of interbedded coal and sand, silt, clay, and volcanic ash layers. The rest of the area is covered by alluvium.

The granite of the Gunung Ledang is pink in color, medium to coarse grained (i.e., grain sizes range from 10 to 40 mm, average about 20 mm) and equigranular [4]. Based on the petrography, the granite is composed predominantly of quartz,



**Fig. 1** Lithological map of the Gunung Ledang and surrounding area (Modified from [4]; [6]). Negative lineaments (which are fractures/faults in this case) have been traced and they are presented in the rose diagram at the right. N-S, NE-SW, and ESE-WNW lineaments are the major sets in Gunung Ledang

orthoclase, plagioclase, and biotite with subordinate muscovite, apatite, zircon, sphene, rutile, and magnetite [4]. Askury Abd Kadir [1] has categorized two units of granitoids in Gunung Ledang: (1) Ledang type (dominant type): pinkish colored, equigranular, medium-grained biotite granite and (2) Bekok type: microgranite which occurs in diameter of few meters to 100 m, with rounded and oval shape that is trapped in the Ledang-type granite.

The radiometric dating of granite samples in Gunung Ledang gave a K-Ar date of  $52 \pm 2$  Ma (biotites) and Rb-Sr date of  $81 \pm 2$  Ma (whole rock mineral isochron), the lower K-Ar ages assumed to be due to argon loss from the biotite [2]. An average radiometric age of 69 Ma has been determined from 5 granite samples by [8]. Hence, the granite of the Gunung Ledang generally is Late Cretaceous in age based on these datings.

The Bekoh Valley at the eastern part of the Gunung Ledang is a fault zone at the boundary of granite metamorphic rocks, and is a dominant set of N-S striking faults

and a less prominent set of SE striking faults [4]. In the aerial photograph, a vertical fault scarp striking in N-S direction can be observed at the eastern edge of the Bekoh Valley. Two sets of faults can be found in the Gunung Ledang granite such as  $\sim$ NNW and  $\sim$ NE striking faults [4]. Kilometer-scale  $\sim$ NNW striking faults are cutting through the middle of the mountain, whereas the  $\sim$ NE striking faults are dominant at the northeastern part. Fault indications such as brecciated/sheared granite, cataclasites, and mylonites are present in these fault zones. Those fracture/fault zones are also infilled by granitic materials.

Four sets of joints have been identified in granitic area, which are  $\sim$ 360°–020°,  $\sim$ 040°–060°, and  $\sim$ 320°–340° with steeply/vertical dipping, and another set striking in 080°–100° [4].

### 3 Methodology

There are two scales of fracture analysis: regional scale and outcrop scale. At the regional scale, negative lineaments (major fractures) of the Gunung Ledang are traced and analyzed. They provide an overview of the fracture trends in this area.

At the outcrop scale, the study is conducted in the Puteri Waterfall located at the south of the Gunung Ledang. This locality has been chosen because of well-exposed fresh rock, existence of systematic fractures, and easy accessibility. The orientations of the fractures were measured, and every fracture planes were described in terms of fracture type, sense of motion, and infilling. At the same time, their crosscutting relationships and interpretation of their relative chronology of the fracture formation were determined. Finally, we will propose a history of the fracture development in this area based on the analysis on regional lineaments and outcrop fractures.

### 4 Results and Discussion

Fracture analysis was conducted at two scales (regional scale and outcrop scale). The results of these two analyses are integrated to construct the structural events of the area.

*A. Regional-scale Lineament Analysis* A total of 30 negative lineaments (fractures/faults) have been traced on the SRTM digital elevation model of the Gunung Ledang (Fig. 1). The major sets of lineament are N-S (000°–009°), NE-SW (050°–059°), and ESE-WNW (290°–299°). The N-S lineaments are clearly truncated along the NE-SW lineaments which are located at the northern and southern foothills of the Gunung Ledang. It may indicate that N-S lineaments were formed prior to NE-SW set.

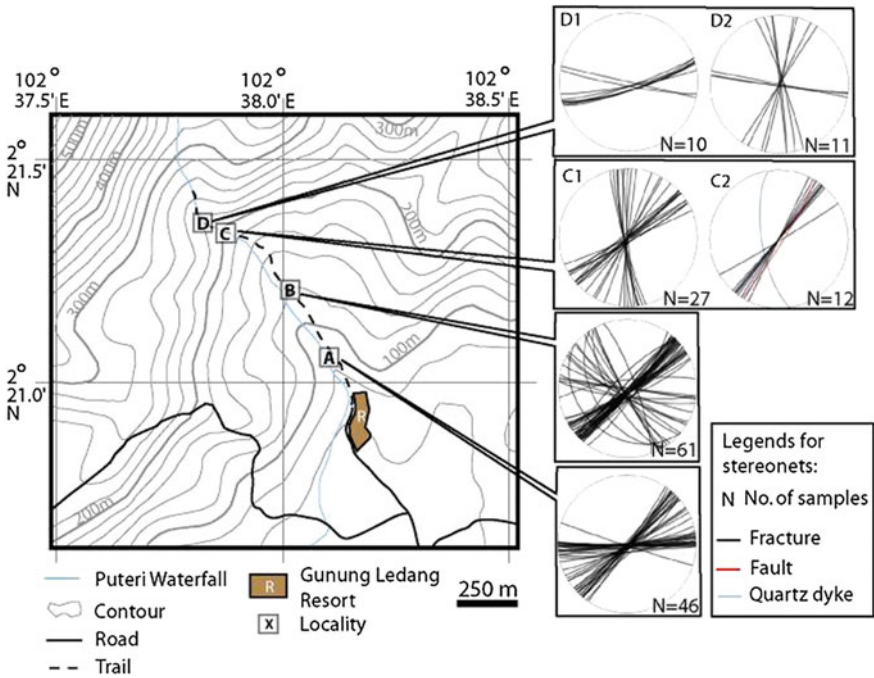


Fig. 2 Stereonets present the distribution of the fractures in the different localities, Puteri Waterfall, Gunung Ledang

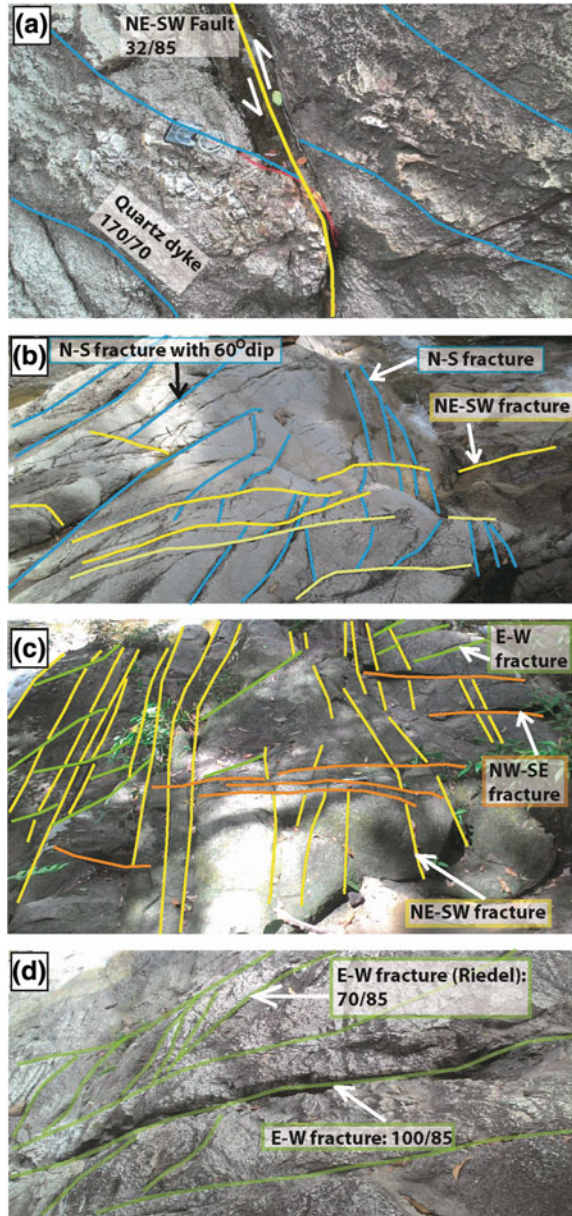
*B. Outcrop-scale Fracture Analysis* Four localities have been visited from the bottom to the peak of the waterfall (Fig. 2) to collect fracture data. All localities are in the granitic area.

Four sets of fractures have been identified in the waterfall, and they are striking in NE-SW, N-S, E-W, and NW-SE directions (Fig. 3). These fracture sets are similar to the joint sets that were recorded by Ong [4]. Nearly all fractures are nearly vertically dipping ( $>75^\circ$ ), commonly  $85^\circ$ – $90^\circ$ . Senses of motion of the fractures would rarely be observed.

The 1st fracture set is NE-SW fractures which are the most dominant and striking in ranges of  $035^\circ$ – $065^\circ$ , often in  $045^\circ$ . The fractures were formed in all localities, however, less occurrence in locality D. The 2nd fracture set is trending in N-S direction and striking varies from  $340^\circ$  to  $020^\circ$  which is found in the locality C and D. A mega-crystal quartz dyke has been observed which is trending in the same direction (N-S) at locality C. At the same locality, few N-S fractures are dipping around  $60^\circ$  toward east and dip toward the downstream of the waterfall. These  $60^\circ$  dipping fractures are not plotted in the stereonet, because they may be exfoliation joints, which are not tectonic induced.



**Fig. 3** **a** Locality C2. N-S quartz dyke in locality C2 has been cut by NE-SW left-lateral strike-slip (or probably oblique-slip) fault. Compass as scale,  $\sim 20$  cm long. **b** Locality C1. NE-SW fractures cut the N-S fractures. The orientation of the steeply dipping ( $\sim 60^\circ$ ) N-S fractures generally followed the trend of the waterfall. **c** Locality B. The possible E-W Riedel fractures associated with the main NE-SW fracture which deduced a  $\sim$  E-W compression. NW-SE fractures cut the NE-SW fractures, which indicated that NW-SE fractures formed later than NE-SW set. **d** A possible Riedel system (left lateral) along  $\sim$  E-W fractures at locality D1



The 3rd fracture set is E-W striking and ranging from  $075^\circ$  to  $105^\circ$ . The fractures mostly occur in  $085^\circ$ – $095^\circ$  and were found in all localities except locality C. The last fracture set (NW-SE) has the lowest occurrence, and they are trending in  $130^\circ$ – $150^\circ$ . This fracture set only occurs at locality B.



*C. Crosscutting Relationship of the Fracture Sets and Its Structural Interpretation* The N-S quartz dyke in locality C has been cut by NE-SW left-lateral strike-slip (or probably oblique-slip) fault (Fig. 3a); it indicates that the quartz dykes are older than NE-SW fractures. The same relationship can be observed in the rest of the locality C (Fig. 3b). The evidences inferred a  $\sim$  N-S compression.

At locality A, B, and C, E-W fractures commonly end at the NE-SW fractures, which may indicate that the E-W fractures are formed earlier than NE-SW set. However, some of the E-W fractures in locality B show curvy profile that resembles Riedel fractures and sometimes crosscut NE-SW set (Fig. 3c). These “possible” Riedel fractures (E-W) have a slight deviation of the strikes compared to the NE-SW fractures (possible primary fractures). Based on the orientations of E-W and NE-SW fracture sets, the Riedel system can be worked when NE-SW fractures have right-lateral motion. This model indicates a  $\sim$  E-W compression.

E-W fractures ( $N = 21$ ) at the locality D can be subdivided into 2 groups which are trending in  $072^\circ$  and another  $100^\circ$ . The fractures are steeply dipping, which is  $75^\circ$ – $80^\circ$ . It clearly shows a Riedel fracture system (Fig. 3d), where  $072^\circ$  fractures are Riedel fractures and  $100^\circ$  fractures are the primary fractures. The Riedel system can deduce a  $\sim$  ENE-WSW compression.

NW-SE fractures cut the NE-SW fractures in the locality B. It clearly shows that NW-SE fractures formed later than NE-SW fractures. It is probably the last set of fractures that formed in this area, since no other fractures crosscut them.

*D. History of the Fracture Formation of the Gunung Ledang area* Four set of fractures found here such as N-S, NE-SW, NW-SE, and N-S, and all are steeply dipping. N-S fracture set is the oldest fracture set which is deduced from the crosscutting relationship, because it is always crosscut by other fractures. The same relationship can be observed in the digital elevation model, and the N-S lineament set is commonly cut by NE-SW lineament set. At least one N-S fracture has been filled by quartz and formed mega-crystal quartz dyke.

NE-SW fractures have the highest occurrence at Puteri Waterfall. A possible right-lateral and also left-lateral motion has occurred along the NE-SW fractures which deduced a  $\sim$  E-W compression and  $\sim$  N-S compression, respectively. The crosscutting relationship of NE-SW fractures and E-W fractures is not consistent. E-W fractures may act as secondary/Riedel fractures to NE-SW fractures.

The NW-SE fractures only occur at locality B. This fracture set often crosscuts other fractures, which shows that it is a late fracture.

## 5 Conclusion

In Gunung Ledang, the regional-scale negative lineaments (fractures) are trending in N-S, NE-SW, and ESE-WNW direction. The outcrop-scale fracture sets of the Puteri Waterfall are striking in N-S, NE-SW, E-W, and NW-SE direction, with steeply to nearly vertical dips. Based on the crosscutting relationship of the fractures in the

outcrop, their relative chronology is N-S set (oldest), followed by NE-SW set and E-W set, and lastly NW-SE set. There is a left-lateral movement, which occurred along the NE-SW fracture, which displaced the N-S quartz dyke and which deduced a  $\sim$  N-S compression. The same NE-SW fractures are likely to form a Riedel system together with E-W fracture set, indicating a right-lateral movement. The NE-SW fractures are reactivated before; however no clear indication/evidence was found to determine the relative chronology of those two events (N-S and E-W compression).

## References

1. Askury Abd Kadir, 1986. Petrology and Petrochemistry of the granites in the Gunung Ledang area, Johor. *Geological Survey Malaysia Annual Report 1986*. pp. 369–384.
2. Bignell, J.D. and Snelling, N.J., 1972. The geochronology of the Tahi-Malay Peninsula. In *Proceedings of the Regional conference on the geology of southeast Asia. Geological Society of Malaysia, annex to newsletter*, 34.
3. Chakraborty, K.R. & Kamineni, D.C., 1978. Chemical characteristics and classification of Segamat volcanics. *Geological Society of Malaysia Warta Geologi*, 4, pp. 85–91.
4. Ong, Y.H., 2001. *Geology and Mineral Resources of the Gunung Ledang area, Melaka and Negeri Sembilan*. Minerals and Geoscience Department Malaysia, Map Report 14, 93 pp.
5. Raj, J.K., Abdul Hadi Abd. Rahman and Mustaffa Kamal Shuib, 1998. Tertiary Basins and inland Peninsular Malaysia: review and tectonic evolution. *Geol. Soc. Malaysia, Bulletin* 42, pp. 211–226.
6. Tate, R.B., Tan, D.N.K. & Ng, T.F., 2008. Geological Map of Peninsular Malaysia. Scale 1:1 000 000. Geological Society of Malaysia & University Malaya.
7. Vijayan, V.R., 1990. Gravity survey of the Layang-Layang Tertiary Basin in Johor, Peninsular Malaysia – A Preliminary Report. *Geol. Soc. Malaysia, Bulletin* 26, pp. 55–70.
8. Yap, F.L., 1980. Isotopic age and petrochemistry of the Gunung Ledang granite. *Geological Survey Malaysia departmental senior officers' conference 1980*, unpubl.
9. Zaiton Harun, 2002. Late Mesozoic - Early Tertiary faults of Peninsular Malaysia. *Geological Society of Malaysia Annual Geological Conference 2002*, Kota Bharu, 26–27 May 2002.

# Sedimentology of Potential Tertiary Fluvial Deposits in Kluang, Johor, Malaysia

Choong Chee Meng, Nur Huda M. Jamin,  
Muhammad Azfar Mohamed and Chin Soon Mun

**Abstract** The occurrences of Tertiary basins in Peninsular Malaysia are localized and limited. Commonly, their boundaries are difficult to define due to limited exposure. They are sometimes difficult to be differentiated from the younger Quaternary alluvium. Hence, the geological knowledge for the most Tertiary basins of the Peninsular Malaysia is not well developed. In this study, two new outcrops with potential Tertiary formation were visited and described in terms of sedimentology. These two outcrops are located at Taman Sri Permai and Taman Saujana, few kms east and west of the Kluang town, respectively. The main lithology of the outcrops is light-coloured poorly sorted medium- to very coarse-grained sandstone or conglomerate which is often not completely consolidated. The dominant minerals present are quartz followed by feldspar. Feldspar is commonly weathered and altered to soft kaolinite. The beds have sharp contact and their thickness varies (~15 to ~150 cm) due to the occurrences of intensive symmetrical channel structures. At the bottom of the channel, the very coarse sands to pebbly grains are commonly aligned and followed the shape of the channel. The very coarse to pebbly sandstones often have a fining upward sequence, which gradually change to finer grains and better sorting sandstones. These fining upward sequences are repeated few times within a bed. The channel structures are symmetrical and consist of fining upward sequences from very coarse sandstone–conglomerate to medium-grained sandstone, which indicates that it was deposited in a braided river environment. However, the cross-bedding (common in fluvial system) was not observed. This palaeo-fluvial system may continue till present day, which incises into the nearby area, e.g. Sg. Mengkibol and Sg. Melantai.

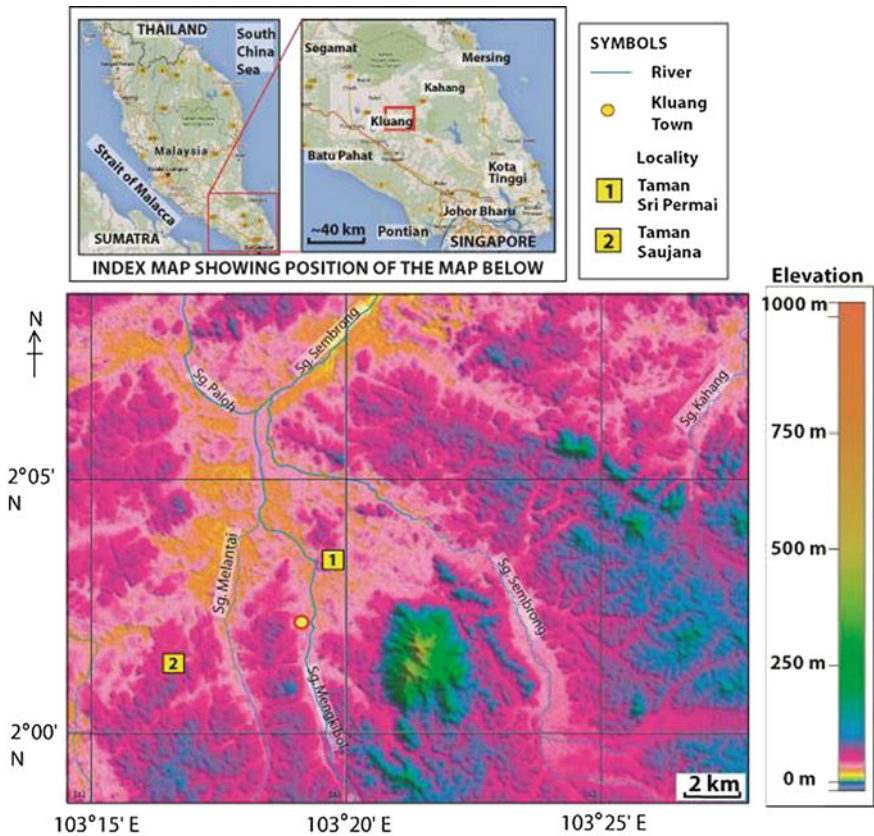
**Keywords** Sedimentology · Tertiary · Channel · Kluang

---

C.C. Meng (✉) · N.H.M. Jamin · M.A. Mohamed · C.S. Mun  
Universiti Teknologi PETRONAS, 32610 Seri Iskandar, Perak, Malaysia  
e-mail: choong.meng@petronas.com.my

# 1 Introduction

Kluang is located at the central of Johor. This area is composed of different lithologies ranging from Palaeozoic to Recent ages. In terms of geography, Kluang is a low-land area surrounded by hilly/mountainous areas with different elevations (Fig. 1). Two outcrops of sedimentary rocks (probably Tertiary age or even younger), namely Taman Sri Permai and Taman Saujana were discovered few kms to the east and west of the Kluang town. Those are new outcrops and no detailed documented sedimentological study so far. The study aims to determine its depositional environment and its relationship with present nearby river development. This study contributes to sedimentology of this region during Tertiary period because Tertiary deposits here are rarely exposed to the surface and hence lack of documentary and study.

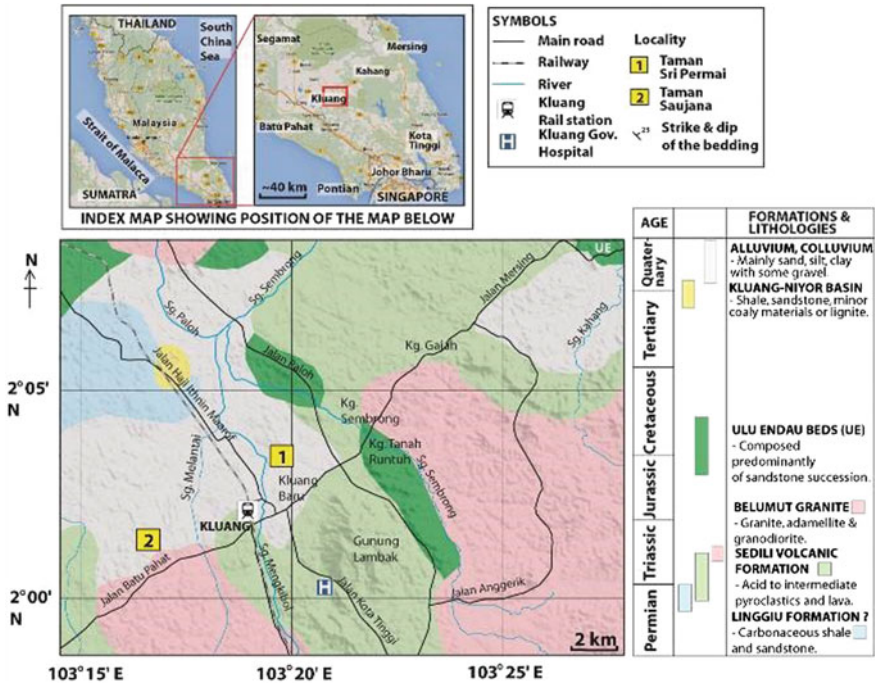


**Fig. 1** Digital elevation model around Kluang area. In the model, *light pink-coloured area* is ~35 m in elevation and *dark pink* is ~50 m. It shows that Kluang is generally a flat low-land area and mostly covered by alluvium. Two outcrops are located in the area with the elevation of around 50 m

Both outcrops are exposed at the slope-cut on top of a hilly area. As both exposures are continuous; few metres in height and about tens of metres in length. The deposits are quite well-bedded and gently/horizontal dipping, and the thickness is quite even in the lateral extension except the channelized deposit features. The lithology is mainly light-coloured, not fully consolidated sandstone with a wide range of grain sizes. Although the exposure of the beds is only a few metres, the grain sizes of the sandstone changed rapidly. Sedimentological logging in different parts of the outcrop was conducted in one of the outcrop (Taman Sri Permai) in order to understand the lateral variation of the depositional environment.

## 2 Tertiary Sedimentary Rock in Johor

Three Tertiary basins were identified in Johor, namely Kg. Durian Chondong Basin, Kluang–Niyor Basin (Fig. 2) and Layang-layang Basin, which are located at the northern, middle and southern parts of this state, respectively. Since the visited outcrops are located in Kluang, these not fully consolidated sandstones have potential to be correlated with Kluang–Niyor Basin. These respective basins will be reviewed in detail as followed.



From the previous geological studies, the occurrence of Kluang–Niyor Basin ranges from Niyor south to Kluang (~8 km) and from Kluang to the west and south-west (over 9.5 km). Stauffer [3] suggested it was probably several kilometres across. This interpretation is based on the field evidences such as variable dip directions of the sediments, rapid lateral thickness changes and depth to older rock (granite and volcanic rocks).

Several exposures were observed and described along the Niyor and Kluang rail stations. Near to Niyor rail station, from milepost (railway) 413.25–417.25, the lithologies are mainly grey and pink, slightly iron-stained alluvium consists of mainly of sub-angular quartz grains. In milepost 414.25, pale grey shale of a compact, fine-grained nature containing numerous concretions of similar materials was exposed beneath alluvium. Poor-quality lignite with NE dipping was seen bedded with alluvium which was observed in milepost 471.75 [2].

In the Kluang rail station area, several borehole drillings were conducted since the 1930s. The shallow depth sediments encountered from drilling were sandy clay, clay, sands and shale. One of the boreholes discovered a 4.5-m-thick shale containing fossil vegetations and little oil indication at the deeper part of the borehole (10.7 m) [2]. Lignite is occasionally found in the sedimentary sequence. The bottom of the wells encountered granite, volcanic rocks and quartzite/tuff at the depth more than 20 m.

Similar sediments were found at Batu Arang and other Tertiary basins of west Malaysia, and thus, it is likely to be Tertiary age [3]. Burton [1], however, mentioned the possibility of a Quaternary age for these sediments, though he considers the unconformity overlying alluvium to be of an Early Pleistocene or even Pliocene age.

### 3 Methodology

The study begun with sedimentary logging in 3 different sections of the Taman Sri Permai outcrop to identify the variation of the lithology in terms of the lateral extension. During logging, the details of the sediments were carefully recorded in detailed, i.e. colour, consolidation state, mineral types, grain sizes, shapes and sorting. The logs were correlated with the outcrop (photopanel) to identify the major trend of lithological changes laterally. In Taman Saujana outcrop, detailed observation on sedimentation was conducted and compared with previous outcrop of Taman Sri Permai. Based on the rock textures/properties, the facies were identified to the sedimentary sequences and their depositional environment was proposed.

### 4 Results and Discussion

This section composed of outcrop descriptions and sedimentary facies of Taman Sri Permai and Taman Saujana. These facies were identified based on the observations, and the deposition environment was proposed.

*A. Outcrop Descriptions*

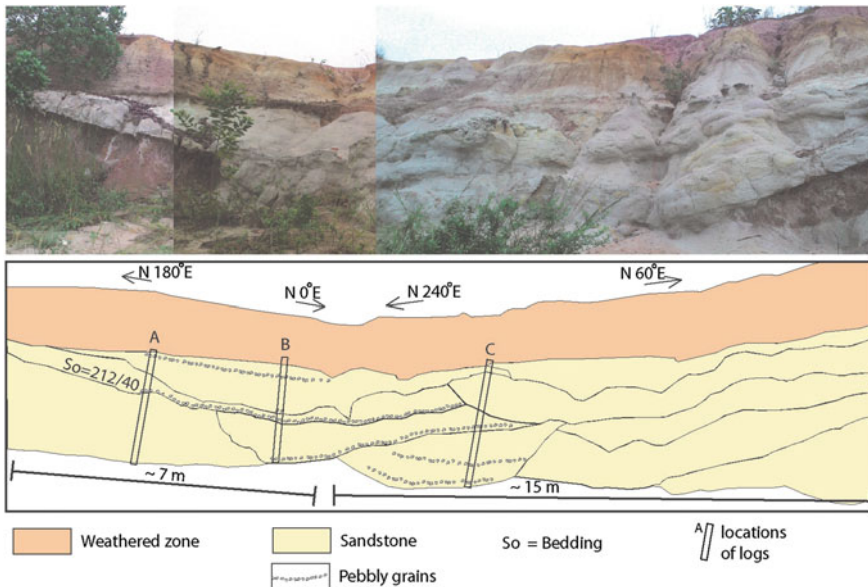
Two outcrops were described, i.e. Taman Sri Permai and Taman Saujana.

**(a) Taman Sri Permai**

An extensive exposure is located in the Taman Sri Permai approximately 2 km east of Kluang Town. The hill-cut is occurred in L-shaped pattern with about 4 m height and extended about 30–40 m (Fig. 3). The thicknesses of the beds vary from 15 to 150 cm. The channel feature at the outcrop will be the focus for this research. This sand-rich succession is characterized by thick- to medium-bedded sandstone facies and partially consolidated. The sandstone is coarse- to medium-grained, light grey in colour, composed of mainly quartz and feldspar grains in various sizes with sub-rounded to sub-angular shaped, poorly sorted and exists as a normal grading bed (Figs. 4 and 5).

**(b) Taman Saujana**

A hill side exposed a horizontal bedded sequence. This outcrop is located approximately 3 km west of Kluang Town. The total exposure of the outcrop is about 100 m, part of the exposure is shown in Fig. 6. The rocks have the similar texture as the outcrop in Taman Sri Permai, i.e., is not completely consolidated, light-coloured due to high percentage of quartz and feldspar grains, various sizes and shapes of grains (poorly sorted). The beds are 50–100 cm thick, but they pinched out to the sides. At the bottom of the channel feature, quartz and feldspar



**Fig. 3** Field photograph (*top*) showing general outcrop view of Taman Sri Permai section and its outcrop sketch (*bottom*)



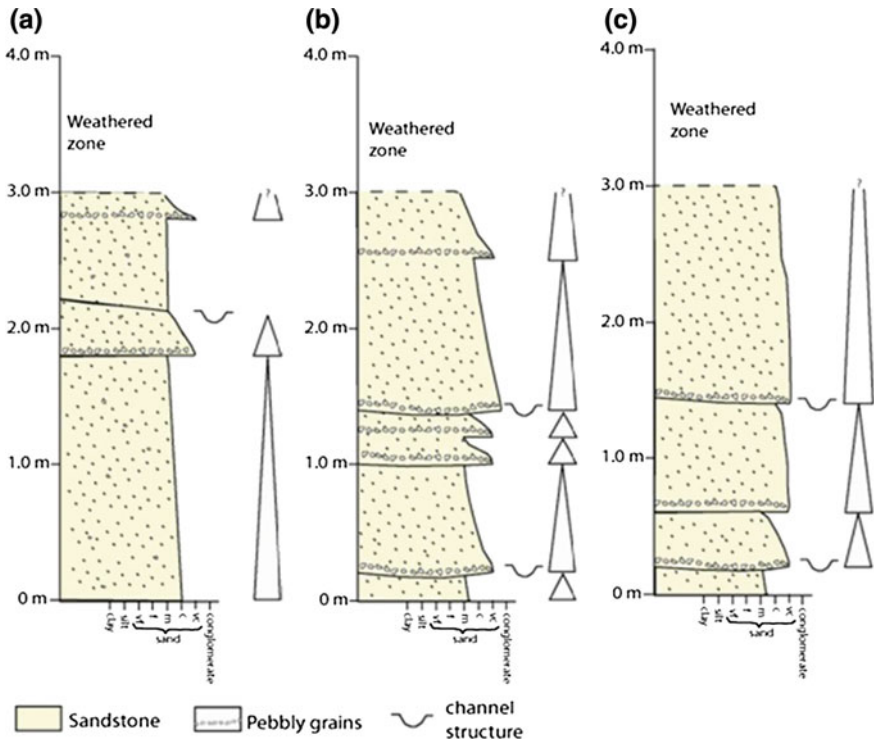
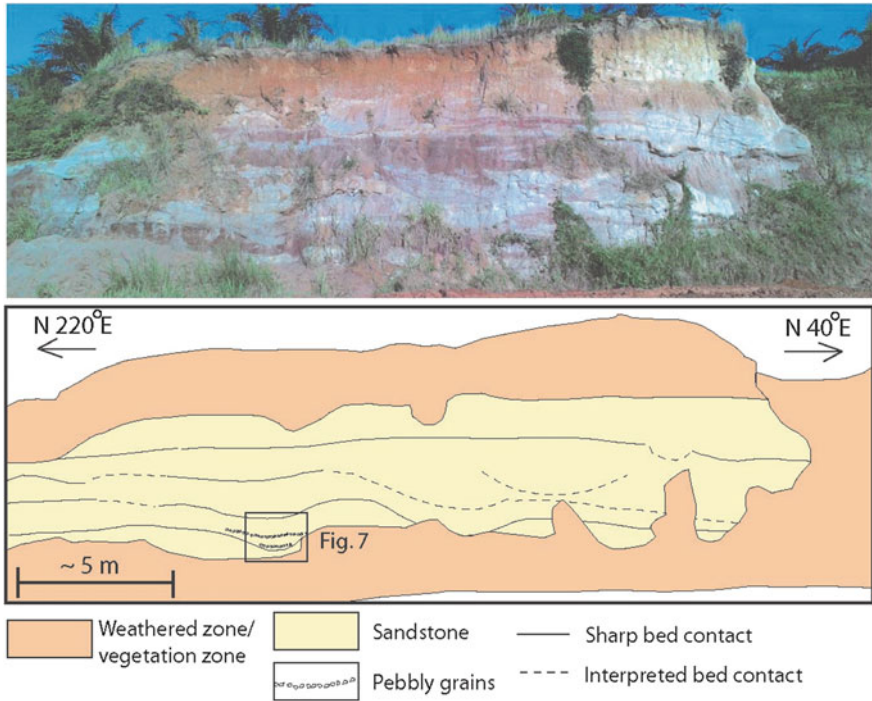


Fig. 4 Sedimentary logs of Taman Sri Permai outcrop shows fining upward trend



Fig. 5 The quartz grains of the conglomerate or very coarse-grained sandstone (F1a, pointed by white arrows) are aligned and sandwiched between medium-grained sandstone (F1b). The photograph taken at ~1.2 m of Log B





**Fig. 6** Field photograph (*top*) and the sketch (*bottom*) for part of the Taman Saujana outcrop

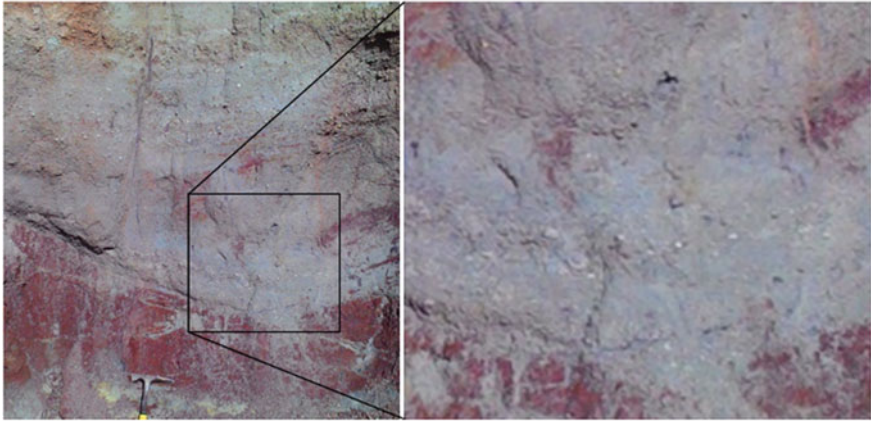
made up 50% of the total grains of the rock. The grain size of quartz is 0.3–5 mm, commonly 0.5 mm; whereas the grain size of feldspar ranging from 0.5 to 3 mm. The symmetrical in channel feature can be easily recognized and its bottom always filled with aligned pebble-sized grains. Fining upward sequence was observed within channel structure (Fig. 7).

**B. Sedimentary Facies**

The main facies that can be observed in both outcrops, i.e. pebble sandstone to medium-grained sandstone fining upward sequence (F1). This facies are divided into two sub-facies: pebbly sandstone/conglomerate (F1a) and medium-grained sandstone (F1b). The fining upward sequence (F1) can be clearly observed in the channel structure. The same sequence can be repeated several times in a single bed.

**(a) Pebbly Sandstone/Conglomerate (F1a)**

This facies commonly formed at the bottom of the bed. The rock is light grey to whitish in colour. The rock is often consolidated. The rock is made up of 85% grains and 15% of matrix. The grains of the rocks are mainly quartz and feldspar (partially to totally weathered into kaolinite). Colourless or translucent quartz grains are commonly in size of 1–3 mm, the grain size can be up to 10 mm. Feldspar grains are also often weathered to whitish kaolinite, and its sizes are mostly in the



**Fig. 7** Alignment of *light-coloured pebbles* (mainly quartz) in the channel sandstone bed. Part of the hammer as scale, ~20 cm long is shown at the *bottom* of the figure. *Black box* is the close-up view of the grains (mainly quartz) alignment

range of 1–2 mm. Occasionally, the coarse feldspar grains remain unweathered and its cleavages are preserved. The range of the grains is ranging from 1 to 3 mm, which indicates that the rocks are very coarse sandstone to conglomerate. The grains are sub-rounded and the sorting of the rock is poor. Weak alignment of the coarse quartz grain can be observed particularly at the bottom of the bed.

#### **(b) Medium-Grained Sandstone (F1b)**

The sandstone is mud poor, light grey to milky white in colour and characterized by medium- to coarse-grained sandstone with good to moderate sorting. This sub-facies is partially consolidated and made up of 80–90% grains. The grains composed dominantly of quartz and feldspar minerals. Quartz grains size varies from 0.2 to 0.3 mm but may be up to 5 mm. The grains are sub-rounded in common. The coarser grains are sometimes found embedded in the rock.

#### *C. Depositional Environment*

The two exposures in Kluang area shown fining upward sequence (F1) which composed of pebbly sandstone/conglomerate (F1a) changing to medium-grained sandstone (F1b). The sequence can be clearly observed in the channel structure in the rock succession. It indicates that the deposition is under a fluvial environment; however, the common braided river's sedimentary structure (cross-bedding) is not observed. This fluvial system may be developed at late Tertiary and continue till Recent. The rivers incised and migrated to the current lower position in nearby area, e.g. Sg. Mengkibol and Sg. Melantai.

Based on the lithological information of these two exposures, it is correlatable to the alluvium unit (horizontal bedded unconsolidated fluvial sands) of Kluang–Niyor Basin summarized by Raj [2].

## 5 Conclusion

Two exposures of potential Tertiary sequences of Kluang (Taman Sri Permai and Taman Saujana) were visited and studied. They are composed of well-bedded, not fully consolidated sandstone ranging from medium-grained to coarse-grained or conglomerate. Those exposures have clear channel features with alignment of coarse sand- or pebble-size grains at its bottom. The sandstone with coarse-grained sand grains commonly has fining upward pattern and changes to medium-grained sandstone. This sequence is named as “pebble sandstone to medium-grained sandstone fining upward sequence (F1)”, with 2 sub-facies, pebbly sandstone/conglomerate (F1a) and medium-grained sandstone (F1b). This facies shows a braided river deposition environment. Since the tectonics are quite stable from Tertiary to Recent, the rivers may have begun to develop at late Tertiary and gradually incised to nearby area till present day, e.g. Sg. Mengkibol and Sg. Melantai, and the remnant of river deposits is now exposed at these two outcrops.

## References

1. Burton, C.K., 1964. The Older Alluvium of Johore and Singapore. *Jour. Trop. Geog.*, 18, 30–42.
2. Raj. J.K., Abdul Hadi Abd. Rahman and Mustaffa Kamal Shuib, 1998. Tertiary Basins and inland Peninsular Malaysia: review and tectonic evolution. *Geol. Soc. Malaysia, Bulletin* 42, pp. 211–226.
3. Stauffer, P.H., 1973. Cenozoic. Chapter 6. In: Gobbett, D.J. and Hutchison, C.S. (Eds.), *Geology of Malay Peninsula*. Wiley-Interscience, U.S.A., pp. 143–176.
4. Tate, R.B., Tan, D.N.K. & Ng, T.F., 2008. *Geological Map of Peninsular Malaysia*. Scale 1:1 000 000. Geological Society of Malaysia & University Malaya.

# 3D Reservoir Characterization of Field Deta, Termit Basin, Niger

Eevon Chang and Lo Shyh Zung

**Abstract** Field Deta is located in the south–west area of Agadem Block. Agadem Block (27516.2 km<sup>2</sup>) covers main part of Termit basin. The Termit basin is believed to be rifting basin (Genik, 1992, *Tectonophysics*, 213(1–2): 169–185) [1] with graben structures. The total studied surface area of Field Deta covered by 3D seismic is about 945 km<sup>2</sup>. There are total of 12 wells drilled in the area of study mentioned above. The hydrocarbon is discovered from Alter Sokor formation which is divided into 6 sand groups: E0, E1, E2, E3, E4, and E5. The average thickness of sand groups ranges from 80 to 140 m. E2–E4 is the major oil zone; meanwhile, partly of the E5 sands had found some compartmentalized gas. Hence, this study aims to understand the highly faulted horst and graben structurally controlled reservoirs. Besides this study also reviews the radioactive sand thickness and low-resistivity pay interval that will affect the hydrocarbon assessment. Radioactive sand can be differentiated and studied using SGR log by plotting Th/K crossplot and density–neutron crossplot. The Shaly-sand intervals interpretation and petrophysical characterization are carried out taking into account the radioactive sand. Aware about the potential low-resistivity pay, resistivity index of deep resistivity log is compared. 3D seismic volume is interpreted with regard to different seismic attributes to enhance structural interpretation.

**Keywords** Rifting basin Radioactive sands Low-resistivity pay Density–neutron crossplot

---

E. Chang (✉) · L.S. Zung (✉)  
Department of Geoscience and Petroleum Engineering, Universiti Teknologi  
PETRONAS, 32610 Bandar Seri Iskandar, Perak Darul Ridzuan, Malaysia  
e-mail: eevonchang@gmail.com

L.S. Zung  
e-mail: losyh.zung@petronas.com.my

# 1 Introduction

Niger is a landlocked country bordered in the north by Libya, Chad to the east, and Nigeria in the south. A portion of Lake Chad is situated in the eastern part of the country. The hydrocarbon potential of Niger is mainly located in the two large sedimentary basins (the Iullemeden basin in the west and the eastern (Chad) basin in the east) [2] that cover about 90% of the national territory. The Agadem Block is part of the Termit-Ténéré Rift formation [3]. The Cretaceous–Tertiary rift basins are filled with Lower Cretaceous to Neogene sedimentary rocks, sediments ranging in thickness from about 3000 m to more than 12,000 m. Sediments mostly were deposited in fluvial, lacustrine, and marine environment [1, 4]. A total of seven discoveries/fields have been found, including this project study area, Field Deta.

Termit basin is an asymmetrical semi-graben, steep in the west and gentle in the east. The study area is filled with high dense of NW–SE-trending normal faults resulting from the several cycles of rifting activities (multiphase) from Lower Cretaceous–Tertiary. Hydrocarbon can be found from the sand package up to 2 km depth of the reservoir (Fig. 1).

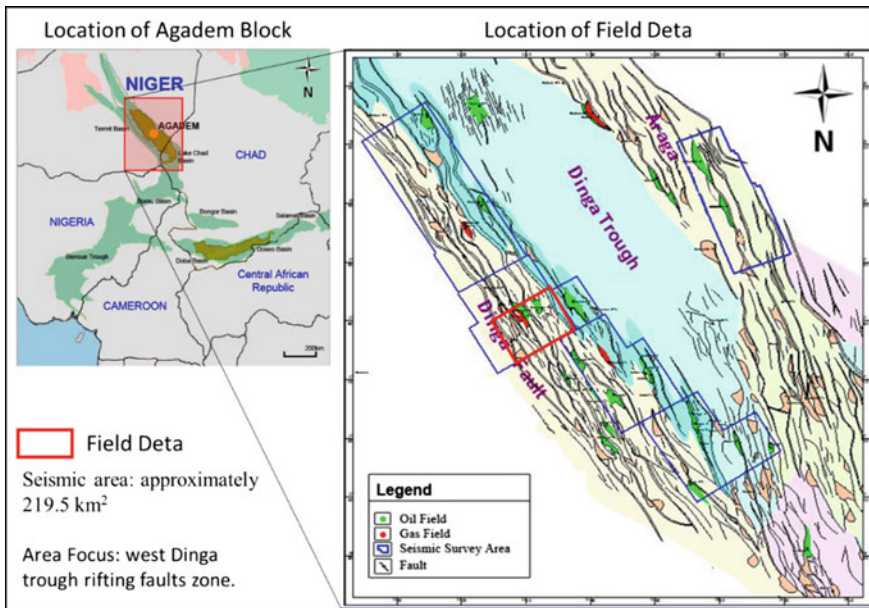
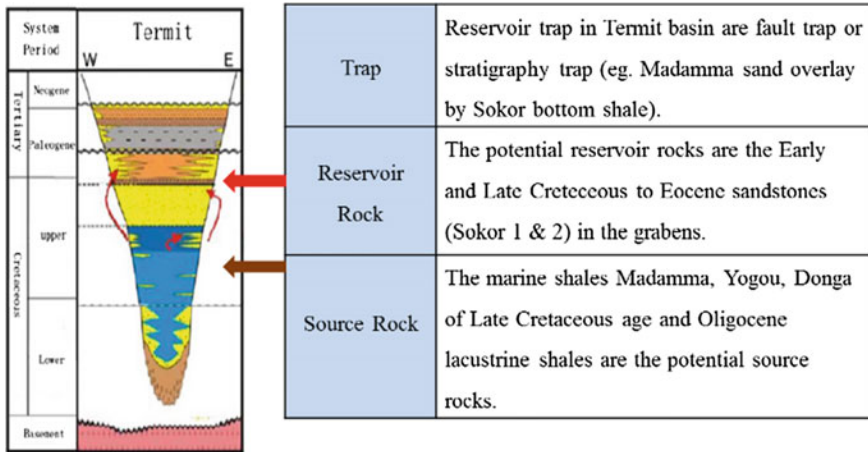


Fig. 1 The study area, Field Deta location map



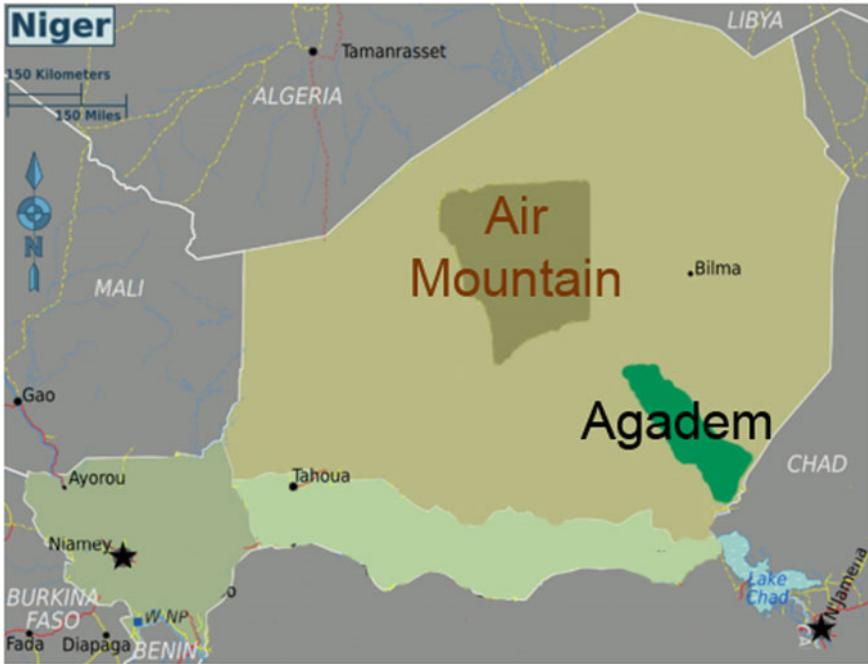
**Fig. 2** The sedimentary fill map of Termit basin showing the relationship of source rock and reservoir rock [9]

Geophysical interpretation had been carried out to investigate the structure-controlled prospect. The main focus of this project is to access the potential of undiscovered and technically recoverable oil and natural gas resources in Field Deta, Agadem Block, Niger.

The general geology had fulfilled the total petroleum system (TPS) concept which includes hydrocarbon source rocks, reservoir rocks, and traps for hydrocarbon accumulation [1]. Reservoir currently producing are from shallow Palaeogene Sokors 1 and 2 sands. The petroleum geology focuses on the source rock and reservoir rock in the field. Hydrocarbon is believed to be generated in the marine shales/mudstone and migrated to be stored in the Eocene sandstone reservoir rock as shown in Fig. 2. The sedimentary rocks ranging in age from Early Cretaceous to Neogene in the east Niger grabens had accumulated up to 10,000 m thick. It consists of mainly siliciclastic with some Late Cretaceous carbonates (Fig. 3).

### 1.1 Radioactive Sand

Air Mountains aged from Precambrian to Cenozoic is the nearest granite mountain to Termit basin. This granite mountain that consists of alkaline granite intrusions might be the source of radioactive sediments deposited in Termit basin. Radioactive sand is sediments sourced from nearby granitic highlands which have not undergone sufficient transportation and weathering. Radioactive sand contains parent



**Fig. 3** The location map of Air Mountains

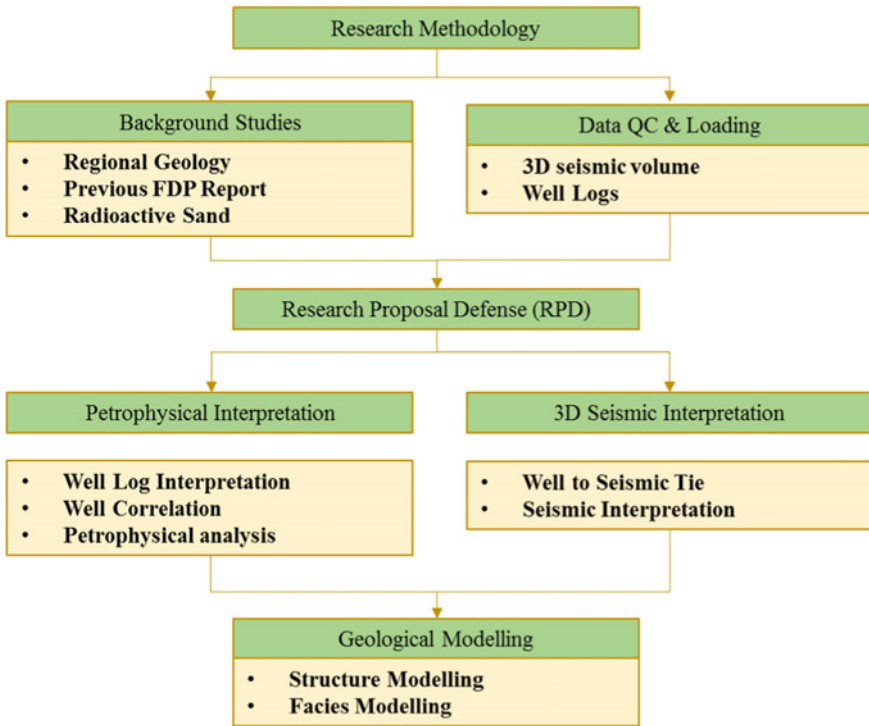
minerals (i.e., zircon, highly arkosic (high feldspar content), micas, glauconite, or uranium-rich water). Sand supposed to give low gamma ray (GR) value, but radioactive sand gives high GR value like shale. Sand intervals interpreted using GR log will be inaccurate.

## ***1.2 Low-Resistivity Pay***

Low-resistivity pay can be referred as resistivity range of 0.5–5  $\Omega\text{m}$  in deep resistivity logs or low contrast in resistivity logs characteristic between pay zone and adjacent shale-bed or water zone [5]. There are mainly two causes of low-contrast resistivity characteristic: conductivity of clay mineral and high irreducible water saturation [5]. Clay mineral gives high cation exchange capacity and therefore results in low resistivity; sandstone with medium-to-high shale content might have clay coating and bridging in pores and have shown low-resistivity value in log test.



## 2 Methodology



## 3 Results and Discussion

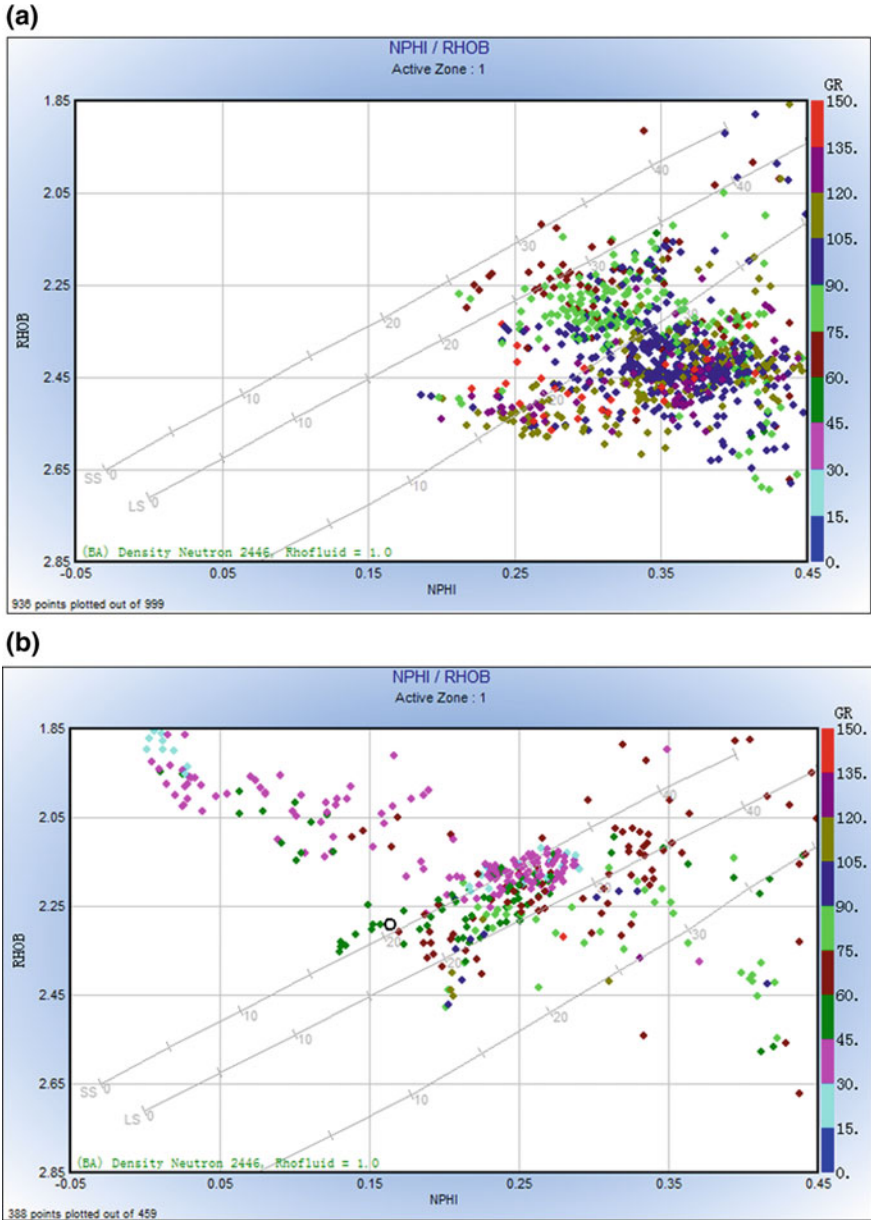
### 3.1 Petrophysical Well Log Interpretation

#### 3.1.1 Radioactive Sandstone

Radioactive sand had been reviewed in all wells to determine the accurate reservoir sand thickness. The possible radioactive sand is interpreted into zones. Two types of crossplot, Th/K crossplot and density–neutron crossplot, include only the data from the selected potential radioactive sand zones which are plotted. The results show that there is a percentage of radioactive sand in the data.

Density–neutron crossplot is used to test the existence of radioactive heavy minerals. Apparently, the matrix density from density–neutron crossplot in Fig. 4a is





**Fig. 4** **a** The conventional density–neutron crossplot with data from the suspected radioactive sand zones in Deta-1. **b** The density–neutron crossplot with data from non-radioactive sand zones in Deta-1

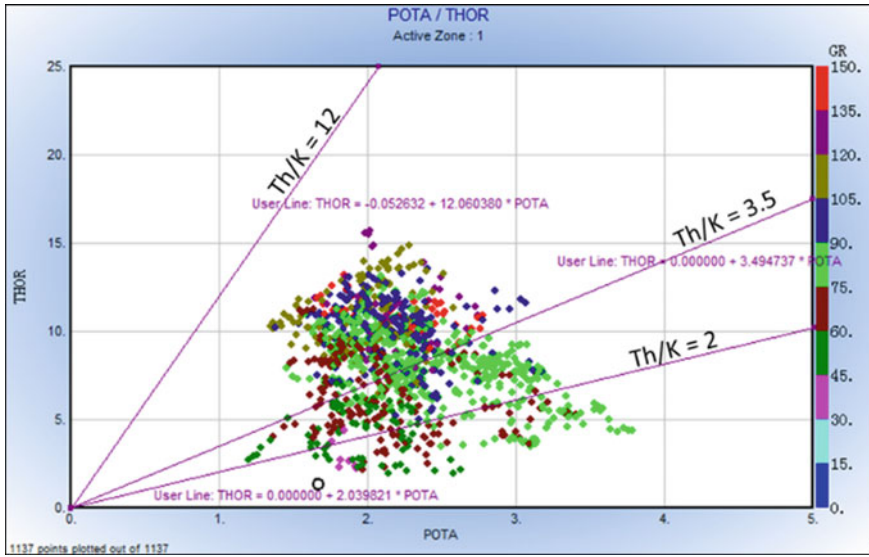


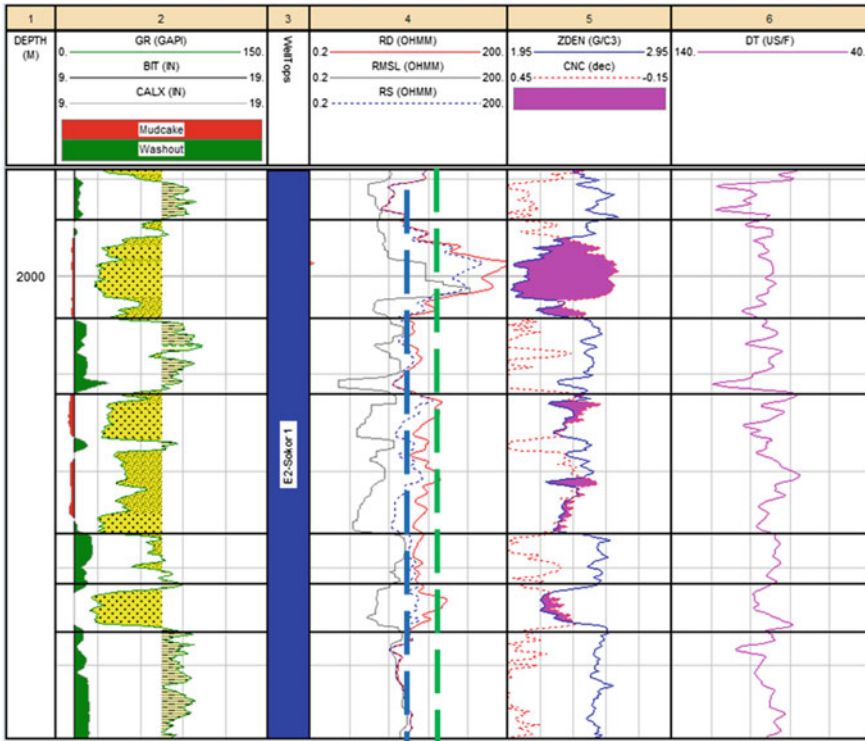
Fig. 5 The Th (ppm) versus K (%) crossplot for the suspected radioactive sand zones in Deta-4

higher due to denser minerals present in radioactive sand. As compared to the non-radioactive (normal) sand, the density–neutron crossplot in Fig. 4b data shows less dense sandstone where all the points of data fall around Rho fluid sandstone line.

The GR log is not reliable for lithology differentiation due to the radioactive substances in the sand, and the separate SGR log is used to help in identifying the exact sand shale interval. In shales, the potassium value indicates the presences of micaceous clay minerals—illite; high uranium concentration indicates organic shales. In sandstone, the thorium value is related as clay content; high potassium concentration is due to the abundance of mica and potassium feldspars [6] in radioactive sandstone. Thorium concentration versus potassium concentration crossplot in Fig. 5 is used to study the presence of radioactive sand.  $Th/K < 3.5$  or  $>12$  will be considered as radioactive substances in the sand zone data.

### 3.1.2 Low-Resistivity Pay Reservoir

Low-contrast characteristic in resistivity is always overlooked by interpreter. The low-resistivity pay with deep resistivity log readings from 7 to 12  $\Omega m$  exhibits a resistivity index of 1–1.7 compared with water zone section. Oil had been proven and produced from the well Deta-E1 low-resistivity pay section in Fig. 6. This low-contrast resistivity pay was also found in some other wells within the Termit basin. The possible lithology reason that leads to this type of low-contrast response is still being investigated, and two high possibilities are low water salinity of the water zone and high clay substances in sandstone.



**Fig. 6** Well section of Deta-E1 showing low contrast of resistivity log between reservoir and non-reservoir interval

### 3.2 Well Correlation and Lithofacies

After the sand interval reviewed, well correlation is carried out from the direction of southwest to northeast. The main focus reservoir is the Sokor 1 with E0–E5 sand groups (refer to Fig. 8). The Sokor 1 reservoir can be differentiated into two compartmentalized reservoirs: west reservoir (depth range: 1180–1280 m) and east reservoir (depth range: 1800–2500 m). The two reservoir compartments are separated by huge fault—Fault L1, between Deta-5 and Deta E-1. Sokor 1 sedimentary facies are characterized as fluvial delta environment moving into lacustrine environment as shown in Fig. 7 [7].

Basic observation from the GR log pattern shows sand column is blocky and cleaning upwards or dirtying upwards signatures in sand package, indicating possible interchange in depositional environment through time between tidal/fluvial

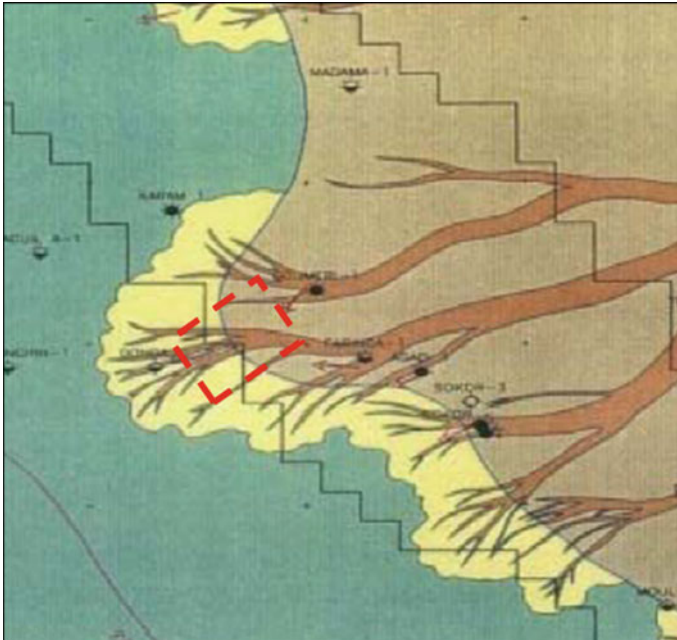


Fig. 7 The analogy of depositional environment for Sokor 1 sand groups

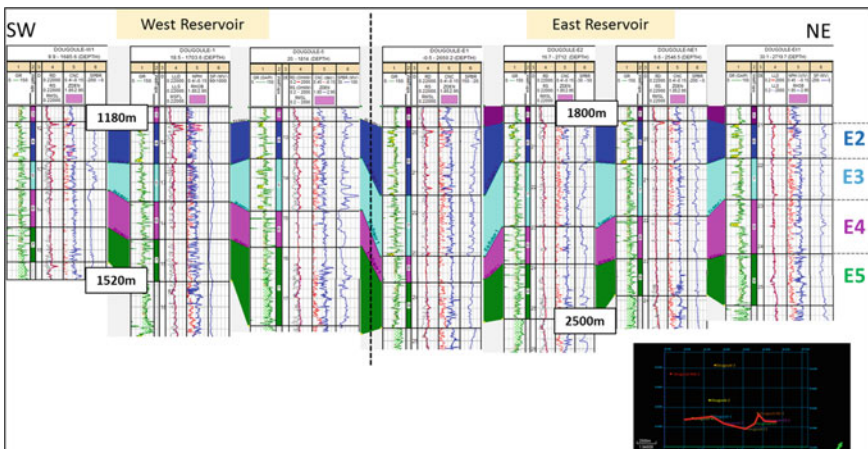


Fig. 8 Sokor 1 reservoir well correlation in direction: (SW) Deta-W1, Deta-1, Deta-5, Deta E-1, Deta E-2, Deta NE-1, and Deta-EX1 (NE)

**Table 1** The summary of lithology description studies from the core samples of E2–E5 sands

Sand	Lithology
E2	Gray mudstone Shaly SS–green fine SS Dark gray–gray SS
E3	Light gray fine SS Gray SS Dark gray SS–gray coarse SS with gravel
E4	Dark gray fine SS Sandstone (SS) Muddy shaly SS
E5	Gray matured SS Gray matured SS interbedded with gray mudstone Dark gray–gray matured SS

SS Sandstone

**Table 2** Fault strike orientation, dipping direction, and type of fault

Fault	Strike	Dipping	Type
L4	NW–SE	SW	Normal
L3	NW–SE	SW	Normal
L2	NW–SE	NE	Normal
L1	NW–SE	NE	Normal
R1	NW–SE	SW	Normal
R1a	NW–SE	NE	Normal
R1b	NW–SE	SW	Normal
R2	NW–SE	SW	Normal
R3	NW–SE	NE	Normal
R4	NW–SE	NE	Normal

channel fills and coastal barrier bar environment [8]. The high serrated GR log pattern at shale zones showed muddy/mudstone characteristic for the lacustrine environment [8]. Core samples of the area are studied and described in Table 1.

### 3.3 Fault Interpretation

The major faults are interpreted to identify reservoir compartments and stratigraphy correlation. The fault strikes are all in northwest–southeast direction following the rifting geological direction and are either dipping in the direction of southwest or northeast. The normal fault results from rifting activities are generally presented with big displacement as observed in the seismic (Table 2).

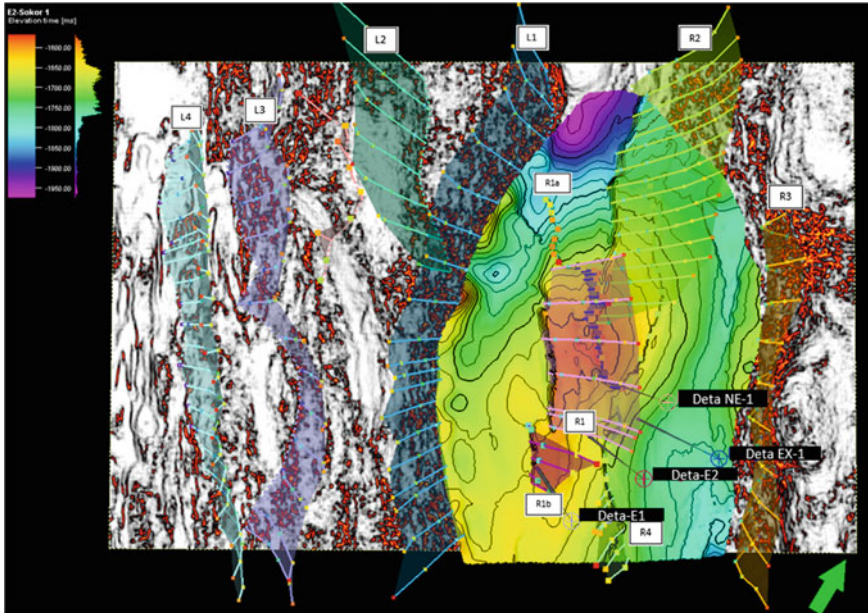


Fig. 9 Interpreted faults on variance time slice (-2000 ms) overlay by east reservoir E2 top map

### 3.4 Horizon Interpretation

Horizon interpretation is focused at Sokor 1 east reservoir. 4 surfaces are interpreted: E2, E3, E4, and E5. The Sokor 1 reservoir found in Deta E-1 and Deta E-2 is mainly controlled by Fault R1 (Refer to Fig. 9). Fault R1 is highly possible sealing that had formed a closure for the two-way dipping E2 top surface towards the northeast direction. As observed, Deta-E1 and Deta-E2 are drilled on the same fault block and Deta NE-1 and Deta EX-1 are drilled on another fault block. The interpreted two-way-time (TWT) maps are converted into depth map by using single function (generated from checkshot) method. The pressure data will be crossplotted to identify the hydrocarbon contact in order to do volumetric calculation (Fig. 10).



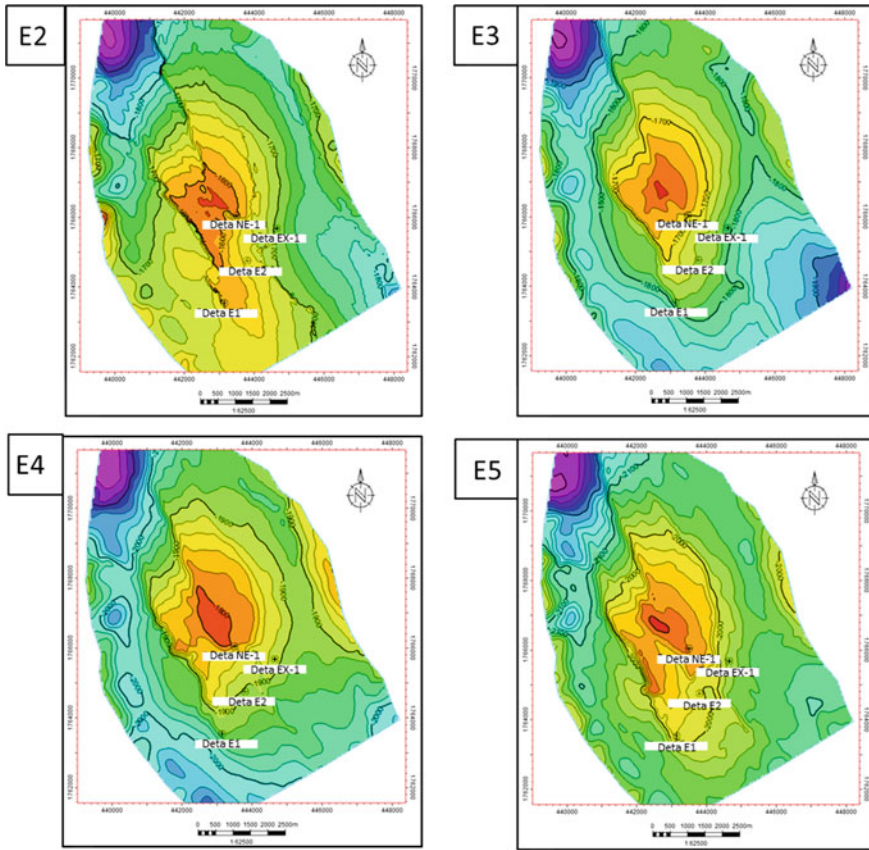


Fig. 10 TWT maps of E2, E3, E4, and E5 interpreted and shown with 4 wells in the reservoir area

## 4 Conclusion

The review on possibility of radioactive sand had increased the net pay thickness of reservoir and the other petrophysical values such as porosity and permeability. The seismic interpretation is carried out to generate the output gross bulk volume (GBV) and study of reservoir connectivity between wells as well as sand distribution. Based on the increase in GBV, the volumetric calculation will show an increase in reserves initial in place. This project had proved that radioactive sands and low-resistivity pay should not be overlooked in reservoir characterization.

## References

1. G. J. Genik, "Regional framework, structural and petroleum aspects of rift basins in Niger, Chad and the Central African Republic (C.A.R.)," *Tectonophysics*, vol. 213, no. 1–2, pp. 169–185, 1992.
2. J. G. Shellnutt, T.-Y. Lee, C.-C. Yang, S.-T. Hu, J.-C. Wu, K.-L. Wang, and C.-H. Lo, "Late Permian mafic rocks identified within the Doba basin of southern Chad and their relationship to the boundary of the Saharan Metacraton," *Geol. Mag.*, vol. 152, no. 06, pp. 1073–1084, 2015.
3. I. Aigbedion, "Reservoir fluid differentiation case study from Oredo field in the Niger Delta—Nigeria," vol. 2, no. June, pp. 144–148, 2007.
4. M. Zanguina, A. Bruneton, and R. Gonnard, "An introduction to the petroleum potential of Niger," *J. Pet. Geol.*, vol. 21, no. 1, pp. 83–103, 1998.
5. M. Zhiqiang, K. Lichun, X. Chengwen, L. Guoxin, Z. Cancan and O. Jian, "Identification and Evaluation of Low Resistivity Pay Zone by Well Logs and the Petrophysical Research in China\*," vol. 4, no. 1, 2007.
6. O. Chudi and R. Simon, "Petrophysical Characterisation of Radioactive Sands- Integrating Well Logs and Core Informations: A Case Study in Niger Delta.," no. Obuaya 1989, pp. 1–8, 2012.
7. L. Wan, J. Liu, F. Mao, M. Lv, and B. Liu, "The petroleum geochemistry of the Termit Basin, Eastern Niger," *Mar. Pet. Geol.*, vol. 51, pp. 167–183, 2014.
8. M. E. Okiator and O.I. Imasuen, "Facies Characterisation of Well A, Field Y, North-Eastern Niger Delta," *Journal of Petroleum Technology and Alternative Fuels*, vol. 2(4), pp. 45–54, 2011.
9. X. Pan, S. Y. Z. Ji, and G. H. L. Liu, "IPTC 17116 Forming Mechanism and Petroleum Geological Features of the Western-Central African Rift Basins (WCARBs)," pp. 1–12, 2013.



# Reservoir Characterization of Lacustrine Environment, Doba Basin, Southern Chad: Radioactive Sand Delineation

M.S. Nur Fathiha, S.Z. Lo and A.S. Ahmed Mohamed

**Abstract** The contribution of lacustrine environment as the hydrocarbon reservoir has been widely known. However, despite of its growing importance, the lacustrine petroleum geology has received far less attention than marine due to its sedimentological complexity [3]. This study therefore aims at developing an understanding of the unique aspects of lacustrine reservoirs which eventually impact the future exploration decisions. Hydrocarbon production in Doba Basin, particularly the northern boundary, for instance, has not yet succeeded due to the unawareness of its depositional environment. The drilling results show that the problems were due to the presence of radioactive sand that will lead to the overlooked reservoir, bad cementing, and failed DST. More advanced detailed interpretations comprising of integration study between geological and petrophysical data are required to further explain the characteristics and features of the lacustrine sand body environment, thus solving the problem encountered in this area.

**Keywords** Reservoir characterization · Lacustrine environment · Doba Basin

## 1 Introduction

Lacustrine-dominated basin is a standing water surrounded by land that mostly feed and drained by river and streams. The water depth, size, salinity, and sedimentation vary from one lake to another. Some lake deposit can act as both source and reservoir. The lacustrine reservoir may have high porosity and permeability values, thus making it known as one of the prolific areas for hydrocarbon exploration where much fields in the world have been produced from this type of environment.

Doba Basin, particularly, has high potential of being a good lacustrine reservoir. It is a Late Mesozoic basin situated in Southern Chad of the Central Africa. The

---

M.S. Nur Fathiha (✉) · S.Z. Lo · A.S. Ahmed Mohamed  
Geoscience Department, Faculty of Geoscience and Petroleum Engineering,  
Universiti Teknologi PETRONAS, 32610 Bandar Seri Iskandar, Perak, Malaysia  
e-mail: Fathiha.Ms@gmail.com

appraisal wells have been drilled in the northern block of Doba Basin; however, no hydrocarbon has been produced yet even though the exploration well proves the presence of it. The drilling results show that the problems were related to the radioactive sand occurrence in the lacustrine depositional environment. Relatively short-distance sedimentation (incomplete weathering cycle) and granitic hill provenance are the ground cause of arkosic and subarkosic sand deposition. This highly radioactive sand content leads to the:

- (i) Misinterpretation reservoir or overlooked reservoir as more radioactive sand being mistaken as shale due to the high gamma ray value (fail differentiation of reservoir and non-reservoir),
- (ii) Bad cementing which eventually affects the DST result (fail or inconclusive).

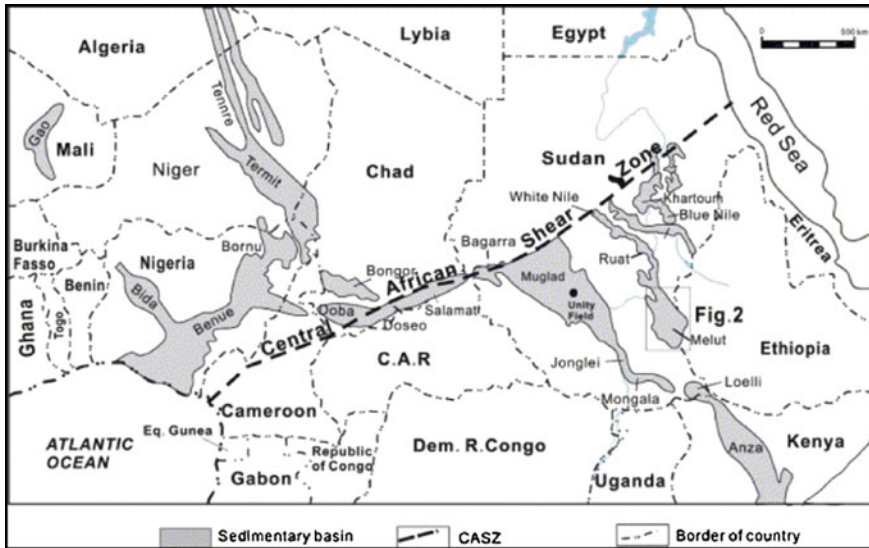
This radioactive sand has some unique character of the wireline logging as compared to the conventional logs. A progressive investigation of the geological and petrophysical characteristics may help in recalibrating the data, thus leading to a better calculation of hydrocarbon volume in Doba Basin which significantly impacts the exploration concept measures. Therefore, to address this issue, an integrated reservoir study on wireline logs, mud logs, thin sections, cores/side wall cores, and the DST results is needed to reveal the more detailed reservoir model for future exploration.

## 2 Geological Setting

### 2.1 *Regional Geology of Africa, Chad, and Its West and Central African Rift System (WCARS)*

Regional tectonic study revealed that the lithosphere of African continent, which was affected by the separation of Gondwana land and the staged expansion of Southern Atlantic Ocean in Early Cretaceous, has experienced drift motion in the direction of northeast under the action of mantle convection. Moreover, Atlantic plate compressed and wedged in the middle of the continent plate which forms the West and Central African Rift System (WCARS) [2]. The strong dextral strike-slip tension of WCARS then developed a series of Late Mesozoic–Cenozoic passive rift basins. The rift is divided into two systems: the West African Rift System (WAS) and the Central African Rift System (CAS) [6–8, 13, 15].

The Republic of Chad comprise of series of Cretaceous-to-Cenozoic sedimentary basins unconformably underlain by Lower Paleozoic and Precambrian basement. These basins are part of WCARS, having a sediment thickness ranging from 7.5 to 14 km with a combined length exceeding 7 km of linked rift system [6]. In the Republic of Chad, only four out of six main basins have the hydrocarbon discoveries, namely Bongor, Chad, Doseo, and Doba. Doba Basin, however, is the primary area of the oil and gas exploration and development where over 50% of the country's wells have been drilled, becoming the current oil production of the country [14] (Fig. 1).



**Fig. 1** Simplified tectonic map of Central African Shear Zone (also called as Central African Rift System) and its major features that form under strong dextral strike-slip tension of Central African Shear Zone (modified from [5] and [12])

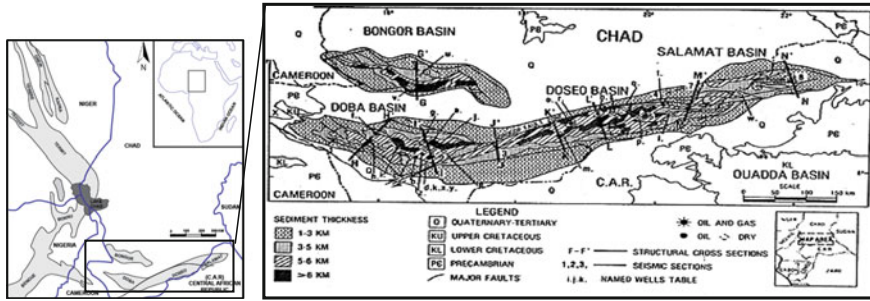
## 2.2 Doba Basin

Doba Basin is located in the northwest of Central African Rift System. This asymmetric basin trends northeast-to-southwest direction that was formed and evolved under the control of movements of Central Africa faults with obvious strike-slip characteristics. For stratigraphic sedimentary characteristics, the basement of all rift basins is composed of Precambrian metamorphic rocks. Doba Basin met the tension and rifted depression with thinner Lower Cretaceous formations, but thicker Upper Cretaceous formations (Fig. 2).

In view of sedimentary environment, the Lower Cretaceous formations mainly contain lacustrine sediments, the sandstone and mudstone interbeds are major reservoir strata, and especially a large set of thick shales are developed at the top Lower Cretaceous, acting as the good regional caprocks. Upper Cretaceous is dominated by abundant fluvial sandstones, with alluvial plain mudstones at the top. Cenozoic formations contain fluvial coarse-grained clastic sediments. In Doba Basin, the total thickness of formation is at most over 7,500 m, and the key exploration target is Lower Cretaceous strata, followed by Upper Cretaceous strata [8].

The petroleum geology of Doba Basin is as follows [1]:

- **Reservoir rock**—Lower Cretaceous (porosity ranges from 35% down to 2%, normally 15–20%) and Upper Cretaceous (porosities range 25–32%) varyingly arkosic sandstones.



**Fig. 2** Maps studied location, Doba Basin of Southern Chad which is a part of Central African Rift System, CAS (after Aremu n.d)

- **Source Rock**—Lower Cretaceous early rift lacustrine shales with the TOC content of typically 1–4% (type I and III organic matters)
- **Seal**—Lower Cretaceous (lacustrine) Mangara shale and Upper Cretaceous (flood plain and interdistributary to lacustrine) Miandoum shale.
- **Hydrocarbon Quality**—Medium-to-high gravity crudes of similar quality in the Lower Cretaceous. The oils are paraffinic with wax content up to 25%.

### 3 Lacustrine Radioactive Sandstone and Cement Bond Logging

#### 3.1 Lacustrine Radioactive Reservoir

The hydrocarbon reservoir potential within lacustrine basins is partially impacted by the overall tectonic setting [10, 11] where within extensional settings, there are (i) limited transport distance and (ii) poorly sorted and immature sedimentation (commonly resulting in poor reservoirs due to both primary properties and their susceptibility to diagenesis).

The radioactive sand, resulted from the limited transport distance, is coarse-grained detrital rocks that have high affinity of radioactive minerals. In principle, sand is usually composed of quartz which give low gamma ray (GR) reading, but the high concentration of radioactive minerals in clean sand causes the increase of GR value. Radioactive sand can be classified into 6 types which are (i) feldspathic sandstone or arkose, (ii) micaceous sandstones, (iii) mixed feldspathic–micaceous sandstone, (iv) greensand or glauconitic sandstones, (v) heavy mineral within sandstones, and (vi) shaly sand and sandstone [4]. This radioactive sand comes from near-by granitic highlands, implying that the detrital materials from the sedimentary source have not undergone sufficient transportation and weathering, and then, the parent minerals such as feldspar (K), micas, glauconite, and heavy minerals would be retained in the sedimentary rock. In this case,

the sands and gravel may be highly arkosic (high feldspar content) with a high content of K40 or may contain zircon enriched with thorium.

### 3.2 Cement Bond Logging

The purpose of cement bond loggings is to determine the quality of the cement bond to the production casing and to evaluate cement fill-up between the casing and the reservoir rock. Poor fill-up of cement leaves large channels behind the pipe that, likewise, allow the flow of unwanted fluids, such as gas or water into an oil well. Both poor bond and poor fill-up problems can also allow fluids to flow to other reservoirs behind casing. This can cause failed or inconclusive DST, thus leading to the serious loss of potential oil and gas reserves.

The interpretation shows that this poor cementing happened at the area of highly radioactive sandstones. The arkosic sandstones cause the cement to be non-solidified and leave spaces between the borehole and casing. The scales range from 0 to 100 where 100 indicates no cement is present (Fig. 3).

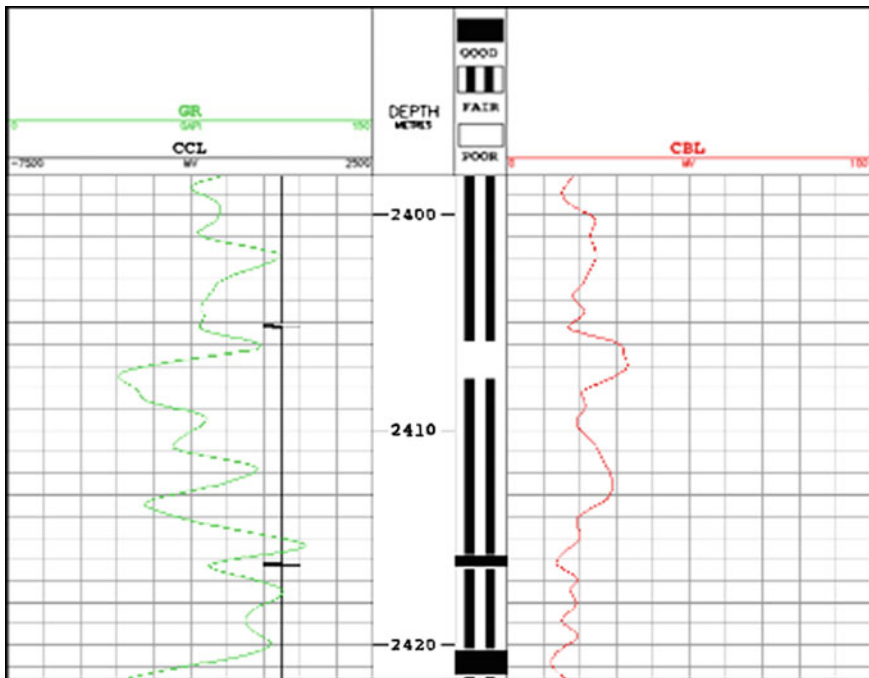


Fig. 3 Cement bond logging shows that the poor cementing occurs at the high gamma ray value, and according to the core sample, it is sand

## 4 Methodology

The methodology used in this study is comprised of (i) integrated study of wireline logging, mud logging, DST, and rock matrix analysis and (ii) core and petrography thin section analysis.

And these are done by using the following steps;

- (M1) Literature review of the geological study area
- (M2) Data collection
  1. **Wireline Logging** (conventional logging, shear wave, and FMI data)
  2. **Mud Logging**
  3. **Thin Sections and Cores**
  4. **DST Results**
- (M3) Analyzing and interpreting data of the study area based on the regional geology, reservoir geology, and petrophysics aspect (By the application of log-based technique and core analysis interpretation, the occurrence and type of radioactive sand can be recognized)
  1. **Natural Gamma Ray Spectroscopy:** To study thorium and uranium (ppm) and potassium (%) content.
  2. **Wireline Log Response and Cross-plot:** To recognize the reservoir and non-reservoir, thus conducting the petrophysical evaluation.
  3. **Petrography Thin Section:** To study the detailed information about mineralogy of detrital matrix and cement composition.
- (M4) Evaluation of the applied potential of the methodology depicted above for its integration in exploration (and production) routines.

## 5 Results and Discussion

Based on the problems listed (overlooked reservoir and bad cementing), there are needs in finding the real reasons of the cause of failure (which later causes the production wells to fail). After the analysis and interpretation, it is confirmed that the prime factor is due to the occurrence of radioactive sand in Doba Basin. Therefore, it is necessary for the geologist to know the presence of it as it will be affecting the whole well, in fact whole block volumetric hydrocarbon exploration decision. Here are the interpretation results of the radioactive sand existence based on the methodologies mentioned earlier.

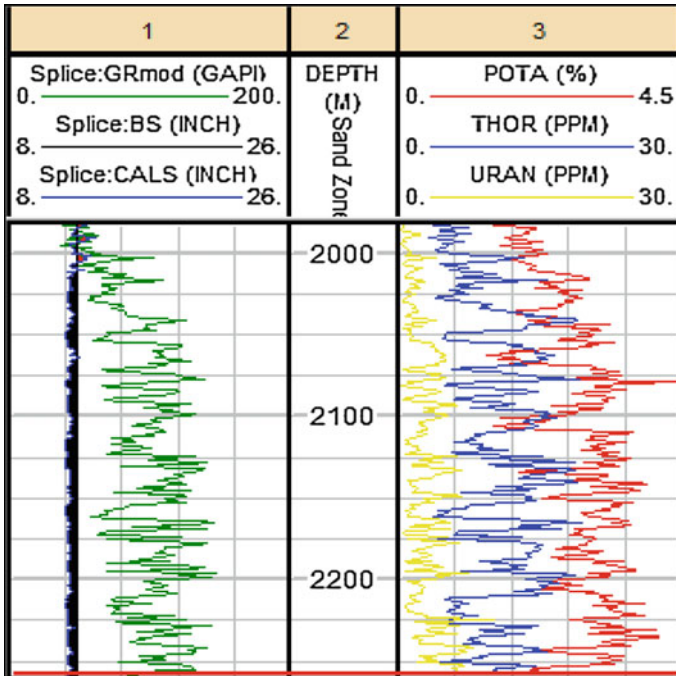


Fig. 4 Using gamma ray spectroscopy to determine the type of radioactive sand

### 5.1 Natural Gamma Ray Spectroscopy

By using the natural gamma ray spectroscopy, the individual sources' gamma ray can be determined, thus helping in interpreting the type of sand in the reservoir. In general, in shales, high potassium indicates micaceous clay, while high uranium indicates organic shale. As for the sandstones, high potassium means arkosic sand, and high thorium and uranium suggest more heavy minerals within the sandstone matrix.

In Doba Basin, one of the wells shows high gamma ray value, but there is a formation of mud cake which is usually associated with sand interval. To refine further, the amount of potassium element in that interval is the highest compared to the uranium and thorium and this concludes that the interval has arkosic sand (Fig. 4).

### 5.2 Wireline Log Response and Cross-Plot

#### 5.2.1 Integration of the Wireline Logs and Cross-Plot

The integration of wireline logs including the FMI and mud log is capable of determining the reservoir interval. Neutron density (NPHI vs. RHOB) on the other

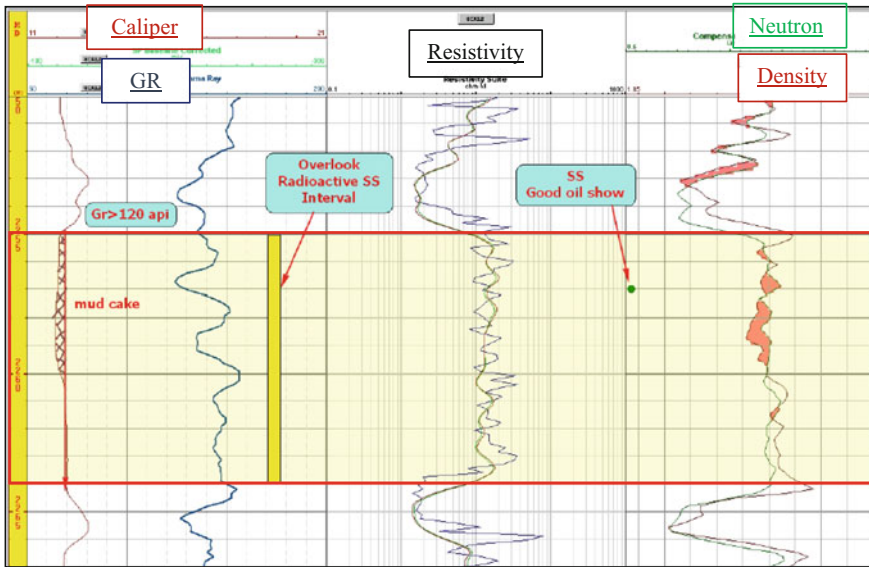


Fig. 5 Formation of mud cake, high resistivity value, and distinct features of neutron density pattern (crossover) show that the interval is the reservoir zone even though it had high gamma ray value

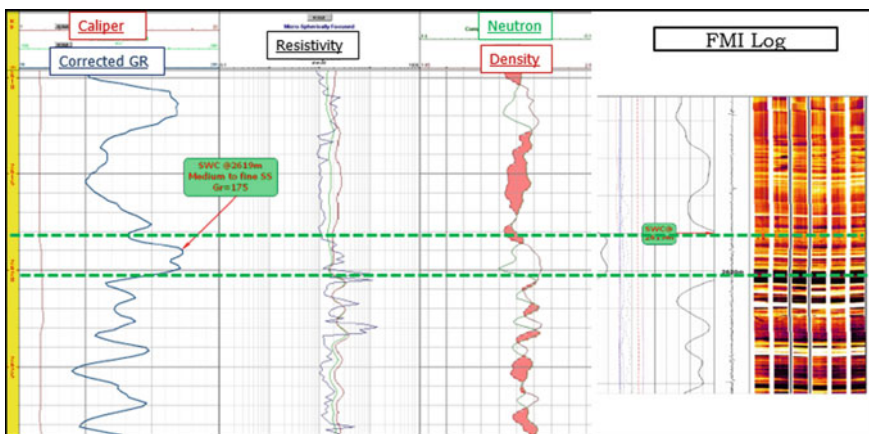
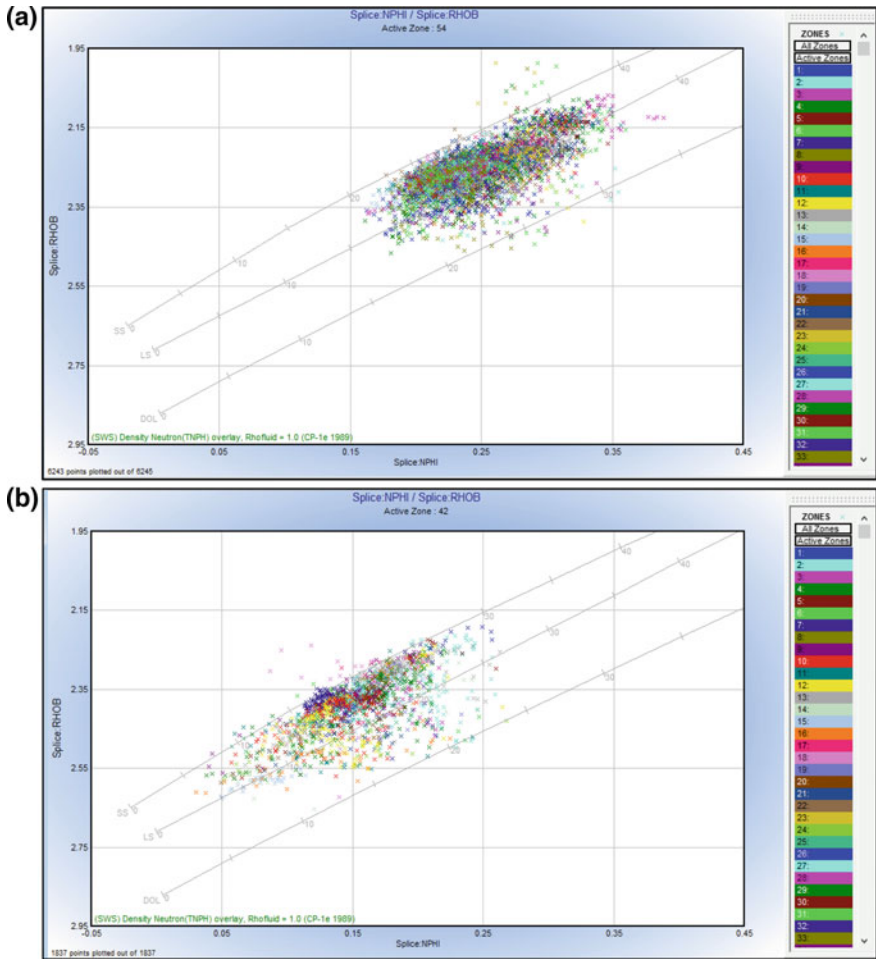


Fig. 6 The integration with FMI log shows that the high gamma ray value is actually sandstone interval (sandstone has bright color, while shale is darker)





**Fig. 7** NPHI versus RHOB cross-plot for sandstone (a) and radioactive sandstone (b) in Well B

hand shows that the radioactive sand has lower neutron but higher density compared to the normal sandstone (Figs. 5, 6, and 7).

### 5.2.2 Failure of DST Due to Poor Cementation

Few DSTs have been run; however, most of them are either failed or inconclusive. After the analysis, the problem is due to the poor cementation as the DST interval and this zone is actually the arkosic interval (Figs. 8 and 9).

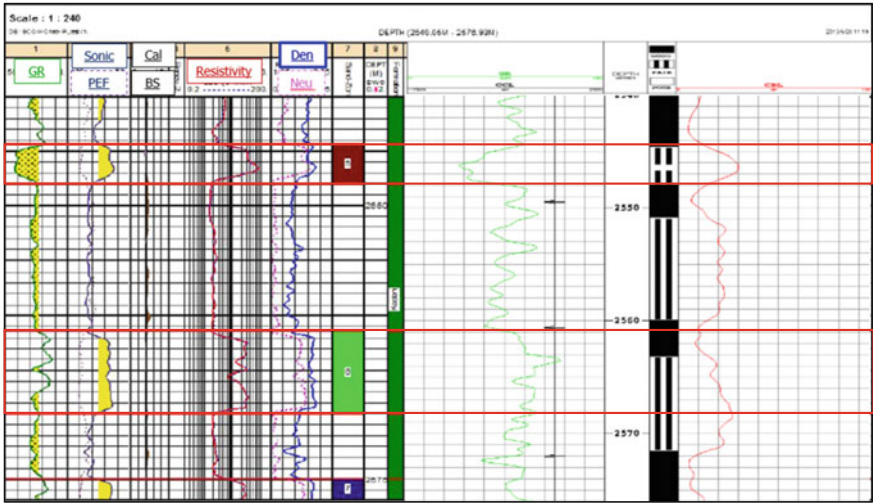


Fig. 8 The occurrence of feldspathic sand in the formation causes the bad or poor cementation (marked by black and white strips)

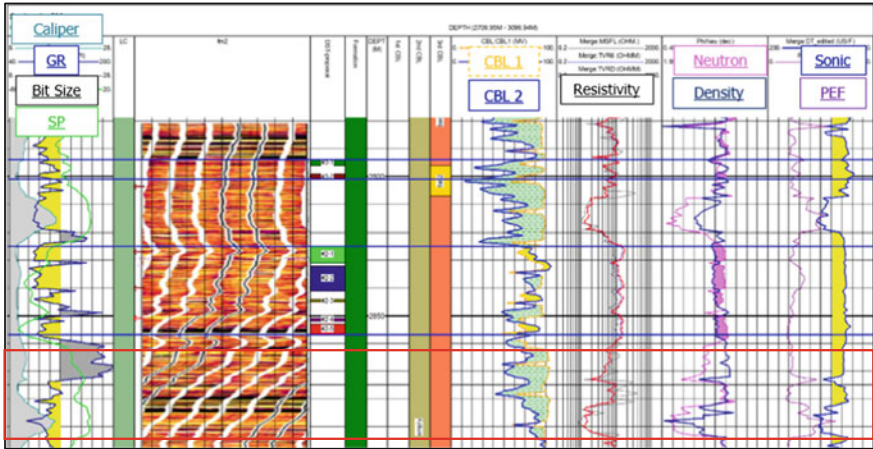


Fig. 9 The bright color of FMI data shows that there is bad or poor cementation at the radioactive sand zone (arkosic interval)



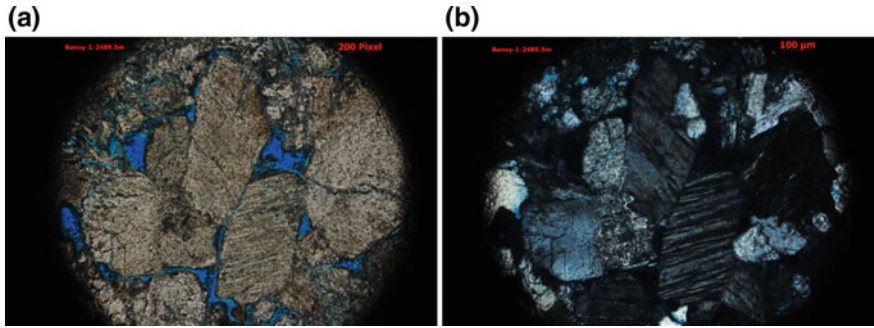
Fig. 10 Sand and shale can be easily identified using rho matrix technique

### 5.2.3 Rho Matrix Analysis

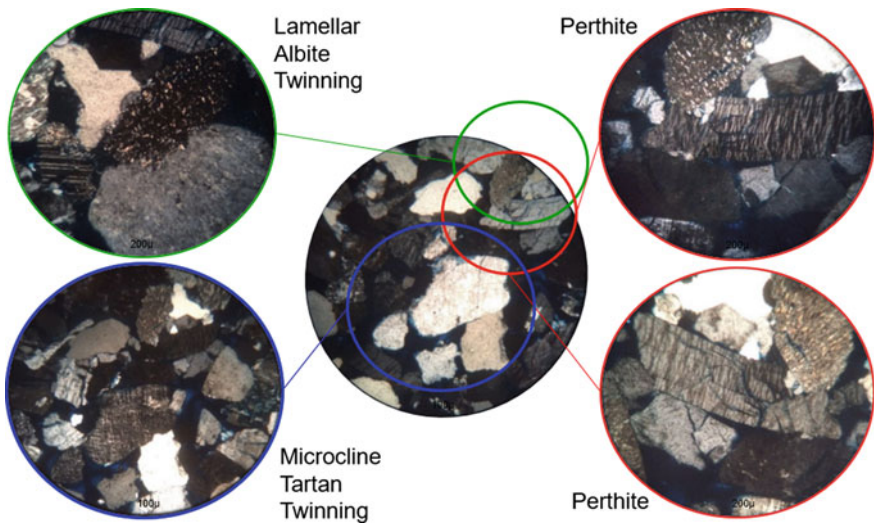
Based on the sonic log, there is no distinct change in its value (which probably means same lithology); however, by using the rho matrix, the sand and shale bed gave totally a different value (Fig. 10).

### 5.3 Petrography Thin Section

Petrographic analysis of thin sections provides the detailed information about the mineralogy of detrital matrix and cement composition. By using the classification system from Petti [9], sandstones are divided into arenites (less than 15% matrix) and wackes (more than 15% matrix). These classes are then subdivided on the basis of a ternary quartz–feldspar–rock fragment diagram. Sandstones with more than 25% feldspar or rock fragment are arkosic or lithic, respectively, whereas rocks with 5–25% feldspar or rock fragment are subarkosic or sublithic. After the point-counting analysis, the results show that sandstone with high gamma ray interval has a high amount of feldspathic mineral (Figs. 11 and 12).



**Fig. 11** Thin section sample under PPL (a) and XPL (b). Sample under XPL shows obvious polysynthetic twinning indicating feldspar mineral



**Fig. 12** Thin section sample XPL. Within one sample, few types of twinning can be seen in which most of them indicate the feldspar mineral

## 6 Conclusion

Radioactivity is the major feature of the lacustrine environment that will give serious impacts to the exploration evaluation;

- The identification of true net pay thickness including radioactive sands is essential in determining the volumetric calculation.
- The drill string test result is unreliable due to the poor cementing along the borehole.

Overall, the integration study between regional and reservoir geology and petrophysics data will lead to the understanding of the lacustrine sand reservoir

characteristics. It is expected that after the evaluation of these integrations, a better volumetric calculation of the reservoir and pay zone can be achieved resulting in a new economic value of the studied area.

## References

1. Aremu, M. (n.d) Chad Prepares to Be an Oil Producers. Oil and Gas Online. Retrieved on September, 29th 2015 from <http://www.oilandgasonline.com/doc/chad-prepares-to-be-an-oil-producer-0001>.
2. Binks, R.M. and Fairhead, J.D. (1992). A Plate Tectonic Setting for Mesozoic Rifts of West and Central Africa. Department of Earth Sciences, University of Leeds, UK. Elsevier Science Publishers B.V.
3. Carroll, A.R. and Bohacs, K.M. (2001). Lake-type Controls on Petroleum Source Rock Potential in Nonmarine Basins. The AAPG Bulletin, Volume 85, No. 6, PP. 1033–1053.
4. Chudi, O., Simon, Roya., SPE, and Warri, SPDC. (2012) Petrophysical Characterisation of Radioactive Sands—Integrating Well Logs and core Information: A Case Study in Niger Delta. Nigeria Annual International Conference and Exhibition, Abuja, Nigeria, August 6–8, 2012.
5. Fairhead, J. D. (1988). Mesozoic plate tectonic reconstructions of the central South Atlantic Ocean: the role of the West and Central African rift system. *Tectonophysics*, 155(1–4), 181–191.
6. Fairhead, J. D. (2009) The Mesozoic West and Central African Rift System: Qualitative Evaluation. AAPG International Conference and Exhibition, Cape Town, South Africa, October 26–29, 2008. Search and Discovery Article #30077.
7. Fairhead, J. D., Green, C. M., Masterton, S. M., and Guiraud, R. (2013) The Role That Plate Tectonics, Inferred Stress Changes and Stratigraphic Unconformities Have on The Evolution of The West and Central African Rift System and The Atlantic Continental Margins. *Science Direct, Tectonophysics* 594, 118–127.
8. Genik, G.J. (1993) Petroleum Geology of Cretaceous-Tertiary Rift Basins in Niger, Chad, and Central African Republic. The AAPG Bulletin, Volume, No. 8, PP. 1405–1434.
9. John, M. K., VanLaerhoven, C. J., & Chuah, H. H. (1972). Factors affecting plant uptake and phytotoxicity of cadmium added to soils. *Environmental Science & Technology*, 6(12), 1005–1009.
10. Katz, B. J. (1995) Factors Controlling The Development of Lacustrine Petroleum Source Rocks - An Update. In Huc, A. Y. (ed.), *Paleogeography, Paleoclimate, and Source Rocks*. Am. Assoc. Petrol. Geol. Studies in Geology 40: PP. 61–79.
11. Katz, B. J. (2001) Lacustrine Basin Hydrocarbon Exploration – Current Thoughts. *Journal of Paleolimnology* 26: 161–179, Kluwer Academic Publishers. Netherlands.
12. Mchargue, T. R., Heidrick, T. L., & Livingston, J. E. (1992). Tectonostratigraphic development of the interior Sudan rifts, Central Africa. *Tectonophysics*, 213(1–2), 187–202.
13. Pan, X.H., Yuan, S.Q., Ji, Z.F., Hu, G.C., and Liu, L. (2013). Forming Mechanism and Petroleum Geological Features of Western-Central African Rift Basins (WCARBs). IPTC 17116, Paper Presentation.
14. United Hydrocarbon International Corp. (2013) Geology. Why Chad. Retrieved on September, 30th 2015 from <http://unitedhydrocarbon.com/cms/why-chad/>.
15. Warren, M.J. (2009). Tectonic Inversion and Petroleum System Implications in the Rifts of Central Africa. Jenner GeoConsulting, Suite 2008, 1235 17th Ave SW, Calgary, Alberta, Canada, T2T 0C2. Frontiers + Innovation, CSPG SCEG CWLS Convention.

# Application of Seismic Imaging for Shallow Crustal Structure Delineation

H. Haiqal Hazreeq and M.N. Khairul Ariffin

**Abstract** Two lines of 2D seismic reflection survey were conducted in Lenggong area to study and delineate the geological contact between the recent alluvium sediments and the meteorite impact crater. Apart from that, the survey was also conducted to understand the seismic response of the impacted rocks in the deeper part of the subsurface in relation to its attributes. Recent studies have only focused on the shallow part of the subsurface and still lacking deeper subsurface geophysical information. The survey uses a 36-kg accelerated weight drop system as well as a 48 channel receivers and 100 m offsets at each receiver end. With 5-m receiver spacing, source is fired at 10-m interval. Two lines of seismic raw data are processed using GeoGiga Seismic Pro, and final stacked data are produced.

**Keywords** Seismic imaging · Seismic reflection · Bukit Bunuh · Impact crater

## 1 Introduction

Bukit Bunuh is one of the most important sites in Malaysia. It is situated in Lenggong Valley, in the upper part of Perak, with a longitude of 100° 58.5' east and 5° 4.5' north of latitude. Situated in one of the most prehistoric sites in the country, Bukit Bunuh is not only famous for the existence of a prehistoric population which existed 40,000 years ago, but recent studies have suggested that Bukit Bunuh may have experience a meteorite impact which dated back approximately 1.74 million years ago.

During the archaeological excavation at Bukit Bunuh in 2001, the excavation team had discovered clusters of cobbles and pebbles of suevite which are also known as impact breccia. The discoveries of suevite and other shock minerals, however, have led to the hypothesis that the area had once been affected by a high

---

H. Haiqal Hazreeq (✉) · M.N. Khairul Ariffin  
Department of Petroleum Geoscience, Universiti Teknologi PETRONAS,  
32610 Seri Iskandar, Tronoh, Perak, Malaysia  
e-mail: eezreeq@gmail.com



velocity impact, most probably a meteorite, which has caused shock metamorphism in the region. This hypothesis of hypervelocity impact is further supported by other evidence such as geophysical anomalies and different geomorphologies in the area which will be discussed later.

## 1.1 Regional Geology

General geology of Lenggong Valley is mostly dominated by three main lithologies, namely granitic rock, alluvium and tefra dust with the granitic rock being the most dominant. According to Mokhtar [2], the dominant granitic rock in Lenggong Valley is formed during the Late Jurassic–Early Carbonaceous era. While the granitic body covers vast area of Lenggong Valley, granitic rock in Bukit Bunuh area is found to be a relatively older unit. The vast granitic body is believed to have been formed during granite intrusions which occurred in Malaysia approximately during Mesozoic era which is around 200 million years ago [1].

## 1.2 Seismic Reflection

Seismic reflection method makes use of the seismic wave traveling downward to the geological interface and bounces back to the surface due to acoustic impedance contrast and get recorded by receivers, also known as geophones or hydrophones (Fig. 1). The receivers record the two-way travel time of the wave. After velocity determination, the depth of the interface can be determined and delineated.

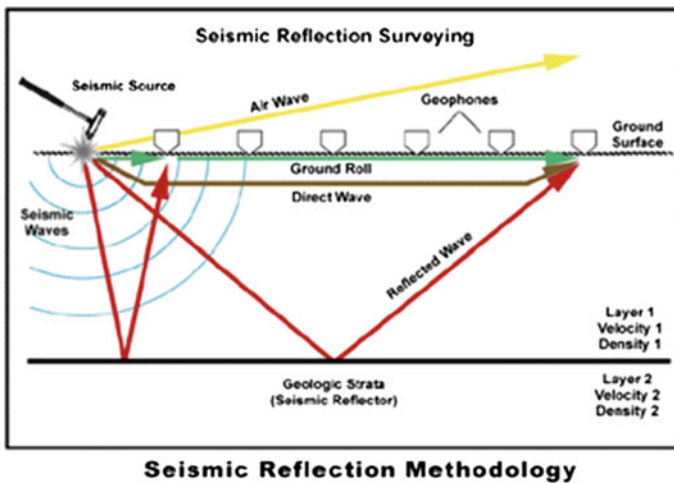


Fig. 1 General seismic reflection survey layout used in the acquisition process for this study

Seismic reflection is preferable in the acquisition, when compared with refraction. This is due to the fact that reflection method requires smaller geophone array dimensions compared to refraction method to image the density contrast of interest (impact crater boundary). In addition, seismic refraction method can only be optimized if the target boundary is more or less near horizontal in geometry. The complex geometry of the impact crater in Lenggong would demand the use of reflection method which could cater to this and produce a more reliable result.

## **2 Methodology**

### **2.1 Acquisition**

Two lines of seismic reflection survey were done in the area of study. The first line is located at a limestone hill in Kg. Batu Berdinding, while the second line is in Kg. Banggol Berdinding south of Lenggong town. Each line utilizes 48 channel geophones with 5-m spacing. About 100-m offset is added on each receiver end except for the second line with just 50-m offset due to dimension limitations.

The source used in the survey is Propelled Energy Generators (PEGs) accelerated weight drop system which is mounted on a SUV. The 36 kg weight is dropped from 43 cm height onto a steel plate. The source is powered by a 12 v electric supply and a motor. Upon impact, the source would generate a source wave with the frequency band of 10–250 Hz.

The acquisition makes use of end-on shooting layout. The shot point is set to be at an interval of 10 m starting from the beginning of the offset. In total, there are 44 shot points except for the last survey which only had 34 shot points. Each data acquired for every shot is then stacked to improve the quality using Terraloc Mk8 Seismograph (Figs. 2 and 3).

In general, these are the key parameters of the survey:

- Maximum offset: 335 m;
- Minimum offset: 0 m;
- Shot interval: 10 m;
- Number of recording channel: 48;
- Direction of shooting: east–west; and
- Geophone spacing: 5 m.

### **2.2 Seismic Data Processing**

The processing procedure was conducted by using GeoGiga Seismic Pro Reflector software. The main aim for the processing step is to increase S/N ratio and produce





Fig. 2 Seismic acquisition design for this research

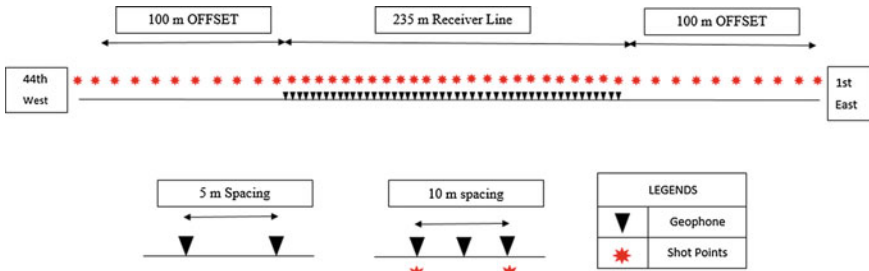
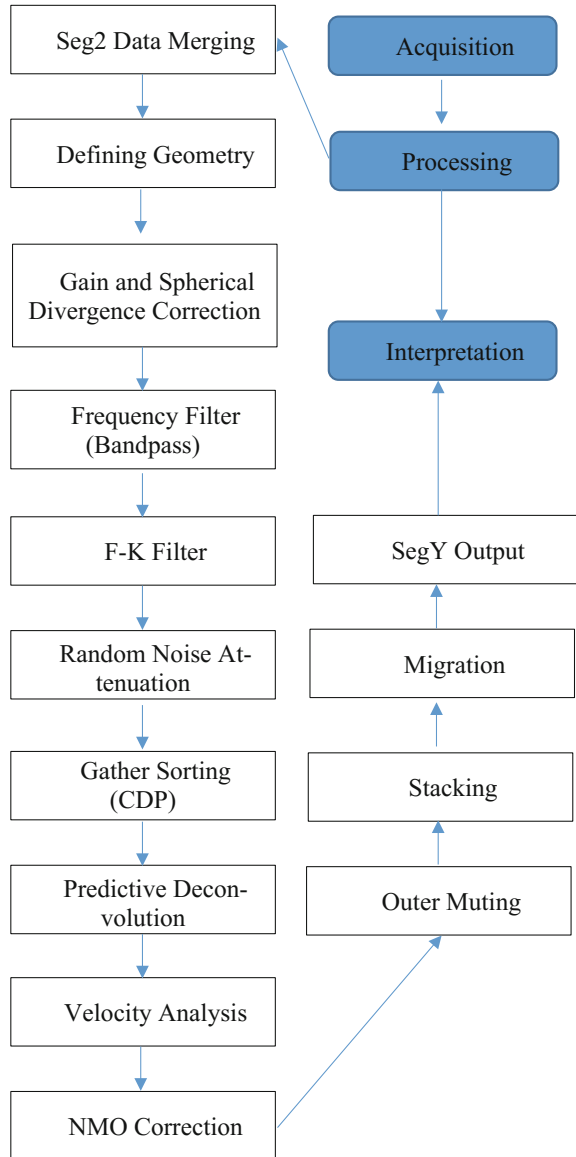
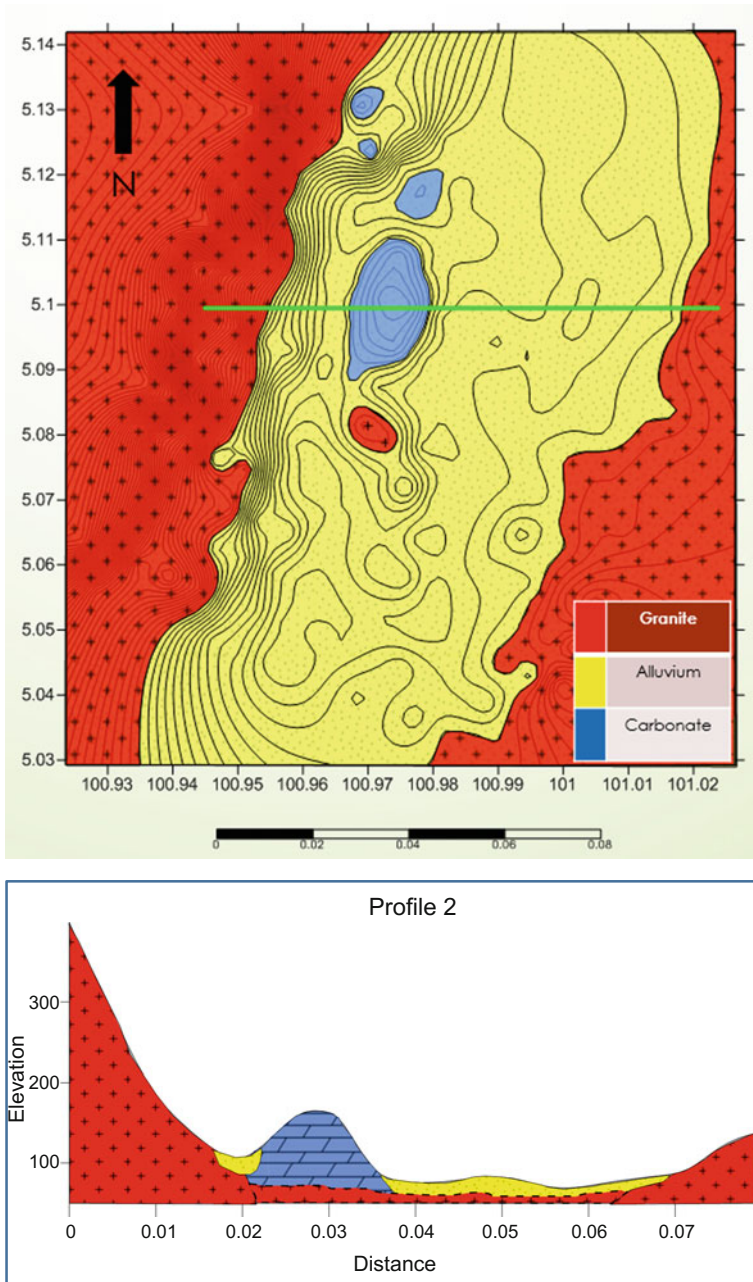


Fig. 3 Survey location. The two red lines indicate the seismic acquisition lines

stacked migrated seismic section for interpretation. For velocity analysis, velocity from the previous rock physics studies from core data is used for reference (Figs 4 and 5).

**Fig. 4** Seismic data processing steps taken to image the crustal structure





**Fig. 5** Geological map generated for the study area. Lithological information is obtained through geological survey of the area. Arbitrary cross-sectional line is taken crossing the area of interest

### 3 Result and Discussion

#### 3.1 Geological Map

#### 3.2 Rock Physics Properties

To study the rock physical properties, 4 samples of granite are collected. Two samples are from Bukit Bunuh, while the other two are from the foothill of Bintang Range. Four rock properties have been measured in the laboratory. They are  $V_p$ ,  $V_s$ , point load strength index (I), and the density. Subsequently, the data are used to calculate the properties such as Poisson's ratio ( $\sigma$ ), bulk modulus (K), shear modulus ( $\mu$ ), and the acoustic impedance (AI) (Tables 1 and 2).

The main objective of this study is to obtain velocity to guide velocity picking during processing. Although the samples are taken relatively shallow, it is still applicable to be used since the depth of interest in the study is also relatively shallow.

Based on the measured rock property table, there is no significant velocity difference between all the granite samples from both localities. The velocity of primary wave ranges from 4700 to 4600 m/s, while the shear wave velocity is around 2800 m/s in general. In terms of point load index, the granite sample BR2 is having the highest value of I which is 5.62 Mpa compared to 3.95 Mpa of point load index of BB1 sample from Bukit Bunuh. The density however does not vary significantly for all the granite samples. This is probably due to the fact that all the samples are taken at a relatively shallow depth.

The way reflection seismic wave responds to a geological interface or boundary is mostly affected by the acoustic impedance contrast between the overlying and underlying rocks. Basically, increasing AI contrast will give positive amplitude

**Table 1** Granite sample measured rock physics properties

Sample	$V_p$ (m/s)	$V_s$ (m/s)	I (Mpa)	P ( $G/cm^3$ )
BB1	4775	2847	3.95	2.65
BB2	4657	2754	4.47	2.73
BR1	4769	2854	4.95	2.77
BR2	4660	2824	5.62	2.74

**Table 2** Granite sample calculated rock physics properties

Sample	SM ( $\mu$ ) (Gpa)	BM (K) (Gpa)	PR ( $\sigma$ )	AI
BB1	21.48	31.78	0.2242	12,653,750
BB2	20.71	31.60	0.2311	12,713,610
BR1	22.56	32.92	0.2210	13,210,130
BR2	21.85	30.36	0.2098	12,768,400

(mostly based on convention) and vice versa. The magnitude however depends on the value of contrast between the two AI values. The bigger the difference, the higher the wave energy recorded.

Having said that, if we were to delineate the boundary between the weathered granite and the impacted granite or the boundary of impacted and non-impacted granite, we want to look for the positive (peak) response in the seismic section. Since AI value depends on the density of the rock itself, those boundaries can be detected because weathered rocks tend to have lower density compared to the non-weathered granite. The same case should apply to impacted and non-impacted granite in which the impacted granite has slight lesser density.

The rock physics study supports the theory where the samples from the Bintang Range (non-impacted granite) are having slightly higher density as well as the AI value, probably because the hypervelocity impact might have altered the rock physical properties such as developing fractures that have reduced the density of the rocks. Apart from that, the mineral content, such as biotite, could also affect the density of the samples and the possibilities are also taken into consideration during the study.

These rock physics values will affect the final seismic data later on. Nevertheless, due to the small variations in the  $V_p$  and AI values between the impacted and non-impacted granite, distinguishing those two from each other in seismic section is quite tricky.

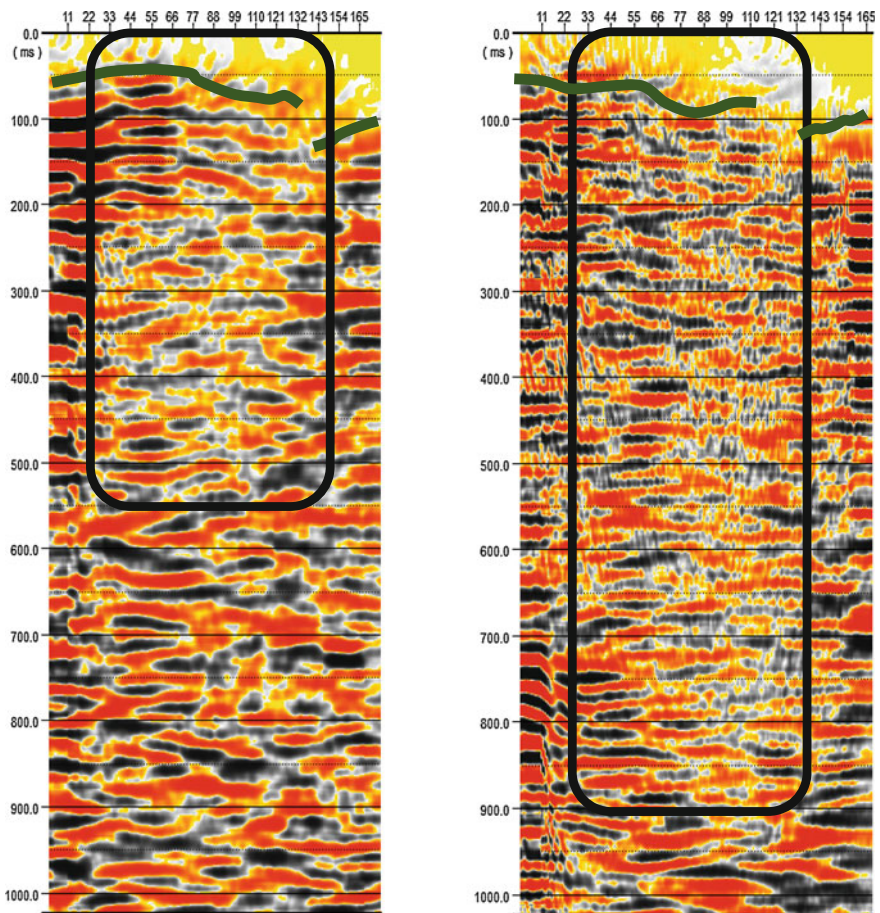
### 3.3 *Seismic Section*

The interpretation of the seismic section begins with the interpretation to the top of bedrock. From Fig. 6, we can see the high impedance contrast between the recent sediments and the top of bedrock that suggests the impact crater. The recent sediments which fill up the crater will have very low density and thus will result in low seismic wave velocity compared to the top of bedrock. Due to this, we can expect hard kick response or peak response which indicates increase in acoustic impedance from the overlying sediments and the underlying bedrock. The boundary between the top of bedrock and the recent sediment fill is denoted by the dashed green line which delineates the blue color reflector.

From the delineation of the top of bedrock as well, we can see that the top of bedrock is somehow dipping toward the east direction. This could very well be the indication of the nature of the crater itself. The dipping direction should point to the likely center of the crater since the impact crater will develop radial pushed down pattern. If we interpolate the dipping direction between the two seismic lines, we could in fact determine the center of the crater where the central uplifting of a complex crater should develop. Nevertheless, it is needed to bear in mind that the bedrock dipping based on the seismic section is an apparent dip and may not represent the actual dipping direction since we only acquire it in 2D.

There are also some displacements in the bedrock reflectors in both of the seismic lines. These fractures could represent the radial fractures that were developed during the hypervelocity impact event. The fractures are position toward the east direction as well, where they are likely to be in the event of hypervelocity impact.

In addition to that, the seismic section also revealed the low-velocity region going down the seismic line depicted by the black box in both sections. The low-velocity region is suspected to be generated by the fault or fractures that occurred in the subsurface. In Fig. 6 (left) which is Line 1 survey, the low-velocity region (low amplitude) only extends until about 550 ms, whereas in Fig. 6 (right), which is Line 2 survey, the low-velocity region extends up to 900 ms. This suggests that the fault radius is larger in Line 2 and suggests that whatever force that give rise to these faults is greater at Line 2. In hypervelocity impact, the force is greater at the



**Fig. 6** (Left) Line 1 Post-stack time migration. (Right) Line 2 Post-stack time migration



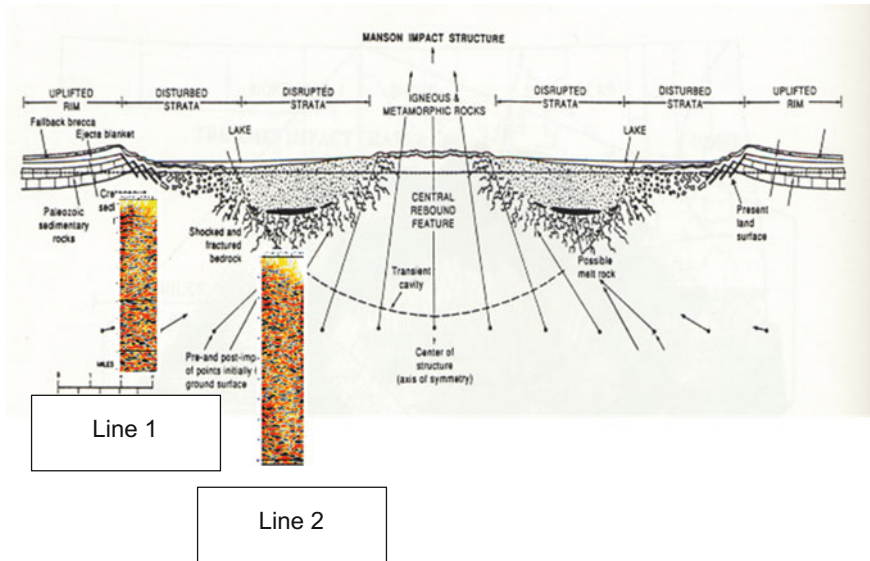


Fig. 7 Likely position of the two survey lines in the complex crater morphology

center of the crater and is reduced going out from the center radially. Thus, this suggests that Line 2 survey is closer to the center of the crater than Line 1 which could possibly be at the outer rim of the crater. This is depicted by Fig. 7, which illustrates the likely position of the two survey lines in the complex crater morphology.

## 4 Conclusion

To delineate and map the impact crater of the meteorite impact in Bukit Bunuh, the use of seismic reflection is proved to be reliable since the acoustic impedance contrast between upper sediments and impacted country rock is significantly large. Delineating the contact between the impacted and fresh granite however is bit complicated since the boundary is not very clear and having low AI contrast. Perhaps, the use of longer survey line and different seismic sources that can produce a higher frequency could help in delineating the interface between the impacted and fresh granite.

**Acknowledgements** The author would like to express his utmost appreciation to his supervisor, Mr. Khairul Ariffin Mohd Noh, who was very motivative, inspiring, and helpful during the project. Highest gratitude also goes to the General Assistance of Geoscience Department who was willing to assist in fieldwork and acquisition works; last but not least, to my parents who were very generous to support the study not only by giving support and encouragement but also for some ideas and insights. Thank You.

## References

1. Alexander J.B. (1962). A short outline of the geology of Malaya with special reference to Mesozoic orogeny: Crust of the Pacific Basin. *Geophysical Monograph*. 6, 81–86.
2. Carpenter, B.N. & Carlson, R. (1992). The Ames impact crater. *Oklahoma Geology Notes* 52(6), 208–223.
3. Hamm, H. & Olsen, R.E. (1992). Oklahoma Arbuckle lime exploration centered on buried astrobleme structure. *Oil and Gas Journal*. 90, 113–116.
4. Jinmin, M., Rosli, S., Saidin, M., Kiu, Bery, A.A. (2013). Electrical Resistivity Survey in Bukit Bunuh, Malaysia for Subsurface of Meteorite Impact Study. *Open Journal of Geology*. 3, 34–37. Retrieved February 8, 2014, from <http://www.scirp.org/journal/PaperDownload.aspx?paperID=38347>.
5. Jinmin, M., Rosli, S., Saidin, M.M., Kiu, Y.C. (2013). Bukit Bunuh Alluvium Thickness With The Effect Of Meteorite Impact Using 2-D Resistivity Method—Second Stage Study. *EJGE*. 18, 1719–1725. Retrieved February 8, 2014, from <http://www.ejge.com/2013/Ppr2013.151lr.pdf>.
6. Majid, Z. (2003). *Archaeology in Malaysia*. Universiti Sains Malaysia: Centre for Archaeological Heritage of Malaysia.
7. Mokhtar, Saidin. 2004. Bukit Bunuh, Lenggong, Malaysia: A new evidence of late Pleistocene culture in Malaysia and Southeast Asia. *10th European Association of Southeast Asian Archaeological Conference, London*. pp. 14–17.
8. Nick, K.E. (1994). Lithologic and stratigraphic evidence for the impact origin of a buried Ordovician age crater and reservoir near Ames, Major County, Oklahoma. *American Association of Petroleum Geologists 1994 Annual Convention Official Program*. p. 224.
9. Samsudin, A.R., Harun, A.R., Arifin, M.H., Hamzah, U., Saidin, M., Karamah., M.S.S. (2012). Gravity Investigation of the Bukit Bunuh Impact Crater at Lenggong, Perak, Malaysia. *Sains Malaysiana*. 41(12), 1629–1634. Retrieved February 8, 2014, from [http://www.ukm.my/jsm/pdf\\_files/SM-PDF-41-12-2012/18%20Abdul%20Rahim.pdf](http://www.ukm.my/jsm/pdf_files/SM-PDF-41-12-2012/18%20Abdul%20Rahim.pdf).
10. Saidin M. (1993). Kajian perbandingan tapak Paleolitik Kampung Temelong dengan Kota Tampan dan sumbangannya terhadap kebudayaan zaman Pleistosein akhir di Asia Tenggara. *Malaysia Museum Journal*. Vol. 32.
11. Saidin M. (1998). Kota Tampan dan Kampung Temelong: Kajian Perbandingan Tapak-tapak Paleolitik di Lembah Lenggong. *Malaysia Museums Journal*. 34, 131–153.
12. Saidin, M. (2007). *Archaeological Heritage of Malaysia*. Universiti Sains Malaysia: Centre for Archaeological Heritage of Malaysia.



# Hydrocarbon Bond Variation in Some Shales from Batu Gajah, Malaysia

Syed Muhammad Ibad Mahmoodi and Eswaran Padmanabhan

**Abstract** This study demonstrates the variation in aliphatic hydrocarbons in shales by Fourier transform infrared (FTIR) spectroscopic characterization from an isolated outcrop of Batu Gajah area, Malaysia. IR spectra of analyzed sample indicate alkanes, alkenes and alkynes groups of aliphatic hydrocarbon. The spectra indicated the variation in the distribution of the aliphatic hydrocarbon groups. =C–H bonds occur as dominant peaks in the spectra. The main peaks in the infrared spectra reflected alkane methyl symmetric C–H stretching, Alkyne C=C stretching, alkene =C–H stretching bonds. Alkyne and alkene aliphatic hydrocarbons have higher peak intensities in samples B1 and B8, respectively. The Presence and absence of alkene aliphatic hydrocarbon in samples of units 2 and 3 also have been observed. Total organic carbon content also has been measured for ten samples. All sample had a variation in TOC values, while B1 sample of unit 1 had an exceptional (3.501%) value of TOC.

**Keywords** Fourier transform infrared spectroscopic · Shales · Aliphatic hydrocarbon · Total organic carbon content · Source rock

## 1 Introduction

The Malay Peninsula is characterized by three north–south belts, the western, central, and eastern belts [1]. Western belt (comprising the “Northwest Domain”) was the part of the NW Australian Gondwana margin through Cambrian–Early Permian times as the Meso-Tethys opened [2–4]. The present study focused on an

---

S.M.I. Mahmoodi (✉) · E. Padmanabhan  
Department of Geosciences, Faculty of Geosciences and Petroleum Engineering,  
Universiti Teknologi PETRONAS, Seri Iskandar, Perak, Malaysia  
e-mail: s.mohammadibad@gmail.com



Fig. 1 Location of Batu Gajah area, Perak, Malaysia

isolated outcrop of Batu Gajah area comprises shales [4], which is found in the Western belt of peninsula Malaysia (Fig. 1).

Influx of low clastic material (low dilution), high primary production of coastal waters, supply of high terrestrial organic matter, a stratified water column, and anoxic bottom waters may increase the formation of organic carbon-rich sediments [5, 6]. Organic carbon-rich, argillaceous sedimentary rocks or so-called black shales [7, 8], are metamorphosed during Carboniferous period.

Geological evidence showed that until the Early Paleozoic period, organic-rich sediments might be deposited in an open shelf [9]. The presence of organic matter in higher amount is also one of the basic criteria for the identification of oil and gas source rocks [10]. The aim of the present study was to see the hydrocarbon presence and variation in shales.

There is a lack of information on the hydrocarbon distribution in these shales at the molecular level. Therefore, the aim of this study was to carry out an evaluation using FTIR on the variability of hydrocarbon distribution in the shales, Batu Gajah area, Malaysia.

## 2 Methodology

The study area focused on isolated outcrops of Batu Gajah area, in northwest Peninsular Malaysia (Fig. 2). Three main units were recognized on the basis of color, texture, joints, hardness, presence and absence of quartz vein, orientation of quartz vein, and presumable competency of the bed (Fig. 3).

FTIR and TOC analyses have been done for the presence of and to see the variation in hydrocarbon in shales. The total organic carbon content was determined by using a Shimadzu total carbon analyzer. For TOC concentrates, ten rock samples were analyzed. The residual constituents were used for TOC through combustion analysis of temperatures in surplus of 850 °C. The evolved gas (CO<sub>2</sub>) was measured simultaneously and quantitatively by infrared detectors and noted down as percentage of carbon. FTIR analysis was done using Agilent FTIR-ATR spectrometer to evaluate the distribution of aliphatic hydrocarbon bonds. The spectra range from 400 cm<sup>-1</sup> to 4500 cm<sup>-1</sup>. Peaks were reported based on % transmittance to given wavelengths. The peaks have been identified from [11].



**Fig. 2** Photograph showing shale outcrop of Batu Gajah. **a** Total thickness of outcrop, **b** close-up picture of unit 1 in sample B1, **c** close-up picture of unit 2 in sample B4, **d** close-up picture of unit 3 sample B10

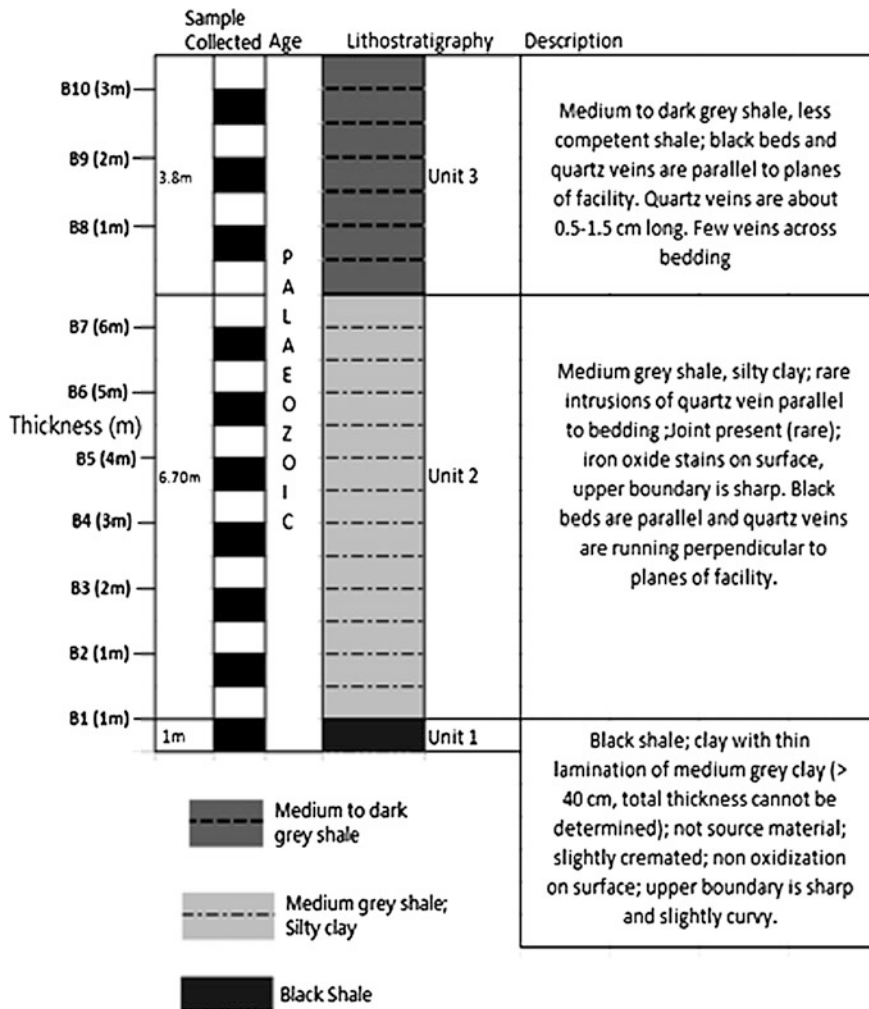
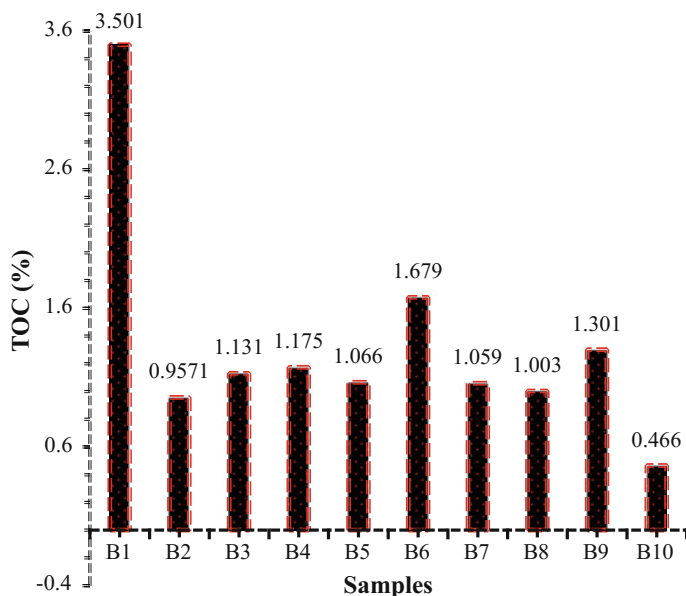


Fig. 3 Lithology of the outcrop studied in Batu Gajah

### 3 Results and Discussions

#### 3.1 TOC Analysis

The total organic carbon analyses in the present study consist of 10 shale samples from the outcrop of Batu Gajah area. The shales are characterized by medium-to-high weight percent of TOC (from 1 to >3%). Quantity of organic matter is variable from unit to unit according to the type of shales and their characteristic attributes (Fig. 4). The shales from unit 1 recorded TOC value of 3.501%.



**Fig. 4** Variation and abundance in TOC values of shale sample from Batu Gajah

The shale samples from unit 1 gave the highest TOC value of 3.501%. The shale samples from unit 2 recorded TOC values of 0.9571, 1.131, 1.175, 1.066, 1.679, and 1.059%, respectively. Unit 3 also shows variable TOC values of 1.003, 1.301, and 0.466%, respectively. Shales have shown drastic variation in TOC values. Units 1, 2, and 3 show high, low-to-intermediate, and very low-to-intermediate TOC values, respectively. Sharp change in TOC values within a same unit can also be observed, e.g., unit 2 has shown low (0.9571%), intermediate (1.175%), and high (1.679%) TOC values. Same variation within similar unit is also present in unit 3. Unit 3 also possesses very low (0.466%) and intermediate (1.301%) TOC values. The possible reason of this drastic change in TOC values may be due to the deposition rates, bottom-water circulation rates, terrestrial organic matter supply rate from the continents, surface water productivity, and degree of oxygenation of bottom water. Changes in these factors may create variation in the quantities of organic carbon [12–15].

### 3.2 FTIR Analysis

Infrared (IR) spectroscopy has been for decades a frequently used method to investigate the structure and bonding properties of the clay minerals [16–23]. IR spectra of six analyzed samples contain three groups of aliphatic hydrocarbon, i.e.,

**Table 1** Characteristic of infrared bands of aliphatic hydrocarbon present in shale samples

Wavenumber (cm <sup>-1</sup> )	B1	B2	B4	B6	B8	B10	Assignment
2960	2960.54	2960.23	2960.56	2960.35	2960.95	2960.67	Alkanes Methyl symmetric C–H stretching
1600	1600.25	1600.45	1600.54	1600.70	1600.78	1600.35	Alkenes
1000–600	1030.82	1030.11	1030.50	1030.29	1030.43	1030.93	C=C stretching
	–	–	–	1007.02	1007.09	–	=C–H out-of-plane bending
	910.32	910.82	910.64	910.84	910.82	911.61	
	797.13	798.23	797.48	797.02	796.90	–	
2260	777.89	–	–	–	–	769.90	Alkynes
700–600	2260.25	2260.45	2260.82	2260.73	2260.65	2260.57	C=C stretching
	694.65	695.76	695.49	695.04	695.76	694.74	=C–H bending

alkanes, alkenes, and alkynes (Table 1). The spectra were identified by [11]. C–H-stretching bands in an aliphatic hydrocarbon are visible in the 3000–2800 cm<sup>-1</sup> range, due to C–H-stretching vibrations. The correct position of the absorption is disturbed by the hybridization of the carbon. All six analyzed samples contain methyl symmetric C–H-stretching bonds at 2960 cm<sup>-1</sup> band, representing the presence of alkane aliphatic hydrocarbon in all samples. Alkene aliphatic hydrocarbon can be seen at 1600, 797.13, 777.89, and 910 cm<sup>-1</sup> bands in all six IR spectra. 1600 cm<sup>-1</sup> indicates C = C-stretching bond, and 797.13, 777.89, and 910 cm<sup>-1</sup> indicate = C–H out-of-plane bending. Sample B8 contains the higher transmittance value at 1600 and 910 cm<sup>-1</sup> as compared to other five samples. 2260 and 694.74 cm<sup>-1</sup> bands also present in all samples, indicating the C = C-stretching bond and =C–H-bending of alkyne aliphatic hydrocarbon. B1 samples contain higher transmittance values of 694.74 cm<sup>-1</sup> bands as compared to other five samples, which shows the higher presence of alkyne aliphatic hydrocarbons in sample B1 (Fig. 5).

All three samples from unit 2 comprise alkane and alkyne aliphatic hydrocarbons at 2960, 2260, and 695 cm<sup>-1</sup>, respectively. Variation within unit 2 can be seen in alkene aliphatic hydrocarbons. 1600, 1030, 910, and 797 cm<sup>-1</sup> bands are present in all three analyzed samples from unit 2, while 1007.02 cm<sup>-1</sup> band is only present in B6 sample of unit 2. The absence of 1007.02 cm<sup>-1</sup> band in samples B2 and B4 indicates that there is no = C–H out-of-plane bending. All shale samples from unit 3 also contain alkane and alkyne aliphatic hydrocarbon, and variation within unit 3 can be observed in alkene aliphatic hydrocarbon, e.g., 769 cm<sup>-1</sup> is present in sample B10 of unit 3, while B8 sample from same unit does not have 769 cm<sup>-1</sup> (Table 1).



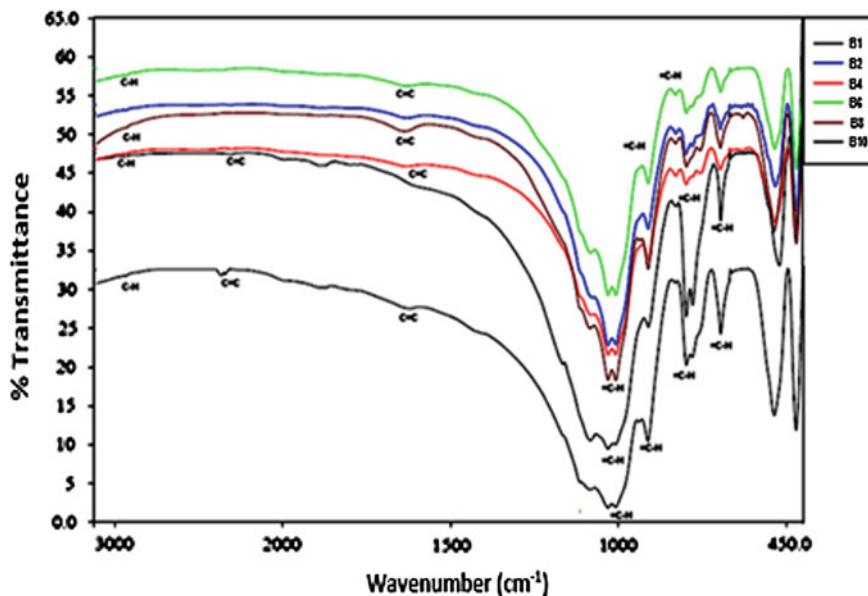


Fig. 5 FTIR spectra showing the distribution of aliphatic hydrocarbons

The toughest bands in the alkenes spectra are those assigned to the carbon-hydrogen-bending vibrations of the  $=C-H$  group. These bands are shown in the region  $1000-600\text{ cm}^{-1}$ . The presence and absence of these bonds in units 2 and 3 indicate the effect of chemical changes present in a same unit sample such as induced electronic-, spatial-, or entropy-related effects.

## 4 Conclusions

The present study comprises insights in the hydrocarbon variation in shales from three different units of an isolated outcrop of Batu Gajah area, Malaysia.

1. All analyzed samples are dominated by aliphatic compounds. The Batu Gajah shales had alkane methyl symmetric  $C-H$ -stretching, alkene  $=C-H$ -stretching, alkene  $C=C$ -stretching, alkyne  $C\equiv C$ -stretching, and alkyne  $=C-H$ -bending bonds.
2. Variation in intensities of aliphatic hydrocarbon can be seen in FTIR results of different units. Result shows that the presence of alkyne aliphatic hydrocarbons is higher in B1 sample of unit 1, while alkene aliphatic hydrocarbon shows higher occurrence in sample B8 of unit 3.

3. Variations within unit 2 and unit 3 also have been seen in FTIR data. Alkene aliphatic hydrocarbon is present and absent in some samples of units 2 and 3, respectively.
4. All samples from 3 different units have shown different (low-to-high) values of TOC. Variation in TOC also has been seen within a same unit. Higher (3.501%) and lower (0.466%) values of TOC are found in samples B1 and B10, respectively.

**Acknowledgements** The author would like to acknowledge and appreciate the Universiti Teknologi PETRONAS for Graduate Assistantship.

## References

1. Metcalfe, I., Tectonic evolution of the Malay Peninsula. *Journal of Asian Earth Sciences*, 2013. 76: pp. 195–213.
2. Metcalfe, I., The Bentong-Raub Suture Zone. *Journal of Asian Earth Sciences*, 2000. 18(6): pp. 691–712.
3. Metcalfe, I., Palaeozoic and Mesozoic tectonic evolution and palaeogeography of East Asian crustal fragments: The Korean Peninsula in context. *Gondwana Research*, 2006. 9(1–2): pp. 24–46.
4. Hutchison, C.S., et al., *Geology of Peninsular Malaysia*. 2009: University of Malaya.
5. Whelan, J.K. and J.W. Farrington, *Organic Matter: Productivity, Accumulation, and Preservation in Recent and Ancient Sediments*. 2013: Columbia University Press.
6. Meyers, P.A., Organic geochemical proxies of paleoceanographic, paleolimnologic, and paleoclimatic processes. *Organic Geochemistry*, 1997. 27(5–6): pp. 213–250.
7. Langrock, U., et al., Paleoenvironment and sea-level change in the early Cretaceous Barents Sea - Implications from near-shore marine sapropels. *Geo-Marine Letters*, 2003. 23(1): pp. 34–42.
8. Larson, R.L., Geological consequences of superplumes. *Geology*, 1991. 19(10): pp. 963–966.
9. Klemme, H.D. and G.F. Ulmishek, Effective petroleum source rocks of the world: stratigraphic distribution and controlling depositional factors. *American Association of Petroleum Geologists Bulletin*, 1991. 75(12): pp. 1809–1851.
10. Dabous, a.a.a., mineralogy, geochemistry and radioactivity of some egyptian phosphorite deposits. 1981, The Florida State University: Ann Arbor. pp. 217–217.
11. Stuart, B.H., *Organic Molecules, in Infrared Spectroscopy: Fundamentals and Applications*. 2005, John Wiley & Sons, Ltd. pp. 71–93.
12. Brooks, J., *Organic maturation studies and fossil fuel exploration*. 1981: Academic Press.
13. Daly, A.R. and J.D. Edman, Loss of organic carbon from source rocks during thermal maturation. 1987. Medium: X; Size: Pages: 546.
14. Heydari, E., W.J. Wade, and L.C. Andersonb, Depositional environments, organic carbon accumulation, and solar-forcing cyclicity in smackover formation lime mudstones, Northern Gulf Coast. *AAPG Bulletin*, 1997. 81(5): pp. 760–774.
15. Tissot, B.P. and D.H. Welte, *Petroleum Formation and Occurrence*. 1984: Springer-Verlag.
16. Farmer, V.C. and J.D. Russell, The infra-red spectra of layer silicates. *Spectrochimica Acta*, 1964. 20(7): pp. 1149–1173.
17. Farmer, V.C., *The Infrared Spectra of Minerals*, 1974.
18. Decarreau, A., O. Grauby, and S. Petit, The actual distribution of octahedral cations in 2:1 clay minerals: Results from clay synthesis. *Applied Clay Science*, 1992. 7(1–3): pp. 147–167.



19. Russell, J.D. and A.R. Fraser, Infrared methods. *Clay Mineralogy: Spectroscopic and Chemical Determinative Methods*, 1994: pp. 11–67.
20. Bishop, J.L., C.M. Pieters, and J.O. Edwards, Infrared spectroscopic analyses on the nature of water in montmorillonite. *Clays and Clay Minerals*, 1994. 42(6): pp. 702–716.
21. Gates, W.P., et al., Electronic and structural properties of reduced-charge montmorillonites. *Applied Clay Science*, 2000. 16(5–6): pp. 257–271.
22. Heller-Kallai, L., Protonation-deprotonation of dioctahedral smectites. *Applied Clay Science*, 2001. 20(1–2): pp. 27–38.
23. Madejová, J., FTIR techniques in clay mineral studies. *Vibrational Spectroscopy*, 2003. 31(1): pp. 1–10.

# Heterogeneity in Hydrocarbon and Organic Matter Distribution Patterns in the Offshore West Baram Delta, Sarawak Basin

J. Ben-Awuah and E. Padmanabhan

**Abstract** The objective of this paper was to evaluate heterogeneities in hydrocarbon and organic matter distribution patterns in the offshore West Baram Delta. A total of 170 samples from seven subsurface wells in the delta have been analyzed using FTIR and UV–Vis spectroscopy, and total organic carbon analyzer. Samples from wells W1, W6, and W3 show the lowest TOC values with averages of <1% indicating organic matter oxidation in these wells. The plot of E4 against E6 for samples from the four different fields shows a strong linear correlation between the two parameters. Such linear relationship between E4 and E6 suggests a fairly consistent supply of organic carbon into the environment during deposition. Generally, the farthest field offshore, i.e., Field C, has the highest E4/E6 ratios averaging 1.37 and decreasing to the most proximal field, i.e., Field A with an average of 1.24 suggesting a depositional environment control on the quality of the organic matter as well. The relative amount of aromatic functional groups generally increases from the samples nearest to the shoreline to the samples farther offshore, whereas the amount of aliphatic functional groups decreases from the nearshore to farther offshore samples. An overlay of the distribution of E5 across the wells shows similar distribution pattern to the aliphatic functional groups. Since a good relationship exists between these two parameters, it indicates that with knowledge on E5 values, hydrocarbon functional groups distribution can be predicted with a good degree of accuracy.

**Keywords** West Baram Delta • Hydrocarbon distribution • Hydrocarbon functional groups • Organic matter

---

J. Ben-Awuah (✉)

Chemical and Petroleum Engineering Department, UCSI University,  
Kuala Lumpur, Malaysia  
e-mail: benawuah@ucsiuniversity.edu.my

E. Padmanabhan

Geosciences Department, Universiti Teknologi PETRONAS, Seri Iskandar, Malaysia

## 1 Introduction

All the fields in the West Baram Delta are matured fields with declining production and therefore being produced through enhanced oil recovery processes (EOR). According to [1], the two main criteria for selecting appropriate EOR method for a particular field are reservoir characteristics (porosity, permeability, hydrocarbon distribution, net thickness, depth, and temperature) and crude oil characteristics (gravity, viscosity, and composition). Knowledge on the distribution and composition of hydrocarbons is therefore essential for the successful implementation of EOR techniques in the West Baram Delta. The current knowledge on hydrocarbon distribution in the West Baram Delta is limited to basin scale studies [2, 3] and do not account for variations in localized distribution of hydrocarbons.

Particularly for the West Baram Delta, the literature on hydrocarbon distribution is very rare. Ingram et al. [3] noted differences in migration patterns of hydrocarbons in NW Borneo and attributed it to tectonic activity and deformation. Ramli et al. [4] identified tremendous spatial and temporal variations in hydrocarbon distribution in the Belait and Lambir Formations from onshore West Baram Delta but failed to properly account for the reasons for such variations.

As petroleum consists of compounds in which carbon is the principal component, determination of the carbon content of sedimentary rocks plays an important role in analyzing petroleum plays [5]. The preservation of organic matter is controlled by various conditions including bottom-water circulation rates, degree of oxygenation of bottom water, organic matter supply rate from the continent, deposition rates, and surface water productivity [6, 7]. The UV–Vis experiment has been used to determine the E4/E6 ratio of organic extracts from the samples. The E4/E6 ratio is an indicator of the type and quality of humic matter [8]. FTIR has been used to determine the compositional variation of hydrocarbon functional groups in the studied samples.

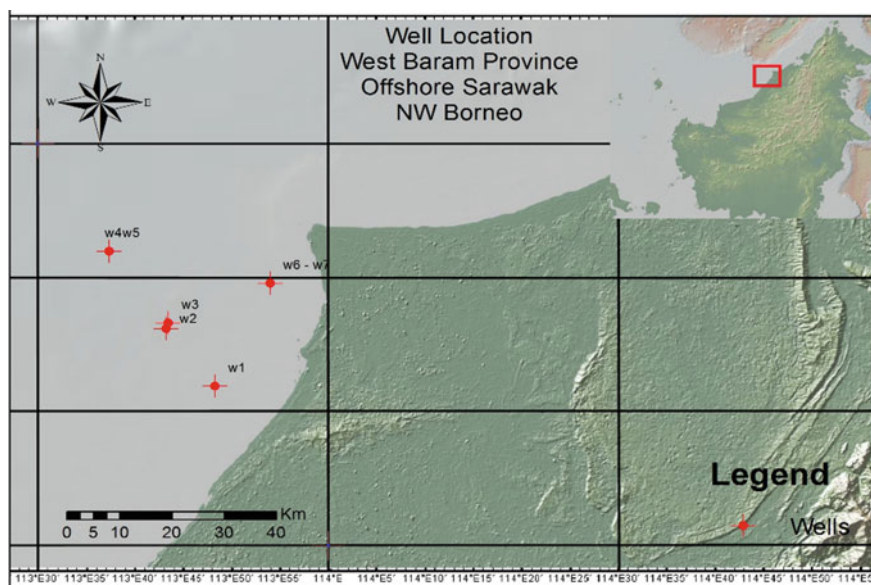
The Baram Delta is one of the seven geological provinces found offshore Sarawak Basin and is the most prolific province of all the geological provinces in the basin [9]. The delta which was discovered in 1969 is estimated to have more than 400 million stock barrels of oil in place with multiple stacked sandstone reservoirs in a shallow offshore environment and has been in production for the past 30 years [10]. Extensive synsedimentary growth faulting with very large throws forms the principal petroleum traps in this area [11]. The offshore stratigraphy of the Baram Delta is characterized by the occurrence of coastal to coastal-fluviomarine sands which have been deposited in a northwestward prograding delta since the Middle Miocene (from Cycle IV onwards) with the Cycle V (Middle-to-Upper Miocene) to Cycle VII (Upper Pliocene) being well developed [9, 12, 13].

## 2 Materials and Methods

About 170 core samples from seven wells in four offshore fields in the West Baram Delta have been used in this study (Fig. 1). The studied reservoir sandstone intervals all belong to the cycles V and VI, Upper-to-Middle Miocene sandstones [9]. Core logging was carried out for all wells. FTIR spectroscopy, UV–Vis spectroscopy, and total organic carbon measurements have been carried out on the samples.

FTIR spectroscopy has been used to determine variations in the composition and distribution of hydrocarbon functional groups in the studied samples. An Agilent Technologies Cary 660 Series FTIR spectrometer equipped with a PIKE MIRACLE diamond attenuated total reflectance spectroscopy (ATR) and mid-infrared (MIR = 4000–400  $\text{cm}^{-1}$ ) source has been used. The limit of detection in the instrument is 0.08%. The spectra obtained are processed and analyzed using the Agilent Resolutions Pro software. The settings used in this study include 16 sample scans, 4  $\text{cm}^{-1}$  resolution, and aperture.

UV–Vis spectroscopy has been used to analyze extracts from the samples to determine their E4/46 ratios. Two standard wavelengths widely employed for one-dimensional UV–Vis characterization of humic matter are measured at 465–665 nm [15–17]. The optical absorbencies measured at these wavelengths are represented by a E4/E6 ratio where E4 is absorbencies at 465 nm and E6 is absorbencies at 665 nm. 0.1 g of each sample uniformly crushed with a rock



**Fig. 1** Location map of study area. Modified after [14]

pulverisette was soaked in 10 ml of solvent for 48 h to extract the organic matter, and the supernatant solutions were analyzed using a PerkinElmer Lambda 750 UV/Vis/NIR spectrophotometer.

In this study, the total organic carbon (TOC) content was measured in order to determine the organic carbon content of the studied samples. The TOC measurement was carried out using the direct method proposed by [18]. Weighed crushed samples were treated with 10% hydrochloric acid to remove the inorganic carbon. The samples were dried in an oven for 3.5 h at a temperature of 110 °C and analyzed for organic carbon by combustion using Analytikjena HT 1300 solids carbon analyzer module at a maximum combustion temperature of 1200 °C.

### 3 Results and Discussion

#### 3.1 Organic Matter Input and Preservation

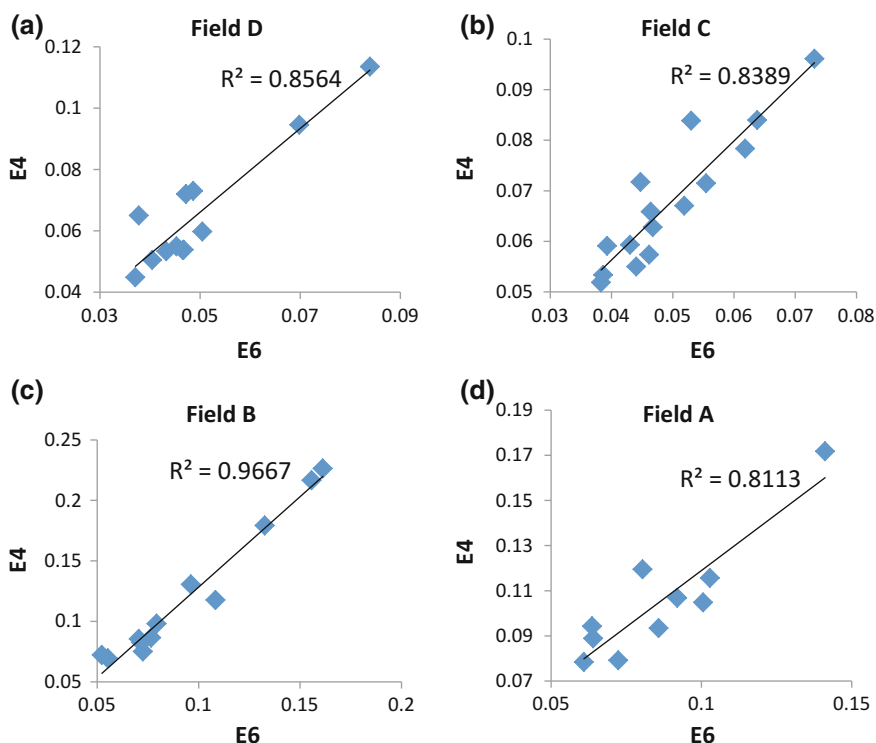
The TOC content in the samples varies a lot possibly due to the numerous factors that affect organic matter deposition and preservation as enumerated above. The maximum TOC value of 6.99% is recorded in W5, whereas the lowest TOC value of 0.19% is recorded in W1 (Table 1). Samples from wells W1, W6, and W3 show the lowest TOC values with averages of <1% (Table 1). The fine-grained lithologies such as the siltstones, mudstones, and very fine-grained sandstones generally have a higher TOC content than the coarse-grained lithologies. This is reflected in the fact that wells with larger intervals of coarse-grained sandstones such as W1 and W6 have lower average TOC values than wells with larger fine-grained intervals such as W5 and W7 (Table 1). This can be attributed to the relatively buoyant nature of organic matter which makes it settle to the sea floor as slowly as fine particles, and therefore, conditions which allow the deposition of fine particles also favor deposition of organic matter [5]. The samples with low TOC may have been deposited in the suboxic conditions where there is oxygen, albeit very low, leading to some organic matter oxidation, whereas the samples with high TOC may have been deposited under reducing/anoxic conditions.

**Table 1** Summary of TOC (wt%) data of samples in the studied wells

Well ID.	Min TOC (wt%)	Max TOC (wt%)	Avg. TOC (wt%)
W1 ( <i>n</i> = 12)	0.19	2.21	0.79
W2 ( <i>n</i> = 24)	0.87	4.28	1.65
W3 ( <i>n</i> = 27)	0.19	2.76	0.95
W4 ( <i>n</i> = 24)	0.27	3.58	1.13
W5 ( <i>n</i> = 23)	0.64	6.99	1.88
W6 ( <i>n</i> = 47)	0.18	2.04	0.67
W7 ( <i>n</i> = 13)	0.28	5.07	1.61

### 3.2 E4, E6, and E4/E6 Ratio

The E4/E6 ratio of extracts from the samples has been calculated to determine the ratio of aliphatic to aromatic compounds in the rocks. The plot of E4 against E6 for samples from the four different fields shows a strong linear correlation between the two parameters with correlation coefficient ( $R^2$ ) values of 0.86, 0.84, 0.97, and 0.81 in Fields D, C, B, and A, respectively (Fig. 2a–d). Such linear relationship between E4 and E6 suggests a fairly consistent supply of organic carbon into the environment during the deposition and similar subsequent organic matter diagenesis. The E4/E6 values for the studied samples range between 1.15–1.72, 1.24–1.6, 1.04–1.49, and 1.03–1.4 for Fields D, C, A, and B, respectively (Table 2). E4/E6 ratios of more than 1.0 generally indicate a dominance of aromatics over aliphatics [16]. The



**Fig. 2** Correlation between E4 and E6 of samples from (a) Field D, (b) Field C, (c) Field B, and (d) Field A

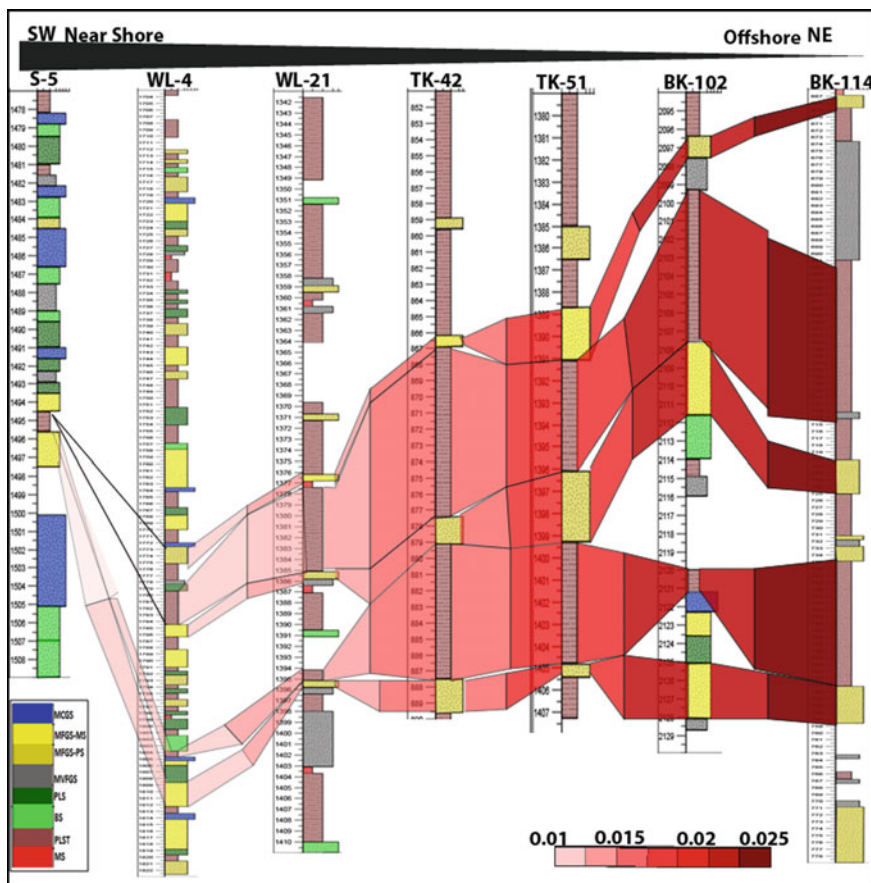
**Table 2** Summary of E4/E6 ratio for studied fields

Field Name	E4/E6 ratio		
	Minimum	Maximum	Mean
Field D	1.15	1.72	1.32
Field C	1.24	1.60	1.37
Field B	1.04	1.49	1.25
Field A	1.03	1.40	1.24

extracts from the samples are therefore dominated by aromatic compounds. Generally, the farthest field offshore, i.e., the Field C, has the highest E4/E6 ratios averaging 1.37 followed by the next farthest field, i.e., Field D, with an average of 1.32 (Table 2). Average E4/E6 ratios therefore seem to follow a definite pattern increasing from the most proximal fields, i.e., Field A (1.24) and Field B (1.25) to the intermediate Field D (1.32) and the most distal Field C (1.37). This suggests a depositional environment control not only in the organic matter content but also in the organic matter quality of the samples. Higher E4/E6 ratios of Field C extracts (Table 2) indicate a dominance of aromatic compounds within these samples.

### 3.3 Variation in Hydrocarbon Functional Groups Across Wells

The relative amount of aromatic functional groups generally increases from the samples nearest to the shoreline to the samples farther offshore (Fig. 3), whereas the amount of aliphatic functional groups decreases from the nearshore to farther offshore samples (Fig. 4). This observation may give credence to the concept of differential migration on the onshore West Baram Delta, which is initially suggested by Ramli and Padmanabhan (2012). The higher molecular weight aromatic bonds have relatively slower migration rate (Ramli and Padmanabhan 2012) and are more concentrated close to the source compared to the lighter weight aliphatic bonds that can migrate much farther from the source rock. The dominance of aromatic bonds in Field C compared to the other fields suggests that Field C may be closer to the source rocks in the offshore West Baram Delta with reference to the current Sarawak shoreline. The heterogeneity in the distribution of hydrocarbons in the delta could also be due to the presence of multiple source rocks or possible

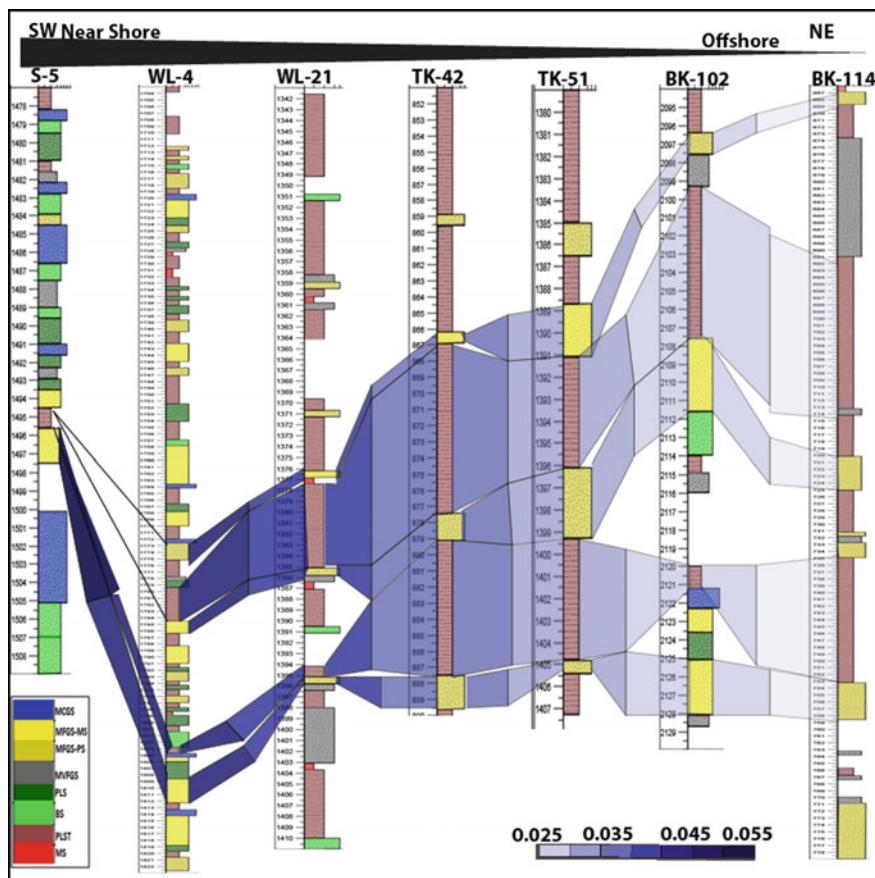


**Fig. 3** Profile of studied wells across the West Baram Delta showing increasing amount of aromatic C = C bond from nearshore to offshore

diagenesis of kerogen in the reservoir rocks. Further study is needed to confirm the possible contribution of these factors to the heterogeneity.

An overlay of the distribution of E5 across the wells shows similar distribution pattern to the aliphatic functional groups (Fig. 5). The E5 values decreases from the nearshore wells to the wells farther offshore with reference to the current Sarawak shoreline. Figure 6 shows a plot of the absorbance of hydrocarbon functional groups from FTIR against the absorbance of hydrocarbons at the standard





**Fig. 4** Profile of studied wells across the West Baram Delta showing decreasing amount of aliphatic C–H bond from near shore to offshore

wavelength, 550 nm (E5), for color coding of organics (Stevenson 1994) from UV–Vis. The plot shows a strong correlation ( $R^2 = 0.87$ ) between FTIR bond absorbance and E5. Since a good relationship exists between these two parameters, it indicates that with knowledge on E5 values, hydrocarbon bond distribution can be predicted with a good degree of accuracy.

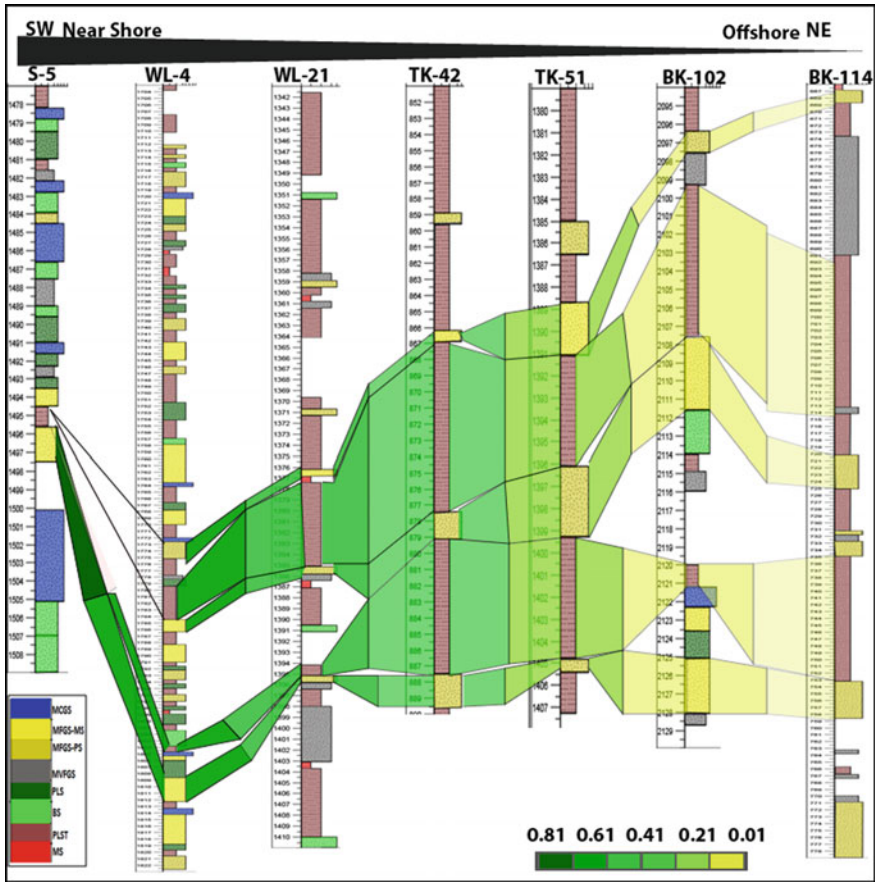


Fig. 5 Profile of studied wells across the West Baram Delta showing decreasing E5 values from nearshore to offshore

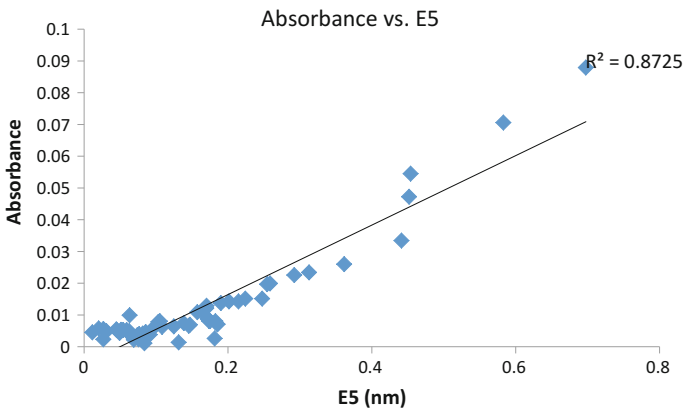


Fig. 6 Absorbance of hydrocarbon functional groups versus E5 showing strong positive correlation ( $R^2 = 0.87$ )

## 4 Conclusions

The E4/E6 values for the studied samples range between 1.15–1.72, 1.24–1.6, 1.04–1.49, and 1.03–1.4 for Fields D, C, A, and B, respectively. The plot of E4 against E6 for samples from the four different fields shows a strong linear correlation between the two parameters with correlation coefficient ( $R^2$ ) values of 0.86, 0.84, 0.97, and 0.81 in Fields D, C, B, and A, respectively. Such linear relationship between E4 and E6 suggests a fairly consistent supply of organic carbon into the environment during deposition. Generally, the farthest field offshore, i.e., Field C, has the highest E4/E6 ratios averaging 1.37 and decreasing to the most proximal field, i.e., Field A, with an average of 1.24, suggesting a depositional environment control on the quality of the organic matter as well. The suboxic to anoxic paleoenvironment of deposition may account for the preservation of significant amount of organic matter in these samples.

Higher E4/E6 ratios of Field C extracts indicate a dominance of aromatic compounds within these samples compared to samples from the other fields. The TOC content in the samples varies a lot possibly due to the numerous factors that affect organic matter deposition and preservation. The maximum TOC value of 6.99% is recorded in well W3, whereas the lowest TOC value of 0.19% is recorded in W1. Samples from wells W1, W4, and W7 show the lowest TOC values with averages of <1% indicating organic matter oxidation in these wells. The fine-grained lithologies such as the siltstones, mudstones, and very fine-grained sandstones generally have a higher TOC content than the coarse-grained lithologies.

**Acknowledgements** The authors will like to acknowledge the insightful contributions of PetroGeo Oil and Gas Consult to this paper and to Universiti Teknologi PETRONAS for funding this study.

## References

1. Taber, J. J., Martin, F. D., and Seright, R. S. (1997). EOR Screening Criteria Revisited Part 1 : Introduction to Screening Criteria and Enhanced Recovery Field Projects. Society for Petroleum Engineers (SPE) Reservoir Engineering, (August), 189–198.
2. Sandal, S. T. (1996). The geology and hydrocarbon resources of Negara Brunei Darussalam (p. 234). Brunei: Brunei Shell Petroleum and Brunei Museum.
3. Ingram, G., Chisholm, T., Grant, C., Hedlund, C., Stuart-Smith, P., and Teasdale, J. (2004). Deepwater North West Borneo: hydrocarbon accumulation in an active fold and thrust belt. *Marine and Petroleum Geology*, 21(7), 879–887.
4. Ramli, M. S., and Padmanabhan, E. (2012). Heterogeneity of the Hydrocarbon Distribution in Tertiary Sediments of North-East Sarawak. In *International Petroleum Technology Conference (IPTC)* (pp. 1–7). Bangkok.
5. Trask, P. D., and Hammar, H. E. (1934). Organic Content of Sediments. *Drilling and Production Practice*, 117–130.
6. Brooks, J. (1981). Organic maturation studies and fossil fuel exploration (p. 441). London: Academic Press.

7. Tissot, B. P., and Welte, D. H. (1984). *Petroleum formation and occurrence* (Second., p. 702). Berlin: Springer-Verlag.
8. Chen, Y., Senesi, N., and Schnitzer, M. (1977). Information Provided on Humic Substances by E4/E6 Ratios. *Soil Science Society of America Journal*, 41(2), 352–358.
9. Tan, D. N. K., Rahman, A. H. B., Anuar, A., Bait, B., and Tho, C. K. (1999). West Baram Delta. In L. K. Meng (Ed.), *The Petroleum Geology and Resources of Malaysia* (pp. 291–341). Kuala Lumpur: Petroliaam Nasional Berhand (PETRONAS).
10. Sudirman, S. B., Samsudin, Y. B., and Darman, N. H. (2007). Planning for Regional EOR Pilot for Baram Delta, Offshore Sarawak, Malaysia : Case Study, Lesson Learnt and Way Forward. Society for Petroleum Engineers Asia Pacific Oil and Gas Conference and Exhibition in Jakarta, Indonesia.
11. Rijks, E. J. H. (1981). Baram Delta geology and hydrocarbon occurrence (Sarawak). *Geological Society of Malaysia Bulletin*, 14, 1–8.
12. Ho, K. F. (1978). Stratigraphic Framework for Oil Exploration in Sarawak. *Bulletin of the Geological Society of Malaysia Geological Society of Malaysia*, 10, 1–13.
13. Hutchinson, C. (2005). *Geology of North West Borneo: Sarawak, Brunei and Sabah* (p. 421). New York: Elsevier.
14. Ryan, W. B. F., Carbotte, S. M., Coplan, J. O., O'Hara, S., Melkonian, A., Arko, R., Zemsky, R. (2009). Global multi-resolution topography synthesis. *Geochemistry Geophysics Geosystems*, 10(3).
15. Schnitzer, M., and Neyroud, J. A. (1975). Further Investigations on the Chemistry of Fungal "Humic Acids." *Soil Biology and Biochemistry*, 7(6), 365–371.
16. Stevenson, F. J. (1994). *Humus Chemistry: Genesis, Composition, Reactions* (p. 496). New York: John Wiley and Sons.
17. Evdokimov, I. N., and Losev, A. P. (2007). Potential of UV-Visible Absorption Spectroscopy for Characterizing Crude Petroleum Oils. *Oil and Gas Business*, 1–21.
18. Dow, W. G., and Pearson, D. B. (1975). Organic Matter in Gulf Coast Sediments. In *Offshore Technology Conference* (pp. 85–95). Texas.

# Characteristics of Pore Pressure and Effective Stress Changes in Sandstone Reservoir Through Velocity Analysis Approach Due to Hydrocarbon Production

Adha Kurniawan, Wan Yusoff Wan Ismail, Lubis Luluan Almanna and Mhd Hanapiah Nurhajeerah

**Abstract** This paper focuses on the use of velocity analysis to identify and characterize the pore pressure and effective stress changes during oil field production since the pore pressure estimation takes an important role in oil and gas industry. Pore pressure estimation is a substantial prerequisite to start drilling and production. Moreover, the precise pore pressure estimation will determine the safety, profits and success in both production and recovery. In order to accomplish the objective of this study, the methodology is composed of several broad stages. It consisted of field mapping to create stratigraphy model, coring/sampling, velocity measurement with saturation and pressure (i.e., pore and confining) variations, velocity analysis for constructing the empirical equation of pressure, saturation, and pore pressure relationship in each facies, pore pressure and effective stress changes estimation model from interval velocity and transit time analysis. The result shows that pore pressure value was reduced due to the decrease in fluid content to represent the production history. The decreasing in pore pressure might soften the elastic mineral frame and has the tendency to possess high velocity. Regarding depth, the pore pressure was slightly increasing where the effective stress decreased gradually; the enhancement of pore pressure values was due to the increasing overburden pressure. In consistent depth or constant overburden pressure (confining pressure), increasing of pore pressure would decrease the velocity gradually. This occurs due to the increase in inflicted interval time ( $t_i$ ) as a consequence of reduced medium (samples) velocity. The alteration in pore pressure by the changes in fluid content or saturation resulted in the alteration of velocity value that had proportionate trend with the effective stress.

---

A. Kurniawan (✉) · W.Y. Wan Ismail · L. Luluan Almanna · M.H. Nurhajeerah (✉)  
Department of Petroleum Geoscience, Universiti Teknologi PETRONAS,  
32610 Seri Iskandar, Tronoh, Perak, Malaysia  
e-mail: kurniawanadhaa@gmail.com

**Keywords** Pore pressure · Effective stress · Hydrocarbon production · Overpressure mechanism · Velocity

## 1 Introduction

This paper presents the study of pore pressure and effective stress analysis through velocity model analysis for carrying out the significant impact of hydrocarbon production inducing pore pressure changes. The samples are carried from one outcrop which represents the Miri formation. The analysis was conducted using 5 samples representing 5 facies of the outcrop and analyzing the velocity trend as the function of saturation variance.

The Miri field is located in South China Sea as a part of West Baram Delta in Tertiary Age. It was deposited in rapid sedimentation yield which produced thick low permeability sediment leading to the development of overpressure. Disequilibrium compaction is the most widely used mechanism, which generates an overpressure zone in this study area. This study used core sample from Miri Field. As the birthplace of Malaysian petroleum industry, the oil exploration began in 1910 in Miri field. The Miri formation consists of sand members that are very important in oil and gas reservoirs, especially in early production in Malaysia. The formation consists of siliciclastic sequence of a succession of clay–sand packages that are coarsening upwards. The age of the formation is Middle Miocene and exposed around Miri city, Serawak, Malaysia, which uplifted part of subsurface, oil-bearing sedimentary strata of the Miri Field, and possibly also for the offshore fields [8, 9].

### 1.1 Problem Statement and Objective

Pore pressure is the pressure which is exerted by the fluid contained inside the pore space of the sediment at particular depth. Without any process or normal conditions, the pore pressure is equal to the hydrostatic pressure. However, in certain sedimentary formation, the pore pressure is not hydrostatic, especially in deep reservoir where the pore pressure increases above the hydrostatic pressure called overpressure zone [2].

The most crucial of the correct pore pressure information is useful for drilling well management, reservoir (hydrocarbon) monitoring (before and during production), geological and geomechanical analysis. Besides preventing geohazards (i.e., Blowout and well collapse), accurate pore pressure estimation is crucial to be successful in both drilling and production.

Hottman and Johnson [13] is probably the first one to define pore pressure prediction from shale properties which is derived from well-log data (acoustic travel time and resistivity) followed by Gardner et al. [14] that proposed an equation combining the normal fluid gradient and overburden stress gradient. The research

on pore pressure prediction is slightly increasing from time to time; many empirical equations for pore pressure prediction were presented based on sonic transit time (P-Wave velocity), resistivity and other well-log or seismic data [1, 2, 3].

Nowadays, interval velocity or sonic transit time approach i.e., Eaton Method (1975) and Bowers Method (1995) are constantly used for pore pressure prediction or overpressure detection. The velocities eternally increase with effective pressure and have negative relation with pore pressure. These velocities are tending to be sensitive with the pore fluid contents and pressure [1, 4, 12].

Most of the conventional methods are unique and used widely, yet very complex with many assumptions and hypothesis that have been made to estimate the true pore pressure. However, as the assumptions made focusing on complex data analysis, some basic properties are being neglected which may have significant impact on the estimation model. After all, the velocity analysis is a widely used and the most appropriate method.

From time to time, the hydrocarbon reserves have continuously been produced for answering world’s energy demands. As the primary energy in the world, oil and gas industry always carries out methods like enhance oil recovery (EOR) for the potential existing oil wells. There are several parameters that would be changed during production, including pore pressure and effective stress.

This study focused on laboratory experiment for analyzing the interval velocity and transit times changes due to different pressure and different fluid saturation for representing hydrocarbon production. The velocity changes were the mandatory parameters which used for determining and analyzing the changes of pore pressure and effective stress.

### 1.2 Pore Pressure and Effective Stress Changes Due to Depletion and Velocity Laboratory Analysis

Pore pressure is the pressure which is formed by the fluid contained in the pores space of rocks maintained at depths. When there is equilibrium, the pore pressure is simply equal to the weight of the overlying fluid, and the total of vertical stress is equal to the weight of the overlying fluid and rock. This pressure is often referred to as “hydrostatic pressure ( $P_h$ )”. In this study, the hydrostatic pressure referred freshwater (0.443 psi/ft). Whereby, the overburden pressure ( $P_o$ ) that of function of density ( $p$ ), thickness ( $hi$ ), and gravity ( $g$ ) is given below:

$$P_o : p_w g h_w + p g h_i \tag{1}$$

However, there are several conditions that can cause the pore pressure to be different from hydrostatic pressure. Pore pressure is defined by Eaton formula [5] where function of overburden pressure ( $P_o$ ) and hydrostatic pressure ( $P_h$ ) with acoustic transit time from the normal compaction trend at depth of investigation ( $tn$ ) and travel time ( $ti$ ), which can be written as follows:

$$Pp : Po - (Po - Ph) * \left(\frac{ti}{tn}\right)^y \quad (2)$$

where the difference between the *overburden pressure* ( $Po$ ) *pore pressure* ( $Pp$ ) is *effective stress* ( $\sigma$ ), which can be written as following Eq. 3 [6].

$$\sigma = Po - PP \quad (3)$$

Due to production, the changes of stress in reservoir were modeled using poroelasticity. Changes in both vertical and lateral stress vary as the pore pressure in reservoir reduces. In reservoir, the changes of the in situ stress are function geometry, elastic properties, grain compressibility of reservoir, and surrounding material [6]. However, in thin tabular reservoir the lateral strain and the vertical stress were assumed constant, since the lateral distribution was much more preponderant than its thickness. By following the linear poroelasticity relationship, where  $\nu$  (*poisson ration*) and  $\alpha$  are Biot's pore elastic constants [5, 10, 11].

$$\sigma/PP = \alpha_b(1/2\nu)/(1-\nu) \quad (4)$$

Equation 4 is applied by performing laboratory experiment to determine  $\nu$  and  $\alpha$ . Since the pore pressure and effective stress are interrelated, changes in pore pressure also cause the changes in effective stress in contravention. The mathematical relationship between stress and pore pressure is defined in terms of the effective stress. Implicitly, the effective stress is that portion of the external load from total stress that is carried by the rock itself. Effective stress ( $\sigma$ ) controls sediment compaction process, in the case the reduction in the effective pressure at certain depth means a reduction in the product of rock compaction pressure.

As mention in introduction, the P-Wave velocity, S-Wave velocity, and velocity derivative (i.e., P-wave, S-Wave,  $Vp/Vs$ ,  $AI$ , and  $\nu$ ) are the mandatory parameters used in this study. Those parameters will be substituted into stratigraphic sequence and correlate with rock properties (i.e., porosity and permeability) for characterizing the pore pressure and effective stress changes due to hydrocarbon production. Although, the timescale of the laboratory experiment is much smaller compared to geologic timescale of the true sedimentation, the laboratory model and analysis are very useful for characterizing the pore pressure changes and overpressure mechanism with better accuracy [3, 6].

## 2 Methodology

There were several stages in the procedures that were conducted in this experiment. The stages involved were collecting data, preparation of samples including coring and cutting of samples, determination of rock properties of samples, velocity determination and analysis, and the development of pore pressure and effective stress model (Fig. 1).



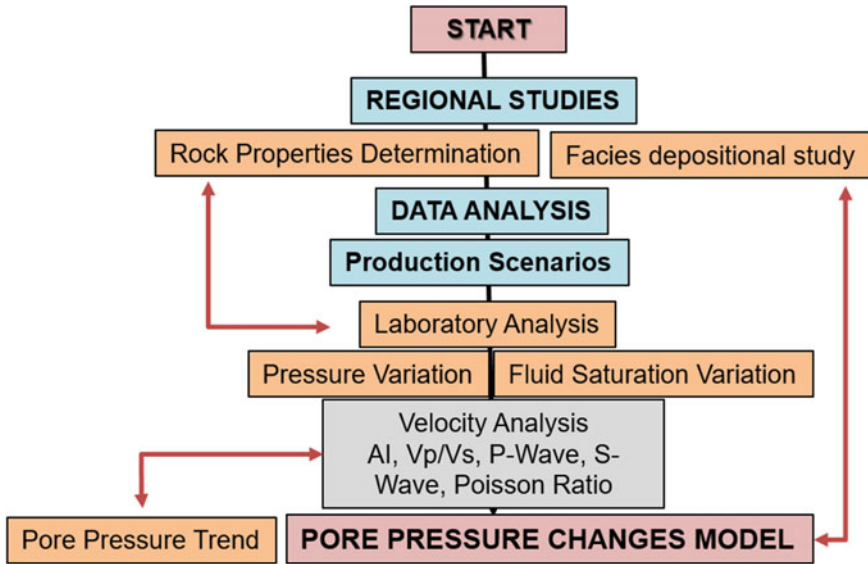


Fig. 1 General procedure of study area

The procedure in this analysis was initiated with data collection, whereas this process involved field study and the building stratigraphy sequence model based on outcrop study followed by coring and cutting sample in 1.5 in. diameter. The samples were cleaned to remove the remaining oil and/or salt before performs porosity and permeability analysis.

The velocity changes were the main parameters that were used for determining and identifying pore pressure and effective stress changes during production. To obtain parameters that were needed to build the model, there were several methods need to be performed.

Direct measurements or laboratory analyses were divided into two main categories: First, laboratory analysis using SONIC OYO equipment was carried out to determine the velocity of the facies in room temperature and pressure. The second analysis was carried out using AutoLab 500 for investigating velocity yield from various confining pressure and different saturation used for perfume production scenario. In this study, the saturation was divided into water saturation, partial oil saturation, full oil saturation, and dry saturation with assumed gas saturation. The oil used was Tapis crude oil, and its properties are shown in Table 1.

The main results from this analysis were velocity variations, which is a product of consistent changes in confining pressure, saturation and pore pressure variation. The velocity variations were derived from alteration values of confining pressure which were used for estimating the pore pressure variation along the sequence model.

**Table 1** Fluid properties for study purposes

Properties	Unit	Tapis oil	Miri oil
Density	g/m <sup>3</sup>	0.82	0.88
Pour point	°C	18	14
Cloud point	°C	27	25
Viscosity	Cp	4.012	4.01
API	API	39.39	31.33
Wax content	%	17.1	4.7

### 3 Result and Discussion

#### 3.1 Facies Studies and Rock Properties

In order to accommodate the laboratory analysis to investigate the changes in pore pressure and effective stress due to hydrocarbon production, a number of reservoir rock samples with different porosity and permeability were selected for this study.

This study used core sample from outcrops within Miri Field. As the birthplace of Malaysian petroleum industry, the oil exploration began in 1910 in Miri field. The core samples from Miri field from Sarawak, Malaysia, were used in this study (Fig. 2), where the formation consists of sandstone reservoir [7]. The study area was divided into sixteen (16) layers and encompassed six facies (A–F) from the outcrop that was used for stratigraphy sequence model (Fig. 3), but this study only conducted experiment to five samples (Facies A to Facies E).

*Facies A: Wavy-Bedded Fine-Grained Sandstone.* These facies were presented at 0, 4.2, and 5 m depth and were characterized by dark gray color with moderately short and very fine-grained sandstone. In addition, asymmetrical-to-symmetrical wavy bedding sediment structures were discovered in this facies. These facies were diffused in several layers, approximately at 0.4–2.3 m. This layer might be laterally up to few to several meters. Based on the observation, the dark color was caused by mud or shale contained in these rocks; the formation of wavy bedding may involve the conditions where the deposition and preservation of both sand and mud were probably formed. Noticing the characteristic of this facies, wavy-bedded facies could be formed in mixed tidal setting (middle-to-upper shore face).

*Facies B: Bioturbated Fine-Grained Sandstone.* These facies were distributed in several layers at below part of this sequence, characterized by the moderate bioturbation activity of vertical to subvertical *ophimorpha*. Facies had light grey color, moderately sorted, slightly rounded shape of grains (subrounded), and absence of carbonates. The thickness of sand varies from 30 cm to several meters. Bioturbation term refers to the condition where the sediment contains irregular disruption of plants and/or animal. The presence of sediment structure (parallel lamination) and grains of this facies (very fine) indicated the periods of low-energy deposition.

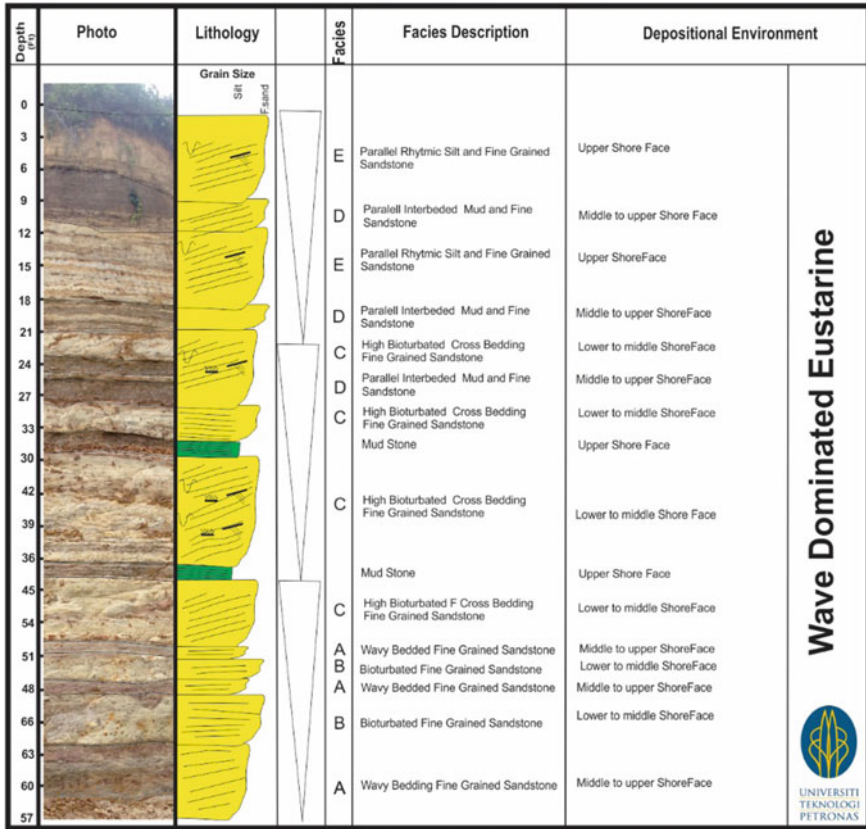


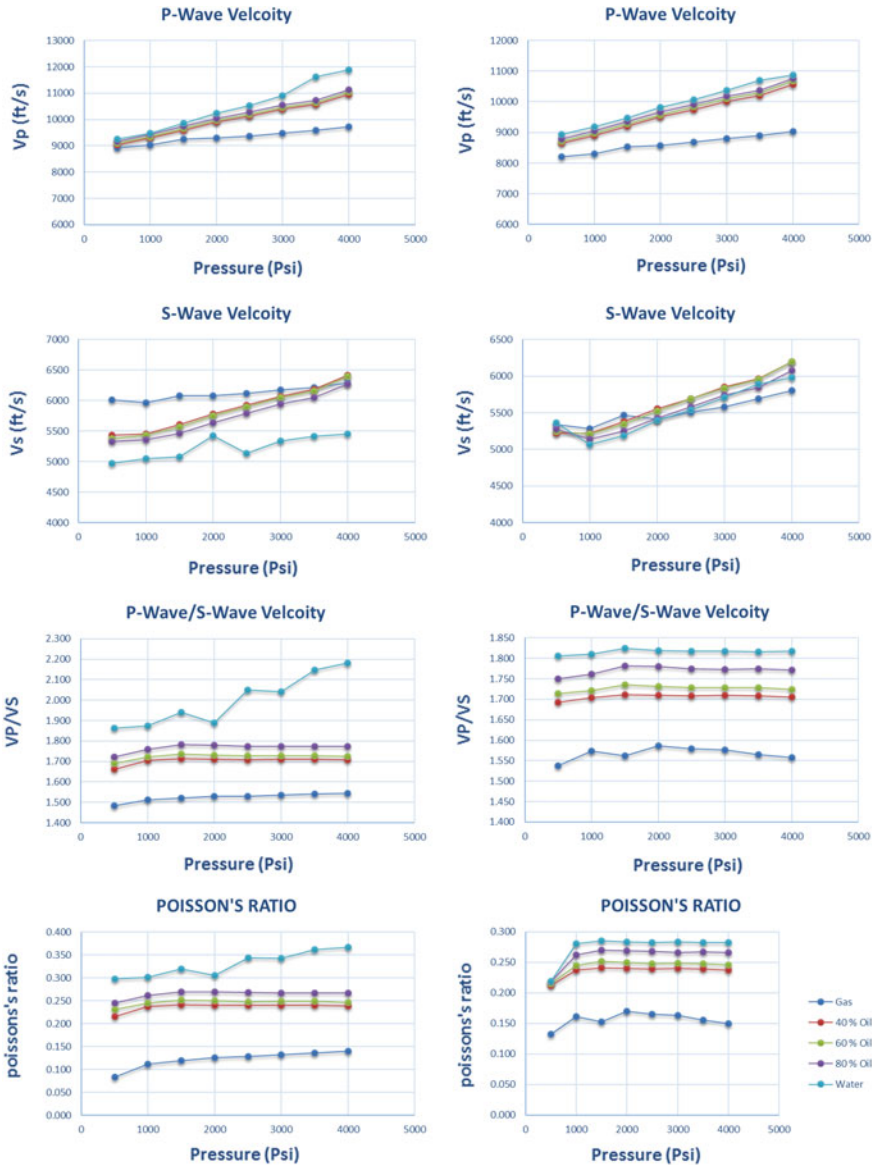
Fig. 2 Stratigraphy of study area

**Facies C: High Bioturbated Cross-Bedding Fine-Grained Sandstone.** These facies often appeared in this sequence and were distributed in several layers. The thicknesses of this facies vary from 40 cm to 3 m. The main characterization of this facies was the presence of high bioturbation activity of *ophimorpha* in vertical-to-subvertical circumstance. Facies had moderately light grey color, moderately sorted, slightly rounded shape of grains (subrounded), and absence of carbonates. These facies were interpreted in lower-to-middle shoreface.

**Facies D: Parallel Inter-bedded Mud and Fine-Grained Sandstone.** These facies come up at several depths, consisting of the interval layers of sandstone and mudstone (shale). But in this facies, mudstone was more dominant compared to sandstone. At this depth, rock mud had parallel laminated light and dark, fine-grained sandstone combined with mud laminations. Moderate grained, light gray sandstone was discovered, which had a medium sorting with subrounded shapes; the depositional processes are interpreted by the condition where storm

Wave Dominated Eustarine





**Fig. 3** Velocity trend changes due to saturation and pressure, Facies A with 14.6% porosity (*left*) and Facies D with 26.1% porosity (*right*)

deposit sequence may be disrupted to varying degrees of bioturbation (gradual changes in bioturbated sandstone and mudstone) during post-storm. Facies D possibly have been formed in shoreface. Moreover, the occurrence of inter-bedding

sandstone and mudstone was indicated by a fair-weather circumstance. Thus, these facies were interpreted as having been formed in middle shoreface.

*Facies E: Cross Inter-bedded Silt and Fine-Grained Sandstone.* Generally, Facies F had similar characteristic with Facies E, where inter-bedded silt with sandstone was encountered. In this facies, existence of silt was dominant than sandstone. These facies were at the top of this model. Facies F had light gray color with good sorted and subrounded shapes; moreover, the alternation of parallel-bedded sandstone in which, burrows rarely disappeared and parallel-stratified sandstone observed, generally indicate a moderate energy environment. And the presence of mudstone laminae indicates that the sediment was deposited in low-to-medium dispositional energy. These facies consisted of alternating thin layers which are different in composition, texture, and color. The reason for repetition is the regular changes in the transport or production material. These regular changes could be caused by short duration processes, i.e., tidal changes, or by long-term changes, i.e., seasonal changes due to transformation in weather or wave conditions. These suggest the considerable variations in sedimentation rates, probably associated with storm or fair-weather deposition. Because of those evidences, facies E was interpreted as having been formed at upper-to-middle shore face environment.

*Facies F: Mud Stone.* These facies had dark colour, very fine grained, good sorted, and subrounded shapes. These facies show parallel lamination with high-to-low depositional energy. Based on the fact, these facies were interpreted in upper shore face.

The Miri formation consists of sand members that are very important in hydrocarbon reservoirs, during early production in Malaysia. The formation consists of siliciclastic sequence of a succession of clays and packages that are coarsening upwards. The age of formation is Middle Miocene and is exposed around Miri city. The grain density shows that the samples were sandstone reservoir with quart minerals. In addition, the samples were representing hydrocarbon reservoirs which show good porosity and permeability with little percentage of fines.

The samples were cut and shaped into cylindrical form with 1.5 inch in diameter. The core samples were cleaned to remove the remaining oil and/or salt before conducting porosity, permeability measurements. Rock property data are given in Table 1.

The samples were saturated with 3 types of fluids, including water, oil and gas, with the intention of performing hydrocarbon reservoir. For oil saturated, the saturation was divided into three types of saturation (i.e., 2, 4, and 6 days of saturation) in 2500 psi pressure saturation.

The result shows that the density and weight of samples were having positive relationship; an increase in saturation would increase both of weight and density, since the fluid filled the pore space with bulk volume of medium. The increase in density was the only alteration in the weight of sample, where the transformation of weight was the product of fluid substitution and total of pore volumes. The more the number of pores, the more possibility of fluid to fill the pores of the medium

**Table 2** Rock properties of samples

Facies	A	B	C	D	E
Core porosity (%)	14.8	16.7	17.3	26.1	24.5
Permeability (Md)	124.74	172.48	175.24	287.4	242.2
Grain volume (cc)	44.5	60.9	62.4	78.9	75.3
Bulk density (g/cc)	2.261	2.604	2.506	2.431	2.591
Pore volume (cc)	6.579	10.182	10.78	20.43	19.38
Pore volume (%)	11.45	12.44	12.76	24.70	23.13
Grain density (g/cc)	2.654	2.67	2.64	2.68	2.72
Bulk volume (cc)	52.24	81.85	84.43	82.7	83.8
Weight (g)	122.18	217.10	217.13	217.93	217.36
Length (mm)	50.03	72.82	72.98	73.77	74.55
Diameter (mm)	36.47	37.84	38.39	37.79	37.84
Volume of fine (cc)	6.4	10.2	10.5	10.7	10.7

(samples), and the difference in pore volume of each facies would distinguish the density of each facies.

Table 2 shows that the D facies had the highest pore volume followed by facies E, C, B, and A in the last position. This result proves the statement where the samples having more pore volume would produce higher density compared to samples with low pore volume when the samples were filled by similar fluid type (Table 3). Furthermore, in the same condition of pore volume (Facies), the variation in density was the function of density of fluids and total saturation of fluids into samples. Sample which was saturated with water had the highest density and weight, followed by oil and gas. In addition, the porosity and permeability had parallel relationship for all samples (Table 3).

By carrying the final model of velocity, the empirical equations (Table 4) were developed for each condition (i.e., Facies and saturation) in different saturation. Those empirical equations would be used for the synthetic model (stratigraphic models).

### 3.2 Velocity Trend Changes Due to Saturation and Pressure

Generally, all samples (Facies A with 14.8% porosity and Facies E with 24.5% porosity) indicate both P-Wave and S-Wave increased due to the increasing of effective pressure (confining pressure) in constant pore pressure. Thus, the velocity was the function of the total time through the medium (samples), by increasing the pressure yielded the closing of grain boundaries, cracked and flowed and made time was going fast. However, in terms of saturation changes P-Wave and S-Wave showed different scenery; P-Wave velocity indicated significant changes from gas to oil and water saturation compared to S-Wave. Full saturated water had the

**Table 3** Saturation with density, weight, bulk volume, and bulk density of samples

Facies	Condition	Condition	Weight (gr)	Volume (cm <sup>3</sup> )	Density (g/cm <sup>3</sup> )
	Days	(%)			
a	Dry	100	122.18	54.06	2.261
	2 days	40	128.67	54.06	2.380
	4 days	58	131.91	54.06	2.440
	6 days	74	148.12	54.06	2.740
	Water	100	152.14	54.06	2.814
b	Dry	100	217.10	85.01	2.604
	2 days	38	221.52	85.01	2.606
	4 days	56	224.32	85.01	2.639
	6 days	73	231.72	85.01	2.726
	Water	100	232.26	85.01	2.732
c	Dry	100	217.13	88.02	2.506
	2 days	42	222.71	88.02	2.530
	4 days	62	224.22	88.02	2.547
	6 days	73	230.26	88.02	2.616
	Water	100	232.60	88.02	2.643
d	Dry	100	217.93	89.64	2.431
	2 days	42	220.78	89.64	2.463
	4 days	59	226.61	89.64	2.528
	6 days	73	237.05	89.64	2.644
	Water	100	237.82	89.64	2.653
E	Dry	100	217.36	87.04	2.591
	2 days	41	225.17	87.04	2.587
	4 days	58	230.36	87.04	2.647
	6 days	75	232.42	87.04	2.670
	Water	100	234.78	87.04	2.697

highest P-Wave velocities then followed by oil and gas saturation. This outcome indicates that P-Wave tended to be more sensitive with saturation compared to S-wave that had less sensitivity with the saturation. Since the S-Wave is a function of shear modulus and density, the shear modulus was not affected by the fluids. This contradicted with the P-Wave velocities where the wave is function of both bulk and shear moduli. When shear modulus is constant, increasing the velocity only affects bulk modulus which is influenced by the density of the fluids. Water had the highest fluid density followed by oil and gas (Fig. 3).

In constant confining pressure or overburden pressure (500 psi), the effective stress ( $\sigma$ ) was going down aligned with the decrease in P-Wave velocity due to parallel increase in pore pressure. In Eq. 4 it is mentioned that the pore pressure and effective stress had contradicted relationship; however, the effective stress had positive relation with P-Wave velocities. The decrease was influenced by the expanded spacing of grain-to-grain contact or opening of pore spacing (increasing

**Table 4** Empirical equation for each facies and saturation condition

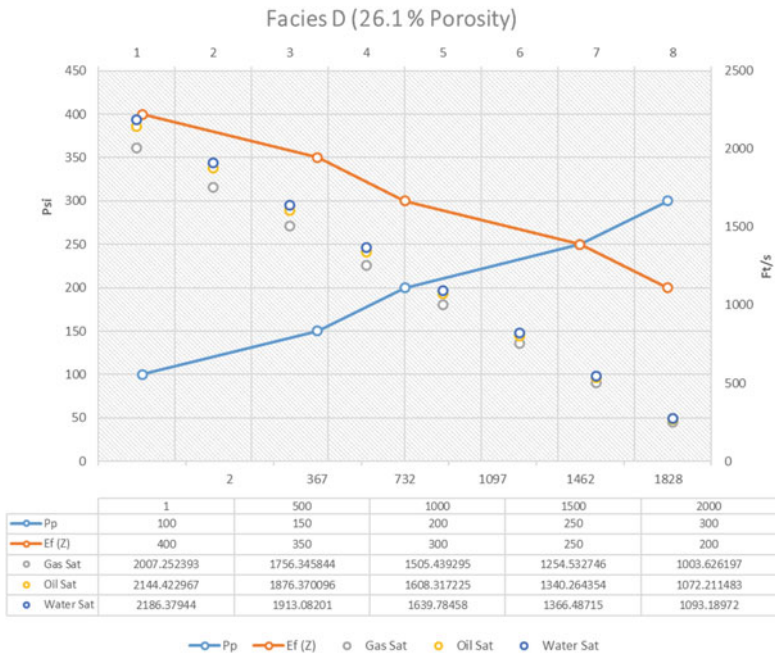
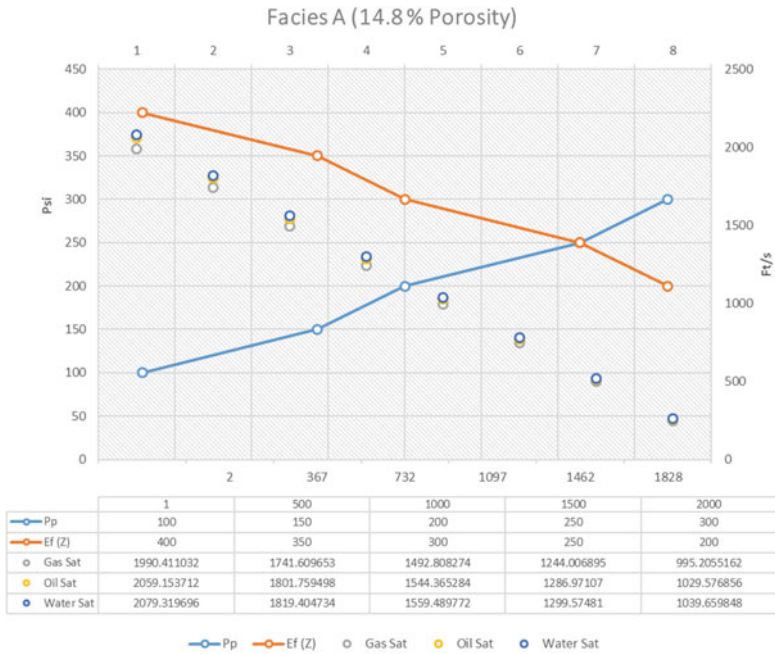
Facies	Condition	P-wave (Ft/s)	S-wave (Ft/s)
A	Gas	$y = 0.218x + 8838.1$	$Y = 0.0837x + 5929.3$
	40% oil	$y = 0.5352x + 8779.3$	$y = 0.287x + 5215.5$
	60% oil	$y = 0.5391x + 8839.2$	$y = 0.2947x + 5167.9$
	80% oil	$y = 0.543x + 8913.2$	$y = 0.278x + 5107.3$
	Water	$Y = 0.7761x + 8726.7$	$y = 0.1347x + 4931.6$
B	Gas	$y = 0.2647x + 8684.6$	$y = 0.1402x + 5825$
	40% oil	$y = 0.4781x + 8570$	$y = 0.2482x + 5103.1$
	60% oil	$y = 0.5342x + 8585.1$	$y = 0.2891x + 5011$
	80% oil	$y = 0.5951x + 8638.9$	$y = 0.323x + 4906.8$
	Water	$y = 0.6599x + 8805.5$	$y = 0.3537x + 4864.4$
C	Gas	$y = 0.2676x + 8719.5$	$y = 0.0723x + 5861.7$
	40% oil	$y = 0.3662x + 8757.7$	$y = 0.1819x + 5213.6$
	60% oil	$y = 0.3879x + 8839.3$	$y = 0.204x + 5159.9$
	80% oil	$y = 0.4166x + 8886.7$	$y = 0.1918x + 5158.7$
	Water	$y = 0.4369x + 9042$	$y = 0.2086x + 5069.6$
D	Gas	$y = 0.223x + 8137.9$	$y = 0.1405x + 5182.7$
	40% oil	$y = 0.537x + 8403.3$	$y = 0.2954x + 4969.3$
	60% oil	$y = 0.5431x + 8462.6$	$y = 0.2781x + 4999.3$
	80% oil	$y = 0.5391x + 8547.2$	$y = 0.2416x + 5007.1$
	Water	$y = 0.5722x + 8631$	$y = 0.2833x + 4820.6$
E	Gas	$y = 0.2305x + 8117.7$	$y = 0.136x + 5204.6$
	40% oil	$y = 0.537x + 8386.9$	$y = 0.2884x + 4988.4$
	60% oil	$y = 0.5506x + 8442.4$	$y = 0.2866x + 4982.2$
	80% oil	$y = 0.5516x + 8520.9$	$y = 0.2563x + 4966.7$
	Water	$y = 0.5752x + 8633.3$	$y = 0.2425x + 4971.4$

crack porosity). This phenomenon led to the slowness of time through the medium (samples).

There are several parameters which must be taken into consideration, such as porosity, pore volume, type of fluid, and rate of saturation. In comparison, Facies A and Facies D had porosity difference of 11.3% and more than 100 mD difference in permeability but in both facies the effective stress and P-Wave velocities were reducing gradually due to the increasing of pore pressure. However, there were different values of P-Wave velocity in the same level of effective stress, saturation, and pore pressure, as in Facies A (oil saturation) with 300 psi effective stress and 200 psi pore pressure; the P-Wave velocity was 1544 ft/s when facies D in same condition was 1608 ft/s (Fig. 4).

In addition, pore volume and rate of saturation were giving crucial influences for the variation of P-Wave velocity in constant confining pore pressure. The saturation was giving significance to the total density (bulk density) where the total density was a combination of grain density and fluid density, and the bulk density was





**Fig. 4** Pore pressure profile, effective stress, and velocity variation in constant confining pressure (Po) 500 psi, Facies A 14.6% porosity (above), Facies D 26.1% porosity (below)

required for  $P_o$  and  $P_h$  determination. Thus, in constant overburden pressure, the rate of saturation was not considered for overburden pressure ( $P_o$ ) but highly crucial for hydrostatic pressure determination, since the different hydrostatic pressure was giving particular different in P-Wave velocities.

In both of facies (Facies A and Facies D), the high velocities were led by water saturation, followed by oil water saturation, oil saturation, and oil and gas saturation, and closed by full gas saturation. The conditions were particularly caused by a change in pore pressure that would change the saturation. The total time to pass through the medium become lower as the fluid density increases. In addition, the high pore was persisting over long periods and might prevent diagenesis and preserve to keep the P-Wave velocities getting lower.

Another derivative parameter, such as  $v_p/v_s$  and Poisson's ratio, pointed out the same trends. Saturated water stood in highest place followed by 80–40 oil saturation and gas saturation in the last place.

In Facies A sample, both  $V_p/V_s$  and Poisson's ratio show significant changes from gas to oil and from water to oil. This was a little bit difference in Facies E sample (24.5% porosity and 242 mD permeability), where water and oil saturation showed parallel changes and significant changes from gas to oil saturation.

In hydrocarbon production, the fluids (i.e., oil or gas) were carried out from reservoir to be produced. Mostly for continuity of the reservoir condition, the fluids were substituted with water. During production, the pore pressure changed due to the activity of fluid substitution in reservoirs followed by changes in other parameters. Many approaches were done by previous researchers to determine and study the changes in pore pressure during the hydrocarbon production. Although, the timescale of laboratory analysis and experiments was much smaller than real geological timescales, the sensitivity of P-wave velocities due to changes saturation can be one of the advantages of this study (models) for application in reservoir scales.

### ***3.3 Pore Pressure Changes in Different Saturation***

This study characterizes the pore pressure based on its function of overburden pressure, hydrostatic pressure, and sonic time velocities. The various saturation illustrated the general production history with no mineral changes assumption during production where only applied changes in fluid were present. The pore pressure was carried out from Eaton equation with exponent 3.

The result shows the pore pressure increased with respect to the increasing of the depth which contradicted with effective stress where it was decreasing gradually to depth. The pore pressure reduced due to production or reservoir depletion.

Reservoir depletion is one of the processes that decreasing of pore pressure and reduction in volume would bring down the pore pressure over time. During oil and/or gas production, the pore pressure within the reservoir reduced. The rates of pore pressure drop were controlled by the rate from the surrounding rocks. The

trend in pore pressure line would reduce, and effective stress was increasing due to production.

Decreasing of pore pressure softened the elastic mineral frame and tended to have high velocity. Changes in pore pressure due to change in contained fluid type or saturation might change the velocity since velocity could be sensitive to saturation and had parallel trend with effective stress.

The values of pore pressure were decreasing gradually with respect to the reduction in fluids (i.e., oil and gas) in these reservoirs. The changes in pore pressure and effective stress were in respect of the depth where the amount of pore pressure and effective stress changes was getting high due to depth (Table 3). In addition, these synthetic reservoirs show that changes in pore pressure and effective stress values were not significant ( $\pm 10\%$ ) as the influence of small laboratory samples. However, these results highly prove that during production the pore pressure was reducing gradually.

The pore pressure was not tied with hydrostatic pressure and going to overburden pressure which this condition was representing abnormal pressure (i.e. overpressure). This phenomenon occurred since this syntactic model (stratigraphic model) is a part of Miri Cycle 5, which is below part of the general stratigraphic sequence that exposing on the surface. Derivative parameters of velocity (i.e.  $V_p/V_s$  and Poisson's ratio) show the similar results where the reducing fluids' contents would reduce the values of them.  $V_p/V_s$  shows more clear changes from oil to gas saturation (Fig. 5).

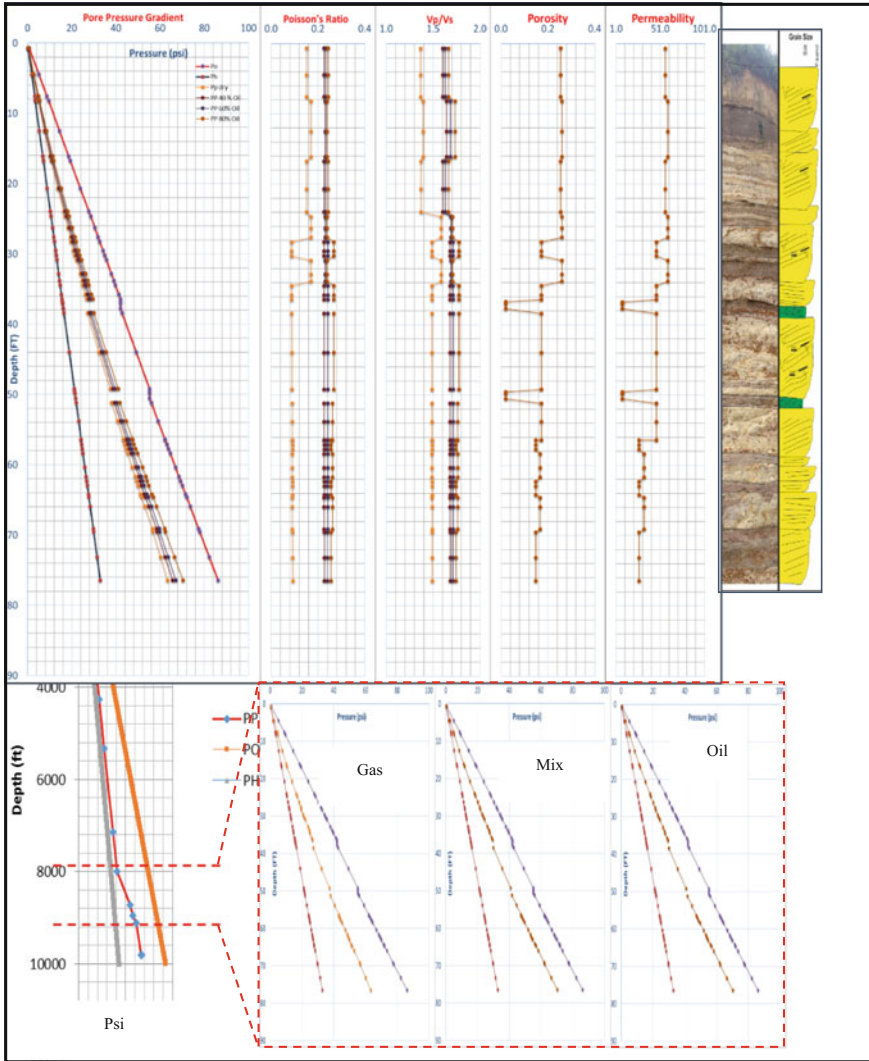
## 4 Conclusion

Velocity analysis is an essential parameter in pore pressure prediction or pore pressure and effective stress characterization prior or during production. The main reason of essential from velocity is that the velocity can be sensitive with burial mechanism, rate of sedimentation, porosity, and rock type. In addition, the velocity is sensitive or influenced by saturation and density. Those characters are interrelated.

When confining pressure is increasing, velocities and effective stress ( $\sigma$ ) are increasing parallel while the pore pressure is reducing gradually. But when overburden pressure is constant, the effective stress ( $\sigma$ ) is going down aligned with decreasing of P-Wave velocity due to parallel increase in pore pressure. The effective stress has positive relation with P-Wave velocity and negative relation with pore pressure. The decrease was influenced of the expanded spacing of grain-to-grain contact or opening of pore spacing (increasing crack porosity).

The empirical formula from velocity, saturation, and pressure were useful for upscaling the data from core scale to outcrop scale. The benefit of the upscaling was for identifying the characteristics of pore pressure changes with respect to depth and production. The changes from different fluids did not show significant changes.

The pore pressure characterization of the outcrop model was influenced by sedimentary environment of deposition. The characteristic of the model shows



**Fig. 5** Pore pressure profile from stratigraphic model (*above*), pore pressure profile from well AK (5) depth (7841) ft top of Miri cycle 5 (*left below*), pore pressure changes due to changes in hydrocarbon (*right below*)

parallel line near to overburden using exponent 3, but with exponent 1, the trend line was parallel and near to hydrostatic pressure. Since the model was the outcrop model of Miri Cycle 5, most likely the reason of overpressure in model was caused by the type of rock and the stratigraphy (Fig. 5).

The pore pressure was decreasing with hydrocarbon production and, respectively, increasing the effective stress. In general, during the production, the

reduction in fluid content or fluid substitution in this case was the horizontal scheme change, and the pore pressure had tendency to get lower. But if the changes were vertical, when the gas came out and the place or the depth where the gas existed before were replaced by oil or water, the pore pressure most probably would be going up.

**Acknowledgements** The authors express their gratitude to Universiti Teknologi Petronas (UTP) for providing laboratory facilities and financial assistance on this study.

## References

1. Bell, D.W., 2002, Velocity Estimation for Pore Pressure Prediction, in Huffman, A. L. and Bowers, G.L., eds, Pressures Regimes in Sedimentary Basin and Their Prediction, AAPG Memoir 76, p. 177–215.
2. Bowers, G. (1995). Pore pressure estimation from velocity data: Accounting for overpressure mechanism besides undercompaction. *SPE Drilling & Completion*, 89–95.
3. Bowers, G. (2002). Detecting high overpressure. *The Leading Edge*, 174–177.
4. G.N Boitnott, et al (2009). Pore Pressure Depletion and Effective Stress Issues in Gulf of Mexico's Lower Tertiary Play. *SPE Annual Technical Conference*. New Orleans.
5. J.E. Streit." Estimating Fluid Pressures that Can Induce Reservoir Failure during Hydrocarbon Depletion", Proceedings of SPE/ISRM Rock Mechanics Conference ISRM, 10/2002.
6. Madon, M. (2006). Overpressure history of the Malay Basin, Offshore Peninsular Malaysia. *Petroleum Geology Conference & Exhibition* (pp. 135–144). Kuala Lumpur: Geological Society of Malaysia.
7. Madon, M., Abolins, P., Hoesni, M., & Ahmad, M. (1999). The petroleum Geology and Resources of Malaysia. In PETRONAS, *Malay Basin* (pp. 173–185). Kuala Lumpur: Petroliam Nasional Berhad (PETRONAS).
8. Sayers, C.M., 2006, An Introduction to Velocity-Based Pore Pressure Estimation, The Leading Edge, December 2006, p. 1496–1500.
9. Tingay, M., Hillis, R., Swarbrick, R., Morley, C., & Damit, R. (2011). Origin of Overpressure and Pore Pressure Prediction in the Baram Delata Province, Brunei. *AAPG Memoir*, 65–85.
10. Tingay, M., Hillis, R., Swardick, R., Morley, C., & Damit, A. R. (2009, January). Origin of overpressure and pore-pressure prediction in the Baram province, Brunei. *AAPG Bulletin*, pp. 51–74.
11. Wahab, M., Asraff, A., Ismail, J., & Ibrahim, A. (2013). Significant Hydrocarbon Accumulation in Deep Overpressured Play of Baram Delta, Malaysia. *EAGE Conference & Exhibition*. London, UK.
12. Zhang, J. "Pore pressure prediction from well logs: Methods, modifications, and new approaches", *Earth-Science Reviews*, 201109.
13. Hottman, C. E., & Johnson, R. K. (1965). Estimation of Formation Pressures from Log-Derived Shale Properties (\*).
14. Gardner, G. H. F., Gardner, L. W., & Gregory, A. R. (1974). Formation velocity and density-the diagnostic basics for stratigraphic traps. *Geophysics*, 39(6), 770–780.

# Taking Seismic Acquisition Artifacts Beyond Mitigation

Mohamed Mahgoub, Deva Ghosh, Abdul Halim Abdullatif and Fernando Neves

**Abstract** Seismic acquisition footprint is an irritating noise type on the seismic data. This footprint noise is the dominated noise on the seismic stacked data; however, the common practice nowadays is removing them by filtering using 3D FKxKy frequency slice notch filter in pre-stack stage on OVT (offset vector tile) minimal data set in the orthogonal acquisition geometry in particular. Any acquisition footprint noise remnants will definitely hinder the accurate fault and fractures lineament seismic interpretation, since any discontinuities in the seismic might be treated as fractures or faults. Elimination, attenuation, or mitigation of this noise is some sort of compromise in this noise removal. Taking acquisition footprint beyond mitigation to be fully suppressed by applying alternative cascaded processing approach is the main goal of this study.

**Keywords** Acquisition footprints · 3D FKxKy · OVT · Cascaded · Mitigation

## 1 Introduction

Seismic data have different types of noise, such as seismic source generated noise, surface waves, mud roll or ground roll linear coherent noise, scattered noise, and acquisition geometry spread layout noise, which is well known as seismic

---

M. Mahgoub (✉) · F. Neves  
Abu Dhabi National Oil Company (ADNOC), Abu Dhabi, UAE  
e-mail: mmahgoub@adnoc.ae

F. Neves  
e-mail: fneves@adnoc.ae

D. Ghosh · A.H. Abdullatif  
Department of Geosciences, Universiti Teknologi PETRONAS, Seri Iskandar, Malaysia  
e-mail: drdeva@utp.edu.my

A.H. Abdullatif  
e-mail: abdulhalim.alatiff@utp.edu.my

acquisition footprints. The acquisition footprint is defined as any phase or amplitude anomaly that is closely correlated with the surface acquisition geometry rather than with the subsurface geology [1]. Two main types of noise could be distinguished; the major familiar one is caused by the sparseness in acquisition geometry in which the source/receiver line spacing is too large. The main cause of acquiring sparse geometry surveys is due to economic constraints where dense sampling acquisition geometry has a higher cost. That sparseness gives rise to spatially periodic changes in the seismic data fold, offsets, and azimuth which in turn resulted a spatial periodicity in signal-to-noise-ratio, AVO response, and normal move out errors [1]. The conventional way in seismic processing industry by conducting limited QCing through looking at only time slices or vertical seismic sections is not accurate any longer to verify the footprints filtering outcome. Many other tools such as amplitude maps, time samples in the wave number domain and times slices in seismic coherency attributes could pave the way to proper parametrization of the and could specify at which time window that filter should be applied and stop the filter application downward that window. Three seismic surveys have been selected from Abu Dhabi, UAE: The first case is 3D offshore OBC, the second one is 3D marine towed streamer, and the third one is 3D onshore data set. The legacy seismic data sets of those three cases have had sparse acquisition geometry types. Those surveys have been selected in particular because they have been reprocessed more than one time because of the existence of strong residual footprints.

The tested processing workflow in this study was the definite solution to get rid of those acquisitions artifacts and to end up the endless loop of reprocessing and establishing a post-stack sensible processing workflow for similar sparser legacy seismic surveys.

## 2 Acquisition Footprint Types

The noise due to the sparseness in acquisition geometry does look like a mirror of surface acquisition spread layout that appears as vertical amplitude stripes on the time slice (Fig. 1), while it is short wave length jitters on the vertical seismic sections (inline and cross-line) (Fig. 2a). The second type of footprints could be processing artifacts caused if any residual aliased noise is not fully attenuated and crept into the seismic data, where multi-channel processing such as stacking, DMO, and migration do usually accentuate those types of noises and give rise to footprints steeply dipping cross-hatching noise induced into the seismic stacked data [1] (Fig. 2b).

In one of the cases selected for this study, a strong acquisition gridded pattern was induced by processing through applying erroneous carving with bad overlapping tapering during the gathering of different adjacent OVTs after pre-stack time migration (Fig. 3). In some cases, the footprints are not prominent on either the



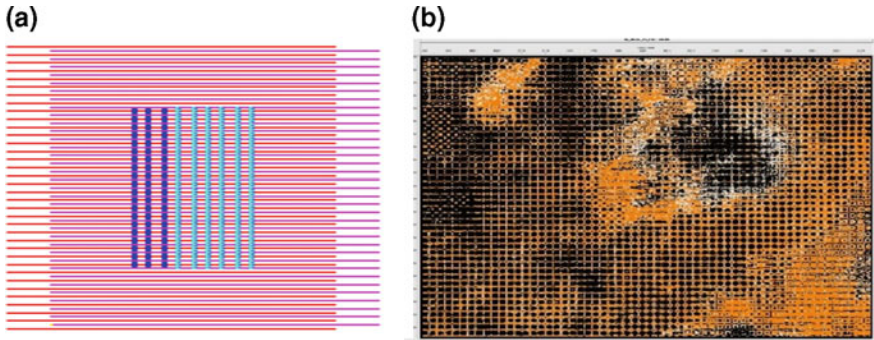


Fig. 1 a Acquisition geometry and b acquisition footprints mirrors

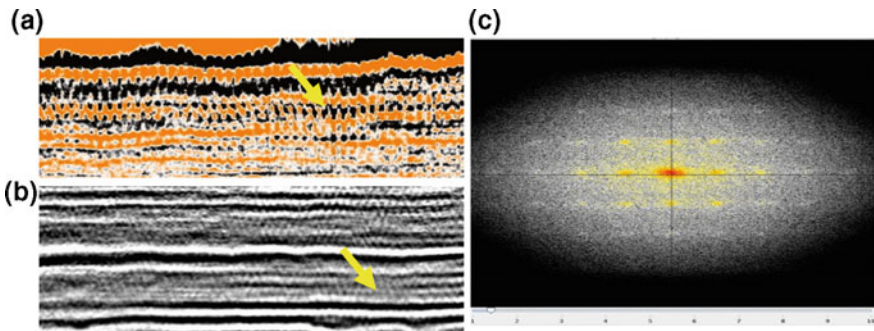


Fig. 2 Vertical seismic section showing a short wavelength acquisition footprints jitters on shallower data, b cross-hatching noise at deeper seismic data, and c periodic spikes in shallow 100-ms time slice in Kx-Ky wave number domain

vertical or the horizontal seismic sections as they are usually being used as routine type of QCing tools while they are pronounced on seismic coherency or curvatures attributes (Fig. 4); therefore, seismic attributes are powerful tools to help, assist, and verify the effectiveness of alternative footprint suppression workflows [2].

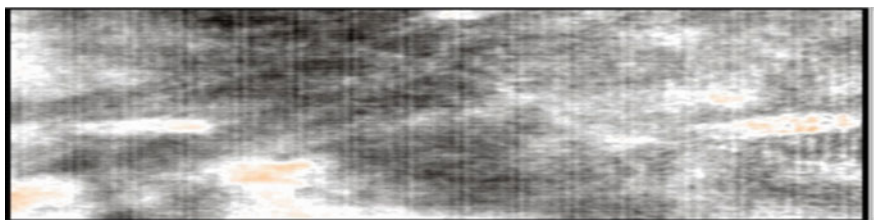
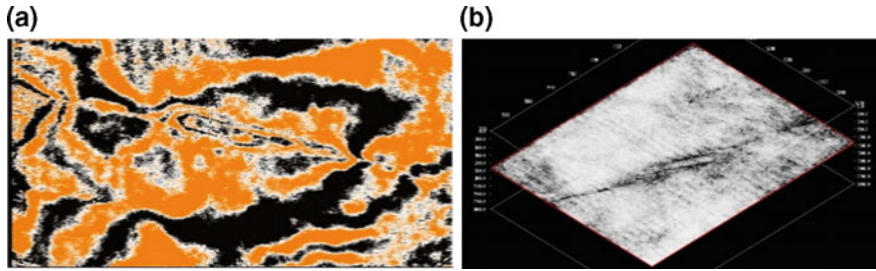


Fig. 3 Carving gridded pattern induced in the seismic data by processing artifacts





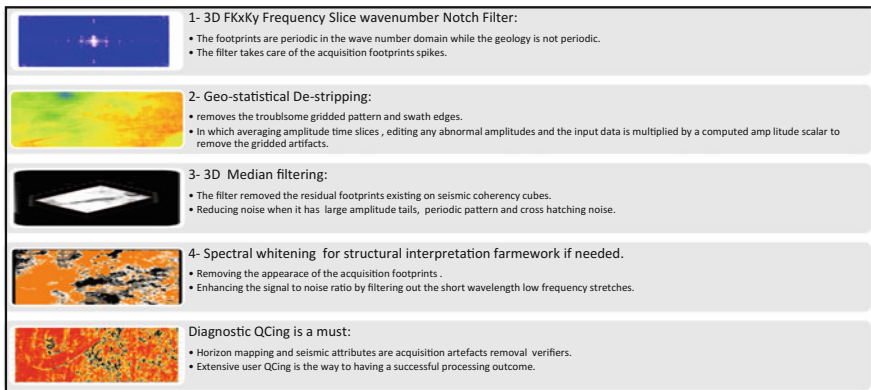
**Fig. 4** **a** Acquisition footprints noises are not so prominent on 1400-ms time slice, **b** while it is pronounced on the corresponding seismic coherency attribute

### 3 Cascaded Reprocessing Workflow

The legacy seismic data of this study because of its sparse acquisition geometry design the single filter approach FKF3D that was not able to fully get rid of the seismic acquisition footprints despite its iterative seismic reprocessing. Extensive optimum quality control methods with reviewing the acquisition spread geometry layout to find out the root cause of footprints derive us to come up with the new cascaded reprocessing workflow (Fig. 5).

#### 3.1 3D Kx-Ky Frequency Slice Wave Number Notch Filter

Since the seismic acquisition footprint noise signature is not stationary in timely manner and it is stronger in the shallower data while it does heal with depth, filtering them out in time domain is eventually impossible. Footprints have spatial

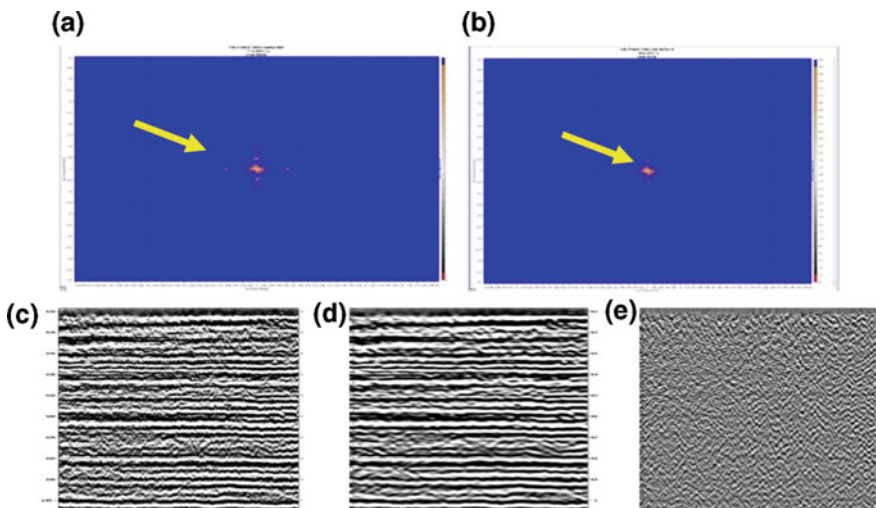


**Fig. 5** Cascaded reprocessing workflow

periodicity in the form of spikes in the wave number domain which can be clearly separated from the signal wave numbers. That was the main reason for the application of the frequency slice wave number notch filtering method on an average Kx-Ky frequency spectrum of the time slice which is called FKF3D method [3]. Nowadays, the 3D FKxKy is a commonplace processing practice of attenuating those footprints noise either pre-stack or post-stack. The fundamental QCing diagnostic plot of the filter is the time slices in the wave number domains (Fig. 6a) on which the footprint periodic spikes will be completely suppressed leaving only the signal with Kx-Ky around the zero value (Fig. 6b). The difference section in this step has shown that the signal of the seismic data has been retained while removing the acquisition footprints noise (Fig. 6e).

### 3.2 Geostatistical De-Stripping

The acquisition footprint filters are basically working when the footprints are spikes in the wave number domains not as the gridded pattern artifacts imposed by processing artifacts in the OBC case study of this paper. Geostatistical methods are becoming widely used in the exploration and reservoir geophysics [4]. Factorial kriging has been extensively applied to seismic data in various noise reduction contexts [5], and modeled factorial kriging is a simply additive model where the spatial variable is modeled by a random function,  $Z(x)$ , segregated as independent factors:



**Fig. 6** Time slice 100 ms in wave number domain; **a** before and **b** after 3D FKF3D in which the periodic spikes (pointed out) have been knocked down significantly. Vertical seismic section; **c** before, **d** after 3D FKF3D application and **e** the difference section is showing the removed noise while there is no signal leak

$$Z(x) = Z1(x) + Z2(x) + Zn(x)$$

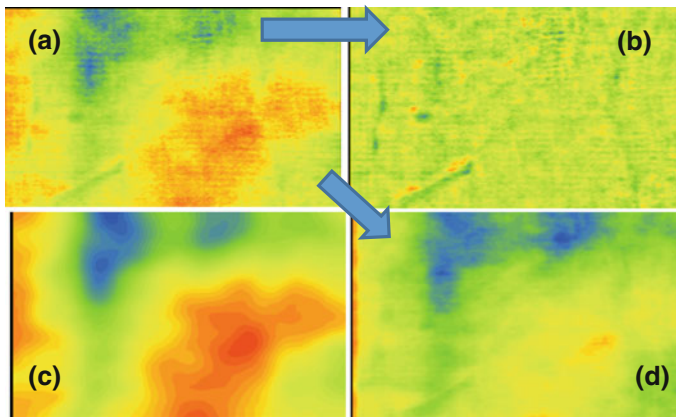
Noise reduction issues can be easily handled by the framework of this model as far as the noise part of a data set can be considered a signal part independent:

$$Z(x) = ZNOISE(x) + ZSIGNAL(x)$$

A factorial kriging, by estimating  $ZSIGNAL(x)$ , allows filtering out the noisy component of a data set. In the same context following this modeled factorial kriging, the geostatistical de-stripping was applied through running a processing patch job scheme. Firstly, by computing average amplitude maps every 100-ms time slice, maps will be edited and the abnormal amplitude will be filtered out and eventually computes a time slice compute scalar to be multiplied by the raw input data. The results show that the gridded pattern processing artifacts have been successfully removed by applying geostatistical de-stripping filter (Fig. 7).

### 3.3 3D Median Filter

It is well known that median filtering is useful for reducing random noise with large amplitude tails and periodic patterns [6], median filters might be used to attenuate coherent wave field [7], and the median filter has the advantage over the mean filter of rejecting outliers and preserving edges [2]. Theoretically, 1D stationary median filtering approach was selected and the median filter is expressed as follows:



**Fig. 7** **a** RMS amplitude map decomposed into **b** high-frequency (structured noise) and **c** low-frequency component (structured geology) **d** RMS amplitude of the final PSR outcome (seismic acquisition artifacts free)

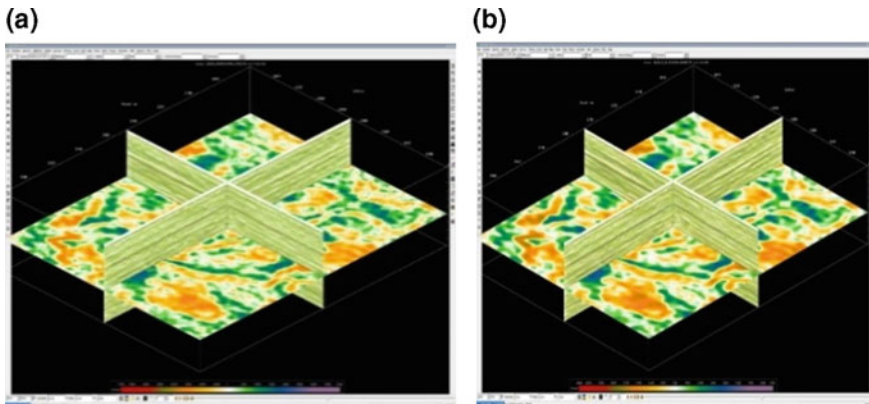
$x_i, j(j = 1, m, , Nx, Ny; j = 1, n, , Nt)$ , where  $i$  is the spatial sample index,  $j$  is the temporal sample,  $Nx$  &  $Ny$  are the numbers of spatial samples in cross-lines and inline directions, and  $Nt$  the numbers of temporal samples. When filter window length,  $C$ , is normally odd [8], for each  $n$ th sample within the  $n$ th time samples and spatial window length  $C$ , the output trace is constructed by taking the median sample between the samples around. Applying the median [ $x_i, j$ ] on all traces achieved the 1D stationary median filtering of the whole seismic cube. In this case study, a 3D temporal and spatial median filtering was tested to remove residual coherent periodic noise. The median filter has definitely filtered out the residual noise as is clearly illustrated in time slice 1300 ms of 3D viewer (Fig. 8).

### 3.4 3D Time-Variant Spectral Whitening

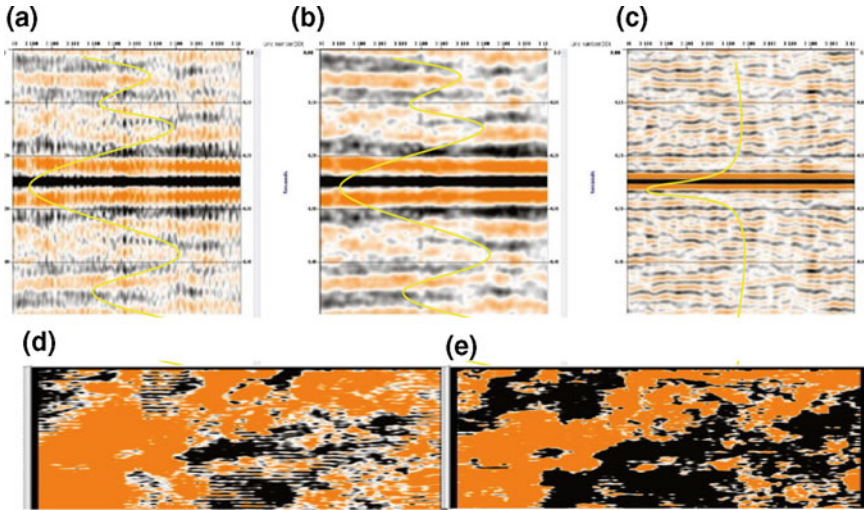
Time-variant spectral whitening involves passing the input data through a narrow band-pass filters and determining the decay rates for every single frequency band, and the amplitude spectrum for the output data has been whitened [9]. The convolution model of the seismic traces is as follows:

$$S(t) = r(t) * w(t) + n(t),$$

where  $s(t)$ : seismic trace,  $r(t)$ : reflectivity function,  $w(t)$ : source wavelet, and  $n(t)$ : noise. The objective of the deconvolution is to remove the wavelet effect from the seismic trace and recover the reflectivity function [9], and the deconvolution operator is depending on the amplitude spectrum;  $\tilde{A}_w^{(w)}$  derived from the



**Fig. 8** 3D viewer (inline, cross-line, and time slice) **a** before and **b** after 3D median filter application



**Fig. 9** Autocorrelation of vertical seismic section **a** raw data, **b** after median filter **c** after spectral whitening, time slice 300 ms **d** before spectral whitening **e** after spectral whitening

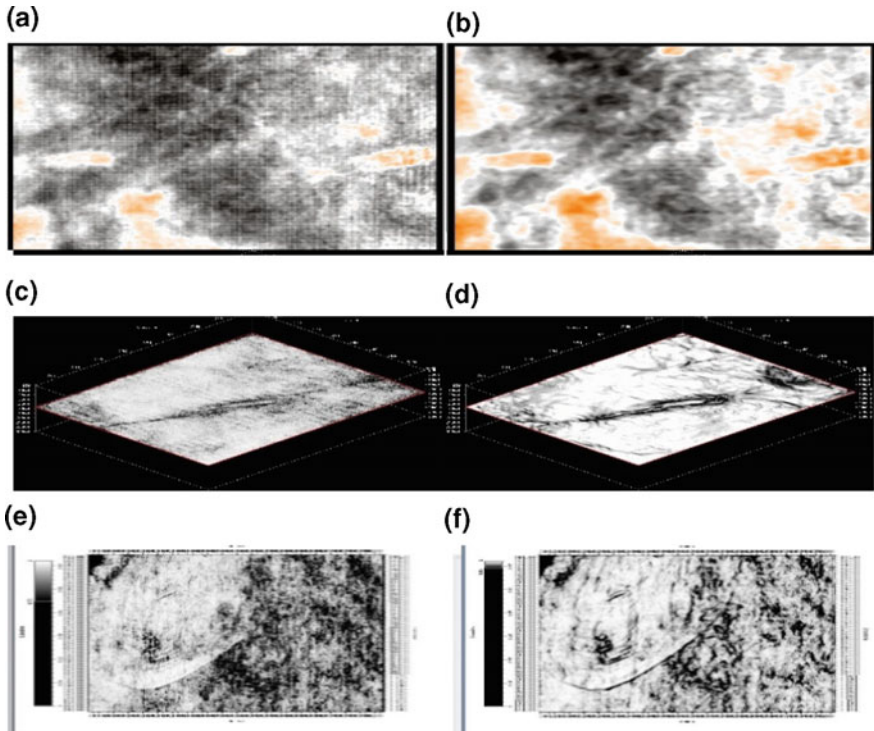
autocorrelation of the seismic trace and the phase spectrum of the source  $\phi_w(w)$  can be expressed as follows:

$$F(w) \cong \frac{e^{-i\phi_w(w)}}{\tilde{A}_w^{(w)}} \tag{1}$$

On the other hand, the spectral whitening in the frequency domain and under the random reflectivity assumption, its operator could be expressed as follows:

$$\lim_{\alpha \rightarrow 0} F(w) = \frac{1}{\tilde{A}_w^{(w)}} \tag{2}$$

From the comparison of the Eqs. (1) and (2), it can be seen that the spectral whitening is similar to the spiking deconvolution; however, it is operating on amplitude spectrum only when the parameter  $\alpha$  is being small. Spectral whitening has compressed the wavelet reducing the ringing side lobes as it is clearly shown in the autocorrelation window (Fig. 9c) and removing the frequency stretching of the acquisition footprint as it is depicted in the shallower 300-ms time slice (Fig. 9e).



**Fig. 10** 3D OBC case; **a** legacy data, **b** after cascaded approach. 3D onshore case; **c** legacy, **d** after cascaded reprocessing approach. 3D towed streamer case; **e** legacy **f** after cascaded approach

## 4 Result and Discussion

The innovative cascaded approach has got rid of the remaining noise of those legacy seismic data definitely and taking the acquisition artifacts beyond mitigation on these three case studies. The most irritating acquisition artifacts noise type that was processing erroneous artifacts has been entirely removed by the cascading processing workflow as it is clearly illustrated in 3D OBC (Fig. 10a, b). On the onshore data case, the cascaded approach has removed the residual footprints revealing the faults definitions clearly (Fig. 10c, d). Moreover, for the 3D towed streamer case, the cascaded seismic reprocessing approach has made uplift in the data quality improvements through unveiling all the faults and fractures details (Fig. 10e, f). The improved seismic data resolution through the application of the cascaded approach workflow has revealed the structure details without any seismic data smearing and it will help seismic interpreters to extract trustable seismic attributes of faults/fractures lineament interpretation.



**Acknowledgements** The authors are grateful to UTP (University Technology of PETRONAS and ADNOC (Abu Dhabi National Oil Company) management for granting permission to publish this paper.

## References

1. Chopra, S., Misra, S., and Marfurt, K.J., Coherence and Curvature attributes on preconditioned seismic data: *The Leading Edge*, 30, no.4, 386–393. (2011)
2. Davogussto, O., and Marfurt, K.J., 2011, Footprint suppressions applied to Legacy Seismic Data Volumes, University of Oklahoma; <http://geology.ou.edu/>(2011).
3. Gulunay, N., Benjamin, N., and Magesan, M., Footprint suppression with wave number notch filtering for various acquisition geometries, 67th EAGE Annual Conference, (2005).
4. Journal, A., Five lessons in geostatistics, American Geophysical Union (1988).
5. Magneron C., et al, Geovariances web site: Noise reduction by M- Factorial kriging *Geovariances\_Abstract\_IAMG\_09*.pd, (2015).
6. Robert R. Stewart, MEDIAN FILTERING: REVIEW AND A NEW F/K ANALOUGE DESIGN, *Journal of the Canadian Society of Exploration Geophysicists*, VOL 21, and NO.1. P. 54–63. (DEC. 1985).
7. Duncan, G., and G. Beresford, Some analyses of 2-D median f-k filters: *Geophysics*, 60, 1157–1168.9, (1995).
8. Liu, Y., et al, A 1-D time-varying median filter for seismic random, spike-like noise elimination, *Geophysics*, 74, V17–V24 (2009).
9. M.W. Lee, Spectral Whitening in the Frequency Domain, Open-File Report 86–108, Department of the Interior, U.S. Geological survey (1986).

# An Innovative Low-Cost Approach for Discontinuity Roughness Quantification of Sandstone at Bukit Merah, Perak, Malaysia

Salimun Norsyafiqah and Abdul Rafek Ghani

**Abstract** An alternative low-cost approach in quantifying the discontinuity roughness of the Semanggol Formation Sandstone at Bukit Merah, Perak, is presented here. In engineering geology, the discontinuity roughness is very important as discontinuities influence the rock mass stability for cut rock slopes, tunnel, and underground excavation. However, limited geomechanical studies have been done on sedimentary rocks, e.g., sandstones in Peninsular Malaysia. Here, the tilt test method is applied in evaluating the correlation between joint roughness coefficient (JRC) and peak friction angle,  $\phi_{\text{peak}}$ , of discontinuities of the Semanggol Formation Sandstone. The tilt test experiment successfully generated a polynomial approximation  $\phi_{\text{peak}} = 0.0424 \text{ JRC}^2 + 1.1286 \text{ JRC} + 29.179$  with coefficient of determination  $R^2 = 0.97$  for the correlation of JRC values with the friction angle of the sandstone discontinuity surfaces. This polynomial approximation provides a low-cost alternative for peak friction angle,  $\phi_{\text{peak}}$ , determination of sandstone.

**Keywords** Joint roughness coefficient • Friction angle • Tilt test

## 1 Introduction

Rock materials have physical and mechanical characteristics. Physically, the color of rocks, textures, and grain sizes can be seen. Meanwhile, the mechanical characteristics are described by the strength of the rock material as well as the roughness and behavior of fractures. The stability of rock masses is influenced significantly by surface roughness of geological discontinuities [3].

---

S. Norsyafiqah (✉) · A.R. Ghani  
Department of Geosciences, Faculty of Geosciences and Petroleum Engineering,  
Universiti Teknologi PETRONAS, Bandar Seri Iskandar, 32610 Tronoh,  
Perak Darul Ridzuan, Malaysia  
e-mail: norsyafiqahsalimun@gmail.com

A.R. Ghani  
e-mail: ghani.rafek@utp.edu.my



## 2 Literature Review

Previous studies published by Ghani et al. [3, 4] use the tilt test approach that mainly focuses on igneous and metamorphic rocks, i.e., Malaysian granites and schists, for either fresh or slight weathered samples. Barton and Choubey [1] defined two main parameters to predict the discontinuity shear strength accurately: joint wall roughness coefficient (JRC) and joint wall compressive strength (JCS). The JCS or uniaxial compressive strength can be measured using rock mechanics tests, while the JRC is measured by using Barton comb profilometer (see Fig. 1), where typical roughness profile for JRC range (see Fig. 2) can be obtained directly from visual estimation [7].

Fecker and Rengers [2] estimate large-scale discontinuity surface roughness using a disk clinometer and geological compass. Previously, Patton [6] used direct shear testing to determine the basic friction angle ( $\phi_b$ ) and dilation angle ( $i$ ) of sawtooth samples. Patton established that the first-order roughness of the samples is the dilation angle itself. The basic friction angle is referred as the angle of friction of smooth planar sliding surfaces. Besides Patton, Goh et al. [3, 6] also used direct shear test using artificially sawn granite discontinuity plane surfaces to determine  $\phi_b$ .

Moreover, Barton and Choubey [1] recommended a method to estimate the peak friction angle,  $\phi_{peak}$ , from joint roughness coefficient (JRC), joint wall compressive strength, the basic friction angle, and normal stress. However, all these mentioned methods involve tedious sample preparation, complex testing procedures, and expensive laboratory testing apparatus. An alternative presented in this study is simpler and low-cost approach using the comb profiler to determine the JRC and tilt test for  $\phi_{peak}$  determination for the corresponding JRC. The polynomial approximation generated can then be applied for the direct determination of the  $\phi_{peak}$  from JRC measurement.

Several researchers have quantified the effects of roughness, filling materials, joint alteration on strength of discontinuity, e.g., Ghani and Goh [3] where the JRC

**Fig. 1** Barton comb profiler



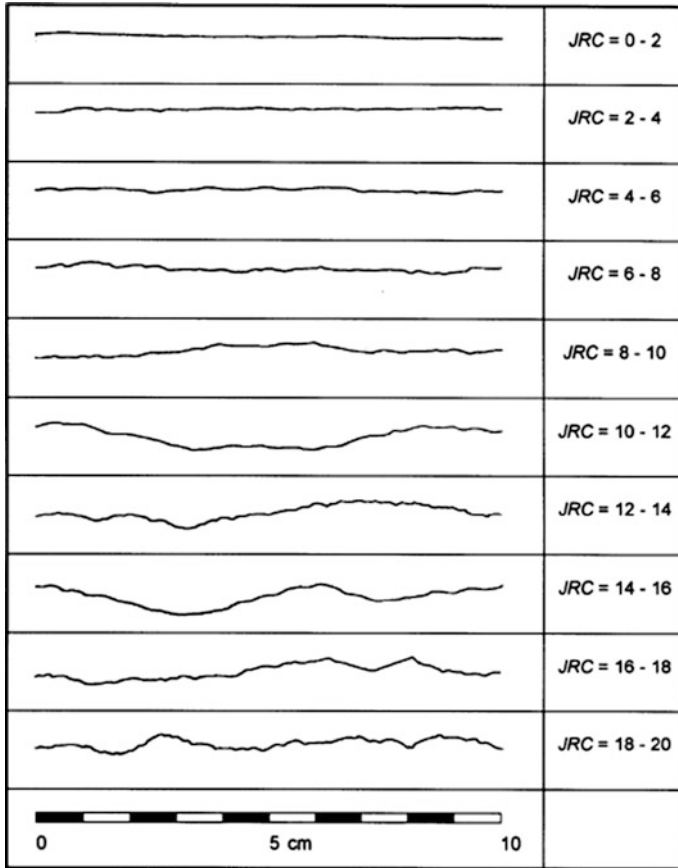


Fig. 2 Typical roughness profile

is correlated with the peak friction angle of discontinuities of Malaysian schist. Recently, Hoek [5] also recommended this method since large number of tests can be conducted and hence improved the results' interpretation and reliability.

### 3 Material and Methodology

The tilt test has been employed to determine the angle of friction of natural discontinuities of slightly weathered sandstone from the Bukit Merah outcrops. Sandstone blocks were collected from the outcrop with different JRC value as defined by Barton and Choubey [1]. The rock samples were then separated along the natural discontinuities, into upper and lower block. The comb profiler (Fig. 1) is the main tool used to measure the surface roughness of the samples. The

**Fig. 3** Tilt test apparatus

measurement as recommended by Barton and Choubey [1] was repeated on four different directions on plane surfaces.

Next, the joint roughness coefficient values are determined using the typical roughness profile as shown in Fig. 2. To measure the peak friction angle,  $\phi_{\text{peak}}$ , of these discontinuity plane surfaces, samples were then tested on a self-fabricated tilt testing apparatus. The pair of sandstone blocks were positioned in the apparatus as shown in Fig. 3. The inclination angle is obtained when the upper blocks slide as the apparatus slowly inclined from horizontal position is the peak value.

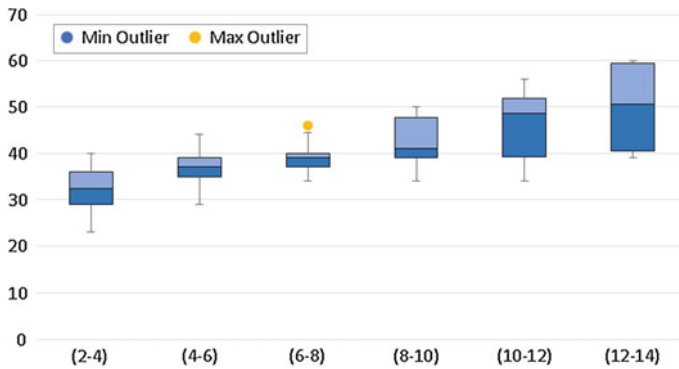
## 4 Results and Discussion

A total of 140 reading were recorded during the testing and are tabulated in Table 1. From the data tabulated, a histogram is constructed to analyze the relationship of JRC values with peak friction angles. For JRC value (2–4), the peak friction angle is  $31^{\circ}$ – $33^{\circ}$ . Meanwhile, the angle for JRC (4–6) and (6–8) is equivalent which is  $37^{\circ}$ – $39^{\circ}$ . JRC (8–10) until (12–14) shows increasing range of angle:  $40^{\circ}$ – $42^{\circ}$ ,  $49^{\circ}$ – $51^{\circ}$ , and  $58^{\circ}$ – $60^{\circ}$ , respectively. The distribution of the angle measured is not uniform for each class of JRC.

The tilt test results were analyzed using the statistical software package SPSS at a 95% confidence level. Figure 4 shows the box plots of tilt tests corresponding to their respective JRC values. A polynomial approximation was determined in equation given by  $\phi_{\text{peak}} = 0.0424 \text{ JRC}^2 + 1.1286 \text{ JRC} + 29.179$  with coefficient of determination  $R^2 = 0.97$  as shown in Fig. 5. The JRC value was taken from the midpoint of the respective JRC range. Thus, using this approximation, the peak friction angle,  $\phi_{\text{peak}}$ , of the discontinuity surface can be estimated without conducting tilt test. Moreover, the basic friction angle for sandstone can be obtained which is the intercept of the polynomial line with a value  $29.2^{\circ}$ . This basic friction angle for this sandstone is lower compared to basic friction angle of metamorphic and igneous rocks [3].

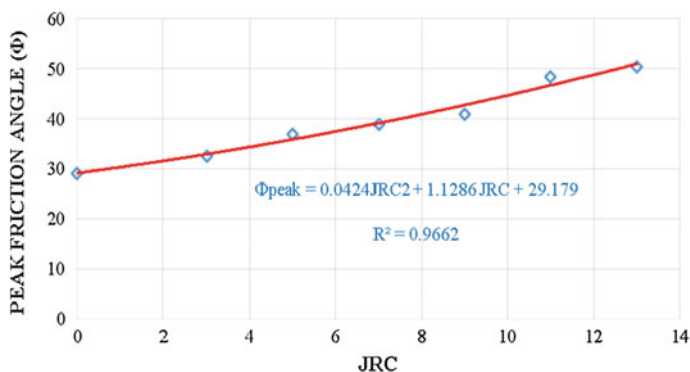
**Table 1** JRC value and angle measured in tilt test

No.	JRC	Sample	Angle	No. of reading	Average
1	(2-4)	J5	36, 40, 38, 36, 39, 32, 32, 34, 36, 35	20	31-33
		J7	29, 27, 25, 29, 23, 39, 38, 39, 36, 37		
2	(4-6)	J2	40, 37, 43, 42, 36, 40, 44, 40, 40, 40	30	37-39
		J5	36, 40, 38, 36, 39, 32, 32, 34, 36, 35		
		J7	38, 39, 39, 39, 39, 33, 29, 33, 31, 31		
3	(6-8)	J2	36, 38, 39, 37, 39, 46, 40, 44, 40, 41	20	37-39
		J3	37, 38, 42, 40, 40, 36, 34, 39, 37, 36		
4	(8-10)	J1	36, 34, 36, 34, 35, 42, 50, 56, 48, 44	30	40-42
		J3	40, 48, 43, 45, 49, 47, 48, 50, 48, 50		
		J4	39, 36, 34, 38, 39, 44, 40, 42, 48, 40		
5	(10-12)	J1	36, 34, 36, 34, 35, 42, 50, 56, 48, 44	30	49-51
		J4	54, 55, 48, 50, 54, 50, 50, 51, 50, 53		
		J6	39, 40, 42, 39, 39, 49, 55, 52, 55, 48		
6	(12-14)	J6	42, 43, 39, 40, 39, 58, 60, 60, 58, 60	10	58-60



**Fig. 4** Box plot of tilt test results for respective JRC

Table 2 presents a comparison of the calculated values based on the equation with mean values from actual tilt test results. Clearly, the percentage difference obtained is less than 5.0%. Therefore, the equation offers tolerable and valid means to estimate the peak friction angle of the same lithology of sedimentary rock, e.g., sandstone.



**Fig. 5** A polynomial approximations of peak friction angle versus JRC for slightly weathered sandstone

**Table 2** Differences of calculated and measured peak friction angles with respective JRC values

Method/JRC	3	5	7	9	11	13
Tilt test	32.5	37	39	41	48.5	50.5
$\phi_{\text{peak}} = 0.0424\text{JRC}^2 + 1.1286\text{JRC} + 29.179$	32.95	35.88	39.16	42.78	46.72	51.02
Difference (%)	-1.36	3.07	-0.40	-4.23	3.73	-1.02

## 5 Conclusion

This study successfully established the equation  $\phi_{\text{peak}} = 0.0424 \text{JRC}^2 + 1.1286 \text{JRC} + 29.179$  with the coefficient of determination  $R^2 = 0.97$ . This equation can be employed for estimating the peak friction angle of discontinuities of sandstones from JRC measurements obtained at the field. This will help discontinuity surface roughness quantification without the need of sampling and testing at early stage of engineering geological investigations.

## References

1. Barton, N.R. and Choubey, V. (1977). The shear strength of rock joints in theory and practice. *Rock Mechanics*. 10 (1–2), p. 1–54.
2. Fecker, E. & Rengers N. (1971). Measurement of large scale roughness of rock planes by means of profilograph and geological compass. *Rock Fracture*, Proc. of Int. Symp. Rock Mech Nancy, 1, p. 18.
3. Ghani, A.R & Goh T.L (2011). Correlation of Joint Roughness Coefficient (JRC) and Peak Friction Angles of Discontinuities of Malaysian Schists. *Earth Science Research* 1(1), p. 57–63.

4. Ghani, A.R., Goh T.L., & Hariri M.A (2011). Field and Laboratory-based Approach for the Determination of Friction Angle of Geological Discontinuities of Malaysian Granites. *ASEAN J. Sci. Technol. Dev.* 28 (2), p. 151–155.
5. Hoek, E. (2007). Practical rock engineering. Course notes, Hoek's Corner. <http://www.rocscience.com>.
6. Patton, F.D. (1966). Multiple modes of shear failure in rock. Proc. *1st International Congress of Rock Mechanics, Lisbon*, 1, p. 509–513.
7. Singh B. & Goel R.K., (1999). *Rock mass classification: A practical approach in civil engineering*. Elsevier publisher, Amsterdam, p. 267.

# Bilinear Extrapolation for Geocellular Reservoir Connectivity and Flow Simulation

Numair Ahmed Siddiqui, Abdul Hadi A. Rahman  
and Chow Weng Sum

**Abstract** Reservoir connectivity is one of the main subsurface uncertainties in the assessment and improvement of many oil and gas fields. The main objective of this paper is to analyze the static and dynamic connectivity of the selected shallow-marine sandstone facies through construction of gridded-based units for flow behavior/patterns. Prior to the generation of the sandstone facies connectivity and flow simulation, outcrop log data are input into the modeling software. The exposer used for the facies connectivity and flow simulation was ranging from 1 to 500 cm. The measurements of permeability values were taken on each of the grid, which were bilinear extrapolated, to populate the surface with permeability variation. Detailed analysis of the sedimentology and interpretation of three major sandstone facies is used as a framework to build the geocellular facies connectivity and flow simulation. The sandstone facies of HCSS shows more uniform and have linear connectivity, fallow by sub-layer gridding. In case of HBCBS, horizontal sweep is more effective as compared to vertical, because of thin mudstone deposited at the base of each layer boundaries which resist to sweep vertically. Whereas TCBS, WFBS, and BS show the distribution of different qualities of sandstones and bioturbation in the grid block model, burrows filled with mud which acts as impermeable pathways within moderate to low-quality sandstone.

**Keywords** Bilinear extrapolation · Permeability · Sandstone facies · Connectivity · Flow simulation

---

N.A. Siddiqui (✉) · A.H.A. Rahman · C.W. Sum  
Department of Geosciences, Universiti Teknologi PETRONAS,  
32610 Seri Iskandar, Perak Darul Ridzuan, Malaysia  
e-mail: numair.siddiqui@utp.edu.my

© Springer Nature Singapore Pte Ltd. 2017  
M. Awang et al. (eds.), *ICIPEG 2016*,  
DOI 10.1007/978-981-10-3650-7\_36

421

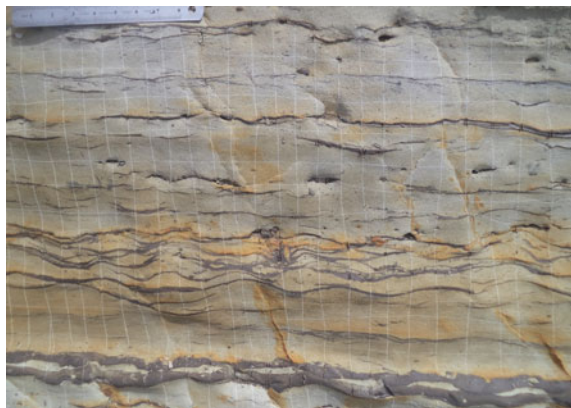
## 1 Introduction

Characterization and modeling of siliciclastic shallow-marine sandstone reservoirs are challenging because of the various scales of heterogeneity that exist between and within shallow-marine deposits [1–5]. Outcrop analogs are more commonly used to improve the understanding of the geological system that has controlled production and are used as a quality check on dynamic models which reveal variance in reservoir flow behavior [6, 7]. Sedimentary rocks usually have complex internal architecture caused by genetic depositional processes and alteration during burial and diagenesis [8–13]. Where heterogeneities are complex and occur at multiple scales, it is difficult to discern a priori which features exert the greatest influence on reservoir flow behavior or to define averaging rules for flow properties [12]. Flow simulations of high-resolution outcrop data quantify effects and interactions of different types and scales of heterogeneity [14]. A variety of both commercial and freely available software can be used to visualize the virtual outcrop. Visual inspection of the data allows improved understanding of bedforms and bedform geometries; the correlation of key surfaces (depending upon the resolution) improved the understanding of facies geometries and transitions. In addition to the qualitative visual inspection, a key utility of the virtual outcrop is the ability to extract quantitative spatial data in either a manual or an automated fashion [15]. This study focuses on reservoir sandstone facies connectivity and flow simulation in some siliciclastic sandstone facies by bilinear extrapolation of permeability.

## 2 Materials and Methods

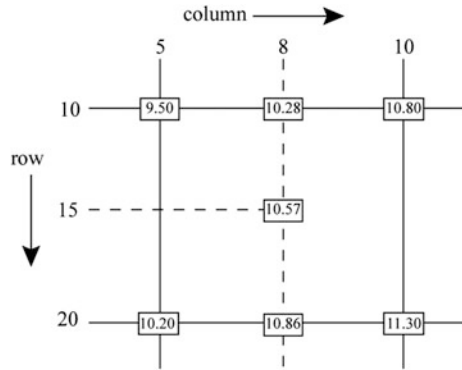
Measurements in different sandstone facies at each of the outcrops were taken on several rectangular regular grids on outcrop facies wall in dry conditions (Fig. 1). Mostly all irregularities and weathered or loose material are removed prior to

**Fig. 1** Example of outcrop facies grid marking for air permeability measurements for the facies flow modeling





**Fig. 2** Example of bilinear interpolation for grid population of permeability values in flow modeling



constructing the grids. The measurement spacing was adjusted to the thickness of lamina, so that the vertical and horizontal spacing is between 2 and 5 cm, and total grid dimension is between 500 cm and 1 m. A total of approximately 100–400 air permeability measurements are made (depending on the surface exposure, weathering, and accessibility of surface) on each sandstone facies and outcrop with different orientation. All permeability data are analyzed and gridded into Petro Mod<sup>®</sup> 2D builder, which bilinear interpolated the value to entire grid blocks. For example (Fig. 2), the intensity value at the pixel is computed to be at row 15, column 8 can be calculated by first linearly interpolating between the values at columns 5 and 10 on each of the rows 10 and 20, giving:

$$I(10, 8) = \frac{10 - 8}{10 - 5} * 9.50 + \frac{8 - 5}{10 - 5} * 10.80 = 10.28$$

$$I(20, 8) = \frac{10 - 8}{10 - 5} * 10.20 + \frac{8 - 5}{10 - 5} * 11.30 = 10.86$$

and then interpolating linearly between these values, giving:

$$I(15, 8) = \frac{20 - 15}{20 - 10} * 10.28 + \frac{15 - 10}{20 - 10} * 10.86 = 10.57$$

### 3 Results and Discussion

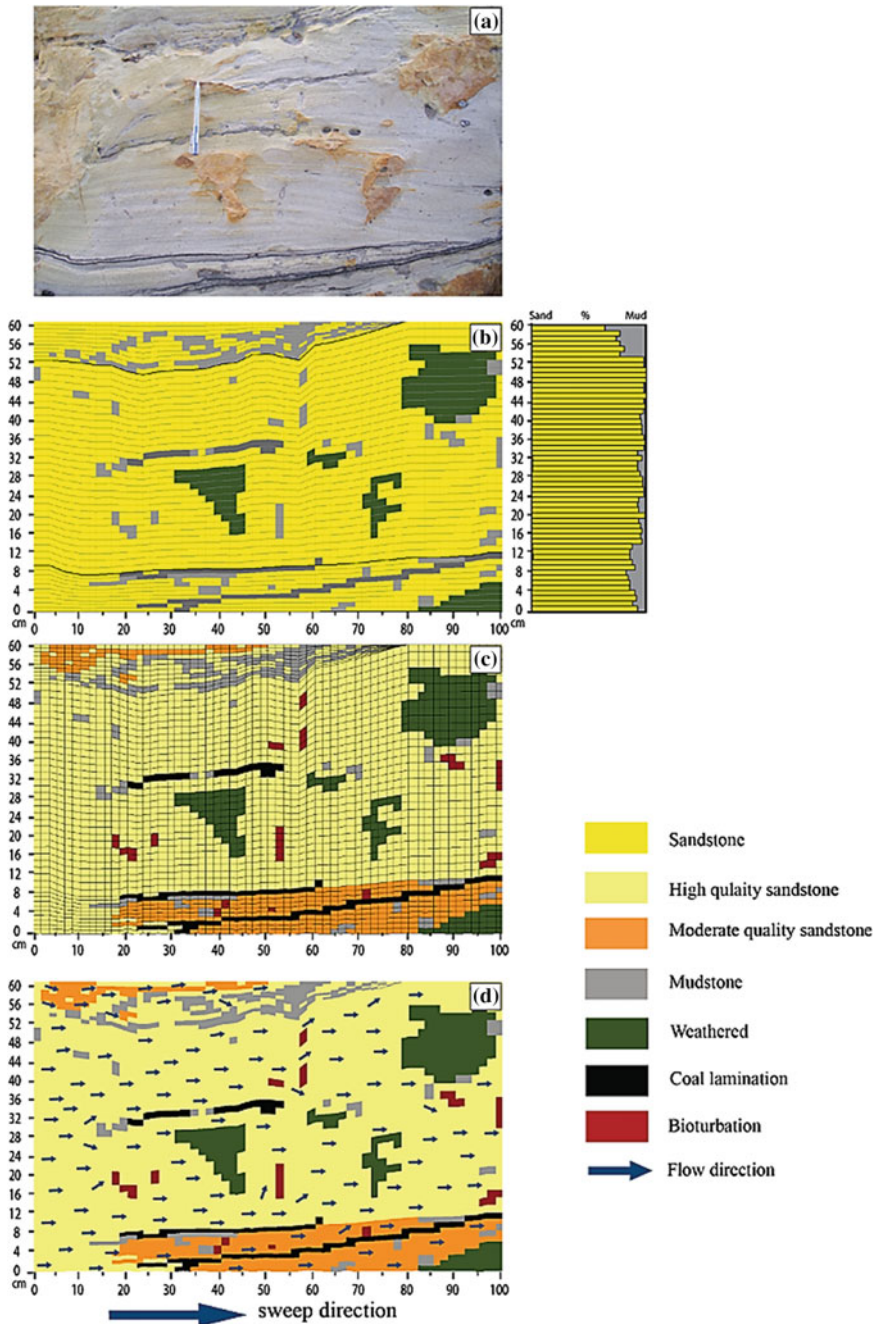
The variation in sandstone quality was marked with high-quality sandstone (HQS), moderate-quality sandstone (MQS), and low-quality sandstone (LQS) within the permeability ranges. Detailed analysis of the sedimentology and interpretation of three major sandstone facies is used as a framework to build the geocellular facies connectivity and flow model.

#### 3.1 *Hummocky Cross-Stratified Sandstone (HCSS)*

This facies (HCSS) represents the most laterally extensive and high-quality sandstone reservoir in terms of porosity and permeability. The exposer use for facies connectivity and flow model is clean sandstone with coal lamination of 100 cm 60 cm (Fig. 3a, b). The first-stage model is the distribution and connectivity of sandstone and mudstone within the boundaries marked in each grid in yellow (sandstone) and gray (mudstone), whereas the weathered surface is marked by green (Fig. 3b). It has been absorbed that percentage of sand in each sub-layer grid block is almost more than 70% in all HCSS facies. The second stage of connectivity modeling is the population of permeability limits for high-quality sandstone (HQS), moderate-quality sandstone (MQS) and low-quality sandstone (LQS) (Fig. 3c). It has been absorbed that the top and bottom sandstone is interfinger with HQS and MQS, whereas the middle section is of HQS mostly. The grids were also marked with bioturbation and coal laminate sandstone which acts as a flow baffles, which is not the severe case in HCSS facies. By simulating the flow through this type of sandstone at centimeter scale (in this case water), the sweep is uniform with less dispersion in HQS and MQS, but rock heterogeneities in terms of mud and coal lamination effect the flow path patterns which allow to move fluid through down-dip or up-dip sub-layers (Fig. 3d). Overall in case of HCSS, the flow is uniform and liner, followed by sub-layer gridding.

#### 3.2 *Herringbone Cross-Bedded Sandstone (HBCBS)*

This type of sandstone facies is among the high- to moderate-quality reservoir sandstone. This facies is well marked in Nyalau Formation, Outcrop 1. The exposer use for facies connectivity and flow model is bidirectional stratification, due to tidal

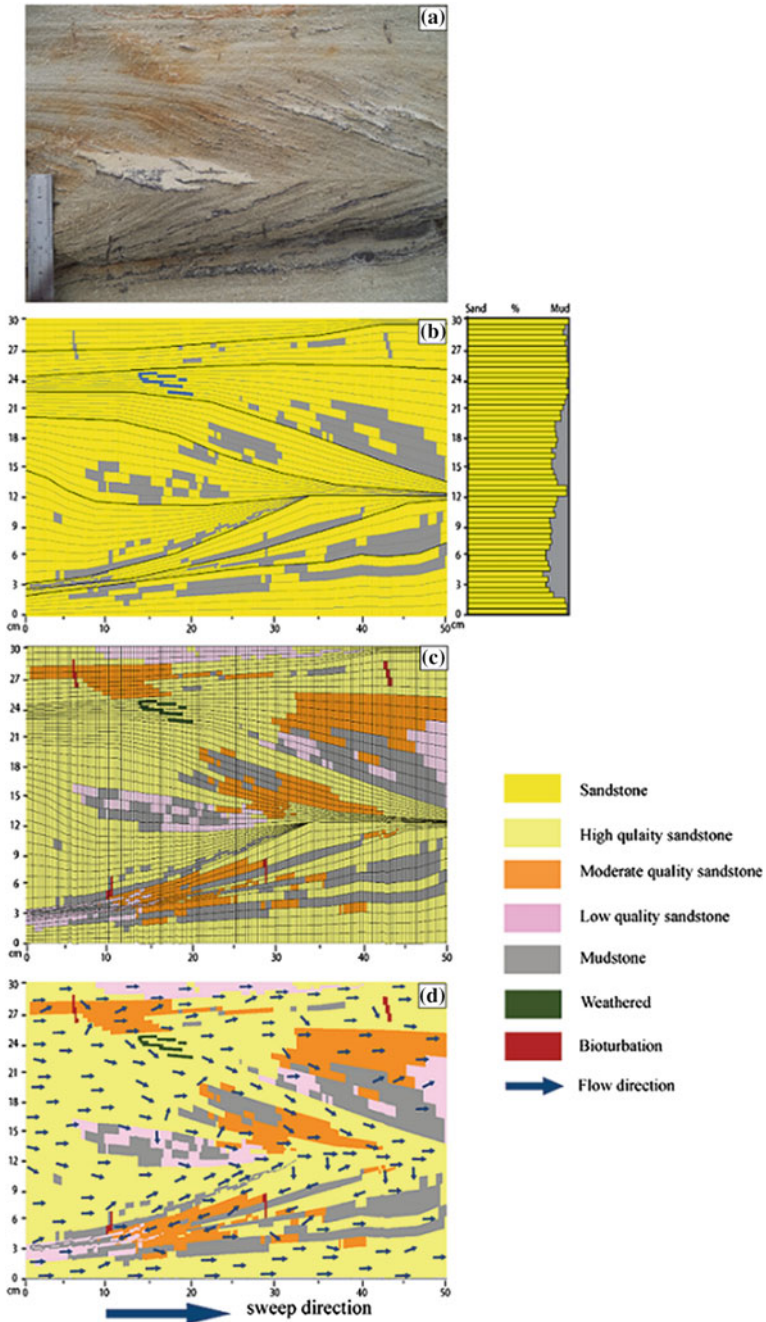


**Fig. 3** An example of outcrop sandstone facies of hummocky cross-stratified sandstone (HCSS). **a** Photomosaic of HCSS facies used for mapping of connectivity and heterogeneity. **b** Distribution of sandstone and mudstone with percentages in each layer and sub-layer grids. **c** Distribution of different qualities of sandstones (HQS, MQS, and LQS) and coal lamination with different internal heterogeneity and permeability distribution. **d** Connectivity and flow heterogeneity with the effect of different lithologies and flow baffles

influence with mud lamination and of 50 cm × 30 cm (Fig. 4a, b). The first-stage model shows the marked layers with bedding which connected laterally either down-dip or up-dip, depending upon the stratification. Each layer show sub-layers with gridding to mark the distribution of sandstone and mudstone lithology. The mudstone is deposited at the bottom of the sub-layers which act baffle in later case for flow model (Fig. 4b). The model shows that the percentage of sand is more than 70% in most cases. After extrapolating the permeability in each grid, it has been seen that the HQS is abundant in distribution, whereas MQS and LQS is distributed mostly down-dip to the stratification (Fig. 4c). The sweep and flow behavior in this case is influenced by heterogeneities in sandstone quality and some bioturbation. At the thickness of 24–30 cm, the water sweeps linearly parallel to the gridding surface from HQS to MQS and LQS. The deflection occurs at bioturbated zonation gridded in red color. In the middle layers (8–23 cm), the sweep direction is moved down-dip to the bedding plain and mostly follows the HQS which drifts back to other bedding plane (Fig. 4d) because of the mudstone and LQS (very fine grained) immediately beneath the HQS, which served as baffles to fluid flow, causing fluids to focus and migrate laterally along the good-quality sandstone. In case of vertical and horizontal movement of fluid, it has been observed that horizontal sweep is more effective as compared to vertical, because of thin mudstone deposited at the base of each layer boundaries which resist to sweep vertically.

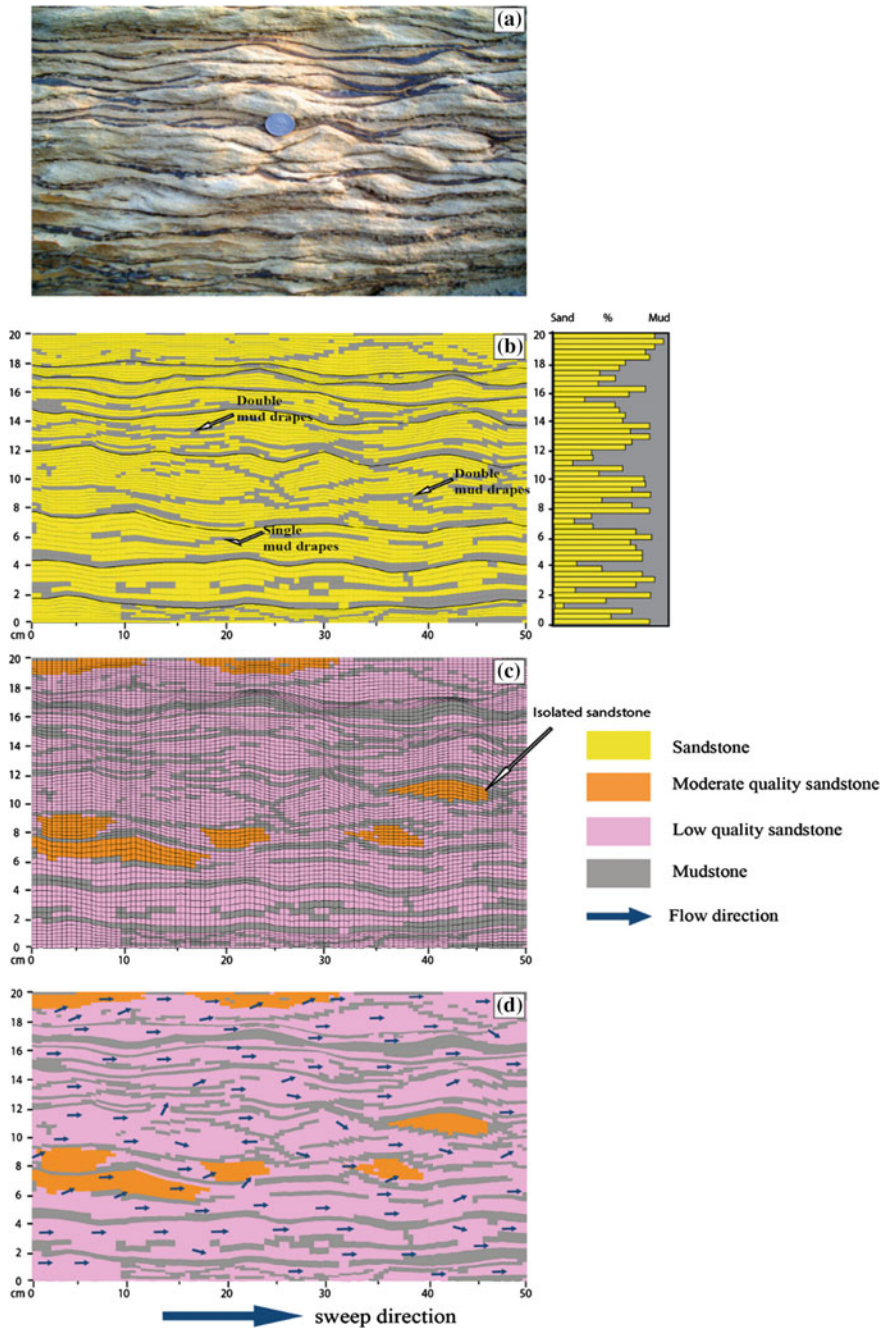
### 3.3 *Wavy- to Flaser-Bedded Sandstone (WFBS)*

The facies grid base model of WFBS allows qualitative analysis of the architecture and connectivity of the sandstone and mudstone layers. The exposer use for this type of facies is either of discontinuous sandstone–mudstone sections or of continuous, which reveals large variations in lateral continuity and vertical connectivity of the lithologies (Fig. 5a). Two conditional scenarios can be possible: either the drapes are commonly bifurcated and connect vertically forming double-mud drapes (Fig. 5b) or they can be continued as a single drape. The percentage of sand–mud randomly distributes, i.e., 50% sand and 50% mud, depending upon the lithological contrast. In terms of sandstone quality and permeability variations, the sandstone is of mostly LQS with some isolated MQS (Fig. 5c). While performing the flow sweep, it has been observed that the vertical flow performance is almost zero due to the discontinuity in layer caking whereas the horizontal sweep is linear to the bedding surface, which only affected by double-mud drapes or bioturbation (Fig. 5d). This heterogeneity can be visualized by individual sandstone and mudstone layers in exposed section that how lateral sandstone and mudstone layers' continuity/connectivity varies with the fraction of sandstone (net-to-gross).



**Fig. 4** An example of herringbone cross-bedded sandstone (HBCBS). **a** Photomosaic of HBCBS facies used for mapping of connectivity and heterogeneity. **b** Distribution of sandstone and mudstone with percentages in each layer and sub-layer grids with bedding which connected laterally either down-dip or up-dip, depending upon the stratification. **c** Distribution of different qualities of sandstones (HQS, MQS, and LQS) and with internal connectivity and heterogeneity. **d** Connectivity and flow heterogeneity with the effect of different lithologies and bedding





**Fig. 5** An example of wavy- to flaser-bedded sandstone (WFBS) facies. **a** Photomosaic of WFBS facies use for mapping. **b** Drapes a commonly bifurcated; they connect vertically forming double-mud drapes with percentages of sand–mud in each layer and sub-layer grids. **c** Distribution of different qualities of sandstones with variations in lateral continuity and vertical connectivity, sandstone is of mostly LQS with some isolated MQS. **d** Connectivity and flow heterogeneity, with zero vertical flow performance and some unswept isolated sandstone

## 4 Conclusion

HCSS shows more uniform and linear connectivity, followed by sub-layer gridding. In case of HBCBS, horizontal sweep is more effective as compared to vertical, because of thin mudstone deposited at the base of each layer boundaries which resist to sweep vertically. Whereas TCBS, WFBS, and BS shows distribution of different qualities of sandstones and bioturbation in the grid block model, burrows filled with mud which acts as impermeable pathways within moderate- to low-quality sandstone. Finally, the flow models can be constructed and analyzed by response surface methods to synthesize the results, which is simpler and cheaper than fine-grid simulations and is more reasonable than using the same pseudo-function for different scenarios.

**Acknowledgements** The authors gratefully acknowledge Universiti Teknologi PETRONAS and PETRONAS Sdn. Berhad for their financial support and funding for this research activity. However, the technical contents and ideas presented in this paper are solely the author's interpretations.

## References

1. Abd Rahman, A. H., Menier, D., and Mansor, M. Y., 2014, Sequence stratigraphic modelling and reservoir architecture of the shallow marine successions of Baram field, West Baram Delta, offshore Sarawak, East Malaysia: *Marine and Petroleum Geology*.
2. Ainsworth, R. B., Flint, S. S., and Howell, J. A., 2008, Predicting coastal depositional style: influence of basin morphology and accommodation to sediment supply ratio within a sequence stratigraphic framework: Recent advances in models of shallow-marine stratigraphy: *SEPM Special Publication*, v. 90, p. 237–263.
3. Howell, J., Vassel, Å., and Aune, T., 2008, Modelling of dipping clinoform barriers within deltaic outcrop analogues from the Cretaceous Western Interior Basin, USA: *Geological Society, London, Special Publications*, v. 309, no. 1, p. 99–121.
4. Matthews, J. D., Carter, J. N., Stephen, K. D., Zimmerman, R. W., Skorstad, A., Manocochi, T., and Howell, J. A., 2008, Assessing the effect of geological uncertainty on recovery estimates in shallow-marine reservoirs: the application of reservoir engineering to the SAIGUP project: *Petroleum Geoscience*, v. 14, no. 1, p. 35–44.
5. Stephen, K. D., Yang, C., Carter, J. N., Howell, J. A., Manocochi, T., and Skorstad, A., 2008, Upscaling uncertainty analysis in a shallow-marine environment: *Petroleum Geoscience*, v. 14, no. 1, p. 71–84.
6. Enge, H. D., Buckley, S. J., Rotevatn, A., and Howell, J. A., 2007, From outcrop to reservoir simulation model: Workflow and procedures: *Geosphere*, v. 3, no. 6, p. 469–490.
7. Pranter, M. J., Ellison, A. I., Cole, R. D., and Patterson, P. E., 2007, Analysis and modeling of intermediate-scale reservoir heterogeneity based on a fluvial point-bar outcrop analog, Williams Fork Formation, Piceance Basin, Colorado: *AAPG bulletin*, v. 91, no. 7, p. 1025–1051.
8. Alpay, O. A., 1972, A practical approach to defining reservoir heterogeneity: *Journal of Petroleum Technology*, v. 24, no. 07, p. 841–848.
9. Hamilton, D., Reservoir Heterogeneity at Seventy-Six West Field Texas: An Opportunity for Increased Oil Recovery From Barrier/Strandplain Reservoirs of the Jackson-Yegua Trend by

Geologically Targeted Infill Drilling, *in* Proceedings SPE Annual Technical Conference and Exhibition 1991, Society of Petroleum Engineers.

10. Meyer, R., and Krause, F. F., 2006, Permeability anisotropy and heterogeneity of a sandstone reservoir analogue: An estuarine to shoreface depositional system in the Virgelle Member, Milk River Formation, Writing-on-Stone Provincial Park, southern Alberta: *Bulletin of Canadian Petroleum Geology*, v. 54, no. 4, p. 301–318.
11. Morad, S., Al-Ramadan, K., Ketzer, J. M., and De Ros, L., 2010, The impact of diagenesis on the heterogeneity of sandstone reservoirs: A review of the role of depositional facies and sequence stratigraphy: *AAPG Bulletin*, v. 94, no. 8, p. 1267–1309.
12. Willis, B. J., and White, C. D., 2000, Quantitative outcrop data for flow simulation: *Journal of Sedimentary Research*, v. 70, no. 4.
13. Wilson, M. D., 1994, Diagenetic mechanisms of porosity and permeability reduction and enhancement.
14. White, C. D., Willis, B. J., Dutton, S. P., Bhattacharya, J. P., and Narayanan, K., 2004, Sedimentology, statistics, and flow behavior for a tide-influenced deltaic sandstone, Frontier Formation, Wyoming, United States.
15. Pringle, J., Howell, J., Hodgetts, D., Westerman, A., and Hodgson, D., 2006, Virtual outcrop models of petroleum reservoir analogues: a review of the current state-of-the-art: *First Break*, v. 24, no. 3.



# Triaxial Compression Test Characteristics of Limestone from Gunung Lang, Malaysia

T.L. Goh, A.S. Serasa, A.G. Rafek, A. Abd Kadir, N. Simon, N. Surip, A. Hussin and K.E. Lee

**Abstract** The shear characteristics of rock materials are input parameters for reservoir geomechanics, wellbore stability, subsidence prediction, and underground structure numerical modeling. One of the most important shear characteristics of rock material is the significant increase in rock material strength with increasing confining pressure. This can be described from the triaxial compression test where rock material samples were subjected to increasing confining pressure in order to investigate the stress–strain relationship that the rock experienced and thus the failure strength envelope. For many years, multistage triaxial compressive strength

---

A.S. Serasa (✉) · N. Surip  
Chemical and Petroleum Engineering Department, Faculty of Engineering and Built Environment, UCSI University, 56000 Kuala Lumpur, Malaysia  
e-mail: Ailie@ucsiuniversity.edu.my

N. Surip  
e-mail: Noraini@ucsiuniversity.edu.my

T.L. Goh · A.S. Serasa · N. Simon · A. Hussin  
Geology Program, School of Environment and Natural Resource Sciences, Faculty of Science and Technology, Universiti Kebangsaan Malaysia, 43600 Bangi, Malaysia  
e-mail: gothianlai@ukm.edu.my

N. Simon  
e-mail: norbsn@ukm.edu.my

A. Hussin  
e-mail: haqqim@ukm.edu.my

A.G. Rafek · A. Abd Kadir  
Department of Geosciences, Universiti Teknologi PETRONAS, Bandar Seri Iskandar, 31750 Perak, Malaysia  
e-mail: ghani.rafek@utp.edu.my

A. Abd Kadir  
e-mail: askury\_akadir@utp.edu.my

K.E. Lee  
Institute for Environment and Development (LESTARI), Universiti Kebangsaan Malaysia, 43600 Bangi, Malaysia  
e-mail: khaiernlee@ukm.my

has been increasingly used by rock mechanics engineers to determine the Mohr–Coulomb failure envelope of rock material. The literature study revealed that there was less publication emphasizing on shear strength of Malaysian limestone using triaxial compression test. With that, this paper presents the result of four sets of multistage triaxial testing with confining pressures ranging from 1 to 15 MPa, conducted on limestone sample from Gunung Lang, Malaysia. From the Mohr–Coulomb failure envelope, the range and mean of friction angle,  $\phi$ , and cohesion,  $C$ , range from  $46^\circ$  to  $54.2^\circ$  with mean of  $49.6^\circ$  and 12–28 MPa and with mean of 14.5 MPa, respectively. With regard to the information presented in this paper, it was anticipated that the presented result will provide important rock strength characteristics for subsequent use in rock strength analysis in Malaysia.

## 1 Introduction

Limestone bedrock has always been a challenge for engineers in Kuala Lumpur [1, 2]. During the past decade or so, the development in Malaysia has becoming very rapid, especially in the development of high-rise buildings, tunnels, and dams. A large number of geotechnical problems have occurred during the construction of the earlier engineering projects in the limestone formation, and this rapid development is anticipated to further grow at an escalated rate in the near future. As larger and taller buildings are being planned and constructed, site investigations for the foundations are becoming more crucial, and it involves a thorough geomechanical analysis as limestone is known for causing serious problems such as sinkhole, surface subsidence, cavities, and underground solution channels.

The shear strength parameters which include cohesion,  $C$ , and friction angle,  $\phi$ , are used to predict how the rock material will behave in large-scale engineering applications. Examples of such application associated from large-scale interaction with surface engineering structures would be prediction of sliding stability of concrete dams and cut slopes, and design of tunnel support and foundation. The frictional characteristic of rock materials is also used in subsurface reservoir geomechanical modeling to simulate the response of reservoir rock and cap rock that undergo stress changes. In investigating the shear properties of limestone, the application of triaxial compression test is gradually increasing as it captures the entire stress stages of material deformation up to failure, seeing shear stress as the main factor causing failure. Despite the relevance of the triaxial compression test, there have been very few studies conducted on the triaxial compression characteristics of rock material in Malaysia due to lack of equipment, cost, and the complexity of the test. With that, this research took the opportunity to conduct and to present the result of triaxial compression strength characteristics of limestone to

guide subsequent rock strength analysis and geotechnical engineering-related problems in Malaysia.

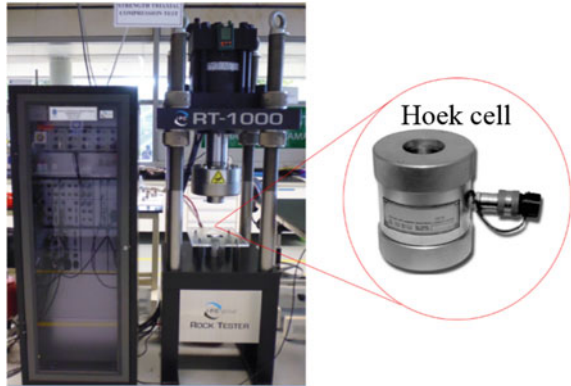
The study of the behavior of rock under stress in applied engineering has been studied from many different points of view. To this end, a number of methods have been developed to investigate the variation of peak stress with confining pressure in describing the deformations of rock material. Among others, the triaxial compression test is recommended as it captures the deformability of rock material for the entire stages of confining pressures. This deformability can be observed in the stress–strain curve used to indicate rock strength limits whereby the parameters are further defined in the Mohr–Coulomb failure envelope. The Mohr–Coulomb failure envelope is a mathematical model commonly used to predict failure when stresses surpass both the cohesion and friction angle of a rock. In a triaxial compression test, the Mohr–Coulomb failure envelope is expressed as a function of major principal stress ( $\sigma_1$ ) and minor principal stress ( $\sigma_3$ ). The advantages of Mohr–Coulomb failure envelope lie on its numerical simplicity, flexibility of input parameters, and general level of acceptance.

The study area is within the vicinity of the Kinta Valley, Ipoh, Malaysia. Raj et al. [3] have reported that the valley floor of Kinta is made up of the Simpang Formation (Old Alluvium) overlain by the Beruas Formation (Young Alluvium). Kinta Valley area is surrounded by the Main Range on the east side that reaches up to 867 m heights above sea level. Kinta Valley has many limestone hill distributions covering an average of 1.08 km<sup>2</sup> area. Based on topographic maps, elevation of the limestone hills is within 161–546 m above sea level. Kinta limestone formation was proposed by Foo [4] based on the abundance of scattered limestone rocks in the vicinity of Kinta Valley. Early researchers had recorded these formations by different names such as Kanthan limestone [5], HS Lee beds, Nam Long beds, Kuan On beds, Thye On beds, and Kim Loong No. 1 beds [6]. Ingham and Bradford [7] have characterized the lithological facies rocks into three main facies rocks: chalk facies, argillaceous facies, and arenite facies. The Kinta limestone formation is generally made up of calcareous facies rocks (limestone sequence), comprising dominantly of calcite and dolomite. Foo [4] reported that the age of Kinta limestone ranges from Silurian to Permian with the deposition of the clastic sediment in a relatively deep marine setting followed by the deposition of limestone following the progressive shallowing of the sea. Figure 1 shows the location of study area.



Fig. 1 Location of study area

**Fig. 2** The apparatus RT-1000 was used to conduct the triaxial compression test. The rock sample was located inside the Hoek cell



## 2 Methods

The multistage triaxial compression test provides a measure of the compressive strength and stress–strain characteristics by simulating in situ confining pressures and measuring the corresponding deformation characteristics of the samples. In this study, the test was performed over a range of confining pressures between 1 and 15 MPa to define the limestone material’s strength envelope according to the recommendation of ASTM D7012-14 Method B [8].

Figure 2 shows the apparatus RT-1000 manufactured by IPC Global used to conduct the triaxial test. Samples were prepared in regular geometry cored to a dimension ratio of 2:1 (height:diameter) with both ends of the surface trimmed to flat and smooth surfaces. During the test, the confining pressures were set constant, while the axial stress was increased gradually until the sample approached its maximum peak strength and failed.

## 3 Result and Discussion

A total of four multistage triaxial compression tests were conducted over the range of confining pressures of 1–15 MPa as shown in Table 1. From the results of triaxial compression test, the stress–strain curve was plotted to maximum peak

**Table 1** Summary of parameters and shear strength results from the triaxial compression test

Sample	Multistage confining pressure (MPa)	Cohesion, C (MPa)	Friction angle, $\phi$ (°)
GL1	4, 8, 12	12	49.3
GL2	1, 5, 10	17	54.2
GL3	3, 7, 11	16	46.0
GL4	5, 10, 15	13	49.0

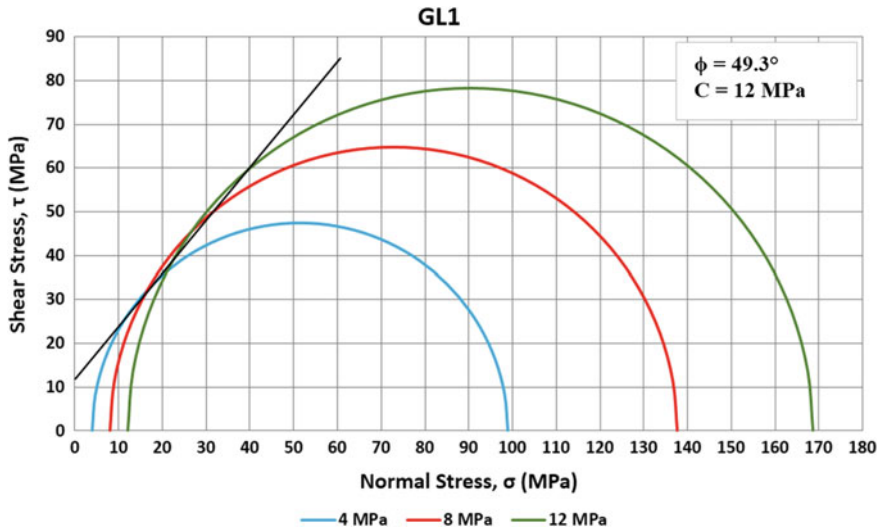


Fig. 3 Mohr–Coulomb failure envelope for sample GL1

loads against corresponding values of confining pressure to build the complete Mohr–Coulomb failure envelope. The result shows that the range of friction angle  $\phi$  of limestone was  $46^\circ$ – $54.2^\circ$  with mean of  $49.6^\circ$ , with the respective cohesion  $C$  ranging from 12 to 28 MPa with mean of 14.5 MPa.

Figure 3 shows the Mohr–Coulomb failure envelope for sample GL1. The cohesion and friction angle were 12 MPa and  $49.3^\circ$ , respectively.

Figure 4 shows the Mohr–Coulomb failure envelope for sample GL2. The cohesion and friction angle were 17 MPa and  $54.2^\circ$ , respectively.

Figure 5 shows the Mohr–Coulomb failure envelope for sample GL3. The cohesion and friction angle were 16 MPa and  $46.0^\circ$ , respectively.

Figure 6 shows the Mohr–Coulomb failure envelope for sample GL4. The cohesion and friction angle were 13 MPa and  $49.0^\circ$ , respectively.

The study revealed that the mean values of friction angle of limestone reported in this study are higher than the range of  $35^\circ$ – $42^\circ$  as reported by Goodman [9] and  $35^\circ$ – $45^\circ$  as reported by Hoek and Bray [10]. This could be due to the reason that the confining pressures applied in this study only range from 1 to 15 MPa, while the confining pressures reported by Goodman [9] ranges from 0 to 203 MPa. The mean values of cohesion for limestone reported in this study are within the range of 7–24 MPa as reported by Hoek and Bray [10] and of 10–30 MPa as reported by Goodman [9].

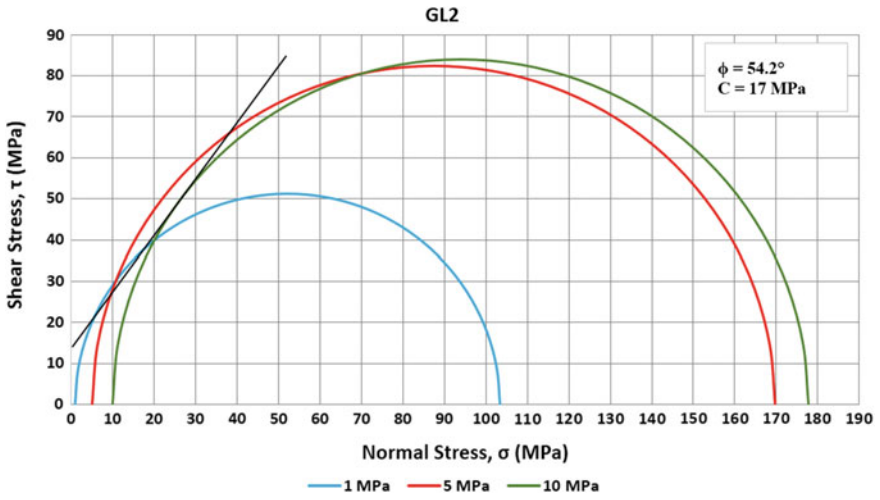


Fig. 4 Mohr-Coulomb failure envelope for sample GL2

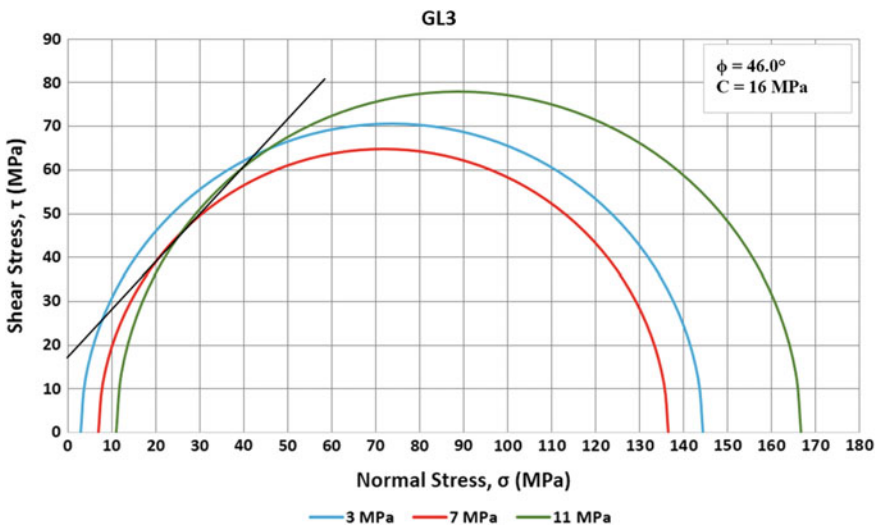


Fig. 5 Mohr-Coulomb failure envelope for sample GL3

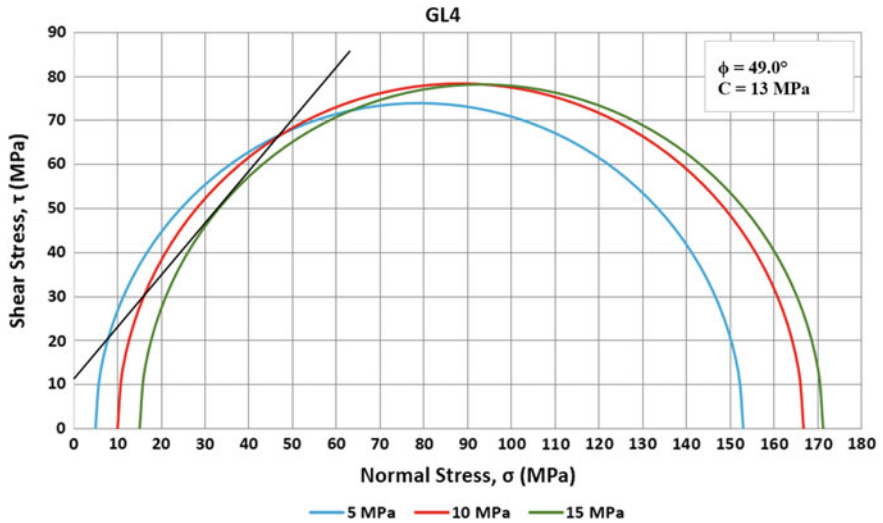


Fig. 6 Mohr–Coulomb failure envelope for sample GL4

## 4 Conclusions

A total of four sets of multistage triaxial compression test were conducted on limestone sample over the range of confining pressure of 1–15 MPa. From the Mohr–Coulomb failure envelope, the range of friction angle  $\phi$  of limestone was  $46^\circ$ – $54.2^\circ$  with mean of  $49.6^\circ$ . The respective cohesion  $C$  ranges from 12 to 28 MPa with mean of 14.5 MPa. The result presented is expected to be useful in subsequent geotechnical and rock strength analysis of limestone in Malaysia.

**Acknowledgements** This publication is funded by CERVIE UCSI University, FRGS/1/2014/STWN06/UKM/02/1, GUP-2016-024, and e-Science Fund Grant Scheme 06-01-SF-1140. The authors would also like to acknowledge the support of the staff and the facilities at the Department of Geosciences, Universiti Teknologi PETRONAS, for the assistance in the laboratory.

## References

1. Tan Yean-Chin and Chow Chee-Ming. 2014. *Foundation Design and Construction in Limestone Formation: A Malaysian Consultant's Experience*. Advances in Foundation Engineering. Research Publishing Services.
2. Ibrahim, O.B. & Fang, H.T. 1985. Piled foundation in limestone formation. In: *Proceedings of the 8th Southeast Asian Geotechnical Conference*, Kuala Lumpur, 11–15 March, 1985, 1. Kuala Lumpur: Organising Committee, 1985, P4/45 - P4/52.
3. Raj, J.K., Tan, D. N. K. & Wan Hasiah Abdullah 2009. Cenozoic Stratigraphy. In Hutchison, C. S. & Tan, D. N. K. (eds.) *Geology of Peninsular Malaysia*. Universiti Malaya and Geological Society of Malaysia Publication, Kuala Lumpur, 133–173.



4. Foo K.Y., 1990. Geology and Mineral Resources of The Taiping-Kuala Kangsar Area, Perak Darul Ridzuan. Geol. Survey Malaysia, Map Rept. 1, 145p.
5. Metcalfe, I. 1981. Permian and Early Triassic conodonts from northwest Malaya. Fourth. *Reg. Conf. Geol. Min. Res. S.E. Asia*, Abstracts of Papers, p. 10.
6. Sunthralingam, T., 1968. Upper Palaeozoic stratigraphy of the area west of Kampar, Perak. *Geol. Soc. Malaysia Bull.*, 1. 1–15p.
7. Ingham, F.F and E.F. Bradford. 1960. “The Geology and Mineral Resources of the Kinta Valley, Perak,” Geological Survey District Memoir, 9p.
8. ASTM D7012-14 Method B. “Standard Test Methods for Compressive Strength and Elastic Moduli of Intact Rock Core Specimens under Varying States of Stress and Temperatures”. ASTM International.
9. Goodman, R.E. 1980. *Introduction to Rock Mechanics*. New York: Wiley.
10. Hoek, E. & Bray, J.E. 1981. *Rock Slope Engineering*. 3rd Edition, London: Inst. Min. Metall.

# Analysis on the Trend of Pore Pressure in Miri Area, Baram Delta

M.H. Nurhajeerah, W.Y. Wan Ismail, A.Z. Muhammad Noor and A. Kurniawan

**Abstract** Studies of overpressure characterization are carried out in oil and gas exploration and production such as to avoid the drilling problem such as blowout, stuck pipe, and gas kick. These concerns can be addressed by enhancing the understanding of overpressure characterization in the field. This research emphasizes in determining the pore pressure trend in the Miri area to assist pore pressure prediction for future hydrocarbon exploration and production. The general pore pressure trends are related to mechanisms that contribute to the overpressure generation. The predominant overpressure mechanism in the region is disequilibrium compaction within the prodelta shales in outer shelf. The other mechanism is the fluid expansion in deltaic sequence of inner shelf area. The objective of this research is to analyze the pore pressure profile of wells for determining vertical and lateral pore pressure trends for various depositional environment facies of Miri area. The techniques such as rock physics analysis and pore pressure are part of the methodology of this research. The relation between the depositional environment facies and pore pressure profile were integrated with the help of seismic attribute and sequence of wells. The characterizations of overpressure trend and hard overpressure depths of selected area are related to the well location within delta setting of depositional environment facies and compaction factor.

**Keywords** Overpressure · Deep overpressure · Hard overpressure · Overpressure mechanism · Baram Delta

## 1 Introduction

The Miri field was located in the South China Sea at the southwestern part of the Peninsular Malaysia in between Kalimantan and Brunei. Miri field is known to be one of the Sarawak Basins, and petroleum in Sarawak is produced from Neogene

---

M.H. Nurhajeerah (✉) · W.Y. Wan Ismail · A.Z. Muhammad Noor · A. Kurniawan  
Department of Petroleum Geoscience, Universiti Teknologi PETRONAS,  
32610 Seri Iskandar, Perak, Malaysia  
e-mail: hana.nurhaj@gmail.com

rocks that occur mostly in the offshore areas of Sarawak Basin [4–6]. Some author (James, 1984, p. 38; Agostinelli et. 1990) claimed that the Sarawak Basin continues westward into Indonesia as the East Natuna Basin and is separated from the Sabah Basin to the east by a major tectonic discontinuity called West Baram Line as a major transform fault [2]. Evidence shows that this fault has significantly influenced the sedimentary evolution of the NW Borneo margin, as separating evolution of the carbonate sedimentation (Central Luconia Province) from deltaic siliclastic sedimentation (Baram Delta Province) [8].

The study of overpressure is compulsory in order to do the pore pressure estimation on the reservoir. The study of overpressure profile based on the well location is significant since the analysis done can be used to set the trend of overpressure in Miri field. Overpressure zone can also be used as the indicator of seal recognition. It will be useful for the study of petroleum system and the trend of overpressure zone which in turn can be used for future finding of reservoir in Miri field. Besides, overpressure zone can be further divided into three different zones which are transition zone, hard overpressure zone, and deep overpressure zone.

In this study, field-scale distribution of overpressure trend is conducted in Miri field and basic analysis of pore pressure characteristic is demonstrated as a first step in pore pressure estimation. Then, the research is continued by investigating the origin of overpressure mechanism generated at other wells in Miri area. This is to provide the essential foundation for subsequent vertical and lateral overpressure trend useful for pore pressure estimation.

### ***1.1 Problem Statement and Objective***

The study of pore pressure and overpressure of the Miri area, Baram Delta is still in progress. High pore pressure is mainly induced when excess pressure is present in that particular zone due to density changes. There is specific mechanism definition to characterize for high55 overpressure zone. This project was performed in high rate of sedimentation in order to acquire the basic understanding of the pore pressure mechanism that causes the overpressure.

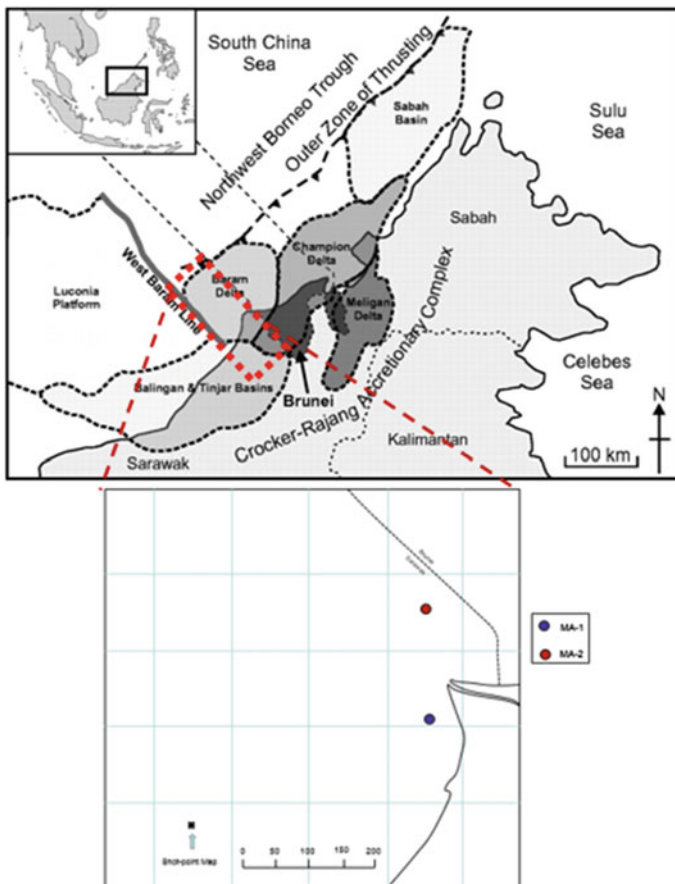
The concern of the research is there is lack in the relationship between overpressure intervals to the environment of deposition. Based on the pore pressure trend, this research tries to correlate the rate of sedimentation, overburden pressure, and volume of shale facies in order to identify the tectonic history experienced in the study area. Thus, these trends can be the indicator to differentiate the depositional environment of the well.

The main objective of this study is to analyze the trend of overpressure profile with respect to depositional environment facies as well as to study the effect of

overburden on the pore pressure at varies stratigraphic and structural styles based on the wells located in Miri area.

### 1.2 Study Area

The location of this research is located at northeastern part of Sarawak, Malaysia. The study area of this project can be divided into two wells which are offshore of Miri area. The wells are known as MA-1 and MA-2. These wells are located proximal to the shelf area of Baram Delta. The distance between these two wells is around 180 km apart as shown in Fig. 1.



**Fig. 1** A map of location of Baram Delta and the well location of MA-1 (blue circle) and MA-2 (red circle) in the Miri area. Modified from (Peter, Derek & Robert, 2015)

Offshore area of Miri field emphasize on understanding and predicting of overpressure zone using well log motif approach. This research will be stressed on the well log, rock physics, and seismic reflection analysis based on log motif.

### 1.3 Scope of Study

The research will begin with overview structural sequence and rock physics data on the outcrops that are located in the Miri area. Subsequently, well log analysis will be done based on gamma ray log, sonic velocity log, density log, resistivity log, and neutron log from wells. Significant crossplot will be created in order to analyze the pore pressure trend. Further analysis will be conducted on the pore pressure analysis for the well located in the Miri area. Hydrostatic, lithostatic, and normal compaction model will be created from well log data collected. Pore pressure analysis will be conducted to see the trend of pore pressure in Miri area. The report on the pore pressure trend that comprises of all the significant analysis will be produced at the end of the research.

## 2 Methodology

See Figure 2.

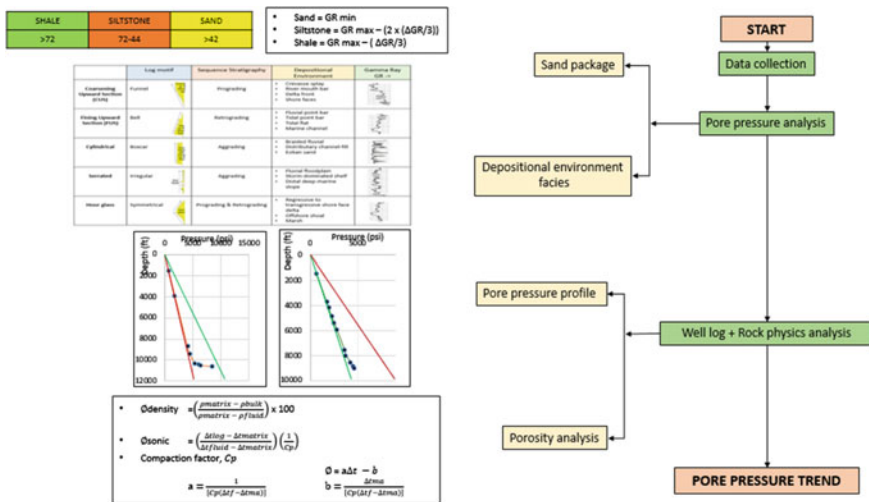


Fig. 2 The methodology of this research study begins with data collection to pore pressure analysis and continues to rock physics analysis in order to achieve the pore pressure trend

### 3 Result and Discussion

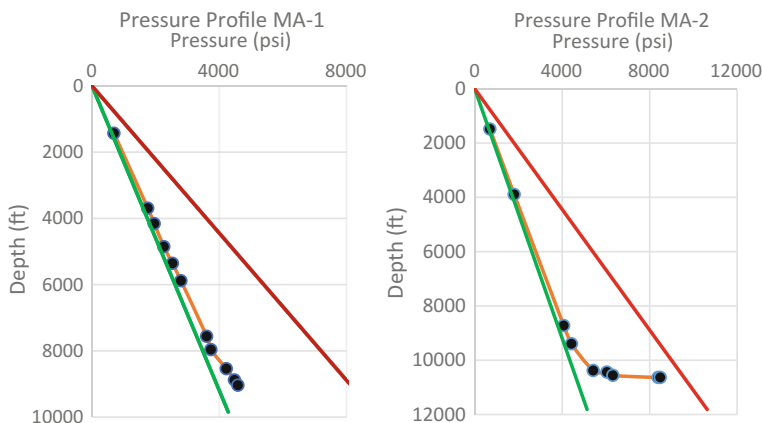
#### 3.1 Pore Pressure Characterization

Pore pressure is the essential parameters for physical properties and for geomechanical and geological analyses. Pore pressure is defined as fluid pressure in the pore spaces in the porous formation. Hydrostatic (normal) pressure is associated with a column of water from surface to depth of interest. Generally, the range of hydrostatic pressure for average density used in sedimentary basin varies from 1.00 to 1.08 g/cm<sup>3</sup>. Hydrostatic pressure in this reservoir shows increases in depth at the rate of 10 MPa/km or 0.44 psi/ft [11, 12].

Meanwhile, lithostatic pressure happens when the pore pressure exceeds the hydrostatic values in a confined pore volume at depth. It means that the pressure in the pores of the rock is equivalent to the weight of the overburden stress. Overburden pressure in this reservoir shows increase in depth at the rate of 0.9 psi/ft.

Figure 3 for MA-1 shows the variation of pore pressure with depth in Miri area. At the shallow depth (about 1000–6000 ft), the hydrostatic pressure is essentially imply continuous. Transition overpressure zone present at 7500–8000 ft is increased gently with depth. At the depth of 8500 ft, the hard overpressure continues with the gentle change in pressure with depth until reach 9200 ft.

MA-2 shows the variation of pore pressure with depth in Miri area. At the shallow depth (about 100–8500 ft), the hydrostatic pressure is essentially continuous. Transition overpressure zone present at 8700–10,300 ft is increased gradually with depth. Hard overpressure present at depth 10,400 ft continues with the sudden change in pressure with depth until it reaches 10,600 ft.



**Fig. 3** Pore pressure profile of MA-1(*left*) and MA-2 (*right*). *Green line* is to indicate the hydrostatic pressure and *red line* is to indicate the lithostatic pressure

Even though MA-1 and MA-2 are located proximal in the shelf area (inner shelf) and overpressure mechanisms were both controlled by disequilibrium compaction, they actually show the different trend of pore pressure. This means that there are some anomalous zones that lead to deviation of the overpressure generation in the well at certain depth. This might be upon to the different lithology and structural style of the well. By having trend of pore pressure, studies can improve the overpressure prediction of the wells for other oil and gas fields.

### 3.2 Facies Characterization

Facies characterization is necessary in order to distinguish the trend of the overpressure in the different sand packages. It gives us better correlation that shows the depositional environment could respond to the pore pressure trend in Miri area. Besides, it enhances the visualization of pore pressure variation on that particular depth interval.

Firstly, facies characterization is done in these studies by identifying the cutoff of gamma ray log for different lithology such as sand, silt, and shale. The cutoff gamma ray for shale, silt, and sand was calculated based on these formulas [1], [2] and [3]. Facies were then further divided based on the log motif as shown in Table 1. Here, log motif is categorized into different trends such as funnel, bell, boxcar, and irregular and symmetrical shape [7, 9, and 10].

$$\text{Shale} = GR_{max} - \left( \frac{\Delta GR}{3} \right) \quad (1)$$








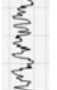


$$\text{Silt} = GR_{max} - \left( 2 \left( \frac{\Delta GR}{3} \right) \right) \quad (2)$$

$$\text{Sand} = GR_{min} \quad (3)$$

Generally, sequence stratigraphy shows the geometry of the sediment change by depth, and each well experiences different sequence stratigraphy. So, identifying log motif is important to recognize the depositional environment of the well. Thus, log motif is useful for the depositional environment analysis of the well located in Miri area.

Based on Appendix 1 and Appendix 2, the result from MA-1 expresses that it dominated with channel and point bar since MA-1 shows mostly fining upward section (FUS). Based on the location of the MA-1 in Fig. 1, it shows that MA-1 was actually located near the provenance. Meanwhile, MA-2 expresses that it dominated with the delta and mouth bar since the observation from the log motif of MA-2

**Table 1** Table of log motif that been used as reference for depositional environment analysis

	Log motif	Sequence stratigraphy	Depositional environment	Gamma ray gr->
Coarsening upward section (CUS)	Funnel 	Prograding	<ul style="list-style-type: none"> <li>• Crevasse splay</li> <li>• River mouth bar</li> <li>• Delta front</li> <li>• Shore faces</li> </ul>	
Fining upward section (FUS)	Bell 	Retrograding	<ul style="list-style-type: none"> <li>• Fluvial point bar</li> <li>• Tidal point bar</li> <li>• Tidal flat</li> <li>• Marine channel</li> </ul>	
Cylindrical	Boxcar 	Aggrading	<ul style="list-style-type: none"> <li>• Braided fluvial</li> <li>• Distributary channel fill</li> <li>• Eolian sand</li> </ul>	
Serrated	Irregular 	Aggrading	<ul style="list-style-type: none"> <li>• Fluvial floodplain</li> <li>• Storm-dominated Shelf</li> <li>• Distal deep marine</li> </ul>	
Hour glass	Symmetrical 	Prograding & Retrograding	<ul style="list-style-type: none"> <li>• Regressive to transgressive shore face delta</li> <li>• Offshore shoal Marsh</li> </ul>	

Picture taken from [www.researchgate.net](http://www.researchgate.net). For the sand package of MA-1 and MA-2, refer Appendix 1 and Appendix 2

mostly shows coarsening upward section (CUS). Thus, MA-2 actually located quiet far from the provenance.

Since MA-1 and MA-2 experienced different depositional environment facies, the location of the well from provenance itself influences the trend of pore pressure [13]. So, sequence stratigraphy studies are important in order to enhance the understanding of the pore pressure for future hydrocarbon discovery.

### 3.3 Porosity Analysis

Porosity gives the meaning of void volume against the total volume. Porosity acts as important role in geology as it can control the fluid storage. Besides, porosity has the relation to the fluid transport and rock properties. Thus, it can be used for pore pressure analysis in the reservoir.

Porosity can further divided into: (1) total porosity is identified by using density log and (2) effective porosity is identified by using sonic log.

Primary porosity is formed by crystallization. Besides, secondary porosity is caused by the variety processes such as deformation (including fracture), metamorphism, hydrothermal alteration, diagenesis, and weathering [3]. Since porosity



influences on the overpressure generation, porosity parameter is reliable in determining the trend of pore pressure in Miri area.

Referring to Appendix 1 and Appendix 2, the result from porosity of density and sonic logs shows the variations based on different facies characterization. Porosity analysis was further analyzed by identifying the compaction factor for sand and shale package for MA-1 and MA-2.

Compaction factor for MA-1 is shown in Fig. 4, sandstone Cp: 0.02 and shale Cp: 0.03. This shows that shale experiences more compaction compare to sandstone. Compaction factor for MA-2 is shown in Fig. 5, sandstone Cp: 0.006 and shale Cp: 0.008. Observation from both wells shows that shale experiences more compaction compare to sandstone.

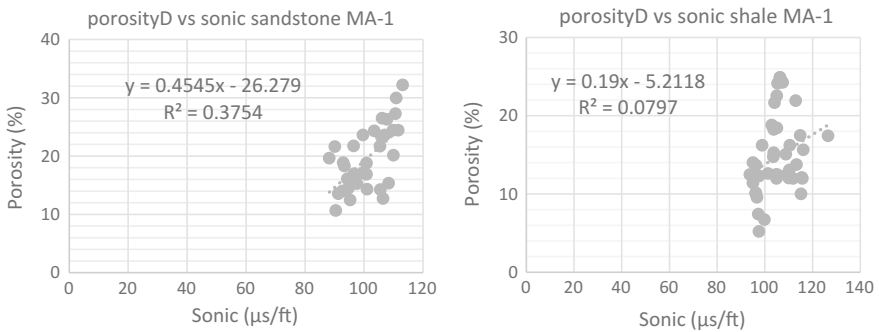


Fig. 4 Compaction factor for MA-1 sandstone (left) and shale (right)

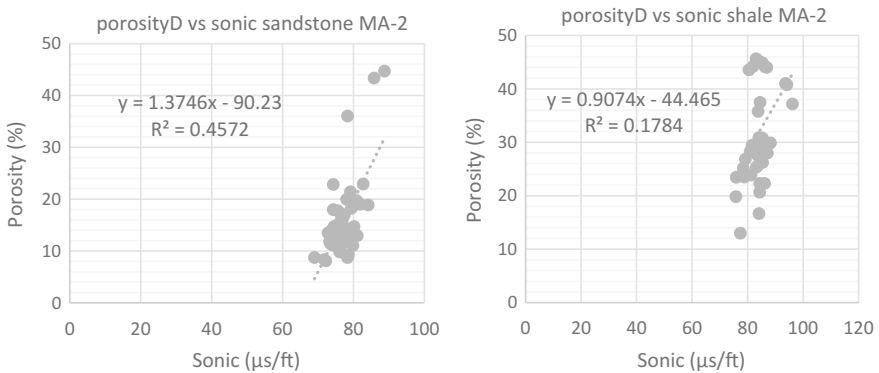


Fig. 5 Compaction factor for MA-2 sandstone (left) and shale (right)

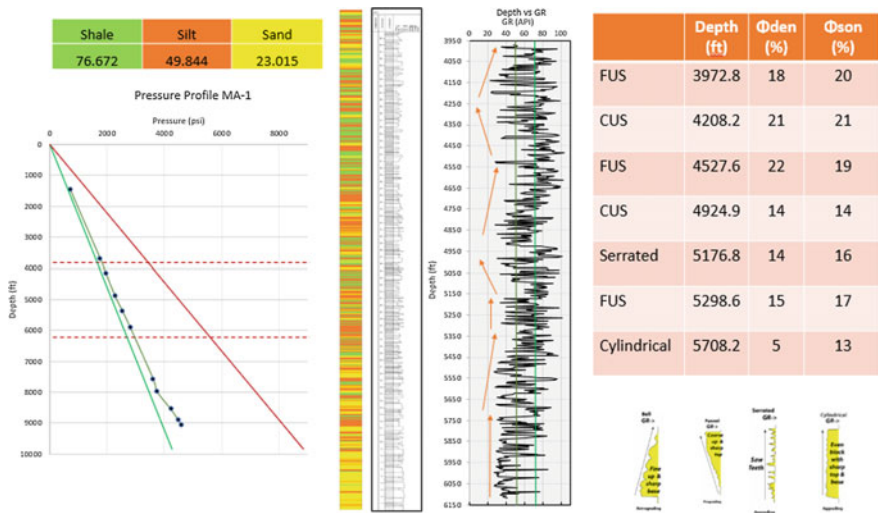
### 4 Conclusion

As the conclusion for the research studies:

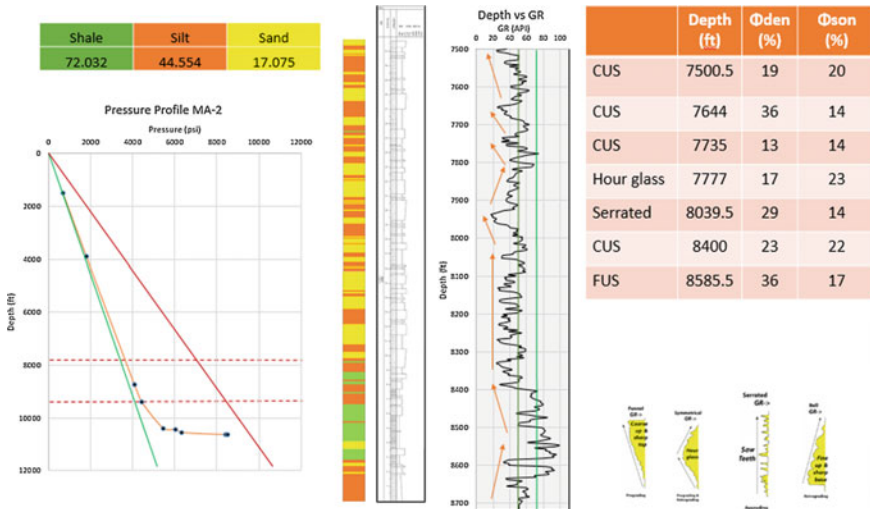
- Depositional environment facies and the location of the well to the provenance influence the trend of the pore pressure.
- Compaction factor shows that shale experienced more compaction compared to sandstone.
- Porosity of sonic and porosity of density show the changes in the log motif and pore pressure trend; however, other parameter is needed to support the changes in the trend of pore pressure.

### 5 Appendix

Appendix 1.



Appendix 2.



**Acknowledgements** I would like to express my deepest gratitude to my supervisor Assoc. Prof. Wan Ismail Wan Yusoff and cosupervisor Muhammad Noor Amin Zakariah for their guide during my studies. I thank all the lectures and Petroleum Geoscience Department of Universiti Teknologi PETRONAS for giving me an opportunity to further the research study. I would like to thank my father, mother, and family as well as colleague for their continuous support. Not forgotten huge thanks go to PETRONAS company for providing me the data for my research studies.

References

1. Bowers, G. (2002). Detecting high overpressure. *The Leading Edge*, pp. 174–177.
2. Hafizan, A. M., & Jennifer, C. (2011). Deep overpressure play: Second Lifeline for West Baram delta, East Malaysia. *Petroleum Geology Conference and Exhibition* (p. 172). Kuala Lumpur: Geological Society of Malaysia.
3. Lawrence M.A., & David R.C., (2015). Characterization and Analysis of Porosity and Pore Structures. Mineralogical Society of America.
4. Madon, M. (2006). Overpressure history of the Malay Basin, Offshore Peninsular Malaysia. *Petroleum Geology Conference & Exhibition* (pp. 135–144). Kuala Lumpur: Geological Society of Malaysia.
5. Mansor, M. Y., Rahman, A. A., Menier, D., & Pubellier, M. (2014). Structural Evolution of Malay Basin, its link to Sunda Block tectonics.
6. Mazlan, H., Abolins, P., Hoesni, M., & Ahmad, M. (1999). The petroleum Geology and Resources of Malaysia. In PETRONAS, *Malay Basin* (pp. 173–185). Kuala Lumpur: Petroliaam Nasional Berhad (PETRONAS).

7. Miller, T., Luk, C., & Olgaard, D. (2002). Interrelationships between overpressure mechanism and in situ stress. *AAPG Memoir*, pp. 145–161.
8. Morley, C., Tingay, M., Richard, H., & Rosalind, K. (2008). Relationship between structural style, overpressure and modern stress, Baram Delta Province, northwest Borneo. *Journal of Geophysical Research*, pp. 1–23.
9. Nogeitzig, A. (2010). Overpressure prediction based on rock physics model for shales. *EAGE Shale Workshop 2010*. Nice, France: EAGE.
10. Satti, I., Ghosh, D., & Yussof, W. (2014). Analysis of Overpressure Mechanism in Field of Southwestern Malay Basin. *Offshore Technology Conference* (pp. 1–5). Kuala Lumpur, Malaysia: OTC.
11. Tingay, M., Hillis, P., Swarbrick, R., Morley, C., Damit, & Razak, A. (2007). ‘Vertically Transferred’ overpressure in Brunei: Evidence for new mechanism for the formation of high-magnitude overpressure. *Geology*, p. 1023.
12. Wahab, M., Asraff, A., Ismail, J., & Ibrahim, A. (2013). Significant Hydrocarbon Accumulation in Deep Overpressured Play of Baram Delta, Malaysia. *EAGE Conference & Exhibition*. London, UK.
13. Yussof, W. I. W. (1993). Geothermics of Malay Basin, offshore Malaysia.

# Fracture Network Analysis of Metasedimentary Rock in East Coast Terengganu—An Analogue to Fractured Basement in Malay Basin

P.C. Ooi, S.N.F. Jamaludin and A.H.A. Latif

**Abstract** Oil and gas explorations have now moved to the basement rocks. Basements are rocks with low matrix porosity and permeability; therefore, fractures provide a path for hydrocarbon flow and storage. The research aims to establish an outcrop that could possibly be an analogue to the fractured basement of the Malay Basin and to apply seismic attributes to enhance the seismic images, thereby reducing the uncertainty of interpretation. Kuala Abang outcrop in Terengganu has been chosen to be an example of exposed basement in the Malay Basin. The metasediments in Kuala Abang are 21 m wide and 8 m tall, with beds dipping at 340°/60°. Fracture measurements were recorded and analysed using rose diagram. Results show the Shear<sub>1</sub>Left is positioned at 340°, whereas the Shear<sub>1</sub> Right I positioned at 270°. Therefore, the maximum stress  $\sigma_1$  is located at NNW-SSE, while the minimum stress  $\sigma_3$  is at ENE-WSW. 3D seismic data of Puteri Field in the Malay Basin were utilized for fracture characterization of the reservoir basement. Seismic interpretation is first done, followed by the interpretation of fractures using seismic attributes as image enhancer. The attributes used are structural smoothing, variance and curvature attributes. Seismic interpretation shows one major fault and four seismic units whereby the lithology is generally sandstone and siltstone in a fluvial environment. The basement is not metasediment due to the presence of feldspar. Fractures are beyond the resolution of seismic data; therefore, the approach to this problem is by analysing the azimuth of the major fault. The stress orientation of the fault is relatable to the stress direction of fractures, as both are within the same stress field. The fault analysis results in a NNW-SSE maximum stress direction. Although it is correlatable with the stress measurements of Kuala Abang, the difficulties faced are the difference in lithology, age and scale of the outcrop and Puteri Field. Nonetheless, the seismic attributes are excellent methods to assist in the study of fractured basement.

**Keywords** Fracture · Attributes · Curvature · Variance · Stress

---

P.C. Ooi (✉) · S.N.F. Jamaludin · A.H.A. Latif  
Department of Geosciences and Petroleum Engineering, Universiti Teknologi Petronas,  
32610 Tronoh, Perak, Malaysia  
e-mail: ooipecychee@gmail.com

## 1 Introduction

The world has been largely dependent on fossil fuels that account for 80% of the world energy consumption [11]. Experts have forecast a steady increase in demand of oil and gas consumption, and yet, there is no strong assurance of hydrocarbon discoveries to keep up with the high demand. The oil and gas industries have thus begun applying technologies such as deepwater exploration and enhanced oil recovery, and the recent interest of explorationist is the fractured basement reservoir. Fractured basement has been proven productive at several basins around the world, with the latest neighbouring discovery being the Cuu Long Basin, Vietnam. Basement is a combination of metamorphic and igneous rocks, with little or no matrix porosity [5]. However, extensive fractures in the basement enhance the reservoir permeability, hence producing a basement reservoir.

As part of this study, fractures on the metasedimentary rocks along the East Coast of Terengganu are studied in Kuala Abang outcrop (Fig. 1) and will act as an analogue to the fractured basement in the Malay Basin. The seismic data of Puteri Field in the Malay Basin are studied for its fractures, with the application of seismic attributes such as structural smoothing, curvature, coherence, dip and azimuth. Seismic attributes, especially the curvature and coherence, improve the seismic image for interpreters to distinguish fractures in a basement [3]. Seismic data may provide a good view of the reservoir structure; however, there are certain limitations to fine details such as identification of the extent of fractures and their connectivity [2]. While studying reservoir analogues, the stress state is also studied, which will characterize the fracture for its ability to conduct fluid. The lithology, structure and stratigraphy of the outcrop, in addition to the stress regimes, will help in the construction of the conceptual fracture models.

## 2 Field Background

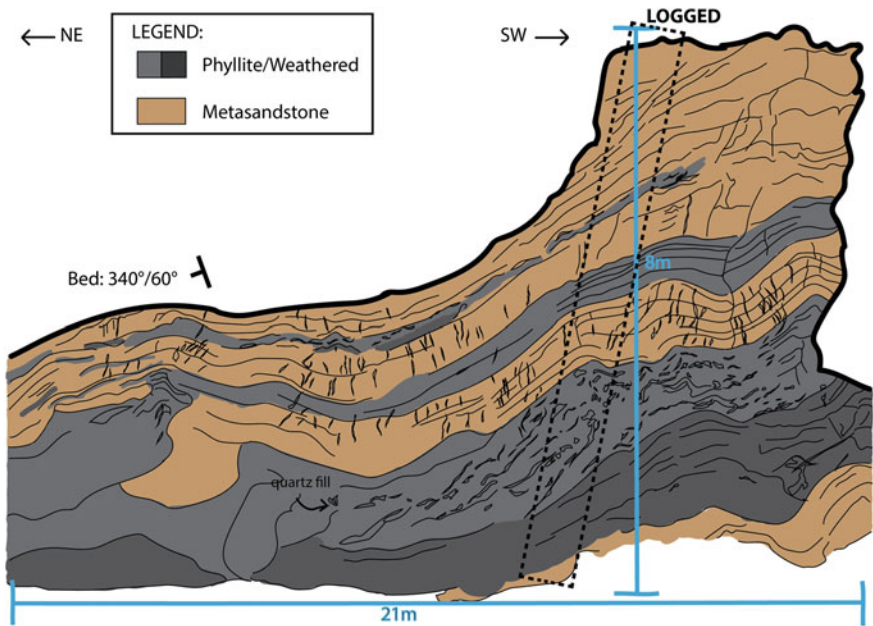
### 2.1 Kuala Abang in Terengganu

Kuala Abang is located about 63.6 km to the south of Kuala Terengganu as shown in Fig. 1. Kuala Abang rock formation is Carboniferous of age with sandstone and siltstone interbedding metasediments. In the Kuala Abang area, studies by Abdullah [1] show the existence of refolding in a recumbent fold, resulting in an open upright fold (Fig. 2), with the folding limb plunging towards the NE direction. This structural orientation is due to compression from the NNE direction and, after that, through the E-W compression, finally forming the conjugate lateral fault system or also known as the strike-slip fault.

The outcrop is also shown to possess brittle deformation. Recumbent fold is also shown to have double or more overlapping fold with both the axial planes of the fold lying parallel and horizontally, with the angle of dipping less than 45°. It is



**Fig. 1** Locations of Kuala Abang outcrop and the Malay Basin where Puteri Field is located. Puteri field is approximately 236 km from Kuala Abang outcrop



**Fig. 2** Kuala Abang outcrop sketch showing the outcrop is 21 m wide and 8 m tall. The lithology is metasandstone and phyllite with bed measurements at 340°/60°

formed during events of high tectonic stress. Open folds have limbs that gently dip away from the crest; naturally, it is a broad fold. It was formed at minimal tectonic stress [9].

## ***2.2 Puteri Field in Malay Basin***

Puteri Field is located in Block PM318 of the Malay Basin, offshore Terengganu. The Block PM318 covers an area of 1600 km<sup>2</sup> and is situated approximately 263 km offshore Kuala Abang. The water depth ranges from 60 to 80 m. The 3D seismic data of Puteri Field obtained is the raw migrated full-stack whereby the seismic attributes will be applied to obtain clearer fracture images.

The tectonic history of the Malay Basin began with the movement of India into Eurasia, causing displacement of the Malaya continental blocks, leading to transtensional shear and crustal extension close to the pre-Tertiary period. Due to the extension of crust began during the Late Eocene–Oligocene to Miocene period, the basin formed a rift-sag structure [7]. Rift-sag basin has led to active faulting, and when sedimentation occurs, the weight of the sediment load causes gravitational loading, in addition to the crustal cooling which causes the crusts to become denser, thus putting more weight on the sediments. This has led to the basin to sag broadly. Through the Early-to-Middle Miocene is when the basin inversion occurred, leading to the formation of axial shear zone.

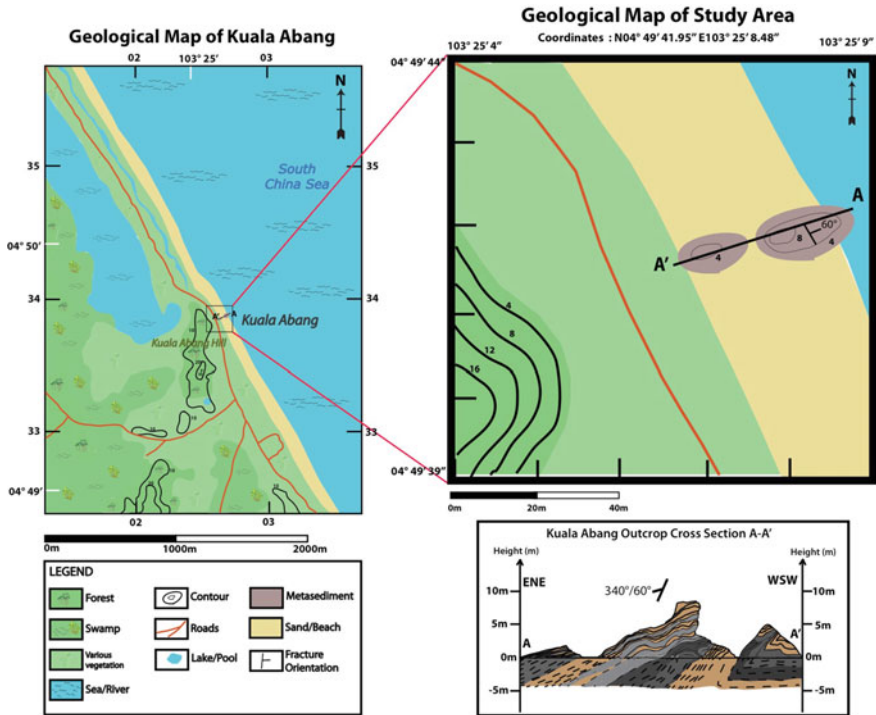
Generally, the Malay Basin was formed during the Tertiary period, but the basement composes of a combination of metasediments, igneous rocks and carbonates that were deposited during the Mesozoic and Palaeozoic era. After the Late–Middle Miocene tectonic uplift and deformation, the pre-Tertiary basement was uplifted to shallow depth trending southeast. The uplifting tectonic had also produced compressional anticlines which are bounded by normal faults at the south of the basement. The faulting trend in two-thirds of the Southern Malay Basin is showing faults trending towards E-W and NW-SE [10].

## **3 Methodology**

### ***3.1 Kuala Abang Outcrop Study***

The study of outcrop (Fig. 3) is first done by mapping whereby GPS readings are taken, and then cross-sectional sketch of the outcrop is made to display the folds, faults and fractures. Then, the lithology is studied by plotting the sedimentary log and formalized using the SedLog software. Fracture analysis is the next step where fracture measurements are first taken by utilizing the Scan-line Method. A total of





**Fig. 3** Geological map showing the location of Kuala Abang outcrop in the East Coast of Terengganu

156 measurements were taken and tabulated into the rose diagram using the Rose.net software to obtain the principal stress direction (Fig. 4).

### 3.2 Puteri Field Fracture Analysis

Upon the completion of the first part of the fieldwork analysis, the 3D seismic data are then loaded into Petrel software for structural and horizon interpretation. Quality control of the data was done.

The Puteri Field is a 3D data with inline ranging from 2721 to 3589, totalling 869 lines. The crossline on the other hand ranges from 2938 to 3852 with a total of 915 lines. It has been observed that the depth of the basement top is on line -2000 ms. Below -3000 ms, it is also observed that the data are filled with low frequency that distorts the quality of the seismic data; therefore, it is virtually cropped below -3000 ms and realized. Realizing and cropping the data ease the effort of working with seismic data in large volumes.



**Fig. 4** Puteri Field is located in Block PM318 of the Malay Basin. PM318 covers an area of 1600 km<sup>2</sup> and located approximately 263 km from Kuala Abang outcrop

Upon identifying the seismic unit below the basement and also the major downthrown fault, the fault polygons and time structure map are produced. Seismic attributes such as structural smoothing, curvature and variance are applied to the surface maps to generate surface attributes and volume attributes. Structural smoothing is applied on the data to enhance the contrast on the seismic lines as stated in the work by Mohammad et al. [8]. Variance attributes or also known as coherence attribute is a measure of discontinuity of waveforms (Fig. 5). Variance attribute is coloured in black, reddish-yellow and white. The waveforms that are coherent indicate lithological homogeneity, which means that the lithology of the rock is similar throughout. However, a non-continuous waveform proves a displacement in the subsurface structure due to faults or fractures and can be better observed in the coherence map [6].

Curvature attribute measures structural deformation [4] and deduce stress regimes that are correlatable with the density and orientation of fractures in the basement. Curvature attribute (Fig. 6) describes the extent of bending at a point on the curve. The parameters are adjusted respectively to obtain the most enhanced image using these attributes. The attributes reduce the uncertainty while measuring fault azimuth along the major downthrown fault that extends from the east to the west. Manual measurements are done using printed surface maps at aerial view using protractor; then, the azimuth values are tabulated into the rose diagram to identify the principal stress direction. Finally, the stress direction from both Kuala Abang outcrop and Puteri Field basement is compared to conclude the project (Fig. 7).

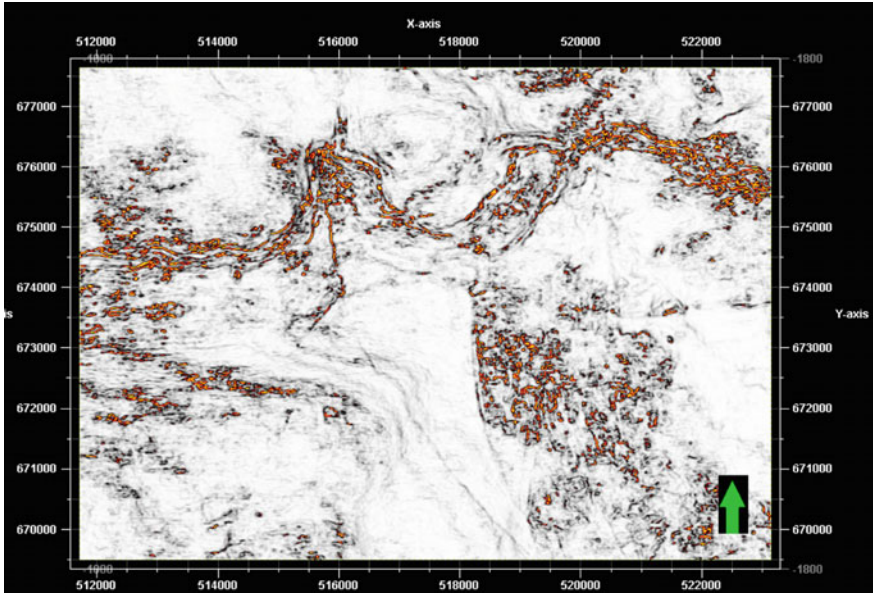


Fig. 5 Timeslice at Z-1800 ms is applied with variance attribute, also known as coherence attribute. Structural features are enhanced to assist in the interpretation process

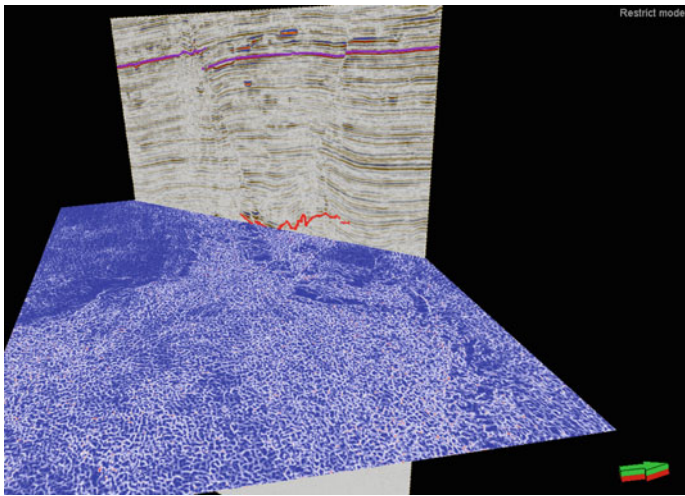


Fig. 6 Blue-coloured timeslice is applied with the curvature attribute. Curvature attribute displays the extent of the bending at a point on the curve, which can be due to channel features, bed foldings or faults. Therefore, by comparing the timeslice and 2D seismic line, the exact structural features can be confirmed

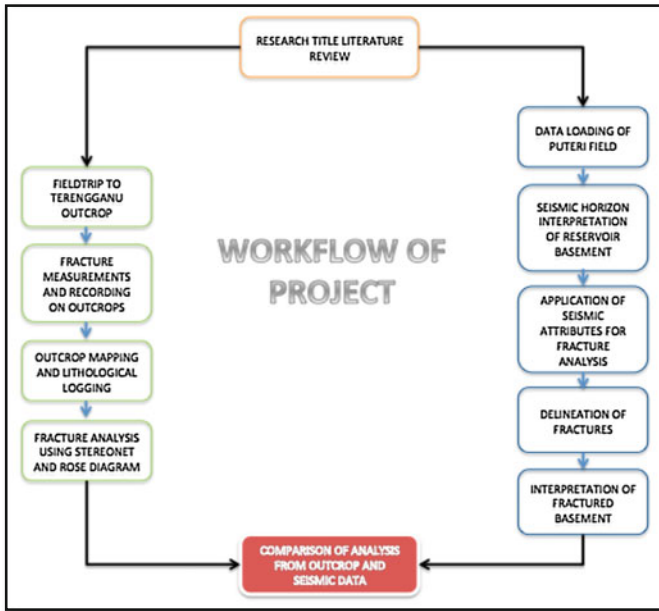


Fig. 7 Methodology/workflow of project

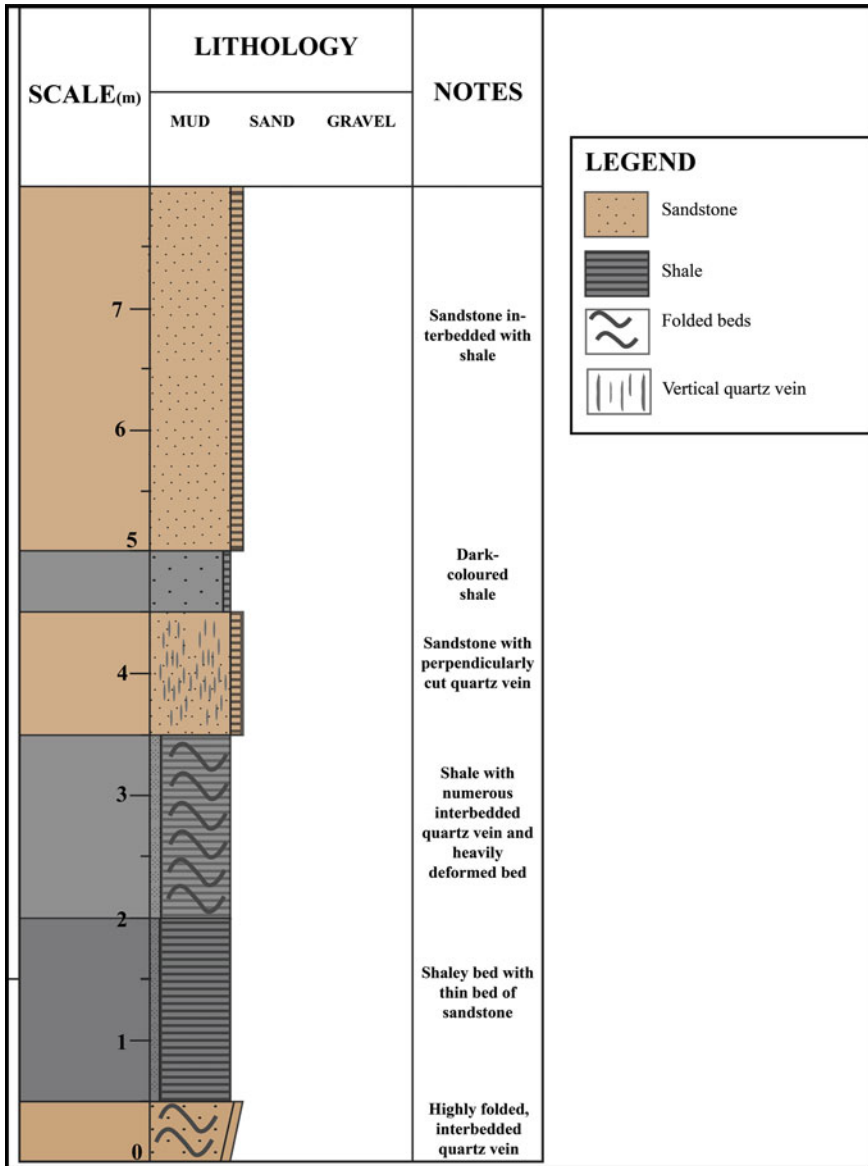
## 4 Results and Discussion

### 4.1 Kuala Abang Outcrop Study

The sedimentary log (Fig. 8) shows that the outcrop is approximately 8 m high, with an open upright folding. The bedding of the outcrop alternates with metasandstone (quartzite) that is interbedded or infilled with quartz vein as shown in the bottommost bed. The bed alternates with the metashale (phyllite) bed that is interbedded with metasandstone (quartzite) layer.

Generally, it is also observed that the bottom half of the outcrop has highly folded beds as shown in number 1 of Table 1. According to Abdullah [1], the Kuala Abang has undergone secondary deformation, thus the evidence of crenulations that were observed on the shaley beds as well as at the top of the outcrop. The other evidence that supports the secondary deformation hypothesis is the recumbent fold found at the SW part of the outcrop, as shown in number 4 of Table 1.





The rose diagram for Kuala Abang has 156 fracture measurements that were recorded using the Scan-line method. The fractures measured were all of non-extensional fractures. Generally, the rose diagram has two petals of the highest density as shown in Fig. 9. The area is interpreted to have a shear fracture labelled Shear<sub>1</sub>. Shear<sub>1</sub> Left is positioned at 340°, whereas the Shear<sub>2</sub> Right is positioned at



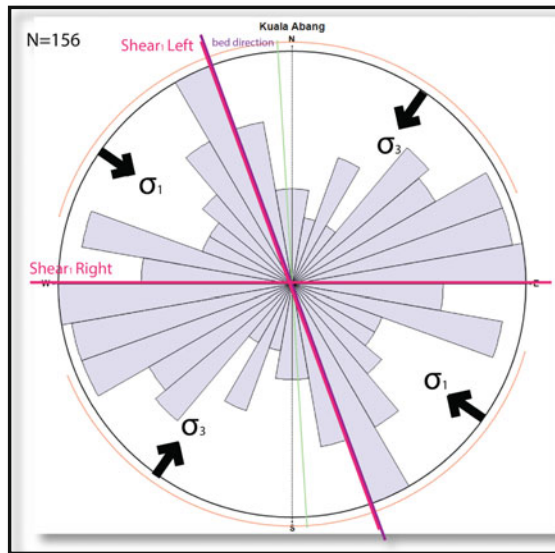
**Fig. 8** Sedimentary log shows the interbed of metasandstone and metashale. The bottom beddings are foldings and crenulations, with quartz vein vertically and horizontally infilled

270°. Therefore, the maximum stress  $\sigma_1$  is located at NNW-SSE, whereas the minimum stress  $\sigma_3$  is at ENE-WSW.

**Table 1** Kuala Abang field study shows deformational and structural features that were formed due to stress

Kuala Abang field observations		
No.	Image	Description
1		Wave-folded bed
2		Quartz infill perpendicular to the folded beds
3		Crenulations
4		Recumbent fold

**Fig. 9** Rose diagram of fractures measured in Kuala Abang outcrop. The maximum stress is at NNW-SSE direction

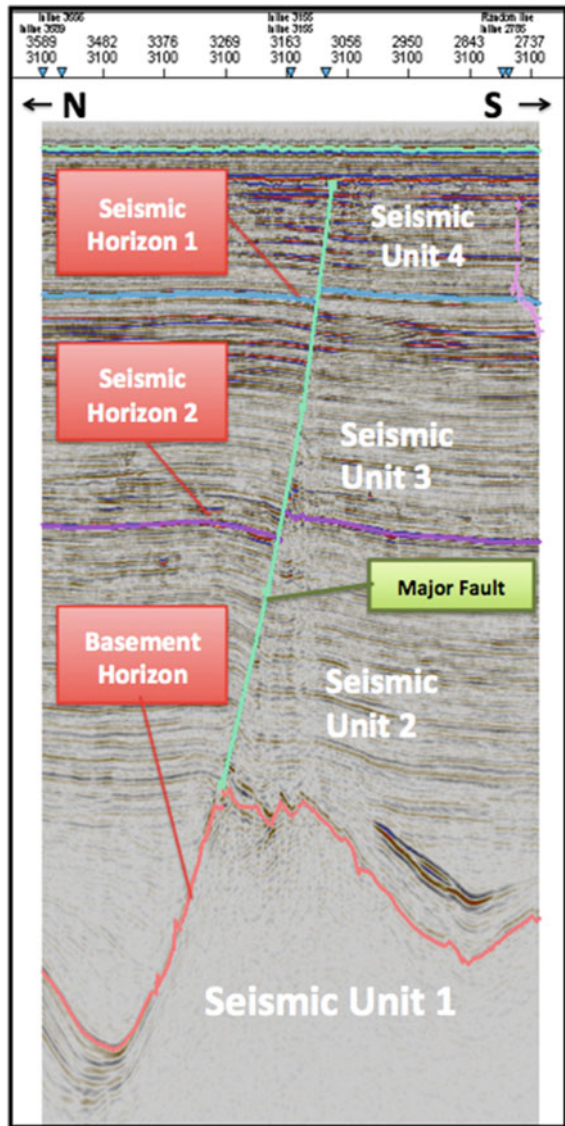




### 4.2 Seismic Interpretation

Puteri field seismic data were interpreted to four (4) horizons, namely the Water Bottom (WB), Seismic Horizon 1, Seismic Horizon 2, and Basement Horizon. The regions between the horizons are labelled starting from the deepest section. The bottommost section is the Seismic Unit 1 (SU 1) followed by Seismic Unit 2 (SU 2), Seismic Unit 3 (SU 3) and Seismic Unit 4 (SU 4). SU 1 is the seismic section below the Basement Horizon, whereas the SU 4 is the region beneath the Water Bottom as shown in Fig. 10, Table 2.

**Fig. 10** 2D inline seismic shows four seismic units that were interpreted. Seismic Unit 1 is the basement

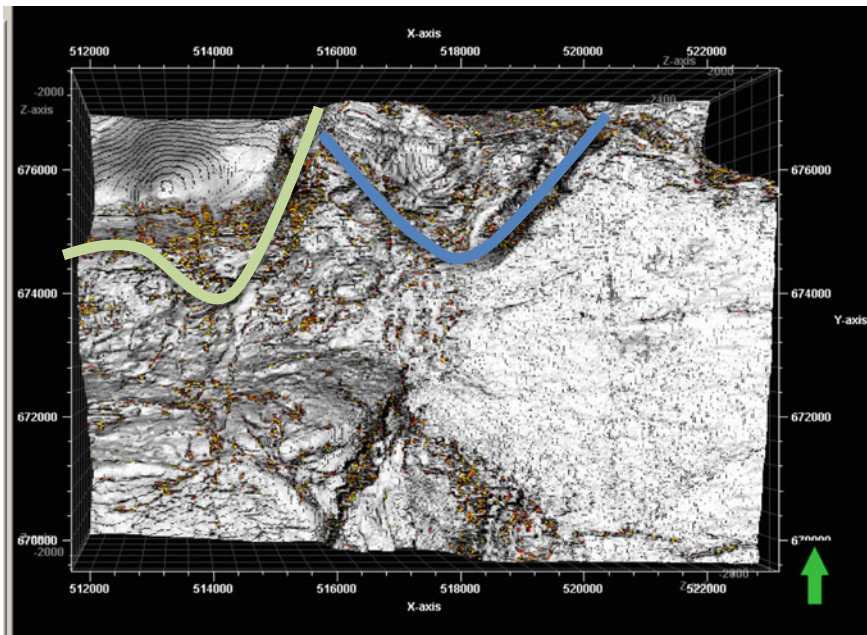


**Table 2** Comparison of data from seismic unit 1–4

Seismic unit	1	2	3	4
Age	Oligocene–lower Miocene	Lower Miocene	Lower–middle Miocene	Middle Miocene
Amplitude strength	Weak	Moderate	Moderate–strong	Strong
Reflection patterns	Chaotic	Parallel, disrupted and chaotic	Parallel, contorted	Parallel
Faults	One major and 15	One major	1 major and 1 minor	1 major and 1 minor
Lithology	Shale and sandstone, metamorphosed	Claystone, siltstone and sandstone	Claystone, sandstone, siltstone and some coal	Claystone, sandstone, siltstone and some coal
Depositional environment	Fluvial–lacustrine	Fluvial–estuarine	Fluvial	Fluvial

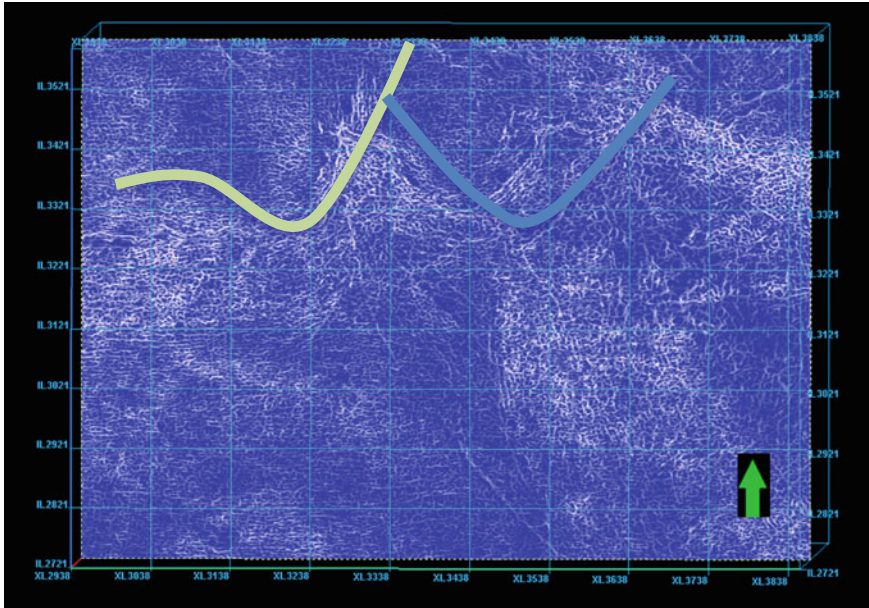
### 4.3 Fracture Analysis on Seismic Attributes

Seismic attributes are the geophysical data which are obtain via computation, calculation and other techniques to ease the geological and geophysical



**Fig. 11** Variance attribute on the basement surface map with the red dotted line showing the major fault in the E-W direction

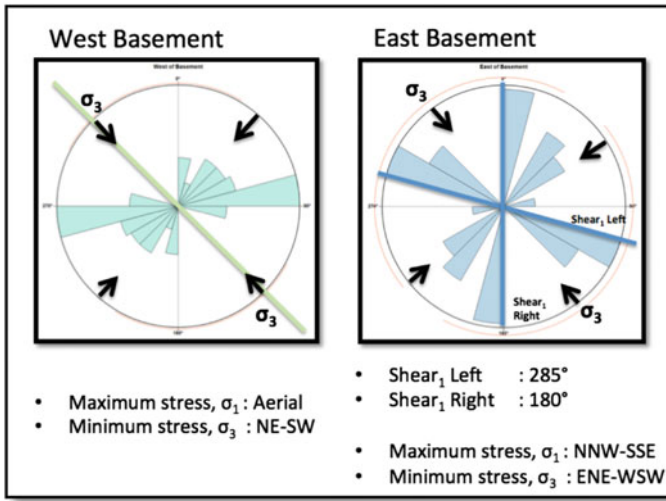




**Fig. 12** Curvature attribute is applied on the timeslice at Z-1800 ms. The *green and blue dotted lines* are the fracture on the west and east side of the basement, respectively. These two sections are where fault azimuth is measured to input into the rose diagram

interpretation by enhancing specific structural features especially the faults or folds. Fractures are not subtle lineaments on seismic data that are not easily delineated as it is beyond the seismic resolution. The method applied in this project for identifying the principal stress is by measuring fault azimuth on the printed surface map in its aerial view. Measurements are made at several points, depending on its orientation and its length. Finally, the measurements are tabulated into the rose diagram to obtain its principal stress direction.

The basement is measured for the azimuth of the major downthrown fault. The analysis has been separated into the west basement and east basement (Figs. 11 and 12). A total of 40 measurements were taken along the fault, and the results are as shown in Fig. 13. The maximum stresses coincide with each other whereby all are at the NNW-SSE direction. The minimum stresses are located at approximately ENE-WSW. For the East Basement region, the  $\text{Shear}_1 \text{Left}$  is at  $285^\circ$ , while the  $\text{Shear}_1 \text{Right}$  is at  $180^\circ$ . The maximum stress also coincides with the principle direction of Kuala Abang fractures.



**Fig. 13** Two rose diagrams were generated through the fault azimuths measured on the west and east side of the fault on the basement

## 5 Conclusion

The objective of the project study is met whereby the number of events that generate the fractures in onshore and offshore is measured. Seismic attributes are also applied effectively to enhance the seismic data for better analysis of fracture networks through the major faults interpreted in the seismic section. A relationship between Kuala Abang outcrop and offshore Puteri Field basement is also established; however, although the principal stress direction or the maximum stress coincides between basement and outcrop, the results show they are still incompatible due to a large difference in scale and age and a slight difference in its lithology.

Therefore, further works will be focused on studying a more suitable outcrop, applying more seismic attributes during the study, applying the shear wave splitting technique during seismic acquisition, and also studying fractures through the FMI well logs by Schlumberger.

**Acknowledgements** I am grateful to my supervisor, Mdm. Siti Nur Fathiyah, for her utmost guidance in conducting my FYP. I also extend my thanks to AP Askury Abdul Kadir, Mr Lo Shyh-Zung and Pn Suhaileen Shahar for their guidance and kind assistance throughout the journey of completing my project.

## References

1. Abdullah, I. (2004). *On the presence of pre-Carboniferous metasediments in the Eastern Belt: A structural view*. Paper presented at the Annual Geological Conference, Perlis, Malaysia.
2. Bratton, T., Canh, D. V., Que, N. V., Duc, N. V., Gillepsie, P., Hunt, D., et al. (2006). The Nature of Naturally Fractured Reservoirs. *Oilfield Review - Schlumberger*, 4–23.
3. Chopra, S., & Marfurt, K. J. (2009). Seismic Attributes for Stratigraphic Feature Characterization. *AAPG Search and Discovery Article*.
4. Chopra, S., & Marfurt, K. J. (2010). Delineating Fractures from Seismic Attributes. *AAPG Journals*.
5. Cuong, T. X., & Warren, J. K. (2009). Bach Ho Field, A fractured granitic basement reservoir, Cuu Long Basin, Offshore SE Vietnam: A “Buried-Hill” Play. *Journal of Petroleum Geology*, 32 (2), 129–156.
6. Jamaludin, S. N. F. (2014). Relationship between syn-depositional faulting and carbonate growth in Central Luconia Province, Malaysia. *Bulletin of the Geological Society of Malaysia*, 60(December 2015), 77–83.
7. Madon, M. (1999). Plate Tectonic Elements and the Evolution of Southeast Asia *The Petroleum Geology and Resources of Malaysia* (pp. 59–73). Kuala Lumpur, Malaysia: Petroliam Nasional Berhad (PETRONAS).
8. Mohammad, H. H., Shamsuddin, A. A. S., & Ghosh, D. P. (2014). *Fracture Pattern and Stress Analysis Based on Borehole Images and Seismic Attributes*. (Bachelors of Technology (Hons) Petroleum Geoscience), Universiti Teknologi PETRONAS, Perak.
9. Nelson, S. A. (2012). Deformation of Rock. *Physical Geology*. from <http://www.tulane.edu/~sanelson/eens1110/deform.htm>.
10. Ngah, K. (1990). Structural Framework of Southeastern Malay Basin. *AAPG Online Journal for E&P Geoscientists*, 1–8.
11. Schlumberger. (2008). Characterization of Fractured Reservoirs. *Schlumberger Carbonate*. Retrieved 10 February 2015, from [www.slb.com/carbonates](http://www.slb.com/carbonates).

# Full Waveform Inversion: A Multiscale Approach to Tackle Gas Cloud Problem

Srichand Prajapati

**Abstract** Acoustic and elastic wave equations are computationally efficient and accurate simulation of complex wave propagation in heterogeneous environments. Both acoustic and elastic FWI with  $Q$ -absorption on synthetic gas cloud model have been used in this study. Inversion results and misfit analysis show the effectiveness of both equations. In the analysis, the elastic FWI results have not significantly changed, even with wrong assumption of  $Q$ -values within the gas cloud. A detailed  $Q$  model is not needed for a successful elastic FWI, as long as appropriate passive long wavelength background  $Q$  model is incorporated.

**Keywords** Inversion · Acoustic · Elastic ·  $Q$ -attenuation

## 1 Introduction

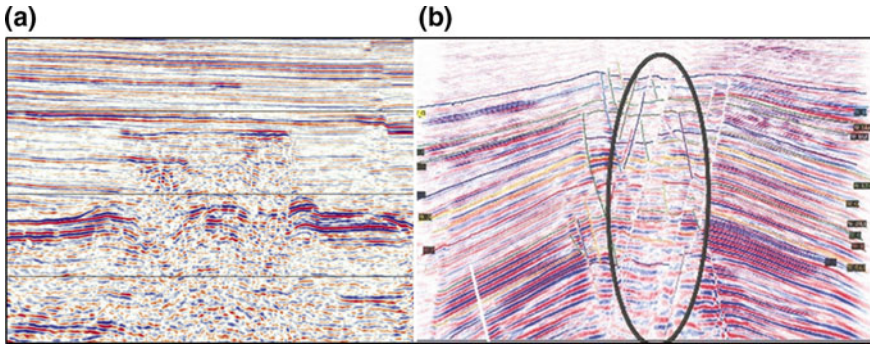
Getting subsurface properties is very critical and challenging especially in complex environment such as low-velocity overburden area. The presence of gas cloud has long been recognized as a significant problem in the seismic data around the world (North Sea, offshore Southeast Asia). In SE Asia, major hydrocarbon-bearing fields are affected by shallow gas clouds, and therefore, data quality often suffers from serious wipeouts due to shallow gas or gas leaking from a deep reservoir. Gas clouds are easily identified by the low  $P$ -wave velocities, whereas their signature is much weaker in the  $V_s$  model (Fig. 1).

Joint inversion for velocity and  $Q$  with viscoacoustic FWI has attracted a lot of interests from the industry; however, it remains a very challenging topic as the joint inversion for both  $V_p$  and  $Q$  is an ill-posed problem, as they are coupled. Based on wave equation, the first imaging through FWI was proposed in the 1980s by [12] using least-squares approach in time domain and later by [10] in frequency domain.

---

S. Prajapati (✉)

Centre for Seismic Imaging, Department of Petroleum and Geosciences,  
Universiti Teknologi PETRONAS, 32610 Seri Iskandar, Perak, Malaysia  
e-mail: srichandprajapati@hotmail.com



**Fig. 1** Gas masking effect: **a** dense shallow gas cloud masking with poor imaging and **b** poor imaging with gas leakage due to poor sealing of hydrocarbon reservoir

The basic idea of FWI is to minimize the misfit between observed and calculated dataset after each optimization during inversion. FWI technique is very sensitive to the initial velocity model especially when real data are considered. In the absence or poor starting velocity model, FWI will tend to converge to one of the many local minima due to the wrapping around the nature of phase in the frequency domain or cyclic-skipping problem in the time domain [3, 11].

Earlier, some studies have been done on low velocity or gas cloud using first arrival tomography [13] and using  $l_2$  norm [2]. Kohn et al. [6] discuss the elastic isotropic FWI and conclude that  $P$ - and  $S$ -velocities and densities are better than using impedances. In the present study, I approached this problem in 2D format using acoustic and elastic wave equations with and without considering the  $Q$ -absorption value in gas cloud.

## 2 Theory

### 2.1 Acoustic Full Waveform Inversion

For 2D acoustic FWI approach, I follow the approach proposed by [8] in frequency domain as follows:

$$A_i(m)u_i = q_i \quad (1)$$

This equation defines a relation between the vector parameters  $m$ ,  $A_i(m)$  is the discretized Helmholtz operator, and the wavefield  $u = [u_1; u_2 \dots]$  and the  $q_i$  represent the discretized source vectors. Starting with the initial model  $m_0$ , assuming that this is closed to the true model with misfit of data.

$$\Delta d = d_{\text{obs}} - d_{\text{cal}}(m) \quad (2)$$

where  $d_{\text{obs}}$  is the observed seismic data,  $d_{\text{cal}}$  is the model seismic data with a function of  $m$ , and  $\Delta d$  is the residual. The misfit function is updated with perturbation model  $m = m_0 + \Delta m$  at every iteration given by

$$\text{Misfit}(m) = \frac{1}{2} \Delta d^t \Delta d \quad (3)$$

where  $t$  denotes the transpose of matrix.

## 2.2 Elastic Full Waveform Inversion

The propagation of waves in an elastic medium can be described by coupled linear partial differential equations. In the isotropic elastic case, a second-order partial differential equation of motion in the time domain can be written as

$$\begin{aligned} \rho \frac{\partial v_i}{\partial t} &= \frac{\partial \sigma_{ij}}{\partial x_i} + f_i \\ \sigma_{ij} &= \lambda \theta \delta_{ij} + 2\mu \varepsilon_{ij} \\ \varepsilon_{ij} &= \frac{1}{2} \left( \frac{\partial v_i}{\partial x_j} + \frac{\partial v_j}{\partial x_i} \right) \end{aligned} \quad (4)$$

where  $v_i$  is known as the displacement velocity vector,  $\sigma_{ij}$  is known as the stress tensor,  $\lambda$  and  $\mu$  are the Lamé parameters,  $\varepsilon_{ij}$  is the strain tensor,  $v_i$  is the particle displacement vector, and  $f_i$  is the body forces.

Since the Lamé parameters,  $\lambda$  and  $\mu$ , do not depend on time, Eq. 4 can be written as

$$\begin{aligned} \rho \frac{\partial v_i}{\partial t} &= \frac{\partial \sigma_{ij}}{\partial x_i} + f_i \\ \frac{\partial \sigma_{ij}}{\partial t} &= \lambda \frac{\partial \theta}{\partial t} \delta_{ij} + 2\mu \frac{\partial \varepsilon_{ij}}{\partial t} \\ \varepsilon_{ij} &= \frac{1}{2} \left( \frac{\partial v_i}{\partial x_j} + \frac{\partial v_j}{\partial x_i} \right) \end{aligned} \quad (5)$$

For this work, time domain is used to minimize the misfit function (Tarantola 1987) as follows:

$$\partial u = u_{\text{obs}} - u_{\text{mod}} \quad (6)$$

where  $u_{\text{mod}}$  is the synthetic data and  $u_{\text{obs}}$  is the observed data calculated using elastic wave equation.

The model is updated using the conjugate gradient method as:

$$m_{n+1} = m_n - \alpha \delta m \quad (7)$$

where  $\alpha$  is the step length.

---

**Algorithm 1 : Conjugate Gradient (CG) algorithm**

---

**Input :** A,  $x_0$ ,  $\text{max.iter}$ ,  $\eta$   
**Output :** x  
Initialize parameters;  
 $r_0 = b - Ax_0$   
 $P_1 = r_0$   
**for**  $k = 1$  **to**  $\text{max.iter}$  **do**  
 $\alpha_k = \frac{r_{k-1}^T r_{k-1}}{P_k^T A P_k}$ ;  
 $x_k = x_{k-1} + \alpha_k P_k$ ;  
 $r_k = r_{k-1} - \alpha_k A P_k$ ;  
 $\beta = \frac{\delta m_n \cdot \delta m_{n-1} - \delta m_{n-1}^2}{\delta m_{n-1} \cdot \delta m_{n-1}}$ ;  
used by Polak-Ribière. The convergence of the Polak-Ribière method is guaranteed by choosing  $\beta = \max[\beta, 0]$ .  
 $P_{k+1} = r_k + \beta_k P_k$ ;  
**if**  $\|Ax_k + b\| < \eta \|b\|$  **then return**  $x_{k-1}$   
**end**

---

**Algorithm 2 : Elastic Full Waveform Inversion**

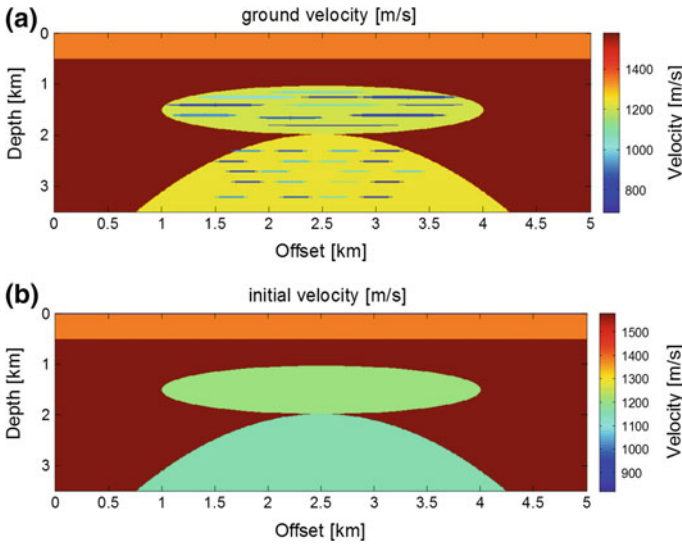
---

**for** each iteration step  $n$  **do**  
**while** (*NOT convergence AND iter < niter<sub>max</sub>*) **do**  
Build forward problem, stated in equation 5 for model  $m_n$   
Build synthetic dataset  $u^{\text{mod}}$  and the wavefield  $u(x, t)$  for each shot.  
Estimate the residual  $\delta u = u^{\text{mod}} - u^{\text{obs}}$ .  
Back propagating the residual to generate wavefield.  
Build gradient vector  $\delta m_n$   
Calculate the conjugate gradient direction for  $\text{iter } n \geq 2$  using algorithm 1  
Update model with equation 7.  
**end while**  
**end for**

---

### 2.3 Numerical Examples Using Acoustic FWI

We use a realistic synthetic gas cloud model which closely represents the shallow gas cloud environments of SE Asia basin (Fig. 2). This model is used to image the overburden properties of horizon or layer of media where the acoustic velocity ( $V_p$ ) is significantly low as the reflection underneath the gas exhibit a ‘push-down’ effect due to localization of the anomaly.

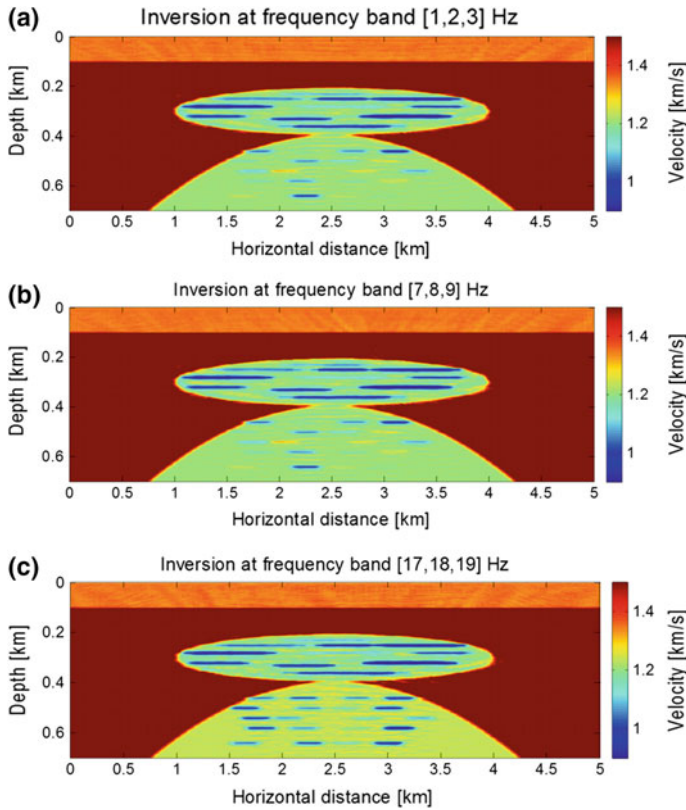


**Fig. 2** **a** True velocity model enriched with Gaussian anomaly to make model more complex and **b** initial velocity model for FWI

We first solve Helmholtz 9-point stencil [5]. In the second step, the  $V_p$  velocity model is reconstructed, which has 5-km long offset and 0.7-km as depth and populates the model with Gaussian anomaly to make data more complex; note that due to Gaussian anomaly, the effect of attenuation and scattering phenomenon is very dominant; however, the adjoint velocity perturbation is less affected. Finally, initial velocity model is used. We use the multiplicative  $l_2$ -norm regularization throughout the inversion process. A number of initial realizations are constructed by adding random variation around the model. For source wavelet, full bandwidth wavelet with 55 Hz is used. The synthetic data are generated at a constant spread length with all the receivers at the same location with 125 shots at offset 40:40:5000 at 50 m depth and with 250 receivers at lateral positions 20:20:5000 m at 20 m depth.

To solve nonlinear optimization problem, we used steepest decent (i.e., gradient) as penalty with l-BFGS (limited-memory Broyden Fletcher Goldfarb Shanno) method, which is a popular quasi-Newton method for solving nonlinear optimization problems. We invert the data in  $l_2$  frequency bands from 3 to 33 Hz where each frequency band contains a group of three frequencies. We use 20 iterations per frequency band. Figure 3 shows the inversion results at some selected frequency band. Due to ill-posed and nonlinear relationship between data and model, inversion needs to be iterated several times to converge toward the local minima of misfit





**Fig. 3** From the inversion results at different frequency bands, it is clear from inversion results that moving toward high frequency, inversion results are more promising

function. This is particularly true, when working on low-frequency model. In this paper, we implement different ways of full waveform inversion for low-frequency model with minimum number of iterations providing a better resolution of inversion results. To mitigate some challenges related to local minima, the appropriate way is to invert the data from low frequencies and gradually to higher frequencies [9].

#### 2.4 Numerical Examples Using Elastic FWI

We use elastic wave equation in time domain to study the role of attenuation for weakly and strongly attentive media in marine environments. We can account attenuation into two ways. Firstly, attenuation may be used as a passive parameter, i.e., as modeling parameter only.

The main aim is to improve the accuracy of the inversion results [1]. Secondly, a multiparameter inversion involves attenuation as an additional inversion parameter [7]. We investigate the impact of attenuation in application of elastic FWI with a passive  $Q_p$  model (Fig. 5). The true  $Q_p$  model is derived from the velocity model (Fig. 4a) by applying  $V_p - Q_p$  relation [4]:

$$\frac{1}{Q_p} = \alpha_p \frac{v_p}{\pi f - \frac{\alpha_p^2 v_p^2}{4\pi f}} \tag{8}$$

where  $\alpha_p$  is the intrinsic attenuation of the velocity model. Using a realistic gas cloud model (Fig. 4), we performed acquisition geometry with number of sources and receivers. The source time function is a Ricker wavelet with a peak frequency 12 Hz. Figure 6 is used for initial model for elastic inversion. Based on true model, their residuals are shown for shot 1 located at  $x = 0$  m (Fig. 7). In the case of two

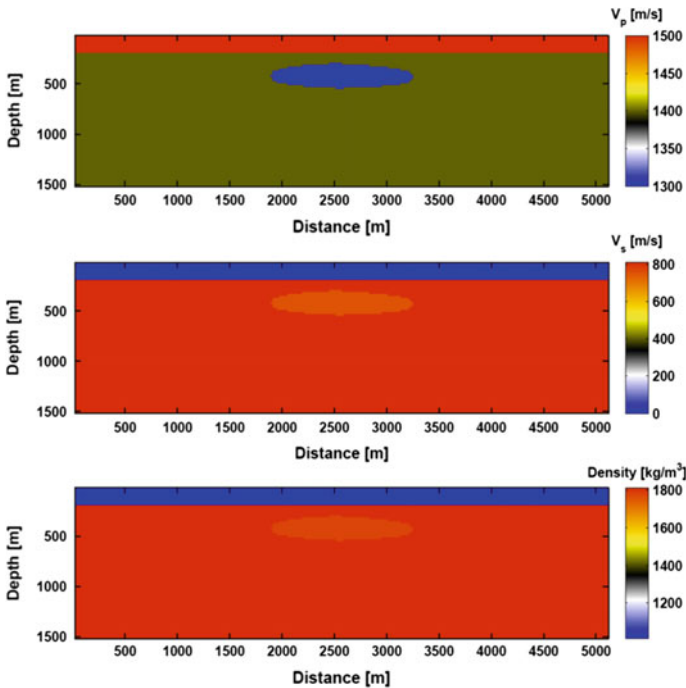


Fig. 4 True velocity and density model for elastic FWI

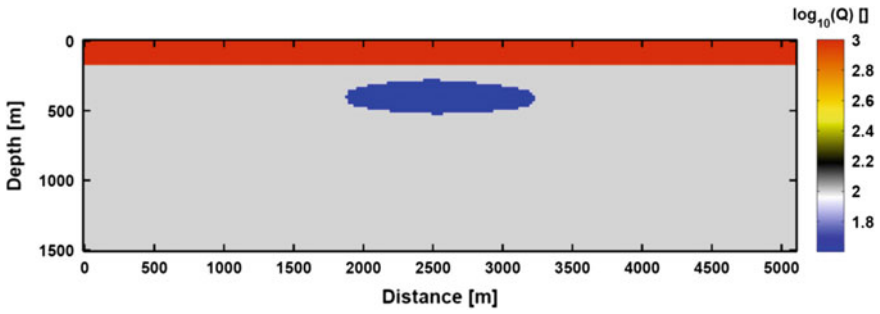


Fig. 5 True  $Q$  model

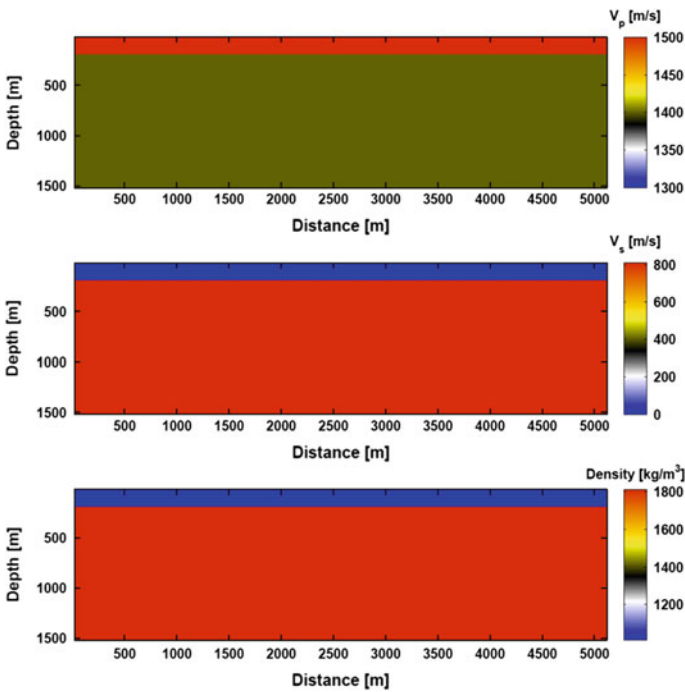


Fig. 6 Initial velocity and density model

layers with overburden model, the velocity and density are assumed as per following:  $Q_p = 1000$  for top layer (i.e., water layer),  $Q_p = 100$  in the sediment and  $Q_p = 40$  in the low velocity zone. Shear wave velocity has been estimated using empirical relation  $V_s = V_p/\sqrt{3}$ , and the density model is estimated using Gardner's relation.

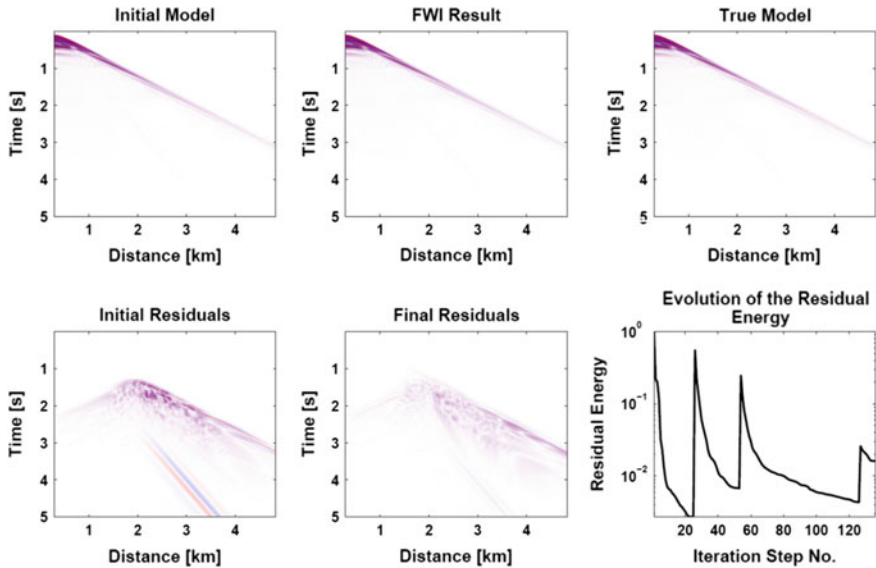
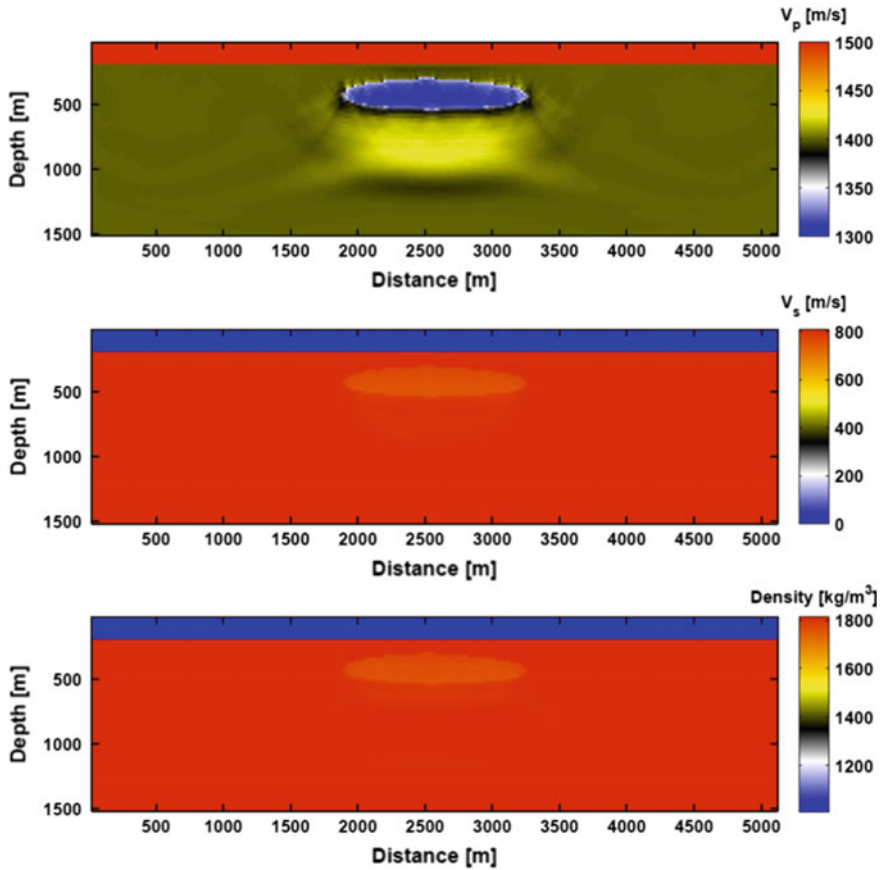


Fig. 7 Shot gathers and corresponding residual plot

Using elastic approach with  $Q$  model, inversion results are very promising as shown in Fig. 8.  $P$ -wave inversion is more effective as compared to  $S$ -wave and inverted density parameters. Exact  $Q$  model (Fig. 5) is used for elastic inversion. However, if uniform  $Q$  model is used, there are much significant effects of attenuation on  $S$ -wave and density parameter.

### 3 Discussion and Conclusions

Acoustic inversion shows promising results with complex model. Inversion from low to high frequency shows that the acoustic full waveform inversion is very effective and it explains well the structural properties of subsurface. In spite of incorporating attenuation, the result is very similar to the velocity model. In practice, a good  $Q_p$  model is usually unknown. Empirical relations can be used to derive a  $Q_p$  model from the initial velocity model. However, in general, they do not account for all rock types and physical conditions occurring in the given subsurface. As mentioned above, a certain choice of a homogeneous passive  $Q_p$  model might cause unsatisfactory results. The availability of a sufficiently good passive quality factor model allows the reconstruction of a reliable velocity model by applying the acoustic inversion scheme. However, such an appropriate good model does not necessarily have to be characterized by a high complexity being close to the true model.



**Fig. 8** Elastic FWI result of each model. There is a significant improvement in  $P$ -wave but not much in  $S$ -wave and density

**Acknowledgements** Authors thank to Centre for Seismic Imaging (CSI) and Universiti Teknologi PETRONAS for giving permission to publish this research work.

## References

1. Brenders, A., and R. G. Pratt, 2007, Full waveform tomography for lithospheric imaging: results from a blind test in a realistic crustal model: *Geophysical Journal International*, 168, 133–151.
2. Brossier, R., S. Operto, and J. Virieux, 2009, Robust elastic frequency-domain full-waveform inversion using the  $l_1$  norm: *Geophysical Research Letter*, 36, L20310.
3. Bunks, C., F. M. S. S. Z., and G. Chavent, 1995, Multiscale seismic waveform inversion: *Geophysics*, 60, 1457–1473.

4. Hamilton, E., 1972, Compressional-wave attenuation in marine sediments: *Geophysics*, 37, 620–646.
5. Jo, C. H., C. Shin, and J. H. Suh, 1996, An optimal 9-point, finite-difference, frequency-space, 2-D scalar wave extrapolator: *Geophysics*, 61, 529–537.
6. Kohn, D., D. D. Nil, A. Kurzmann, A. Przebindowska, and T. Bohlen, 2012, On the influence of model parametrization in elastic full waveform tomography: *Geophysical Journal International*, 191, 325–345.
7. Liao, Q., and G. A. McMechan, 1995, 2.5d full-wavefield viscoacoustic inversion: *Geophysical Prospecting*, 43, 1043–1059.
8. Prajapati, S., and D. Ghosh, 2015, Acoustic 2d full waveform inversion to solve gas cloud challenges: *Annals of Geophysics*, 58, S0426.
9. Pratt, R., Z. Song, P. Williamson, and M. Warner, 1996, Two-dimensional velocity models from wide-angle seismic data by wavefield inversion: *Geophysical Journal International*, 124, 232–340.
10. Pratt, R. G., C. Shin, and G. H. Hicks, 1998, Gauss-newton and full newton methods in frequency-space seismic waveform inversion: *Geophysical Journal International*, 133, 341–362.
11. Sirgue, L., and R. G. Pratt, 2004, Efficient waveform inversion and imaging: A strategy for selecting temporal frequencies: *Geophysics*, 69, 231–248.
12. Tarantola, A., 1984, Inversion of seismic reflection data in the acoustic approximation: *Geophysics*, 49, 1259–1266.
13. Virieux, J., and S. Operto, 2009, An overview of full waveform inversion in exploration geophysics: *Geophysics*, 74, WCC1–WCC26.

# Feasibility Study of Various Litho-Fluid Indicators for Better Hydrocarbon Prediction in Malay and Adjacent Basin

Syaza Zuhaira Shamsuddin, Maman Hermana, D.P. Ghosh  
and Ahmed Mohamed Ahmed Salim

**Abstract** The application of lithology and fluid indicators has helped the geophysicists to discriminate reservoirs to non-reservoirs from a field. This analysis is conducted to select the most suitable lithology and fluid indicator for the Malay basin that could lead to better eliminate pitfalls of amplitude. This paper uses different rock physics analyses such as Poisson's impedance, acoustic impedance, shear impedance, elastic impedance, LambdaMuRho (LMR), and  $SQ_p-SQ_s$  attribute. Poisson's impedance (PI) log is generated by using the method by determining the constant from AI-SI gradient. Then, litho-elastic impedance log is generated by correlating the gamma ray log with extended elastic impedance (EEI) log. The same application is used for fluid-elastic impedance by correlation of EEI log with water saturation or resistivity. The work is done on several well log data collected from different fields in Malay basin and its neighboring basin. Preliminary observations are done for three wells: Well 1, Well 2, and Well 3. The constant  $c$  in PI log for Well 2 is 1.305 and 1.58 for Well 3. There is an excellent separation between hydrocarbon sand and background shale for Well 3 from different cross-plot analyses. The similar method done on the Well 2 shows fair separation of silty sand and gas sand using  $SQ_p-SQ_s$  attribute which can be correlated with well log data. Meanwhile, the third well shows good separation in LMR plot. Based on the point distribution histogram plot, different lithology and fluid can be separated clearly. There are many attributes available in the industry used to separate the lithology and fluid; however, some of the methods are not suitable for the application to the basins in Malaysia.

**Keywords** Litho-fluid indicator · Poisson impedance ·  $SQ_p-SQ_s$  · EEI

---

S.Z. Shamsuddin (✉) · M. Hermana · D.P. Ghosh  
Center for Seismic Imaging, Universiti Teknologi Petronas,  
31750 Bandar Seri Iskandar, Perak, Malaysia  
e-mail: syazashamsuddin90@gmail.com

A.M.A. Salim  
Department of Geosciences, Universiti Teknologi Petronas,  
31750 Bandar Seri Iskandar, Perak, Malaysia  
e-mail: mohamed.salim@petronas.com.my

## 1 Introduction

Malaysia has been producing hydrocarbons from various fields since the early 1900s, with the first field found in onshore Miri, Sarawak. The following major discoveries were made offshore in Sarawak, Sabah, and Malay Basins. The location of Malay Basin is at the eastern side of Peninsular Malaysia and surrounded by Pattani Basin at north, West Natuna Basin at south, Sarawak and Sabah basins at its southeastern part. Malay basin is known to be an extensional pull-apart basin with anticlines trending from east to west direction including series of half-grabens. Primarily, the basin is formed during the late Eocene to early Oligocene, followed by thermal subsidence leading to sedimentation in the Early Miocene. Later in the Middle Miocene, regional stress fields changed and the basin inverted forming east–west anticlines trend [6].

One of the geophysical issues faced by the interpreters is the pitfalls of amplitude, for example, coal, soft shale, and high-porosity brine sand. Coal has been the excellent source rock for Malay basin reservoirs and good horizon markers; however, the presence of coal masks interferes with the reservoirs underneath by forming strong soft negative impedance. This is due to the acoustic properties of coal that are low density and low velocity [1], which show similar acoustic impedance response to the gas sand. Another issue is that good porosity brine sand shows similar amplitude versus offset (AVO) response to hydrocarbon sand. In the case of poor quality gas sand, the reflectivity shows positive impedance which might be misguided as non-reservoir [2]. In addition, soft shale that composed of unconsolidated rocks (especially younger sediments) produces lower acoustic impedance than the surrounding rocks, similar response as hydrocarbon sand. It is difficult to differentiate the amplitude anomalies based on acoustic impedance alone, whether they are caused by the lithology or fluid content. Therefore, it is important to determine which elastic parameters are able to separate hydrocarbon sand from the background lithology.

The main objective of this paper was to choose the best or the most suitable lithology and fluid indicator for Malay basin and its adjacent basin that could lead to better interpretation of its hydrocarbon reservoirs.

## 2 Methodology

This paper addresses different applications of rock physics analysis such as acoustic and shear impedance, Poisson's impedance, extended elastic impedance, Poisson ratio,  $SQ_p$ – $SQ_s$  attribute, and Lambda-Mu-Rho (LMR). The work is done on several well log data collected from different fields in Malay basin and its adjacent basin. In the beginning, various elastic properties are generated using different rock physics from the well log data, and the interest zones are identified for each well. Later, cross-plot analyses are done using logs to observe which attributes can



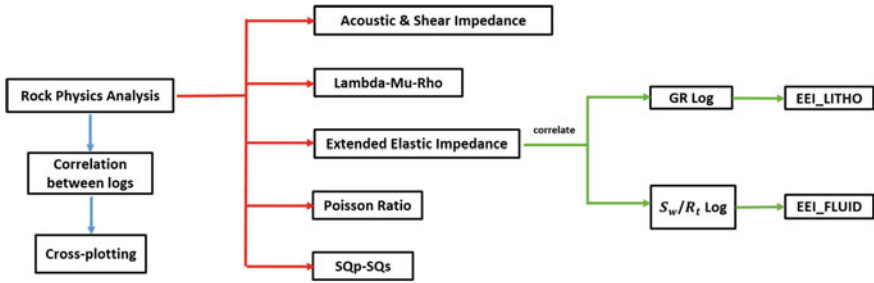


Fig. 1 Workflow of the project

separate lithology and fluid better. The cross-plotting analysis and EEI correlation is done at a certain depth (including reservoir target) to omit the effect of depth trend (Fig. 1).

### 2.1 Poisson Impedance

The Poisson impedance (PI) analysis is adopted from the method introduced by Quakenbush et al. [3]. PI practices the rotation of axis in AI–SI cross-plot to maximize the separation of litho–fluid. The method uses constant  $c$  derived from the gradient of AI versus SI plot in order to obtain Poisson impedance value based on Eq. (1).

$$AI - cSI = PI \tag{1}$$

The Poisson impedance log is generated for two constant values; (1) 1.41 (theoretical) and (2) derived from well to compare the suitable Poisson impedance for the well.

### 2.2 Extended Elastic Impedance

Whitcombe [4] extended the elastic impedance (EI) theory to maximize the separation of fluid or lithologies by introducing the angle  $\chi$ . The normalization of elastic impedance equation, where the angle  $\theta$  is replaced by  $\chi$ , is shown in Eq. (2).

$$\text{EEI}(\chi) = V_{p0}\rho_0 \left(\frac{V_p}{V_{p0}}\right)^p \left(\frac{V_s}{V_{s0}}\right)^q \left(\frac{\rho}{\rho_0}\right)^r, \quad (2)$$

where  $p = \cos \chi + \sin \chi$ ,  $q = -8K \sin \chi$ ,  $r = \cos \chi - 4K \sin \chi$

The EEI logs are correlated with gamma ray log to produce EEI\_litho log and resistivity or water saturation log to obtain EEI\_fluid log.

### 2.3 $SQ_p$ - $SQ_s$

These attributes are derived based on attenuation concept—rock physics approximation:

$$SQ_p = \frac{5 [(M/G) - 2]^2}{6\rho [(M/G) - 1]} \quad (3)$$

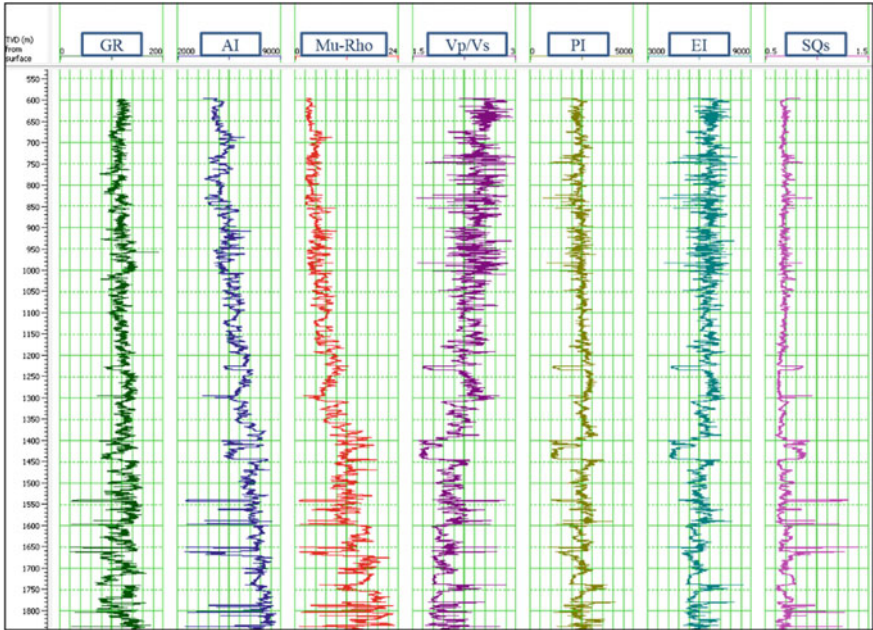
$$SQ_s = \frac{10}{3\rho} \frac{M/G}{[3(M/G) - 2]} \quad (4)$$

$SQ_p$  is defined as scaled inverse quality factor of p-wave which is used as lithology indicator, while  $SQ_s$  is used as pore fill indicator [5]. From Eqs. (3) and (4), the M, G, and  $\rho$  represent bulk modulus, shear modulus, and density, respectively. The M/G is approximated as  $(V_p/V_s)^2$ .

## 3 Results

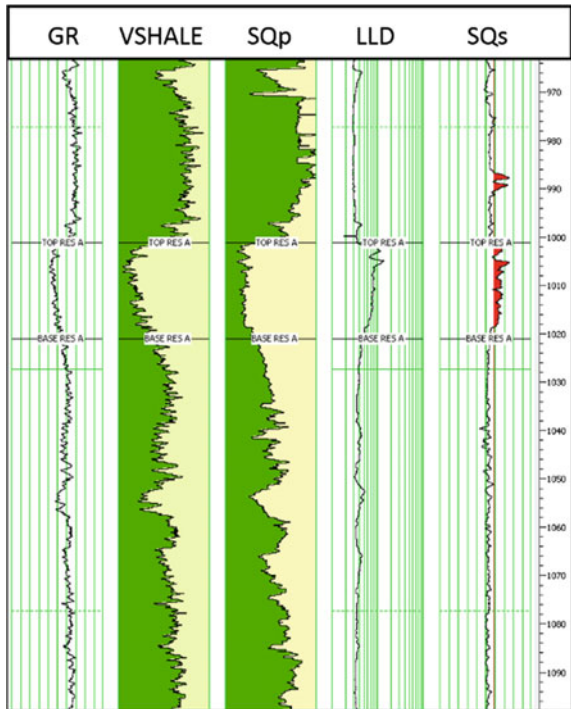
Three wells are used for the observations, namely Well 1, Well 2, and Well 3. Overall, PI  $SQ_p$ ,  $SQ_s$  and EEI logs are the logs which are not affected by depth trend as shown in Fig. 2; as the depth increases, the compaction trend affects the rock properties. If the reservoir target is at shallow depth, it would be easier to distinguish the lithology; however, most of the reservoirs are present at deeper formation. The example from Well 3 shows that the attribute  $SQ_p$  manages to imitate the gamma ray log but with high value of coal, while attribute  $SQ_s$  is similar to the true resistivity log (Fig. 3). In case of PI log, Well 2 has constant value of 1.305, which is almost similar constant value to the theoretical value, 1.41. On the other hand, Well 3 shows better impedance contrast when “c” value is 1.58.

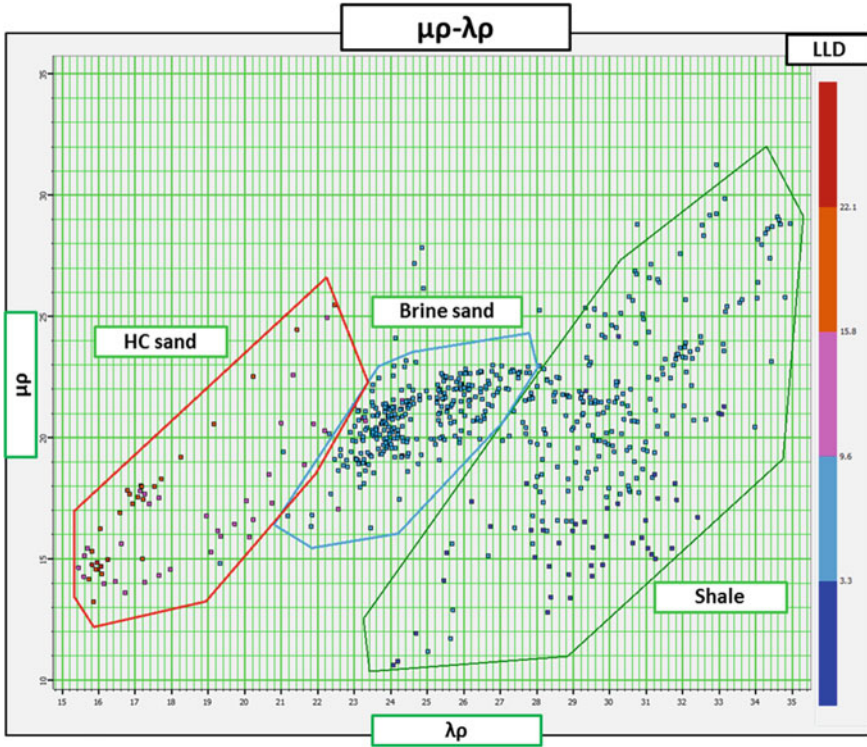
There is an excellent separation between hydrocarbon sand and background shale from several cross-plots generated. The first well, the lithology in Well 1, is



**Fig. 2** Logs from Well 2 showing that PI, EI, and SQ<sub>s</sub> do not have the presence of compaction trend

**Fig. 3** Comparison of SQ<sub>p</sub> and SQ<sub>s</sub> logs in Well 3 with gamma ray log and resistivity log, respectively

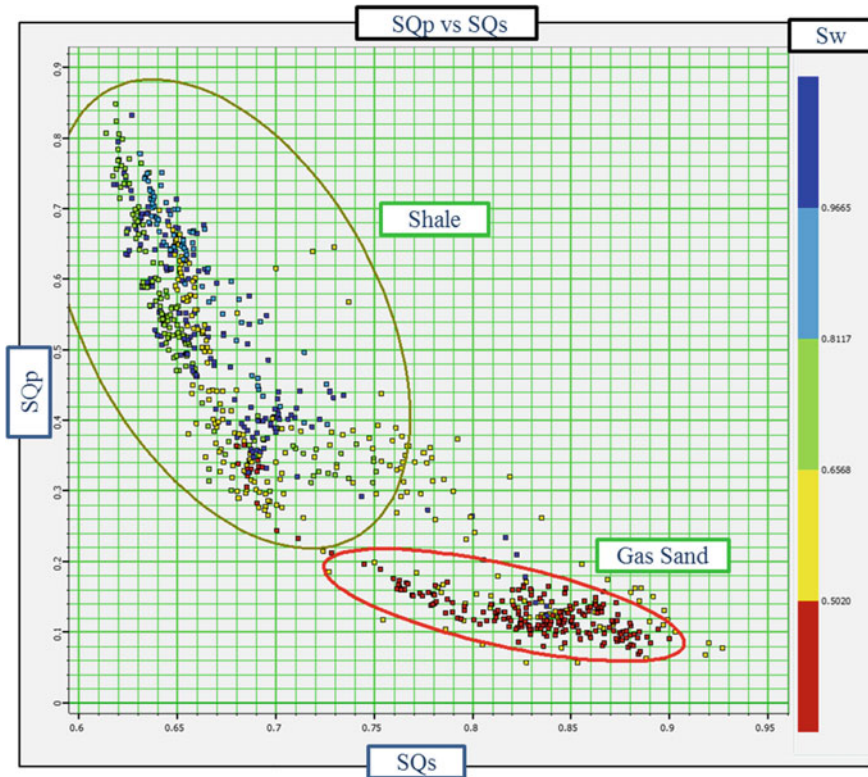




**Fig. 4** Cross-plot of Lambda-Rho from Well 1 manages to differentiate three lithology

distinguished the best in LMR plot as it manages to separate clearly the gas sand from the brine sand and shale (Fig. 4). The gas sand cluster is represented by the low-to-high values of Mu-Rho and low values of Lambda-Rho.  $SQ_p-SQ_s$  attributes are able to discriminate the lithology for Well 2 lithology, where in Fig. 5, the hydrocarbon sand cluster is deviated away from the wet trend. The correlated EEI cross-plot in Fig. 6 shows good separation of gas sand from shale, which can be difficult to differentiate from logs only. The gas sand cluster is represented by the combination of low EI\_litho and EI\_fluid values from Well 3.

The occurrence of different lithology can be determined much clearer using the histogram plot. Figure 7 shows a summary of the point distribution constructed from four different elastic properties at Well 2. Each lithology can be defined based on the distribution curves trends by assuming the points are normally distributed. In



**Fig. 5** Cross-plot of  $SQ_p$  and  $SQ_s$  attributes. Color key is represented by water saturation values

the case of Poisson ratio, the curves can be grouped into three different lithology: gas sand, silty sand, and shale (Fig. 7a). This case is applicable for Lambda-Rho ( $\lambda\rho$ ) and elastic impedance (EI) distributions (B and C, respectively) with three lithology types can be defined. However, both EI and  $\lambda\rho$  do not show distinct separation between silty sand (yellow) and shale (green), as silty sand and shale curves might overlap with each other. Hence, it is possible for other interpreters to group the lithology into two classes only. Meanwhile,  $SQ_s$  attribute presents four clear distribution curves. From the well display on its right, lithology can be categorized separated into shale (gray), poor silty sand (yellow), silty sand (green), and gas sand.



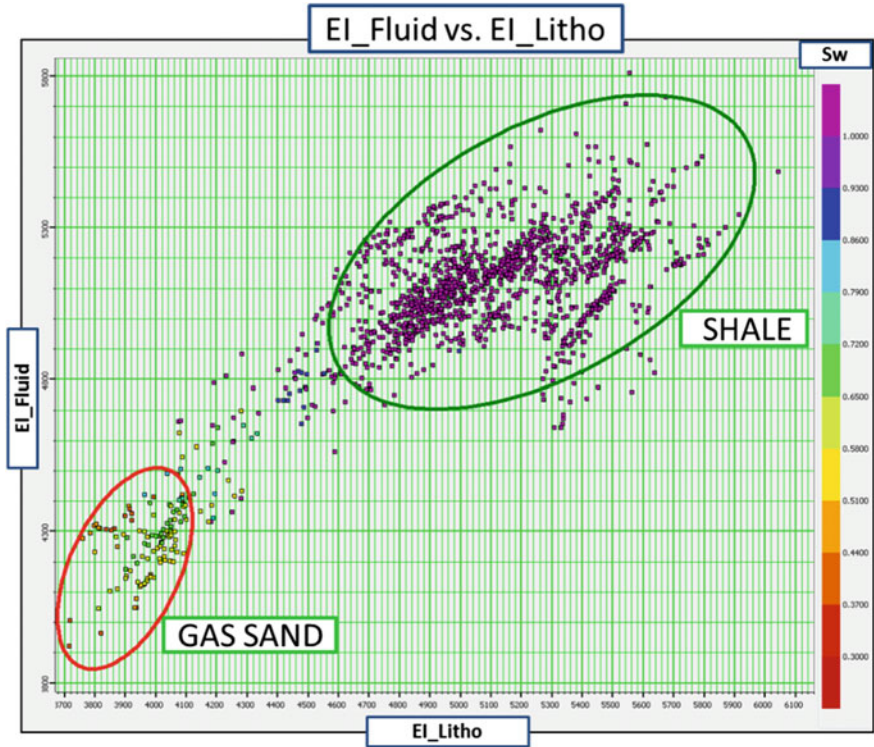


Fig. 6 Cross-plot of elastic impedance based on Connolly (1999). Color key represents the water saturation values

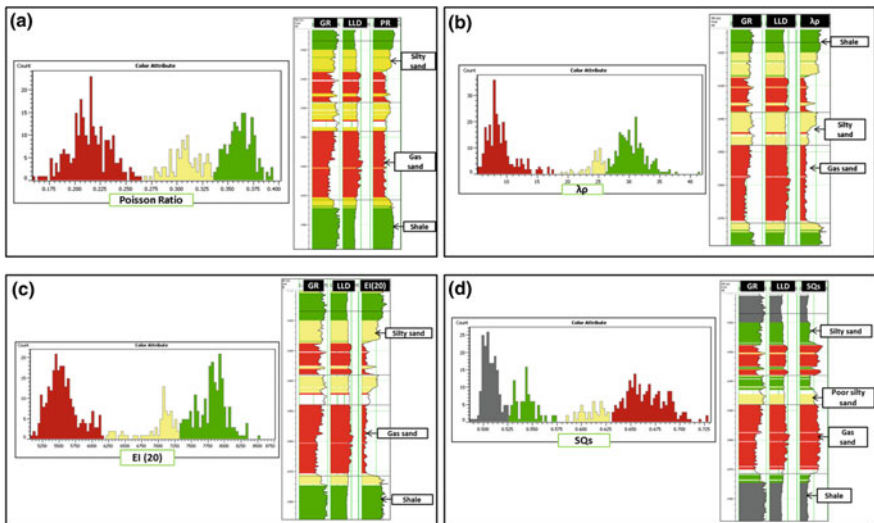


Fig. 7 Plot a represents the frequency of Poisson ratio distribution, b represents Lambda-Rho, c displays the plot of elastic impedance at 20° angle, and d shows the distribution of SQs points. On the right side of each histogram shows the lithology type at well location with GR, resistivity, and elastic parameters log (from left to right in order)

## 4 Conclusions

Various methods are available in the industry to delineate reservoir from non-reservoir. However, the methods are not applicable to all fields worldwide. For the shale-dominated well or well that has distinct lithology variables, it would be convenient to use conventional rock physics methods to separate the lithology and fluid. On the other hand, if the well is dominated by silty sand, it is difficult to distinguish the pay sand based on the available rock physics methods only. The analyses suggest that the most suitable method for the silty sand-dominated formation is the  $SQ_p$ – $SQ_s$  attribute as they manage to display clear separation of hydrocarbon sand from the background trend and different lithology. The LMR method is able to distinguish clearly the gas and brine sand from shale-dominated formation. This analysis explained in this paper is based on a well domain only. However, implementation of inversion of pre-stack seismic data could further analyze the effect of selected methods on larger scale.

**Acknowledgements** We would like to express our deepest gratitude to the parties involved in completing this paper especially Yayasan Universiti Teknologi Petronas (YUTP) for funding this project, PETRONAS for providing the well log data, and the Center for Seismic Imaging (CSI) for the complete facilities and to the members for the never-ending support.

## References

1. Q. Yao and D. Han, "Acoustic properties of coal from lab measurement," in *SEG Las Vegas 2008 Annual Meeting*, Nevada, 2008.
2. D. P. Ghosh and M. Brewer, *Interpretation of Amplitudes: Pitfalls & Lessons Learnt*, PETRONAS CARIGALI, 2007.
3. M. Hermana, D. P. Ghosh and S. W. Chow, "Optimizing the Lithology and Pore Fluid Separation using Attenuation Attributes," in *Offshore Technology Conference Asia*, Kuala Lumpur, 2016.
4. P. Connolly, "Elastic Impedance," *The Leading Edge*, pp. 438–452, April 1999.
5. M. Quakenbush, B. Shang and C. Tuttle, "Poisson Impedance," *The Leading Edge*, pp. 128–138, February 2006.
6. D. Ghosh, M. F. Abdul Halim, M. Brewer, B. Viratno and N. Darman, "Geophysical issues and challenges in Malay and adjacent basins from an E&P perspective," *The Leading Edge*, pp. 436–449, April 2010.

# Growth Timing of Southern Field High Carbonates, Central Luconia Province

W.K. Chung and D. Ghosh

**Abstract** The growth timing of the studied carbonate platform at Central Luconia Province is approximately 4 million years governed by series of third-order sea-level fluctuations and syndepositional tectonics. The prevalent sea-level fluctuations during the Miocene developed a flat-topped limestone interval, capped by a relatively thin dolomitic interval. The first karstification period occurred during the sea-level drop in the Burdigalian stage, over a complex horst and graben setting. The complex surfaces were believed to be predominantly configured by the seafloor expansion of the South China Sea, prior to the carbonate initiation and growth. The second subaerial exposure stage was highlighted as the most prominent karstification period during the Langhian stage, with sporadic distribution of sinkholes, paleocollapse caves, and Uvalas. The third subaerial exposure period is deemed to be a minor karstification stage where a slight fall in the sea level led to buildout and expansion of the carbonate platforms. The final growth horizon is finally drowned during the Serravallian without any further subaerial exposure. A growth timing log is developed based on seismic time slices evidences, sea-level curves, and tectonic information highlighting karstification stages of the carbonate platform.

**Keywords** Karstification · Carbonate platform · Central Luconia · Growth timing

## 1 Introduction

The growth timing of the selected carbonate platform remained limited in information using only palynological estimates of the overlying clastic sediment age. Karst evidences and platform morphology on the time slices provided an alternate insight of the growth timing for the carbonate platform. Thus, further seismic evidences allow an alternate timing estimate in the form of log to be constructed. The platform growth initiation of the 200 buildups in Central Luconia Province is

---

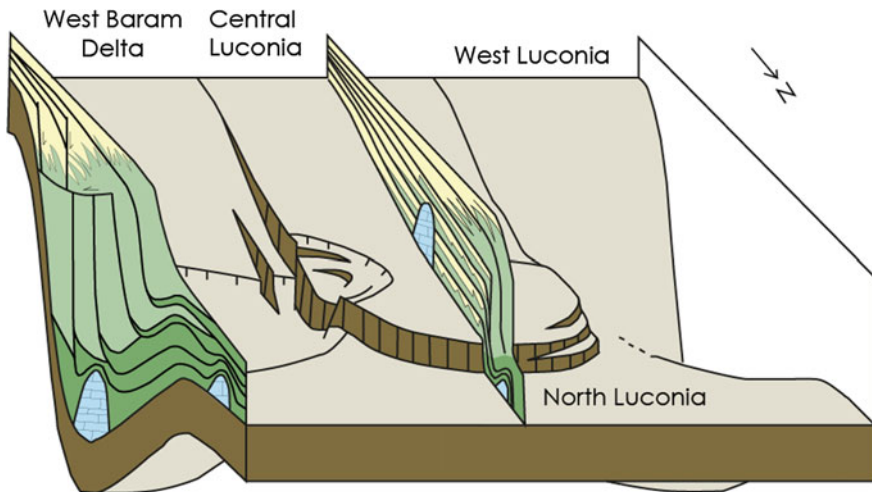
W.K. Chung · D. Ghosh (✉)  
Universiti Teknologi Petronas, 31750 Tronoh, Perak, Malaysia  
e-mail: drdeva@petronas.com.my



asymmetrical as some platforms appear to grow as early as the Late Oligocene while some later right after the Middle Miocene Unconformity (MMU) [1–5]. Submerged tropical karst landforms in the southern Ryukyu Islands, Japan exhibit various types of tropical karst landforms including fluviokarst, doline karst, cockpit karst, polygonal karst, Uvalas, and mega dolines [6].

## 2 Tectonic Setting

The studied platform is developed over the southern region of Central Luconia Province, covering an area of approximately 200 km<sup>2</sup> with 14 km in length. Central Luconia Province is noted as an independent shallow shelf microcontinent as shown in Fig. 1, which provided a pedestal for approximately 200 carbonate buildups during the Oligo-Miocene period. The active tectonics initiated by the seafloor spreading of the South China Sea at about 45 Ma [7] led to the development of complex syndepositional tectonic horst and graben system, thus impacting the growth morphology of carbonate platform in Central Luconia. The seafloor spreading age is initially thought to be ceased around 15.5 Ma; however, the cessation timing is further revised to 20.5 Ma [8, 9].



**Fig. 1** Generalized horst and graben structural framework of Central Luconia Province suggesting eight regressive clastic cycles overlying the Oligo-Miocene carbonate platforms (modified after Kosa 2015)

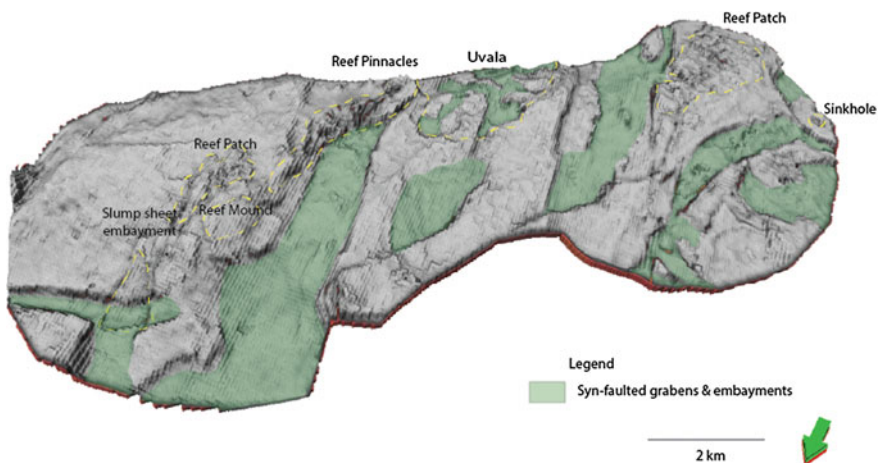
### 3 Data and Methodology

A high-resolution 3D pre-stacked time migrated seismic volume of the selected carbonate platform, 14 km in length, was acquired offshore Sarawak in 2003 and processed from November 2003 to October 2004. An array of seismic sections consisting 226 inline seismic and 1125 crossline seismic section forms the volume cube with an inline interval of 25 and 12.5 m for the crossline interval. The parameters used for the seismic processing involve data resampling at 3 ms and a low cut filter of 5 Hz. 18 dB/Oct. Corrections such as spherical spreading, tidal, residual statics, and water bottom deghosting were applied to remove noises and unwanted artifacts. The data are zero-phased. Seismic data conditioning and attribute application were conducted prior to the interpretation. The major growth episodes were interpreted at every interval on true amplitude reflectivity, prior in producing a horizon to crosscut the attribute cube. Additional information such as palynological analysis of overlying clastic interval provides further insight of the plausible timing estimate of the carbonate platform's demise. Sea-level curve [10] is then correlated with the time slices evidences [11] and horizon model to establish a growth timing log.

## 4 Result and Discussion

### 4.1 Burdigalian Stage Karstification (~17 Ma)

The first major carbonate growth shown in Fig. 2 grew in a patchy trend around the complex horst and graben setting of the field, governed by a series of rotation,

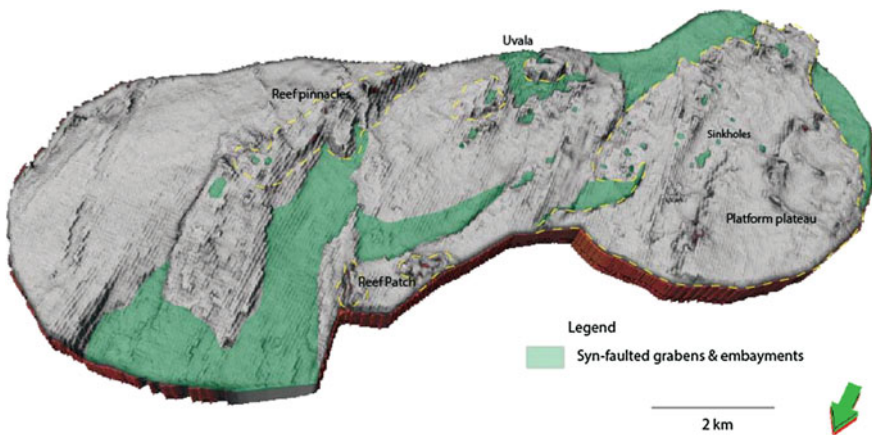


**Fig. 2** Interpreted karstified horizon model showing various forms of karstification including sinkholes, Uvalas, and tower pinnacles

tilting, and elevation. A sea-level drop period during the Burdigalian stage about 16.5 Ma led to a period of minor karstification of the carbonate platform. Isolated subcircular sinkhole depression with dimension of 250 m in length and 165 m in width was present, however, to very limited extent. Uvalas denote a mass interconnected paleocave collapse forming an enclosed elongated depression. Reef pinnacles were developed over the tilt-elevated edge of the sheared grabens while reef patch developments were more common on flat pedestals. A slump sheet embayment of 950 m in length and up to 690 m in width modeled exhibits an acute slumping angle of meteoric drainage incision. A T-shaped embayment formed by the complex syndepositional tectonics perpendicular to the slump sheet slope is of 250 m in width with a catchment area length of more than 750 m.

#### 4.2 Langhian Stage—Period of Major Karstification (~15.5 Ma)

The Langhian stage shown in Fig. 3 is highlighted as a prominent period of karstification with a sporous distribution of paleocollapse cave up plaguing the carbonate platform. Isolated cave depressions exhibit subcircular characteristics generally having a length ranging from 160 to 200 m and width ranging from 50 to 100 m. A depression deepening observed at the Uvalas flanking a tower karst body with a dimension of 505 m in length and 285 m in width denotes the severity of the tropical paleoclimate denudation. Reef patches visible on the northern elevated flank denote submerged shallow shelf environment, which maintains reefal patch growth, and at the same time denude subaerially exposed regions. The embayments were highlighted as down dipping depression. It is repositories for younger

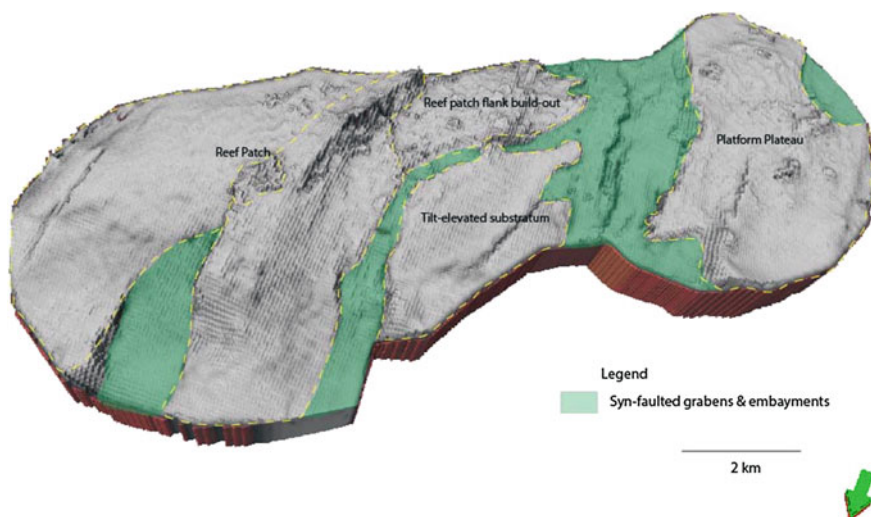


**Fig. 3** Langhian stage period showing the severity of the karstification period with the sporous distribution of the isolated sinkholes and paleocollapse caves

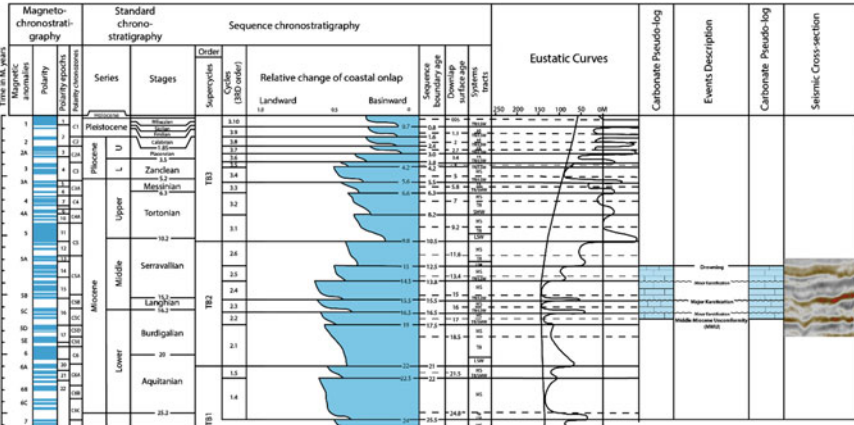
carbonate sediments whether biogeochemically precipitated in situ or as a catchment area for eroded reefal materials.

### 4.3 *Serravallian Stage Karstification (13 Ma)*

Prominent karst evidences on the pre-demise horizon shown in Fig. 4 are very limited to nonexistent. Carbonate buildout features are evident with an estimate of 3.3 km reefal patch buildout of overgrowth burying the existing Uvalas in this field. The generic preference of reefal growth observed has a higher tendency to be centralized along the apex of the tilted edge of the substratum. Minor evident of karst features on this horizon implies post-burial karstification instead of subaerial denudation. Time slices evidences has shown a slight drop of sea level correlating to the sea-level fall in the Langhian stage ( $\sim 14.5$  Ma) which shows a sudden expansion and buildout highlighted as a period of minor karstification. It is debatable that some authors believed that the demise of the development of carbonate platform ceased with the advent of siliciclastic influx, however, on this selected platform shows no sign of clastic heterogeneities, though drowning characteristics of reefal bodies; failing to catch up with the surge of sea level is evident. The model implies that the selected carbonate platform in this field was drowned with the prevalent surge of sea level with no evidence of further subaerial exposure. The influx of the younger clastic sediments for this platform, an overlying shale, is



**Fig. 4** The pre-demise growth horizon exhibits reefal buildout and catch-up, however, showing very minor or limited karstification signs



**Fig. 5** Growth timing log of studied carbonate platform, Central Luconia Province, offshore Sarawak (correlated with sea-level curve by, Haq et al. 1987)

estimated to be of Tortonian stage from palynological analysis, which suggested a period of nondeposition in the transition.

### 4.4 Carbonate Platform Growth Timing Log

A major carbonate buildout is denoted during the Middle Miocene Unconformity period (~17 Ma) in the absence of the clastic deposition shown in Fig. 5. A short-term sea-level drop during the Burdigalian stage (~16.5 Ma) exposed the carbonate platform to meteoric waters. A major sea-level drop during the Langhian stage (~15.5 Ma) leads to prominent paleocollapse cave feature. The visibility on the 2D inline seismic cross section is obvious, which correlates to the severity of the karstification. A mild decline of sea level during the Langhian stage (~14.5 Ma) in a failed attempt in platform drowning [11] resulted in platform expansion observed on the time slices. The platform’s final growth horizon is of a capping dolomitic layer with an estimated age of 13 Ma via strontium isotope analyses [12].

## 5 Conclusion

A growth timing log of the studied carbonate platform is constructed, highlighting one major and two minor karstification stages, governed by several third-order eustatic fall during the Miocene. The first decline of sea level during the Burdigalian stage at about 16.5 Ma subaerially exposed the carbonate platform imprinting large meteoric drainage sheet patterns. A second major karstification

stage is highlighted during the Langhian stage around 15.5 Ma that leads to severe karstification plaguing the platform with collapsed caves. The final subaerial exposure period of this platform is estimated to be during Langhian at about 14.5 Ma, which leads to very minor karstification denoted by the evidences of platform sudden expansion. The final growth horizon around 13 Ma implies that the platform does not resurface after being completely drowned prior to the siliciclastic influxes from proto-Borneo during the Tortonian stage.

**Acknowledgements** The authors gratefully acknowledge PETRONAS and Universiti Teknologi PETRONAS for financial support and funding for this research activity.

## References

1. K. K. Ting, B. J. Pierson, O. Al-Jaadi, and P. F. Hague, "Effects of syn-depositional tectonics on platform geometry and reservoir characters in Miocene carbonate platforms of Central Luconia, Sarawak," in *International Petroleum Technology Conference*, 2011.
2. S. F. Jamaludin, M. Pubellier, and D. Menier, "Relation of Syn-Depositional Faulting with Carbonate Growth using Miocene Carbonate Platforms of Central Luconia Province, Malaysia," 2014.
3. D. Menier, B. Pierson, A. Chalabi, K. K. Ting, and M. Pubellier, "Morphological indicators of structural control, relative sea-level fluctuations and platform drowning on present-day and Miocene carbonate platforms," *Marine and Petroleum Geology*, vol. 58, pp. 776–788, 2014.
4. V. Zampetti, W. Schlager, J.-H. van Konijnenburg, and A.-J. Everts, "Architecture and growth history of a Miocene carbonate platform from 3D seismic reflection data; Luconia province, offshore Sarawak, Malaysia," *Marine and Petroleum Geology*, vol. 21, pp. 517–534, 5// 2004.
5. E. Koša, "Sea-level changes, shoreline journeys, and the seismic stratigraphy of Central Luconia, Miocene-present, offshore Sarawak, NW Borneo," *Marine and Petroleum Geology*, vol. 59, pp. 35–55, 2015.
6. H. Kan, K. Urata, M. Nagao, N. Hori, K. Fujita, Y. Yokoyama, *et al.*, "Submerged karst landforms observed by multibeam bathymetric survey in Nagura Bay, Ishigaki Island, southwestern Japan," *Geomorphology*, vol. 229, pp. 112–124, 2015.
7. A. Cullen, P. Reemst, G. Henstra, S. Gozzard, and A. Ray, "Rifting of the South China Sea: new perspectives," *Petroleum Geoscience*, vol. 16, pp. 273–282, 2010.
8. U. Barchhausen, M. Engels, D. Franke, S. Ladage, and M. Pubellier, "Evolution of the South China Sea: Revised ages for breakup and seafloor spreading," *Marine and Petroleum Geology*, vol. 58, Part B, pp. 599–611, 12// 2014.
9. S. Steuer, D. Franke, F. Meresse, D. Savva, M. Pubellier, and J.-L. Auxietre, "Oligocene–Miocene carbonates and their role for constraining the rifting and collision history of the Dangerous Grounds, South China Sea," *Marine and Petroleum Geology*, vol. 58, pp. 644–657, 2014.
10. B. U. Haq, J. Hardenbol, and P. R. Vail, "Chronology of fluctuating sea levels since the Triassic," 1987.
11. W. K. Chung, D. Menier, S. N. F. Jamaludin, and D. Ghosh, "Geomorphology and Karstification of the Southern Field High Carbonates, Central Luconia Province," *Offshore Technology Conference Asia 2016*, 2016.
12. Y. Ali, "M. and Abolins, P.[1999] Central Luconia Province," *The Petroleum Geology and Resources of Malaysia*. PETRONAS, p. 381, 1999.

# Seismic Wave Simulation Using a TTI Pseudo-acoustic Wave Equation

S.Y. Moussavi Alashloo, D. Ghosh and W.I. Wan Yusoff

**Abstract** The significance of considering anisotropy in seismic processing and imaging is extensively recognized by geophysicists. Seismic wave equation operates as a kernel of imaging and inversion algorithms. Although seismic anisotropy is inherently an elastic phenomenon, the elastic anisotropic wave equation is used rarely in anisotropic imaging techniques due to its heavy computing process. In this paper, we aim to employ a pseudo-acoustic TTI wave equation to simulate the seismic wave propagation in anisotropic media. First, the theory of deriving the TTI pseudo-acoustic coupled equations is described, and then, the results of wave modeling are demonstrated. Finally, we investigate the accuracy and efficiency of the considered technique.

**Keywords** Seismic anisotropy · Wave propagation · TTI · VTI

## 1 Introduction

The significance of considering anisotropy in seismic processing and imaging is extensively recognized by geophysicists. The primary causes of seismic anisotropy in the subsurface are alignment of mineral grains, fractures network, and thin layering. In P-wave imaging, isotropic imaging algorithms have been mostly developed for tilted transverse isotropy (TTI) and vertical transverse isotropy (VTI) media [1–3]. Transverse isotropy, the simplest form of anisotropy, exists when thin bed sequences, perpendicular to symmetry axis, are isotropic. A medium is called VTI where thin beds are horizontal, and it is called TTI where layers are tilted due to tectonic activities (Fig. 1). VTI anisotropy commonly exists in sedimentary media where lithification ordinarily happens by the vertically oriented

---

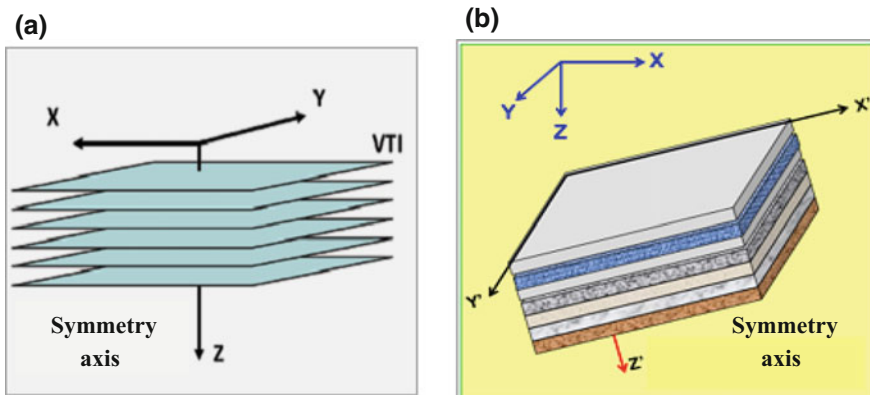
S.Y. Moussavi Alashloo (✉) · D. Ghosh · W.I. Wan Yusoff  
Center of Seismic Imaging, Department of Geoscience,  
Universiti Teknologi PETRONAS, 32610 Seri Iskandar, Malaysia  
e-mail: y.alashloo@gmail.com



compaction pressure. Strong tectonic stress can also create cracks and fractures in thin bed interfaces, which results in an azimuthal anisotropy [4–6].

Seismic wave equation operates as a kernel of imaging and inversion algorithms. Although seismic anisotropy is inherently an elastic phenomenon, the elastic anisotropic wave equation is used rarely in anisotropic imaging techniques due to its heavy computing process. Pseudo-acoustic approximations were suggested to mitigate the computational cost [7]. Alkhalifah [8] first demonstrated that by setting the vertical S-wave velocity to zero for VTI media, one can extract much simpler dispersion relation than the elastic expression. He thereafter developed an acoustic VTI wave equation by using the dispersion relation which yielded acceptable approximations to the elastic equation [9]. Several pseudo-acoustic wave equations were later derived based on Alkhalifah's dispersion relation [10, 11]. Another approach, to obtain a pseudo-acoustic wave equation, uses Hooke's law and the equations of motion in which the vertical S-wave velocity is also considered equal to zero [12, 13]. In both mentioned methods, by taking the tilt of symmetry axis into account, the pseudo-acoustic TTI approximations can be achieved [14].

In this paper, we aim to employ a pseudo-acoustic TTI wave equation to simulate the seismic wave propagation in anisotropic media. First, the theory of deriving the TTI pseudo-acoustic coupled equations is described, and then, the results of wave modeling are demonstrated. Finally, we investigate the accuracy and efficiency of the considered technique.



**Fig. 1** Anisotropic models: **a** VTI and **b** TTI



## 2 Methodology

Following Alkhalifah's work, several alternatives of the coupled equations are suggested. Here, we present the theory of the TTI pseudo-acoustic wave equation proposed by Fletcher et al. [13]. Next, the method to create anisotropic synthetic data is demonstrated.

### 2.1 Theory

Alkhalifah's dispersion relation, where  $V_{sz}$  is assumed to be zero in the exact TTI dispersion relation, is given by:

$$\omega^4 = \left[ v_{px}^2 (\hat{k}_x^2 + \hat{k}_y^2) + v_{pz}^2 \hat{k}_z^2 \right] \omega^2 + v_{pz}^2 (v_{pn}^2 - v_{px}^2) (\hat{k}_x^2 + \hat{k}_y^2) \hat{k}_z^2 \quad (1)$$

where  $\omega$  is angular frequency,  $\hat{k}$  is wavenumber and the hat demonstrates its direction in a rotated coordinate system aligned with the symmetry axis,  $v_{pz}$  is the P-wave vertical velocity,  $v_{pn}$  is the P wave normal moveout (NMO) velocity which is defined by  $v_{pn} = v_{pz} \sqrt{1 + 2\delta}$ ,  $v_{px}$  is the P-wave horizontal velocity given by  $v_{px} = v_{pz} \sqrt{1 + 2\varepsilon}$ ,  $v_{sz}$  is the Sv-wave vertical velocity, and  $\varepsilon$  and  $\delta$  are Thomsen's parameters.

The rotated wavenumbers can be defined as:

$$\begin{aligned} \hat{k}_x &= k_x \cos\theta \cos\varphi + k_y \cos\theta \sin\varphi + k_z \sin\theta \\ \hat{k}_y &= -k_x \sin\varphi + k_y \cos\varphi \quad \hat{k}_z = -k_x \sin\theta \cos\varphi - k_y \sin\theta \sin\varphi + k_z \cos\theta, \end{aligned} \quad (2)$$

where  $\theta$  is the angle between the wavefront normal and the vertical axis, and  $\varphi$  is the tilt angle which is the angle between the symmetry axis and the vertical axis. After substituting Eq. (2) into Eq. (1) and applying an inverse Fourier transform, the following differential operators are generated:

$$\begin{aligned} H_1 &= \sin^2\theta \cos^2\varphi \frac{\partial^2}{\partial x^2} + \sin^2\theta \sin^2\varphi \frac{\partial^2}{\partial y^2} + \cos^2\theta \frac{\partial^2}{\partial z^2} + \sin^2\theta \sin 2\varphi \frac{\partial^2}{\partial x \partial y} \\ &+ \sin 2\theta \sin\varphi \frac{\partial^2}{\partial y \partial z} + \sin 2\theta \cos\varphi \frac{\partial^2}{\partial x \partial z} \end{aligned} \quad (3)$$

$$H_2 = \frac{\partial^2}{\partial x^2} + \frac{\partial^2}{\partial y^2} + \frac{\partial^2}{\partial z^2} - H_1. \quad (4)$$

By using the auxiliary function

$$q(\omega, k_x, k_y, k_z) = \frac{\omega^2 + (v_{pn}^2 - v_{px}^2)f_2}{\omega^2} p(\omega, k_x, k_y, k_z), \tag{5}$$

the new wave equations are defined as follows:

$$\begin{aligned} \frac{\partial^2 p}{\partial t^2} &= v_{px}^2 H_2 p + v_{pz}^2 H_1 q \\ \frac{\partial^2 q}{\partial t^2} &= v_{pn}^2 H_2 p + v_{pz}^2 H_1 q. \end{aligned} \tag{6}$$

The above-mentioned pseudo-acoustic equations are derived for 3D media, yet one can use them as a 2D propagator by removing one of the spatial variables.

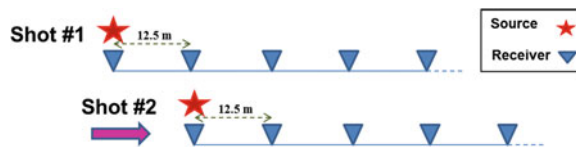
### 2.2 Forward Modeling

Seismic forward modeling is a numerical procedure which uses a geological model to simulate a seismic data acquisition experiment. Marmousi model is utilized as our geological model. The seismic survey is simulated by the Madagascar seismic package, open-source software, to record the subsurface responses by solving an acoustic VTI wave equation using the finite difference technique. An off-end array is employed where the source is placed past the beginning of receiver line, and the array is moving forward with interval of 12.5 m (Fig. 2). Several parameters need to be set for executing the seismic acquisition survey such as the source interval and group settings. Properties of the survey are demonstrated in Table 1. The Ricker wavelet is used for the source, and its frequency is defined as follows:

$$f_{\max} \leq \frac{V_{\min}}{2\Delta x} \tag{7}$$

where  $f_{\max}$  is the maximum frequency which can be defined for the source wavelet,  $V_{\min}$  is the minimum velocity of the model, and  $\Delta x$  is the interval between two grid points, in meter.

**Fig. 2** Off-end array with 12.5-m interval between receivers and shots



**Table 1** Survey parameters used for seismic forward modeling

Survey Parameters	
Source frequency	30 Hz
Source depth	8 m
Shot interval	12.5 m
Group depth	10 m
Group length	800 m
Receiver spacing	12.5 m
Sampling time	2.8 s
Time step	0.2 ms
Number of shots	673

The sampling interval  $\Delta t$  is given as follows:

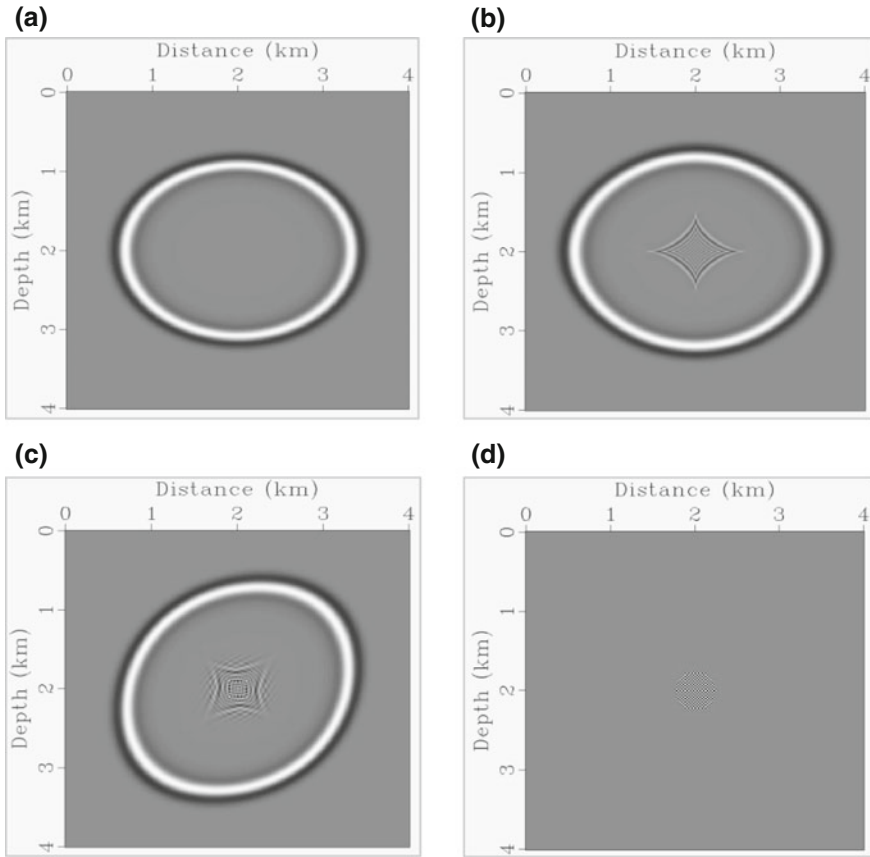
$$\Delta t \leq \frac{\sqrt{2}}{\pi} \frac{\Delta x}{V_{\max}} \quad (8)$$

where  $V_{\max}$  is the maximum velocity in the model. Fulfilling Eqs. (7) and (8) along with the right number of sampling ensures the stability of the finite difference modeling. Density model is an another input which we define it for both models as  $\rho = \text{velocity}/1.7$ .

### 3 Results and Discussion

2D wave simulation is conducted in a homogenous TI medium by employing the finite difference technique. Figure 3 illustrates wavefield snapshots for different TI conditions at time  $t = 0.8$  s. The wavefield produced in an elliptical VTI medium, where  $\varepsilon$  and  $\delta$  are equal to 0.25 (Fig. 3a), is completely free of Sv-waves, and only P-wave is propagated. In Fig. 3b and 3c, the anisotropic parameters are set as  $\varepsilon = 0.22$  and  $\delta = 0.12$ , and the tilt angles are  $\varphi = 0^\circ$  and  $\varphi = 45^\circ$ , respectively. It can be clearly seen that a diamond-shaped Sv wavefield, which is known as an artifact or spurious Sv-wave, appears along with P wavefield. Figure 3d, with  $\varepsilon = 0.06$  and  $\delta = 0.12$ , shows that if the condition  $\varepsilon - \delta \geq 0$  is violated, the finite difference modeling results in a null output.

Although the pseudo-acoustic approximation performs well in isotropic and elliptical anisotropic conditions, for an ellipticity, where  $\varepsilon \neq \delta$ , the Sv-wave velocity is only zero along the symmetry axis. In other directions, S-wave velocity has a value, and when the approximation is applied for imaging, Sv-wave components add noises to images. One way to remove S-wave artifacts is to locate the source in either isotropic or elliptical anisotropic environments. One can eliminate the converted Sv-waves either by adding finite Sv-wave velocities along the axis of symmetry which also fixes the instability problem [14] or by implementing a filter at each output time step.



**Fig. 3** Pseudo-acoustic wavefields in a medium with  $V_{pz} = 3$  km/s and anisotropic condition **a**  $\epsilon = 0.25$  and  $\delta = 0.25$ , **b**  $\epsilon = 0.22$  and  $\delta = 0.12$ , **c**  $\epsilon = 0.22$ ,  $\delta = 0.12$  and  $\varphi = 45^\circ$ , and **d**  $\epsilon = 0.06$  and  $\delta = 0.12$

Before running seismic modeling for whole Marmousi model, the stability and efficiency of the finite difference algorithm need to be checked. Several single shots were conducted to obtain optimum parameters. The main parameters affecting seismic modeling are the sampling time and source frequency. When the time step and frequency are following Eqs. (7) and (8), respectively, the number of samplings needs to have a minimum value where less than that, the algorithm does not result any data, and it is not stable. After defining the minimum sampling time, we optimized sampling time and frequency where we can collect sufficient high-quality data for migration. Finally, the full forward modeling was executed, and synthetic seismograms are generated. The resulted shot gathers are raw data which need preprocessing. Unwanted signals, primarily, the direct wave, are muted and removed by applying a filter. Figures 4 and 5 illustrate the Marmousi velocity and Eta model, and processed common shot gathers, respectively.

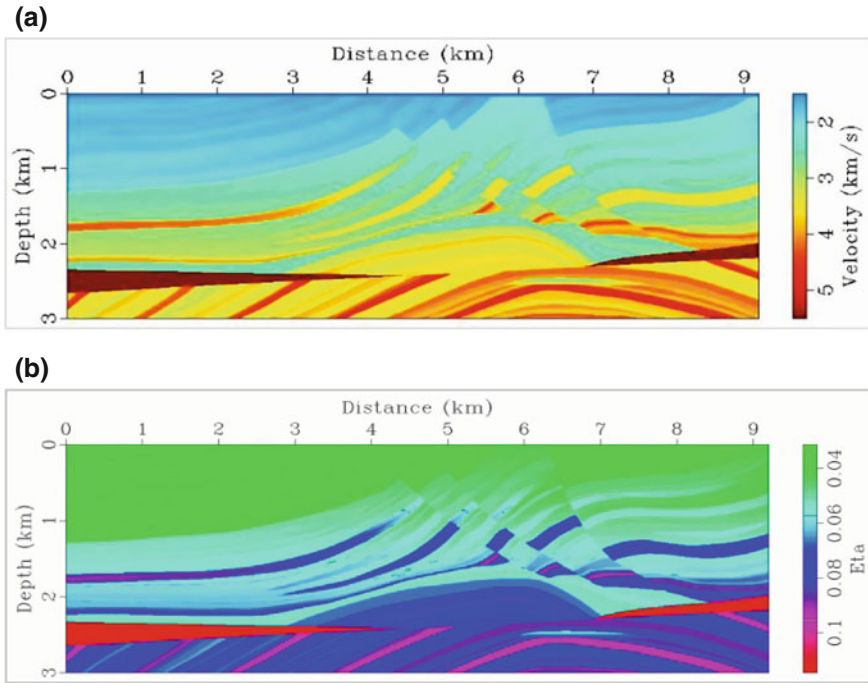


Fig. 4 a Marmousi velocity model and b its Eta model

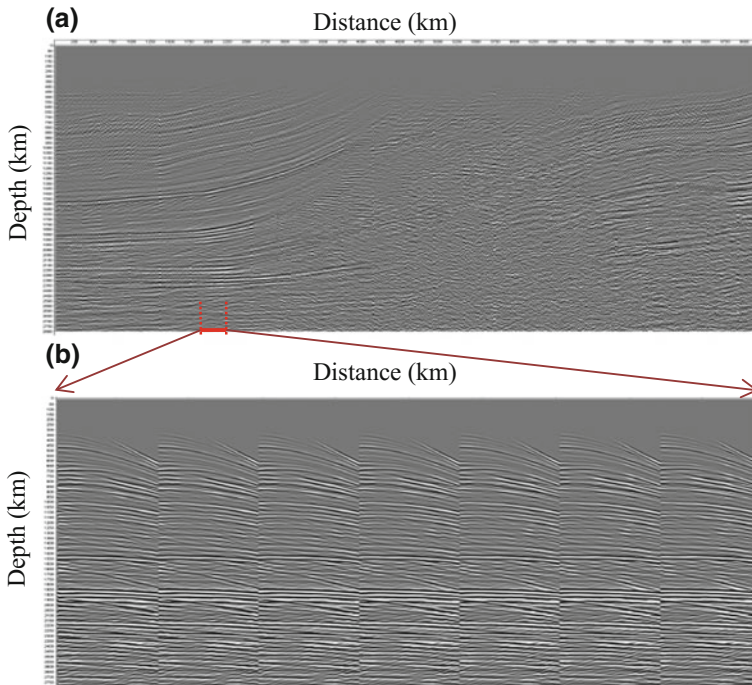


Fig. 5 Forward modeling for Marmousi model which a shows all shot gathers and b is a zoomed section

## 4 Conclusions

A TTI pseudo-acoustic coupled wave equation is employed for a wave modeling algorithm. Although the pseudo-acoustic approximation performs well in isotropic and elliptical anisotropic conditions, for an ellipticity, the Sv wavefield appears along with P wavefield. Sv-wave components can add noises during imaging. One way to remove S-wave artifacts is to locate the source in either isotropic or elliptical anisotropic environments. One can eliminate the converted Sv-waves either by adding finite Sv-wave velocities along the axis of symmetry which also fixes the instability problem or by implementing a filter at each output time step. The result of anisotropic forward modeling on Marmousi model confirmed that the produced synthetic data are satisfactory and the modeling algorithm can be used for forward modeling as well as for imaging purposes.

**Acknowledgements** This work is funded by grant PETRONAS Petroleum Research Fund. The authors acknowledge the contribution of PETRONAS and Universiti Teknologi PETRONAS (UTP) advisors.

## References

1. T. Alkhalifah and S. Fomel, 2009 "Angle gathers in wave-equation imaging for VTI media," *79th International Exposition and Annual Meeting*, pp. 2899–2903.
2. Z. Koren, *et al.*, 2010 "Moveout approximation for horizontal transversely isotropic and vertical transversely isotropic layered medium. Part II: effective model," *Geophysical Prospecting*, vol. 58, pp. 599–617.
3. L. Behera, *et al.*, 2011 "Anisotropic P-wave velocity analysis and seismic imaging in onshore Kutch sedimentary basin of India," *Journal of Applied Geophysics*, vol. 74, pp. 215–228.
4. H. B. Lynn, *et al.*, 2011 "Introduction to this special section Practical applications of anisotropy," *The Leading Edge*, vol. 30, pp. 726–730.
5. S. Sinha and R. Ramkhelawan, 2008 "P-wave azimuthal anisotropy from a full-wave seismic field trial in Wamsutter: 78th Annual International Meeting," presented at the SEG, Expanded Abstracts.
6. P. J. Fowler and R. J. King, 2011 "Modeling And Reverse Time Migration of Orthorhombic Pseudo-acoustic P-waves," presented at the 2011 SEG Annual Meeting.
7. R. Fletcher, *et al.*, 2008 "A new pseudo-acoustic wave equation for TI media," presented at the SEG Annual Meeting, Las Vegas.
8. T. Alkhalifah, 1998 "Acoustic approximations for processing in transversely isotropic media," *Geophysics*, vol. 63, pp. 623–631.
9. T. Alkhalifah, 2000 "An acoustic wave equation for anisotropic media," *Geophysics*, vol. 65, pp. 1239–1250.
10. X. Du, *et al.*, 2007 "Anisotropic reverse time migration for tilted TI media," *Geophysical Prospecting*, vol. 55, pp. 853–869.

11. S. Hestholm, 2007 “Acoustic VTI modeling using high-order finite-differences,” presented at the 2007 SEG Annual Meeting.
12. E. Duvencek, *et al.*, 2008 “Acoustic VTI wave equations and their application for anisotropic reverse-time migration,” presented at the 78th Annual International Meeting.
13. Y. Zhang and H. Zhang, 2009 “A stable TTI reverse time migration and its implementation,” presented at the 2009 SEG Annual Meeting.
14. R. P. Fletcher, *et al.*, 2009 “Reverse time migration in tilted transversely isotropic (TTI) media,” *Geophysics*, vol. 74, pp. WCA179–WCA187.

# Separation of Seismic Diffraction and Reflection Using Dip Frequency Filtering

Yasir Bashir, Deva P. Ghosh and Chow Weng Sum

**Abstract** An existing theory of diffraction imaging from the zero-offset seismic section explains the geometric pattern of the subsurface reflectors. Curvature of diffraction hyperbola is mainly dependent on the velocity of the medium and depth of discontinuous reflector. These diffraction hyperbolas are indication of fault, fracture, and pinch-outs. During the imaging because of choosing incorrect aperture and processing parameters, we might lose the information of diffraction. In this research work, diffraction imaging is performed by separating the diffractions from reflection data. We have developed a new workflow using f-k domain which is called frequency filter for separating only diffraction depending on the dipping angle of reflectors. The validation of method is completed on synthetic seismic reflection data set from one of Malay Basin field. Geological model comprises of a small part of the field which incorporates highly dipping faults and fractures.

**Keywords** Seismic diffraction · Reflection · Diffraction hyperbola · F-k spectrum · Frequency filter

## 1 Introduction

Diffraction patterns frequently occur in seismic section because of the abrupt lateral change in impedance contrast and discontinuity of subsurface reflector. It was a very serious objection on the application of theory follows from distinguishing that stacked seismic data are not true zero-separation data. It is subtle that the results of stacking the data recorded over a wide range of source–receiver separations will reasonably approximate the results of true zero-separation recording, insofar as diffraction amplitudes are concerned [1]. Barryhill, in 1977, has explained the concept and compared the zero-separation theory with nonzero-separation

---

Y. Bashir (✉) · D.P. Ghosh · C.W. Sum  
Center of Seismic Imaging (CSI), Geoscience Department,  
Universiti Teknologi PETRONAS (UTP), Seri Iskandar, Malaysia  
e-mail: Yasir.bashir@live.com; yasir.bashir@utp.edu.my



source-geophone distance (SGD). He concludes that diffraction amplitudes at nonzero source–receiver separation are well ordered almost completely by the location of the source–receiver midpoint [1].

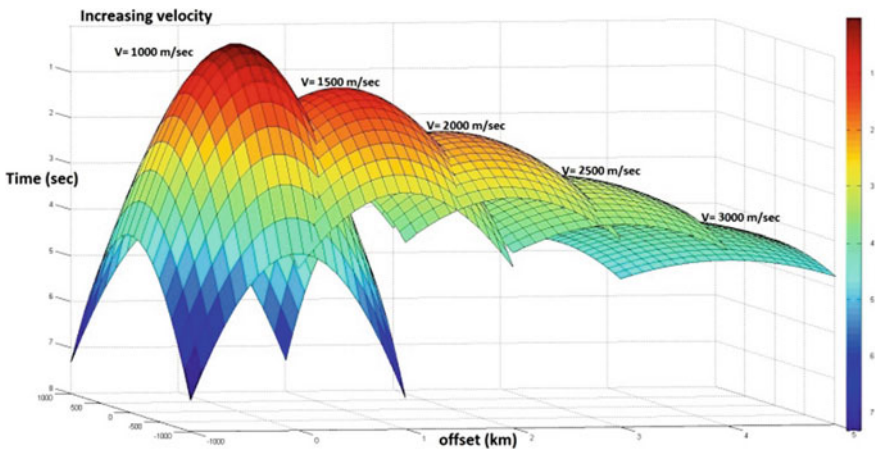
As we are familiar with the wave propagation and geometric path, a point diffractor gives rise to a hyperbolic pattern on the stacked section. It is well understood that curvature of hyperbola is depended on the velocity of the medium, and apex of hyperbola is an indicator of fault location as shown in Fig. 1, where we can see the hyperbolas on different velocities starting from 1000 m/sec to 3000 m/sec. Hyperbola is being spread out when velocity increases.

In reflection seismology for exploration geophysics, we use the wave propagation phenomena to estimate the properties of earth’s subsurface reflector. A diffraction phenomenon is also concerned with reflection because of the properties of subsurface as defined above. The acoustic (seismic) impedance,  $Z$ , is defined by the equation:

$$Z = V\rho$$

where  $V$  is the seismic wave velocity and  $\rho$  is density.

Seismic migration is the one of the primary imaging tools, but the earliest analog seismic record was the illustration of single-fold simply. These records were occupied by diffracted energy and random noise but those records still give an interpretation of the earth’s subsurface. Mechanical migration removed the structural misrepresentation on early seismic data, and the CMP stack condensed the amount of random noise when diffracted energy is preserving.



**Fig. 1** Diffraction hyperbola on different time and velocities, showing the curvature of a hyperbola is not dependent only on velocity but depth also [2]

## 2 Methodology

### 2.1 Finite Difference Modeling

Here, for modeling process, we take velocity and density as input and output is the seismic data. For seismic inversion case, input is traces and output is the structural image. These both common quantities are required to be calculated. These quantities consist of the following [3]:

$\vartheta$	Propagation angle
$\tau$	Travel time
$\beta$	Incident angle from source or receiver
$\sigma$	Running ray parameter
$\partial\beta/\partial x$	Geometrical spreading parameter

For each source or receiver, the above quantities satisfy the following equation [3]:

$$\left(\frac{\partial\tau}{\partial x}\right)^2 + \left(\frac{d\tau}{dx}\right)^2 = \frac{1}{v^2(x, z)} \quad (1)$$

$$\sin\vartheta = v \frac{d\tau}{dx} \quad (2)$$

$$\frac{\partial\sigma}{\partial x} \frac{\partial\tau}{\partial x} + \frac{\partial\sigma}{\partial z} \frac{\partial\tau}{\partial z} = 1 \quad (3)$$

$$\frac{\partial\beta}{\partial x} \frac{\partial\tau}{\partial x} + \frac{\partial\beta}{\partial z} \frac{\partial\tau}{\partial z} = 1 \quad (4)$$

$$\frac{\partial}{\partial z} \left( \frac{\partial\beta}{\partial x} \right) + \frac{\partial}{\partial x} \left[ \mu(x, z) \frac{\partial\beta}{\partial x} \right] = 0 \quad (5)$$

where  $v(x, z)$  is the velocity and

$$\mu(x, z) = \frac{\partial\tau}{\partial x} \left[ \frac{\partial\tau}{\partial z} \right]^{-1}$$

Equation (1) is eikonal equation, Eqs. (3) and (4) are derived by Pusey and Vidale (1991). Equation (5) follows from Eq. (3).

## 2.2 Geological Model Building

The geological model is taken from one of the producing fields from Malay Basin. The model contains four superimposed layers of different velocities/densities, with major faulting because of uplifting of the sub-layer during tectonic activities. The synthetic seismic data is obtained using finite difference wave equation modeling technique.

In finite difference method, we chose a zero-offset recording survey design and the parameters are as follows:

Source distance ( $dx_s$ )	10 m
Receiver distance ( $dx_r$ )	10 m
No. of source	1001
Frequency	50 Hz
Sampling interval	2 ms

## 3 Separation of Difractions and Reflection

Wavelength to frequency equation can be defined as follows:

$$f = \frac{v}{\lambda}$$

where  $f$  is frequency,  $v$  is velocity, and  $\lambda$  is the wavelength.

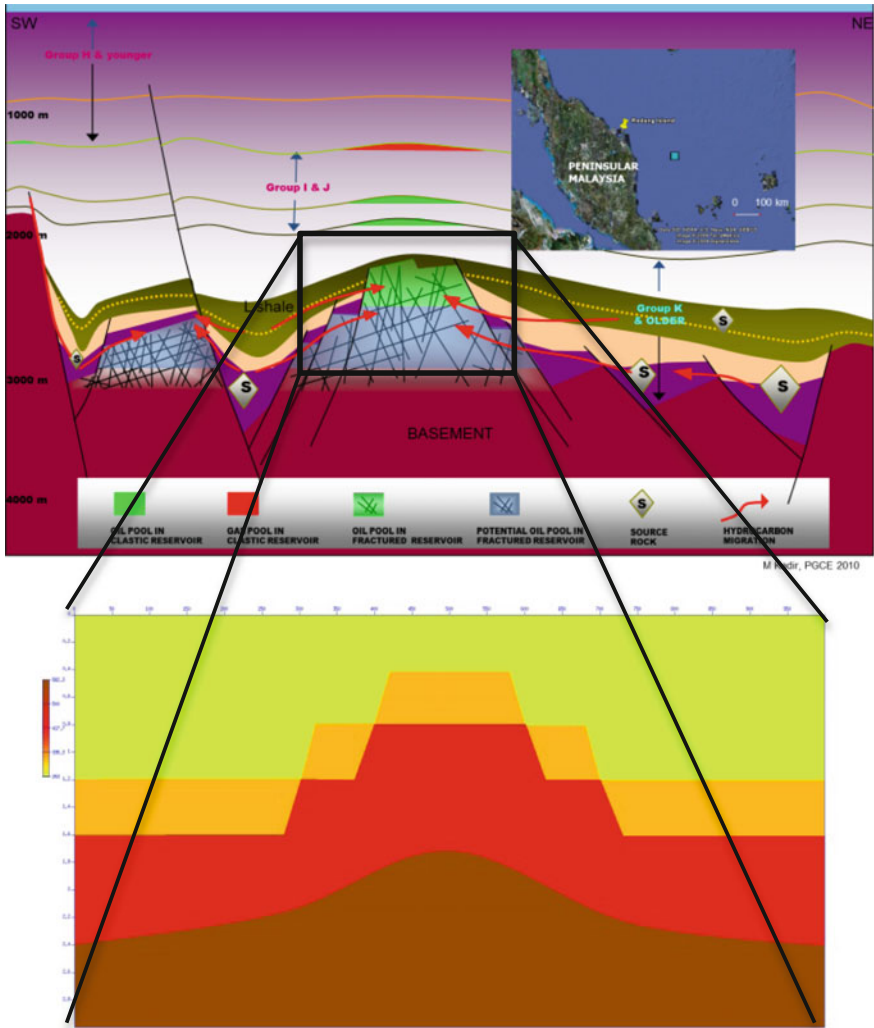
Wave number is the total number of complete wave cycles, and wave number is related to the wavelength.

$$k = \frac{1}{\lambda}$$

As reflection seismology is concerned with both reflection and diffraction phenomena, wide varieties of techniques/methods are used for the separation of diffraction and reflection energy from the seismic data such as amplitude and travel time [4] and plane-wave destruction (PWD) filter [5].

In this research work, we have developed a new workflow using frequency filtering in  $f$ - $k$  domain to achieve our objective.

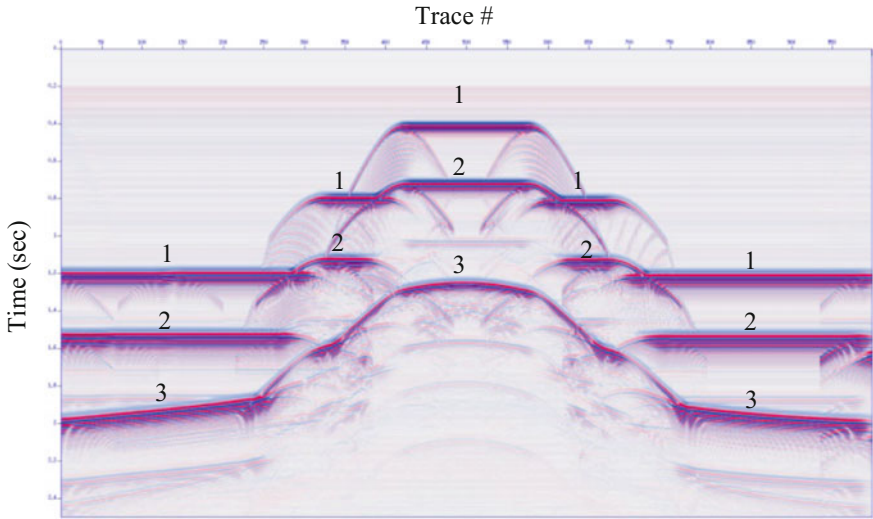
1. Development of velocity model from one of Malay Basin field (Fig. 2).
2. Zero-offset data acquisition using finite difference modeling (Fig. 3).
3. Preprocessing to improve the data quality.
4. Apply Fourier transform to observe the spectrum (Fig. 4).



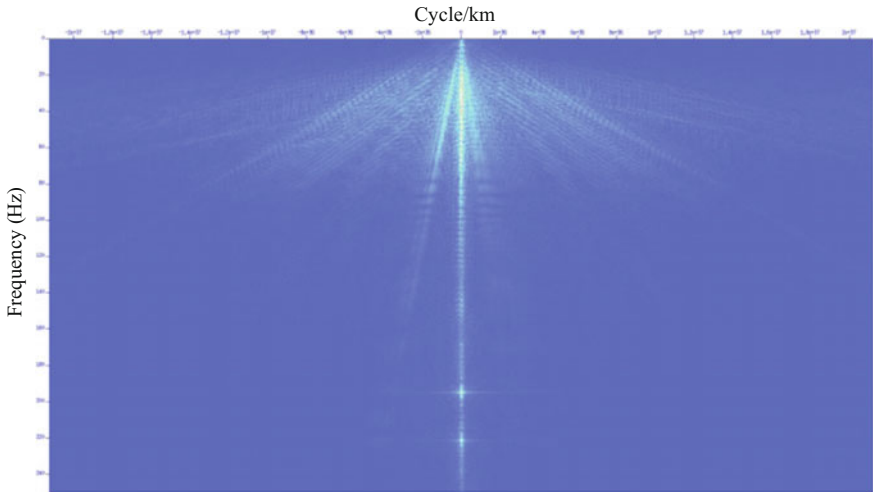
**Fig. 2** A geological model from Malay Basin field [6] extracted velocity model for study purpose with highly dipping faults

5. Development of filter on the basis of reflector dip in  $(dt/dx)$  plane.
6. Frequency filtering to remove the horizontal reflectors depending on the slope (Fig. 5).
7. Inverse Fourier transforms to get the results back in seismic diffraction section (Fig. 6).

This workflow is a complete procedure to separate the diffraction and reflection from a seismic section. Depending on the dip filtering, we can separate either reflection or diffraction section. In this paper, we have separate diffraction section

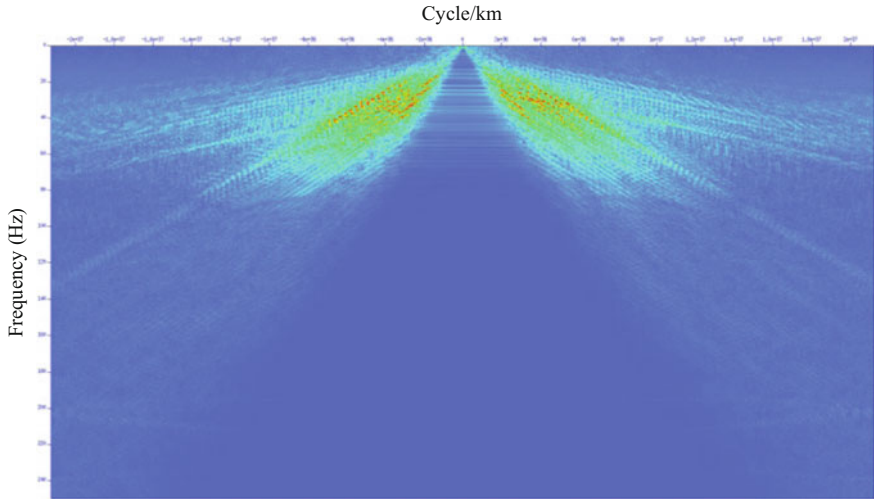


**Fig. 3** Zero-offset seismic gather using finite difference modeling technique. Diffraction hyperbolas are produced on the fault plane with phase change of 180° and amplitude decay exponentially

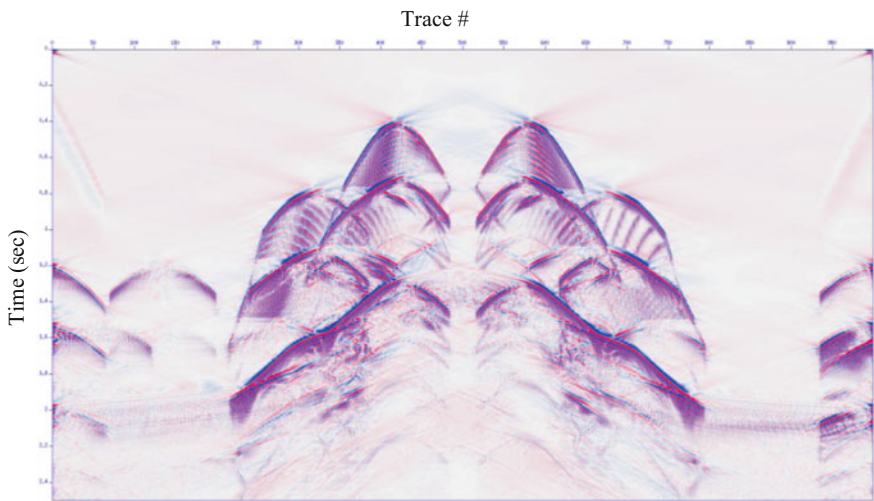


**Fig. 4** f-k spectrum of seismic data, showing the horizontal reflection energy at minimum wave number

only as our objective to study the diffraction phenomena to detect the faults and fracture for highly dipping angle in complex geological condition that contributes to improve the imaging results.



**Fig. 5** After filtering, the wave frequency of the reflectors 1, 2, and 3. Diffraction energy is distributed and enhanced



**Fig. 6** Separated seismic diffraction section after dip frequency filtering

## 4 Results and Discussion

First, we try to remove the reflection of 1, 2, and 3 reflectors as shown in Fig. 3. Since the dip ( $dt/dx$ ) of the wave is near to zero in  $t$ - $x$  plane, we design a filter that removes the energy around zero dip in  $f$ - $k$  plane,

The workflow described in methodology will double Fourier transform in  $t$  and  $x$  directions and will create  $f-k$  spectrum as shown in Fig. 4. In display spectrum, we can observe the reflector 1, 2 and 3 are around zero in  $t-x$  plane. In this study, a filter that can remove the energy around zero dip has been developed.

Figure 5 shows the  $f-k$  spectrum after applying filter on the basis of slopes that are not quantified. Figure 6 is the output after filtering data and shows diffraction section only.

## 5 Conclusion

Separation of diffraction and reflection energy is an alternative way to improve imaging results in complex region especially in faulted and fractured basement. The proposed research is a unique way to separate the diffraction from reflection data and gives opportunity to study diffraction imaging. This method is mainly depending on the frequency filtering in  $f-k$  domain. In  $f-k$  domain, the frequency from the horizontal reflection appears at the minimum wave number and diffraction energy at maximum wave number. Design filter from our workflow gives satisfactory result and separates the diffractions. Sometime, because of choosing wrong dipping angle of frequency filter will distort the data. Interpretations of diffraction section will help to mark the faults and fracture, as apex of each hyperbola is the best indicator of subsurface discontinuity. After separating, diffraction energy can be converted to the geological information by using diffraction stacking or Kirchhoff migration for further imaging.

**Acknowledgements** We are thankful to Universiti Teknologi PETRONAS (UTP), Geoscience department, and the Centre of Seismic Imaging (CSI) for providing facilities for this research. In this work, I have used Seismic Unix from CSM.

## References

1. J. R. Berryhill, "Diffraction Response For Nonzero Separation Of Source And Receiver," *GEOPHYSICS*, vol. 42, no. 6, pp. 1158–1176, 1977.
2. Y. Bashir, D. Ghosh, and C. W. Sum, "Detection of Fault and Fracture using Seismic Diffraction and Behavior of Diffraction Hyperbola with Velocity and Time," in *Seismic Driven Reservoir Characterization and Production Management*, 2015.
3. N. Bleistein, "Two-And-One-Half Dimensional In-Plane Wave Propagation\*," *Geophys. Prospect.*, vol. 34, no. 5, pp. 686–703, 1986.
4. R. Zhang, "Imaging the earth using seismic diffractions by means of Radon transform," in *CSEG National Convention, Canada*, 2005.
5. S. Tyiasning, D. Merzlikin, D. Cooke, and S. Fomel, "A comparison of diffraction imaging to incoherence and curvature," *Lead. Edge*, vol. 35, no. 1, pp. 86–89, 2016.
6. M. B. Kadir, "Fractured Basement Exploration Case Study in Malay Basin," in *PGCE 2010*, 2010.

# Locating Optimum Receiver Position in Seismic Acquisition: Example from Carbonate Region

Abdul Halim Abdul Latiff, Zulfadhli Mohd Zaki,  
Siti Nur Fathiyah Jamaludin and Nurul Mu'azzah Abdul Latiff

**Abstract** The existence of carbonate pinnacle disrupts the propagation of seismic wave from source to receivers, thus creating un-illuminated reflectors image. In previous years, several methods have been studied and applied in order to improve the subsurface data by restoring true reflectivity, with certain degrees of success. We can improve the seismic images in hand either by the implementation of complex migration algorithm or by conducting a fresh seismic data acquisition within the affected region. Following the seismic value chain, we can easily analyse the quality of the seismic images before any new acquisition took place through the forward modelling procedure using synthetic data for illumination analysis. In current illumination procedure, the required inputs are velocity model, acquisition set-up and the wave propagation. Although velocity information and wave propagation parameters are generally consistent within a basin, the seismic acquisition set-up needs to be revolutionized in order to bring a higher subsurface illumination. In this work, we proposed an optimum receiver position by using the particle swarm optimization approach, for better seismic images in carbonate-affected region.

**Keywords** Seismic acquisition · Receiver optimization · Carbonate

---

A.H.A. Latiff (✉) · Z.M. Zaki · S.N.F. Jamaludin  
Department of Geosciences, Universiti Teknologi PETRONAS,  
32610 Bandar Seri Iskandar, Perak, Malaysia  
e-mail: abdulhalim.alatiff@utp.edu.my

Z.M. Zaki  
e-mail: zfaba.a@gmail.com

S.N.F. Jamaludin  
e-mail: fathiyah.jamaludin@utp.edu.my

N.M.A. Latiff  
Faculty of Electrical Engineering, Universiti Teknologi Malaysia,  
81310 Skudai, Johor, Malaysia  
e-mail: muazzah@fke.utm.my



# 1 Introduction

Locating the new and rich hydrocarbon reservoir has become extremely difficult for geoscientist. Major industry players are now shifting their focus for bigger discovery in the extreme terrain and environment as well as previously abandoned region which was not optimized due to poor interpretation of seismic data. The latter case normally occurs in the field that has been exploited for shallow reservoir, but was predicted to have a larger hydrocarbon reserve beneath the subsurface anomaly such as salt dome and carbonate platform. In south-east Asia region, Luconia, Natuna and Palawan basins are the hydrocarbon-producing fields associated with carbonate structures. The carbonate sediments in these basins were formed by organic and inorganic processes with higher rate than siliciclastic sedimentation process. The Luconia block (Fig. 1) and oil and gas exploration industry are facing a lot of problems in producing a good seismic data quality because of the carbonate platform, which consequently lead to inadequate seismic wave amplitude detected on the surface level. This is partly due to the extreme velocity variations between carbonate build-ups compared to surrounding sediments, thus affecting the seismic signal propagation from source to receivers.

In Malaysia, there has been no production from the pre-carbonate sequence so far, despite the proven outcrops analogue elsewhere in Malaysia [2]. This lack of successful well drilling has been related to poor interpretation as the quality of seismic data is low. The resulting interpretation thereby makes the trap identification and selection of suitable drilling locations highly ambiguous (Fig. 2).

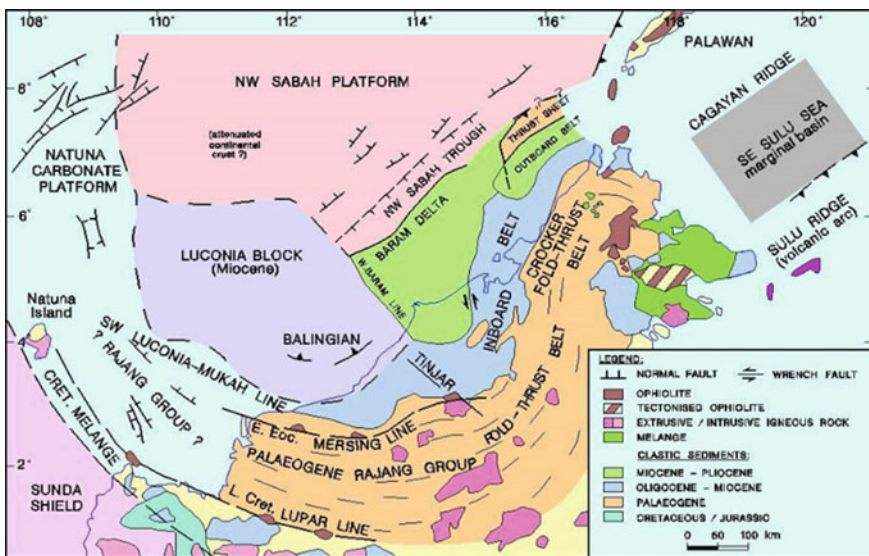
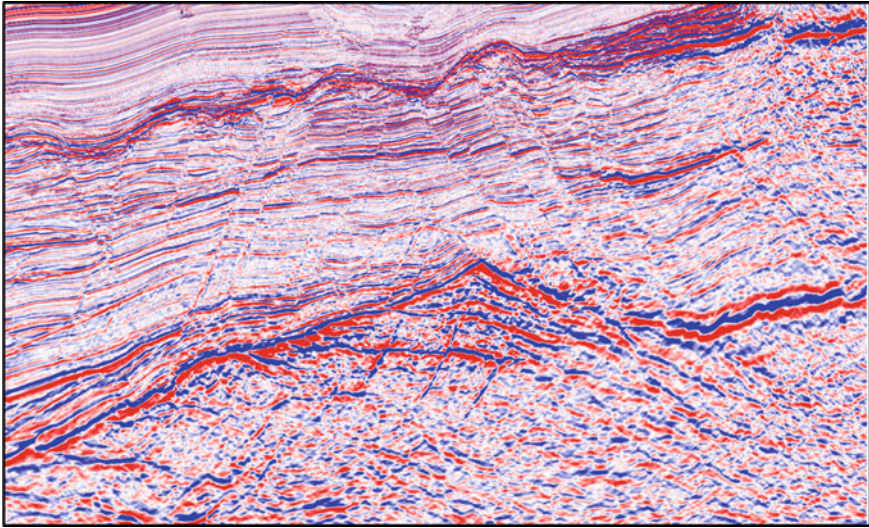


Fig. 1 Map showing the location of Luconia block located in offshore Malaysia [1]



**Fig. 2** Example of carbonate build-up in Luconia block, offshore Malaysia. The area beneath carbonate (known as pre-carbonate sequence) suffers from poor illumination as a result of wave scattering and attenuation [2]

The basic of carbonate structure lies in a stratal geometry, which occurred due to sea-level changes. The carbonate data appear to have strong amplitude at the top and the base of carbonate. Within the carbonate area itself, weaker amplitude has been observed, causing the uncertainty in well positioning. Based on this discovery, several seismic wave characteristics in carbonate reservoir are discussed as follows:

- The area within carbonate region has a high seismic velocity and density which was originated from complicated pore systems [3]. As a result, it produces a complex wave propagation and non-uniform velocity information.
- At the top and base of carbonate, strong amplitude is observed, which is due to high reflection coefficient contrast between carbonate and its surrounding environment. Meanwhile, the area inside carbonate structure as well as dipping reflector located beneath the carbonate platform suffered from poor quality data due to weak amplitude signal recorded. This low illumination data were attributed to non-uniform wave propagation once the wave encounters the high impedance contrast of carbonate body [4]. Instead of being reflected, these waves are refracted and did not reached the surface level, thus creating an illumination gap at certain portions of the data.
- Another general characteristic of carbonate structure is the low seismic frequency signal that exhibits dispersion phenomena, as the seismic wave velocity changes with the frequency. The high-frequency attenuation from the wave propagation is also as an indication of hydrocarbon presence inside the carbonate structure. However, the low-frequency generalization is not always true.

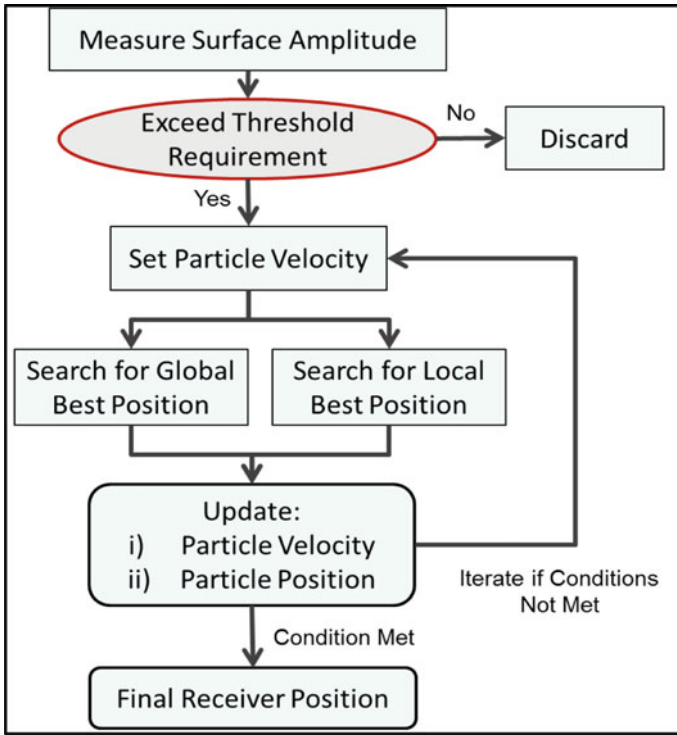
In one of the observations, the seismic frequency detected in two of the carbonate basins in Central China exhibits a high-frequency anomaly which surprisingly turned out as a good carbonate reservoir [5].

Therefore, the most viable option to enhance the seismic data quality is by deploying a new seismic data acquisition in the area, as the current imaging algorithm is unable to improve the data. However, the re-deployment of vessel and streamers without identifying the best acquisition system first is not ideal, as this will not provide any improvement to the existing seismic data. Besides seismic enhancement, a proper acquisition planning is also beneficial for time-lapse 4D seismic study, as changes in reservoir dynamic may contribute to a new reservoir discovery. In a case study, the application of cross-well technique was used to evaluate the stratigraphy and image of the structure [6]. In addition, some researchers also use multicomponent acquisition technology to improve the image of fractured carbonate at onshore Texas [7]. These two works prove that the carbonate images can be improved significantly if a proper approach was taken, with re-acquisition method being far more desirable compared to the development of seismic imaging algorithm.

However, there is a shortcoming in determining poor illumination in subsurface seismic data. According to seismic value chain [8], the earth's depth section can be obtained after proper acquisition, following suitable processing and migration techniques before an illumination analysis can be carried out. To overcome this drawback, a method called focal beam analysis was developed [9, 10], which allows us to perform a quick illumination analysis once a velocity model of the subsurface has been known. Another popular method commonly used for illumination analysis is hit count in ray tracing method [11].

## 2 Methodology

In this work, the integrated method used is illustrated in Fig. 3 [12], where the focal beam method merged with particle swarm optimization (PSO) technique [13, 14]. The PSO method works by incorporating a real particle swarming movement where it is constantly looking for the optimum parameters involve from nearest available position. Before the analysis begins, we develop a suitable fitness function for scaling the particle's movement between its original position and their global best position. From the early findings, multiple global positions existed as there are many optimum receiver positions; therefore, the fitness function solution needs to include every global best (*gbest*) location. This can only be done by obtaining knowledge from particles' past best position, *pbest*, along with chosen *gbest* position, before each particle optimized solution is evaluated; the corresponding particle velocity and position will be updated. Once all information is acquired, we simulate the next particle position by adjusting the particle's velocity equation,  $V_n$ , before updating its movement equation,  $x_n$ .

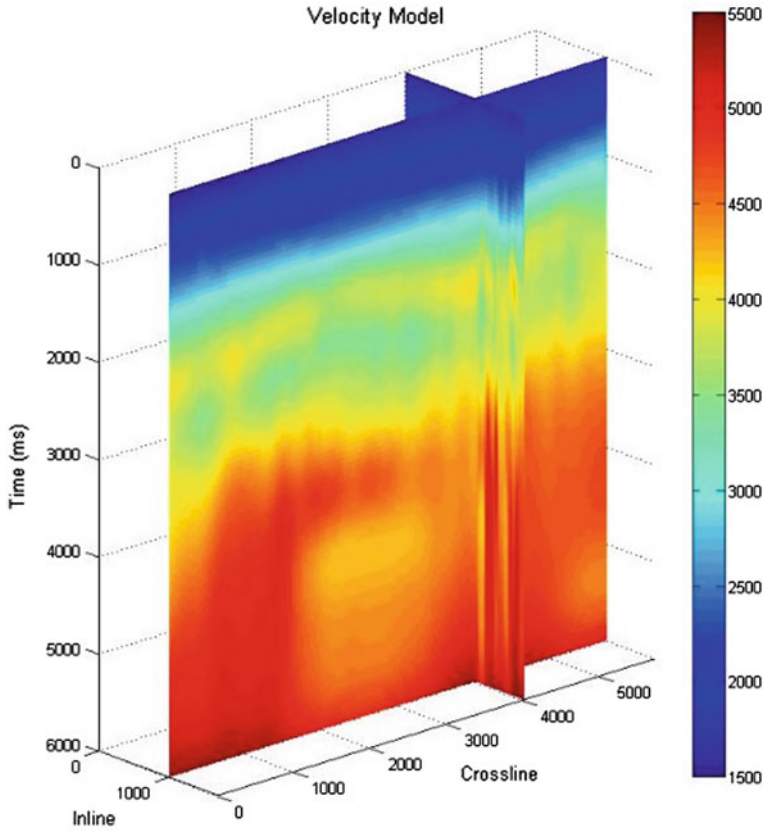


**Fig. 3** New acquisition design workflow. This methodology incorporates the particle swarm optimization technique which contributes to better receiver positioning [12]

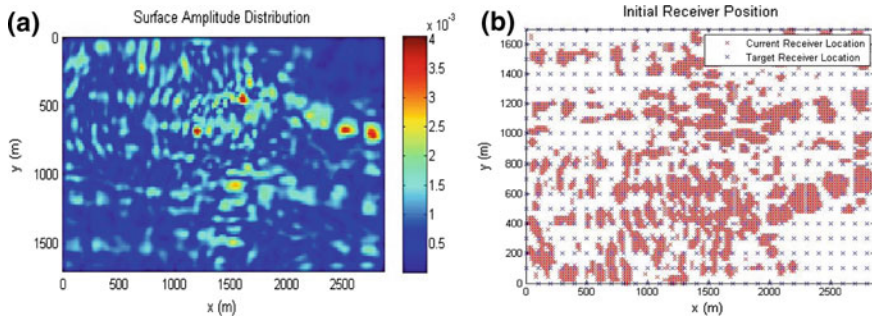
### 3 Receiver Optimization

Before any optimization process begins, the field velocity model (Fig. 4) was built according to the migration velocity information from the completed seismic data processing sequence. We set the target reflection point to be studied is at coordinate (3000 m, 1000 m, 6000 ms). From the target reflection point, a wave operator is propagated upward by using recursive  $xy-\omega$  depth sequences. Once the wave operator reaches the surface level, amplitude distribution is measured (Fig. 5a) to determine the initial suitable receiver position. This amplitude positioning will be converted into particle’s locations that require optimization (Fig. 5b). Before implementing PSO algorithm, an array of target located 100 m apart from each other (maximum source and receiver spacing in real seismic survey) was created in both  $x$  and  $y$  directions. This will enable the current particles to choose their global locations based on the PSO algorithm.

The receiver particles begin their iterations to search for the optimal location based on the specified algorithm. However, since there is a possibility that the optimization process might continue infinitely, a criterion is set to stop all

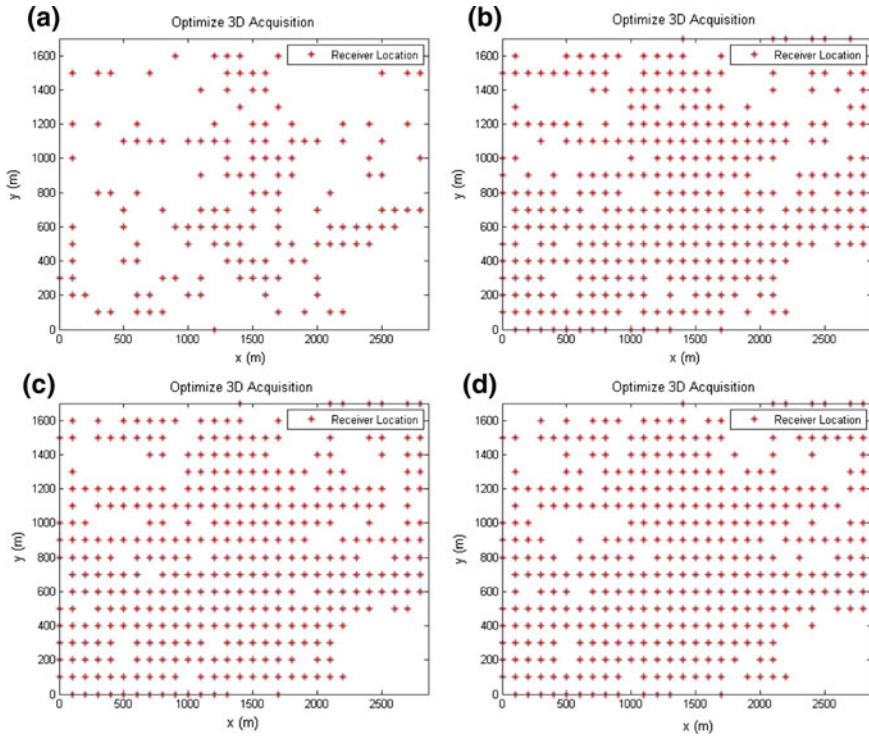


**Fig. 4** Field velocity model used throughout the optimization and focal beam analysis. Three target depth points were chosen for analysis; 2 s depth, 4 s depth and 6 s depth



**Fig. 5** **a** Recorded amplitude distribution once the wave amplitude reached the surface level. **b** From the amplitude distribution outputs, a threshold criterion was applied, and the wave amplitude was transformed into an initial receiver position for optimization process





**Fig. 6** a Receiver locations after single iteration, b after 25th iterations, c after 50th iterations and d after 100th iterations

optimization processes if the counter hits 100. In Fig. 6, we demonstrate the best particle’s position with respect to the number of iteration, by capturing its position in carbonate region after 1st, 25th, 50th and 100th consecutive iterations. We might conclude that after 25th iteration (Fig. 6b), only few improvements can be detected. However, it should be noted that only optimized particles will be considered for final survey design configuration as well as for subsurface illumination analysis. This means that any particle that did not find its best location will be discarded from receiver location solution.

## 4 Conclusions

From the results obtained, the proposed approach has successfully improved the receiver position according to the velocity model obtained earlier. It give an advantage to the new acquisition procedure to be proposed as the cost of new seismic re-acquisition will be cheaper as new source and receiver positioning is no

longer subject to standard acquisition geometry design. Eventually, it is hoped that a better subsurface image can be obtained from the outcome of this optimized seismic survey approach.

**Acknowledgements** The authors would like to thank PETRONAS for granting permission to use data in this research project. The authors also appreciate the rigorous reviews and positive feedbacks from external reviewers to further improve this research work.

## References

1. M. Madon, *The petroleum geology and resources of Malaysia*: PETRONAS, 1999.
2. S. K. Chandola, L. C. Foo, M. F. Akalin, R. Alai, A. A. Muhamad, M. Bayly, K. Myers, T. Brice, G. Nyein, S. Hydal, "Large Scale Seismic Modelling of the Pre-Carbonate Geology, Offshore Malaysia, a Multidisciplinary Approach - Running the Seismic Method Backwards", presented in *International Petroleum Technology Conference*, Kuala Lumpur, 2014.
3. Z. Wang, "Seismic Properties of Carbonate Rocks," in *Carbonate Seismology*, I. Palaz and K. J. Marfurt, Eds., ed Tulsa: Society of Exploration Geophysics, 1997.
4. J. F. Sarg and J. S. Schuelke, "Integrated seismic analysis of carbonate reservoirs: From the framework to the volume attributes," *The Leading Edge*, vol. 22, pp. 640–645, 2003.
5. Y. Li, X. Zheng, and Y. Zhang, "High-frequency anomalies in carbonate reservoir characterization using spectral decomposition," *Geophysics*, vol. 76, pp. 47–57, 2011.
6. R. T. Langan, S. K. Lazaratos, J. M. Harris, A. A. Vassiliou, T. L. Jensen, and J. W. Fairborn, "Imaging of a stratigraphically complex carbonate reservoir with crosswell seismic data," in *Carbonate Seismology*, I. Palaz and K. J. Marfurt, Eds., ed Tulsa: Society of Exploration Geophysicist, 1997.
7. X. Y. Li and M. C. Mueller, "Case studies of multicomponent seismic data for fracture characterization: Austin Chalk examples," in *Carbonate Seismology*, I. Palaz and K. J. Marfurt, Eds., ed Tulsa: SEG, 1997.
8. A. J. Berkhout, "The data-driven seismic value chain, providing a business context for the velocity issue," *Geophysical Prospecting*, vol. 52, pp. 481–487, 2004.
9. Berkhout, A.J., Ongkiehong, L., Volker, A.W.F., Blacquièrè, G., "Comprehensive assessment of seismic acquisition geometries by focal beams—Part I: Theoretical considerations," *Geophysics*, Vol. 66, p 911–p917, 2001.
10. Volker, A.W.F., Blacquièrè, G., Berkhout, A.J., Ongkiehong, L., "Comprehensive assessment of seismic acquisition geometries by focal beams—Part II: Practical aspects and examples," *Geophysics*, Vol. 66, p 918–p931, 2001.
11. Van Veldhuizen, E.J., "Integrated approach to 3D seismic acquisition geometry analysis," *Delft University of Technology, PhD thesis*, 2006.
12. A. H. Abdul Latiff, "Development of Hybrid Illumination and Optimised Survey Design Techniques for Shallow Gas Cloud Fields," *Universiti Teknologi PETRONAS, MSc Thesis*, 2014.
13. Eberhart, R.C., Shi, Y., "Particle swarm optimization: development, application and resources," *IEEE Congress on Evolutionary Computation*, p 81–p86, 2001.
14. Kennedy, J., Eberhart, R.C., "Particle swarm optimization," *IEEE International Conference on Neural Networks*, vol. 4. Perth, Australia, pp. 1942–1948, 1995.

# Seismic Waveform Classification of Reservoir Properties Using Geological Facies Through Neural Network

Afiqah Zahraa and Deva Ghosh

**Abstract** Seismic waveform classification is a very powerful tool to explore hydrocarbon especially in area with sparse well data. However, dependency on seismic data remains small without any geological or physical evidence such as well logs that are able to support the interpretation. Hence, numerous efforts have been made to establish strong relationship between geology and geophysics using different methods and techniques throughout the years. This paper focuses on seismic waveform classification to different classes using neural network and to link them to geological facies derived from well log data. The interpretation of seismic facies or waveform classification map provides a better understanding toward depositional environment and helps to identify significant reservoir rock. The produced facies model can also be used to reduce uncertainty in exploration and production, especially for reservoir productivity enhancement and stratigraphic identification.

**Keywords** Facies model · Neural network · Stratigraphic traps · Waveform classification

## 1 Introduction

Quantitative approach to characterize seismic facies has been used as early as 1969 by Mathieu and Rice to identify lateral changes in sand and shale environment using discriminant analysis that makes use of linear combination of a larger number of

---

A. Zahraa (✉) · D. Ghosh  
Center for Seismic Imaging, Universiti Teknologi Petronas, 32610 Bandar Seri Iskandar,  
Perak, Malaysia  
e-mail: afiqahzahraa@gmail.com

D. Ghosh  
e-mail: drdeva@petronas.com.my

D. Ghosh  
Department of Geosciences, Universiti Teknologi Petronas, 32610 Bandar Seri Iskandar,  
Perak, Malaysia



variables [10]. Hagen introduced the use of principal component analysis (PCA) to detect the subtle changes in seismic traces and to group them based on the variation of lateral porosity of a reservoir [8]. The PCA technique used supervised method with known well data and location as clustering center to classify the amplitude envelope and instantaneous frequency seismic to different petrophysical properties. The same principal component technique was later used by Fuller and Smithson to detect the edges of thin reservoir facies [7]. Hagen, Conticini and Fuller and Smithson recognized the importance of seismic attributes at delineating the changes of seismic facies that are usually very subtle and difficult to be identified [8, 4, 7]. Conticini suggested automatic and semiautomatic method for seismic facies clustering to group them to similar character, to interpret the lithological and fluid content of different facies classes, and to study the distribution and areal extent of the reservoir [4]. Study by Dumay and Fournier introduced the learning and predictive steps in multivariate statistical analyses or automatic facies recognition [5]. The study shows the importance of principal component analysis to validate the learning traces and multidimensional analyses, clustering technique, and factor analyses to point out the parameters that best represent or discriminate the facies. An and Moon and An et al. revealed the advantages of using feedforward neural network for reservoir characterization and reservoir property estimation [1, 2]. The same neural network method has also been used for waveform classification using supervised and unsupervised method [12, 6]. The waveform classification map is also integrated with other seismic attributes to delineate the properties of reservoir [3, 14]. The neural network method is also combined with other clustering techniques such as hierarchical and hybrid to produce the optimum result for seismic facies classification [9]. Saggaf et al. used competitive neural network for the unsupervised and supervised analyses to classify and identify the reservoir facies from the seismic [13]. Neural network is also being utilized to predict the rock parameters or log properties as studied by Mohaghegh et al. and Sun et al. [11, 15].

Neural network is the best automatic method used to identify and to classify the seismic facies due to its ability to suppress the noise, insensitive to absolute changes in amplitude, and able to handle the complex and large database. It also has the ability to eliminate the need of complex statistical technique with no prior knowledge or established relationship between the seismic parameters and geologic variations is needed. Hence, this paper focuses on the neural network method to classify the seismic waveform into different classes and to relate them to geological facies and lithology prediction.

## 2 Methodology

PETREL software by Schlumberger is used to support the interpretation and analysis process of geological and geophysical data. Hampson-Russell and StratiMagic are used mainly for statistical analysis and neural network pattern recognition and identification.

## **2.1 Geological Interpretation**

Well log correlation: The sand and shale packages are characterized and correlated based on the similar well log value. Each of the packages corresponds to different facies and environment of deposition. It is also characterized according to the related stratigraphic sequences such as maximum flooding surfaces and sequence boundaries that are crucial for log motif definition in describing the geological facies of the studied area.

## **2.2 Seismic-to-Well Tie**

Time-to-depth conversion using raw checkshot and calibrated sonic is used to tie geological data to the geophysical information. Different types of sand or shale exhibit unique seismic response depending on its character such as velocity and density. It is important to achieve the highest percentage of correlation to ensure the log motif, or geology is properly correlated to correct the seismic traces in time domain since this log motif and its corresponding seismic traces will be used as an input for neural network training. Inaccurate input will cause unreliable training which later will be affecting the waveform classification process.

## **2.3 Geophysical Analysis**

- Seismic interpretation: The target sand or shale is interpreted in the time domain/seismic. Seismic traces are constraint along the interpreted horizons at certain interval to reduce the redundancy of seismic traces used at unnecessary target.
- Seismic attributes: Lateral variation in attribute patterns suggests the changes in stratigraphy or facies which are able to define the limits of the reservoir production [19]. Seismic attribute maps such as RMS amplitude map, sweetness map, and variance map are created using the interpreted horizon. The redundancy of seismic attributes used can be reduced by using principal component analysis (PCA) in which it helps to normalize the unit without taking away the dimensionality of the seismic itself. The correct combination of seismic attributes is able to bring out the facies features such as channel or sand plain in seismic slice. The seismic attributes are later inputted into neural network for the training purpose.

## **2.4 *Petrophysical Analysis***

The petrophysical analysis includes the porosity, saturation, and net-to-gross of the reservoirs. Petrophysical parameters explain the quality and productivity of the potential reservoir rock. Depositional environment of sand and shale package can also be described in terms of its proximity to source and provenance by using these parameters.

## **2.5 *Neural Network Application***

Neural network identification: The identification system requires two critical steps, namely learning steps and predictive steps. The initial learning method depends on the type of network used: supervised or unsupervised. The supervised system requires the known facies information relationship with the seismic response as training input. Neural network is a method that mimics the way human brain works. It needs the training of neurons in which they learn how to cluster themselves to a different number of classes according to the input vector. The training requires the number of iterations to ensure that neurons are not undertrained and properly classified. Overtraining also needs to be avoided in some cases. The training input vector consists of geologically defined log motif and its seismic response. Hence, well with the complete geological information is chosen as input for the training. Each of the log motifs is characterized by different facies and seismic facies. In this study, supervised method is developed using blocking method which also utilizes the neural network analysis for waveform classification but in a supervised manner by calibrating it to the available wells.

In predictive steps, the wavelet or seismic response away from the wells is classified according to the relevant class. The method is very crucial as it provides the integration of seismic and geological data derived from log motif and its facies. It also introduces the constrained clustering technique by limiting the classification only to the trained log motif. The produced waveform classification map is interpreted by integrating both supervised and unsupervised methods.

## **3 Results**

The workflow has been applied to real data in Malay basin. Four wells are correlated for X reservoir with the thickness ranging from 10 to 15 m. Post-stack inversion seismic cube is generated using velocity and density data which are then used as input for waveform classification using neural network method. Principal component analysis is utilized to remove the noise, redundant data and for dimension reduction. The PCA indicates y-axis showing eigenvalues and x-axis the

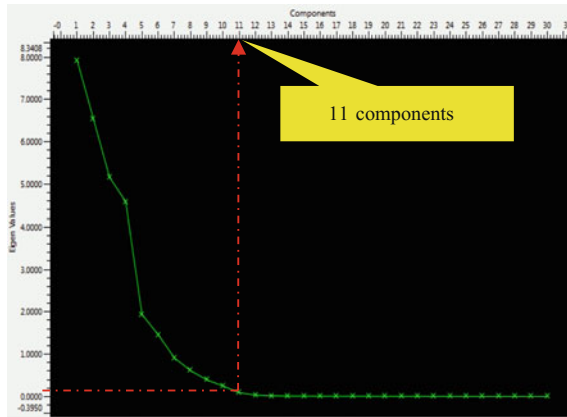


Fig. 1 Principal component analysis of post-stack inversion cube

components consisting of seismic traces. The best cases are only eigenvalues more than one selected to represent the data cloud. However, 11 components are used for projection to avoid losing any detailed changes in seismic traces even though the percentage of contribution is rather small (Fig. 1). The components bigger than 11 are not used as the data points are not contributing to any changes to the cloud point indicated by constant slope starting from the 11th component.

Using neural network, the post-stack inversion cube that had undergone PCA is classified into six classes of seismic traces. The time window used is  $-26 + 33$  ms and X reservoir as a reference horizon (Fig. 2). It is very crucial to use the ideal value of time window in order to capture as much the geological features and its lithological differences. In this case, the time window is restricted to only  $-26$  ms

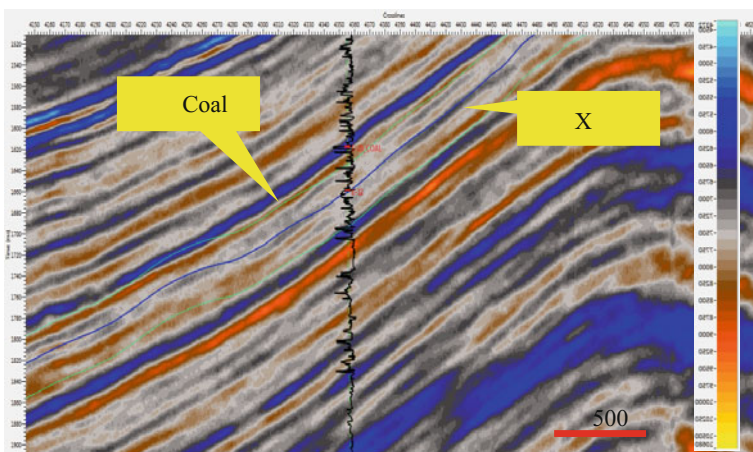


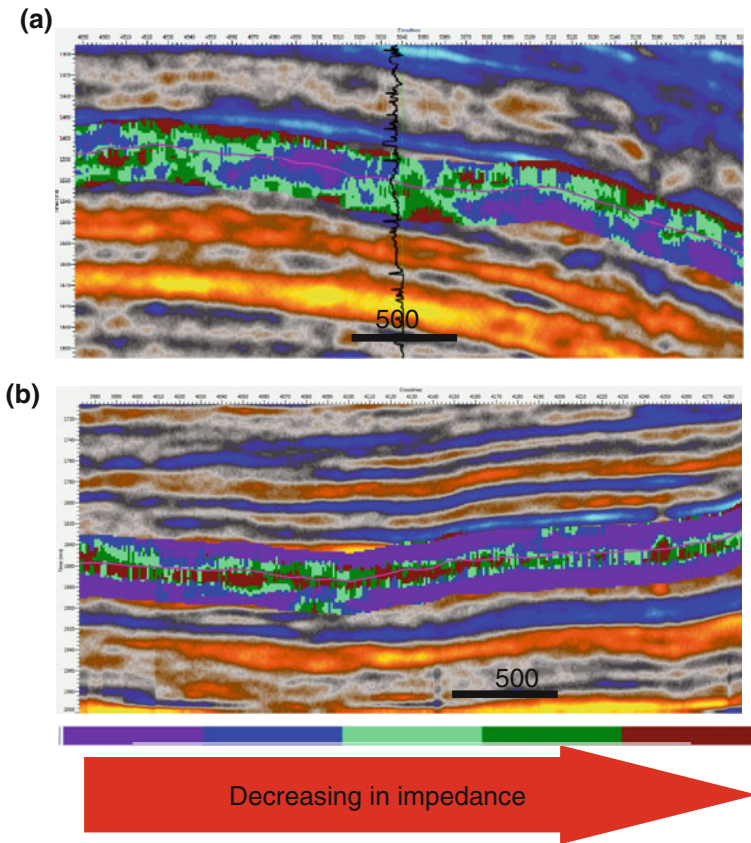
Fig. 2 The time window is indicated using the green line; meanwhile, blue line is the X sand

above the reservoir sand to avoid the strong impedance coal above which can cause the masking effect and 33 ms is stretched below the horizon to capture the changes in lithology between reservoir sands and shale (Fig. 2).

Each of the seismic trace classes corresponds to different colors, indicating its different shape and morphology. The unsupervised classification is done based only on seismic data without any correlation with wells. The trace model viewer (Fig. 6) shows six classes and their corresponding cumulative differences between traces. The ideal case of this line is straight sloping line representing facies equally different from its neighbors. Too much classes will show flat line; meanwhile, sudden bend of line indicates that the number of classes is not sufficient or indicates the significant geological boundary such as fault. The waveform classification map produces straight and steady sloping line showing that the number of classes used is optimal and reliable in representing the geological differences or facies in region (Fig. 6).

To perform the supervised waveform classification, another method called blocking is conducted to correlate the classification classes with the lithology in the well log. Blocking is a data compression method in which the interval is sliced into several microlayers based on zero crossing, maximum, minimum, or inflection points. The produced classification has higher vertical frequency compared to the previous method. However, the propagation of lateral continuity using this method is limited. The same neural network technique is used for classification purposes after performing blocking. The inflection points are used to define the smaller zone interval with the same time interval used for unsupervised classification and fifth number of classes are selected. Each of the classes has their own unique color. The blocking result shows that the green color is sand; meanwhile, blue color is shale based on the well observation (Fig. 3). Hence, transitioning of green (3rd class) to blue (2nd class) indicates the changes from sand to shale lithology (Fig. 3a). The changes of color from greenish to red and blue to purple show the change of impedance of sand and shale, respectively (Fig. 3b).

The cross-plot between P-impedance value and gamma ray is plotted to see the relationship between lithology and impedance in which high impedance indicates the shale lithology and low impedance is high-quality sand (Fig. 4). Increasing impedance represents the transition of good-quality sands to shale lithology. By comparing the impedance result with blocking color, hence, red is defined as high-quality sand, followed by greenish color (lower quality of sand), blue (sandy shale), and purple (shale). An X horizon slice map is produced based on the blocking volume and compared to the waveform classification map (Fig. 5). The area of high-quality sand based on the blocking map fits the red color or 6th class in the waveform classification. Hence, 6th class is interpreted as high-quality sand and decreasing in quality as the number of classes starts to decrease.



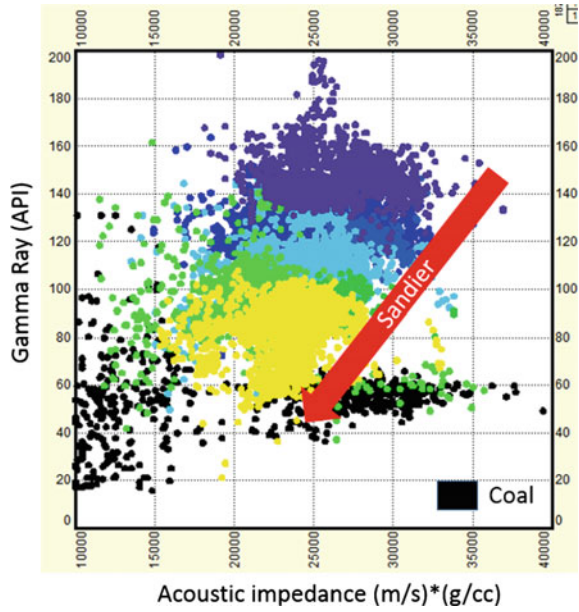
**Fig. 3** **a** The blocking method is calibrated with well for geological and lithological definition. *Green* means sand, while *blue* is shale. **b** The in-between color of *green* and *blue* represents the changes in impedance with high-quality sand corresponding to *red* class, and shale is *purple* and *blue*

All the wells are positioned in the 4th class except for B-4 (Fig. 6a). It is important to note that the changes in class do not only signify in the changes of lithology but also in the changes of sand thickness. B-4 waveforms are grouped in the first class, indicating the decrease in sand quality and the changes in sand thickness. B-4 well indicates no lithological changes vertically along the time window, with sand dominating the whole interval. Hence, the contrast between shale and sand is small, and the impedance of the sand itself is intermediate contributing to the factors the wells to be grouped in 1st class.

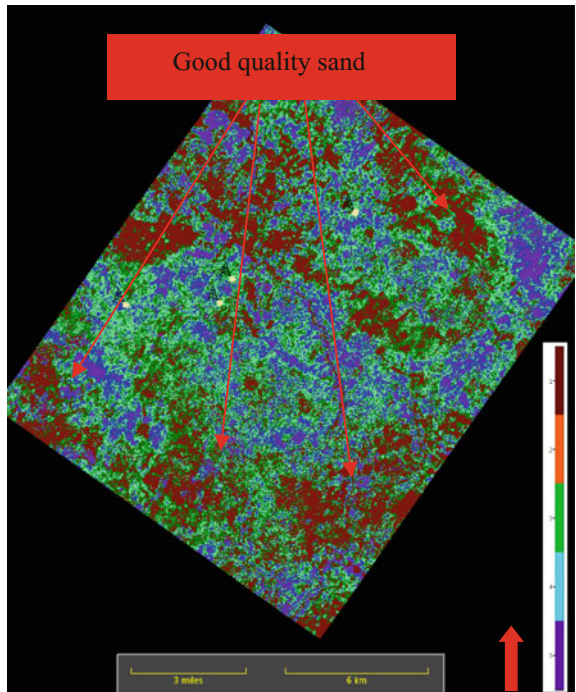
Waveform classification map is integrated with 'blocking' method map to predict lithological definition of each of the classes. High-quality sand dominates in the

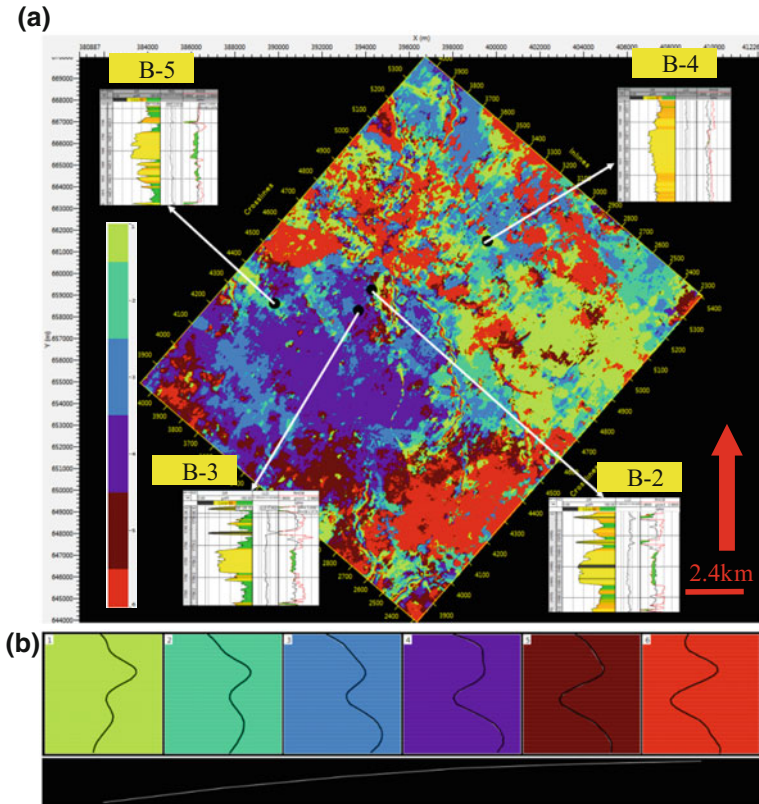


**Fig. 4** The P-impedance and gamma ray cross-plot indicate the high impedance consists of shale and low impedance consists of coal and sand



**Fig. 5** Horizon slicing of *blocking cube* shows high-quality sand is in red color or the class 1. The lithology interpretation of the map fits the different classes in waveform classification map





**Fig. 6** **a** The waveform classification map shows sixth number of classes that corresponds to different traces morphology and geological facies, which is closely related to lithological prediction and log motif. **b** The trace model shows the shape of each of the waveforms and its cumulative differences between classes

southern area and becomes decreasing in quality in both the west and east directions. Some indicators of good-quality sand can also be found along the direction of southern-to-northern area.

## 4 Conclusions

Waveform classification using neural network is to predict the lithology distribution and to analyze the environment of deposition of the studied area. The method involves a lot of uncertainty as seismic traces can be heavily influenced by external factors such as fluid and porosity. The integration with blocking method helps to



reduce the uncertainty and to define the waveform classification using well calibration. Careful analysis must be made during PCA as numbers of components play an important role in representing the seismic traces to be used.

**Acknowledgements** Special gratitude goes to PETRONAS for allowing me to utilize the data and for providing me the financial support throughout my research. My special appreciation and thanks to my advisor Professor Dr. Deva Ghosh, you have been a tremendous mentor for me. I thank our colleagues CSI/UTP who provided insight and expertise that greatly assisted the research.

## References

1. An, P., and Moon, W. M. (1993) Reservoir characterisation using feedforward neural networks: 63<sup>rd</sup> Ann. Internat. Mtg., Soc. Expl. Geophys., Expanded Abstracts, CT4.8, 258–262.
2. An, P., Moon, W. M., and Kalantzis, F., (2001) Reservoir characterization using seismic waverform and feedforward neural network: Geophysics, 66, 1450–1456.
3. Basman II, Y.V. (2015). Seismic Waveform Classification: Renewng the Interest in Barrolka Field, SW Queensland, Copper Basin. 24<sup>th</sup> Internatial Geophysics Conference and Exhibition.
4. Conticini, F. (1984) Seismic facies quantitative analysis: New tool in stratigraphic interpretation. SEG Technical Program Expanded Abstracts 1984, 680–682.
5. Dumay, J., & Fournier, F. (1988). Multivariate statistical analyses applied to seismic facies recognition. Geophysics, 53(9), 1151–1159.
6. Farzadi, P. & Hesthammer, J. (2007). *Diagnosis of the Upper Cretaceous Paleokarst and Turbidite System from the Iranian Persian Gulf using Volume-based Multiple Seismic Attribute Analysis and Pattern Recognition*. Department of Earth Science, University of Bergen.
7. Fuller, B. N., & Smithson, S. B. (1989). Multivariate pattern recognition of seismic data for exploitation. SEG Technical Program Expanded Abstracts 1989, 723–725.
8. Hagen, D.C. (1982) The applications of principal components analysis to seismic data sets: Geoexplor., 20, 93–111.
9. Marroquin, I. D. (2013). A Knowledge-integration Framework for Interpreting Seismic Facies Classifications. *SEG Houston 2013 Annual Meeting*, pp. 2464–2469.
10. Mathieu, P. G., & Rice, G. W. (1969). Multivariate analysis used in the detection of stratigraphic anomalies from seismic data. Geophysics, 34(4), 507–515.
11. Mohaghegh, S., Arefi, R., Ameri, S., & Hefner, M. H. (1994, January). A methodological approach for reservoir heterogeneity characterization using artificial neural networks. In SPE Annual Technical Conference and Exhibition. Society of Petroleum Engineers.
12. Neri, P. (1997, May). Revolutionary Software for Seismic Analysis. *WORLD OIL magazine*, 90–93.
13. Saggaf, M. M. and Marhoon, M. I (2001) Seismic facies mapping by competitive neural networks. Society of Exploration Geophysicists Source 2001 SEG Annual Meeting, 9–14 September, San Antonio, Texas.
14. Singavarapu, A., Singh, S. K., Alvarez, M., Al-Owihan, H., Al-Ajmi, A. & Al-Rashidi, S. (2014). Seismic Attributes & Wave form Classification: An Emerging Tool for Exploration of Shallow Oil Play, Kuwait. *SEG Denver 2014 Annual Meeting*, pp. 1538–1542.

15. Sun, X., Sun, S. Z., Jiang, S., Yang, H., Luo, C., & Pan, W. (2013). Application of Probabilistic Neural Network on Complex Carbonate Reservoir Prediction. In IPTC 2013: International Petroleum Technology Conference.
16. Taner, M. T., Koehler, F. & Sheriff, R.E (1979). Complex Seismic Trace Analysis. *Geophysics*, 44(6), 1041–1063.

**Part V**  
**Advanced Geological Concepts**  
**in Carbonates and Sedimentary Basins**

# The Isoelectric Points of Some Selected Black Shales from the Setap Formation—Sarawak Basin

E.L. Fosu-Duah, E. Padmanabhan and J.A. Gámez Vintaned

**Abstract** The isoelectric points of four shale samples from the Setap Formation, Sarawak basin, Malaysia, were determined and characterised using electrophoretic mobility analysis. The values recorded are relatively low within the acidic range of 2.61–4.87. These values were accounted for by the presence of organic matter and kaolinite mineralogical composition. A positive correlation existed between recorded IEPs and TOC. An average IEP of 3.69 was assigned to the Setap Formation. All the IEPs reported for the samples were relatively lower than the native pH of the samples which suggested that the shales from the Setap Formation will predominantly exhibit cation exchange capacity in situ.

**Keywords** Isoelectric point · Kaolinite · Organic matter

## 1 Introduction

Isoelectric point (IEP) of a shale is the pH at which the net electrical potential of its particles at the hydrodynamic shear is zero [1, 2] This implies that either equal densities of positively and negatively charged particles migrate towards the anode and cathode, respectively, or there is no particulate migration due to the absence of charged sites under the influence of an electric field [3]. IEP is a result of particles in suspension preserving electroneutrality from an unstable microenvironment caused by electrical potential imbalances at the solid-surface interfaces.

IEP is an important parameter of particulate shales dominated by clays with amphoteric surfaces [4]. It defines the pH boundary where suspended shales predominantly exhibit a cation exchange capacity (CEC—exchange of one positive ion by another when the pH of the surrounding is greater than the IEP) or have an electrostatic anion retention abilities [5–7]. Most geological materials have IEP in

---

E.L. Fosu-Duah (✉) · E. Padmanabhan · J.A. Gámez Vintaned  
Faculty of Petroleum Engineering and Geosciences,  
Universiti Teknologi PETRONAS, 32610 Seri Iskandar, Perak Darul Ridzuan, Malaysia

the acidic range and are thus negatively charged at near neutral pH [3]. Although IEP of most pure crystalline oxides, hydroxides and carbonates are well defined, shales can exhibit a variety of IEP(s) due to heterogeneities in mineralogy and/or organic carbon (OC) [7]. Despite the possible continuum of ionic mobilities caused by heterogeneities, the IEP of shales can still be semiquantitatively estimated from ab initio methods proposed by the study [8] on the basis of mineralogical composition. For instance, at a pH of 5, shales composed of goethite only (IEP =  $\sim 8$ ) and kaolinite ( $\sim 4$ ) will have IEP which is approximately the mean of the IEP(s) of the two mineralogical constituents [8, 9]. The ratio of goethite to kaolinite will, of course, play a significant role in the value of IEP.

There is a strong evidence in the literature indicating the intricate relationship between IEP and many geological processes. For example, the works of Tombácz [10] and recently Chukwuma and Nmegbu [11] have thrown more light on the dependency of physicochemical properties such as flocculation, coagulation, dispersion, aggregation and sedimentation on IEP. The parameter has also been shown to influence in organic matter (OM) accumulation in fine-grained sediments (source rocks) [12, 13], in oil or water wettability, and in fluid flow rates [14] in reservoirs. IEP is also known to be the single factor that contributes the most to the control of fluid distribution in pore spaces [15]. Studies of Wasan and Mohan [16] and then Pillai et al. [17] have also added to the understanding of how IEP can strongly and favourably affect the displacement efficiency of oil gangalia by changing the interfacial tension, surface viscosity and electric repulsion of the gangalia entrapped in the pores of the shale.

Although all these studies have well-published data, they are mostly restricted to geological strata in the USA and/or Canada. For this reason, determining, characterising and documenting the IEPs of some selected shales from the Setap Formation of the Sarawak basin, which has never been done, is a crucial contribution to the literature.

## 2 Geological Setting

The Setap Formation is a monotonous and extensive succession of shales with thin lenses of sandstone layers and a few of limestone. It occupies the low-lying country, from Batu Niah north-eastwards to the base of the Lambir Hills and inland towards Limbang and beyond Mulu [18, 19]. In the north-east, the formation grades into the Nyalau Formation [19]. Outcrops of the Setap Formation show a NNW-SSE trend. The main lithologies are grey shale and mudstone, thin lenses of sandstone and minor limestone, with a variable degree of induration which increases towards the Mulu Anticlinorium.

Records from pelagic foraminifera by the Shell Paleontological Laboratory allow to date the Setap Formation as Upper Oligocene to Lower Miocene in age. The OM contained is known to be terrigenous in origin. The Setap Formation correlates with the formations of the prolific offshore sedimentary cycle III [19].

### 3 Materials and Methods

Powders of four (4) onshore samples labelled (S1–S4) from the Setap Formation were used for the study.

Pertinent properties of the shales used in this study were obtained using standard methods. Total organic carbon (TOC) was determined on a Model 240C Perkin-Elmer elemental analyzer (Perkin-Elmer Corp., Norwalk, CT) and reported on a dry weight basis [20]. All 4 shale samples belong to the clay textural classification [21]. The mineralogical compositions were qualitatively determined for this study by X-ray diffraction (XRD) on a Bruker D8 Advance X-ray diffractometer and interpreted using the methods proposed by Macedo [21] and by Fourier transform infrared spectroscopy (IR) using an Agilent technologies Cary 660 Series FTIR Spectrometer equipped with a pike miracle diamond attenuated total reflectance spectroscopy (ATR) and mid-infrared (MIR = 4000–400  $\text{cm}^{-1}$ ).

$\zeta$ -potential measurements of the samples were made with an Anton Paar Surpass<sup>TM</sup> Electrokinetic Analyzer at  $25 \pm 0.1$  °C.

### 4 Results and Discussion

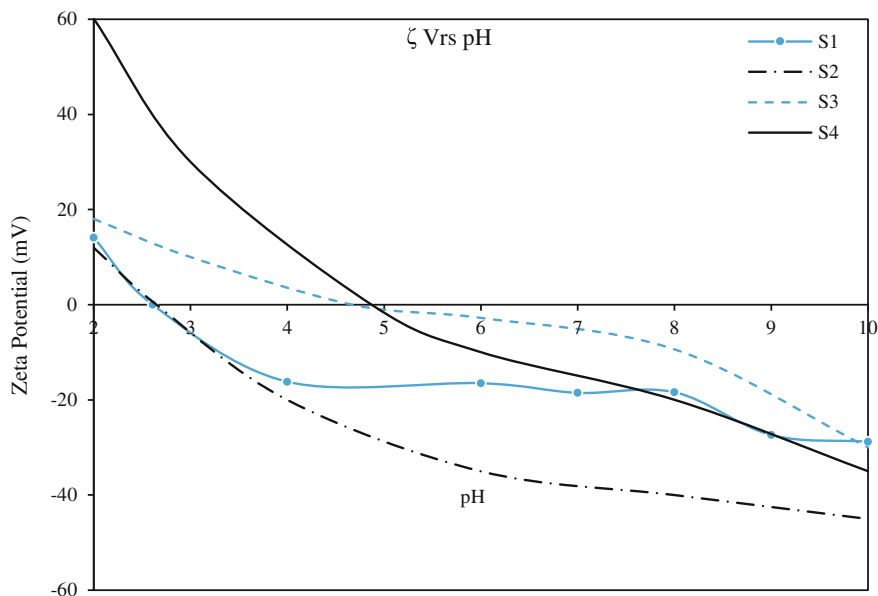
The summary of results from XRD, TOC analysis and pH measurement are presented in Table 1. Detailed qualitative mineralogical study of XRD diffractograms shows that the composition of the four samples is fairly homogeneous, with kaolinite and quartz being the most common minerals among all the samples. Only the presence of goethite makes a slight difference in sample S4.

#### 4.1 Electrophoresis

Figure 1 shows the zeta potential of the four samples as a function of pH. The four samples reported IEP values within the pH range of 2.61–4.87 (Table 1 and Fig. 1). The precise reason for such relatively low (acidic) IEP values must be related to the composition of the shales. For similar geological materials that differ only in their

**Table 1** Pertinent sample characteristics

Sample ID	Sample mineralogy from XRD			Surface properties		
				TOC	pH_H2O	IEP
S1		Kaolinite	Quartz	0.97	3.32	2.61
S2		Kaolinite	Quartz	0.99	4.09	2.65
S3		Kaolinite	Quartz	1.19	5.0	4.61
S4	Goethite	Kaolinite	Quartz	6.20	5.10	4.87



**Fig. 1** Zeta potential of studied shales as a function of pH

organic matter contents, authors like Rajj and Peech [22] and then Morais et al. [23] suggested that TOC inversely correlates with IEP. An experimental evidence from [24] confirmed this hypothesis even though [3] showed the irrelevance of TOC on surface charge properties such as IEP in their study.

OM owes its charge to dissociable functional groups ( $-\text{COOH}$ ), despite the fact that protonation constants of such functional groups according to Tanford [25] are mostly  $>4$  which is incapable of such acidic IEP values (Table 1) [3]. However, for complex multifunctional macromolecules like the ones present in the OM in shale, interaction between neighbouring sites may alter dissociation constants and account for low IEP such as those reported in this study (Fig. 1).

As it is shown in Table 1, IEP correlates positively with TOC. Appel [6] and Fox [26] reported similar results in their work. This finding may suggest the association of OM with mineral constituents possibly absorbed onto aluminol sites of the kaolinite in the samples.

The mineralogical suite of a heterogeneous material such as shale must have a reflection on the surface charge characteristics such as IEP. Several studies have demonstrated this using binary systems (silicon/aluminium—[27]) and can be extrapolated to multicomponent mixtures [8]. Recalling from Table 1, the IEPs reported for the four samples fall within the range of values mostly assigned in the literature to kaolinitic samples [28, 29]. Kaolinite is the commonest clay mineral samples under investigation and may possibly be the determinant of surface charge characteristics in these shales.

Differences in the IEPs may be accounted by variations in kaolinite amounts per sample. The presence of goethite in S4 (IEP = 4.87) was expected to have shifted the IEP towards basic values, but it seems to have had an insignificant effect on the IEP of the sample despite its highest reported IEP. This is because S3 (IEP = 4.61) lacks goethite (composition is mainly kaolinite) but reported comparable IEP values (Table 1). This may indicate that the aluminol sites of the kaolinite in samples S3 (IEP = 4.61) and S4 (IEP = 4.87) have a higher influence on their surface charge properties as compared to S1 (IEP = 2.61) and S2 (IEP = 2.65) which may solely be influenced by the silanol sites [2, 30]. The ratios of Si/Al ratios in kaolinite may, therefore, account for variations in IEP in either the aluminol or silanol sites.

## 5 Conclusions

IEP positively correlates with the TOC, which is an abnormal relationship, and further work is needed to elucidate this relationship.

Using electrophoretic mobility to determine and characterise the surface charge properties of the Setap Formation, it has been shown that:

- The average IEP of the shale is approximately 3.69, which implies that the shales will predominantly be receptive to positively charged ions in situ.
- IEP positively correlates with the TOC, which is an abnormal relationship, and further work is needed to elucidate this relationship.

## References

1. R. J. Hunter, *Zeta potential in colloids science*. Academic Press, NY, 1981.
2. E. Tombácz and M. Szekeres, "Surface charge heterogeneity of kaolinite in aqueous suspension in comparison with montmorillonite," *Appl. Clay Sci.*, vol. 34, pp. 105–124, 2006.
3. H. A. Elliot and D. L. Sparks, "Electrokinetic behaviour of a paleudult profile in relation to mineralogical composition," *Soil Sci.*, pp. 1–8, 1981.
4. The Society for Sedimentary Geology (SEPM-1988), "Clay Minerals for Petroleum Geologists and Engineers. Short Course Notes 22," 2012.
5. R. O. James and G. A. Parks, "Characterization of aqueous colloids by their electrical double-layer and intrinsic surface chemical properties.," *Surf. Colloid Sci.*, vol. 12, pp. 119–216, 1982.
6. W. Stumm and J. J. Morgan, *Aquatic chemistry*, 3rd ed. John Wiley and Sons, New York, 1996.
7. C. Appel, L. Q. Ma, R. Dean Rhue, and E. Kennelley, "Point of Zero Charge Determination in Soils and Minerals via Traditional Methods and Detection of Electroacoustic Mobility," *Geoderma*, vol. 113, pp. 77–93, 2003.
8. G. A. Parks, "The isoelectric points of oxides, solid hydroxides and aqueous hydroxo complex systems," *Chem. Rev.*, vol. 65, pp. 177–198, 1965.



9. G. A. Parks, "Aqueous Surface Chemistry of Oxides and Complex Oxides Minerals-Isoelectric Point and Zero Point of Charge," *Adv. Chem.*, vol. 67, pp. 121–160, 1967.
10. M. Kosmulski, *Surface charging and points of zero charge*. New York: CRC Press, 1956.
11. E. Tombácz and M. Szekeres, "Colloidal behaviour of aqueous montmorillonite suspensions: the specific role of pH in the presence of indifferent electrolytes," *Appl. Clay Sci.*, vol. 27, pp. 75–94, 2004.
12. G. J. Chukwuma and J. S. Nmegbu, "Chemical flocculation of microorganisms in the reservoir during MEOR," *J. Eng. Adv. Technol.*, vol. 3, pp. 2249–2258, 2014.
13. J. I. Hedges and R. G. Keil, "Sedimentary organic matter preservation: an assessment and speculative synthesis," *Mar. Chem.*, vol. 49, pp. 81–115, 1995.
14. E. A. Jenne, "Controls on Mn, Fe, Co, Ni, Cu, and Zn concentrations in soils and water—the significant role of hydrous Mn and Fe oxides," in *Trace Inorganics in Water, Advances in Chemistry Vol 73*, American Chemical Society, Washington, 1968, pp. 337–387.
15. J. R. Kanicky, S. Pandey, and D. O. Shah, "Surface chemistry in the petroleum industry," *Handb. Appl. Surf. Colloid Chem.*, pp. 252–267, 2002.
16. D. T. Wasan and V. Mohan, "Interfacial rheological properties of fluid interfaces containing surfactants," in *Improved Oil Recovery by Surfactant and Polymer Flooding*, D. O. Shah and R. S. Schechter, Eds. New York: Academic Press, 1977.
17. V. Pillai, J. R. Kanicky, and D. O. Shah, "Applications of microemulsions in enhanced oil recovery," in *Handbook of Microemulsion Science and Technology*, Kumar P. and Mittal, K. L., Marcel Dekker, Ed. 1999, pp. 743–753.
18. E. Agostinelli, M. R. Tajuddin, E. Antonielli, and M. M. Aris, "Miocene - Pliocene paleogeographic evolution of a tract of Sarawak offshore between Bintulu and Miri Bulletin of the Geological Society of Malaysia," vol. 27, pp. 117–136, 1990.
19. C. S. Hutchison, *Geology of North West Borneo: Sarawak, Brunei and Sabah*, 1st ed., vol. VI. Elsevier, NY, USA., 2005.
20. W. G. Dow and D. B. Pearson, "Organic matter in gulf coast sediments," in *Technology Conference*, 1975.
21. J. Macedo and R. B. Bryant, "Morphology, mineralogy, and genesis of a hydrosequence of oxisols in Brazil," *Soil Sci. Soc. Am.*, vol. 51, pp. 690–698., 1987.
22. V. Rajj and M. Peech, "Electrochemical Properties of Some Oxisols and Alfisols of the Tropics," *Soil Sci. Soc. Am. Proc.*, vol. 36, pp. 587–593, 1972.
23. F. L. Morais, A. L. Page, and L. J. Lund, "The effect of pH salt concentration and nature of electrolytes on the charge characteristics of Brazilian tropical soils," *Soil Sci. Soc. Am.*, vol. 40, pp. 521–527, 1976.
24. W. H. Hendershot and L. M. Lavkulich, "The Effect of Sodium Saturation and Organic Matter Removal on the Value of Zero Point of Charge," *Soil Sci.*, vol. 128, pp. 136–141, 1979.
25. C. Tanford, *Physical chemistry of macromolecules*. New York: John Wiley and Sons Inc, 1961.
26. R. L. Fox, "Some highly weathered soils of Puerto Rico: 3. Chemical properties.," *Geoderma*, vol. 27, pp. 139–179, 1982.
27. T. J. Smoilik, M. Harman, and D. W. Fuerstenau, "Surface characteristics and flotation behaviour of aluminosilicates.," *Trans Am. Inst. Min. Met. Eng.*, vol. 235, pp. 367–375, 1966.
28. Y. Hu and X. Liu, "Chemical composition and surface property of kaolins," *Miner. Eng.*, vol. 16 (11), pp. 1279–1284, 2003.
29. J. D. Miller, J. Nalaskowski, B. Abdul, and D. Hao, "Surface characteristics of kaolinite and other selected two layer silicate minerals," *Can. J. Chem. Eng.*, vol. 85, pp. 617–624, 2007.
30. Y.-H. Hu, W. Sun, X.-W. Liu, and D.-Z. Wang, "Cleavage Nature, Electrokinetics, aggregation and dispersion of kaolinite," *Trans. Nonferrous Met. Soc. China*, vol. 13, no. 6, pp. 1430–1434, 2003.

# Diagenetic Process and Their Effect on Reservoir Quality in Miocene Carbonate Reservoir, Offshore, Sarawak, Malaysia

Hammad Tariq Janjuhah, Ahmed Mohammad Ahmed Salim,  
Deva Parsed Ghosh and Ali Wahid

**Abstract** The carbonate platforms form one of the genetic gas reservoirs in the subsurface in Central Luconia, offshore, Sarawak, Malaysia. A detailed investigation of available core and thin sections revealed that different diagenetic parameters influence the reservoir quality in Central Luconia. Marine diagenesis, dissolution, and burial are the three main diagenetic environments that have affected the carbonate rocks in Central Luconia. Micrite envelop, cementation, fracture, compaction, and dissolution are the dominant diagenetic parameters which are identified in the current field of study. Among all the observed diagenetic features, dissolution feature was formed as a result of subaerial exposure during the meteoric diagenesis and contribute to porosity enhancement and reservoir quality. The compaction and cementation (calcite and dolomite) have a negative impact on the reservoir behavior. Based on the observed qualitative porosity types and their quantitative distribution in Well A of Central Luconia, the porosity in Central Luconia is a combination of depositional, diagenetic and fracturing. The diagenetic porosity is the far more dominant types of porosity, and the carbonate reservoir in Central Luconia is the type of diagenetic reservoirs.

**Keywords** Diagenetic processes · Porosity types · Reservoir quality

---

H.T. Janjuhah (✉)

South East Asia Carbonate Research Laboratory, Department of Geosciences,  
University Technology PETRONAS, 32610 Seri Iskandar, Perak, Malaysia  
e-mail: Hammadtariq013@gmail.com

A.M.A. Salim · A. Wahid

Department of Geosciences, University Technology PETRONAS,  
32610 Seri Iskandar, Perak, Malaysia  
e-mail: mohamed.salim@petronas.com.my

A. Wahid

e-mail: aliwahid@live.com

D.P. Ghosh

Centre for Seismic Imaging, Department of Geosciences, University Technology  
PETRONAS, 32610 Seri Iskandar, Perak, Malaysia  
e-mail: drdeva@petronas.com.my

## 1 Introduction

Central Luconia is found to be a prolific gas exploration target for many oil companies since it was proven to contain numerous amount of hydrocarbon. These carbonates in Central Luconia are economically significant, containing 65 trillion cubic feet of gas in place with minor contribution of oil [1, 2]. In addition, more than 120 carbonate buildups still remain undrilled.

In order to have a good understanding of the carbonate rocks at reservoir scales, the first step is to understand them at the pore scale. Carbonate rocks are very complex to predict the porosity and permeability. Porosity in carbonate rock is distributed into three genetic categories, chronologically the first step during deposition, then diagenesis (Vuggy, Moldic, etc.), and later on due to compaction (fracture porosity). In order to predict the reservoir quality, it is necessary to understand the origin of porosity and its effect on reservoir properties. However, the diagenesis and the effect of diagenetic processes on reservoir properties in Central Luconia carbonate rock were still missing prior to the present study. The objective of this study is to highlight the different diagenetic processes which affect the carbonate rock in Central Luconia and different porosity types with quantitative distribution to determine the reservoir quality.

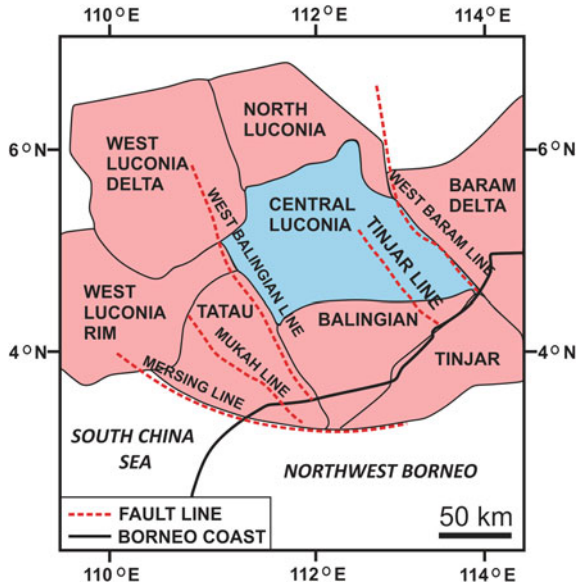
## 2 Regional Geology

Central Luconia is one of the biggest gas provinces in Sarawak basin, offshore NW Borneo (Fig. 1). It is dominated by the large development of middle Miocene to recent carbonate [3]. The west Baram line to the west distinguished the Central Luconia from Baram delta [4], and to the south is the Balingian Province that extended into Central Luconia (Fig. 1).

Several geologic provinces surrounded by Central Luconia have been identified based on their structural and stratigraphic pattern. Central Luconia is flanked by deep basins on the west, north, and east sides, respectively [3]. Basement-involved extensional tectonics, strike-slip, and wrench tectonic structures are represented in the different parts of Central Luconia basin [4, 5].

The southern part of Central Luconia during the Oligocene to Early Miocene was defined as a coastal plain to inner neritic setting [4, 6, 7], whereas inner and outer neritic was described for the northern part of Central Luconia. The extensional forces during the Late Oligocene to Early Miocene time divided the Central Luconia into several half graben and graben structures heading SSW–NNE orientation, which are the products of normal faults [8, 9]. The normal fault negatively impacted the carbonate growth in Central Luconia. During the Middle Miocene time, the dextral strike-slip fault deformation dominantly representing the extensional setting and these dextral strike-slip faults affected the internal stratigraphy or the growth of carbonate platform that grew on the heights of fault-bounded.

**Fig. 1** Offshore Sarawak's location and structural map showing the boundaries of the carbonate platform of the Central Luconia Province. Modified from [3]



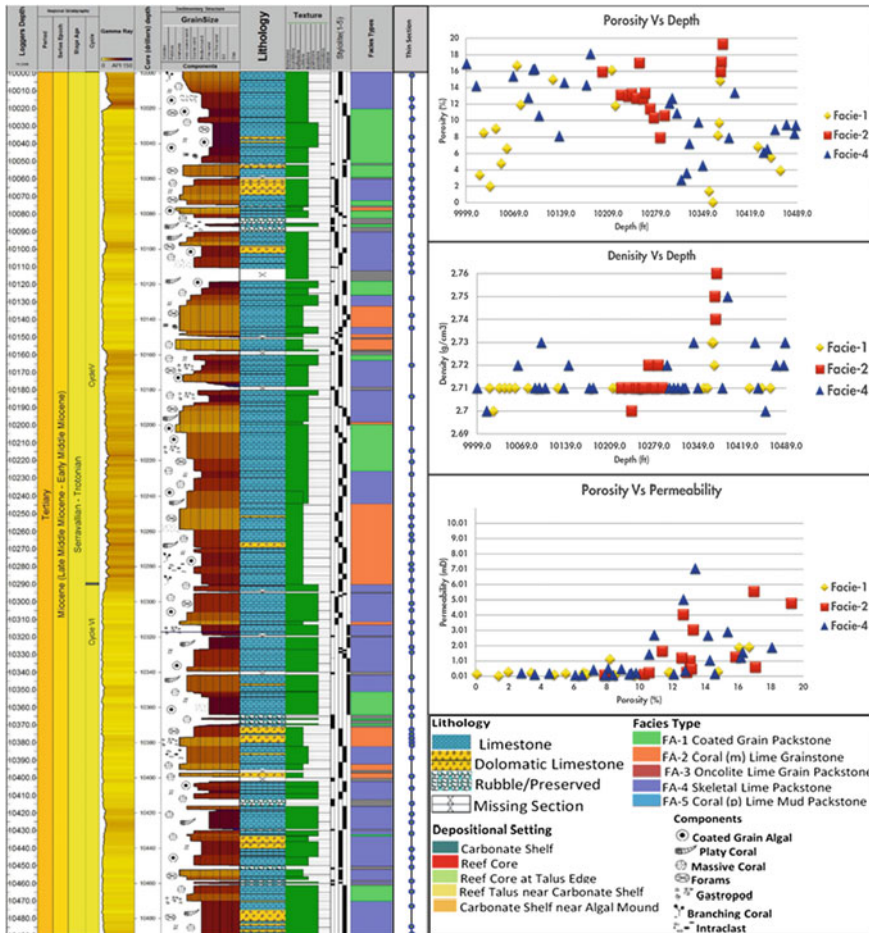
### 3 Materials and Methods

The available core of 492 ft of Well A from Central Luconia is studied in this research to observe different parameters such as lithology, texture, grain size, porosity, and allochems. To carry out the petrographic study, 80 thin sections were prepared from a depth interval of 9999–10489 ft (Fig. 2). These thin sections represent different facies and different lithologies based on grain density, different porosity, and permeability variation with depth (Fig. 2). These thin sections were stained and studied under the polarized light microscope to identify the different diagenetic parameters, such as micritic envelop, cementation, dissolution, mechanical compaction, chemical compaction, and stylolite. In order to classify the porosity types, the classification by Choquette and Pray [10] was used. The quantitative distribution of different porosity types was also studied in each selected thin section (Fig. 3) to understand the quality of the reservoir.

### 4 Results

#### 4.1 Diagenesis

Petrography reveals a variety of diagenetic features. Detailed accounts of diagenetic features are presented below.



**Fig. 2** Sedimentological log showing the location of selected thin section based on stratigraphic position, gamma ray, density, porosity, permeability, and facies types

### 4.1.1 Micrite Envelopes

Micrite envelopes are the first diagenetic phase, and it takes place in the marine diagenesis environment of limestone. Micrite envelopes have original aragonitic mineralogical composition. Aragonite dissolves in the early phase of diagenesis and is replaced by calcite. The evidence of the presence of micrite evaporates locally at the depth of 10036 ft (Fig. 4a) and 10164.3 and 10374 ft (Fig. 4b), forming crusts around echinoderm plate and some other bioclasts. In the next phase, the aragonite dissolved into grains containing aragonitic minerals and precipitated as calcite cement.

Depth core (ft)	Facies	Porosity Type					total
		Mouldic (%)	Intraparticle (%)	Interparticle (%)	Fracture (%)	Vugs (%)	
10000 ft	FA-4	45	30	5	0	20	100
10014.6 ft	FA-4	45	20	10	0	25	100
10019.2 ft	FA-1	35	25	5	5	30	100
10025.3 ft	FA-1	40	25	10	0	25	100
10035 ft	FA-1	35	30	5	0	30	100
10043 ft	FA-1	50	20	5	0	25	100
10051.1 ft	FA-1	40	25	10	0	25	100
10059.9 ft	FA-1	45	10	15	0	30	100
10064 ft	FA-4	20	40	25	0	15	100
10069.3 ft	FA-4	35	30	15	0	20	100
10074.6 ft	FA-1	30	40	15	0	15	100
10080.2 ft		45	20	10	0	25	100
10091.6 ft	FA-4	40	30	10	0	20	100
10098.3 ft	FA-4	35	30	10	0	25	100
10101.2 ft	FA-4	45	30	5	0	20	100
10107.4 ft	FA-4	40	45	5	0	10	100
10112.1 ft	Missing Section	35	30	10	0	25	100
10127.7 ft	FA-1	30	40	5	0	25	100
10137.1 ft	FA-4	40	30	10	0	20	100
10144.8 ft	FA-4	35	35	10	0	20	100
10165.3 ft		45	30	10	0	15	100
10177.8 ft	FA-4	40	25	15	0	20	100
10183.5 ft	FA-4	40	35	5	0	20	100
10201.4 ft	FA-2	30	30	10	0	30	100
10214.8 ft	FA-1	35	30	5	0	30	100

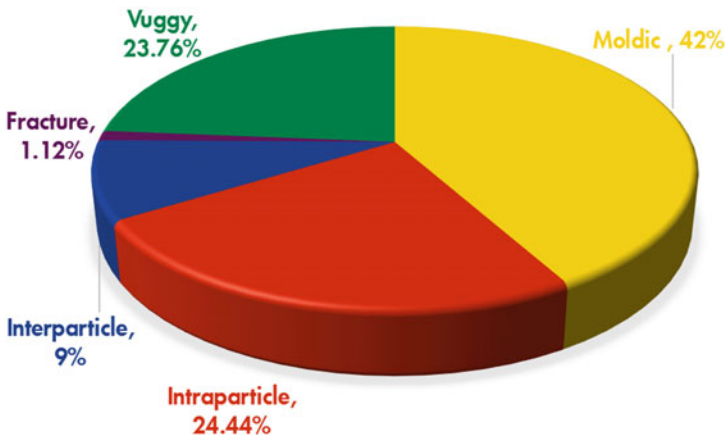
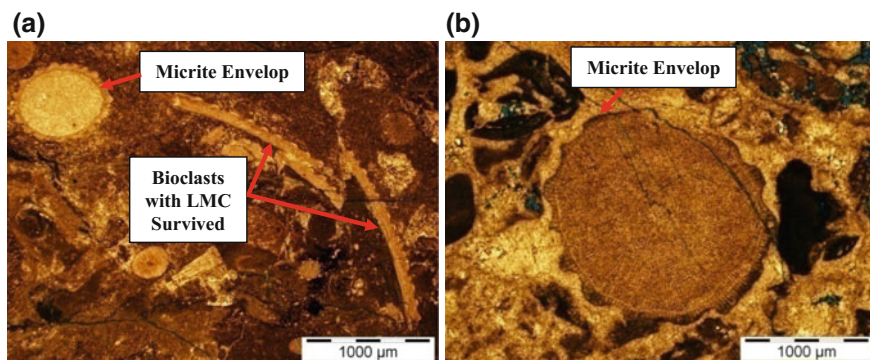


Fig. 3 Quantitative distribution of porosity types in Well A, Central Luconia, Sarawak, Malaysia

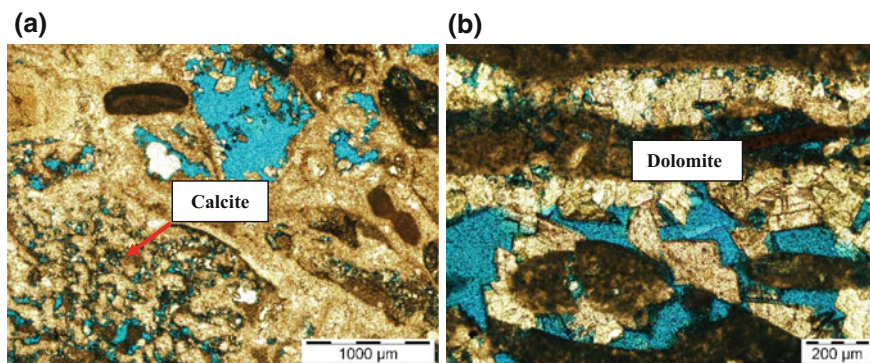
In some cases, all the internal structures are destroyed and no internal structures are observed, but outer structures and morphology of these grains are preserved. The micrite envelopes affected permeability by filling up the pore spaces (Fig. 4b).



**Fig. 4** Photo-micrograph representing features of diagenesis. **a** Diagenetic process of Echinodermate and bioclasts (1) HMC nature of echinoderm plates leads to neomorphism (2) Bioclasts with LMC survived at the depth of 10036 ft. **b** Diagenetic process of Echinodermate at the depth of 10165 ft, Echinodermplate neomorphosed and fractured during telodiagenesis

#### 4.1.2 Cementation

The cementation of carbonate sediments is always taken into an important diagenetic process. Based on the petrographic investigation, two types of cements, calcite and dolomite, occurred in Well A. On a certain occasion, the calcite cementation is followed by stylolization. Toward the younger/upper part of the Well A, the appearances of calcite cement become dominant (Fig. 5a). At the depth of 10375 ft, the dolomitic cement filled up the pore spaces (Fig. 5b). Its crystals are smaller in size at margins and get larger toward the center of pores as per the available accommodation spaces.



**Fig. 5** Photo-micrograph of microfacies and features of diagenesis. **a** Calcite cement filling up the pore spaces at the depth of 10062 ft. **b** Dolomitization occurred, dolomite filling up the pore spaces and reducing porosity, with sample depth 10375.7 ft



### 4.1.3 Mechanical Compaction

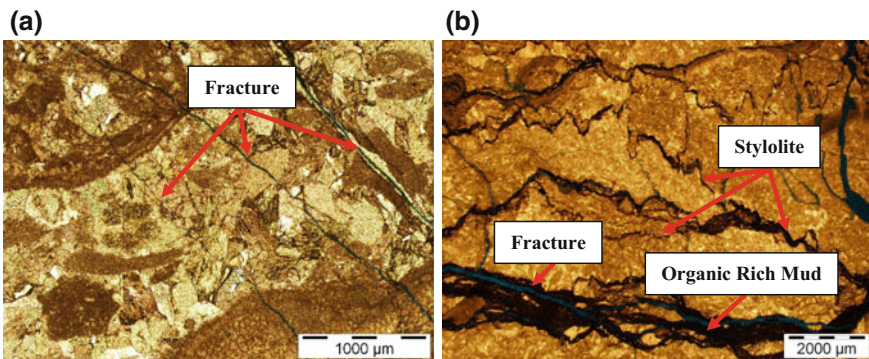
The next diagenetic event is mechanical compaction. In the case of thin section observation, the poorly cemented components are broken down as a result of an increase of mechanical compaction (Fig. 4a). Mechanical compaction also plays an important role in enhancing porosity and permeability by forming fractures.

### 4.1.4 Fracture

Tectonic stresses, overburden pressure, and pre- and post-cementation phase lead to fractures. Various horizontal and vertical fracture veins are found in the measured section at different depths (Figs. 5a and 6a). Different phases of fractures, along with stylolization, have been observed. The development of stylolite in the organic-rich mud has also been observed at the depth of 10043 ft which disrupts the fractures' growth (Fig. 6b). The investigated sections reveal the enhancement of effective porosity and permeability due to the occurrence of various phases of fractures forming interconnectivity. Moreover, the filling of host area creates additional porosity, which took place in the process of dissolution.

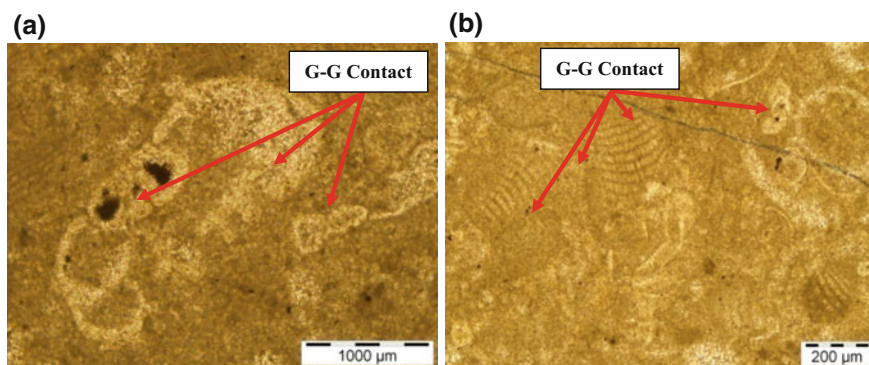
### 4.1.5 Chemical Compaction

In the last stage of diagenesis, the compaction increases as a result of overburden pressure or due to tectonic stress. The grain-to-grain contact took place, which is clearly observed at the depth of 10363.8 ft (Fig. 7a, b). The chemical compaction results in the reduction of the overall pore throat size and volume as well. The embayment of one grain into another is also observed.



**Fig. 6** Photo-micrograph of fractures. **a** Dissolution, overburden, or tectonic activity resulting in fracture at the depth of 10364.8 ft. **b** Calcified algal mounds with bedding parallel late-stage fractures and different levels of stylolites filled with organic matter at the depth of 10043 ft





**Fig. 7** Photo-micrograph representing grain-to-grain contact. **a** Representing grain-to-grain contact at the depth of 10363.8 ft. **b** Representing the grain-to-grain contact at the same depth at 10363.8 ft

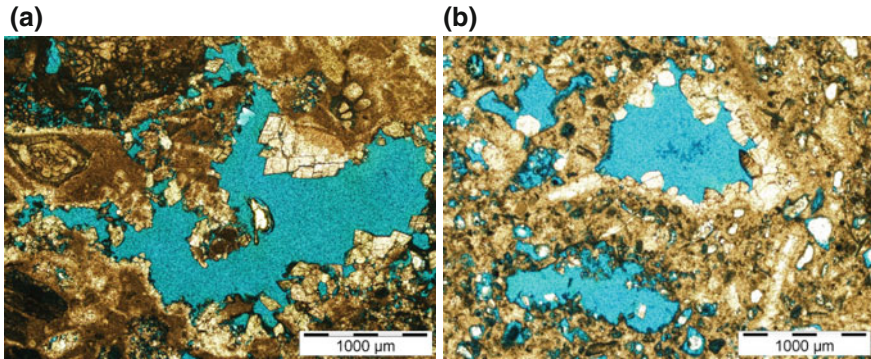
#### 4.1.6 Stylolite

The stylolites develop as a result of pressure dissolution or chemical compaction. The formations of stylolites are the product of continuous dissolution of compacted grains. In the recorded thin sections, the indication of pressure solution seams and the development of stylolites are observed, which are the indications of chemical compaction due to the result of tectonic activities or overburden pressure. The various levels of stylolites are observed in the studied thin sections, ranging from low-amplitude stylolite (Fig. 6b) to high-amplitude stylolite which is found in mudstone. However, the stylolites are frequently found throughout the core in this study.

#### 4.1.7 Dissolution

Dissolution is one of the important diagenetic processes which has a positive impact on porosity and permeability. The secondary porosity is formed by the mechanism of dissolution. Vuggy, moldic, and interparticle porosity is generated by the process of dissolution, as a result of cement dissolution. In Well A, the dissolution formed vuggy porosity, which is in the form of touching and connected vugs (Fig. 8a).

The size of these vugs reached up to 1 cm. It is variable with a matrix background. The vuggy porosity enhances the reservoir quality, but some of these pores have subsequently been filled with cement and have a negative impact on reservoir quality (Fig. 8b). The meteoric freshwater is the place where dissolution thought to take place.



**Fig. 8** Photo-micrograph representing dissolution process. **a** Dissolution process forming connected vugs at the depth of 10186 ft and **b** Vugs formed by the process of dissolution and later filled with cement at the depth of 10278 ft

## 4.2 Porosity

The different types of porosity (Fig. 9) are observed in thin sections along with their quantitative distribution (Fig. 10) in Well A as described below.

### 4.2.1 Moldic Porosity

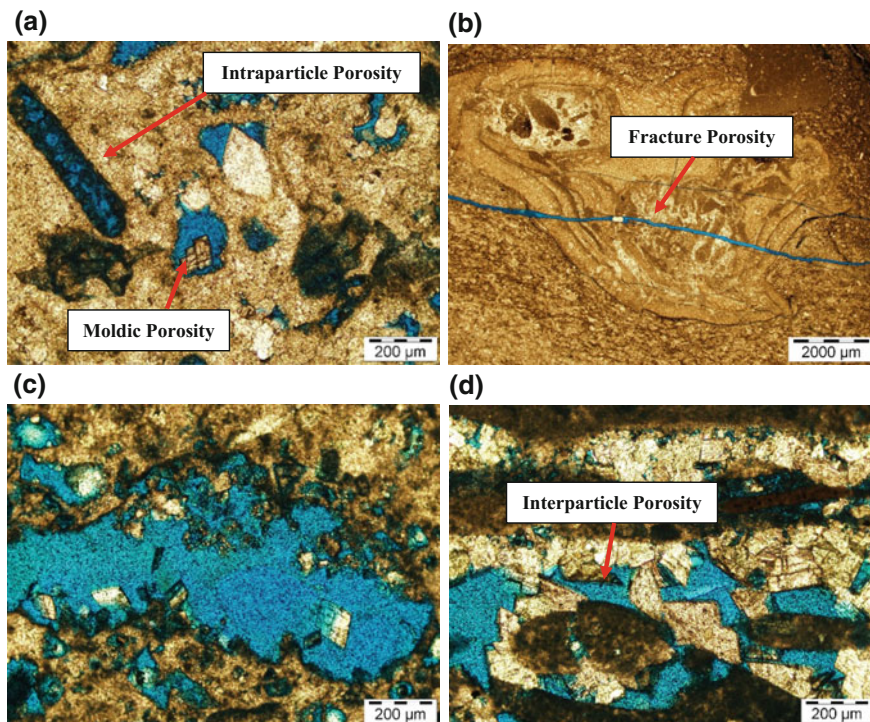
The moldic porosity is the dominant porosity type in Well A. The dissolution of unstable shell fragments results in moldic porosity. The average amount of moldic porosity in thin sections is up to 40% (Fig. 10). In some samples, the moldic porosity (Fig. 9a) reduced dramatically by the plugged of calcite cement.

### 4.2.2 Vuggy Porosity

The vuggy porosity is the second dominant porosity type. The formation of vuggy porosity is the cause of non-fabric selective dissolution, which is commonly observed throughout all the selected study samples (Fig. 9c) in the form of either connected vugs or disconnected vugs as a result of cement. The vuggy porosity ranges from 20 to 25% (Fig. 10).

### 4.2.3 Intraparticle Porosity

The intraparticle porosity is the primary and fabric selective. It occurred mostly in different types of bioclasts (Fig. 9a), such as foraminifera and red algae. The amount of intraparticle porosity ranges from 15 to 20% (Fig. 10).



**Fig. 9** Photo-micrograph representing different types of porosity. **a** Intraparticle and moldic porosity at the depth of 10090 ft. **b** Fracture porosity at the depth of 10250 ft. **c** Vuggy porosity at the depth of 10259 ft. **d** Interparticle porosity at the depth of 10357.7 ft

#### 4.2.4 Intraparticle Porosity

The intraparticle porosity (Fig. 9a) in the current study is an average amount of 10%.

#### 4.2.5 Fracture Porosity

Fracture porosity is rarely observed in Well A (Fig 9b). The identified fractures are open to semifilled with calcite cement, but the open fractures are the dominant ones (Fig. 9b).

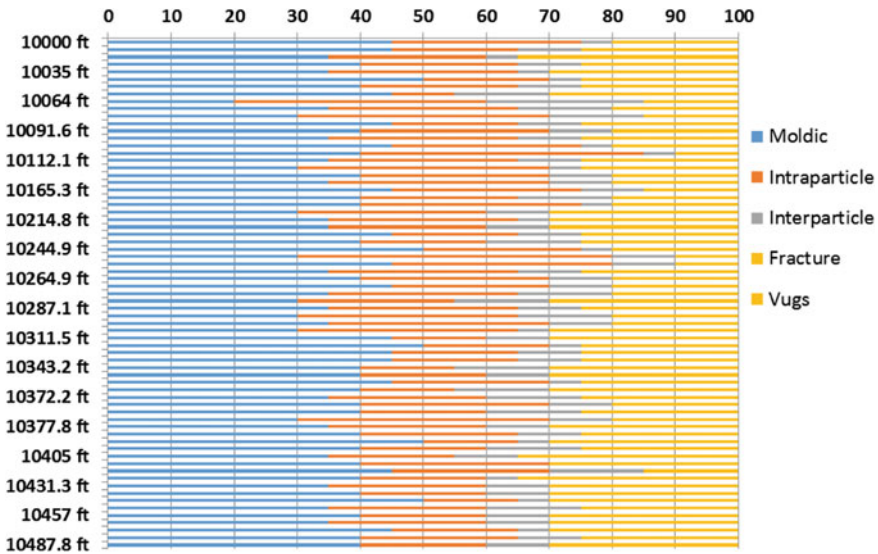


Fig. 10 Quantitative distribution of porosity types in Well A, Central Luconia, Offshore Sarawak, Malaysia

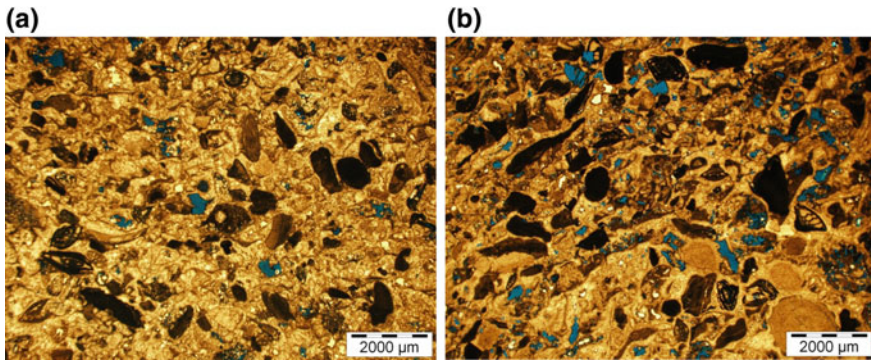
## 5 Discussion

In the current study, three diagenetic processes affected the diagenetic alteration, which are marine diagenesis, dissolution, and burial. Marine environment is the first process of diagenetic alteration. The most important marine diagenetic features include micrite envelopes, microcrystalline, and peloid cements [11]. The presence of algae activity in the allochems is the result of micritization [12]. The formation of micrite envelop around the bioclasts takes place by the alteration of bioclastic grain or below by endolithic algae in a quieter water area [13]. Micritization of allochems is observed by the presence of algae, which took place in the early stage of diagenesis on the seafloor. Micritization process is an early diagenetic process characteristic of the shallow marine setting [12, 14]. Firstly, around the allochems, the micrite envelopes are formed (Fig. 4a, b). Based on this action, the allochems are replaced by micrite. Since the endolithic algae action is intense, most of the other allochems and skeletal grains are highly micritized as observed at the depth of 10154.5 (Fig. 11a) and 10165.5 ft (Fig. 11b).

After the deposition of carbonate in Central Luconia, the meteoric diagenesis affected the formation. Undersaturated meteoric water affected the carbonate rock as a result of dissolution by forming vuggy porosity at different depths (Figs. 8a and 9c).

The burial diagenetic processes have also affected the carbonate rock. Compaction, fracture, calcite, and dolomitization are the major burial events. Fitted fabric and shell breakage (Fig. 4a) are the result of overburden pressure during the





**Fig. 11** Photo-micrograph representing highly micritized skeletal grains. **a** Randomly oriented, multiple types of bioclasts with highly micritized grains at the depth of 10154.5 ft. **b** Bioclasts with varied textural maturity. Randomly oriented, multiple types of bioclasts with high micritization at the depth of 10165.5 ft

shallow burial environment. With respect to the increase of burial depth, the overburden pressure increased and solution seams and stylolites (Fig. 6b) and fracture (Figs. 4b, 5a, 6a and 9b) are formed. The source of calcite cement which is dissolved during the formation of stylolite is probably as a result of overburden pressure.

Calcite and dolomite cement play an important role in decreasing the porosity. Calcite cement filled in the vugs (Fig. 8b) and decreased the void spaces. The deep burial stage was associated with extensive neomorphism (Fig. 4a) that had converted the bioclasts, matrix, and mesogenetic cement spars into regionally varying sized clumpy. These processes sealed all the pores that were present in the rock. The accurate timing of dolomitization is difficult to determine, but it seems that fine crystal dolomites are formed early (Fig. 9c) than coarse crystalline dolomites (Fig. 9d). The rate of dolomitization increases with time.

### ***5.1 Diagenetic Processes and Its Effect on Reservoir Quality***

Diagenetic processes were responsible in Central Luconia for the modification of reservoir quality. Micritization, cementation, compaction, dissolution, and dolomitization are the more significant diagenetic processes that influence the reservoir quality of the Central Luconia carbonate reservoir. The influence of diagenetic processes on Central Luconia carbonate rocks is categorized into two classes which are enhancing porosity and decreasing porosity. Generally, the reservoir quality is diagenetically controlled [12, 15, 16]. The micritization usually fills up the pore throats which have an effect on permeability. During burial compaction, sometimes porosity reduction is prevented due to micritization [15]. In micritization processes, most of the bioclastic grains are totally micritized by the

action of intensive endolithic algae action and caused the formation of micrite envelop which have negative impact on permeability. The dissolution process plays an important role in increasing the porosity [17]. Three types of porosity, vuggy, moldic, and enlarged intergranular, are generated in the process of dissolution [10]. Vuggy porosity (Fig. 9c) and moldic (Fig. 9a) porosity are the results of dissolution process. Dissolution process has a positive effect on reservoir quality. Fracture appeared (Fig. 4B, 5a, 6a and 9b) in the study interval as well.

Reservoir quality is highly affected by the most important diagenetic feature which is cementation [12]. In the studied thin sections, calcite cement has a negative effect on reservoir quality. Calcite cement replaced bioclasts with minor-to-no visible porosity.

## 6 Conclusion

In summary, micritization, cementation, dissolution, compaction, and dolomitization are the most important diagenetic processes which affected the Central Luconia carbonate rock. Among all, cementation, dolomitization, and compaction reduce porosity, whereas dissolution increases porosity. Although the effect of dissolution began during meteoric diagenesis in the studied rock and it did not expose for a long time, it increased porosity but not effectively compared to Persian Gulf.

**Acknowledgements** The author would like to thank Sarawak Shell Sdn Bhd and Petronas Sdn Bhd for providing data and supporting the Ph.D. work. The author also thanks Prof Michael. C. Poppelreiter and Dr. Mumtaz shah for their skilled help.

## References

1. N. F. M. Khazali, S. Osman, and C. Abdullah, "The awakened giants," in *Petroleum Geoscience Conference & Exhibition 2013*, 2013.
2. A. Abdullah, J. Singh, S. Osman, and C. Abdullah, "Unravel New Exploration Opportunity in Central Luconia," in *PGCE 2012*, 2012.
3. E. Koša, "Sea-level changes, shoreline journeys, and the seismic stratigraphy of Central Luconia, Miocene-present, offshore Sarawak, NW Borneo," *Marine and Petroleum Geology*, vol. 59, pp. 35–55, 2015.
4. S. Olave Hoces, "Controls on isolated carbonate platform evolution and demise, Central Luconia province, South China Sea," Texas A&M University, 2006.
5. C. Morley, R. King, R. Hillis, M. Tingay, and G. Backe, "Deepwater fold and thrust belt classification, tectonics, structure and hydrocarbon prospectivity: a review," *Earth-Science Reviews*, vol. 104, pp. 41–91, 2011.
6. I. Mat-Zin and R. Swarbrick, "The tectonic evolution and associated sedimentation history of Sarawak Basin, eastern Malaysia: a guide for future hydrocarbon exploration," *Geological Society, London, Special Publications*, vol. 126, pp. 237–245, 1997.
7. K. Ho, "FUI, 1978. Stratigraphic framework for oil exploration in Sarawak," *Geological Society of Malaysia, Bulletin*, vol. 10, pp. 1–13.

8. M. Madon, C. L. Kim, and R. Wong, "The structure and stratigraphy of deepwater Sarawak, Malaysia: implications for tectonic evolution," *Journal of Asian Earth Sciences*, vol. 76, pp. 312–333, 2013.
9. K. Ting, E. Chung, and O. Al Jaaidi, "Evolution and controlling factors of Miocene carbonate build-up in Central Luconia, SE Asia: Insights from integration of geological and seismic characterization," *Integrated Petroleum Engineering and Geosciences (ICIPEG)*, vol. 15, p. e17, 2010.
10. P. W. Choquette and L. C. Pray, "Geologic nomenclature and classification of porosity in sedimentary carbonates," *AAPG bulletin*, vol. 54, pp. 207–250, 1970.
11. E. Gischler, A. L. Thomas, A. W. Droxler, J. M. Webster, Y. Yokoyama, and B. R. Schöne, "Microfacies and diagenesis of older Pleistocene (pre-last glacial maximum) reef deposits, Great Barrier Reef, Australia (IODP Expedition 325): A quantitative approach," *Sedimentology*, vol. 60, pp. 1432–1466, 2013.
12. A. Shakeri and S. Parham, "MICROFACIES, DEPOSITIONAL ENVIRONMENT, AND DIAGENETIC PROCESSES OF THE MAUDDUD MEMBER, IN THE PERSIAN GULF," *Journal of Petroleum Science and Technology*, vol. 4, pp. 67–78, 2014.
13. M. E. Tucker and V. P. Wright, *Carbonate sedimentology*: John Wiley & Sons, 2009.
14. K. Bjorlykke, *Petroleum geoscience: From sedimentary environments to rock physics*: Springer Science & Business Media, 2010.
15. A. A. Taghavi, A. Mørk, and M. A. Emadi, "Sequence stratigraphically controlled diagenesis governs reservoir quality in the carbonate Dehluran Field, southwest Iran," *Petroleum Geoscience*, vol. 12, pp. 115–126, 2006.
16. V. Tavakoli, H. Rahimpour-Bonab, and B. Esrafil-Dizaji, "Diagenetic controlled reservoir quality of South Pars gas field, an integrated approach," *Comptes Rendus Geoscience*, vol. 343, pp. 55–71, 2011.
17. B. Esrafil-Dizaji and H. Rahimpour-Bonab, "Effects of depositional and diagenetic characteristics on carbonate reservoir quality: a case study from the South Pars gas field in the Persian Gulf," *Petroleum Geoscience*, vol. 15, pp. 325–344, 2009.

# Lithostratigraphy of Paleozoic Carbonates in the Kinta Valley, Peninsular Malaysia: Analogue for Paleozoic Successions

Haylay Tsegab, Chow Weng Sum and Jasmi Ab Talib

**Abstract** Tectonics of the Paleo-Tethys resulted in the formation of three distinct stratigraphic zones in Peninsular Malaysia, namely western, central, and eastern zones. The western zone encompasses extensive carbonate sediments, among which is the Kinta Limestone, which forms a major Silurian to Permian lithological unit. Subjection to diagenetic and thermal alteration of this succession and paucity of unweathered and accessible outcrop sections posed constraints on precise characterization of lithofacies. A few localities in the northern part of the valley indicate preservation of primary sedimentary/geochemical features with variable thermal alteration. Drilling campaign to recover a continuous succession, followed by geophysical logging allowed lithological characterization and detection of stratigraphic surfaces. The present study attempts to characterize the other monotonous Kinta Limestone into mappable units with defined stratigraphic surfaces that were not obvious from outcrops. Core profiles, natural gamma-ray, density, and caliper logs were used to interpret stratigraphic surfaces. Low gamma-ray and density values with near-shale baseline spontaneous potential were noted on the studied sections. Major caving and higher peaks of gamma-ray corresponding to siliciclastics were resulted perhaps from potassium and thorium. The lower gamma-ray readings of the Kinta Limestone may also show presence of little detrital mixing in the carbonates. This is in good agreement with the mineralogical composition that showed the dominant occurrences of calcite, followed by dolomite and low detrital silica. The stratigraphic surfaces between the siliciclastics and limestone are represented by sharp contact surfaces. The logs showed synergy with lithological and stratigraphic interpretations on the cores and outcrops, and this may facilitate local and regional correlations. This may advance the understanding of the Paleozoic basins and serve as analogue for wireline log signature in the Paleo-Tethys basins.

---

H. Tsegab (✉) · C.W. Sum · J.A. Talib  
Department of Geosciences, Universiti Teknologi PETRONAS,  
32610 Seri Iskandar, Perak, Malaysia  
e-mail: haylay.tsegab@petronas.com.my; haylish@gmail.com

H. Tsegab  
South East Asia Carbonate Research Laboratory, Universiti Teknologi  
PETRONAS, 32610 Seri Iskandar, Perak, Malaysia



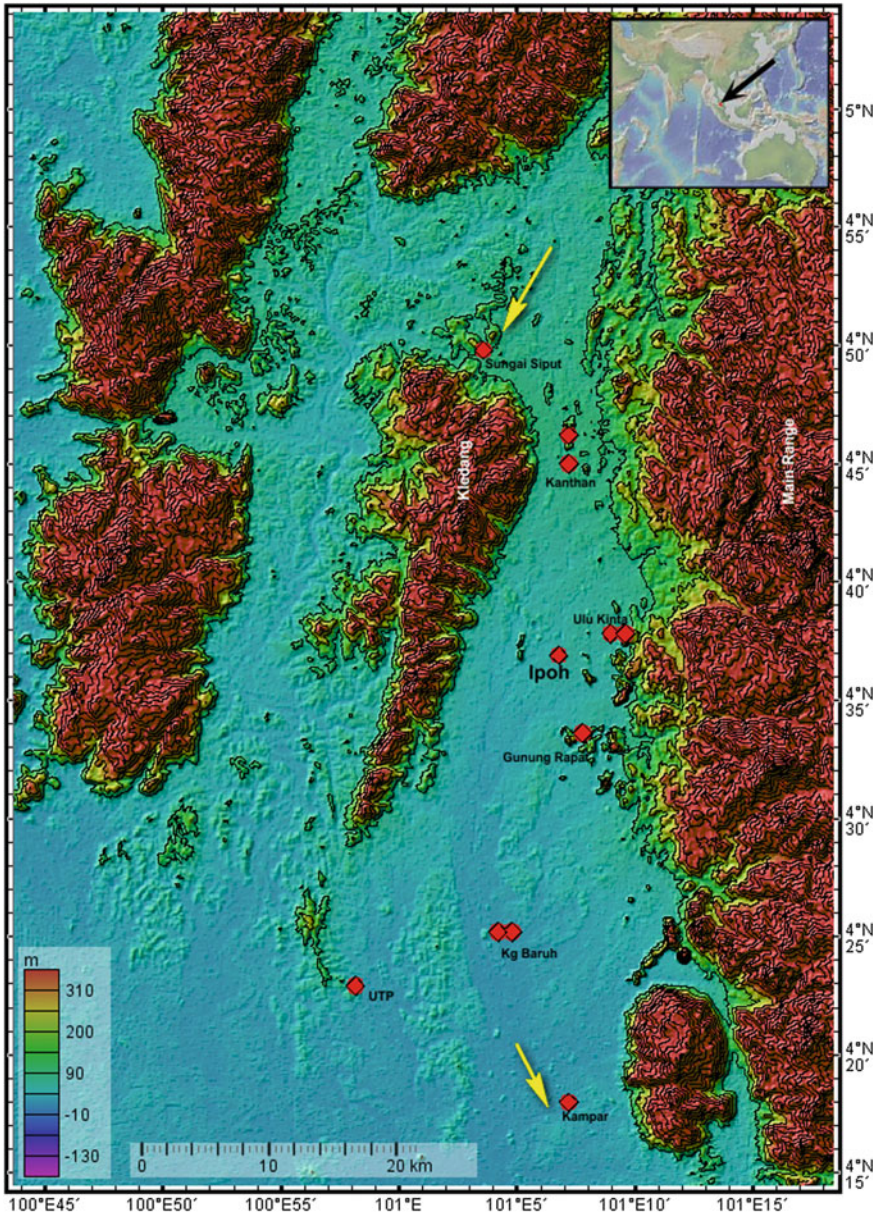
**Keywords** Geophysical logs · Stratigraphic surfaces · Paleozoic · Sea-level fluctuation · Regional correlation

## 1 Introduction

The Paleozoic tectonics of Southeast Asia has resulted in complex configuration of basins and continental terranes. Peninsular Malaysia is the southernmost part of the mainland Asia. It comprises three stratigraphic zones, namely the western, central, and eastern zones each with distinct stratigraphy, structure, magmatism, and geophysical signatures [3, 14]. The tectonic setting of the Western Belt is related to the closure of the Paleo-Tethys during the Late Triassic [8, 13]. After the closure of the Paleo-Tethys, tectonothermal and diagenetic events affected the sedimentary successions in the Western Belt [3, 5, 8]. The Kinta Valley, which forms a major part of this Western Belt, is characterized by tower karst remnant limestone hills sandwiched between Late Triassic and Early Jurassic granitic intrusions [5] of the Kledang in the west and the main range in the east (Fig. 1).

The Paleozoic sedimentary sequences of the Kinta Valley are represented by limestone, shale, siltstone, and their metamorphosed equivalents such as slate, phyllite, schist, quartzite, and marble [11]. The Silurian–Permian Kinta Limestone forms one of the major stratigraphic units in the region [11, 18]. The age of the limestone and associated siliciclastics has been a topic of discussion [9, 11] owing to the nonavailability of unaltered, unweathered, accessible, and continuous exposures. This state of affair is further compounded by the thick successions of Quaternary deposits burying the accessible limestone and also due to the granitic intrusions which resulted in the thermal alteration of Kinta Limestone [6, 10, 11, 16]. Although the Kinta Limestone is under study since the 1960s [9, 11], its lithic, stratigraphic, and chronologic details are far from better understanding, which in turn thwart regional correlation and petroleum exploration.

Given cognizance to these, it is perceived that investigating the geophysical properties may offer nondestructive and noninvasive methods of study and can help overcome natural, geological difficulties in characterizing the buried successions of the least altered intervals in the Kinta Limestone. In addition, it is also noted during the reconnaissance survey that a few pockets of limestone outcrops in the Valley such as in Sungai Siput have preserved primary sedimentary features and seemingly endured minimal thermal alteration [6]. Therefore, this paper is focused on examining the geophysical properties of the Kinta Limestone to define the stratigraphic relationships of the lithofacies and to unveil stratigraphic surfaces which might have chronostratigraphic significance with the intention to serve as analogue for Paleozoic basin studies in the region.



**Fig. 1** Location of the study area. The red circles represent outcrop locations, and the yellow arrows indicate the drilling locations for the Sungai Siput and Kampar areas in the Kinta Valley. Arrow in the inset map shows the location of the study area in peninsular Malaysia

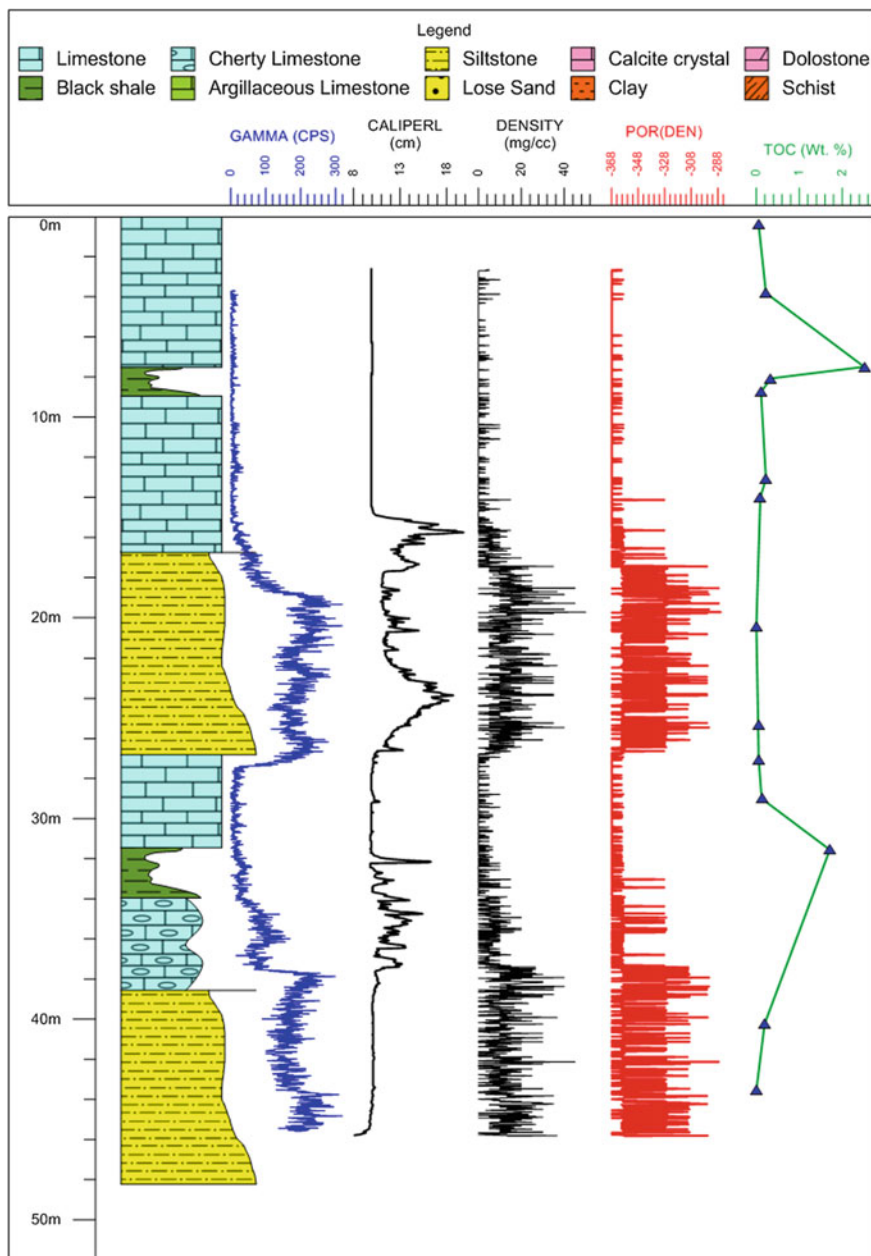
## 2 Materials and Methods

Three conventional boreholes were drilled to retrieve continuous cores and to examine the subsurface stratigraphy of the Kinta Limestone from least metamorphosed localities in the Kinta Valley. Two of the boreholes are located at about 1 km apart from the Sungai Siput. These boreholes have intercepted carbonate mudstone, shale, and siltstone. The recovered cores were cut into two equal parts. One part was utilized for subsampling for laboratory analyses; the other half was preserved for archiving. It was followed by description of lithological heterogeneities and recognition of stratigraphic contacts. The boreholes were also logged for geophysical wireline logs and comparisons of the wireline logs, petrophysical measurements, and the lithofacies descriptions were made. The wireline log data acquisition and processing were carried out using a wellsite laptop loaded with the “log” and “display” software developed by Century Geophysical Corporation. The tools were tested in the year 2012 while our logging campaign was carried in the 2013. Geophysical wireline logging was carried out in air-filled uncased borehole environment. Logs were measured during the ascending direction for better depth control. Default units were used during the data acquisition. Therefore, the GR and density are measured as counts per second (cps) and g/cc, respectively. Results of natural gamma-ray readings, density, resistivity, spontaneous potential (SP), and caliper logs were compared to the interpreted stratigraphic surfaces from the cores. Total organic carbon (TOC) and elemental geochemical analyses were also conducted on 14 samples to complement the lithological and the geophysical measurements. In this paper, we described and discussed the continuous core section recovered from one of the boreholes (SGS-02) in northern part of the Kinta Valley and examined the log signatures of this section as analogue for uncored intervals in deeper part of the basin or in similar geological setting of other Paleozoic basins.

## 3 Results

Cores of 48.92 m thick from a borehole (SGS-01) located in the northern part of the Kinta Valley are described in this paper. The lithostratigraphic description shows that the bottom of the drill hole is characterized by 10-m-thick siltstone and followed by 5 m of cherty limestone. Above that, the cherty limestone is of 2-m-thick black shale followed toward top by 5-m-thick limestone. The pattern is repeated again in such a way that, above the 5-m-thick limestone, another 10-m-thick siltstone is followed by 8-m-thick limestone. Again, about 2-m-thick black shale and another 7-m-thick limestone (Fig. 2) are occurred. The limestones are dark gray to black in color and dominated by carbonate mudstone texture while the siltstones are light brownish in color and contain red-colored cements probably iron oxide.

The intercalations of thin-to-thick-bedded horizontal to subhorizontal dark greyish-to-black carbonate mudstone, light brownish siltstone, and black shale units





◀**Fig. 2** Comparison of lithological, wireline logs and total organic content of the section. This figure shows the comparison of the lithological description and the geophysical wireline logs for Borehole SGS-02 in the Sungai Siput. The three main lithologies (limestone, shale, and siltstone) in this borehole showed a cyclic pattern with almost similar thickness and lithofacies characteristics. The borehole is located at about 1 km to the east of the first borehole in the northern part of the Kinta Valley

with chert also show distinct trends in the gamma-ray, caliper, density, and porosity logs. The intercalated carbonate mudstone and siltstone have shown unique wireline signatures which is low in gamma-ray, smooth borehole environment on the caliper log and low density and por(den) readings. While the carbonate mudstones are characterized by lower gamma-ray values, the siliciclastic units show higher gamma-ray values which are associated with higher density readings. The caliper log clearly documented the contact between the limestone and the siliciclastic intervals, which was portrayed by caving in the siliciclastic while the limestone is characterized by smooth borehole environment (Fig. 2). The SP log is not diagnostic; however, it detects the lower porous siliciclastic material. The shale unit is characterized with high TOC content that reached to 2.5 wt% in this section. The carbonate mudstone has less than 1 wt% of TOC and the siltstone has showed minimal amount of TOC (Fig. 2). The geochemical compositions of the samples also complemented the lithological variation described on the cores of this borehole.

## 4 Discussion

The lithostratigraphic log shows good agreement with the trends of gamma-ray, caliper, density, and porosity logs. This relationship is interpreted in such a way that the carbonate intervals are less dense and contains low natural radioactive elements or devoid of detrital materials, whereas the siliciclastic is relatively richer in radioactive materials and found to be relatively denser than the carbonate mudstone.

The petrophysical measurements and rock fabric descriptions provide a basis for quantifying geological descriptions with petrophysical properties [12]. To have continuous petrophysical data in order to support the geochemical analyses, wireline geophysical logs of pressure, caliper, natural gamma-ray, density, and resistivity were recorded in the two boreholes drilled in the northern part of the Kinta Valley. It was to characterize the lithology and identify stratigraphic surfaces and compare the recognized geophysical signatures with the core descriptions. As these log signatures could be useful for lithofacies identification in other uncored sections of the Kinta Limestone or in other basins with similar sedimentation history.

The gamma-ray was applied to distinguish lithologies, which have high natural gamma-ray values and to trace the original facies which may be grain- or wackestone-dominated carbonates [12]. However, the grain type cannot be identified from wireline logs and need to be integrated with core description of

lithofacies. Gamma-ray measures the natural gamma-ray emission strength present in the rock successions. The natural radiations could have emanated from uranium, potassium, and thorium in the rock. K and Th are concentrated in the minerals that constitute the insoluble residue of carbonate rocks such as rock fragments and clays. Shale, siliciclastic, silt intervals, and organic-rich beds typically display high K and Th radiation [12, 17]. Many carbonate facies can be correlated with current energy and, thus, with K and Th radiation since the amount of residue is thought to be inversely proportional to the current energy. This implies that grainstones and grain-dominated packstones are deposited in high-energy environments and characterized with low gamma-ray activity. Conversely, the mud-dominated packstones, wackestones, and mudstones are deposited in low-energy environments and are expected to have high gamma-ray counts. However, the Kinta Limestone is characterized by low gamma-ray on the carbonate mudstone and high in the siliciclastic beds which might be more related to provenance than the energy level. The presence of high gamma-ray value corresponds to the fine-grained intervals which are interpreted as siltstone and shale units in the cored intervals of the studied sections. The source of the gamma-ray might be the combination of three main radioactive elements, K, Th, and U [1]. However, in the elemental analysis of samples from the Kinta Limestone [19], Uranium was not detected, which implies that the main source of the total gamma-ray might be K and Th. The siliciclastic intervals in the Kinta Valley are characterized by higher concentration of K as evident from the bulk geochemical analyses [7]. Thus, it is interpreted that the high values of gamma-ray in the shale and siltstone beds of the Kinta Limestone are derived from the radioactivity of K. This inference is consistent with the absence of Th and U in the nearby sections. It is also in agreement with the low value of Mn/Sr ratio which indicates that the studied section is not subjected to significant change of oxidation state [19]. The log response of relative abundances of K has an implication to the provenance and the depositional environment of the Kinta Limestone. Depositional environments of cyclic carbonate and siliciclastic units have been correlated to relative sea-level changes [15, 20, 21]. Deposition of the fine-grained carbonate on top of the fine-grained siliciclastic units is an indication of depositional environment change from siliciclastic to carbonate and then back to carbonate. These lithofacies changes might be associated with sea-level fluctuations. This inference is consistent with the global sea-level change during the Upper Paleozoic [4]. In addition, the lower value of the gamma-ray response of the lithofacies in the Sungai Siput section showed that the limestone was less affected by meteoric diagenetic fluids. It is further affirmed by [2] who reported that most of U in carbonates is controlled by diagenetic processes. From this perspective also, it is evidenced that the limestones have not undergone significant diagenetic, particularly meteoric diagenetic imprints could influence the measured geophysical signatures. The organic-rich interval which is below the resolution of the wireline logs might indicate anoxic depositional condition of organic matter and probably transgression in the Paleo-Tethys. The other logs have confirmed the lithological identification and provided clues on possible challenges to drill on similar basins and maintain the geometry of the boreholes. For instance, the caving is more

common in the siliciclastic intervals than the carbonates. This may be due to the fact that the carbonate mudstones are tight and compact, whereas the siltstone and shale are relatively porous and fractured which would affect the strength of the beds to resist drilling pressure. Therefore, the lithological and geophysical log signatures might help in understanding the stratigraphy in the basin in particular and in other similar geological settings in general.

## 5 Conclusions

In addition to demonstrating the stratigraphic variations in lithofacies characteristics and primary/bulk mineralogical and major geochemical compositional differences, the geophysical properties managed to detect the stratigraphic surfaces in the Kinta Limestone. The geophysical log data demonstrated that it could be useful to substantiate the chronostratigraphic boundaries. This relationship could be used as an analogue for basins in similar geological settings and may also contribute to minimize costs of coring during for petroleum exploration campaign in the region. The correlation of the mineralogical composition with the natural gamma-ray log may help in the characterization of the Paleozoic sequences and may also signify regional correlation based on geophysical log signatures. These relationships may also help in deciphering the provenance and aid in paleogeographic and regional correlation.

**Acknowledgements** We express our gratitude to South East Asia Carbonate Research Laboratory (SEACARL) and Universiti Teknologi PETRONAS for funding this project. We appreciate Sime Darby Plantation and JMG for allowing access to their lands for drilling. Prof. Michael Poppelreiter, Head of SEACARL, is thanked for his valuable comments.

## References

1. Dypvik H, Eriksen D (1983) Natural radioactivity of clastic sediments and the contributions of U, Th and K. *Journal of Petroleum Geology* 5 (4):409–416.
2. Ehrenberg S, Svånå T (2001) Use of spectral gamma-ray signature to interpret stratigraphic surfaces in carbonate strata: An example from the Finnmark carbonate platform (Carboniferous-Permian), Barents Sea. *AAPG Bull* 85 (2):295–308.
3. Foo KY The Paleozoic Sedimentary Rocks of Peninsular Malaysia-Stratigraphy and Correlation. In: Nutalaya P (ed) Workshop on Stratigraphic Correlation of Thailand and Malaysia Thailand, September 8–10 1983. Geological Society of Thailand, Thailand, pp 1-19.
4. Haq BU, Schutter SR (2008) A chronology of Paleozoic sea-level changes. *Science* 322 (5898):64–68. doi:[10.1126/science.1161648](https://doi.org/10.1126/science.1161648).
5. Harbury NA, Jones ME, Audley-Charles MG, Metcalfe I, Mohamed KR (1990) Structural evolution of Mesozoic Peninsular Malaysia. *J Geol Soc London* 147 (1):11–26. doi:[10.1144/gsjgs.147.1.0011](https://doi.org/10.1144/gsjgs.147.1.0011).

6. Haylay TG, Hunter AW, Sum CW (2014) Depositional Environment of the Kinta Limestone, Western Peninsular Malaysia. In: AAPG International Conference & Exhibition Istanbul, Turkey, 14–17 September 2014. AAPG, p 36.
7. Haylay Tsegab G, Sum CW, Hunter AW, R. P. Major, Talib JA Paleothermal Effects on and Organic Carbon Records of Paleozoic Carbonate Rocks of Peninsular Malaysia, Southeast Asia. In: International Sedimentological Congress (accepted), Geneva, Switzerland, 18–22, August 2014. International Sedimentological Association.
8. Hutchison CS (1994) Gondwana and Cathaysian blocks, palaeotethys sutures and cenozoic tectonics in South-east Asia. *Geol Rundsch* 83 (2):388–405. doi:[10.1007/bf00210553](https://doi.org/10.1007/bf00210553).
9. Ingham FT, Bradford EF (1960) The geology and Mineral Resources of the Kinta Valley. 1st edn. Geological Survey Headquarters, Malaysia.
10. Jones CR (1973) The Geology and Mineral resources of the Girk Area, Upper Perak., vol 11. 1st edn. Geological survey West Malaysia district Memoir, New York.
11. Lee CP (2009) Palaeozoic Stratigraphy. In: Hutchison CS, Tan DNK (eds) Geology of Peninsular Malaysia. 1st edn. Geological Society of Malaysia, Malaysia, pp 55–86.
12. Lucia FJ (2007) Carbonate reservoir characterization. 1st edn. Springer, Berlin.
13. Metcalfe I (2000) The Bentong–Raub Suture Zone. *J Asian Earth Sci* 18 (6):691–712. doi:[10.1016/s1367-9120\(00\)00043-2](https://doi.org/10.1016/s1367-9120(00)00043-2).
14. Metcalfe I (2013) Tectonic evolution of the Malay Peninsula. *J Asian Earth Sci* 76 (0):195–213. doi:<http://dx.doi.org/10.1016/j.jseaes.2012.12.011>.
15. Posamentier H (1988) Eustatic controls on clastic deposition I—conceptual framework.
16. Rastall R (1927) The Limestone of the Kinta Valley, Federated Malay States. 1st edn. Cambridge Univ Press, Malaysia.
17. Rider H (2002) The Geological Interpretation of Well Logs. 2nd edn. Rider-French Consulting Limited, Scotland.
18. Tsegab H, Hunter WA, Pierson BJ, Chow WS Review on Fossil records of the Kinta Valley Limestones. In: First EAGE South-East Asia Regional Geology Workshop-Workshop on Palaeozoic Limestones of South-East Asia and South China, 2011.
19. Tsegab H, Sum CW, Hunter AW (2015) Preservation of Marine Chemical Signatures in Upper Devonian Carbonates of Kinta Valley, Peninsular Malaysia: Implications for Chemostratigraphy. In: Awang M, Negash BM, Md Akhir NA, Lubis LA (eds) ICIPEG 2014. Springer Singapore, pp 291–302. doi:[10.1007/978-981-287-368-2\\_28](https://doi.org/10.1007/978-981-287-368-2_28).
20. Vail PR (1987) Seismic stratigraphy interpretation using sequence stratigraphy: Part 1: Seismic stratigraphy interpretation procedure.
21. Van Wagoner J, Mitchum Jr R, Posamentier H, Vail P (1987) Seismic Stratigraphy Interpretation Using Sequence Stratigraphy: Part 2: Key Definitions of Sequence Stratigraphy.



# Sedimentology of the Lambir Formation (Late Miocene), Northern Sarawak, Malaysia

A.R. Abdul Hadi, K. Zainey, M.S. Ismail and N. Mazshurraiezal

**Abstract** The Late Miocene Lambir Formation is extensively exposed along the road from Bekenu to Miri near the Bukit Lambir National Park. This formation is characterized by a succession of poorly consolidated sandstone and sand interbedded with soft clay in several exposures. Four sedimentary facies from three (3) outcrops of the Lambir Formation have been identified and interpreted. These sedimentary facies are categorized into three main units depending on their major lithology type: (1) mud-dominated unit: bioturbated heterolithic mudstone (F2); (2) sandstone-dominated facies: hummocky cross-bedded sandstone (F1) and trough cross-bedded sandstone (F2); (3) interbedded sandstone/mudstone unit: interbedded hummocky cross-bedded with bioturbated mudstone (F3). These four (4) facies are grouped into three (3) facies association which are (1) lower to middle shoreface, (2) upper shoreface and (3) offshore. The pattern of facies and presence of marker pollen species imply that these facies were deposited in the shallow marine setting with pronounced storm, wave and tidal influence along the paleo-margin. Acme of *Zonocostites ramonae* and high proportion back mangrove pollen suggest a former mangrove belt that was developed in conjunction with back mangrove swamp within coastal area. Pollen analysis suggests this sediment was deposited during Middle-to-Late Miocene period.

**Keywords** Sedimentology · Sedimentary facies · Shallow marine · Lambir formation · Sarawak

---

A.R. Abdul Hadi · M.S. Ismail · N. Mazshurraiezal (✉)  
Department of Geoscience, Universiti Teknologi Petronas,  
32610 Bandar Seri Iskandar, Perak, Malaysia  
e-mail: rizal\_geo@ymail.com

K. Zainey  
Geological Department, Bukit Jelutong Business and Technology Centre,  
15 & 17 Jalan Astaka U8/84, 40150 Shah Alam, Selangor, Malaysia

## **1 Introduction**

The integration of sedimentology and palynology offers a more precise image of the depositional conditions of any investigated sedimentary succession. This research presents an integrated sedimentological and palynological investigation and the interpretation of the Lambir Formation exposed along the Bekenu–Miri rural road within the Lambir area, Sarawak. This formation has developed through the interplay of tectonics, sea level changes and sediment supply during the Middle-to-Late Miocene period.

Three (3) outcrops have been completely logged and described to investigate the facies and facies association within this formation (Fig. 1). Eighteen (18) samples have been sent to the laboratory analysis to investigate the pollen content within this rock succession.

### ***1.1 Problem Statement***

The Lambir Formation (Late Miocene) was deposited within the Sarawak Tertiary Basin in response to the uplift and erosion of the Rajang Group during Late Neogene to Quaternary, Madon [1]. To date, no detail studies on the sedimentological and palynological characteristics have been carried out since the general geological investigations by Liechti et al. [2] and Wilford [3]. Newly exposed outcrops of the Lambir Formation in Northern Sarawak allow new investigations to be carried out in order to reconstruct the depositional environment of the Lambir Formation.

### ***1.2 Objective***

The main objective of this research is to evaluate and integrate sedimentological and palynological data to unravel the depositional environment of the Lambir Formation. The outcome will enhance our understanding of the interrelationships between relative sea level changes, the sediment supply and the temporal–spatial distribution of depositional environments.

## **2 Result and Discussion**

### ***2.1 Facies***

Four (4) facies are identified in the patches of outcrop along the Bekenu–Miri rural road, Lambir area. These facies are differentiating based on its sedimentological and



### 2.1.1 F1—Hummocky Cross-Bedded Sandstone

Macroscopic characteristic: the facies consists of fine-grained sandstone, which is pale white in colour and well to moderately sorted. It is characterized by low angle, hummocky cross-stratified with thickness from 0.5 m up to 2.0 m. Within the facies are sparse thin carbonaceous laminae which usually lined the internal stratification including isolated rounded to subangular muddy pebbles which present in variable size (0.3–1.0 cm) in diameter.

Ichnological characteristic: the facies is sparsely bioturbated with BI: 0–1 that is commonly characterized by clay-lined burrows of *Ophiomorpha*.

Palynological characteristic: poor palynomorph is characterized by reworked palynodebris and sparse mangrove pollen and spores.

Interpretation: the formation of HCS has been explained by Southard et al. [4] as the product of strong and purely oscillatory flows which is formed during major storm. HCS is generally preserved in areas of weak tidal activity and results from strong and complex wave processes that mainly lie below fair-weather wave base (Collinson and Thompson [5]; Walker and Plint [6]).

### 2.1.2 F2—Trough Cross-Bedded Sandstone

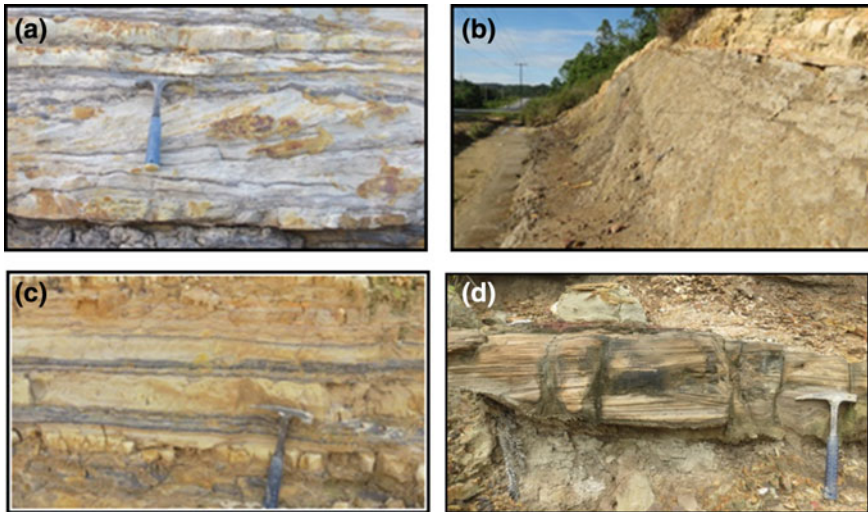
Macroscopic characteristic: the trough cross-bedded sandstone is medium grained, greyish white and moderate to well sorted. There are common isolated mud partings and lenses with (1–2 cm) in thickness. Flaser bedding is abundant with sparse muddy intercalated. F2 sandstones show well-developed erosional and scour basal contact (Fig. 2a). The thickness of the facies is ranged from 0.5 up to 1.0 m with good lateral continuity as observed in the field.

Ichnological characteristic: the facies is sparsely bioturbated with BI: 0–1. Palynological characteristic: poor palynomorph is characterized by reworked palynodebris and sparse mangrove pollen and spores.

Interpretation: trough cross-stratifications occur in many different settings, from fluvial environment to shallow marine areas. In shallow marine setting, the trough cross-stratification denotes high-energy environments, probably rip up and long-shore currents in the shoreface area (Clifton et al. [7]; Reineck and Singh [8]; Collinson and Thompson [5]).

### 2.1.3 F3—Interbedded Hummocky Cross-Bedded with Bioturbated Mudstone

Macroscopic characteristic: the facies consists of interbedded thin-bedded hummocky cross-stratified sandstone and bioturbated mudstone (Fig. 2b). The sandstone shows sharp, slightly scour base and slight ripple top. The mudstone within this facies has a thickness varying from 10–20 cm. Within the mudstone layer, isolated thin sand/silt streaks were observed.



**Fig. 2** Bekenu–Miri rural road outcrop photographs. **a** Trough cross-bedded sandstone. **b** Interbedded thin hummocky cross-bedded sandstone with bioturbated sandstone. **c** Bioturbated heterolithic mudstone. **d** Hummocky cross-bedded sandstone

**Inchnological characteristic:** the facies is moderately bioturbated with BI: 1–2 especially within the mudstone layer. The sandstone is sparsely bioturbated with small clay-lined burrow of *Ophiomorpha*. **Palynological characteristic:** abundant mangrove palynomorph such as *Zonocostites ramonae* and very common back mangrove pollen.

**Interpretation:** the interbedded sandstone and mudstone reflect a fluctuation and alternation of high-energy and low-energy conditions. During fair-weather conditions, the area experience relatively mixed energy conditions with continuous deposition of mud from suspension and wave actions.

#### 2.1.4 F4—Bioturbated Heterolithic Mudstone

**Macroscopic characteristic:** the bioturbated heterolithic mudstone facies consists of grey and silty mudstone with common thin-isolated silty and sandy streaks (Fig. 2c). Within the mudstone is rare isolated thin silt/very fine-grained sand layer which is locally intercalated including starved ripples.

**Inchnological characteristic:** this facies is intensely bioturbated with B.I = 4 and dominated by *Skolithos*, *Thalassinoides* and *Diplocraterion*.

**Palynological characteristic:** abundant mangrove palynomorph such as *Zonocostites ramonae* and very common back mangrove pollen.

**Interpretation:** this facies reflects deposition within mixed energy environment with relative influences of storm and wave processes. The fluctuation of high-energy

conditions generated by storm event and quite period during non-storm condition has produced an alternation in sediment supplying into a depositional area.

## **2.2 *Facies Association***

### **2.2.1 Lower to Middle Shoreface**

Lower to middle shoreface facies association is dominated by grey, sharp and erosive-based, thick-bedded, fine- to medium-grained well-sorted sandstone with hummocky cross-stratification and interbedded thin hummocky cross-bedded sandstone with bioturbated mudstone (F1 and F3). The heterolithic facies in this facies association are interpreted to be the results of deposition in oscillatory and occasionally combined flow in Lower to middle shoreface during fair-weather conditions.

Hummocky cross-bedded sandstone within this facies association is generally preserved in the areas of weak tidal activity and results from strong and complex wave processes that mainly lie below fair-weather wave base (Collinson and Thompson [5]; Walker and Plint [6]).

### **2.2.2 Upper Shoreface**

The upper shoreface facies association comprises of thin- to thick-bedded, medium- to coarse-grained, trough cross-stratified sandstones. Based on Clifton et al. [7]; Reineck and Singh [8]; Collinson and Thompson [5], trough cross-stratification represents migration of bars and dunes along the shoreline due to either rip currents or longshore currents in the upper shoreface.

The coarser portion along with sparse or lack of bioturbation also suggests deposition in agitated high-energy conditions (Pemberton et al. [8]). The strong currents and coarser portion during the high-energy interval in upper shoreface did not allow suitable substrate and time for biological activities.

### **2.2.3 Offshore**

Offshore facies association is dominated by grey and silty mudstone with common thin-isolated silty and sandy streaks (F4). This facies association is interpreted to have been deposited within offshore environment below fair-weather wave base. The high diversity suite of trace fossils is clearly indicative of a well-oxygenated infaunal environment (Figs. 3, 4 and 5).

(a)



(b)



Fig. 3 Bekenu–Miri rural road outcrop photographs. a Outcrop 1 (01) b Outcrop 2 (02)

### 2.3 Palynological Analysis

In general, mangrove species are dominantly characterized by *Zonocostites ramonae*, including important marker species for Southeast Asia region such as *Florschuetzia meridinalis*, *Florschuetzia levipoli* and *Florschuetzia trilobata*. Other mangrove species includes *Acrostichum aureum*, *Excoecaria aggulocha*, *Spinizinicolpites echinatus*, *Avicennia* and *Oncosperma*. Most of these taxa have long stratigraphic range except for the *F. trilobata*-, *F. levipoli*- and *F. meridionalis*-type pollen, which are very significant in dating the Neogene sediments particularly in North West Sarawak region.

In addition, other pollen and spores sources are derived from peat swamp and riparian vegetation including montane, coastal and seasonal pollen component. However, their occurrences are scarce. Some of dominant species which is originated from peat swamp vegetation includes *Dicolpopolis*, *Palaquium*, *Dactylocladus*, *Blumeodendron*, *Stemonurus*, *Calophyllum*, *Cyrthostachys*, *Pandanus* *Eugenia*, *Ilex* and *Elaeocarpus*.

Low percentage of freshwater–brackish algae is characterized by *Bosedinia*-type algae and *Pediastrum*. The *Pediastrum* are chlorococcale green algae which are exclusively freshwater species usually derived from lacustrine lakes. The oily



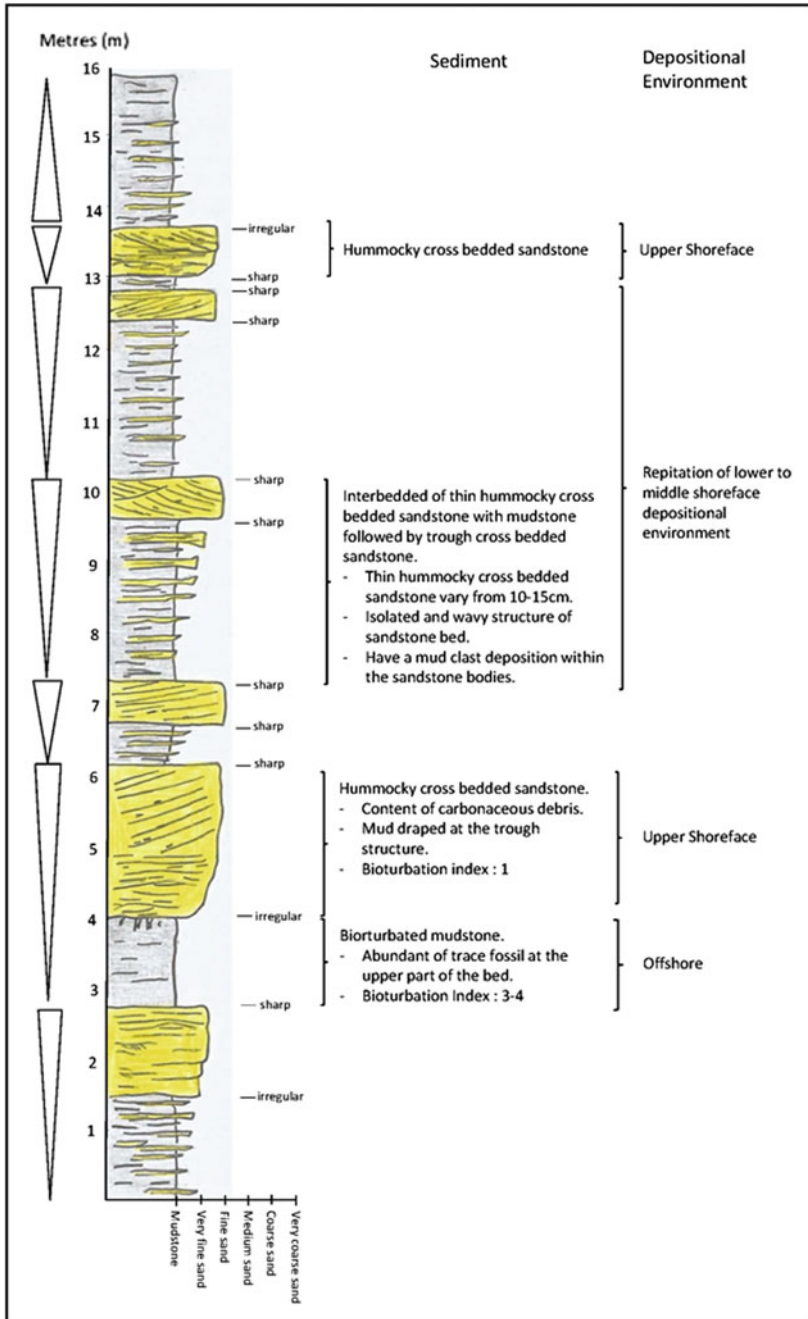


Fig. 4 Stratigraphic log for a Outcrop 1 (O1)



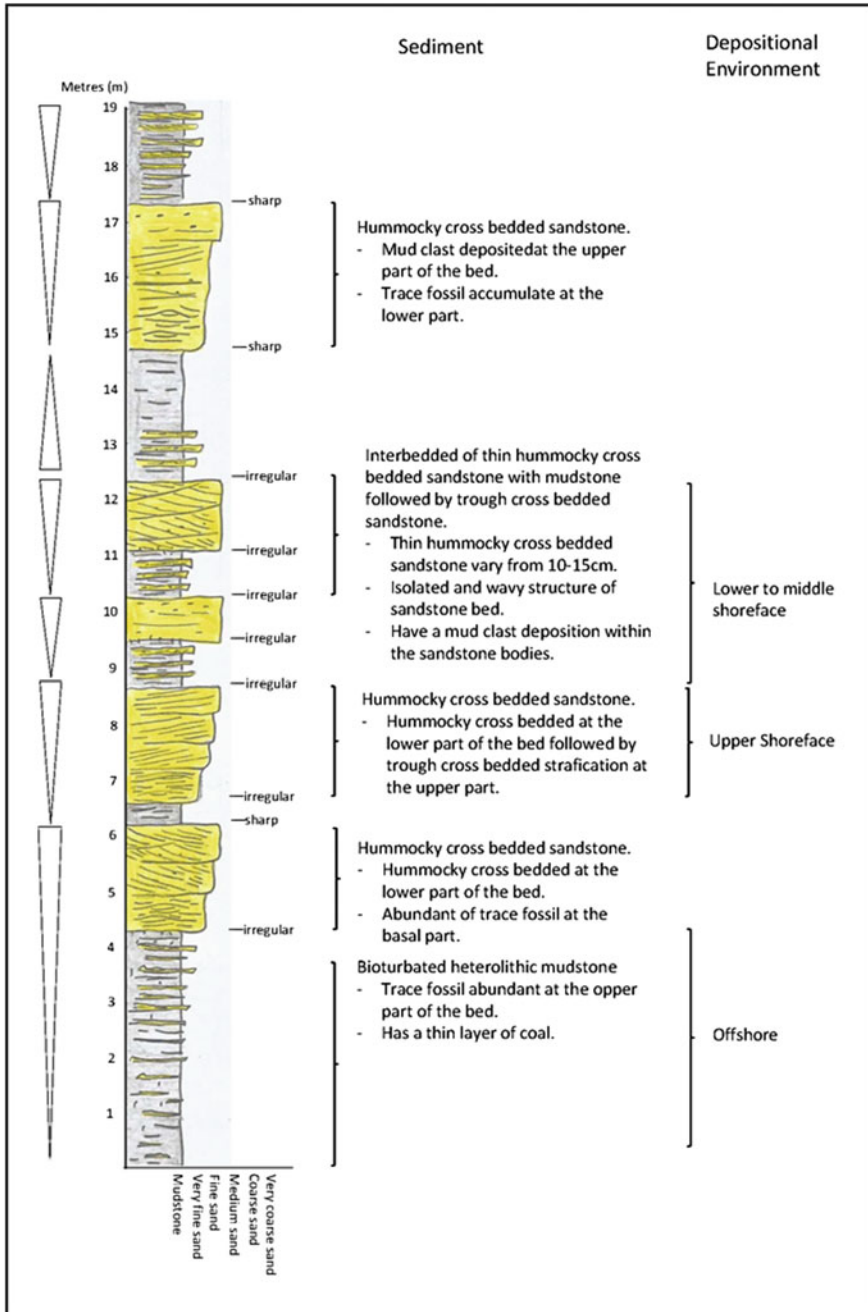


Fig. 5 Stratigraphic log for b Outcrop 2 (O2)

composition of the species makes them highly buoyant (Burns 1982) and often easily transported or re-deposited in much deeper environment. They are commonly flushed out of deltaic areas and become quite dominant in adjacent shelf sediments (Loh et al. 1986).

Some species of open marine dinoflagellate cysts are also common to regular, which is represented by *Operculodinium* sp., *Lingulodinium* sp. and *Spiniferites* spp. Foraminifera test lining is also regularly present within the samples.

The acme of mangrove palynomorphs which is dominated by *Zonocostites ramonae* including high proportion back mangrove pollen suggests a former mangrove belt that was developed in conjunction with back mangrove swamps within coastal areas. This event is probably associated with transgression phase or relative sea level rise.

### 2.3.1 Palynological Zonation

The occurrence of palynomorphs from the study area is compared to the palynological zonation published by Germeraad et al. [9] and Morley [10] which is developed for Southeast Asia region. Analysis of outcrop samples from the study area has revealed that the marker species for Southeast Asia region such as *Florschuetzia* group occurs consistently in each sample. The defined zones for this study are based on the presence of restricted taxa summarized below based on Morley [10] Germeraad et al. [9].

*Stenochlaenidites papuanus*: Late Miocene–Pliocene

*Florschuetzia meridionalis*: Intra Middle Miocene–Recent

*Florschuetzia levipoli*: Late Miocene–Recent

*Florschuetzia trilobata*: Late Eocene–Late Miocene

The results show the samples can be assigned into Middle–to–Late Miocene palynostratigraphic zones (Fig. 6) by comparing to the zonation published by Morley [10]. The pollen zone published by Morley [10] is used as the basis for zonal interpretation and comparison as it is developed for Southeast Asia region and not for specific area.

Morley [10] in his zone has modified the age range of *F. trilobata* to include sediments no younger than Late Oligocene and proposed to subzones within the *F. meridionalis* zone. These are *F. trilobata* and *F. meridionalis* subzone. Both of the subzones have clear definition where the *F. trilobata* subzone is defined based on the presence of *F. trilobata*. Meanwhile, the *F. meridionalis* subzone is defined where *F. trilobata* is absent. The presence of *Stenochlaenidites papuanus* in respective R4b and U7 samples may delineate at least Late Miocene age. This is considering, there is no marker species that are younger than *S. papuanus* such as the *Podocarpus imbricatus* found in the samples.

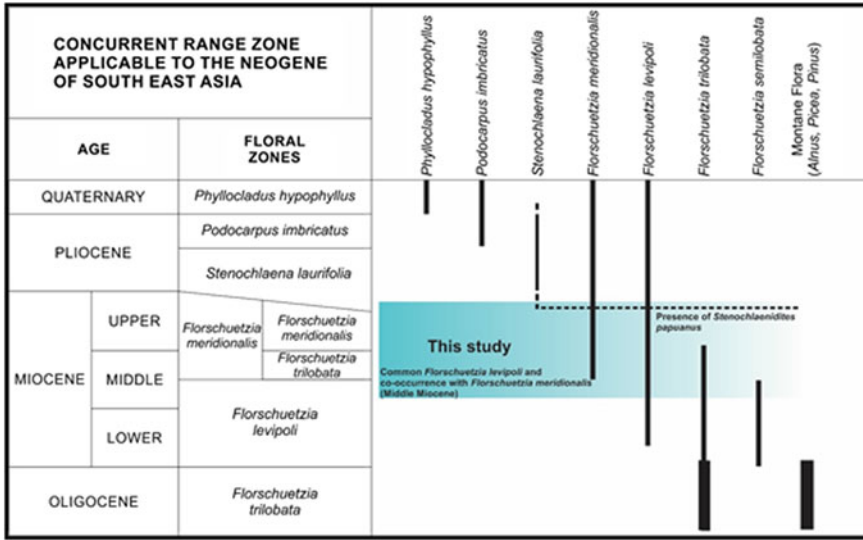


Fig. 6 Palynological zonation of the study area. Modified from Morley [10]

### 3 Conclusion

Three (3) main conclusions have been determined which are as follows:

- (1) Four facies has been identified within the Lambir Formation in Lambir area, which are F1—hummocky cross-bedded sandstone, F2—trough cross-bedded sandstone, F3—interbedded thin hummocky cross-bedded with bioturbated mudstone and F4—bioturbated heterolithic mudstone.
- (2) These four facies have been grouped into three (3) facies association, which are lower to middle shoreface, upper shoreface and offshore.
- (3) Acme of *Zonocostites ramonae* and high proportion back mangrove pollen suggest a former mangrove belt that was developed in conjunction with back mangrove swamp within coastal area. Pollen analysis suggests this sediment was deposited during Middle-to-Late Miocene period.

### References

1. Madon, M., 1999. Chapter 5 In: The Petroleum Geology and Resources of Malaysia, ISBN 983-9738-10-0, 275-286 p.
2. Liechti, P., Roe, F.W. and Haile, N.S. (1960). The geology of Sarawak, Brunei and Western part of North Borneo. British Borneo Geological Survey Bulletin 3, pp 360.

3. G.E. Wilford., 1961. The geology and mineral resources of Brunei and adjacent parts of Sarawak with description of Seria and Miri Oilfield. Geological Survey Department, British Territories in Borneo, Memoir 10, pp 319.
4. Southard, J.B., Lambie, J.M., Federico, D.C., Pile, H.T., and Weidman, C.R., (1992). Experiments on bed configurations in fine sands under bidirectional purely 209 oscillatory flow, and the origin of hummocky cross-stratification, *Journal Sediment. Petrol.* v. 60, pp. 1–17.
5. Collinson, J.D. and Thompson, D.B., 1989. *Sedimentary Structures*. Unwin Hyman Ltd, 207 pp.
6. Walker, R.G., and Plint, A.G., 1992. Wave- and storm- dominated shallow marine systems, In: Walker, R.G., and James, N.P., eds., *Facies Models: Response to Sea Level Change*: St. John's, Newfoundland: Geological Association of Canada, pp. 219–237.
7. Clifton, H.E., Phillips, R.L. and Hunter, R.E. 1971. Depositional structures and processes in the non-barred high-energy nearshore. *Journal of Sedimentary Petrology*, 41: 651.
8. Reineck, H.E. and Singh, I.B., 1980. *Depositional sedimentary environments*. Berlin, Heidelberg, New York, Springer Verlag, 549 pp.
9. Germeraad, J.H., Hoving, C.A., and Muller, J., 1968. Palynology of Tertiary sediments from tropical areas, *Review of Palynology and Paleobotany*, v. 6, pp. 189–348.
10. Morley, R.J., 1978. Palynology of Tertiary and Quaternary sediments in Southeast Asia. *Proc. 6th Ann. Conv. Indonesian Petro Assn.*, pp. 255–276.
11. Wannier, Lesslar, Lee, Raven, Sorkhabi, and Ibrahim (2011), *Geological Excursion Around Miri, Sarawak*.
12. Pemberton, S.G., Maceachern, J.A. and Frey, R.W., 1992a. Trace fossil facies models; environmental and allostratigraphic significance. In: *Facies models; response to sea level change* (Eds R.G. Walker and D.P. James), Geological Association of Canada. p. 47.

# Sandstone Facies Reservoir Properties and 2D-Connectivity of Siliciclastic Miri Formation, Borneo

Numair Ahmed Siddiqui, Abdul Hadi A. Rahman, Chow Weng Sum and Muhammad Murtaza

**Abstract** Reservoir connectivity and modeling in siliciclastic deposits are quite challenging in terms of its distribution and quality prediction. The objective of this paper is to demonstrate the different aspects of reservoir properties to construct static connectivity model and its heterogeneity distribution in siliciclastic Miri Formation, Borneo. Field description in terms of facies, distribution, and dimensions of sand bodies and rock samples, for grain-size and petrographic analysis, were used to quantify and examine seven different types of sandstones: (i) hummocky cross-stratified sandstones, with medium- to fine-grained sand with 86.4% sand and 13.6% mud,  $\phi = 20.4\text{--}32.07\%$ ,  $k = 6.78$  md; (ii) herringbone cross-bedded, with coarse to fine-grain having 92.7% sand and 7.3% mud,  $\phi = 12.2\text{--}31.3\%$ ,  $k = 17.7$  md; (iii) trough cross-bedded sandstones, with very-fine- to medium-sized grains having 86.6% sand and 13.4% mud,  $\phi = 16.8\text{--}35.5\%$ ,  $k = 5.97$  md; (iv) wavy- to flaser-bedded, silty sand to very-fine-grained sand with 48.1% sand and 51.9% mud,  $\phi = 7.6\text{--}19.4\%$ ,  $k = 2.31$  md; thickness varies from 2–9 m; (v) cross-bedded sandstone, with fine to medium grain having 89.2% sand and 10.8% mud,  $\phi = 10\text{--}12.8\%$ ,  $k = 12.2$  md; thickness from 2–3 m; (vi) bioturbated sandstone, having silty sand to fine-grained sand with 72–86% sand and 28–14% mud,  $\phi = 2.4\text{--}6.8\%$ ,  $k = 5.2$  md; the sandstone thickness from 1–3 m; and (vii) massive sandstone, with very fine to medium grain representing 94.8% sand and 5.2% mud,  $\phi = 14\text{--}25.8\%$ ,  $k = 4.3$  md; thickness from 1–5 m. The results show that sandstones of HCSS and HBSC are better sorted, with minimal mud content, with the depositional pattern with increasing vertical and lateral connectivity, even in bioturbated rich sand, as compared to other sandstone facies. On the other hand, sandstones of BS and CB are of poor quality in terms of grain sorting and poro-perm. This may reflect the heterogeneity in different facies and affect the connectivity within sand bodies.

---

N.A. Siddiqui (✉) · A.H.A. Rahman · C.W. Sum · M. Murtaza  
Department of Geosciences, Universiti Teknologi PETRONAS,  
Bandar Seri Iskandar, 32610 Tronoh, Perak Darul Ridzuan, Malaysia  
e-mail: numair.siddiqui@utp.edu.my

**Keywords** Facies characteristics · Outcrop geometry · Static connectivity · Reservoir sandstone properties

## 1 Introduction

Shallow marine sandstones are formed within the depositional systems that exist between the landward influence of marine and the seaward influence of fluvial process [1, 2]. A significant percentage of the world's hydrocarbon reserves are found in these rocks. The characteristics of these shallow marine sandstones from outcrop geometry and its vertical and lateral connectivity in terms of a static reservoir connectivity model is a challenging task for a successful exploration and production [3–6]. To identify this scale-dependent issues, outcrop analogues of well-exposed shallow marine sandstone deposits of Miri formations were evaluated in terms of its facies, reservoir properties, and static connectivity model. The outcrops are located near Miri towns, which are the analogue of offshore cycle I and II and Baram Delta, Oilfield, Sarawak.

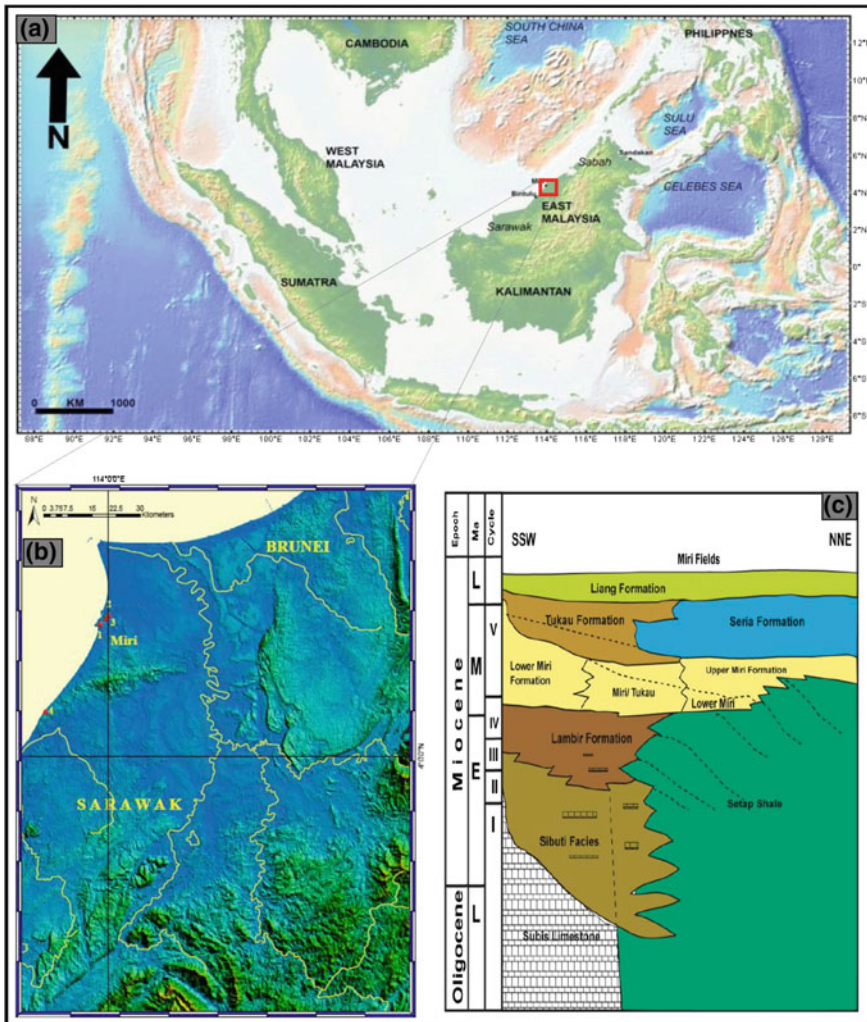
Detailed 2D static connectivity model of well-exposed rocks from Miri was constructed using field data and measurements. Therefore, we believe that these results of outcrop model are applicable to varieties of other well-exposed outcrops in these areas.

## 2 Study Area

The study area is near to Miri town, Sarawak, East Malaysia, and bounded by latitude N 04°21' 52.2" to N 04°07' 30.2"; longitude E 113°58' 46.4" to E 113°49' 12.4" for Miri formations. For this study, four outcrops from Miri formation have been studied as located in Fig. 1a–c.

## 3 Geological Background

The rock exposed around the Miri town, which belongs to the Middle to Late Miocene age, is the uplifted part of the subsurface, oil-bearing sedimentary strata of the offshore West Baram Delta and is exposed predominantly as an arenaceous succession [7]. Its outcrops are restricted to the narrow coastal region around Miri. The basal contact with the underlying Setap Shale Formation is a gradual transition from an arenaceous succession downward into a predominantly argillaceous succession. The Miri Formation is subdivided into lower and upper units, [7–9]. The maximum total thickness of the Miri Formation is approximated to 1830 m. The lower Miri unit consists of interbedded shales and sandstones and passes downward



**Fig. 1** a Illustrating the Southeast Asia map and location of study area in Miri, East Malaysia, b Outcrop locations of Miri Formation near Miri town, Sarawak, East Malaysia, c Stratigraphic framework for the onshore northwest Sarawak represents the units of Miri Formation. Modified from [10]

into the underlying Setap Shale Formation, which interfinger with Lambir Formation (SW) (Fig. 1c). The upper Miri unit is rapidly recurrent and irregular sandstone-shale alternation, and more arenaceous laterally.

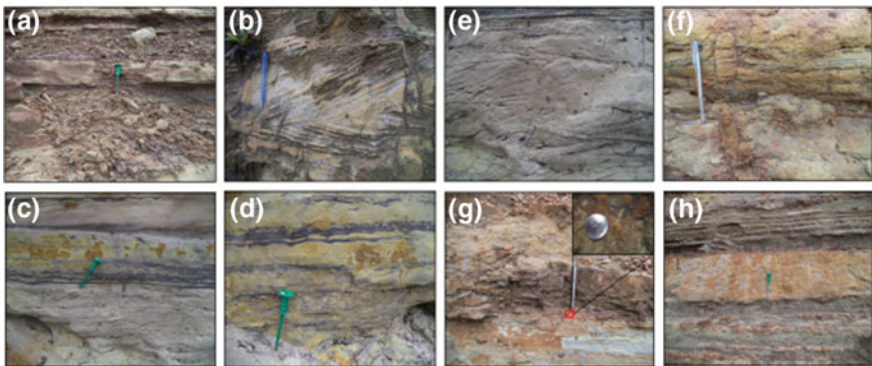


## 4 Sedimentology and Facies Description

Detailed sedimentologic observation and measurements were collected from different outcrops in Miri area. On the basis of lithology, geometry, sedimentary structures, and sandstone quality, the Miri formations are divided into seven different types of sandstone facies based on four stratigraphic sections as follows.

### 4.1 Hummocky Cross-Stratified Sandstone (HCSS)

The hummocky cross-stratified sandstone is characterized by light-gray to yellowish fine- to very-fine-grained, well-sorted sandstone. This facies is identified in all the outcrops; the thickness of this sandstone varies from 1 to 4 m between predominantly sand and shale of tidal origin. This sandstone displays low-angle cross-stratification (Fig. 2a). Bioturbation is quite frequent and is normally limited to the upper part of the formation, as in Outcrop 1. The base of this facies is founded with some mud-clasts of some thin beds. Hummocky cross-stratified sandstone deposited and reworked by storms in the offshore transition zone, between the fair-weather wave base and storm wave base on storm-dominated shelves [11]. Therefore, the occurrence of hummocky bed forms clearly indicates a storm origin for the sandstone beds in a shallow marine environment. Trace fossils (Chondrites and Ophiomorpha) in this facies show that the sandstone was deposited in a shallow marine environment.



**Fig. 2** Major sandstone Facies of Miri Formation, **a** hummocky cross-stratified sandstone (HCSS), **b** herringbone cross-bedded sandstone (HCBS), **c** trough cross-bedded sandstone (TCB), **d** wavy- to flaser-bedded sandstone (W-FBS), **e** cross-bedded sandstone (CB), **f** Bioturbated sandstone (BS), **g** Coarse-grained bioturbated sandstone, with fossilized mollusk seashell in small picture and **h** Massive sandstone (MS)



## **4.2 *Herringbone Cross-Bedded Sandstone (HBCBS)***

Herringbone cross-bedded sandstone is typically brown–light gray, fine- to very-fine-grained, well-sorted and with thickness varies from 1–7 m. This sandstone occurs as a distinct facies within the large trough cross-bedded units in outcrop of Miri Formation, with well-defined, low- to high-angle planar cross-bedded and hummocky cross-bedded features preserved locally (Fig. 2b). Some of them are preserved with mud-clasts and mud drapes. This has been seen in a single vertical section showing alternating directions of migration of ripples or dunes which results from a unidirectional tidal current flow for a period of time span, followed by an abrupt change in an opposite tidal flow direction for another time span.

## **4.3 *Trough Cross-Bedded Sandstone (TCBS)***

This facies consists of yellow to yellowish-gray, fine- to medium-grained, moderately sorted to well-sorted sandstone. This variety of sandstone facies varies from large to small-scale TCBS. It consists of mixed mud-clasts and mud-draped. The large-scale TCB found in between clean thick sandstones mostly shows a fair and moderate weather-based deposition. Bioturbation is common and abundant with trace fossils comprising mostly ophiomorpha and is typical of a shallow marine environment (Fig. 2c). The overall stratification recommends that the TCBS in Miri formations was deposited in a tide-dominated estuary in a shallow sub-tidal environment with major sub-tidal bed load transport. Some of this facies show scour-and-fill structures that are normally formed at channel bottoms, with flow over an unconsolidated surface. Overall, this sandstone facies resulted as a small, shallow tidal channel-fill, which comprises fine- to medium-grained sand, due to the migration of three dimensional flows [12].

## **4.4 *Wavy- to Flaser-Bedded Sandstone (W-FBS)***

Wavy- to flaser-bedded sandstone is light-yellowish-gray, very-fine- to silty sand, moderately sorted to well-sorted with dominating non-heterolithic bedding (Fig. 2d). It consists of flaser bedding (typically bifurcated-wavy or, more rarely, wavy) with numerous intercalation of mud. The bedding is wavy due to wavy layers of rounded asymmetrical sand ripples with mud draping on top. Its thickness varies from 2 to 9 m. These bedding are commonly formed in tidal flat sediments where there is a variation of sediment supply and the level of wave (or current)

activity is in a constant mode with adequate deposition and preservation of both sand and mud. In some of the cases, it is deposited on mixed intertidal flats [13].

#### **4.5 *Cross-Bedded Sandstone (CBS)***

Other than hummocky, herringbone, and trough cross-bedded sandstone, CBS facies is also found randomly in Outcrops. It is usually gray- to light-gray, fine- to medium-grained sandstone with poorly sorted grain and composed of quartz grains. It is usually formed with horizontal units that are composed of inclined thin layers of sandstone with some mud drapes and thin fragmented coal layers, so referred to as cross-strata (Fig. 2e).

#### **4.6 *Cross-Bedded Sandstone (CBS)***

This sandstone facies consists of light-gray, fine- to very-fine-grained, moderate to well-sorted sandstone and the thickness of this sandstone facies ranges from 1 to 3 m, averaging 1 m. This facies has a high degree of bioturbation and is also identified within HCSS in Outcrop 1, Outcrop 2, and Outcrop 4 (Fig. 2b). It is characterized as thin layers of coarse-grained sandstone with abundant body fossils, such as whole brachiopod shells, fossilized mollusk sea shells, and skeletal fragments and other well-preserved fossils (Fig. 2f, g). Remnant sedimentary structures include parallel stratification with coal fragments. The occurrence of Ophiomorpha burrows suggests a low-energy and a sandy shallow marine setting. In most of the sections, its bioturbated index is more than 5 which do not show any clean internal bedding. In some cases, this BS facies is overlain by fine-grained sandstone with equally distributed HCSS facies. This relationship suggests a period of very high energy current deposition brought by storm reworking.

#### **4.7 *Massive Sandstone (MS)***

This massive sandstone facies consists of poorly to moderately sorted, fine- to coarse-grained sandstone with no internal structures. This sandstone occurs as individual beds that are separated by HCS sandstone facies above and interbedded thin sand and silt below (Fig. 2h). The loose grain-supported framework suggested that the sandstone has modest compaction and shows dewatering structure, suggesting deposition in a fluidized condition.

## 5 Grain-Size Analysis

Grain-size analysis was carried out by using the sieving method and observation under a binocular microscope. Representative samples were collected from each of the facies. The sieving results were plotted as histograms frequency % (for sorting, textural group, skewness, mode, and mean values) curve to represent the grain size distribution (Figs. 3 and 4).

### 5.1 Facies HCSS

The sandstone sample from the HCSS facies has a grain size in the range of the phi values  $-1$  to  $5$ , according to Folk and Ward method, with a mode of phi  $3.36$ , which is very-fine-grained and moderately sorted (Table 1). The sandstone type is unimodal with  $96.3\%$  sand and  $3.7\%$  mud. Visual examination under binocular microscope, however, shows the sandstone is moderately sorted to sorted with coarse- to very-fine-grained sandstone.

### 5.2 Facies HBCBS

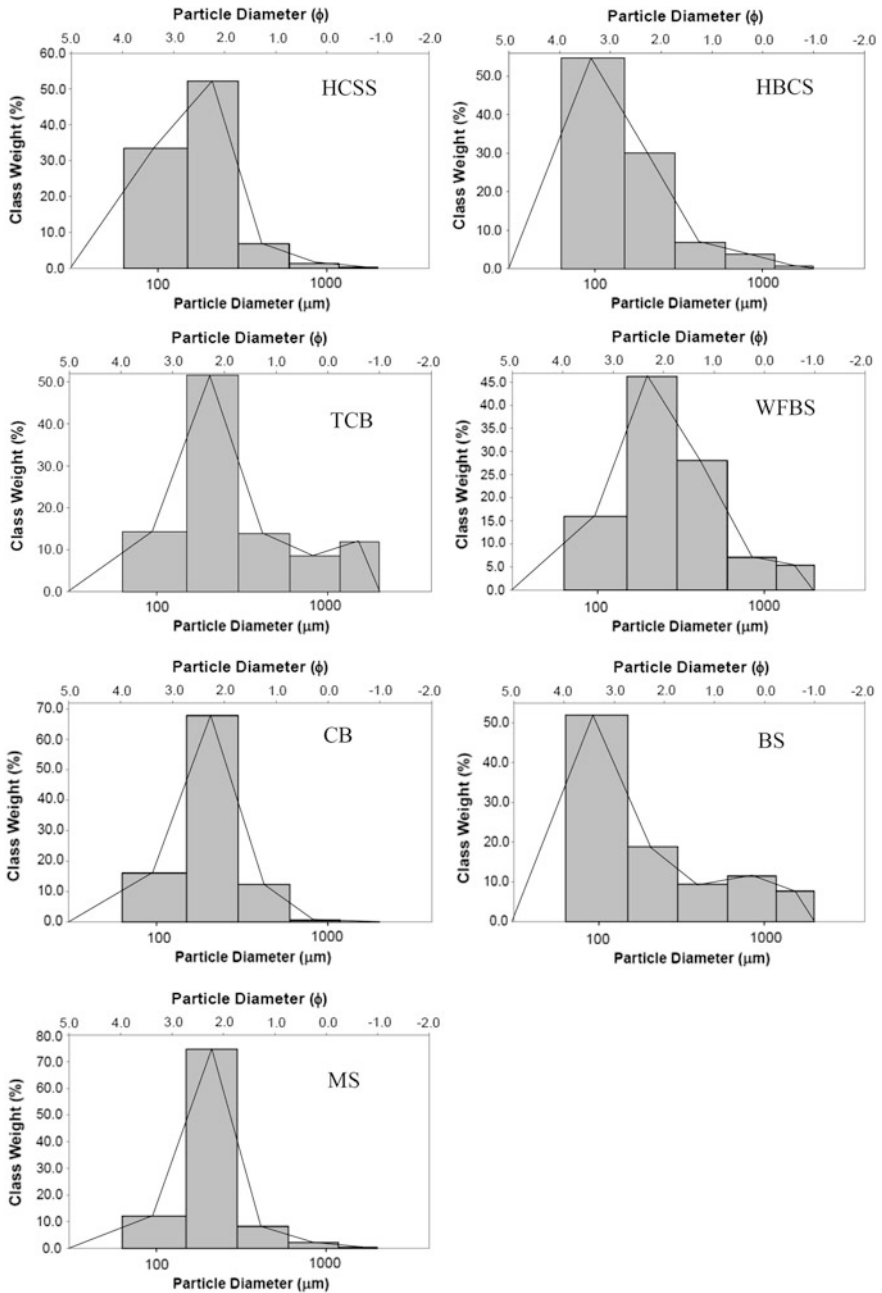
The sample from HBCBS has a grain size in the range of phi value  $-1$  to  $5$ , with a mode of phi  $2.24$ . This sandstone is moderately sorted and comprises very fine sand according to the distribution pattern (Table 1). The sandstone type is unimodal (Fig. 3) with  $94.7\%$  sand and  $5.3\%$  mud. Visual examination shows sorted grains with fine- to very-fine-grain-size sandstone.

### 5.3 Facies TCBS

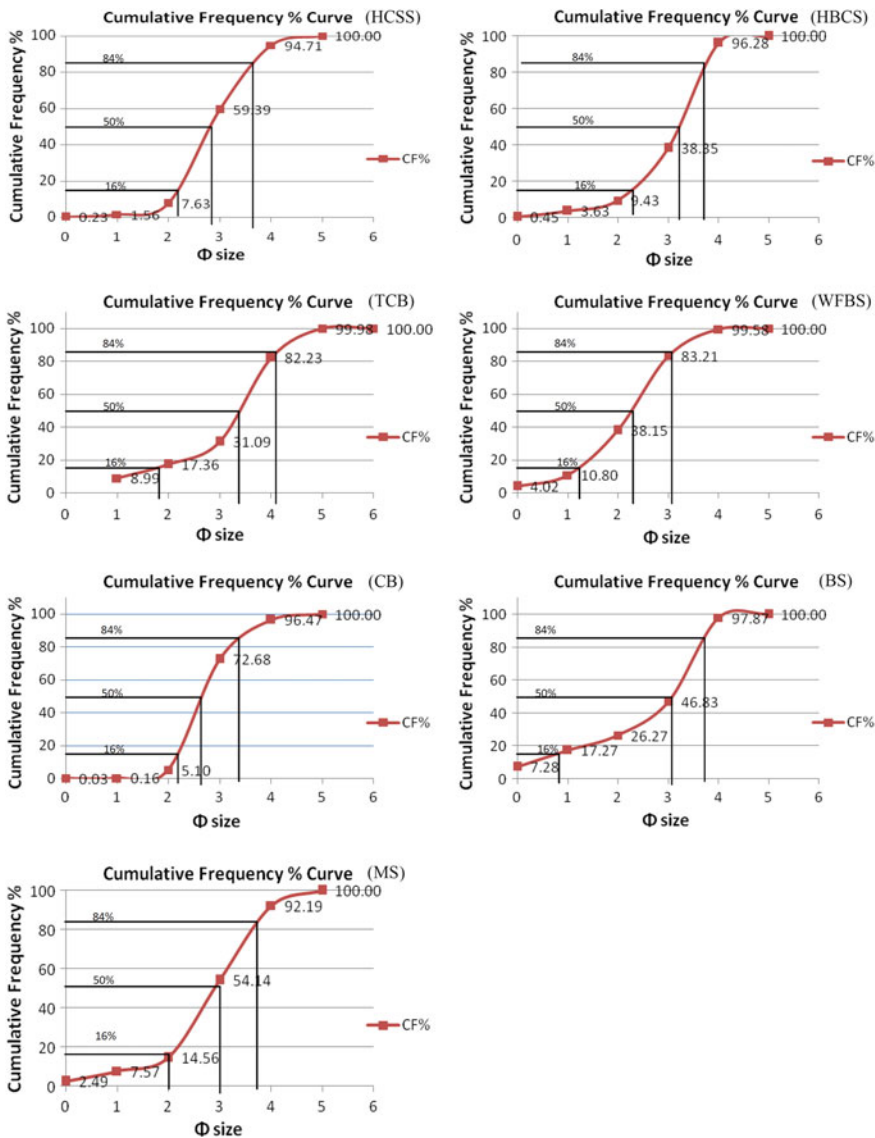
The trough cross-bedded sandstone has a grain size in the range of  $-1$  to  $5$  phi, with a mode of phi  $2.24$  and is poorly sorted (Table 1). The sandstone type is bimodal (Fig. 3) with  $100\%$  sand. Visual examination of the sandstone shows moderately to well-sorted, with fine- to very-fine-grained sandstone.

### 5.4 Facies W-FBS

The sandstone sample from the W-FBS facies has a grain size in the range of the phi  $-1$  to  $5$  values with mostly very-fine-grained sandstone (i.e., mode value of



**Fig. 3** The columns of the histograms of each of the facies, which have a width proportional to the size range of grains (expressed using the phi scale) for each sample split. Only *TCB* and *BS* are bimodal in distribution



**Fig. 4** Cumulative frequency % curve for seven (7) different sandstone facies of Miri Formation for mean, median, mode, and skewness calculation by using the values of phi at 16, 50, and 84%, according to Folk & Ward method

2.24 phi) and is poorly sorted (Table 1). The sandstone type is unimodal mostly with 99.6% sand and 0.4% mud. Visual examination shows fine- to very-fine-grained sandstone and moderately sorted to well-sorted grains.

**Table 1** Grain-size distribution and statistical analysis

Method	Outcomes	SM1 3 (HCSS)	SM1 1 (HBSC)	SM4 6 (TCB)	SM4 2 (W-FBS)	SM4 5 (CB)	SM2 5 (MS)	SM3 3 (BS)
Sieving	Sieving error	3.0%	3.0%	3.0%	3.0%	3.0%	5.0%	2.0%
	Sample type	Unimodal, moderately sorted	Unimodal, moderately sorted	Bimodal, poorly sorted	Unimodal, poorly sorted	Unimodal, moderately sorted	Unimodal, moderately well-sorted	Bimodal, poorly sorted
	Textural group	Sand	Sand	Sand	Sand	Sand	Sand	Slightly gravelly sand
	Sediment name	Moderately sorted very fine sand	Moderately sorted fine sand	Poorly sorted fine sand	Poorly sorted fine sand	Moderately sorted fine sand	Moderately well-sorted fine sand	Slightly very fine gravelly medium sand
Folk and Ward method (φ)	Mean	2.892	2.688	1.849	1.908	2.352	2.270	1.460
	Standard deviation	0.893	0.868	1.209	1.034	0.721	0.644	1.875
	Skewness	-0.257	0.185	-0.306	-0.135	0.147	0.064	0.168
Folk and Ward method (Description)	Mean	Fine sand	Fine sand	Medium sand	Medium sand	Fine sand	Fine sand	Medium sand
	Standard deviation	Moderately sorted	Moderately sorted	Poorly sorted	Poorly sorted	Moderately sorted	Moderately well-sorted	Poorly sorted
	Skewness	Coarse skewed	Fine skewed	Very coarse skewed	Coarse skewed	Fine skewed	Symmetrical	Fine skewed
	Mode 1 (φ)	3.363	2.237	2.237	2.237	2.237	2.237	1.237
	Mode 2 (φ)	-	-	-0.619	-	-	-	-0.619

(continued)

**Table 1** (continued)

Method	Outcomes	SM1 3 (HCSS)	SM1 1 (HBCS)	SM4 6 (TCB)	SM4 2 (W-FBS)	SM4 5 (CB)	SM2 5 (MS)	SM3 3 (BS)
	% Gravel	<b>0.0%</b>	<b>0.0%</b>	<b>0.%</b>	<b>0.0%</b>	<b>0.0%</b>	<b>0.0%</b>	<b>2.1%</b>
	% Sand	<b>96.3%</b>	<b>94.7%</b>	<b>100.%</b>	<b>99.6%</b>	<b>97.3%</b>	<b>96.6%</b>	<b>89.7%</b>
	% Mud	<b>3.7%</b>	<b>5.3%</b>	<b>0.0</b>	<b>0.4%</b>	<b>2.7%</b>	<b>3.4%</b>	<b>8.1%</b>

### 5.5 *Facies CBS*

The cross-bedded sandstone has a grain size in the range of  $-1$  to  $5$  phi, with a mode of phi 2.24 and is moderately sorted with fine grains (Table 1). The sandstone type is unimodal (Fig. 3) with 97.3% sand and 2.7% mud. Visual examination of the sandstone shows moderately to well-sorted, with fine- to very-fine-grained sandstone.

### 5.6 *Facies BS*

The sample from BS shows a phi value that ranges from  $-1.5$  to  $5$  and is poorly sorted with very fine sand to slightly gravelly medium sand. It has a mode of phi 1.23–3.36 (Table 1). The sandstone type is bimodal (Fig. 3) with 89.7–97.9% sand and 2.1–8.1% mud. Visual examination shows that the sandstone is sorted and fine- to very-fine-grained in distribution.

### 5.7 *Facies MS*

The massive sandstone has a grain size in the range of  $-1$  to  $5$  phi, with a mode of phi 2.24 and is poorly to moderately well-sorted (Table 1). The sandstone type is unimodal (Fig. 3) with 96.6–92.2% sand and 3.4–7.4% mud. Visual examination the sandstone shows moderately sorted to sorted, with fine- to very-fine grains.

## 6 Static Connectivity

The two-dimensional (2-D) outcrop models are constructed from well-exposed outcrops based on different lithologies [3], shale cutoffs, observed grain-size trend and poro-perm properties with lateral and vertical extent as by [14–17] (Fig. 5). These results show that sandstones of HCSS and HBSC are better sorted, with minimal mud content, and the depositional pattern indicates increasing vertical and lateral connectivity, even in bioturbated rich sand, as compared to other sandstone facies. On the other hand, sandstones of BS and CB are of poor quality in terms of grain sorting and poro-perm. Based on these results, a 2-D outcrop model is constructed providing additional insight into the significance of small-scale heterogeneity and static connectivity of siliciclastic shallow marine sandstone deposits.



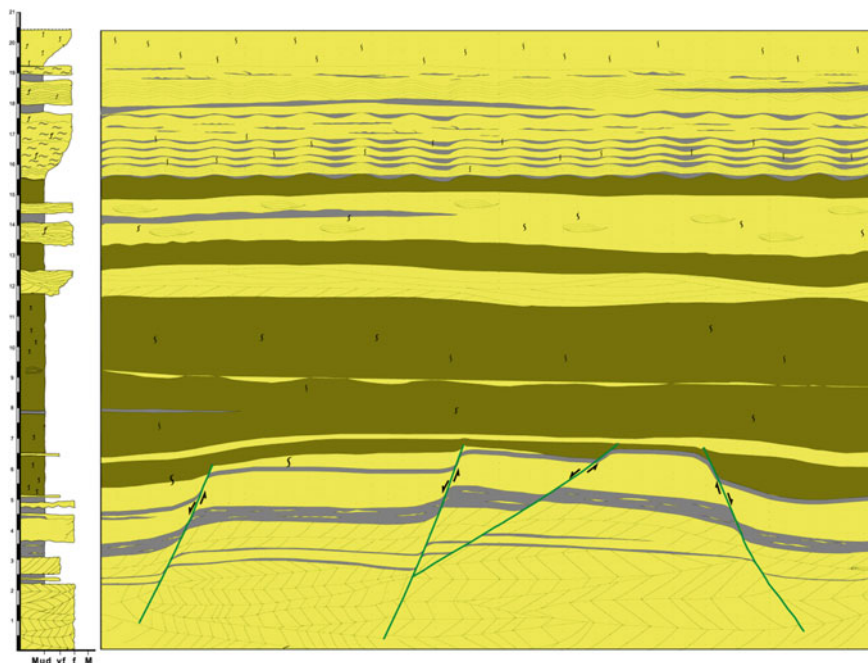


Fig. 5 The two-dimensional (2D) static connectivity outcrop model

## 7 Poro-Perm

See Table 2.

**Table 2** Results of porosity–permeability by porosimeter of seven different sandstone

Sample	Porosity (%)	Permeability (md)
Hummocky cross-stratified sandstones	29.31	$794.93e-3 \mu\text{m}^2 = 805$
Herringbone cross-bedded sandstones	30.41	$138.96e-2 \mu\text{m}^2 = 1408$
Trough cross-bedded sandstone	34.41	$386.61e-2 \mu\text{m}^2 = 3917$
Wavy- to flaser-bedded sandstone	22.04	$336.8e-5 \mu\text{m}^2 = 3.37$
Bioturbated sandstone	9.74	$130.78e-3 \mu\text{m}^2 = 132$
Massive sandstone	25.80	$130.86e-4 \mu\text{m}^2 = 13.2$
Cross-bedded sandstone	34.35	$217.01e-1 \mu\text{m}^2 = 21,988$

## 8 Conclusion

On the basis of sedimentology, lithology, grain size, texture, and sedimentary structure, the Miri and Lambir formations are divided into seven (7) major sandstone facies; (i) hummocky cross-stratified sandstones; (ii) herringbone cross-bedded sandstones; (iii) trough cross-bedding sandstones; (iv) wavy-flaser-bedded sandstone; (v) cross-bedded sandstone; (vi) bioturbated sandstone; and (vii) massive sandstone. The sandstones of HCS and HBSC are better sorted sandstones, with minimal mud content. This may have contributed to the high poro-perm values as compared to other sandstone facies. On the other hand, the sandstone of BS is of poor quality in terms of grain sorting. This reflects the heterogeneity in facies characteristic and reservoir quality. Further analysis must be done for quality and overall achievement of the project in terms of poro-perm and petrography analysis.

**Acknowledgements** I would like to thank Universiti Teknologi PETRONAS (UTP) for granting me scholarship under GA scheme to complete my Ph.D. research. I also like to extend my sincere thanks to my supervisors AP. Dr. Abdul Hadi Abd Rahman and AP. Dr. Chow Weng Sum for all the guidance and support to fulfill the Ph.D. requirement in paper writing and data collection with analysis.

## References

1. J. Howell, Å. Vassel, and T. Aune, "Modelling of dipping clinoform barriers within deltaic outcrop analogues from the Cretaceous Western Interior Basin, USA," Geological Society, London, Special Publications, vol. 309, pp. 99–121, 2008.
2. J. A. Howell, A. Skorstad, A. MacDonald, A. Fordham, S. Flint, B. Fjellvoll, et al., "Sedimentological parameterization of shallow-marine reservoirs," Petroleum Geoscience, vol. 14, pp. 17–34, 2008.
3. R. Labourdette, "Stratigraphy and static connectivity of braided fluvial deposits of the lower Escanilla Formation, south central Pyrenees, Spain," AAPG bulletin, vol. 95, pp. 585–617, 2011.
4. T. Aigner, U. Aspiron, J. Hornung, W.-D. Junghans, and R. Kostrewa, "Integrated outcrop analogue studies for Triassic alluvial reservoirs: examples from southern Germany," Journal of Petroleum Geology, vol. 19, pp. 393–406, 1996.
5. G. H. Graham, M. D. Jackson, and G. J. Hampson, "Three-dimensional modeling of clinoforms in shallow-marine reservoirs: Part 1. Concepts and application," AAPG Bulletin, vol. 99, pp. 1013–1047, 2015.
6. N. Siddiqui, A. Rahman, C. Sum, M. Mathew, D. Menier, and H. Muhammad, "Modeling of Littoral Sandstones Reveal Variance in Reservoir Flow Patterns: An Example from Nyalau Formation, East Malaysia," Research Journal of Applied Sciences, Engineering and Technology, vol. 11, pp. 176–184, 2015.
7. P. Liechti, F. W. Roe, N. S. Haile, and H. Kirk, "The geology of Sarawak, Brunei and the western part of North Borneo," 1960.
8. C. S. Hutchison, *Geology of North-West Borneo: Sarawak, Brunei and Sabah*: Elsevier, 2005.
9. C. S. Hutchison, *Geological evolution of South-east Asia*. Oxford [Oxfordshire]; New York: Clarendon Press; Oxford University Press, 1989.

10. PETRONAS, *The Petroleum geology and resources of Malaysia: Petronas*, 1999.
11. R. J. Cheel and D. A. Leckie, "7 Hummocky cross-stratification," *Sedimentology Review* 1, vol. 31, p. 103, 2009.
12. M. Collins, C. Amos, and G. Evans, "Observations of some sediment-transport processes over intertidal flats," 1981.
13. R. W. Dalrymple, B. A. Zaitlin, and R. Boyd, "Estuarine facies models: conceptual basis and stratigraphic implications: perspective," *Journal of Sedimentary Research*, vol. 62, 1992.
14. I. Fabuel-Perez, D. Hodgetts, and J. Redfern, "Integration of digital outcrop models (DOMs) and high resolution sedimentology-workflow and implications for geological modelling: Oukaimeden Sandstone Formation, High Atlas (Morocco)," *Petroleum Geoscience*, vol. 16, pp. 133–154, 2010.
15. I. Fabuel-Perez, J. Redfern, and D. Hodgetts, "Sedimentology of an intra-montane rift-controlled fluvial dominated succession: the Upper Triassic Oukaimeden Sandstone Formation, Central High Atlas, Morocco," *Sedimentary Geology*, vol. 218, pp. 103–140, 2009.
16. J. E. Funk, R. M. Slatt, and D. R. Pyles, "Quantification of static connectivity between deep-water channels and stratigraphically adjacent architectural elements using outcrop analogs," *AAPG bulletin*, vol. 96, pp. 277–300, 2012.
17. N. Siddiqui, A. H. bin Abd Rahman, C. W. Sum, M. J. Mathew, and D. Menier, "Facies Characteristics and Static Reservoir Connectivity of Some Siliciclastic Tertiary Outcrop Successions in Bintulu and Miri, Sarawak, East Malaysia," *AAPG Search and Discovery*, vol. Article # 51035 2014.

# Review of Tectonic Evolution of Sabah, Malaysia

Samira Ghaheri and Mohd Suhaili Bin Ismail

**Abstract** Sabah's geological structure and tectonic history show that this region had undergone several tectonic events, of which the most important were the South China Sea floor spreading and the Sulu Sea subduction. The South China Sea subducted beneath the northern Borneo margin forming a basin that was filled with Middle Eocene–Early Miocene sediments. The Celebes Sea subduction occurred during Late Oligocene, this sea subducting northward beneath the Dent Peninsula. These subductions led to shallower sedimentation in north, east, and west of Sabah. During the Upper Oligocene–Middle Miocene, active rifting of the South China Sea Basin took place. The N–S compression formed in the west led to general shallowing of sedimentary facies and formed the NW–SE fold and thrust belt in the northern and eastern part of Sabah. During the Early–Middle Miocene, the circular basins in the eastern part of Sabah formed and it is thought to be related to SE Sulu Sea Basin rifting. The volcanic arc in Dent Peninsula also formed during this time which was due to the southward subduction of the Sulu Sea. In Late Miocene, the SE Sulu Sea Basin rifting ceased.

**Keywords** Sabah · Tectonic evolution

## 1 Introduction

Sabah is located in the northern part of Borneo which is tectonically very active. Since Tertiary, this region had undergone considerable tectonic stress, but the main tectonic activity occurs during the Middle Miocene. Sabah is located between three different seas which greatly influenced the tectonic evolution of the region. It is bordered on the west and north by the South China Sea which currently is covered

---

S. Ghaheri (✉) · M.S. Bin Ismail  
Department of Geosciences, University Teknologi PETRONAS,  
32610 Bandar Seri Iskandar, Perak, Malaysia  
e-mail: s.ghaheri@yahoo.com

**Fig. 1** Sabah is located between three different seas which greatly influenced the tectonic evolution of this region (modified from [6])



by carbonate platform known as Dangerous Ground [33]. From the east, it lies next to the Sulu Sea, and from the south, it lies adjacent to the Celebes Sea.

Sabah is one of the important regions in Malaysia in terms of hydrocarbon exploration. A better understanding on the geology structures and tectonic evolution of the region can be a great assistance for further oil and gas field development. Sabah region was studied by many authors for the past few decades [1–3, 5, 8, 10, 11, 14, 15, 21–24, 26–30, 32].

This paper attempts to integrate all studies and come out with the overall pictures of the tectonic evolution of Sabah. This review will follow the formal works of previous authors, identifying the events according to the geology and tectonic (Fig. 1).

## 2 Sedimentology

A brief account on the sedimentology of Sabah region is given here on tectonic evolution closely associated with basin sediment.

Tongkul [33] divided Sabah rock formation based on their age and lithologies to the five main groups. The oldest rock in Sabah is the basement rock. The basement rock units also known as Chert-Spilite formation that consist metamorphic and igneous rocks association of cherts interbedded with red shale [12, 19, 20]. These basement rocks indicate as Triassic–Cretaceous based on radiometric age determination [17, 20]. The second rock group consists of Eocene–Lower Miocene sediments. These sediments lie unconformably on the basement rock in western and northern Sabah [33]. He interpreted the sediments deposited in shallow to deep marine and includes thick sandstone and shale beds, with internal limestone and tuffs lenses. The third deposits mostly occur in eastern Sabah in Dent and Semporna peninsulas [33]. These rocks may form from volcanic activity during Early–Middle Miocene in this region. These pyroclastic deposits overlie the older basement rocks with marked unconformity. The fourth rock group is the sediment deposits that named Middle Miocene chaotic deposits and melanges. These deposits include

chaotic mixtures of single-lithology blocks or different lithology blocks [33]. Tongkul believed that the melanges developed in eastern and southeastern Sabah also occur in smaller outcrops in western and northern Sabah. Noad [23] suggested that a series of melange deposits ranging across eastern Sabah and comprises the Garinono, Ayer, and Kuamut mélanges. These deposits are characterized by the diversity of sediments such as sandstone, shale, chert, limestone, and igneous rocks. The origin of the chaotic deposits is varied, and it is argued that in eastern Sabah the melange was produced by submarine slope failure of Labang sediments and slumped Kulapis material [4, 23]. Also Tongkul showed that most of the tuffaceous sediments were derived from the Kalumpang Formation and most of the igneous and metamorphic rocks are from the basement rocks. It was suggested that the common characteristics of these blocks are the small-scale faults and fractures that filled by calcite veins [33]. The last sediment deposit group is characterized by sandstone, shale, conglomerates, and limestone. These sediments unlike the other groups are rich in fossils and show age of Early–Late Miocene. The sediments in most part lie unconformably on older rocks. Tongkul [33] argued that these sediments deposited in isolated, circular-shaped basins.

### 3 Tectonic Evolution

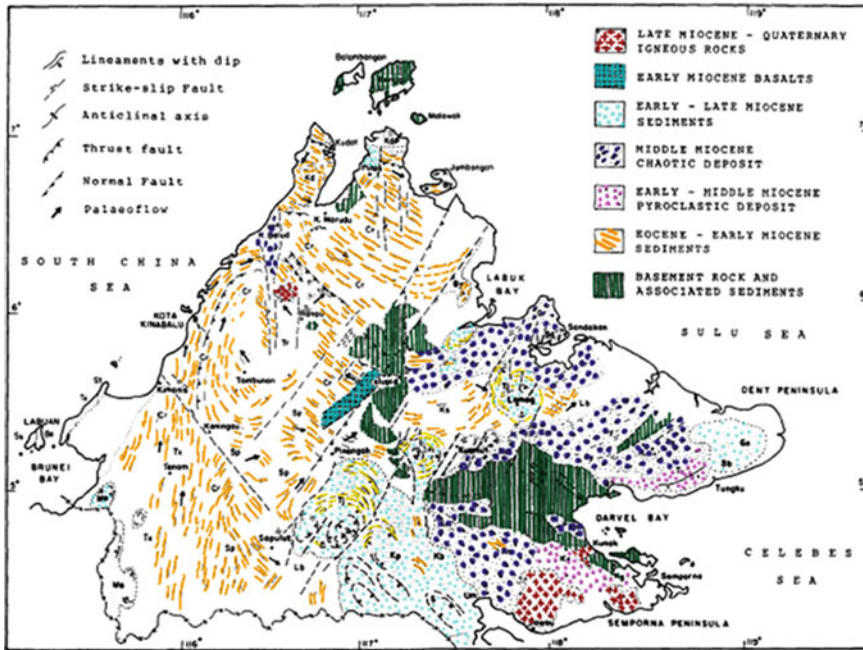
The tectonic evolution of Sabah is described in three parts: Cretaceous to Early Eocene, Middle Eocene to Middle Oligocene, and Late Oligocene to recent. The earliest tectonic event in this region is believed to begin in Early Cretaceous (Fig. 2).

#### 3.1 *Cretaceous to Early Eocene*

The Sabah basement rock mostly includes metamorphic, igneous, ultrabasic rock, and cherts (Chert–Spilite Formation) associated with ophiolite complex that formed during Early Cretaceous [33]. Based on the presence of ophiolites, Hutchison [13] interpreted this unit as oceanic crust although some authors such as Reinhard and Wenk [25] and Leong [20] believe that the origin of the basement rock is probably continental crust based on the existence of granitic and metamorphic rock and from the interpretation of gravity data. It is suggested SW Borneo is a continental block rifted from the west Australian margin, and during Early Cretaceous joined to the Sundaland [7].

In Early Cretaceous, the basement rock unit was uplifted [33] and during Paleocene to Eocene, this unit was uplifted again as indicated by the presence of limestones during this time in the most part of Sabah [18, 32, 33].

At the same time, the SE portion of the South China Sea subducted beneath the northern Borneo margin [6, 14]. The Rajang Group also started to deposit in deep



**Fig. 2** Tectonic map of Sabah (modified from [33]) (Formations: *Cr* = Crocker, *Sp* = Sapulut, *Tr* = Trusmadi, *Tx* = Temburong, *Lb* = Labang, *Ks* = Kulapis, *Kd* = Kudat, *Tj* = Tanjong, *KI* = Kalabakan, *Kp* = Kapilil, *Sd* = Sandakan, *Me* = Meligan, *Be* = Belait, *Ss* = Setap Shale, *By* = Bongaya, *Ay* = Ayer, *Wr* = Wariu, *Km* = Kuamut, *Sb* = Sebahat, *Gn* = Ganduman, *Tu* = Tungku, *Ln* = Libong Tuffite, *Kg* = Kalumpang, and *Um* = Umas-Umas.)

marine [14] and the Labang Formation in the Central Sabah Basin (in eastern of Sabah) was developed by eroded sediments of the accretionary wedge [23]. Noad [23] had suggested that the Central Sabah Basin was a back-arc basin to the subduction zone to the north. During Eocene to Lower Miocene, Crocker, and Kudat formations that covered mostly the north part of Sabah began to deposit [34]. The Crocker Formation formed in deep marine as turbidite deposit while Kudat Formation deposited in deep to shallow marine [34] (Fig. 3).

### 3.2 Middle Eocene to Middle Oligocene

It is suggested a basin extending NE–SW through southwestward to Sarawak was formed as a result of the southeastward subduction of the South China Sea under western part of the Celebes Sea [33]. The Trusmadi, Labang, Crocker, Kulapis, part of Sapulut, Kudat, and Temburong formations were formed as deep marine deposits in the central part of this basin and some part of Kudat, Temburong, and Labang. At

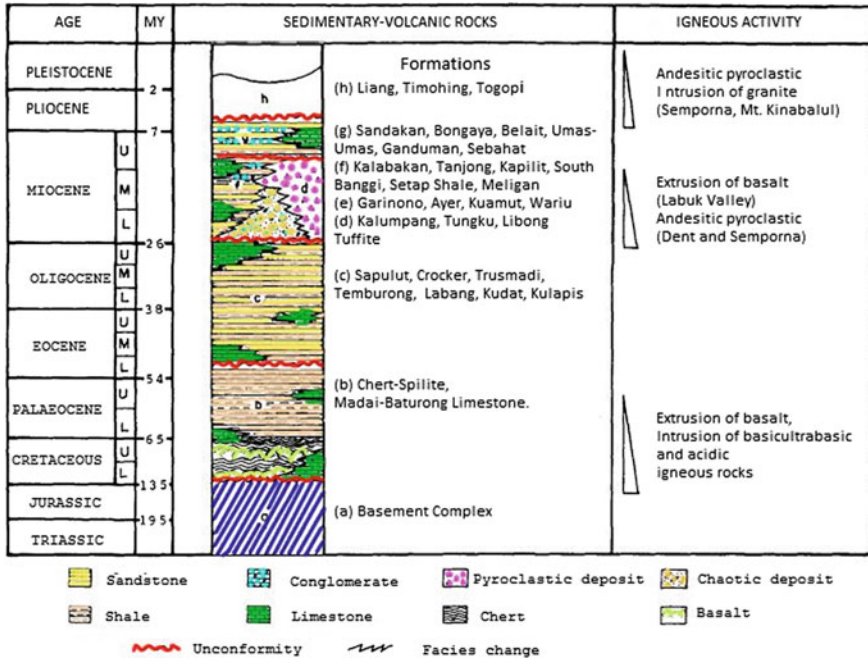


Fig. 3 Stratigraphy of Sabah (modified from Wilford [35] and Rangin et al. [24])

the same time, the Kulapis Formation was deposited in shallower water at the edge of the basin [33]. In the Middle Eocene, the Celebes Sea was formed due to seafloor spreading [6].

### 3.3 Late Oligocene to Recent

During Late Oligocene, the Celebes Sea subducted northward beneath the Dent Peninsula. The southern margin of the Central Sabah Basin was uplifted by this subduction [23] and Labang High was formed due to this subduction [4]. This subduction led to compression northward of Sabah. During this time, Gomantong Limestone deposited on shallow shelf area of the basin [23]. Tongkul [33] also noted during the Upper Oligocene to Early Miocene, widespread carbonate platform and reef formed due to uplifted of the area.

On the other hand, the Crocker accretionary wedge was uplifted due to compression in eastern Sabah that was caused by southward subduction of the South China Sea at the northern Borneo margin.

In the Late Oligocene to Early Miocene, the local plate movement changed due to the cessation of subduction of the South China Sea beneath Borneo, and it caused the Miri Zone attached to the Luconia Platform [23].



Inversion of the Miocene sequence in eastern Sabah appears to be limited to the edges of basement blocks which were moved by far-field tectonic stresses. Post-Middle Miocene basin evolution in the onshore (Central Sabah Basin) and adjacent parts of the Sulu Sea offshore (Sandakan Basin) has been strongly influenced by mud diapirism and gravitational sagging of progradational sand-rich sediments into underlying muds and melange units [7].

At the end of the Early Miocene, oceanic spreading ceased in the South China Sea Basin as a series of collisions were initiated between the continental blocks derived from the Asian mainland and the northwestern margin of Borneo. This tectonic event caused a major period of uplift and erosion which produced the Deep Regional Unconformity (DRU). While these events were occurring at the southern margin of the South China Sea, the Sulu Sea was undergoing extension stress in the northwest and ocean spread in the southeast [3, 4, 23].

Noad [23] also pointed out that Sabah during this time was under both extensional and compressional stresses. Seismic survey in Sabah offshore area shows that the DRU can be traced from the South China Sea into the Sulu Sea on a boundary between two depositional systems that are both represented in sedimentary section onshore eastern Sabah [7].

The Upper Oligocene–Middle Miocene was the period of most important tectonic activity occurred in the Sabah region [30, 31, 33]. The N–S compression led to general shallowing of sedimentary facies especially in the west part of the Sabah basin and also formed the NW–SE fold and thrust belt in the northern and eastern part of Sabah [33]. This compression was the result of active rifting of the South China Sea Basin [26, 28].

Eastern Sabah changed from an environment of deep marine clastic deposition in the Oligocene and Early Miocene, to shallow marine and terrestrial sedimentation in the Mid- to Late Miocene, with a major period of sedimentary Melang Formation occurring at the time of the Deep Regional Unconformity (DRU).

In Early–Middle Miocene, SE Sulu Sea Basin started to rifting [4, 16, 23]. The Sulu Sea seafloor spreading reconstructed the Central Sabah Basin in the west part of Sabah and trending the basin to the south. The host and graben structures in the west of Sabah that made the circular basin are related to this extension [23, 33]. During this time, a volcanic arc in the Dent Peninsula was formed related to the southward subduction of the Sulu Sea [23, 33]. The volcanic activity continues until the end of the Middle Miocene [23]. This compression and extension reconstructed the formations. In northern and western part of Sabah, the melange formation (broken formation) was formed along NW–SE fold and thrust belt [33]. In eastern Sabah, this formation was formed due to slumping and shearing of unstable sediment [4].

The SE Sulu Sea Basin rifting ceased during the Late Miocene [9] and the NW–SE large transform fault formed in eastern Sabah [4, 9, 23] that detached the east part of Sabah from Sulu Sea [23].

## 4 Conclusion

Sabah tectonic started during the Early Cretaceous. The tectonic evolution of this region greatly affected by surrounding seas (South China Sea, Sulu Sea, and Celebes Sea). The South China Sea subduction under western part of Celebes Sea formed a basin extending NE–SW through southward to Sarawak. This basin was filled by Middle Eocene–Early Miocene sediments.

The Sabah region is tectonically active and continues to be under extension and compression stresses until today. The presence of mud volcano in many parts of Sabah supported this idea [33].

**Acknowledgements** I would like to thank University Teknologi PETRONAS for supporting my study in this university and make it possible to produce this paper. I wish to thank the Mineral and Geoscience Department of Malaysia, Sabah for their support and allowing access to the reports. My special thanks to Dr. Noad for kindly providing his thesis.

## References

1. Bell, R. M. and Jessop, R. G. C. 1974. Exploration and geology of the West Sulu Basin, Philippines. *Aust. Petrol. Explore. Assoc. J.* 1, 21–28.
2. Bernard, F., M filler, C., Letouzey, J., Rangin, C. and Tahir, S. 1990. Evidence of multiphase deformation in the Rajang-Crocker Range (Northern Borneo) from Landsat Imagery Interpretations: Geodynamic implications. *Tectonophysics* 183, 321–339.
3. Bol, A. J. and Hoorn, B. v. 1980. Structural Styles in Western Sabah Offshore. *Geological Society of Malaysia Bulletin* 12: 1–16.
4. Clennell, M. B. 1996. Far-field and gravity tectonics in Miocene basins of Sabah, Malaysia. In: *Tectonic Evolution of Southeast Asia*, ed. Hall, R. and Blundell, D. Special Publication no. 106: 307–320. Geological Society of London.
5. Haile, N. S. 1969. Geosynclinal theory and the organizational pattern of the NW Borneo Geosyncline. *J. Geol. Soc. Lond.* 124, 171–194.
6. Hall, R. 1996. Reconstructing Cenozoic SE Asia. In: *Tectonic Evolution of Southeast Asia*, ed. Hall, R. and Blundell, D. Special Publication no. 106: 153–184. Geological Society of London.
7. Hall, R., Clements, B., and Smyth, H., 2009. Sundaland: Basement Character, Structure, and Plate Tectonic Development. Proceedings, Indonesian Petroleum Association 33, May 2009.
8. Hamilton, W. 1979. Tectonics of the Indonesian region. U.S. Geol. Surv. Prof. Paper 1078.
9. Hinz, K., Fritsch, J., Kempter, E. H. K., Mohammad, A. M., Meyer, J., Mohamed, D., Vosberg, H., Weber, J., and Benavidez, J. 1989. Thrust tectonics along the north-western continental margin of Sabah/Borneo. *Geologische Rundschau* 78 (3): 705–730.
10. Hinz, K., and Schluter, H. U. 1985. Geology of the Dangerous Grounds, South China Sea, and the continental margin off Southwest Palawan—results of Sonne Cruises SO-23 and SO-27. *Energy* 10, 297–315.
11. Holloway, N. H. 1982. The North Palawan Block, Philippines, its relationship to the Asian mainland and its role in the evolution of the South China Sea. *Bull. Geol. Soc. Malaysia* 14, 19–59.
12. Hutchison, C. S. 1975. Ophiolite in Southeast Asia. *Geol. Soc. Am. Bull.* 86, 797–806.
13. Hutchison, C. S. 1978. Ophiolite metamorphism in northeast Borneo. *Lithos* 11: 195–208.

14. Hutchison, C. S. 1988. Stratigraphic-tectonic model for E. Borneo. *Bulletin of the Geological Society of Malaysia* 22: 133–151.
15. Hutchison, C. S. 1989. *Geological Evolution of Southeast Asia. Oxford Monographs on Geology and Geophysics* No. 13. Clarendon Press, Oxford, 386 pp.
16. Hutchison, C. S. 1992. The Southeast Sulu Sea, a Neogene marginal basin with outcropping extensions in Sabah. *Bulletin of the Geological Society of Malaysia* 32: 89–108.
17. Hutchison, C. S. and Dhonau, T. J. 1969. Deformation of an Alpine ultramafic association in Darvel Bay, East Sabah, Malaysia. *Geol. Mijnb.* 48, 481–493.
18. Jasin, Basir and Selvarajah, M. 1988. Palaeogene planktonic foraminifera from Pulau Kalamumpunan Kecil, Sabah. *Sains Malaysiana* 17, 99–113.
19. Kirk, H. J. C. 1962. The geology and mineral resources of the Semporna Peninsula, N. Borneo. *Geol. Surv. Malaysia Mere.* 14. Kirk, H. J. C. 1968.
20. Leong, K. M. 1974. The Geology and Mineral Resources of the Upper Segama Valley and Darvel Bay area. Memoir 4 (revised). Geological Survey of Malaysia.
21. Levell, B. K. 1987. The nature and significance of regional unconformities in the hydrocarbon-bearing Neogene sequence offshore West Sabah. *Geol. Soc. Malaysia Bull.* 21, 55–90.
22. Mascle, A. and Biscarrat, P. A. 1978. The Sulu Sea: a marginal basin in Southeast Asia. *Geological and Geophysical Investigations of Continental Margins* (Edited by Watkins, J. S., Montadert, L., and Pickering, P. J.). *Am. Assoc. Petrol. Geol. Mem.* 29, 373–381.
23. Noad, J.J. 1998. The sedimentary evolution of the Tertiary of Eastern Sabah, Northern Borneo. Ph.D. thesis, research school of geological and Geophysical Sciences, Birbeck College and university collsge, University of London, 123–128.
24. Rangin, C., Bellon, H., Bernard, F., Letouzey, J., Miller, C. and Sanudin, T. 1990. Neogene arc-continent collision in Sabah, Northern Borneo (Malaysia). *Tectonophysics* 183, 305–319.
25. Reinhard, M., and Wenk, E. 1951. The Geology of the Colony of North Borneo. *British Borneo Region Geological Survey Bulletin* 1: 7–15.
26. Ru, Ke, and Piggot, J. D. 1986. Episodic rifting and subsidence in the South China Sea. *AAPG Bull.* 70(9), 1136–1155.
27. Tan, D. N. K. and Lamy, J. M. 1990. Tectonic evolution of the NW Sabah continental margin since the late Eocene. *Geol. Soc. Malaysia Bull.* 22, 237–251.
28. Taylor, B. and Hayes, D. E. 1983. Origin and history of the South China Sea Basin. In: *Tectonic and Geologic Evolution of Southeast Asian Seas and Islands, Part 2. American Geophysical Union Geophysical Monograph* 27, 23–56.
29. Tjia, H. D. 1988. Accretion tectonics in Sabah: Kinabalu suture and East Sabah accreted terrane. *Geol. Soc. Malaysia Bull.* 22, 237–251.
30. Tongkul, F. 1987. The sedimentology and structure of the Crocker Formation in the Kota Kinabalu area, Sabah, Malaysia. Unpublished Ph.D. thesis, University of London.
31. Tongkul, F. 1989a. The sedimentology and structure of the Crocker Formation in the Kota Kinabalu area, Sabah. *GEOSEA VI Proceedings, Jakarta 1987. Indonesian Assoc. Geol.*, 135–156.
32. Tongkul, F. 1990. Structural styles and tectonics of Western and Northern Sabah. *Bull. Geol. Soc. Malaysia* 27, 227–240.
33. Tongkul, F. 1991. Tectonic Evolution of Sabah, Malaysia, Southeast Asia Earth Sciences, vol.6, No, 3/4., 395–405.
34. Tongkul, F. 2003. The Structural Style of Lower Miocene sedimentary Rocks, Kudat Peninsula, Sabah. Petroleum Geology Conference, 2003.
35. Wilford, G.E., 1967. Geological map of Sabah, scale 1:500,000. Geological Survey of Malaysia.

# Stratigraphy and Palaeoichnology of “Black Shale” Facies: Chert Unit of the Semanggol Formation, Perak

Farahana Azwa Drahman and José Antonio Gámez Vintaned

**Abstract** The exposed area of Bukit Putus, one of the Semanggol abandoned quarries in Bukit Merah (NNW of Taiping, Perak, Peninsular Malaysia) has allowed us to start a detailed study of the “black shales” of the chert unit of the Semanggol Formation. Presently, no integrated palaeoichnological-stratigraphical studies have ever been performed in the Semanggol Formation. The chert unit in particular is claimed to have been deposited in a deep oceanic basin under the influence of different regimes of transportation (Basir Jasin and Zaiton Harun [2]). The analysis conducted herein aims to reconstruct the palaeoenvironmental evolution, contrasting with previous interpretations. Description of sedimentary facies and facies associations was done at the main outcrop. Samples collected have been studied through thin sections, total organic content (TOC) analysis, scanning electron microscope (SEM)–EDX, and photography and image enhancement. As a result, palaeontological and sedimentological data indicate that as far as the “black shale” facies is concerned, the basin evolved from mid-distal continental shelf settings into shallower sublittoral conditions. The general evolution is compatible with the dynamics of a deltaic apparatus prograding seawards (prodelta facies evolving into lower delta front ones). At the outcrop of the Bukit Putus quarry, several levels bearing abundant specimens of *Claraia* sp.—an Early Triassic pectinid bivalve—have been found. Questionable brachiopods of the order Lingulida also seem to be present. In short, results from the integration of stratigraphical and paleoichnological data support the palaeoenvironmental conclusions obtained in this study.

**Keywords** Semanggol Formation • Permo-Triassic • Trace fossils • *Cruziana* ichnofacies • Bivalvia • Brachiopoda

---

F.A. Drahman (✉) · J.A.G. Vintaned  
Petroleum Geoscience Department, Universiti Teknologi PETRONAS,  
Seri Iskandar, Malaysia  
e-mail: farahanaazwa.drahma@petronas.com.my

## 1 Introduction

A few geological studies have been conducted on the Semanggol Formation which is widely exposed in north Perak, as well as in south and north Kedah (Peninsular Malaysia). Burton (1973) [3] divided the formation—from the bottom to the top—into three informal members, namely the chert member, the rhythmite member and the conglomerate member; they were later called “units” by [7]. The age of the Semanggol Formation was previously assigned to the Triassic based on the bivalves found [3]. Nevertheless, the age is now recognized as Early Permian to mid-Triassic as proposed by [1] based on the radiolarian present in the chert unit in Kedah. Most of the studies were conducted in the Kedah area as compared to Perak. Hence, an outcrop has been herewith selected at Bukit Merah (Perak) to further study the Semanggol Formation.

The present study of the Semanggol Formation at Bukit Merah focuses on the stratigraphy and palaeoichnology of the “black shale” facies of the chert member. The application of Palaeoichnology in sedimentary geology is consolidated and being recognized today as a capable apparatus to reconstruct the palaeoenvironment, to perform facies interpretation and to identify discontinuities, among other topics, and has accumulated a vast knowledge used for prospection and exploration of hydrocarbon resources. This is mostly because trace fossils are not susceptible to post-mortem displacement; they are virtually always found *in situ* [4]. Trace fossils are good facies indicators, as they record the behaviour of the producers, typically as a response to subtle changes in environmental parameters such as salinity, oxygen and food supply [6].

The siliciclastic succession of Bukit Merah has been described by Hutchison and Tan in 2009 [5], who interpreted the succession as mainly deposited in deepwater environments across the Semanggol Basin. The presence of radiolarians supports this vision. However, until now no integrated ichnological and stratigraphical studies have ever been performed. More precise interpretations can be done on the Semanggol Formation by using the trace fossil evidence which is present in the rock. In particular the ichnological analysis may prove valuable in detailing the environmental evolution of the basin.

## 2 Geological Setting

The Semanggol Formation is widely exposed at three separate locations, namely Padang Terap (north Kedah), Kulim-Baling (south Kedah) and Gunung Semanggol (north Perak). As previously mentioned in Chap. 1, the stratigraphy of the

Semanggol Formation at Gunung Semanggol consists of three units: the chert unit, rhythmite unit and conglomerate unit. The outcrops exposed at the Padang Terap area show all of the units, and they are conformably overlying the Permian Kubang Pasu Formation. Meanwhile, in the south of Kedah, at Kulim-Baling only two units are identified, namely the chert and the rhythmite units. As for the area of interest, Gunung Semanggol, three units are represented: the chert unit, the rhythmite unit and the conglomerate unit. All of them were later intruded by a Late Triassic granitic intrusion [2].

### **3 Methodology**

#### **3.1 *Field Techniques***

1. Stratigraphic Logging and Sampling—A log of ca. 50 m has been made, with multipurpose sampling at regular intervals.

#### **3.2 *Laboratory Techniques***

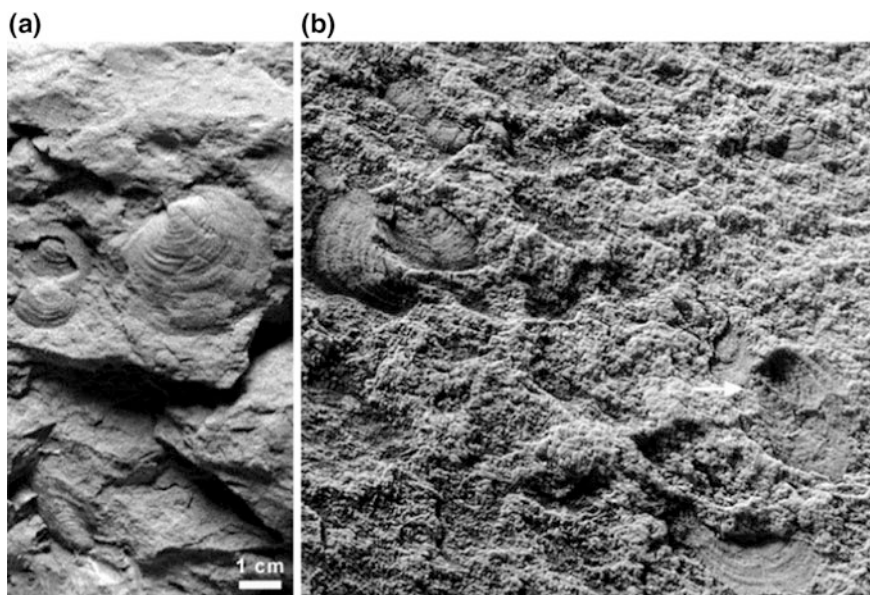
1. Polished (macroscopic) sections and thin (microscopic) sections—these techniques, combined with others of staining and/or impregnation, are essential to enhance the visibility of trace fossils in bioturbated fabrics, apart from allowing the study of ichnological systematics on the samples.
2. Scanning electron microscopy (SEM) with EDX—selected, sample is studied at the SEM, and analysed where necessary with EDX. This allows the study of the ethological structures in detail.
3. Photography and image enhancement—an important method to enhance the visibility of biogenic structures after sectioning and polishing the rock samples.
4. Total organic content (TOC)—the colour of the “black shale facies” ranges from dark to light grey, depending on weathering. TOC analyses determine the carbon content of a rock attributable to the organic matter preserved on it.
5. Whitening of samples for photography—most samples of body fossils and bioturbation structures benefit from being “whitened” with ammonium chloride in order to improve the visibility of the 3D morphology by increasing the contrast.

## 4 Results

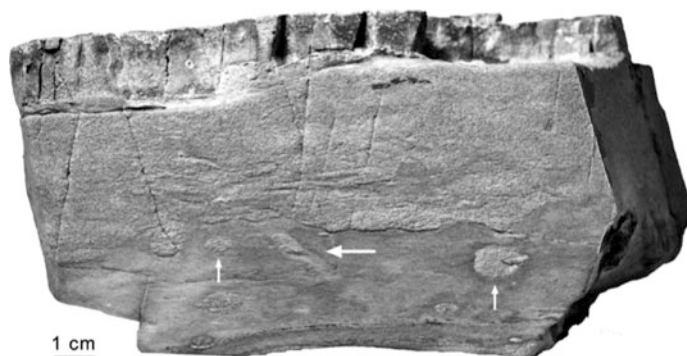
Palaeontological evidences found at the stratigraphic section BM1 are compatible with the sedimentological ones, both indicating a shallowing-upward trend, from mid-sublittoral shelfal environments—located above the storm wave base—to shallower sublittoral conditions. The basin was probably receiving muddy sediments from a deltaic apparatus.

### 4.1 Data from Body Fossils

Abundant specimens of the pectinid genus *Claraia* (Fig. 1a)—an Early Triassic bivalve—and also scarce questionable brachiopods of the order Lingulida (Fig. 1b) are found at several levels, indicating the presence of epifaunal (*Claraia*) and shallow infaunal (lingulids) suspension-feeder invertebrates. The complete array of sizes found among the valves of *Claraia*—although disarticulated—talks in favour of a short-distance transportation of these shell assemblages, if any transportation existed at all.



**Fig. 1** **a** Different-sized specimens (*inner moulds*) of the bivalve *Claraia* sp. **b** Probable outer mould of a brachiopod of the order Lingulida, showing the migration line of the pedicle (*arrowed*). Level BM1/16



**Fig. 2** Longitudinal section of oblique *Skolithos* (big arrow) and transverse sections of *Palaeophycus* (smaller). Level BM1/16

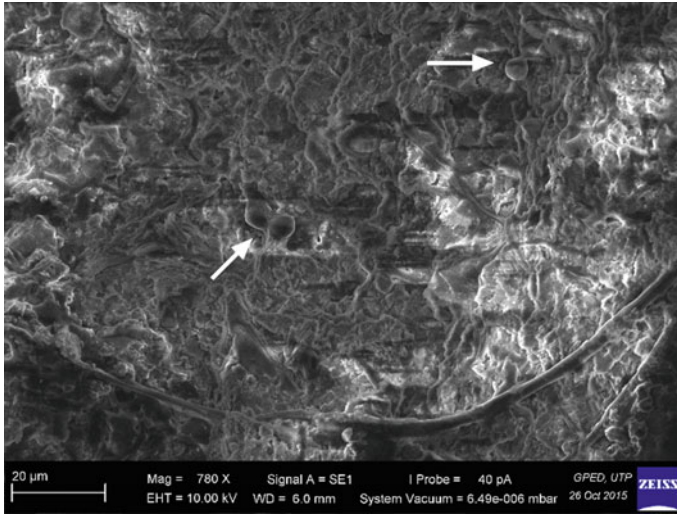
#### 4.2 Data from Ethological Structures

The benthic fossil communities identified were composed not only of shelly, suspension-feeder invertebrates but also of soft-bodied invertebrates which left bioturbation structures (ethological structures, in which action can be semiquantitatively measured by means of the bioturbation ichnofabric index), as well as bioarrangement structures (another kind of ethological structures) left by microbial mats. From the present study of the ethological structures, we may perform a more complete study of the benthic living communities populating the sea bottom.

The identified bioturbation ichnogenera are a total of nine: *Cochlichnus*, *Cylindrichnus*, *Diplocraterion*, *Palaeophycus* (Fig. 2), *Planolites*, *Scolicia*, *Skolithos* (Fig. 2), *Torrowangea* and *Psammichnites*. They all indicate the presence of a diversified benthic fauna populating the sea bottom. Most of the ichnological contents represent the *Cruziana* ichnofacies, although suites dominated by dwelling, oblique burrows may indicate the *Skolithos* ichnofacies developed at deeper conditions than normal, below the fair-weather wave base. The *Cruziana* ichnofacies is indicative of mid-distal continental shelf settings, slightly below the normal wave base and exposed to the action of storms (i.e. above the storm wave base).

At a lesser scale of the producer's body size, the phenomenon of cryptobioturbation has been identified under microscope observations in thin sections of parallel laminated mudstone and silty mudstone at levels BM1/3 and BM1/4. Cryptobioturbation may eventually produce intense mixing of the sediment, with deep alteration or destruction of the sedimentary fabric. Nevertheless, in such cases, the bioturbation ichnofabric index is not of common use at all.





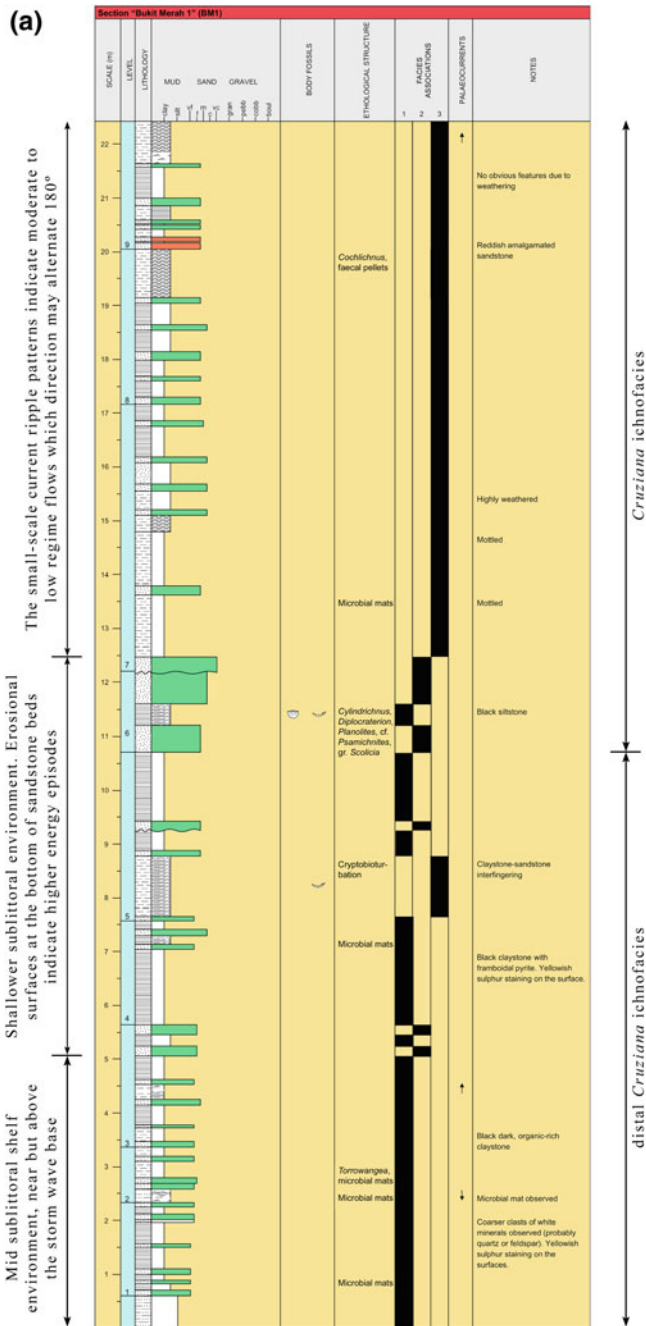
**Fig. 3** Three 5- $\mu$ m-wide coccoids (*arrows*) and filaments (*below*) spotted in a microbial mat sample, level BM1/7

At several levels of the section, thin microlaminated intervals are interpreted as fossil microbial mats (bioarrangement structures), most probably of cyanobacterial origin. Under the SEM, they show minute coccoids and filaments of either cyanobacterial or fungal origin (in the latter case, fungi would be interpreted as eating on the mat) (Fig. 3).

### **4.3 Data from TOC (Total Organic Content)**

In terms of palaeoxygenation of the benthos (i.e. the seafloor bed), a preliminary analysis has been carried out based on the TOC. The analysis has been conducted on shale samples from levels 5 and 16 (Fig. 4), indicating TOC values of 0.342 and 0.497%, respectively, which are very low, most probably due to modern weathering.

The presence of organic carbon talks in favour of early diagenetic conditions which have favoured its preservation, which ultimately entails a deficit of oxygen during burial so that some of the organic carbon—despite the low values measured—is eventually preserved from oxygenation.



**Fig. 4** (opposite page) Integrated stratigraphical and palaeoichnological log at section BM1 (lower part). Legend, in **b**. Key for facies associations: 1, dark grey mudstone with few centimetric, very fine-grained sandstone; 2, decimetric, erosive, medium-grained sandstone; 3, dark grey mudstone with centimetric, len-ticular, fine-grained sandstone. **b** (opposite page) Integrated stratigraphical and palaeoichnological log at section BM1 (upper part). Facies associations, as in **a**.

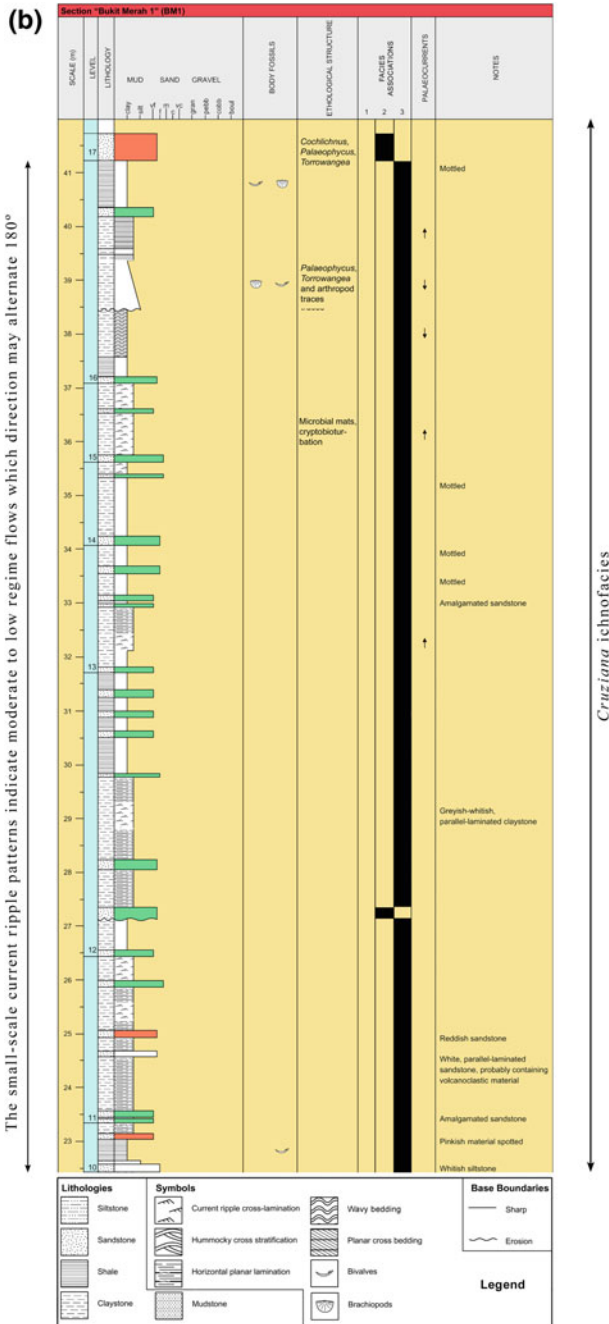


Fig. 4 (continued)

## 5 Conclusions

An integrated study of the palaeoichnology and the stratigraphy of the Semanggol Formation, focused on the Bukit Merah area, has shown its potential to certainly improve our understanding of the facies distribution and interpretation, environmental evolution and palaeoecological reconstruction of the basin.

Evidence of benthic fauna traces—mostly of the *Cruziana* ichnofacies—populating the sea bottom indicate that the basin evolved—during the time of deposition of the “black shale” facies—from a distal-mid continental shelf setting into a more proximal one with shallower sublittoral conditions, above the storm wave base but always below the action of the fair weather wave base. Lithostratigraphic and sedimentological evidences also indicate a shallowing-upward trend: from mid-sublittoral shelfal conditions—above the storm wave base—to shallower sublittoral conditions. Thus, trace and body fossil data are in agreement with the sedimentological ones throughout the 41.8-m-thick stratigraphic log obtained. The general sedimentary evolution is compatible with the dynamics of a deltaic apparatus prograding seawards, as indicated in the integrated stratigraphy given herein (Fig. 4).

The “black shale” facies are only in a few cases reflecting true anoxic conditions during deposition (i.e., those intervals lacking completely benthic life or their palaeoichnological evidences). Most of the dark grey facies visible at the studied section reached anoxia in phases after burial, during diagenesis, since they showed moderate-to-high contents of palaeontological remains indicative of benthic life.

All these observations and concluding remarks will contribute to the palaeogeographical knowledge of the Semanggol Basin and its geotectonic setting.

## References

1. Basir Jasin, 1997. Permo-Triassic radiolaria from the Semanggol formation, northwest Peninsular Malaysia. *Journal of Asian Earth Sciences*, 15(1), 43-53. doi: [http://dx.doi.org/10.1016/S0743-9547\(96\)00079-7](http://dx.doi.org/10.1016/S0743-9547(96)00079-7).
2. Basir Jasin, & Zaiton Harun., 2007. Stratigraphy and Sedimentology of the chert unit of the Semanggol Formation. *Bulletin of Geological Society of Malaysia*, 53, 103–109.
3. Burton, C.K., 1973. Mesozoic. In: Gobbett D.J. & Hutchison, C.S. (eds.) *Geology of the Malay Peninsula*. Wiley Interscience, New York and London, 97–141.
4. Ekdale, A.A., Bromley, R.G. & Pemberton, S.G., 1984. *Ichnology. The Use of Trace Fossils in Sedimentology and Stratigraphy: Society of Economic Paleontologists and Mineralogists. Short Course*, 15, 1–317.
5. Hutchison, C.S., & Tan, D.N.K., 2009. *Geology of Peninsular Malaysia*. University Malaya and Geological Society of Malaysia, Kuala Lumpur, 67–131.
6. Mángano, M.G., Rindsberg A.K., Buatois, L.A., 2002. Carboniferous Psammichnites: Systematic Re-Evaluation, Taphonomy and Auteology. *Ichnos*, 9, 1–22.
7. Teoh, L.H., 1992. *Geology and mineral resources of the Sungai Tiang area, Kedah Darulaman*. Geological Survey of Malaysia, Map Report, 5, 1–9.

**Part VI**  
**Drilling, Well Completion, Production**  
**and Operation**

# Advanced Porosity Modeling and Lithology Analysis Based on Sonic Log and Core Data for Arkose Sandstone Reservoir: Habban Field

A. Al-Hasani, I.M. Saaed, A.M. Salim and H.T. Janjuhah

**Abstract** Porosity represents the rock's capacity to trap fluid. It is the main quality indicator for hydrocarbon-bearing reservoirs. The reservoir porosity is a crucial input to estimate hydrocarbon reserves by volumetric method, which is known as oil originally in place (OOIP). It also plays a key role in the hydraulic unit identification, rock typing, net reservoir, and net pay analyses to determine the best potential oil-bearing layers for perforation and oil production. The porosity is also a required input to establish the reservoir static and dynamic models. The quantitative evaluation of porosity is challenging especially during reservoir characterization. Many factors such as mineralogical composition, type and amount of cement, rock texture, grain-packing pattern, and rock compaction would affect its value. A good quantitative evaluation of porosity requires using integrated methods between well logs and core data. The present study is part of an integrated workflow to characterize arkose sandstone reservoir called Kuhlan Formation in the Habban field located in Republic of Yemen. It is one of the most important oil-producing formation in East Yemen region, located in the sedimentary basin called Shabwa–Marib basin. It is deposited in transitional continental environment in the Jurassic Age. The compressional sonic log is initially used in this analysis from five key wells. The sonic porosity by using linear and nonlinear methods is computed over the reservoir depth interval. The sensitivity analysis for fluid slowness, matrix slowness, and compaction factor is conducted. Core samples were taken from two wells and analyzed by using both conventional and special core analyses in the laboratory. Core porosity by using helium method was measured, and the grain density was determined. The X-ray diffraction analyses were conducted on core samples to fully understand the rock lithology and mineralogical bulk composition for this reservoir. Understanding the details of the reservoir lithology and mineralogy is extremely important in the reservoir characterization and production improvement treatments. The comparisons between log porosity and core porosity have been made. The log analysis results show that the linear method is highly

---

A. Al-Hasani (✉) · I.M. Saaed · A.M. Salim · H.T. Janjuhah  
Petroleum Engineering & Geosciences Department, Universiti Teknologi PETRONAS,  
31750 Bandar Seri Iskandar, Tronoh, Perak, Malaysia  
e-mail: aalhasani2@gmail.com

sensitive to the changes of matrix slowness and compaction factor. The nonlinear method is insensitive to the changes of fluid slowness and slightly sensitive to the changes of matrix slowness. The analysis also shows that the porosity based on the nonlinear method has a good match with core porosity. The X-ray diffraction analysis shows that the dominant mineral is quartz with average dry weight of 52%; however, this reservoir contains a significant amount of feldspar minerals. The cement is of calcareous nature, and its concentration is more at the upper part of this formation. The clay type is illite, and its volume ranges between 10 and 13%. The average porosity for this reservoir varies between 6 and 11%.

**Keywords** Porosity · Reservoir · Core · Sonic · Log · X-ray diffraction · MATLAB · Kuhlan

## 1 Introduction

Habban field is located in Alsabatayn sedimentary basin. This basin is one of the Mesozoic sedimentary basins of Yemen [1, 2]. It was generated as a rift basin formed as a consequence of an extensional phase related to the separation of India from Africa–Arabia. In this field, the main hydrocarbon-bearing formation is arkose sandstone formation called Kuhlan Formation [3, 4]. The stratigraphic subdivision of the basin fill is displayed in Fig. 1. The Kuhlan Formation consists of a basal transgression unit, poorly sorted coarse sandstone (eolian sandstone), filling the topographic lows in the basement. The Kuhlan Formation conformably grades up into the platform carbonates of Shuqra Formation, which was part of a wider Tethys shelf on the passive margin of the Arabian plate [3, 4]. The minerals detected in Kuhlan Formation by X-ray diffraction analyses are quartz, plagioclase, orthoclase, mica, clay, and some fragments. Within the last years, the sonic logging systems have been developed with the ability to digitally record the entire acoustic waveforms and compute travel time or sonic slowness with good quality [5]. The technique used to extract slowness from the acoustic waveform is called slowness time coherence (STC) technique [6–8]. Several factors disturb the sonic log such as lithology, mineralogy, fluid type, porosity, and rock compaction. The main influence on the sonic log is the porosity [8]. The compressional wave speed or travel time dependence on porosity is well known [8]. The relationship between sonic travel time and rock porosity has been described by mathematical models such as Wyllie and Raymer–Hunt equations. Sonic porosity is the suitable option to calculate porosity for hydrocarbon reservoirs in case of absence of other porosity logs such as bulk density and neutron logs. It is also improving the porosity interpretation in the presence of porosity logs [6, 9]. In this study, the sonic data have been acquired by modern array system sonic tools in five key wells and the sonic logs were extracted by using STC technique. P-waves are processed to compute the compressional slowness. The porosity is computed along the logged reservoir depth interval by using Wyllie and Raymer–Hunt equations, since the sonic porosity is

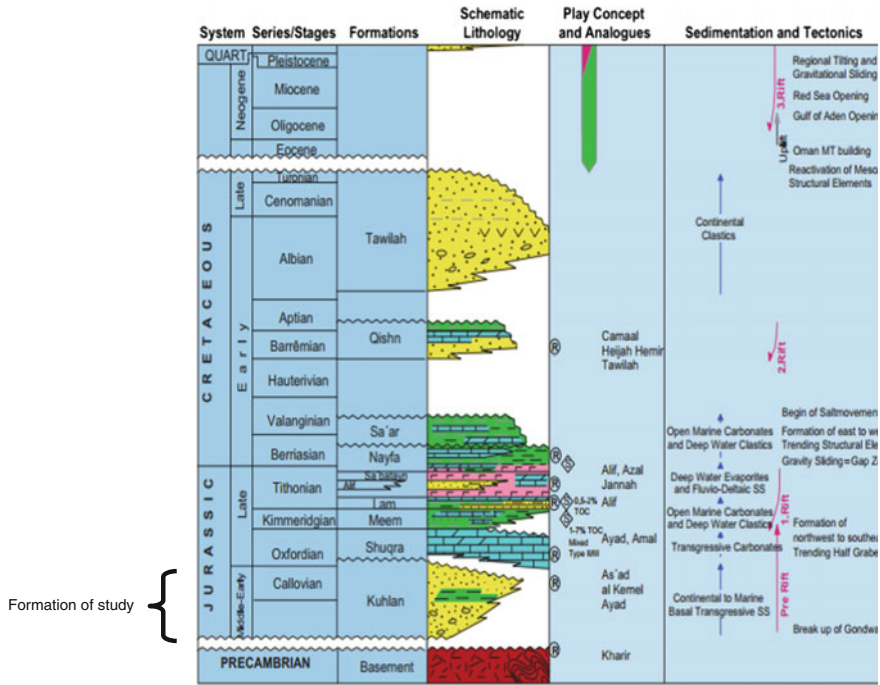


Fig. 1 Generalized stratigraphy of the Habban field [3, 4]

lithology dependent; the equations are sensitive to some factors such as matrix slowness (DTmx, us/ft), fluid slowness (DTf; us/ft), and compaction correction factor (Cp) [10–14]. The numerical modeling approach is used to investigate the effect of those factors one by one on porosity determination by the sonic log. The aim is to obtain the best quality porosity log representing reservoir porosity. The results have been correlated with core data for validation purpose.

## 2 Materials and Methods

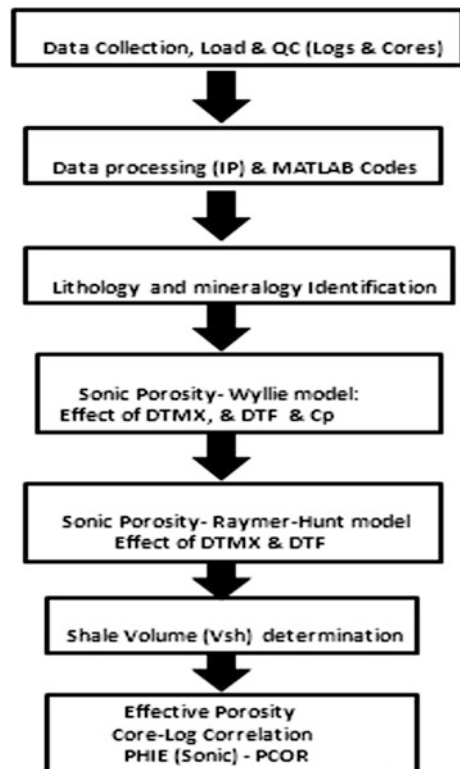
The main data used in this work are sonic logs and core data. Full open-hole log sets including compressional sonic slowness logs have been collected from five wells drilled in Kuhlan Formation: Well-A (reservoir interval: 2697–2715 m MDRT) and Well-B (reservoir interval: 2645–2662 m MDRT), Well-C (reservoir interval: 2794–2817 m), Well-D (reservoir interval: 2376–2386 m), and Well-E (reservoir interval: 2670–2692 m). The nineteen (19) sidewall core samples have been taken from two key wells: Well-A and -B. The core samples have been



analyzed by routine core analysis (RCA) to obtain the main reservoir properties: porosity and permeability. MATLAB and computer-assisting IP software\* (Interactive Petrophysics) have been used in this study. The core samples from the two key wells were analyzed to determine helium porosity and dry weights of minerals by X-ray diffraction. The X-ray diffraction analysis results (dry weight %) have been visualized by bar and pie plots using Microsoft Excel application to display the bulk mineralogical composition for core samples. The sonic porosity was computed by both Wyllie and Raymer–Hunt models, and the final results are validated by correlation with core porosity. The shale volume is determined to use it in the further computation of the effective porosity [15]. The integrated workflow applied in this study including both well logs and core data is illustrated in Fig. 2.

The data inventory is described in Table 1. The triple-combo open-hole logs from five wells have been collected and processed. These data include natural gamma ray (GR), formation bulk density (RHOB), photoelectrical factor (PEF), thermal neutron porosity (NPHI), and sonic compressional slowness (DTCO).

**Fig. 2** The integrated workflow of core sonic porosity modeling and lithology identification analysis



**Table 1** Data inventory of core samples and open-hole logs

Well-ID	Well-A	Well-B	Well-C	Well-D	Well-E
GR	✓	✓	✓	✓	✓
S-GR	✓	✓	✓	✓	✓
RHOB	✓	✓	✓	✓	✓
NPHI	✓	✓	✓	✓	✓
PEF	✓	✓	✓	✓	✓
DTCO	✓	✓	✓	✓	✓
Core samples	✓	✓	n/a	n/a	n/a

## 2.1 Data Processing and Quality Control (QC)

The open-hole logs and measured core results have been loaded into IP software\* (Interactive Petrophysics). The wireline open-hole logs are data acquired in fill-in fluid hole so the essential environmental corrections have been applied as per oil industry standards and the final logs have been produced. The depth match between logs has also been performed. The MATLAB software has been used to perform the required modeling and sensitivity analysis for porosity.

## 2.2 Reservoir Lithology Identification

The reservoir lithology could be determined by drilled cuttings [16]. X-ray diffraction analysis method provides a fast and reliable tool for routine mineral and lithology identification. This method complements other mineralogical methods, including optical light microscopy, electron microprobe microscopy, and scanning electron microscopy [17]. The bulk mineralogical composition analysis was conducted for 19 samples from Well-A and -B by X-ray diffraction analysis to obtain quantitative information on the content of minerals in the rock. Samples were initially cleaned of contaminants and hydrocarbon. Samples were then transferred to distilled water and powdered. Dried powders were loaded into a metal sample holder for randomly oriented mounts for whole rock analysis. A separate sample split was used for clay mineral analysis by dispersing the sample in distilled water using a sonic probe. Suspensions were size-fractionated by centrifugation to separate clay-size material (<4  $\mu\text{m}$  equivalent spherical diameter) for analysis. The suspensions were vacuum-deposited on nylon membrane filters and exposed to ethylene glycol vapor for 12 h to fully expand swelling clays. XRD results were obtained with a Siemens D500 automated powder diffractometer equipped with a copper X-ray source (40 kV, 30 mA) and a scintillation X-ray detector. The whole rock samples were evaluated from 5–60° two theta at 1° per minute.

### 2.3 Computing Sonic Porosity by Wyllie and Raymer–Hunt Models

The Wyllie et al. time-average equation is a linear relationship between the porosity and interval transit time (slowness) of the P-waves [18, 19]. It has been widely used due to its simplicity [20]. It can be expressed by Eq. 2 as follows:

$$DTCO - DTmx(1 - \phi) + DTf \cdot \phi \quad (1)$$

By rearranging Eq. 1, we obtain:

$$\phi = \frac{1}{Cp} \frac{DTCO - DTmx}{DTf - DTmx} \quad (2)$$

The main problem associated with the transformation of sonic transit time into porosity involves the selection of the proper matrix transit time [20]. The numerical modeling approach is applied to investigate the effect of those factors on sonic porosity specifically for this reservoir. The Raymer–Hunt equation is based on field observation to address the weakness in Wyllie equation [18–21]. The application of this equation results in more accuracy determination for porosity from transit time [9, 22]. This equation is expressed by Eq. 4 as follows:

$$\frac{1}{DT} = \frac{1 - \phi^2}{DT_{mx}} - \frac{\phi}{DT_f} \quad (3)$$

By rearranging Eq. 3, we obtain:

$$\phi^2 + \phi \left( \frac{DT_{mx}}{DT_f} - 2 \right) - \left( \frac{DT_{mx}}{DT_f} - 1 \right) = 0 \quad (4)$$

where

DTCO: compressional slowness, us/ft

DTmx: matrix slowness, us/ft

DTf: fluid slowness, us/ft

Cp: compaction correction factor

Phis: sonic porosity, fraction

$\phi$ : porosity, fraction

### 2.4 Clay Volume Determination

The clay volume is necessary input to determine the effective porosity from logs [15]. The common method in the oil industry to compute clay volume, VCL, is

linear GR method. This method could overestimate clay volume for arkose sandstone reservoir such as Kuhlan Formation due to high natural radioactivity caused by orthoclase mineral [16]. This kind of lithology is known as hot sandstone showing high natural radioactivity (gAPI) due to potassium and thorium contents. The alternative method is using double indicators: neutron–density logs [16]. The model used in this method is described by Eq. 5 as follows:

$$VCLND = \frac{(Dencl2 - Dencl1) * (Neu - NeuCl1) - (Den - Dencl1) * (Neucl2 - Neucl1)}{(Dencl2 - Dencl1) * (Neuclay - Neucl1) - (Denclay - Dencl1) * (Neucl2 - Neucl1)} \quad (5)$$

where

VCLND: clay volume computed by neutron–density method, fraction

Den: bulk formation density log, g/cc

Neu: neutron log, dec

DenCl1, DenCl2, NeuCl1, NeuCl2: end points of clean line

Denclay, Neuclay: end points of clay

## 2.5 Correlation with Core Porosity

The core porosity provides important constraints for the range of porosity estimations [23, 24]. The porosity calculated by sonic logs has been correlated with core porosity for validation purpose. In this study, the sonic porosity computed by Wyllie and Raymer–Hunt models has been compared with core porosity in two key wells: A and B. This correlation has been achieved using IP software package and MATLAB platform.

## 3 Results and Discussions

The reservoir lithology and porosity for arkoses sandstone Kuhlan reservoir are determined using re sonic log and core analysis from five key wells. The parameters effecting porosity modeling have been investigated and modeled. The final findings from this study could be divided into the following:

### 3.1 Core Porosity Results

The core porosity analysis shows high heterogeneity in this reservoir. The porosity varies from 0.7% up to 14%. The average core porosities in wells A and B are 8 and 12%, respectively. The results are presented in Tables 2 and 3.

**Table 2** Core porosity measurement results of Well-A

Sample ID	Depth (m)	Core porosity (%)
1	2715.5	0.72
2	2713.5	7.89
3	2710	11.81
4	2708.5	13.69
5	2707.5	10.7
6	2706.5	7.91
7	2705.5	4.29
8	2704.5	6
9	2703	2
10	2701.9	7.07
11	2699.4	8.62

**Table 3** Core porosity measurement results of Well-B

Sample ID	Depth, m	Core porosity (%)
1	2645.5	13.33
2	2646.6	2.98
3	2649.3	17.41
4	2650.6	16.14
5	2652.4	4.36
6	2654	12.38
7	2657.1	12.55
8	2659	14.28

### 3.2 Reservoir Lithology Identification

The X-ray diffraction analyses have been conducted for (11) sidewall core samples taken from Well-A (Figs. 3 and 8) sidewall core samples taken from Well-B (Fig. 4). The main minerals detected in this formation are quartz, orthoclase, plagioclase, calcite, and illite. In core samples of Well-A, the average dry weights of quartz, orthoclase, plagioclase, calcite, and illite are 49, 15.2, 14, 7, and 9%, respectively. In core samples of Well-B, the average dry weights of quartz, orthoclase, plagioclase, calcite, and illite are 53.5, 19, 16, 11, and 9%, respectively. The calcite has not been detected in Well-B resulting in good reservoir properties in this well.

Generally, the analysis results show that the dominant mineral in this reservoir is quartz. The calcite is existing as calcareous cement especially in the upper part of this reservoir. The presence of calcite cement could interpret the reduction of effective porosity and permeability in this reservoir. The results also show the presence of feldspars (albite and orthoclase) as the second most abundant minerals in this reservoir. The clay type has been identified as illite. The lithology description and mineralogical composition analysis could lead to describe this reservoir as feldspathic or arkose sandstone formation deposited in a transitional continental environment.

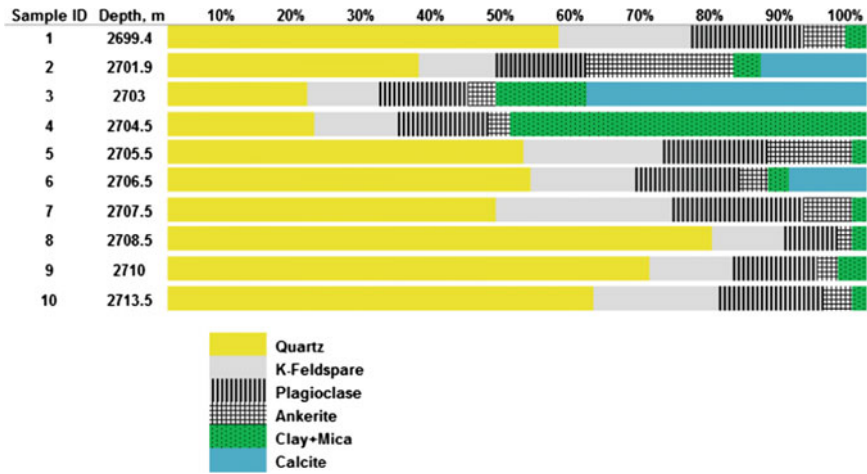


Fig. 3 X-ray diffraction analysis results (dry weight %), Well-A

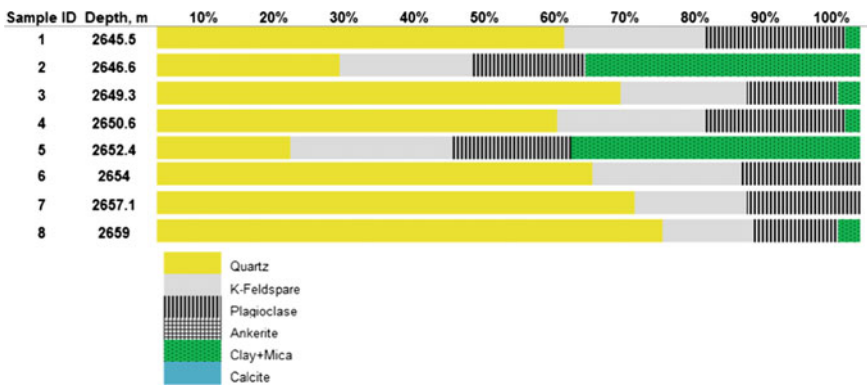


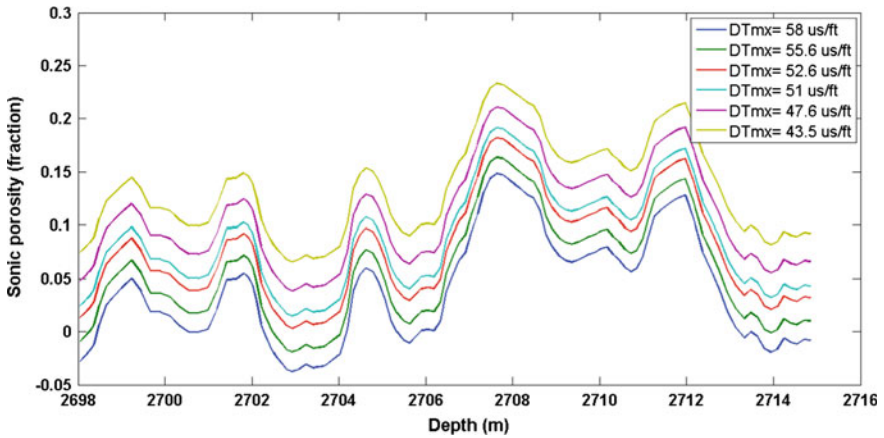
Fig. 4 X-ray diffraction analysis results (dry weight %), Well-B

### 3.3 The Effect of Lithology Matrix Slowness

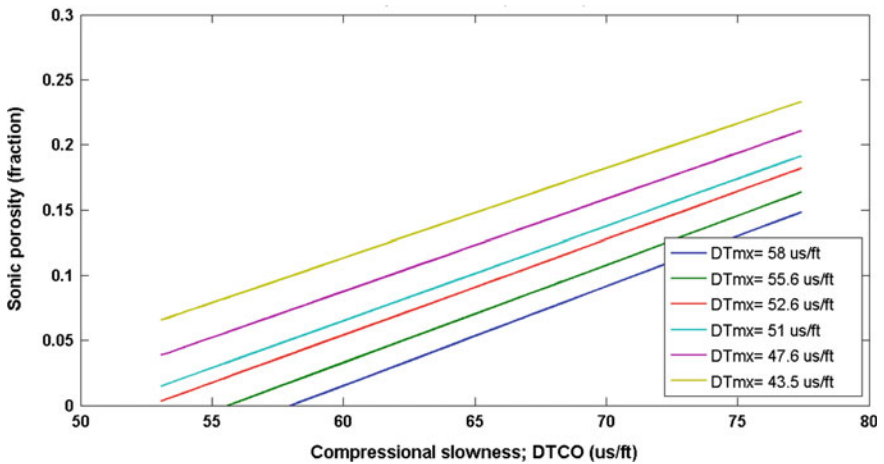
The matrix slowness varies according to the mineralogical composition of reservoir rocks [7, 25, 26]. Since the sonic porosity is lithology-dependent property, the porosity will differ accordingly. The effect of this factor is inspected by assuming various values for matrix slowness as per Table 4. The investigation has been accomplished on both Wyllie and Raymer–Hunt models which are used to transfer the compressional slowness log to porosity. The statistical analysis has been performed, and the results are displayed in Table 4 and Figs. 5, 6, 7, and 8.

**Table 4** Average sonic porosity at different lithology matrix slowness

Lithology matrix slowness; us/ft/Well	Average sonic porosity, Wyllie model					Average sonic porosity, Raymer-Hunt model				
	Well-A	Well-B	Well-C	Well-D	Well-E	Well-A	Well-B	Well-C	Well-D	Well-E
58	0.04	0.052	0.025	0.064	0.025	0.102	0.119	0.086	0.13	0.092
55.6	0.06	0.069	0.043	0.081	0.04	0.070	0.087	0.054	0.098	0.061
52.6	0.08	0.089	0.064	0.10	0.068	0.101	0.116	0.085	0.127	0.090
51	0.09	0.10	0.074	0.11	0.078	0.083	0.099	0.066	0.110	0.072
47.6	0.11	0.12	0.097	0.13	0.10	0.091	0.108	0.075	0.119	0.081
43.5	0.13	0.14	0.12	0.15	0.12	0.091	0.108	0.075	0.119	0.081



**Fig. 5** The effect of matrix slowness, DTmx, on sonic porosity computed by Wyllie model, depth versus sonic porosity plot



**Fig. 6** The effect of matrix slowness, DTmx, on sonic porosity computed by Wyllie model, compressional slowness versus sonic porosity plot

The relationship between sonic porosity and variations of matrix slowness factor has been illustrated in Figs. 5, 6, 7, and 8. The analysis results show that the matrix slowness has the major influence on both Wyllie and Raymer–Hunt models.

Sonic porosity varies from 4 to 13% in Wyllie model and from 9 to 10% in Raymer–Hunt model as the lithology slowness varies from 58 to 43.5 us/ft. The matrix slowness has an influence on Raymer–Hunt models less than Wyllie model.



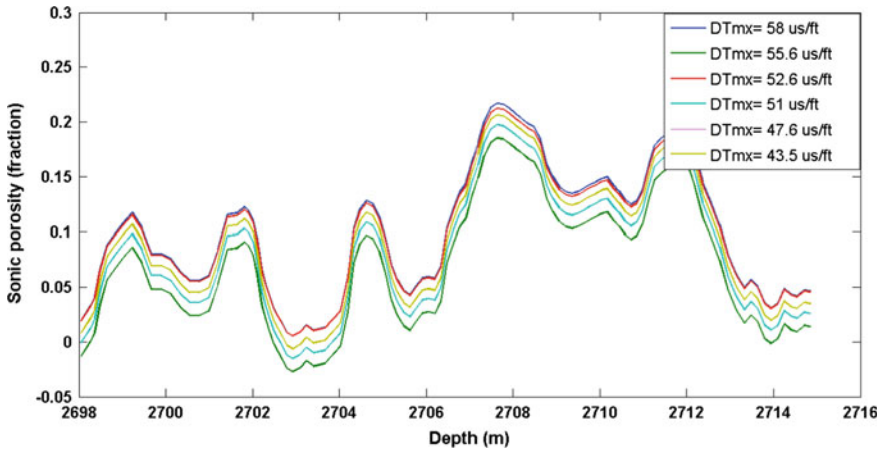


Fig. 7 The effect of matrix slowness, DTmx, on sonic porosity computed by Raymer–Hunt model, depth versus sonic porosity plot

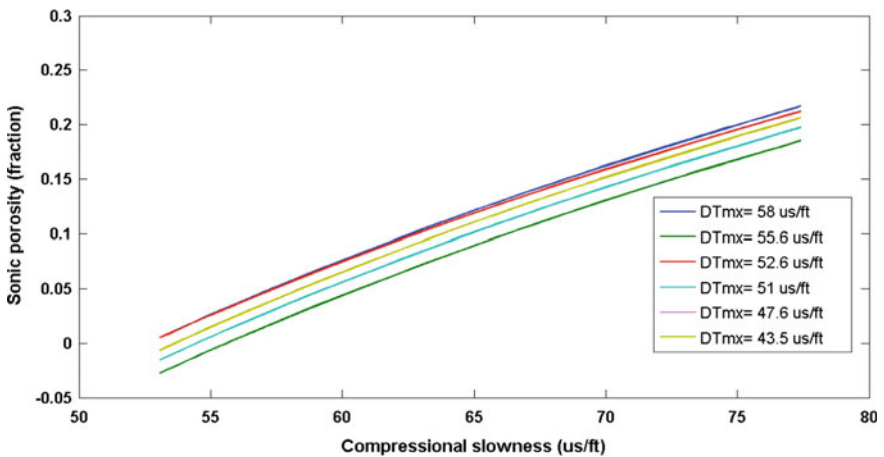


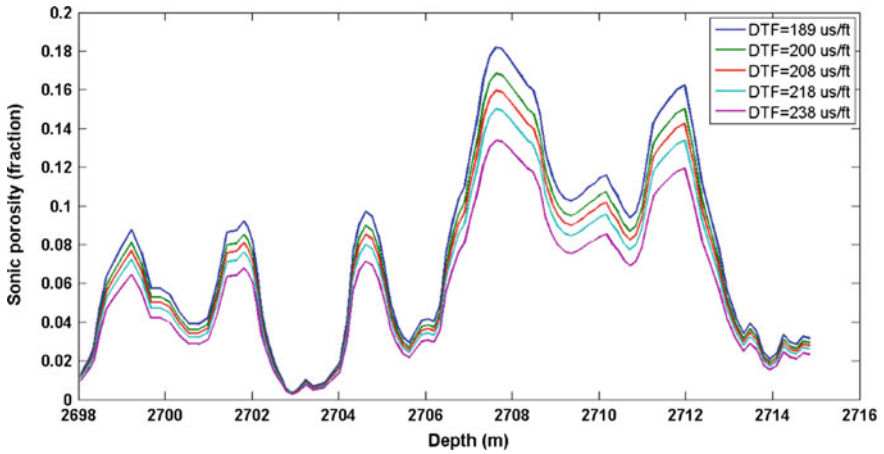
Fig. 8 The effect of matrix slowness, DTmx, on sonic porosity computed by Raymer–Hunt model, compressional versus sonic porosity plot

It indicates that the Raymer–Hunt model is less sensitive to variation in matrix slowness resulting from complexity in reservoir lithology. It makes this model more reliable to compute total porosity in the clastic reservoir which has complex lithology and mineralogical composition.

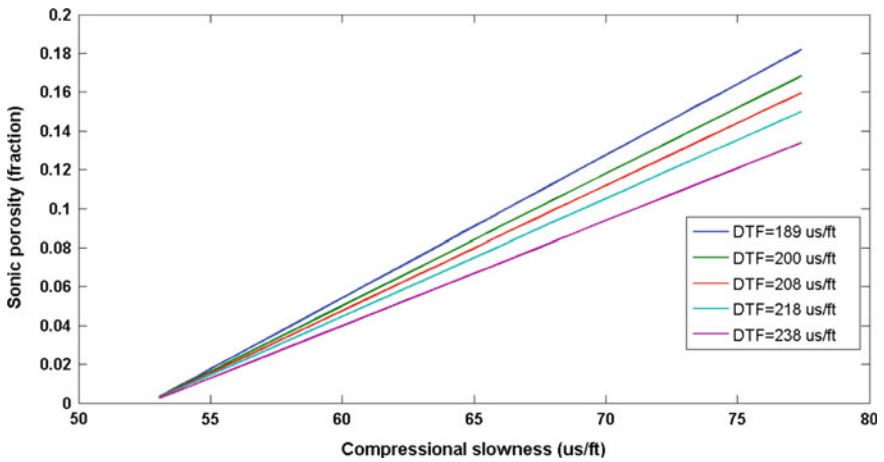
The modeling results show that lithology matrix slowness has a significant effect on sonic porosity computed by both Wyllie and Raymer–Hunt models; however, the magnitude of this effect is minimum in Raymer–Hunt model. This effect is

**Table 5** Average sonic porosity at different types of fluids

Fluid slowness; us/ft/Well	Average sonic porosity, Wyllie model					Average sonic porosity, Raymer–Hunt model				
	Well-A	Well-B	Well-C	Well-D	Well-E	Well-A	Well-B	Well-C	Well-D	Well-E
189	0.078	0.089	0.064	0.101	0.068	0.10	0.116	0.085	0.127	0.09
200	0.072	0.082	0.059	0.093	0.063	0.099	0.115	0.084	0.126	0.089
208	0.068	0.078	0.056	0.088	0.059	0.099	0.114	0.083	0.125	0.088
218	0.064	0.073	0.052	0.083	0.056	0.098	0.113	0.083	0.124	0.088
238	0.058	0.065	0.047	0.074	0.050	0.097	0.112	0.082	0.122	0.087



**Fig. 9** The effect of fluid slowness, DTF, on sonic porosity computed by Wyllie model, depth versus sonic porosity plot



**Fig. 10** The effect of fluid slowness, DTF, on sonic porosity computed by Wyllie model, compressional slowness versus sonic porosity plot

negligible in the low porosity range (e.g., 3–5 %) (Table 4 and Figs. 5, 6, 7, and 8). This leads to a conclusion that Raymer–Hunt model is less sensitive to the differences of lithology matrix slowness and would provide more accurate porosity in this reservoir.

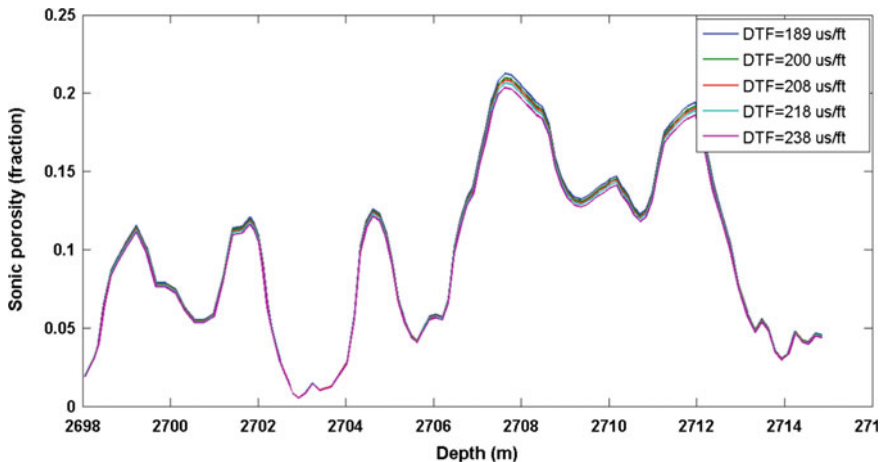
### 3.4 The Effect of Fluid Slowness

The slowness of fluid trapped in the rock pores has an influence on sonic porosity computed by compressional slowness [27]. This effect is modeled by introducing fluid slowness as a variable into Wyllie and Raymer–Hunt models. The compressional slowness logs acquired in Kuhlman Formation in the five wells have been introduced into the both models. The common fluids in subsurface hydrocarbon reservoirs and its sonic slowness are presented in Table 5. The relationship between sonic porosity and the fluctuations of fluid slowness has been illustrated in Figs. 9, 10, 11, and 12.

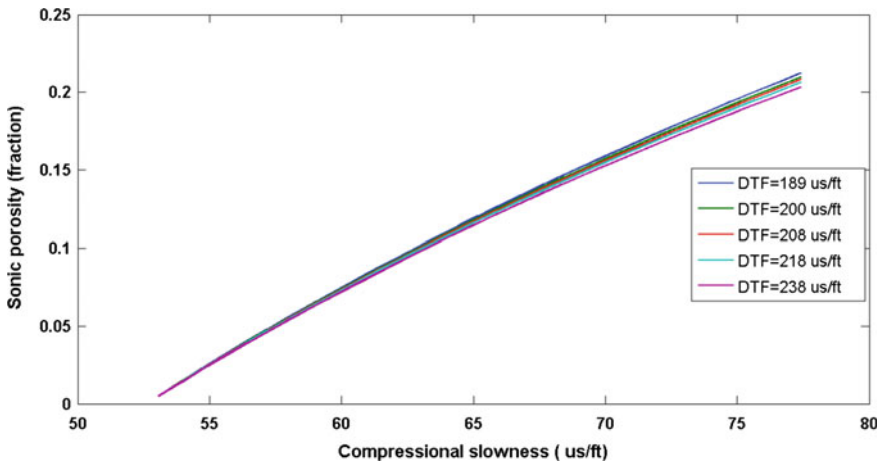
The modeling results (Table 5 and Figs. 9, 10, 11, and 12) show a minor influence caused by fluid slowness on both Wyllie and Raymer–Hunt models. The sonic porosity varies from 6 to 9% in Wyllie model and from 9 to 10% in Raymer–Hunt model as the fluid slowness varies from 189 to 238 us/ft. The effect of this factor is negligible in Raymer–Hunt model especially in the low porosity range which makes this model more dependable to deliver porosity from sonic compressional slowness.

### 3.5 The Effect of Compaction Correction Factor

Compaction is the loss in overall volume porosity after deposition with pressure from the weight of overlying material, usually in a non-elastic way, i.e., by grain



**Fig. 11** The effect of fluid slowness, DTF, on sonic porosity computed by Raymer–Hunt model, depth versus sonic porosity plot



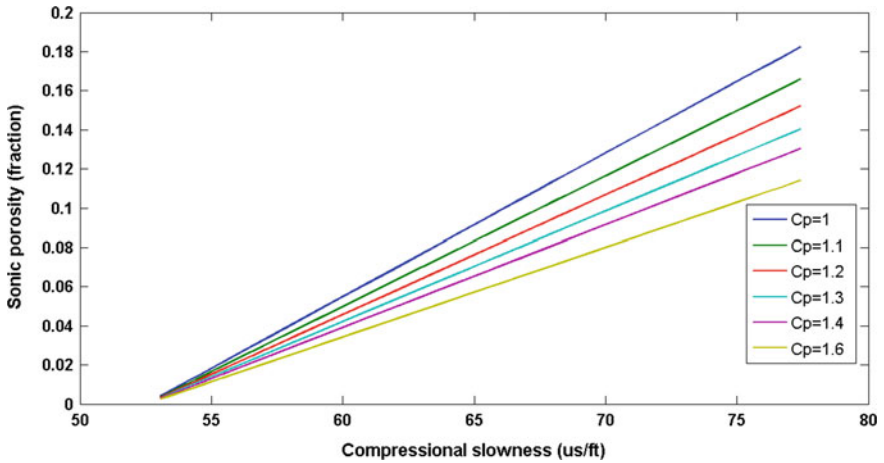
**Fig. 12** The effect of fluid slowness, DTF, on sonic porosity computed by Raymer–Hunt model, compressional slowness versus sonic porosity plot

deformation, repacking, and crystallization. The compaction factor should always be greater than one [28, 29]. This factor is considered only in Wyllie model. It considers the lithology compaction in the unconsolidated sand when the sonic compressional slowness is used to compute porosity based on Wyllie model. In Raymer–Hunt model, this factor does not exist and this is a significant advantage of using this model. The influence of this factor is inspected, and the modeling results (Table 6) show important effect caused by this factor on sonic porosity determination as per Fig. 13.

Based on the previous modeling analysis, the end point selection of matrix slowness and fluid slowness for this formation has been optimized. The lithology matrix slowness and fluid slowness (DTmx & DTF) used in the further computation for porosity are 52.5 and 189 us/ft, respectively. The Raymer–Hunt model has been selected to compute reservoir porosity from sonic compressional slowness.

**Table 6** Average sonic porosity at different compaction correction factors

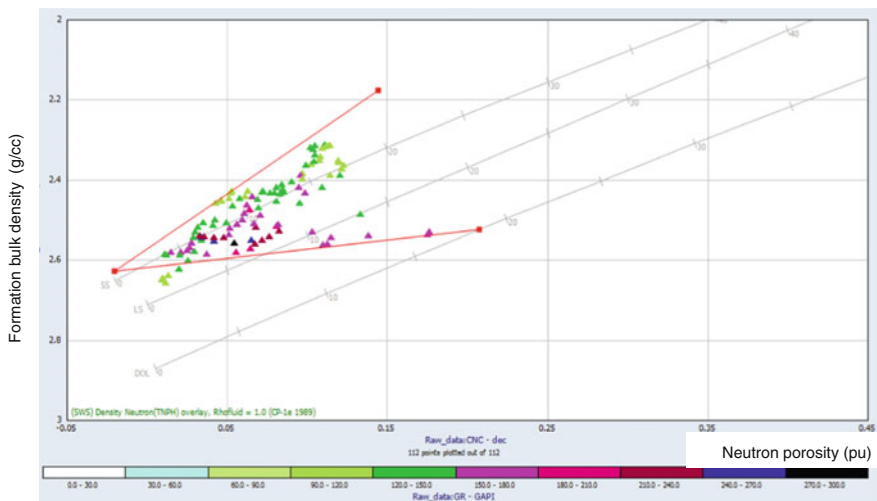
Compaction correction factor, Cp/Well	Average sonic porosity, Wyllie model				
	Well-A	Well-B	Well-C	Well-D	Well-E
1	0.079	0.09	0.064	0.10	0.068
1.1	0.071	0.082	0.058	0.093	0.062
1.2	0.065	0.075	0.053	0.085	0.057
1.3	0.061	0.069	0.049	0.078	0.052
1.4	0.056	0.064	0.046	0.072	0.049
1.6	0.048	0.056	0.040	0.063	0.042



**Fig. 13** The effect of compaction factor, Cp, on sonic porosity computed by Wyllie model, compressional slowness versus porosity lot

### 3.6 Clay Volume Determination

Since this sandstone formation contains radioactive mineral such as orthoclase, the double indicator method is recommended to compute the volume of clay. This method uses bulk density–neutron logs as main inputs (Figs. 15 and 16). The end points of bulk density (RHOB) and neutron porosity (NPHI) for sand and clay lines have been determined by using the interactive plot (Fig. 14).



**Fig. 14** Bulk density–neutron porosity end points for clean sand and clay lines

The end points have been entered in the Eq. 5 to compute clay volume. The clay volumes for the five wells have been computed, and multi-well histogram has been plotted (Fig. 15). The VCL processing results show that average VCL ranges between 10 and 15% which perfectly matches with clay volume measured by X-ray diffraction for core samples (Figs. 15, 20 and 21).

### 3.7 Statistical Analysis

The effective porosity (PHIE) has been statistically determined from total sonic porosity by taking to account clay fraction (Fig. 16 and Table 6). The total sonic porosity has been gained in advance by using the end point parameters for matrix slowness and fluid slowness. The core porosity (PCOR) has been correlated with log porosity as per Figs. 17, 18, 19, and 20. The correlation shows a good match between both effective porosity and core porosity when Raymer–Hunt model has been used as per Table 7. This confirms that this methodology can be propagated to other wells in this field. The statistical analysis of average reservoir porosity for the five wells is presented in Table 7.

The final statistical results for the five wells have been displayed in Table 7.

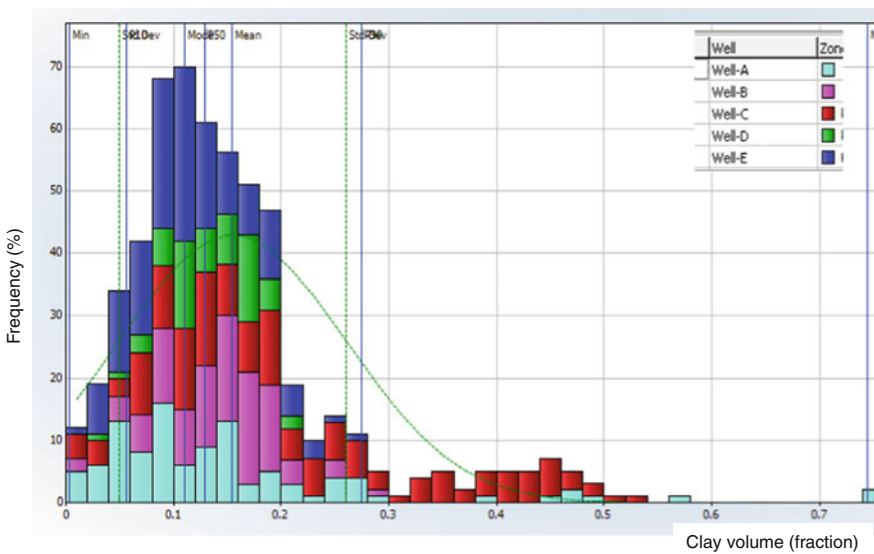


Fig. 15 Multi-well histogram of clay volume, VCL for wells A, B, C, D, and E

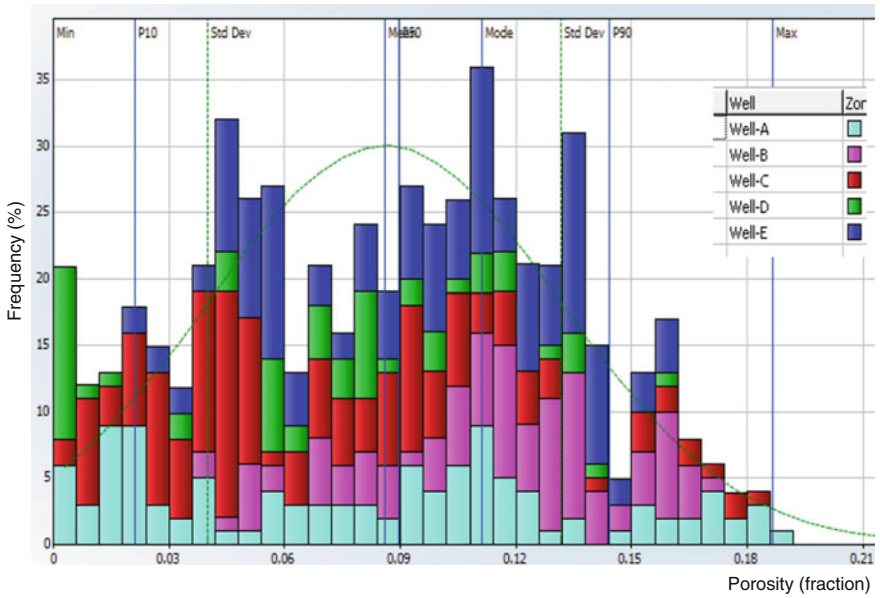


Fig. 16 Multi-well histogram for sonic porosity (PHIS)

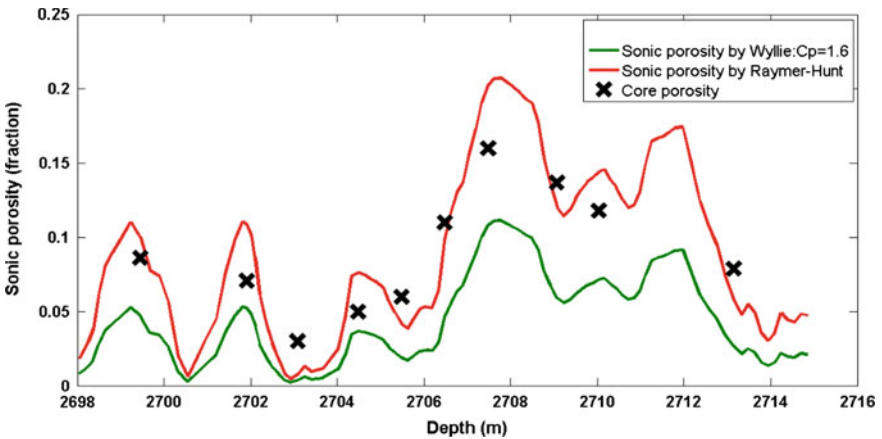


Fig. 17 Core-log porosity correlation, Well-A



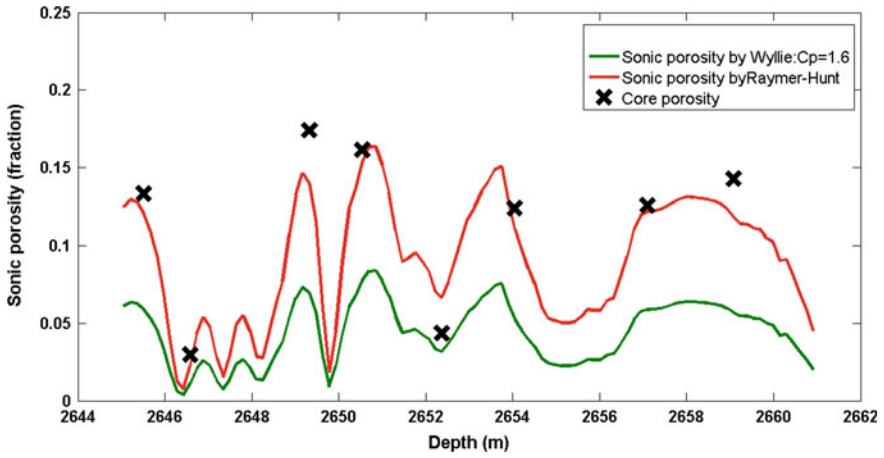


Fig. 18 Core-log porosity correlation, Well-B

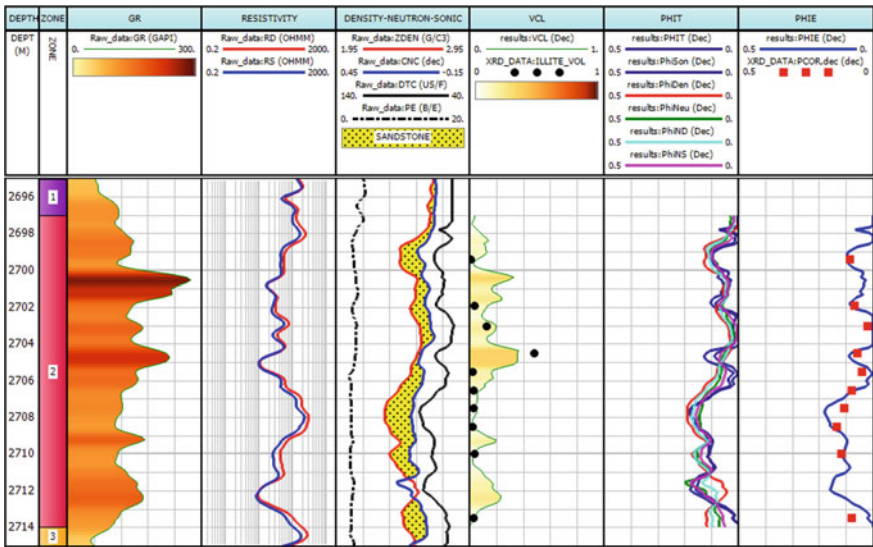
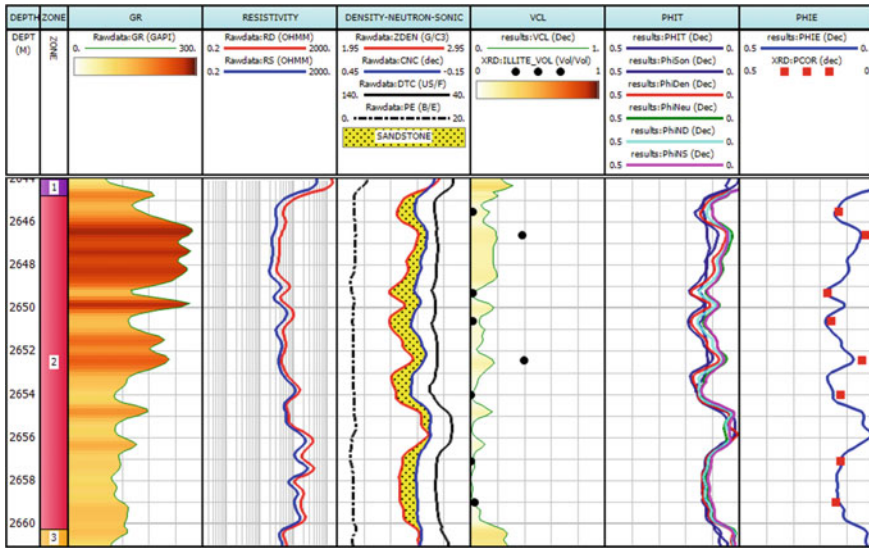


Fig. 19 Well-A open-hole logs-VCL-PHIT-PHIE correlation; Track 1 depth, MDRT; Track 2 reservoir zonation; Track 3 gamma ray, GR; Track 4 shallow and deep resistivity; Track 5 sonic compressional, DT; bulk density, RHOB, and neutron porosity, NPHI; Track 6 clay volume, VCL; Track 7 total porosity, PHIT; Track 8 core and effective porosity



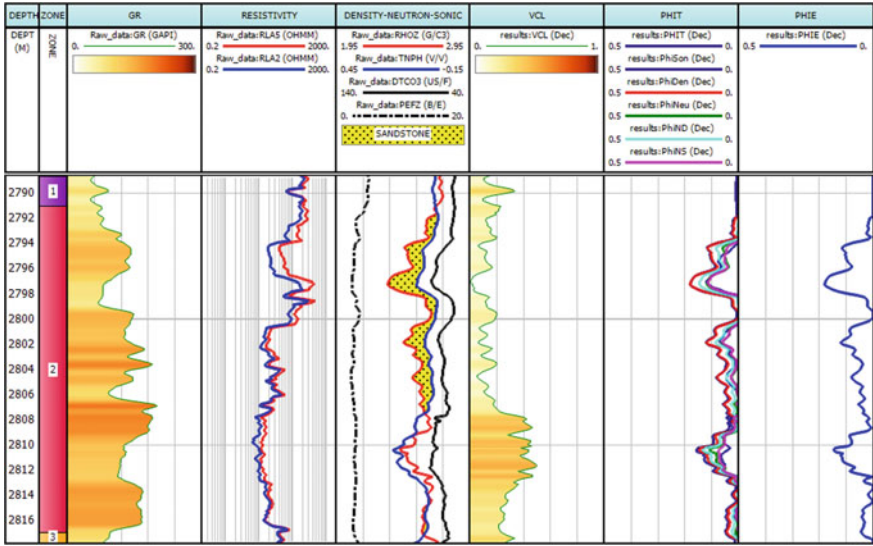
**Fig. 20** Well-B open-hole logs-VCL-PHIT-PHIE correlation; *Track 1* depth, MDRT; *Track 2* reservoir zonation; *Track 3* gamma ray, GR; *Track 4* shallow and deep resistivity; *Track 5* sonic compressional, DT; bulk density, RHOB, and neutron porosity, NPHI; *Track 6* clay volume, VCL; *Track 7* total porosity, PHIT; *Track 8* core and effective porosity

**Table 7** Core-log average porosity correlation

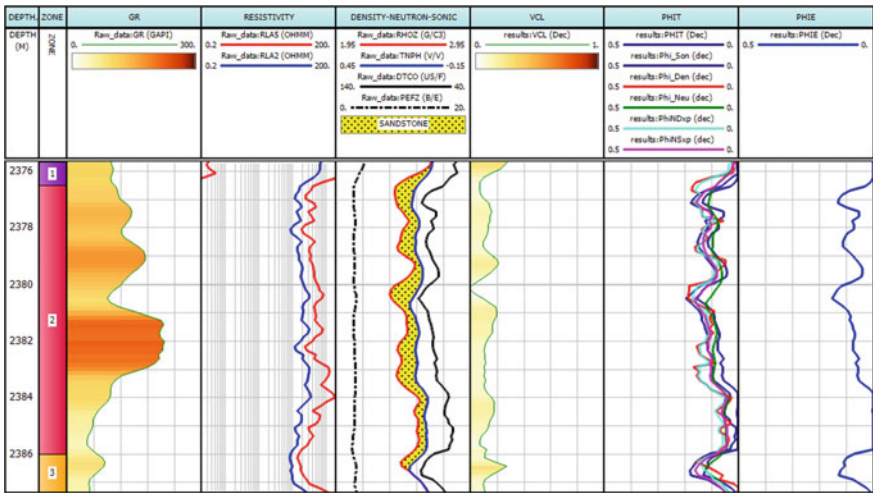
Well	Average log porosity	P10	P50	P90	Average core porosity
Well-A	0.07	0.001	0.07	0.15	0.073
Well-B	0.10	0.04	0.10	0.13	0.11
Well-C	0.06	0.01	0.05	0.11	n/a
Well-D	0.06	0.001	0.06	0.11	n/a
Well-E	0.09	0.04	0.09	0.13	n/a

### 3.8 The Final Log-Core Correlations

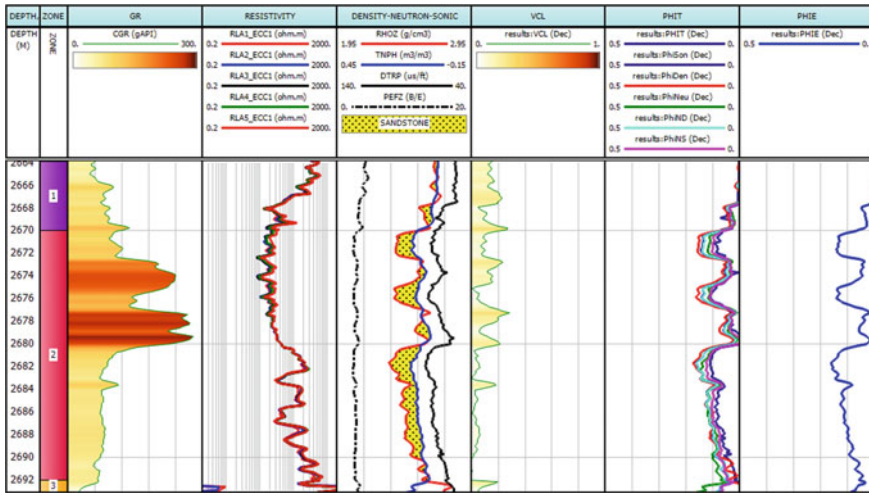
The final correlations between open-hole logs, clay volume (VCL), log porosity, and core porosity (PCOR) have been carried out (Figs. 17, 18, 19, 20, 21, and 22). These figures show good consistent results for VCL and porosity. This agreement has been confirmed by core data in Well-A and -B (Figs. 17, 18, 19, and 20). The sonic porosity has a good match with density and neutron porosity in the log-log correlation composites (Figs. 19, 20, 21, 22, and 23). The maximum porosity is observed in Well-B which is around 10%, and the minimum porosity is observed in Well-D which is around 6%.



**Fig. 21** Well-C open-hole logs-VCL-PHIT-PHIE correlation; *Track 1* depth, MDRT; *Track 2* reservoir zonation; *Track 3* gamma ray, GR; *Track 4* shallow and deep resistivity; *Track 5* sonic compressional, DT; bulk density, RHOB, and neutron porosity, NPHI; *Track 6* clay volume, VCL; *Track 7* total porosity, PHIT; *Track 8* effective porosity



**Fig. 22** Well-D open-hole logs-VCL-PHIT-PHIE correlation; *Track 1* depth, MDRT; *Track 2* reservoir zonation; *Track 3* gamma ray, GR; *Track 4* shallow and deep resistivity; *Track 5* sonic compressional, DT; bulk density, RHOB, and neutron porosity, NPHI; *Track 6* clay volume, VCL; *Track 7* total porosity, PHIT; *Track 8* effective porosity



**Fig. 23** Well-E open-hole logs-VCL-PHIT-PHIE Correlation; *Track 1* depth, MDRT; *Track 2* reservoir zonation; *Track 3* gamma ray, GR; *Track 4* shallow and deep resistivity; *Track 5* sonic compressional, DT; bulk density, RHOB, and neutron porosity, NPHI; *Track 6* clay volume, VCL; *Track 7* Total porosity, PHIT; *Track 8* effective porosity

## 4 Conclusions

From the results as obtained and discussed earlier, X-ray diffraction analysis method has been successfully used to characterize the lithology and mineralogical bulk composition of this reservoir. It is exposed that this reservoir could be classified as arkose sandstone or feldspathic sandstone. The dominant mineral is quartz; however, this reservoir contains a significant amount of feldspar minerals. The cement between grains is calcareous, and its amount is concentrated more at the upper part of this formation. The clay type is illite, and its volume ranges between 10 and 15%. The optimal method to compute the clay volume is double indicator method by using formation bulk density–neutron porosity logs. The reservoir porosity has been precisely determined by compressional sonic slowness log. There are two models used for this purpose. The first model is Wyllie model, and the other one is Raymer–Hunt model. Wyllie model is based on a linear relationship between sonic velocity,  $V_p$ , or sonic slowness and porosity. This model requires compaction correction factor. Raymer–Hunt model is based on a nonlinear relationship between sonic velocity,  $V_p$ , and porosity. The analyses for porosity determination revealed that the average porosity for this reservoir ranges between 6 and 11%. The Raymer–Hunt model results have a good match with core data better than Wyllie model. The optimum selection for matrix slowness and fluid slowness for this reservoir is 52.6 and 189 us/ft, respectively. Well-B has average porosity more than other wells. The sonic slowness extracted from sonic waves by slowness time coherence (STC) technique is more accurate than first motion detection technique, FMD. The

accuracy of porosity computed by sonic log depends highly on the sonic log quality itself and on the accuracy of lithology matrix slowness determination, and with less degree, it depends on the accuracy of fluid slowness determination. In Raymer–Hunt model, the influence of matrix slowness on the sonic porosity is more significant than the influence of fluid slowness. The fluid slowness effect is negligible. The effect of lithology matrix slowness on Raymer–Hunt outputs is less than that on Wyllie model outputs. The effect of matrix slowness is significantly more than the effect of fluid slowness on both models. It is observed that the effect of matrix slowness is negligible in the low porosity ranges. This effect increases with the increase of porosity. The effect of fluid slowness on porosity determined by Raymer–Hunt model is certainly negligible. There is a significant advantage of using Raymer–Hunt model over Wyllie model to compute reservoir porosity. The Raymer–Hunt model does not require compaction correction factor to be considered, whereas the Wyllie model requires that correction factor to be considered which leads to less accuracy in the results of porosity determined by Wyllie model. The results are validated by core data which make this methodology reliably applicable for all wells that drilled in this reservoir. The sonic porosity has good agreement with density and neutron porosity in the log–log correlation composites.

**Acknowledgements** Authors would like to extend sincere thanks and gratitude to Mr. Graham Melvin and IP support team in Senergy Company, Malaysia branch for their support and assistance. We also would thank the management of Petroleum Exploration and Production Authority (PEPA) in the Republic of Yemen for support and encouragement. We are grateful for Dr. Mohsen Shabib from Enhanced Oil Recovery Center (EOR) in University Teknologi PETRONAS for valuable advises and review.

## References

1. R. F. Sachsenhofer, A. Bechtel, R. W. Dellmour, A. F. Mobarakabad, R. Gratzer, and A. Salman, "Upper Jurassic source rocks in the Sab'atayn Basin, Yemen: Depositional environment, source potential and hydrocarbon generation," *GeoArabia, Journal of the Middle East Petroleum Geosciences*, vol. 17, pp. p. 161–186., 2012.
2. M. H. Hakimi and W. H. Abdullah, "Thermal maturity history and petroleum generation modelling for the Upper Jurassic Madbi source rocks in the Marib-Shabowah Basin, western Yemen," *Marine and Petroleum Geology*, vol. 59, pp. 202–216, 2015.
3. M. A. As-Saruri, R. Sorkhabi, and R. Baraba, "Sedimentary basins of Yemen: their tectonic development and lithostratigraphic cover," in *Lithosphere Dynamics and Sedimentary Basins: The Arabian Plate and Analogues*, ed: Springer, 2013, pp. 361–373.
4. Z. Beydoun, M. As-Saruri, and R. Baraba, "Sedimentary basins of the Republic of Yemen: their structural evolution and geological characteristics," *Revue de l'Institut Français du Pétrole*, vol. 51, pp. 763–775, 1996.
5. R. W. Siegfried and J. P. Castagna, "Full waveform sonic logging techniques," in *SPWLA 23rd Annual Logging Symposium*, 1982.
6. H.-P. Valero, M. Tejada, and D. Murray, "Improved First-Motion Algorithm to Compute High-Resolution Sonic Log," in *SPE Annual Technical Conference and Exhibition*, 2004.
7. W. John and M. Welx, "FULL WAVE SONIC LOGGING: A BRIEF PERSPECTIVE," *SPWLA TWENTY-SEVENTH ANNUAL LOGGING SYMPOSIUM, JUNE 9–13, 1986*, 1986.

8. H. D. Leslie and F. Mons, "Sonic waveform analysis: applications," in *SPWLA 23rd Annual Logging Symposium*, 1982.
9. J. Dvorkin and A. Nur, "Time-average equation revisited," *Geophysics*, vol. 63, pp. 460–464, 1998.
10. K. Holliger and J. O. Robertsson, "Sonic log velocity variations and crack-porosities in crystalline rocks," in *1995 SEG Annual Meeting*, 1995.
11. B. E. Hornby, I. William, M. I. H.-I. Liu, and K. Hsu, "Full Waveform Sonic Logging in a North Sea Reservoir CH4. 6," 1990.
12. J. Market and W. Canady, "Multipole Sonic Logging In High-Angle Wells," in *SPWLA 50th Annual Logging Symposium*, 2009.
13. C. Poster, "Acoustic characterization of permeable zones from full waveform array sonic data," in *Middle East Oil Show*, 1989.
14. V. Saxena, "Fresh sonic interpretation in limestone through modulus decomposition," in *SPE India Oil and Gas Conference and Exhibition*, 1998.
15. P. Spooner, "Lifting the Fog of Confusion Surrounding Clay and Shale in Petrophysics," in *SPWLA 55th Annual Logging Symposium*, 2014.
16. R. A. Hussein and M. E. B. Ahmed, "Petrophysical Evaluation of Shaly Sand Reservoirs in Palouge-Fal Oilfield, Melut Basin, South East of Sudan," *Engineering and Computer Sciences (ECS), Journal of Science and Technology*, vol. 13, 2012.
17. N. F. M. Henry, H. S. Lipson, and W. A. Wooster, *The interpretation of X-ray diffraction photographs*: McMillan, 1960.
18. J. Garat, M. Krief, J. Stellingwerf, and J. Ventre, "A petrophysical interpretation using the velocities of P and S waves (full-waveform sonic)," *The Log Analyst*, vol. 31, 1990.
19. J. Raiga-Clemenceau, J. Martin, and S. Nicoletis, "The concept of acoustic formation factor for more accurate porosity determination from sonic transit time data," in *SPWLA 27th Annual Logging Symposium*, 1986.
20. L. Yadav, K. Prasad, and A. Bhattacharya, "GENERALISED SONIC POROSITY TRANSFORM FOR UPPER ASSAM OIL FIELDS, INDIA," *5th Conference & Exposition on Petroleum Geophysics, Hyderabad-2004, India PP 95–100*, vol. 5th Conference & Exposition on Petroleum Geophysics, Hyderabad-2004, India PP 95-100, 2004.
21. W. M. Mabrouk, "An Approach for Estimating Porosity from Sonic-Logs in Shaly Formations," 2007.
22. J. Dvorkin and I. Brevik, "Diagnosing High-porosity Sandstones: Permeability From Porosity And Velocity," in *1997 SEG Annual Meeting*, 1997.
23. R. J. Jenkins, "Accuracy of porosity determinations," *The Log Analyst*, vol. 7, 1966.
24. S. Calvert, M. Lovell, P. Harvey, J. Samworth, and J. Hook, "Porosity Determination In Horizontal Wells," in *SPWLA 39th Annual Logging Symposium*, 1998.
25. R. Hoard, "Sonic waveform logging: a new way to obtain subsurface geologic information," in *SPWLA 24th Annual Logging Symposium*, 1983.
26. S. Huang and C. Torres-Verdin, "Sonic Spatial Sensitivity Functions and Inversion-Based Layer-by-Layer Interpretation of Borehole Sonic Logs," in *SPWLA 56th Annual Logging Symposium*, 2015.
27. L. Yadav, K. Prasad, and A. Bhattacharya, "Generalised Sonic Porosity Transform for Upper Assam Oil Fields," in *5th Conference and Exposition on Petroleum Geophysics, India, 2004*, p. 95100.
28. R. K. Bratli, J. M. Daines, and P. F. Worthington, "Comparative Evaluation Of Core Compaction Corrections For Clastic Reservoirs," 1997/9/1/.
29. I. Tamunobereton-ari, V. Omubo-Pepple, and N. Tamunobereton-ari, "Compaction correction factor in the South-East Niger Delta, Nigeria: A function of porosity and density of formation materials," *J. Basic Appl. Sci. Res.*, vol. 1, pp. 464–470, 2011.

# The Roles of Polar Compounds in the Stability and Flow Behavior of Water-in-Oil Emulsions

A.A. Umar, I.M. Saaid and A.A. Sulaimon

**Abstract** This paper summarizes an investigation of the roles of asphaltenes and other polar compounds in forming and stabilizing water-in-oil emulsions. Two crude oils with entirely different starting properties from Canada and Malaysia were used for the study. Asphaltenes and polar compounds were isolated from the crude oils using silica columns, and emulsions were prepared with the asphaltenes-free crude oils. These investigations have confirmed that water-in-oil emulsions formed by amphiphiles with the highest molecular weight play the most important roles in stabilizing W/O emulsions. Rheological as well as stability studies were conducted for emulsions formed by the crude oils with and without asphaltenes. The study shows that the viscosity of emulsions formed by the crude oils with asphaltene at a shear rate of one reciprocal second is about three orders of magnitude greater than that of the starting oil. An unstable emulsion is formed with the asphaltene-free crude oils, and thus, the viscosity of the emulsion is not more than about 20 times greater than that of the starting oil. A stable emulsion has a significant elasticity, whereas an unstable emulsion does not. A mesostable emulsion has properties between stable and unstable, but breaks down within a few days of standing. The usual situation is that emulsions are either obviously stable, mesostable, or unstable. The type of emulsion produced is determined primarily by the properties of the starting oil. The most important of these properties are the asphaltene and resin content and the viscosity of the oil. The composition and property ranges of the starting oil that would be required to form each of the water-in-oil states are discussed in this paper.

**Keywords** Emulsions · Isolation · Asphaltene · Emulsifiers · Water-in-oil emulsion · Surfactants · Polar compounds

---

A.A. Umar (✉) · I.M. Saaid · A.A. Sulaimon  
Department of Petroleum Engineering, Universiti Teknologi PETRONAS,  
Bandar Seri Iskandar 32610, Perak Darul-Ridzuan, Malaysia  
e-mail: abubakar\_g02934@utp.edu.my

© Springer Nature Singapore Pte Ltd. 2017  
M. Awang et al. (eds.), *ICIPEG 2016*,  
DOI 10.1007/978-981-10-3650-7\_55

643

## 1 Introduction

The formation of crude oil emulsions is a costly problem in the oil and gas industry. Although water and oil are immiscible, highly stable water-in-oil emulsions (W/O) do form during the production, transportation, and processing of crude oil [1, 2]. An emulsion is defined as a system of immiscible liquids in which one of the liquids is intimately dispersed in the other as small droplets under the influence of interfacially active materials. These interfacially active materials (such as asphaltenes, resins, and fine particles) are also known as ‘emulsifiers.’ Among other factors, the presence of these surface-active agents is a necessary condition for a stable emulsion to form, and they control the stability of the emulsions [2–9]. Other authors proposed that, it is the asphaltene particles that gather at the oil–water interface and form a mechanical skin are responsible for a stable W/O emulsion. This ‘skin’ was suggested to contain waxes, tar particles, and other polar compounds. Microcrystals of wax were also hypothesized to stabilize emulsions [7, 8, 10]. It is a general belief among researchers that these components adsorb as surfactants or as particles at the oil/water interface, resulting in rigid films that encapsulate water droplets and inhibit their coalescence. This leads to the stabilization of the emulsion by (1) repulsive charges on the surfaces of the dispersed phase and (2) adsorbed films that, being preferentially wetted by the external phase, act as a physical barrier to prevent contact between the dispersed droplets [6, 9, 11]. Depending on the crude oil aliphatic/aromatic ratio which controls the solubility of asphaltene–resins and their interfacial activity, three main stabilization mechanisms of W/O emulsion exist: (1) steric stabilization due to an adsorbed layer of asphaltene at a low concentration of asphaltene–resin submicron particles; (2) depletion destabilization due to an excluded volume effect, leading to attraction between water droplets; and (3) structural stabilization due to long-range colloidal structure formation inside the film in the presence of a sufficient effective volume fraction of colloidal particles. Generally, an emulsion system is expected to have a combination of these three mechanisms [7, 12–14].

This study investigates the roles of asphaltenes and other polar compounds in the stability and flow behavior of water-in-crude oil emulsions. Both static bottle test and the light scattering methods were used to determine the stability of emulsions prepared by crude oils with and without polar compounds. The rotational rheometry technique is used to determine the flow behaviors of the emulsions.

## 2 Methodology

### A. Crude Oil Samples

As mentioned earlier, the same crude oil was used to prepare both emulsions. However, asphaltenes and other polar compounds were chemically removed from the other sample, thus giving a sample with asphaltene and other polar compounds



and one without. Table 1 shows some of the properties of the crude oil samples used in the study. While some crude oils form emulsions, some do not form at all. Oils with very low viscosities of the range  $<50$  mPa s do not form emulsions and so also high viscosity oils with viscosity values  $>200,000$  mPa s [15, 16].

### B. Simulated Distillation—SimDist (GC-FID)

The simulated distillation was carried out on the crude oil samples, using the method provided in ASTM (American Society for Testing Materials) D2887. It is a known fact that the emulsions formed by light and intermediate fractions of crude oil that distill at temperatures below  $520$  °C are not stable. Hence, most stable emulsions form with the fraction of crude that distilled at temperatures greater than  $520$  °C. This suggests that the amphiphiles with the highest molecular weight, i.e., resins and asphaltenes, play a major role in the protection of water droplet against coalescence, thus making the emulsion more stable.

### C. Polar Compound Isolation from Crude oils

Asphaltenes and other polar compounds that are naturally found in the crude oil have been recognized as the primary emulsion stabilizers [17]. Being more polar than alkanes, asphaltenes tend to stick to the oil–water interface, and due to their large molecular size, they sterically prevent droplet coalescence. This is done either by sterically preventing the drops to come together, close enough for coalescence to occur, or by making the droplet interfacial film too rigid to favor coalescence. This study employs the method used by Sjoblom et al. (1992) (with slight modifications) in chemically isolating asphaltene and other polar compounds from the crude oil. In this study, 10 g of brown silica beads with minimum absorbent capacity of 22.0% (supplied by Sorbead India) was added into a 100 mL plastic beaker. 20 mL of Orente crude oil was added, and n-hexane was added into the beaker to dilute the crude oil to 100 mL. The beaker was gently stirred, and a Whatman filter paper #42 was used to filter the mixture. The silica was discarded, and the procedure was repeated until the silica beads lose its brown color. The filtrate was again filtered through a  $0.45\text{-}\mu\text{m}$  syringe filter into another clean beaker. A rotary evaporator was then used to evaporate off the hexane at  $65\text{--}70$  °C until the original 20 mL of the crude oil was recovered. This is repeated until 100 mL of the isolated crude oil was gathered. It was then stored in a glass bottle for further use.

**Table 1** Physicochemical properties of crude oils used in the study

Crude oil samples	Physical properties		
	$\rho$ ( $\text{g}/\text{cm}^3$ )@25 °C	Viscosity (cP)	Wax content (%)
Orente	0.9891	15.54	16.67
Isolated Orente	0.8089	13.40	16.23
Dulang	0.9788	17.50	25.41
Isolated Dulang	0.9844	16.10	24.20

#### D. Emulsion Sample Preparations

Emulsions used in this study were prepared using Orente crude oil. One of the emulsions (A) was prepared from an original sample of Orente (as received), while the other sample (B) was prepared from a sample of the same crude oil, but with asphaltenes and other polar compounds isolated. For this study, all emulsions were prepared from 30% brine as discontinuous phase and 70% crude oil as the continuous phase. The types of prepared emulsions were verified using filter paper, and only the W/O types were used in this study. The emulsions were prepared by stirring both crude oil and water at 1000 rpm for 10 min, using a standard blade stirrer. Prior to mixing, both the crude oil and brine were kept in an oven at 45 °C for 10 min, to ensure homogeneity. Dulang and Orente with high wax contents were, however, kept for 30 min at 75 °C. Checking the emulsion type involves placing some drops of the emulsion to be tested on a filter paper placed flat on a table. An emulsion that spreads up the filter paper is considered an O/W emulsion. An emulsion that does not spread is, however, considered a W/O emulsion.

#### E. Emulsion Stability Measurement—Bottle Test method

The most widely used method of assessing the stability of emulsions in the oil and gas industry is the batch test (bottle test method). The method follows the gravity separation technique, where the quantity of separated water is being observed over time and taken as a measure of the emulsion stability. All prepared emulsions were kept in a calibrated measuring cylinder and left to settle. The percentage of water separated was calculated using the equation below:

$$W\% = \frac{V_{ws}}{V_{ow}} \times 100 \quad (1)$$

$W\%$  is the percentage of water separated

$V_{ws}$  = volume of water separated, in mL

$V_{ow}$  = volume of original water used to prepare the emulsion, mL

The stability of the emulsions from the crude oil samples with and without polar compounds was tested, the results are presented under the results and discussions section of this work.

#### F. Emulsion Stability Measurement—Multiple Light Scattering method

The Turbiscan is quite a newly developed method. The technique allows for the scanning of the turbidity profile of a sample (emulsion) along the height of a glass tube filled with the emulsion. The portion of the equipment called the reading head is made up of a pulsed near-IR light source ( $\lambda = 850$  nm) and two synchronous detectors. The transmission (T) detector collects the light which goes through the sample ( $0^\circ$ ), while the backscattering (BS) detector receives the light backscattered

by the sample ( $135^\circ$ ). The transmission and backscattering data are acquired by the Turbiscan head every 40 mm along the vertical length of the cell. Hence, the scan of a 60-mm-high sample provides configurations, comprising 1,500 points of measurements in less than 20 s. Therefore, by repeating the scan of a sample at different time (t) intervals, the stability or instability of dispersions can be studied in detail.

### G. *Emulsion Flow Behavior (Bulk rheology)*

Among the important properties of an emulsion is its flow behavior (Rheology). Emulsion rheology involves the flow of emulsions and their deformation when subjected to some stress. Emulsion rheology, especially its viscous behavior, is very vital in handling produced crude oil that normally comes along with water especially in mature oil field. The use of rotational rheometry technique for the measurement of complex shear rheology for all kinds of materials has been so vital. It is perfect for discriminating essential and compositional changes of materials, which can be critical controlling factors in flow and deformation properties. In this study, MCR Anton Paar HPHT Rotational Rheometry was used. The MCR viscometer is very easy and user-friendly to measure shear stress and shear rate at specific rotational speed and plot the flow curve automatically by the Rheoplus software.

## 3 Results and Discussions

### A. *Crude Oil and Water Samples*

Some of the physicochemical properties of the crude oil samples measured are recorded in Table 1. It is a known fact that certain crude oils do not form stable emulsions, as a result of the properties they possess. These crude oils are either of low viscosity or of high viscosities. The low viscosity oils are those whose viscosities are less than 50 mPa s. On the other hand, those crude oils considered to be of high viscosities have their values ranging above 200,000 mPa s. One of the reasons we have to characterize our crude oil samples and measure their physicochemical properties is to know whether our crude oils have the potentials or not, to form stable emulsions.

### B. *Simulated Distillation (SimDist)*

Crude oil consists of light and heavy fractions. Investigations have revealed that crude oils with higher percentage of heavy fractions do form stable emulsions. On the contrary, light and intermediate fraction crude oils do not form stable emulsions. Heavy fractions distill at temperatures higher than  $520^\circ\text{C}$  and thus have a very high potential of forming stable emulsions. Asphaltenes and resins are amphiphiles with

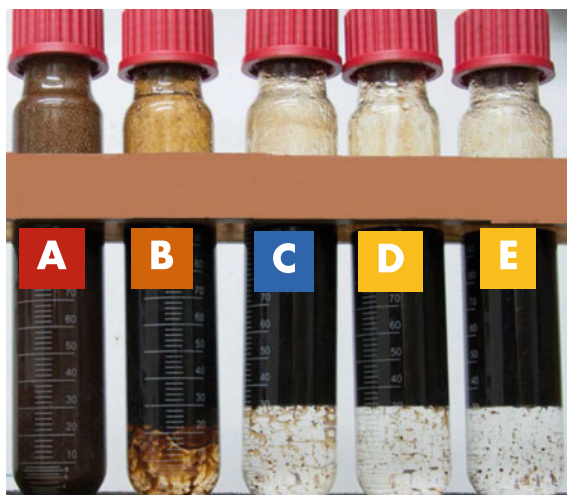
the highest molecular weight and therefore play major roles in preventing droplet coalescence. The SimDist results from this study showed that the original crude oils (before isolating the asphaltene and other polar compounds) distill at temperature as high as 547.48–550.57 °C. Upon isolation of the polar compounds, the temperatures were seen to be lower than 439.2 °C. Thus, the absence of significant heavy fractions is one of the reasons that the crude oil without asphaltene and other polar compounds could not form stable emulsion.

Asphaltenes and other polar compounds that are naturally found in the crude oil are seen as the primary emulsion stabilizers. Being more polar than alkanes, asphaltenes tend to stick to the oil–water interface, and due to their large molecular size, they sterically prevent droplet coalescence.

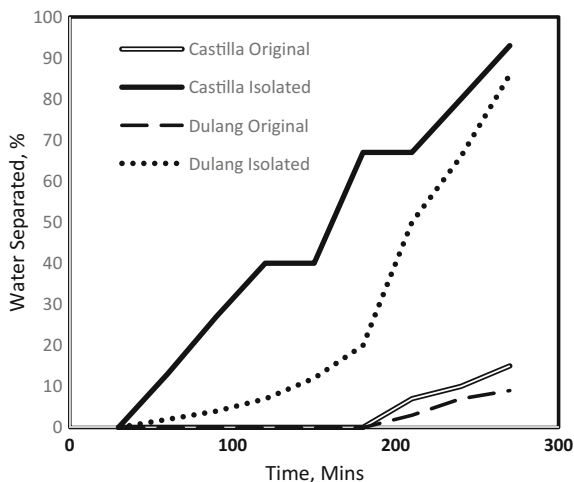
### C. Emulsion Stability Measurement—Bottle Tests and Light Scattering Method

The bottle test method is by far the most common method of determining emulsion stability in oil fields. It is done by measuring the amount of water separated over time in an undisturbed emulsion. The Turbiscan (light scattering) technique is, however, a valid and more accurate method of determining emulsion stability. Both methods are used in this study. As mentioned in Sect. 2, subsection E, emulsions were prepared with different water cut (30/70 v/v). As shown in Fig. 1, bottles A and B are the emulsions that form when original crude oil samples of Orente and Dulang were used. These emulsions are more stable than those prepared with isolated samples of the two crude oils (shown in bottles C, D, and E). In Fig. 1, bottle A is the emulsion that remained very stable throughout the duration of the test (over a month). In Fig. 1, bottle B is also a stable emulsion, because it persisted for over 21 days before water broke out. For emulsions in bottles C, D, and E in Fig. 1, they were prepared using isolated samples of Dulang 1, Dulang 2,

**Fig. 1** Bottle test results



**Fig. 2** Bottle tests stability measurements—isolated and original



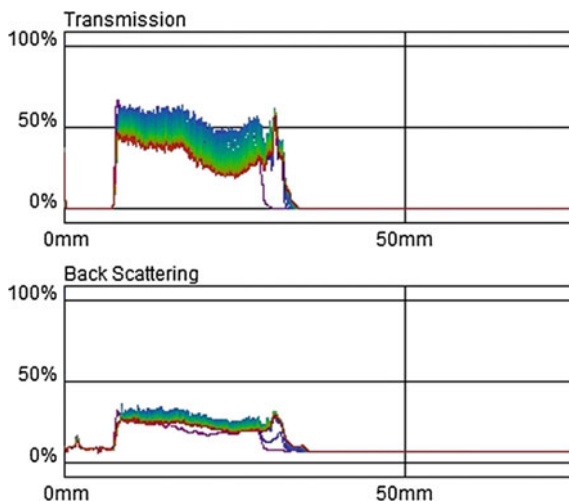
and Orente crude oils. As shown, the crude oil and water are separated into their respective phases without the addition of any demulsifier nor heat. This can be attributed to the absence of high molecular weight polar compounds in the crude oils used. These compounds act as natural emulsifiers. Certain crude oil components such as resins, fatty acids such as naphthenic acids, porphyrins, and wax crystals also may act as natural emulsion stabilizers when found in crude oils, although they may not be able to produce a stable emulsion alone.

Figure 2 shows the water separation pattern for the emulsions prepared by original crude oils and those prepared by crude oils from which asphaltene has been isolated. As can be seen, less than 15% of the water content in emulsions prepared with original Castilla and Dulang was separated from the emulsion after the whole period of study. This is against almost 95% water separated from emulsions formed by the isolated crude oils. This is evident that emulsions formed by crude oils containing asphaltene and resin are much more stable than those formed by crude oils with no such high molecular weight polar compounds.

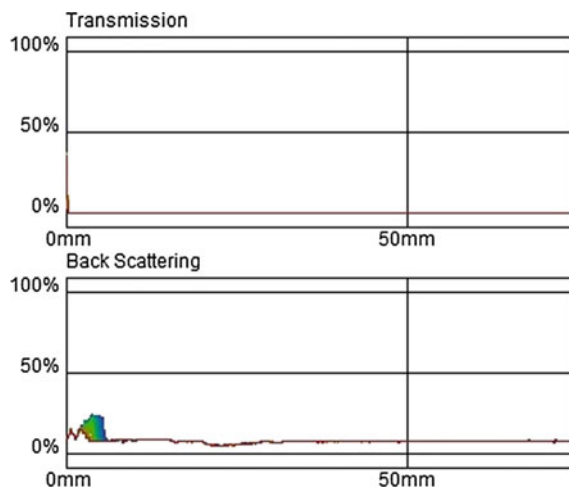
To further study the stability of the emulsions, the Turbiscan MA2000 optical analyzer was used. The equipment permits for assessing the droplet sedimentation behavior within a white opaque column, where the emulsion shows a visual stability. This behavior is shown by the transmission versus time profile shown in Figs. 3 and 4. The transmission (T) and backscattering (BS) strengths represent the emulsion stability with respect to height.

As shown in Fig. 4, there is no indication of particle movement on the profile, suggesting the emulsion is stable over the entire period of study. However, Fig. 3 shows light transmission along the length of the tube, indicating that water separates within this region. Beyond this region, no further transmission was recorded, suggesting that the separation of the emulsion has finished, and no further separation would occur.

**Fig. 3** Transmission and backscattering profiles for crude oil emulsions (without asphaltene and resins in the oil sample)



**Fig. 4** Transmission and backscattering profiles for crude oil emulsions (with asphaltenes and resins in the oil sample)

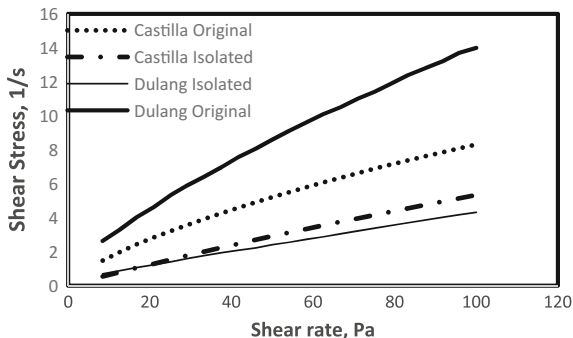


#### D. Emulsion Bulk Rheology

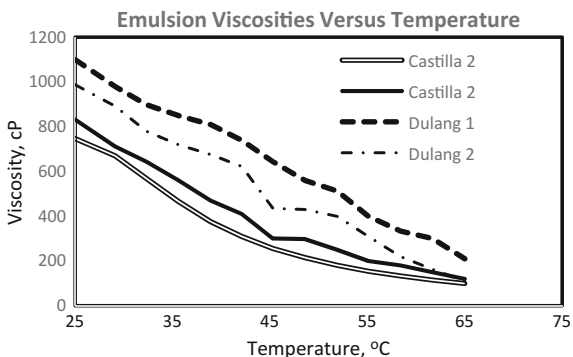
Emulsions show exceedingly wide-ranging rheological behaviors which are both useful and intriguing. The relationships between stress and strain in emulsions depend extremely on the composition, droplet structure, and size, as well as the interfacial interactions within the emulsions.

In Fig. 5, the relationship between the shear rate and shear stress of the studied emulsions is shown. As shown, the shear stress/shear rate relationship is almost constant and is linear for emulsions formed by original samples of the crude oils. However, the flow behaviors for emulsions formed by the isolated crude oils are non-Newtonian (shear thinning).

**Fig. 5** Shear stress versus shear rate behaviors of different emulsions

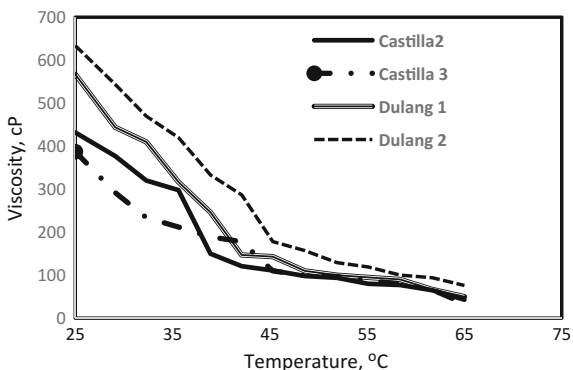


**Fig. 6** Viscosities versus temperature for emulsions formed by crude oils



In Figs. 6 and 7, the effect of temperature on emulsion flow behavior is shown. As seen, decrease in viscosity is observed with increasing temperature due to an increase in the deformation of the emulsion as well as an increase in coalescence as temperature increases. Generally, emulsions formed by crude oils containing asphaltenes and resins have higher viscosities when compared to those crude oils

**Fig. 7** Viscosities versus temperatures for emulsions prepared by isolated crude oil



from which asphaltenes were isolated. Although there is a decrease in the viscosities in both cases, the viscosities of the emulsions that form when the original crude oils were used are quite higher than those of the isolated crude oils.

## 4 Conclusions

This study investigated the effect of asphaltene and other polar compounds in the stability and flow behavior of water-in-oil emulsions. It has been found that the presence of asphaltene and other polar compounds significantly affect the stability of crude oil emulsions. Also, emulsion rheology is significantly affected by the presence of polar compounds in the oil phase. Thus, the viscosities of emulsions with asphaltenes and resins are generally higher than those without.

## References

1. M. Nikkhah, T. Tohidian, M.R. Rahimpour, A. Jahanmiri., Efficient demulsification of water-in-oil emulsion by a novel nano-titania modified chemical demulsifier. *Chemical Engineering Research and Design*, p. 164–172 (2015).
2. S.L. Kokal, Crude oil emulsions: A state-of-the-art review. *SPE Production & facilities*, 20 (01): p. 5–13 (2005).
3. P. Meyer, Chemelectric Treating a New Phase in the Electrical Dehydration of Oil Emulsions. In *SPE Production Automation Symposium*. Society of Petroleum Engineers (1964).
4. H.V. Smith, K.E. Arnold, Crude oil emulsions. *Petroleum engineering handbook*. 3rd ed. Richardson: Society of Petroleum Engineers, p. 19.1–19.34 (1992).
5. B. Mokhtari, K. Pourabdollah, Separation and Determination of Diol Pollutants from Demulsifier in the Produced Water of Oil Fields. *Journal of Environmental Research and Development Vol*, 8(2) (2013).
6. J. Strassner, Effect of pH on interfacial films and stability of crude oil-water emulsions. *Journal of Petroleum Technology*, 20(03): p. 303–312 (1968).
7. O.C. Mullins, E.Y. Sheu, Structures and dynamics of asphaltenes. *Springer Science & Business Media* (2013).
8. M. Fingas, B. Fieldhouse, J. Mullin, Water-in-oil emulsions results of formation studies and applicability to oil spill modelling. *Spill Science & Technology Bulletin*, 5(1): p. 81–91 (1995).
9. R.F. Lee, Agents which promote and stabilize water-in-oil emulsions. *Spill Science & Technology Bulletin*, 5(2): p. 117–126 (1999).
10. M. Fingas, Water-in-oil emulsion formation: A review of physics and mathematical modelling. *Spill Science & Technology Bulletin*, 2(1): p. 55–59 (1995).
11. M.B. Sadeghi, Experimental Investigation of Rheological and Morphological Properties of Water in Crude Oil Emulsions Stabilized by a Lipophilic Surfactant. *Journal of Dispersion Science and Technology*, 34(3): p. 356–368 (2013).
12. K. Kumar, A. Nikolov, D. Wasan, Mechanisms of stabilization of water-in-crude oil emulsions. *Industrial & engineering chemistry research*, 40(14): p. 3009–3014 (2001).
13. J.D. McLean, P.K. Kilpatrick, Effects of asphaltene solvency on stability of water-in-crude-oil emulsions. *Journal of Colloid and Interface Science*, 189(2): p. 242–253 (1997).



14. A.P. Sullivan, N.N. Zaki, J. Sjoblom, P.K. Kilpatrick, The Stability of Water-in-Crude and Model Oil Emulsions. *The Canadian Journal of Chemical Engineering*, 85(6): p. 793–807 (2007).
15. M. Fingas, A Simplified Procedure to Predict Water-in-Oil Emulsions. *Journal of Spill Science*, (2014).
16. M. Fingas, B. Fieldhouse, Studies on crude oil and petroleum product emulsions: Water resolution and rheology. *Colloids and Surfaces A: Physicochemical and Engineering Aspects*, 333(1): p. 67–81 (2009).
17. Z. Wang, Characteristics of spilled oils, fuels, and petroleum products: 1. Composition and properties of selected oils. United States Environmental Protection Agency, 2003.

# Geomorphology and Hydrology of 2014 Kelantan Flood

A.R. Abdul Hadi, M.R.A. Ghani, Jasmi Talib and I. Nur Afiqah

**Abstract** The December 2014 Kelantan floods were the worst on records in terms of depth and extent of inundation as well as damages to properties and infrastructure. Therefore, a comprehensive and integrated flood monitoring, forecasting, and warning methods are needed to allow planning of responses to potential future floods by the government and related environmental agencies. The Kelantan state has been affected by floods every year in modern times. Meteorological and hydrological records have shown that the Kelantan River often overflows during the NE monsoon season. This preliminary due to heavy rainfall, causing an almost annual recurrence of floods to the state between the end of November till March (DID 2014/2015). Excessive land use changes such as deforestation (i.e. logging and clearing for agriculture) and increased precipitation intensity and frequency are the possible causes for this change. However, little research has been conducted to understand and quantify how these factors contribute to changes in the magnitude and frequency of flooding in the area. This research will attempt to integrate geomorphological, hydrological and meteorological data and evaluate their impact on the recurrence of the annual flood in Kelantan. The main objective of this research project is to study all factors that contribute to the flooding events in Kelantan and propose a strategy to minimize the impact of future flooding events. The methodology planned to achieve the specific objectives for this research comprises of: (i) analysis of satellite imagery and remote sensing images to map general geomorphology of Kelantan; (ii) analysis of medium-term climatic data (temperature and rainfall data) to evaluate the impact of hydrology on the flooding events. From the Digital Elevation Model (DEM) map, the geomorphology of Kelantan can be clearly seen where at the southern part of Kelantan (Gua Musang and Kuala Krai area) is more hilly and highly elevated, and toward northern parts of Kelantan

---

A.R. Abdul Hadi · M.R.A. Ghani · J. Talib · I. Nur Afiqah (✉)  
Department of Geosciences, Universiti Teknologi Petronas,  
32610 Bandar Seri Iskandar, Perak, Malaysia  
e-mail: nurafiqahismail92@gmail.com

which cover area Kota Bharu, Pasir Puteh, Tumpat, Bachok, Pasir Mas, Tanah Merah, the elevation more gentle since it near to coastal region area. This lowland geomorphology allows becoming an escape route for the water and later transported to the nearby delta before escaping to the sea which is the main basin. The fluvial geomorphology at the Kelantan Delta area is meandering since it located at downstream area. More than that, the urbanization aggressively increases at floodplain area and also forces the flooding to occur. Meanwhile the data could also identify the water flow from rivers in southern upstream highland region (Lebir River and Galas River) to Kelantan Delta area. The existence of bottle necks in southern parts of Kelantan area such as Dabong, Manek Urai, and Kuala Krai can be identified under the image whereby the river flows through a narrow or obstructed section from catchment area. It could assist to decelerate the water flow to Kelantan River in the event of flood and long duration rainfall. However, river-bottle neck will accelerate the rise of flood level in southern upstream highland area. The Kelantan River Basin experiences the northeast (NE) monsoon climate which is responsible for the heavy rains that hits the east coast of the Peninsular Malaysia, such as the state of Kelantan, Terengganu, and Pahang, and frequently cause overflow of riverbank flooding. The flooding that occurred in 2014/2015 was caused by heavy rains brought by the northeast monsoon winds blown from November to March. Floods in 2014 showed the total rainfall in rural areas is more dense (>60 mm) than the coastal areas (DID 2014/2015). Heavy rain began to fall in the Gunung Gagau on December 16, 2014, in which a total of 6648.0 mm in the coastal areas have been covered by 6 new stations in Kota Bharu, Tumpat, Pasir Mas, Machang, Bachok, and Pasir Puteh while in rural areas of 7373.0 mm, which also includes 6 stations, namely Dabong, Jeli, Gua Musang, Laloh, Aring and Gunung Gagau for the month of December. Continuous heavy rains until early January as recorded stations involved. Based on the preliminary geomorphological and hydrological analysis, DEM and satellite data, future development plan of residential areas, reforestation and plantation, town planning, and river engineering projects for Kelantan state should incorporate the details of the studies. Several *flood management strategies* are proposed here. In the southern upstream areas, desilting of the river system needs to be carried out. The deforestation projects should be stopped in the areas which forms large rainfall catchment areas. The logging activities should be limited to non-catchment, intermediate, and lowland areas. In the lowland, Kelantan delta areas, urbanization and river engineering projects need to be re-evaluated. Construction of large monsoon drains may help to distribute the floodwaters more efficiently.

**Keywords** Kelantan • Flood • Upstream • Downstream • Delta • Highland

# 1 Introduction

Kelantan is situated in the East Coast of Peninsular Malaysia. The state is exposed to the northeast monsoon and experiences floods almost every year. This is the result of extreme and widespread rainfall brought by the northeast monsoon across Kelantan from November to March the following year, and urbanization [1]. During the monsoon season, continuous and heavy rainfall in the Sungai Kelantan and Sungai Golok basin will transport excess volume of water downstream. Ten districts are known to be flood-prone areas; they are—Kota Bharu, Kuala Krai, Machang, Pasir Mas, Pasir Puteh, Tanah Merah, Jeli, Bachok, Tumpat, and Gua Musang.

According to previous records, flooding begins from the month of December and continues until January the following year. Table 1 shows the comparison between major flooding events that have occurred in Kelantan [2].

In 2014, one of the worst recorded floods occurred in Kelantan. During November and December 2014 and as well as early 2015 monsoon, three episodes of flooding were recorded in Kelantan [2]. The first flood duration was seven days starting from November 17, 2014, until November 23, 2014, and this affected the districts of Pasir Mas (Rantau Panjang) and Tumpat. The second flood lasted for 21 days from December 14, 2014, to January 3, 2015, affecting Gua Musang, Kuala Krai, Tanah Merah, Machang, Pasir Mas, Kota Bharu, Tumpat, Jeli, Pasir Puteh, and Bachok. The last episode, a minor flood, lasted for two days from January 10, 2015, until January 11, 2015. The floods affected all of the districts from the Sungai Kelantan and Sungai Golok basin. The annual rainfall in 2014 record exceeded the average annual rainfall; this 2700 mm was linked to the heavy rainfall in the Gunung Gagau rural areas. The floods in 2014 and 2015 had resulted in the movement of flood victims up to 319,156 people with a death toll of fourteen people, while the total loss had been estimated to be almost RM 155,956,468.00 [2].

**Table 1** Major flood events in Kelantan

Major flood event (year)	Total average annual rainfall (mm/year)
1926	No record
1967	No record
1971	No record
1983	2, 860.50
1988	3, 163.85
2004	2, 492.75
2014	3, 495.25

## 2 Problem Statement and Objectives

The Kelantan state has been affected by floods every year in modern times. Meteorological and hydrological records have shown that the Sungai Kelantan often overflows during the NE monsoon season. This is primarily due to heavy rainfall, causing an almost annual recurrence of floods to the state between the end of November till March [2].

Excessive land use changes such as deforestation (i.e., logging and clearing for agriculture) and increased precipitation intensity and frequency are the possible causes for this change. However, little research has been conducted to understand and quantify how these factors contribute to changes in the magnitude and frequency of flooding in the area. This research will attempt to integrate geomorphological, hydrological, and meteorological data and evaluate their impact on the recurrence of the annual flood in Kelantan.

The main objective of this study was to evaluate the available data related to the 2014 Kelantan flood and to determine the major causes of the flood. The conclusions derived from this study will provide an assessment of the flood risk in Kelantan and can be incorporated in the development of risk management strategies. Effective and meaningful flood risk analysis and management requires the integration of geomorphological and hydrological approaches and data. To achieve the objectives of the study, we have taken the following approaches.

This research will focus on three main areas listed below:

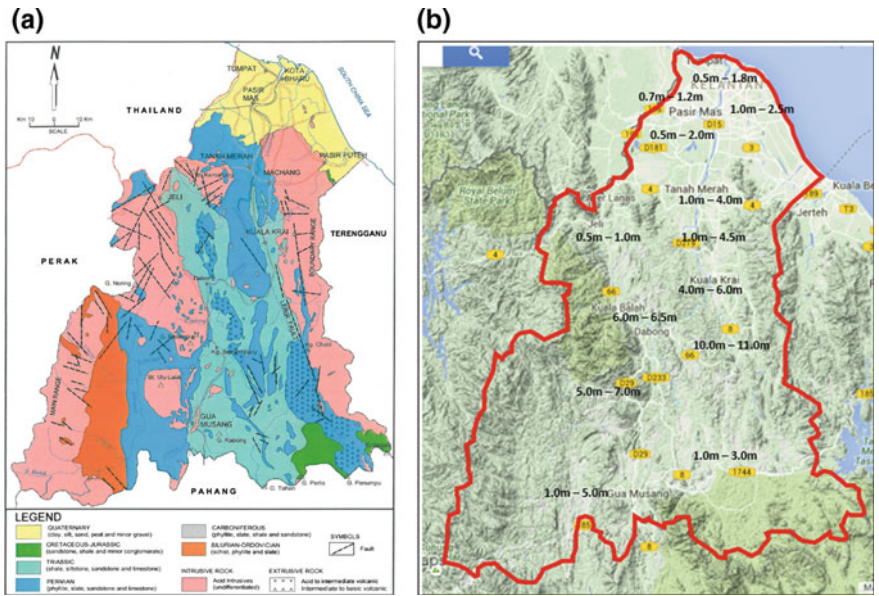
1. To evaluate the impact of the geomorphology of the Kelantan state and its rivers on floods;
2. To assess the effects of climate change and rainfall on the magnitude and frequency of floods in Kelantan;
3. To identify the major causes contributing to the Kelantan flood and to suggest potential flood risk management strategies.

## 3 Results and Discussion

### 3.1 *The Kelantan 2014 Flood*

#### 3.1.1 Geology and Geomorphology of Kelantan

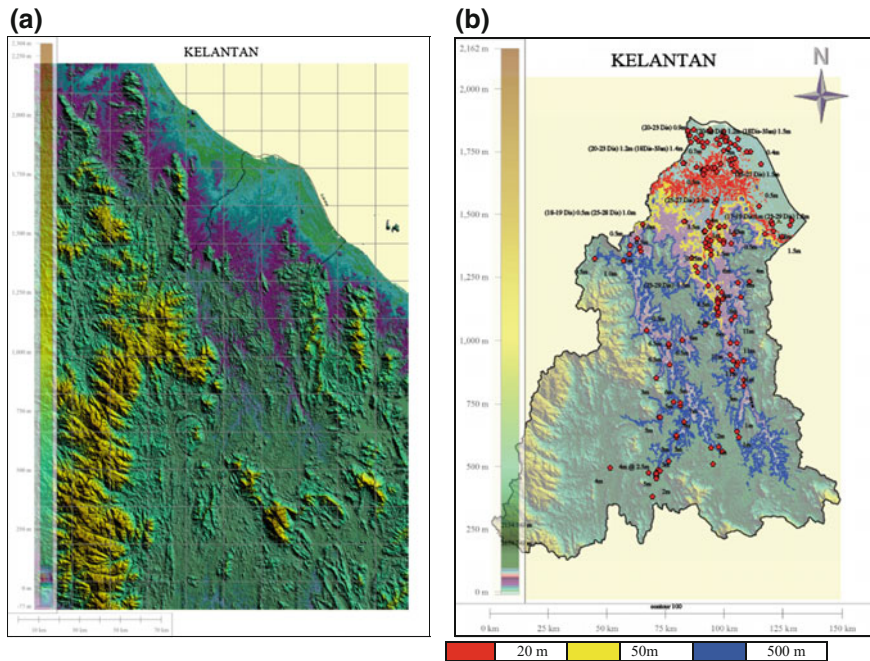
Geologically, the Kelantan state is underlain by four rock types (Fig. 1a): (1) granitic rocks; (2) sedimentary and meta-sedimentary rocks; (3) volcanic rocks; and (4) unconsolidated sediments. Granitic rocks of the boundary range fence the eastern border of Kelantan with the Terengganu state. Felsic intrusive granite belonging to the main range forms the mountainous region in the southwest and western part of the state. The Silurian-Ordovician meta-sediments encircle the main



**Fig. 1** a Geological map of Kelantan, showing the major rock types within the state. *Courtesy of JMG*; b Terrain map (Google map) of Kelantan, showing the southern highland areas and the northern delta plain. The numbers at the different locations are showing the level of floodwaters during the peak of the 2014–2015 flood

range granite in the southwest; these are schists, phyllites, and slates. These areas are marked by steep gradients and are covered by soils such as alluvium, clay-loam-sand soil which support thick tropical forest. Permian and Triassic sedimentary rocks occupy areas in the central, highland valley of Kelantan, and the region is characterized by high-to-moderate gradients. The rocks here are shales, sandstones, conglomerate, quartzite, limestone, siltstone, and mudstone. Permian volcanic rocks have been mapped in the southeast, bordering the boundary range granite. Quaternary alluvium (i.e., gravel, sand, silt, and clay) covers much of the northern, Kota Bharu–Tumpat–Pasir Mas areas. Topographically, coastal-flood plain region shows elevation less than 75 m above mean sea level.

The generated Digital Elevation Model (DEM) map, supported by satellite images, clearly displays the geomorphology and topography of the Kelantan state. In general, the southern part of Kelantan (Gua Musang and Kuala Krai area) is marked by high elevation, while the northern parts around the area of Kota Bharu, Pasir Puteh, Tumpat, Bachok, Pasir Mas, and Tanah Merah is characterized by gentle-to-flat topography. Detailed examination of the DEM allows us to delineate



**Fig. 2** **a** DEM geomorphological, terrain map of Kelantan. This geomorphological framework channels surface waters from the mountainous and highland areas in the south toward the north-northeast delta plain of Pasir Mas–Kota Bharu–Tumpat areas; **b** Interpreted DEM map of Kelantan, defining the different elevation zones. *i* The mountainous region in the west and southeast. This region, characterized by granitic mountains, shows elevation of 500 m to the highest point of 2157 m; *ii* The highland areas around Dabong–Kemubu–Manek Urai–Kuala Krai are between 50 and 500 m high; *iii* The foothill zone of Tanah Merah–Machang with elevation between 20 and 50 m, and *iv* The flat, floodplain and coastal-deltaic plain stretching around Pasir Mas–Kota Bharu–Tumpat

at least four (4) geomorphic zones: (i) the mountainous region in the west and southeast. This region is characterized by granitic mountains, with elevations from 100 m to the highest point of 2157 m; (ii) The highland areas around Dabong–Kemubu–Manek Urai–Kuala Krai are between 30- and 100-m elevation; (iii) The foothill zone of Tanah Merah–Machang, with elevation between 15 and 30 m, and (iv) The flat, floodplain, and coastal-deltaic plain stretching around Pasir Mas–Kota Bharu–Tumpat with elevation less than 15 m (Fig. 2a, b).

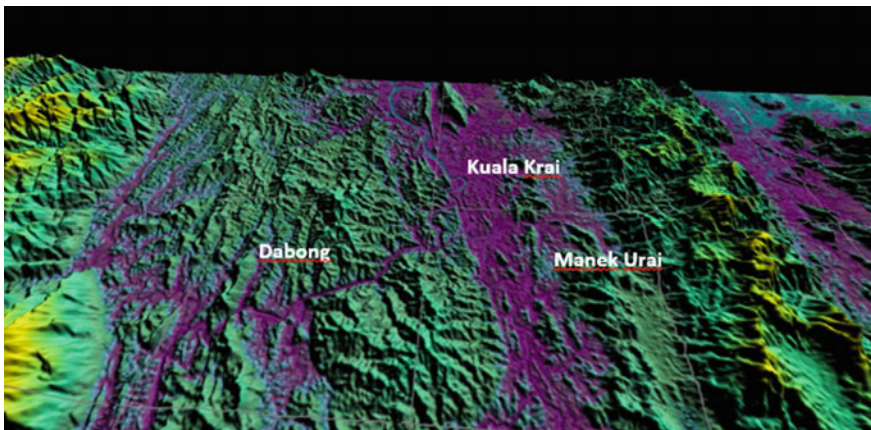
This geomorphological framework channels surface waters toward the north-northeast, from the mountainous and highland areas in the south to the flat-lying coastal-deltaic plain of Pasir Mas–Kota Bharu–Tumpat areas. From the Digital

Elevation Model (DEM) map, the geomorphology of Kelantan can be clearly seen where the southern part of Kelantan (Gua Musang and Kuala Krai area) is more hilly with high elevations and toward the northern parts of Kelantan which covers the areas of Kota Bharu, Pasir Puteh, Tumpat, Bachok, Pasir Mas, and Tanah Merah; the elevation are lower since it is near to coastal region. This lowland geomorphology allows an escape route for the water and later transported to the nearby delta before escaping to the sea which is the main basin (Fig. 2a).

The Sungai Kelantan emerges at the confluence of the Sungai Galas and the Sungai Lebir near Kuala Krai and meanders over the coastal plain, until it finally reaches the South China Sea, approximately 12 km north of Kota Bharu. The Sungai Galas and the Sungai Lebir themselves have many tributaries, which provide the flow into the main Sungai Kelantan. These tributaries rise in the forested mountains of Peninsular Malaysia. Four major towns are located along the Kelantan River including Kota Bharu, Pasir Mas, Tumpat, and Kuala Krai. The Kota Bharu sub catchment is one of the major flood-prone areas in Sungai Kelantan Basin. Meanwhile, data from Drainage Irrigation Department [2] shows the last 2014/2015 flooding areas are situated at valleys which became escape routes for the water (Fig. 2).

### 3.1.2 The Southern Upstream Highlands Area Lojing–Gua Musang–Kuala Krai

SRTM DEM data show the existence of geological obstacle features in southern parts of Kelantan area such as Dabong, Manek Urai, and Kuala Krai as shown in Fig. 3 and can be identified under the image whereby the river flows through a



**Fig. 3** Location geological obstacle features in Dabong, Kuala Krai, and Manek Urai. *Source* DEM image

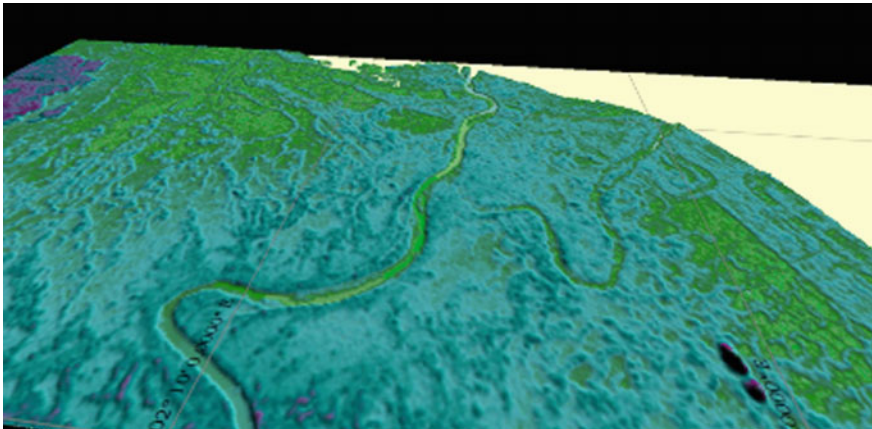


narrow or obstructed section from catchment area. It could assist to decelerate the water flow to Sungai Kelantan in the event of floods and long duration rainfall. However, the obstacles will accelerate the rise of flood level in southern upstream highland area [3].

### 3.1.3 The Northern Kelantan Delta Plain–Kota Bharu

The fluvial geomorphology at the Kelantan Delta area is meandering since it is located at downstream area. Besides the fluvial geomorphology, this area seems shallower with u-shaped channel compared with the upstream fluvial geomorphology. Therefore, the fluvial can only support only a small volume of water. Moreover, the aggressive urbanization increases within the floodplain area forcing the flooding to occur.

An ancient riverbed located in the middle of Kota Bharu district was identified by SRTM DEM data (Fig. 4). The ancient relic riverbed is identified to be appropriate route for the water flow in order to minimize the effect of floods in the Kota Bharu area. The ancient riverbed could be a natural pond for the residents, and dredging works has to be carried out [3].



**Fig. 4** DEM of Sungai Kelantan that shows the ancient riverbed

### 3.2 Climate Change and Rainfall Trends

#### 3.2.1 Recent Climate Change and Its Impact on Rainfall

Figure 5 shows that the global temperature changes occur on land and ocean. The graph seems increasing drastically starting from 1980s. The effect of warming water and melting ice on sea-level rise are expected to vary depending on location, where some places are expected to see higher-than-average increases, and a few places may even see decreases.

According to NASA, the consequences of global sea-level rise could be even more frightening than the worst-case scenarios predicted by the dominant climate models, and the sea level is already rising without knowing the speed of the water rise. Meanwhile, 97% of climate scientists agreed that the rate of global warming trends the planet is now experiencing is not a natural occurrence, but is primarily the result of human activity.

Kelantan state can be classified as relatively humid, with mild winds and heavy monsoonal rainfall during the NE monsoon season when the high-velocity NE winds bring heavy rain to this area. About 40% of the annual rainfall received in the Kelantan catchment can be divided into two climate regions according to its land surface elevation and effect of rainfall: The first is northern Kelantan region climate or the coastal area (lowland) and secondly, southern Kelantan region or the rural

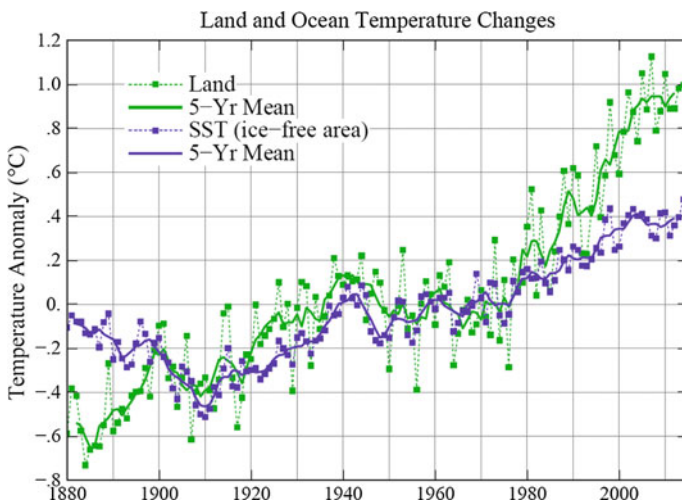
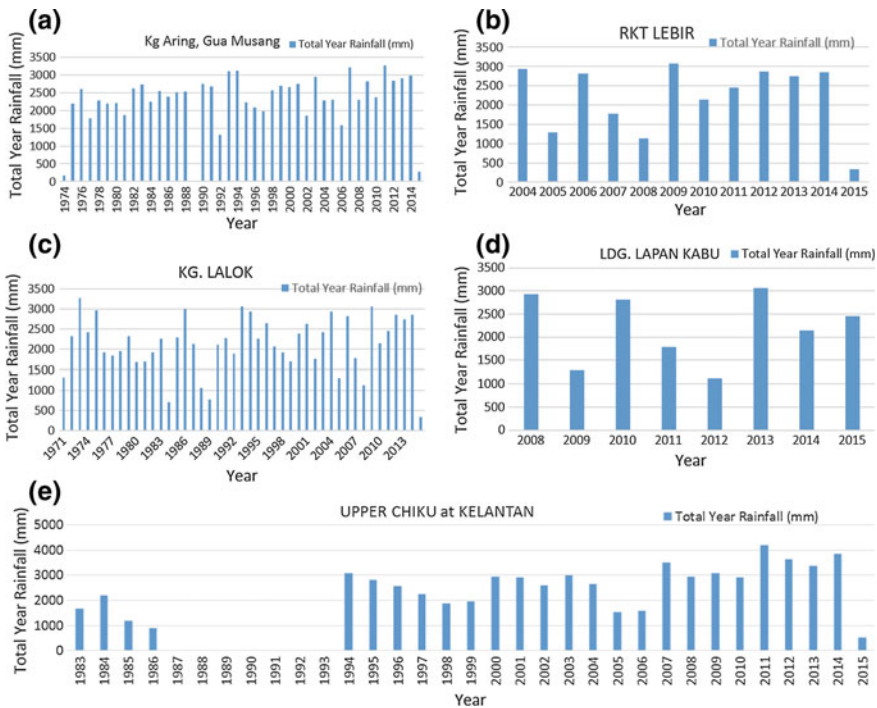


Fig. 5 Global land and ocean temperature changes

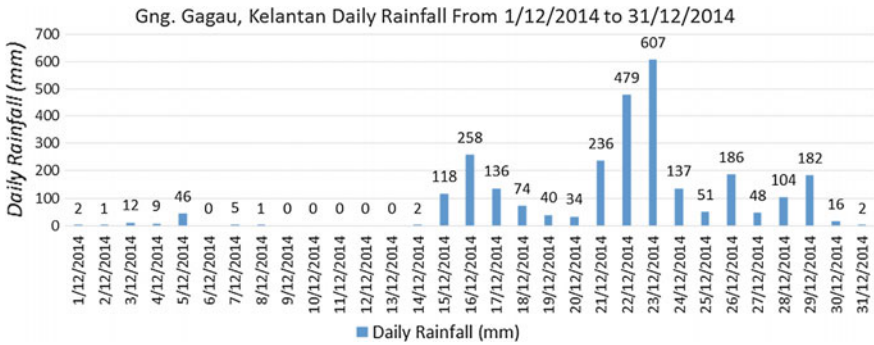
area (highland). The northern Kelantan climate is normally associated with relatively stable climate conditions (i.e., dry and wet conditions through the year). Meanwhile, the southern Kelantan region is associated with relatively cooler climate and less rainfall compared to the northern region. But during 2014/2015, southern Kelantan experienced heavier rainfall compared to the northern region. This heavy rainfall at the highland area contributed to the high stream flow of Sungai Galas and Sungai Lebir which are located at the southern parts of Kelantan.

### 3.2.2 Medium-Term Rainfall Trends in Kelantan (1970s–2014)

Figure 6 shows total year rainfall (mm) from the previous years starting from 1970s until 2014 at 5 rainfall stations located at Kg Aring, Gua Musang, RKT Lebir, Kg Lalok, Ldg Lapan Kabu and Upper Chiku, Gua Musang. From the graphs, we can see that the rainfall distribution throughout years is having the same pattern. There are no drastic differences in total yearly rainfall volume in 2014 when compared to



**Fig. 6** Total year rainfall (mm) in **a** Kg. Aring, Gua Musang; **b** RKT Lebir; **c** Kg. Lalok; **d** Ldg. Lapan Kabu, and **e** Upper Chiku. *Source* JPS



**Fig. 7** Daily rainfall in the Gunung Gagau from December 1, 2014, to December 31, 2014. Source JPS

the previous years, although flooding event in 2014 was marked as the most catastrophic flooding event that had occurred in Kelantan. Therefore, rainfall is not the only reason that contributes to the flooding event.

**3.2.3 Short-Term Rainfall Trends in Kelantan (2010–2014)**

Precipitation in Kelantan state is not uniformly distributed throughout the year. Two weather conditions are experienced in this area: a wet period and a dry period. As described earlier, wet conditions coincide with the NE monsoon. In the extreme NE, monsoon season rainfall has been recorded of about 100–300 mm per day [4]. The dry period normally is characterized by weak prevailing winds or usually by calm atmospheric conditions. In 2006, the mean annual rainfall for Kelantan was recorded as 326.7 mm, with maximum rainfall received of 654.4 mm in December (during monsoon) and minimum rainfall of 114.2 in March [5].

The flooding that occurred in 2014/2015 was caused by heavy rains brought by the northeast monsoon winds blowing from November to March each year. Floods in 2014 showed the total rainfall in December 2014 in rural areas was more dense (>60 mm) than the coastal areas [4]. Heavy rain began to fall at Gunung Gagau on December 16, 2014 (refer Fig. 7), in which a total of 6648.0 mm in the coastal areas have been covered by 6 new stations in Kota Bharu, Tumpat, Pasir Mas, Machang, Bachok, and Pasir Puteh, while in rural areas of 7373.0 mm, which also includes 6 stations, namely Dabong, Jeli, Gua Musang, Lahoh, Aring, and Gunung Gagau for the month of December (Table 2). Continuous heavy rains were recorded until early January the stations involved.

**Table 2** Percentage of total annual rainfall in Kelantan (December 2014)

No.		Station	Month												Total
			January	February	March	April	May	June	July	August	September	October	November	December	
1		Kota Bharu @ Jet Kastam	80.0	2.0	30.0	6.0	127.0	146.0	74.0	239.0	121.0	264.0	837.0	994.0	2920.0
2		Tumpat @ Pengkalan Nangka	69.0	1.0	58.0	8.0	75.0	118.0	138.0	140.0	137.0	278.0	660.0	803.0	2485.0
3		Pasir Mas @ Kasar	135.0	0.0	39.0	0.0	75.0	193.0	148.0	166.0	112.0	367.0	586.0	959.0	2780.0
4		Machang @ Kusial	316.0	6.0	58.0	40.0	117.0	195.0	221.0	283.0	237.0	280.0	487.0	1686.0	3926.0
5		Bachok Serdang Gunung Barat	45.0	0.0	30.0	1.0	152.0	312.0	120.0	237.0	165.0	216.0	1021.0	970.0	3269.0
6		Pasir Puteh g Bkt. Gedombak	262.0	1.0	60.0	21.0	122.0	176.0	234.0	314.0	443.0	197.0	816.0	1236.0	3882.0
		Total rainfall monthly	907.0	10.0	275.0	76.0	668.0	1140.0	935.0	1379.0	1215.0	1602.0	4407.0	6648.0	19262.0
		Coastal average	151.17	1.67	45.83	12.67	111.33	190.00	155.83	229.83	202.50	267.00	734.50	1108.00	3210.33
		Accum. coastal average	151.17	152.83	198.67	211.33	322.67	512.67	668.50	898.33	1100.83	1367.83	2102.33	3210.33	
1		Da bong	178.0	0.0	16.0	0.0	146.0	129.0	56.0	427.0	258.0	227.0	262.0	967.0	2666.0
2		Jeli	432.0	6.0	225.0	245.0	368.0	251.0	198.0	446.0	301.0	451.0	442.0	1542.0	4907.0
3		Gua Musang	136.0	3.0	196.0	169.0	225.0	215.0	90.0	618.0	489.0	313.0	175.0	591.0	3220.0
4		Laloh	152.0	8.0	74.0	98.0	199.0	73.0	151.0	282.0	172.0	148.0	354.0	706.0	2417.0
5		Aring	174.0	5.0	251.0	144.0	206.0	251.0	130.0	306.0	495.0	545.0	233.0	881.0	3621.0
6		Gunung Gagau	171.0	22.0	208.0	59.0	461.0	192.0	317.0	341.0	562.0	252.0	576.0	2686.0	5847.0
		Total rainfall monthly	1243.0	44.0	970.0	715.0	1605.0	1111.0	942.0	2420.0	2277.0	1936.0	2042.0	7373.0	22678.0
		Rural area average	207.17	7.33	161.67	119.17	267.50	185.17	157.00	403.33	379.50	322.67	340.33	1228.83	3779.67
		Accum. rural area average	207.17	214.50	376.17	495.33	762.83	948.00	1105.00	1508.33	1887.83	2210.50	2550.83	3779.67	
		Total average	179.17	4.50	103.75	65.92	189.42	187.58	156.42	316.58	291.00	294.83	537.42	1168.42	
		Total accum. average	179.17	183.67	287.42	353.33	542.75	730.33	886.75	1203.33	1494.33	1789.17	2326.58	3495.00	

Source JPS

## 4 Conclusion

The *Upstream, highland flood* is marked by maximum high waters of 11.0 m in Kuala Krai–Manek Urai areas. The main and major cause for this flood is the uncontrolled deforestation in the southern catchment, Ulu Kelantan areas. Increasing the impact of deforestation is the current (2014–2015) region-wide replantation of oil palms in Gua Musang–Lojing areas. This is recorded by satellite images and manifested by the excessive log debris in the rivers during and after the 2014 flood. The rapid rise of the river water level was due to the (1) rapid discharge of water from the upstream, barren highlands; (2) shallowed river channels due to the sedimentation of eroded soils; and (3) formation of temporary dams by accumulated log debris.

The *Lowland, Kelantan delta flood* is an annual event. It is widely recognized that this lowland flood is caused by excessive floodplain urbanization and river engineering, without proper drainage system. An immediate solution to this flood is the construction of suitable drainage system for the Kota Bharu town. An ancient riverbed (paleochannel) located in the middle of Kota Bharu district was identified by SRTM data. The relic paleochannel is identified to be the appropriate route for the water flow in order to minimize the effect of flood in Kota Bharu area. Further study of SRTM data will be beneficial to produce the geomorphology map of Kelantan and to improve the understanding of the flood behavior in Kelantan.

The *flood management strategies* that can be done to solve the problems are by improving the drainage system. Removing the excess sediments and also by cleaning the river system, so that the space for the water flow can be reclaimed, can increase the efficiency of the drainage system. The deforestation project should be stopped in the area which is potentially the large catchment area for the rainfall which is usually happened to be hill or highland area. The logging activities should be limited to the lowland area and stopped in the critical area which is prone to the erosion. The planning for any activity which is potential can disrupt the water drainage and should be revised so that there will be no more problem regarding the drainage system.

**Acknowledgements** The authors wish to express their gratitude for funding from the FRGS-MOE 2015-1 Flood Disaster Management Grant (FRGS/1/2015/STWN06/UTP/02/2) for making this research possible, and the Research Innovation Office of Universiti Teknologi PETRONAS (UTP) for facilitating the research.

## References

1. Adnan, N.A., and Atkinson, P.M., 2011. Exploring The Impact of Climate and Land Use Changes on Streamflow Trends in A monsoon Catchment. *International Journal of Climatology*, 31: 815–831.
2. DID (Drainage and Irrigation Department), 2014/2015. Annual Flood Report of DID (2014/2015) for Kelantan. Unpublished Report DID. Kelantan.

3. Hidayat M. Y., M. Naufal. M. B., Matthew. N., Abdullah. A., 2015. Application of Light Detection and Ranging (LiDar), Interferometric Synthetic Aperture Radar (IFSAR) and Shuttle Radar Mission (SRTM) Topography Technology to Understand Flood Behaviour of Kelantan State.
4. DID (Drainage and Irrigation Department), 2016. Rainfall Data.
5. DID (Drainage and Irrigation Department), 2004/2005. Annual Flood Report of DID (2004/2005) for Kelantan. Unpublished Report DID. Kelantan.

# Nano Additives in Water Based Drilling Fluid for Enhanced-Performance Fluid-Loss-Control

Ali Samer Muhsan, Norani M. Mohamed, Usman Siddiqui  
and Muhammad U. Shahid

**Abstract** Drilling fluid which is also known as drilling mud is a crucial element in oil and gas exploration process as it used to aid the drilling of boreholes into the earth. Among other functions, drilling fluid needs to carry drill cuttings to the surface of the well, support the walls of the well bore, provide hydrostatic pressure to prevent formation fluids from entering into the well bore, cool and lubricate the drill bit, prevent drill-pipe corrosion, facilitate the attainment of information about the formation being drilled, and create a thin low-permeability cake that protects permeable production formations. Water-based mud (WBM) is the most common drilling fluid used in oil industry. WBM is an expensive complex chemical system that is usually mixed with filtration-loss-prevention additives such as clay, lignite, or organic polymers, with bentonite clays being very common to control the fluid-loss during drilling process. These traditional additives are able to give an average fluid loss of 7.2 mL over 30 min and leaving a filter cake  $\sim 280 \mu\text{m}$  thick. Graphene, as a single layer of graphite which is also considered nano-additive, has become the subject of much research interest for its unique materials properties. A pristine graphene monolayer has a theoretical surface area of  $2965 \text{ m}^2/\text{g}$  and has been shown to form a membrane impermeable even to helium gas. This work presents the recent progress of using nano-materials such as graphene as an additive in WBM. Most recent report showed that graphene has the potential to decrease the fluid loss by  $\sim 15\text{--}20\%$  (due to its large surface area with very thin 2D layer, only 1 atom thick) compared to that of WBM with conventional additives, and to reduce

---

A.S. Muhsan (✉) · U. Siddiqui  
Petroleum Engineering Department, Universiti Teknologi PETRONAS,  
32610 Seri Iskandar, Perak, Malaysia  
e-mail: alisameer2007@gmail.com; ali.samer@utp.edu.my; ali.samer@petronas.com.my

N.M. Mohamed · M.U. Shahid  
Fundamentals and Applied Sciences Department, Universiti Teknologi PETRONAS,  
32610 Seri Iskandar, Perak, Malaysia



the filter cake thickness up to  $\sim 20\text{--}50\ \mu\text{m}$ , which in turn can help to increase the oil production rate. In addition, adding graphene to WBM solutions is expected to lead to greater shear thinning and higher temperature stability compared to clay-based fluid loss additives.

**Keywords** Graphene • Nano-additives • Water-based mud • Fluid loss control

## 1 Introduction

The chemicals and additives used in the formation of a drilling fluid play a significant role in the preparation of mud, though the aspects of choosing the drilling mud and additives are complicated. The additives must focus on to cope with the drilling challenges in a cost-effective manner and reduction in exploitation risk. The formulation of drilling mud with the addition of one nano-material additive with specific properties and characteristics is likely to mitigate challenges and hazards such as sour gas environment, deep and geothermal drilling, shallow water flow problems, unconsolidated formation, borehole instability, lost circulation, torque and drag, pipe sticking, gumbo and bit balling, gas hydrates zone, and HPHT environment. Furthermore, nano-additive increases ROP significantly with the reduction of solid materials in the drilling fluid, and they are also influenced on the rheological properties of fluid such as plastic viscosity, yield point, and gel strength.

The major challenge that occurs during drilling is the loss of fluids that escapes into the formation as the fluid encroachment on the porous formation can result in reservoir damage, and drilling fluid in the hydrocarbon flow path can result in formation collapse or reduction in productivity. The majority of the additives used are conventional micro or macro which is less stable than nano-material, and industries are more conscious about the drilling challenges occurring; thus, they require more stable additives.

The focus of this research is to use a nano-additive in water-based drilling mud which can form a barrier to avoid the infiltration of drilling fluid into the formation due to its high specific surface area with an enormous area of interaction. For this, a nano-additive of graphene oxide can form a thin film which is directly associated with the drilling time and cost and differential torque required to rotate drilling pipe.

The available research and information proves that graphene oxide is the effective nano-additive to control fluid losses in water-based mud, and when methylating the graphene oxide through esterification process, a much more stable graphene oxide is produced and well productivity is increased due to its unique properties of forming non-erodible, thin and impermeable mud cake.

## ***1.1 Drilling Fluids***

Drilling mud also known as drilling fluid is a crucial element in the building of the well that is circulated in the well bore through the drilling process. Besides, the major functions of drilling fluid are to transmit drill cuttings to the surface, to cool and lubricate the drilling bit, to prevent drill-pipe corrosion, to protect the walls of the well bore from low-permeability, mud to protect producing formation.

The oil industry faces severe drilling challenges, depending on pressure profile, geographical location, geological history, and features of the formation. The drilling challenges that occurs like shallow water flow problem, poorly consolidated formations, lost circulation of drilling mud, increase in torque and drag, differential pipe sticking, bit balling in gumbo shale, blowout situation in subsurface hydrate-bearing zones, emission of deadly acidic gases ( $\text{CO}_2$  and  $\text{H}_2\text{S}$ ), high pressure, and high temperature wells not only results in the rise of the cost but also results in the abandonment of the well. Due to these severe drilling challenges, oil industry today focuses on different factors for the preparation of drilling mud, such as the mud must be thermally stable, biologically degradable, mechanically strong, physically small, environmental friendly, and must be of minimal cost.

## ***1.2 Fluid Loss Control***

The macro- and micro-based material does not possess much potential to tackle the drilling challenges. Thus, an addition of nano-additive due to its ultrafine size, higher surface area-to-volume ratio, gelling and suspension properties, thermal conductivity, tolerance to high pressure and temperature, capability of creating thin mud cake, sealing and strengthening potential and lower concentration requirement could offer solutions to the problems associated with drilling operation and increase the benefits of petroleum production.

The loss circulation of the drilling fluid is the major and the frequent challenge that occurs in the wells. The loss circulation may be due to highly consolidated sand formations, in situ stresses in the vicinity of thief zone or due to use of improper mud weight, in formation with narrow mud weight window [1]. The prevention of fluid losses by macro- or micromaterial shows minimal success and makes job extremely difficult, thus resulting in borehole collapse and decrease in productivity due to the presence of drilling mud in hydrocarbon flow path. A nano-additive used for fluid loss control forms a filter cake due to its potential to form a structural barrier according to the paths around the well bore to stop the invasion of the drilling mud into the formation. An ideal nano-additive is very effective at low concentration, and a constant dispersion in brine solutions [2] is developed.

### ***1.3 Nano-Materials and Nano-Additives***

Nano-materials are extremely fine particles and nano-scale particle dimension, smaller than microparticles but larger than an atom cluster and so have a high specific surface area with vast area of interaction. Nano-materials provide higher fluid properties at an extremely reduced or low additive concentration. Nano-materials also possess inhibition potential, whether it is external or internal [3].

Nano-material is classified as single functional or multifunctional on the basis of their functions. A single functional nano-additive can perform single job in the fluid systems, whereas multifunctional nano-additive can perform multiple tasks with an intense decrease in drilling mud cost and as well as the reduction in chemical and solid contents of the fluid [1].

### ***1.4 Nano-Additives in Oil and Gas Exploration***

Drilling fluids that comprise at least one additive with particle size in the range of 1–100 nm are defined as nano-based drilling fluids. Therefore, the application of nano-additive in formulating oil- and water-based mud has the potential to mitigate the drilling challenges faced now and in future. The large surface area-to-volume ratio of nano-materials when compared to the macro- and micromaterials has decreased the borehole challenges. The ability of nano-additive to form well-dispersed plastering effect on the borehole wall improves the performance of drilling and drilling fluid [4]. For example, the huge surface area-to-volume ratio of nano-based mud additive improves the thermal conductivity of nano-based fluids. Therefore, the improved thermal conductivity of drilling mud cools the drill bit efficiently. In particular in high-pressure and high-temperature environment, excessive equipment failure occurs due to poor heat transfer and thermal degradation effect of high temperature. In this case, the formulation of nano-based drilling mud with nano-additive possessing high thermal stability and heat transfer can minimize cost dramatically associated with equipment repair, failure, or replacement or equipment damage.

The wear and tear of down drilling equipment is a major challenge occurred while drilling, particularly in horizontal, deviated, and extended wells. One of the major factor contributing to this is abrasiveness of drilling fluid and cuttings. Because of very minute size of nano-materials, the wear and tear of down hole equipment due to the abrasive action of the nano-sized material is minor because of less kinetic energy impact of nano-particles as compared to micro- and macroparticles.

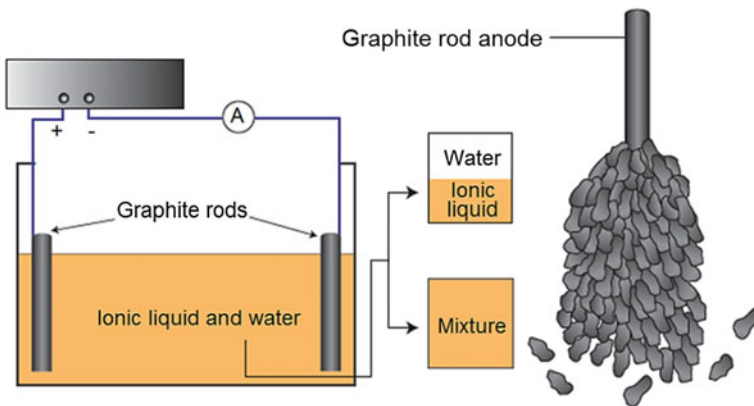
Along with wear and tear problem, the loss circulation of the drilling fluid is also the major problem because this problem is frequently observed. The loss circulation may be due to extremely consolidated sand formations, in situ stresses in the vicinity of thief zone or as a result of using incorrect mud weight [5]. The inhibition of fluid losses through macro- or micromaterial indicates negligible success and makes drilling very challenging, thus resulting in borehole damage. A nano-additive designed for fluid loss control forms a thin filter cake around the well bore to avoid the infiltration of drilling fluid into the formation.

From an environmental point of view, the use of nano-material in drilling mud design may turn a nano-based mud highly environment friendly due to its low concentration.

## 2 Experimental

### 2.1 Preparation of Graphene and Graphene Oxide in Flakes Shape

Various techniques to produce graphene and graphene oxide via chemical/physical method (top-down approach) will be investigated. The main focus will be on techniques that are capable to produce graphene and graphene oxide in aqueous solutions such as electrochemical intercalation (see Fig. 1) and electrolytic exfoliation.



**Fig. 1** Schematic illustration of graphene synthesis using electrochemical intercalation

## 2.2 Potential of Using Graphene as an Additive for Fluid Loss Control in Drilling Process

Graphene as a single layer of graphite has become an area of interest due to its distinctive properties and large surface area. Due to its great sealing ability, it acts as the best pore-plugging filter in drilling fluids. High-pressure graphene sheets form a barrier to prevent encroachment of drilling mud on the formation. While lowering the pressure during production phase of hydrocarbon, the hydrocarbon pushes the barrier off the bore wall formed by the graphene as shown in Fig. 1. The large graphene shavings create difficulties in water-based mud on dispersing in aqueous medium. However, oxidized graphene obtained from graphite oxide acts as a more stable material for dispersion in aqueous medium, thus forming the filter cake on the formation [6]. This could be beneficial for making a thin impermeable film, to prevent fluid loss in the well bore as shown in Fig. 2. Since GO sheets are well exfoliated, they could be used at substantially lower concentrations than clay-based additives to obtain the desired performance. More importantly, the nano-meter thickness of the GO flakes could also result in much thinner filter cakes than that obtained using clay-based materials. The thickness of a well bore's filter cake is directly and strongly correlated with the differential torque needed to rotate the pipe during drilling, to the drilling time and to drilling costs [7]. GO is further appealing in that it offers the prospect of an environmentally friendly and inexpensive technology [8, 9].

Furthermore, chemical processes of graphene oxide result in better performance in drilling mud. For instance, esterification of graphene oxide can make drilling mud more stable in saline solutions. However, methylated graphene oxide (MeGO) is used in high-salinity water-flooding media because graphene oxides precipitate in highly saline solution. On combining larger flakes of graphene oxide with

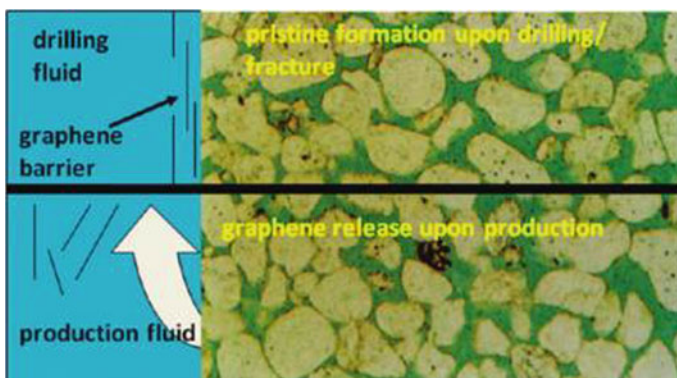


Fig. 2 Graphene barrier on high and low pressure

powdered graphene oxide as a reinforcing agent, filtration properties are increased. At low concentration of 4 g/L by carbon content, the mixture resulted in less filtration loss and thin filter cake [2].

### 3 Conclusion

Using graphene and graphene oxide as an additive in WBM is expected to decrease the fluid loss by  $\sim 15\text{--}20\%$  compared to that of WBM with conventional additives and to reduce the filter cake thickness up to  $20\text{--}50\ \mu\text{m}$ , which in turn helps to increase the oil production rate. Adding GO to WBM solutions can also result a greater shear thinning and higher temperature stability compared to clay-based fluid loss additives, demonstrating potential for high-temperature well applications. However, an alternative mixing technique of graphene oxide as stable additives with improved dispersion in saline and fresh WBM should be proposed.

**Acknowledgements** The authors would like to thank “Universiti Teknologi PETRONAS” for providing funds and laboratory facilities to support this project.

### References

1. Moore, P. L. *Drilling Practices Manual*; the Petroleum Publishing Co.: Tulsa, OK, (1974).
2. Ayotamuno, M. J., et al. “Chromium removal from flocculation effluent of liquid-phase oil-based drill-cuttings using powdered activated carbon.” *Applied energy* 84.10 (2007): 1002–1011.
3. Kosynkin, Dmitry V., et al. “Graphene Oxide as a High-Performance Fluid-Loss-Control Additive in Water-Based Drilling Fluids.” *ACS applied materials & interfaces* 4.1 (2011): 222–227.
4. Patel, Arvind D., Emanuel Stamatakis, and Eric Davis. “Shale hydration inhibition agent and method of use.” U.S. Patent No. 6,247,543. 19 Jun. 2001.
5. Allen, Matthew J., Vincent C. Tung, and Richard B. Kaner. “Honeycomb carbon: a review of graphene.” *Chemical reviews* 110.1 (2009): 132–145.
6. Luo, Jiayan, et al. “Graphene oxide nanocolloids.” *Journal of the American Chemical Society* 132.50 (2010): 17667–17669.
7. Ayotamuno, M. J., et al. “Chromium removal from flocculation effluent of liquid-phase oil-based drill-cuttings using powdered activated carbon.” *Applied energy* 84.10 (2007): 1002–1011.
8. Salas, Everett C., et al. “Reduction of graphene oxide via bacterial respiration.” *ACS nano* 4.8 (2010): 4852–4856.
9. Segal, “Selling graphene by the ton.” *Nature nanotechnology* 4.10 (2009): 612–614.

# Effect of Different Injection Rates of Biopolymer Drag-Reducing Agent (DRA) on Formation Permeability

Muhammad Luqman Bin Hasan, Jagathesh Jantararas  
and Juhairi Aris B. Mohd Shuhli

**Abstract** At point of depletion in a reservoir, secondary recovery methods such as water injection are usually introduced to combat the pressure decline within the reservoir and increase well production. However, water injection systems are subjected to form of pressure drop due to an opposing drag force acting along the injection wellbore and formation resulting in the requirement additional pumps. An efficient solution to this problem is to add drag-reducing agents (DRAs) which can effectively reduce drag in this system, thus maintaining the pressure. The problem arises when the available DRA such as surfactants and synthetically produced polymers pose a threat to the environment as they easily seep into the formation and accumulate overtime. Therefore, this study will concentrate on extracting DRA from a natural source (coconut residues) to substitute synthetic and chemically produced DRA with a natural DRA known as carboxymethyl cellulose (CMC). A water injection system faces another crucial problem which is formation permeability reduction due to the mechanical erosion and skin development within the formation and wellbore. Therefore, a benchtop permeability test is run at 3 injection rates of DRA (1 and 5 cc/min) to investigate the change in permeability at different injection rates of DRA. The test is run using CMC as well as a synthetic polymer known as polyacrylamide (PAM). The results are then compared and quantitatively analysed. It is found that at low injection rates, the CMC biopolymer DRA causes a smaller permeability drop within the core sample, whereas at higher injection rate, the CMC biopolymer DRA causes a larger permeability drop within the core when compared to the synthetic PAM DRA. These findings also show that the CMC biopolymer DRA can retain its molecular structure better as compared to PAM DRA at higher injection rates.

**Keywords** Drag-reducing agent (DRA) · Polyacrylamide (PAM) · Coconut residue · Permeability reduction

---

M.L.B. Hasan (✉) · J. Jantararas · J.A.B.M. Shuhli  
Universiti Teknologi PETRONAS, 32610 Darul Ridzuan,  
Seri Iskandar, Perak, Malaysia  
e-mail: luqman.hasan@petronas.com.my

## 1 Introduction

When reservoirs approach depletion, it experiences a large pressure drop as compared to its early production history. In addition, water production would increase as the reservoir matures (Muda et al. n.d). In order to maximise hydrocarbon production, most oil and gas companies will result in the usage of secondary recovery methods such as water injection to aid the reservoirs to drive mechanism and increase the reservoir pressure. According to a paper written by Rochan et al. [5], there are many oil fields that use water injection to perform two major roles which are sweeping oil towards the production wells and maintaining pressure. Water injection is one of the most common and efficient available methods as it is able to increase the pressure in the reservoir and ensure production continues at a higher rate. However, the efficiency of this method is compromised by the presence of drag. Drag causes a restriction in flow that in turn reducing the pressure of the system.

Drag occurs when a fluid flowing through a space is opposed by object around it. In the case of water injection wells, the injected water is opposed by the walls of the wellbore and the formation pore spaces. In pipelines and injection wells, the drag force becomes more prominent when a turbulent flow of fluid is present. Therefore, drag-reducing agent (DRA) is used in water injection systems in order to maintain the pressure with minimal exertion by the mechanical equipments such as pumps. The concept of drag reduction is applied widely especially in the oil and gas industry due to the ability to prevent large pressure drop with a small amount of DRA [1].

DRA comes in different forms. In paper written by Truong [6], the different types of DRA include polymer solutions, surfactants, microbubbles, electromagnetic turbulence control, and hybrid methods which use any of these combinations. During water injection, synthetic polymer used as DRA can seep into the ground or formation and cause detrimental effect as they accumulate in excess [2]. Therefore, the solution to this issue is to use biopolymers which are biodegradable. Therefore, this study will investigate on the potentials of carboxymethyl cellulose (CMC) that can be synthesised from coconut residues which are used as a substitute for synthetic polymers. The advantages of using this biopolymer are cost-efficient and environmentally friendly. This study mainly focuses on different injection rate of water with biopolymer and how it affects the permeability ( $k$ ) of the formation.

## 2 Research Methodology

### 2.1 *Synthesising Carboxymethyl Cellulose (CMC)*

The process of synthesising biopolymer CMC from coconut husk is divided into 2 stages: (1) basification (alkalisation) and (2) esterification (carboxymethylation).

- (1) **Basification Stage:** Accumulated coconut residues are dried in the oven at 60 °C for 24 h. The dried coconut residues are then cooked and stirred with 1 M of



sodium hydroxide (NaOH) in 1 litre (L) beaker for 1 h (h) at temperature of 100 °C. A reddish residue is obtained and washed with water and dried in the oven at 60 °C for 24 h. After drying for 24 h, the residue is weighed and dried every 1 h until there is no longer any weight reduction. A measured weight of 40 g of dried cellulose is stirred with 100 ml of 60% concentration NaOH and 900 ml of Isopropanol for 0.5 h.

- (2) **Esterification Stage:** 36.0 g of monochloroacetic acid of 99% concentration is then added and stirred for another 30 min. The mixture is then left to settle for 4 h until it is observed that there is a separation of solid and liquid phases. The solid residues are separated from the liquid and suspended in 100 ml of 70% concentration ethanol for overnight. Glacial acid is then added as a part of a neutralisation process of the solid residues in the methanol. The solid residues are then filtered out and suspended in 70% concentration ethanol for 10 min (min) to remove unwanted products. Then, the solid residue is washed using 300 ml of methanol until the residue looks clean. This residue is then dried in the oven at 60 °C for 24 h. The CMC produced is grinded to a fine powder form using a mortar grinder. The process is then repeated for 5 cycles to observe the trend for the amount of CMC that can be produced from the process.

## 2.2 *Titration to Determine CMC Concentration*

The procedure is adopted from a previously done study of CMC extraction from Sagu plants by academics of Monash University Malaysia and University Putra Malaysia. The process flow for producing acid carboxymethyl is as follows: A portion of the CMC product is added to 60 mL of 95% ethanol and stirred for 1 h. 10 ml of nitric acid of 2 M concentration is then added and stirred for 2 min. The mixture is then heated and stirred further for 15 min. It is then left to settle until a solid precipitate phase and liquid phase are observed. The solid precipitate is then filtered out from the liquid. This precipitate is then washed with 80 ml of 95% ethanol. The washing is continued further with 80% ethanol and heated up at temperature of 60 °C until all acid and salts are removed. This precipitate is then washed with methanol and heated using a hotplate magnetic stirrer until all alcohol present within the solid is removed. This solid precipitate is then dried in an oven for 3 h at 105 °C. Acid-based titration steps are as follows: 0.5 g of the acid carboxymethyl is dissolved in 100 ml of distilled water by stirring for 4 h in an Erlenmeyer flask. Then, 25 ml of 0.5 M sodium hydroxide is added and boiled for 15 min. This solution is then titrated against 0.3 M of hydrochloric acid using phenolphthalein as an indicator. The phenolphthalein indicator is used to indicate the presence of base solution (pink) and turns colourless when the solution is neutral or acidic. The second and third steps are then repeated without the presence of the acid carboxymethyl. The concentration of carboxymethyl is then calculated using the equation:

$$\text{CM}\% = (V2 - V1)0.058/M \times 100 \quad (1)$$

where  $V1$ : volume of 0.3 M HCl used to titrate solution with sample acid carboxymethyl (ml),  $V2$ : volume of 0.3 M HCl used to titrate solution without acid carboxymethyl (ml) and  $M$ : mass of acid carboxymethyl used (g).

### 2.3 Benchtop Permeability Experiment

The steps to the benchtop permeability experiment are as follows: CMC biopolymer solution is prepared by mixing 0.248 g of CMC with 1000 ml of brine to create a DRA solution with 100 ppm concentration. Flood core with brine for 1 cc/min until permeability is stabilised, and record the final permeability to obtain initial permeability ( $k_{\text{initial}}$ ). Flood it again with DRA solution at the same injection rate for 30 min to obtain permeability reduced due to the DRA ( $k_{\text{DRA}}$ ). Run backflow process using 10000 ppm brine at a high injection rate of 8 cc/min to recover back the permeability loss due to the polymer injection. Inject brine at 1 cc/min to obtain a final permeability reading, and record the permeability reading as permeability recovered ( $k_{\text{recovered}}$ ). Repeat the test for different injection rates of 3 and 5 cc/min. Repeat steps 1–6 for synthetic polymer DRA which is polyacrylamide (PAM). The reduction and recovered permeability can be calculated using the following formula:

$$k_{\text{reduction}}(\%) = (k_{\text{initial}} - k_{\text{DRA}})/k_{\text{initial}} \times 100 \quad (2)$$

$$k_{\text{recovered}}(\%) = (k_{\text{final}} - k_{\text{DRA}})/(k_{\text{initial}} - k_{\text{DRA}}) \times 100 \quad (3)$$

## 3 Results and Discussion

### 3.1 CMC Extraction

See Table 1.

It is observed from the table above that the average mass of CMC extracted from every cycle is 25.274 g with a percentage average of 63.17%.

**Table 1** Percentage of CMC extracted from 40 g of CR

Cycle	Initial CR mass (g)	Final CMC extracted mass (g)	Percentage of CMC produced (%)
1	40.008	26.381	65.94
2	40.003	24.734	61.83
3	40.006	23.829	59.56
4	40.010	27.489	68.71
5	40.009	23.939	59.83
Average	40.007	25.274	63.17

### 3.2 Titration to Determine CMC Concentration Results

See Table 2.

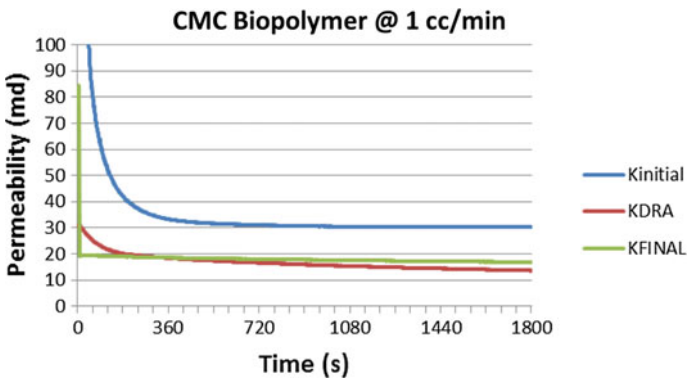
It is observed that the average concentration of CMC produced from each cycle is 40.31%.

### 3.3 Benchtop Permeability Test

See Fig. 1.

**Table 2** Concentration of CMC extracted

Cycle	Mass of acid carboxymethyl (g)	Volume of HCl (L)	Concentration %
1	0.5	41.1	41.76
	0.8	39	41.325
	1	37.6	41.18
2	0.5	41.2	40.6
	0.8	39.1	40.6
	1	37.8	40.02
3	0.5	41.4	38.28
	0.8	39.4	38.425
	1	38	38.86



**Fig. 1** Graph of permeability ( $k$ ) versus time at injection rate 1 cc/min of CMC biopolymer solution

$$k_{\text{reduction}} = (30.233 - 13.621)/30.233 \times 100 = 54.94 \%$$

$$k_{\text{recovered}} = (16.835 - 13.621)/(30.233 - 13.621) \times 100 = 19.35 \%$$

See Figure 2.

$$k_{\text{reduction}} = (19.461 - 13.982)/19.461 \times 100 = 28.15 \%$$

$$k_{\text{recovered}} = (16.538 - 13.982)/(19.461 - 13.982) \times 100 = 46.65 \%$$

See Figure 3.

$$k_{\text{reduction}} = (19.853 - 6.722)/19.853 \times 100 = 66.14 \%$$

$$k_{\text{recovered}} = (8.224 - 6.722)/(19.853 - 6.722) \times 100 = 11.44 \%$$

See Fig. 4.

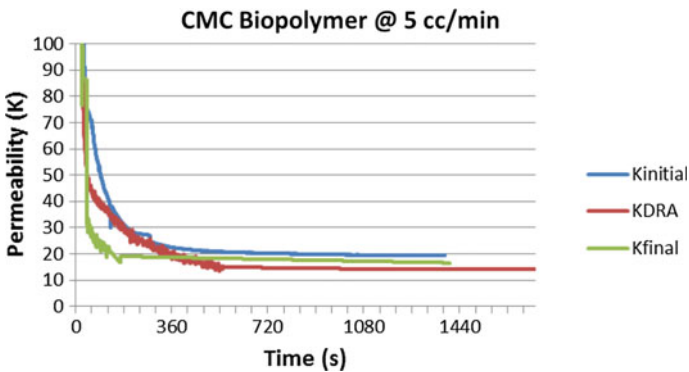


Fig. 2 Graph of permeability (*k*) versus time at injection rate 5 cc/min of CMC biopolymer solution

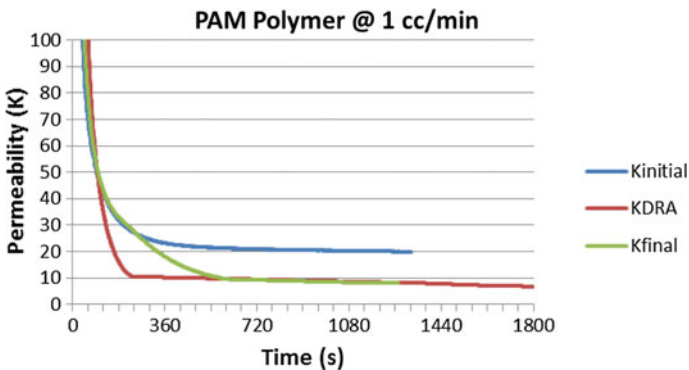
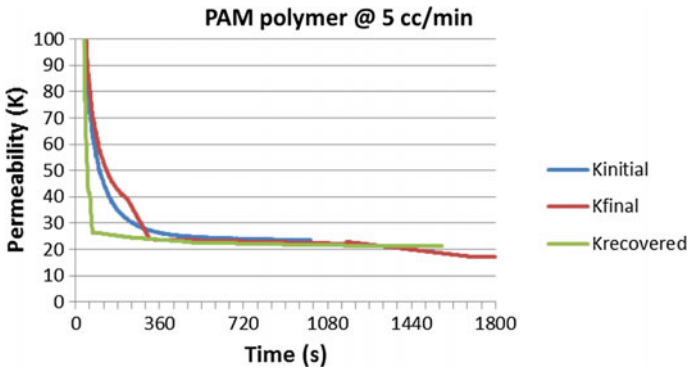


Fig. 3 Graph of permeability (*k*) versus time at injection rate 1 cc/min of synthetic polymer solution



**Fig. 4** Graph of permeability (*k*) versus time at injection rate 5 cc/min of synthetic polymer solution

$$k_{\text{reduction}} = (23.471 - 17.892)/23.471 \times 100 = 23.77 \%$$

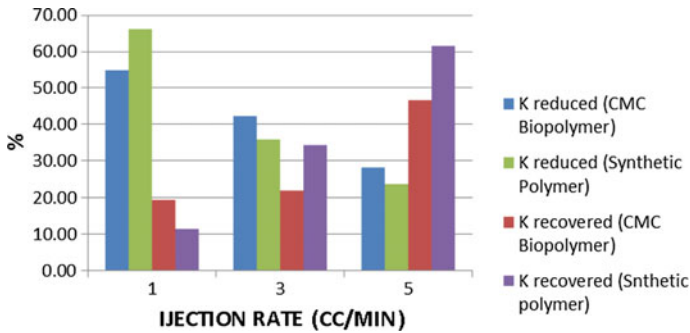
$$k_{\text{recovered}} = (21.332 - 17.892)/(23.471 - 17.892) \times 100 = 61.66 \%$$

### 3.4 Performance Comparison

Table 3 summarizes the results of permeability reduced and permeability recovered at different injection rates. It is observed that in general as the injection rate increases, the percentage of permeability reduction decreases. And the permeability able to be recovered increases with increase in the injection rates. The permeability reduced by PAM polymer is higher at low injection rates as compared to CMC biopolymer. For CMC polymer, it is higher at high injection rates when compared to PAM polymer. The *K* recovered using PAM polymer is higher at high injection rates when compared to CMC biopolymer, whereas the recovery for CMC biopolymer is higher for low injection rates as compared to PAM polymer. This shows that PAM polymer clogs the core lesser as compared to CMC biopolymer at

**Table 3** Summary of CMC biopolymer and PAM polymer effects on formation permeability

Injection rate (cc/min)	CMC biopolymer		PAM polymer	
	<i>K</i> <sub>reduced</sub> (%)	<i>K</i> <sub>recovered</sub> (%)	<i>K</i> <sub>reduced</sub> (%)	<i>K</i> <sub>recovered</sub> (%)
1	54.95	19.35	66.14	11.44
3	42.15	22.04	35.80	34.42
5	28.15	46.65	23.77	61.66



**Fig. 5** Bar chart of performance comparison between natural polymer and synthetic polymer as DRA

high injection rates and CMC biopolymer clogs the core lesser at low injection rates. At the injection rate of 3 cc/min, the  $K$  reduced by CMC biopolymer appears to be higher and the difference to PAM polymer injection is 6.35% (Fig. 5).

The pattern of permeability change is caused due to the tendency of degradation for the two different polymer chains. PAM polymer has a dense polymer chain, and this leads to a greater deposition at low injection rates leading to a larger permeability decrease. However, the polymer chain is weaker compared to CMC biopolymer causing it to go through a greater mechanical gradation at high injection rates. A greater degradation of the polymer makes its polymer chains smaller, and the tendency to be deposited in the core is less.

## 4 Conclusion

Based on the result, if the injection rates are higher, the permeability decrease is lower and permeability to be recovered is higher. For an example, when using CMC biopolymer, the permeability reduced is 28.15% and permeability recovered is 46.65% at 5 cc/min as compared to permeability reduced is 54.94% and permeability recovered is 19.35% at 1 cc/min. This can be due to the rapid pressure build up in the formation when injection rates increase and also a shearing of polymer which does not allow the polymer to clog the core. It is also observed that the permeability reduction using natural CMC biopolymer is lower than PAM polymer at low injection rates of 1 cc/min, which is 54.94% for CMC biopolymer and 66.14% for PAM synthetic polymer. However, the permeability reduced for CMC biopolymer is higher at high injection rates of 5 cc/min when compared to PAM polymer which is 28.15% for CMC biopolymer and 23.77% for PAM synthetic polymer. Therefore, it is safe to conclude that PAM polymer tends to undergo a greater mechanical degradation as compared to CMC biopolymer at higher injection rates because its effects on permeability reduction are decreasing at higher rates.

The mechanical degradation of the polymer causes them to break down to smaller chains. This lead to less deposition of polymers in the formation, resulting in a lesser permeability reduction. This smaller chain can also be removed easily when brine is back-flowed causing the permeability recovered to be higher.

DRA effectiveness reduces with mechanical degradation, meaning at a higher injection rate, CMC biopolymer would serve as a better DRA for water injection wells. However, this using CMC biopolymer would cause a larger drop in formation permeability at higher injection rates. Its difference from PAM polymer in terms of permeability reduction is 4%. Therefore, it can be concluded that CMC biopolymer can be used as DRA in substitute for industrial used PAM, because of its ability to withstand larger injection rates, and is more environmentally friendly when to compare to PAM polymer. Although the permeability drop caused by CMC biopolymer is higher at high injection rates, its difference from PAM polymer is small and its permeability reduction caused by CMC biopolymer at low injection rates is lower.

However, the polymer properties are also affected by many other factors such as concentration and temperature. Therefore, further study should also include the effect of different injection rates on the formation permeability reduction at different DRA concentrations and different formation pressures. To further understand the reasons behind the permeability reduction, a further qualitative study should be carried out using a scanning electron microscope which can help in understanding how the different polymers cause and reduce in permeability at different injection rates.

## References

1. Al-Anazi, H. A., Al-Faifi, M., Tulbah, F. M., & Gillsepie, J. (2006). Evaluation of Drag Reducing Agent (DRA) for Seawater Injection System: Lab and Field Cases.
2. Gurchran, H. K., & Dr Azuraieen, J. (2013). Study of Drag Reduction Ability of Naturally Produced Polymers from a Local Plant Source. International Petroleum Technology Conference. International Petroleum Technology Conference.
3. Muda, R. A., & Jasmani, M. (n.d.). Comparison Between Two Surfactant (Sodium Oleate and Sodium Sterate) as Drag Reducing Agent in Water System. Perak, Malaysia: University Teknologi Petronas.
4. Pushpamalar, V, Langford, S.J, & Ahmad, M.. (n.d.). Optimisation of reactio condition for preparing carboxylmethyl cellulose from sago waste. Monash University Malaysia. University Putra Malaysia.
5. Rochon, J., Creusot, M. R., & Rivet, P. (1996). Water Quality for Injection Wells. SPE Formation Damage Control Symposium. Lafayette, U.S.A: SPE 31122.
6. Truong, V. (2001). Drag reduction technologies; DTIC Document.

# Examination and Improvement of Salama Model for Calculation of Sand Erosion in Elbows

Mysara Eissa Mohyaldinn, Mokhtar Che Ismail, Muhammad Ayoub and Syed Mohammad Mahmood

**Abstract** Sand erosion is a problem recognized in many facilities and piping components used in production, treatment, and transportation of oil and gas. Proper controlling of sand erosion requires early prediction at different conditions and within various ranges of flow parameters. Numerous models and correlations are available for sand erosion prediction in various components. The applicability and accuracy of the available models depends on many factors such as the range of conditions and the number of parameters that are taken into account in developing the model. One of the models widely used for sand erosion prediction is Salama model, which is used for calculation of sand erosion in elbows and tees. In spite of Salama model's simplicity, it is not recommended to use in many cases due to decrease in accuracy. Salama model accuracy, in general, decreases when it is applied to viscous fluids flow and low gas–liquid-ratio multiphase flow. In this paper, the discrepancy of Salama model with field data was confirmed by comparing its output with published measured data. The model was, then, improved by comparing its results with three sets of measured sand erosion data for pure gas, high gas–liquid-ratio fluids, and low gas–liquid-ratio fluids. The model improvement results in three models for prediction of sand erosion in elbows with higher accuracy.

**Keywords** Sand · Erosion · Model · Salama

---

M.E. Mohyaldinn (✉) · M. Ayoub · S.M. Mahmood  
Petroleum Engineering Department, Universiti Teknologi PETRONAS,  
32610 Bandar Seri Iskandar, Perak, Malaysia  
e-mail: mysara.eissa@utp.edu.my

M.C. Ismail  
Mechanical Engineering Department, Universiti Teknologi PETRONAS,  
32610 Bandar Seri Iskandar, Perak, Malaysia



## 1 Literature Review

Pipes and facilities carrying high velocity singlephase or multiphase fluids containing solid particles are frequently suffering erosion resulting from impingement of the particles on internal walls. The erosion is generally proportional to sand concentration and is more recognized at locations where flow diverts or accelerates (e.g., elbows, valves, chokes, and tees). The erosion is affected by many interacted factors that are related to pipe geometry, sand characteristics, and flow characteristics. This fact causes difficulties and high degree of uncertainties in predicting the magnitude of erosion (so-called sand erosion). One and major reason of this difficulty is the fact that the fluid exhibits complex multiphase flow composed of sand particles dispersed in a continuous phase [1]. The severity of the erosion rate depends on many factors related to the fluid, sand particles, and target material [2–6]. Barton [4] has arranged the components, where the erosion takes place according to erosion vulnerability, in eight ranks ranging from chokes as the most vulnerable component to straight pipes as the least vulnerable component. The serious attempt to predict erosion rate is dated back to 1960, when Fannie [7] has developed an empirical model relating erosion rate to particle impingement velocity and some empirical constants that depend on material's properties and the angles of impingement. This attempt has been followed by valued efforts by subsequent researchers who developed models either for general application or for specific-purpose application. One of the specific-purpose erosion rate prediction applications is number of models used to calculate erosion rate at different pipes and fittings used in petroleum and petrochemical industry. In petroleum industry, sand erosion has been studied at different subsurface and surface components such as sand control screen [8], choke [9], valve [10], plugged tee, and elbow [11].

Many models have been developed for sand erosion prediction in elbows [12]. Among these models, Salama empirical models that developed by Salam and his co-workers have shown acceptable agreement with experimental data for gas flow and multiphase flow with high gas volume fraction. It is believed that this accuracy would not be valid for viscous liquids flow due to high discrepancy between the continuous phase velocity and the dispersed sand velocity. In this paper, the discrepancy of Salama model with field data was confirmed by comparing its output with published measured data. The model was, then, improved by comparing its results with three sets of measured sand erosion data for pure gas, high gas–liquid-ratio fluids, and low gas–liquid-ratio fluids. The model improvement results in three models for prediction of sand erosion in elbows with higher accuracy.

## 2 SALAMA Model Improvement

### 2.1 Sand Erosion Empirical Models

In sand erosion empirical methods, erosion is predicted for a component by using the fluid velocity (no particles or bubbles tracking). The methods are commonly based on simple empirical correlations that predict erosional threshold velocity (the velocity above which erosion occurs) and erosion rate, and are more applicable to gas flow where the dispersed phase (particles or bubbles) is almost flowing at the fluid mean velocity. The erosional velocity,  $V_e$ , is usually predicted using the American Petroleum Institute Recommended Practice equation (API RP 14 E) [13].

$$V_e = \frac{C}{\sqrt{\rho_f}} \quad (1)$$

where  $C$  is constant, its value as proposed by API RP 14 E is 100 for continuous service and 125 for intermittent service, and  $\rho_f$  is the density of fluid.

Many investigators have questioned the accuracy of Eq. 1 on the ground of neglecting some important factors such as particles' size and shapes, component geometries, and fluid viscosity. Therefore, many attempts were made to enhance the accuracy and to extend the applicability of API RP 14 E equation. Salama and Venkatesh proposed a model for prediction of penetration rate in elbows and tees. Assuming a sand density of  $2650 \text{ kg/m}^3$ , their model can be written in SI units as follows:

$$ER = 37.585 \frac{WV^2}{PD^2} \quad (2)$$

where  $ER$  is the erosion rate (mm/year),  $W$  is sand production rate (kg/s),  $V$  is the fluid flow velocity (m/s),  $P$  is the hardness parameter (Bar), and  $D$  is the pipe diameter (m). Salama and Venkatesh used Eq. 2 to calculate the erosional velocity for steel pipes using value of  $P 1.05 \times 10^4$  bar for allowable erosion rate of 0.254 mm/year. This resulted in the following equation for erosional velocity.

$$V_e = \frac{0.0152D}{\sqrt{W}} \quad (3)$$

The shortcomings of Salama and Venkatesh model (Eq. 2) are its neglect of sand particles size and shape, and its inapplicability to two-phase (liquid-gas) flow. Their model also neglects solid particles fragmentation and hardness, but since the model only deals with sand particulates where their hardness varies slightly, so we believe that neglecting the hardness is logical. The material hardness is also not considered due to the fact that the model only deals with carbon steel materials. Salama incorporated the effect of two-phase mixture density and particle size into Eq. 2 and proposed the following equation.

**Table 1** Geometry-dependent constant  $S_m$  in salama equation (Salama 2000)

Geometry	Elbow (1.5 and 5D)	Seamless and cast elbows (1.5–3.25 D)	Plugged tee (gas–liquid)	Plugged tee (gas flow)
$S_m$	5.5	33	68	1379

$$ER = \frac{11.574 WV_m^2 d}{S_m D^2 \rho_m} \tag{4}$$

where  $V_m$  and  $\rho_m$  are mixture velocity (m/s) and density (kg/m<sup>3</sup>), respectively. In Eq. 4,  $S_m$  is a geometry-dependant constant as given in Table 1.

Equation 4 was developed through numerous tests that were carried out using water and nitrogen gas. Since water and gas viscosities are almost constant, therefore the viscosity parameter has not been included in the equation. Salama, however, expected that higher viscosity will result in reduction of erosion rate.

## 2.2 Examination of Salama Model Accuracy

Salama model results have been compared with published measured data. The erosion rate in the published data is expressed in unit of mm/kg, which means material loss in mm for every kg of sand hits the target. The predicted erosion rate in mm/year is converted to mm/kg using the following relationship:

$$E(L/M) = \frac{1}{CF} \frac{ER(L/T)}{W(M/T)} \tag{5}$$

where  $W$  is sand production rate, and  $CF$  is a conversion factor for converting unit of sand production rate to kg/year. The value of  $CF$  for different unit of  $W$  is contained in Table 2 provided that  $ER$  unit is in mm/year.  $L$ ,  $M$ , and  $T$  denote dimensions of length, mass, and time, respectively.

Table 3 and Fig. 1 show that the predicted results by Salama model overestimates the measured data.

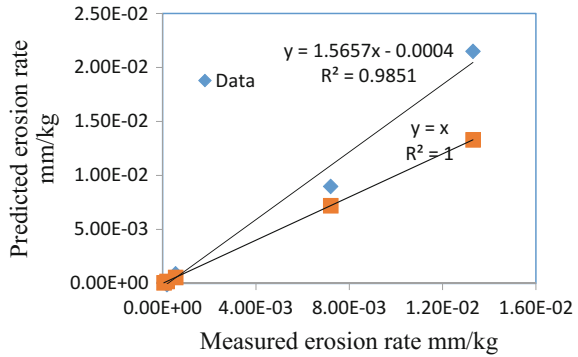
**Table 2** Values of  $CF$  for different unit of sand production rate ( $W$ )

Unit of sand production rate ( $W$ )	$CF$
kg/s	31536000
kg/day	365
kg/hr	8760

**Table 3** Validation of the code results (Salama model) using published data

Vl m/s	Vg m/s	Density kg/m <sup>3</sup>	D sand μ	D pipe mm	ER measured	ER predicted
1	30	34.48	150	49	5.52E-04	8.83E-04
5.8	20	226.59	150	49	5.19E-05	9.16E-05
6.2	9	413.5	250	26.5	1.80E-04	9.93E-05
0.5	34.3	24.1	250	26.5	7.20E-03	8.98E-03
0.7	52	23	250	26.5	1.33E-02	2.15E-02

**Fig. 1** Validation of Salama model



### 2.3 Salama Model Improvement

An attempt is made to improve the accuracy of Salama model. Another set of data measured by Bourgoyne and Tolle and Greenwood has been added to the data in Table 3. The whole data is categorized into three groups according to the gas–liquid ratio (GLR) as follows:

Pure gas flow at

$$\frac{V_{sl}}{V_{sg}} = 0 \tag{6}$$

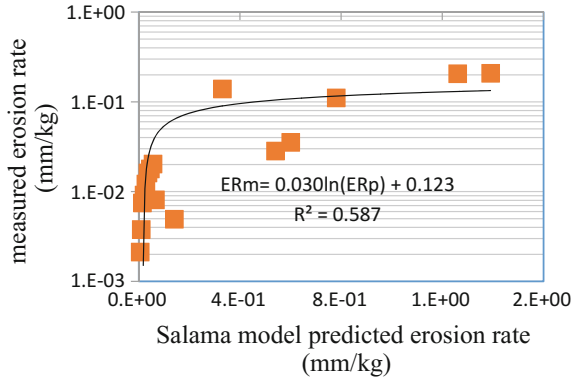
$$0 < \frac{V_{sl}}{V_{sg}} \leq 0.155 \tag{7}$$

$$\frac{V_{sl}}{V_{sg}} > 0.155 \tag{8}$$

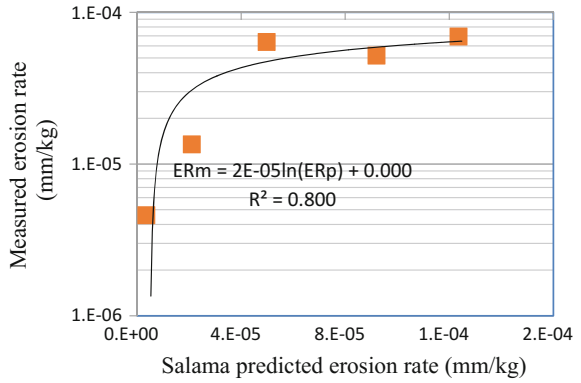
Figures 2, 3, and 4 show the correlations between the sand erosion values calculated using Salama model and the measured values for pure gas, low GLR, and high GLR.

From Figs. 2, 3, and 4, the measured values are related to the predicted values for the three types of flow as follows:

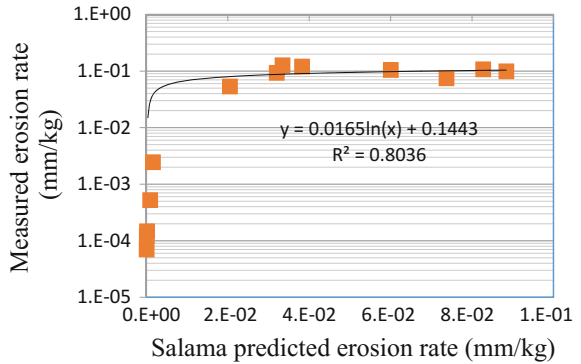
**Fig. 2** Comparison of salama model predicted values with measured data (pure air)



**Fig. 3** Comparison of salama model predicted data with measured data (low gas-liquid ratio)



**fig. 4** Comparison of salama model predicted data with measured data (high gas-liquid ratio)



Pure gas flow:

$$\log ER_m = 0.296 \ln(ER_p) - 0.985 \quad (9)$$

High gas–liquid-ratio flow:

$$\log ER_m = 0.462 \ln(ER_p) + 0.349 \quad (10)$$

Low gas–liquid-ratio flow:

$$\log ER_m = 0.347 \ln(ER_p) - 0.99 \quad (11)$$

where  $ER_m$  is the erosion rate calculated using Salama equation (Eq. 4).

Considering the value of  $S_m$  for elbow, the erosion rate ( $ER$ ) unit is converted from mm/year to mm/kg (the unit of the collected data) as follows:

$$ER = \left[ \frac{11.578 WV_m^2 d_p}{5.5 D^2 \rho_m} \right] \times \frac{1}{W} \times \frac{1}{3600 \times 24 \times 365} \quad (12)$$

$$ER = 6.66 \times 10^{-8} \left[ \frac{V_m^2 d_p}{D^2 \rho_m} \right] \quad (13)$$

By substituting  $ER$  in Eq. 13 for  $ER_p$  in Eqs. 9–11, the modified erosion rate prediction equations can be written for the three flow types as follows:

$$\log(ER_{act}) = \begin{cases} 0.296 \ln \left( \left[ \frac{V_m^2 d_p}{D^2 \rho_m} \right] \right) - 7.621 & \frac{V_{sl}}{V_{sg}} = 0 \\ 0.462 \ln \left( \left[ \frac{V_m^2 d_p}{D^2 \rho_m} \right] \right) - 10.009 & 0 < \frac{V_{sl}}{V_{sg}} \leq 0.155 \\ 0.347 \ln \left( \left[ \frac{V_m^2 d_p}{D^2 \rho_m} \right] \right) - 6.7895 & \frac{V_{sl}}{V_{sg}} > 0.155 \end{cases} \quad (14)$$

where

- $ER_{act}$  Actual erosion rate, mm/kg.
- $W$  Sand production rate in kg/s.
- $V_m$  Mixture flow rate, m/s.
- $D$  Elbow diameter, m.
- $d$  Particles size,  $\mu$ .
- $\rho_m$  Mixture density,  $\text{kg/m}^3$ .

### 2.4 Demonstrating Example for the New Model

Figures 5, 6, and 7 show comparisons of results obtained from original Salama model and the proposed models. The figures show variation of erosion rate (mm/kg) with air/oil mixture velocity. The input data are as shown in Table 4.

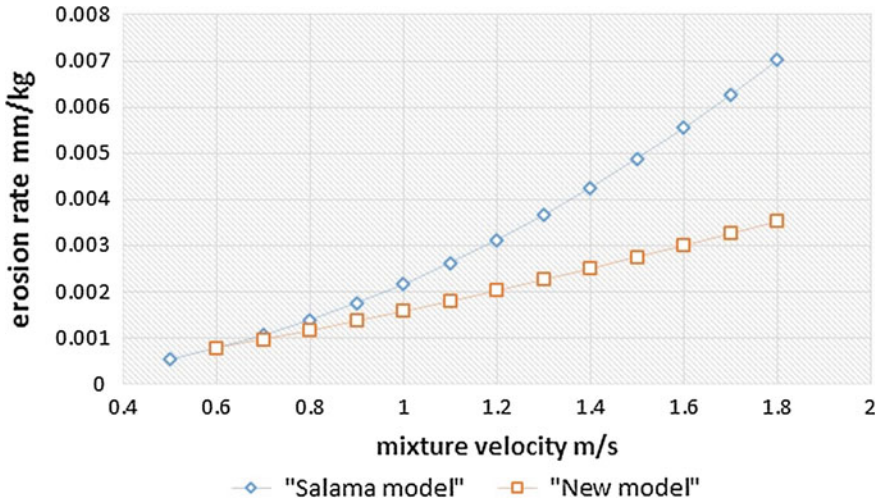


Fig. 5 Variation of erosion rate with mixture velocity for pure air

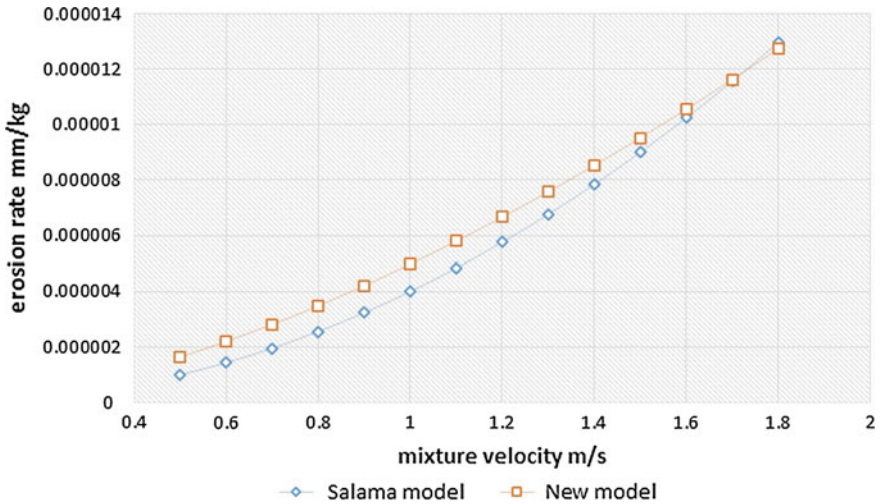


Fig. 6 Variation of erosion rate with mixture velocity for LGLR

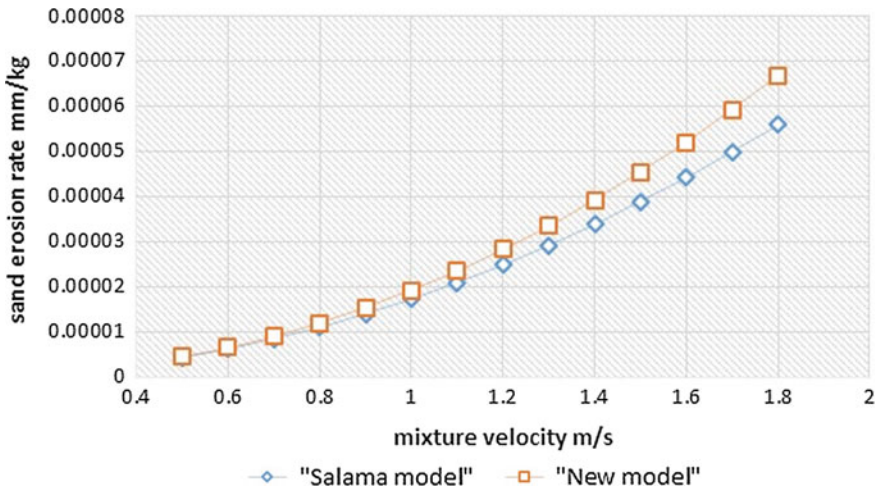


Fig. 7 Variation of erosion rate with mixture velocity for HGLR

Table 4 Example input data

Parameter	Unit	Value
Flow velocity	m/s	0.5–1.8
Mixture density	Kg/m <sup>3</sup>	1.2, 650, 150.96*
Elbow diameter	m	0.08
Sand particle size	μ	250

\*Calculated based on GLR (for pure air, LGLR, and HGLR)

In all cases, sand erosion rate increases with increase in mixture velocity. For pure gas, the new model results are lower than the original Salama model results, whereas for LGLR and HGLR Salama model results are slightly lower than the new model results.

### 3 Conclusion

Salama sand erosion prediction model has been examined against a set of measured data and then improved utilizing comparison with another set of measured data for pure gas, low gas–liquid-ratio, and high gas–liquid-ratio fluids. A new model as an improvement of Salama model is proposed. The main features of the proposed model as compared to Salama model are as follow:

1. For pure gas, the new model results are lower than the original Salama model results, whereas for LGLR and HGLR Salama model results are slightly lower than the new model results.



2. For pure air and high gas–liquid ratio, Salama models agrees with the new model at low flow velocities and the discrepancy is getting larger at higher velocities.
3. For low gas–liquid ratio, the results from Salama model and the new model are getting closer with increasing flow velocity.

## References

1. Bastien Chopard, Alexandre Masselot, Alexandre Dupuis, “A lattice gas model for erosion and particles transport in a fluid, computer physics communication”, 129 (2000), pp. 167–176.
2. Finnie, I. (1972). “Some observations on the erosion of ductile materials.” *Wear* 19, pp. 81–90.
3. Deng, T., Chaudhry, A. R., Patel, M., Hutchings, I. and Bradley, M. S. A. (2005). “Effect of particle concentration on erosion rate of mild steel bends in a pneumatic conveyor.” *Wear* 258: pp. 480–487.
4. Barton, N. A. (2003). Erosion in Elbows in hydrocarbon production systems: Review document.
5. Ahlert, K. (1995). The effects of particle impingement angle and surface wetting on solid particle erosion on AISI 1018 steel, U of Tulsa. M Sc.
6. Karelin, C. G. D. A. V. Y. (2002). Abrasive erosion and corrosion for hydraulic machinery Vol 2, Imperial college press.
7. Finnie I. 1960. Erosion of surfaces by solid particles, *Wear* 3(2): pp. 87–103.
8. Colwart, G., Burton, R. C., Eaton, L. F. and Hodge, R. M. (2007). Lessons Learned on Sand-Control Failure and Subsequent Workover at Magnolia Deepwater Development. SPE/IADC Drilling Conference, Amsterdam.
9. Haugen, K., Kvernfold, O., Ronold, A. and Sandberg, R. (1995). “Sand erosion of wear-resistant materials: erosion in choke valves.” *Wear* 186–187, pp. 179–188.
10. Mazur, Z., Campos-Amezcu, R. and G. Urquiza-Beltr an, A. G.-G. (2004). “Numerical 3D simulation of the erosion due to solid particle impact in the main stop valve of a steam turbine.” *Applied Thermal Engineering* 24: pp. 1877–1891.
11. Chen, X., Mclaury, B. S. and Shirazi, S. A. (2006). “Numerical and experimental investigation of the relative erosion severity between plugged tees and elbows in dilute gas/solid two-phase flow.” *Wear* 261: pp. 715–729.
12. Rakesh Meshra, S.N. Singh, V. Seshadri, 1998. Study of wear characteristics and solid distribution in constant area and erosion-resistant long-radius pipe bends for the flow of multisized particulate slurries, *Wear* 217: pp. 297–306.
13. Api (1991). API RP 14 E Recommended Practice for Design and Installation of Offshore Production Platform Piping Systems. Washington DC, American Petroleum Institute: p. 22.

# Total Acid Number Reduction in Naphthenic Acids Using Ionic Liquid-Assisted Hot Water

P.C. Mandal, N.F.B. Salleh and D. Ruen-ngam

**Abstract** Naphthenic acids (NAs) found in hydrocarbon deposits is responsible for the acidity of petroleum oils. This aim of this study was to explore the capability of mixture of ionic liquid (IL) and hot water for reducing the acidity of NAs without the addition of any catalyst. The reaction kinetics and mechanism are also discovered for large-scale reactor design. The experiments were carried out in a 25-ml autoclave reactor (China) at temperatures of 60–80 °C, NA, IL, and water ratio of 1:0.1:1, reaction times of 0–60 min. The total acid number (TAN) content of the samples was analyzed using American Society for Testing Materials (ASTM) D 974 techniques. The reaction products were identified with the help of GC/MS. Experimental results reveal that TAN reduction in NAs was increasing with the increasing reaction temperature and time. Approximately 31.68% TAN was reduced at a temperature of 80 °C and a reaction time of 60 min. Experimental data revealed that TAN removal reaction kinetics followed first-order kinetics with an activation energy of 10.96 kcal/mol and a pre-exponential factor of 998.9 s<sup>-1</sup>. Therefore, mixture of IL and hot water is able to reduce TAN of NAs without the addition of any catalyst.

**Keywords** Petroleum oil · Naphthenic acid · Ionic liquid · Hot water · Total acid number

---

P.C. Mandal (✉)

Department of Petroleum Engineering, Universiti Teknologi PETRONAS,  
32610 Bandar Seri Iskandar, Perak, Malaysia  
e-mail: pradip.mandal@petronas.com.my

P.C. Mandal

Titas Gas Transmission and Distribution Co. Ltd., 105, Kazi Nazrul Islam Avenue,  
Kawran Bazar, Dhaka 1215, Bangladesh

N.F.B. Salleh

Department of Petroleum Engineering, Universiti Teknologi PETRONAS,  
31750 Bandar Seri Iskandar, Tronoh, Perak, Malaysia

D. Ruen-ngam

Department of Biology Faculty of Science, King Mongkut's Institute of Technology  
Ladkrabang, Bangkok 10520, Thailand

## 1 Introduction

The demand of petroleum oil is increasing day by day, and petroleum oil is becoming heavier. Heavy crude oil is one kind of unconventional petroleum oil having high viscosity and API gravity between 10 and 20 [1]. Heavy oil is considered as low-value oil due to the presence of impurities, for example sulfur, asphaltene, metals, nitrogen, and naphthenic acid (NA). NAs contain one or more cycloalkyl groups having molecular weight 120–700 a.u., and are the primary contributors to the acidity of heavy oil [2]. Acidity of petroleum oils is expressed in terms of total acid number (TAN) and the amount of potassium hydroxide in milligrams that is required to neutralize the acids present in 1 g of oil [3]. Research results revealed that corrosion happens at TAN level of 1.5 mg KOH/g and above [4]. Acidic crude oil accelerates serious corrosion of equipment [5, 6] during oil production, storage, transportation, and refinement. It can also deactivate refinery catalyst and create foam during refinement of petroleum oils. As a result, high-TAN content crude oil is often considered as low-value crude [7] oil. The removal or reduction in NAs is now considered as an indispensable issue due to its corrosive nature, creation of specific refinement and disposal problems, and reduction in product quality.

Lot of TAN reduction techniques have been proposed by previous researchers to reduce acidity in crude oil. Ding et al. [8] have classified TAN reduction techniques into two methods—(1) destructive methods, such as thermal cracking and hydrogenation process and (2) non-destructive methods, such as adsorption and solvent extraction. The physical separation techniques, such as adsorptive separation and solvent extraction, isolate naphthenates from crude oil without altering their chemical state [1, 9]. In reality, solvent extraction produces stable emulsion and excessive industrial wastewater, making the process non-selective. On the other hand, adsorption process is said to be less efficient to treat highly viscous crude oil. The thermal deacidification technique breaks down thermally weak NAs into hydrocarbons and carbon dioxide. This method, however, requires elevated temperature (400 °C), implying high cost. Rudolf [10] also found that this process consumed more time, and decomposition of NA for some cases was incomplete. Chemical decomposition techniques, such as esterification and neutralization, can reduce the acidity of crude oil by chemical decomposition of NAs into salt that can be removed. Ester can be decomposed into fatty acids again at crude oil refinement conditions creating corrosion in distillation column. Hydrogenation is an alternative way of chemical destruction of NAs; however, a large amount of hydrogen gas is required at plant side for continuous treatment [11], making the process inefficient.

Nowadays, researches have concentrated their works of acidity reduction in NAs using green processes. Ionic liquid (IL)-based and supercritical fluid (SCF)-based technologies are extensively exercised as a green process in different fields of chemical industries. SCF-based processes are considered expensive process due to the requirement of elevated temperature and pressure. In reality, total acid number (TAN) of NAs need to reduce at a temperature less than distillation temperature of

crude oil and low pressure for reducing corrosion in production, storage, and transportation of heavy oil. Low-temperature IL-based technology can open a new window for treating high NAs containing crude oil.

An ionic liquid (IL) is one kind of salt that can remain liquid at room temperature and below 100 °C. It generally consists of a cation, a bulk organic structure with low symmetry, and an anion. Though the field of IL is not new, their applications as solvents in different chemical processes and catalysis have become an advance technology nowadays. This interesting field started in 1914 after the formulation of ethylammonium nitrate ( $[\text{C}_2\text{H}_5\text{NH}_3][\text{NO}_3]$ ) by Paul Walden [12–14]. The fields of ILs were drawn international attention in 1970s as aluminum chloride-based molten salts were utilized for the preparation of nuclear warheads batteries. But they were extensively used as a solvent in the late 1990s. The properties of IL can be changed by adjusting the theory to make it widely usable. ILs are now used in many potential applications, such as microwave-assisted organic synthesis, catalysis, biocatalysis, separation, extraction, electrochemistry, nanomaterials synthesis, polymerization reactions, and corrosion inhibitors [15]. IL-based technologies are also utilizing in petrochemical industry to reassess and optimize existing technologies and processes.

The aim of this technical paper was to explore the capability of mixture of IL and hot water for reducing acidity of NAs. In addition, TAN removal kinetics is also explored at temperatures of 60–80 °C, NA, IL, and water ratio of 1:0.1:1, and reaction times of 0–60 min.

## 2 Methodology

### 2.1 Materials Used

NAs (grade: technical, density: 0.92 g/mL at 20 °C) used in this study were purchased from Sigma-Aldrich and used without further treatment. NAs are water insoluble and brown-colored liquid with an offensive smell. They have the potential to pollute soil and may contaminate nearby water. The stable hygroscopic IL, 1-ethyl-3-methylimidazolium chloride ([EMIm]Cl) is used in this study. It is a light yellowish solid having an empirical formula  $\text{C}_6\text{H}_{11}\text{ClN}_2$ , molecular weight of 146.62 g/mol, relative density 1.11 g/mL, and melting point at 77–79 °C. The [EMIm]Cl was also purchased from Sigma-Aldrich and used without further treatment. Other reagents, toluene, 2-propanol, potassium hydroxide, and phenolphthalein, were obtained from EMD Corporation and were used without further treatment. The mixture of toluene and 2-propanol at a ratio of 1:1 was used as solvent for collecting the samples and determining TAN.

## 2.2 Equipment

All experiments were performed in 25-ml autoclave reactor fabricated by Shanghai Yanzheng Experiment Instrument Co., Ltd., China, for maximum temperature of 230 °C and pressure of 3 MPa (gauge). The reactor is a stainless steel structure, which is durable, and gas-tight. Inner chamber of the reactor is made of polytetrafluoroethylene (PTFE) to minimize corrosion.

## 2.3 Experimental Procedure

Approximately 1.0 g of NAs, 0.10 g of IL, and 1.0 g of water were charged into the autoclave reactor. The reactor was then loaded into a furnace that was preheated to the planned temperature. After a specific reaction time, the reactor was removed from the furnace and kept it in a water bath by allowing sufficient time to cool the reactor at room temperature. Finally, the products were collected in sample bottles by washing the reactor interior at least three times with solvent. The reaction products were separated into two parts—one is water-insoluble organic portion and another was water-soluble portion. Water-soluble portion was analyzed using pH meter, and water-insoluble organic portion was analyzed using titration, gas chromatography–mass spectrometry (GC/MS), and Fourier transform–infrared spectroscopy (FT-IR).

## 2.4 Analytical Procedure

Mandal et al. [3] disclosed that American Society for Testing Materials (ASTM) D 974 has sufficient accuracy for evaluating TAN value. This method was used in this study for evaluating TAN value. In this process, a mixture of toluene and 2-propanol in 1:1 ratio was used as solvent, and phenolphthalein was used as an indicator for detecting end point. A recently prepared approximately 0.05 mol/L standard potassium hydroxide solution was utilized as a titrant. The following terms are used in this study.

Titration was conducted to estimate the acidity of NAs. TAN was calculated by identifying the amount of potassium hydroxide needed to neutralize 1 g of NA using the following equation:

$$\text{TAN} \left( \frac{\text{mg KOH}}{\text{g NA}} \right) = \left[ \frac{V_{\text{KOH}} \times N_{\text{KOH}} \times 56.10}{W_{\text{NA},0}} \right] \quad (1)$$

where  $V_{\text{KOH}}$  is volume of KOH in ml,  $N_{\text{KOH}}$  is the concentration of KOH in mmol/ml, and  $W_{\text{NA},0}$  is the amount of NA in g.

TAN reduction was calculated in order to identify the extent of reduction in acidity in NAs using the equation shown below:

$$\text{TAN reduction}(\%) = \frac{\text{TAN}_0 - \text{TAN}_t}{\text{TAN}_0} \times 100 \quad (2)$$

where  $\text{TAN}_0$  is the initial TAN in loaded NAs, and  $\text{TAN}_t$  is the TAN at reaction time of  $t$ .

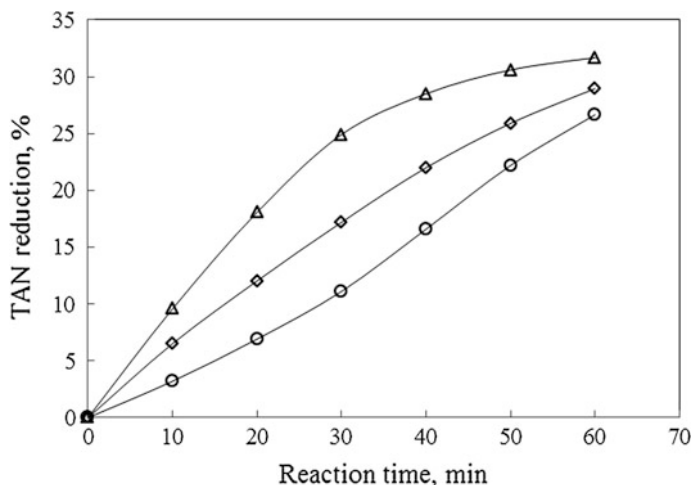
The reaction products were also analyzed using GC/MS method for identifying reaction products. The column, BPX5 non-polar and low-bleed capillary column, 30 m long by 0.25 mm diameter, was used. The samples were diluted by adding methylene chloride before charging the samples in GC/MS analyser at a specified temperature program.

All experiments were conducted three times to achieve accurate result. The error margin of the achieved data was less than 5% with confident level of 95%.

### 3 Results and Discussion

#### 3.1 TAN Reduction

Mandal et al. [6] discovered that supercritical water (SCW) has the capability of reducing approximately 83% TAN of NAs at a temperature of 490 °C and a water partial pressure (WPP) of 45 MPa. Quiroga-Becerra et al. [16] discovered that approximately 95% TAN was reduced from NAs obtained from Colombian heavy crude oil at temperature of 250 °C, reaction time of 600 min, and a methanol-to-acid ratio of 20:1. Mandal et al. in 2013 [3] disclosed that SC-MeOH can reduce 100% TAN at a temperature of 350 °C, a MPP of 10 MPa, and a reaction time of 60 min. But this condition is very high to treat heavy oil for reducing corrosion as a pre-treatment. Shi et al. [12] has proposed a green method to separate NAs from highly acidic crude oils by forming ILs. They used 2-methylimidazole solution in ethanol for acidity removal achieving 67% acid removal rate. Jing et al. [17] have reached 75.9% deacidification rate using [BMIm]Br-AlCl<sub>3</sub> that showed catalytic performance. Sun and Shi in 2012 revealed that the ILs of imidazole anion having strong alkalinity had fantastic performance on deacidification. Duan et al. [14] have studied on pyridinium-, imidazolium-, and imidazolide-based ionic liquids at different alkalinity. They showed that the deacidification rate increased with the increase in the strength of alkalinity of ILs. Anderson et al. [15] have studied a number of tetraalkylammonium- and tetraalkylphosphonium amino acid-based ILs to remove NAs from crude oil. Their results show that the tributylmethylammonium lysinate IL has the highest acid removal rate (approximately 46%) at a temperature of 25 °C. It is no doubt that ILs and heated water can reduce acidity of NAs. To observe the capability of mixture of IL and hot water for TAN reduction in NAs, approximately eighteen experiments were performed at temperature of 60–80 °C and

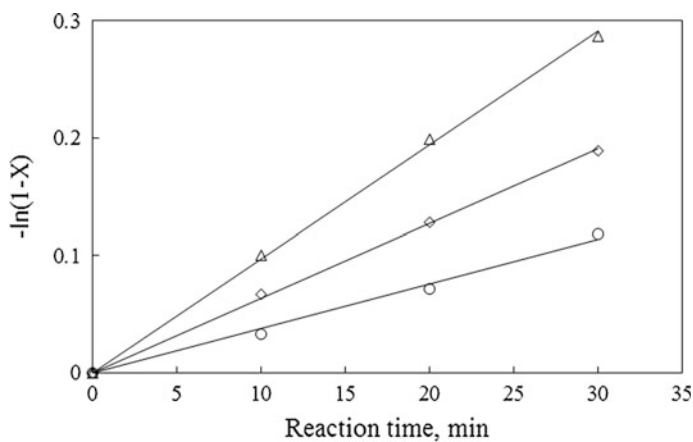


**Fig. 1** Variation in TAN reduction at a function of temperature and reaction time (Symbol: ○, at a temperature of 60 °C; ◇, at a temperature of 70 °C; △, at a temperature of 80 °C)

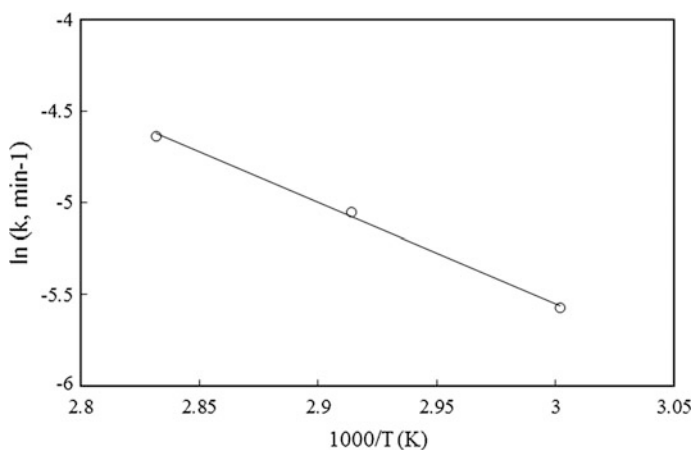
reaction times of 0–60 min. The mixture of NAs, IL, and water used in this study had an initial TAN value 235.50 mg KOH/g NA. Figure 1 shows that TAN removal of NAs was increasing with increasing reaction temperature and time. Approximately 31.68% TAN was removed at a temperature of 80 °C, a reaction time of 60 min. The water at a temperature of 100 °C and a reaction time of 90 min can produce more maltene by reducing the asphaltene content of crude oil showing that hot water is active to produce more maltene [18]. Mandal et al. [19] discovered that [EMIm]Cl can reduce 25% TAN of NAs at a temperature of 80 °C, reaction time of 60 min, and an IL/NA ratio of 1:1. This value was lesser than the result obtained in this study, indicating that hot water was active during reaction. NAs, IL, and water were mixed properly with increasing temperature, thereby increasing the collision between them to increase the rate of reaction.

### 3.2 TAN Reduction Kinetics and Mechanism

Reaction kinetics is very important to design chemical reactor. Mandal et al. [3] shows that kinetics of the reaction of NA and SCW follow first-order kinetics. To discover the reaction order of the reaction between NAs and mixture of IL and water, a plot of  $\ln(1-X)$  versus reaction time is plotted (Fig. 2). Each set of data gives straight line which, obtained with the least square method, passes almost exactly through the origin indicating first-order kinetics with respect to TAN removal. The reaction kinetics analysis of this study was tested and evaluated to a maximum of 24.92% TAN removal as kinetics data were more compatible with



**Fig. 2** TAN reduction kinetics plot (Symbol: ○, at a temperature of 60 °C; ◇, at a temperature of 70 °C; △, at a temperature of 80 °C)

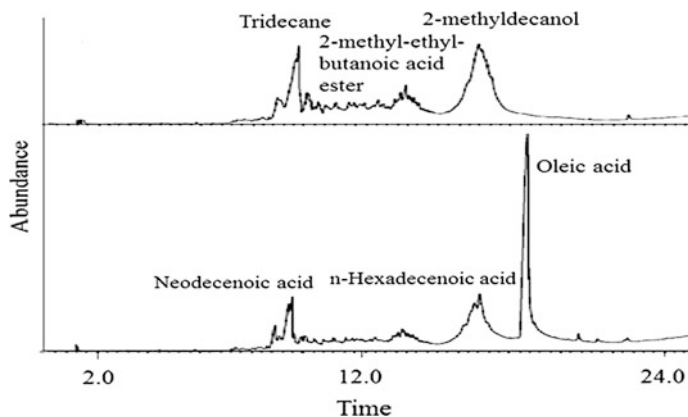


**Fig. 3** Arrhenius plot

second-order kinetics at this extent [20]. An Arrhenius-type temperature dependency acidity removal rate constant is presented in Fig. 3. By exploring this plot, the activation energy and pre-exponential factor of the said reaction was discovered, and the values were 10.96 kcal/mol and  $998.9 \text{ s}^{-1}$ , respectively. Thus, the Arrhenius equation can be rewritten as follows:

$$k_{\text{IL}+\text{water}} = 998.9e^{\frac{-10.96}{RT}} \quad (3)$$

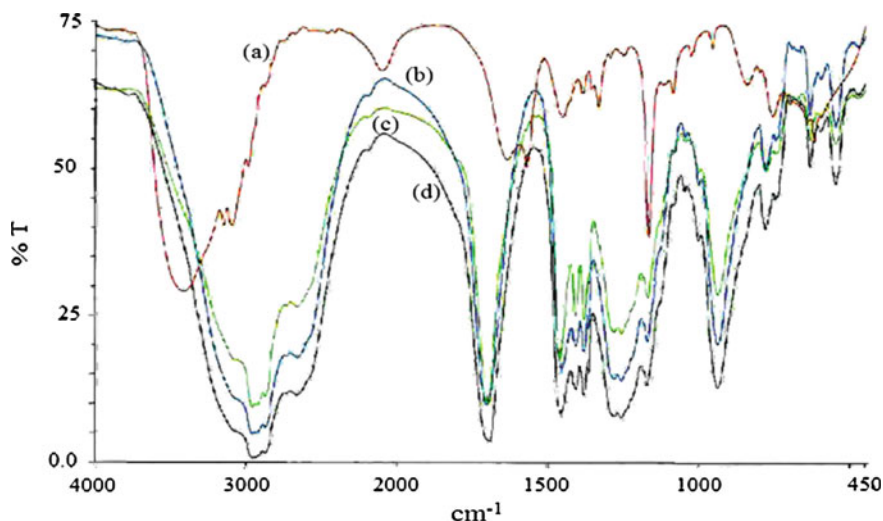




**Fig. 4** GC/MS chromatogram of NAs before reaction (*bottom*) and after reaction (*top*) at temperature of 80 °C, reaction time of 30 min

The activation energy for reaction between SCW and NAs is 15.78 kcal/mol Mandal et al. [6]. Thus, IL-assisted hot water requires lower energy than SCW, indicating that IL was active during TAN reduction process.

Mandal et al. [6] have disclosed that NAs decomposed into saturated hydrocarbons, naphthalene, phenanthrene, anthracene, pyrene, and their derivatives and gaseous products such as carbon dioxide (CO<sub>2</sub>), carbon monoxide (CO), petroleum gas by the action of SCW. Current study showed that reaction products contained (Fig. 4) in ester (like 2-methyl-ethyl butanoic acid ester), alkane (like dodecane), cyclohexane (like 1,1,3-trimethyl-cyclohexane), ketone (like octahydro-8a-methyl-cis-1(2H)-naphthalenone,) and alcohol (like 2-methyl-1-decanol). [EMIm]Cl decomposition products were not detected by GC/MS. [EMIm]Cl is generally dissolved in water but insoluble in NAs. The water used in this study has a pH value of 7. When [EMIm]Cl was added into the water, the pH was reduced to 4.73, indicating the acidic behavior of [EMIm]Cl. After reaction at a temperature of 80 °C, a reaction time of 30 min, the pH of the water soluble portion was reduced to 4.19, indicating that a small quantity of acid was dissolved in water after reaction. FT-IR spectra (Fig. 5) revealed that [EMIm]Cl was not dissolved in organic reaction products. [EMIm]Cl molecules were probably acting as a catalyst during the course of reaction. Sun and his coworker [21, 22] explained NAs removal mechanism using ILs with the help of techniques proposed by Holbrey et al., in 2003 [23]. During the reaction, water and NAs molecules were trapped into cage structure of [EMIm]Cl. IL molecules also helped to weaken the bond that expedited the reaction of NAs and water molecules. Mandal et al., in 2012 [6] depicted that hydrothermal reaction is controlled by ionic reaction mechanism at high water density and low temperature. Thus, under experimental conditions water molecule is able to produce H and OH ions that can react with NAs to produce non acidic hydrocarbons.



**Fig. 5** FT-IR spectra of **a** IL, [EMIm]Cl **b** after reaction at a temperature of 80 °C **(c)** after reaction at a temperature of 70 °C **d** mixture of NAs, IL, and water before reaction

## 4 Conclusions

The capability of IL-assisted hot water on TAN reduction in NAs was explored in this study. TAN reduction was affected by the reaction temperature and treatment time and was increasing with increasing reaction time and temperature. IL-assisted hot water reduced approximately 31.68% TAN of NAs at a temperature of 80 °C, and a reaction time of 60 min. The kinetics of TAN reduction in NAs using IL-assisted hot water without the addition of catalyst at specified reaction conditions was adjusted to a first-order rate law with respect to the TAN reduction in NAs. The calculated activation energy of the reaction is 10.96 kcal/mol. This value is lower than the reaction of SCW with NAs at temperatures of 400–490 °C. This investigation determined the global reaction. So future work is necessary in order to optimize the reaction toward the TAN reduction and propose suitable reaction mechanism.

**Acknowledgements** This work was financially supported by the Short-Term Internal Research Fund (STIRF), Universiti Teknologi PETRONAS, Malaysia.

## References

1. C. Hardacre, P. Goodrich, K. Anderson, Processing for removing organic acids from crude oil and crude oil distillates. US Pat No. 20120132564 A (2012).
2. Y.-Z. Wang, J.-Y. Li, X.-Y. Sun, H.-L. Duan, C.-M. Song, M.-M. Zhang, Y.-P. Liu, Removal of naphthenic acids from crude oils by fixed-bed catalytic esterification. *Fuel* 116, 723–728 (2014).
3. P.C. Mandal, Wahyudiono, M. Sasaki, M. Goto, Non-catalytic reduction of total acid number (TAN) of naphthenic acids (NAs) using supercritical methanol. *Fuel Process Technol.* 106, 641–644 (2013).
4. R. Kane, M. Cayard, A comprehensive study on naphthenic acid corrosion. Corrosion, NACE International, Houston, USA, Paper No. 02555, 1–16 (2002).
5. A. Lucia, Extraction of naphthenic acid from Indonesian crude oils by methanol-ammonium solution. *Lemigas Scientific Contributions* 34 (1), 91–94 (2011).
6. P.C. Mandal, Wahyudiono, M. Sasaki, M. Goto, Reduction of total acid number (TAN) of naphthenic acid (NA) using supercritical water for reducing corrosion problems of oil refineries. *Fuel* 94, 620–623 (2012).
7. N.M. Shukri, W.A. Bakar, J. Jaafar, Z.A. Majid, Removal of naphthenic acids from high acidity Korean crude oil utilizing catalytic deacidification method. *J. Ind. Eng. Chem.* 28, 110–116 (2015).
8. L. Ding, P. Rahimi, R. Hawkins, S. Bhatt, Y. Shi, Naphthenic acid removal from heavy oils on alkaline earth-metal oxides and ZnO Catalyst. *Appl. Catal. A-Gen.* 371(1–2), 121–130 (2009).
9. A. Zhang, Q. Ma, K. Wang, Y. Tang, W.A. Goddard, Improved processes to remove naphthenic acids. Final Technical Report, California Institute of Technology, Pasadena, CA, DE-FC26-02NT15383, 1–96 (2005).
10. M.F. Rudolf, Process for removing naphthenic acids from hydrocarbon oils. US Pat No. US 2227811 A (1941).
11. H.Y. Oh, J.H. Park, Y.W. Rhee, J.N. Kim, Decarboxylation of naphthenic acid using alkaline earth metal oxide. *J. Ind. Eng. Chem.* 17(4), 788–793 (2011).
12. L. Shi, B. Shen, G. Wang, Removal of naphthenic acids from Beijing, crude oil by forming ionic liquids. *Energy & Fuels* 22(6), 4177–4181 (2008).
13. Y. Sun, L. Shi, Basic ionic liquids with imidazole anion: New reagents to remove naphthenic acids from crude oil with high total acid number. *Fuel* 99, 83–87 (2012).
14. J. Duan, Y. Sun, L. Shi, Three different types of heterocycle of nitrogen-containing alkaline ionic liquids treatment of acid oil to remove naphthenic acids. *Catalysis Today* 212, 180–185 (2013).
15. K. Anderson, P. Goodrich, C. Hardacre, A. Hussain, D. Rooney, and D. Wassell, Removal of naphthenic acids from crude oil using amino acid ionic liquids. *Fuel* 108, 715–722 (2013).
16. H. Quiroga-Becerra, C. Mejia-Miranda, D. Laverde-Cataño, M. Hernandez-López, M. Gomez-Sánchez, A kinetic study of esterification of naphthenic acids from a Colombian heavy crude oil. *CT&F- Ciencia, Tecnología y Futuro* 4(5), 21–32 (2012).
17. L. Jing, S. Yu, S. Li, Study on Removal of Naphthenic Acids from White Oil by [BMIm] Br-AlCl<sub>3</sub>. *China Petroleum Processing & Petrochemical Technology* 12 (4), 46–51 (2010).
18. P.C. Mandal, Md.A.B. Alias, Investigation of asphaltene under subcritical water treatment, IACT, 6th International Conference on Mechanical, Industrial, and Manufacturing technologies (MIMT 2015), The Hotel Equatorial Melaka, Malaysia (2015).
19. P.C. Mandal, Md. A. Abdalla, Md. Moniruzzaman, Acidity reduction of naphthenic acid using imidazolium chloride based ionic liquids. International Conference on Science, Technology and Management (ICSTM 2015), IPN-IWNEST 2015, Melia Hotel (2015).
20. P.C. Mandal, T. Shiraiishi, Wahyudiono, M. Sasaki, M. Goto, Kinetics and reaction pathways of heptylbenzene decomposition in supercritical water, *J. Chem. Eng. Jpn.* 44(7), 486–493 (2011).

21. S. Keskin, D. Kayrak-Talay, U. Akman, O. Hortacsu, A review of ionic liquids towards supercritical fluid applications. *J. Supercrit. Fluids* 43, 150–180 (2007).
22. M. Koel, *Ionic liquid in chemical analysis*. Mihkel Koel, CRC Press, Taylor & Francis (2009).
23. R. Martinez-Palou, R. Luque, Applications of ionic liquids in the removal of contaminants from refinery feedstocks: an industrial perspective. *Energy Environ. Sci.* 7, 2414–2447 (2014).

# Pressure Transient Behaviour of Horizontal Wells in a Bounded Reservoir with Gas Cap and Aquifer

Tsani Sabila and Azeb Habte

**Abstract** Increased productivity can be seen as a result of horizontal well applications in certain reservoir conditions. Consequently, there exists the need to monitor the performance of the horizontal wells and characterise the reservoir surrounding it. The literature provides limited study on pressure transient behaviour of horizontal wells in a reservoir with vertical constant pressure boundaries. Moreover, even lesser investigated completely bounded reservoir (in all X-, Y-, and Z-directions) coupled with vertical constant pressure boundaries. An analytical solution is thus presented for the pressure transient response of horizontal wells in an anisotropic, rectangular, homogeneous reservoir, bounded by gas cap and aquifer and, laterally, by no-flow boundaries. Solutions were formulated using Green's and source function method in combination with Newman's product method. Type curves analysis and detailed discussion of each flow regime exhibited are thoroughly investigated. It could be observed that the pressure behaviour and flow regimes exhibited depend on the type of outer boundaries, distance of the well to the nearest boundary, and length of horizontal well itself. Common flow regimes usually associated with horizontal wells were masked by the constant pressure behaviour.

**Keywords** Bounded reservoir · Vertical constant pressure boundary · Flow regimes · Horizontal well · Gas cap · Aquifer

## List of symbols

k<sub>x</sub> Formation permeability in the X-direction, md  
k<sub>y</sub> Formation permeability in the Y-direction, md  
k<sub>z</sub> Formation permeability in the Z-direction, md

---

T. Sabila (✉)  
Institute of Petroleum Engineering, Heriot-Watt University,  
EH14 4AS, Edinburgh, UK  
e-mail: st46@hw.ac.uk

A. Habte  
Faculty of Geosciences and Petroleum Engineering,  
Universiti Teknologi PETRONAS (UTP), 31750 Seri Iskandar, Perak, Malaysia  
e-mail: azeb.habte@petronas.com.my

rw	Wellbore radius, ft
t	Time, hr
tD	Dimensionless time
Xe	Half of the distance to the boundary in the X-direction, ft
Xw	X coordinate of the production point
Ye	Half of the distance to the boundary in the Y-direction, ft
Yw	Y coordinate of the production point
Zw	Z coordinate of the production point
ct	Compressibility, 1/psi
h	Formation thickness, ft
L	Total length of horizontal well, ft
Lw	Half length of horizontal well, ft
P	Pressure, psi
PD	Dimensionless pressure
Pi	Initial pressure, psi
Pwf	Flowing well pressure, psi
A	Drainage area, ft <sup>2</sup>
B	Oil volumetric factor, RB/STB
Q	Oil well flow rate per unit length of horizontal well, B/D/ft
q	Oil well flow rate, B/D

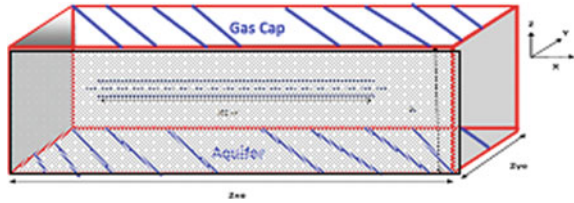
## 1 Introduction

The strategic practicalities and profitability of horizontal wells in certain reservoir situations have been widely recognised and well established in the oil and gas sector. Improved well productivity, reduction of the effects of damaged zones, and higher oil recovery due to better sweep efficiency are all among direct results of using horizontal wells [1].

Due to its advantageous nature, over the past two decades, there has been rapid surge in the implementation of horizontal wells technology. As a consequence of this, there also exists the need to develop analytical models that can evaluate the performance of these horizontal wells. An analytical model is used here because the analytical solution is able to give direct “meaning”; as opposed to numerical solution. Hence, transient pressure analysis techniques have emerged as an auspicious method for the assessment of horizontal well productivity and performance as well as reservoir characterisation.

The literature provides limited study for an analytical solution pertaining horizontal wells in a reservoir bounded by vertical constant pressure boundaries apart from the research conducted by Stewart and Du [2] and later by Lu [3]. Yet, both research studies still did not consider completely bounded reservoir geometry in lateral directions (they considered laterally infinite boundaries, only finite in

**Fig. 1** Reservoir geometry configuration



Y-direction). Fewer researchers in the past investigated the reservoir bounded in all three directions (X, Y, and Z) with the exceptions of the analytical works carried out by [1, 4, 5]. Nevertheless, all of these previous studies focused on bounded reservoir with vertical no-flow boundaries. Hence, it is for this reason that this research is conducted.

In this study, focus is directed in analysing pressure behaviour of horizontal wells in a homogeneous, rectangular-shaped reservoir bounded by vertical constant pressure boundaries (aquifer and gas cap) and also bounded by two no-flow boundaries laterally. The diffusivity equation to be solved is for 3D, anisotropic medium with Cartesian coordinates. Solutions for this reservoir geometry are formulated and developed based on the principles of Green’s and source functions [6] merged with Newman’s product method [7]—combining with the definitions of dimensionless variables defined in Al Rbeawi and Tiab’s work [1]. The assumption of slightly compressible fluid is applied throughout the medium. In addition, effects of gravity are negligible. For simplicity, wellbore storage and mechanical skin effects are not considered. Type curves are generated using MATLAB software (Fig. 1).

## 2 Discussion

The mathematical model in dimensionless form for pressure transient behaviour in a bounded reservoir with gas cap and aquifer is modelled as shown in Eq. (1).

$$P_D = \pi.X_eD Y_eD \tag{1}$$

$$\left. \begin{matrix} \text{id} \\ \int \\ 0 \end{matrix} \right\} \times \left[ \begin{matrix} 1 + \frac{4}{\pi X_eD} \sum_{n=1}^{\infty} \frac{1}{n} \exp\left(-\frac{\pi^2 n^2 X_{gd}^2 \tau D}{4}\right) \sin\left(n\pi \frac{X_{gd}}{2}\right) \\ \cos\left(n\pi \frac{X_wD}{2}\right) \cos\left(\frac{n\pi}{2} (XD X_eD + X_wD)\right) \end{matrix} \right] \times \left. \begin{matrix} \\ \\ \end{matrix} \right\} d\tau D$$

$$\left[ \begin{matrix} 1 + 2 \sum_{n=1}^{\infty} \exp\left(-\frac{\pi^2 n^2 Y_{gd}^2 \tau D}{4}\right) \cos\left(n \frac{Y_wD}{2}\right) \\ \cos\left(\frac{n\pi}{2} (Y_D Y_eD + Y_wD)\right) \end{matrix} \right] \times \left[ \begin{matrix} \sum_{n=1}^{\infty} \exp\left(-n^2 \pi^2 L_D^2 \tau D\right) \sin(n \pi z_{wD}) \\ \sin\left(n\pi (z_D L_D + Z_wD)\right) \end{matrix} \right]$$

Consequently, as shown in Eq. 1, based on Lord Kelvin's and Newman's product method in solving 3D heat conduction problems, when the reservoir is not considered to be of infinite extent in all directions, having straight boundaries that are maintained either as no-flow or constant pressure boundaries (or mixed), the bounded reservoir can be replaced by an infinite reservoir in all directions by taking images in the bounding planes [1]. Hence, the solution of a three-dimensional problem can be solved as equivalent to the product of solutions of three one-dimensional problems.

## 2.1 Model Validation

### 2.1.1 Validation Against Literature

Type curves generated are validated against Al Rbeawi and Tiab's study [1] since the definitions of dimensionless variables were adapted from their paper. Validation of the mathematical model can only be done at early times. This is due to the fact that Al Rbeawi and Tiab's study differed in their vertical boundary conditions (theirs were no-flow boundaries) while the reservoir geometry currently under this study possesses vertical constant pressure boundaries. It is observed that indeed, the mathematical model matched and was validated against literature starting at the early times of 0.00303 h as displayed in Figs. 2 and 3; see the pressure derivative trend between dimensionless time  $tD = 0.0001$  to  $tD = 0.001$ .

### 2.1.2 Validation Against Numerical Differentiation

The pressure derivative was calculated through numerical differentiation by means of adjacent points as referred from [10]—see Eq. 2. It is concluded that the analytical solution used in this study also matches with the numerical solution calculated—see Fig. 3

$$\begin{aligned}
 t \left( \frac{\partial p}{\partial t} \right)_i &= t_i \frac{(t_i - t_{i-1}) \Delta p_{i+1}}{(t_{i+1} - t_i)(t_{i+1} - t_{i-1})} \\
 &+ \frac{(t_{i+1} + t_{i-1} - 2t_i) \Delta p_i}{(t_{i+1} - t_i)(t_i - t_{i-1})} \\
 &- \frac{(t_{i+1} - t_i) \Delta p_{i-1}}{(t_i - t_{i-1})(t_{i+1} - t_{i-1})}
 \end{aligned} \tag{2}$$



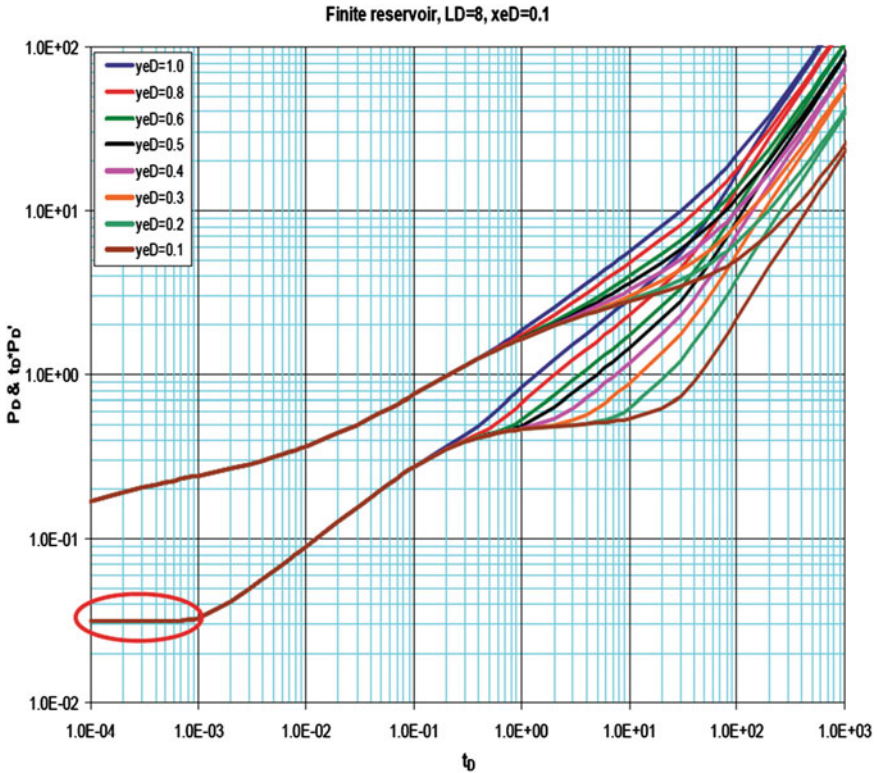
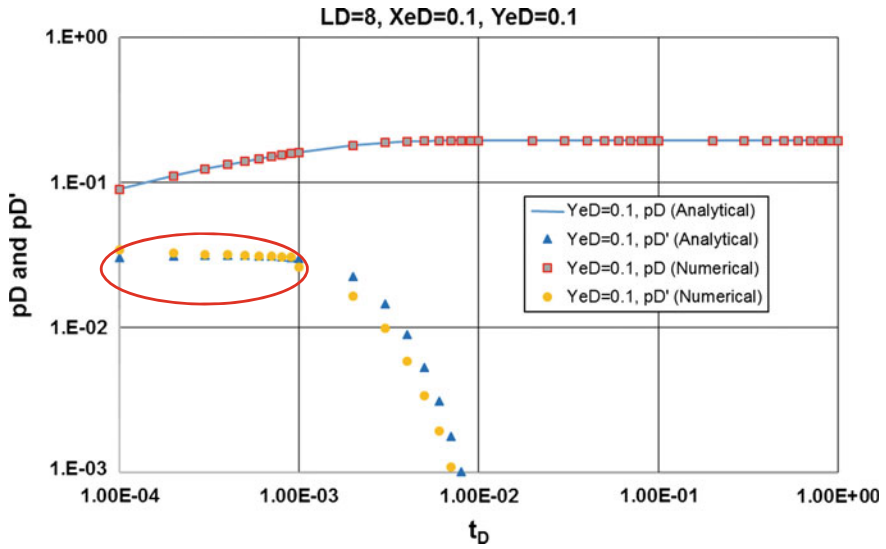


Fig. 2 Type curve for short horizontal well in bounded reservoir with vertical no-flow boundaries for  $LD = 8, XeD = 0.1$  (Adapted from [1])

### 2.2 Flow Regimes

Generally, in a bounded reservoir with vertical no-flow boundaries, five flow regimes could be observed [1]. The following are the commonly occurring flow regimes: early radial flow, early linear flow, pseudo-radial flow, channel flow (late linear flow), and pseudo-steady-state flow. Lee et al. [8] as strengthened by [1] explained that the early linear flow occurs when the pressure has already reached both vertical no-flow boundaries. Furthermore, pseudo-radial flow is observed when the fluid flows to the wellbore from beyond the ends of the well. Finally, the late pseudo-steady-state flow regime could be seen when the bounded reservoir has been produced for a long time and is marked by a unit slope line as a consequence of the pressure being influenced by all four closed boundaries.

However, with regard to the reservoir under this study possessing constant pressure boundaries, only the early radial flow and constant pressure behaviour could be detected. Based on the results obtained, it is thus concluded that the commonly occurring flow regimes associated with horizontal wells are masked by constant pressure behaviour.



**Fig. 3** Analytical and numerical differentiation solution—type curve for short horizontal well in bounded reservoir with constant pressure boundaries for  $LD = 8$ ,  $XeD = 0.1$ ,  $YeD = 0.1$

### 2.2.1 Early Radial Flow

As shown in Fig. 3, the early radial flow is observed. In his study, [9] stated that elliptic cylindrical flow is the first pattern before the flow becomes radial. Short-time approximation for this flow is defined by [1]—see Eq. 3:

$$t_D = \frac{(1 - x_D)^2}{20} \tag{3}$$

### 2.2.2 Late Linear Flow

Normally, the late linear flow occurs when the pressure has diffused and reached the lateral no-flow boundaries [1, 8, 9]. However, under the realistic physical reservoir thickness, the late linear flow regime could not be observed for the reservoir under study. Table 1 below displays the reservoir parameter used in this study as adapted from [1]. Short horizontal wells as compared to reservoir thickness are defined as  $LD < 20$  while longer horizontal wells are defined as  $LD > 20$ .

**Table 1** Reservoir thickness used in this study

Parameter limit	Reservoir thickness (ft)	Dimensionless variable
Max	400	$LD = 1$
Min	12	$LD = 32$

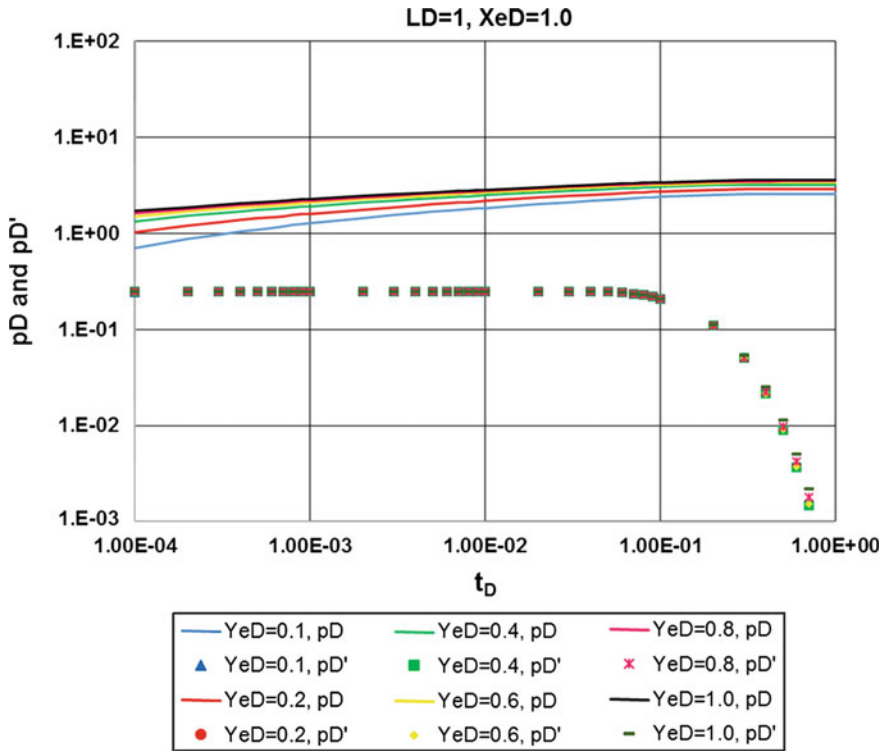
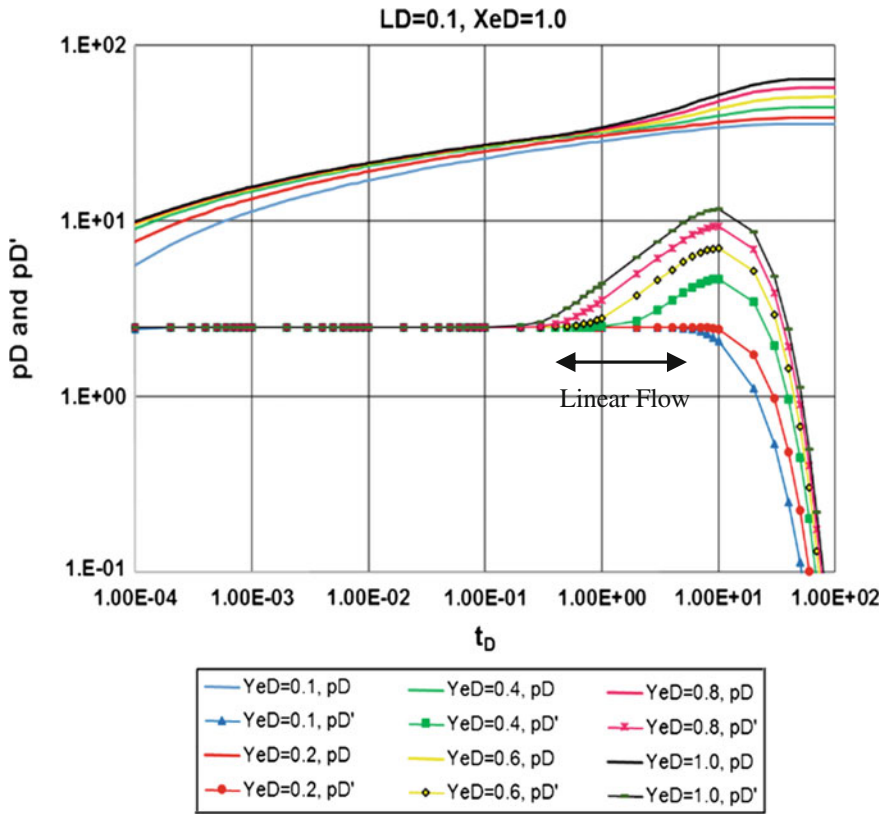


Fig. 4 Type curve for short horizontal well,  $LD = 1$ ,  $XeD = 1.0$ ,  $h = 400$  ft

For the sake of research purpose, the reservoir thickness was varied to 4000 ft. Distance to boundary in X-direction ( $XeD$ ) is kept constant, but reservoir thickness is varied. It was discovered that the late linear flow does exist as illustrated in Fig. 5 ( $h = 4000$  ft) in comparison with Fig. 4 ( $h = 400$  ft). Pressure tends to diffuse faster vertically than horizontally. Hence, for this case as shown in Fig. 5, it is deduced that due to the large extent of reservoir thickness, the pressure is “felt” sooner at the lateral boundaries as opposed to the vertical constant pressure boundaries. Thus, the late linear flow regime appeared before the constant pressure behaviour.

Based on Fig. 5, it is observed that as the distance to the lateral boundary in the Y-direction decreases ( $YeD$  increases), the linear flow regime thus becomes more pronounced and the duration of the flow is longer. On the other hand, it is clearly seen that when  $YeD = 0.1$  (larger distance of lateral boundary in Y-direction), this enables the pressure to diffuse faster vertically to constant pressure boundaries and ultimately, masked other consequent flow regimes.



**Fig. 5** Type curve for short horizontal well,  $LD = 0.1$ ,  $XeD = 1.0$ ,  $h = 4000$  ft (thickness varied only for research purpose)

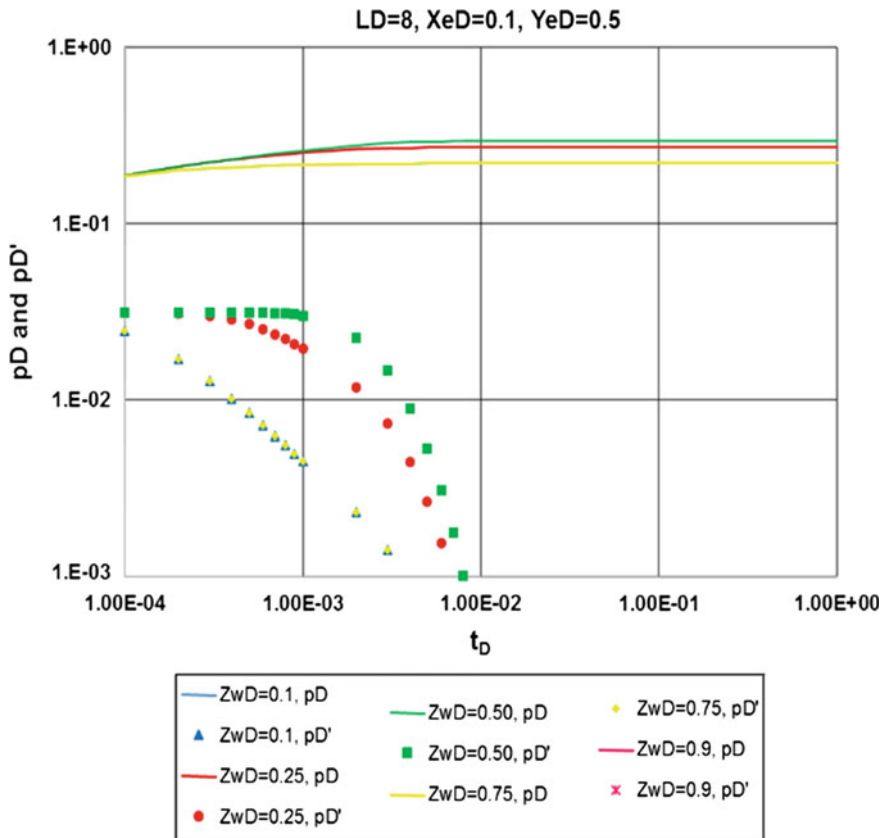
### 2.2.3 Constant Pressure Behaviour

It is concluded based on the type curves generated that varying  $YeD$  and  $XeD$  (distance to lateral boundaries) do not have significant effect on pressure derivatives, rather only the pressure value changes for the reservoir geometry under study. However, pressure derivative is only significantly affected by the ratio of the wellbore length to the reservoir thickness ( $LD$ ). This phenomenon reported actually eases the practice of type curves as users would only need to match with the pressure trend, since all pressure derivatives are showing similar trend/values.

### 2.3 Varying Location of Well in Vertical Direction

Wellbore location is varied in the vertical direction to investigate the pressure behaviour especially when the wellbore is closer to any of the vertical constant pressure boundaries. The Z-coordinate starts at 0 from the aquifer and ends at 1 with the gas cap.

Based on Fig. 6, it is understood that when the well is set closest to the aquifer ( $Z_{wD} = 0.1$ ), the pressure derivative value and trend are exactly equivalent as to the situation when the wellbore is located nearest to gas cap ( $Z_{wD} = 0.9$ ). It is thus concluded that due to both gas cap and aquifer being constant pressure boundaries, the equation is not able to differentiate between them both and hence, type curve matching is not suitable for the purpose of investigating well location in vertical



**Fig. 6** Pressure behaviour as a result of varying reservoir thickness (varying well location in vertical direction, hence, distance to vertical constant pressure boundaries)

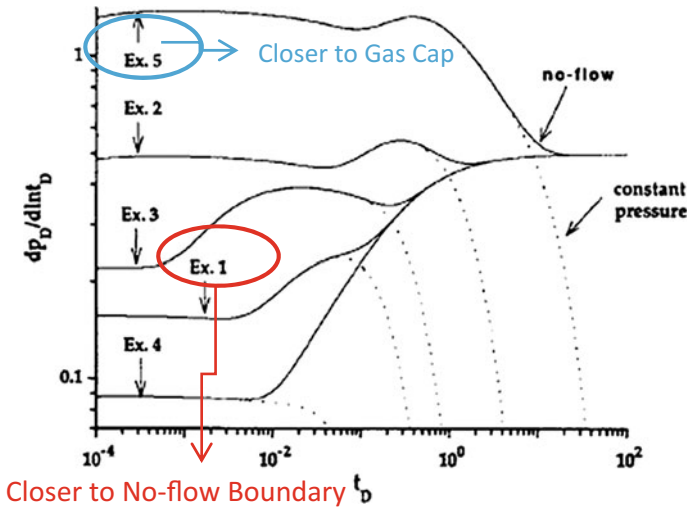


Fig. 7 Graph showing no-flow boundary model (solid line) and mixed boundary model (dotted line). Adapted from [9]

direction. On the contrary, [9] in his study (though with infinite lateral boundaries) have indicated that if the vertical boundaries are either mixed boundaries and/or no-flow boundaries, then the model could be used to analyse pressure behaviour when the well location is varied in the vertical direction as shown in Fig. 7.

### 3 Conclusion

Many comprehensive analytical solutions for horizontal wells have been proposed in the literature including, Laplace, Fourier transforms, and Green’s function for both isotropic and anisotropic reservoirs. Using these solutions and dimensionless variables, it is possible to generate pressure and pressure derivative type curves for varying horizontal well parameters.

It is concluded based on this study that:

1. Pressure behaviour and flow regimes of horizontal wells acting in bounded reservoirs are affected significantly by how fast the pressure can be felt at the vertical or lateral boundaries. The impact of the lateral boundaries on pressure responses and fluid flow regimes occurs at late time production. Since pressure tends to diffuse faster vertically than horizontally, pressure is usually “felt” sooner at vertical constant boundaries and may mask other commonly occurring flow regimes as a result of lateral boundaries (pressure diffusion in horizontal direction). Thus, only early radial flow and constant pressure behaviour could be mainly observed in this study. However, only when reservoir thickness is

increased significantly (which gives more time before effects of vertical boundaries can be “felt”; we see other common flow regimes as a result of lateral boundaries.

2. Pressure derivative is not significantly impacted by distance to lateral boundary in both X and Y directions but only affected by the ratio of the wellbore length to the reservoir thickness (variable  $LD$ ).
3. The pressure behaviour of the long horizontal well, i.e.  $LD > 20$ , is similar to the behaviour of vertical fractures. Early radial flow cannot be seen for long horizontal wells.

## References

1. S. J. H. Al Rbeawi and D. Tiab, “Transient Pressure Analysis of Horizontal Wells in a Multi-Boundary System,” in SPE Production and Operations Symposium, 2013.
2. K.-F. Du and G. Stewart, “Analysis of Transient Pressure Response of Horizontal Wells in Bounded Reservoirs Using Derivative Approach,” 1994/3/1/ 1994.
3. J. Lu, “A Mathematical Model of Horizontal Wells Productivity and Well Testing Analysis,” Virginia Polytechnic Institute and State University, 1998.
4. F. Daviau, G. Mouronval, G. Bourdarot, and P. Curutchet, “Pressure analysis for horizontal wells,” SPE Formation Evaluation, vol. 3, pp. 716–724, 1988.
5. L. C. Wang Xiaodong, “Horizontal Well Pressure Analysis In Box-Bounded Reservoirs,” Appl. Math. Mech. -Engl. Ed., vol. 19, pp. 315–320, 1998-04-18 1998.
6. A.C. Gringarten and H. J. Ramey Jr, “The use of source and Green’s functions in solving unsteady-flow problems in reservoirs,” *SPE Journal*, vol. 13, pp. 285–296, 1973.
7. B. Newman, “Heating and cooling rectangular and cylindrical solids,” *Industrial & Engineering Chemistry*, vol. 28, pp. 545–548, 1936.
8. J. Lee, J. B. Rollins, and J. P. Spivey, *Pressure transient testing*: Richardson, Tex.: Henry L. Doherty Memorial Fund of AIME, Society of Petroleum Engineers, 2003.
9. F. Kuchuk, P. Goode, D. Wilkinson, and R. Thambynayagam, “Pressure-transient behavior of horizontal wells with and without gas cap or aquifer,” *SPE Formation Evaluation*, vol. 6, pp. 86–94, 1991.
10. Horne, R. N. *Modern Well Test Analysis*. Petroway Inc, 1995.

# Effect of Synthesized Biopolymer from Coconut Residue as Drag Reducing Agent in Water Injection Well

T.M. Alghuribi, M.S. Liew and N.A. Zawawi

**Abstract** Over the past 20 years, commercial polymers have been utilized in oil and gas industries as drag reducing agent (DRA) to minimize the pressure drop and improve the injectivity in water flooding systems. Several studies have been carried out to find an alternative for commercial polymers as drag reducing agents (DRAs) from natural and biodegradable polymers such as carboxymethylcellulose (CMC) which are more environmental friendly, yet performing as good as the synthetic polymer. In this paper, a new eco-friendly DRA is extracted from organic materials (coconut residue) to replace the commercial polymer, due to its abundance and ability to perform as effective as commercial polymer in lowering pressure losses and accelerating the flow in oil and gas pipelines. The objective of this study was aimed to demonstrate the synthesizing process of biopolymer from coconut residue, then test biopolymer DRA impacts on formation permeability after injecting them into the reservoir, and finally studying the mechanical degradation of biopolymer DRA by exposing the solutions to a high mechanical stirring speed using viscometer device. An experimental study is conducted using a benchtop permeability system to justify if the DRAs have any impact on formation permeability. Three core samples were flooded with brine solution of 10000 ppm and DRA solution of 50 ppm at three different injection rates 1 ml/min, 3 ml/min, and 5 ml/min consecutively. The mechanical degradation of the DRA is examined by exposing 0.5–1.0% solutions of biopolymer to a high stirring speed ranged from

---

T.M. Alghuribi (✉)

Department of Petroleum Engineering, Universiti Teknologi PETRONAS,  
Seri Iskandar, Perak, Malaysia  
e-mail: utp.tareq@gmail.com

M.S. Liew

Faculty of Petroleum Engineering and Geoscience, Universiti Teknologi PETRONAS,  
Seri Iskandar, Perak, Malaysia  
e-mail: shahir\_liew@petronas.com.my

N.A. Zawawi

Department of Civil Engineering, Universiti Teknologi PETRONAS, Seri Iskandar,  
Perak, Malaysia  
e-mail: amilawa@petronas.com.my



500 rpm to 1500 rpm for 60 min to perceive whether such influence is noticeable. The result showed the solution of 1.0% concentration has higher mechanical degradation compared to a lower molecular weight solution of 0.5% concentration.

**Keywords** Biopolymer extraction · Coconut residue · DRA · Formation permeability · Mechanical degradation

## 1 Introduction

Optimizing the production in oil and gas industries is undoubtedly very important and has positive consequences such as increasing the efficiencies and maximizing the economic revenue. The excessive usage of operational pumps in handling pressure drop across the pipeline leads to severe financial consequences forcing oil and gas industries to look for an appropriate alternative. Commercial polymers known as drag reducing agents were later acknowledged to be the best alternative to replace high-power pumps, since they have the ability to demonstrate the turbulent flow behaviors [1, 2]. The usage of commercial polymers as drag reducing agents (DRAs) has been proven to be successful in minimizing the effect of frictional forces along the injection tubing of water injection system as well as enhancing the system deliverability [3]. Practically, commercial polymers are introduced in oil and gas industries by injecting them into the system in order to boost flow throughput and lower pressure losses in the line.

The excessive usage of commercial polymers such as polyacrylamide has ringed the alarm of increasing the risks negatively toward the environment, due to the degradation of their chemical compositions in high turbulent flow [4]. These environmental impacts have pushed oil and gas industries to dig for a new environmentally friendly replacer for commercial polymer. Meanwhile, this paper presents eco-friendly biopolymers extracted from coconut residue which have been testified to be the best alternative for commercial polymers as well as a successful DRA [5]. Injecting small amount of these additives into turbulent flow regime will result out in a less pressure drop and enhancement in water flooding operations without changing the pipeline conditions [6]. Based on the reduction theory, drag reduction occurs as a result of the suppression of the energy dissipation by turbulent eddy flows near the pipe wall during turbulent flow regime [7]. DRA performance is dependable upon several parameters, namely concentration, viscosity, solubility, and molecular weight of the chemical additives [8, 9]. Yet these parameters are the main factors in controlling the effectiveness of drag reducing agents in turbulent flow regime. The synthesized drag reducing agents from coconut residue are only effective in overcoming the drag forces throughout turbulent flow regime. Turbulent flow occurs whenever the Reynolds number is equal or greater than 4000 [10]. The Reynolds number is calculated by using Eq. (1):

$$R_e = \frac{\rho VL}{\mu} \quad (1)$$

where  $\rho$  is the density of the fluid,  $V$  is fluid velocity,  $L$  is the length or diameter of the pipe, and  $\mu$  is the viscosity of fluid.

### ***1.1 Mechanism of Biopolymer DRA***

The extracted drag reducing agent (DRA) from coconut residue is a highly molecular weight chemical and potentially effective agents in reducing drag forces along the inner wall of the injection tubing and boosting the flow rate significantly [9]. During the water flooding operation, DRAs have been used to optimize the production and accelerate the flooding process which definitely helps oil and gas operators to reduce the number of injection wells [11]. In a turbulent drag reducing flow, biopolymer DRAs have the ability to control the slug frequency as well as the thickness of liquid film, which eventually diminish the disorder patterns of the flowing fluid, and accelerate the flowing fluid in the line [12]. Despite all the advantages DRAs provide for oil and gas industries, they still rapidly lose their efficiencies at intense turbulent flow, due to either chemical reactions or mechanical forces causing a rupture of biopolymer's chains. This rupture weakens the biopolymer molecules and makes it difficult to overcome the induced frictional forces across the flow line [13]. The usage of these biopolymers in practical applications has been severely limited due to their poor mechanical stability in turbulent flow.

The reduction in DRA efficiency in turbulent flow with exposure time is just evident of mechanical degradation which is observable once exposing such solution to a high stirring speed. Mechanical degradation is a very common phenomenon in drag turbulent flow regime, which is often observed when the additives are subjected to high fractional forces for a sufficient time [14]. Mechanical degradation of DRAs is tangible in turbulent flow whereby a breakage of agglomerate chains of biopolymers is caused by high mechanical forces throughout the operation. Degradation rate is experimentally determined through viscosity test measurement as a probable change in the average molecular weight accompanied with changes in biopolymer's efficiency [15].

## **2 Methodology**

### ***2.1 Extraction of Cellulose***

Coconut residue was collected and then rinsed with water for cleaning purpose, and then, it was dried in the oven at 50 °C for 2 days. The dried sample was later

grinded before cooking it with 1 M of NaOH at 150 °C using magnetic stirrer (200 rpm) for 1 h. Afterward, it was filtered using a tea bag filter to separate the solid phase from the liquid phase. The powder was washed with plenty of water until it is kept clean. Finally, the pulp was dried again at 55 °C for 24 h.

## 2.2 Preparation of Carboxymethyl Cellulose (CMC)

The extraction of carboxymethyl cellulose is initiated with two reactions, namely alkalization reaction and carboxymethylation reaction. The alkalization reaction was initiated by mixing 15 grams of obtained cellulose with isopropanol and 40% of NaOH, whereas the carboxymethylation reaction was conducted by adding 18 grams of chloroacetic acid. The entire extraction process of CMC is summarized in Fig. 1.

## 2.3 Sample Preparation

The preparation process of all sample concentration is achieved by utilizing Eq. (2):

$$ppm = \frac{\text{mass of DRA}(g)}{\text{volume of distilled water}(ml)} \times 10^6 \quad (2)$$

Permeability reduction is determined by Eq. (3):

$$K_{\text{reduction}} = \frac{K_{\text{before}} - K_{\text{after}}}{K_{\text{before}}} \times 100\% \quad (3)$$

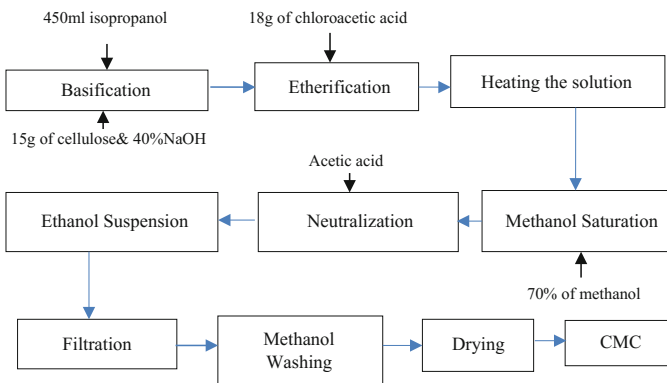


Fig. 1 CMC preparation process

Recovered permeability is calculated by using Eq. (4):

$$K_{\text{recovered}} = \frac{K_{\text{final}} - K_{\text{after}}}{K_{\text{before}} - K_{\text{after}}} \times 100\% \quad (4)$$

### 2.4 Mechanical Shear Degradation of DRA

Two biopolymer solutions of 0.5–1.0%wt concentrations were prepared initially and then exposed to shear rates ranged from 500 rpm to 1500 rpm for exposure time of 60 min. The viscosity of the solutions was measured after 15, 30, 45, and 60 min with regard to stirring speed in order to determine the mechanical degradation of the solutions. The viscosity was recorded using viscometer device. The viscosity reduction (%RV) is achievable by using Eq. (5) which assesses the viscosity of the solution before and after exposing it to such mechanical stirring speed to attain the mechanical degradation of DRA if any.

Viscosity reduction (RV) is defined as in Eq. (5):

$$\%RV = \frac{\mu_{\text{before}} - \mu_{\text{after}}}{\mu_{\text{before}}} \times 100\% \quad (5)$$

## 3 Results and Discussion

This chapter demonstrated the collected data from experimental analysis to attain the objectives of this paper. The results are depicted in the following pages and then interpreted accordingly.

### 3.1 Collected Mass of CMC from Coconut Residue

In this result section, the collected mass (g) of carboxymethyl cellulose (CMC) from coconut residue at 40% sodium hydroxide concentration and at various reaction temperature, and reaction time were tabulated in Table 1 accordingly.

Table 1 shows that CMC mass was achieved based on three reaction factors including concentration of NaOH, reaction temperature, and reaction time. The concentration of NaOH was set to be 40%wt for 6 runs, because a higher mass of CMC was collected under 40%wt concentration as proven by [6]. The highest mass of 27.10 g was collected when the sample undergone a reaction temperature of 50 °C for 60 min, but immediately declined as the reaction time doubled to 120 min. Hence, the reaction time is likely to be the crucial factor in controlling the

**Table 1** Extracted mass of CMC from coconut residue

Run no	Concentration of NaOH(%)	Reaction temperature (°C)	Reaction time (min)	Collected mass of carboxymethylcellulose (g)
1	40	50	60	26.872
2	40	50	60	27.100
3	40	50	60	23.665
4	40	50	120	22.030
5	40	55	60	19.511
6	40	55	240	24.745

amount of CMC mass. In the fifth run, as the reaction temperature increased to 55 °C while maintaining the reaction time constant, the amount of yield CMC mass dropped to 19.511 g. The reason behind this drop is the degradation of coconut residue cellulose as temperature increases.

### 3.2 Permeability Test

The main purpose of this test is to analyze the associated impacts of DRAs on the formation permeability once DRAs were injected into the reservoir. The DRAs effects on formation permeability were investigated by flooding three core samples with DRA solution at different injection rates as illustrated in Figs. 2, 3, and 4.

Figure 2 shows that the core was initially flooded with brine at 1 ml/min until the permeability's curve stabilized. The stabilization phase was noticeable after 60 min with a permeability value of 14.565 md. However, a drop to about 8.12 md was observed after flooding the core with biopolymer DRA solution at the same injection rate.

A significant permeability reduction to about 44.34% was induced after injecting biopolymer DRA into the reservoir. The core was then reversed, and a back flow process was carried out at 8 cc/min for 15 min to restore the permeability. Eventually, the core was flooded with brine again for 1 h at 1 ml/min to obtain the final permeability; hence, final permeability was recorded to be 9.122 md. It can be said that the restored permeability was observed to be 15.51%. Hence, the test is ceased once the pressure profile stabilized at almost a constant value.

Similarly, Fig. 3 describes the flooding process of the core sample with brine and then with biopolymer DRA solution at 3 ml/min injection rate for 60 min. After one hour, the permeability of the formation dropped from 10.13 md to 7.65 md, due to the presence of biopolymer DRA in the formation. A back flow process was carried out in order to achieve the final permeability by which the core sample was reversed and then flooded at 8 ml/min for 15 min. Obviously, the higher the injection rate, the lower the permeability reduction will be. The pressure

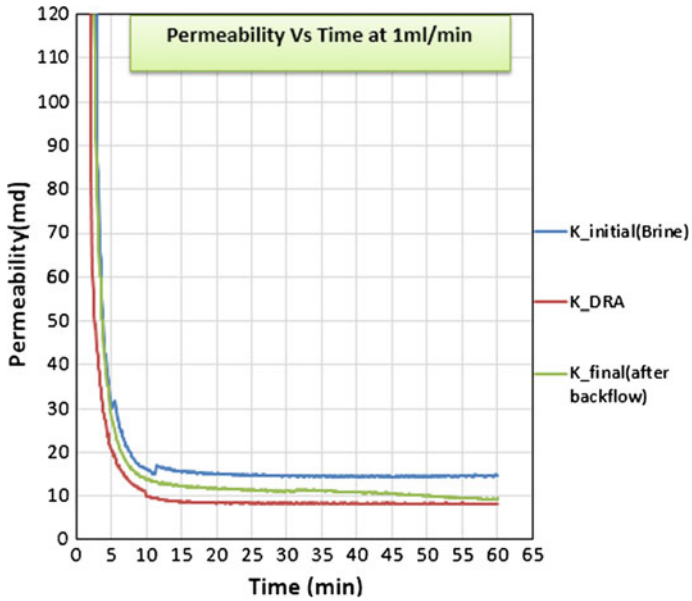


Fig. 2 Biopolymer DRA performance at 1 ml/min

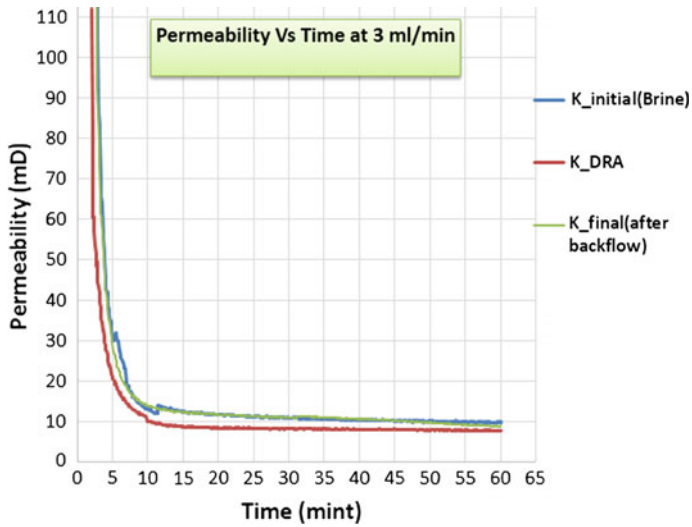


Fig. 3 Biopolymer DRA performance at 3 ml/min

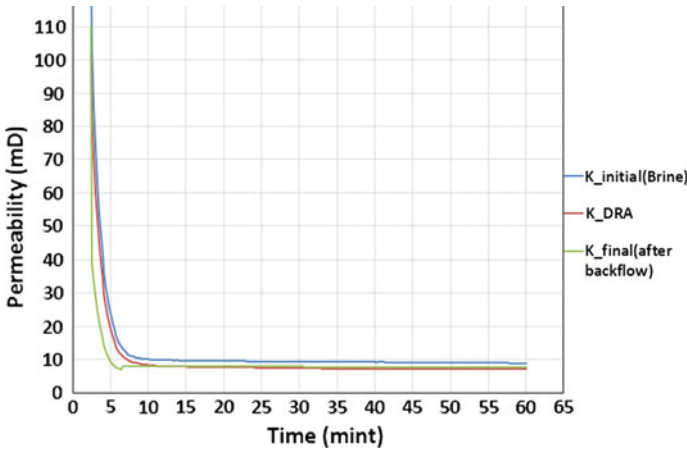


Fig. 4 Biopolymer DRA performance at 5 ml/min

profile shows that the pressure increases at the beginning of each run and becomes constant as the permeability reaches a constant value.

According to Fig. 4, the impact of biopolymer DRA on the formation permeability at injection rate of 5 ml/min was insignificant. It can be clearly seen that permeability was reduced from 8.037 md to 7.037 md after flooding the core sample with biopolymer DRA solution. Subsequently, the core sample was subjected to a back flow process to retrieve the initial permeability of the formation. The final permeability was attained by flooding the core with brine solution at 5 ml/min by which it was perceived to be 7.607 md after 1 h.

As a result, the permeability reduction can be overcome by increasing the injection rate of DRA, so the higher the injection rate, the lower the reduction value of the permeability will be.

Figure 5 summarized the permeability reduction and the restored permeability percentage after injecting the biopolymer DRA into the reservoir. At injection rate

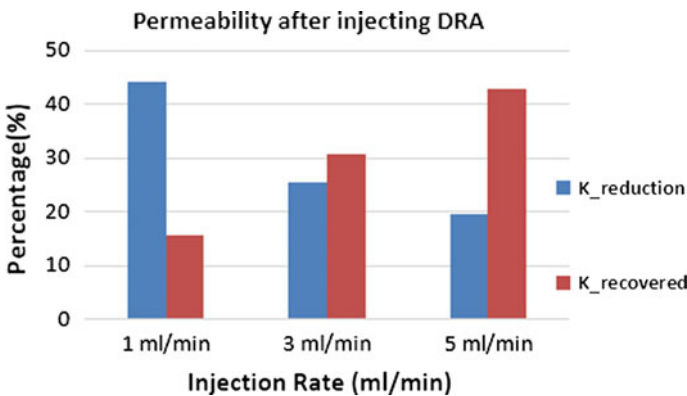


Fig. 5 Permeability reduction and recovered versus injection rate

of 1 ml/min, a reduction of 44.34% was computed, and recovered permeability was beyond 15%. As the injection rate increases, the opposite observation was witnessed. For instance, at injection rate of 5 ml/min, the reduction in formation permeability was only 19.47% and the recovered permeability was triple the recovered permeability at 1 ml/min injection rate. This shows that permeability reduction is a function of injection rate, and the higher the injection rate, the lower the reduction in the formation permeability will be.

In contrast, the recovered permeability is dependable upon the injection rate where it raised to 43% at 5 ml/min, followed by 30.34% at 3 ml/min, and finally it dropped to 15.54% at 1 ml/min. Therefore, permeability reduction decreases with increasing the injection rate of the system and vice versa for the recovered permeability.

### 3.3 Mechanical Effects on Biopolymer as DRA

Biopolymer DRA was exposed to high mechanical stirring 500 rpm, 1000 rpm, and 1500 rpm to investigate the viscosity changes of biopolymer. Two solutions of 0.5% and 1.0% of DRA were prepared to certify the stirring speed influence on the viscosity of the solution.

From Fig. 6, it is shown that a gradual reduction in viscosity was noticed with respect to the exposure time. Exactly, after 1 h of stirring, the viscosity dropped

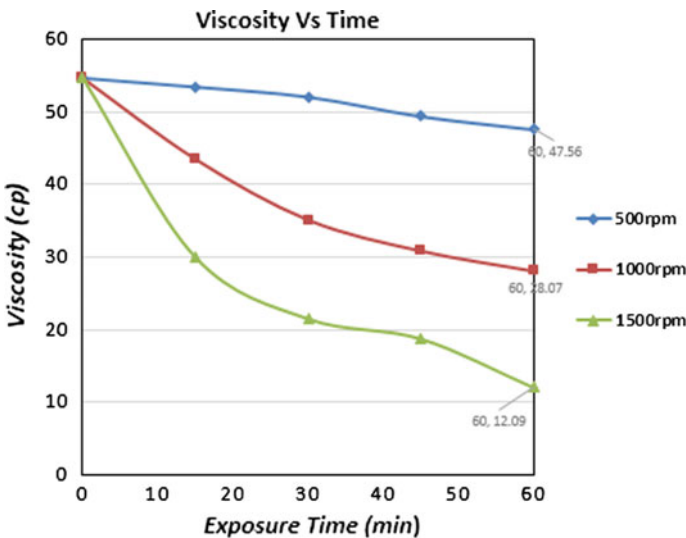
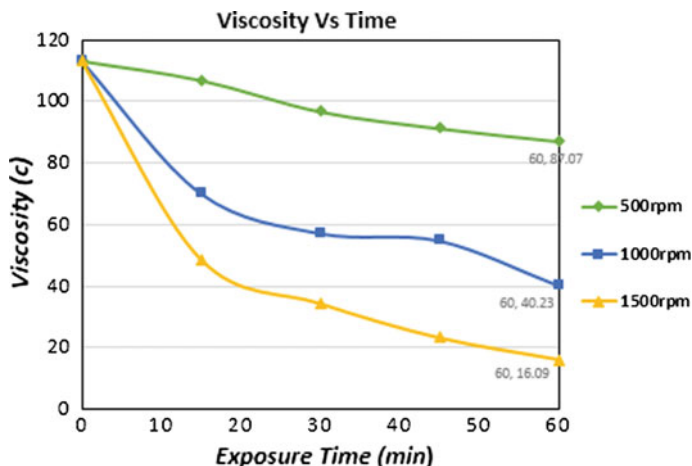


Fig. 6 Effect of exposure time and stirring speed on the viscosity of 0.5% biopolymer solution





**Fig. 7** Effect of exposure time and stirring speed on the viscosity of 1% biopolymer solution

from 54.62 cp to 47 cp at 500 rpm, followed by a significant reduction from 54.62 cp to merely 28 cp at 1000 rpm. Hence, a high mechanical stirring leads to a higher lowering in the viscosity.

A gradual decrease in biopolymer solution viscosity with increasing time of shearing is shown in Fig. 7. The test was conducted for 1.0%wt biopolymer solution at 500, 1000, and 1500 stirring speed consecutively. The reduction in biopolymer viscosity was observed, and after 1 h of stirring, the viscosity changed sharply from 56 to 47.56 cp, 28.07 cp, and 12.09 cp for biopolymer solution of 1.0%wt. Based on this, higher molecular weight biopolymer undergoes higher mechanical degradation which causes them to lose their efficiency faster when subject to tremendous turbulent flow.

Both Figs. 8 and 9 indicated that solutions with higher concentrations are more vulnerable to lose their effectiveness when exposed to higher mechanical forces. Additionally, a remarkable reduction was noticeable as the stirring speed increases. After 60 min of the test, viscosity reduction of 0.5 biopolymer DRA solution at 500, 1000, and 1500 rpm was 13.95, 48.73, and 78.03%, respectively, while for 1.0% biopolymer DRA solution, viscosity reduction was 87.61% at 500 rpm, 66.37% at 1000 rpm, and 23% at 1500 rpm.

Therefore, the results of both Figs. 8 and 9 are evident of susceptibility of biopolymer DRA for mechanical degradation as their molecular weight gets higher. This is because biopolymer chains for low concentration solutions are unlikely to be destroyed faster by the turbulent flow forces which make their effectiveness last longer with compared to high concentration solutions. Generally, mechanical degradation is acknowledged whenever the viscosity reduction is above 10%.

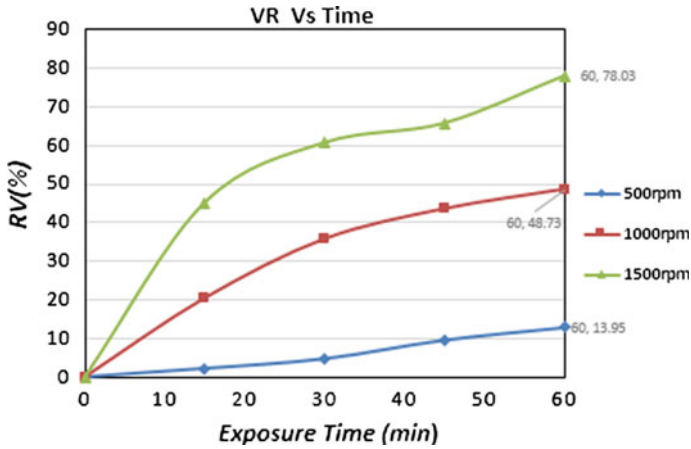


Fig. 8 Viscosity reduction of 0.5% biopolymer DRA

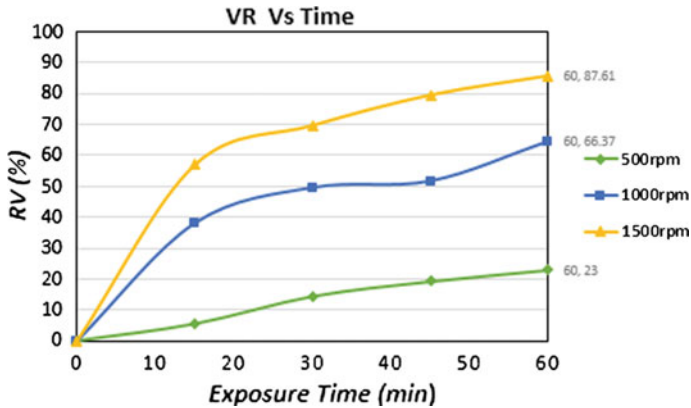


Fig. 9 Viscosity reduction of 1.0% biopolymer DRA

### 4 Conclusion

As a result, the extracted DRA from coconut residue has yet proven their ability in overcoming the flow line frictional forces and enhancing the flow rate throughout the pipeline. The usage of biopolymer DRA in water flooding system is effective despite the disadvantages that might lead to a permeability reduction. Thus, precaution needs to be taken to ensure the reduction in permeability is negligible. The reduction in the formation permeability depends on the injection rates: A higher injection rate gives a lower permeability reduction compared to lower injection rate. In contrast, the recovered permeability percentage also depends on the injection rates with high injection rates, and a higher recovery of formation permeability is perceived. Therefore, permeability reduction is a function of injection rate; the higher the

injection rate, the lower the reduction percentage will be. Finally, mechanical degradation of biopolymer DRA was studied by subjecting the solutions to a high stirring speed for adequate exposure time. It was perceived that biopolymer DRAs with high concentration solutions lost their efficiency faster with compared to those solutions that have low concentrations. The reduction in viscosity is due to the degradation of biopolymer molecules that weakens and breaks their chains and makes their effectiveness to vanish faster.

## References

1. H. Karami and D. Mowla, "Investigation of the effects of various parameters on pressure drop reduction in crude oil pipelines by drag reducing agents," *Journal of Non-Newtonian Fluid Mechanics*, vol. 177, pp. 37–45, 2012.
2. H. A. A. Bari, K. Letchmanan, and R. M. Yunus, "Drag Reduction Characteristics Using Aloe Vera Natural Mucilage: An Experimental Study," *Journal of Applied Sciences*, vol. 11, pp. 1039–1043, 2011.
3. A. Rahman, "Effect of Drag Reducing Agents (DRA) in Water Injection Well," Universiti Teknologi Petronas, 2012.
4. W. Brostow, "Drag reduction in flow: Review of applications, mechanism and prediction," *Journal of industrial and Engineering Chemistry*, vol. 14, pp. 409–416, 2008.
5. M. Campolo, M. Simeoni, R. Lapasin, and A. Soldati, "Turbulent Drag Reduction by Biopolymers in Large Scale Pipes," *Journal of Fluids Engineering*, vol. 137, p. 041102, 2015.
6. H. Kaur, G. Singh, and A. Jaafar, "The Study of Drag Reduction Ability of Naturally Produced Polymers from Local Plant Source," in *IPTC 2013: International Petroleum Technology Conference*, 2013.
7. H. A. Abdulbari, A. Shabirin, and H. Abdurrahman, "Bio-polymers for improving liquid flow in pipelines—A review and future work opportunities," *Journal of Industrial and Engineering Chemistry*, vol. 20, pp. 1157–1170, 2014.
8. C. Kang and W. Jepson, "Multiphase flow conditioning using drag-reducing agents," in *SPE Annual Technical Conference and Exhibition*, 1999.
9. J. Nelson, "Optimising production using drag reducing agents in water injection wells," *Offshore Engineer*, vol. 29, pp. 47–49, 2004.
10. S.-Q. Yang, "Drag reduction in turbulent flow with polymer additives," *Journal of Fluids Engineering*, vol. 131, p. 051301, 2009.
11. R. Paige, L. Murray, J. Martins, and S. Marsh, "Optimising water injection performance," in *Middle East Oil Show*, 1995.
12. M. Daas and D. Bleyle, "Computational and experimental investigation of the drag reduction and the components of pressure drop in horizontal slug flow using liquids of different viscosities," *Experimental thermal and fluid science*, vol. 30, pp. 307–317, 2006.
13. A. JOSEPH and J. A. AJIENKA, "Use of Drag Reducer in Improving Water (Flooding) Injectivity in Ukpokiti Field, Niger Delta," *Leonardo Electronic Journal of Practices and Technologies*, vol. 16, pp. 177–188, 2010.
14. M. W. Liberatore, S. Baik, A. J. McHugh, and T. J. Hanratty, "Turbulent drag reduction of polyacrylamide solutions: effect of degradation on molecular weight distribution," *Journal of non-newtonian fluid mechanics*, vol. 123, pp. 175–183, 2004.
15. A. A. Hamouda and O. T. Moshood, "Effect of temperature on degradation of polymer drag reduction and heat transfer in non-Newtonian fluid," in *International Symposium on Oilfield Chemistry*, 2007.

# Rheological Performance of Potassium Formate Water-Based Muds for High-Temperature Wells

T.N. Ofei, R.M. Al Bendary and A.D. Habte

**Abstract** Drilling mud plays a crucial role during drilling operation as they not only enhance efficient transport of drilled-cuttings from the drill bit to the surface, but also maintain their rheological properties especially in harsh environments to suspend drilled-cuttings when drilling operations stop. Although water-based muds are known to be environmentally friendly and less expensive as compared to oil-based and synthetic-based muds, they exhibit poor performance with less stability when circulating in high-temperature wells particularly with shale formations. Water-based mud systems with potassium brine have proven better results in shale formations; nonetheless, very little is known about their performances in high-temperature environments. This study examines the performance of water-based muds with synthetic polymers and potassium formate brine as additives in high-temperature conditions up to 300 °F. The drilling muds were formulated using the Taguchi Design of Experiment (TDOE) approach. The muds were prepared and tested in laboratory conditions under the guidelines of safety and drilling fluid testing using the American Petroleum Institute (API) standard. The experimental data obtained showed that the combinations of synthetic polymers and potassium formate brine were able to stabilize the rheology of the water-based muds at elevated temperatures. The usage of potassium formate brine at concentrations of 3.2, 6.7, and 10% aided in stabilizing the drilling mud's rheological properties after dynamic aging at 300 °F. Rheological properties such as plastic viscosity and yield point were also found to be almost identical for both static and dynamic aging conditions. Therefore, this study serves as optimization guide to design water-based muds applicable to high-temperature formations.

**Keywords** Water-based mud · Potassium formate brine · Synthetic polymers · Design of experiment · Fluid rheology

---

T.N. Ofei (✉) · R.M. Al Bendary · A.D. Habte  
Petroleum Engineering Department, Universiti Teknologi PETRONAS,  
Seri Iskandar, Malaysia  
e-mail: titus.ofei@utp.edu.my.com.my

## 1 Introduction

The oil and gas industry is always on the move toward exploring harsher and more extreme environments.

Drilling to reach deeper target depths comes with the risks of uncertainty in formations, extreme pressures and temperatures, and high-risk investment. Drilling high-pressure/high-temperature (HTHP) wells is typically high in both risk and capital investment, which makes justifying the costly drilling operations in such extreme environment a tough task especially with pressures up to 40,000 psi and temperatures reaching 500 °F or more [1]. Drilling fluids system that is intended for use in HTHP environments should not experience decomposition of its components because of the excessive heat. It should provide a safe environment for the drilling operations while easing the daily operations of drilling and logging, and at the same time not causing formation damage especially when interacting with clays and shale or any other wellbore problems.

WBMs face a number of challenges when subjected to HTHP conditions. One challenge is the instability of the fluid's chemical additives when exposed to high temperatures for extended periods of time. Another challenge is the environment of the drilling operation. Most HTHP wells are common to have shale formations that react to the presence of WBM and cause drilling problems such as stuck pipes.

Drilling fluids are of thixotropic features in most cases, and they are continuously affected by the changing environment in which they are operated. Factors such as pressure, temperature, rheological history, chemical compositions, and internal chemical reactions all affect the performance of the whole drilling fluid simultaneously [2, 3]. It is therefore extremely difficult to separate the conditions affecting the performance of any given drilling fluid especially under high-pressure and high-temperature circumstances. Several studies have attempted to measure the effects of high pressure and temperature as well as sagging time on the performance of drilling fluids.

It is reported from previous experimental work that the increase in temperature causes a decrease in effective and plastic viscosity, yield point, and gel strength as well as decreases in shear stresses corresponding to increase in shear rates in case of increasing temperatures [3]. Gel strength, however, is reported to generally increase in certain cases where temperature is above 250 °F [4, 5]. The difference of reported behavioral outcomes may be caused by the differences of the drilling fluids being tested or the equipment employed in the experimental setup for each case.

This paper discusses the formulation of water-based muds with synthetic polymers and potassium formate brine and their rheological properties at high-temperature conditions.

## 2 Materials and Methods

The formulation of the drilling muds consisted of three main compositions: Driscal D and Dristemp as synthetic polymers, and potassium formate brine. Other chemicals used in the formulations include soda ash, bentonite, sodium asphalt sulfonate, and hydro-Rez (see Table 1). The Taguchi Design of Experiment approach was adopted to characterize the mud compositions. Table 1 shows the compositions of the drilling mud.

The mud samples were prepared and characterized at both static (before hot roll) and dynamic (after hot roll) conditions using a Fann viscometer model 35SA. During the dynamic test, aging cells were used to contain the mud samples and a roller oven was used to hot roll the mud samples. At static conditions, the muds rheological properties were measured at atmospheric conditions, whereas, at dynamic conditions, the muds rheological properties were measured after being hot-rolled under dynamic condition for sixteen (16) h at 300 °F. Table 2 presents the design matrix of the mud sample tests conducted.

The drilling fluid additives were mixed using OFITE fixed-speed mixer. Rheological properties were first measured at atmospheric condition using Fann 35 viscometer. A Fann viscometer is a coaxial rheometer that is widely used in the industry to measure rheological properties of drilling fluids. OFITE 1100 HTHP viscometer was used to record the fluid's rheological properties at elevated temperatures and pressures. All sixteen drilling fluids formulated were dynamically aged at 300 °F for 16 h. Rheological properties were measured before and after hot-rolling (BHR and AHR) and performance comparison of the rheological properties was carried out between BHR and AHR values to understand the mud stability and overall performance. The dial readings from the viscometer were used to calculate plastic viscosity (PV), yield point (YP), and gel strength (GS) values.

**Table 1** Drilling mud formulation

Product	Specific gravity	Concentration
Freshwater	1	Calculated from material balance
Potassium formate	1.575	0%, 3.2%, 6.7%, 10%
Water (prehydrated gel)	1	90.2 lb/bbl
Bentonite	2.6	8 lb/bbl
soda ash	2.53	0.25 lb/bbl
Caustic soda	2.13	0.25 lb/bbl
Driscal D	1.44	1, 2, 3, 4 lb/bbl
Dristemp	1.5	1, 2, 3, 4 lb/bbl
Hydro-Rez	1.5	10 lb/bbl
Soltex	1.3	8 lb/bbl
Drill bar	4.4	Calculated from material balance

**Table 2** Summary of mud design matrix

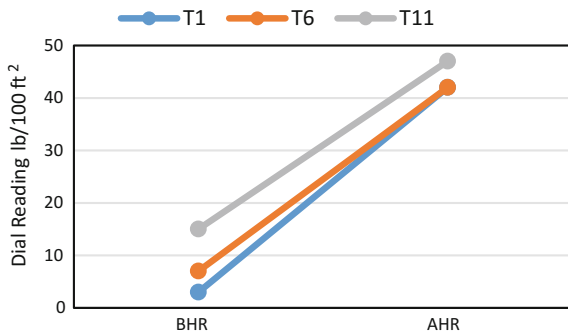
Run	Driscal D (lb/bbl)	Dristemp (lb/bbl)	Potassium formate
T1	1	1	0% (freshwater)
T2	1	2	3.2%
T3	1	3	6.7%
T4	1	4	10%
T5	2	1	3.2%
T6	2	2	0% (freshwater)
T7	2	3	10%
T8	2	4	6.7%
T9	3	1	6.7%
T10	3	2	10%
T11	3	3	0% (freshwater)
T12	3	4	3.2%
T13	4	1	10%
T14	4	2	6.7%
T15	4	3	3.2%
T16	4	4	0% (freshwater)

The ratio PV/YP is considered as an important indicator of the stability of the WBM performance before and after dynamic aging as it is used to evaluate the fluid’s rheological stability.

### 3 Results and Discussion

Samples T1, T6, and T11 exhibited a typical behavior for WBMs when exposed to high temperatures, where the observed viscosity of the mud was proved to increase after dynamic aging. There was a dramatic increase of about 70–80% in the low-end rheological properties which represents a challenge in moving and pumping the mud in real conditions as shown in Fig. 1.

**Fig. 1** Effect of dynamic aging on WBM without potassium formate at 3RPM



**Fig. 2** Effect of dynamic aging on PV/YP ratio (0 wt% potassium formate)

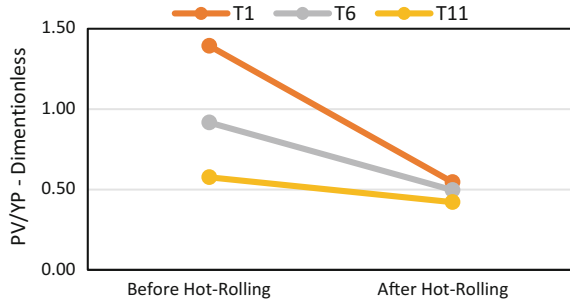
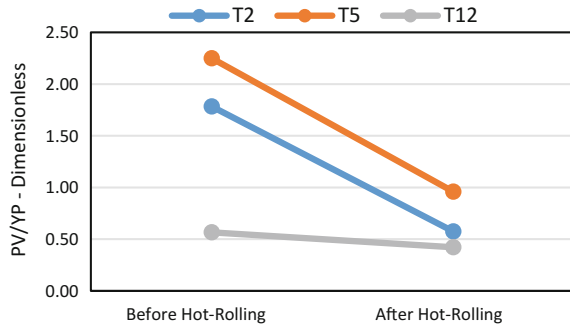


Figure 2 shows the change in PV/YP ratio after hot-rolling reaches high percentages of difference from 27 to 60% of the original ratio before hot-rolling. When introducing potassium formate into the system in different concentrations, the changes in PV/YP ratios decrease in comparison with systems that have no potassium formate. This indicates that the increase in potassium formate concentration in the system up to a certain level will increase the stability of the drilling mud system at elevated temperatures. However, excessive usage of potassium formate or when saturated potassium formate is used to formulate drilling muds, there is no free water particles to react with the viscosifying polymers and the polymers essentially lose their ability to dissolve in water.

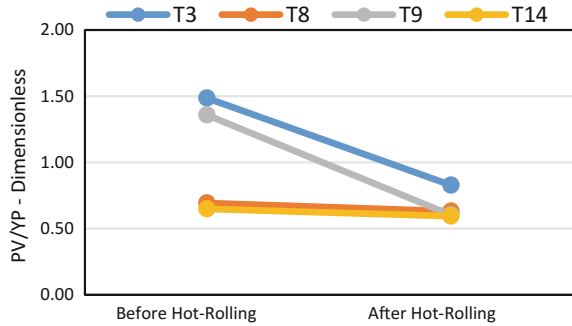
The relationship between PV/YP ratio before and after hot-rolling is observed to be also related to the concentrations of Driscal D and Dristemp polymers as well as the concentration of potassium formate. Figures 3, 4, and 5 show the effect on PV/YP ratio under different concentrations of potassium formate brine. They all indicated that the use of potassium formate is useful in stabilizing the drilling fluid systems when exposed to high temperatures although flocculation in the absolute difference percentage between PV/YP ratios was observed. The fluid samples that exhibited most resistance to temperature were found to be the samples containing relatively high concentrations of Driscal D and Dristemp (50% or more of the upper level used for DOE for one or both of the additives combined).

**Fig. 3** Effect of dynamic aging on PV/YP ratio (3.2 wt% potassium formate)

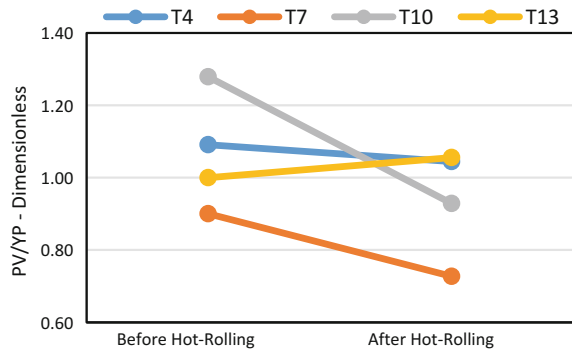




**Fig. 4** Effect of dynamic aging on PV/YP ratio (6.7 wt % potassium formate)



**Fig. 5** Effect of dynamic aging on PV/YP ratio (10 wt % potassium formate)



**Fig. 6** Shear stress versus shear rate plots for mud samples T2, T5, and T12 measures BHR and AHR at 3.2 wt% potassium formate brine

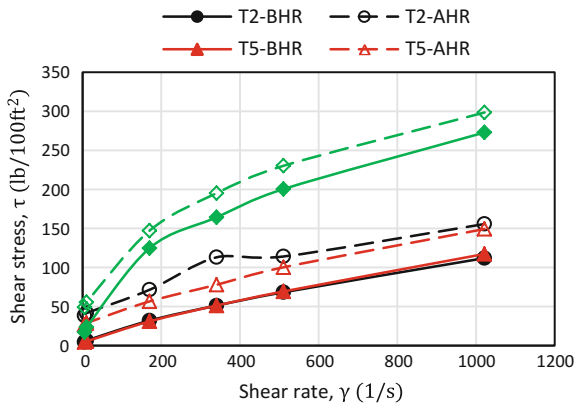


Figure 6 shows the shear stress versus shear rate plots for mud samples T2, T5, and T12 with 3.2 wt% potassium formate brine measured BHR and AHR. It is observed that the rheogram of the mud samples BHR exhibited shear thinning and pseudoplastic effect, while the measured mud samples AHR exhibited a yield

pseudoplastic behavior. There is an increase in shear stress for all mud samples measured AHR as shear rate increased. Furthermore, the rheological behavior of mud sample T2 was compared closely to mud sample T5 measured BHR and AHR. In addition, the shear stress values of mud samples AHR are far greater than that of mud samples BHR, an indication of high equivalent circulating density (ECD) in the wellbore with AHR mud samples.

## 4 Conclusions

The experiment showed that the usage of potassium formate at concentrations of 3.2, 6.7, and 10 wt% aided in stabilizing the drilling fluid's rheological properties after dynamic aging at 300 °F. The stability of the drilling fluid is characterized by calculating the ratio PV/YP before and after hot-rolling. It was found that the usage of 10% concentration by weight of potassium formate provided the most stable drilling fluids with a change of PV/YP by only 5%. Furthermore, mud samples BHR exhibited a pseudoplastic shear-thinning behavior, while mud samples AHR showed a yield pseudoplastic behavior. There is the tendency of high equivalent circulating density (ECD) in the wellbore with AHR mud samples.

**Acknowledgements** This work was financially supported by STIRF Grant with cost center: 0153AA-D15 from Universiti Teknologi PETRONAS, Malaysia.

## References

1. A. Shadravan and M. Amani, "HPHT 101: What Every Engineer or Geoscientist Should Know about High Pressure High Temperature Wells," 2012, Society of Petroleum Engineers. SPE-163376-MS. DOI [10.2118/163376-MS](https://doi.org/10.2118/163376-MS).
2. N.J. Alderman, A. Gavignet, D. Guillot and G.C. Maitland, "High-Temperature, High-Pressure Rheology of Water-Based Muds," 1988, Society of Petroleum Engineers [10.2118/18035-MS](https://doi.org/10.2118/18035-MS).
3. M.S. Ali and M.A. Al-Marhoun, "The Effect of High Temperature and Aging on Water-Based Drilling Fluids," 1990, Society of Petroleum Engineers. 21613-MS SPE General.
4. M. Amani and M. Al-Jubouri, "The Effect of High Pressures and High Temperatures on the Properties of Water Based Drilling Fluids," Energy Science and Technology, 2012, 1 (4), [10.3968/j.est.1923847920120401.256](https://doi.org/10.3968/j.est.1923847920120401.256).
5. S. Wenjun, T. Shixian, F. Fan, Y. Weimin and Z. Zhitao, "Research on the Drilling Fluid Technology for High Temperature over 240 °C," Procedia Engineering, 2014. **73**: pp. 218–229.

# A Pre-drill Computer Model for Predicting Post-drill Well Gradients

T.N. Ofei and D.J. Jorge

**Abstract** Drilling wildcat or exploration wells without the knowledge of the well gradients (pore gradient, fracture gradient, and overburden gradient) poses a great risk to operators economically and operationally. This project proposes a simple but robust computer model for predicting pre-drill well gradients. Two-way time (TWT) and average velocity (AV) from a field seismic data were adopted in the model development. Results obtained from the pre-drill well gradient model were validated against post-drill well gradient data from three wells in the same field. A very good statistical agreement between the pre-drill model and the post-drill field data was achieved. The pre-drill model predicted the post-drill gradient data with mean absolute percent error (MAPE) from 4.64 to 6.23%, thus indicating the robustness of the proposed model. Similarly, regression success index,  $R^2$ , values between the pre-drill and post-drill well gradient data ranged from 0.830 to 0.985 for all datasets (DS1), (DS2), and (DS3). Information from this study is very essential in making better and sound decisions about mud weight design and casing program before drilling wildcat wells especially in deep offshore environment where there is a narrow window between the pore and fracture gradients.

**Keywords** Well gradients · Seismic data · Two-way time · Average velocity · Wildcat well

## 1 Introduction

The accurate prediction of well gradients such as pore gradient, fracture gradient, and overburden gradient is of great importance in designing drilling program for wildcat or exploratory wells. The unavailability of offset or near-well data in a new field usually requires that the estimation of pre-drill well gradients be made using

---

T.N. Ofei (✉) · D.J. Jorge  
Petroleum Engineering Department, Universiti Teknologi PETRONAS,  
Seri Iskandar, Malaysia  
e-mail: titus.ofei@utp.edu.my

seismic data which includes two-way time (TWT) and average velocity (AV). The estimation of these well gradients is a prerequisite for designing an effective mud weight and casing program, thus ensuring the drilling operations are carried out safely and economically. The knowledge of the subsurface pressure enables the drilling operator to prevent critical drilling problems such as formation fracture and loss of drilling mud, as well as avoiding potential influx of formation fluids into the wellbore which may eventually lead to a blowout if uncontrolled. A further use of pre-drill well gradients helps the drilling team to design cementing program, casing setting points, and casing design. Additionally, pre-drill well gradients are also useful for the optimization of hydraulic program, bit selection, blowout preventers (BOPs) and well head selection, drilling rig dimensioning, equipment selection, detection of potential hole problems, and forecast of operation costs.

By applying an appropriate transformation model, two-way time and average velocities adopted from seismic data are used to provide an estimation of the pre-drill well gradients. Estimated well gradients using seismic data are not truly representative of the actual gradients that are measured down hole while drilling the well; however, these predicted gradients serve as a guide for designing the well drilling program. Therefore, drilling a wildcat or exploratory well demands an effective contingency plan and awareness of the drilling events during the operations.

Banik and Wagner [1] emphasized that the understanding of formation pressure is vital in well planning because it allows the drilling engineer to design a safe mud weight which is below the fracture gradient in order not to fracture the formation and lose the drilling fluid into the formation. On the other hand, a safe mud weight should be designed above the pore pressure gradient, so that formation fluids will not flow into the wellbore (kick) which can eventually culminate in a blowout if the kick is not controlled [2].

Pre-drill well gradient estimation involves estimating the pore pressure gradient, fracture pressure gradient, and overburden gradient before the well is drilled in a given area. As stated by Godwin [3], if offset wells are available in the vicinity, then offset data such as well logs can be used to predict the formation pressure in the new well to be drilled. However, if the well to be drilled is a wildcat, this entails that area is new and no wells have been drilled before in the surrounding; thus, little knowledge is known about the pressure in the subsurface. Therefore, the only method to estimate the well gradients (pore gradient, fracture gradient, and overburden gradient) will rely on seismic data which involves using two-way time and average velocity [4].

According to Suwannasri et al. [5], drilling through overpressured zones is quite problematic; thus, it can lead to well control incidents such as influx of formation fluids into the well, which can potentially result in a blowout if the drilling crew fails to control the influx. The prediction of pore pressure is relatively easy for formations having normal pore pressure gradient (1.03–1.07 kg/cm<sup>2</sup>/10 m or 0.447–0.464 psi/ft). However, the estimation of formation pore pressure in geopressured (overpressured) zones is critical and relevant. Furthermore, knowledge

about well gradients is important for well planning as it provides the drilling engineer key information for designing the mud weight and casing program of the well. With a safe mud weight, one is able to drill through overpressured zones and zones with wellbore instability without incurring severe problems, thus allowing the well to be completed effectively [6]. On the other hand, a well-designed mud weight based on accurate estimation of pore pressure and fracture pressure can greatly reduce the chances of having well control related issues such as influx, blowouts, and lost circulation, as well as avoid drilling events such stuck pipes, packoff, and wellbore collapse. When fewer problems are encountered during drilling operations, this gives the operator an opportunity to achieve the target in a cost-effective manner [7].

A study conducted by Chatterjee et al. [8] emphasized that the need for an accurate estimation of well gradients is substantial; hence, in order to predict pore pressure in overpressured zones, it is first necessary to have a background understanding with regard to how overpressures are generated. The understanding of formation pressure helps identify drilling hazards encountered when drilling through overpressured zones. Overpressures are more critical and cause more problems in drilling operations if not addressed properly. Yan and Han [9] and Li et al. [10] studies explained that the origin of overpressure is due to the rapid deposition of sediments which preclude sufficient time for pore fluids to escape. As a result, the pore fluids become trapped in the pores due to a phenomenon termed undercompaction. These trapped fluids build high pressures within the pore spaces in which they are trapped, and when intercepted during drilling operations, high-pressure fluids will be released, hence increasing the likelihood of having an influx if the mud weight is less than formation pore pressure [11].

By using seismic data to estimate well gradients, it was documented that seismic interval velocity can accurately predict pore pressure and the onset of overpressure of a given geologic formation [12]. The seismic data which include two-way time and average velocity are acquired during seismic survey. The two-way time and average velocity required to estimate the seismic interval velocity are presented in a mathematical relation as [13].

$$V_N^2 = \frac{(V_{2,rms}^2 \cdot t_{N,2} - V_{1,rms}^2 \cdot t_{N,1})}{(t_{N,2} - t_{N,1})} \quad (1)$$

According to Zhang [14], the interval velocity can further be used to estimate parameters such as interval transit time, depth interval, and depth reference which aid toward the process of estimating the well gradients. Although seismograms are used mainly by geophysicists and geologists for subsurface structural and lithological interpretation, since the beginning of the 1970s, they have also become of great interest and help to the drilling engineers. In fact, two of the most important applications of seismic data for drilling purposes consist in detecting formations

characterized by geopressures (overpressures) and provide an estimation of pore pressure gradient, overburden gradient, and fracture gradient. Experience has shown that when good seismic data are available and proper interpretation is performed, it is possible in most cases to locate the overpressure tops and estimate the well gradients. Naturally, the determination of fracture gradients is strictly dependent on the quality of pore pressure gradient evaluation since better approximations are obtained in the calculation of overburden gradients [15]. The ultimate objective is to predict the pore pressure gradient, fracture pressure gradient, and overburden gradient from seismic interval velocity through a transformation model.

## 2 Materials and Methods

### 2.1 Overburden Gradient Estimation

The overburden gradient for a formation can be computed in  $\text{kg/cm}^2/10 \text{ m}$  as follows:

$$G_{OB} = \frac{P_{OB} \times 10}{z} \quad (2)$$

The sum of the pressures applied by the overlaying sediment columns for different intervals is given in  $\text{kg/cm}^2$  as follows:

$$P_{OB}^n = \frac{\delta_{\text{sed}}^1 \times \Delta z^1}{10} + \frac{\delta_{\text{sed}}^2 \times \Delta z^2}{10} \dots \frac{\delta_{\text{sed}}^n \times \Delta z^n}{10} \quad (3)$$

The average density,  $\delta_{\text{sed}}$ , between two seismic reflectors is expressed as follows:

$$\delta_{\text{sed}} = \delta_{\text{max}} - 2.11 \left( \frac{1 - \frac{v_i}{v_{\text{max}}}}{1 + \frac{v_i}{v_{\text{min}}}} \right) \quad (4)$$

From field practice,  $\delta_{\text{max}} = 2.75 \text{ g/cm}^3$ ,  $v_{\text{max}} = 7000 \text{ m/s}$ , and  $v_{\text{min}} = 1500 \text{ m/s}$ .

The TWT and AV obtained from a seismic data can be used to compute the interval velocity,  $v_i$ , as follows:

$$v_i = \sqrt{\frac{v_{m2}^2 \cdot t_2 - v_{m1}^2 \cdot t_1}{t_2 - t_1}} \quad (5)$$

The transit time in  $\mu s/ft$  and depth reference in  $m$  can be expressed, respectively, as follows:

$$\Delta t = \frac{304,800}{v_i} \tag{6}$$

$$H_i = \sum_i \left( \frac{t_2 - t_1}{2} \right) v_i \tag{7}$$

### 2.2 Pore Gradient Estimation

The pore gradient can be estimated using the equivalent depth method (EDM) where the transit time is plotted against depth on a semi-log graph to define the normal compaction trend (NCT) as below [16] (Fig. 1).

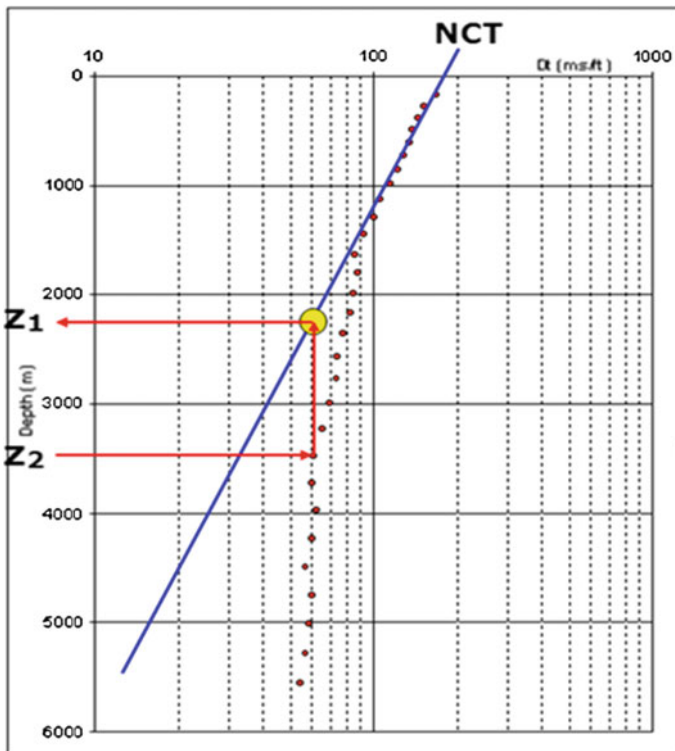


Fig. 1 Equivalent depth versus transit time [16]

The pore gradient is estimated using the expression,

$$G_{p,2} = \frac{P_{p,2} \times 10}{z_2} \quad (8)$$

The pore pressure,  $P_p$ , is computed from the difference between the overburden pressure,  $P_{OB}$ , and effective pressure,  $P_{eff}$  as follows:

$$P_{p,2} = P_{OB,2} - P_{eff,2} \quad (9)$$

where

$$P_{OB,2} = \frac{G_{OB} \times z_2}{10} \quad (10)$$

and

$$P_{eff,1} = P_{eff,2} = \frac{(G_{OB} - G_p) \times z_1}{10} \quad (11)$$

### 2.3 Fracture Gradient Estimation

The Eaton's correlation is used to estimate the fracture gradient as a function of the Poisson ratio which is given as follows:

$$G_{frac} = G_p + \frac{\sigma}{1 - \sigma} (G_{OB} - G_p) \quad (12)$$

Typically, the Poisson ratio,  $\sigma$ , value commonly used is 0.4.

The mean absolute percent error (MAPE) between the actual values (post-drill data) and forecast values (pre-drill data) is estimated as follows:

$$MAPE = \frac{1}{n} \sum_{t=1}^n \left| \frac{A_t - F_t}{A_t} \right| \quad (13)$$

### 2.4 Computational Procedure

The pre-drill well gradients were computed using the combined equations from (1) to (12). A computer model was developed using C++ codes where the input data



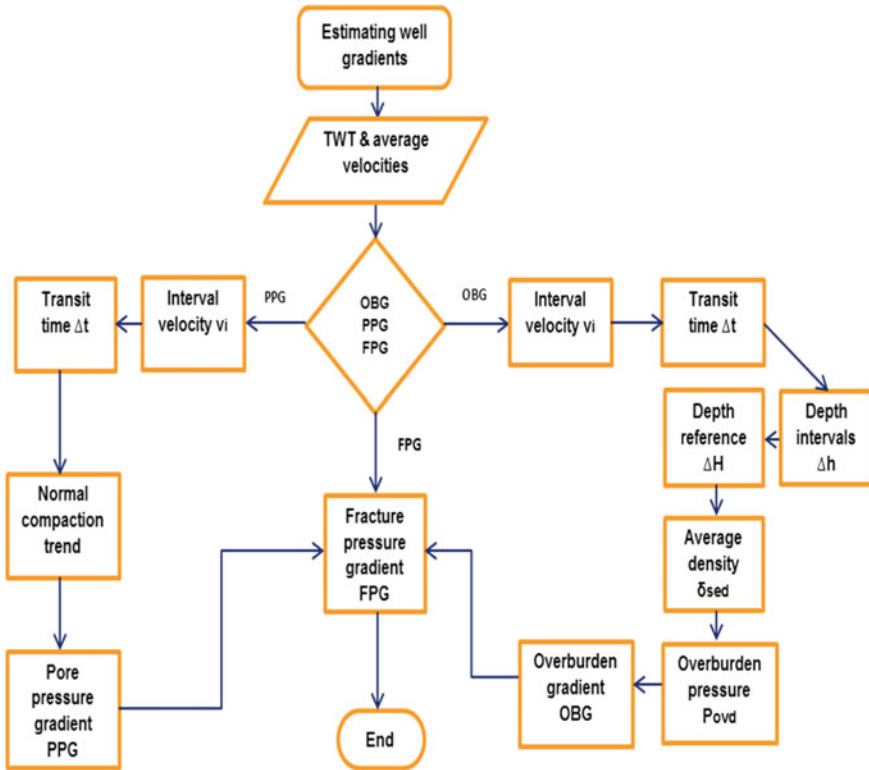


Fig. 2 Computer model workflow

were TWT and AV, all obtained from field seismic data. To validate the model, post-drill well gradient data from three (3) wells in the same field were utilized. The model workflow is presented in Fig. 2.

### 3 Results and Discussion

Table 1 presents the input data for TWT and AV obtained from the field seismic data for three wells. The computer program prompts the user to provide the input data (seismic data) and then estimates various parameters mathematically, and the end result is to estimate the pre-drill well gradients. The total vertical depth for the wells from DS1, DS2, and DS3 is 20,057 m, 23,402 m, and 7444 m, respectively.

In Fig. 3, it is evident that the pre-drill well gradients were compared closely with the post-drill well gradient for DS1, and this is desirable as it reduces the

**Table 1** Computed two-way time (TWT) and average velocity (AV) from three field seismic data [16]

Dataset (DS1)		Dataset (DS2)		Dataset (DS3)	
TWT	AV	TWT	AV	TWT	AV
s	m/s	s	m/s	s	m/s
0.04	1700	0.04	1650	0.04	1600
0.47	1860	0.51	1900	0.34	1750
0.70	1890	0.83	2000	0.65	1850
1.04	2090	1.03	2070	0.89	2000
1.20	2190	1.25	2200	1.45	2320
1.73	2540	2.05	3100	1.70	2500
2.20	2940	2.40	3325	2.00	2600
3.72	3740	3.55	3900	2.30	3000
5.00	4000	8.00	4000	3.40	3300
8.00	5300	9.50	5500	4.30	3600

drilling risk when drilling wildcat wells using seismic data. This close match is attributed to the accuracy of seismic data which is a key requirement for better prediction. Furthermore, it can be observed that the pre-drill models accurately predicted the overpressured zone which is located in about 1100 m which was confirmed by the post-drill data. This accurate prediction is crucial for enhancing drilling efficiency and reducing well control incidents. The pre-drill pore gradient slightly overpredicted the post-drill pore gradient at the depth below 1900 m. Overpredicting the pore gradient by a slight margin will not affect the design of the mud systems since the mud weight will be below the fracture gradient.

Cross-plots for the pre-drill and post-drill well gradients on DS1 as shown in Figs. 4, 5, and 6 reveal relatively small errors of 4.64, 5.78, and 5.31% for pore gradient, fracture gradient, and overburden gradient, respectively. Linear regression models were also proposed for predicting post-drill well gradients for DS1.

The pre-drill well gradients presented in Fig. 7 are compared closely with the post-drill well gradients for DS2. The overpressured zone is closely predicted to lie below 1100 m. However, at the depth below 2000 m, the pre-drill pore gradient is quite overestimated. On the other hand, both predicted fracture and overburden gradients are slightly lower than the post-drill fracture and overburden gradient below the depth of 1100 m. It must be noted that underpredicting the post-drill pore gradient may result in underdesigning the drilling mud system. This will cause formation fluid influx or kick into the wellbore which will result in a catastrophic blowout if uncontrolled.

Figures 8, 9, and 10 depict the cross-plots of dataset DS2 for pre-drill well gradients and post-drill well gradients. The mean absolute percent error recorded between the pre-drill and post-drill data for DS2 is 4.98, 5.46, and 6.14% for pore gradient, fracture gradient, and overburden gradient data, respectively. Furthermore,

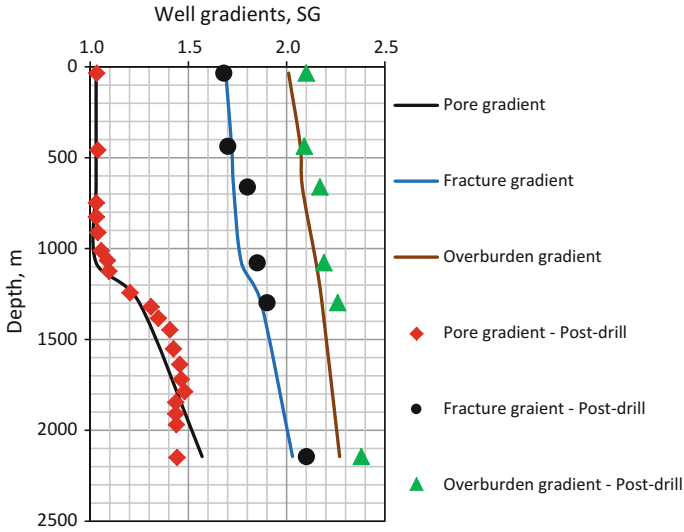


Fig. 3 Comparison of pre-drill and post-drill well gradients for DS1

Fig. 4 Comparison of pre-drill and post-drill pore gradients for DS1

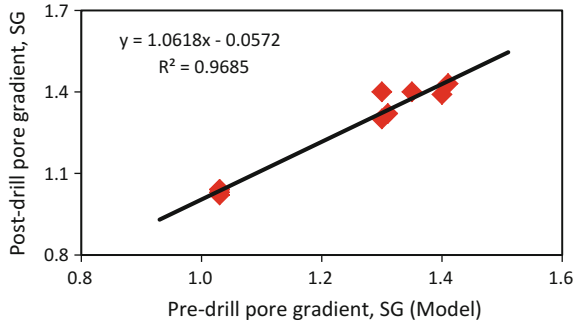
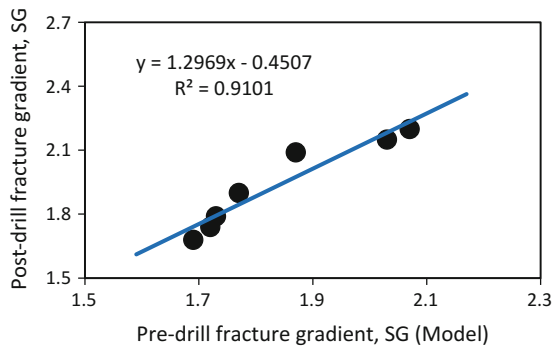


Fig. 5 Comparison of pre-drill and post-drill fracture gradients for DS1



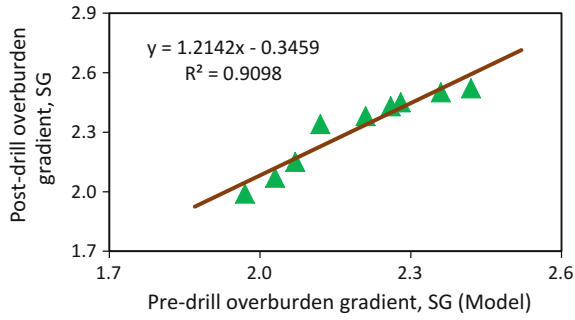


Fig. 6 Comparison of pre-drill and post-drill overburden gradients for DS1

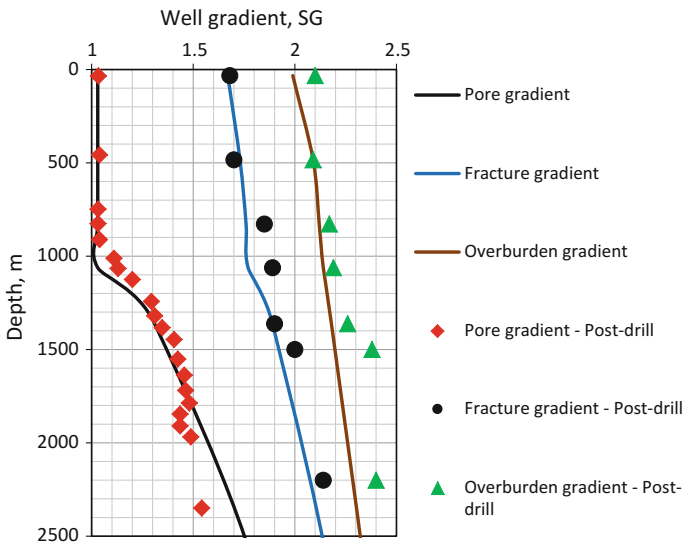
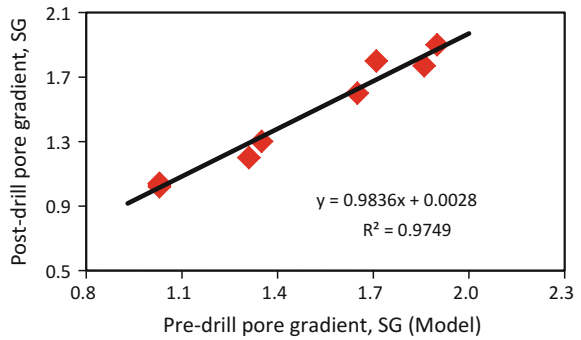
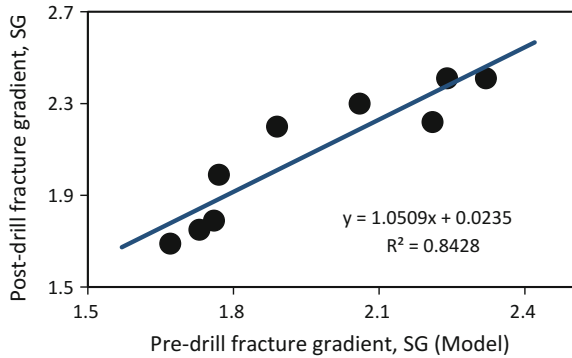


Fig. 7 Comparison of pre-drill and post-drill well gradients for DS2

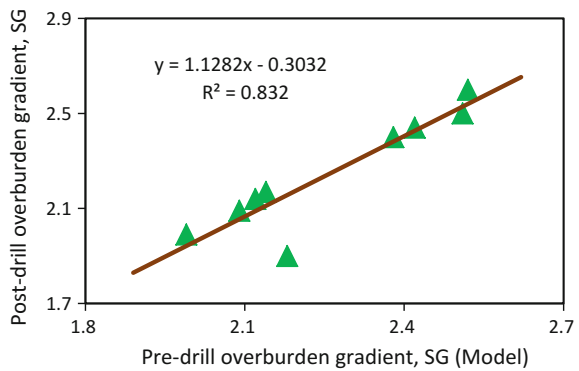
Fig. 8 Comparison of pre-drill and post-drill pore gradients for DS2



**Fig. 9** Comparison of pre-drill and post-drill fracture gradients for DS2



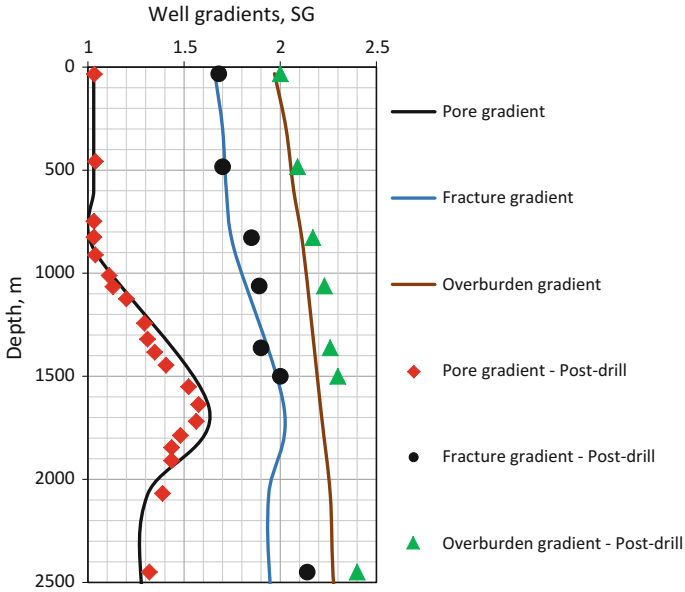
**Fig. 10** Comparison of pre-drill and post-drill overburden gradients for DS2



linear regression models have been proposed for predicting the post-drill well gradients with good degree of accuracy.

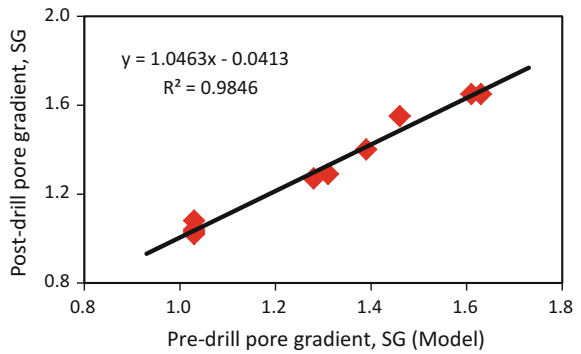
From Fig. 11, the pre-drill pore gradient is slightly overestimated from the post-drill pore gradient between the depths of 1200 and 1900 m from DS3. However, this slight overestimation would not pose critical drilling problems provided that the pre-drill fracture gradient lies below the post-drill fracture gradient and therefore no fluid loss (formation fracture) would occur. Nonetheless, the pre-drill fracture gradient and overburden gradient slightly underestimated the post-drill fracture and overburden gradients at a depth of approximately 1500 and 840 m, respectively. Again, the overpressured formation was accurately predicted at the well depth of about 800 m.

As shown in Figs. 12, 13, and 14 for DS3, linear regression models are proposed for predicting the post-drill well gradients with mean absolute percent errors between the pre-drill and post-drill data as 5.74, 6.23, and 6.07% for pore gradient, fracture gradient, and overburden gradient, respectively.

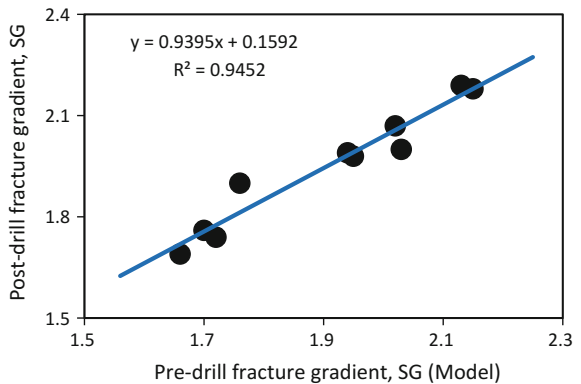


**Fig. 11** Comparison of pre-drill and post-drill well gradients for DS3

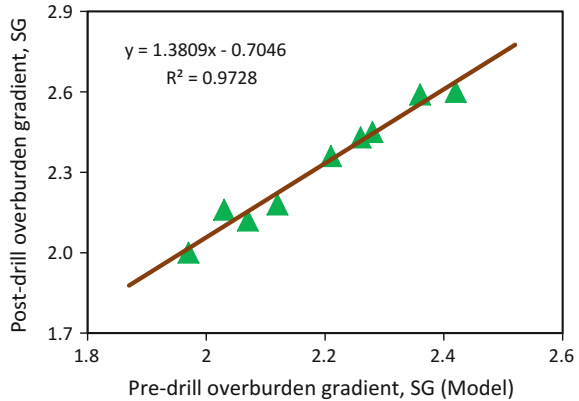
**Fig. 12** Comparison of pre-drill and post-drill pore gradients for DS3



**Fig. 13** Comparison of pre-drill and post-drill fracture gradients for DS3



**Fig. 14** Comparison of pre-drill and post-drill overburden gradients for DS3



## 4 Conclusions

A computer model has been proposed for estimating pre-drill well gradients. The accuracy of the model was successfully tested against post-drill well gradient data from three wells in the same fields, where very good agreement was achieved.

The mean absolute percent error recorded between the pre-drill and post-drill well gradient data ranges between 4.64 and 6.23%, thus indicating the robustness of the proposed model.

The use of field seismic data can be adopted to predict well gradients in wildcat or exploratory wells with high degree of accuracy.

For better accuracy of the estimated well gradients, it is recommended that input data (two-way time and average velocity) obtained from seismic data are accurate. If the seismic data are not the representative of the field where the data are measured, it would lead to poor estimation of the well gradients, thus increasing operational and economical risk of drilling operations.

**Acknowledgements** This work was financially supported by STIRF Grant with cost center: 0153AA-D15 from Universiti Teknologi PETRONAS, Malaysia.

## References

1. N. Banik and C. Wagner, "Pre-drill Prediction of Subsalt Pore Pressure from Seismic Data," Offshore/OTC, Schlumberger (2014).
2. J. Narciso, "Pore Pressure Prediction Using Seismic Velocities," Instituto Superior Técnico, Lisboa (2014).
3. E. Godwin, "Pore-Pressure Prediction from Seismic Data in Parts of the Onshore Niger Delta Sedimentary Basin," Department of Physics, University of Port Harcourt, Nigeria, (2013).

4. N. Francis, "Analytical Model to Predict Pore Pressure in Planning High Pressure, High Temperature (HPHT) Wells in Niger Delta," Department of Petroleum and Gas Engineering, University of Port Harcourt, Rivers state, Nigeria (2013).
5. K. Suwannasri, N. Pooksook, P. Suthisripok, S. Utitsan, H. Sognnes and V. Chaisomboonpan, "Seismic Velocity-based Pore Pressure and Fracture Gradient Prediction in High Temperature Reservoirs: Bongkot Field," Gulf of Thailand (2013).
6. M. Pervukhina, C. Piane, D. Dewhurst, M. Clennell and H. Bolås, "Estimation of Pore Pressure in Shales from Sonic Velocities," Statoil (2013).
7. B. Kumar, S. Niwas and B. Mangaraj, "Pore Pressure Prediction from Well Logs and Seismic Data," 9th Biennial International Conference & Exposition on Petroleum Geophysics, (2012).
8. A. Chatterjee, S. Mondal and P. Patel, "Pore Pressure Prediction Using Seismic Velocities for Deepwater High-Temperature High-Pressure Well in Offshore Krishna Godavari Basin, India," SPE oil and gas Conference and Exhibition, Mumbai, (2012).
9. F. Yan and D. Han, "A New Model for Pore Pressure Prediction," Rock Physics Lab, University of Houston Keyin Ren, Nanhai West Corporation, CNOOC, (2012).
10. S. Li, J. George and C. Purdy, "Pore-Pressure and Wellbore-Stability Prediction to Increase Drilling Efficiency," SPE, Landmark Halliburton, (2012).
11. S. O'Connor, R. Swarbrick, J. Hoesni and R. Lahann, "Deep Pore Pressure Prediction in Challenging Areas, Malay Basin, SE Asia," Thirty-Fifth Annual Convention & Exhibition, May (2011).
12. S. Babu and A. Sircar, "A Comparative Study of Predicted and Actual Pore Pressures in Tripura, India," School of Petroleum Technology, Raisan, Gandhinagar-382007, Gujarat, India, (2011).
13. V. Rabinovich, "Pore Pressure and Fracture Pressure Prediction of Deepwater Subsalt Environment Wells in Gulf of Mexico," The University of Texas at Austin, (2011).
14. J. Zhang, "Pore Pressure Prediction from Well Logs: Methods, Modifications, and New Approaches," Shell Exploration and Production Company, Houston, Texas, USA, (2011).
15. Y. Shykhaliyev, A. Feyzullayev and I. Lerche, "Pre-drill Overpressure Prediction in the South Caspian Basin Using Seismic Data," Vol. 28, no. 5, pp. 397–410 397, (2010).
16. Eni SpA—E&P Division Drilling, Completion and Production Optimization Well Operating Manuals (2010).



# A Comparison of Drilling Fluid Power for Coiled Tubing Drilling of Microholes in Hard Rock: Water Versus Supercritical CO<sub>2</sub>

Xianhua Liu, Brian Evans and Ahmed Barifcani

**Abstract** Given the scenario of using a coiled tubing rig for drilling into deep hard rock formations, the energy delivery efficiency required to drive the high-speed down-hole motor for bit rotation and to transport cuttings up to surface becomes a major issue if water is used as a drilling fluid. High-speed rotary drilling in hard rock formations enables the diamond-impregnated drill bit to cut the rock into powder form particles, which requires a large amount of cutting power. In addition, the very long small diameter coiled tubing and a narrow annular space will also result in a lot of frictional pressure energy loss. Water is incompressible and hence can only deliver hydraulic power. As a result, water as drilling fluid can only supply limited drilling power for coiled tubing drilling. By contrast, supercritical CO<sub>2</sub> (SC-CO<sub>2</sub>) is a compressible dense fluid, has lower viscosity hence has the potential to deliver drilling fluid power more efficiently. This paper focuses on comparing the power delivery of water and SC-CO<sub>2</sub> for coiled tubing drilling of deep microholes in hard rock. It shows that, in addition to the transfer of hydraulic power, the SC-CO<sub>2</sub> drilling fluid can store and release thermodynamic power to the down-hole drilling system, can have less frictional pressure energy loss, can absorb heat energy generated during drilling and later release that energy in the form of thermal expansion. It shows that SC-CO<sub>2</sub> has the potential to provide constant power to the down-hole motor for high-speed drilling with a relatively low operating pressure. This low operating pressure will enable a longer fatigue life of the coiled tubing and associated drilling components.

**Keywords** Coiled tubing drilling · Hard rock · Drilling fluid power · Supercritical CO<sub>2</sub>

---

X. Liu (✉)

Petroleum Engineering Department, Universiti Teknologi PETRONAS,  
Seri Iskandar, Malaysia  
e-mail: xianhua.liu@utp.edu.my

B. Evans · A. Barifcani

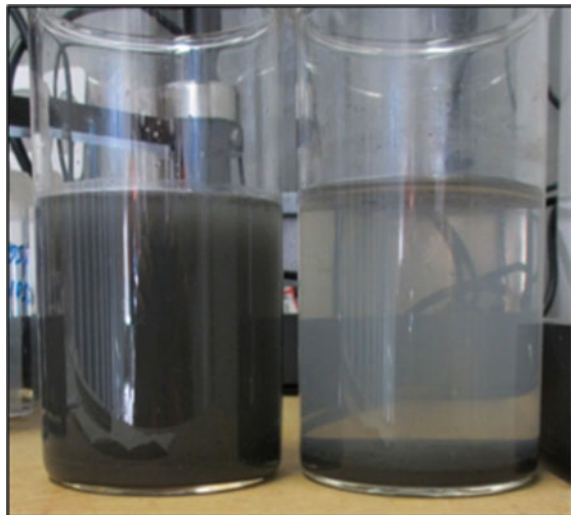
Deep Exploration Technologies CRC, Department of Petroleum Engineering,  
Curtin University, Perth, Australia

## 1 Introduction

For developing a next-generation drilling technology for mineral exploration, the DET CRC drilling research team proposed to use coiled tubing drilling of microholes into deep hard rock formations. It is believed that coiled tubing drilling technology can achieve the goal of drilling deeper, cheaper, faster and with small foot imprint for mineral exploration. The coiled tubing is  $\text{Ø}38.1$  or  $\text{Ø}44.5$  mm (1.5–1.75 in.) size, the drill bit is diamond impregnated and the cuttings are powder form particles as shown in Figs. 1 and 2 (DET CRC eNewsletter July 2013, [5]). The cuttings particle size distribution is in the range of 1–1000  $\mu\text{m}$  with the majority being less than 100  $\mu\text{m}$  (Kamyab et al. 2013, [9]). Coiled tubing drilling of microholes is expected to achieve the goal of drilling cheaper, deeper, faster and with small environmental footprint. By microhole, the Los Alamos National Laboratory definition is for borehole size range from 32 to 61 mm (1–1/4" to 2–3/8") (Albright et al. 1994).

For hard rock deep microhole drilling, using a diamond-impregnated bit is considered to allow low weight on bit (WOB) and very high rotation speed, e.g. up to 7000–10000 rpm, to achieve a high rate of penetration (ROP) (DET CRC eNewsletter February 2014, [4]). The cut depth of each revolution is small; hence, each revolution does not require a high degree of energy. However, the drilling process does consume a large amount of energy due to the very high rotation speed, large ROP per second and cutting hard rock into powder. For example, a laboratory drilling experiment has shown that the diamond-impregnated bit can drill in a red granite hard rock at 4 GPA specific energy cost at a normal drilling condition of 100  $\mu\text{m}$  penetration per revolution (DET CRC eNewsletter July 2013, [5]). Specific energy is the energy cost of cutting out a unit volume of hard rock. Such a situation

**Fig. 1** Powder form cuttings 1–1000  $\mu\text{m}$  with majority being less than 100  $\mu\text{m}$  generated by diamond-impregnated bit drilling (DET CRC eNewsletter July 2013)



**Fig. 2** Brukunga core and corresponding cuttings by diamond-impregnated drill bit collected and packed in sequence (DET CRC eNewsletter July 2013)



requires a drilling fluid of efficient energy delivery for driving the down-hole motor to rotate the drill bit at high speed to cut the hard rock. In addition, the drilling fluid should reserve sufficient energy for overcoming the frictional pressure loss through the long but narrow coiled tubing and annulus for transporting drilled cuttings up to the surface.

Water or water-based drilling fluid is widely used. However, it is believed that water cannot deliver the cutting power efficiently through a very long but small diameter coiled tubing and a narrow cuttings return annulus due to its incompressibility and high viscosity. In particular, when the drilled cuttings are as small as powder form particles, the mixing of water and the powder will significantly increase the viscosity of the drilling fluid resulting significant frictional pressure loss in the annulus (Kamyab et al. 2013, [9]). This requires a fast increase of pump pressure as the drilling depth increases. High pressure will reduce the fatigue lifespan of the coiled tubing, and very high pressure has the potential to burst the coiled tubing. According to Kellé (2000, 2002, [10, 11]) “conventional steel CT is subject to fatigue and will fail after about 200 trips at operating pressure of around 35 Mpa. Doubling the operating pressure to 70 Mpa reduces the fatigue life to under 20 cycles with significant risk of premature failure”. However, it is preferred to use water-based drilling fluid to drill at least shallow microholes. By shallow and deep microholes, the following classification is proposed (Liu 2014, [12]):

Shallow	0–500 m
Medium	500–1000 m
Deep	1000–1500 m
Ultra deep	1500–2000 m

For finding an efficient energy delivery or powerful drilling fluid for deep microhole drilling of hard rock, we turned our attention to compressible and low viscosity fluid. As such, SC-CO<sub>2</sub> has been identified to be one of the powerful drilling fluids. These physical properties enable SC-CO<sub>2</sub> to achieve efficient energy delivery to the down-hole motor and to transport drilled cuttings to the surface at much lower coiled tubing inlet pressure than water. By efficient energy delivery, we consider the amount of energy provided by a unit mass of drilling fluid at selected pressure difference between the inlet pressure of the coiled tubing and the outlet pressure of the annulus as well as the useful work done by the amount of energy. It will determine the pressure needed for pumping a drilling fluid into the coiled tubing for a desired drilling ROP which will in turn affect the coiled tubing fatigue life. To quantify the above theoretical reasoning, this paper calculates and compares water and SC-CO<sub>2</sub> in terms of energy delivery in relation to fluid pressure for hard rock deep microhole drilling. First, it is necessary to have a brief review of related drilling technologies and equipment.

## 2 Coiled Tubing Drilling and CO<sub>2</sub> Work Fluid Research

Coiled tubing drilling for mineral exploration is a new area being developed by the DET CRC which is performing research into high-speed rotary drilling using low WOB. This results in reducing the axial and torque loads acting on the bit with the conceptual consequence that the down-hole motor and coiled tubing should have an increased fatigue lifespan. High-speed rotation should in principal increase the drilling ROP in order to achieve fast drilling. For this approach to be successful, four challenging tasks must be carried out successfully:

- Use of a drilling fluid and a corresponding fluid system to provide sufficient power to the down-hole motor to rotate drill bit, to transport drilled cuttings to the surface and to provide sufficient cooling and lubrication of the drill bit face.
- Develop a down-hole motor that can be run by the drilling fluid at high speed with sufficient shaft power output.
- Select or develop a suitable drill bit.
- Ensure that the high-speed rotation rock cutting process does not cause extensive vibration of the drill bit and the motor or develop a mechanism to control any excessive vibration.

The DET CRC is developing a turbine motor driven by water drilling fluid (Mokaramian et al. 2012, [14]). The turbine is concentric and can run much faster with less vibration than a positive displacement motor (PDM). Water is the conventionally accepted, safe drilling fluid. However, turbines are best run by compressible fluids if they are to have high rotation speed and high power output, such as a steam turbine in a thermal power station (which will be discussed later). A compressible fluid can therefore potentially provide more power than water to

run a down-hole turbine at a high rotation speed. Hence, the next stage of development for this project is to find a suitable compressible drilling fluid, design and test the corresponding turbine with an optimum drilling fluid system. A literature survey was performed to find the best drilling fluid, and as a result, CO<sub>2</sub> was identified as a potential drilling fluid.

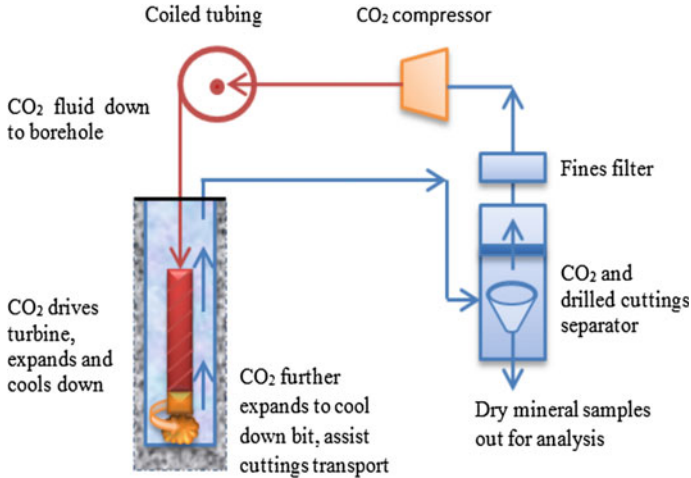
The idea of CO<sub>2</sub> as a drilling fluid was first proposed by Kollé in 2000 and 2002 [10, 11]. He stated in his SPE paper that “*Small-scale pressure drilling tests have also been carried out in shale with SC-CO<sub>2</sub> using microbit with a drag cutter. The rate of penetration in Mancos Shale with CO<sub>2</sub> was 3.3 times the rate with water. The increased drilling rate was accompanied by reduced drilling torque so that the drilling SE is only 20% that observed while drilling with water*”. Note that SE—specific energy—was defined by Kollé as the energy expended for cutting and removing a unit volume of rock. Gupta et al. compared supercritical CO<sub>2</sub> and foam drilling fluids for underbalanced drilling in 2005 [6]. They concluded that the liquid-like density and gas-like viscosity of CO<sub>2</sub> are advantageous in its role as a drilling fluid and these properties allow it to run the down-hole motor. Shen and Wang et al. [16, 17] also studied the feasibility of coiled tubing drilling and cuttings transport with supercritical CO<sub>2</sub> in 2010 and 2011. They concluded that coiled tubing drilling with supercritical CO<sub>2</sub> will bring an innovation in drilling technology and will become an efficient drilling technique for special reservoir development.

As discussed earlier, supercritical CO<sub>2</sub> has been identified as a highly efficient work fluid for electric power generation to substitute steam at thermal power stations (e.g. see Ho and Lillo et al. 2004, [8]; Hey 2011, [7]; Wright 2011, [21]). The supercritical CO<sub>2</sub> turbine is much smaller than a steam turbine leading to a much smaller footprint for thermal power stations as described in Persichilli and Kacludis et al. in 2012 [15]. The SC-CO<sub>2</sub> Power Cycle Symposium, which is now held every 2 years, is a demonstration of the perception of using CO<sub>2</sub> as the future drive fluid for electric power generation. The engineering principle of using CO<sub>2</sub> as a drive fluid is that an efficient energy delivery work fluid for driving a turbine allows it to rotate at high speed with high shaft power output.

### 3 Water Versus CO<sub>2</sub> Drilling Fluid Systems

A water drilling fluid system in coiled tubing drilling is consisted of Water Tank, Pump, Coiled Tubing, Down-hole Motor, Drill Bit, Annulus, Well Head, Mud Separator and Water Tank. The corresponding down-hole motor is usually a PDM type. For hard rock microhole drilling, a water-driven turbine is being developed and its capability is to be tested (e.g. see Mokaramian and Rasouli et al. 2012, [14]).

A possible CO<sub>2</sub> drilling fluid system is shown in Fig. 3. This system is based on maximizing energy conservation. In this closed-loop system, any CO<sub>2</sub> loss is replenished either before or after the compressor. Starting at the compressor, CO<sub>2</sub> gas is compressed to an increased pressure and temperature to be a supercritical



**Fig. 3** Illustration of supercritical CO<sub>2</sub> drilling fluid system for hard rock drilling

fluid (above 7.4 Mpa, and above 31.1 °C), which would then flow down through the coiled tubing to the down-hole turbine; when it enters the turbine, it rotates the turbine while expanding and reducing temperature as it passes over the blades with some of its pressure and thermal energy transforming to mechanical rotation energy in the turbine; the CO<sub>2</sub> passes through the nozzles of the drill bit with further expanding and cooling down; the impact force of CO<sub>2</sub> jet flow discharged from the bit nozzles assists breaking the rock; it then removes drilled cuttings and cools the drill bit; the CO<sub>2</sub> fluid also absorbs thermal energy from the drilled cuttings and further expands as it flows up through the annulus to bring drilled cuttings up to the surface; then the CO<sub>2</sub> fluid is separated from drilled cuttings in a separator and further filtered in a fines filter. It then reaches the inlet of the compressor for being recompressed. The drilled cuttings at the separator are dry mineral samples for analysis. The separation of cuttings from a gas using conventional filtration methods is far easier than removing cuttings from water.

Such a CO<sub>2</sub> fluid system is an energy-efficient system with most of the energy devoted to drilling and cuttings transport with the following advantages:

- A closed-loop system with its returned and contained CO<sub>2</sub> allows efficient energy reuse.
- Energy conversion due to the pressure and thermal energy of CO<sub>2</sub> being transformed into mechanical shaft rotation energy of the turbine; some of the mechanical energy is transformed to heat during the cutting process; the heat is absorbed by the CO<sub>2</sub> causing its expansion and increased flow speed for transporting drilled cuttings.

- The high-density compressed supercritical CO<sub>2</sub> fluid is suitable for efficiently driving the high-speed turbine and is more effective in terms of energy transfer than water.

There are methods for controlling the inlet pressure, temperature and flow rate of the drilling fluid by a combined use of a compressor, pump, chiller or cooler. We can adjust the outlet pressure of the annulus by a valve before or after the separator. The question is, given a set of defined inlet pressure, temperature and flow rate, how capable the CO<sub>2</sub> can be in energy delivery as compared with water?

## 4 Comparison of Total Energy Delivery

Water is used as the benchmark for evaluating the energy delivery efficiency of CO<sub>2</sub> drilling fluid. The comparison is based on the same mass flow rate and at specified pressure differences. We define the pressure difference between the inlet pressure of the coiled tubing and the outlet pressure of the annulus. The first step is to calculate and compare the total energy that can be delivered by a unit mass of water and CO<sub>2</sub> at specified pressure difference. The total energy expended is in three parts: friction energy loss within the coiled tubing, energy loss for driving the turbine which rotates the drill bit and energy loss in the annulus due to friction and cuttings transport. We then calculate and compare the friction energy loss between water and CO<sub>2</sub> in the coiled tubing. Finally, we calculate and compare the turbine power output at a specified pressure differential of the turbine. The drilling data is set as below:

- Coiled tubing of 1.5 in. diameter and 0.175 in. wall thickness (38.1 mm OD, 4.45 mm wall thickness)
- Borehole diameter 50 mm and depth to 2 km
- Equal mass flow rate 1 kg/s for water and CO<sub>2</sub>

The coiled tubing size is from the Tenaris Coiled Tubes technical data [18]. It is considered appropriate to choose a larger wall thickness for increased strength and stiffness of the small diameter coiled tubing for deep microhole drilling. Water has a very large bulk modulus  $2.2 \times 10^9$  Pa and hence is regarded as an incompressible fluid. Its density is 1 kg/L and hence 1 kg/s mass flow rate can be converted to 1 L/s volume flow rate. On the other hand, CO<sub>2</sub> is compressible and its volume flow rate  $Q_v$  is a function of its mass flow rate  $Q_m$  and density  $\rho$  which depends on its pressure and temperature. The flow speed  $V$  can be calculated from the volume flow rate and the cross-sectional area  $A$  of the flow.

Once the inlet and outlet conditions of a drilling fluid are given, the energy delivered by the fluid can be calculated by considering only the fluid energy states at the inlet and outlet. Assuming a fully developed turbulent flow and a non-compressible fluid, water delivers hydraulic energy which can be expressed by Eq. (1). It includes pressure energy  $E_p$ , kinetic energy  $E_k$  and gravity potential energy  $E_z$ . The energy difference between the inlet and outlet is the energy delivered

by the fluid, which is shown in Eq. (2). Setting the outlet pressure to be 0.5 Mpa, the energy delivered by a unit mass flow rate of water corresponding to different inlet pressure is calculated and plotted in Fig. 4.

$$E = E_p + E_k + E_z = pQ_v + \frac{1}{2}Q_m V^2 + Q_m g z \quad (1)$$

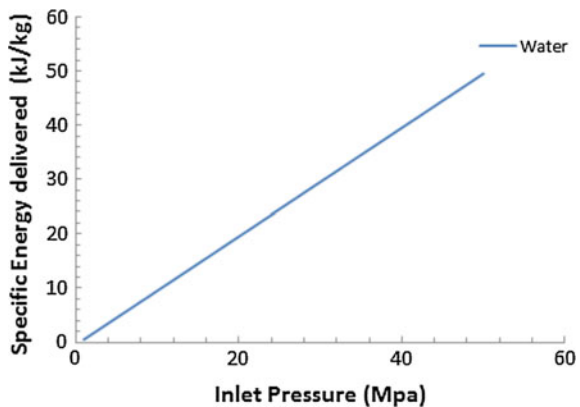
$$\Delta E = E_{in} - E_{out} \quad (2)$$

The straight line in Fig. 4 shows a linear relationship between the energy delivered by water and its inlet pressure. In the calculation, the inlet and outlet have been assumed about the same height so that the gravity potential energy terms are cancelled; the kinetic energy is 1.1 kJ/kg at the inlet and 0.7 kJ/kg at the outlet. Hence, only 0.4 kJ/kg energy is delivered due to the velocity difference, which is too small to be noticed in Fig. 4. As a result, the energy delivery of water is almost solely relying on the pressure difference between the inlet and the outlet. For a 1 kg mass flow rate, an increase of 1 Mpa inlet pressure will provide an increase of 1 kJ/kg pressure energy to the down-hole drilling system.

The pressure energy is not an internal energy stored in water. It is the work done by the pump and is transferred by the water flow driven by the pressure difference. For a volume flow rate  $Q_v$  through the inlet of the coiled tubing, the work done is  $pAV$ , i.e.  $pQ_v$ , per second. Here,  $A$  is the cross-sectional area and  $V$  is flow speed.

For a compressible drilling fluid such as  $CO_2$ , the energy delivery mechanism involves the internal energy stored in the compressible fluid and hence is a function of pressure, temperature and the thermodynamic properties of the fluid. Considering the  $CO_2$  fluid flow across a section of the coiled tubing or the annulus, its energy state can be expressed by Eq. (3). Here,  $U$  is internal energy of the fluid. The combination of internal energy and pressure energy is defined as enthalpy  $H$  in thermodynamics which is expressed by Eq. (4). Hence, we have Eq. (5) for calculating the energy delivery of  $CO_2$ .

**Fig. 4** Hydraulic energy delivered by water drilling fluid (outlet pressure 0.5 Mpa)





$$E = U + E_p + E_k + E_z = uQ_m + pQ_v + \frac{1}{2}Q_m V^2 + Q_m g z \tag{3}$$

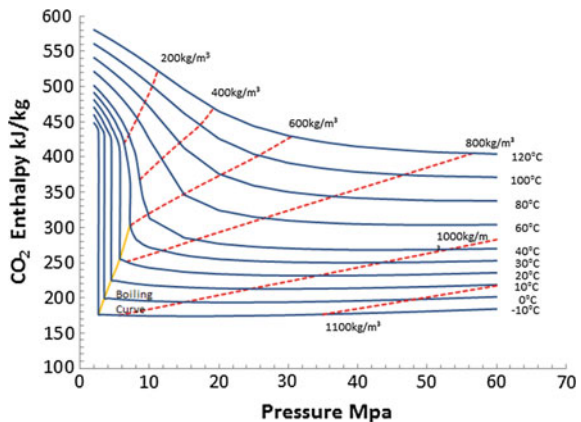
$$H = U + E_p = uQ_m + pQ_v \tag{4}$$

$$E = H + E_k + E_z = H + \frac{1}{2}Q_m V^2 + Q_m g z \tag{5}$$

The enthalpy of a matter is usually measured and stored in a thermodynamic database for the convenience of energy balance calculation. There are also pressure–enthalpy or temperature–enthalpy charts available for use. A pressure–enthalpy chart is created and plotted in Fig. 5 for the convenience of illustration and description in this paper. We are indebted to Berndt Wischnewski for the online CO<sub>2</sub> property calculation website [20]. In Fig. 5, each solid line is a pressure–enthalpy curve at a constant temperature. Each dotted line is a pressure–enthalpy curve of constant density. The pressure range of up to 60 Mpa and temperature range from -10 to 120 °C are plotted in the figure.

Figure 5 shows that CO<sub>2</sub> has the potential to work at a wide range of densities depending on the operating pressure and temperature. Different ranges of CO<sub>2</sub> drilling fluid operation conditions can be chosen to achieve underbalanced, balanced or overbalanced drilling, which in some drilling scenarios is beneficial for well control and drilling optimization. It is important to note that there exists a boiling curve at the lower pressure, lower temperature region which is below the CO<sub>2</sub> critical point (7.38 Mpa, and 31.1 °C). If the turbine outlet pressure is below 7.4 Mpa, there is a possibility that the turbine will be operating across the CO<sub>2</sub> boiling curve which is shown in Fig. 5. It is better for the turbine to carry out drilling operations away from the CO<sub>2</sub> boiling condition in order to avoid cavitation erosion problem. The outlet pressure of the turbine should be set to be greater than 7.38 Mpa; otherwise, the outlet CO<sub>2</sub> temperature should be well above the critical temperature 31.1 °C.

**Fig. 5** Pressure enthalpy chart of CO<sub>2</sub>

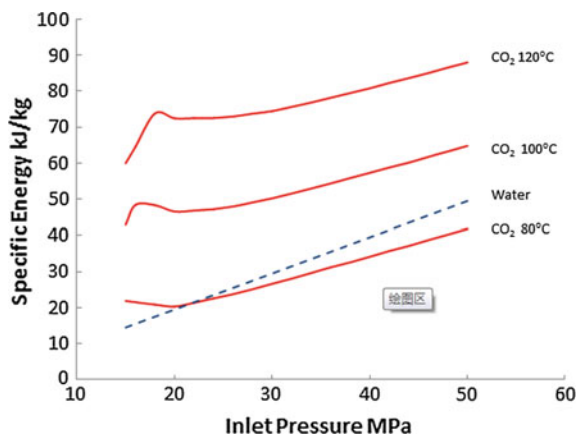


A complex drilling fluid such as CO<sub>2</sub> is pressure and temperature dependent. Setting the inlet and outlet pressure requires considering the temperature in order to calculate the energy delivered. However, the outlet temperature cannot be set to a fixed value because it will change as a function of the inlet pressure and temperature as well as the changing drilled hole depth. In fact, it is difficult to accurately calculate the energy delivery without a detailed knowledge of energy consumption in the coiled tubing, the down-hole turbine and the annulus. Instead, estimation is made of the potential capability of energy delivery of CO<sub>2</sub> drilling fluid. For estimation purposes, the outlet pressure of the annulus is set to 8 Mpa and the outlet CO<sub>2</sub> fluid density set to 75% of the corresponding inlet density due to expansion. The total energy delivery is calculated based on Eq. (5) and plotted in Fig. 6.

Figure 6 shows that, within the common operation pressure range of 20–40 Mpa and at 120 °C, the CO<sub>2</sub> fluid can generally provide two to three times of the energy provided by water. At 100 °C, CO<sub>2</sub> can provide 1.5–2 times of the energy by water, while at 80 °C, CO<sub>2</sub> fluid generally provides about the same amount of energy as water. This demonstrates that temperature is an important factor for CO<sub>2</sub> fluid to provide drilling power. Temperature is a measure of thermal energy contained in compressible fluids. In order to maintain the thermal energy for turbine rotation, it is better to retain the CO<sub>2</sub> heat, i.e. not cool it down after it is compressed and its temperature increased. Since CO<sub>2</sub> drilling fluid can provide much more energy than water, the CO<sub>2</sub> drilling fluid can operate at lower pressure than water drilling fluid for delivering the same amount of energy, which will result in a long life of the coiled tubing.

The thermodynamic energy of CO<sub>2</sub> is transformed into mechanical shaft rotation energy in the turbine. The mechanical rotation energy enables the drill bit to cut the rock. The rock cutting process generates a lot of heat, which is then recovered by the CO<sub>2</sub> fluid. The recovered thermal energy can assist the cuttings transport in the annulus. Assume  $W_M$  is the turbine motor shaft work output and  $Q_{in}$  is the heat recovered by the CO<sub>2</sub> fluid at the bottom of the hole. These two parameters have a

**Fig. 6** Energy delivery comparisons between CO<sub>2</sub> and water drilling fluids (CO<sub>2</sub> outlet pressure 8 Mpa and water outlet pressure 0.5 Mpa)



proportional relationship which can be expressed by Eq. (6). Here,  $\alpha$  is a proportional factor which depends on the efficiency of the drill bit and the turbine. If the drill bit can cut the rock efficiently without producing a lot of heat, then  $\alpha$  will be a small value; otherwise, it is a larger value. By the mechanism of heat recovery and reuse, the efficiency of the drilling fluid energy delivery is increased. An energy balance equation is shown in Eq. (7). Here,  $E_f$  is the friction energy loss in the coiled tubing and the annulus,  $W_{TC}$  is the work done by transporting cuttings up to surface and  $Q_l$  is the heat energy loss to a surrounding environment. Equation (7) can be reorganized into Eq. (8), which is a clear expression of the increase of energy efficiency.

$$Q_{in} = \alpha W_M \quad (6)$$

$$E_{out} = E_{in} - E_f - W_M - W_{TC} + Q_{in} - Q_l \quad (7)$$

$$E_{in} + Q_{in} = E_{out} + E_f + W_M + W_{TC} + Q_l \quad (8)$$

The energy terms in Eq. (8) are worth careful study for optimized drilling operations. In the next section, the friction energy loss  $E_f$  of CO<sub>2</sub> inside the coiled tubing will be compared with that of water.

## 5 Comparison of Friction Energy Loss Inside the Coiled Tubing

Friction energy loss occurs inside the coiled tubing and annulus. It reduces the energy available for the turbine and for cuttings transport. The deeper the hole is drilled, the longer the coiled tubing and annulus will become and the larger the frictional energy loss. Friction energy loss is characterized by a friction factor and can be calculated in terms of friction pressure loss for a pipe by Eq. (9). Here,  $f$  is the Fanning friction factor,  $\rho$  the fluid density,  $L$  the length and  $D$  the inside diameter of the pipe [1]. Friction factor is a function of the wall roughness  $\varepsilon$  and the fluid flow Reynolds number  $R_e$  as expressed by the Colebrook Eq. (10) [3]. A simplified Eq. (11) is by Tomita in 1959 [19]. The wall roughness  $\varepsilon$  depends on the pipe material and the manufacturing process. For coiled tubing, the Tenaris technical data [18] suggests an internal wall roughness of new coiled tubing to be 0.001 in. (0.00254 mm). The Reynolds number  $R_e$  is a function of the fluid density  $\rho$ , dynamic viscosity  $\mu$  and flow speed as expressed in Eq. (12).

$$\Delta P_{loss} = f \frac{2\rho L V^2}{D} \quad (9)$$

$$\frac{1}{\sqrt{f}} = 3.48 - 4 \log \left( \frac{2\varepsilon}{D} + \frac{9.35}{R_e \sqrt{f}} \right) \quad (10)$$

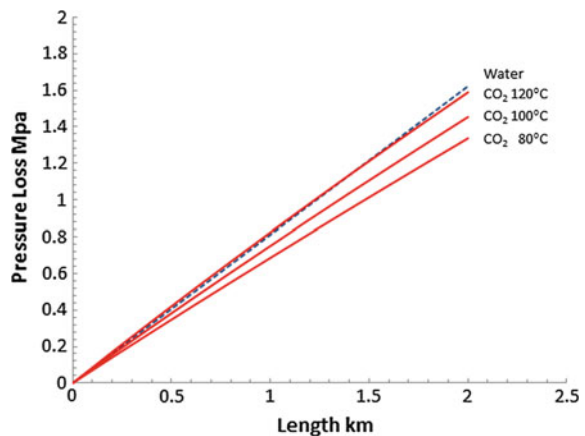
$$\frac{1}{\sqrt{f}} = 2.28 - 4 \log \left( \frac{\varepsilon}{D} + \frac{21.25}{R_e^{0.9}} \right) \quad (11)$$

$$R_e = \frac{\rho V D}{\mu} \quad (12)$$

Based on the above equations, the friction pressure loss within the coiled tubing can be calculated. The dynamic viscosity of freshwater is taken to be  $890 \times 10^{-6}$  Pa s at 25 °C. The viscosity of CO<sub>2</sub> is small and yet changes with both temperature and pressure. For example at 120 °C, it is  $54.2 \times 10^{-6}$  Pa s under 30 Mpa of pressure and  $70.2 \times 10^{-6}$  Pa s under 50 Mpa of pressure. Dividing the whole length of the coiled tubing into 200-m length sections and using the average pressure, density, flow rate and viscosity of CO<sub>2</sub> fluid for each section and setting the inlet pressure to be 30 Mpa, the calculated results are plotted in Fig. 7 against the length of the coiled tubing in a vertical hole. The friction pressure loss of CO<sub>2</sub> at 120 and 100 and 80 °C are calculated and compared with that of water.

Figure 7 shows the friction pressure loss curves of water and CO<sub>2</sub>. At 2000-m coiled tubing length, water has a 1.62 Mpa friction pressure loss and CO<sub>2</sub> has 1.59, 1.45 and 1.34 Mpa friction pressure losses at 120, 100 and 80 °C, respectively, which are lower than that of water. The friction factor of freshwater is 5.3E-3. The low viscosity of CO<sub>2</sub> fluid has resulted in small friction factors of 3.43E-3, 3.48E-3 and 3.55E-3 at 120, 100 and 80 °C, respectively. However, the higher flow speed of CO<sub>2</sub> has increased its friction pressure loss. The decrease in temperature and increase in pressure will enable the CO<sub>2</sub> density to increase which will result in a decrease in volume flow rate and hence a decrease of friction pressure loss. Figure 7 is for freshwater and pure CO<sub>2</sub> fluid. In practice, the drilling fluids are reused in the circulating drilling fluid system and are contaminated by drilled cuttings and additives, and hence, the viscosity of real drilling fluid inside the coiled tubing is larger and needs to be measured under real field drilling conditions.

**Fig. 7** Friction pressure loss of CO<sub>2</sub> and water fluid inside the coiled tubing (inlet pressure 30 Mpa)



There is much greater friction pressure loss in the annulus than in the coiled tubing. The hard rock cuttings are very fine particles like powder. When mixed with the drilling fluid, it dramatically increases the viscosity of the fluid. This phenomenon has been found true for water drilling fluid and is under careful study at the DET CRC drilling research group (see e.g. Kamyab, Rasouli and Cavanough 2013, [9]). The CO<sub>2</sub> drilling fluid viscosity in the annulus ideally should be less than water because CO<sub>2</sub> has low viscosity. However, the exact situation for CO<sub>2</sub> drilling fluid viscosity and pressure loss in the annulus needs to be carefully studied by laboratory experiments and field drilling tests in the future. There is a need of having high-quality fine particle filtering in the system to ensure that the CO<sub>2</sub> being as clean as possible inside the coiled tubing.

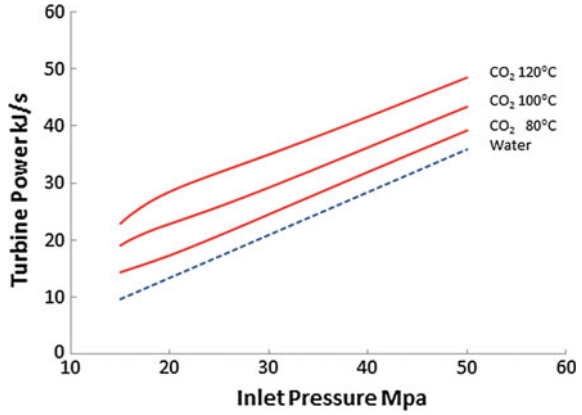
## 6 Comparison of Power Output of Down-hole Turbines

Shaft power output of a down-hole turbine plays a vital role in the drilling ROP. It is this power that drives the drill bit to cut the rock. Therefore, it is necessary to compare drilling fluids in terms of their turbine power outputs. The turbine power output at a given inlet pressure and temperature and outlet pressure can be calculated by software such as Aspen HYSYS and MegaWatSoft [2, 13]. Setting coiled tubing inlet pressure in the range of 15–50 Mpa and inlet temperature to be 80, 100 and 120 °C, respectively, and the outlet pressure to be 8 Mpa, the CO<sub>2</sub> turbine power output can be calculated. Setting the inlet pressure to be in the range of 15–50 Mpa and outlet pressure of water to be 0.5 Mpa, the water turbine power output is calculated. Both CO<sub>2</sub> turbine and water turbine are assumed to have 75% energy efficiency. The MegaWatSoft calculation results are plotted in Fig. 8. It shows that a CO<sub>2</sub> turbine can have much more power output than a water turbine. For example, at an inlet pressure of 30 Mpa, a CO<sub>2</sub> turbine can have 24.5, 29.2 and 35 kJ/s of power output for 80, 100 and 120 °C inlet temperature, respectively, which are 1.17, 1.40 and 1.67 times of the water turbine power output 20.9 kJ/s. Mr. Nicholas Ted, a postgraduate student, did verification calculation and confirmed that HYSYS obtained almost exactly the same result as MegaWatSoft result shown in Fig. 8.

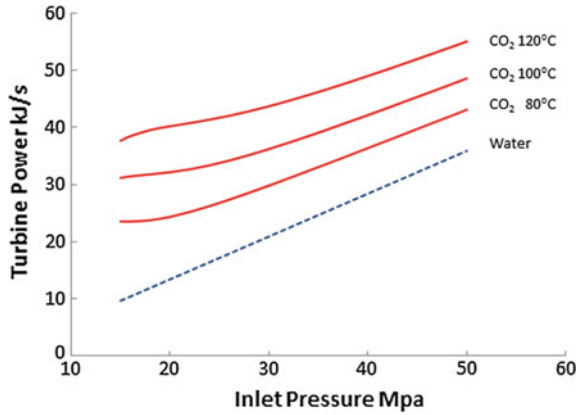
Setting the outlet pressure of the CO<sub>2</sub> turbine to be 0.5 Mpa so that both CO<sub>2</sub> and water turbines work under the same differential pressure, the MegaWatSoft calculation results are obtained and shown in Fig. 9. It shows that reducing the outlet pressure of CO<sub>2</sub> can significantly increase the turbine power output. For example, at an inlet pressure of 30 Mpa, a CO<sub>2</sub> turbine can have 29.8, 36.2 and 43.7 kJ/s power outputs at 80, 100 and 120 °C of CO<sub>2</sub> inlet temperature, respectively, which are 1.43, 1.73 and 2.09 times of the water turbine power output 20.9 kJ/s. This demonstrates the additional capability of energy delivery of CO<sub>2</sub> as a turbine drive fluid.

As drilling continues, the friction pressure loss and the energy cost for cuttings to be transported in the annulus will increase as a function of the hole depth, therefore making less energy available for the turbine. By simply assuming that the energy

**Fig. 8** Power outputs of CO<sub>2</sub> and water turbines as a function of their inlet pressure (CO<sub>2</sub> turbine outlet pressure 8 Mpa and water turbine outlet pressure 0.5 Mpa)



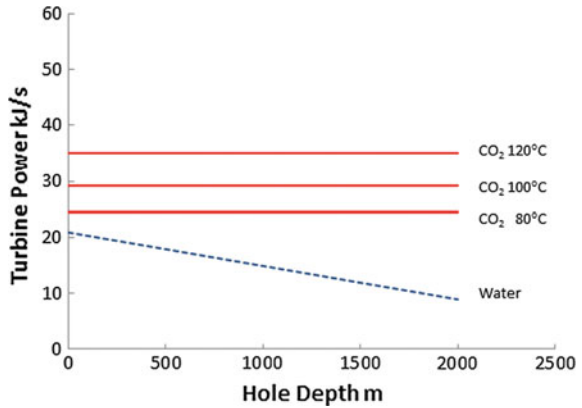
**Fig. 9** Power outputs of CO<sub>2</sub> and water turbines as a function of their inlet pressure (CO<sub>2</sub> and water turbine outlet pressure is 0.5 Mpa)



loss of water drilling fluid in the annulus due to friction and cuttings transport is  $\beta$  times that inside the coiled tubing, the calculated water turbine power output as a function of hole depth at a fixed coiled tubing inlet pressure 30 Mpa and the annulus outlet pressure 0.5 Mpa are plotted as a dotted line in Fig. 10 when  $\beta = 10$ . This shows that the water turbine has a power output of 20.9 kJ/s at the start of drilling and has only 8.9 kJ/s at the end of drilling which is a 57% power reduction. This factor of 10 is an assumption for illustration purposes only. In fact, it can be within a wide range of values depending on the concentration and the size of cuttings in the annulus fluid (see e.g. Kamyab et al. 2013, [9]), and more accurate values only come from drilling measurements, initially in the laboratory.

For CO<sub>2</sub> as a drilling fluid, we are able to keep the turbine power output constant throughout the hole depth by gradually reducing the annulus outlet pressure but still keeping the down-hole turbine outlet pressure above 8 Mpa. Figure 10 shows two solid horizontal lines for the CO<sub>2</sub> turbine power output at 80, 100 and 120 °C inlet temperatures, respectively. In fact because the density of CO<sub>2</sub> fluid inside the coiled

**Fig. 10** Power output of CO<sub>2</sub> and water turbines as a function of drill hole depth (coiled tubing inlet pressure 30 Mpa, water outlet pressure 0.5 Mpa, CO<sub>2</sub> turbine outlet pressure >8 Mpa)

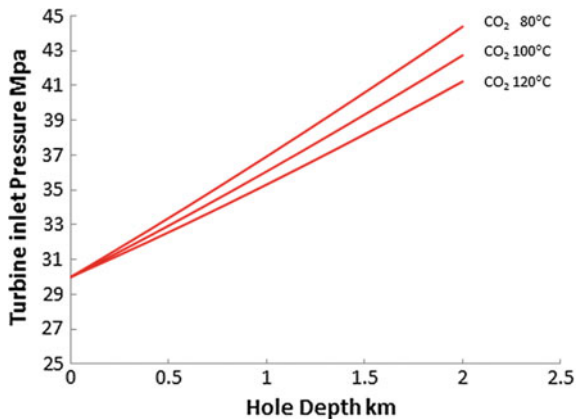


tubing is much higher than in the annulus (resulting in a faster increase of the inlet pressure than the outlet pressure of the turbine), the CO<sub>2</sub> turbine is capable of producing more power output.

Figure 11 shows the inlet pressure increase of the turbine while keeping the coiled tubing inlet pressure at 30 Mpa. It shows that, at 2-km hole depth, the turbine inlet pressure increases by 11.2, 12.7 and 14.4 Mpa for 120, 100 and 80 °C CO<sub>2</sub> fluid, respectively. This means that by gradually reducing outlet pressure of annulus to keep the turbine outlet pressure to be constantly at 8 MPa while hole depth increases can actually produce more drilling power. Water drilling fluid does not have this advantage since its annulus outlet pressure is already minimum value at the starting of drilling, i.e. at zero hole depth.

In addition, CO<sub>2</sub> drilling fluid has less friction pressure loss than water in the coiled tubing, and it can recover heat energy by absorbing heat generated during the rock cutting process. We now can conclude that CO<sub>2</sub> is a fluid for providing much more drilling power than water and making efficient use of that power by

**Fig. 11** CO<sub>2</sub> turbine inlet pressure increases as a function of hole depth while the coiled tubing inlet pressure is fixed at 30 Mpa



recovering heat energy generated during the rock cutting process to transport cuttings up to the surface.

## 7 Conclusions and Future Work

This paper has theoretically calculated and compared the energy delivery capabilities of CO<sub>2</sub> and water drilling fluids for deep microhole hard rock drilling for mineral exploration. It has found that water as an incompressible drilling fluid can only deliver hydraulic energy to the drilling system. The total hydraulic energy of water has a linear relationship with its total pressure difference between the inlet of the coiled tubing and the outlet of the annulus at the surface. The water turbine power output has a linear relationship with the differential pressure between its inlet and outlet. The kinetic energy difference of water between the inlet and the outlet is very small and negligible. The friction pressure energy loss of water has a linear relationship with the pipe length.

On the other hand, it is found that CO<sub>2</sub> is a more complex drilling fluid than water. It is compressible allowing the manipulation of the energy delivery mechanism. Apart from pressure which allows the transfer of hydraulic power, the pressure, temperature and thermodynamic properties of CO<sub>2</sub> also enable it to store and release internal energy by absorbing heat and expansion. It is found that CO<sub>2</sub> drilling fluid can offer much more energy to the drilling system than water. The higher the pressure and temperature, the more energy that CO<sub>2</sub> can store and supply. Due to its low viscosity, CO<sub>2</sub> also has smaller friction energy loss than water. While water will lose turbine power output significantly as the hole depth increases, the CO<sub>2</sub> drilling fluid can keep a constant or increasing turbine power output with the increase of hole depth, which is crucial for ensuring fast drilling with increasing depth. In addition, CO<sub>2</sub> can increase its energy utilization efficiency by absorbing heat energy produced during the drilling process and then reuse it by further expansion in the annulus for increased flow speed to bring the cuttings up to surface. This power delivery capability of CO<sub>2</sub> allows drilling at lower pressure which is beneficial for extending the fatigue life of the coiled tubing. We conclude that CO<sub>2</sub> is a much more powerful, more efficient energy delivery and utilization drilling fluid than water.

This paper performed a theoretical analysis by comparing the energy delivery capability and efficiency of CO<sub>2</sub> with water. It evaluates CO<sub>2</sub> as a new drilling fluid by taking conventional water drilling fluid as a benchmark. There is a lot of work to be done for developing a working coiled tubing drilling system with CO<sub>2</sub> as drilling fluid, for example experimental comparison of the fatigue life of the coiled tubing between using water and CO<sub>2</sub> at different temperature and pressure; selecting a suitable pump or compressor; developing equipment for separating CO<sub>2</sub> and drilled cuttings; developing a down-hole CO<sub>2</sub> turbine which can use supercritical CO<sub>2</sub> as work fluid; as well as the high-speed drill bit and other associated components. It is also important to carry out detailed theoretical and experimental studies on the



two-phase thermodynamic flow behaviour of the mixture of CO<sub>2</sub> and drilled cuttings in the annulus. This will enable a better understanding of cuttings transport and the energy utilization in the annulus and provide detailed data for calculation and development of a drilling operation strategy.

**Acknowledgements** The authors acknowledge the financial support from the Deep Exploration Technologies Cooperative Research Centre whose activities are funded by the Australian Government's Cooperative Research Centre Program. This paper presents some of the research work for DET CRC when the first author was at the Curtin University.

## References

1. Azar, J. J. and Samuel, G. R. 2007. Drilling Engineering. PennWell Corporation, Tulsa, Oklahoma, USA.
2. Aspen HYSYS V7.2. <http://www.aspentech.com/products/aspen-hysys.aspx>.
3. Colebrook, C. F. 1938. Turbulent Flow in Pipes with Particular Reference to the Transition Region between the Smooth and Rough Pipe Laws. *Journal of the Institute of Civil Engineers*, London 11: 133–156.
4. DET CRC 2014. ROP Continues to Improve in High Speed, Low WOB Trials. DET CRC eNewsletter February 2014. <http://detcrc.com.au/enewsletter/explore-february-2014/>.
5. DET CRC 2013. Efficient Solids Removal for Drilling Fluids – The Results Are Clear. DET CRC eNewsletter July 2013. <http://detcrc.com.au/enewsletter/explore-july-2013/>.
6. Gupta, A. P., Gupta, A. and Langlinais, J. 2005. Feasibility of Supercritical Carbon Dioxide as a Drilling Fluid for Deep Underbalanced Drilling Operations. SPE Annual Technical Conference and Exhibition, Dallas, Texas, USA, 9–12 October.
7. Hey, N. 2011. Exit the Steam Turbine, Enter the CO<sub>2</sub> Turbine? *Innovation, America's Journal of Technology Commercialization*, 9 (3). <http://www.innovation-america.org/exit-steam-turbine-enter-co2-turbine>.
8. Ho, C., Lillo, T., Windes, W. et al 2004. Development of a Carbon Dioxide Brayton Cycle: Improving PBR Efficiency and Testing Material Compatibility. Idaho National Engineering and Environmental Laboratory, USA.
9. Kamyab, M., Rasouli, V., Mandal, S. et al. 2013. Rheological Properties and Fluid Behaviour in Hard Rock Drilling. *Mining Technology*, 122 (4): 185–192. <http://dx.doi.org/10.1179/1743286313Y.0000000047>.
10. Kollé, J. J. 2000. Coiled –Tubing Drilling with Supercritical Carbon Dioxide. SPE/Petroleum Society of CIM International Conference on Horizontal Well Technology, Calgary, Alberta, Canada, 6–8 November.
11. Kollé, J. J. 2002. Coiled Tubing Drilling with Supercritical Carbon Dioxide. United States Patent US 6,347,675, B1. Feb. 19.
12. Liu, X. 2014. A Borehole Size Optimization Method Based on Drilling Fluid Power for Maximizing the Rate of Penetration in Coiled Tubing Drilling of Hard Rock Formations. SPE Drilling & Completion (submitted).
13. MegaWatSoft. <http://www.megawatsoft.com/>.
14. Mokaramian, A., Rasouli, V. and Cavanough, G. 2012. CFD Simulation of Turbodrill Performance with Asymmetric Stator and Rotor Blades Configuration. Ninth International Conference on CFD in the Minerals and Process Industries CSIRO, Melbourne, Australia, 10–12 December.
15. Persichilli, M. and Kauludis, A. et al 2012. Supercritical CO<sub>2</sub> Power Cycle Developments and Commercialization: Why sCO<sub>2</sub> Can Displace Steam. Presented at Power-Gen India & Central Asia, 19–21 April, Pragati Maidan, New Delhi, India.

16. Shen, Z., Wang, H. and Li, G. 2010. Feasibility analysis of coiled tubing drilling with supercritical carbon dioxide. *Petroleum Exploration and Development*, 37(6): 743–747.
17. Shen, Z., Wang, H. and Li, G. 2011. Numerical simulation of the cutting-carrying ability of supercritical carbon dioxide drilling at horizontal section. *Petroleum Exploration and Development*, 38(2): 233–236.
18. Tenaris 2013. Coiled Tubes Technical Data. <http://www.tenaris.com/en/Products/CoiledTubing.aspx>.
19. Tomita, Y. 1959. *Bulletin J.S.M.E.*, 2: 469. Tomita, Y. 1961, *Bulletin J. S. M. E.*, 4: 77.
20. Wischnewski, B. 2013. Online CO<sub>2</sub> Calculation. [http://www.peacesoftware.de/einigewerte/co2\\_e.html](http://www.peacesoftware.de/einigewerte/co2_e.html).
21. Wright, S. A. 2011. Break-even Power Transients for Two Simple Recuperated S-CO<sub>2</sub> Brayton Cycle Test Configurations. *Supercritical CO<sub>2</sub> Power Cycle Symposium*, May 24–25, Boulder, Colorado, USA.

# Drilling Hydraulic Power Optimization in Coiled Tubing Drilling of Hard Rock

Xianhua Liu

**Abstract** Coiled tubing drilling of hard rock for mineral exploration is a new technology being developed by the Deep Exploration Technologies CRC, Australia. Coiled tubing drilling of small holes in hard rock relies on sufficient drilling fluid power for breaking the rock and transporting cuttings up to the surface. High-speed rotating diamond-impregnated bit cuts hard rock into powder form particles, which consumes a large amount of power; meanwhile, cuttings transported through the narrow annular space also cost a lot of hydraulic power. The drilling power supply becomes an issue if water is used as drilling fluid since it is incompressible and can only transmit hydraulic power. In such a case, it is necessary to optimize the use of drilling fluid power for achieving maximum rate of penetration. The drilling power optimization here is different from that of the conventional rotary drilling for oil and gas production. This paper analyses the difference and proposes optimizing the borehole size for achieving the optimum use of drilling fluid power and maximum rate of penetration. An optimization algorithm is developed, and an example is presented.

**Keywords** Coiled tubing drilling · Hard rock · Hydraulic power optimization · Borehole size

## 1 Introduction

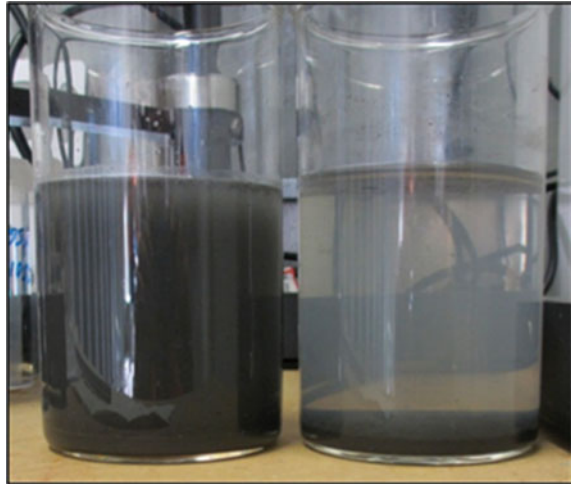
For developing a next-generation drilling technology for mineral exploration in the mining industry, the DET CRC drilling research team has proposed to use coiled tubing drilling in hard rock formation. It is believed that coiled tubing drilling technology can drill deeper, cheaper, and faster, with small foot imprint. The coiled tubing is  $\varnothing 38.1$  or  $\varnothing 44.5$  mm (1.5–1.75 in.) in size, the drill bit is diamond-impregnated

---

X. Liu (✉)

Petroleum Engineering Department, Universiti Teknologi PETRONAS,  
Seri Iskandar, Malaysia  
e-mail: xianhua.liu@utp.edu.my

**Fig. 1** Hard rock cuttings generated by diamond-impregnated bit drilling. *Left* bottle before cutting removal; *Right* bottle after cutting removal



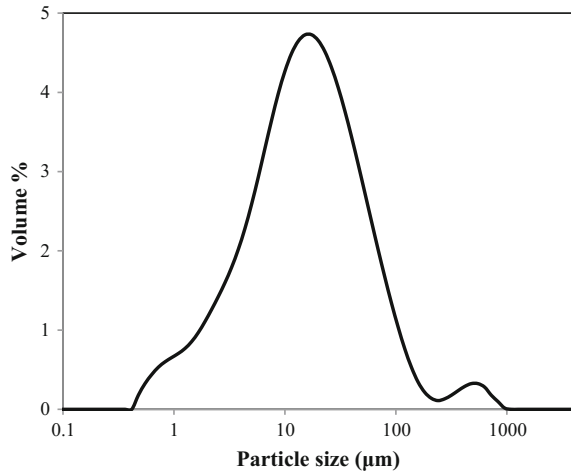
**Fig. 2** Core samples (*top*) and drilled hard rock cuttings (*bottom*) by diamond-impregnated drill bit



type, and the cuttings are powder form particles as shown in Figs. 1 and 2. The cutting particle size distribution is from 1 to 1000  $\mu\text{m}$  with the majority being less than 100  $\mu\text{m}$ , as shown in Fig. 3 [1, 2]. The mixture of such micrometre-sized particles with water is a kind of low-concentration slurry. According to Chien's correlation (1994) [3], a 1-mm-diameter spherical cutting has only a slip velocity of about 0.13 m/s in water. On the other hand, coiled tubing drilling usually has higher cutting transport velocity than conventional rotary drilling. Hence, cutting transport itself is not an issue. The issue is the inefficiency of drilling fluid power for drilling deep holes.

Water is incompressible and can only transmit hydraulic power. The high frictional pressure loss in the narrow annular space caused by high flow velocity and

**Fig. 3** Cutting particle size distribution generated by diamond-impregnated drill bit [1]



increased viscosity of the slurry like mixture of water and cuttings will cost a lot of hydraulic power resulting insufficient power left for the downhole motor to rotate the drill bit. In such a case, it is necessary to optimize the use of the available drilling fluid-transmitted hydraulic power for maximum rate of penetration (ROP).

This paper proposes to optimize the use of drilling hydraulic power through borehole size optimization for achieving maximum ROP. For a fixed-diameter coiled tubing rig with given hydraulic power, drilling a large-sized borehole will cost a large amount of power for cutting a large amount of hard rock; hence, the ROP will be small, while drilling a too small borehole will cost a lot of drilling fluid power to overcome the large frictional pressure loss in a very narrow annulus due to increased flow speed. Hence, there is an optimum borehole size that enables the optimized use of the available drilling hydraulic power. The borehole size can be an optimizing parameter because mineral exploration drilling is only for collecting mineral samples for analysing mineral content, which is a different purpose from drilling for oil and gas production [4, 5]. An optimization algorithm is developed, and an optimization example is presented.

## 2 Drilling Fluid Power Optimization

### 2.1 Drilling Fluid Power Equations

The total hydraulic power of drilling fluid  $E_t$  at any cross section of the drilling system can be expressed by Eq. 1. It includes pressure power  $E_p$ , kinetic power  $E_k$ , and gravity potential power  $E_z$ . The total power consumption  $\Delta E_t$  of the downhole drilling fluid system from the inlet of the coiled tubing to the outlet of the annulus

can be calculated by Eq. 2. The inlet and outlet can be assumed at the same elevation so that the gravity potential energy terms are cancelled.

$$\begin{aligned}
 E_t &= E_p + E_k + E_z \\
 &= pQv + 1/2Qmv^2 + Qmgz
 \end{aligned}
 \tag{1}$$

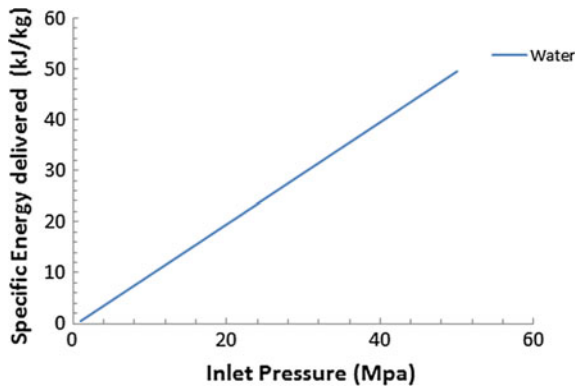
$$\begin{aligned}
 \Delta E_t &= E_{ti} - E_{to} \\
 &= (p_i - p_o)Qv + 1/2Qm(v_i^2 - v_o^2) + Qmg(z_i - z_o) \\
 &\approx \Delta pQv + 1/2Qm(v_i^2 - v_o^2)
 \end{aligned}
 \tag{2}$$

The kinetic energy difference between the inlet and outlet is negligible. For example, using a coiled tubing of Ø38.1 mm diameter to drill 50-mm-sized borehole, the power delivered by a unit volume flow rate in litres per second of water as drilling fluid corresponding to the different inlet pressure is calculated. The kinetic energy at the inlet is 1.1 kJ/L and at the outlet 0.7 kJ/L; hence, the difference is only 0.4 kJ/L, which is a constant value and small enough to be negligible. Set the outlet pressure to be 0.5 Mpa, and the power delivered by a unit mass flow rate of water corresponding to the different inlet pressure is calculated and plotted in Fig. 4. It shows a linear relationship between inlet pressure and the power delivered per unit flow rate. An increase of 1 Mpa inlet pressure will provide an increase of 1 kJ/L power to the downstream drilling system. This power is the work done by the surface pump and transmitted downstream by the water flow.

The drilling fluid power is consumed for performing several functions: cutting the hard rock  $E_c$ , frictional pressure loss within coiled tubing  $E_{ft}$ , within downhole motor  $E_{fm}$ , within annular space  $E_{fa}$ , cuttings lift to surface  $E_{cl}$ . The energy conservation is expressed by Eq. 3. The power for cutting the hard rock comes from the downhole motor shaft power output; hence, the total power consumption of the motor is expressed by Eq. 4, where  $\eta$  is the efficiency of the downhole motor.

$$\Delta E_t = E_c + E_{ft} + E_{fm} + E_{fa} + E_{cl}
 \tag{3}$$

**Fig. 4** Hydraulic energy delivered by water drilling fluid (outlet pressure 0.5 Mpa)



$$E_m = E_c + E_{fm} = E_c/\eta \quad (4)$$

Based on Eqs. 1–4, an optimization method can be derived for achieving the maximum drilling ROP by maximizing the downhole motor shaft power output for a given drilling fluid power supply from the surface mud pump. This leads to an algorithm of borehole size optimization.

## 2.2 Cutting Power, Borehole Size, and Rate of Penetration

Let us define the rock cutting specific energy  $E_s$  as the energy cost of the drill bit for cutting a unit volume of hard rock [6, 7]. The volume of rock that is cut out per unit time is expressed by Eq. 5. Here,  $E_c$  is the cutting power available from the downhole motor. The volume increase of the borehole is also a function of its size and ROP as expressed in Eq. 6. Combining the two equations leads to Eq. 7 for ROP.

$$V_c = E_c/E_s \quad (5)$$

$$V_c = \pi/4d_h^2ROP \quad (6)$$

$$ROP = 4E_c/(\pi E_s d_h^2) \quad (7)$$

The ROP is inversely proportional to the borehole size and proportional to the drilling power input  $E_c$  from the downhole motor shaft to drive the drill bit. When the borehole size is reduced, the flow velocity of annular space will increase causing an increase of frictional pressure loss  $E_{fa}$ . As a result, the pressure drop across the downhole motor will be decreased leading to a decreased output of cutting power  $E_c$ . When the borehole size is reduced to some extent, there will be a rapid increase of frictional pressure loss in the annular space causing rapid decrease of cutting power. As a result, for a given drilling fluid power supply from the surface mud pump, there is an optimum borehole size that leads to the maximum drilling ROP.

## 2.3 The Optimization Equations

Combining Eqs. 3, 4, and 7, the drilling ROP can be expressed by Eq. 8, which is a function of drilling fluid power supply, borehole size, and instant drilling depth  $z$ . Let the target borehole depth be  $D$ , and the total drilling time would be expressed by Eq. 9.

$$\begin{aligned}
 ROP(z) &= 4E_c(z)/(\pi d_h^2 E_s) \\
 &= 4\eta[\Delta E_t(z) - E_{ft}(z) - E_{fa}(z) - E_{cl}(z)]/(\pi d_h^2 E_s)
 \end{aligned}
 \tag{8}$$

$$\begin{aligned}
 t_D(d_h) &= \int_0^D ROP(z)^{-1} d(z) \\
 &= \pi E_s d_h^2 / (4\eta) \int_0^D [\Delta E_t(z) - E_{ft}(z) - E_{fa}(z) - E_{cl}(z)]^{-1} d(z)
 \end{aligned}
 \tag{9}$$

For drilling a borehole of target depth  $D$ , the optimization objective is to find the optimum borehole size from Eq. 9 so that the total drilling time  $t_D$  is a minimum value, i.e. the average ROP is a maximum value. The total power  $E_{ti}$  at the inlet of coiled tubing can be assumed constant, i.e. a constant power output from the surface mud pump to the downhole drilling fluid system. Strictly speaking, all the power terms in Eq. 9 are functions of the borehole size and drilled depth because they influence the frictional pressure loss in the annular space, which in turn causes a redistribution of the flow rate, inlet pressure, and frictional pressure loss inside the coiled tubing and the downhole motor [8].

### 2.4 The Optimization Algorithm

A numerical optimization algorithm can be developed by letting  $d_h = d_{he} \pm \Delta d_h, \pm 2\Delta d_h, \dots$  and calculate  $t_D(d_h)$ . Here,  $d_{he}$  is an initial estimated borehole diameter. For example, let  $d_{he}$  be the borehole diameter that gives equal flow speed in the annular space and the coiled tubing. A numerical optimization algorithm can be expressed by a flow chart in Table 1.

**Table 1** Flow chart of the optimization algorithm

1. Input original data, such as drilling fluid flow rate, rheology, coiled tubing size and length, downhole motor and rock cutting specific energy, target borehole depth.
2. Calculate an initial estimated borehole size $d_{he}$
3. Divide total target depth $D$ into $n$ sections of equal length.
4. Calculate frictional pressure losses in coiled tubing and annular space for each section.
5. Calculate drilling fluid power left for downhole motor for drilling in each section.
6. Calculate the total time cost $t_D(d_{he})$
7. Decide borehole diameter change step size, e.g. $\Delta d_h = 1$ mm.
8. Calculate total time costs for $t_D(d_{he} \pm \Delta d_h)$
9. If $t_D(d_{he} - \Delta d_h) < t_D(d_{he}) < t_D(d_{he} + \Delta d_h)$ , calculate $t_D(d_{he} - 2\Delta d_h), t_D(d_{he} - 3\Delta d_h) \dots$ till the time cost began to increase; otherwise, calculate $t_D(d_{he} + 2\Delta d_h), t_D(d_{he} + 3\Delta d_h), \dots$ till the time cost began to increase.
10. The optimum borehole size $d_{ho}$ is the one that enables minimum time cost $t_D$ in the above calculation.



### 3 Optimization Examples

#### 3.1 The Drill Test

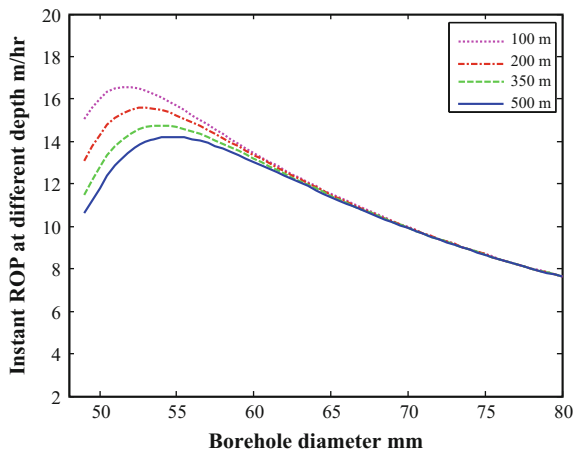
A drilling rig with coiled tubing size  $\varnothing 44.5 \times 3.2$  mm is to drill a borehole of target depth 500 m in hard rock. A rough estimate of borehole size is 59 mm. In the optimization, the target depth is divided into 50 equal length sections. Assume that the mud pump has a normal working condition of 3 L/s flow rate with 15 or 20 Mpa output pressure and the downhole motor has a normal working condition of 3 L/s flow rate as well. The drilling operation will be at constant weight on bit.

The hard rock is red granite, which has an unconfined compressive strength of 149 MPa and a Mohr’s hardness of 5.5. The diamond-impregnated bit can drill the hard rock at 4 Gpa specific energy cost at a normal drilling condition of 100  $\mu$ m penetration per revolution. The specific energy  $E_s$  is a constant; hence, its value does not affect the optimum borehole size but the ROP.

#### 3.2 The Optimization Results

The optimization results for 20 Mpa pump outlet pressure case are plotted in Figs. 4, 6, and 7. Figure 5 shows the instant drilling ROP at a different depth. It demonstrates that at each depth, there is an instant optimum borehole size that enables an instant maximum ROP. For example, when drilling at 500 m depth, the optimum borehole size is 55 mm which achieves a maximum average ROP of 14 m/h; when drilling at 100 m depth, the optimum borehole size is 52 mm which achieves a maximum ROP of 16.5 m/h.

**Fig. 5** Instant ROP at a different depth for constant weight on bit and start drilling pump pressure 20 Mpa and flow rate 3.0 L/s



**Fig. 6** Average ROP for drilling to a different target depth under constant weight on bit and start drilling pump pressure 20 Mpa and flow rate 3.0 L/s

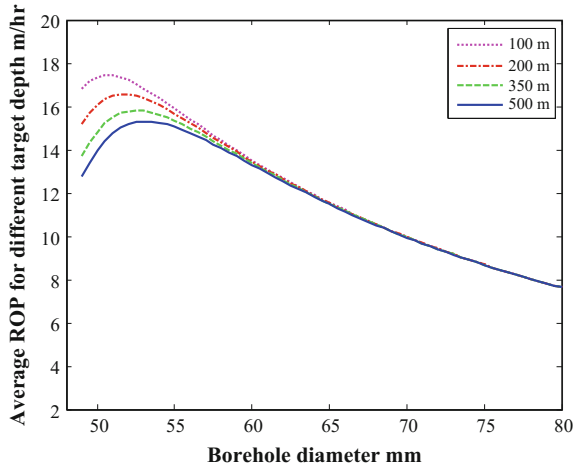
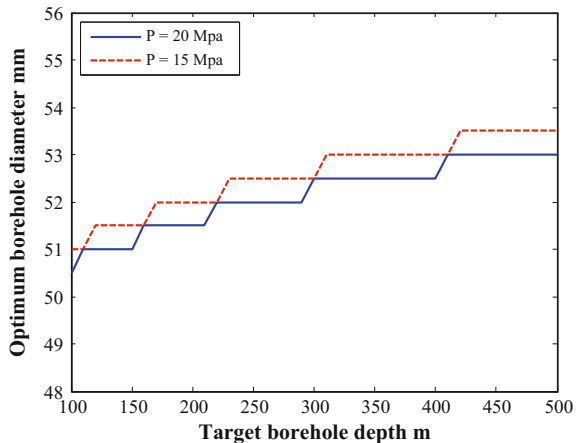


Figure 6 shows the average drilling ROP from surface through to different target depths. It indicates that for each target depth, there is an optimum borehole size that enables a maximum average ROP. For example, when the target depth is 500 m, the optimum borehole size is 53 mm which achieves a maximum average ROP of 15 m/h; when the target depth is 100 m, the optimum borehole size is 50.5 mm which achieves a maximum ROP of 17.5 m/h. The instant ROP and average ROP curves obtained for the 15 Mpa pump output pressure to start drilling are similar to the 20 Mpa pump pressure case except for a lower ROP and larger optimum borehole size. For example, when the target depth is 500 m, the optimum borehole size is 53.5 mm for achieving a maximum average ROP of 10.5 m/h.

Figure 7 compares the optimum borehole sizes for different target depths between 15 and 20 Mpa drilling pump pressure. It shows that the optimum borehole

**Fig. 7** Optimum borehole size for drilling to a different target depth under constant weight on bit and start drilling pump pressure 15 or 20 Mpa and flow rate 3.0 L/s



size will increase as the target depth increases, which is due to the need of reducing the frictional pressure loss; the optimum borehole size will also increase when pump pressure decreases, which is due to the fact that the pump pressure is becoming precious, and hence, there is a need to reduce frictional pressure loss.

## 4 Conclusion and Discussion

This paper has studied hydraulic power problem for coiled tubing drilling of hard rock formation. It has found that the borehole size is an important drilling parameter for optimizing the use of drilling fluid power for maximum ROP. A borehole size optimization method is derived, and a corresponding algorithm is proposed. An optimization example is presented. The optimization can be carried out under constant pump power output and constant weight on bit.

In the optimization example, the viscosities of drilling fluids inside the coiled tubing and annulus are assumed approximate values. This approximation does not in any way affect the validity of the optimization method. However, when applying the optimization algorithm for practical drilling, more accurate viscosity values should be used. These values can be obtained by the lab-on-rig test facility for drilling fluid property measurement in the drilling field.

**Acknowledgements** The author acknowledges the financial support from the Deep Exploration Technologies Cooperative Research Centre whose activities are funded by the Australian Government's Cooperative Research Centre Program. This paper presented some of the research work for DET CRC when the author was at Curtin University. Special thanks to Trevor Zwar of DET CRC for providing results' summary of the initial drilling test with downhole motor and full-face bit and to Peter Kanck of DET CRC for his comments during the writing up of this paper.

## References

1. DET CRC 2013. Efficient Solids Removal for Drilling Fluids—The Results Are Clear. DET CRC eNewsletter July. <http://detcrc.com.au/enewsletter/explore-July-2013/>.
2. Kamyab, M., Rasouli, V., Mandal, S. et al. 2013. Rheological Properties and Fluid Behaviour in Hard Rock Drilling. *Mining Technology*, 122 (4): pp. 185–192. <http://dx.doi.org/10.1179/1743286313Y.0000000047>.
3. Chien, S.F. 1994. Settling Velocity of Irregular Shaped Particles. *SPE Drilling & Completion*, 9 (4): pp. 281–289. SPE-26121-PA. <http://dx.doi.org/10.2118/26121-PA>.
4. Azar, J.J. and Samuel, G.R. 2007. *Drilling Engineering*. PennWell Corporation, Tulsa, Oklahoma, USA.
5. B. Guo and G. Liu 2011. *Applied Drilling Circulation Systems*. Gulf Professional Publishing, ISBN: 978-0-12-381957-4.

6. DET CRC 2013. E-S Diagram Balances Matrix/Diamond Wear in Real Time. DET CRC eNewsletter July.
7. DET CRC 2013. Full Face Drill Bit Trials Guide Next Generation Bit Design. DET CRC eNewsletter July. <http://detcrc.com.au/enewsletter/explore-July-2013/>.
8. RIO Technical Services 2004. Current Capabilities of Hydraulic Motors, Air/Nitrogen Motors and Electric Downhole Motors. Final Report. Department of Energy National Petroleum Technology Office, USA.

# Optimizing Well Structures and Trajectories for Maximizing Oil Recovery

Noorfadzreena Mahmud and Xianhua Liu

**Abstract** This project investigates the significant role of different well structures and trajectories to the oil recovery rate. The structure, trajectory and location of injector well to inject fluid into the reservoir are the vital aspects in order to have effective oil sweeping efficiency. While copious and diverse research papers have theoretically concluded that horizontal well offers significant commercial advantages to the oil recovery rate as compared to the conventional vertical well due to the greater drainage coverage, this project investigates the validity of the statement experimentally through Petrel E&P software for injection and production wells. Using conventional approach (theoretical) to locate optimal location and trajectory of injection well is a lengthy process as the outcome is dependent on the ability to understand reservoir behaviour and its operational limits. Thus, an alternative approach is proposed by utilizing Petrel E&P software to evaluate the change in the oil recovery rate with change in well trajectory. Specifically, the difference in the oil recovery rate is observed between vertical and horizontal wells with two types of wells (injection and production) placed in a grid, simulated in three different cases. First case (base case), both injection and production wells were placed vertically in the grid while in the sensitivity cases, the wells were placed horizontally. Several cases have been simulated in the model and the outcomes are significantly promising, and it is proven that the structure, trajectory and location of injector well have significant effects to the oil recovery rate.

**Keywords** Improved oil recovery · Well trajectories · Cumulative oil production

---

N. Mahmud (✉) · X. Liu  
Petroleum Engineering Department, Universiti Teknologi PETRONAS,  
Ipoh, Perak, Malaysia  
e-mail: noorfadzreena@gmail.com

X. Liu  
e-mail: xianhua.liu@utp.edu.my

# 1 Introduction

## 1.1 Background of Study

Oil recovery refers to the processes by which crude oil is extracted beneath the Earth's surface. It can be further categorized into three phases, namely primary, secondary and tertiary recovery method. Primary oil recovery uses natural pressure to push crude oil to the surface or by using artificial lift devices, such as pump jacks and gas lift devices. Secondary recovery employs pressurized water and gas injection, displacing the oil and driving it to the surface. The way to further the increase oil production is through the tertiary recovery method or EOR where different materials are being injected into the reservoir to improve the flow between oil, gas and rock. Used in fields that exhibit heavy oil, poor permeability and irregular fault lines, EOR entails changing the actual properties of the hydrocarbons, which further distinguishes this phase of recovery from the secondary recovery method.

Improved oil recovery (IOR) methods are known as the potential oil recovery methods with the objective of boosting the oil recovery rate using the injection of substances into the reservoir especially for depleted reservoir. There are many methods for improved oil recovery such as water injection, gas injection, thermal injection and chemical injection, and each poses different characteristics to make it a more desirable choice based on specific reservoir challenges and other parameters. The production potential for these IOR methods can take up to 40% of produced oil. Until present, gas injection process is the most commonly used approach in enhanced oil recovery. Through a miscible displacement process, reservoir pressure is maintained and oil displacement is improved due to the reduction in interfacial tension between oil and water.

However, the methods mentioned are only able to extract another 10–15% of the initially available hydrocarbons, leaving much left behind. Thus, another alternative of enhancing IOR production is proposed in this paper by altering the design of well architecture which is mainly composed of trajectory and completions functionality. This can be achieved by positioning the injection wells directionally, or vertically, depending on the reservoir characteristic in order to efficiently sweep off the residual oil in place thus, increasing reservoir performance.

## 1.2 Problem Statement

The current oil recovery techniques such as water, gas, thermal and chemical injection (IOR techniques) have been used in the industry for a long period, but the application and volume of oil recovered are limited due to the technical, operational and economic difficulties faced by the industry. The uses of injecting fluids in oil recovery techniques contribute to the higher drilling cost borne by oil companies,

but the reserves are yet to be recovered fully. In addition, IOR techniques require multiple injection wells to be drilled for the use of injecting fluids in the drilling process which leads to the increasing number of drilled wells and subsequently, increasing the cost. Hence, a new approach is introduced in this project which aims to maximize oil recovery by optimizing the well structures and trajectories.

### ***1.3 Objectives and Scopes of Studies***

This study aims to investigate the change in the oil recovery rate with the change in production and injection well trajectory (vertical and horizontal injection wells) using Petrel E&P software. The significance of the structure, trajectory and location of well to the oil sweeping efficiency will also be investigated. The scope of the study can be expressed as the following:

- (1) To generate reservoir model using Petrel E&P software.
- (2) To correlate different types of well trajectories with oil production rate.
- (3) To propose an optimal design of well trajectory by comparing between trajectories and recovery rate.

## **2 Literature Review**

Diversified research work related to oil recovery and well trajectory will be further discussed in this section. While some studies are focusing on the vast outcome of conventional improved oil recovery (IOR) methods, others have explored the effectiveness of well-planned trajectory in optimizing the oil recovery rate.

### ***2.1 Improved Oil Recovery***

The general mechanism of oil recovery is the movement of hydrocarbons to production wells due to a pressure difference between the reservoir and the production wells (Pwaga et al. 2010). Improved oil recovery deals with the measurement of how much oil production can be increased from a depleted reservoir that is unable to produce oil naturally. That is when IOR is introduced as the last phase of useful oil production above that obtained through the natural reservoir energy with the first production of oil begins by the expansion of volatile components pumping wells, thus stimulate early production by natural means. Generally, the production of oil will, after a period, decline as the reservoir energy depletes, and IOR phase will begin after supplemental energy is added by injection of water to assist the production. As the difference between the profit obtained through production of oil and

the cost for water treatment becomes too narrow, the tertiary or last phase of production takes place known as enhanced oil recovery (EOR) by using the advancements in technology and equipment that is different from conventional extraction means. EOR is also known as one of the IOR techniques.

According to Latil (1980) [3], water injection programme has been used in the industry for quite a long time, and it is the oldest assisted recovery method and remains the most. He added that almost 80% of the oil produced by recovery techniques in the USA in 1970 was produced by water injection. Water injection maintains the reservoir pressure when the expansion of gas cap is insufficient. Water injection can also be used to dispose brine produced along with oil if surface discharge is not possible. Water may be injected into underlying or neighbouring aquifer. However, the addition of alienated substances or surfactant through EOR methods can cause major damage to the reservoir and also increase drilling cost, but the total oil recovered is yet to be recovered fully. In other words, the current EOR techniques are still unable to efficiently sweep the residual hydrocarbons in the reservoir with only 60% of recovered oil from the total hydrocarbon in place.

## ***2.2 Well Structures and Trajectories***

Well trajectory also plays an important role in optimizing oil recovery. There are several types of well trajectory available in the industry such as horizontal trajectory, vertical trajectory and combination of the two. Horizontal trajectory allows access to previously unattainable bottom-hole target. It is applicable for thin oil zone with water and gas coning problems. Theoretically, by increasing the reservoir's contact area, the productivity from low permeability reservoir will be maximized. As stated by Bond et al. (2006) [1], horizontal wells are more preferred to develop oil and gas fields in many applications than conventional vertical wells. The significant difference in drainage patterns of horizontal wells when compared with vertical wells makes it critical that the formation has to have a certain minimum vertical permeability for a horizontal well to be productive (Bond et al. 2006). Bond statement is supported by Joshi (2006), in which he explained that horizontal wells generally provide better economics than conventional wells with 2–5 times greater production rate than vertical wells. Joshi also added that the cumulative oil and gas produced by a horizontal well is about 2–6 times more than that of a conventional vertical well. Drilling a horizontal well is intended to increase the well productivity (Al-Hadad, S.M. and Craton, J.W. 1991).

Nghiem et al. (1992) [4] have conducted a simulation about horizontal and deviated wells in naturally fractured reservoir and they have concluded that in naturally fractured reservoirs (also in high-permeability reservoirs), wellbore hydraulics in horizontal and deviated wells affect significantly the inflow along the wellbore. According to them, relative location of injection and production well is dependent relatively to the above factor. It is important to consider wellbore



hydraulics and relative injection/production locations in the design of horizontal and deviated wells.

Based on the literature review, it can be concluded that deviated (horizontal) wells are more preferred due to the higher oil recovery rate as compared to the conventional vertical wells. To further validate the statement, a simple reservoir model is built using Petrel E&P software with two different trajectories (vertical and horizontal) placed in the model to observe the difference in the oil recovery rate.

### 3 Methodology

The project was conducted by applying different designs of well trajectory, especially for deviated wells using Petrel E&P software in order to obtain a set of different production rates for different well trajectories. The injection pattern used in this study is based on 5-spot injection pattern (producer well is placed at the centre of the model).

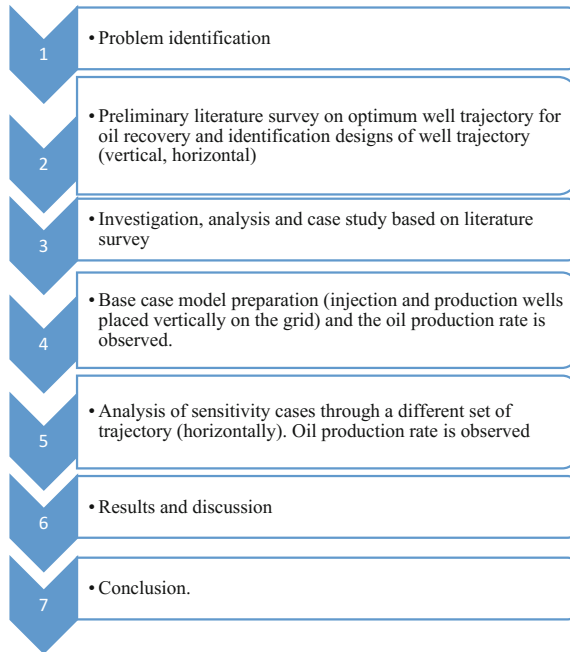
Reservoir characteristic selected for this study was homogenous, fairly high oil saturation (80%) due to no fault identified to hinder movement of oil in the project. A grid with dimension of 11 ft by 11 ft by 11 ft was built for reservoir modelling by using Petrel E&P software. This unit represents the behaviour of the basic production architecture where in actual operation the size of the block can be larger depending on the field length. Reservoir properties such as porosity, permeability and net to gross were inserted in the model, depicting real reservoir conditions in a dynamic model form. The same grid configuration was used in all simulation cases to avoid grid orientation effect.

In the early simulation stage, it was recognized that in the model, only a small percentage of the original oil in place (OOIP) was recovered during the production of primary phase due to the depletion of the reservoirs' natural energy. Additional recovery methods were then needed to produce the large quantity of the remaining oil. The execution of the project is based on the process flow as shown in: Chart 1

### 4 Results and Discussions

The three cases were simulated, and the cumulative oil production rate for each case was observed. The simulation results below show that base case (both injector and producer wells were built vertically) produced a cumulative oil production of 4841 MSTB, sensitivity case I with 5460 MSTB and sensitivity case II with 6865 MSTB of produced oil. Table 1 shows the trajectory settings for both producer and injector wells in the three cases (Table 2).

The reservoir oil initially in place (STOIP) is calculated to be 11,857 MSTB. By natural means, the recovery factor of oil production can only achieve as high as



**Chart 1** Research methodology flow chart

**Table 1** Trajectory settings for production and injection wells

Case name	Well inclination angle	
	Production wells' inclination angle (°)	Injection well's inclination angle (°)
Base case	0° (Vertical)	0° (Vertical)
Case 1	90° (Horizontal)	0° (Vertical)
Case 2	90° (Horizontal)	90° (Horizontal)

**Table 2** Simulation Results

Case name	Cum oil production rate (MSTB)	Recovery factor (%)
Base case	4841	40.8
Case 1	5460	46.1
Case 2	6865	57.9

10% of the STOIP volume. Thus, in order to boost oil production, water flooding programme was introduced in the reservoir and the recovery factor is increasing (as expected) to 40.8% with base case and 46.1 and 57.9% with the sensitivity cases. It is observed that the recovery factor of sensitivity cases is higher than the amount of oil recovered by base case. In sensitivity case I, a 5.3% increase, and in case II 17.1% increase in recovery factor were observed (Fig. 1).

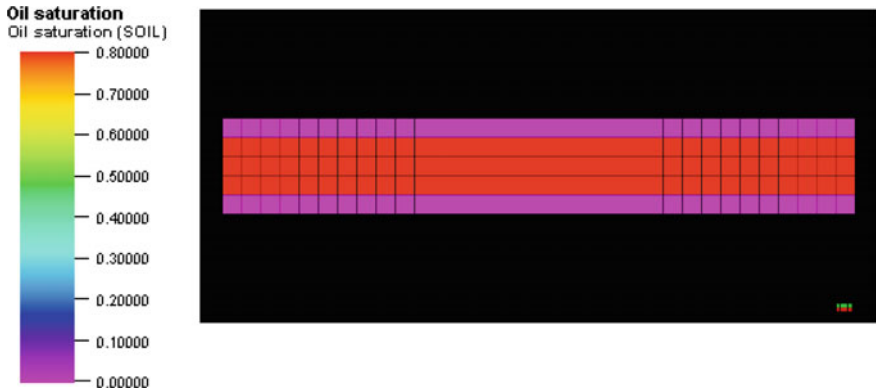


Fig. 1 Initial oil saturation for all cases

Table 3 Final oil saturation

Case name	Oil saturation (at oil layer)
Base Case	0.15–0.65
Sensitivity Case I	0.15–0.65
Sensitivity Case II	0.15–0.30

At the initial phase of the three cases, oil saturation is set to 0.8 uniformly throughout oil layer.

Water flooding programme was then applied to the cases, and the final oil saturation at oil layer obtained in the three cases is shown in Table 3.

The grid is viewed from the top; yellow indicates high saturation of oil while blue indicates low saturation. Figure 2 shows the final oil saturation for both cases, and it can be seen that much lower, uniform final oil saturation is observed in horizontal

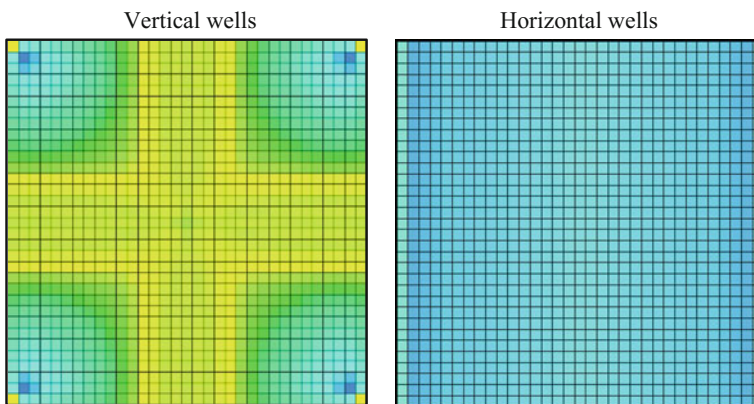
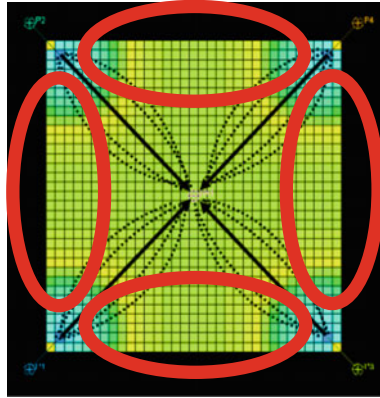
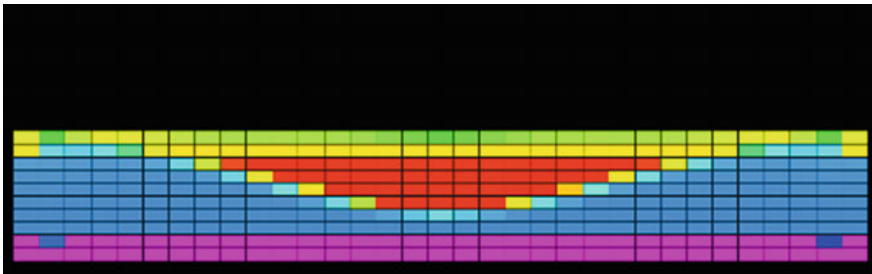


Fig. 2 Final oil saturation for vertical and horizontal well simulation cases (top view)



**Fig. 3** Water flow pattern in vertical well (Dead zones are circled in red)



**Fig. 4** Dead zone (Red indicates high saturation of oil—low sweeping efficiency of oil)

wells simulation case as compared to vertical wells. Low final oil saturation also indicates high sweeping oil efficiency (high initial saturation to low final saturation) Sensitivity Case II (Figs. 3, 4, 5 and 6). Figures 7 and 8 show the field cumulative oil production and field oil in place, respectively, for the three cases.

The possible reason of the observed discrepancy may be the influence of water flood front pattern, where in the vertical wells water tends to move through the shortest path between producer and injector, and while in the horizontal well, water moves in a more parallel and laminar flow resulting in a much more complete areal of displacement. Higgins and Leightons [2] have introduced a technique to analyse waterflood using what has been termed as streamtubes, or stream channels, and using the concept of streamlines.

Streamlines are the paths that fluid particles follow when they move from the injector to the producer. When water is injected into the oil zone through the water injection wells, an edge water drive will push oil towards the production well. Occasionally, a wider channel between the injector and producer wells will begin to develop at the shortest path between the two wells. Leaving the much longer path to be a slow- or dead-flow region resulting to a lesser amount of oil to be recovered.

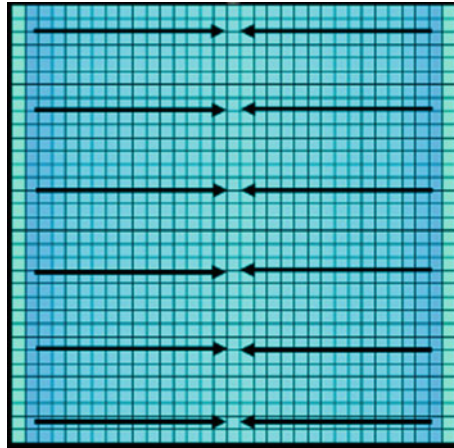


Fig. 5 Water flow pattern in horizontal well

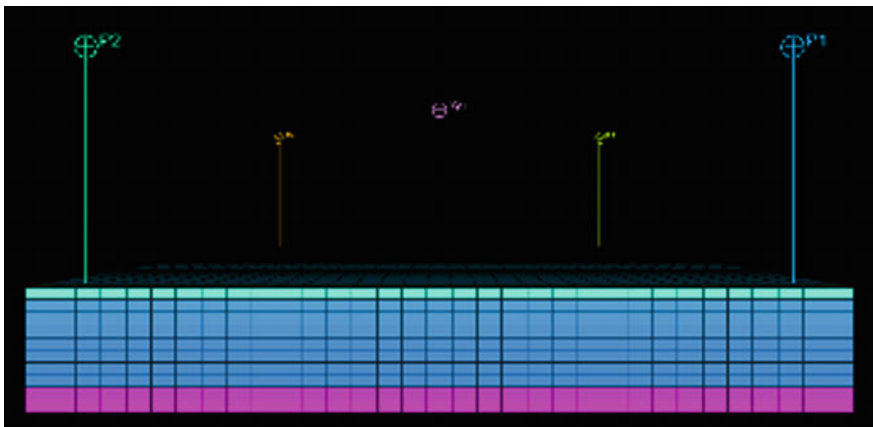


Fig. 6 Uniform displacement in horizontal well

Thus, by maximizing the horizontal and vertical contact areas, dead zones will be reduced, areal of displacement will increase and subsequently oil production will be maximized.

In base case where the wells were built vertically, water tends to flow through the shortest path between the injector and producer wells (arrow and dotted lines). The red circles indicate the dead-flow region, where the flow of water is minimum throughout the region, thus leading to low oil sweeping efficiency.

Horizontal wells were used in the sensitivity cases, providing a much larger extensive reach area and more vertical intersections in a single wellbore. Water tends to flow in a laminar, parallel and wider pattern from injector to producer wells

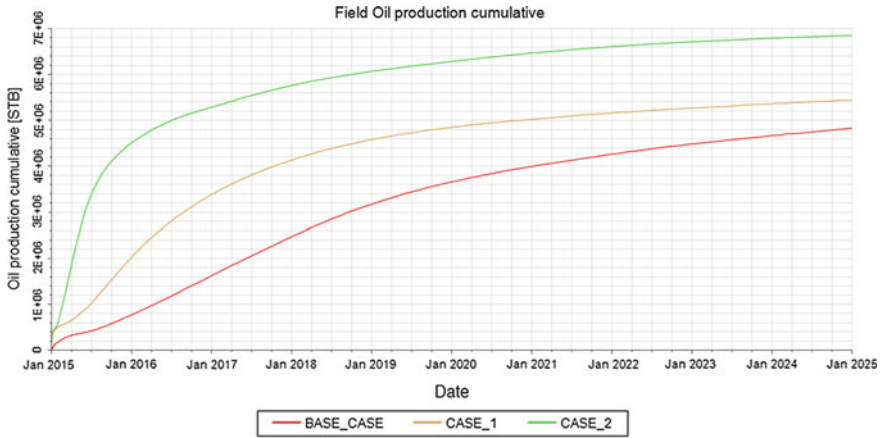


Fig. 7 Field cumulative oil production

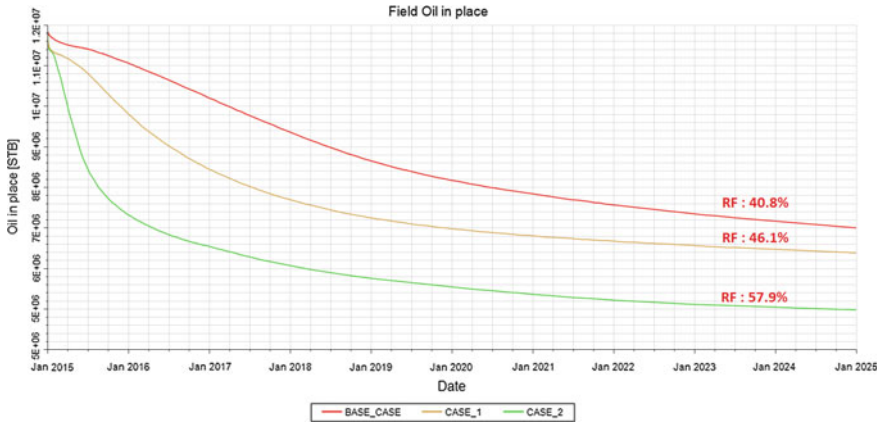


Fig. 8 Field oil in place

due to the consistent distance between the two wells (no shorter path). This results in the reduction of dead-flow regions, thus increasing the oil production since oil is being swept uniformly.

## 5 Conclusion

In this study, a novel injection and production architecture is proposed to enhance water injection process where vertical and horizontal wells are used for injector well. Larger drainage area is created by extending the perforation interval

horizontally, thus allowing more water to be injected into the reservoir and subsequently improve the oil recovery. Extensive simulation studies were done to select an optimum well structure strategy and understand the effect of trajectory to the reserves production. Two graphs have been plotted in order to illustrate the relationship between trajectory and oil production. The most productive case is sensitivity case II that has both producer and injector wells drilled horizontally and achieves 58% in recovery factor, a 17.1% increase as compared to the base case of achieving recovery factor of 41%. This production difference can be explained by easier and increased water injection and production in horizontal wells and most importantly thorough sweeping; that is, no dead-flow regions left in the reservoir. The net recovery factor and cumulative water injected suggest that horizontal well trajectory should be the optimum design of trajectory. In a nutshell, the objectives of the study have met, where different cases using different trajectories have been simulated to foresee the impact on the oil recovery rate. The hypothesis is proven to be true that well trajectory do play a significant role in recovering the oil, and the higher the sweeping efficiency is, the greater the reservoir performance will be.

**Acknowledgements** The authors acknowledge the support from Universiti Teknologi PETRONAS and Petroleum Engineering Department for providing the facilities and software for this research to be carried out smoothly. The authors also acknowledge with profound gratitude and reverence the help and guidance of one and all in completing this project.

## References

1. Bond., A. Zhu, D., and Kamkon, R. (2006). "The Effect of Well Trajectory on Horizontal Well Performance," in SPE International Oil and Gas Conference and Exhibition 2006, China.
2. Higgins, R.V. and Leighton, A.J. 1974. Matching Calculated With Actual Waterflood Performance by Estimating Some Reservoir Properties. *J Pet Technol* 26 (5): 501–506. SPE-4412-PA.
3. Joshi, S.D.: "Production Forecasting Methods for Horizontal Well: Appendices A and B", paper SPE 17580, Presented at the SPE International Meeting on Petroleum Engineering, held in Tianjin, China, November 1–4, 1988.
4. Manrique, E., Thomas, C., Ravikiran, R., Izadi, M., Lantz, M., Romero, J., and Alvarado, V. (2010) "EOR: Current Status and Opportunities" in SPE Improved Oil Recovery Symposium 2010, Tulsa, Oklahoma, pp. 1–21.

# Anionic Surfactant for Enhancing the Performance of Water-Based Mud

Putri Yunita, Sonny Irawan, Dina Kania and Deni Subara

**Abstract** Drilling fluid that has better rheological properties and fluid loss controls is required for optimum performance of oil well drilling. In this paper, an anionic surfactant was mixed to the formulated water-based mud (WBM) as an additive to improve the rheological properties of WBM. The rheological tests were conducted after the mud being hot-rolled for 16 h at 250 and 275 °F. The filtration tests were carried out at temperature up to 300 °F. It was found that WBM containing anionic surfactant improved the stability of the mud at high temperature and reduced up to 46% of fluid loss.

**Keywords** Anionic surfactant · Water-based mud · Drilling fluid · Rheology

## 1 Introduction

Drilling fluid or mud is one of the important components in the oil well drilling process. Selection of drilling fluid depends on formation oil field [1–4]. The functions of drilling fluid are to carry cutting toward the surface, cooling the bit, and to control formation pressure [1]. Drilling fluid was classified into two based on system: water-based mud (WBM) and oil-based mud (OBM). The performance of

---

P. Yunita (✉) · S. Irawan  
Petroleum Engineering Department, Universiti Teknologi PETRONAS,  
32610 Seri Iskandar, Darul Ridzuan, Perak, Malaysia  
e-mail: putriyunita89@gmail.com

D. Kania  
Chemical and Environmental Engineering Department, Universiti Putra Malaysia,  
43400 Serdang, Selangor, Malaysia

D. Subara  
Biotechnology Engineering Department, International Islamic University Malaysia,  
53100 Kuala Lumpur, Selangor, Malaysia



OBM is better than WBM. OBM provides excellent wellbore stability, lubricity, and temperature resistant at difficult well condition but non-environmental friendly [3–6]. In other hand, WBM is commonly used in drilling operation due to its cheaper and non-toxic characteristics. However, their rheological properties' stability at high temperature is generally poor [3, 4]. Therefore, it is necessary to find an additive to improve the performance of WBM.

From the previous studies, several researchers had reported that surfactant might improve the rheology, reduce the fluid loss, risk of water blockage, oil/water emulsifier, and could be used as lubricant [7–10]. In this study, we propose to use anionic surfactant as an additive to optimize the WBM performance. The mud property measurements include plastic viscosity, yield point, gel strength, and filtration loss up to 300 °F temperature condition.

## **2 Materials and Methods**

### **2.1 *Water-Based Mud (WBM)***

WBM used in this study consisted of water and various mud additives. Mud formulation was comprised basically of the following ingredients: water-based fluid, organophilic clay bentonite, and barite as weight agents. The ingredients of mud were mixed using the Hamilton Beach Model 3 mixer at 45 min.

### **2.2 *Surfactant***

Surfactant is a compound that could reduce interfacial tension or surface tension between two liquid or between solid and liquid. This study used anionic surfactant alkyl benzene sulfonate. Surfactant had a good result from enhanced oil recovery (EOR) process.

### **2.3 *Rheological Test***

Rheological properties' test of mud was measured based on API (American Petroleum Institute) standard procedure [11]. Plastic viscosity (PV), yield point (YP), and gel strength (GS) of mud are measured by FANN VG viscometer.

## 2.4 Filtration Test

Filtration test measured the filtration loss volume of mud using filtration press at 30 min. API filtration test was conducted at ambient temperature under 100 psi condition. HPHT (high pressure, high temperature) test was conducted at temperature 300 °F and 500 psi.

## 3 Result and Discussion

The rheological properties of the mud were controlled to provide their optimum performance. The important properties to control are viscosity and gel strength. They are related to release cuttings at the surface, holding cutting when not circulated and removal of cuttings [12]. The results of the rheological properties of the mud in the presence of surfactant are given in Table 1.

Rheological properties of mud contained surfactant had high stability compared to the mud without surfactant. In this experiment, plastic viscosity (PV) of mud changed from 33 to 36 and muds are more viscous when added the surfactant. A long chain of surfactant possibly makes the mud more viscous compared to a short chain when added in same concentration [13]. After hot-rolled (AHR) at 250 275 °F, PV of M1 (mud without surfactant) changed from 33 cP to 21 cP and 16 cP, PV of M2 (mud with surfactant) changed from 36 cP to 26 cP and 19 cP (Fig. 1). PV decreased when temperatures increased [14].

Yield point (YP) reflects the resistance to initial flow or the stress required to initiate fluid movement [15]. YP of M1 increased from 37 lb/100 ft<sup>2</sup> to 44 lb/100 ft<sup>2</sup> when surfactant added to mud. Moreover, the YP of M1 decreased from 37 lb/100 ft<sup>2</sup> to 1 lb/100 ft<sup>2</sup> after aging at temperature 275 °F for 16 h. M2 appeared to have more improved YP at high temperature, and YP of M2 decreased

**Table 1** Rheological properties of muds

Properties	M1			M2		
	BHR	AHR 250 °F	AHR 275 °F	BHR	AHR 250 °F	AHR 275 °F
PV	33	21	16	36	26	19
YP	37	11	1	44	23	9
GS 10 s	12	7	7	12	7	9
GS 10 min	34	29	23	34	28	29
Filtration loss	5	26	85	3.8	10	46

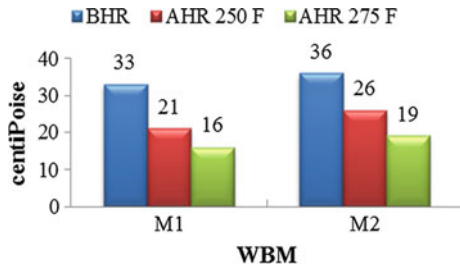
*M1* mud without surfactant

*M2* mud with surfactant

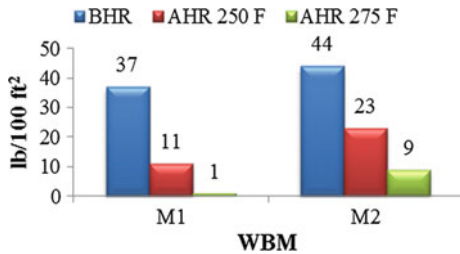
*BHR* before hot-rolled

*AHR* after hot-rolled

**Fig. 1** Plastic viscosity of WBM with and without surfactant



**Fig. 2** Yield point of WBM with and without surfactant

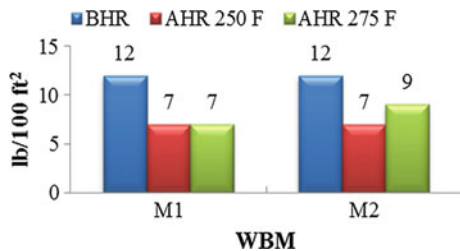


from 44 lb/100 ft<sup>2</sup> to 9 lb/100 ft<sup>2</sup> (Fig. 2). Surfactant showed improvement in WBM compared with WBM without surfactant. YP decreased after aging condition [16]. The strength bonding between particles is weakening when temperature increases, and this effect is explained the decreased in the yield point [13].

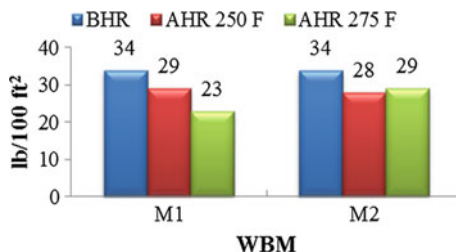
Gel strength (GS) depends on concentration colloidal clay in mud. The surfactant used in his study caused water-based mud to be more viscous without affecting the value of GS that is shown in Table 1. The GS of mud formulation M1 and M2 after aging was reduced. Gel strength decreases when temperature increases [17]. 10s GS of M1 decreased from 12 lb/100 ft<sup>2</sup> to 7 lb/100 ft<sup>2</sup> after aging at 275 °F and GS of M2 decreased from 12 lb/100 ft<sup>2</sup> to 9 lb/100 ft<sup>2</sup> (Fig. 3).

10 min GS of M1 decreased from 34 lb/100 ft<sup>2</sup> to 29 lb/100 ft<sup>2</sup> AHR 250 °F and 23 lb/100 ft<sup>2</sup> AHR 275 °F. GS of M2 decreased from 34 lb/100 ft<sup>2</sup> to 28 lb/100 ft<sup>2</sup> AHR 250 °F and 29 lb/100 ft<sup>2</sup> AHR 275 °F (Fig. 4). High value of GS 10 s and 10 min is not desirable; the meaning of high value has becoming hard to break the gel [18].

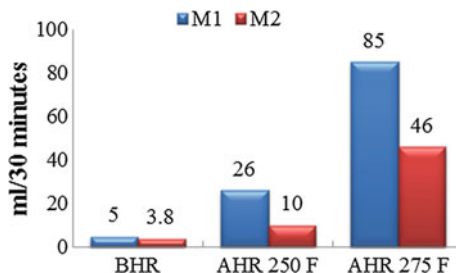
**Fig. 3** 10 s gel strength of WBM with and without surfactant



**Fig. 4** 10 min gel strength of WBM with and without surfactant



**Fig. 5** Filtration test of WBM with and without surfactant



The fluid loss of water-based mud was reduced in the presence of surfactant additive. Molecules of surfactant were suspected to block the pore of mud cake; hence, lower filtrate is collected. Therefore, in API test, mud with surfactant reduces filtration loss from 5 to 3.8 ml. In HPHT test, surfactant additive reduces filtration loss from 26 to 10 ml and 85 to 46 ml as shown in Fig. 5.

## 4 Conclusion

The rheology of water-based mud mixed after aging for 16 h at 275 °F was improved in addition to anionic surfactant. It was also found that anionic surfactant additive reduced the fluid loss up to 46% by blocking the permeable pore of filter paper.

**Acknowledgements** The authors would like to thank Universiti Teknologi PETRONAS (UTP) for providing the laboratory facilities to perform the experiment.

## References

1. H. C. H. Darley and G. R. Gray, "Introduction to Drilling Fluids," *Compos. Prop. Drill. Complet. Fluids*, pp. 1–37, 1988.
2. J. M. Neff, "Biological effects of drilling fluid, drill cuttings and produced water," *Long-term Environ. Eff. offshore oil gas Dev.*, pp. 469–538, 1987.

3. M. Khodja, J. P. Canselier, F. Bergaya, K. Fourar, M. Khodja, N. Cohaut, and A. Benmounah, "Shale problems and water-based drilling fluid optimisation in the Hassi Messaoud Algerian oil field," *Appl. Clay Sci.*, vol. 49, no. 4, pp. 383–393, Aug. 2010.
4. A. Audibert, L. Rousseau, I. Français, J. Kieffer, and S. N. F. Floerger, "Novel High-Pressure/High Temperature Fluid Loss Reducer for Water-Based Formulation," *Soc. Pet. Eng.*, vol. SPE 50724, 1999.
5. M. Amanullah, "Physio-Chemical Characterisation of Vegetable Oils and Preliminary Test Results of Vegetable Oil-based Muds," in *SPE/IADC Middle East Drilling Technology Conference & Exhibition*, 2005.
6. B. Demirdal, U. Alberta, S. Miska, N. Takach, U. Tulsa, and J. C. Cunha, "Drilling Fluids Rheological and Volumetric Characterization Under Downhole Conditions," *Soc. Pet. Eng.*, vol. SPE 108111, 2007.
7. T. Huang, J. B. Crews, D. E. Clark, and B. Hughes, "Protecting the Reservoir With Surfactant Micellar Drill-In Fluids in Carbonate-Containing Formations," *SPE Annu. Tech. Conf. Exhib.*, vol. 26, pp. 492–498, 2011.
8. L. F. Nicora, W. and M. McGregor, "Biodegradable Sutfactants for Cosmetics Find Application in Drilling Fluids," *IADC/SPE Drill. Conf.*, pp. 723–730, 1998.
9. A. Audibert-Hayet and C. Dalmazzone, "Surfactant system for water-based well fluids," *Colloids Surfaces A Physicochem. Eng. Asp.*, vol. 288, no. 1–3, pp. 113–120, Oct. 2006.
10. J. M. González, F. Quintero, J. E. Arellano, R. L. Márquez, C. Sánchez, and D. Pernía, "Effects of interactions between solids and surfactants on the tribological properties of water-based drilling fluids," *Colloids Surfaces A Physicochem. Eng. Asp.*, vol. 391, pp. 216–223, Nov. 2011.
11. API, "Recommended Practice for Field Testing Water-based Drilling Fluids API Recommended Practice 13B-1 Petroleum and natural gas industries, Field testing of drilling fluids, Part I, Water based fluids," 2003.
12. N. A. Negm, S. M. Tawfik, M. I. Abdou, E. A. Badr, and F. M. Ghuiba, "Evaluation of Some Nonionic Surfactants Derived from Tannic Acid as Additives for Water-Based Mud," *J. Surfactants Deterg.*, Aug. 2014.
13. M. M. A. El-Sukkary, F. M. Ghuiba, G. H. Sayed, M. I. Abdou, E. A. Badr, S. M. Tawfik, and N. A. Negm, "Evaluation of some vanillin-modified polyoxyethylene surfactants as additives for water based mud," *Egypt. J. Pet.*, vol. 23, no. 1, pp. 7–14, Mar. 2014.
14. S. Mahmoud and M. Dardir, "Synthesis and evaluation of a new cationic surfactant for oil-well drilling fluid," *J. Surfactants Deterg.*, vol. 14, pp. 123–130, 2011.
15. X. Meng, Y. Zhang, F. Zhou, and P. K. Chu, "Effects of carbon ash on rheological properties of water-based drilling fluids," *J. Pet. Sci. Eng.*, vol. 100, pp. 1–8, 2012.
16. F. Wang, X. Tan, R. Wang, M. Sun, L. Wang, and J. Liu, "High temperature and high pressure rheological properties of high-density water-based drilling fluids for deep wells," *Pet. Sci.*, vol. 9, no. 3, pp. 354–362, 2012.
17. F. Growcock and T. Harvey, "Drilling fluids," in *Drilling Fluids Processing Handbook*, Elsevier Inc, 2005, pp. 15–68.
18. R. Caenn, H. C. H. Darley, and G. R. Gray, "The Rheology of Drilling Fluids," *Compos. Prop. Drill. Complet. Fluids (Sixth Ed.)*, pp. 179–269, 2011.

# Hydrocarbon Fire and Explosion's Safety Aspects to Avoid Accident Escalation for Offshore Platform

Muhammad Imran, M.S. Liew, Mohammad Shakir Nasif,  
Usama Muhammad Niazi and Airil Yasreen

**Abstract** Offshore platforms are never 100% secure from fire hazard despite of using advanced technology. Hydrocarbon fire and explosion accidents are among commonly reported incidents in the oil and gas process-related activities. In April, 2015, PEMEX-operated oil platform caught fire—45 injured and four died. Accidents such as Piper Alpha have recorded greatest loss of human live on offshore platform in history. A total of 167 persons perished victim of the tragedy confluence of design flows, human error, and bad luck. Saving lives and property in such disaster is extremely a challenging job for engineers. Hydrocarbon fire and explosion produce extreme pressure and temperature, which cause fatalities and structural damages at large scale within a fraction of time. The experimental studies are restricted due to limited facilities available for fire and explosion testing for offshore structure. In previous studies, individual structure member was tested, which cannot represent the behaviour of the entire structure. Therefore, structural safety is always being a main issue to prevent property damage or least-obtained safe evacuation before structural collapse. To understanding the behaviour of structural modelling

---

M. Imran (✉)

Civil Engineering and Environmental Engineering,  
Universiti Teknologi PETRONAS, Seri Iskandar, Perak, Malaysia  
e-mail: engrimran\_ce@hotmail.com

M.S. Liew

Civil Engineering and Environmental Engineering Universiti  
Teknologi PETRONAS, 32610 Seri Iskandar, Perak, Malaysia  
e-mail: shahir\_liew@petronas.com.my

M.S. Nasif · U.M. Niazi

Department of Mechanical Engineering, Universiti Teknologi PETRONAS,  
Seri Iskandar, Perak, Malaysia  
e-mail: mohammad.nasif@petronas.com.my

U.M. Niazi

e-mail: ukniaxi@gmail.com

A. Yasreen

Department of Civil Engineering, Universiti Teknologi PETRONAS,  
Seri Iskandar, Perak, Malaysia  
e-mail: airil.yasreen@petronas.com.my

techniques allow to study the possible behaviour of the platform. These techniques entirely depend on personal experience and modelling practice adopted in oil and gas sector. Therefore, simulation should be verified by a full-scale experimental study on combined structural members. The standard experimental studies should be conducted and data should be easily available after testing for validation for future simulation and to overcome lack of data issues.

**Keywords** Disaster · Explosion · Fire · Human · Hydrocarbon · Offshore · Safety · Structure

## 1 Introduction

Malaysian economy imparts 30% in oil and gas operations. These operations are extremely hazardous due to the presence of highly flammable hydrocarbon fuel [1–4]. Hydrocarbon fuels in funnels are the worst-case scenarios for any offshore facilities which caused massive engineering disasters such as Piper Alpha and Deep Water Horizon. The major hazard among all process-related hazards happened throughout the offshore operation is hydrocarbon fire followed by an explosion or vice versa [5]. The temperature of the fire can exceed more than 1000 °C less than 10 min [6]. Similarly, pressures of explosion released in microseconds, which is extremely challenging to secure structure in time [5]. Lessons learnt from past accidents are not sufficient to predict the safety of structure under such hazardous conditions due to limited experimental data [7, 8]. The Piper Alpha is one of significant disasters in human and oil and gas industry—as happened during Piper Alpha in which 20,000 ton rig vanished just in 1 h 30 min after the chain of events leaving only flare tower and causing 167 precious lives. Indeed, the safety perspectives will be entirely changed because of this accident. Then another devastating incident occurred which shook the entire oil and gas industry that was Deepwater Horizon 2010. It caused a massive oil spill in the Gulf of Mexico, which affected entire marine life almost 5 million barrel oil was spilled in Gulf of Mexico [9, 10]. These types of incidence are not only a loss of property, but also precious lives and company reputation. In case of deepwater horizon only cleaning operation was more than 20 billion USD [11, 12]. Hazard assessment studies such as qualitative or quantitative risk assessment (QRA) [13, 14], fault tree analysis [8], and event tree analysis [15] can predict potential hazard related to process, but it cannot predict the behaviour of structure under extreme fire and explosion condition. Due to limited data from the past event and experiment, it is difficult to predict structural behaviour.

Some platforms are found to be well organised or safety measures are strong that they can evacuate platform safely during accident without any loss of life. For example on 16 February 2007 from Rough 47/3-B platform, during accident all crew were safely evacuated. But unfortunately these examples are extremely rare in oil and gas sector. An example is Ocean Ranger, on 15 February 1982 none of the

crew survived when emergency evacuation took place in harsh weather condition. Rescue operation was not performed during such harsh condition. Proper planning and risk assessment safe evacuation strategy while structure in intact could be an ideal condition [16]. Therefore, ensuring safe operation and human safety HSE audit is becoming compulsory for every oil and gas process unit yearly to control these deadly accidents.

These accidents are still not controlled. Recently in April 2015 another offshore platform caught fire in Gulf of Mexico which took 4 workers lives [18, 19]. The purpose of this review was to highlight the need for future studies by reviewing previous studies on the issues causing major fatalities and structural damage due to hydrocarbon fire and explosion, and understand the behaviour of structure under extreme conditions.

## 2 Offshore Accidents and Damages

Major blast and fire incidents in the offshore industry are caused by human error [20]. The biggest incident which shocked offshore industry was occurred on July 1988 in North Sea. Piper Alpha was extremely productive platform and a largest living facility for more than 200 workers in North Sea. It can produce up to 360,000 barrels oil per day [21, 22]. After first blast and a series of incidents, within 40 min the platform was completely vanished, leaving only the flare tower. The main reason was a minor human error in routine maintenance, which caused a loss of 167 lives out of 228 workers on board. It is known as 'World Deadliest Offshore Industry Disaster'. The accident highlighted various safety issues such as maintenance documentations, poor planning and communication, and failure of safety provisions.

Despite of lesson learnt from past accidents on April 2010 the biggest accident in US history has occurred in Gulf of Mexico on BP's oil rig Deepwater Horizon. The accident occurred on the next day of maintaining its 7 years of safety record. Rig completely sunk within 36 h of continuous burning in Gulf of Mexico. This incident caused 27 billion USD property and 11 precious lives. The blowout resulted massive oil spill in Gulf of Mexico over several months, which entirely disturbed ecosystem of sea [7]. BP has to pay a billion dollars of federal fines to compensate losses. Almost identical sequences Montara well to blow out in Australia just 8 months earlier than Deepwater Horizon [15].

Accidents can be due to sudden blowout of the platform may be due to ship collision, human error, helicopter crash, or natural disaster such as rough weather. It may cause sudden release of hydrocarbon gasses/fuel. These uncontrolled incidents are always threat for billion dollar property, precious human lives, and company reputations for investors [21]. These accidents also cause large-scale environmental damages. Similarly, Montara incident in Australia caused continuous oil spill to 74 days, expected 30,000 barrels oil [23]. Deepwater Horizon on the other hand caused almost 5 million barrels oil spill in Gulf of Mexico [6] which affect marine



life. Therefore, it is important to identify expected risks for hydrocarbon blast and explosion to minimise live losses, environmental pollution, and property damages. There are various techniques used to assess hazard related to fire and explosion. The details will be discussed in the next section.

### 3 Process-Related Hazards

Hydrocarbon fuel is processed through main separator after being extracted from the reservoir. The crude oil is mixed with oil and gases separated through a sequence of subprocess [7]. The process diagram for oil and gas is described in Fig. 1. It is essential to understand the potential sources of fire and explosion on offshore platform. These sources require special attention to mitigate hazard. A study was conducted by Khan et al. in 2002 to identify process-related hazard [14].

A study was conducted by Khan and Husain in 2002 on risk-based safety assessment to measure the potential hazard related to processing facilities. The hazard was reduced to an acceptable level for offshore facilities using risk-based safety management. The risk for process activities was measured using feedback from detailed qualitative analysis. Different methods and process for predicting potential risk were presented such as event tree analysis (ETA) and fault tree analysis (FTA) [24, 25].

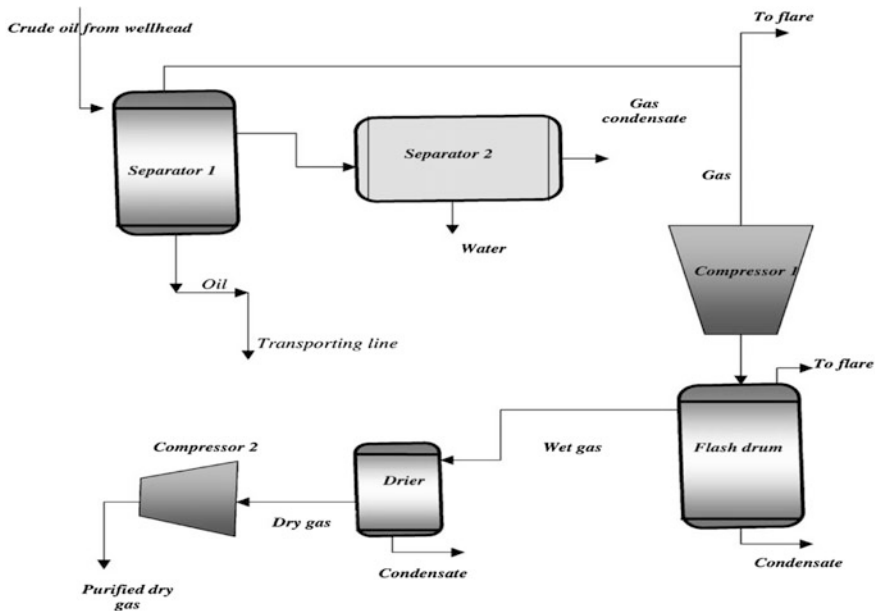


Fig. 1 Hydrocarbon fuel separation unit and process diagram [14]

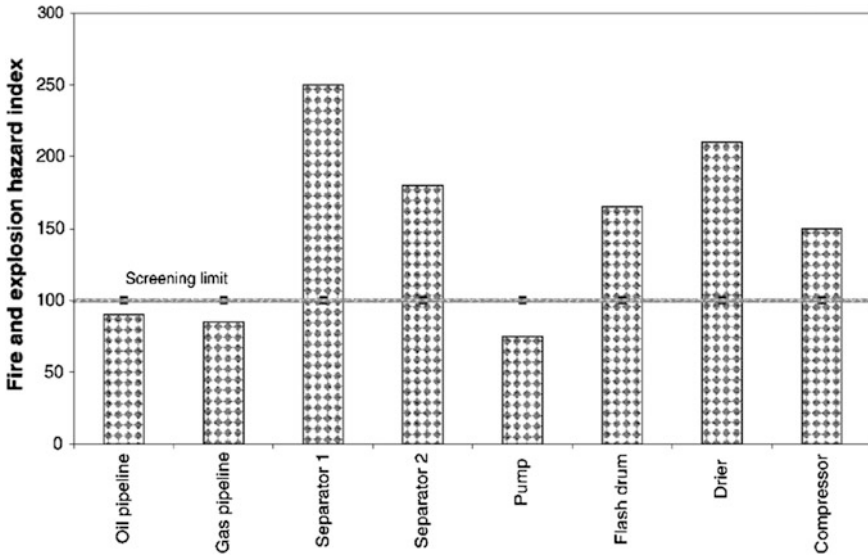


Fig. 2 Hazard Identification Index [14]

The study revealed the severity of each processing unit possessing highest hazard such as separators, compressors, drier, and flash drum. On the other hand, high-pressure oil and gas pipelines were under moderate hazard as shown in Fig. 2. The values of FAR exceed the ALARP acceptance range. These processing units required detailed analysis and safety precaution in order to reduce values to an acceptable range [14]. Compressor 1 has been always in high risk of fire and explosion due to the highest frequency of leakage—critical operation [26]. But it does not mean to avoid other processing units. The risk assessment tools can be used such as quantitative risk assessment (QRA) to assess risk and mitigate as low as reasonable practice without increasing cost of mitigation.

## 4 Hydrocarbon Fire

The temperature of hydrocarbon can be raised unexpectedly high compared to normal or cellulosic fire [27]. How long structure can sustain during the hydrocarbon fire and explosion for safe evacuation. Steel is most commonly used in offshore structure. Steel lose its mechanical property when exposed to 400 °C. The strength significantly reduces as temperature exceeds 600 °C [28]. The temperature of hydrocarbon fire can exceed more than 1000 °C less than 10 min. This extreme temperature is hazardous to human and causes major damage to structure.

This temperature can immediately cause fatality as temperature increases. The drastic change in temperature causes worst effects on structure as well. The strength

of steel structure can significantly reduce between the ranges of 400–600 °C but when the structure is loaded it immediately lose stability. The steel under elevated temperature causes joints to weak under fire. Impact loading would cause serious effects depending upon the type of loading, but the effect is not significant [29]. They involve an extreme explosion and heat flux, which have hazardous consequences for safety, health, and the surrounding environment [24]. The effect on the human body can get third-degree burns when exposed to 72 °C. The temperature of hydrocarbon fire can cause 100% fatalities in a few minutes. Simulation steel uses finite element (FEM) to overcome limitations of the study [30]. Hydrocarbon explosions and fires are extremely hazardous for offshore installations.

## 5 Hydrocarbon Explosion

The explosion effects are devastating in any oil and gas processing unit. Hydrocarbon fuel explosion can cause extreme pressure instantaneously depending upon the type of leak source. Usually at 10 psi overpressure can cause fatality and structural damage. The human body can survive relatively high blast overpressure without experiencing barotrauma. A 5 psi blast overpressure will rupture eardrums in about 1% of subjects, and a 45 psi overpressure will cause eardrum rupture in about 99% of all subjects. The threshold for lung damage occurs at about 15 psi blast overpressure. A 35–45 psi overpressure may cause 1% fatalities, and 55–65 psi overpressure may cause 99% fatalities [31]. During Piper Alpha, series of explosion and fire caused 20,000 ton steel rig to collapse in an hour and 30 min [21, 22]. Major fatality occurred when living quarters felt down into the North Sea due to instability of structure. Of the total 167 worker killed, 83 workers were in living quarter waiting for rescue operation [6]. Careful considerations should be taken in designing of the structure, equipment layout or arrangement of the facilities to minimise the effects of mishaps or structure instability [32]. Hydrocarbon fuel can cause evolvable massive explosion over pressure and heat flux, which have harmful consequences for structural safety, health, and the surrounding environment [24].

Despite of deep understanding, accidents are still uncontrolled. Individual experimental studies on the structural member cannot represent the behaviour of the entire platform by such studies. The effects could be more severe when member combined loaded member. Testing full-scale offshore platform is not only costly, but also nearly impossible [6]. The only process by which behaviour of entire structure can be observed is through simulation. Only protection arrangement (Active and Passive Fire Protection) is not sufficient to secure structure integrity. The area of risk fire intensity and loading condition played significant role in structural integrity.

## 6 Conclusion

Following are the conclusions drawn based on the current review:

1. Accidents such as Piper Alpha and Deepwater Horizon are the examples of the worst-case scenario of oil and gas industry. Despite of learning lessons from these accidents, they are not completely prevented. On offshore processing unit Separator 1 possess highest risk of explosion and fire than any other processing unit and required extra attention.
2. During the event of hydrocarbon fire time is extremely crucial to save lives and property damages. As the temperature increased more than 1000 °C less than 10 min within that human body can get third-degree burn at the temperature of 37 °C or when exposed to thermal radiation of 1000 (kW/m<sup>2</sup>)<sup>4/3</sup>s. Similarly, 100% fatality observed if body received pressure more than 20 psi. Improved analysis of risk assessment, proper planning, and structure protection hindrance such as blast/fire wall can prevent lives and structural damages, and delay heat radiation/pressure to spread out to other units.
3. The individual experimental study cannot represent the behaviour of the entire offshore platform during fire and explosion. Therefore, it is essential to observe behaviour through simulation and validate results from which experimental study on full-scale frame.

## References

1. A. Rajendram, F. Khan, and V. Garaniya, "Modelling of Fire Risks in an Offshore Facility," *Fire Safety Journal*, vol. 71, pp. 79–85, 2015.
2. C. H. Vervalin, "Fire Protection Manual for Hydrocarbon Processing Plants," 1985.
3. A. T. Paterson, *Offshore fire safety*: Pennwell Corp, 1993.
4. J. K. Paik and A. K. Thayamballi, *Ship-Shaped Offshore Installations: Design, Building, and Operation*: Cambridge University Press, 2007.
5. D. Lord, A. Luketa, C. Wocken, S. Schlasner, T. Aulich, R. Allen, *et al.*, "Literature Survey of Crude Oil Properties Relevant to Handling and Fire Safety in Transport," Sandia National Laboratories (SNL-NM), Albuquerque, NM (United States) 2015.
6. M. Imran, M. S. Liew, and M. S. Nasif, "Experimental Studies on Fire for Offshore Structures and its Limitation: A Review," *Chemical Engineering Transactions*, vol. 45, pp. 1951–1956, 2015.
7. N. Khakzad, F. Khan, and P. Amyotte, "Safety analysis in process facilities: Comparison of fault tree and Bayesian network approaches," *Reliability Engineering & System Safety*, vol. 96, pp. 925–932, 2011.
8. F. I. Khan and S. Abbasi, "Major Accidents in Process Industries and an Analysis of Causes and Consequences," *Journal of Loss Prevention in the process Industries*, vol. 12, pp. 361–378, 1999.
9. OGP's, "OGP Risk Assessment Data Directory," International Association of Oil & Gas Producers, England 2010.
10. T. Haidar. (2015, The 10 Biggest Oil Spills In World History - 3 Deepwater Horizon Oil Spill. Available: <http://www.oilandgasiq.com/integrity-hse-maintenance/articles/the-10-biggest-oil-spills-in-world-history-part-8/>.

11. M. Dadashzadeh, F. Khan, K. Hawboldt, and P. Amyotte, "An integrated approach for fire and explosion consequence modelling," *Fire Safety Journal*, vol. 61, pp. 324–337, 2013.
12. M. Dadashzadeh, R. Abbassi, F. Khan, and K. Hawboldt, "Explosion Modeling and Analysis of BP Deepwater Horizon Accident," *Safety science*, vol. 57, pp. 150–160, 2013.
13. A. Brandsæter, "Risk Assessment in the Offshore Industry," *Safety Science*, vol. 40, pp. 231–269, 2002.
14. F. I. Khan, R. Sadiq, and T. Husain, "Risk-Based Process Safety Assessment and Control Measures Design for Offshore Process Facilities," *Journal of hazardous materials*, vol. 94, pp. 1–36, 2002.
15. C. Jerzy and J. K. Paik, "Paradigm Change in Safety Design Against Hydrocarbon Explosions and Fires," in *FABIG Newsletter, SCI, Issue 60*, ed, 2012, pp. 30–38.
16. Y. Pan and L. A. Louca, "Experimental and numerical studies on the response of stiffened plates subjected to gas explosions," *Journal of Constructional Steel Research*, vol. 52, pp. 171–193, 11// 1999.
17. J. Paik, J. Czujko, J. H. Kim, Sung In Park, MD Shafiqul Islam, and D. H. Lee, "A New Procedure for the Nonlinear Structural Response Analysis of Offshore Installations in Fires," *Transactions SNAME*, vol. Vol. 121, 2013, 2013.
18. REUTERS, "Accident Aboard Pemex Jack-Up Kills Two, Injures 10" in *Maritime News Today*, ed, 2015.
19. Reuters, "Fire Out at Pemex Processing Platform," in *gCaptain*, ed, 2015.
20. J. Vinnem, R. Bye, B. Gran, T. Kongsvik, O. Nyheim, E. Okstad, *et al.*, "Risk Modelling of Maintenance Work on Major Process Equipment on Offshore Petroleum Installations," *Journal of Loss Prevention in the Process Industries*, vol. 25, pp. 274–292, 2012.
21. M. E. Paté-Cornell, "Learning from the Piper Alpha Accident: A Postmortem Analysis of Technical and Organizational Factors," *Risk Analysis*, vol. 13, pp. 215–232, 1993.
22. D. Drysdale and R. Sylvester-Evans, "The Explosion and Fire on the Piper Alpha Platform, 6 July 1988. A Case Study," *Philosophical Transactions Mathematical Physical and Engineering Sciences*, vol. 356, pp. 2929–2951, 1998.
23. P. Hart. (2010, 14/February). *Montara Oil Spill: "A Failure of Sensible Oilfield Practice"*. Available: <http://www.theoil Drum.com/node/7193>.
24. J. Paik and J. Czujko, "Explosion and Fire Engineering of FPSOs (EFEP JIP): Definition of Design Fire Loads," *FABIG Newsletter*, pp. 15–28, 2011.
25. J. K. Paik and J. Czujko, "Assessment of Hydrocarbon Explosion and Fire Risks in Offshore Installations: Recent Advances and Future Trends," *The IES Journal Part A: Civil & Structural Engineering*, vol. 4, pp. 167–179, 2011.
26. Y. Jin and B. S. Jang, "Study on the Probabilistic Scenario Based Fire Risk Analysis of FPSO Topside Module," in *ASME 2014 33rd International Conference on Ocean, Offshore and Arctic Engineering*, 2014, pp. V04BT02A007-V04BT02A007.
27. Promat. (2014, 05–03–15). *Fire Curves*. Available: <http://www.promat-tunnel.com/en/advices/fire-protection/fire%20curves>.
28. C. International. PFP Systems [Online]. Available: <http://www.pfpsystems.com/assets/Uploads/HydrocarbonBook1.pdf>.
29. W. Yu, J. Zhao, H. Luo, J. Shi, and D. Zhang, "Experimental Study on Mechanical Behavior of an Impacted Steel Tubular T-joint in Fire," *Journal of Constructional Steel Research*, vol. 67, pp. 1376–1385, 2011.
30. M. Jin, J. Zhao, M. Liu, and J. Chang, "Parametric Analysis of Mechanical Behavior of Steel Planar Tubular Truss under Fire," *Journal of Constructional Steel Research*, vol. 67, pp. 75–83, 2011.
31. R. K. Zipf and K. Cashdollar, "Effects of blast pressure on structures and the human body," *National Institute for Occupational Safety and Health (NIOSH)*, 2006.
32. API, "API RP2A-WSD: Recommended Practice for Planning, Designing and Constructing Fixed Offshore Platforms–Working Stress Design," in *Twenty*, ed, 2000.

# Developing Optimum Production Strategy of Kailashtilla Gas Field and Economic Analysis

H. Mahmud, M.M. Huque and P.C. Mandal

**Abstract** This study focuses on the utilization of integrated production optimization of Kailashtilla Gas Field (KGF), Bangladesh. KGF has a current production rate of 60 MMscfd gas with three producing wells. According to a previous study in 2009 by RPS Energy, gas initially in place of this field was 3.54 Tcf. However, only 640 Bcf gas has been produced over the last 30-year period from 1983 to 2014. Only 39.39% recovery is achievable using the present field production strategy over next 25 years. The ultimate goal of this study is to discover an optimum field development strategy to increase the production from KGF. The proposed augmentation program is based on recovery factor, plateau, and economic outcome. The tasks have been divided into well modeling, reservoir modeling, and surface facility modeling. Finally, some cases studies and economic analysis have been done including net present value and benefit–cost ratio. This study involves reservoir, wells, and surface facilities in an integrated model to investigate different field development strategies. Effect of changing production systems such as upgrading separator, changing tubing size, lowering separator pressure, and adding new well in the system have been studied. This study estimates total reserve of this field as 3.013 Tcf by material balance method from three sand layers: Upper Gas Sand (UGS), Middle Gas Sand (MGS), and Lower Gas Sand (LGS). Comparative analysis of the various prediction cases with economic analysis suggests three optimum field development strategies for next 25 years as follows: (a) drilling one

---

H. Mahmud (✉)

Petroleum and Mineral Resources Engineering Department, Bangladesh University of Engineering and Technology, Dhaka 1000, Bangladesh  
e-mail: hmplus02@gmail.com

M.M. Huque

Process Engineering (Oil and Gas Program), Memorial University of Newfoundland, St. John's, NL A1C 5S7, Canada

P.C. Mandal

Chemical Engineering Department, Universiti Teknologi PETRONAS, 32610 Bandar Seri Iskandar, Perak, Malaysia

new well in UGS and one in MGS with 180 MMscfd plateau; (b) drilling two new wells in UGS with 180 MMscfd plateau; and (c) changing the tubing size of existing two wells with 120 MMscfd plateau. Current study yields a maximum recovery of 63.02% from UGS, 80.03% from MGS, and 79.0% from LGS by implementing the recommended development strategies.

**Keywords** Gas reservoir • Production optimization • Water drive • Economic analysis • Field development

## 1 Introduction

Natural gas plays a major role in the energy matrix of Bangladesh as it accounts for about 70% of the total commercial primary energy of the country. Currently, the country produces around 2600 MMscfd gas from 20 gas fields but it suffers from 500 MMscfd shortages [1]. As there is no recent discovery, several augmentation programs are required to boost up the gas production from existing gas field to meet this demand.

Kailashtilla Gas Field is one of the largest reserves in Bangladesh. It was first recognized in 1960 by shell. The reserves are primarily contained within three distinct horizons: UGS, MGS, and LGS. A total number of six wells have been drilled in this field since 1961 from which KTL-2, KTL-3, and KTL-6 are currently in production. In 2009, RPS Energy estimated GIIP of UGS, MGS, and LGS to be 1.79, 0.72, and 1.10 Tcf, respectively [2]. The cumulative gas and condensate production from this field are 640 Bcf and 4.04 MMstb, respectively [3]. Currently the field produces 60 MMscfd of gas and 500 bbl condensate per day. Summary of current producing wells is shown in Table 1.

This study focused on integrated production modeling of the reservoir, wells, and surface facilities to ensure optimum production by using the commercial simulator. This study covers material balance for updating GIIP and estimating reservoir drive mechanism, production optimization of the wells as well as the whole field, future performance prediction, and economic analysis to find out optimum development plan.

**Table 1** Summary of current producing wells [3]

Wells	Sand	Gas rate (MMscfd)	FWHP (psig)	WGR (bbl/MMscf)	CGR (bbl/MMscf)
KTL-2	UGS	19.32	2240	0.19	8.21
KTL-3	UGS	16.10	2530	0.20	8.21
KTL-6	UGS	23.80	2510	0.15	8.21

## 2 Methodology

### 2.1 Model Preparation

Model preparation consists of well modeling, reservoir modeling, and integrated production modeling of reservoir, wells, and surface facilities. In well modeling, IPR and VLPs were generated for measuring the optimum flow of each well. Reservoir model was prepared by history matching using material balance technique. The prepared wells and reservoir models were incorporated with surface facilities in an integrated model for forecasting reservoir performances under several preset conditions.

### 2.2 Well Modeling

In well modeling, black oil method was used for PVT analysis. Inflow performance relationship (IPR) curve for each well had been generated using the production test data. There are several multiphase correlations available for well modeling such as Duns Ros Original, Hagedorn and Brown, Beggs and Brill, Gray, and Petroleum Expert [4]. The multiphase flow correlations were compared against the field well test measurement. It was compared for both pressure and gas rate. Once the best correlation was found, the vertical lift performance (VLP) curve had been created using the best-matched tubing correlation. The summary of the well model is shown in Table 2. A very good match of measured data and calculated data gives a high level of confidence on well model [5].

### 2.3 Reservoir Modeling

Reservoir modeling includes history matching and simulation using material balance technique. In this work, history matching and simulation of the three main

**Table 2** VLP/IPR matched data and well test data of KTL-2, KTL-3, and KTL-6

Wells	Parameters	Measured	Calculated	% difference
KTL-2	Gas rate (MMscfd)	18.800	19.067	1.42
	BHP(psig)	3435.6	3439.0	0.10
KTL-3	Gas rate	14.240	14.222	0.13
	BHP	3132.82	3132.63	0.01
KTL-6	Gas rate	15.86	16.334	2.99
	BHP	3184	3192.38	0.26



sand layers of Kailashtilla namely UGS, MGS, and LGS had been performed separately. For an example, model preparation for UGS has been discussed. At first, the basic fluid data was matched with the laboratory measured PVT data [6]. Production history of UGS is shown in Fig. 1. Corey functions were used to determine relative permeability parameters as these were not determined during core analysis [7]. From the early history of the field, the sand was assumed as depletion drive.

In history matching, reservoir drive mechanism can be recognized from Cole plot response [8]. For depletion drive reservoir, ideal response of Cole plot is a horizontal line. For Kailashtilla UGS, Cole plot as in Fig. 2 clearly indicates a deviation from flat line that is found normally when an external energy support is available.

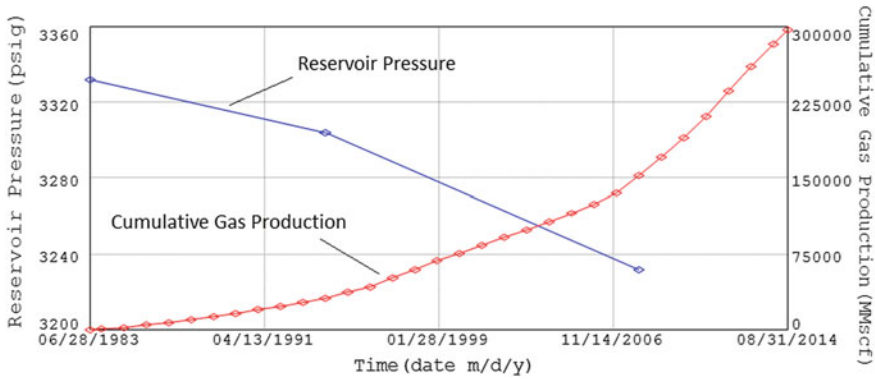


Fig. 1 Production history of UGS

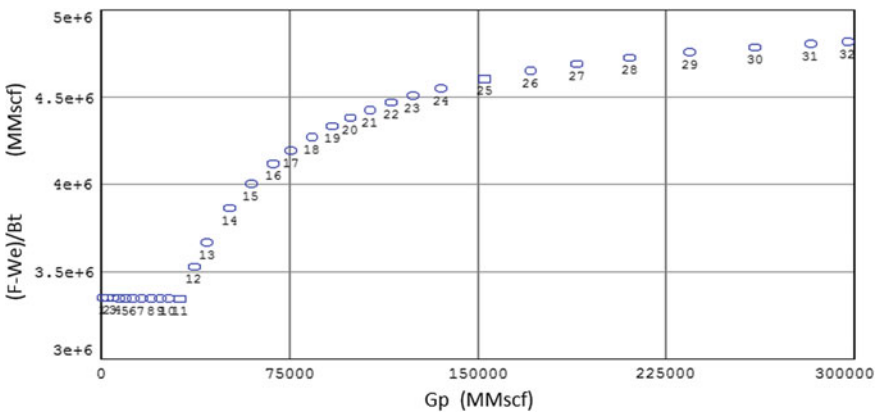


Fig. 2 Cole plot without aquifer support for UGS

Therefore, the model was reconstructed with an aquifer. The most common Van Everdingen–Hurst’s model was incorporated in this study [9]. Then, Cole plot response as in Fig. 3 was nearly straight line and represents that this sand is aquifer driven.

An iterative nonlinear regression had been performed to find the best mathematical fit by analytical method. GIIP previously calculated from Cole plot was matched with the model by analytical plot as shown in Fig. 4. For Kailashstilla UGS, GIIP was found to be 2.18 Tcf.

A simulation was run for comparing the production history and checking the validity of the model. Comparison of the history with simulated reservoir pressure reflects a very good matching that is shown in Fig. 5.

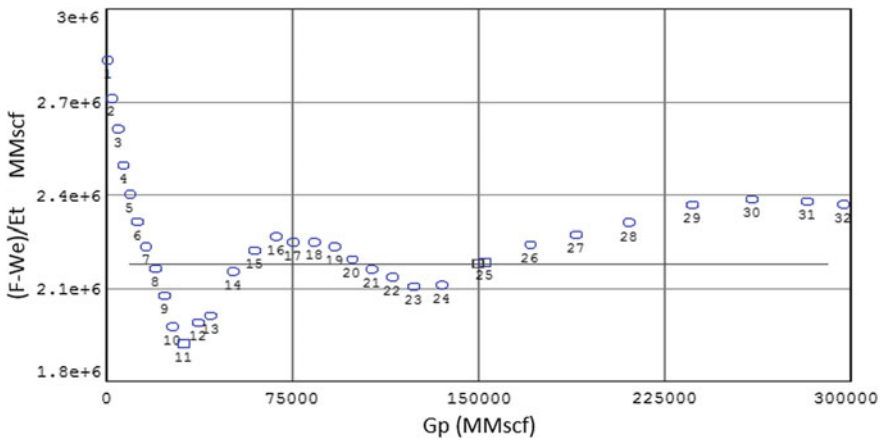


Fig. 3 Cole plot with aquifer support for UGS

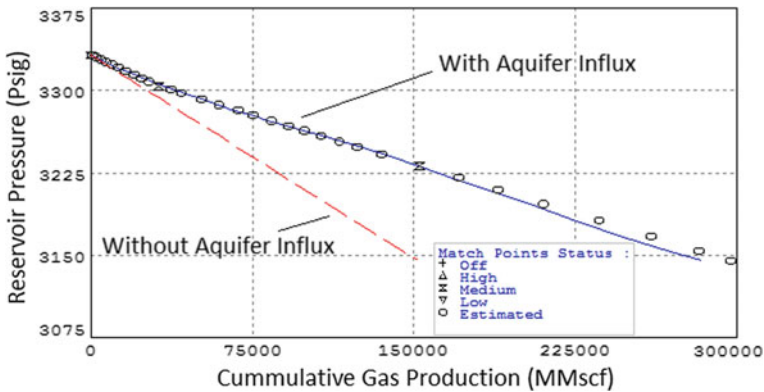


Fig. 4 Analytical plot for UGS

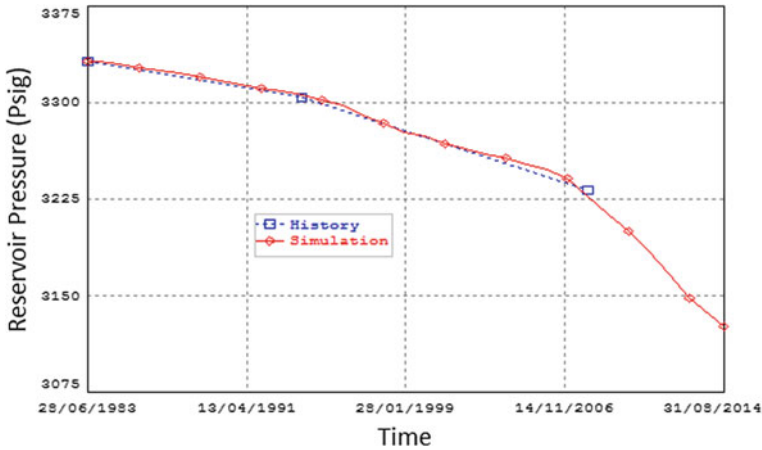


Fig. 5 History and simulated reservoir pressure

### 2.4 Network Modeling

In network modeling, reservoir, wells, and surface facilities were integrated in a single model using the previously generated well and reservoir models. Test data for surface pipeline performances is not available. Thus, for industry standard pipeline correlation, Mukherjee-Brill had been chosen for all pipelines section. Separator capacities and pipeline geometries were also included in the model. The model was validated with the current production data. The field model validation is shown in Table 3 and reflects that KTL-2 matched very well where other 2 wells matched within 4.5% of the field case [7].

### 2.5 Case Studies

Several cases with predetermined constraints had been studied for determining the prospective cases in terms of gas recovery and plateau duration. The studied cases are shown in Table 4.

Table 3 Network model validation

Wells	Measured gas rate (MMscfd)	Calculated gas rate (MMscfd)	% difference
KTL-2	19.630	19.728	+0.50
KTL-3	16.100	15.381	+4.47
KTL-6	24.009	24.999	-4.12

**Table 4** List of predictive cases

Case	Plateau rate	WHC	Proposed modification
1	60	900	Existing condition
2(a)	120	1200	Change tubing size
2(b)		2400	Change tubing size
2(c)			Lowering separator pressure to 400 psig
3(a)	150	3000	Drill 1 new well in UGS
3(b)			Drill 2 new wells(1 in UGS, 1 in MGS)
4(a)	180	3600	Drill 2 new wells in UGS
4(b)			Drill 3 new wells(1 in UGS, 1 in MGS, and 1 in LGS)
4(c)			Drill 2 new wells(1 in UGS, 1 in MGS)

Note Water handling capacity (WHC) is in bbl and plateau rate is in MMscfd

### 2.6 Economic Analysis

Network model provides future performance of the studied cases in terms of plateau duration, recovery factor, and cumulative production. Economic analysis offers this performance as net present value (NPV) and benefit–cost ratio (BCR) to determine the optimum development plan. The cost for drilling new well, installing and upgrading separator, changing tubing size, and installing compressor in case of lowering separator pressure and the benefit of additional gas and condensate production were considered during economic analysis [10].

## 3 Results and Discussion

Gas reserve and drive mechanisms obtained from reservoir modeling are shown in Table 5. Again, production forecasting and economic analysis results are shown in Table 6.

Table 6 shows that case 2(b), 4(a), and 4(c) are promising for field augmentation program in terms of net present value as well as benefit–cost ratio.

**Table 5** Gas reserves and drive mechanism

Parameter	Sands	Results	
		RPS study [1]	This study
GIIP, Tcf	UGS	1.89	2.17
	MGS	0.66	0.647
	LGS	0.99	0.196
Reservoir drive mechanism	UGS	Combination of depletion and water drive	
	MGS		
	LGS		

**Table 6** Results from production forecasting and economic analysis

Case	Production prediction		Economic analysis	
	Plateau period	Overall recovery %	NPV, Million \$	BCR
1	25	39.96	–	–
2(a)	13	51.22	87.35	3.06
2(b)	16	55.77	92.96	7.83
2(c)	16	55.77	84.22	4.77
3(a)	13	59.96	114.87	3.88
3(b)	16	61.37	123.83	3.70
4(a)	12	63.02	147.21	4.11
4(b)	15	65.18	159.45	3.30
4(c)	14	64.71	168.38	4.53

Note Plateau period is in years. Prediction period is 25 years

## 4 Conclusion

The GIIP was estimated as 3.013 Tcf by material balance method, which is about 0.327 Tcf lower than the previous RPS Energy's estimation in 2009. Based on the existing condition, a recovery of only 39.39% and full life plateau are achievable using the existing wells over a 25-year prediction period.

Comparative analysis of the various predictive cases with economic analysis suggests the three optimum production strategies:

- (a) Drilling two additional wells (one in MGS and one in UGS) and upgrading the separator capacity to 180 MMscfd gas and 3600 bbld water. This can produce 180 MMscfd plateau for 14 years with 64.71% recoveries. Economic analysis shows NPV 168.38 Million USD and BCR 4.53.
- (b) Drilling two additional wells in UGS and upgrading the separator capacity to 180 MMscfd gas and 3600 bbld water. This can produce 180 MMscfd plateau for 12 years and 63.02% recovery with 147.21 Million USD NPV and 4.11 BCR.
- (c) Changing the tubing size of KTL-2 and 3 wells from 3-1/2 in. to 4-1/2 in. and upgrading the separators capacity to 120 MMscfd gas and 2400 bbld water. This can produce 120 MMscfd plateau for 16 years and 55.77% recovery with a net present value of 92.96 Million USD and BCR of 7.83.

## References

1. Petrobangla, MIS reports of 2015 (2015). Retrieved from [www.petrobangla.org.bd](http://www.petrobangla.org.bd).
2. RPS Energy, Kailashtilla Petroleum Engineering Report. Prepared for Petrobangla (2009).
3. Sylhet Gas Field Limited (2015). Retrieved from [www.sgfl.org.bd](http://www.sgfl.org.bd).
4. B. H. Dale, Gas Production Operation. OGCI Publications, Tulsa (1985).

5. M. M. Huque, M. Rahman, Model Development and Performance Analysis of Gas Well. Proceedings of 3rd International Conference of Chemical Engineering, Bangladesh.2011. pp 263–267.
6. Shoaib Memon, Asif Zameer, To Develop the Optimum Field Development Plan for Condensate Well Using Integrated Production Modeling(IPM). Presented at SPE Saudi Arabia Young Professional Technical Symposium, Dhahran, Saudi Arabia. 19–21 March 2012. SPE 160924.
7. A. Mantopoulos, D. A. Marques, S. P Hunt, S. Ng, M. Haghighi, Best Practice and Lessons Learned for The Development and Calibration of Integrated Production Models for The Cooper Basin, Australia. Presented at SPE/IATMI Asia Pacific Oil and Gas Conference and Exhibition, Nisa Dua, Bali, Indonesia. 20–22 October 2015. SPE-176131-MS.
8. T. Ahmed, P. D. McKinney, Advanced Reservoir Engineering. ELSEVIER. (2005).
9. B.C. Craft, M. Hawkins, Applied Petroleum Reservoir Engineering. Prentice-Hall, Inc, USA (1990).
10. L. Saputelli, G. Mijara, J. A. Rodriguez, D. Deaton, S. Sankaran, Integrating Production Optimization and Economics Under Certain Conditions. Presented at SPE digital Energy Conference and Exhibition held in Huston, Texas, U. S. A., 11–12 April 2007. SPE 107482.

# Erratum to: Pressure-Transient Behavior of Injection/Falloff Tests

A.D. Habte, M. Onur, I.B.M. Saaid and T.N. Ofei

**Erratum to:**  
**Chapter “Pressure-Transient Behavior of Injection/Falloff Tests” in: M. Awang et al. (eds.), *ICIPEG 2016*, DOI [10.1007/978-981-10-3650-7\\_7](https://doi.org/10.1007/978-981-10-3650-7_7)**

The original version of the book was inadvertently published without the following corrections:

- The interchanged affiliations of co-authors, Prof. M. Onur and I.B.M. Saaid, have to be corrected.
- The reference citations [9, 10], which were removed earlier, have to be retained in Sect. 3.1.
- The references of [9, 10] have to be included in the reference list.

The erratum chapter and the book have been updated with the changes.

---

The updated online version for this chapter can be found at [http://dx.doi.org/10.1007/978-981-10-3650-7\\_7](http://dx.doi.org/10.1007/978-981-10-3650-7_7)